

From fundamental design to applications of supramolecular polymer bottlebrushes

Dissertation
(kumulativ)

zur Erlangung des akademischen Grades doctor rerum naturalium
(Dr. rer. nat.)

vorgelegt dem Rat der Chemisch-Geowissenschaftlichen Fakultät der
Friedrich-Schiller-Universität Jena
von M.Sc. Franka Viola Gruschwitz
geboren am 20.08.1993 in Kronach

Gutachter:

1. Dr. Johannes C. Brendel, Friedrich-Schiller-Universität Jena
2. Prof. Dr. Ulrich S. Schubert, Friedrich-Schiller-Universität Jena

Tag der öffentlichen Verteidigung: 15.11.2021

Table of contents

Documentation of authorship	4
1. One-dimensional (1D) nanostructures by self-assembly	9
1.1. SPBs resulting from π - π interactions of aromatic systems	11
1.2. Structure formation by hydrogen-bonds	12
1.3. Applications of SPBs	16
1.4. Motivation.....	17
2. Prerequisites for 1D supramolecular self-assembly of SPBs in water	20
2.1. The influence of the packing parameter on the self-assembly.....	20
2.2. Overcoming the packing parameter - Influence of the interaction strength on 1D aggregation	25
2.3. Limiting factors for the 1D supramolecular self-assembly	31
3. Kinetics of the self-assembly - on the way to size adjustment	37
4. Formation of dynamic hydrogels by crosslinking of SPBs.....	48
5. Summary	57
6. Zusammenfassung.....	60
7. References	64
List of abbreviations	73
Curriculum vitae	75
Publication list	76
Acknowledgement	78
Declaration of authorship	79
Appendix	80

Documentation of authorship

This election contains a list of the individual author's contributions to the publications reprinted in this thesis.

<i>Supramolecular polymer bottlebrushes</i>				
P1	F. V. Gruschwitz, ^{1,‡} T. Klein, ^{2,‡} S. Catrouillet, ³ J. C. Brendel, ⁴ <i>Chem. Commun.</i> 2020 , 56, 5079-5110.			
Author	1	2	3	4
Conceptual contribution	×	×		×
Preparation of the manuscript	×	×		
Correction of the manuscript	×	×	×	×
Supervision of F. V. Gruschwitz				×
Proposed publication equivalent	0.5			

[‡] These authors contributed equally to this work.

<i>The influence of directed hydrogen bonds on the self-assembly of amphiphilic polymers in water</i>						
P2	T. Klein, ^{1,‡} F. V. Gruschwitz, ^{2,‡} S. Rogers, ³ S. Hoepfner, ⁴ I. Nischang, ⁵ J. C. Brendel, ⁶ <i>J. Colloid Interface Sci.</i> 2019 , 557, 488-497.					
Author	1	2	3	4	5	6
Conceptual contribution	×	×				×
Synthesis	×	×				
Polymer characterization	×	×				
Aggregate characterization	×	×	×	×	×	
Preparation of the manuscript	×	×				
Correction of the manuscript	×	×		×	×	×
Supervision of F. V. Gruschwitz						×
Proposed publication equivalent		0.75				

[‡] These authors contributed equally to this work.

Documentation of authorship

Unraveling Decisive Structural Parameters for the Self-Assembly of Supramolecular Polymer Bottlebrushes Based on Benzene Trisureas

P3 F. V. Gruschwitz,¹ M.-C. Fu,² T. Klein,³ R. Takahashi,⁴ T. Higashihara,⁵ S. Hoepfener,⁶ I. Nischang,⁷ K. Sakurai,⁸ J. C. Brendel,⁹ *Macromolecules* **2020**, *53*, 7552-7560.

Author	1	2	3	4	5	6	7	8	9
Conceptual contribution	×								×
Synthesis	×	×							
Polymer characterization	×	×							
Aggregate characterization	×	×		×	×	×	×		
Preparation of the manuscript	×								
Correction of the manuscript	×	×	×	×	×	×	×	×	×
Supervision of F. V. Gruschwitz									×
Proposed publication equivalent	1								

Impact of amino acids on the aqueous self-assembly of benzenetrispeptides into supramolecular polymer bottlebrushes

P4 T. Klein,¹ H. F. Ulrich,² F. V. Gruschwitz,³ M. T. Kuchenbrod,⁴ R. Takahashi,⁵ S. Fujii,⁶ S. Hoepfener,⁷ I. Nischang,⁸ K. Sakurai,⁹ J. C. Brendel,¹⁰ *Polym. Chem.* **2020**, *11*, 6763-6771.

Author	1	2	3	4	5	6	7	8	9	10
Conceptual contribution	×									×
Synthesis	×	×								
Polymer characterization	×	×								
Aggregate characterization	×	×	×	×	×	×	×	×		
Preparation of the manuscript	×									
Correction of the manuscript	×	×	×	×	×	×	×	×	×	×
Supervision of F. V. Gruschwitz										×
Proposed publication equivalent			0.25							

Documentation of authorship

Overcoming the Necessity of a Lateral Aggregation in the Formation of Supramolecular Polymer Bottlebrushes in Water

P5 T. Klein,¹ H. F. Ulrich,² F. V. Gruschwitz,³ M. T. Kuchenbrod,⁴ R. Takahashi,⁵ S. Hoepfener,⁶ I. Nischang,⁷ K. Sakurai,⁸ J. C. Brendel,⁹ *Macromol. Rapid Commun.* **2020**, 2000585.

Author	1	2	3	4	5	6	7	8	9
Conceptual contribution	×								×
Synthesis	×	×							
Polymer characterization	×	×							
Aggregate characterization	×	×	×	×	×	×	×		
Preparation of the manuscript	×								
Correction of the manuscript	×	×	×	×	×	×	×	×	×
Supervision of F. V. Gruschwitz									×
Proposed publication equivalent			0.1						

Kinetically controlling the length of self-assembled polymer nanofibers formed by intermolecular hydrogen bonds

P6 F. V. Gruschwitz,^{1,‡} T. Klein,^{2,‡} M. T. Kuchenbrod,³ N. Moriyama,⁴ S. Fujii,⁵ I. Nischang,⁶ S. Hoepfener,⁷ K. Sakurai,⁸ U. S. Schubert,⁹ J. C. Brendel,¹⁰ *ACS Macro Lett.* **2021**, 837-843.

Author	1	2	3	4	5	6	7	8	9	10
Conceptual contribution	×	×								×
Synthesis	×	×								
Polymer characterization	×	×								
Aggregate characterization	×	×	×	×	×					
Preparation of the manuscript	×	×								
Correction of the manuscript	×	×				×	×	×	×	×
Supervision of F. V. Gruschwitz										×
Proposed publication equivalent	1									

[‡] These authors contributed equally to this work.

Documentation of authorship

<i>Adjusting the length of supramolecular polymer bottlebrushes by top-down approaches</i>					
P7 T. Klein, ^{1,‡} <u>F. V. Gruschwitz</u> , ^{2,‡} M. T. Kuchenbrod, ³ S. Hoepfener, ⁴ J. C. Brendel, ⁵ <i>submitted</i> .					
Author	1	2	3	4	5
Conceptual contribution	×	×			×
Aggregate characterization	×	×	×	×	
Preparation of the manuscript	×	×			
Correction of the manuscript	×	×	×	×	×
Supervision of F. V. Gruschwitz					×
Proposed publication equivalent		0.75			

[‡] These authors contributed equally to this work.

<i>Dynamic hydrogels from crosslinked supramolecular polymeric nanofibers</i>								
P8 <u>F. V. Gruschwitz</u> , ¹ F. Hausig, ² P. Schüler, ³ J. Kimmig, ⁴ D. Pretzel, ⁵ U.S. Schubert, ⁶ S. Catrouillet, ⁷ J. C. Brendel, ⁸ <i>submitted</i>								
Author	1	2	3	4	5	6	7	8
Conceptual contribution	×						×	×
Synthesis	×							
Polymer characterization	×							
Gel characterization	×	×	×	×	×		×	
Preparation of the manuscript	×						×	
Correction of the manuscript	×	×	×	×	×	×	×	×
Supervision of F. V. Gruschwitz								×
Proposed publication equivalent	1							

Erklärung zu den Eigenanteilen des Promovenden sowie der weiteren Doktoranden/Doktorandinnen als Koautoren an Publikationen und Zweitpublikationsrechten bei einer kumulativen Dissertation

Für alle in dieser kumulativen Dissertation verwendeten Manuskripte liegen die notwendigen Genehmigungen der Verlage („Reprint permissions“) für die Zweitpublikation vor.

Die Co-Autoren der in dieser kumulativen Dissertation verwendeten Manuskripte sind sowohl über die Nutzung als auch über die oben angegebenen Eigenanteile informiert und stimmen dem zu.

Die Anteile der Co-Autoren an den Publikationen sind in den vorausgehenden Tabellen aufgeführt.

Ich bin mit der Abfassung der Dissertation als publikationsbasiert, d.h. kumulativ, einverstanden und bestätige die vorstehenden Angaben. Eine entsprechend begründete Befürwortung mit Angabe des wissenschaftlichen Anteils des Doktoranden an den verwendeten Publikationen werde ich parallel an den Rat der Fakultät der Chemisch-Geowissenschaftlichen Fakultät richten.

Dr. Johannes C. Brendel

Jena, den

Franka V. Gruschwitz

Jena, den

1. One-dimensional (1D) nanostructures by self-assembly

Parts of this chapter have been published in P1) F. V. Gruschwitz, T. Klein, S. Catrouillet, J. C. Brendel, *Chem. Comm.* **2020**, *56*, 5079-5110.

In natural systems such as proteins or membranes, hierarchical structuring is a key factor for functional structures. Inspired by the elongated shape of actin filaments or microtubules of the cytoskeleton,^[1-3] chemists try to transfer these concepts to synthetic materials.^[4] Utilizing supramolecular chemistry,^[5] the design of molecules featuring intrinsic self-assembly properties into 1D aggregates, resembling the cylindrical structures from nature, is feasible.^[6-7] The synthesis of cylindrical aggregates from low molar mass compounds employing hydrogen bonds^[8] or π -interactions^[9] has already been widely investigated (Figure 1 right).^[10] By controlled polymerization methods, anisotropic structures with narrow size distributions are accessible.^[11] In contrast to covalently linked materials,^[12-14] here, dynamic processes are facilitated^[10, 15-18] which renders these anisotropic particles suitable for a range of applications, for instance in rheology,^[19-22] organic electronics,^[23-25] and nanomedicine.^[26-27] The possible degradation due to supramolecular erosion and thus renal clearance, is beneficial to circumvent accumulation in the body. Furthermore, the high surface area of the cylindrical aggregate, combined with high modularity^[28] and functional variety, improves the uptake of the particle compared to spherical analogs.^[29-30]

However, matching the complexity found in natural assemblies remains a challenge considering nature's capability to organize large macromolecules and proteins into well-defined nanostructures. One way to take this structuring as a blueprint, chemists have come up with the concept of block copolymer self-assembly (Figure 1 left). Here large macromolecules consisting of incompatible blocks (e.g. a solvophobic and a solvophilic block) tend to assemble into different morphologies in solution. The solvophobic block minimizes its contact area with the surrounding solvent and forms the energetically favored morphology of spheres, cylinders, vesicles, or bilayers, depending on the volume fractions of the two blocks, the degree of polymerization, and the interaction parameter specifying the (in-)compatibility of all components (polymer blocks, solvents, and non-solvents) in the solution.^[31] At certain conditions e.g. a packing parameter p of $\frac{1}{3} < p < \frac{1}{2}$ cylindrical morphologies are favored. However, the prediction of the morphology is quite often very difficult since various other parameters (see above) can influence the structure formation and thus mixtures of different morphologies can be observed.^[32-36] Additionally, slow dynamics and the possibility of kinetical trapping complicate the prediction of the resulting morphologies.^[37] Nevertheless, the

One-dimensional (1D) nanostructures by self-assembly

self-assembly of polymers for instance into worm-like micelles results in interesting rheology and improved processability of the materials.^[38-39] This renders the resulting cylindrical polymer micelles additionally suitable for application in electronics or nanomedicine.^[40-43]

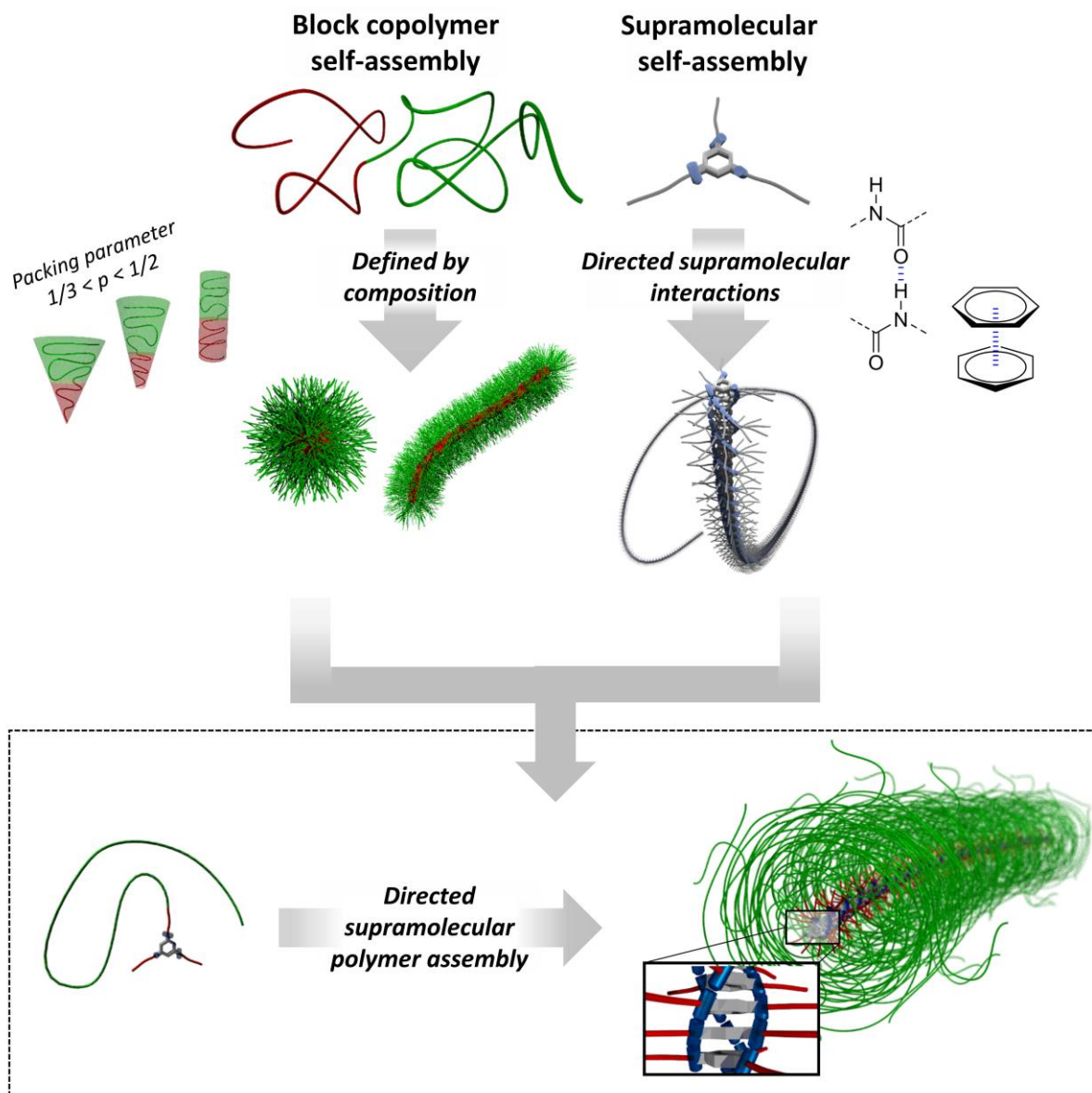


Figure 1 Schematic representation of different methods to form cylindrical (polymer) aggregates by self-assembly of block copolymers (left) or and supramolecular polymerization of low molar mass compounds (right). By the combination of supramolecular polymerization and polymeric self-assembly, a directed supramolecular polymer assembly into supramolecular polymer bottlebrushes is possible (bottom).

By combining the self-assembly of copolymers based on solvophobic effects and the supramolecular polymerization with its directed interactions, a versatile system is formed yielding cylindrical assemblies of macromolecular building blocks (Figure 1 bottom). The resulting columnar cylindrical aggregates with pendant polymer chains are termed supramolecular polymer brushes (SPBs) in correspondence to their covalent analogs. Here, in

contrast to crystallization driven self-assembly (CDSA) which relies on the epitaxial crystallization of one polymer block,^[44-45] directed non-covalent interactions such as hydrogen bonds or π -interactions of supramolecular building blocks, functionalized with polymer chains, add an additional driving force to generate anisotropic structures.^[8-10] The combination of these self-assembly motifs with polymer chains increases the dynamics and thus paves the way to a variety of responsive materials.^[46-47] Furthermore, by combination of supramolecular building blocks with polymers, modular systems with versatile functionalization are accessible.^[18] However, so far, only an exclusive selection of structural motifs capable to self-assemble, are reported to be suitable for the creation of supramolecular polymer bottlebrushes since it requires stronger forces to overcome the additional steric demands of the attached polymer chains. In chapters 1.1 and 1.2 a selection of these self-assembly motifs divided by the nature of their directing interactions and their application in SPBs is presented.

1.1. SPBs resulting from π - π interactions of aromatic systems

Among the first materials used for the formation of supramolecular polymer bottlebrushes in solution, planar unsaturated cyclophanes were of great interest due to their strong van der Waals and π - π interaction.^[48-50] Oligo ethylene glycol substituted cyclophanes form large columnar aggregates in solution due to the additional solvophobic effect.^[51] Supramolecular polymer bottlebrushes could be obtained by the attachment of polystyrene (PS) chains (degree of polymerization (DP) = 25) to a phenylene-ethynylene macrocycle, forming a block-like *coil-(rigid) ring-coil* polymer structure which resulted in the formation of hollow cylindrical structures in *cyclo*-hexane (Figure 2A).^[52-53] Apart from these structures, also aromatic rod-coil amphiphiles are capable of assembling into supramolecular fibers in solutions via π - π interaction.^[54-56] Supramolecular polymer bottlebrushes from oligo phenylene-vinylene blocks, for instance, could be synthesized in very dilute THF/water mixtures by combining them with longer polyethylene oxide (PEO) (DP = 45) or poly(propylene oxide) (PPO) chains (Figure 2C).^[57-58]

Another very prominent self-assembly motif of rigid aromatics relying on π - π stacking are rylene-type aromatic systems (Figure 2B). π - π interaction of the large aromatic systems, as in perylenes, favor the stacking of single molecules in either J- or H-type aggregates.^[59-60] Utilizing hydrophilic substituents, it is possible to render these very hydrophobic systems water-soluble.^[61-62] Hereby, PEO-functionalized supramolecular perylene bisimide brushes (PDIs) have shown pathway-dependent self-assembly. Direct dissolution in water favored slipped stacking of the aromatic cores (J-aggregation) in contrast to face-to-face stacking

One-dimensional (1D) nanostructures by self-assembly

(H-aggregation) when a gradual solvent-switch from THF to water was performed.^[63] This shows that the self-assembly can be strongly influenced by the solvent composition, temperature, and chain length of the polymer.^[64] Structural very similar naphthalene diimides are also able to form SPBs with lengths of ~ 300 nm when they are equipped with additional bisurea groups to compensate for the smaller aromatic system compared to PDIs.^[65]

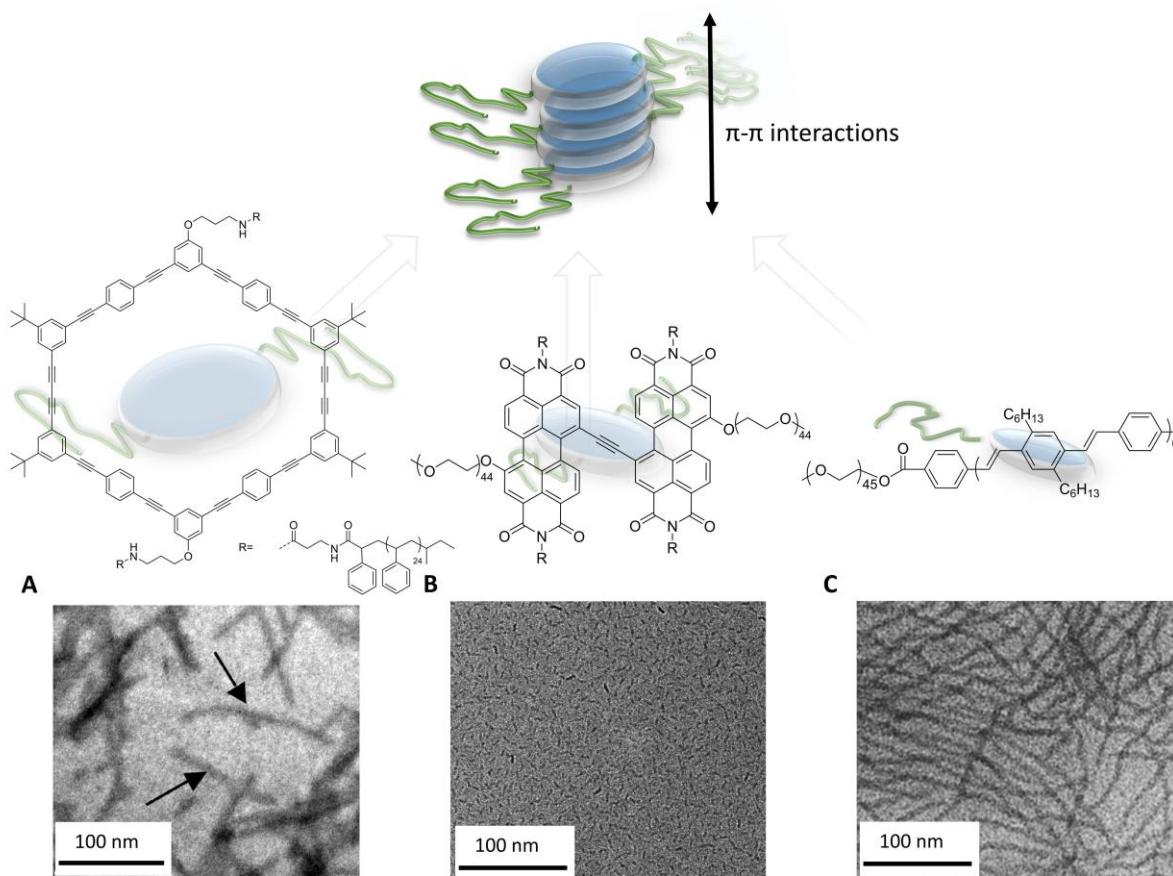


Figure 2 Self-assembly to supramolecular polymer bottlebrushes in water by π - π interactions of phenylenevinylene macrocycles (A) (adapted with permission from ref. ^[66] Copyright (2010) American Chemical Society), perylene dyes (B) (adapted with permission from ref. ^[63] Copyright (2014) John Wiley and Sons) and aromatic rod-coil amphiphiles (C) (adapted with permission from ref. ^[57] Copyright (2000) American Chemical Society)

1.2. Structure formation by hydrogen-bonds

Slightly stronger and more directional interactions compared to π - π interactions are hydrogen bonds.^[67] The most prominent example for these interactions which can also be found in nature are peptides.^[68] Their ability to form directional hydrogen bonds, e.g in β -sheet structures, makes them interesting candidates for the synthesis of polymeric supramolecular structures in solution.^[69-70] However, the self-assembly of small linear oligopeptides in solution to cylindrical structures mostly requires additional interactions such as aromatic moieties at the

N-terminus to induce 1D aggregation.^[69, 71-72] This restriction can be overcome by employing peptide amphiphiles.^[73] Due to additional aliphatic chains, the structures phase separate and thus initiate fiber formation. By combination of the peptide amphiphiles with hydrophilic macromolecules, the rather limited solubility of the aggregates, resulting from β -sheet structures, can be circumvented (Figure 3A).^[74-78] With the development of new strategies in solid-phase peptide synthesis^[79-80] a great variety of supramolecular polymer bottlebrush structures was obtained.^[81-88] Some could even show their potential in nanomedicine.^[81, 89] Further research on such systems revealed a very delicate interplay of the steric demand of the hydrophilic polymer chains and the composition of the peptide motif.^[86, 90] For instance, it could be shown that an increase in molar mass of the hydrophilic polymer resulted in a decreased fiber size due to increased steric hindrance.^[91]

Apart from linear peptides their cyclic analogues comprised of alternating D- and L- α -amino acids, possess the ability to self-assemble into hollow nanotubes.^[92-93] Adopting a flat-ring conformation where all amide groups are oriented perpendicular to the ring plane, the cyclic peptide ring can form strong intramolecular hydrogen bonds. The stacking of the cyclic peptides on top of each other results in the formation of poorly soluble cyclic peptide nanotubes (CPNT).^[94-95] Employing 4 to 12 amino acids, the tuning of the void volume inside the nanotubes is possible and further substitution of adjacent amino side chains allows for a great variety of functionalization possibilities without interfering with the stacking.^[96] This makes the CPNT applicable in fields of electronics,^[97-99] or nanomedicine, where they are used as membrane channels^[100-102] or antiviral agents.^[103] The limited solubility of CPNTs can be overcome with the linkage of a polymeric exterior to the cyclic peptide ring (Figure 3B).^[48, 104-107] The combination of cyclic octapeptides with polymer chains paved the way for additional functionalization and stimuli-responsiveness.^[108-113] Their possible applications range from drug delivery to their use as membrane channels.^[112-119] Since for an application in nanomedicine a profound knowledge and control over the size of the structures is necessary,^[29, 120] first studies to control the length of cyclic peptide polymer nanotubes (CPPNTs) by variation of the size of the polymer exterior were conducted.^[116, 121-122] It could be shown, that an increased number of polymer arms or bulkier polymers resulted in a reduction of the length, due to the higher steric demand of the polymer exterior. Apart from the possibility of functionalization due to the polymer chains, additionally, the CPPNTs exhibited increased dynamics that can even be tuned by incorporation of further hydrophobic segments, kinetically trapping the structures.^[123-124]

One-dimensional (1D) nanostructures by self-assembly

The rather complicated and demanding synthesis of cyclic peptides is still a challenge. In contrast to that, the straightforward synthesis and almost endless possibilities for functionalization render 1,3,5-substituted benzenes perfectly suitable for the design of supramolecular polymer brushes. By employing amide groups as hydrogen bonding units, and thus the formation of intramolecular threefold hydrogen bonds between the centrosymmetric molecules, helical structures can be synthesized.^[125-129] Their applications range from hydrogelators,^[20, 130] nucleation agents,^[131-134] filtration material^[135] to the cellular delivery of siRNA in nanomedicine.^[26-27, 136-137] Similar to the CPPNT a dynamic exchange of the building blocks from different fibers for this system could be proven.^[138-139] Nonetheless, supramolecular polymer bottlebrushes employing benzene trisamides (BTAs) are difficult to realize since the low number of possible hydrogen bonds of the amide groups does not account for the steric demand of a polymeric exterior and thus results in the formation of mostly spherical aggregates.^[140-141] Further work on the hurdles of anisotropic self-assembly, that have to be overcome to yield SPBs by using amides are introduced in chapter 2.

If benzene amides are modified with additional peptide groups, this results in increased interactions and thus the formation of stable supramolecular helical structures (Figure 3C).^[142-145] With the use of Coulomb interactions of charged amino acid sequences, pH-responsive structures could be obtained.^[146-147] Employing a nonaphenylalanin peptide at the 1,3,5-positions of a benzene molecule, the fiber formation could even tolerate the addition of dendritic oligo ethylene glycol side chains. Due to the size of the molecule, this can already be regarded as a type of SPBs. Another example for SBPs based on benzene trispeptides is the combination of this benzene trisnonaphenyl motif with polyglutamates. Nevertheless, to form SPBs high concentrations and the addition of salt is necessary.^[148-149] Further work on SPBs derived from 1,3,5-substituted benzenes employing peptide groups is introduced in chapter 2.

One-dimensional (1D) nanostructures by self-assembly

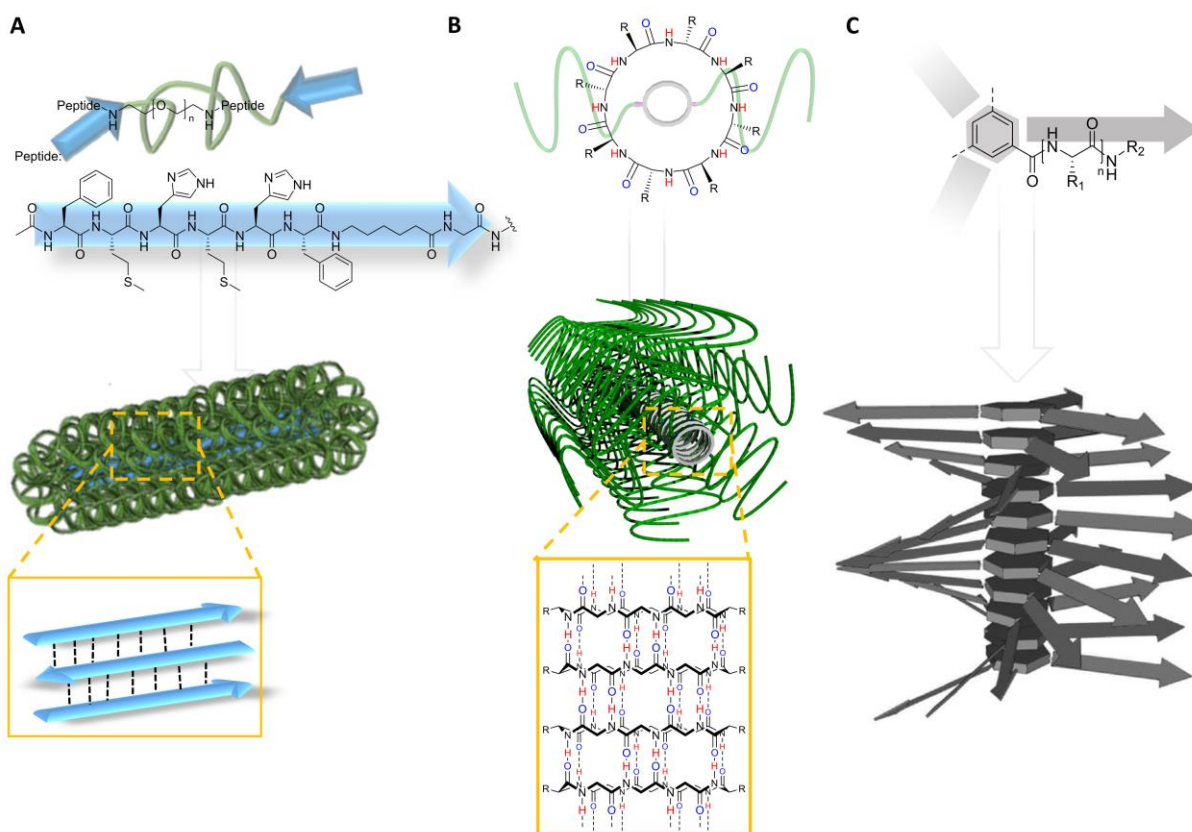


Figure 3 Self-assembly of linear peptides (A), cyclic peptides (B) and centrosymmetric benzene tricarboxamide peptides (C) to supramolecular polymer bottlebrushes. Adapted with permission of ref.^[150] Copyright (2018) Royal Society of Chemistry and ref.^[151] Copyright (2013) American Chemical Society.

Situated in between the interaction strength of amides and peptides, ureas have already been applied frequently in supramolecular chemistry.^[152-154] The strong hydrogen bonds, due to bidentate interactions of the two hydrogen donors (N-H-group) with their neighboring molecules, makes them interesting candidates, for instance, in the use as (organo)gelators (Figure 4A).^[128, 144, 154-157] Furthermore, an intriguingly straightforward synthesis by adding amines to isocyanates certainly paved the way for their frequent application in supramolecular chemistry. Since an increase in interaction strength simultaneously enhances cooperativity and promotes aggregation, it's been proven that bis- or trisureas promote the growth of larger structures. Therefore, often several connected urea groups are employed as a self-assembly motif to build up SPBs. By combination of aliphatic^[158-160] or aromatic bisureas with macromolecules, the directional interactions of the urea groups are already strong enough to overcome the entropic penalty of the macromolecule and thus yield SPBs (Figure 4A).^[161-164] Increasing the number of urea groups by utilizing trisureas, even longer SPBs could be obtained, using the same size of polymer exterior.^[163]

One-dimensional (1D) nanostructures by self-assembly

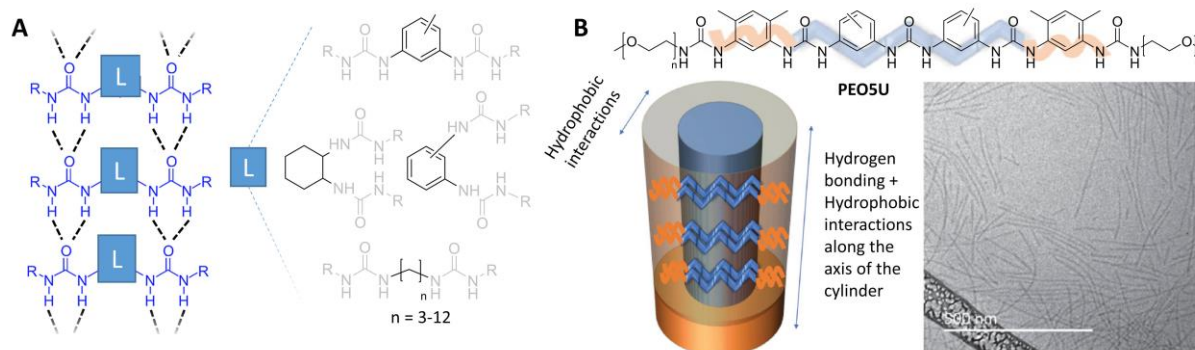


Figure 4 Interactions between two bis-ureas and possible structures of rigid aromatic or flexible aliphatic linkers (A). Schematic depiction of the self-assembly of **PEO5U** in water (cryoTEM of **PEO5U** at $c = 0.5 \text{ g L}^{-1}$) (B). adapted with permission from ref. ^[165] Copyright (2019) John Wiley and Sons.

As already mentioned for CPPNTs, the degree of polymerization of the polymer and thus steric demand influences the size of the resulting SPBs.^[162] Apart from the size of the hydrophilic exterior and the interaction strength of the self-assembly unit, the length of hydrophobic segments separating the hydrogen-bonding unit from the polymer and shielding it in an aqueous environment is considered crucial.^[166] Variations of polymer length and the distance of the polymer arms to an aromatic trisurea motif lead to the observation that longer alkyl chains in combination with polystyrene (DP = 10) resulted in the formation of longer fibers in toluene, whereas higher DPs of the polymer chains (DP = 30) formed solely spherical aggregates.^[167] The necessity for shielding can only be circumvented by increasing the number of hydrogen bonding units. SPBs in water without alkyl spacer could, for instance, be obtained by employing 5 consecutive urea groups separated by aromatic moieties connected to a PEO chain (DP=50) (Figure 4B).^[165] The straightforward synthesis, great possibilities for functionalization, and high interactions-strength render urea-derived SPBs, apart from other prominent self-assembly motifs, for instance, ureidopyrimidinones, potential candidates for eg. application in hydrogels.^[168-170] The application of SPBs derived from 1,3,5-trisurea benzenes in hydrogels will be highlighted in chapter 4.

1.3. Applications of SPBs

Apart from that, several already mentioned advantages of SPBs over their covalent analogs, render SPBs very interesting for a plethora of applications. One of their advantages, namely their modularity, enables SPBs to be applicable as biofunctionalities in nanomedicine (e.g. targeting agents, sensors, etc.). By simple mixing of differently functionalized unimers in the desired molar ratio supramolecular polymers with synergistic effects are obtained, which could already be proven for non-polymeric supramolecular building blocks.^[77, 136, 171-172] Additionally, the higher surface area of cylindrical morphologies increases the possible

interaction sites for specific groups and thus increases the uptake of the particles.^[173-175] Apart from that, the dynamics arising from their unique backbone, the potential stimuli-responsiveness, and the plethora of functionalities lay the foundation for their use in nanoarchitectonics^[176] as smart actuators^[177] or electronics.^[178]

For most of the applications, defined sizes and low dispersity are desirable. Nevertheless, control over the size distributions of supramolecular polymers is still a milestone to be reached. Taking nature as a blueprint,^[1] first works on chain-growth supramolecular polymerization have been conducted.^[11, 179] Either self-assembly pathway complexities can be exploited to gain kinetic control over the polymerization,^[180-181] or meta-stable unimers that have to be activated by supramolecular initiators^[182] can be used to yield defined assemblies with low dispersity. Another way to control supramolecular polymerization is by addition of small seeds to induce the polymerization.^[183-187] Due to the intrinsic dynamics of SPBs, gaining kinetic control is challenging and thus a living growth as observed for non-polymeric supramolecular molecules will perhaps be beyond reach for these systems.^[123-124] First insights into the kinetics of the self-assembly of SPBs and approaches to tune the length of the aggregates with simple methods are presented in chapter 3.

1.4. Motivation

The structuring of macromolecules employing supramolecular polymerization results in interesting dynamics, a high modularity, and defined morphologies. Supramolecular polymer bottlebrushes may feature several advantages over supramolecular polymers from small molecules or structures obtained from block-copolymer self-assembly in diverse fields of application, for instance, in nanomedicine, electronics, and rheology. However, a fundamental understanding of prerequisites for the formation of 1D structures in water from macromolecular building blocks is necessary. Furthermore, a knowledge of size, size distributions, and interaction of the fibers is beneficial for the application-oriented design of supramolecular polymer bottlebrushes.

In this work, a 1,3,5-substituted benzene with hydrogen bonding groups (e.g. amides) was chosen as a starting point for the design of a central structural motif to direct the self-assembly of macromolecules (Figure 5). This centrosymmetric motif is utilized to guide the self-assembly of polymers into cylindrical aggregates with a brush-like structure in aqueous solution. 1-dimensional growth is induced by threefold intermolecular hydrogen bonding between the

One-dimensional (1D) nanostructures by self-assembly

functionalized benzene molecules and a 1-dimensional stacking of the latter into columnar helical assemblies.

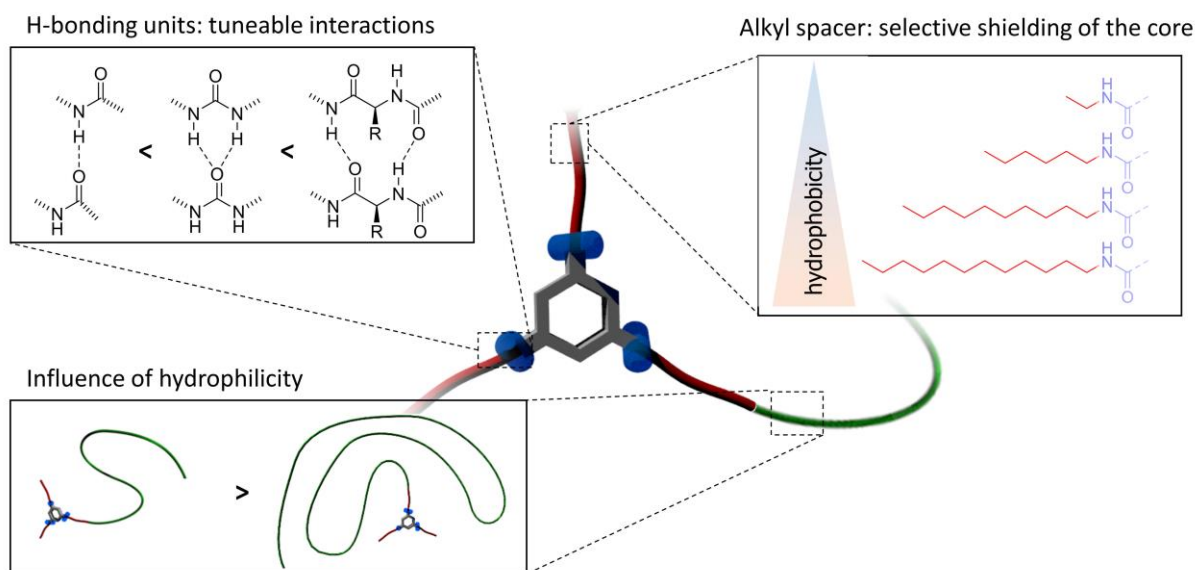


Figure 5 Structural parameters of the benzene self-assembly motif to influence the formation of SPBs in water.

Based on the benzene motif, the prerequisites for 1D self-assembly of macromolecules to form SPBs in solution are evaluated. Here, it has to be assessed whether the packing parameter, similar to the self-assembly of block-copolymers, or the aggregation by the hydrogen bonds is the main driving force for aggregation. Therefore, the influence of the hydrophobic to hydrophilic ratio of the functionalized macromolecule on the resulting structure formation will be evaluated. To do so, alkyl spacers of different lengths are investigated to shield the hydrogen bonding units from surrounding water molecules which would disrupt the structure formation. But even if sufficient shielding is provided, the formation of the desired 1D assembly requires overcoming the additionally created surface area. In this regard, the necessary interaction strength between the self-assembly units to form columnar assemblies is tuned by varying the number of possible hydrogen bonds via the incorporation of amides (BTA), ureas (BTU), or peptides (BTP) as hydrogen bonding units. Here, the influence of the hydrophilic polymer exterior, which solubilizes the formed helical structures and builds up the brush-like structure, additionally has to be taken into account. Since a strong dependency of the structure formation on the hydrophobic/hydrophilic ratio of the building block and thus a pronounced hydrophobic effect in the self-assembly can often lead to kinetically trapped morphologies, the energetic landscape of the self-assembly of these SPBs will be subject to further studies. Combining the knowledge of the prerequisites for 1D self-assembly in water with kinetic aspects of the self-assembly mechanism, ways to influence the size distributions of the resulting structures are

One-dimensional (1D) nanostructures by self-assembly

accessible (Figure 6). Apart from this bottom-up approach, top-down methods as ultrasonication might represent alternatives to adjust the size of the SPBs. Finally, first prerequisites for the application of SPBs hydrogel in, for instance, biomedicine are studied. Due to the supramolecular interactions and the brush-like structure, the hydrogels should feature interesting dynamics and stress-responsiveness.

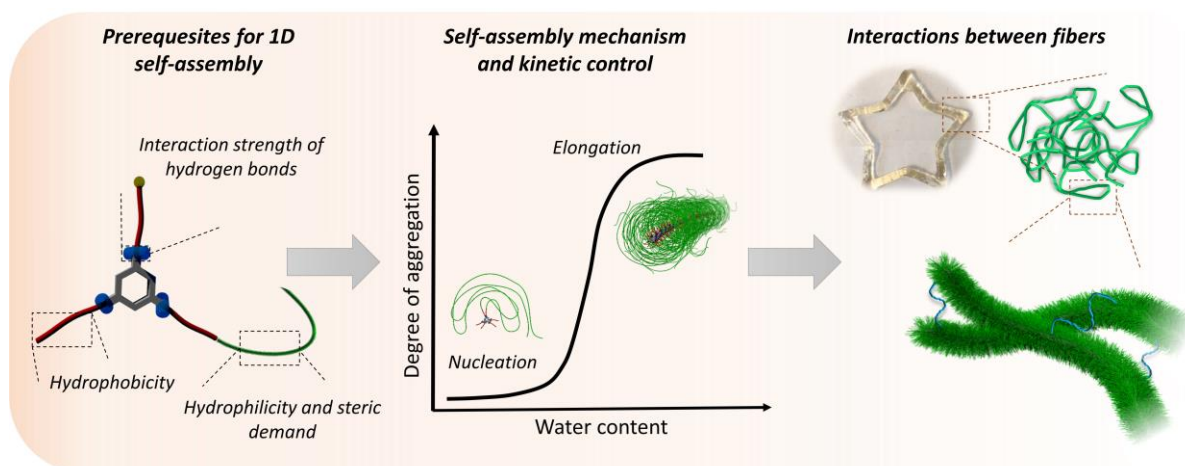


Figure 6 By knowing the prerequisites of 1,3,5 substituted benzenes for the formation of SPBs in water and the kinetics of the self-assembly, adjustment of the size of the resulting SPBs is possible. With the formation of μm sized fibers and their entanglement, combined with the introduction of crosslinkers, the application of these SPBs in stress-responsive hydrogels is feasible.

In summary, this thesis aims to estimate the prerequisites for hierarchical macromolecular self-assembly employing supramolecular chemistry. The overall goal is to form supramolecular polymer bottlebrushes with adjustable size, gain an understanding of their self-assembly mechanism, and evaluate first potential applications such as the formation of a biocompatible hydrogel.

2. Prerequisites for 1D supramolecular self-assembly of SPBs in water

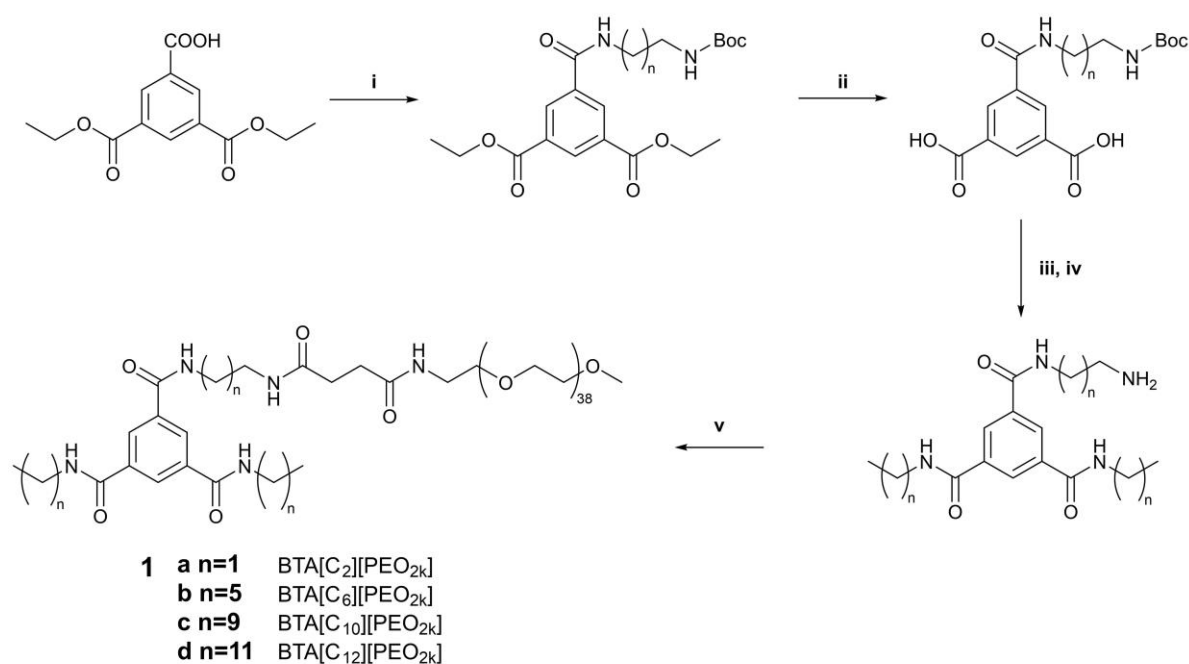
2.1. The influence of the packing parameter on the self-assembly

Parts of this chapter have been published in: P2) T. Klein, F. V. Gruschwitz, S. Rogers, S. Hoepfener, I. Nischang, J. C. Brendel, *J. Colloid Interface Sci.* **2019**, *557*, 488-497.

In this chapter, the influence of the composition of the PEO-functionalized building block on the formation of SPBs, and thus, the impact of changes in the hydrophilic/hydrophobic block ratio on the formation of SPBs will be examined. Therefore, a BTA with alkyl chains of different lengths is conjugated to a PEO-polymer of 2 kD, resulting in an amphiphilic structure. By systematically varying the length of the alkyl chains (2 to 12 methylene groups), the influence of the hydrophilic/hydrophobic block ratio on the self-assembly is assessed. In general, the hydrophobic effect drives the self-assembly of amphiphiles in water if no additional interactions are present. Since it is energetically favored for the hydrophobic part to minimize its contact area to water, the hydrophilic part of the molecule forms a corona surrounding the hydrophobic part. This results in the formation of micellar morphologies, such as spheres or worms, depending on the ratio of hydrophobic to hydrophilic domain. This ratio is termed packing parameter p and is defined for small molecules as $p = V_c / (a_0 \cdot l_c)$ where V_c is the volume of the hydrophobic tail, a_0 the surface area of the hydrophilic head group of the aggregate, and l_c the length of the hydrophobic chain. With knowledge of the packing parameter, an estimation of the resulting morphologies is feasible. For polymeric amphiphiles as the herein used BTA-PEO conjugate, it is challenging to predict the surface area of the polar block and thus the resulting morphologies. Nevertheless, with careful estimations, an equilibrium surface area a_e will be calculated to make a statement about the driving force for the resulting morphologies of the BTA-PEO conjugates in water.

The BTA-PEO conjugates could be synthesized from cheap starting materials and circumventing tedious purification procedures. Addition of a semi-protected diamine of different length to 3,5 bis(ethoxycarbonyl)benzoic acid, subsequent saponification of the esters and addition of primary amines, gave, after deprotection and addition of NHS-PEO ester via click-chemistry, compound **1**. (Scheme 1, Further information on the synthetic procedure can be found in the Supporting Information of **P1**)

Prerequisites for 1D supramolecular self-assembly of SPBs in water



Scheme 1 Synthetic routes toward BTA compounds **1a-d**. i) Semi-protected amine, DMAP, EDC, DCM, 25 °C, overnight; ii) KOH in EtOH/H₂O 9:1, 80 °C, 30 min; iii) Alkylamine, DMAP, EDC, DCM, 25 °C, overnight; iv) TFA/TIPS/H₂O, DCM, 25 °C, 2 h; v) Methoxy-PEG-NHS, TEA, DMF, 25 °C, overnight; vi) Alkylamine, DMAP, EDC, DCM, 25 °C, overnight; vii) TFA/TIPS/H₂O, DCM, 25 °C, 2 h; viii) Methoxy-PEO-NHS, TEA, DMF, 25 °C, overnight.

Characterization of the solution assemblies of the BTAs **1a-d** in water with small-angle neutron scattering (SANS), cryo transmission electron microscopy (cryo-TEM), and analytical ultracentrifugation (AUC), yielded no aggregation for **1a**, spherical micelles for **1b-c**, and a mixture of spherical particles with a minority of anisotropic structures for **1d** (Figure 7).

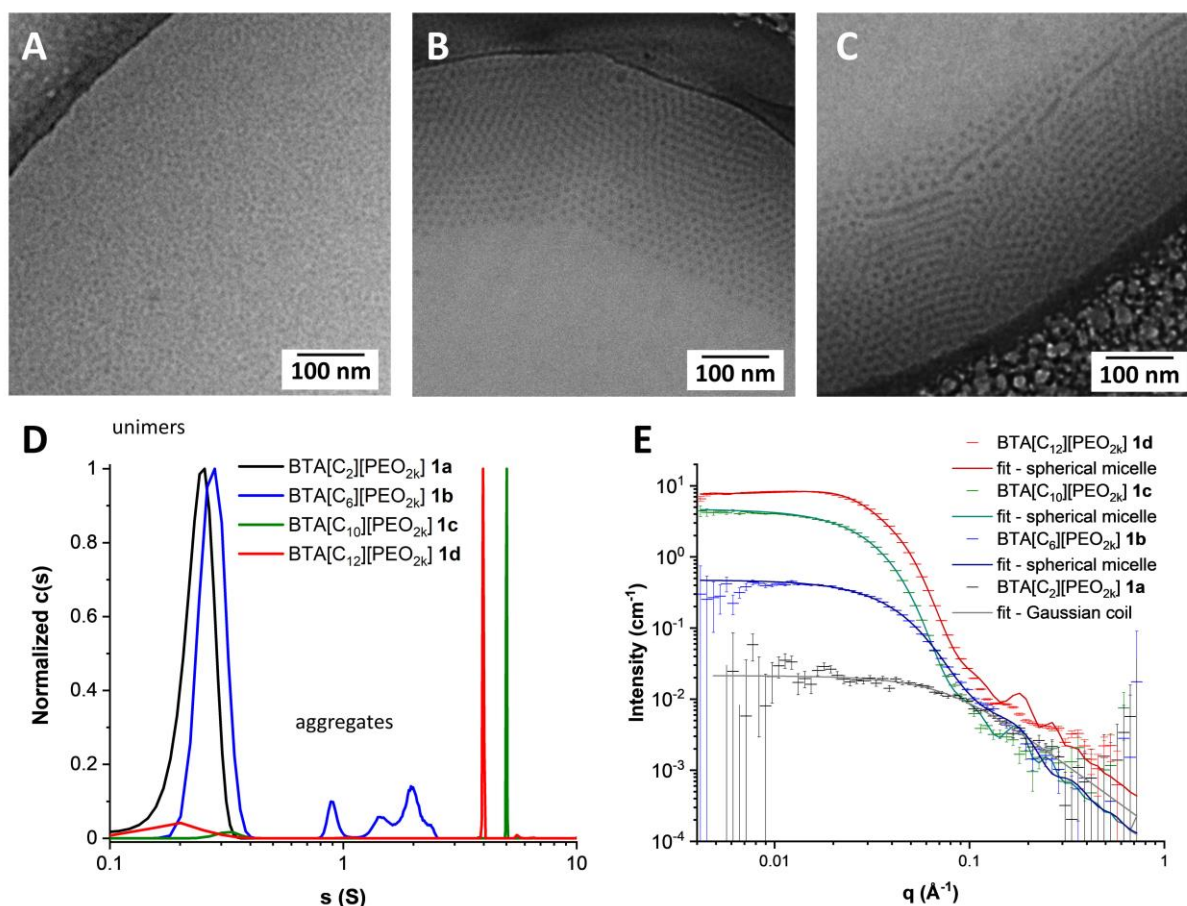


Figure 7 cryo-TEM images of **1b** (A), **1c** (B) and **1d** (C) ($c = 3 \text{ mg mL}^{-1}$). Normalized differential distribution of sedimentation coefficients, s , of BTA samples **1a-d** from sedimentation-diffusion analysis, $c(s)$, at a comparable solution concentration of $c = 3 \text{ mg mL}^{-1}$ (semi-logarithmic scale) (D). Scattering profiles of compound **1d** (red, $c = 10 \text{ mg mL}^{-1}$), **1c**, **1b**, and **1a** ($c = 3 \text{ mg mL}^{-1}$) obtained by SANS. The respective continuous lines represent the fit for a spherical micelle for each sample. Adapted with permission of ref. ^[188] Copyright (2019) Elsevier.

Utilizing the shortest spacer of 2 methylene units for the synthesis of **1a**, resulted in the presence of only unimers in solution. Via AUC measurements it could be observed, that BTA-C₂ **1a** showed a narrow distribution of readily small sedimentation coefficients derived from sedimentation-diffusion analysis (black trace in Figure 7D). f/f_{sph} values are not concentration-dependent and in good agreement with the values reported for end-functionalized PEGs in solution.^[189] The molar mass of **1a** was calculated to $M_{s,f} = 2200 \text{ g mol}^{-1}$, corresponding to the molar mass of a single molecule. In agreement with this, SANS data for **1a** can be fitted by the typical scattering pattern of a Gaussian coil (Figure 7E), proving the presence of solely unimers for **1a** in solution. By increasing the number of methylene units to 6, the equilibrium is shifted to spherical morphologies for **1b**. Cryo-TEM images reveal the presence of micelles with a diameter of approximately 6 nm (Figure 7A), which can also be proven by the q^0 decay in the scattering profile for **1b** obtained by SANS (Figure 7E blue line). Nevertheless, as seen in AUC experiments, this spherical fraction is not the majority. A big fraction of unimers is still present.

This number of unimers is significantly decreased when a C₁₀ alkyl chain is used and well-defined aggregates with a molar mass of $M_{s,f} \approx 340\,000\text{ g mol}^{-1}$ and a number of aggregation N_{agg} of 140 can be calculated (Figure 7D green line). However, in the cryo-TEM images of **1c** still solely spherical micelles with a diameter of 8 nm can be observed (Figure 7B). The increase in diameter compared to **1b** correlates well to the increased spacer length. To further increase the hydrophilic/hydrophobic ratio of the amphiphile, an alkyl chain of 12 methylene units was used for the synthesis of BTA[C₁₂][PEO_{2k}] **1d**. Here, a small minority of anisotropic aggregates next to a majority of micellar structures could be observed in cryo-TEM images (Figure 7C). Nonetheless, in AUC measurements and SANS data of **1d** mostly spherical particles were detected, resembling the ones of **1c**. That means, despite the ability of literature-known non-polymeric BTAs with spacers consisting of 11 methylene units to form anisotropic columnar supramolecular assemblies,^[126] polymeric BTAs cannot overcome the limitation of directional growth by the packing parameter. These findings already emphasize that hydrophobic BTA moiety needs to have a certain size compared to the hydrophilic PEO to enable assembly in water. This corroborates the findings for non-polymeric BTA-derivatives.^[190] To connect these observations to the packing parameter, theoretical considerations can be drawn by employing the equilibrium surface area, a_e which is based on repulsive forces between adjacent chains instead of a_0 . The equilibrium surface area, a_e can be calculated from the spherical fit of the SANS data via the surface of a sphere, A , of a radius, r_c , divided by the aggregation number also calculated from fitted SANS data. Assuming the observed solution morphologies to represent a thermodynamic equilibrium, the value for a_e derived from the spherical micelle fits results in a significantly increased available surface area per PEO chain for BTA[C₆][PEO_{2k}] **1b** in comparison to **1c** and **1d** (Figure 8). Since in all cases the same size of hydrophilic exterior is attached, for the BTAs **1c** and **1d** stronger repulsive forces are expected. The resulting increased crowding of chains results in a transition from spherical to cylindrical structures due to a lower overall energy level.^[191-192]

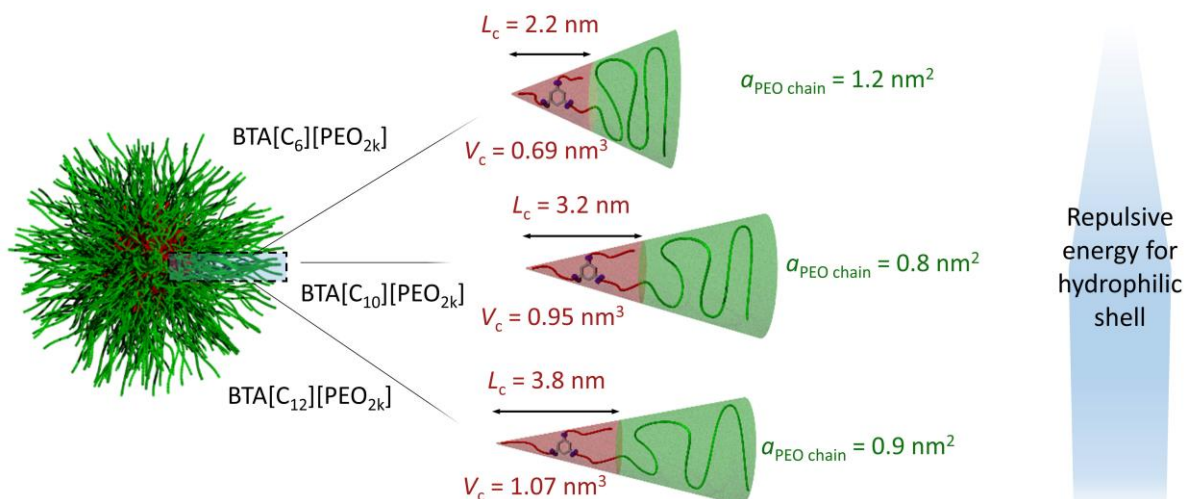


Figure 8 Schematic representation of the configuration of BTA molecules in the spherical micelles; the given values for a theoretical maximum length, L_c , and the theoretically occupied volume for each unit, V_c , are estimated from geometric considerations, while the surface area per PEO chain, $a_{\text{PEO chain}}$, was calculated from the representative spherical micelle fits. Adapted with permission of ref. ^[188] Copyright (2019) Elsevier.

These considerations support the assumption that for BTAs, the transition from spherical to cylindrical structure is dependent on the composition (i.e. the ratio of hydrophobic to hydrophilic domain), and not the presence of directed hydrogen bonds in the BTA motif itself. This hypothesis is again supported by comparison of the BTA compounds to a compound lacking the hydrogen bonding units. The benzenediesteramide-PEO with C_{10} alkyl chains BDEA[C_{10}][PEO $_{2k}$] **2** forms an increased number of fiber-like morphologies in water compared to the BTA analogs (Figure 9, the synthetic procedure can be found in Supporting Information of P1). Since BTA[C_{10}][PEO $_{2k}$] **1c** does not form any anisotropic structures, the packing parameter can be regarded as the structure-directing factor. Due to the hydrogen bonds in BTA[C_{10}][PEO $_{2k}$] **1c** a denser packing of the molecules in the core can be expected, thus resulting in a lower volume V_c of the hydrophobic part as for **2**. As the surface area and the size of the hydrophilic part is the same, the packing parameter p is lower and a transition from spherical ($p \leq 1/3$) to cylindrical ($1/3 \leq p \leq 1/2$) structures is observable for **2**.

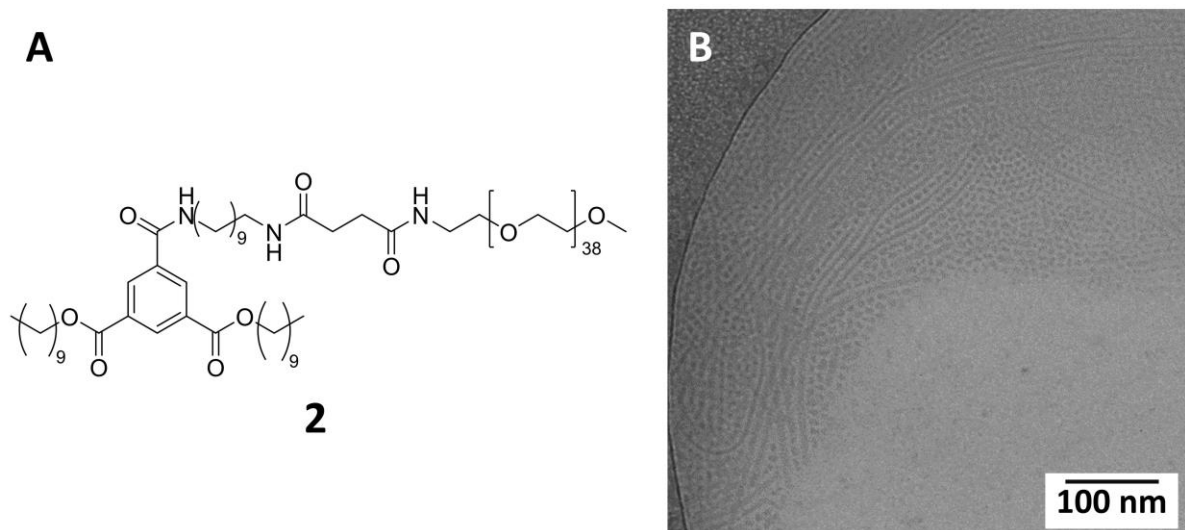


Figure 9 Chemical structure of BDAE **2** (A) and cryoTEM image of **2** ($c = 3 \text{ mg ml}^{-1}$) (B). Adapted with permission of ref. ^[188] Copyright (2019) Elsevier.

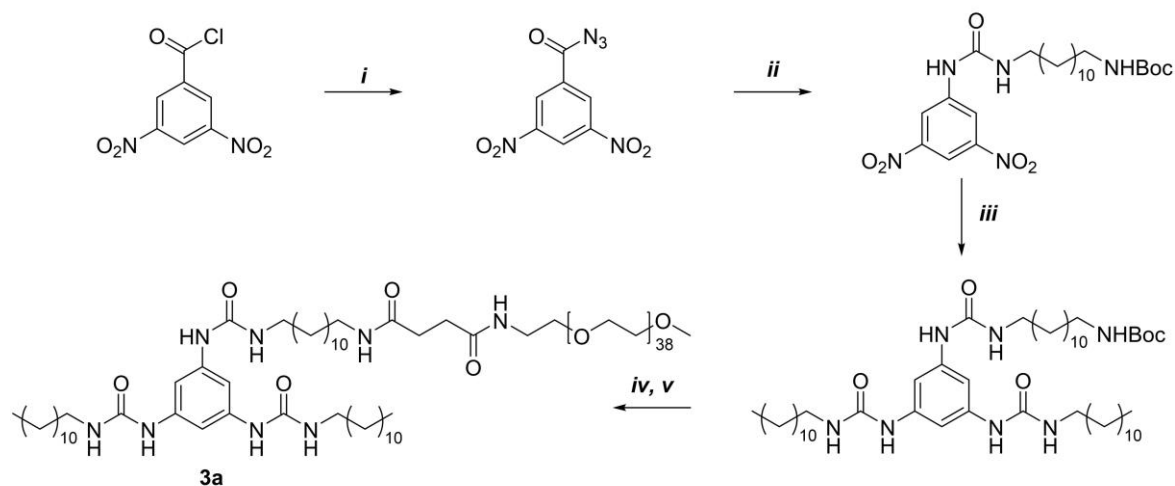
Therefore, by employing the BTA motif the synthesis of SPBs is not feasible. Additional or stronger directional forces are necessary to induce 1D growth. However, the size of the hydrophobic part is of great importance to generally allow for the synthesis of 1D aggregates in aqueous solution.

2.2. Overcoming the packing parameter - Influence of the interaction strength on 1D aggregation

Parts of this chapter have been published in: P3) F. V. Gruschwitz, M.-C. Fu, T. Klein, R. Takahashi, T. Higashihara, S. Hoepfner, I. Nischang, K. Sakurai, J. C. Brendel, *Macromolecules* **2020**, *53*, 7552-7560 and P4) T. Klein, H. F. Ulrich, F. V. Gruschwitz, M. T. Kuchenbrod, R. Takahashi, S. Fujii, S. Hoepfner, I. Nischang, K. Sakurai, J. C. Brendel, *Polym. Chem.* **2020**, *11*, 6763-6771.

To overcome the limitations derived from the packing parameter, the number of hydrogen bonds and thus the interaction strength has to be increased. Employing urea groups as hydrogen bonding units instead of amides, the interaction strength increases and thus results in stronger directional growth. Via a straightforward synthesis, employing isocyanate chemistry, benzene trisurea – PEO conjugate **3a** was obtained (Scheme 2). Commercially available 3,5-dinitrobenzoyl chloride was reacted to its carbonyl azide and subsequent Curtius rearrangement yielded the isocyanate. This was *in situ* reacted with a mono *boc*-protected

dodecyl diamine. After hydrogenation of the nitro groups, dodecyl-isocyanates were attached to the resulting amino groups to finalize the trisurea core motif. After deprotection of the *boc*-group, poly(ethylene oxide) polymers (PEO) were connected to the core by amide groups, which were formed from an activated *N*-hydroxysuccinimide (NHS) ester.



Scheme 2 Synthetic procedure for the synthesis of the BTU-C₁₂-PEO_{2k} **3a** : (i) NaN₃ aq.; (ii) *tert*-butyl *n*-aminoalkylcarbamate; (iii) H₂, Pd/C, alkylisocyanate; (iv) TFA; (v) NHS-PEO, TEA.

Upon dissolution of the compound **3a** in water, aggregation into pure fiber morphology could be proven by cryoTEM, where fibers with an apparent diameter of 7.6 nm can be distinguished (Figure 10B). The length of the fibers is difficult to consider from these images since the ends partly exceed the dimensions of the imaged area. This result already indicated that by simply changing from amide groups to urea the limitation of the packing parameter can be overcome and pure fiber formation can be observed for BTU[C₁₂][PEO_{2k}] **3a** in comparison to BTA[C₁₂][PEO_{2k}] **1d**. Further insight into the fiber morphology of **3a** could be obtained by small-angle x-ray scattering (SAXS) (Figure 10A). For compound **3a** the scattering intensity $[I(q)]$ scales with q^{-1} at low q -values, which is indicative of the formation of cylindrical structures. To extend the accessible window of observation, the sample was analyzed by static light scattering (SLS). Even at lower q -values, the continuation of the q^{-1} dependence can be observed, however, a plateau is formed at q -values below $9 \times 10^{-3} \text{ nm}^{-1}$. By combination of both scattering data,^[167] a model of a cylinder with a radius R_{cyl} of 5.0 nm and a length L_{cyl} of 311 nm can be fitted. By a cross-sectional plot of the SAXS data, the cross-sectional radius R_{cs} could be determined to be 6.2 nm. This does not correlate well with the relationship of $R_{\text{cs}} = R_{\text{cyl}} / \sqrt{2}$ described for a solid cylinder. Nonetheless, the more complex core-shell structure of the cylindrical aggregate has to be considered. Hereby, the hydrophilic polymer

chains will protrude into the solvent inducing a gradient in the electron density profile, which will not be correctly represented by the applied cylindrical model. However, this radius seems reasonable in correspondence with the radius obtained from cryoTEM, which is also slightly smaller since the contrast of the adjacent PEO chain is not big enough to exhibit a high enough contrast to measure the polymer corona. This radius however raises the question of whether the fiber consists of a single columnar stack of unimers or bundling of columnar stacks is favored. The overall mass of the aggregates was determined by SLS to be $9.5 \times 10^6 \text{ g mol}^{-1}$ which results in a number of aggregation of unimeric building units $N_{\text{agg}} = 3\,500$ per cylinder considering a molar mass of $2\,800 \text{ g mol}^{-1}$ for the unimer. If the length of 311 nm per aggregate and an average distance of 3.6 \AA between the stacked molecules is considered, there is a mismatch that can only be explained by the presence of 4 molecules per cross-section (Figure 10C).

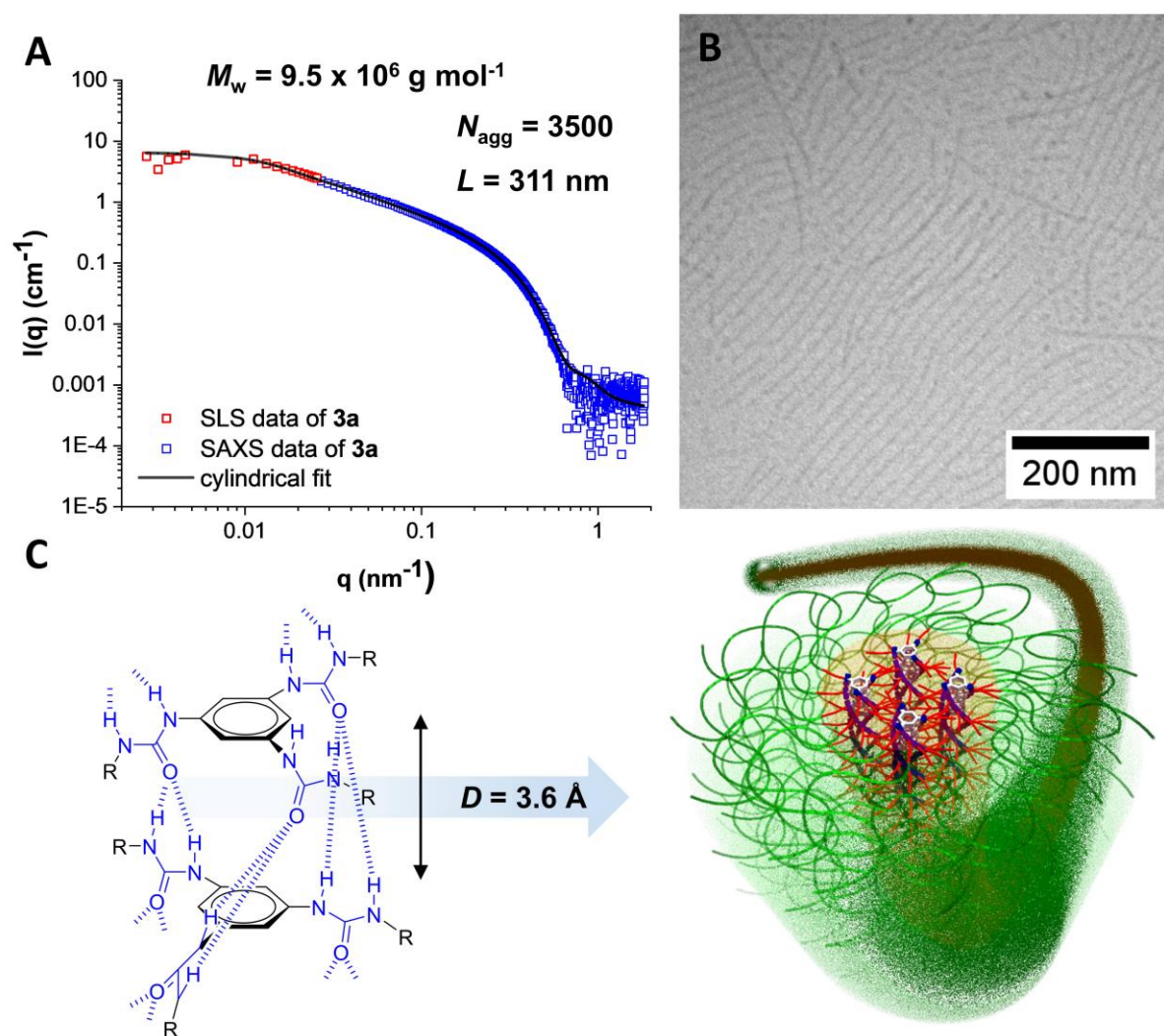


Figure 10 Scattering profile of BTU[C₁₂][PEO_{2k}] **3a** obtained by SLS (red squares) and SAXS (blue squares) and a cylindrical fit (black line) of the combined data ($c = 1.5 \text{ mg mL}^{-1}$) (A). cryoTEM image of **3a** ($c = 5 \text{ mg mL}^{-1}$) (B). The proposed arrangement of BTU[C₁₂][PEO_{2k}] molecules (C). Adapted with permission of ref. ^[193]. Copyright (2020) American Chemical Society.

Stepping further, it is possible to increase the interaction strength even more by employing peptide groups as hydrogen bonding units. Especially the choice of amino acids allows for fine-tuning of the interaction strength. Varying the type of amino acid from alanine, leucine to phenylalanine results in the creation of SPBs derived from benzene trispeptides (BTPs) (Figure 11B). The synthetic route towards compounds **4a-c** can be found in the Supporting Information of P4. Sticking to the previously used alkyl spacer length of 12 methylene units and a 2kD PEO chain, the influence of the amino acid on the structure formation in water is evaluated. Hypothetically, these SPBs will be longer in comparison to **3a** due to the higher interaction strength of the peptide units. This applies to BTP[A][C₁₂][PEO_{2k}] **4a** which features fibers with lengths up to one micron observed by cryoTEM (Figure 11A). By changing the amino acid to Leucine, smaller structures of maximal 600 nm could be obtained (Figure 11C), which is at first thought not expected. A further variation to the β -sheet forming Phenylalanine results in the formation of the shortest fibers observed for BTPs of around 250 nm (Figure 11E). From cryoTEM images, it seems, that despite the high interaction strength of the peptide groups, the structures are smaller compared to **3a** and even some small micelles can be observed. Since in SAXS measurements of **4b** and **4c** a continuous q^{-1} decay, indicative for the presence of cylindrical aggregates, is measured, the small structures are expected to be truncated cylindrical aggregates instead of spherical particles (Figure 11D). This assumption is further supported by the absence of smaller sedimentation coefficients in AUC measurements for **4b** and **4c** (Figure 11F). This unexpected tendency for **4b** and **4c** to form smaller structures compared to **4a** and **3a** (Figure 11B and C), can be explained by the strong increase in hydrophobicity of **4b** and **4c** due to the combination of a hydrophobic amino acid with the long alkyl chain of 12 methylene units, resulting in an increased hydrophobic core. Its free diffusion through the water is thus hindered and the formation of kinetically trapped structures occurs. Therefore it is necessary to not only consider the increased interaction due to hydrogen bonds but also the hydrophobic interactions as already mentioned in chapter 2.1. Further work on the kinetics of BTU and BTP assembly is presented in Chapter 3.

Prerequisites for 1D supramolecular self-assembly of SPBs in water

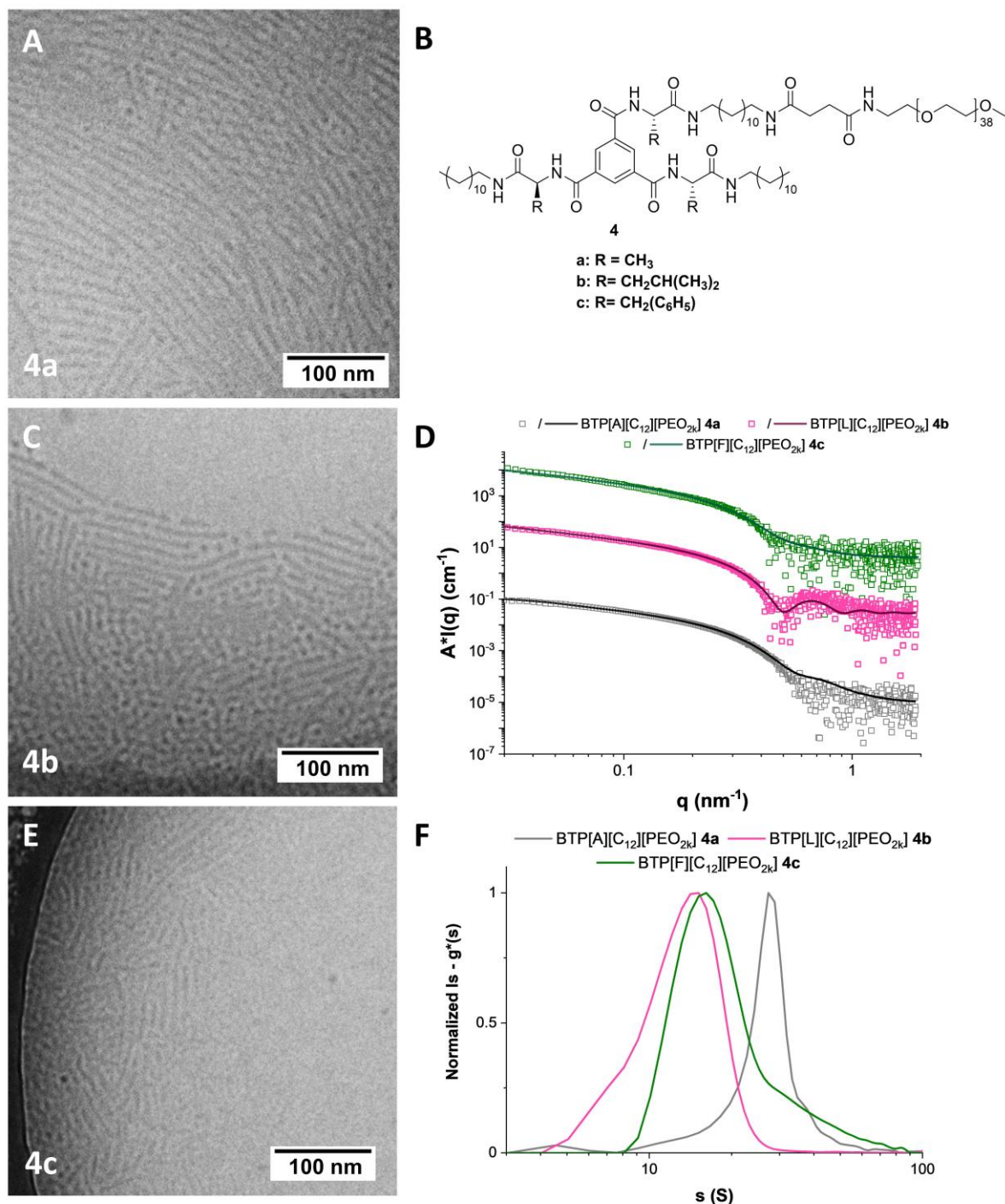


Figure 11 CryoTEM images of **4a-c** in water ($c = 3 \text{ mg mL}^{-1}$) (A, C, E). SAXS scattering profiles of the samples **4a** (grey), **4b** (magenta), and **4c** (green), measured in water ($c = 1.5 \text{ mg mL}^{-1}$). The traces of were shifted by multiplication for reasons of clarity (D). Normalized differential distribution of sedimentation coefficients, $Is - g^*(s)$, of compounds **4a** (grey), **4b** (magenta), and **4c** (green) from sedimentation analysis in water ($c = 3 \text{ mg mL}^{-1}$) (E). Adapted with permission of ref. ^[194] Copyright (2020) Royal Society of Chemistry.

By comparing amide- (**1d**), urea- (**3a**), and peptide-derived (**4a**) PEO-conjugates (without the capability to form additional β -sheet structures), an increase in sedimentation coefficients in AUC and thus an increase in the size of the aggregates can be observed (Figure 12B). Additionally, in SAXS measurements, a q^{-1} decay can be observed for peptide and urea-derived

PEO-conjugates **4a** and **3a**, in contrast to a q^0 decay for the micellar structures of amide-derived PEO conjugate **1d**. This difference amplifies the need for a high interaction strength of the hydrogen bonding units to ensure 1D growth and thus the formation of SPBs in water (Figure 12A).

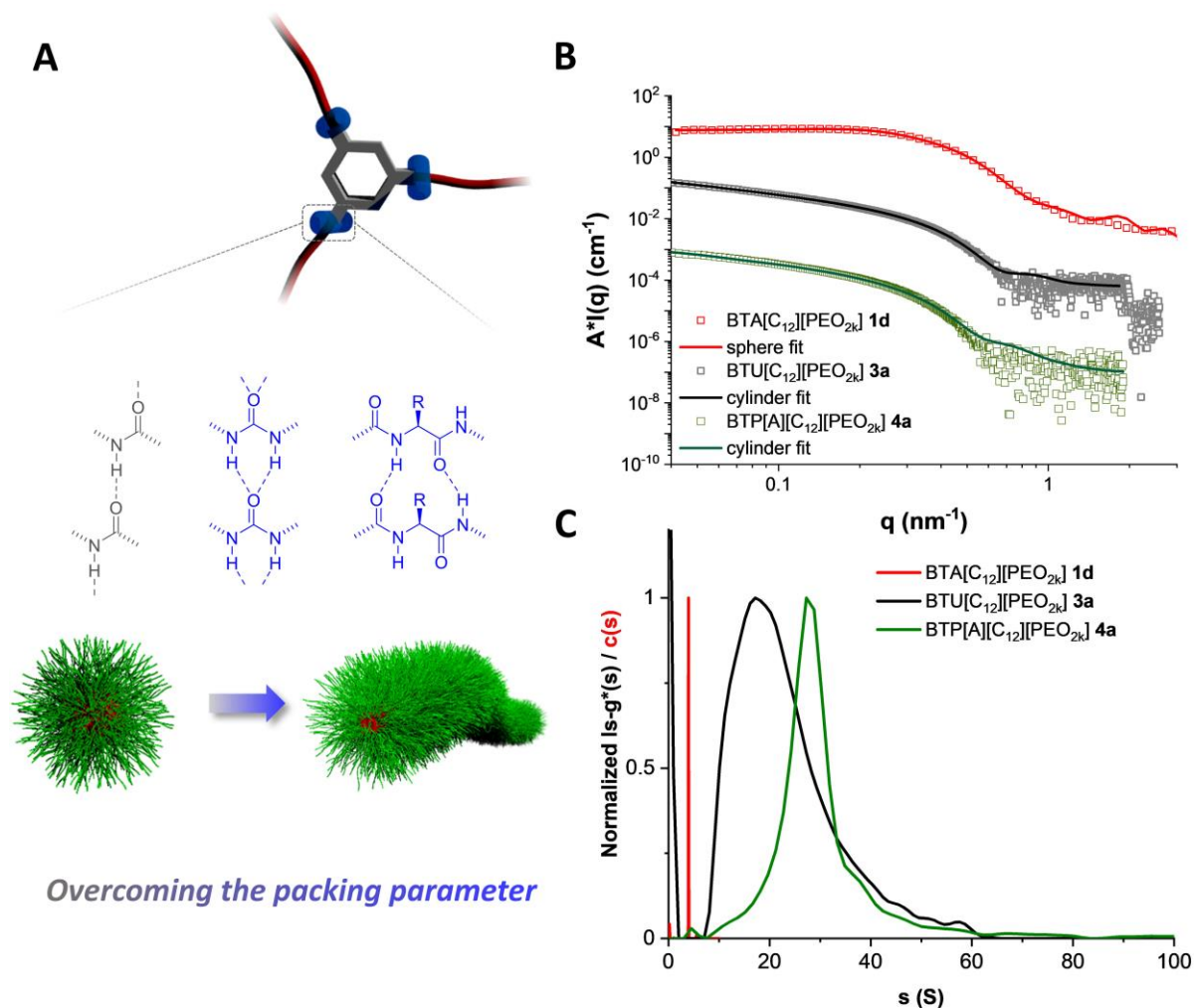


Figure 12 Schematic depiction of the interactions in the self-assembly of benzene trisureas and -peptides in comparison to the analogous amides to form supramolecular polymer bottlebrushes (A). SAXS (B) and AUC (C) measurements of amide- (**1b**), urea (**3a**) and peptide-derived (**4a**) PEO-conjugates. Adapted with permission of ref. [193]. Copyright (2020) American Chemical Society.

Overall, these results corroborate the impact of the interaction strength by the presence of urea or peptide groups, to shift the boundaries of the phase transition from spherical to anisotropic aggregation. Nevertheless, the influence of hydrophobic interactions and the packing parameter should not be neglected.

2.3. Limiting factors for the 1D supramolecular self-assembly

Parts of this chapter have been published in: P3) F. V. Gruschwitz, M.-C. Fu, T. Klein, R. Takahashi, T. Higashihara, S. Hoepfener, I. Nischang, K. Sakurai, J. C. Brendel, *Macromolecules* **2020**, *53*, 7552-7560. P5) T. Klein, H.F. Ulrich, F. V. Gruschwitz, M.T. Kuchenbrod, R. Takahashi, S. Hoepfener, I. Nischang, K. Sakurai, J. C. Brendel, *Macromol. Rapid Commun.* **2020**, 2000585.

As the packing parameter and thus the structure formation cannot only be influenced by the hydrophobic but also by the hydrophilic part of the molecule, the size, and type of the latter has to be chosen carefully to still form cylindrical SPBs in water. Since an increase in the size of the hydrophilic part, will increase a_c and thus decrease the packing parameter, this will result in a shift of the equilibrium morphologies from cylindrical to spherical ones. However, since these SPBs do not solely rely on the packing parameter but also on the hydrogen bond interactions that favor a 1-dimensional growth once they are strong enough, the influence of the dimensions of the hydrophilic exterior on the cylindrical morphologies should be lower. This means, larger variations in the size of the hydrophilic exterior should be tolerable still yielding cylindrical aggregates, as one would expect from the packing parameter if no additional non-covalent interactions would be present. In the following chapter, the boundaries of SPB formation are evaluated by variation of the size of the hydrophilic polymer exterior of BTU[C₁₂]-derived PEO-conjugates.

By increasing the length of the PEO-polymer from the previously known 2 000 g mol⁻¹ to 6 000 g mol⁻¹ and 11 000 g mol⁻¹, the influence of the degree of polymerization (DP) on the formation of SPBs will be assessed. In comparison to BTU[C₁₂][PEO_{2k}] **3a**, BTU[C₁₂][PEO_{6k}] **3b** forms mostly micellar structures however fiber-like aggregates can be observed in cryoTEM images (Figure 13A). Increasing the PEO-corona of the aggregates even more, for BTU[C₁₂][PEO_{11k}] **3c** solely rather ill-defined micelles can be observed in cryoTEM (Figure 13B). Due to the big and highly hydrated PEO-corona, the contrast in cryoTEM is rather low, which complicates the estimation of the length and diameter of the formed aggregates. The loss of anisotropy with increasing hydrophilic part of the molecule can also be depicted by SAXS measurements. In comparison to the q^{-1} decay for **3a**, **3b** and **3c** exhibit a plateau at q values $< 0.2 \text{ nm}^{-1}$, indicative for the formation of micelles. Since the arrangement of the unimers into spherical aggregates might be difficult, due to the limited extension of the hydrophobic domain, the observed micellar structures might be very short fibers with lengths in the size range of their fiber diameter, thus appearing as spherical structures. Fitting the SAXS data with

a cylindrical structure factor, an adequate fit for a cylinder with dimensions of $L_{\text{cyl}} = 14.7$ nm and with a R_{cyl} of 8.0 nm is obtained (Figure 13D). With an overall mass of the aggregate of 1.0×10^6 g mol⁻¹ an aggregation number of N_{agg} of approximately 165 was calculated, which still corresponds well to the tetramolecular cross-section we observed for **3a**. For **3c**, a spherical fit with a radius R_{sphere} of 10.5 nm can be fitted. However, similar adequate fits were obtained using a cylindrical model with L_{cyl} of 17.2 nm and a R_{cyl} of 10.6 nm. With a molar mass of 1.1×10^6 g mol⁻¹ ($N_{\text{agg}} = 98$), only two molecules can be present in the cross-section. Due to the relatively large polymer chain, stronger steric demands are expected and thus the lateral aggregation might be decreased for **3c** in comparison to **3a** and **3b**. AUC measurements, corroborate the shift from bigger structures to smaller ones by increasing the hydrophilic exterior of the aggregates (Figure 13C).

These findings represent the impact of composition on the boundaries of anisotropic self-assembly of urea-derived PEO-conjugates. This means that the window of anisotropic self-assembly can be widened by employing urea groups as hydrogen bonding units in comparison to no or less strong directional interactions as in amide-derived PEO-conjugates. However, even the utilization of peptide groups to obtain SPBs could not tolerate PEO chains of lengths > 2kD, implying the tremendous influence of the size of the hydrophilic domain on the self-assembly.

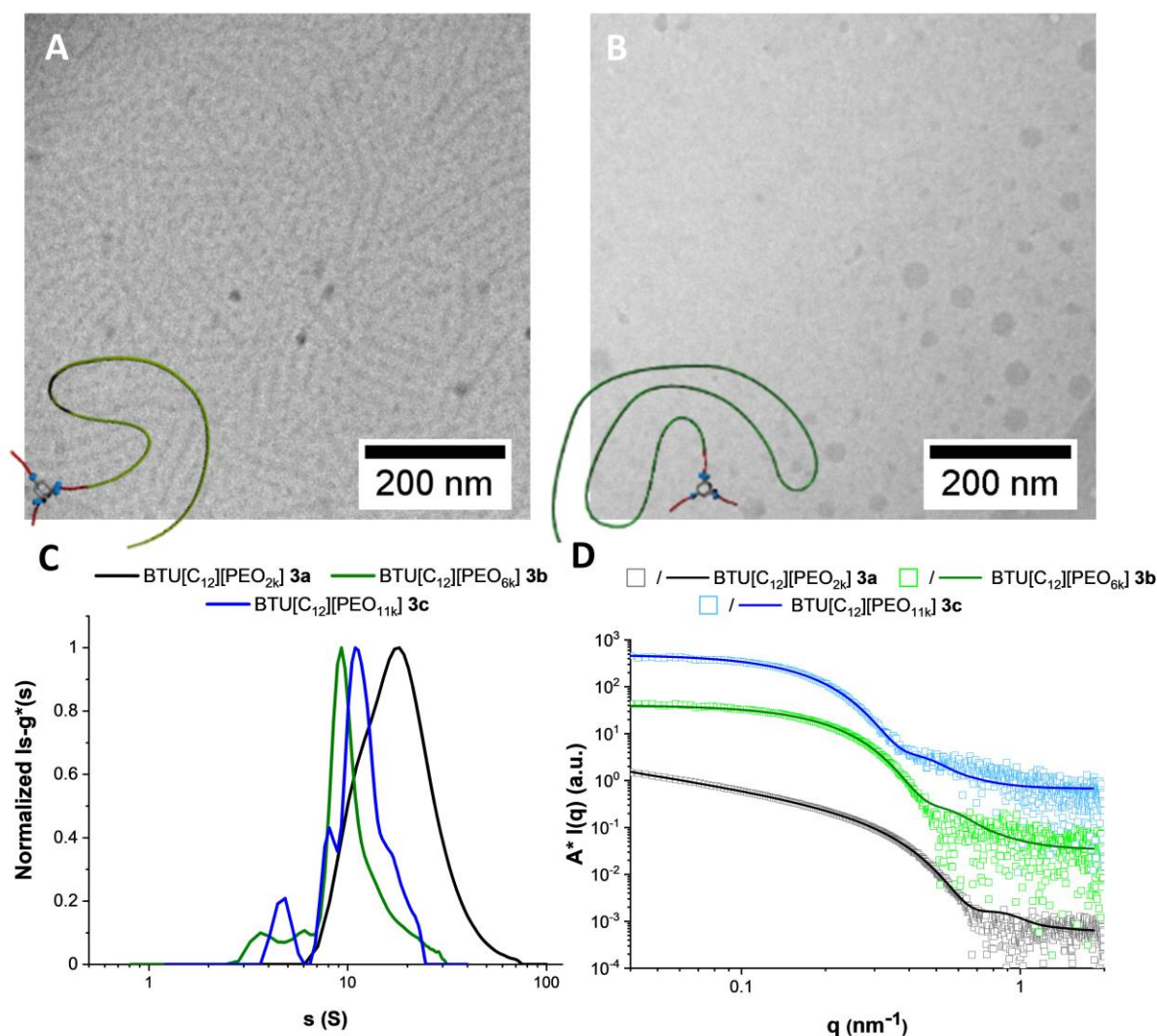


Figure 13 cryoTEM images of **3b** (A) and **3c** (B) in water ($c = 5 \text{ mg mL}^{-1}$). AUC (C) and SAXS (D) data ($c = 1.5 \text{ mg mL}^{-1}$) of BTU[C₁₂]-PEO conjugates with varying DP of the PEO chain. Adapted with permission of ref. [193]. Copyright (2020) American Chemical Society.

Apart from varying the size of the hydrophilic part, it is also possible to change the architecture of the amphiphile to resemble a bolaamphiphilic structure. Comprising two or three polymer chains attached to the core motifs, the compounds BTU[C₁₂][PEO_{2k}]₂ **5a** and BTU[C₁₂][PEO_{2k}]₃ **5b** were synthesized to evaluate the effect of the arrangement of the hydrophilic exterior on the formation of SPBs (Figure 14A). (The synthetic procedure can be found in the Supporting Information of P3).

BTU[C₁₂][PEO_{2k}]₂ **5a** exhibits mostly fiber-like aggregation with a few micellar structures in cryoTEM images (Figure 14B), which is supported by a $q^{-0.5}$ decay in SAXS measurements that can be fitted by the combination of two models for smaller spherical or cylindrical structures and long cylinders (Figure 14D). Both combinations give adequate results of either R_{sphere} of 5.1 nm and a R_{cyl} of 4.3 nm for the spheres and cylinders, or $R_{\text{cyl_short}}$ of 4.8 nm and a $R_{\text{cyl_long}}$ of

4.3 nm for the short and long cylinders, respectively. A further increase of the number of polymer arms to three (BTU[C₁₂][PEO_{2k}]₃ **3b**) resulted in a purely micellar morphology (Figure 14C). Again both, a spherical fit with R_{sphere} of 4.2 nm and a cylinder fit resulting in a L_{cyl} of 5.8 nm and a R_{cyl} of 5.3 nm, were in good agreement with the SAXS data. In contrast to **3a** which is consistent with a tetramolecular cross-section and **5b** where the number of molecules in the cross-section cannot be determined, the aggregates of **5c** ($N_{\text{agg}} = 16$) consist of a single molecule in the cross-section (stacking distance = 3.6 Å). The symmetrical attachment of three polymers impedes the lateral aggregation completely, thus forming a unimolecular cross-section and resulting in the formation of very short structures of micellar shape, although the overall size of the hydrophilic and hydrophobic domains of **5b** is similar as for **3c** (BTU[C₁₂][PEO_{6k}]). This already might be a hint, that the additional lateral aggregation enhances 1-dimensional growth, due to compensation of defects in the stacked, hydrogen bond-forming trisurea benzenes by the parallel alignment of neighboring stacks in such bundles of aggregates. This effect has already been observed for other supramolecular systems.^[195-196] This necessity of lateral aggregation to obtain long SPBs can only be overcome by increasing the interaction strength even more. Only a combination of a urea group with two leucine units induces hydrogen bonds strong enough to yield long fibers with a unimolecular cross-section even if three pendant polymer chains are present.

Prerequisites for 1D supramolecular self-assembly of SPBs in water

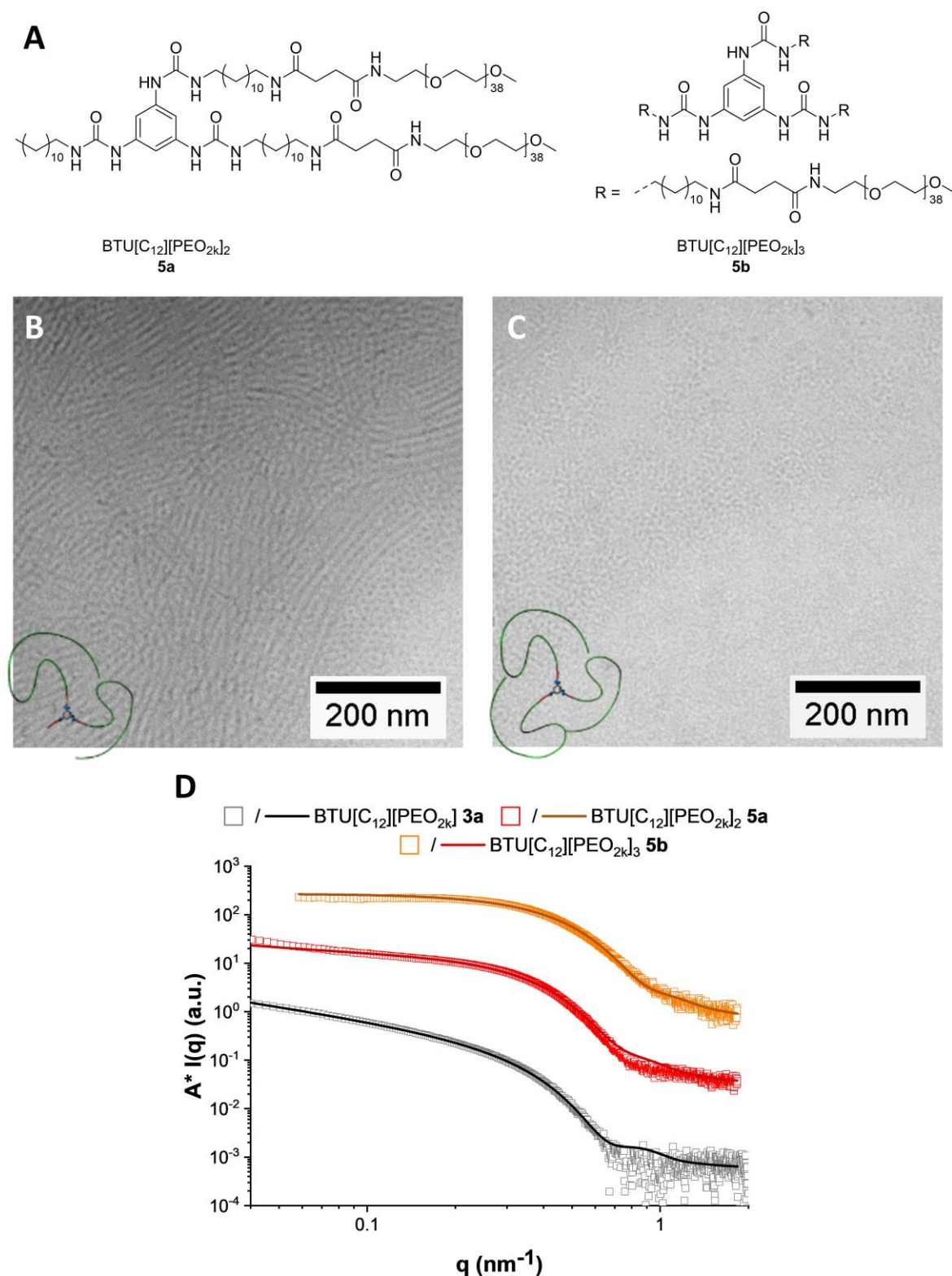


Figure 14 cryoTEM images of **5ba** (B) and **5b** (C) in water ($c = 5 \text{ mg mL}^{-1}$). SAXS (D) data ($c = 1.5 \text{ mg mL}^{-1}$) of BTU[C₁₂]-PEO conjugates with varying architecture of the amphiphiles. Adapted with permission of ref. ^[193]. Copyright (2020) American Chemical Society.

To sum it up, increasing the number of polymer chains and thus changing the architecture of the amphiphile, results in a loss of anisotropy similar to the shift to micellar structures observed

for increasing polymer chain lengths. This amplifies the influence of the packing parameter on the assembly even if stronger directional interactions, for instance, urea instead of amide groups are present. The enhanced interaction seems only to shift the phase boundaries of the morphology transitions, since decreasing the ratio of hydrophobic to hydrophilic part, again results in the transition towards isotropic structures (Figure 15 left). Nonetheless, a change in the structural arrangement affects the molecular packing of the building units in the cross-section of the assemblies (Figure 15 right).

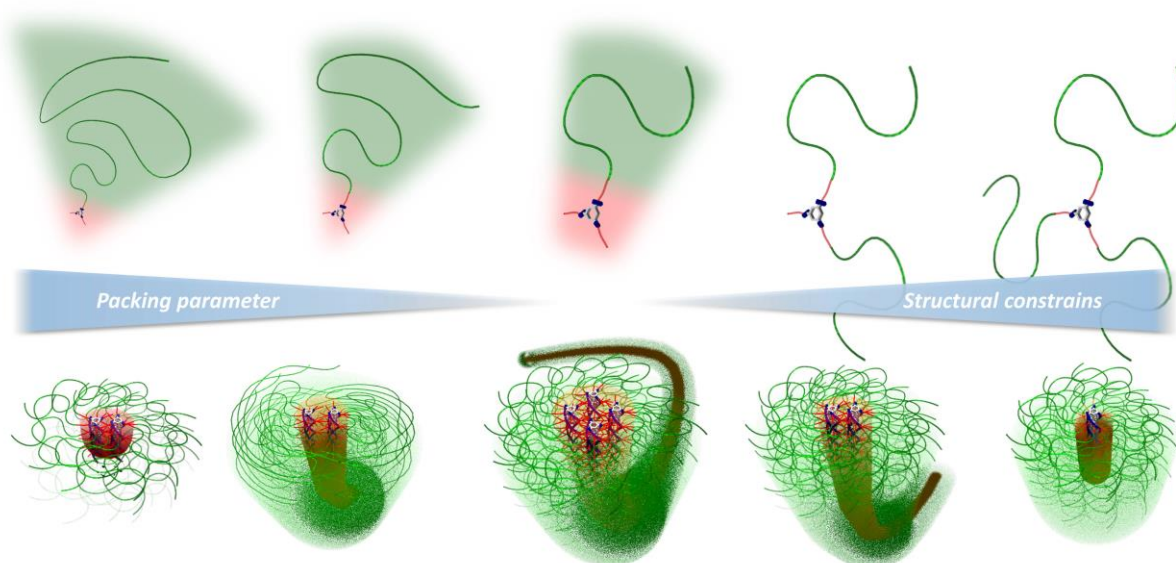


Figure 15 Schematic depiction of the different assembly patterns (bottom) observed for benzene trisurea derived PEO-conjugates, which are either governed by the packing parameter (left) or the structural arrangement of the amphiphiles (right). adapted with Permission of ref. ^[193]. Copyright (2020) American Chemical Society.

For the synthesis of SPBs from 1,3,5 substituted benzenes in water, it is, therefore, crucial to maintaining a balance between a favorable packing parameter ($\frac{1}{3} \leq p \leq \frac{1}{2}$), hydrophobic interactions (alkyl chain ≥ 12 methylene units), directional interactions of hydrogen bonds (interaction strength \geq urea groups), and steric restrictions (number of polymer chains < 2).

3. Kinetics of the self-assembly - on the way to size adjustment

Parts of this chapter have been published in: P6) F. V. Gruschwitz, T. Klein, M. T. Kuchenbrod, N. Moriyama, S. Fujii, I. Nischang, S. Hoepfner, K. Sakurai, U. S. Schubert, J. C. Brendel, *ACS Macro Letters*, **2021**, 837-843.

and P7) T. Klein, F. V. Gruschwitz, M. T. Kuchenbrod, I. Nischang, S. Hoepfner, J. C. Brendel, *Beilstein J.* **2021**, submitted.

After evaluation of the prerequisites for the formation of SPBs in water employing 1,3,5-substituted benzenes, it is necessary to focus on the self-assembly process itself, since a fundamental understanding of the kinetics and thermodynamics governing the self-assembly can help to gain control over the aggregation process. This control over size and size distributions would again be beneficial e.g. in biomedical applications where low dispersity and exact particle sizes are desirable.

By simple dissolution in water solely anisotropic morphologies could be obtained for BTU[C₁₂][PEO_{2k}] **3a** and BTP[F][C₁₂][PEO_{2k}] **4c**. However, for supramolecular self-assembly, the possibility of the formation of kinetically trapped structures, which do not represent the thermodynamic equilibrium morphologies, exists.^[11] Especially aqueous media are appealing for the formation of kinetically trapped structures, due to the strong hydrophobic interactions, which result in high kinetic barriers. Switching between equilibrium structures and non-equilibrium morphologies would open up the way to controlled formation of different structures of one building block and non-covalent synthesis would be significantly augmented.^[197] This pathway-dependent self-assembly has already been observed for amphiphilic block copolymers.^[198-199] Strong hydrophobic interactions and slow dynamics of the polymer chains, favor the formation of kinetic products. Even in supramolecular self-assembly, for instance, for perylene dyes, this pathway dependence is observed.^[200] Due to their planar π surfaces, they should self-assemble into 1D aggregates resulting from equal binding constants of both π -surfaces if no steric hindrance by substituents is present. Hereby two aggregation models are possible.^[201-202] Isodesmic growth is characterized by one binding constant for both monomer addition and dimer formation ($k_{\text{nuc}} = k_{\text{elong}}$). The cooperativity factor $\sigma = k_{\text{nuc}}/k_{\text{elong}}$ equals 1. However, for most of the supramolecular systems, the nucleation is disfavored, which means, due to, for instance, crowding of substituents or polymer chains as in the assembly of SPBs, the assembly follows a nucleation-elongation mechanism.^[203] Hereby, a nucleus is formed with a lower association constant k_{nuc} . If the nucleus reaches a certain size, cooperative effects result

in a higher association constant k_{elong} for further monomer addition and the polymerization speeds up ($\sigma \ll 1$). Therefore, in cooperative supramolecular polymerization, an immediate formation of long aggregates besides residual monomer can be observed. Similar to chain-growth characteristics in the synthesis of covalent polymers, no larger oligomers are present in significant quantity. If multiple non-covalent interactions are present, the structure formation is often governed by kinetics rather than thermodynamics. Here, the preparation pathway is determining the structural outcome. By manipulating temperature, solvent, or external stimuli, different metastable or kinetically trapped structures are accessible.^[204-206] Combination of kinetics and knowledge of the thermodynamic landscape of the polymerization enables control over the polymerization to yield kinetic intermediates or even highly defined structures by living supramolecular polymerization.^[207-208] For the supramolecular polymerization of low molar mass compounds, "living" systems featuring size control based on thermodynamics and kinetics have already been reported.^[182, 185-186, 209] However for polymeric building block crystallization-driven self-assembly (CDSA) remains the only viable method to gain control over the size distributions of fibers especially in aqueous environment.^[187, 210-212]

Since the SPBs in this work are based on different types of interaction, like hydrogen bonds and hydrophobic interactions, the anisotropic structures observed e.g. for BTU[C₁₂][PEO_{2k}] **3a** might not be the thermodynamically favored morphologies. Additionally as mentioned in chapter 2.2, BTP[F][C₁₂][PEO_{2k}] **4c** shows the formation of surprisingly shorter SPBs compared to BTP[A][C₁₂][PEO_{2k}] **4a** with decreased interaction strength compared to **4c** due to a lack of β -sheet formation. The hydrophobicity of the phenylalanine substituted benzene core might result in high kinetic barriers in the assembly in water. Since it has already been observed for poly(ethylene oxide) (PEO) modified bolaamphiphile comprising five urea groups that direct dissolution in water significantly limited the aggregation, while a slow transition from DMSO to water resulted in the formation of long SPBs,^[165] this preparation-pathway is transferred to the herein presented systems. BTU[C₁₂][PEO_{2k}] **3a** and BTP[F][C₁₂][PEO_{2k}] **4c** are dissolved in an organic solvent where no aggregation is observed and subsequently a solvent-switch to water is carried out. This solvent switch- or exchange strategy is performed by adding water to the solution of the compound in organic solvent at different addition speeds up to a final water content of 80 v% to evaluate the kinetics of fiber formation (sample are denoted as **BTU solvent** and **BTP solvent**). The remaining organic solvent is removed via dialysis. To carry the influence of addition speed to its extreme, additionally, a "quenching" (denoted as "(qu)") procedure was applied. Hereby, the organic solution of the compounds was directly added into an excess of water, corresponding to a very fast solvent-switch.

For both compounds **BTU 3a** and **BTP 4c**, significantly larger structures can be obtained when performing a solvent switch from THF with a water addition at 1 mL h^{-1} (**BTU/BTP THF 1 mL h⁻¹**) compared to the direct dissolution in water (**BTU/BTP H₂O direct**). This corroborates the hypothesis of trapped structures upon direct dissolution in water (Figure 16A, C, E, and F). The observed fibers for **BTU** and **BTP THF 1 mL h⁻¹** exceed several micrometers in size and thus the linear region of light scattering. This means, the size analysis for structures where $R_g > 80 \text{ nm}$ via Zimm plot of light scattering data with the herein used multi-angle laser light scattering setup is not possible. Nonetheless, it can be said that performing a solvent switch from THF to water, enhances the growth of supramolecular polymer bottlebrushes and thus emphasizes the impact of the preparation pathway on the resulting morphologies. To evaluate the influence of the addition speed of water to the organic solvent, the syringe pump speed was varied from slow (1 mL h^{-1}) to fast (100 mL h^{-1}) water addition. By AF4-measurements and cryoTEM images, a significant decrease in size with increasing addition speed could be proven for **BTP THF 10 to 50 mL h⁻¹** (Figure 16E). For **BTU THF** only minor differences between the addition rates could be observed (Figure 16F). The fastest water addition achieved by the quenching of an organic BTP or BTU solution in water resulted for both compounds in smaller structures, whereby **BTP THF(qu)** exhibited only a fraction of small micellar aggregates and **BTU THF(qu)** still consisted of larger anisotropic structures up to 100 nm in length (Figure 16B and D, and E and F). In contrast to repeatable results for the size distribution of **BTP THF(qu)**, the size distributions of **BTU THF(qu)** were not completely repeatable, and often even larger structures comparable to **BTU THF** at 20 to 50 mL h^{-1} water addition speed were obtained. This already emphasizes the effect of different aggregation strengths on the self-assembly. The less pronounced dependency of **BTU** on the addition rate leads to the assumption of a faster aggregation compared to **BTP**.

Kinetics of the self-assembly - on the way to size adjustment

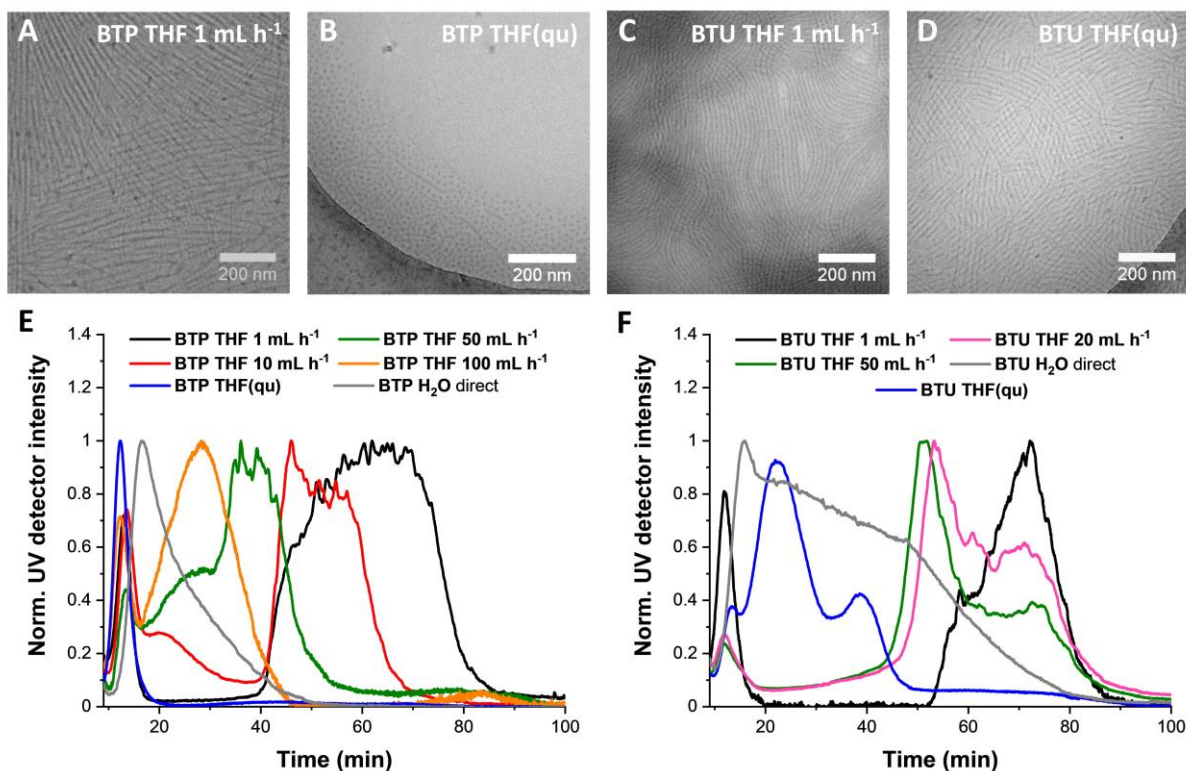


Figure 16 cryoTEM images of A) **BTP THF** 1 mL h⁻¹, B) **BTP THF(qu)**, C) **BTU THF** 1 mL h⁻¹, D) **BTU THF(qu)** ($c = 1 \text{ mg mL}^{-1}$). AF4-UV traces of **BTP THF** and **BTP THF (qu)** (E) and **BTU THF** and **BTU THF(qu)** (F). The injection peaks were omitted for clarity. Adapted with permission of ref.^[213] Copyright (2021) American Chemical Society.

This pathway dependence of **BTP 4c** and **BTU 3a** could also be proven if other solvents than THF were used. Self-assembly via a solvent switch from either acetone, ethanol or DMF to water at 1 mL h⁻¹ resulted in size distributions comparable to THF 1 mL h⁻¹ for both compounds. Nonetheless, for **BTU** a slight difference between THF, EtOH, and DMF, and Acetone could be observed. For THF and EtOH, longer fibers could be obtained. DMF and Acetone favored the formation of decreased fiber lengths, still in the range of several hundred nanometers to micrometers. This indicates that **BTU** might be more sensitive to changes in the solvent than **BTP**.

In AF4-measurements, a fraction of considerable small structures can be detected next to the large aggregates. This might already be a hint that the self-assembly of **BTU** and **BTP** follows a nucleation-elongation mechanism. By monitoring the structure formation via DLS with increasing water addition to an organic solution of **BTP** or **BTU**, a sudden increase in count rate can be noted (Figure 17A and B). This sudden structure formation at a certain threshold water content is indicative of a nucleation-elongation mechanism. Interestingly, the onset of self-assembly of **BTU** and **BTP** is different, starting at 37 or 50 v% water, respectively. The influence of the organic solvent on the onset of aggregation was evaluated by testing DMF.

Here, the assembly starts already at lower water contents of 20 and 15 v% water for **BTP** and **BTU**, respectively. This might be because DMF solvates the compounds slightly worse than THF and thus, even small amounts of water, the poor solvent for the hydrophobic core, lead to a minimization of the exposed surface and initiates nucleation and in the end fiber formation. The faster aggregation of **BTU 3a** in comparison to **BTP 4c** might result from its lower sterical hindrance of the core structure. Due to its benzyl substituents, **4c** needs time for rearrangement to form an energetically favored stacking. The slightly slower aggregation of **BTP** renders it interesting for further research on assembly kinetics. Performing this self-assembly experiment from THF to water for **BTP** while monitoring the stability of the aggregation at certain water contents via DLS showed that at 53 v% of water, the derived count rate increases up to one hour, but then remains constant (Figure 17C). Reaching 55 v% of water, only a slight increase is visible for the first 10 min, whereas for 58 v% water, the count rates remain constant. This indicates an immediately completed assembly at water contents > 55 v%. By changing from THF to DMF, again the subtle influence of the choice of solvent can be proven since with DMF the assembly of **BTP** at 20 to 27 v% water shows no time dependency and immediate structure formation. To elucidate whether some intermediate morphologies can be observed in the structure formation of **BTP DMF**, SAXS measurements at certain DMF/H₂O ratios were conducted (Figure 17D). The absence of aggregation below water contents of 23 v% could be proven. At water contents ≥ 23 v%, immediate formation of cylindrical aggregates can be detected due to the q^{-1} dependency at low q -values. This means there is no intermediate spherical phase in the self-assembly process. Increasing the water content further leads to no increase in the cylinder radius, meaning that the number of **BTP** molecules inside the fiber, which was determined to be two, stays the same throughout the whole assembly process (Figure 17E).

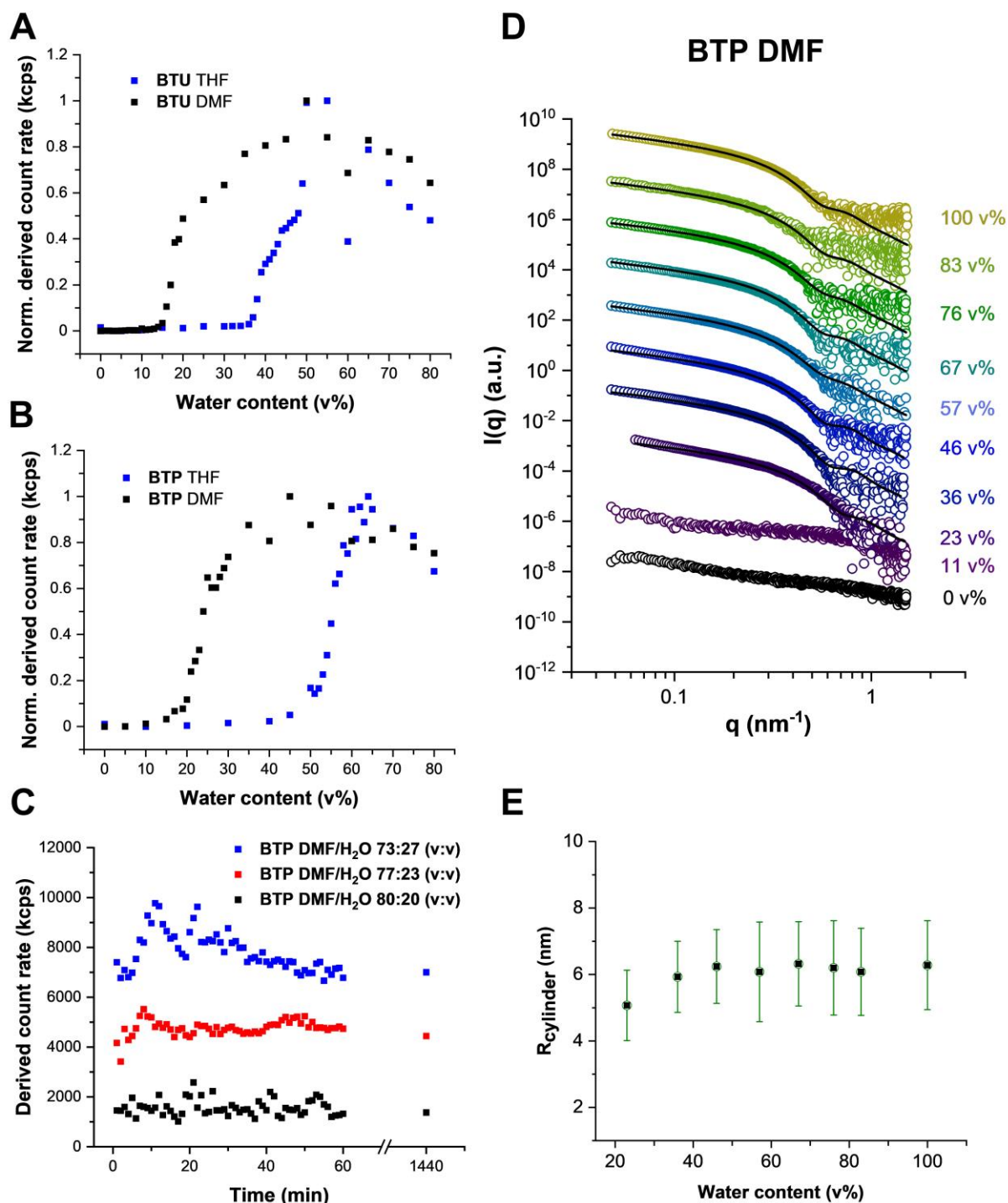


Figure 17 DLS measurements of the solvent switch procedure at different water contents. The compound was molecularly dissolved in THF or DMF and water was slowly added. The count rate was determined for each solvent mixture composition and plotted versus the water content for A) **BTU DMF** (black), and **BTU THF** (blue), and B) **BTP DMF** (black), and **BTP THF** (blue). C) Time-dependent evolution of derived count rates for **BTP THF** at 53, 55, and 58 v% water. D) SAXS scattering profiles of **BTP DMF** (dots) and the respective cylinder fits (lines) for different water volume contents. The traces were shifted by multiplication for reasons of clarity. E) Evolution of the cylinder radius with increasing water content, obtained from the respective cylindrical fits. Adapted with permission of ref.^[213] Copyright (2021) American Chemical Society.

Further insights into the structural changes upon self-assembly of **BTP** could be gained by employing circular dichroism (CD) at specific water/THF ratios (Figure 18B). At high THF

contents, a pre-aggregation into left-handed helical structures due to the hydrogen bonds can be observed.^[214-215] However, this pre-aggregation does not seem to form large aggregates since the count rate in THF is rather low as proven by DLS measurements. The good solubility in THF enables a relatively free orientation of the attached polymer chains in the small stacks according to their steric demands (Figure 18A). Increasing the water content, the hydrophobic parts of the molecule are shielded, favoring an additional lateral aggregation which is accompanied by the inversion of the helicity. The lateral aggregation at critical water content forces the chains of the individual stacks to point in similar directions. To maintain the hydrogen bonds, the helical structure in the individual stacks has to be rearranged during the hydrophobic assembly finally resulting in the right-handed helix in aqueous solution. Surpassing a water content of 60 v%, an irreversible 1D growth of the structures to long fibers featuring cooperative characteristics can be observed. Therefore it can be concluded that the hydrogen bonds seem to induce a pre-aggregation of a few BTP units into very small aggregates but with increasing water content, the hydrophobic effect becomes the predominant driving force in this assembly, inducing the strong cooperativity.^[216-218] This hypothesis is further supported by the fact, that the addition speed of water does not influence the aggregation onset. Nevertheless, the hydrogen bonds introduce the directionality needed for 1D growth, once critical nuclei sizes are reached, and define the local arrangement of the molecules. This aggregation and increasing hydrophobic shielding of the core can also be visualized by ¹H-NMR measurements,^[219] where the aromatic proton signals shift and adjacent signals appear until all signals start to vanish with increasing water content (Figure 18C)

Kinetics of the self-assembly - on the way to size adjustment

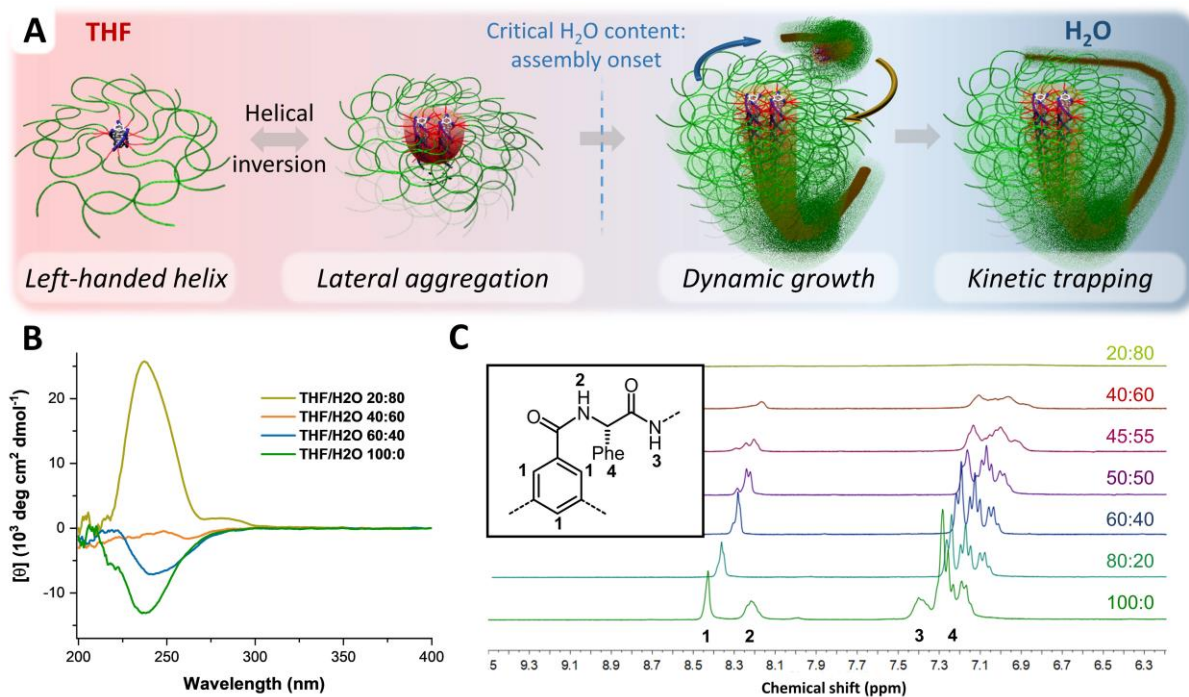


Figure 18 Schematic depiction of the self-assembly process of **BTP** upon changing from THF to H₂O (A). CD-measurements of **BTP** in THF:H₂O (v:v) mixtures (B). ¹H-NMR measurements of **BTP** in different solvent compositions (v:v d₃-THF:D₂O), where the hydrophobic shielding of the aromatic units of **BTP** can be visualized by the vanishing of the respective signals with increasing D₂O content (C). Adapted with permission of ref.^[213] Copyright (2021) American Chemical Society.

Since the nucleation-elongation mechanism of the self-assembly can possibly be exploited in a seeded-growth approach to yield particles with small dispersity,^[179, 220] the addition of further BTP to a solution of **BTP THF(qu)** was tested. At low THF content (~ 10 v%), no growth of the structures could be observed but additional small quenched structures, corroborating the trapped state of the aggregates. However at a THF content higher than the initial composition where aggregation starts (32 v% THF) a small shift to larger sizes can be noted (Figure 19A). This correlates with the expectations for a seeded growth mechanism. However, a competing aggregation process can be measured featuring much larger structures. Similarly, the addition of pure THF to the sample **BTP THF(qu)** also results in an increase of size when THF concentrations of 32 v% of THF are reached (Figure 19B). That means, the system is kinetically trapped at lower THF content and the growth at the chain ends is impeded which we assume is related to an increased shielding from the water and thus limited accessibility for further addition of unimers.^[221] At higher THF contents above the solvent composition at the initial aggregation point, the dynamics of the system are increased and further growth is enabled resulting in broad size distributions. The addition of more THF (≥ 58 v%) finally results in the disassembly of all aggregates (Figure 19C). Since at high THF contents also high dynamics are present, a living growth as observed for other systems is not feasible.^[179, 220]

Kinetics of the self-assembly - on the way to size adjustment

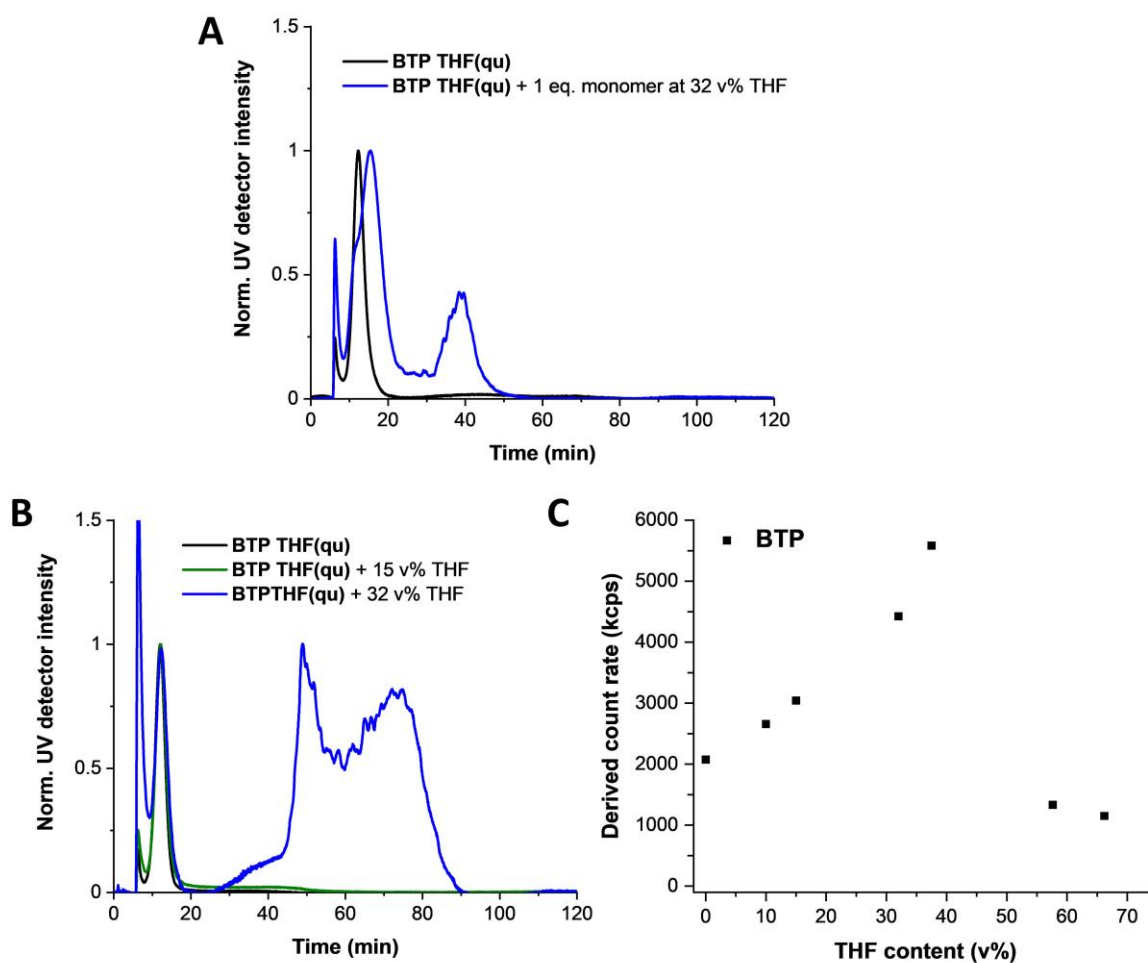


Figure 19 AF4-UV traces of **BTP THF(qu)** after addition of further BTP in THF at the specified THF content (A) and AF4-UV traces of **BTP THF(qu)** after addition of THF (B). The THF was evaporated subsequently and the concentration was adjusted to approx. 1 mg mL^{-1} by addition of water for each sample. DLS measurement of the count rate of **BTP** in solution dependent on the THF content (C). Adapted with permission of ref.^[213] Copyright (2021) American Chemical Society.

The kinetic trapping of **BTU** and **BTP** in water furthermore enables great long-term stability of the formed structures. Via DLS the stability of the formed aggregates could even be monitored over one year and no change in the correlation curves was observable. Apart from that, mixtures of small and large structures stay intact over time as observed in AF4-MALLS and the exchange of unimers is hindered. Therefore, it can be concluded that in water stable and especially defined structures are obtained.

In contrast to the utilization of pathway complexities and especially kinetically trapped morphologies, top-down methods, for instance, ultrasonication are suitable to target structures of intermediate sizes (100 nm – 500 nm), which are often required for application of such fibrillary structures in e.g. biomedical applications.^[222]

Employing the longest structures formed by **BTU THF** 1 mL h^{-1} and exposing them to strong shear forces arising from ultrasonication (US) results in the fragmentation of the structures into smaller fibers dependent on the strength (or amplitude) and period of US. Already after short

sonication times of 1 s at 200 W, a strong decrease in size can be observed in AF4 measurements (Figure 20A). The peak maximum at 80 min decreases and shifts to lower elution times. Additionally, a new peak is formed at 10 to 20 min resulting from small oligomeric particles. From this trend, we assume that, besides the fragmentation, the US shears off small oligomers from the ends of the SPBs. With increasing US times, the length distribution becomes narrower once again and is shifted further towards lower elution times corresponding to smaller aggregates. After 30 s of US, small fibers with lengths of approximately 100-150 nm can be observed in cryoTEM (Figure 20B). Apart from this method, which mostly results in structures of approx. 100 nm, dual asymmetric centrifugation (DAC) can be used to tune the length of the aggregates. Due to the second rotation of the sample, besides a rotation of the main rotor, a continuous change of the direction of the centrifugal field is obtained thus resulting in harsh forces. The generated shear forces can fragment dispersants such as these supramolecular assemblies. By varying the speed (2500, 1000, and 500 rpm) and time (1, 5, 10 min, and 3 h) the influence of dual asymmetric centrifugation on the size distributions can be assessed (Figure 20C and D). For assemblies of **BTU THF 1 mL h⁻¹**, high centrifugation speed results in the formation of small structures comparable to US times of > 30 s. The resulting distributions, however, are slightly narrower compared to the ones obtained from a US procedure. Apart from that also gentle centrifugation speeds (500 rpm) can be used to obtain slightly bigger structures, however, the resulting distributions are very broad and feature even bimodal characteristics.

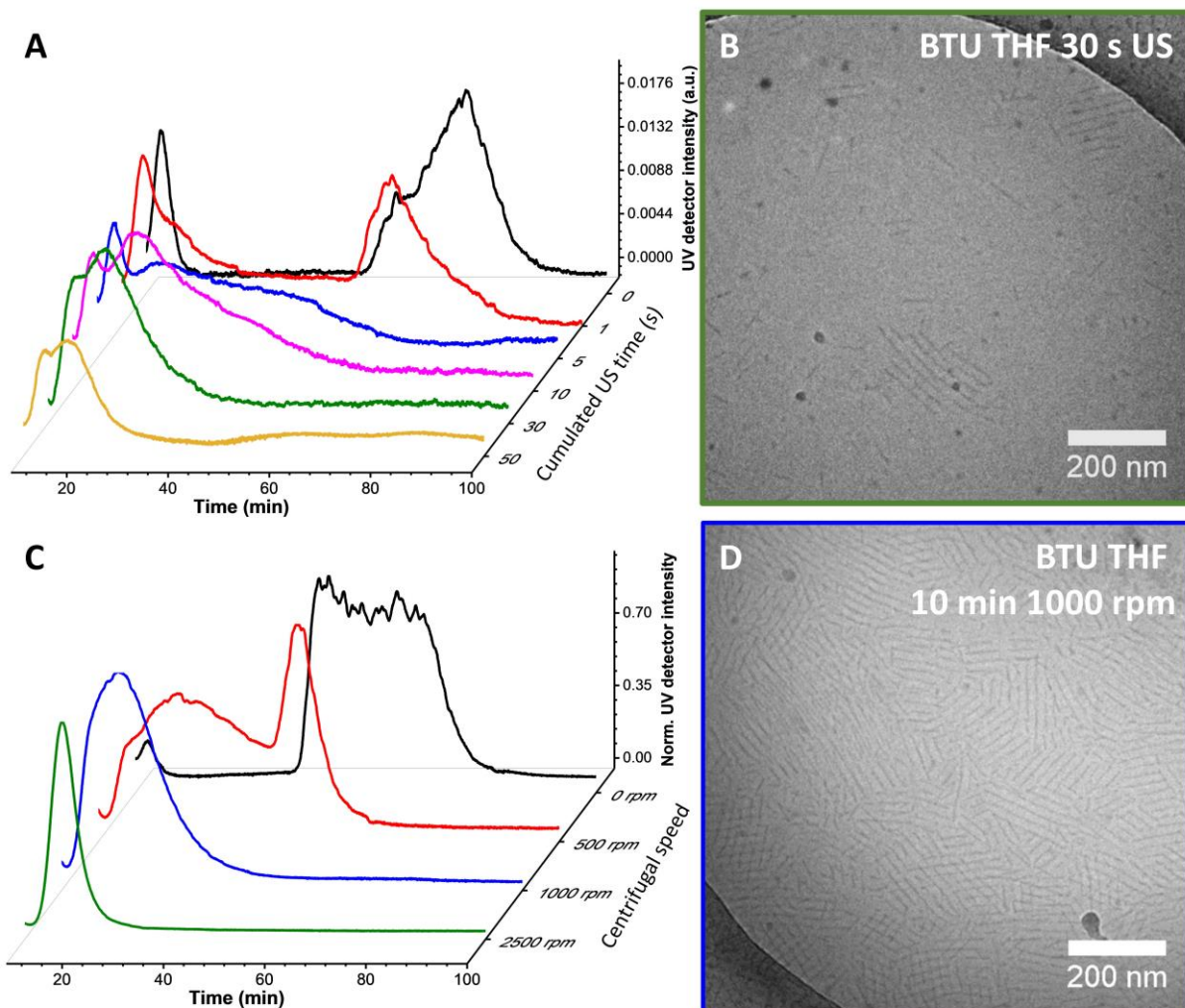


Figure 20 AF4-UV Traces of **BTU THF 1 mL h⁻¹** after 0 to 50 s ultrasonication (200 W) and **BTU THF 1 mL h⁻¹** after 10 min of dual asymmetric centrifugation at 2500, 1000, and 500 rpm. (C) The injection peaks were omitted for reasons of clarity. CryoTEM images of **BTU THF 30 s US** (B) and **BTU THF 10 min DC 1000 rpm** (D) ($c = 1 \text{ mg mL}^{-1}$).

Due to the kinetic entrapment in water, similar to the high aspect ratio structures obtained from **BTU THF**, these small structures resulting from US or DAC treatment exhibit remarkable stability in water over long times. Nonetheless, the control over size distributions of these supramolecular polymer bottlebrushes is still far away from living/controlled polymerizations known for supramolecular polymers of low molecular weight building blocks.^[181, 208] Control over the length of the assemblies of amphiphilic polymers, in contrast, is still a challenge.^[11, 179] Crystallization-driven self-assembly (CDSA) remains the only viable method to gain real control of the fiber length. Nevertheless, particularly aqueous systems are scarce.^[45, 223] So the herein presented utilization of pathway complexities and top-down approaches may be a legitimate try to adjust the size range of the formed structures from micrometers to several nanometers and from aspect ratios of 100 to micellar structures to render these SPBs suitable, for instance, in biomedical application.

4. Formation of dynamic hydrogels by crosslinking of SPBs

Parts of this chapter have been published in: P8) F. V. Gruschwitz, F. Hausig, P. Schüler, J. Kimmig, D. Pretzel, U. S. Schubert, S. Catrouillet, J. C. Brendel, *Adv. Func. Mater.* **2021**, submitted.

In the solvent exchange experiments (Chapter 3), very large fibers of several micrometers could be observed e.g. for **BTU THF**. Surprisingly, these fiber-containing solutions are still liquid at a concentration of 1-3 mg mL⁻¹. Typically, low molar mass substances forming similar fibers by intermolecular hydrogen bonds are known to gel solutions at such concentrations which is related to entanglements between the supramolecular nanofibers. Therefore, these substances are referred to as low molecular weight gelators (LMWG) which are commonly based on peptides,^[224-228] π -gelators^[229] or ureas.^[230-231] In contrast to covalently-linked networks,^[232] which are often static and quite restricted, supramolecular hydrogels feature dynamics and even self-healing abilities. The basis for gelation in fibrillary hydrogels is often the formation of entanglements, bundling, or branching.^[233] Apart from the aforementioned LMWG, also worm-like micelles obtained by block-copolymer self-assembly can form such hydrogels at higher concentrations (~ 10 wt%) due to entanglement.^[38, 234-238] In contrast to LMWG, the brush structure of worm-like micelles features several advantages, as stimuli-responsiveness and the possibility for additional functionalization of the polymer shell.^[38, 239-243] The synergistic effects of both supramolecular polymers and worm-like micelles could be incorporated into hydrogels by employing supramolecular polymer bottlebrushes. A combination of the dynamics observed for LMWG with the functionalities of worm-like micelles paves the way to dynamic, responsive, yet stable gels bearing different functionalities. First studies in this area have already been conducted.^[86, 244-245] Nonetheless, high concentrations ~ 10 wt% are necessary, or the system is limited to oligomer chains instead of a brush-structure originating from polymeric building blocks. Stimuli-responsiveness and the possibility of degradation due to supramolecular erosion could render these gels especially suitable for the application in nanomedicine,^[86, 168, 246-247] e.g. as injectable hydrogel drug reservoir^[168, 170, 172, 244, 248-250]

To obtain hydrogels from SPBs, the concentration necessary for the entanglement of the BTU nanofibers was assessed by inverted vial tests. Only at concentrations > 20 mg mL⁻¹ of BTU fibers obtained from the previously explained solvent switch method (**BTU THF**) showed the formation of a self-supporting gel. In comparison to LMWG which can already gelate at concentrations of 1 mg mL⁻¹,^[251] this is extremely high. The overlap concentration for the SPBs of e.g. 1 to 3 μ m (diameter 10 nm), however, was calculated to be in the range of 0.5 to

0.05 mg mL⁻¹. This means that the fibers are remarkably stiff and do not tend to entangle easily since the concentration of gelation and thus pronounced entanglement is 400 times higher. A reason for that might already be the highly hydrated polymer corona of the SPBs. Due to steric constraints and repulsion between individual fibers, an entanglement will be prevented at low concentrations. Rheological measurements will be used to gain further insight into the interactions between the fibers. Frequency-sweep measurements of the 25 mg mL⁻¹ **BTU** gel exhibit a plateau with a storage modulus G' of 10 Pa which is typical for the entanglements of the supramolecular polymers (Figure 21B green curve). Due to the supramolecular nature of the SPB fibers, the gel is furthermore responsive to stress. Upon applying certain stress onto the material, the fibers deform and break. The storage modulus drops to about 16% of its initial strength and the gel liquefies (Figure 21C). When removing the applied deformation the gel recovers immediately (< 5 s) to its initial gel strength. This memory effect can be repeated many times without a loss of strength. This effect may be based on the rupture of the supramolecular interactions upon deformation and subsequent formation of “active chain ends”. Due to the hydrophobic effect, these ends reassemble as soon as the stress is relieved. Since the gel strength is recovered to 100 % each cycle, nearly every active chain end will re-assemble again. This property features a great potential for the application for instance in nanomedicine.^[244-245, 252-253] However, the strength of a gel consisting of pure BTU-PEO fibers is rather low. A strategy to increase gel strength is to introduce a higher degree of crosslinking by the addition of a bifunctional crosslinker, consisting of a PEO chain of 20 kD and BTU endgroups, before the solvent switch (Figure 21A).^[22] By incorporation of the endgroups of the crosslinker in two distinct nanofibers, the number of crosslinking points increases, the network gets denser, and thus the moduli rise. Combining the entangled fibers of BTU **3a** with just 1% of crosslinker **6a** at an overall concentration of 25 mg mL⁻¹, the strength of the gelation can significantly be improved while still preserving the stress-responsiveness and self-healing behavior (Figure 21B and C black curve). Even the pure crosslinker **6a** features gel properties, however, its response to stress results only in a limited shear-thinning compared to the mixture (Figure 21B and C gray curve).

Formation of dynamic hydrogels by crosslinking of SPBs

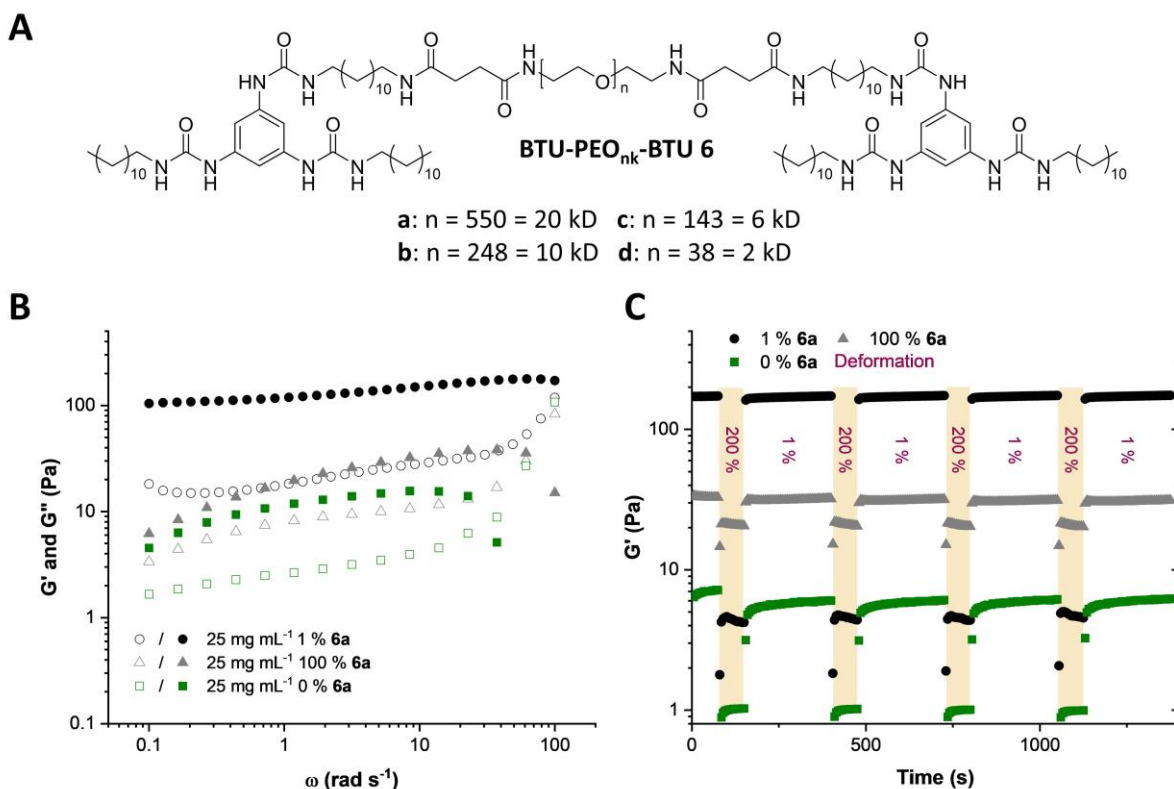


Figure 21 Chemical Structure of **BTU-PEO_{nk}-BTU 6** (A). Frequency-sweep (B) and step-strain measurements (C) of **3a** (green), **3a** with 1% **6a** (black) and **6a** hydrogels at a concentration of 25 mg mL⁻¹.

This gel containing 1% **6a** at 25 mg mL⁻¹ is already very stable and can be easily shaped and structured. Via a molding technique compact gel structures can be obtained, that keep their form on a glass slide for more than an hour at which point severe drying is observed. It is also possible to cut and rearrange the gel. Additionally, even if the gel is immersed in water no degradation, swelling, or changes in rheological properties can be observed even after weeks. The gel formation also tolerates THF contents up to 33 v% which do not alter the mechanical properties to great extent. Even very acidic (pH 2) and basic media (pH 11), the presence of salt and serum proteins are tolerated and still very stable gels are obtained. This again holds great potential for an application *in vitro* and *in vivo*. However, the most important factor for future application in a cellular environment is to ensure biocompatibility. The biocompatibility of a gel of **3a** with 1% **6a** at 25 mg mL⁻¹ was checked by incubation with L929 cells over 24 h and calculation of the cell viability via PrestoBlue assay. By testing two preparation procedures, one where first the gel was placed in the well and then the cell suspension was added (preparation way 1) and one where the gel was added later to the cell suspension (preparation way 2) an influence of the preparation procedure is distinguishable. Generally, the gel seems to be non-toxic since viabilities of 81 % and 96 % could be estimated for preparation way 1 and 2, respectively. The difference might be attributed to the lower amount of space on the bottom of the well or cells

being trapped in the gel when seeded if preparation way 1 is used. Due to the PEO-functionalization of the gel, a stealth behavior is expected, meaning no cells will adhere to the gel. This was proven in microscopy images of gels incubated with L929 cells for 24 h. As expected no cells could adhere to the PEGylated gel structure however already at the border of the gel, cells could be detected proliferating without any signs of detrimental effects on the bottom of the well. It can be concluded that high biocompatibility is ensured. The suppressed interaction of the cells with the gel further opens up the opportunity for selective and controlled cell adherence if specific ligands or binding motifs are introduced. This is already an interesting fact for further research on structured cell scaffolds, which might be accessible by further functionalization of this hydrogel system as already shown for LMWH.^[71]

For the application of this hydrogel as a cell scaffold or as a drug delivery reservoir, additionally to good stability and biocompatibility, the prerequisites for the diffusion of substances in the gel should be given. Pulse-field gradient NMR spectra were recorded to get an impression of the diffusion of macromolecules in the gel. Poly(ethyl oxazoline) (PEtOx) of different molar masses were incorporated in the pure BTU gel (**3a**, 25 mg mL⁻¹) and the crosslinked BTU gel (**3a** + 1% **6a**, 25 mg mL⁻¹) while the assembly process. By comparison of the free diffusion coefficient D_0 of the PEtOx in water to the diffusion coefficient D of PEtOx in the gel, strong retardation, however, no complete trapping can be observed for PEtOx in both gels. This might result from the highly hydrated brush structure where the PEO chains of the SPBs extend far into the water and prevent the free diffusion along the network pores of the PEtOx significantly. Additionally, this diffusion was monitored by measuring the fluorescence intensity of gels covered with water (Figure 22). TRITC-labeled dextrans were incorporated into the gel while the assembly process, similar to the PEtOx polymers in PFG-NMR experiments, and the time-dependent increase of the fluorescence intensity in a supernatant aqueous solution was measured (Figure 22A).^[254] In the first minutes, a fast release is detected, where presumably the probe molecules at the outside of the gel or in close contact with water are measured. After several hours the release is slowed down. By fitting an exponential model, a similar exponent could be calculated for all dextran sizes, meaning the same diffusion mechanism independent of the size of the probe molecule can be expected. This slow release over days is already favorable for the application in nanomedicine to ensure delivery of active pharmaceutical ingredients over larger time scales at a constant level. Apart from large molecules also small substances can be incorporated into the gel, however, their release is much faster. Employing the sodium salt of fluorescein as a probe molecule, an exponential function can be fitted with

Formation of dynamic hydrogels by crosslinking of SPBs

an exponent of 0.5 resembling a Fickian diffusion (Figure 22B). A 100% release, meaning an even distribution of the probe in the whole cuvette volume, is achieved after 80 h.

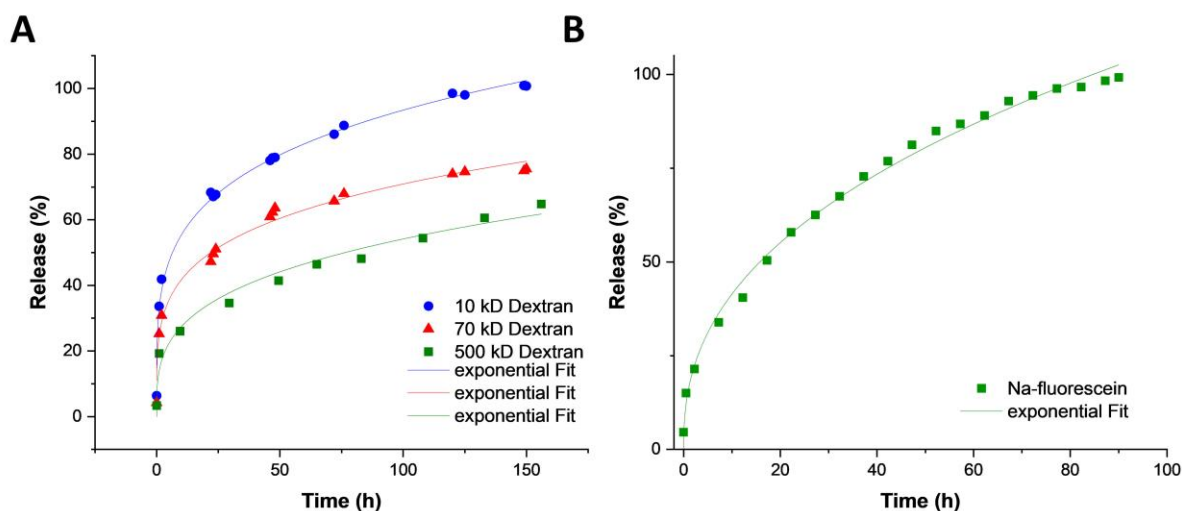


Figure 22 Diffusion kinetics of TRITC-dextran of different molar mass (A) and Na-fluorescein (B) in gels of **3a** with 1 % **6a** at 25 mg mL⁻¹ followed by fluorescence spectroscopy.

Application of such hydrogel in the cellular environment requires apart from biocompatibility, stability, and the possibility of diffusion additionally a careful design of the mechanical properties. Elasticity and surface modification can influence cell attachment and proliferation. In the herein presented versatile system, several parameters can be altered to tune the rheological behavior. Since already 1 % of an additional crosslinker yielded significantly stronger gels, the influence of the crosslinker content on the gel strength was tested (Figure 23A). In frequency-sweep measurements of gels at 25 mg mL⁻¹ with different amounts of 20 kD crosslinker **6a** a maximum strength can be observed for gels with 10 % crosslinker. Higher crosslinker contents lead to the formation of micellar aggregates and increased backfolding, as already observed for other supramolecular gel systems.^[244] Additionally, the length of the linker can be varied to tune the mechanical properties of the hydrogel (Figure 23B). Frequency sweep measurements of the gels at 25 mg mL⁻¹ and 1 % of crosslinker revealed, that a decrease of the linker length from 20 (**6a**) to 10 kD (**6b**) already decrease the gel strength. The lower probability of incorporation of the crosslinker in two distinct fibers if the crosslinker is shorter might be the reason for this. Two fibers would need to get into closer proximity which is unfavorable due to the PEO corona. Surprisingly, this decrease in crosslinking probability can already be observed for crosslinker lengths which are still 5 times the size of the PEO corona (2 kD) of the SPB. This correlation is further emphasized when even smaller crosslinkers of 6 kD (**6c**) and 2 kD (**6d**) are used. Since two nanofibers equipped with a 2kD PEO corona will not get in close proximity for crosslinker **6d** to link them, very weak

Formation of dynamic hydrogels by crosslinking of SPBs

gels are obtained. This means backfolding of the PEO chain of the crosslinker will be favored. Another often used parameter to tune the gel strength is the concentration. If the concentration of the hydrogel is increased, a strong increase in storage and loss modulus can be observed, due to an overall higher number of fibers (Figure 23C). Therefore, also an increasing number of entanglements and crosslinks in the network can be expected which further enhances the overall gel strength. Interestingly, a plateau is reached at a concentration of 50 mg mL^{-1} . Therefore the optimum composition for the strongest gel of this system with a storage modulus of around 1 kPa could be observed for a gel with a concentration of 50 mg mL^{-1} and 10 % crosslinker **6a** (Figure 23D).

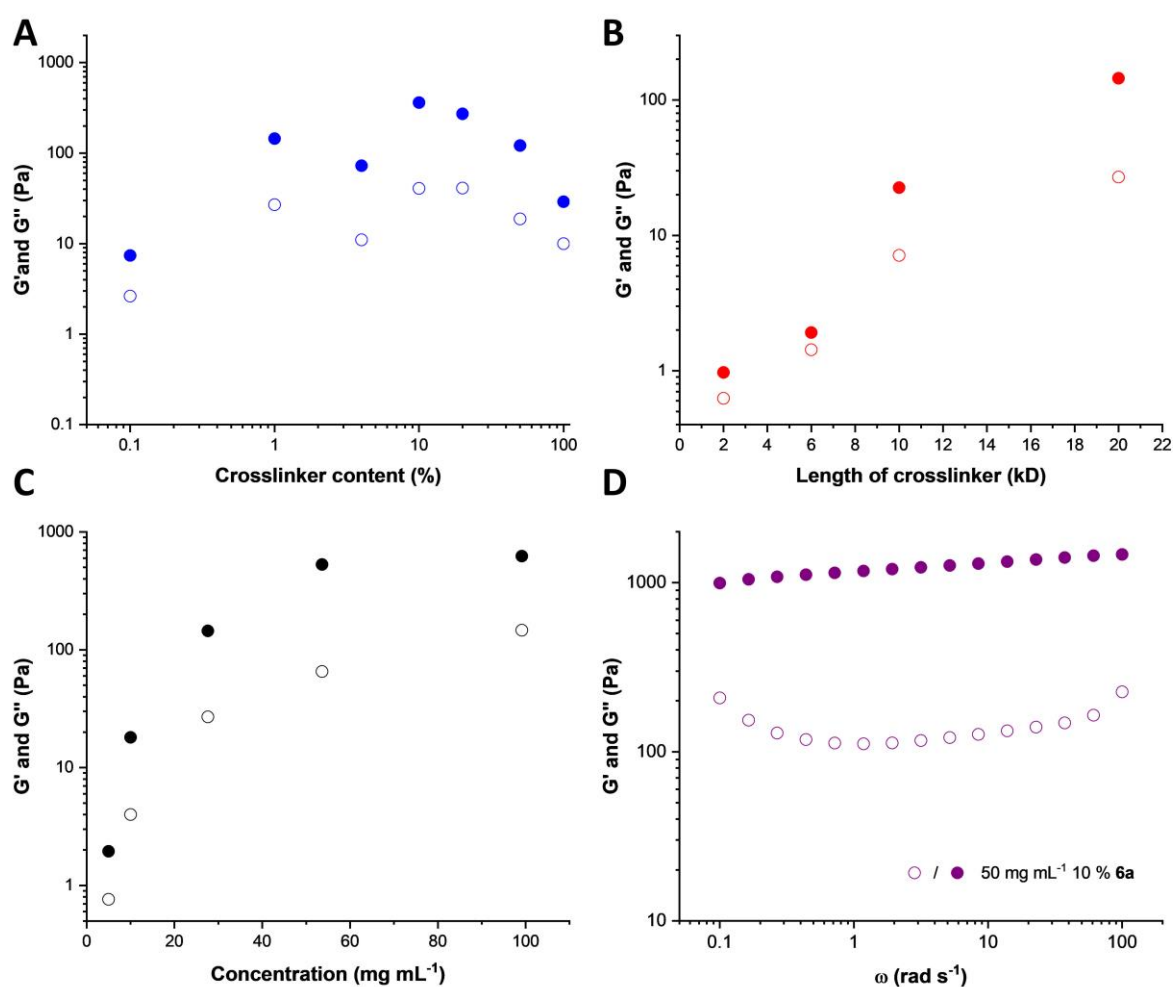


Figure 23 Plateau modulus of hydrogels with different amounts of crosslinker **6a** ($c = 25 \text{ mg mL}^{-1}$) (A), plateau modulus of hydrogels with 1 % crosslinker of different lengths ($c = 25 \text{ mg mL}^{-1}$) (B), and concentration-dependent plateau modulus of hydrogels with 1 % of **6a** crosslinker (C). Frequency-sweep measurement of a hydrogel of **3a** with 10 % of **6a** at 50 mg mL^{-1} (D).

As already observed for gel **3a** with 1 % **6a** at 25 mg mL^{-1} , the gel features stress-responsiveness with self-healing characteristics, due to the supramolecular nature of the fibers. This dynamic behavior could be observed in step-strain measurements of all gel compositions. The gel

consisting of **3a** + 10% **6a** at 25 mg mL⁻¹ features the highest ratio between G' at high and low strain, respectively, giving a factor of 90 in step-strain measurements while recovering < 5 s. On the contrary, the gel formed by the pure crosslinker **6a** reveals only a factor of 1.5 in such experiments and the weak gel formed by pure **3a** gives only a factor of 6. The significant enhancement therefore nicely corroborates the synergistic effect the few crosslinks induce for the shear-thinning behavior of these supramolecular gels. Strong shear-thinning behavior can be observed by evaluation of the proportionality of the shear rate $\dot{\gamma}$ on the resulting shear stress σ . This is exemplarily shown for a gel of **3a** with 1 % **6a** and the non-crosslinked gel **3a** (Figure 24D). The viscosity decreases to a factor of 10 lower values for non crosslinked gel **3a** compared to the gel of **3a** + 1% **6a**. At low shear rates of 0.01 s⁻¹, gels containing crosslinker **6a** showed viscosities > 10⁴ Pa s. However, increasing the shear rates to 1 s⁻¹ the viscosity drops to values < 50 Pa. This makes the gel applicable as injectable hydrogel since the thinning behavior limits the resulting shear stress and for instance, reduces the formation of hematoma at the injection site and facilitates subcutaneous injection.^[244, 247] Sufficient strength, pronounced shear-thinning properties, rapid recovery after stress relief and high stability distinguishes these supramolecular polymer brush gels from many other presented systems. A unique set of properties opens up the opportunity to simply extrude the gel out of a syringe or a nozzle followed by immediate reinforcement without the need for any additional trigger or reaction in this process. Such characteristics simplify the design of injectable drug reservoirs or 3D printing of hydrogel scaffolds since also heat-sensitive materials such as cell-loaded polymers can be processed.^[255-262] With a simple modification a commercial 3D printer can be employed to print prototypes. Starting by printing straight single lines of the gels with 1 % **6a** at 10, 25, and 50 mg mL⁻¹, it could be seen that for the highest concentration of 50 mg mL⁻¹ it was not possible to print a continuous line at a syringe pump speed of 10 mL/min (Figure 24A). The viscosity of such concentrated gel solutions, even at increased shear rates, was too high and leads to clogging of the capillary at some moments. With lower concentrations of 25 and 10 mg mL⁻¹, no clogging and smooth extrusion could be observed. For both gels, the viscosity at the apparent shear rate is low enough to facilitate the extrusion through the nozzle. Apart from a good extrusion through the needle, the gel should reform immediately after the needle tip, meaning the gel should exhibit no or weak thixotropy to form defined structures. Additionally, the formed structures should be stable, implying the gel to be of a certain strength. These prerequisites are met by the gel with 1 % crosslinker **6a** at 25 mg mL⁻¹. Due to its suitable balance between shear-thinning and mechanical strength at zero stress, defined lines could be printed. Since the gel recovers directly after the needle tip, thin lines and even the printing of

Formation of dynamic hydrogels by crosslinking of SPBs

lines on top of each other are feasible. By this approach, even a hollow self-supporting cylinder could be printed as a proof of concept (Figure 24B). Additionally, “non-round” structures, such as stars, were printed to prove the variability of the 3D printing approach (Figure 24C). This processability of the gels in 3D printing methods could pave the way for a future application e.g. as a bioscaffold for tissue engineering.^[256, 260, 263-264]

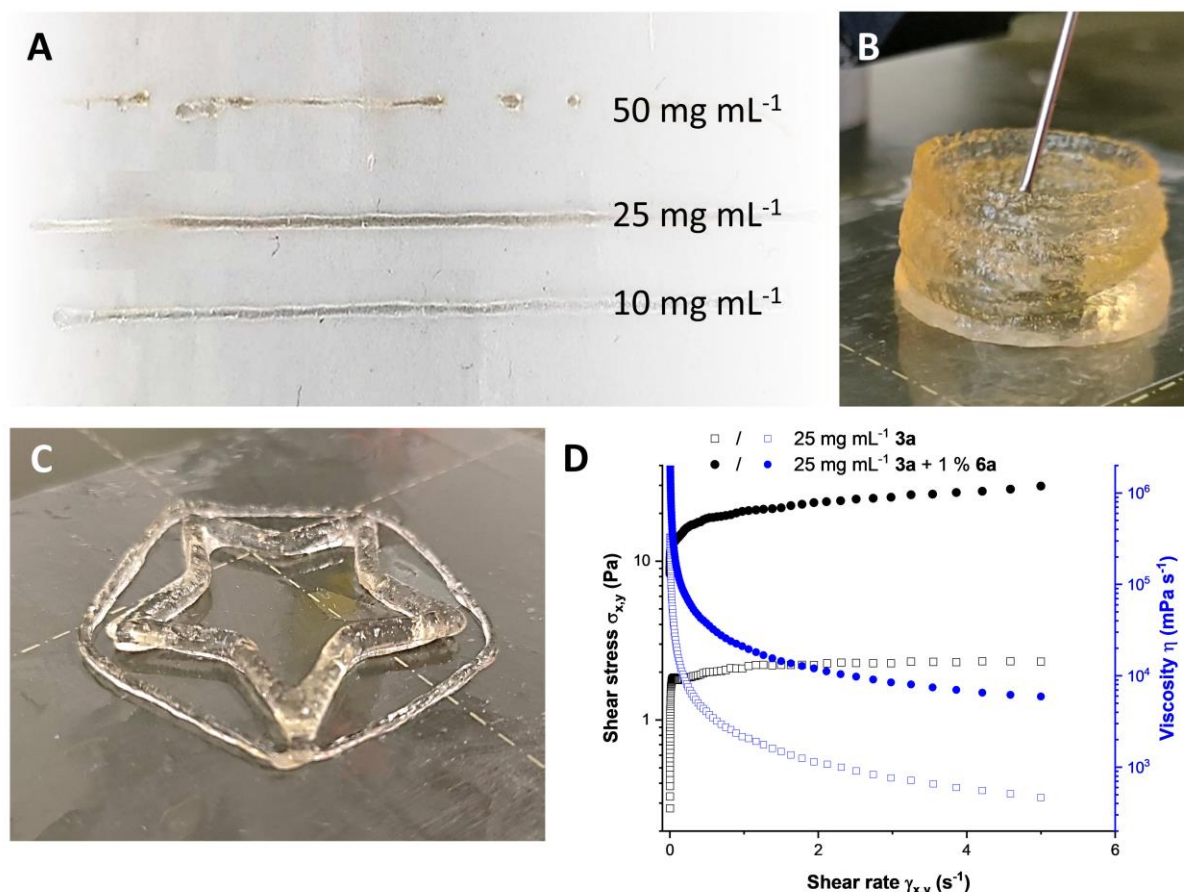


Figure 24 Printed straight lines of 50, 25 and 10 mg mL⁻¹ gels of **3a** with 1 % **6a** (A). 3D printed hollow cylinder with a gel of **3a** with 1 % **6a** ($c = 25$ mg mL⁻¹) (B). 3D printed star with a gel of **3a** with 1 % **6a** ($c = 25$ mg mL⁻¹) (C). Shear stress and apparent viscosity of gel **3a** and **3a** with 1 % **6a** ($c = 25$ mg mL⁻¹) (D).

In conclusion, hydrogels from SPBs have shown to be of excellent stability and tolerate the presence of organic solvents, salts, and even proteins. Their shear-thinning and highly dynamic characteristics in combination with biocompatibility render them to be interesting candidates for 3D printing methods to obtain, for instance, scaffolds for 3D culture or tissue engineering. Due to the resemblance of fibrillary hydrogels to the extracellular matrix (ECM), the incorporation of cells into the gel may lead to further advances in this area of research.^[233, 265] Here, the brush-structure bears significant advantages as already shown for block-copolymer worm-like micelles that have been applied in the culture of human pluripotent stem cells and lung epithelial cells.^[242, 266-267] Further advantages from fibrillar hydrogels of LMWG, as

Formation of dynamic hydrogels by crosslinking of SPBs

improved mass transport, compared to molecular hydrogels, and the easy functionalization with e.g. growth factors and cell-adhesive ligands renders supramolecular polymer brush gels applicable for future research on biocompatible and even biomimetic hydrogels.^[233] However, the effect of the nanoscale structure on stress relaxation remains elusive so far. Apart from that, further research has to be conducted on functionalized SPB hydrogels to improve cell adhesion and proliferation. Nonetheless, their responsiveness, stability, and biocompatibility pave the way for further interesting research and application possibilities.

5. Summary

Inspired by the complexity in nature's molecular assemblies, scientists thrive to transfer these concepts to the field of synthetic chemistry. By employing supramolecular chemistry, dynamic materials of different size and shape, however mostly lacking the complexity found in nature, are accessible. Nature's ability to organize macromolecular building blocks into hierarchical 1D structures inspired chemists to employ an interplay between polymer science and non-covalent synthesis to generate various anisotropic supramolecular polymeric systems with interesting properties, such as stimuli-responsiveness and a dynamic character. One way to form 1-dimensional, supramolecular polymer structures, is to employ weak directed interactions such as hydrogen bonds.

This thesis aimed to evaluate the prerequisites for the formation of supramolecular polymer bottlebrushes (SPBs) via the self-assembly of 1,3,5-benzene trisamides (BTA) equipped with polymer chains in water (Figure 25 lower left). To do so, the influence of interaction strength between the self-assembly units, the hydrophobic shielding, and the hydrophilicity of the polymer exterior was evaluated. Here, the strong effect of the packing parameter and thus the hydrophilic/hydrophobic ratio of the building block could be observed. Increasing the hydrophobic part by employing a larger alkyl spacer of 12 methylene units, the aggregation obtained for the assembly of BTA could not be shifted to a pure fiber morphology phase. The necessity of an increased number of hydrogen bonds could be proven for the formation of SPBs if a PEO chain of 2kD is attached to the self-assembly motif. To do so, urea groups have been employed instead of amides, to overcome the strong influence of the packing parameter. Larger PEO-chains shifted the morphology again to micellar phases or even the dissolution into unimers in solution. Changes in the structural appearance of the amphiphiles by incorporation of an increased number of polymer arms resulted in isotropic morphology phases, too. The steric constraints and increased hydrophilicity could only be counterbalanced by an increased number of hydrogen bonds. Solely, benzene trisureapeptides (BTUPs) have shown the formation of columnar aggregates even if 3 polymer chains were attached.

Furthermore, the assembly mechanism of the resulting SPBs and the possibility of employing kinetic control over the system to tune the resulting sizes of the SPBs were examined (Figure 25 upper left). The hydrophobic effect, which is beside the hydrogen bonding the main driving force for the self-assembly, often leads to the formation of kinetically trapped states and pathway-dependent morphology phases, whose presence could also be proven for the herein presented system. By employing a solvent-switch method, where water was added slowly to

Summary

organic solutions of BTU and BTP to induce self-assembly, micrometer-sized fibers could be obtained. The size of the fibers could be adjusted dependent on the water addition rate (Figure 25 upper right). By increasing the addition speed smaller structures could be synthesized. The smallest structures featuring micelles for BTP could be generated by utilizing a quenching method, where the organic solution of the building block was immersed into an excess of pure water. However, employing the solvent switch method, mostly broad size distributions were obtained. A real living assembly of these SPBs to form fiber distributions with low size dispersity is therefore still beyond reach. Nonetheless, controlling the processing parameters to adjust the length of these SPBs, paves the way to a straightforward synthesis of tailored 1D polymer assemblies, which has so far only been achieved by crystallization-driven self-assembly for macromolecules. Apart from kinetical control over the length distributions, two top-down approaches by the utilization of ultrasonication and dual asymmetric centrifugation were tested. This approach yielded even small oligomeric particles, dependent on the time and shear forces applied. To understand the fiber formation on the molecular level, the self-assembly mechanism was studied. The aggregation proceeds in a cooperative manner, which can be concluded from the rapid onset of aggregation into readily big particles after a nucleation phase. It could be observed, that in e.g. THF already a pre-aggregation into oligomeric particles takes place. Increasing the water content, a helical inversion with additional lateral aggregation occurs, resulting in immediate cooperative growth of the fibers without the presence of micellar phases.

Further research has been conducted on the interaction between fibers from BTU obtained by pathway-dependent self-assembly at higher concentrations (Figure 25 lower right). Surprisingly, gelation can only be observed at concentrations 400 times bigger than the calculated overlap concentration. From that, high stiffness and decreased fiber interactions due to the polymer corona can be concluded. At high concentrations the systems gels due to the entanglement of the SPB fibers. Since these gels are of supramolecular nature, the aggregates can be reversibly broken. This dynamic could be measured for BTU hydrogels, which exhibited stress-responsiveness and self-healing abilities. The gel strength could recover to 100 % even after high strains of 200 % were applied. Here, the nanofiber is ruptured upon high deformation and thus “active chain ends” are formed. Due to the hydrophobic effect, these ends reassembly immediately upon stress relief. This behavior could be preserved even after the reinforcement of the gel via additional crosslinkers. Improved gel strengths could be measured when 1 % of a bivalent BTU-PEO-BTU conjugate was added. The amount of crosslinker, however, was crucial to obtain strong gels. Crosslinker contents > 10 % led to decreased gel strength due to

Summary

increased backfolding and the formation of micellar structures. Further changing the length of the crosslinker and the overall concentration of the gel, the gel strength and responsiveness could be tuned. By utilizing a gel with 1 % crosslinker of 20 kD at an overall concentration of 2.5 wt%, stable, stress-responsive and even biocompatible hydrogels could be synthesized. Since these gels can be processed by 3D printing because of their shear-thinning properties, and still allow for the diffusion of macromolecules and small substances, this system may be applicable as an injectable hydrogel drug reservoir or in tissue engineering as a 3D cell scaffold.

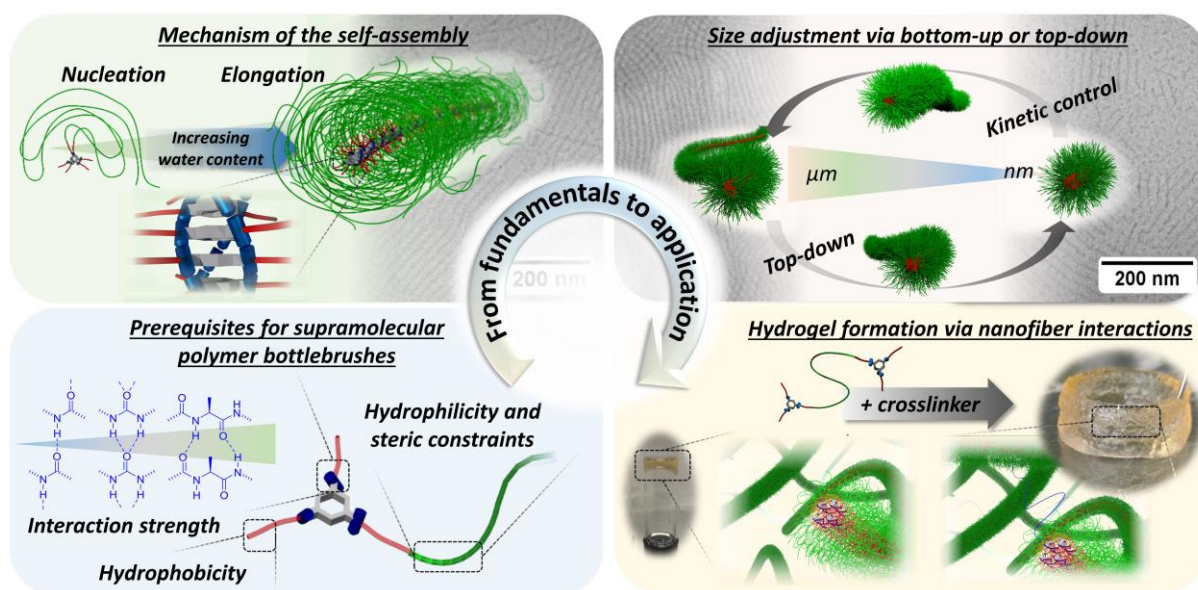


Figure 25 Thematic overview of the thesis: Evaluation of the premises for the formation of SPBs based on a 1,3,5-substituted benzene motif (lower left), studies about the mechanism of self-assembly (upper left) and the exploitation thereof to adjust the size distributions of the nanofibers by either exhibiting kinetic control or top-down methods, such as ultrasonication or dual asymmetric centrifugation of the nanofibers (upper right). Employing the interactions between nanofibers to synthesize dynamic, biocompatible hydrogels by additional crosslinking (lower right).

6. Zusammenfassung

Inspiziert von der Komplexität der molekularen Strukturen in der Natur versuchen Wissenschaftler bis heute, diese Konzepte auf die synthetische Chemie zu übertragen. Mit Hilfe der supramolekularen Chemie lassen sich dynamische Materialien unterschiedlicher Größe und Form herstellen, denen es jedoch meist an der in der Natur vorkommenden Komplexität mangelt. Die Fähigkeit der Natur, makromolekulare Bausteine in hierarchischen eindimensionalen Strukturen anzuordnen, hat Chemiker dazu inspiriert, ein Zusammenspiel zwischen Polymerwissenschaft und supramolekulare Chemie zu nutzen, um verschiedene anisotrope, supramolekulare, polymere Systeme mit interessanten Eigenschaften wie einer hohen Dynamik und Reaktionsfähigkeit gegenüber äußeren Reizen zu erzeugen. Eine Möglichkeit eindimensionale, supramolekulare Polymerstrukturen zu bilden, besteht darin, schwache gerichtete Wechselwirkungen wie Wasserstoffbrücken zu nutzen.

Ziel dieser Arbeit war es, die Voraussetzungen für die Bildung von supramolekularen Polymer-Flaschenbürsten (SPBs) durch die Selbst-Assemblierung mit Polymerketten funktionalisierter 1,3,5-Benzoltriamide in Wasser zu untersuchen (Abbildung 1). Dazu wurde der Einfluss der Wechselwirkungsstärke zwischen den Selbstassemblierungseinheiten, der hydrophoben Abschirmung und der Hydrophilie der Polymerhülle untersucht. Dabei konnte der starke Einfluss des Packungsparameters und damit des hydrophilen/hydrophoben Verhältnisses des Bausteines beobachtet werden. Durch die Erhöhung des hydrophoben Anteils über die Verwendung einer größeren Alkylkette von 12 Methyleneinheiten konnten jedoch keine reinen Fasermorphologien erhalten werden, wenn Amidgruppen verwendet wurden. Die hohe Hydrophilie durch die Funktionalisierung mit PEO (2kD) macht eine erhöhte Anzahl von Wasserstoffbrückenbindungen notwendig. Durch die Verwendung von Harnstoffgruppen anstelle von Amidgruppen konnte der starke Einfluss des Packungsparameters überwunden werden. Größere PEO-Ketten verschieben die Morphologie wieder zu mizellaren Phasen oder sogar unimeren Lösungen. Veränderungen im strukturellen Erscheinungsbild der Amphiphile durch den Einbau einer erhöhten Anzahl von Polymerarmen führten ebenfalls zu isotropen Morphologiephasen. Die hohen sterischen Ansprüche mehrerer Polymerketten und die damit einhergehende erhöhte Hydrophilie konnten nur durch eine größere Anzahl von Wasserstoffbrückenbindungen ausgeglichen werden. Lediglich bei Benzol-Trisureapeptiden (BTUP) konnte die Bildung eindimensionaler Aggregate auch bei Funktionalisierung des Bausteins mit 3 Polymerketten nachgewiesen werden. Hier wurde zudem die, für diese Systeme oftmals beobachtete, laterale Aggregation komplett unterbunden.

Zusammenfassung

Darüber hinaus wurden der Assemblierungs-Mechanismus der resultierenden SPB und die Möglichkeit einer kinetischen Kontrolle des Systems zur Beeinflussung der resultierenden Größen der SPB untersucht. Der hydrophobe Effekt, der neben der Wasserstoffbrückenbindung die Haupttriebkraft für die Selbstorganisation ist, führt häufig zur Bildung von kinetisch gefangenen Zuständen und Morphologiephasen, welche abhängig vom Präparationsweg sind. Diese konnten auch für das hier vorgestellte System nachgewiesen werden. Durch die Anwendung einer Solvent-Switch-Methode, bei der Wasser langsam zu organischen Lösungen von BTU und BTP hinzugegeben wurde, um die Selbstorganisation zu induzieren, konnten mikrometergroße Fasern erhalten werden. Die Größe der Fasern konnte in Abhängigkeit von der Zugabegeschwindigkeit des Wassers eingestellt werden. Durch schnellere Zugabe konnten kleinere Strukturen synthetisiert werden. Die kleinsten Strukturen mit Mizellen für BTP konnten mit Hilfe einer Quench-Methode erzeugt werden, bei der die organische Lösung des Bausteins zu einem Überschuss an reinem Wasser gegeben wurde. Generell wurden jedoch meist breite Größenverteilungen erhalten. Eine echtes lebendes Wachstum dieser SPBs und somit die Bildung von Größenverteilungen mit geringer Dispersität ist daher noch nicht möglich. Nichtsdestotrotz ebnet die Kontrolle über die Assemblierungsparameter der SPB den Weg zu einer unkomplizierten Synthese maßgeschneiderter 1D-Polymer-Assemblies, die bisher nur durch kristallisationsgesteuerte Selbstassemblierung für Makromoleküle erreicht werden konnte. Neben der kinetischen Kontrolle wurden zwei Top-down-Ansätze unter Verwendung von Ultraschall und dualer asymmetrischer Zentrifugation zur Kontrolle der Größenverteilung getestet. Dieser Ansatz ergab sogar kleine oligomere Partikel, abhängig von der Zeit und den angewandten Scherkräften. Um die Faserbildung auf molekularer Ebene zu verstehen, wurde der Mechanismus der Selbstassemblierung untersucht. Die Aggregation verläuft nach einem kooperativen Mechanismus, was sich aus dem raschen Beginn der Aggregation zu großen Partikeln nach einer Nukleierungsphase schließen lässt. Es konnte beobachtet werden, dass z.B. in THF bereits eine Voraggregation zu oligomeren Partikeln stattfindet. Mit steigendem Wassergehalt kommt es zu einer Inversion der gebildeten Helix und einer zusätzlichen lateralen Aggregation, die zu einem sofortigen kooperativen Wachstum der Fasern führt. Interessanterweise werden keine mizellaren Zwischenmorphologien erzeugt sondern direkt ein 1D Wachstum zu zylindrischen Aggregaten.

Weitere Untersuchungen wurden zur Interaktion zwischen Fasern aus BTU durchgeführt, die durch pfadabhängige Selbstorganisation bei höheren Konzentrationen gewonnen wurden. Überraschenderweise kann die Gelierung erst bei Konzentrationen beobachtet werden, die 400 Mal größer sind als die berechnete Überlapp-Konzentration. Daraus lässt sich eine hohe

Zusammenfassung

Steifigkeit und eine verringerte Faserinteraktion aufgrund der Polymerkorona ableiten. Bei hohen Konzentrationen geliert das System aufgrund der Verschlaufung der SPB-Fasern. Aufgrund ihrer supramolekularen Eigenschaften, können die Aggregate reversibel zerlegt und erneut aufgebaut werden. Diese Dynamik konnte bei BTU-Hydrogelen gemessen werden, die auf Belastungen reagierten und Selbstheilungsfähigkeiten aufwiesen. Die Festigkeit des Gels konnte sich selbst nach hohen Deformationen von 200 % vollständig erholen. Dabei wird die Nanofaser bei starker Verformung zerrissen und es bilden sich "aktive Kettenenden". Aufgrund des hydrophoben Effekts fügen sich diese Enden sofort wieder zusammen, wenn keine Krafteinwirkung vorhanden ist. Dieses Verhalten konnte auch nach der Verstärkung des Gels durch zusätzliche Vernetzer beibehalten werden. Bei Zugabe von 1 % eines bivalenten BTU-PEO-BTU-Konjugats konnten verbesserte Gelstärken gemessen werden. Die Menge des Vernetzers war jedoch entscheidend, um starke Gele zu erhalten. Vernetzergehalte $> 10\%$ führten zu einer verminderten Gelfestigkeit aufgrund eines verstärkten Einbaus in einer Nanofaser und der Bildung mizellarer Strukturen. Durch weitere Veränderung der Länge des Vernetzers und der Gesamtkonzentration des Gels konnten die Festigkeit und die Dynamik des Gels eingestellt werden. Bei Verwendung eines Gels mit 1 % Vernetzer mit einer Länge von 20 kD bei einer Gesamtkonzentration von 2,5 Gew.-% konnten stabile, selbst-heilende und sogar biokompatible Hydrogele synthetisiert werden. Da diese Gele aufgrund ihrer scherverdünnenden Eigenschaften im 3D-Druckverfahren verarbeitet werden können und dennoch die Diffusion von Makromolekülen und kleinen Substanzen ermöglichen, könnte dieses injizierbare Hydrogel als Arzneimittelreservoir oder in der Gewebekonstruktion als 3D Zellgerüst eingesetzt werden.

Zusammenfassung

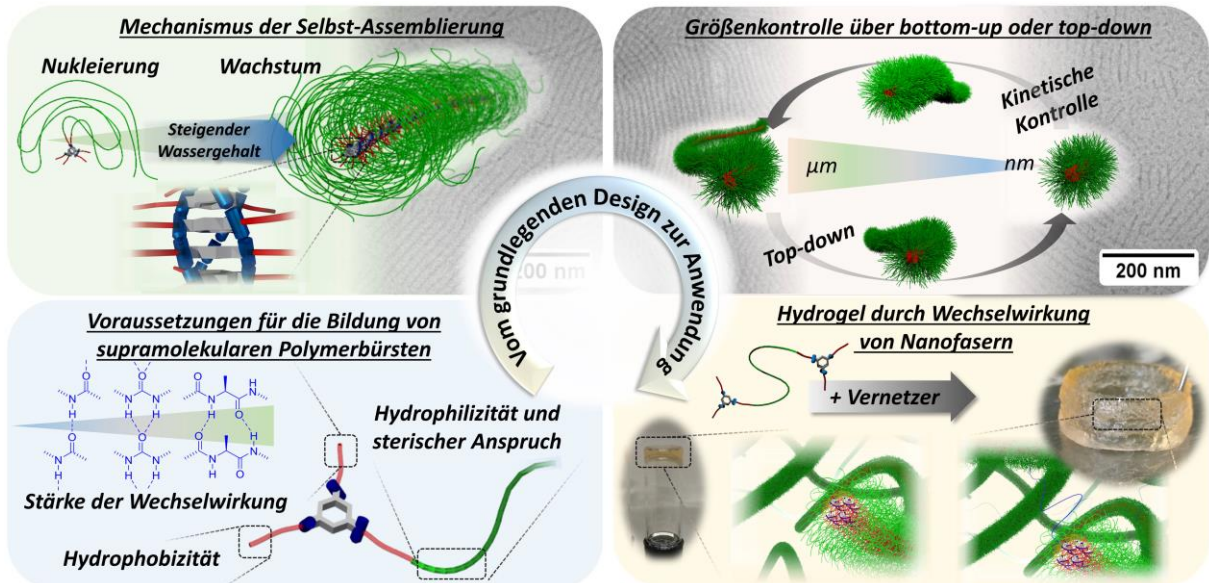


Abbildung 1: Übersicht der behandelten Themen: Voraussetzungen für die Bildung von supramolekularen Polymerbürsten basierend auf einem 1,3,5-substituiertem Benzol (unten links), Studien zum Mechanismus der Selbst-Assemblierung (oben links) Einstellung der Größenverteilung der Nanofasern über kinetische Kontrolle („bottom-up“) oder „top-down“ Methoden (oben rechts). Bildung von dynamischen, biokompatiblen Hydrogelen aufgrund der Wechselwirkungen zwischen Nanofasern und zusätzlicher Vernetzung (unten rechts).

7. References

- [1] D. A. Fletcher, R. D. Mullins, *Nature* **2010**, *463*, 485-492.
- [2] K. C.-W. Wu, C.-Y. Yang, C.-M. Cheng, *Chem. Commun.* **2014**, *50*, 4148-4157.
- [3] H. Hess, J. L. Ross, *Chem. Soc. Rev.* **2017**, *46*, 5570-5587.
- [4] S. I. Stupp, L. C. Palmer, *Chem. Mater.* **2013**, *26*, 507-518.
- [5] J. M. Lehn, *Science* **2002**, *295*, 2400-2403.
- [6] Y. Zhao, F. Sakai, L. Su, Y. Liu, K. Wei, G. Chen, M. Jiang, *Adv. Mater.* **2013**, *25*, 5215-5256.
- [7] J. C. Foster, S. Varlas, B. Couturaud, Z. Coe, R. K. O'Reilly, *J. Am. Chem. Soc.* **2019**, *141*, 2742-2753.
- [8] L. J. Prins, D. N. Reinhoudt, P. Timmerman, *Angew. Chem. Int. Ed.* **2001**, *40*, 2382-2426.
- [9] M. D. Watson, A. Fechtenkötter, K. Müllen, *Chem. Rev.* **2001**, *101*, 1267-1300.
- [10] E. Krieg, M. M. Bastings, P. Besenius, B. Rybtchinski, *Chem. Rev.* **2016**, *116*, 2414-2477.
- [11] M. Wehner, F. Würthner, *Nat. Rev. Chem.* **2019**.
- [12] S. S. Sheiko, B. S. Sumerlin, K. Matyjaszewski, *Prog. Polym. Sci.* **2008**, *33*, 759-785.
- [13] R. Verduzco, X. Li, S. L. Pesek, G. E. Stein, *Chem. Soc. Rev.* **2015**, *44*, 2405-2420.
- [14] T. Pelras, C. S. Mahon, M. Müllner, *Angew. Chem. Int. Ed.* **2018**, *57*, 6982-6994.
- [15] M. B. Baker, L. Albertazzi, I. K. Voets, C. M. Leenders, A. R. Palmans, G. M. Pavan, E. W. Meijer, *Nat. Commun.* **2015**, *6*, 6234.
- [16] R. M. P. da Silva, D. van der Zwaag, L. Albertazzi, S. S. Lee, E. W. Meijer, S. I. Stupp, *Nat. Commun.* **2016**, *7*, 11561.
- [17] B. N. S. Thota, X. Lou, D. Bochicchio, T. F. E. Paffen, R. P. M. Lafleur, J. L. J. van Dongen, S. Ehrmann, R. Haag, G. M. Pavan, A. R. A. Palmans, E. W. Meijer, *Angew. Chem. Int. Ed.* **2018**, *57*, 6843-6847.
- [18] B. Qin, Z. Yin, X. Tang, S. Zhang, Y. Wu, J.-F. Xu, X. Zhang, *Prog. Polym. Sci.* **2020**, *100*, 101167.
- [19] W. Zhang, B. Charleux, P. Cassagnau, *Soft Matter* **2013**, *9*, 2197-2205.
- [20] C. M. A. Leenders, T. Mes, M. B. Baker, M. M. E. Koenigs, P. Besenius, A. R. A. Palmans, E. W. Meijer, *Mater. Horiz.* **2014**, *1*, 116-120.
- [21] M. Golkaram, L. Boetje, J. Dong, L. E. A. Suarez, C. Fodor, D. Maniar, E. van Ruymbeke, S. Faraji, G. Portale, K. Loos, *ACS Omega* **2019**, *4*, 16481-16492.
- [22] E. Vereroudakis, M. Bantawa, R. P. M. Lafleur, D. Parisi, N. M. Matsumoto, J. W. Peeters, E. Del Gado, E. W. Meijer, D. Vlassopoulos, *ACS Cent. Sci.* **2020**, *6*, 1401-1411.
- [23] J. P. Hill, W. Jin, A. Kosaka, T. Fukushima, H. Ichihara, T. Shimomura, K. Ito, T. Hashizume, N. Ishii, T. Aida, *Science* **2004**, *304*, 1481-1483.
- [24] G. M. Miyake, V. A. Piunova, R. A. Weitekamp, R. H. Grubbs, *Angew. Chem. Int. Ed.* **2012**, *51*, 11246-11248.
- [25] X.-H. Jin, M. B. Price, J. R. Finnegan, C. E. Boott, J. M. Richter, A. Rao, S. M. Menke, R. H. Friend, G. R. Whittell, I. Manners, *Science* **2018**, *360*, 897-900.
- [26] K. Petkau-Milroy, M. H. Sonntag, A. H. van Onzen, L. Brunsveld, *J. Am. Chem. Soc.* **2012**, *134*, 8086-8089.
- [27] S. P. W. Wijnands, W. Engelen, R. P. M. Lafleur, E. W. Meijer, M. Merckx, *Nat. Commun.* **2018**, *9*, 65.
- [28] M. H. Bakker, R. E. KIELTYKA, L. Albertazzi, P. Y. W. Dankers, *RSC Adv.* **2016**, *6*, 110600-110603.

References

- [29] N. P. Truong, M. R. Whittaker, C. W. Mak, T. P. Davis, *Expert Opin. Drug. Deliv.* **2015**, *12*, 129-142.
- [30] R. A. Meyer, J. J. Green, *Wiley Interdiscip. Rev. Nanomed. Nanobiotechnol.* **2016**, *8*, 191-207.
- [31] Y. Mai, A. Eisenberg, *Chem. Soc. Rev.* **2012**, *41*, 5969-5985.
- [32] J. C. Brendel, F. H. Schacher, *Chem Asian J* **2018**, *13*, 230-239.
- [33] B. Karagoz, L. Esser, H. T. Duong, J. S. Basuki, C. Boyer, T. P. Davis, *Polym. Chem.* **2014**, *5*, 350-355.
- [34] S. L. Canning, G. N. Smith, S. P. Armes, *Macromolecules* **2016**, *49*, 1985-2001.
- [35] M. J. Derry, L. A. Fielding, S. P. Armes, *Prog. Polym. Sci.* **2016**, *52*, 1-18.
- [36] U. Tritschler, S. Pearce, J. Gwyther, G. R. Whittell, I. Manners, *Macromolecules* **2017**, *50*, 3439-3463.
- [37] R. C. Hayward, D. J. Pochan, *Macromolecules* **2010**, *43*, 3577-3584.
- [38] R. Verber, A. Blanazs, S. P. Armes, *Soft Matter* **2012**, *8*, 9915-9922.
- [39] C. A. Dreiss, *Soft Matter* **2007**, *3*, 956-970.
- [40] C. Cummins, R. Lundy, J. J. Walsh, V. Ponsinet, G. Fleury, M. A. Morris, *Nano Today* **2020**, *35*, 100936.
- [41] D. J. C. Herr, *J. Mater. Res.* **2011**, *26*, 122-139.
- [42] J. K. Kim, S. Y. Yang, Y. Lee, Y. Kim, *Prog. Polym. Sci.* **2010**, *35*, 1325-1349.
- [43] H. Cabral, K. Miyata, K. Osada, K. Kataoka, *Chem. Rev.* **2018**, *118*, 6844-6892.
- [44] H. A. Klok, S. Lecommandoux, *Adv. Mater.* **2001**, *13*, 1217-1229.
- [45] J. Schmelz, F. H. Schacher, H. Schmalz, *Soft Matter* **2013**, *9*, 2101-2107.
- [46] J. Rzayev, *ACS Macro Lett.* **2012**, *1*, 1146-1149.
- [47] H. I. Lee, J. Pietrasik, S. S. Sheiko, K. Matyjaszewski, *Prog. Polym. Sci.* **2010**, *35*, 24-44.
- [48] J. Couet, M. Biesalski, *Soft Matter* **2006**, *2*, 1005-1014.
- [49] A. S. Shetty, J. Zhang, J. S. Moore, *J. Am. Chem. Soc.* **1996**, *118*, 1019-1027.
- [50] R. B. Martin, *Chem. Rev.* **1996**, *96*, 3043-3064.
- [51] S. Lahiri, J. L. Thompson, J. S. Moore, *J. Am. Chem. Soc.* **2000**, *122*, 11315-11319.
- [52] S. Rosselli, A.-D. Ramminger, T. Wagner, B. Silier, S. Wiegand, W. Häubler, G. Lieser, V. Scheumann, S. Höger, *Angew. Chem. Int. Ed.* **2001**, *40*, 3137-3141.
- [53] S. Höger, *Chem. Eur. J.* **2004**, *10*, 1320-1329.
- [54] C.-L. Liu, C.-H. Lin, C.-C. Kuo, S.-T. Lin, W.-C. Chen, *Prog. Polym. Sci.* **2011**, *36*, 603-637.
- [55] J.-H. Ryu, D.-J. Hong, M. Lee, *Chem. Commun.* **2008**, 1043-1054.
- [56] F. J. M. Hoeben, P. Jonkheijm, E. W. Meijer, A. P. H. J. Schenning, *Chem. Rev.* **2005**, *105*, 1491-1546.
- [57] H. Wang, H. H. Wang, V. S. Urban, K. C. Littrell, P. Thiyagarajan, L. Yu, *J. Am. Chem. Soc.* **2000**, *122*, 6855-6861.
- [58] H. Wang, W. You, P. Jiang, L. Yu, H. H. Wang, *Chem. Eur. J.* **2004**, *10*, 986-993.
- [59] F. Würthner, *Chem. Commun.* **2004**, 1564-1579.
- [60] F. Würthner, C. Thalacker, S. Diele, C. Tschierske, *Chem. Eur. J.* **2001**, *7*, 2245-2253.
- [61] S. Rehm, V. Stepanenko, X. Zhang, T. H. Rehm, F. Würthner, *Chem. Eur. J.* **2010**, *16*, 3372-3382.
- [62] A. Arnaud, J. Belleney, F. Boué, L. Bouteiller, G. Carrot, V. Wintgens, *Angew. Chem. Int. Ed.* **2004**, *43*, 1718-1721.
- [63] J. Baram, H. Weissman, Y. Tidhar, I. Pinkas, B. Rybtchinski, *Angew. Chem. Int. Ed.* **2014**, *53*, 4123-4126.
- [64] E. Cohen, H. Weissman, I. Pinkas, E. Shimoni, P. Rehak, P. Král, B. Rybtchinski, *ACS Nano* **2018**, *12*, 317-326.

References

- [65] T. Choisnet, D. Canevet, M. Salle, E. Nicol, F. Niepceron, J. Jestin, O. Colombani, *Chem Commun (Camb)* **2019**, 55, 9519-9522.
- [66] M. Fritzsche, S.-S. Jester, S. Höger, C. Klaus, N. Dingenouts, P. Linder, M. Drechsler, S. Rosenfeldt, *Macromolecules* **2010**, 43, 8379-8388.
- [67] J. W. Steed, J. L. Atwood, *Supramolecular Chemistry*, Wiley, **2009**.
- [68] G. Fichman, E. Gazit, *Acta Biomater.* **2014**, 10, 1671-1682.
- [69] D. J. Adams, *Macromol. Biosci.* **2011**, 11, 160-173.
- [70] C. Tomasini, N. Castellucci, *Chem. Soc. Rev.* **2013**, 42, 156-172.
- [71] M. Zhou, A. M. Smith, A. K. Das, N. W. Hodson, R. F. Collins, R. V. Ulijn, J. E. Gough, *Biomaterials* **2009**, 30, 2523-2530.
- [72] Z. Yang, G. Liang, M. Ma, Y. Gao, B. Xu, *J. Mater. Chem.* **2007**, 17, 850-854.
- [73] H. Cui, M. J. Webber, S. I. Stupp, *Pept. Sci.* **2010**, 94, 1-18.
- [74] G. W. M. Vandermeulen, C. Tziatzios, R. Duncan, H.-A. Klok, *Macromolecules* **2005**, 38, 761-769.
- [75] I. W. Hamley, *Angew. Chem. Int. Ed.* **2007**, 46, 8128-8147.
- [76] H. G. Börner, H. Schlaad, *Soft Matter* **2007**, 3, 394-408.
- [77] R. Otter, P. Besenius, *Org. Biomol. Chem.* **2019**.
- [78] T. S. Burkoth, T. L. S. Benzinger, D. N. M. Jones, K. Hallenga, S. C. Meredith, D. G. Lynn, *J. Am. Chem. Soc.* **1998**, 120, 7655-7656.
- [79] J. Hentschel, M. G. J. ten Cate, H. G. Börner, *Macromolecules* **2007**, 40, 9224-9232.
- [80] J. Hentschel, E. Krause, H. G. Börner, *J. Am. Chem. Soc.* **2006**, 128, 7722-7723.
- [81] V. Castelletto, R. J. Gouveia, C. J. Connon, I. W. Hamley, *Eur. Polym. J.* **2013**, 49, 2961-2967.
- [82] V. Castelletto, I. W. Hamley, *Biophys. Chem.* **2009**, 141, 169-174.
- [83] V. Castelletto, J. E. McKendrick, I. W. Hamley, U. Olsson, C. Cenker, *Langmuir* **2010**, 26, 11624-11627.
- [84] V. Castelletto, G. Cheng, S. Furzeland, D. Atkins, I. W. Hamley, *Soft Matter* **2012**, 8, 5434-5438.
- [85] I. W. Hamley, I. A. Ansari, V. Castelletto, H. Nuhn, A. Rösler, H. A. Klok, *Biomacromolecules* **2005**, 6, 1310-1315.
- [86] I. W. Hamley, G. Cheng, V. Castelletto, *Macromol. Biosci.* **2011**, 11, 1068-1078.
- [87] R. Otter, C. M. Berac, S. Seiffert, P. Besenius, *Eur. Polym. J.* **2019**, 110, 90-96.
- [88] R. Otter, N. A. Henke, C. Berac, T. Bauer, M. Barz, S. Seiffert, P. Besenius, *Macromol. Rapid Commun.* **2018**, 0, 1800459.
- [89] S. Wiczorek, A. Dallmann, Z. Kochovski, H. G. Börner, *J. Am. Chem. Soc.* **2016**, 138, 9349-9352.
- [90] S. Kirkham, V. Castelletto, I. W. Hamley, M. Reza, J. Ruokolainen, D. Hermida-Merino, P. Bilalis, H. Iatrou, *Biomacromolecules* **2016**, 17, 1186-1197.
- [91] V. Castelletto, G. E. Newby, Z. Zhu, I. W. Hamley, L. Noirez, *Langmuir* **2010**, 26, 9986-9996.
- [92] D. T. Bong, T. D. Clark, J. R. Granja, R. M. Ghadiri, *Angew. Chem. Int. Ed. Engl.* **2001**, 40, 988-1011.
- [93] I. W. Hamley, *Angew. Chem. Int. Ed. Engl.* **2014**, 53, 6866-6881.
- [94] P. de Santis, S. Morosetti, R. Rizzo, *Macromolecules* **1974**, 7, 52-58.
- [95] R. M. Ghadiri, J. R. Granja, R. A. Milligan, D. E. McRee, N. Khazanovich, *Nature* **1993**, 366.
- [96] R. Chapman, M. Danial, M. L. Koh, K. A. Jolliffe, S. Perrier, *Chem. Soc. Rev.* **2012**, 41, 6023-6041.
- [97] R. J. Brea, L. Castedo, J. R. Granja, M. Á. Herranz, L. Sánchez, N. Martín, W. Seitz, D. M. Guldi, *Proc. Natl. Acad. Sci. U.S.A* **2007**, 104, 5291-5294.

References

- [98] C. Reiriz, R. J. Brea, R. Arranz, J. L. Carrascosa, A. Garibotti, B. Manning, J. M. Valpuesta, R. Eritja, L. Castedo, J. R. Granja, *J. Am. Chem. Soc.* **2009**, *131*, 11335-11337.
- [99] N. Ashkenasy, W. S. Horne, M. R. Ghadiri, *Small* **2006**, *2*, 99-102.
- [100] R. M. Ghadiri, J. R. Granja, L. K. Buehler, *Nature* **1994**, *369*, 301-304.
- [101] R. García-Fandiño, M. Amorín, L. Castedo, J. R. Granja, *Chem. Sci.* **2012**, *3*, 3280-3285.
- [102] J. R. Granja, M. R. Ghadiri, *J. Am. Chem. Soc.* **1994**, *116*, 10785-10786.
- [103] W. S. Horne, C. M. Wiethoff, C. Cui, K. M. Wilcoxon, M. Amorin, M. R. Ghadiri, G. R. Nemerow, *Biorg. Med. Chem.* **2005**, *13*, 5145-5153.
- [104] J. Couet, M. Biesalski, *Macromolecules* **2006**, *39*, 7258-7268.
- [105] J. Couet, M. Biesalski, *Small* **2008**, *4*, 1008-1016.
- [106] J. Couet, J. D. J. S. Samuel, A. Kopyshhev, S. Santer, M. Biesalski, *Angew. Chem. Int. Ed.* **2005**, *44*, 3297-3301.
- [107] S. Loschonsky, J. Couet, M. Biesalski, *Macromol. Rapid Commun.* **2008**, *29*, 309-315.
- [108] R. Chapman, P. J. M. Bouten, R. Hoogenboom, K. A. Jolliffe, S. Perrier, *Chem. Commun.* **2013**, *49*, 6522-6524.
- [109] R. Chapman, G. G. Warr, S. Perrier, K. A. Jolliffe, *Chem. Eur. J. A* **2013**, *19*, 1955-1961.
- [110] S. Catrouillet, J. C. Brendel, S. Larnaudie, T. Barlow, K. A. Jolliffe, S. Perrier, *ACS Macro Lett.* **2016**, *5*, 1119-1123.
- [111] S. C. Larnaudie, J. C. Brendel, K. A. Jolliffe, S. Perrier, *ACS Macro Lett.* **2017**, *6*, 1347-1351.
- [112] M. Hartlieb, S. Catrouillet, A. Kuroki, C. Sanchez-Cano, R. Peltier, S. Perrier, *Chem. Sci.* **2019**.
- [113] M. Danial, C. M. Tran, K. A. Jolliffe, S. Perrier, *J. Am. Chem. Soc.* **2014**, *136*, 8018-8026.
- [114] S. C. Larnaudie, J. C. Brendel, I. Romero-Canelon, C. Sanchez-Cano, S. Catrouillet, J. Sanchis, J. P. C. Coverdale, J. I. Song, A. Habtemariam, P. J. Sadler, K. A. Jolliffe, S. Perrier, *Biomacromolecules* **2018**, *19*, 239-247.
- [115] S. C. Larnaudie, J. Sanchis, T.-H. Nguyen, R. Peltier, S. Catrouillet, J. C. Brendel, C. J. H. Porter, K. A. Jolliffe, S. Perrier, *Biomaterials* **2018**, *178*, 570-582.
- [116] M. Danial, C. My-Nhi Tran, P. G. Young, S. Perrier, K. A. Jolliffe, *Nat. Commun.* **2013**, *4*, 2780.
- [117] B. M. Blunden, R. Chapman, M. Danial, H. Lu, K. A. Jolliffe, S. Perrier, M. H. Stenzel, *Chemistry* **2014**, *20*, 12745-12749.
- [118] J. G. Binfield, J. C. Brendel, N. R. Cameron, A. M. Eissa, S. Perrier, *Macromol. Rapid Commun.* **2018**, *39*, e1700831.
- [119] J. C. Brendel, J. Sanchis, S. Catrouillet, E. Czuba, M. Z. Chen, B. M. Long, C. Nowell, A. Johnston, K. A. Jolliffe, S. Perrier, *Angew. Chem. Int. Ed. Engl.* **2018**, *57*, 16678-16682.
- [120] S. Venkataraman, J. L. Hedrick, Z. Y. Ong, C. Yang, P. L. Ee, P. T. Hammond, Y. Y. Yang, *Adv. Drug. Deliv. Rev.* **2011**, *63*, 1228-1246.
- [121] R. Chapman, M. L. Koh, G. G. Warr, K. A. Jolliffe, S. Perrier, *Chem. Sci.* **2013**, *4*, 2581-2589.
- [122] E. D. H. Mansfield, M. Hartlieb, S. Catrouillet, J. Y. Rho, S. C. Larnaudie, S. E. Rogers, J. Sanchis, J. C. Brendel, S. Perrier, *Soft Matter* **2018**, *14*, 6320-6326.
- [123] J. Y. Rho, J. C. Brendel, L. R. MacFarlane, E. D. H. Mansfield, R. Peltier, S. Rogers, M. Hartlieb, S. Perrier, *Adv. Funct. Mater.* **2017**, 1704569.
- [124] J. Y. Rho, H. Cox, E. D. H. Mansfield, S. H. Ellacott, R. Peltier, J. C. Brendel, M. Hartlieb, T. A. Waigh, S. Perrier, *Nat. Commun.* **2019**, *10*, 4708.

References

- [125] D. Weiss, K. Kreger, H. W. Schmidt, *Macromol. Mater. Eng.* **2017**, *302*, 1600390-n/a.
- [126] S. Cantekin, T. F. de Greef, A. R. Palmans, *Chem. Soc. Rev.* **2012**, *41*, 6125-6137.
- [127] M. A. Gillissen, M. M. Koenigs, J. J. Spiering, J. A. Vekemans, A. R. Palmans, I. K. Voets, E. W. Meijer, *J. Am. Chem. Soc.* **2014**, *136*, 336-343.
- [128] L. Bouteiller, *Adv. Polym. Sci.* **2007**, *207*, 79-112.
- [129] D. Ogata, T. Shikata, K. Hanabusa, *J. Phys. Chem. B* **2004**, *108*, 15503-15510.
- [130] A. Bernet, R. Q. Albuquerque, M. Behr, S. T. Hoffmann, H.-W. Schmidt, *Soft Matter* **2012**, *8*, 66-69.
- [131] F. Abraham, S. Ganzleben, D. Hanft, P. Smith, H.-W. Schmidt, *Macromol. Chem. Phys.* **2010**, *211*, 171-181.
- [132] F. Abraham, H. W. Schmidt, *Polymer* **2010**, *51*, 913-921.
- [133] N. Mohmeyer, N. Behrendt, X. Q. Zhang, P. Smith, V. Altstadt, G. M. Sessler, H. W. Schmidt, *Polymer* **2007**, *48*, 1612-1619.
- [134] M. Blumenhofer, S. Ganzleben, D. Hanft, H.-W. Schmidt, M. Kristiansen, P. Smith, K. Stoll, D. Mäder, K. Hoffmann, *Macromolecules* **2005**, *38*, 3688-3695.
- [135] D. Weiss, D. Skrybeck, H. Misslitz, D. Nardini, A. Kern, K. Kreger, H. W. Schmidt, *ACS Appl. Mater. Interfaces* **2016**, *8*, 14885-14892.
- [136] M. H. Bakker, C. C. Lee, E. W. Meijer, P. Y. Dankers, L. Albertazzi, *ACS Nano* **2016**, *10*, 1845-1852.
- [137] M. Á. Alemán García, E. Magdalena Estirado, L.-G. Milroy, L. Brunsveld, *Angew. Chem. Int. Ed.* **2018**, *57*, 4976-4980.
- [138] L. Albertazzi, F. J. Martinez-Veracoechea, C. M. A. Leenders, I. K. Voets, D. Frenkel, E. W. Meijer, *Proc. Natl. Acad. Sci. U.S.A* **2013**, *110*, 12203-12208.
- [139] L. Albertazzi, D. van der Zwaag, C. M. Leenders, R. Fitzner, R. W. van der Hofstad, E. W. Meijer, *Science* **2014**, *344*, 491-495.
- [140] A. Duro-Castano, R. M. England, D. Razola, E. Romero, M. Oteo-Vives, M. A. Morcillo, M. J. Vicent, *Mol. Pharm.* **2015**, *12*, 3639-3649.
- [141] A. Duro-Castano, V. J. Nebot, A. Nino-Pariente, A. Arminan, J. J. Arroyo-Crespo, A. Paul, N. Feiner-Gracia, L. Albertazzi, M. J. Vicent, *Adv. Mater.* **2017**, *29*, 1702888.
- [142] K. J. van Bommel, C. van der Pol, I. Muizebelt, A. Friggeri, A. Heeres, A. Meetsma, B. L. Feringa, J. van Esch, *Angew. Chem. Int. Ed. Engl.* **2004**, *43*, 1663-1667.
- [143] A. Friggeri, C. van der Pol, K. J. van Bommel, A. Heeres, M. C. Stuart, B. L. Feringa, J. van Esch, *Chemistry* **2005**, *11*, 5353-5361.
- [144] M. de Loos, J. H. van Esch, R. M. Kellogg, B. L. Feringa, *Tetrahedron* **2007**, *63*, 7285-7301.
- [145] P. Besenius, G. Portale, P. H. Bomans, H. M. Janssen, A. R. Palmans, E. W. Meijer, *Proc. Natl. Acad. Sci. U.S.A* **2010**, *107*, 17888-17893.
- [146] H. Frisch, Y. Nie, S. Raunser, P. Besenius, *Chem. Eur. J.* **2015**, *21*, 3304-3309.
- [147] P. Ahlers, H. Frisch, R. Holm, D. Spitzer, M. Barz, P. Besenius, *Macromol. Biosci.* **2017**, *17*, 1700111.
- [148] O. Zagorodko, T. Melnyk, O. Rogier, V. J. Nebot, M. J. Vicent, *Polym. Chem.* **2021**, *12*, 3478-3487.
- [149] O. Zagorodko, V. J. Nebot, M. J. Vicent, *Polym. Chem.* **2020**.
- [150] R. Otter, K. Klinker, D. Spitzer, M. Schinnerer, M. Barz, P. Besenius, *Chem. Commun.* **2018**, *54*, 401-404.
- [151] H. Frisch, J. P. Unsleber, D. Ludeker, M. Peterlechner, G. Brunklaus, M. Waller, P. Besenius, *Angew. Chem. Int. Ed. Engl.* **2013**, *52*, 10097-10101.
- [152] J. Jadzyn, M. Stockhausen, B. Zywucki, *J. Phys. Chem.* **1987**, *91*, 754-757.
- [153] M. George, G. Tan, V. T. John, R. G. Weiss, *Chem. Eur. J.* **2005**, *11*, 3243-3254.
- [154] J. van Esch, R. M. Kellogg, B. L. Feringa, *Tetrahedron Lett.* **1997**, *38*, 281-284.

References

- [155] F. Lortie, S. Boileau, L. Bouteiller, C. Chassenieux, B. Demé, G. Ducouret, M. Jalabert, F. Lauprêtre, P. Terech, *Langmuir* **2002**, *18*, 7218-7222.
- [156] T. Pinault, B. Isare, L. Bouteiller, *ChemPhysChem* **2006**, *7*, 816-819.
- [157] A. J. Carr, R. Melendez, S. J. Geib, A. D. Hamilton, *Tetrahedron Lett.* **1998**, *39*, 7447-7450.
- [158] A. Pal, S. Karthikeyan, R. P. Sijbesma, *J. Am. Chem. Soc.* **2010**, *132*, 7842-7843.
- [159] G. Mellot, J. M. Guigner, J. Jestin, L. Bouteiller, F. Stoffelbach, J. Rieger, *Macromolecules* **2018**, *51*, 10214-10222.
- [160] G. Mellot, J. M. Guigner, L. Bouteiller, F. Stoffelbach, J. Rieger, *Angew. Chem. Int. Ed. Engl.* **2019**, *58*, 3173-3177.
- [161] S. Pensec, N. Nouvel, A. Guilleman, C. Creton, F. Boué, L. Bouteiller, *Macromolecules* **2010**, *43*, 2529-2534.
- [162] S. Catrouillet, L. Bouteiller, E. Nicol, T. Nicolai, S. Pensec, B. Jacquette, M. Le Bohec, O. Colombani, *Macromolecules* **2015**, *48*, 1364-1370.
- [163] S. Catrouillet, C. Fonteneau, L. Bouteiller, N. Delorme, E. Nicol, T. Nicolai, S. Pensec, O. Colombani, *Macromolecules* **2013**, *46*, 7911-7919.
- [164] C. Fonteneau, S. Pensec, L. Bouteiller, *Polym. Chem.* **2014**, *5*, 2496-2505.
- [165] S. Han, E. Nicol, F. Niepceron, O. Colombani, S. Pensec, L. Bouteiller, *Macromol. Rapid Commun.* **2019**, *40*, e1800698.
- [166] E. Obert, M. Bellot, L. Bouteiller, F. Andrioletti, C. Lehen-Ferrenbach, F. Boue, *J. Am. Chem. Soc.* **2007**, *129*, 15601-15605.
- [167] S. Y. Han, G. Mellot, S. Pensec, J. Rieger, F. Stoffelbach, E. Nicol, O. Colombani, J. Jestin, L. Bouteiller, *Macromolecules* **2020**, *53*, 427-433.
- [168] M. M. C. Bastings, S. Koudstaal, R. E. Kieltyka, Y. Nakano, A. C. H. Pape, D. A. M. Feyen, F. J. van Slochteren, P. A. Doevendans, J. P. G. Sluijter, E. W. Meijer, S. A. J. Chamuleau, P. Y. W. Dankers, *Adv. Healthcare Mater.* **2014**, *3*, 70-78.
- [169] M. M. E. Koenigs, A. Pal, H. Mortazavi, G. M. Pawar, C. Storm, R. P. Sijbesma, *Macromolecules* **2014**, *47*, 2712-2717.
- [170] G. M. Pawar, M. Koenigs, Z. Fahimi, M. Cox, I. K. Voets, H. M. Wyss, R. P. Sijbesma, *Biomacromolecules* **2012**, *13*, 3966-3976.
- [171] M. J. Webber, R. Langer, *Chem. Soc. Rev.* **2017**, *46*, 6600-6620.
- [172] M. J. Webber, E. T. Pashuck, *Adv. Drug Del. Rev.* **2021**, *172*, 275-295.
- [173] R. Toy, P. M. Peiris, K. B. Ghaghada, E. Karathanasis, *Nanomedicine (Lond)* **2014**, *9*, 121-134.
- [174] M. F. Zhang, A. H. E. Muller, *J. Polym. Sci., Part A: Polym. Chem.* **2005**, *43*, 3461-3481.
- [175] M. E. Fox, F. C. Szoka, J. M. Frechet, *Acc. Chem. Res.* **2009**, *42*, 1141-1151.
- [176] S. Hecht, *Angew. Chem. Int. Ed.* **2003**, *42*, 24-26.
- [177] S. M. Chin, C. V. Synatschke, S. Liu, R. J. Nap, N. A. Sather, Q. Wang, Z. Álvarez, A. N. Edelbrock, T. Fyrner, L. C. Palmer, I. Szleifer, M. Olvera de la Cruz, S. I. Stupp, *Nat. Commun.* **2018**, *9*, 2395.
- [178] A. T. Haedler, K. Kreger, A. Issac, B. Wittmann, M. Kivala, N. Hammer, J. Kohler, H. W. Schmidt, R. Hildner, *Nature* **2015**, *523*, 196-U127.
- [179] M. Hartlieb, E. D. H. Mansfield, S. Perrier, *Polym. Chem.* **2020**, *11*, 1083-1110.
- [180] T. Fukui, S. Kawai, S. Fujinuma, Y. Matsushita, T. Yasuda, T. Sakurai, S. Seki, M. Takeuchi, K. Sugiyasu, *Nat. Chem.* **2017**, *9*, 493-499.
- [181] J. S. Valera, R. Gómez, L. Sánchez, *Small* **2018**, *14*, 1702437.
- [182] J. Kang, D. Miyajima, T. Mori, Y. Inoue, Y. Itoh, T. Aida, *Science* **2015**, *347*, 646-651.
- [183] T. Fukui, N. Sasaki, M. Takeuchi, K. Sugiyasu, *Chem. Sci.* **2019**, *10*, 6770-6776.

References

- [184] X. Ma, Y. Zhang, Y. Zhang, Y. Liu, Y. Che, J. Zhao, *Angew. Chem. Int. Ed.* **2016**, *55*, 9539-9543.
- [185] S. Ogi, N. Fukaya, Arifin, B. B. Skjelstad, Y. Hijikata, S. Yamaguchi, *Chem. Eur. J.* **2019**, *25*, 7303-7307.
- [186] S. Ogi, K. Sugiyasu, S. Manna, S. Samitsu, M. Takeuchi, *Nat. Chem.* **2014**, *6*, 188-195.
- [187] M. E. Robinson, D. J. Lunn, A. Nazemi, G. R. Whittell, L. De Cola, I. Manners, *Chem. Commun.* **2015**, *51*, 15921-15924.
- [188] T. Klein, F. V. Gruschwitz, S. Rogers, S. Hoepfener, I. Nischang, J. C. Brendel, *J. Colloid Interface Sci.* **2019**, *557*, 488-497.
- [189] I. Muljajew, C. Weber, I. Nischang, U. S. Schubert, *Materials (Basel)* **2018**, *11*, 528.
- [190] C. M. A. Leenders, M. B. Baker, I. A. B. Pijpers, R. P. M. Lafleur, L. Albertazzi, A. R. A. Palmans, E. W. Meijer, *Soft Matter* **2016**, *12*, 2887-2893.
- [191] R. Nagarajan, *Langmuir* **2002**, *18*, 31-38.
- [192] R. Nagarajan, *Adv. Colloid Interface Sci.* **2017**, *244*, 113-123.
- [193] F. V. Gruschwitz, M.-C. Fu, T. Klein, R. Takahashi, T. Higashihara, S. Hoepfener, I. Nischang, K. Sakurai, J. C. Brendel, *Macromolecules* **2020**, *53*, 7552-7560.
- [194] T. Klein, H. F. Ulrich, F. V. Gruschwitz, M. T. Kuchenbrod, R. Takahashi, S. Fujii, S. Hoepfener, I. Nischang, K. Sakurai, J. C. Brendel, *Polym. Chem.* **2020**, *11*, 6763-6771.
- [195] W. P. J. Appel, G. Portale, E. Wisse, P. Y. W. Dankers, E. W. Meijer, *Macromolecules* **2011**, *44*, 6776-6784.
- [196] A. J. P. Teunissen, M. M. L. Nieuwenhuizen, F. Rodríguez-Llansola, A. R. A. Palmans, E. W. Meijer, *Macromolecules* **2014**, *47*, 8429-8436.
- [197] D. N. Reinhoudt, M. Crego-Calama, *Science* **2002**, *295*, 2403.
- [198] L. Zhang, A. Eisenberg, *Macromolecules* **1999**, *32*, 2239-2249.
- [199] H. Cui, Z. Chen, S. Zhong, K. L. Wooley, D. J. Pochan, *Science* **2007**, *317*, 647.
- [200] Y. Tidhar, H. Weissman, S. G. Wolf, A. Gulino, B. Rybtchinski, *Chem. Eur. J.* **2011**, *17*, 6068-6075.
- [201] M. M. Smulders, M. M. Nieuwenhuizen, T. F. de Greef, P. van der Schoot, A. P. Schenning, E. W. Meijer, *Chem. Eur. J. A* **2010**, *16*, 362-367.
- [202] C. Kulkarni, E. W. Meijer, A. R. A. Palmans, *Acc. Chem. Res.* **2017**, *50*, 1928-1936.
- [203] C. Rest, R. Kandaneli, G. Fernandez, *Chem. Soc. Rev.* **2015**, *44*, 2543-2572.
- [204] S. A. P. van Rossum, M. Tena-Solsona, J. H. van Esch, R. Eelkema, J. Boekhoven, *Chem. Soc. Rev.* **2017**, *46*, 5519-5535.
- [205] A. Sorrenti, J. Leira-Iglesias, A. J. Markvoort, T. F. A. de Greef, T. M. Hermans, *Chem. Soc. Rev.* **2017**, *46*, 5476-5490.
- [206] E. Mattia, S. Otto, *Nat. Nanotechnol.* **2015**, *10*, 111-119.
- [207] D. van der Zwaag, P. A. Pieters, P. A. Korevaar, A. J. Markvoort, A. J. H. Spiering, T. F. A. de Greef, E. W. Meijer, *J. Am. Chem. Soc.* **2015**, *137*, 12677-12688.
- [208] S. Sarkar, A. Sarkar, S. J. George, *Angew. Chem. Int. Ed.* **2020**, *59*, 19841-19845.
- [209] W. Wagner, M. Wehner, V. Stepanenko, S. Ogi, F. Wurthner, *Angew. Chem. Int. Ed.* **2017**, *56*, 16008-16012.
- [210] J. R. Finnegan, X. He, S. T. G. Street, J. D. Garcia-Hernandez, D. W. Hayward, R. L. Harniman, R. M. Richardson, G. R. Whittell, I. Manners, *J. Am. Chem. Soc.* **2018**, *140*, 17127-17140.
- [211] L. MacFarlane, C. Zhao, J. Cai, H. Qiu, I. Manners, *Chem. Sci.* **2021**, *12*, 4661-4682.
- [212] S. T. G. Street, Y. He, X.-H. Jin, L. Hodgson, P. Verkade, I. Manners, *Chem. Sci.* **2020**, *11*, 8394-8408.

References

- [213] F. V. Gruschwitz, T. Klein, M. T. Kuchenbrod, N. Moriyama, S. Fujii, I. Nischang, S. Hoepfener, K. Sakurai, U. S. Schubert, J. C. Brendel, *ACS Macro Lett.* **2021**, *10*, 837-843.
- [214] S. Cantekin, D. W. Balkenende, M. M. Smulders, A. R. Palmans, E. W. Meijer, *Nat. Chem.* **2011**, *3*, 42-46.
- [215] M. M. J. Smulders, T. Buffeteau, D. Cavagnat, M. Wolffs, A. P. H. J. Schenning, E. W. Meijer, *Chirality* **2008**, *20*, 1016-1022.
- [216] L. Jiang, S. Cao, P. P.-H. Cheung, X. Zheng, C. W. T. Leung, Q. Peng, Z. Shuai, B. Z. Tang, S. Yao, X. Huang, *Nat. Commun.* **2017**, *8*, 15639.
- [217] D. Chandler, *Nature* **2005**, *437*, 640-647.
- [218] C. R. Martinez, B. L. Iverson, *Chem. Sci.* **2012**, *3*, 2191-2201.
- [219] S. Yagai, T. Iwashima, T. Karatsu, A. Kitamura, *Chem. Commun.* **2004**, 1114-1115.
- [220] D. van der Zwaag, T. F. A. de Greef, E. W. Meijer, *Angew. Chem. Int. Ed.* **2015**, *54*, 8334-8336.
- [221] J. Baram, H. Weissman, B. Rybtchinski, *J. Phys. Chem. B* **2014**, *118*, 12068-12073.
- [222] X. Liu, F. Wu, Y. Tian, M. Wu, Q. Zhou, S. Jiang, Z. Niu, *Sci. Rep.* **2016**, *6*, 24567.
- [223] C. E. Boott, E. M. Leitao, D. W. Hayward, R. F. Laine, P. Mahou, G. Guerin, M. A. Winnik, R. M. Richardson, C. F. Kaminski, G. R. Whittell, I. Manners, *ACS Nano* **2018**, *12*, 8920-8933.
- [224] G. Cheng, V. Castelletto, C. M. Moulton, G. E. Newby, I. W. Hamley, *Langmuir* **2010**, *26*, 4990-4998.
- [225] Y. Gao, F. Zhao, Q. Wang, Y. Zhang, B. Xu, *Chem. Soc. Rev.* **2010**, *39*, 3425-3433.
- [226] S. Zhang, M. A. Greenfield, A. Mata, L. C. Palmer, R. Bitton, J. R. Mantei, C. Aparicio, M. O. de la Cruz, S. I. Stupp, *Nat. Mater.* **2010**, *9*, 594-601.
- [227] A. Chalard, M. Mauduit, S. Souleille, P. Joseph, L. Malaquin, J. Fitremann, *Addit. Manuf.* **2020**, *33*, 101162.
- [228] H. Yokoi, T. Kinoshita, S. Zhang, *Proc. Natl. Acad. Sci. U.S.A* **2005**, *102*, 8414.
- [229] S. S. Babu, V. K. Praveen, A. Ajayaghosh, *Chem. Rev.* **2014**, *114*, 1973-2129.
- [230] D. Higashi, M. Yoshida, M. Yamanaka, *Chem. - Asian J.* **2013**, *8*, 2584-2587.
- [231] L. A. Estroff, A. D. Hamilton, *Angew. Chem. Int. Ed.* **2000**, *39*, 3447-3450.
- [232] L. Saunders, P. X. Ma, *Macromol. Biosci.* **2019**, *19*, 1800313.
- [233] E. Prince, E. Kumacheva, *Nat. Rev. Mater.* **2019**, *4*, 99-115.
- [234] P. Malo de Molina, M. Gradzielski, *Gels* **2017**, *3*, 30.
- [235] Y.-Y. Won, H. T. Davis, F. S. Bates, *Science* **1999**, *283*, 960.
- [236] Y.-Y. Won, K. Paso, H. T. Davis, F. S. Bates, *J. Phys. Chem. B* **2001**, *105*, 8302-8311.
- [237] S. R. Raghavan, J. F. Douglas, *Soft Matter* **2012**, *8*, 8539-8546.
- [238] J. R. Lovett, L. P. D. Ratcliffe, N. J. Warren, S. P. Armes, M. J. Smallridge, R. B. Cracknell, B. R. Saunders, *Macromolecules* **2016**, *49*, 2928-2941.
- [239] A. Blanazs, R. Verber, O. O. Mykhaylyk, A. J. Ryan, J. Z. Heath, C. W. I. Douglas, S. P. Armes, *J. Am. Chem. Soc.* **2012**, *134*, 9741-9748.
- [240] N. J. W. Penfold, J. R. Whatley, S. P. Armes, *Macromolecules* **2019**, *52*, 1653-1662.
- [241] M. Sponchioni, C. T. O'Brien, C. Borchers, E. Wang, M. N. Rivolta, N. J. W. Penfold, I. Canton, S. P. Armes, *Chem. Sci.* **2020**, *11*, 232-240.
- [242] A. L. A. Binch, L. P. D. Ratcliffe, A. H. Milani, B. R. Saunders, S. P. Armes, J. A. Hoyland, *Biomacromolecules* **2021**, *22*, 837-845.
- [243] M. K. Gupta, J. R. Martin, T. A. Werfel, T. Shen, J. M. Page, C. L. Duvall, *J. Am. Chem. Soc.* **2014**, *136*, 14896-14902.
- [244] J. Cheng, D. Amin, J. Latona, E. Heber-Katz, P. B. Messersmith, *ACS Nano* **2019**, *13*, 5493-5501.
- [245] R. E. Kieltyka, A. C. H. Pape, L. Albertazzi, Y. Nakano, M. M. C. Bastings, I. K. Voets, P. Y. W. Dankers, E. W. Meijer, *J. Am. Chem. Soc.* **2013**, *135*, 11159-11164.

References

- [246] S. Strandman, X. X. Zhu, *Gels* **2016**, *2*, 16.
- [247] S. Correa, A. K. Grosskopf, H. Lopez Hernandez, D. Chan, A. C. Yu, L. M. Stapleton, E. A. Appel, *Chem. Rev.* **2021**.
- [248] Z. Xu, J. Peng, N. Yan, H. Yu, S. Zhang, K. Liu, Y. Fang, *Soft Matter* **2013**, *9*, 1091-1099.
- [249] P. Y. W. Dankers, T. M. Hermans, T. W. Baughman, Y. Kamikawa, R. E. KIELTYKA, M. M. C. Bastings, H. M. Janssen, N. A. J. M. Sommerdijk, A. Larsen, M. J. A. van Luyn, A. W. Bosman, E. R. Popa, G. Fytas, E. W. Meijer, *Adv. Mater.* **2012**, *24*, 2703-2709.
- [250] P. Y. W. Dankers, M. J. A. van Luyn, A. Huizinga-van der Vlag, G. M. L. van Gemert, A. H. Petersen, E. W. Meijer, H. M. Janssen, A. W. Bosman, E. R. Popa, *Biomaterials* **2012**, *33*, 5144-5155.
- [251] V. Jayawarna, M. Ali, T. A. Jowitt, A. F. Miller, A. Saiani, J. E. Gough, R. V. Ulijn, *Adv. Mater.* **2006**, *18*, 611-614.
- [252] J. Y. C. Lim, Q. Lin, K. Xue, X. J. Loh, *Mater. Today Adv.* **2019**, *3*, 100021.
- [253] X. Du, J. Zhou, J. Shi, B. Xu, *Chem. Rev.* **2015**, *115*, 13165-13307.
- [254] V. Hagel, T. Haraszti, H. Boehm, *Biointerphases* **2013**, *8*, 36.
- [255] N. Paxton, W. Smolan, T. Bock, F. Melchels, J. Groll, T. Jungst, *Biofabrication* **2017**, *9*, 044107.
- [256] L. Moroni, J. A. Burdick, C. Highley, S. J. Lee, Y. Morimoto, S. Takeuchi, J. J. Yoo, *Nat Rev Mater* **2018**, *3*, 21-37.
- [257] P. R. A. Chivers, D. K. Smith, *Nat. Rev. Mater.* **2019**, *4*, 463-478.
- [258] M. C. Nolan, A. M. Fuentes Caparrós, B. Dietrich, M. Barrow, E. R. Cross, M. Bleuel, S. M. King, D. J. Adams, *Soft Matter* **2017**, *13*, 8426-8432.
- [259] N. A. Sather, H. Sai, I. R. Sasselli, K. Sato, W. Ji, C. V. Synatschke, R. T. Zambrotta, J. F. Edelbrock, R. R. Kohlmeyer, J. O. Hardin, J. D. Berrigan, M. F. Durstock, P. Mirau, S. I. Stupp, *Small* **2021**, *17*, 2005743.
- [260] R. Landers, A. Pfister, U. Hübner, H. John, R. Schmelzeisen, R. Mülhaupt, *J. Mater. Sci.* **2002**, *37*, 3107-3116.
- [261] L. A. Hockaday, K. H. Kang, N. W. Colangelo, P. Y. C. Cheung, B. Duan, E. Malone, J. Wu, L. N. Girardi, L. J. Bonassar, H. Lipson, C. C. Chu, J. T. Butcher, *Biofabrication* **2012**, *4*, 035005-035005.
- [262] B. Duan, L. A. Hockaday, K. H. Kang, J. T. Butcher, *J. Biomed. Mater. Res. A* **2013**, *101*, 1255-1264.
- [263] K. Schacht, T. Jüngst, M. Schweinlin, A. Ewald, J. Groll, T. Scheibel, *Angew. Chem. Int. Ed.* **2015**, *54*, 2816-2820.
- [264] Y. Wang, J. Li, Y. Li, B. Yang, *Nano Today* **2021**, *39*, 101180.
- [265] J. Boekhoven, S. I. Stupp, *Adv. Mater.* **2014**, *26*, 1642-1659.
- [266] K. A. Simon, N. J. Warren, B. Mosadegh, M. R. Mohammady, G. M. Whitesides, S. P. Armes, *Biomacromolecules* **2015**, *16*, 3952-3958.
- [267] I. Canton, N. J. Warren, A. Chahal, K. Amps, A. Wood, R. Weightman, E. Wang, H. Moore, S. P. Armes, *ACS Cent. Sci.* **2016**, *2*, 65-74.

List of abbreviations

List of abbreviations

1D	One-dimensional
AF4	Asymmetrical flow field-flow fractionation
AUC	Analytical ultracentrifugation
BDEA	Benzenediesteramide
<i>boc</i>	<i>tert</i> -Butyloxycarbonyl
BTA	Benzene trisamide
BTU	Benzene trisurea
BTUP	Benzene trisureapeptide
BTP	Benzene trispeptide
CDSA	Crystallization-driven self-assembly
cryoTEM	Cryo transmission electron microscopy
CPNT	Cyclic peptide nanotube
CPPNT	Cyclic peptide polymer nanotube
DCM	Dichloromethane
DLS	Dynamic light scattering
DMAP	4-Dimethylaminopyridine
DMF	Dimethylformamide
DP	Degree of polymerization
EDC	1-Ethyl-3-(3-dimethylaminopropyl)carbodiimide
EtOH	Ethanol
DAC	Dual asymmetric centrifugation
DP	Degree of polymerization
kD	Kilodalton
LMWG	Low molecular weight gelator
MALLS	Multi angle laser-light scattering
NHS	<i>N</i> -Hydroxysuccinimide
PDI	Perylene bisimide

List of abbreviations

PEO	Poly(ethylene oxide)
PEtOx	Poly(ethyloxazoline)
PPO	Poly(propylene oxide)
PS	Polystyrene
RI	Refractive index
RT	Room temperature
SANS	Small angle neutron scattering
SAXS	Small angle x-ray scattering
SEC	Size exclusion chromatography
siRNA	Silencing ribonucleic acid
SLS	Static light scattering
SPB	Supramolecular polymer bottlebrush
TEA	Triethylamine
TFA	Trifluoroacetic acid
THF	Tetrahydrofuran
TIPS	Trisopropylsilane
US	Ultrasonication

Curriculum vitae



- 20/08/1993 Born in Kronach, Germany
- 2005-2012 Kaspar Zeuß Gymnasium, Kronach
General qualification for university entrance
- 2012-2015 Academic studies in Chemistry (B.Sc.)
University of Bayreuth
- 2015 Bachelor thesis in the group of Prof. Dr. Agarwal
University of Bayreuth, MCII
Title: Antibacterial modification of silk fibers (*bombyx mori*)
- 2015-2017 Academic studies in Polymer Science (M.Sc.)
University of Bayreuth
- 2017 Student assistant in the group of Prof. Dr. Weber
University of Bayreuth, ACII
- 2017 Master thesis in the group of Prof. Dr. Strohriegl
University of Bayreuth, MCI
Title: Synthesis of polycarbazoles by controlled Suzuki-Miyaura polycondensation
- 2017-2021 PhD student at the Laboratory of Organic and Macromolecular Chemistry (IOMC) at the Friedrich Schiller University Jena in the group of Dr. Johannes C. Brendel
Thesis: From fundamental design to applications of supramolecular polymer bottlebrushes

.....

Franka V. Gruschwitz

Publication list

Peer reviewed publications

T. Klein[‡], F. V. Gruschwitz[‡], S. Rogers, S. Hoepfner, I. Nischang, J. C. Brendel, “The influence of directed hydrogen bonds on the self-assembly of amphiphilic polymers in water”, *J. Colloid Interface Sci.* **2019**, 557, 488-497.

DOI: 10.1016/j.jcis.2019.09.046

F. V. Gruschwitz, M.-C. Fu, T. Klein, R. Takahashi, T. Higashihara, S. Hoepfner, I. Nischang, K. Sakurai, J. C. Brendel, “Unraveling decisive structural parameters for the self-assembly of supramolecular polymer bottlebrushes based on benzene trisureas”, *Macromolecules* **2020**, 53, 7552-7560.

DOI: 10.1021/acs.macromol.0c01361

F. V. Gruschwitz[‡], T. Klein[‡], S. Catrouillet, J. C. Brendel, “Supramolecular polymer bottlebrushes”, *Chem. Commun.* **2020**, 56, 5079-5110.

DOI: 10.1039/d0cc01202e

T. Klein, H. F. Ulrich, F. V. Gruschwitz, M. T. Kuchenbrod, R. Takahashi, S. Fujii, S. Hoepfner, I. Nischang, K. Sakurai, J. C. Brendel, “Impact of amino acids on the aqueous self-assembly of benzenetrispeptides into supramolecular polymer bottlebrushes”, *Polym. Chem.* **2020**, 11, 6763-6771.

DOI: 10.1039/d0py01185a

T. Klein, H. F. Ulrich, F. V. Gruschwitz, M. T. Kuchenbrod, R. Takahashi, S. Hoepfner, I. Nischang, K. Sakurai, J. C. Brendel, “Overcoming the Necessity of a Lateral Aggregation in the Formation of Supramolecular Polymer Bottlebrushes in Water”, *Macromol. Rapid Commun.* **2021**, 42, e2000585.

DOI: 10.1002/marc.202000585

F. V. Gruschwitz[‡], T. Klein[‡], M. T. Kuchenbrod, N. Moriyama, S. Fujii, I. Nischang, S. Hoepfner, K. Sakurai, U. S. Schubert, J. C. Brendel, “Kinetically Controlling the Length of Self-Assembled Polymer Nanofibers Formed by Intermolecular Hydrogen Bonds”, *ACS Macro Lett.* **2021**, 837-843.

DOI: 10.1021/acsmacrolett.1c00296

Submitted manuscripts

T. Klein[‡], F. V. Gruschwitz[‡], I. Nischang, S. Hoepfner, J. C. Brendel, “Adjusting the length of supramolecular polymer bottlebrushes by top-down approaches”, *Beilstein J.* **2021**, submitted.

F. V. Gruschwitz, F. Hausig, P. Schüler, J. Kimmig, D. Pretzel, U.S. Schubert, S. Catrouillet, J. C. Brendel, “Dynamic hydrogels from crosslinked supramolecular polymeric nanofibers”, *Adv. Func. Mater.* **2021**, submitted.

E. Gardey, F. H. Sobotta, D. Haziri, P. C. Grunert, M. T. Kuchenbrod, F. V. Gruschwitz, S. Hoepfner, M. Schumann, N. Gaßler, A. Stallmach, J. C. Brendel, “Selective uptake into inflamed human intestinal tissue and immune cell targeting by wormlike polymer micelles”, *Nat. Comm.* **2021**, submitted.

Publication list

F. H. Sobotta, M. T. Kuchenbrod, F. V. Gruschwitz, G. Festag, P. Bellstedt, S. Hoepfener, J. C. Brendel, “ Tuneable time delay in the burst release from oxidation sensitive polymersomes made by PISA”, *Angew. Chem. Int. Ed.* **2021**, submitted.

‡ These authors contributed equally to this work.

Poster presentations

Bayreuth Polymer Symposium (Bayreuth, Germany)

F.V. Gruschwitz, T. Klein, J.C. Brendel (2019): Formation of supramolecular polymer bottlebrushes by benzentrisamides, -ureas or -peptides.

Acknowledgment

Acknowledgment

Last but not least, I want to thank all the people who helped and supported me in the last 4 years. At first, I have to thank my supervisor Johannes C. Brendel for his unbridled scientific enthusiasm, his sheer incredible amount of knowledge about nearly every research area, and his willingness to educate and help his students to improve and develop the necessary scientific and personal skills. I am still amazed by your patience in long discussions and your great encouragement. Thanks for an interesting and fulfilling 4 years in your group and I wish you all the best for the future.

Moreover, I want to express my gratitude to Prof. Ulrich S. Schubert for giving me the chance to work in an inspiring, highly equipped environment – I appreciate the interdisciplinary and productive working conditions.

The DFG is to be thanked for funding.

My warmest gratitude goes to PD Dr. Stephanie Höppener and Maren T. Kuchenbrod for a tremendous amount of awesome cryo-TEM images. Thanks to Dr. Ivo Nischang for all the long and fruitful discussions. Furthermore, I would like to thank all the helpful people, who assisted with measurements: Dr. Grit Festag, Nicole Fritz, Renzo Paulus, Kristin Schreyer, and Sandra Köhn. I also want to thank Dr. Uwe Köhn for his work and help concerning bureaucratic problems. In this context, a big thank you also to the secretaries: Sylvia Braunsdorf and Katja Gattung.

Additionally, I have to thank my practical students (Anne Skotnicki, Pascal Scharfenberg, Xhesilda Fataj), who helped me work on several topics.

Of course, there are more people, without whom I would not have accomplished this! Thanks to Nicole Ziegenbalg, Franziska Hausig and Marcel Enke! I think we were a great office-team offering good support for all of us! Furthermore: Thank you APS group – Tobias Klein, Fabian Sobotta, Hans F. Ulrich for all the helpful discussions and good corporations in all projects but also the great atmosphere and fun activities. The same goes out for the “CEEC-guys” – Thanks for the good times and keeping the fun in “fundamental research”. I will miss you all!

And finally, I want to express my gratitude to my family who encouraged me and supported me all my life. And thank you, Steffen, for having my back in tough times and giving me the strength to accomplish everything I aim for.

Declaration of originality

Declaration of originality

Ich erkläre, dass ich die vorliegende Arbeit selbständig und unter Verwendung der angegebenen Hilfsmittel, persönlichen Mitteilungen und Quellen angefertigt habe.

Jena, den

.....

Franka V. Gruschwitz

Appendix

Publications P1 to P8

P1: Reprinted by permission of Royal Society of Chemistry. Copyright 2020.

P2: Reprinted by permission of Elsevier. Copyright 2019.

P3: Reprinted by permission of the American Chemical Society. Copyright 2020.

P4: Reprinted by permission of Royal Society of Chemistry. Copyright 2020.

P5: Reprinted by permission of John Wiley and Sons. Copyright 2020.

P6: Reprinted by permission of American Chemical Society. Copyright 2021.

P7: Reproduced by permission of T. Klein, F. V. Gruschwitz, I. Nischang, S. Hoepfner, J. C. Brendel.

P8: Reproduced by permission of F. V. Gruschwitz, F. Hausig, P. Schüler, J. Kimmig, D. Pretzel, U.S. Schubert, S. Catrouillet, J. C. Brendel.

Publication P1

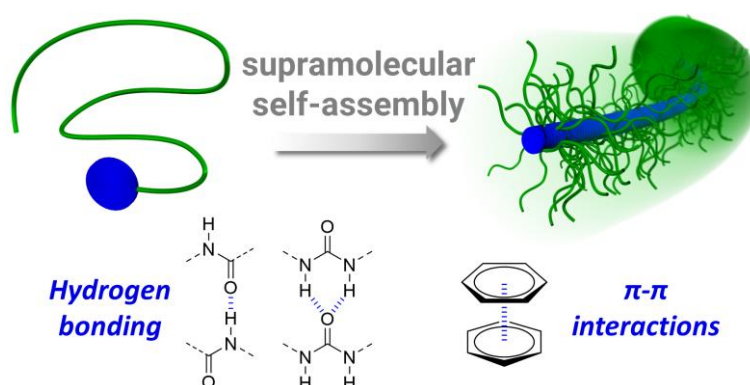
Supramolecular polymer bottlebrushes

F. V. Gruschwitz[‡], T. Klein[‡], S. Catrouillet, J. C. Brendel, *Chem. Commun.*
2020, *56*, 5079-5110.

Reproduced by permission of Royal Society of Chemistry. Copyright © 2020.

The paper as well as the supporting information is available online:

doi.org/10.1039/d0cc01202e



[‡] Equal contribution.



Cite this: *Chem. Commun.*, 2020, 56, 5079

Supramolecular polymer bottlebrushes

Franka V. Gruschwitz,^{†ab} Tobias Klein,^{ib} ^{†ab} Sylvain Catrouillet^c and Johannes C. Brendel^{ib}*^{ab}

The field of supramolecular chemistry has long been known to generate complex materials of different sizes and shapes *via* the self-assembly of single or multiple low molar mass building blocks. Matching the complexity found in natural assemblies, however, remains a long-term challenge considering its precision in organizing large macromolecules into well-defined nanostructures. Nevertheless, the increasing understanding of supramolecular chemistry has paved the way to several attempts in arranging synthetic macromolecules into larger ordered structures based on non-covalent forces. This review is a first attempt to summarize the developments in this field, which focus mainly on the formation of one-dimensional, linear, cylindrical aggregates in solution with pendant polymer chains – therefore coined supramolecular polymer bottlebrushes in accordance with their covalent equivalents. Distinguishing by the different supramolecular driving forces, we first describe systems based on π - π interactions, which comprise, among others, the well-known perylene motif, but also the early attempts using cyclophanes. However, the majority of reported supramolecular polymer bottlebrushes are formed by hydrogen bonds as they can for example be found in linear and cyclic peptides, as well as so called sticker molecules containing multiple urea groups. Besides this overview on the reported motifs and their impact on the resulting morphology of the polymer nanostructures, we finally highlight the potential benefits of such non-covalent interactions and refer to promising future directions of this still mostly unrecognized field of supramolecular research.

Received 14th February 2020,
Accepted 15th April 2020

DOI: 10.1039/d0cc01202e

rsc.li/chemcomm

^a *Laboratory of Organic and Macromolecular Chemistry (IOMC), Friedrich Schiller University Jena, Humboldtstraße 10, 07743 Jena, Germany. E-mail: johannes.brendel@uni-jena.de*

^b *Jena Center for Soft Matter (JCSM), Friedrich Schiller University Jena, Philosophenweg 7, 07743 Jena, Germany*

^c *ICGM, Université de Montpellier, CNRS, ENSCM, Montpellier, France*

[†] These authors contributed equally to this work.

1. Introduction

The design of one dimensional (1D) polymer nanostructures still represents a challenge for material scientists, but their unique properties, for example in rheology or transport behavior have also been an incentive to various developments in fields



Franka V. Gruschwitz

Franka V. Gruschwitz completed her BSc degree in chemistry at the University of Bayreuth in 2015. She then proceeded with her MSc in polymer chemistry at the University of Bayreuth and received her degree in 2017 at the chair Macromolecular Chemistry I. Since 2017 she has been working on the aqueous self-assembly of functional supramolecular polymer bottlebrushes as a PhD student in the group of Dr Brendel at the Friedrich-Schiller-University Jena.



Tobias Klein

Tobias Klein received his BSc degree in chemistry at the University of Bayreuth in 2014. Afterwards, he was a visiting research student in the group of Prof. Perrier at the University of Warwick investigating the self-assembly of cyclic peptide polymer conjugates. He then commenced his MSc in polymer chemistry at the University of Bayreuth and received his MSc degree in 2017 after completing his master's thesis at the Monash Institute of Pharmaceutical Sciences in Melbourne. Since 2017 he has been working as a PhD student in the group of Dr Brendel at the Friedrich-Schiller-University Jena on the aqueous self-assembly of supramolecular polymer bottlebrushes.

such as nanomedicine,^{1–3} rheology modifiers^{4–6} or electronics and photonics.^{7–10} In combination with the plethora of available polymers, anisotropic nanostructures have been built up featuring a variety of functionalities¹¹ or stimuli-responsive behavior.¹² To highlight only one potential application, such 1D polymer nanostructures promise several advantages such as longer circulation lifetime or higher affinity for target cells over their spherical analogs in nanomedicine.^{13–20}

So far, the dominating method to yield such nanostructures relies on the self-assembly of block copolymers. By adjusting the fraction of the blocks, not only spherical or lamellar structures are accessible, but also cylindrical.^{21–26} However, despite several decades of research, the certain prediction of morphologies in block copolymer self-assembly, especially in solution remains difficult and often mixtures of different morphologies are obtained.^{27–31} Extremely slow dynamics and kinetically trapped states further cause pathway-dependent differences and thus complicate the overall process.²³ In order to overcome these obstacles, additional directional driving forces based on hydrogen bonds³² or π - π interactions³³ were introduced to the block copolymers favoring the formation of fiber-like structures. The most promising attempt for controlled assembly of block copolymers so far is certainly the crystallization driven self-assembly (CDSA) process which relies on the epitaxial crystallization of one polymer block resulting in a living growth of the nanostructures.^{34–41} Another concept is based on liquid crystals, which found widespread application in the structuring of polymers in particular in the bulk.⁴² This leads to interesting properties and dynamics and favors the development of a variety of functional supramolecular materials exhibiting ferroelectric, photonic or conductive properties.^{43–47} Interested readers are here referred to the given literature, while overlapping aspects with our topic are discussed in Section 2.2.^{48–54}

In this context, reference should also be made to quasi block copolymers since they occupy an intermediate position, combining the microphase segregation of BCPs and the dynamic

properties of directed supramolecular self-assemblies.^{55,56} Hereby, the hierarchical self-assembly of polymeric structures can further be achieved by employing coordination complexes *via* metal-ligand^{57,58} or host-guest interactions.^{59–64}

In contrast to the above mentioned supramolecular forces involved in the block copolymer self-assembly, 1D polymer nanostructures can also be built up by covalent bonds. Such covalent polymer bottlebrushes are synthesized by different grafting strategies (mainly grafting-to, grafting-from, and grafting-through) which create a densely grafted polymer backbone resulting in a stretched conformation of the polymer arms.⁶⁵ Several excellent reviews summarize their synthesis, the resulting properties, and potential applications of these covalently bound bottlebrushes.^{66–73} With the continuous development of efficient synthetic tools, these very large macromolecules can still be tuned in terms of their length or their diameter⁷⁴ which makes them particularly attractive for applications in nanomedicine.^{75–82}

The herein summarized supramolecular polymer bottlebrushes (SPB)[‡] represent a hybrid between supramolecular polymers and the previous mentioned covalent bottlebrushes to create 1D nanostructures by physical interactions. In contrast to the self-assembly of block copolymers, defined low molar mass building blocks are utilized to create directed interactions and, thus, a supramolecular polymer backbone to which covalent polymer chains are densely grafted (Fig. 1). Numerous organic molecules have been reported to date, which form supramolecular polymers and even might feature a controlled or living assembly.^{20,83–89} The structures range from small gelators to complex aromatic transport systems and their assembly is in most cases well understood including the underlying thermodynamics (causing, for example, isodesmic or cooperative assembly pathways,

[‡] The term supramolecular polymer bottlebrush was deliberately chosen as a compromise between supramolecular polymer brush and supramolecular bottlebrush which were both used in literature. The rearrangement in the terminology should further emphasize the contrast to common bottlebrush polymers and their covalent backbones.



Sylvain Catrouillet

Sylvain Catrouillet completed his PhD in 2014 at the University du Maine (Le Mans, France), his research focused on the self-assembly of supramolecular nanocylinders by hydrogen bonded block copolymers. He completed his post-doctoral position in the group of Prof. Sébastien Perrier at the University of Warwick, researching the self-assembly of cyclic peptide-polymer conjugates. In 2016, he joined the Institut Charles Gerhardt at the University of Montpellier,

where he is currently working as an assistant professor. His research interests include the development of new dynamic architectures by polymer synthesis and hydrogen bonding self-assembling systems.



Johannes C. Brendel

Johannes C. Brendel received his PhD in 2013 (University of Bayreuth) working on semiconducting polymers. After his PhD, he was awarded with a research fellowship of the German Research Foundation (DFG) for a postdoctoral project at the University of Warwick and the Monash Institute of Pharmaceutical Sciences (MIPS). Since 2016, he is an independent research group leader within the Jena Center for Soft Matter (JCSM) at the Friedrich-Schiller-University Jena where he

was awarded with a research grant of the Emmy-Noether program in 2017. His research interests include the synthesis of well-defined polymer architectures and their hierarchical self-assembly into anisotropic nanostructures.

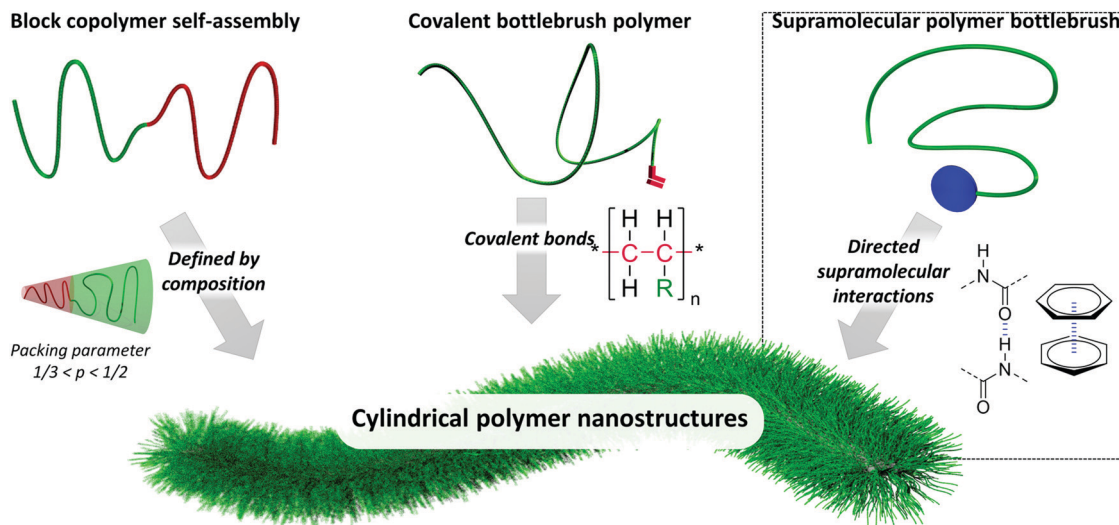


Fig. 1 Schematic illustration of different strategies to obtain polymer based, bottlebrush-like structures. From left to right: block-copolymer self-assembly defined by the packing parameter, covalent polymerization (here depicted: grafting-through approach), and supramolecular self-assembly by directed supramolecular interactions as summarized in this review.

which was nicely described by Meijer *et al.*⁹⁰ So far only an exclusive selection of such molecules have been reported to be suitable for the creation of supramolecular polymer bottlebrushes, which requires stronger forces to overcome the additional steric demands of the attached polymer chains.

However, the combination of polymers and supramolecular building blocks promises advantages of both sides, *e.g.* the versatile functionalities within the macromolecule and an element for reversible hierarchical organization. Nature gives the best example for such a combination when the self-assembly of proteins is considered. These macromolecules are for example able to form dynamic micrometer-sized filaments, the microtubules, by supramolecular interactions that not only act as part of the skeleton of a eukaryotic cell but also provide the platform for cellular transport mechanism.^{91–95} Synthetic chemistry is still far from the complexity of nature, but the assembly of polymeric units into more ordered structures such as the presented supramolecular polymer bottlebrushes represents a promising development for more complex hierarchical structures.^{85,96–105} In particular, the dynamics and the modularity of supramolecular self-assembly offers a unique

potential for the design of functional anisotropic nanostructures in solution.⁸⁸ In contrast to covalent bonds and the strong forces created by crystallization, the relatively weak non-covalent interactions are at the origin of the dynamic nature which facilitates a triggerable assembly or disassembly of the supramolecular structures. However, the construction of a supramolecular backbone in a polymer bottlebrush requires to overcome the repulsion forces arising from the steric demands of the polymer chains. The much lower bond energies of typical supramolecular forces such as hydrogen bonds, π -stacking or van der Waals interactions compared to covalent bonds necessitate often the combination of multiple interaction sites to enable the assembly. For comparison, covalent bonds have homolytic dissociation energies in the range of 100–400 kJ mol⁻¹, while for example the dissociation of hydrogen bonds requires energies between 10–65 kJ mol⁻¹ (Fig. 2).¹⁰⁶ Moreover, these forces need to be directional for the creation of ordered systems, *i.e.* the interaction of two units or the addition of another building block is only favored in one particular position aligning the overall assembly. This prerequisite excludes, for example, most ionic or van der Waals interactions.

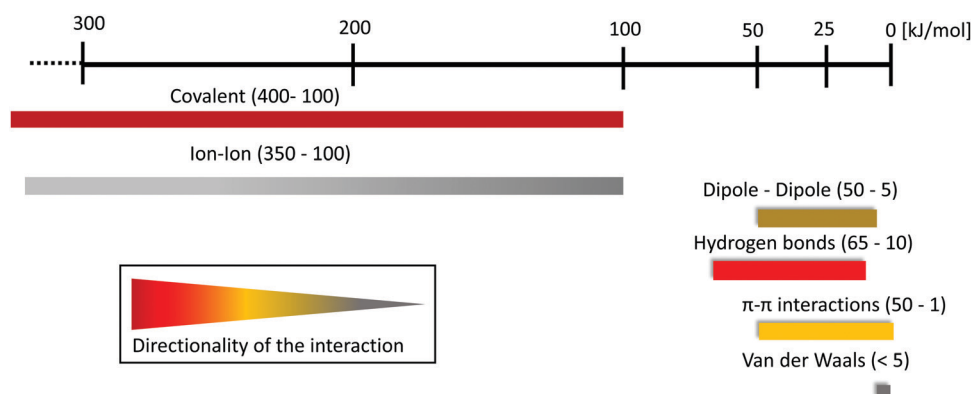


Fig. 2 Bond energies according to J. W. Steed and J. L. Atwood, *Supramolecular Chemistry*, Wiley, 2009.¹⁰⁶

Overall, a fine balance of interactions is required in such materials to guarantee their assembly but still ensure their processing and preserve their dynamic nature. Therefore, it is no surprise that only about a dozen of structural motifs have so far been reported for the formation of supramolecular polymer bottlebrushes. Within this review, we aim at summarizing these different self-assembly motifs and highlight some potential candidates for the future. The interactions between the structures rely mostly on the formation of strong hydrogen bonds or π -stacking between rather large planar aromatic systems. In each case, we first describe the self-assembly of the individual motifs on some selected examples. The focus, however, will remain on developments to integrate these materials into polymers to generate supramolecular polymer bottlebrushes.

2. Structure formation by π - π interactions of aromatic systems

2.1. Planar unsaturated cyclophanes

These rigid, shape-persistent macrocycles consist of a framework of unsaturated hydrocarbons, which adopt a mostly planar conformation. This conformation of the conjugated phenylene and ethynylene units maximizes the contact area between adjacent rings and enables the formation of strong van der Waals and π - π interactions (Fig. 3). These structures are among the first materials used for the formation of supramolecular polymer bottlebrushes in solution.¹⁰⁷ The exterior of these macrocycles can be modified with different substituents to improve their solubility or to exploit additional solvophobic effects and hence, enhance their self-assembly.¹⁰⁸ The synthesis of these rigid macrocycles involves several steps of metal-catalyzed coupling reactions.^{109,110} Their aggregation in chloroform was first reported in 1992 by Zhang and Moore when they observed a concentration-dependent proton shift of the aromatic protons in ¹H-NMR experiments.^{111,112} In general, ring size, solvent choice and steric hindrance *e.g.* by introduction of bulky substituents such as *tert*-butyl groups are the main parameters influencing the stacking of these rigid macrocycles. The solubility in a broader range of solvents, including for example acetone and DMSO was improved with the addition of (ethylene glycol) ester side chains. As a consequence, Lahiri *et al.* found that a solvophobic effect in

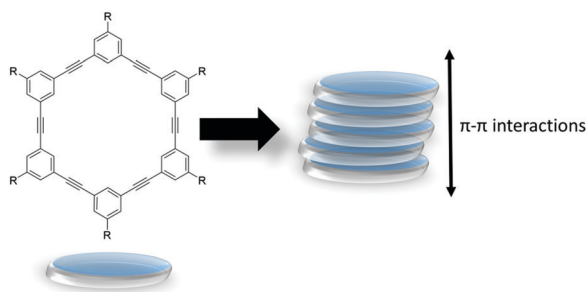


Fig. 3 Possible self-assembly pattern of phenylene ethynylene macrocycle to fibrillar structures.

the more polar solvents enhances the π -stacking which led to the formation of larger aggregates than dimers.¹¹³

Apart from small oligo ethylene glycol (OEG) substituents, also polymeric side chains that are incompatible with the cyclic framework can be attached. Upon dissolution in a selective solvent of the polymeric side chains, a block-like coil-(rigid) ring-coil polymer structure is formed. Rosselli and coworkers attached polystyrene (PS) chains (DP = 25) to a phenylene-ethynylene macrocycle **1** (Fig. 4a), resulting in a birefringent material in cyclohexane that formed a gel upon cooling. The gelation occurred due to the aggregation of the cyclic backbone when cooled, whereas the side chains remain solubilized. Careful choice of the length of the polymeric side chain is crucial to still achieve solubility while maintaining aggregation. Small angle X-ray scattering (SAXS) and ultra-small angle X-ray scattering (USAXS) measurements revealed the existence of hollow cylindrical structures with an external diameter of 10 nm and a lumen of 2 nm. Transmission electron microscopy (TEM) and atomic force microscopy (AFM) (Fig. 4b) showed the formation of ribbon-like structures with a large radius of curvature indicative of their rigidity.^{114,115} After slow evaporation of the cyclohexane, the resulting films were investigated by X-ray analysis. The scattering profiles showed a microphase separation of the crystallized macrocycles from the amorphous PS phase (Fig. 4d).¹¹⁶ The assembly and disassembly of this system were studied in temperature-dependent SAXS measurements. Below 40 °C, a solution of the macrocycle with PS side chains (DP = 25) in cyclohexane formed large tubular structures with a length of about 400 nm besides some unimers. This behavior was assigned to the θ -temperature of 34 °C for PS chains in cyclohexane. Above this temperature, the swelling of polymer chains increases continuously and, therefore, more space is occupied by the PS side chains causing a disassembly. In conclusion, at temperatures below 34 °C the concentration of unimeric macrocycles is declining and below 25 °C there is a narrow temperature range where only tubular structures are present. Increasing the temperature leads to increased solubility of the macrocycles. Therefore, the concentration of aggregated macrocycles decreases and at 40 °C all macrocycles are molecularly dissolved. Hereby, the cylinder length remained high over the whole temperature range, while only the concentration of aggregated macrocycles in the solution is declining with increasing temperature,¹¹⁷ indicating cooperative self-assembly.¹¹⁸ Furthermore, the kinetics of the temperature-induced aggregation of the PS modified macrocycle **1** were investigated using magnetic-field-induced solution birefringence (Fig. 4c). Hereby, solutions of the molecularly dissolved macrocycles in cyclohexane were cooled down to various temperatures between 10 °C and 18 °C to cover the temperature region where no molecularly dissolved macrocycles are present and analyzed over a time range of up to 400 h. This technique allows to distinguish ordered and disordered macrocycle aggregates and gives insight into the large time scales that are necessary to form aggregates. With the use of solution birefringence at temperatures below 18 °C, three consecutive stages of molecular formation could be distinguished: disordered objects, ordered fibers (after 10–50 h) and finally the formation of large networks (> 50 h).¹¹⁹

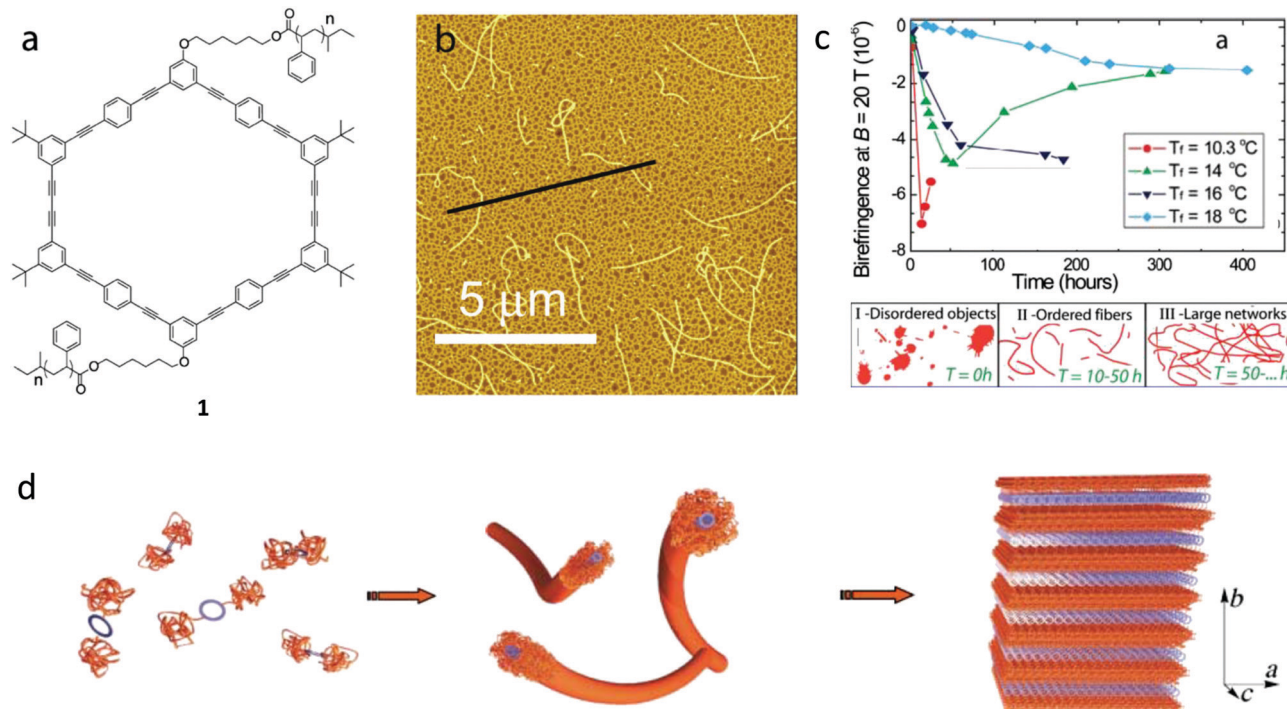


Fig. 4 (a) Structure of the coil-ring-coil macrocycle **1** ($n \approx 25$). (b) AFM image of a 10^{-6} M solution of macrocycle **2** drop-casted on mica. (c) Time-dependent solution birefringence at $B = 20$ T and at different temperatures. (II) Shows the development of ordered fibers from the disordered state (I). Eventually, large networks are formed (III). Adapted with permission from ref. 96 Copyright (2009) American Chemical Society.¹¹⁹ (d) Aggregation of molecularly dissolved coil-ring-coil macrocycles to supramolecular polymer bottlebrushes in solution and formation of lamellar structures in the solid phase. Adapted with permission from ref. 116 Copyright (2003) John Wiley and Sons.¹¹⁶

Additionally to these findings, the kinetics of aggregate formation were investigated *via* AFM measurements of amine-functionalized shape-president phenylene-ethynylene macrocycles **2** modified with polystyrene (Fig. 5a). These macrocycles bear amide moieties on the side chains which are hydrogen bonds promoting groups in addition to the π -stacking of the macrocycles. It could be shown that the self-assembly starts from small isotropic aggregates. The anisotropic growth and therefore, the building of larger supramolecular polymer bottlebrushes (Fig. 5b) is slower compared to the macrocycles without additional amide moieties. No enhanced aggregation due to the additional intermolecular hydrogen bonds could be observed compared to macrocycles lacking amide groups.¹²⁰

In comparison to the following motifs, these planar cyclophanes have received less attention for the formation of SPBs in recent years, but they have certainly inspired subsequent developments in the field.

2.2. Linear rigid aromatic units

Another substance class capable of assembling into supramolecular fibers in solutions are aromatic rod-coil amphiphiles. These consist of a hydrophobic, rigid rod-like aromatic structure to which hydrophilic, flexible coil-like blocks are attached. They are known to form a rich variety of liquid crystalline phases in the bulk state, which is driven by the microphase segregation as a consequence of the incompatibility of the dissimilar blocks.¹²¹ The defined length of their rigid aromatic segment distinguishes

them from the class of rod-coil-block-copolymers.¹²² The latter ones are structurally similar, but contain a rigid aromatic block that exhibits a length distribution. The observed orientational organization is the result of the stiff rod-like conformation of the aromatic block. Turning the focus to solutions, many different supramolecular architectures can be obtained in organic solvents,¹²³ water¹²⁴ or mixtures thereof¹²⁵ as nicely reviewed by Hoeben *et al.*¹²⁶ These architectures can be tailored by the variation of the relative volume fractions of the respective blocks as well as by the geometry of the stiff aromatic blocks. The group of Lee nicely demonstrated the impact of the relative volume ratio of the dissimilar blocks on the resulting morphology of the supramolecular assemblies in water (Fig. 6).¹²⁷ Whereas the rod-coil molecule **3** based on a tetra-*p*-phenylene rod block and a flexible PEG (DP = 23) block formed small spherical micelles in water, the analogous molecule **4** with a decreased PEG length (DP = 12) resulted in the formation of vesicular structures. In contrast to that, cylindrical aggregates were obtained for molecule **5** with a twin-rod block.

Helical nanofibers in water could be obtained with dumbbell-shaped¹²⁸ as well as with rigid-flexible macrocycles.¹²⁹ A rigid aromatic macrocycle with flexible PEG dendrons in its periphery was shown to form several hundred nanometers long SPBs in water and in addition to be a suitable solubilizer for single-walled carbon nanotubes in water.¹³⁰ The Lee group was also able to obtain supramolecular polymer bottlebrushes with T-shaped rod-coil amphiphiles.¹³¹ Due to their OEG dendrons, these molecules exhibited a thermoresponsive behavior and a sol-to-gel transition

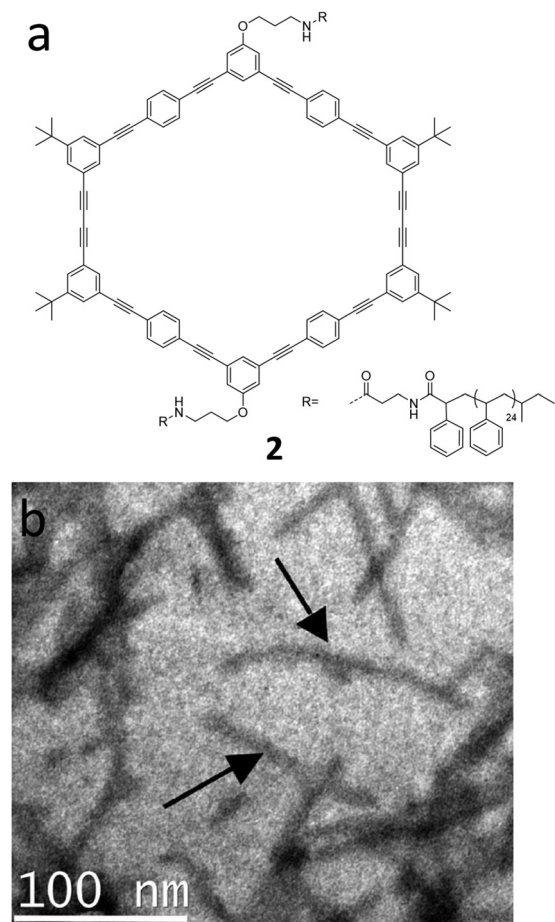


Fig. 5 (a) Structure of coil-rod-coil macrocycle with additional amide functionalities. (b) TEM micrograph of fibers of macrocycle **2** in cyclohexane. Adapted with permission from ref. 120 Copyright (2010) American Chemical Society.¹²⁰

upon heating. This transition was caused by the cleavage of hydrogen bonds between the OEG units and surrounding water molecules, resulting in a higher hydrophobicity and hence stronger interaction between the brushes. Furthermore, the group of Jin could show the potential of an aromatic rod-coil amphiphile consisting of four biphenyl groups connected to PEG with a DP of 17 to assemble into cylindrical aggregates.¹³² These were able to act as a nanoreactor for a Suzuki cross-coupling in aqueous solution. Apart from using rather short polymeric coil segments, also longer PEG chains (DP = 45) have been used in combination with oligo phenylene-vinylene blocks to obtain fibers even in very dilute THF/water mixtures (Fig. 7a).¹²⁵ The same group also reported a fiber formation in water/THF mixtures when poly(propylene oxide) (PPO) chains were attached (Fig. 7b).¹³³ SANS and SAXS measurements proved that the cylindrical structures consisted of an inner core built up by oligo(phenylene vinylene) and a PEG or PPO corona for **6** and **7**, respectively.

An example for the gelation properties of aromatic rod-coil amphiphiles was reported in a study by Zubarev *et al.* in which they synthesized a block-like polymer, consisting of a hydrophilic dendron core linked by a rigid rod biphenyl segment to an oligomeric isoprene coil segment (DP = 9).^{134,135} They defined this system as a dendron-rod-coil molecule. This molecule could induce gelation in several organic solvents. The formation of nanoribbons could even be verified in DCM at a very low concentration of 0.2 wt% and is triggered by noncovalent interactions including hydrogen bonding of the hydroxyl functionalities at the exterior of the dendron and the π -stacking of the biphenyl units of the rod structure.

2.3. Rylene-type aromatics

Already a century ago Jelley and Scheibe discovered the formation of stacked aggregates of cyanine dyes, which were named after

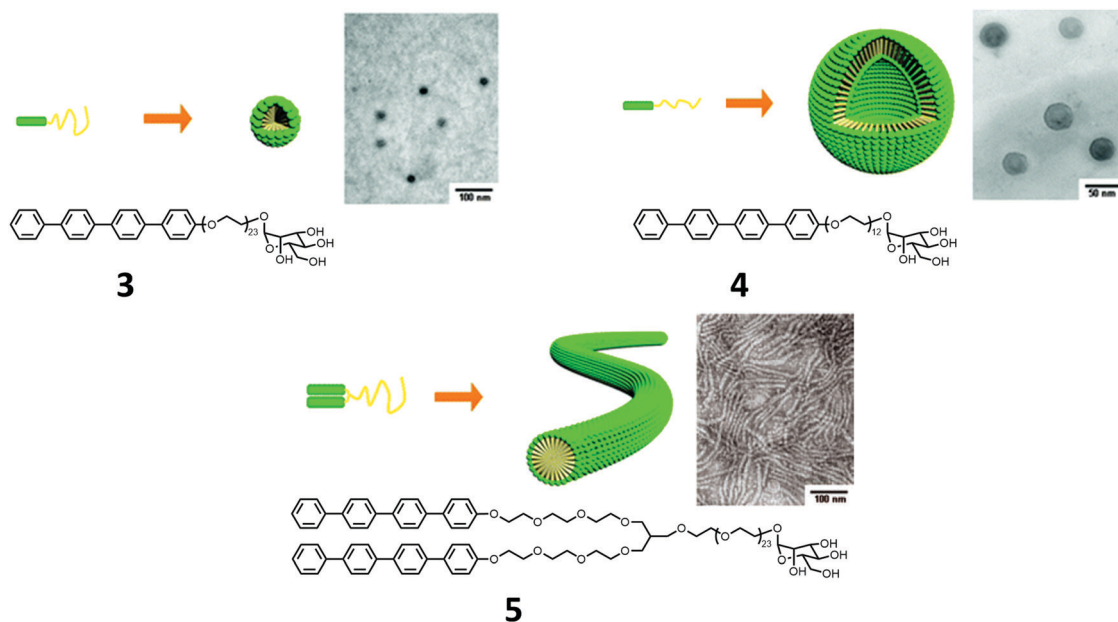


Fig. 6 Molecular structures of **3–5**, schematic representation of their aqueous self-assemblies and their respective TEM images. Adapted with permission from ref. 124 Copyright (2008) Royal Society of Chemistry.¹²⁴

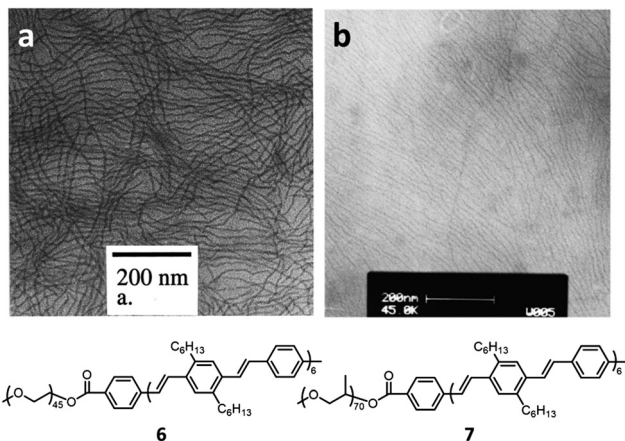


Fig. 7 TEM image of (a) **6** and (b) **7** cast from 0.5 mg mL⁻¹ solutions in THF/H₂O mixture onto a copper grid. (a) Adapted with permission from ref. 101 Copyright (2000) American Chemical Society.¹²⁵ (b) Adapted with permission from ref. 133 Copyright (2004) John Wiley and Sons.¹³³

their discoverer, J-type aggregates.^{136–138} Apart from those cyanine dyes, a very prominent motif for self-assembly by π - π interactions are rylene-type dyes, such as for example perylenes.^{139–144} Perylene dyes also show a tendency to form columnar stacks due to the π - π interaction of the large π -systems.¹⁴⁵ By the introduction of bay-substituents to perylene-bisimides, the interaction between the π -systems is decreased, resulting in a bathochromic shift that is characteristic for the formation of J-type aggregates.¹⁴⁶ Hereby, the dyes exhibit a longitudinal shift in the aggregation pattern, forming a ladder-type structure. For perylene-bisimides without bay-substituents and therefore very planar π -system, a hypsochromy can be observed, resulting from H-aggregation. Whether the type of off-set is of longitudinal, transverse or rotational nature is often difficult to elucidate. In water or alcohol, the strength of the π - π interaction increases, because water cannot solvate well the π -systems. This fact can be employed for the self-assembly of perylene bisimides (PDIs) in water. By utilizing solubilizing substituents, one-dimensional aggregates can also be obtained in aqueous environment.^{147,148} This solubility led to different application possibilities as *e.g.* hydrogelators.¹⁴⁹ Combining the perylene bisimide with Newkome-type dendrimers linked *via* chiral amino acids opened the way to develop chiral supramolecular structures in water.¹⁵⁰ Self-assembly into well-defined helically wound nanorods¹⁵¹ in water could further be obtained for PDIs equipped with short OEG chains due to strong π -stacking of the planar aromatic cores. Exemplarily, the general self-assembly behavior of perylene dyes is depicted in Fig. 8.¹⁵² With increasing concentration fusion and fission processes could be observed, where nanorods merged or divided in a side-by-side manner.

An example of a kinetically controlled PDI polymerization was recently reported by Wagner.¹⁵³ They successfully used PDI derivatives in a kinetically controlled seed-induced polymerization to yield supramolecular block copolymers by hydrogen bond induced intermolecular aggregation. This seeded growth mechanism has already been used to obtain fibers with controllable lengths and low dispersities in a living supramolecular polymerization.^{154,155}

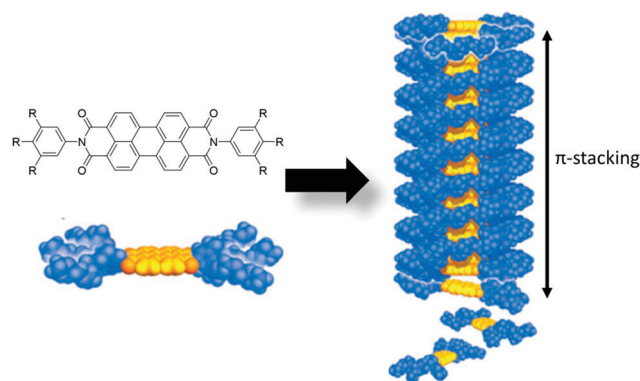


Fig. 8 Schematic depiction of the general self-assembly of perylene bisimide dyes with rotational off-set to long rigid nanorods. Adapted with permission from ref. 152 Copyright (2014) John Wiley and Sons.¹⁵²

The group of Frauerath conducted extensive research on oligomer and polymer functionalized PDIs. For instance, polyisoprene (DP = 15) modified PDI with β -sheet forming peptides self-assembled in dichloromethane or trichloroethane (TCE) into fibrils.¹⁵⁶ With the incorporation of peptides, the formation of hydrogen bonds and π -stacking could be strengthened and facilitated independently of each other. Microfibers could be obtained by solution-spinning of a nanofiber solution in TCE into MeOH. These microfibers can allow for efficient charge transport and can thus be used as a model system in organic semiconductors.¹⁵⁷ This study also evidences the necessity of a careful design of the building blocks and a good balance of the interaction forces required to achieve well-defined one-dimensional structures. Indeed no aggregation was observed for the previous structural motif without peptide sequences.¹⁵⁸

Further work on the self-assembly of PDIs was done by the group of Rybtchinski, who conducted extensive research on polymer functionalized PDIs and their aggregation into one-dimensional structures.^{144,159} In a first work, they found out that a perylene bisimide dye equipped with PEG substituents (DP = 17) can be reduced in water to obtain a stable dianion (Fig. 9).¹⁶⁰ Due to its extended π -system upon reduction, a higher aromatic stabilization makes protonation in water very unfavorable and leads to the formation of a very stable dianion.¹⁶¹ This reduction can be reversed by oxidation with oxygen. Employing this property, it could be shown that a PDI chromophore which is linked to another PDI unit through a planar acetylene linker could self-assemble in water/THF mixtures *via* its extended rigid π -system.¹⁶² Reduction of this compound in water/THF mixture resulted in disassembly of the aggregates. Upon oxidation this process is reversible. Substitution of the acetylene linker with a bipyridyl linker made the system suitable

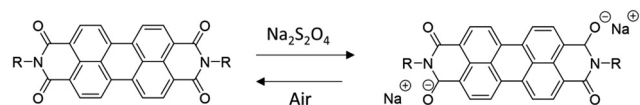


Fig. 9 Oxidation and reduction of the perylene bisimide.

to build up a multi-stimuli responsive supramolecular gel.¹⁶³ Once a reducing agent is added, the supramolecular gel converts into a fluid state due to the charging of the perylene units. The repulsion breaks up the aggregates and a liquid is obtained. By exposition to air, the process is reversible again. Also temperature dependent behavior was observed. At temperatures above 100 °C the gel collapsed and, in contrast to other gels where a sol-gel transition is observed at higher temperatures, here, a rapid deswelling was monitored. This process is of reversible nature. The gel can be very slowly swelled again over 24 h by cooling to room temperature or faster by sonication of the gel at 40 °C.

To obtain a higher structural diversity, further metal-ligand interactions were incorporated to yield a two-level self-assembly motif.¹⁶⁴ Hereby, the hydrophobic PDI motif was equipped with a terpyridine moiety were different metal ions can be coordinated. Coordination of Pd in a square-planar complex favored the formation of tubular structures in water/THF (9:1 v/v) mixtures *via* face-to-face stacking (H-aggregates). *Via* incorporation of Pt or Ag, the morphologies shifted from vesicular to a platelet structure, respectively. Kinetically trapped states can be accessed when additional peptide ligands were attached to the PDI complexed with Pt.¹⁶⁵ Metastable morphologies could be observed which strongly depend on the pathway of assembly. Furthermore, the influence of increased hydrophobicity of the PDIs and its impact on fiber formation were studied. The addition of perfluoroalkyl groups to the perylene core and therefore an enhanced hydrophobicity of the derivative strengthened the supramolecular interactions in water. This led to a higher association constant in 75:25 water/THF solution compared to alkyl chain functionalized derivatives.¹⁶⁶

When they increased the size of the PEG chains from the previous DP of 17 to a DP of 44, fiber formation could still be observed (Fig. 10a). Due to longer PEG chains, the previously mentioned system of two PDI units which are linked through an acetylene group self-assembled even in neat water. They proved that the applied self-assembly procedure is crucial for the type of aggregates formed. Dissolution of the PEG-functionalized PDI directly in water favored slipped stacking of the aromatic cores (J-aggregation; Fig. 10b), whereas the gradual solvent switch from THF to water promoted face-to-face stacking (H-aggregates; Fig. 10c). The THF allows for a rearrangement of the building blocks since it weakens the hydrophobic interactions and thus enables a higher overlap of the aromatic cores.¹⁴¹ This also applied to the system consisting of a bipyridyl linker, whose self-assembly appeared to be dependent on solvent composition, temperature and the chain length of the PEG exterior.¹⁶⁷

A different type of self-assembly to tubular structures could be obtained by a much bigger system **9** consisting of a hex-substituted benzene scaffold with three or six amphiphilic PDI substituents (Fig. 11).¹⁶⁸ They form defined supramolecular polymers in aqueous medium through pairwise directional hydrophobic and π -stacking interactions. This should enable exciton confinement, which is not common for stacked systems. In contrast to the previously mentioned systems, the hydrophobic surfaces of the PDIs arranged hereby parallel to the axis of the resulting polymer (Fig. 11). Each PDI is slightly

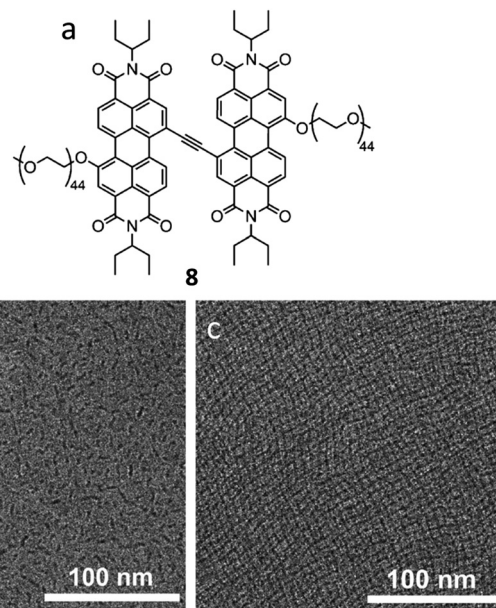


Fig. 10 (a) Chemical structure of PDI **8**. (b) CryoTEM of **8** directly dissolved in water ($c = 10^{-4}$ M). (c) CryoTEM of **8** after 1.5 h at 40% THF content, evaporation of THF and dissolution in water ($c = 10^{-4}$ M). Adapted with permission from ref. 141 Copyright (2014) John Wiley and Sons.¹⁴¹

overlapping with a PDI from the neighboring molecule. This “slipped stack” leads to tubular aggregates in THF/water (3:7) mixtures.

Apart from perylenes also smaller aromatic systems such as naphthalenes are capable of aggregation in one-dimensional structures if additional non-covalent directional forces such as hydrogen bonds are contributing to the driving force of the assembly.^{169–172} Naphthalene on its own without the hydrogen bonding sites of the diimide does not exhibit a high enough driving force to obtain one-dimensional growth. Nevertheless, the naphthalenes are listed here since the general motif is structurally similar to the rylene-type molecules.

The naphthalene diimide motif has also been combined with different polymers such as methacrylates or methacrylamides. The reported molecules self-assemble in water due to π -stacking and additional hydrogen bonds from hydrazide or amide linkers. The amide linker resulted in the initial formation of spherical micelles, which can transform into cylindrical morphologies upon aging of the solutions.^{173,174} More recently, Choisnet *et al.* reported NDIs which are equipped with bisurea groups and formed highly stable and robust self-assemblies (Fig. 12). The fiber formation in aqueous solution was reinforced by a combination of hydrogen bonding, hydrophobic interactions, and π -stacking to yield lengths of ~ 300 nm (Fig. 12).¹⁷⁵ Nevertheless, always the combination of the naphthalene unit with additional hydrogen bonding units as *e.g.* ureas or amides is necessary to obtain one-dimensional structures.

The rylene structures represent certainly one of the most prominent motifs in supramolecular assembly, which is also related to their unique optical and electrical properties. Despite this success, a limited number of examples for structuring polymeric units have been reported so far, but we are convinced

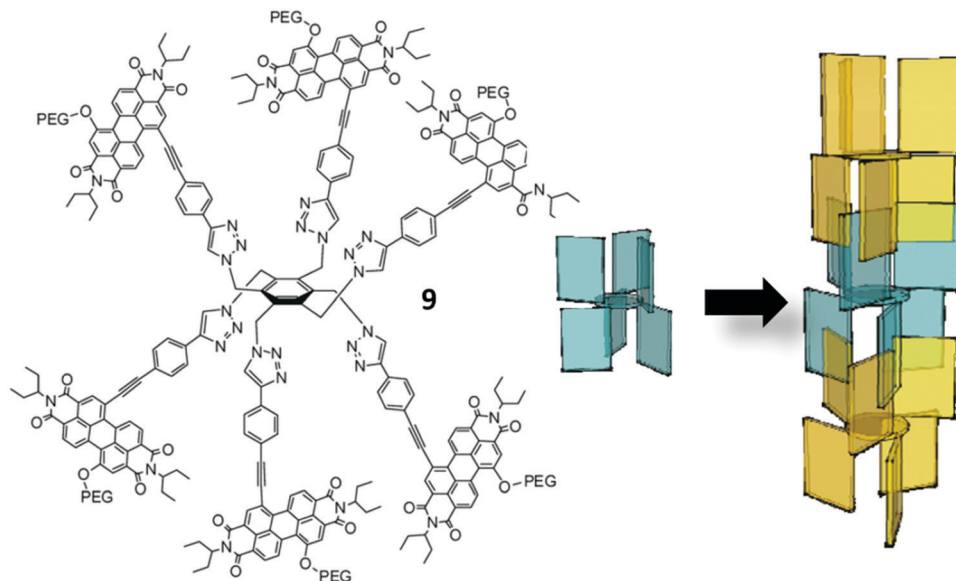


Fig. 11 Schematic depiction of the assembly pattern of compound **9**. Adapted with permission from ref. 168 Copyright (2011) American Chemical Society.¹⁶⁸

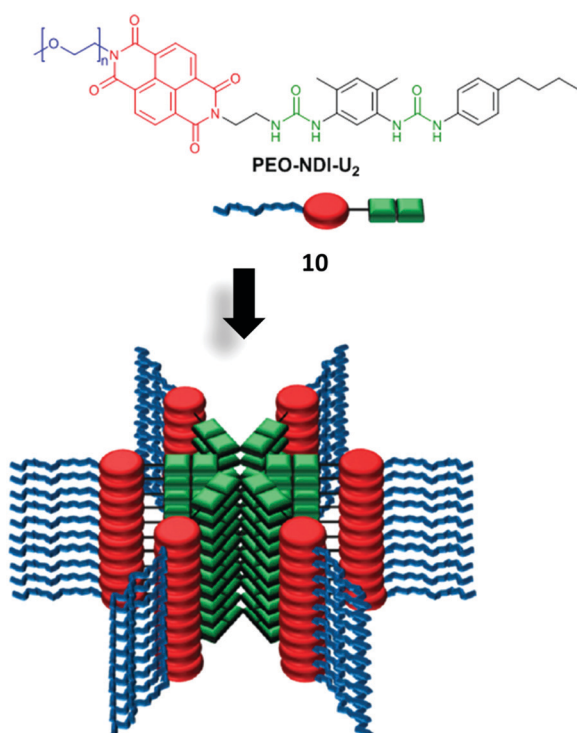


Fig. 12 Bisurea-functionalized naphthalene-diimide **10** (PEO-NDI-U₂) ($n = 38$) and possible model of self-assembly into cylindrical structures in water driven by hydrogen bonds and additional hydrophobic interactions. Adapted with permission from ref. 175 Copyright (2019) Royal Society of Chemistry.¹⁷⁵

that further milestones are just a matter of time. In particular, the latter described naphthalene units often involve hydrogen bonds to direct interactions, and such hybrid compounds might represent an interesting approach to merge their interesting

electronic and optical properties with stronger and more directional interactions, as they are summarized in the following chapters.

3. Hydrogen bond-driven structures

3.1. Benzenetrisamides

It requires only a centrosymmetric attachment of three amide groups to a benzene unit to create one of the most prominent supramolecular building blocks often only known by the abbreviation BTA for benzenetrisamide. The straightforward synthesis of this hydrogen bond-forming unit certainly laid the foundation for its success in the field of supramolecular polymerization.^{176–178} However, to the best of our knowledge 1D assemblies into SPBs based on the pure BTA motif have not been reported so far. We still dedicated an individual chapter to this motif as it clearly inspired the development of the subsequently mentioned centrosymmetric materials. BTAs can stack above each other due to the formation of threefold hydrogen-bonds between the amide groups. Due to the slightly tilted amide groups with respect to the benzene plane, the hydrogen bonds tend to arrange in a helical structure (Fig. 13).^{179,180}

Extensive research on low molar mass BTAs has been performed by the group of Meijer.^{181,182} Apart from their use as hydrogelators,⁶ even as a photoluminescent one¹⁸³ or as air filtration material¹⁸⁴ BTAs have become famous for their application as nucleation agents.^{185–188} More recently, these materials gained interest in nanomedicine as for instance the cellular delivery of siRNA by positively charged BTAs.^{189–192} The mechanism of polymer growth for BTAs in water is usually of cooperative nature.^{193–195} BTAs equipped with bulky 3,3'-diamino-2,2'-bipyridine units, however, demonstrate isodesmic self-assembly behavior in organic solvent (methylcyclohexane) due to intramolecular hydrogen bonding.^{196,197} These differences emphasize that small

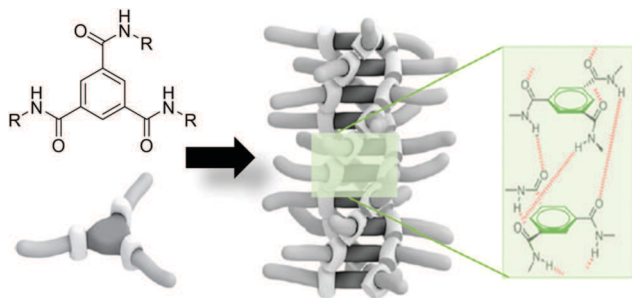


Fig. 13 Schematic depiction of the stacking of BTA units due to threefold hydrogen bonds. Adapted with permission from ref. 176 Copyright (2012) Royal Society of Chemistry.¹⁷⁶

variations in structure and solvent can affect the self-assembly mechanism to a large extent.⁹⁰ With Förster-resonance energy transfer (FRET) experiments and stochastic optical reconstruction microscopy (STORM) measurements, Albertazzi and coworkers proved a dynamic exchange of the building blocks causing an intermixing of monomers from different fibers.^{198,199} Similar methods were used to study the influence of molecular recruiters and the exchange rates in multicomponent systems.^{199,200} Another well-investigated aspect of the BTA assembly is the influence of chirality and chiral amplification, which follows the so-called sergeant-and-soldier principle.^{201–203}

Although SPBs based on BTA could not be realized so far, these motifs were still applied to guide the assembly of polymers. One example is the formation of single-chain polymeric nanoparticles where the incorporation of BTAs into the side chain induces a reversible folding of the chain into a spherical assembly.^{204–210} The closest to a SPB came from the materials reported by Mes and Roosma *et al.* They attached BTAs at the end-group of poly(ethylene-*co*-butylene) leading to the formation of phase segregated nanorods in the bulk.^{211,212} Further bulk studies followed, where the BTA unit was introduced in the middle block of an ABA triblock copolymer.²¹³ In another approach, three armed polymers were prepared from BTAs at the branching point to improve the self-healing properties in the bulk.²¹⁴ Only recently, we analyzed the assembly of such BTAs attached to polymers in solution.²¹⁵ Our aim was to evaluate the influence of the composition on the assembly behavior by variation of the length of the alkyl chains directly connected to the BTA while keeping the molar mass of the hydrophilic PEG constant (2000 g mol⁻¹) (Fig. 14). In contrast to our expectations, the BTA units cannot generate interactions strong enough to promote directional self-assembly into fiber-like morphologies. A few fibers were observed only when a C₁₂ alkyl spacer was introduced between the amide function and the PEG arms. However, the comparison to a similar-sized hydrophobic unit lacking the amide groups revealed that this transition is due to the increased size of the hydrophobic domain and, therefore, the packing parameter is decisive for the morphology.

Symmetrically substituted BTAs with pendant polymers were reported by the group of Vicent. Using the BTA motif as a BF₄ salt-based initiator in a ring-opening polymerization of

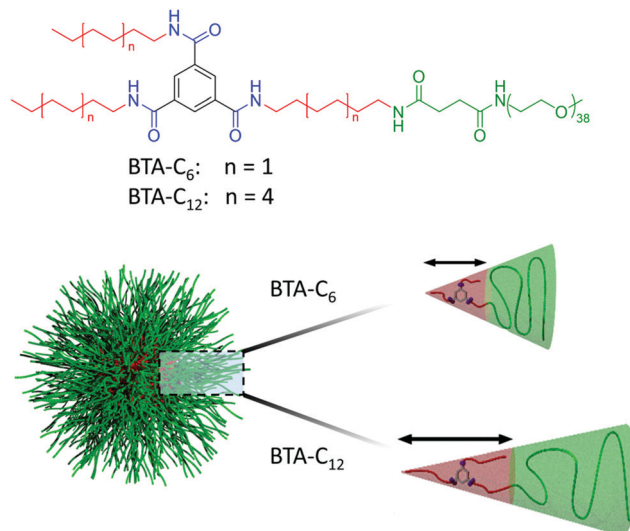


Fig. 14 Schematic depiction of the assembly by the different BTA units (hexyl vs. dodecyl spacer) and the difference in required and available space for the hydrophobic and hydrophilic domain, respectively. (b) Adapted with permission from ref. 215 Copyright (2019) Elsevier.²¹⁵

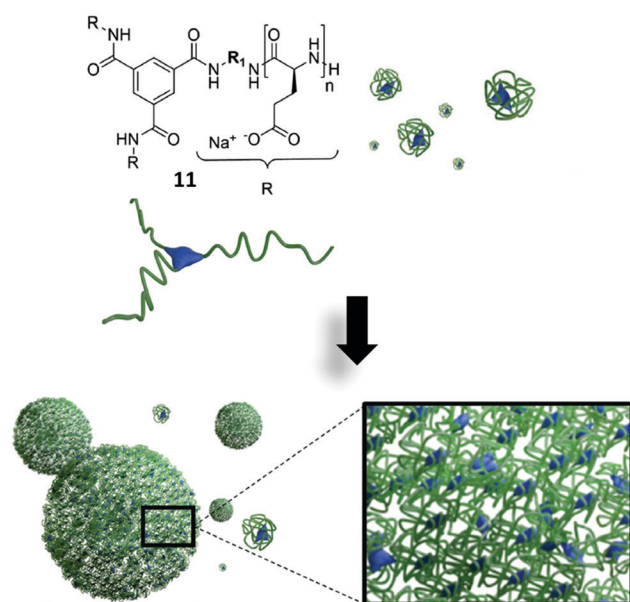


Fig. 15 Star shaped polyglutamates **11** and their assembly to spherical objects in water. Adapted with permission from ref. 217 Copyright (2017) John Wiley and Sons.²¹⁷

benzyl-L-glutamate *N*-carboxyanhydrides results in the formation of 3-arm star-shaped polyglutamates which can assemble into larger aggregates in solution. However, only spherical objects and no anisotropic supramolecular polymer bottlebrushes could be observed (Fig. 15).^{216,217}

3.2. C₃-Symmetric peptide structures

While the BTA motif might not be suitable for the preparation of SPBs, the planar centrosymmetric structure represents a basis for the design of a whole set of materials involving

multiple hydrogen bond sides created by peptide units, which we summarize in this chapter.

Interestingly, this modification was initially reported for symmetric cyclohexane based gelators. In addition, the groups of van Esch and Feringa could demonstrate that these cyclohexane cores are actually superior to the benzene cores as they induce gelation in more different solvents and at lower concentrations.^{218–220} Nevertheless, the modification of BTAs with additional peptide bonds did also result in stronger interactions, improving, for example, the thermal stability of formed gels in cyclo-hexane and *n*-hexane.²²¹ Combining the hydrogen-bonding ability of peptides and the π -stacking of benzene cores, the group of Meijer equipped a benzene-1,3,5-tricarboxamide core with dipeptide fragments and mesogenic groups on the periphery.²²² This resulted in the formation of stacks in chloroform and/or heptane depending on the chirality of the amino acid residual groups. More recently, the influence of the bulkiness of the amino acids and the order of the dipeptide sequence was analyzed.²²³ An early attempt to control the assembly of such materials was reported in 2010. The same C_3 -symmetrical benzene-1,3,5-tricarboxamide was therefore modified with fluorinated *L*-phenylalanine and connected to a peripheral charged gadolinium complex. The repulsive Coulomb interactions due to the charged metal complex counteract the attractive hydrogen bonds induced by the core and provide a lever to control columnar aggregation in water.²²⁴ Hereby, the hydrophobic shielding *via* solvophobic interactions was later found to be important for the stabilization of the aggregates in solution.²²⁵ Apart from hydrophobicity, the self-assembly can also depend on the ionic strength of the solution. For the gadolinium-functionalized benzene cores, a transition from isodesmic growth at low ionic strength to a self-assembly in a cooperative manner at high ionic strength could be observed.²²⁶

The group of Besenius later used a system of C_3 -symmetric peptide amphiphiles equipped with pentapeptides.²²⁷ They synthesized two complementary co-monomers with either acid or basic side groups incorporated in the pentapeptide sequence (Fig. 16b). Upon aggregation in water, a multi-component

supramolecular polymer consisting of a 1 : 1 monomer ratio will be formed by Coulomb interaction and hydrogen bonding of the different co-monomers in an alternating fashion (Fig. 16a). Changes in pH trigger the disassembly of the aggregates once the side groups are not charged and the salt bridges are disrupted.^{228,229}

In contrast to the C_3 -symmetric peptide amphiphiles where charges are incorporated in the peptide sequence, compounds consisting of a nonaphenylalanine peptide attached to the C_3 -symmetrical benzene core (three amino acids per arm) were reported (Fig. 17). These materials even featured macromolecular modification based on a Newkome-type dendron. This way, the exterior was modified with either carboxylate groups or oligo-(ethylene glycol) units which provide solubility and the possibility to deprotonate the carboxylic acid groups at lower pH. In water, one-dimensional aggregates are formed, which can independently be tuned by changes of ionic strength or pH. Repulsive forces due to cationic charges at low pH can be screened by the addition of salt (NaCl) and resulting in the (re-)formation of one-dimensional supramolecular structures. Utilizing this frustrated growth mechanism the mean length of the polyanionic fibers could be adjusted.^{230–235}

Similar systems have also been investigated for application in biomedicine^{236,237} or as multi-stimuli responsive hydrogelators.²³⁸ Furthermore, a type of layer-by-layer assembly was obtained by kinetically controlled sequential growth on a gold-coated surface. This method could pave the way for 3D resolved biomaterials or optoelectronics.^{239,240}

Considering the size of the different dendritic modifications reported so far, these systems should clearly be suitable for the formation of supramolecular polymer bottlebrushes if linear polymers are attached to the C_3 -symmetric peptide motif. However, only very recently such a combination based on polyglutamate was reported, which indeed resulted in the formation of supramolecular polymer bottlebrushes.²⁴¹ Only the previously mentioned non-aphenylalanine based motif was able to form rods and fibers with polymeric side chains (DP 10 or 15), although the charged polyglutamate necessitated high concentrations or the addition of salt (Fig. 18). At low concentrations, the molecules behave

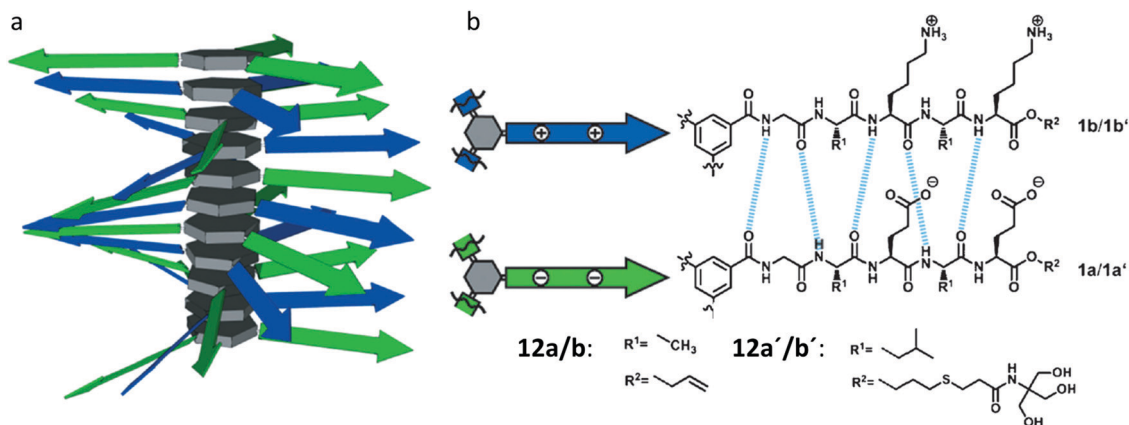


Fig. 16 Schematic depiction of the supramolecular copolymer (a) formed by anionic/cationic β -sheet-encoded dendritic co-monomers **12a/b** and **12a'/b'** (b). Adapted with permission from ref. 227 Copyright (2013) John Wiley and Sons.²²⁷

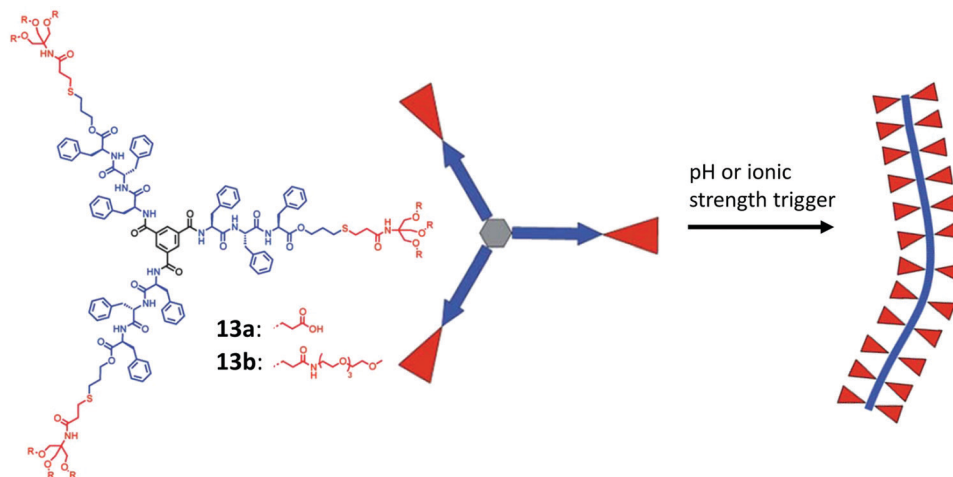


Fig. 17 Chemical structure of the nonaphenylalanin amphiphile **13** and schematic depiction of the self-assembly. Adapted with permission from ref. 230 Copyright (2013) Royal Society of Chemistry.²³⁰

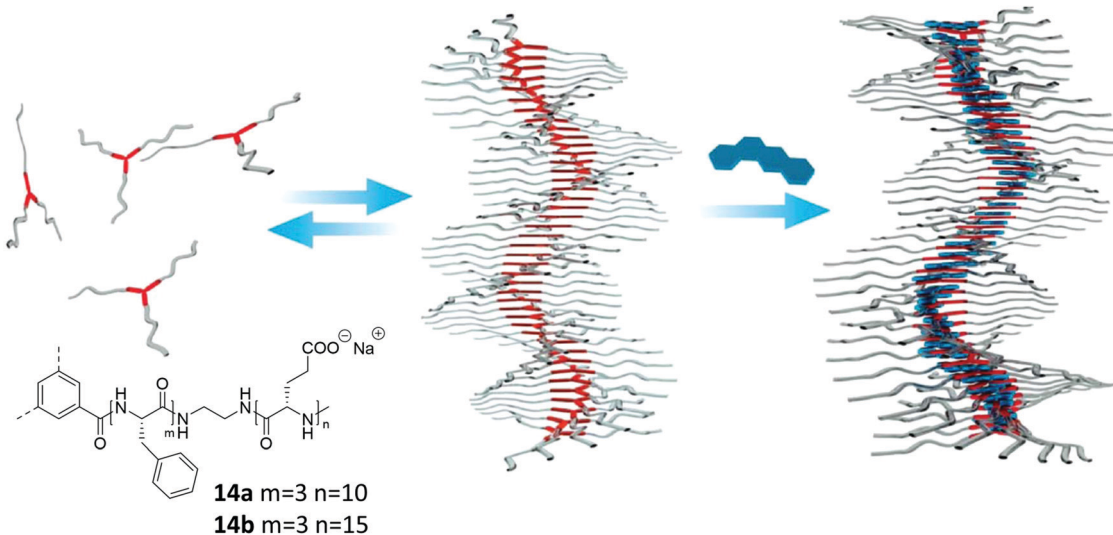


Fig. 18 Schematic depiction of the self-assembly of star-shaped polyglutamates **14** and the stabilization of the aggregates by the integration of small hydrophobic drugs. Adapted with permission from ref. 241. Copyright (2020) Royal Society of Chemistry.²⁴¹

like electrolytes. The group of Vicent further demonstrated that the addition of hydrophobic drugs such as doxorubicin stabilizes the nanorods on account of their encapsulation in the hydrophobic core and consequently reduced the critical aggregation concentration. Due to their versatility and interesting morphologies, this class of substances might be promising for application in biomedicine.

3.3. Linear peptides

Linear peptides have long been known to be able to form fibrillar structures.²⁴² Even very short peptides, consisting only of two linked amino acids, are able to form fibers and act as low molecular weight hydrogelators.^{243,244} For these short oligopeptides to gel, an additional driving force is required to induce the assembly, which usually comprises aromatic moieties at their N-terminus, such as fluorenylmethoxycarbonyl (Fmoc),^{245,246}

carboxybenzyl,²⁴⁷ naphthalene,^{248,249} or pyrene²⁵⁰ groups (see also Section 2.3). The aromatic moieties facilitate peptide assembly in water due to their π -stacking and hydrophobic interactions. Even single amino acids conjugated to Fmoc^{251,252} or pyrene^{253,254} moieties have been used as low molecular weight hydrogelators.

Peptide amphiphiles forming β -sheets do not even require the adjacent aromatic groups to self-assemble in water. Although many peptides are highly hydrophilic, simple aliphatic chains attached to the N- or C-terminus are enough to cause the initial phase separation in water, which further initiates the fiber formation by the β -sheet-like hydrogen bond interaction.²⁵⁵ Such peptide sequences usually contain a domain with a high propensity to form β -sheets adjacent to the alkyl chain followed by charged amino acids to prevent lateral aggregation in water. The amphiphilic character of the peptide favors the location of the hydrophilic and often charged amino acids at the surface

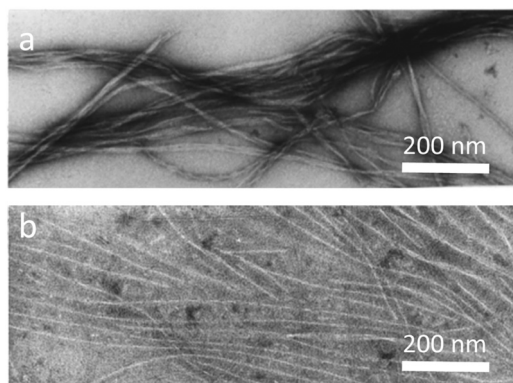


Fig. 19 TEM images of (a) $A\beta(10-35)$ and (b) $A\beta(10-35)$ – PEG_{3k} conjugate stained with uranyl acetate. Adapted with permission from ref. 269 Copyright (1998) American Chemical Society.²⁶⁹

of the resulting aggregates, making them accessible as biological epitopes²⁵⁶ and appealing for biomedical applications.^{257,258} The self-assembly of peptide amphiphiles is significantly influenced by the molecular structure^{259,260} (hydrophilic/hydrophobic domain ratio, amino acid sequence) as well as by solution conditions (ionic strength, pH and temperature).^{261,262}

The strong propensity of β -sheet forming peptides to assemble into fibrillar structures often imposes a major limitation due to an irregular aggregation and very limited solubility in water. A successful strategy to circumvent these limitations is to conjugate hydrophilic synthetic polymers to these peptides.^{263–266} This strategy was first reported in a seminal series of papers by Lynn and coworkers in which they conjugated PEG with a molar mass of 3 kDa to the central hydrophobic domain of the amyloid β -peptide (here: $A\beta(10-35)$).^{267–269} This sequence is a major

component of the plaques found in the brain of patients suffering from Alzheimer's disease. The conjugation with PEG resulted in the formation of well-dissolved fibrillar structures in aqueous solution as resolved in TEM images. In contrast, fibers from pristine $A\beta(10-35)$ tend to laterally assemble into bundles (Fig. 19).

Further contrast matching studies with SANS revealed that the PEG chains form a corona around the central peptide fibril, which acts as a stabilizer preventing the lateral aggregation. Moreover, the PEG-attachment made the β -fibrillization a reversible process controlled by pH and concentration. Collier and Messersmith synthesized a small library of PEG-*b*-peptides to examine the impact of the molecular architecture (diblock *vs.* triblock) as well as the length of the PEG chain on the aqueous self-assembly structures.²⁷⁰

A limitation in employing long peptide sequences in peptide-*b*-polymer conjugates is the tendency of these peptides to aggregate during standard solid-phase peptide synthesis. The Börner group was able to overcome this hurdle by introducing temporary structure breaking defects such as pseudoproline units and so-called switch ester segments into the primary peptide structure.^{271,272} In this strategy, the pseudoproline units introduce conformational kinks in the peptide backbone whereas the switch ester moieties disrupt the amide backbone. Together, these temporary structure defects effectively prevent peptide aggregation. Treatment with TFA transforms the pseudoproline units into serine and threonine, reestablishing an all-*trans* backbone conformation. Afterwards, the amide disruption can be reversed and the peptide backbone restored through a pH-induced *O* \rightarrow *N* acyl transfer, enabling its self-assembly in water (Fig. 20). Long microscopic fibers were spontaneously formed due to the strong propensity of the valine-threonine

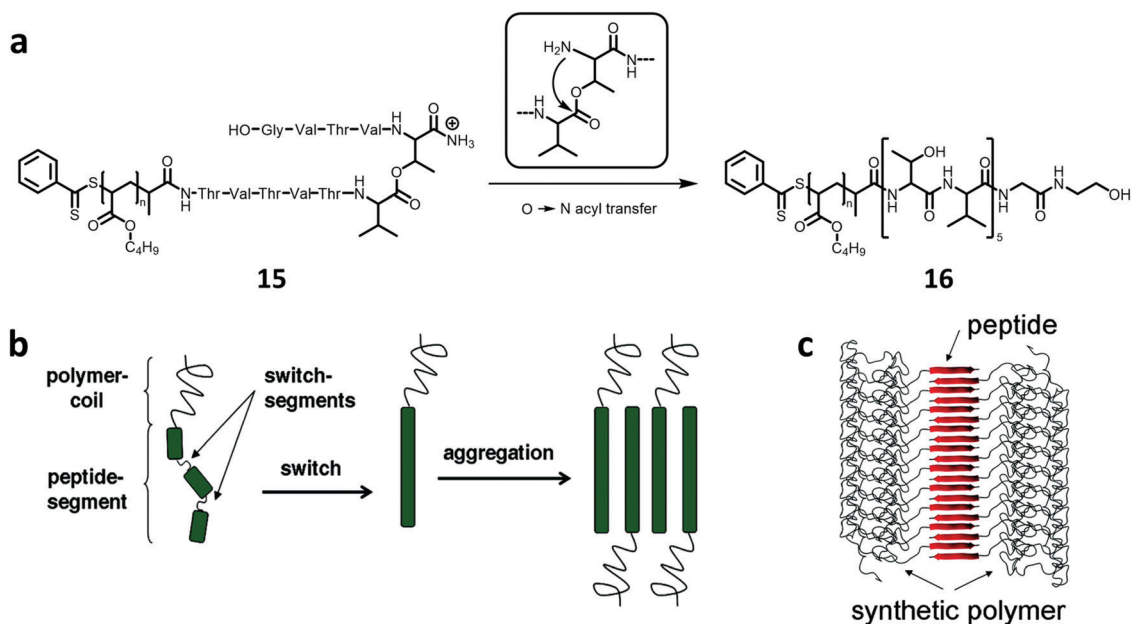


Fig. 20 (a) pH-Induced *O* \rightarrow *N* acyl transfer of the switch peptide–polymer conjugate **15** to the undisturbed peptide **16**; (b) schematic illustration of the pH induced switch and the subsequently enabled conjugate assembly with the resulting SPB in (c). Adapted with permission from ref. 271 Copyright (2007) American Chemical Society.²⁷¹

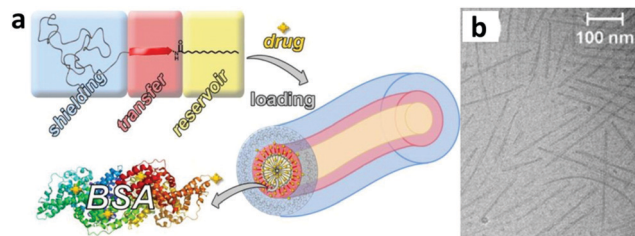


Fig. 21 (a) Scheme of palmitic acid-*b*-peptide-*b*-PEG triblock copolymer that can host drugs and its assembly to fibers. Drug molecule transfer to BSA is mediated through the peptide interlayer. (b) CryoTEM image of the triblock conjugate. Adapted with permission from ref. 274 Copyright (2016) American Chemical Society.²⁷⁴

motif to form β -sheets.²⁷² Besides this, they could also show a peptide-driven PEG assembly into fibers by rational design of a pre-organized dipeptide-strand motif, whose initial pre-organization facilitated the later brush growth.²⁷³

In a recent publication, the Börner lab reported the potential of supramolecular peptide-*b*-PEG bottlebrushes to act as drug delivery systems with extraordinary high drug payload capacities.²⁷⁴ They synthesized a palmitic acid-*b*-peptide-*b*-PEG triblock copolymer in which the peptide sequence was chosen after a combinatorial screening to specifically interact with the incorporated drug, in this case, *m*-tetrakis(hydroxyphenyl)chlorin (*m*-THPC). The triblock conjugate formed fibers of around 20 nm in diameter and a few hundred nanometers in length and was capable of incorporating 0.86 mmol of drug per mmol conjugate (Fig. 21). In addition to its high loading capacities, the peptide sequence also allowed to regulate the *m*-THPC release rate and mediated the transfer to bovine serum albumin (BSA) through the peptide interlayer.

Extensive studies on the self-assembly behavior and structure-property relationships have been reported by the group of Hamley. They investigated the impact of PEG-conjugation to short peptide sequences and their aqueous self-assembly.^{275–280} In 2009, they conjugated PEG with a molar mass of 5 kDa to a hydrophobic peptide sequence comprising of four phenylalanine units.²⁷⁶ CD and fluorescence spectroscopy measurements revealed that above the critical aggregation concentration (CAC) self-assembly in water takes place due to the hydrophobic interaction between the tetra-phenylalanine (FFFF) segments, and well-defined β -sheets are developing at higher concentrations. Drying the conjugates resulted in the formation of macroscopic spherulites and fibers due to the crystallization of PEG, as seen in polarized optical microscopy, dry TEM and X-ray diffraction. The conformational properties of the FFFF-PEG conjugate in aqueous solution were then studied using quantum mechanical calculations and atomistic molecular dynamics simulations.²⁸¹ Backbone-side chain interactions involving the N-H moiety of the amide groups and the π -electron clouds of the phenyl rings were identified to play a significant role in stabilizing the observed conformations in water. Surprisingly, the hydrophobic FFFF unit as well as the hydrophilic PEG chain organize themselves rather independently from each other. They also examined the effect of the PEG molar mass (1, 2, and 10 kDa) on the aqueous self-assembly of the peptide FFKLVFF, a modified sequence of the

amyloid β -peptide.²⁷⁷ As expected, decreased fiber sizes were observed for increasing PEG-length due to the increased steric hindrance. Later, Hamley reported the synthesis of several (hetero)telechelic PEG-conjugates (1.5 kDa) with dityrosine and diphenylalanine units at both PEG-ends that were protected with none, one or two Fmoc end-groups and studied the influence of these subtle structural variations on their self-assembly and rheological properties.²⁷⁸ The conjugates with two Fmoc end-groups were insoluble in water. The dityrosine-conjugate without Fmoc groups was fully water-soluble and did not form any fibrillar structures, probably because of a lack of hydrophobicity as supposed by the authors. All other conjugates form fibers in water as seen *via* cryoTEM, but only the dityrosine compound **17** with one Fmoc group was able to form a self-supporting hydrogel (Fig. 22). Shear rheometry experiments of **17** showed its thermoresponsive behavior close to body temperature. In a follow-up publication, Kirkham and coworkers synthesized a triblock peptide-conjugate consisting of PEG with a molar mass of 2 kDa and 6 kDa that was flanked at each side by five tyrosine amino acids.²⁸² Despite a similar molecular structure compared to the previously reported study²⁷⁸ and formation of short fibrils, no hydrogel formation could be observed, even at very high concentrations. This shows the significant impact of the delicate interplay between the molar mass of the polymeric unit and the length and composition of the peptide segments on the macroscopic properties.

The same group synthesized a DGRFFF-PEG_{3kDa} conjugate containing an RGD unit, which is well-known to enhance cell adhesion.²⁸⁰ Again, fibrillar structures of several hundred nanometers were obtained in water, however, no increase in cell-adhesion was observed. The authors hypothesized that due to

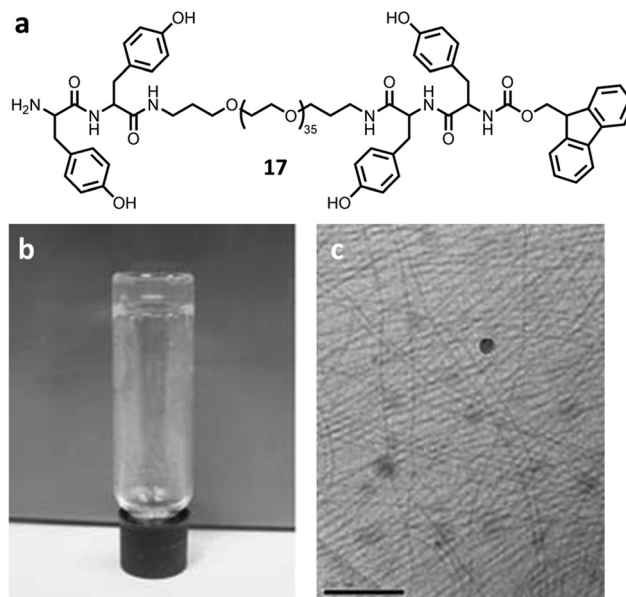


Fig. 22 (a) Molecular structure of compound **17**; (b) hydrogel formation of **17** in water; (c) cryoTEM of **17** showing the formation of micrometer-sized fibers. Scale bar represents 200 nm. Adapted with permission from ref. 278 Copyright (2011) John Wiley and Sons.²⁷⁸

the fibrillar structure the RGD units reside inside the core of the fibers and, hence, are not accessible for interactions with the cells.

Recently, the group of Besenius reported two studies in which they synthesized triblock peptide-*b*-polymer-*b*-peptide conjugates that contained pentapeptide segments of alternating phenylalanine and histidine at each end of the polymer block.^{283,284} In the first report, polysarcosines of different lengths were heterotelechelicly functionalized with two complementary FHFHF pentapeptide units, that were deliberately designed to assemble into antiparallel β -sheets.²⁸³ Nanofibers of an average length of approximately 50 nm length were obtained in water at neutral pH. However, the histidine moieties get protonated at $\text{pH} < 6.0$ and CD spectroscopy revealed a transition from ordered structures towards a molecular disordered state. In a subsequent study, they compared the aforementioned conjugates which form antiparallel β -sheets with similar triblocks but featuring parallel β -sheet forming FHFHF units.²⁸⁴ The latter conjugates also self-assembled into fibers in water at neutral/slightly basic pH which can be dissolved at a pH below 6.0. However, in contrast to the antiparallel β -sheet forming conjugates from the first study, these materials were capable of forming hydrogels at solid weight contents of 1.5% w/v. The authors assumed a physical cross-linking of bridging conjugates between individual fibers causing the hydrogel formation. The introduction of methionine units into the hexapeptide FMHMHF further yielded PEG-conjugates that were pH- and redox-responsive (Fig. 23a).²⁸⁵ These conjugates formed spherical aggregates at acidic pH or after oxidation (Fig. 23b and c), whereas in the reduced state fibers are present in water at neutral pH (Fig. 23d).

Taking advantage of an enzymatic H_2O_2 formation from glucose oxidase, the authors were able to tune the rate of oxidation by adjusting the amounts of glucose oxidase and, thus, the temporal stability of the hydrogels from 1–12 h.

3.4. Cyclic peptides

Topologically related to linear peptides are their cyclic analogs. In particular, cyclic peptides (CP) comprising alternating *D*- and *L*- α -amino acids gained considerable interest for their ability to assemble into nanotubes.^{286,287} Already in 1974, de Santis *et al.* proposed that these CP would adopt a flat ring-type conformation with all amide groups oriented perpendicular to the ring plane, but it took until 1993 for these materials to be synthesized and characterized by Ghadiri and coworkers.^{288,289} In particular the latter was challenging, as the geometric features (all amide bonds align perpendicular to the plane, see Fig. 24) enable these peptides to form strong intermolecular hydrogen bonds by stacking on top of each other, which results in the formation of almost insoluble large cyclic peptide nanotubes (CPNT).

Here, we only briefly summarize the key features important for the formation of SPBs, but an excellent review on different types of CPs, their self-assembly, and applications was published by Chapman *et al.*²⁹⁰ CPs usually consist of 4 to 12 amino acids. The internal diameter of these CPNT can be easily tailored with high accuracy by adjusting the number of amino acids per ring. The perpendicular orientation of the amide groups with regard

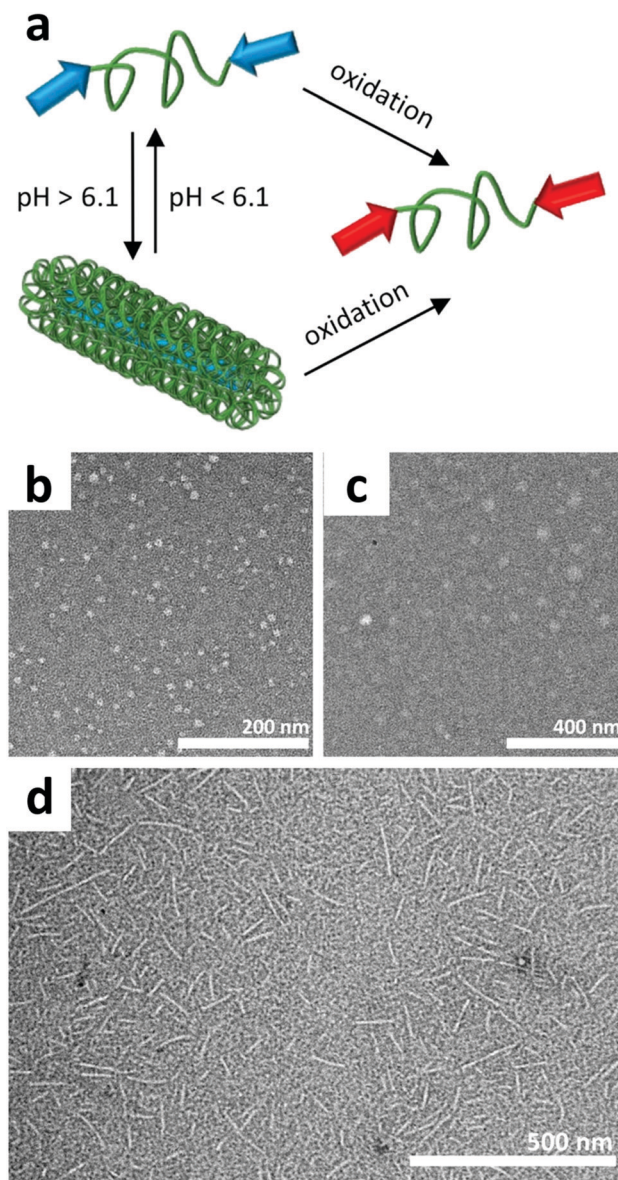


Fig. 23 (a) Schematic representation pH-dependent parallel β -sheet directed supramolecular self-assembly into nanofibers and oxidation-induced disassembly; negatively stained TEM images at pH 2.8 (b), at pH 7.4 after oxidation (c) and at pH 7.4 (d). Adapted with permission from ref. 285 Copyright (2019) Elsevier.²⁸⁵

to the ring-plane results in a protrusion of the amino acid side chains, which allows a functionalization of the outer surface of the CPNT without interfering directly with the stacking. Besides the exterior, also functionalization of the inner ring is possible if γ -amino acids are incorporated.^{291,292} Applications for CPNT range from antibacterial²⁹³ and antiviral²⁹⁴ agents, electronics,^{295–297} ion sensors^{298,299} hydro- and organogels³⁰⁰ to transmembrane^{301–303} or ion channels.³⁰⁴

Similar to their linear analogs, CP exhibit a very poor solubility due to a propensity to laterally aggregate into bundles that can reach widths of 0.5 μm and lengths up to 30 μm .²⁸⁹ A successful strategy to circumvent this limited solubility is the attachment of polymers to the CP scaffold as first shown by the

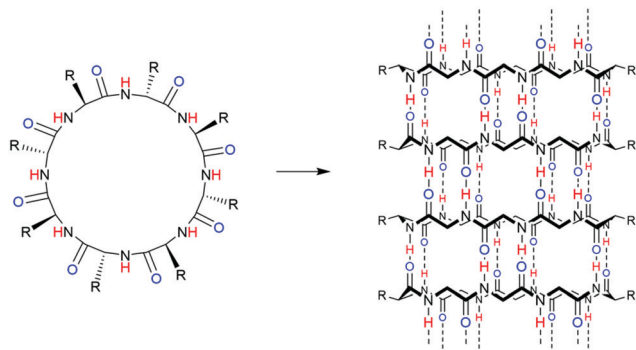


Fig. 24 Cyclic octapeptide with alternating D- and L-amino acids (left) and its assembly into peptide nanotubes formed by intermolecular hydrogen bonds (right). Adapted with permission from ref. 289 Copyright (1993) Springer Nature.²⁸⁹

groups of Biesalski and Börner.^{107,305–309} Polymer conjugation to CP inhibits their lateral aggregation and also reduces their axial growth due to the steric hindrance imposed by the tethered polymer chains. Furthermore, solubility in various solvents can be imparted when solvophilic polymers are attached. These cyclic peptide polymer nanotubes (CPPNT) can either be synthesized by convergent coupling of polymers to the CP or by divergent growth of the polymer chain from the CP scaffold.³¹⁰ So far, exclusively cyclic octapeptides were used for the attachment of polymers, as these demonstrated the strongest self-assembly tendency.^{290,311} In recent years, the group of Perrier was particularly active in the field of CPPNT.^{310,312–334} This group demonstrated in several reports that the attachment of polymers can be used to impart CP-based materials with additional properties. In this way, CPPNT were created that are responsive to changes in temperature,^{314,319} pH^{323,324,335} and reducing agents.^{331,333} In a very recent example, Song *et al.* reported CPPNT that showed reversible assembly–disassembly caused by host–guest interactions.³³² To this end, they synthesized a CP with two phenylalanine moieties attached to opposite sides of the CP ring. A PEG (5 kDa) was conjugated to the CP to make it soluble in water. This CP–polymer conjugate assembled into cylindrical structures in water, but upon addition of cucurbit[7]uril, a disassembly of the CPPNT is observed, which is caused by the binding of this bulky macrocyclic host to the phenylalanine units. Interestingly, the reversible nature of this host–guest interaction allows a re-assembly of the nanotube, if the competitive guest 1-adamantanamine, which has a much stronger binding affinity towards cucurbit[7]uril than the phenylalanine (Fig. 25).

The group of Perrier was also able to show the applicability of CPPNT as membrane channels^{318,319,326,329,331} and for drug delivery applications.^{320,327,328} Larnaudie and coworkers, for instance, introduced highly potent organoiridium anticancer complexes to the side chains of the polymers in the CPPNT.³²⁸ The drug-loaded CPPNT exhibited a lower half-maximal inhibitory concentration (IC_{50}) than the free drug and the corresponding linear polymer, which lacked the central CP moiety. In each case, a similar percentage of iridium entered the cells, indicating that the low IC_{50} value of the CPPNT might be the result of a more efficient

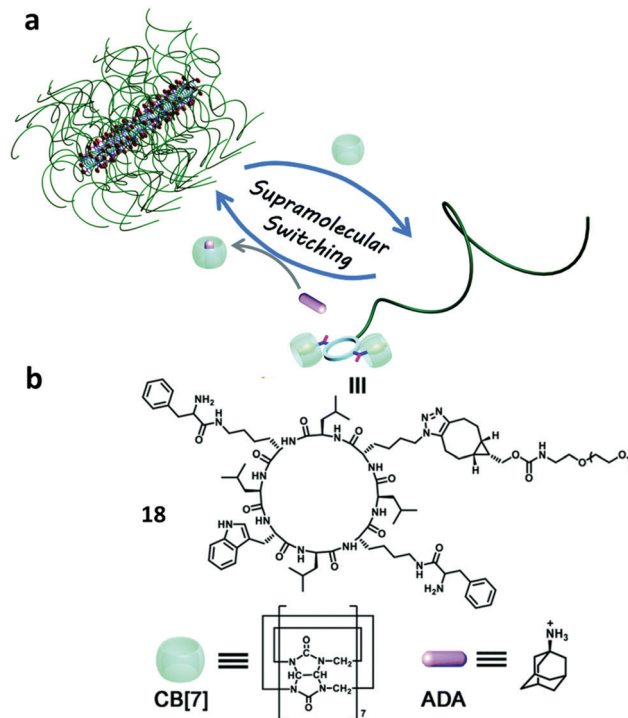


Fig. 25 (a) Schematic representation of the reversible self-assembly of CPPNT via host–guest interactions. (b) Chemical structures and illustrative symbols of the cyclic peptide **18**, cucurbit[7]uril (CB[7]) and 1-adamantanamine (ADA). Adapted with permission from ref. 332 Copyright (2019) Royal Society of Chemistry.³³²

mode of action caused by the assembly. The same group also conducted several systematic studies in which they attempted to control the length of the CPPNT *via* the number, length, and bulkiness of the attached polymer.^{316,318,336} Mansfield and coworkers, for instance, demonstrated that the number of aggregation and thus the lengths of CPPNT in water were reduced with increasing number of polymer arms and increasing bulkiness of the attached polymers due to the higher steric hindrance imposed by the polymer arms.³³⁶ This control of the length of CPPNT is of particular interest in the field of nanomedicine, where the overall size and aspect ratio of anisotropic drug delivery carriers has been shown to be of high importance.^{337,338} Rho and coworkers provided the first evidence that CPPNT are highly dynamic assemblies in water in spite of the strong interaction.³²⁵ To prove this, CPs were functionalized with polymers and complementary dyes, here either cyanine 3 (Cy3) or cyanine 5 (Cy5), which facilitate a Förster resonance energy transfer (FRET) if brought in close proximity. Upon mixing the preassembled CPPNT labelled with the respective dyes, a dynamic exchange of the single building blocks was monitored by the continuous increase of the FRET ratio (Fig. 26). Such a dynamic exchange could even be confirmed in complex biological systems such as mammalian cells, where the individually taken up CPPNT still mix, if they end up in the same compartments.

In a subsequent study, Rho and coworkers reported the synthesis of supramolecular block copolymers based on a cyclic octapeptide equipped with two (butyl acrylate)₄₀-*b*-(dimethyl acrylamide)₁₀ block copolymers on opposite sides of the cyclic

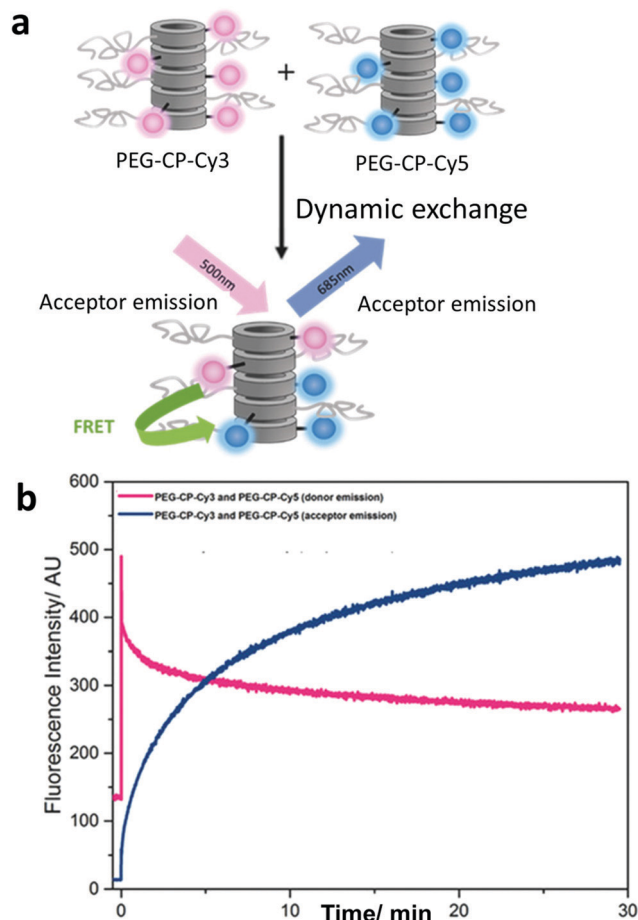


Fig. 26 (a) Schematic illustration of the performed FRET experiment: separately assembled CPPNT with either Cy3 or Cy5 dyes are mixed and start to dynamically exchange single building blocks resulting in mixed CPPNT in which Cy3 and Cy5 dyes are in close proximity to each other. Excitation of the donor (Cy3), followed by the FRET to the acceptor (Cy5) and the acceptor emission. (b) Corresponding fluorescence donor (Cy3) and acceptor (Cy5) emission upon mixing of the CPPNT. Adapted with permission from ref. 325 Copyright (2017) John Wiley and Sons.³²⁵

peptide ring.³³⁴ The inner hydrophobic butyl acrylate block stabilized the hydrogen bond driven self-assembly in water significantly compared to a control molecule lacking the hydrophobic block. Whereas the control CP reached a plateau in the FRET ratio within 60 min, the CP equipped with block copolymers needed 7 days. Even after this prolonged time span, only a low degree of mixing of 41% was achieved, suggesting that the differently labelled CPPNT are not fully mixed. To prove if discrete sections within the CPPNT remain unchanged, stochastic optical reconstruction microscopy (STORM) was applied. As can be seen in Fig. 27 the CPPNT after mixing consisted of differently colored sections as opposed to yellow sections in the case of a complete molecular mixing which are the origin of FRET.

3.5. Urea-based building blocks

The direct comparison of a single amide bond with a urea group gets to the heart of why these units become frequently

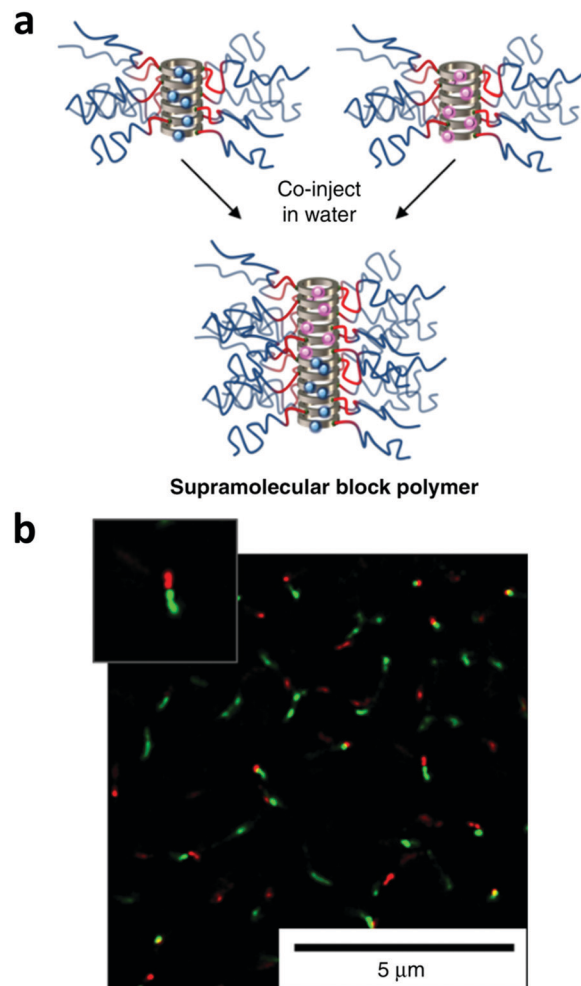


Fig. 27 (a) Schematic illustration of mixing differently labelled CPPNT that do not fully mix due to their slow dynamics. (b) Corresponding STORM image showing CPPNT with discrete sections (red and green). Adapted with permission from ref. 334 Copyright (2019) Springer Nature.³³⁴

applied in supramolecular chemistry. The symmetric arrangement featuring two hydrogen donors (N–H-group) allows a bidentate binding towards neighboring carbonyl groups or simplified a higher number of hydrogen bonds per molecule.³³⁹ In addition to the strong interaction, these materials are intriguingly straightforward to synthesize by the addition of amines to isocyanates, which certainly paved the way for their success in supramolecular chemistry. Among the first materials utilizing the strong hydrogen bond formation are gelators which can be as simple as *N,N'*-dimethylurea.^{340,341} Most commonly, bis-urea compounds are used, because they show enhanced cooperativity in their aggregation compared to building blocks consisting of only one urea group. Consequently, the formation of short oligomers triggers the development of large fibers in a cooperative fashion similar as previously described for BTAs (see Section 3.1). However, the final design of the molecules is rather versatile, which is why we have chosen to represent it by a generic structure motif (Fig. 28).^{342–345}

The group of Bouteiller revealed that the orientation of bis-urea groups forming a bidentate interaction with neighboring molecules is one of the favorable motifs for the formation of

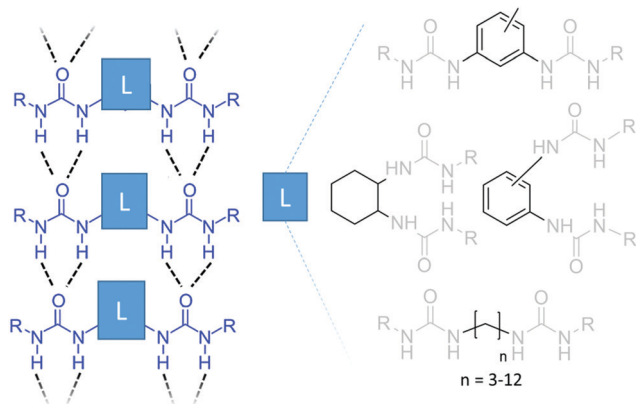


Fig. 28 Interactions between two bis-ureas and possible structures of rigid or flexible linkers.

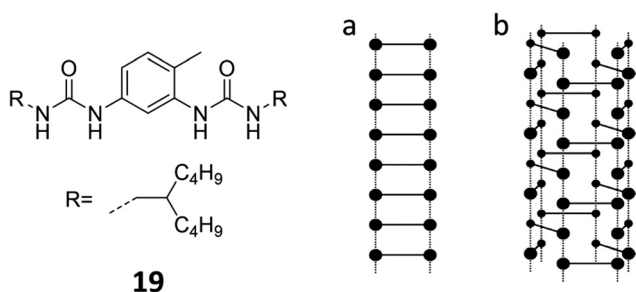


Fig. 29 Possible supramolecular arrangements of 2,4-substituted bis-urea **19** (bis-ureas are depicted as dumbbell shape with dotted lines representing the hydrogen bonds between the urea groups) with a monomolecular (a) or trimolecular (b) cross-section. Adapted with permission from ref. 350 Copyright (2005) American Chemical Society.³⁵⁰

one-dimensional aggregates in the case of a rigid linker.^{346–349} In particular, several variations of a 2,4-substituted toluene bis-urea unit have been studied in detail. It could be shown, that these molecules can form different supramolecular structures in solution depending on the solvent, temperature and composition (Fig. 29).^{347,350} The methylene group of the rigid toluene linker introduces asymmetry and prevents the lateral aggregation or crystallization, which is crucial to maintain the distribution of the individual assemblies or fiber structures, respectively, for their application as gelators.³⁴⁶

Apart from benzene cores, also cyclohexane derived urea-functionalized compounds or ureas linked by alkyl chains were able to induce gelation.^{340,344,345,351} Further reports even increased the number of involved urea groups, as for example in C_3 -symmetrical benzene- or cyclohexane tris-ureas which even induce gelation in polar solvents such as ethanol.²²¹ For more detailed information on motifs for low molecular weight gelators, we refer interested readers to some comprehensive reviews on the topic.^{180,342,352–355}

So far only a few of the above-mentioned structures have been used to create supramolecular bottlebrushes, but despite their low diversity the urea motifs are certainly among the most commonly examined materials for this purpose and many interesting correlations were discovered. The applied structures

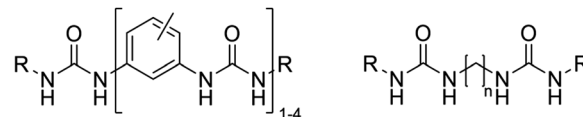


Fig. 30 Schematic overview of aromatic (left) and aliphatic (right) urea motifs used to prepare supramolecular polymer bottlebrushes.

can be divided into the more rigid 2,4-substituted toluene (or in some cases xylene) derivatives and bis-ureas linked by aliphatic units (Fig. 30). As for both systems, the term ‘sticker’ is commonly used, we like to distinguish between them by calling the first aromatic bis/tris/tetra-ureas and the other aliphatic bis-ureas.

In the early attempts to introduce polymers, aromatic bis-ureas have been combined with polyisobutene (PIB). Due to strong self-association of the urea motif and the good solubility of PIB in organic solvents, the resulting supramolecular polymer bottlebrushes featured a dynamic backbone. In very polar solvents such as THF no aggregation was observed. However, for solvents of lower polarity (e.g. chloroform, toluene, and heptane), self-assembly occurred due to the decreased interaction with the hydrogen bond-forming ureas. Mixing these polymeric building blocks with matching low molar mass aromatic bis-ureas³⁴⁷ enabled a control of the average number of PIB chains per self-assembling unit.³⁵⁶

As the steric repulsion of the polymer chains still prevents the formation of long fibers, a straightforward approach was the increase of interaction strength to overcome this energetic penalty. Therefore, three urea groups were combined to form an aromatic tris-urea motif, which resulted in much longer supramolecular polymer bottlebrushes (Fig. 31).³⁵⁷ In more detail, the PIB arms have to adapt a stretched backbone conformation if they are confined within the SPB, which is unfavorable for the overall entropy of the system. In the case of the aromatic bis-urea motif **20**, the enthalpic gain by the hydrogen bonds was not sufficient to account for this entropic penalty of the polymer arms. Aromatic tris-ureas **21**, on the other hand, formed additional hydrogen bonds and therefore compensated this effect which finally results

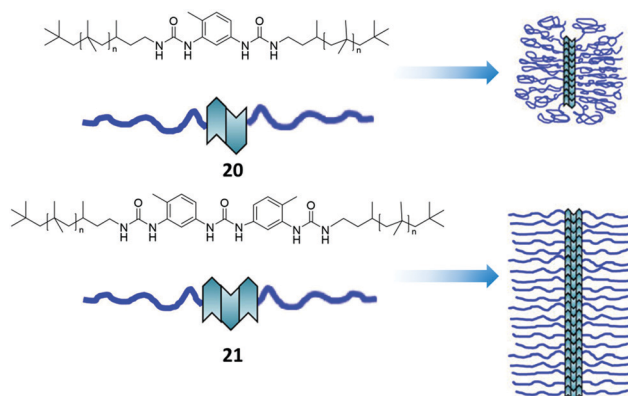


Fig. 31 Formation of supramolecular polymer bottlebrushes of different length depending on the usage of bis- or tris-urea-functionalized polymers. Adapted with permission from ref. 357 Copyright (2013) American Chemical Society.³⁵⁷

in large supramolecular brushes with a persistence length exceeding 300 nm.

This control over the length of the supramolecular polymer bottlebrushes with careful choice of the polymeric side chains could also be demonstrated with polystyrene chains.³⁵⁸ In general, the self-assembly strongly depends on the nature of the monomer and the degree of polymerization of the polymeric side chain. With a higher degree of polymerization, the steric demand is increased and the anisotropic aggregates become shorter. The bulkiness of the monomer itself is also decisive for the length of the resulting bottlebrush, as it has also been reported for the previously mentioned cyclic peptide nanotubes (see Section 3.4).³³⁶ Comparing isobutene to the much bulkier styrene as monomer of the polymeric side chains decorating a tris-urea motif, the latter monomer gave much smaller bottlebrushes than the ones made of PIB. Similar to the previous reports, Fonteneau *et al.* synthesized aromatic bis- and tris-urea units modified with ATRP-initiators which were used to polymerize *n*-butyl acrylates.³⁵⁹ Only the strong interaction of the aromatic tris-ureas initiated the formation of SPBs with poly(*n*-butyl acrylate) side chains in toluene confirming the previous assumptions. Based on these investigations, even more sophisticated control of the microstructure was achieved with PS-*b*-PIB block copolymers where the aromatic tris-urea unit was inserted between the blocks. Patchy supramolecular polymer bottlebrushes were obtained in cyclohexane by phase segregation of the PS and PIB domains.³⁶⁰ Only very recently, further details on the key criteria for fiber-like assembly were discovered by the groups of Colombani and Bouteiller. Therefore, both the polymer length and the distance of the polymer arms to the aromatic tris-urea motif were varied using different aliphatic spacers (Fig. 32).³⁶¹ While all combinations with a large polymer (DP = 30) formed spherical particles in toluene, shorter oligostyrenes of DP 10 were able to form rods in combination with

long (L) or short (S) spacers, whereas the first also gives the longest aggregates. Interestingly, a direct conjugation (no spacer, N) of this very same polymer to the aromatic tris-urea unit also interfered with the rod formation and resulted only in spherical aggregates. These findings emphasize the need for separation of the bulky polymer from the urea groups to enable efficient hydrogen bonding.

The influence of spacer units becomes particularly important if water is used as solvent. Water itself forms strong hydrogen bonds with urea groups and consequently interferes with their ability to stack. Using oligo(ethylene glycol) units as solubilizing side chains, Obert *et al.* revealed that the presence of hydrophobic spacers of sufficient lengths is crucial to obtain fibers in water, as they can act as shields for the hydrogen bonding units.³⁶² For the compounds with large spacers, long fibrillar objects were obtained in water which confirmed the presence of hydrogen bonds between the urea groups. As the diameter of the fibers was larger than for the structures in acetonitrile, the authors further concluded on an additional lateral packing of the unimers due to hydrophobic interactions in water (Fig. 33). In toluene, however, only rather short fibers are observed, which was related to the absence of a solvophobic effect or the formation of intramolecular hydrogen bonds with oxygen atoms of the oligo(ethylene glycol) chains (Fig. 33c).

Recently, a report by Han *et al.* proved that such urea-based supramolecular motifs can self-assemble in water even without the shielding effect of the hydrophobic alkyl chains.³⁶³ Yet, this is only possible when the shielding is compensated by an increasing number of hydrogen bonds. The use of a large aromatic penta-urea motif **PEO5U** was the key to induce assembly of supramolecular fibers (Fig. 34). Moreover, this motif even tolerated a rather large polymer arm (PEG with a DP of 50). Interestingly, the previously observed lateral aggregation was reduced due to the lack of hydrophobic interaction. Decreasing the number of hydrogen bonds by using a smaller building block of only four urea units already resulted in a loss of aggregation.

As already mentioned above aromatic as well as aliphatic ureas were already used to create SPBs so far. An interesting intermediate between both was the application of semi-flexible diacetylene bridged bis-ureas. Equipped with OEG arms, these materials formed fiber-like structures in water, which could even be covalently crosslinked by photo-polymerization of the acetylene groups.³⁶⁴ However, besides the aromatic units, the use of flexible alkyl linkers is most commonly reported. The combination of these more flexible motifs with additional aliphatic spacers was particularly interesting for the formation of fibers in water. Pal and coworkers, for example, synthesized aliphatic bis-ureas comprising OEG side chains, an alkyl spacer of 10 methylene units for sufficient hydrophobic shielding, and variable aliphatic linkers between the urea groups (Fig. 35).³⁶⁵ The authors demonstrated that compounds with 3, 4, 6 and 7 methylene units as linker were able to build fibers in water. Longer alkyl linkers, however, resulted in precipitation, which emphasizes the impact of the additional hydrophobic interaction.

A promising attempt to employ such aliphatic ureas for the assembly of SPBs in water was presented by the groups of

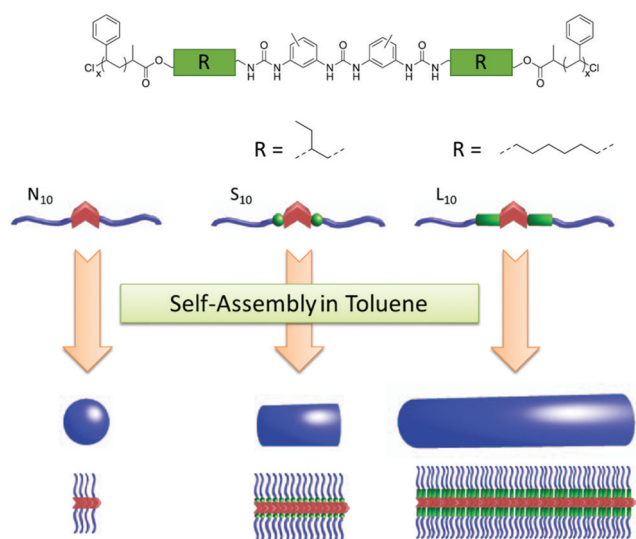


Fig. 32 Self-assembly behavior of tris-urea compounds N_{10} , S_{10} and L_{10} in toluene depending on the spacer length. Adapted with permission from ref. 361 Copyright (2020) American Chemical Society.³⁶¹

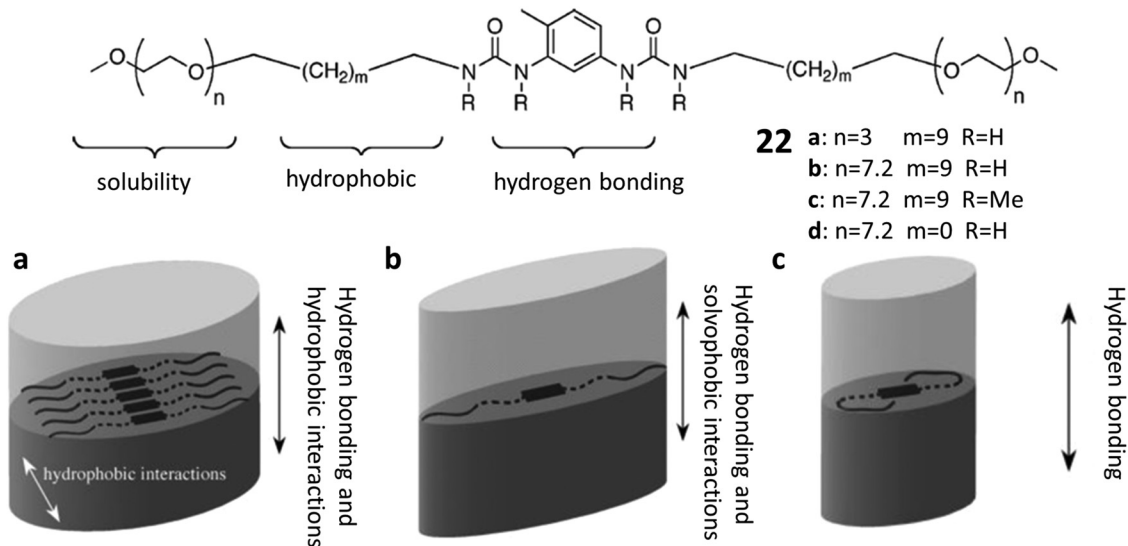


Fig. 33 Aggregation pattern of **22b** in water (a), acetonitrile (b) and toluene (c). Adapted with permission from ref. 362 Copyright (2007) American Chemical Society.³⁶²

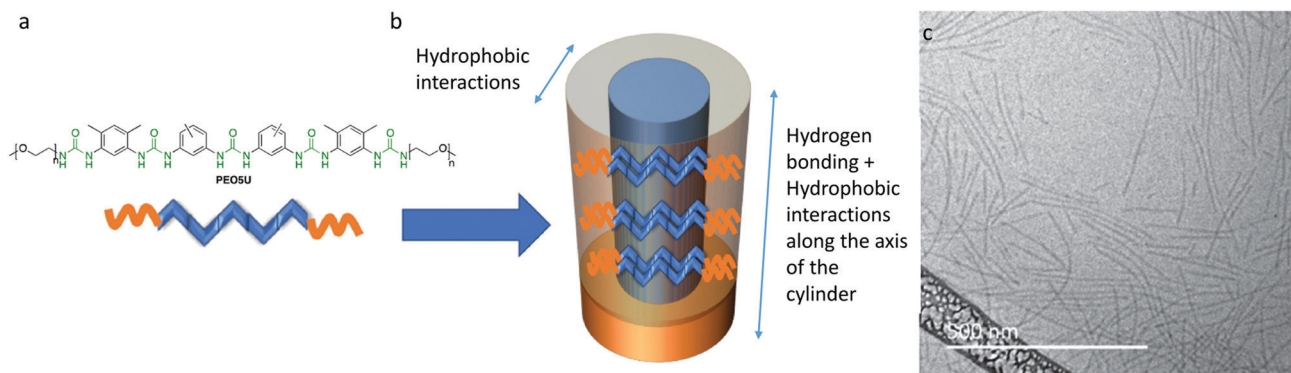


Fig. 34 (a) Chemical structure of **PEOSU**. (b) Schematic depiction of the self-assembly of **PEOSU**. (c) CryoTEM of **PEOSU** in water ($c = 0.5 \text{ g L}^{-1}$). Adapted with permission from ref. 363 Copyright (2019) John Wiley and Sons.³⁶³

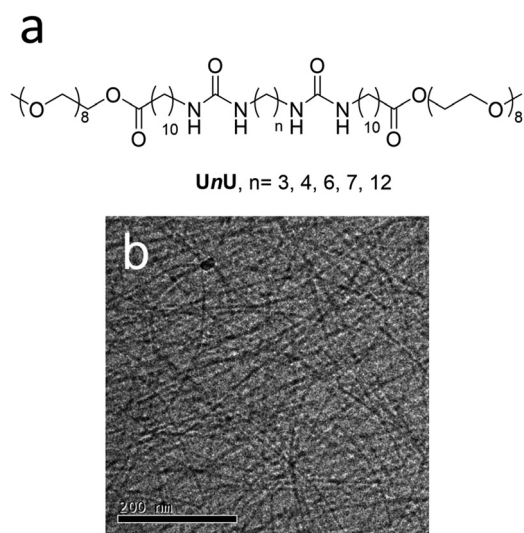


Fig. 35 (a) Chemical structure of bis-ureas **UnU**. (b) CryoTEM of 1 wt% **U7U**. Adapted with permission from ref. 365 Copyright (2010) American Chemical Society.³⁶⁵

Rieger and Stoffelbach. They prepared an urea-functionalized RAFT-agent to polymerize hydrophilic monomers such as *N,N*-dimethylacrylamide, acrylic acid, acrylamide, or 2-(*N,N*-dimethylamino)ethyl acrylate, which spontaneously formed SPBs in water. Their results again confirmed the strong influence of the size of the adjacent polymer as larger DPs inhibited the fiber formation. ITC measurements proved that the aggregation is enthalpy-driven and thus the hydrogen bonds are the main driving force for fiber formation.³⁶⁶ Interestingly, the process could further be adapted to induce morphology changes in the self-assembly of amphiphilic block copolymers (Fig. 36).³⁶⁷

Further work on aliphatic ureas in polymeric building blocks was conducted by the group of Sijbesma. They even obtained SPBs with large PEG (DP of 350) chains, which were attached to aliphatic bis-ureas with rather large spacers and linkers, thus, resembling an amphiphilic triblock copolymer. Interestingly, also the use of similar hydrophobic units lacking the urea groups, resulted in the formation of fibers. However, further tests revealed that the urea groups significantly increased the strength of interaction between the molecules.³⁶⁸ These urea-functionalized polymers with PEG

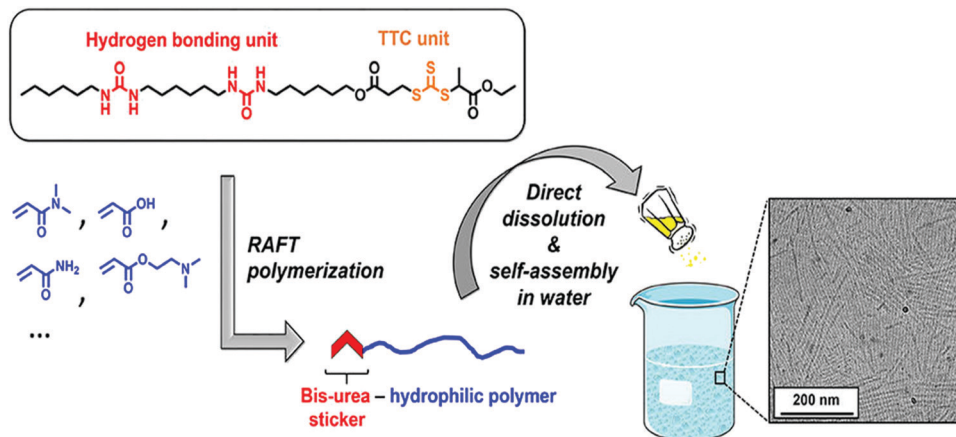


Fig. 36 Fiber-formation of a bis-urea-functionalized RAFT agent after polymerization with different acrylic monomers. Reprinted with permission from ref. 366 Copyright (2018) American Chemical Society.³⁶⁶

chains up to 20 kDa could potentially be applied as hydrogels, due to their interesting rheology behavior, resembling those of physically cross-linked networks.³⁶⁹

3.6. Ureidopyrimidinones

A special class of self-assembling molecules are ureidopyrimidinones (UPys).^{202,370–372} More than twenty years ago, the formation of stable UPy dimers in chloroform due to quadruple hydrogen-bonding was reported.^{373,374} UPys are mostly known for their strong dimerization, which is sufficient to even create long supramolecular chains if bifunctional molecules are applied. Their association strength ($K_{\text{dim}} = 2 \times 10^7 \text{ L mol}^{-1}$) is not solely due to the high number of hydrogen bonds but also caused by electrostatic interactions and a preorganization in

the structure.¹⁸⁰ Four-fold hydrogen bonds between donors (D) and acceptor groups (A) arrange in a DDAA array which is exemplarily depicted in Fig. 37.

In 1997, Meijer used this functionality as associating end groups to build up a reversible supramolecular polymer from bi- and trifunctional ureidopyrimidinones.³⁷⁵ Via main-chain hydrogen bonding, a reversible linear polymeric or cyclic oligomeric structure is formed (Fig. 38). They already realized its potential and designed polydimethylsiloxane with UPy as end groups exhibiting thermoelastic properties. Also, telechelic poly(ethylene/butylene), polyethers, polyesters, and polycarbonates can be modified by this approach to yield better processability due to a lower melt viscosity than conventional covalently bond macromolecules.³⁷⁶ By mixing monovalent compounds, so-called chain stoppers, with the bivalent molecules, it is possible to control the DP of the formed supramolecular polymer.^{375,377}

Among the first examples that these dimers can form columnar stacks, was reported for small molecules in dodecane.³⁷⁸ Whether continuously linked polymeric columns (Fig. 39a) are formed or stacks of dimers (Fig. 39b) are present, is quite difficult to elucidate.

Due to their convenient synthesis,³⁷⁹ UPys were utilized in several attempts to design new supramolecular materials as e.g. bioactive scaffold materials for cells^{380,381} or supramolecular thermoplastic elastomers.^{382–384} The procedure for the synthesis of the bivalent polymers which should eventually be used as

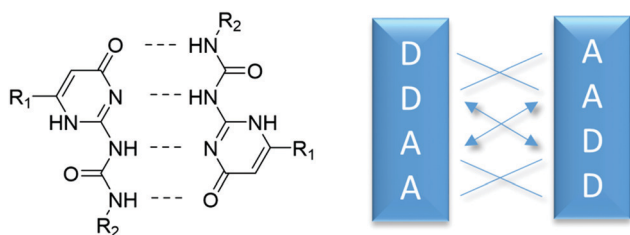


Fig. 37 Self-complementary hydrogen-bonding motif of UPy. Adapted with permission from ref. 180 Copyright (2004) John Wiley and Sons.¹⁸⁰

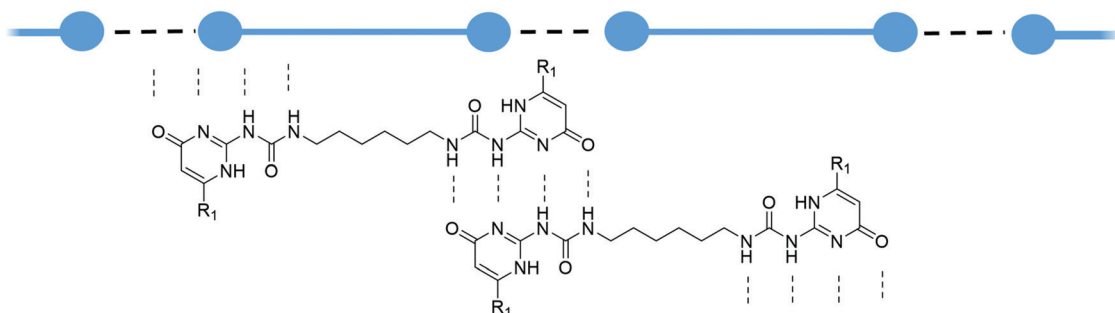


Fig. 38 Main-chain hydrogen-bonded supramolecular polymer from bifunctional ureido-pyrimidinones.

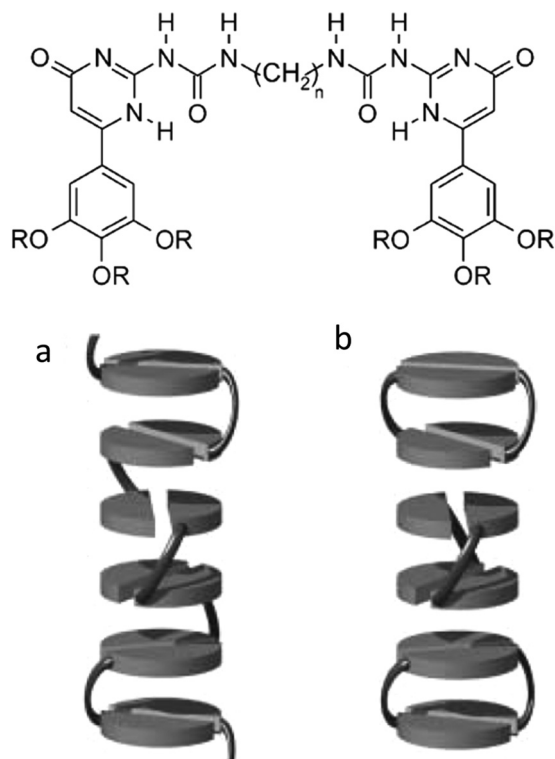


Fig. 39 Exemplary illustration of a bivalent UPy and its self-assembly to polymeric columns (a) or stacks of cyclic dimers (b). Adapted with permission from ref. 378 Copyright (2003) John Wiley and Sons.³⁷⁸

thermoplastic elastomers introduces an additional urea group. Due to amine end groups, which were activated using 1,10-carbonyldiimidazole and coupled to the amino-functionalized UPy unit, urea groups are present in the polymer.³⁸³ Here, not only a main chain hydrogen bonding of UPy units is present, additionally, the urea groups favor a lateral stacking into columnar assemblies (Fig. 40).

Apart from the use in thermoplastic elastomers and hence in bulk, UPys also showed self-assembly into columnar aggregates

in solution.³⁸⁵ The monovalent UPy motif 24,³⁸⁶ depicted in Fig. 41, has furthermore found application in the delivery of siRNA. By synthesizing the UPy 24 with an additional urea group and solubilizing hepta(ethylene oxide) chains, a molecular building block was generated, which could be functionalized with dyes or cationic moieties for complexation of siRNA. Through simple mixing of differently functionalized monomers (Fig. 41a 1, 2 and 3), a multifunctional system was produced that was able to complex and deliver siRNA into cells (Fig. 41b). *Via* two pathways, a 34% reduction of the targeted mRNA expression could be achieved, demonstrating its potential as siRNA delivery system.

Gelation of a bivalent UPy system (Fig. 42) could furthermore be induced by kinetic trapping of self-assembled dimers of 25 in stacked columnar phases.³⁸⁷ UPy 25 was present in its monomeric state in hot chloroform. Upon slow cooling of the solution, a low-viscosity solution was formed, caused by the formation of linear chains. If external stimuli such as shaking or stirring were applied while cooling, a weak gel consisting of stacked aggregates was obtained. Stirring for time ranges longer than three hours enforced this stacking and resulted in the formation of a strong gel. Heating of the gels created stable low viscosity solutions that could be reversibly converted into strong or weak gels again. A mechanism was postulated by the authors in which the breakage of urethane-UPy interactions by mechanical stress results in the formation of nuclei consisting of stacked dimers. These nuclei are stabilized by their intermolecular hydrogen bonds between the urethane groups and induce the growth of larger structures (Fig. 42).

If polymers are attached to the UPy unit, increased dynamics could be observed.³⁸⁵ A low molar mass monovalent UPy 26 formed long fibers in water, whereas the end-functionalization of a PEG chain with two UPy motifs 27 resulted in the formation of shorter fibers with an increased exchange of monomers monitored *via* FRET (Fig. 43). The polymer chain had a destabilizing effect on the assembly of unimers resulting from sterical hindrance and entropic effects.

By simply mixing of monovalent low-molar mass and polymeric bifunctional UPy compounds, Kielyka and coworkers were able to

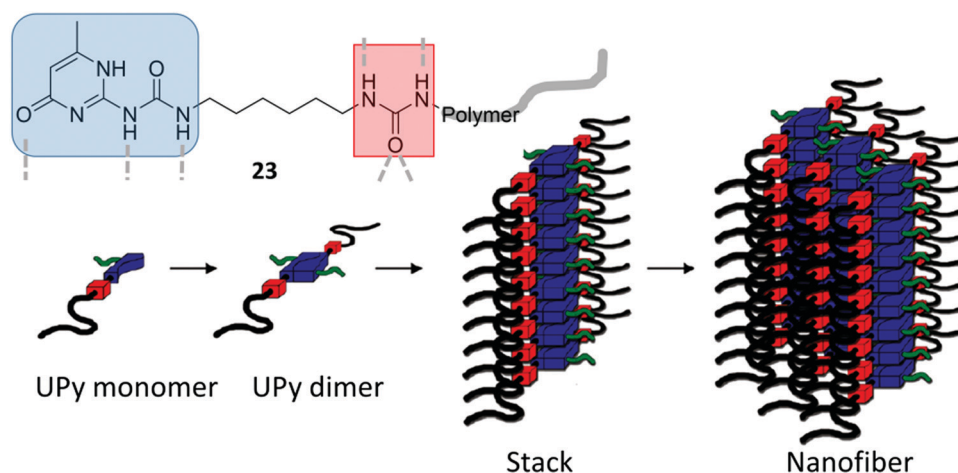


Fig. 40 Aggregation pattern of UPy end groups (blue) and urea (red) functionalized polymers 23. Adapted with permission from ref. 383 Copyright (2011) American Chemical Society.³⁸³

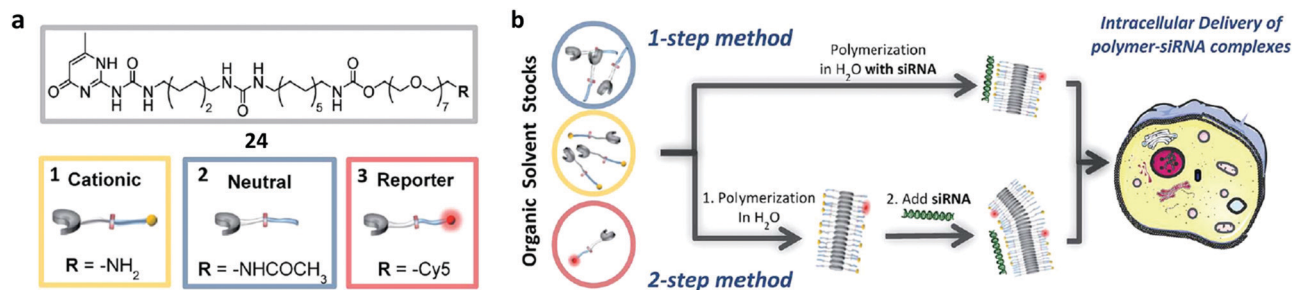


Fig. 41 (a) Design of a multifunctional self-assembly system based on ureidopyrimidinone motif **23**. (b) Two pathways to complex and deliver siRNA to cells. Adapted with permission from ref. 386 Copyright (2016) Royal Society of Chemistry.³⁸⁶

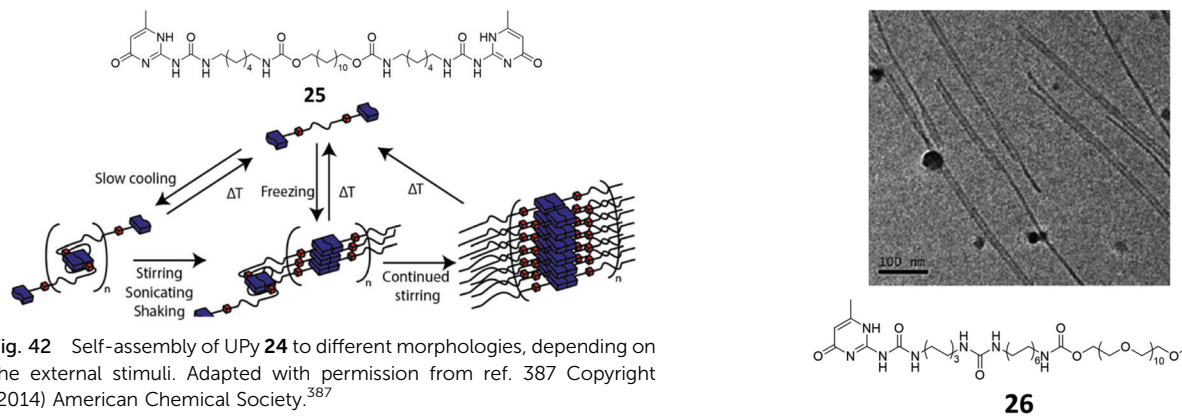


Fig. 42 Self-assembly of UPy **24** to different morphologies, depending on the external stimuli. Adapted with permission from ref. 387 Copyright (2014) American Chemical Society.³⁸⁷

modulate the hierarchical interaction of the fibers and thus tune the hydrogel properties.³⁸⁸ Additional “switching-properties” arose due to the pH-dependent enolate formation of the UPy motif in basic conditions, where electrostatic repulsion disassembled the aggregates. Acidification reconverted the structures to the keto/enol tautomers forming a transient network based on the non-covalent interactions.³⁸⁸ The same group could further show that a combination of peptides with the UPy motif also yields fibrillar structures in water. The conjugation of biomolecules to UPys makes these structures promising for application in regenerative medicine.³⁸⁹

As previously shown for the self-assembly of urea motifs (Section 3.5), the length of the polymer attached to the UPy end groups has to be chosen carefully. The group of Dankers observed that an increasing alkyl spacer length favored the network formation in solution.³⁸¹ With increasing length of the PEG chain (2000–35 000 g mol⁻¹) however, the opposite effect was observed and again smaller aggregates could be detected. By cooling or increasing the concentration, a hydrogel could be formed. Due to the formation of supramolecular cross-links, fiber bundles, and phase separation, the gel increased in strength after approximately one day of aging. These properties make the system applicable as a protein carrier or hydrogel drug reservoir administered *via* minimal invasive injection.³⁹⁰

It can be easily seen that strictly separating the self-assembly of mono- and bivalent UPys from each other is rather difficult since both building blocks are often combined to archive *e.g.* impressive gel-forming properties.^{385,388} Nevertheless, the UPy motif is a very prominent example of supramolecular self-assembly especially in

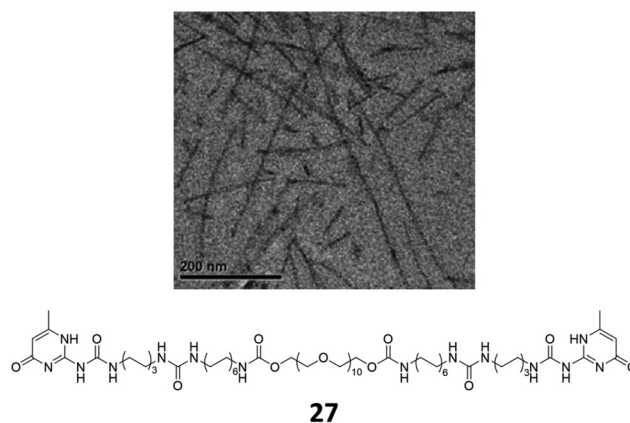


Fig. 43 CryoTEM images of UPy **26** ($c = 482$ mM) and UPy **27** ($c = 474$ mM). Adapted with permission from ref. 385 Copyright (2004) Royal Society of Chemistry.³⁸⁵

the bulk. Its rather unusual assembly *via* dimerization and additional lateral stacking due to urea groups paves the way for a plethora of applications.

3.7. Squaramides

A structural motif that was just recently used for the first time for the supramolecular assembly of polymers are squaramides. Squaramides are an intriguing supramolecular motif as they possess two C=O hydrogen bond acceptors opposite to two N-H hydrogen bond donors on a cyclobutene ring (Fig. 44).

Furthermore, theoretical considerations predict partial aromaticity caused by the delocalization of the nitrogen lone pairs

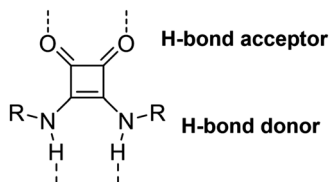


Fig. 44 Hydrogen bond acceptor and donor ability of squaramides.

over the cyclobutenedione system complying with Hückel's rule ($(4n+2) \pi$ electrons, $n = 0$). The remarkable hydrogen bond-forming propensity of squaramides is further amplified by an increase in this aromatic character upon hydrogen bond formation.³⁹¹ Another attractive aspect of squaramides is their high synthetic accessibility through straightforward amidation of commercially available squaric esters with the respective primary or secondary amines. Besides the recent introduction to supramolecular polymer chemistry, squaramides have found applications in anion recognition,³⁹² catalysis,^{393,394} bioconjugations,³⁹⁵ medicinal chemistry³⁹⁶ and to produce algogels³⁹⁷ and hydrogels.^{398,399}

The gain in aromaticity upon hydrogen bond formation was exploited by the Kieltyka group to create the first example of supramolecular polymer bottlebrushes based on squaramides.⁴⁰⁰ They synthesized a bis(squaramide) bolaamphiphile consisting of two squaramides in the hydrophobic core flanked by hydrophilic OEG chains at each end to guarantee water solubility (Fig. 45a).

CryoTEM images of **28a** revealed micrometer-long brushes with a uniform diameter. Interestingly, short bottlebrushes of approximately 12 nm were obtained upon sonication. However, these bottlebrushes slowly reassembled into the initially observed micrometer-long bottlebrushes, nicely illustrating their dynamic nature. A q^{-1} -dependence in the SAXS scattering profile supported the existence of bottlebrushes in aqueous solution. Furthermore, the SAXS measurement allowed the determination of a cross-sectional mass per unit length, indicating that approximately 10–30 squaramide bolaamphiphiles can be found per nm along the brush axis. Derived from these numbers, the authors propose a direction of the hydrogen-bonding and π - π interactions within the brushes as illustrated in Fig. 45b and c. Depolymerization of the fiber was achieved by the addition of hexafluoroisopropanol (HFIP), a well-known hydrogen bond-disrupting solvent. Simulations further indicated an increase in aromaticity upon polymerization which significantly contributes to the overall stability.

The impact of defined structural variations on the aqueous self-assembly was further investigated on a library of bis(squaramide) bolaamphiphiles with variable hydrophilic and hydrophobic domain sizes (Fig. 46).⁴⁰¹ By varying the aliphatic chain length from 2 to 12 methylene groups and the OEG chains from 11 to 36 repeating units, the hydrophilic/hydrophobic domain size ratio was systematically changed. At a constant chain length of 11 OEG units ($n = 11$), a minimum length of 8 to 10 hydrophobic methylene groups is required to induce self-assembly to supramolecular polymer bottlebrushes in water. For shorter alkyl chain lengths, surrounding water molecules can penetrate into the hydrophobic core and disrupt the hydrogen bonds between the

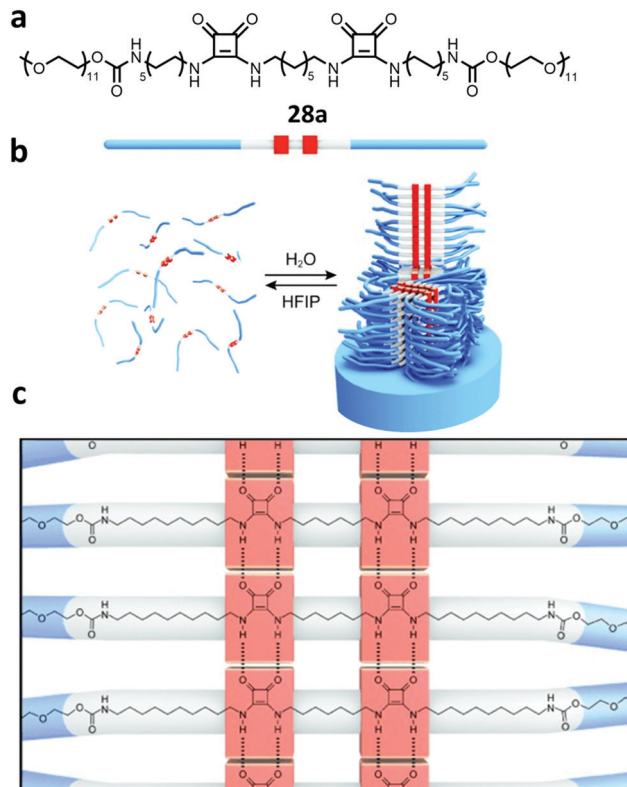


Fig. 45 (a) Structure of the bis(squaramide) bolaamphiphile. (b) Polymerization and depolymerization (by addition of HFIP) of **28a** into supramolecular polymer bottlebrushes. Within the brush, π -interactions are proposed to occur between squaramide bolaamphiphiles in the lateral direction while hydrogen bonds occur parallel to the brush axis. (c) Proposed hydrogen bond formation between squaramide bolaamphiphiles. Adapted with permission from ref. 400 Copyright (2015) John Wiley and Sons.⁴⁰⁰

bis(squaramide) bolaamphiphiles. On the contrary, increasing the OEG chain length resulted in a morphological transition from anisotropic brushes to isotropic micelles at a fixed length of 10 methylene groups, which is most likely due to an amplified steric hindrance.

Moreover, the Kieltyka group used a DNA end-functionalized bis(squaramide) bolaamphiphile in a proof-of-concept study to demonstrate that supramolecular polymer bottlebrushes thereof can be addressed by DNA-functionalized gold nanoparticles.⁴⁰² Furthermore, an on-demand erasing and rewriting of these nanoparticles is possible by means of DNA-strand replacement, illustrating the potential of squaramide-based supramolecular polymer bottlebrushes to function as reversible labeling platform for complex biological compounds such as proteins, peptides or DNA. Very recently, the same group injected fluorescent, squaramide-based supramolecular aggregates of different morphologies (fibres, rods + spheres, spheres) into transparent zebrafish embryos and investigated the impact of the aggregate morphology onto the *in vivo* distribution.⁴⁰³ The fibrous aggregates exhibited a low circulation time with rapid association with venous endothelial cells. In contrast, the spherical squaramide aggregates displayed a significantly prolonged circulation time with an increased overall distribution over the zebrafish.

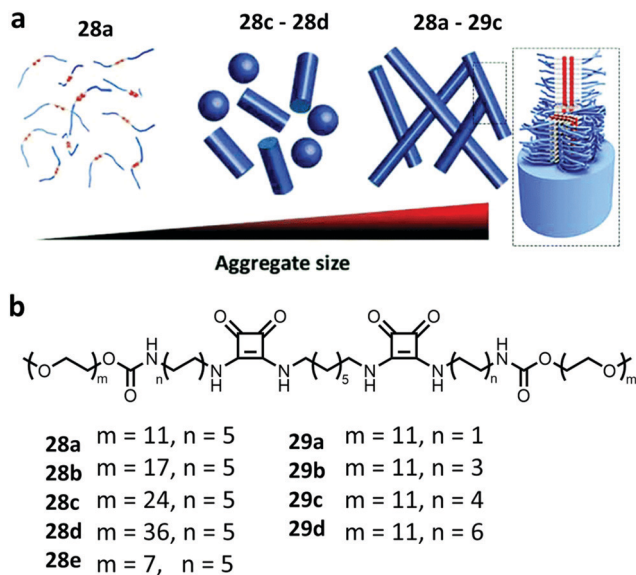


Fig. 46 (a) Summary of the obtained supramolecular polymer bottlebrush morphologies in aqueous solution for the respective compounds. (b) Corresponding chemical structures of the investigated bis(squaramide) bolaamphiphile library. Adapted with permission from ref. 401 Copyright (2019) Royal Society of Chemistry.⁴⁰¹

4. Potential applications of SPBs

SPBs had certainly been an academic niche for several years starting with the early attempts on the planar cyclophanes, while at the same time supramolecular polymers were already on the rise and gained significant attention.^{371,404} Nonetheless, their unique nature combining advantages of supramolecular chemistry and the versatility of polymers renders them an attractive material. Especially the dynamics of the interaction arising from their unique backbone, their potential responsivity to external stimuli, and the large variety of possible functionalities lay the foundation for their use in the rapidly growing field of nanoarchitectonics.⁴⁰⁵ Their application in this field will still require a better control over the dynamic nature of the self-assemblies, but if realized, the disturbance introduced by fluctuations in the environment, such as temperature or concentration, should facilitate the growth or depolymerization, respectively, in response to these stimuli. Moreover, it would be imaginable to create cooperating systems which surpass these fluctuation effects and work in harmony to form nano- to submicro-sized organized systems with complex functionalities as nature is already demonstrating, although it is still a long way to go.

But there are more imminent applications that can be foreseen. The versatile functionality and stimuli responsivity of these systems render them for example good candidates for their use as scaffolds in the development of new porous materials. While for example polyionic complex (PIC) micelles are frequently used as structuring agent for creation of mesoporous organosilica,⁴⁰⁶ the anisotropic nature of SPBs could give access to more hierarchical structures and the additional options for functionalization of the organosilica. In addition to their use as sacrificial template, SPBs could also act as a dynamic platform for the cooperative alignment of catalytic centers.

Only recently Wijnands *et al.* demonstrated that with such a supramolecular approach the formation of protein complexes is amplified which significantly enhanced the enzymatic activity.⁴⁰⁷

Their application in electronics is also conceivable. Indeed, recent work by Haedler *et al.* already demonstrated that large anisotropic structures formed by carbonyl-bridged triaryl amines *via* H-type stacking were able to efficiently transport singlet excitons at ambient conditions over more than 4 μm .⁴⁰⁸ The only limitation in the transport range lies in the finite length of the fiber. The combination of such materials with polymer side chains as in SPBs further opens up multiple options to include for example conjugated polymers or embed these fibers into a flexible polymer matrix and enable unprecedented applications in organic nanophotonic devices or quantum information technologies.

Further potential lies in the formation of smart actuators. The groups of Stupp and Olvera de la Cruz already demonstrated an impressive example based on a hydrogel tube comprising a supramolecular skeleton made of aggregating peptides which are functionalized with an ATRP initiator.⁴⁰⁹ Oligo(ethylene glycol) methacrylate crosslinked by *N,N'*-methylenebisacrylamid were grafted from this supramolecular scaffold. The polymer arms feature LCST behavior which trigger a retraction of the tube at high temperature, due to a hierarchical ordering of the supramolecular skeleton. Key for this actuation was the covalent attachment of polymers to the macroscopically aligned supramolecular scaffold. Compared to conventional materials, the supramolecular building blocks will add an additional level of control thanks to their dynamic rearrangement. Hence, adaptive actuators are imaginable for specific applications on demand, which for example change the direction of the resulting force. Gaining control on these dynamics in stimuli responsive supramolecular building blocks and designing such active matter which is molecularly encoded are the grand challenges for the future development of sophisticated soft actuators.

One of the biggest benefits of supramolecular systems, namely their modularity, has stimulated already commencing applications in the field of nanomedicine, as it has already been demonstrated for BTAs.¹⁹⁰ Further exciting work is certainly to be expected on the design of supramolecular vaccines – a pioneering idea by the Besenius group, which is currently under investigation.^{266,410} An inherent advantage of such SPBs for biomedical application resides in the anisotropic, cylindrical shape. Due to the higher surface area of these structures targeted interactions (*e.g.* by cell specific ligands) can be increased and thus these materials get uptaken more selectively and faster.⁴¹¹ The straightforward supramolecular assembly is further beneficial to achieve synergistic effects in multiple drug approaches, where individually loaded building blocks can simply be mixed at the desired molar ratios.⁴¹² However, for the bench-to-bedside transition, many more milestones are still to be reached.

5. Conclusion and outlook

As summarized in this review, the materials suitable to form supramolecular polymer bottlebrushes (SPBs) range from

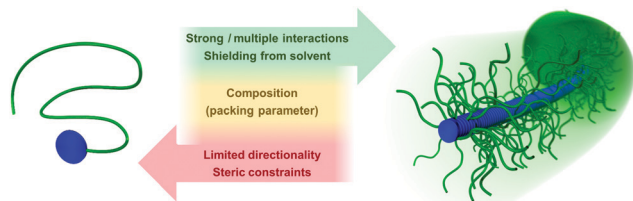


Fig. 47 Summary of key aspects significantly influencing the formation of supramolecular polymer bottlebrushes in a positive (green arrow) or negative (red arrow) manner.

π - π -interaction-based systems such as aromatic rod-coil-amphiphiles, cyclophanes or rylene dyes to hydrogen bond-based systems such as squaramides, benzenetrisamides, urea-based structures, ureidopyrimidinones, linear and cyclic peptides. A summary of a few key aspects that significantly impact the formation of anisotropic SPBs in water such as interaction strength, hydrophobic shielding, overall composition, limited directionality and the steric constraints imposed by the attached polymers are depicted in Fig. 47.

The growing number of molecular platforms has certainly accelerated the recent research, but still the field of SPBs is in its infancy. One of the most challenging milestones yet to reach is certainly the control over the unimer distribution within these SPBs and a guided structuring in the resulting assemblies. This is in particular challenging due to the dynamic nature of the supramolecular polymers, which tend to homogenize the unimer distribution *via* intra- and interchain unimer exchange.^{413,414} A recent achievement in this regard was the fabrication of supramolecular block copolymers based on a cyclic octapeptide functionalized with two block copolymers on each side of the peptide rings as reported by Rho *et al.*³³⁴ Other supramolecular block copolymers based on low molar mass building blocks have also been reported for hexabenzocoronenes,^{415,416} triblock peptides,⁴¹⁷ triarylamine trisamides,^{418,419} and perylene bisimides.¹⁵³

The aspect of control in the unimer order is accompanied by another crucial milestone on the way to advanced SPBs: controlling the length of the assembly. It is rather difficult to control the degree of polymerization in a supramolecular polymer, because of its often spontaneous aggregation without need for initiators.¹¹⁸ In nature, self-organization *via* a controlled/living supramolecular polymerization can often be observed, for instance in the dynamic instability of microtubules in the cytoskeleton.⁹⁴ Taking this as a blueprint while mimicking nature, supramolecular systems that polymerize in a chain-growth manner, and that does not rely on crystallization as the driving force, have been designed.⁴²⁰⁻⁴²² Performing supramolecular polymerizations under kinetic control is considered as the key strategy to obtain supramolecular materials of defined dimensions, as supramolecular polymerizations under thermodynamic equilibrium results in assemblies with broad size distributions.⁴²³ Gaining this kinetic control is however also challenged by the intrinsic dynamic nature of supramolecular polymers. This aspect has so far hardly been addressed for supramolecular polymer bottlebrushes,^{325,334} whereas several

studies report on examining the dynamics of supramolecular fibers based on non-polymeric BTA^{198,200,203,424-426} or UPy³⁸⁵ molecules. Further studies on this topic have certainly to be expected for SPBs in near future, although it clearly remains a significant challenge. However, if we are able to control the dynamic nature, the order of unimers, and the length of such supramolecular systems, an exciting door is opened to new generation of materials and a wealth of opportunities, not only in nanomedicine, where size and aspect ratio are key factors in the efficacy of carrier systems,^{16,427} but also in the other above mentioned fields of electronics, actuators, or scaffold design.

Conflicts of interest

There are no conflicts to declare.

Acknowledgements

The authors thank Ulrich S. Schubert for his continuous support and the excellent working environment. JCB, TK, and FVG further thank the German Science Foundation (DFG) for generous funding within the Emmy-Noether Programme (Project-ID: 358263073). Furthermore, the DFG is acknowledged for funding within the Collaborative Research Centre PolyTarget, project A05 (Project-ID: 316213987 – SFB 1278).

References

- J. A. Champion and S. Mitragotri, *Proc. Natl. Acad. Sci. U. S. A.*, 2006, **103**, 4930–4934.
- P. Decuzzi, R. Pasqualini, W. Arap and M. Ferrari, *Pharm. Res.*, 2008, **26**, 235.
- R. A. Meyer and J. J. Green, *Wiley Interdiscip. Rev.: Nanomed. Nanobiotechnol.*, 2016, **8**, 191–207.
- R. Verber, A. Blanazs and S. P. Armes, *Soft Matter*, 2012, **8**, 9915–9922.
- W. Zhang, B. Charleux and P. Cassagnau, *Soft Matter*, 2013, **9**, 2197–2205.
- C. M. A. Leenders, T. Mes, M. B. Baker, M. M. E. Koenigs, P. Besenius, A. R. A. Palmans and E. W. Meijer, *Mater. Horiz.*, 2014, **1**, 116–120.
- O. Azzaroni, *J. Polym. Sci., Part A: Polym. Chem.*, 2012, **50**, 3225–3258.
- G. M. Miyake, V. A. Pionova, R. A. Weitekamp and R. H. Grubbs, *Angew. Chem., Int. Ed.*, 2012, **51**, 11246–11248.
- G. Sun, S. Cho, C. Clark, S. V. Verkhoturov, M. J. Eller, A. Li, A. Pavia-Jiménez, E. A. Schweikert, J. W. Thackeray, P. Trefonas and K. L. Wooley, *J. Am. Chem. Soc.*, 2013, **135**, 4203–4206.
- X.-H. Jin, M. B. Price, J. R. Finnegan, C. E. Boott, J. M. Richter, A. Rao, S. M. Menke, R. H. Friend, G. R. Whittell and I. Manners, *Science*, 2018, **360**, 897–900.
- J. Rzyayev, *ACS Macro Lett.*, 2012, **1**, 1146–1149.
- H.-i. Lee, J. Pietrasik, S. S. Sheiko and K. Matyjaszewski, *Prog. Polym. Sci.*, 2010, **35**, 24–44.
- Y. Geng, P. Dalhaimer, S. Cai, R. Tsai, M. Tewari, T. Minko and D. E. Discher, *Nat. Nanotechnol.*, 2007, **2**, 249–255.
- K. Zhang, R. Rossin, A. Hagooly, Z. Chen, M. J. Welch and K. L. Wooley, *J. Polym. Sci., Part A: Polym. Chem.*, 2008, **46**, 7578–7583.
- D. A. Christian, S. Cai, O. B. Garbuzenko, T. Harada, A. L. Zajac, T. Minko and D. E. Discher, *Mol. Pharmaceutics*, 2009, **6**, 1343–1352.
- M. Elsbahy and K. L. Wooley, *Chem. Soc. Rev.*, 2012, **41**, 2545–2561.
- N. Doshi, B. Prabhakarandian, A. Rea-Ramsey, K. Pant, S. Sundaram and S. Mitragotri, *J. Controlled Release*, 2010, **146**, 196–200.
- M. Müllner, S. J. Dodds, T.-H. Nguyen, D. Senyashyn, C. J. H. Porter, B. J. Boyd and F. Caruso, *ACS Nano*, 2015, **9**, 1294–1304.
- M. Müllner, K. Yang, A. Kaur and E. J. New, *Polym. Chem.*, 2018, **9**, 3461–3465.

- 20 J. C. Foster, S. Varlas, B. Couturaud, Z. Coe and R. K. O'Reilly, *J. Am. Chem. Soc.*, 2019, **141**, 2742–2753.
- 21 T. Shimizu, M. Masuda and H. Minamikawa, *Chem. Rev.*, 2005, **105**, 1401–1444.
- 22 D. Chandler, *Nature*, 2005, **437**, 640–647.
- 23 R. C. Hayward and D. J. Pochan, *Macromolecules*, 2010, **43**, 3577–3584.
- 24 F. S. Bates, M. A. Hillmyer, T. P. Lodge, C. M. Bates, K. T. Delaney and G. H. Fredrickson, *Science*, 2012, **336**, 434–440.
- 25 Y. Mai and A. Eisenberg, *Chem. Soc. Rev.*, 2012, **41**, 5969–5985.
- 26 S. Song, A. Song and J. Hao, *RSC Adv.*, 2014, **4**, 41864–41875.
- 27 S. L. Canning, G. N. Smith and S. P. Armes, *Macromolecules*, 2016, **49**, 1985–2001.
- 28 B. Karagoz, L. Esser, H. T. Duong, J. S. Basuki, C. Boyer and T. P. Davis, *Polym. Chem.*, 2014, **5**, 350–355.
- 29 M. J. Derry, L. A. Fielding and S. P. Armes, *Prog. Polym. Sci.*, 2016, **52**, 1–18.
- 30 U. Tritschler, S. Pearce, J. Gwyther, G. R. Whittell and I. Manners, *Macromolecules*, 2017, **50**, 3439–3463.
- 31 J. C. Brendel and F. H. Schacher, *Chem. – Asian J.*, 2018, **13**, 230–239.
- 32 L. J. Prins, D. N. Reinhoudt and P. Timmerman, *Angew. Chem., Int. Ed.*, 2001, **40**, 2382–2426.
- 33 M. D. Watson, A. Fechtenkötter and K. Müllen, *Chem. Rev.*, 2001, **101**, 1267–1300.
- 34 J. Qian, M. Zhang, I. Manners and M. A. Winnik, *Trends Biotechnol.*, 2010, **28**, 84–92.
- 35 J. B. Gilroy, T. Gädt, G. R. Whittell, L. Chabanne, J. M. Mitchels, R. M. Richardson, M. A. Winnik and I. Manners, *Nat. Chem.*, 2010, **2**, 566.
- 36 J. Du and R. K. O'Reilly, *Chem. Soc. Rev.*, 2011, **40**, 2402–2416.
- 37 N. Petzetakis, A. P. Dove and R. K. O'Reilly, *Chem. Sci.*, 2011, **2**, 955–960.
- 38 S. K. Patra, R. Ahmed, G. R. Whittell, D. J. Lunn, E. L. Dunphy, M. A. Winnik and I. Manners, *J. Am. Chem. Soc.*, 2011, **133**, 8842–8845.
- 39 J. Schmelz, A. E. Schedl, C. Steinlein, I. Manners and H. Schmalz, *J. Am. Chem. Soc.*, 2012, **134**, 14217–14225.
- 40 W.-N. He and J.-T. Xu, *Prog. Polym. Sci.*, 2012, **37**, 1350–1400.
- 41 S. Ganda and M. H. Stenzel, *Prog. Polym. Sci.*, 2020, **101**, 101195.
- 42 T. Kato, J. Uchida, T. Ichikawa and B. Soberats, *Polym. J.*, 2018, **50**, 149–166.
- 43 U. Kumar, J. M. J. Fréchet, T. Kato, S. Ujiie and K. Timura, *Angew. Chem., Int. Ed. Engl.*, 1992, **31**, 1531–1533.
- 44 J. Ruokolainen, R. Mäkinen, M. Torkkeli, T. Mäkelä, R. Serimaa, G. t. Brinke and O. Ikkala, *Science*, 1998, **280**, 557–560.
- 45 H. Kosonen, J. Ruokolainen, M. Knaapila, M. Torkkeli, K. Jokela, R. Serimaa, G. ten Brinke, W. Bras, A. P. Monkman and O. Ikkala, *Macromolecules*, 2000, **33**, 8671–8675.
- 46 C. Osuji, C.-Y. Chao, I. Bitá, C. K. Ober and E. L. Thomas, *Adv. Funct. Mater.*, 2002, **12**, 753–758.
- 47 T. Cherian, D. R. Nunes, T. G. Dane, J. Jacquemin, U. Vainio, T. T. T. Myllymäki, J. V. I. Timonen, N. Houbenov, M. Maréchal, P. Rannou and O. Ikkala, *Adv. Funct. Mater.*, 2019, **29**, 1905054.
- 48 T. Kato and J. M. J. Frechet, *Macromolecules*, 1989, **22**, 3818–3819.
- 49 C. Fouquey, J.-M. Lehn and A.-M. Levelut, *Adv. Mater.*, 1990, **2**, 254–257.
- 50 H. Kihara, T. Kato, T. Uryu and J. M. J. Fréchet, *Chem. Mater.*, 1996, **8**, 961–968.
- 51 T. Kato, Y. Kubota, T. Uryu and S. Ujiie, *Angew. Chem., Int. Ed. Engl.*, 1997, **36**, 1617–1618.
- 52 T. Kato, N. Mizoshita and K. Kanie, *Macromol. Rapid Commun.*, 2001, **22**, 797–814.
- 53 F. Würthner, S. Yao, B. Heise and C. Tschierske, *Chem. Commun.*, 2001, 2260–2261, DOI: 10.1039/B106413D.
- 54 O. Ikkala and G. ten Brinke, *Chem. Commun.*, 2004, 2131–2137, DOI: 10.1039/B403983A.
- 55 E. Weiss, K. C. Daoulas, M. Müller and R. Shenhar, *Macromolecules*, 2011, **44**, 9773–9781.
- 56 R. A. Sanguramath, P. F. Nealey and R. Shenhar, *Chem. – Eur. J.*, 2016, **22**, 10203–10210.
- 57 J. B. Beck, J. M. Ineman and S. J. Rowan, *Macromolecules*, 2005, **38**, 5060–5068.
- 58 P. Wei, X. Yan and F. Huang, *Chem. Soc. Rev.*, 2015, **44**, 815–832.
- 59 M. Zhang, D. Xu, X. Yan, J. Chen, S. Dong, B. Zheng and F. Huang, *Angew. Chem., Int. Ed.*, 2012, **51**, 7011–7015.
- 60 X. Ji, Y. Yao, J. Li, X. Yan and F. Huang, *J. Am. Chem. Soc.*, 2013, **135**, 74–77.
- 61 M. Dionisio, L. Ricci, G. Pecchini, D. Masseroni, G. Ruggeri, L. Cristofolini, E. Rampazzo and E. Dalcanale, *Macromolecules*, 2014, **47**, 632–638.
- 62 Y. Wang, M. Zhong, J. V. Park, A. V. Zhukhovitskiy, W. Shi and J. A. Johnson, *J. Am. Chem. Soc.*, 2016, **138**, 10708–10715.
- 63 X. Ji, H. Wang, Y. Li, D. Xia, H. Li, G. Tang, J. L. Sessler and F. Huang, *Chem. Sci.*, 2016, **7**, 6006–6014.
- 64 Y. Tsunoda, M. Takatsuka, R. Sekiya and T. Haino, *Angew. Chem., Int. Ed.*, 2017, **56**, 2613–2618.
- 65 S. S. Sheiko, B. S. Sumerlin and K. Matyjaszewski, *Prog. Polym. Sci.*, 2008, **33**, 759–785.
- 66 M. Zhang and A. H. E. Müller, *J. Polym. Sci., Part A: Polym. Chem.*, 2005, **43**, 3461–3481.
- 67 Z. Li, K. Zhang, J. Ma, C. Cheng and K. L. Wooley, *J. Polym. Sci., Part A: Polym. Chem.*, 2009, **47**, 5557–5563.
- 68 Y. Xia, J. A. Kornfield and R. H. Grubbs, *Macromolecules*, 2009, **42**, 3761–3766.
- 69 J. Yuan, A. H. E. Müller, K. Matyjaszewski and S. S. Sheiko, in *Polymer Science: A Comprehensive Reference*, ed. K. Matyjaszewski and M. Möller, Elsevier, Amsterdam, 2012, ch. 6.06, vol. 6, pp. 199–264.
- 70 A. X. Gao, L. Liao and J. A. Johnson, *ACS Macro Lett.*, 2014, **3**, 854–857.
- 71 A. O. Burts, L. Liao, Y. Y. Lu, D. A. Tirrell and J. A. Johnson, *Photochem. Photobiol.*, 2014, **90**, 380–385.
- 72 R. Verduzco, X. Li, S. L. Pesek and G. E. Stein, *Chem. Soc. Rev.*, 2015, **44**, 2405–2420.
- 73 P. Théophile, C. S. Mahon and M. Markus, *Angew. Chem., Int. Ed.*, 2018, **57**, 2–15.
- 74 S. L. Pesek, X. Li, B. Hammouda, K. Hong and R. Verduzco, *Macromolecules*, 2013, **46**, 6998–7005.
- 75 S. Zhang, *Nat. Biotechnol.*, 2003, **21**, 1171–1178.
- 76 L. Liao, J. Liu, E. C. Dreaden, S. W. Morton, K. E. Shopsowitz, P. T. Hammond and J. A. Johnson, *J. Am. Chem. Soc.*, 2014, **136**, 5896–5899.
- 77 M. A. Sowers, J. R. McCombs, Y. Wang, J. T. Paletta, S. W. Morton, E. C. Dreaden, M. D. Boska, M. F. Ottaviani, P. T. Hammond, A. Rajca and J. A. Johnson, *Nat. Commun.*, 2014, **5**, 5460.
- 78 J. Zou, Y. Yu, Y. Li, W. Ji, C.-K. Chen, W.-C. Law, P. N. Prasad and C. Cheng, *Biomater. Sci.*, 2015, **3**, 1078–1084.
- 79 Y. Yu, C.-K. Chen, W.-C. Law, H. Sun, P. N. Prasad and C. Cheng, *Polym. Chem.*, 2015, **6**, 953–961.
- 80 C. Hörtz, A. Birke, L. Kaps, S. Decker, E. Wächtersbach, K. Fischer, D. Schuppan, M. Barz and M. Schmidt, *Macromolecules*, 2015, **48**, 2074–2086.
- 81 M. Müllner, *Macromol. Chem. Phys.*, 2016, **217**, 2209–2222.
- 82 M. Müllner and A. H. E. Müller, *Polymer*, 2016, **98**, 389–401.
- 83 T. Aida, E. W. Meijer and S. I. Stupp, *Science*, 2012, **335**, 813–817.
- 84 J. Kang, D. Miyajima, T. Mori, Y. Inoue, Y. Itoh and T. Aida, *Science*, 2015, **347**, 646–651.
- 85 E. Busseron, Y. Ruff, E. Moulin and N. Giuseppone, *Nanoscale*, 2013, **5**, 7098–7140.
- 86 E. Yashima, N. Ousaka, D. Taura, K. Shimomura, T. Ikai and K. Maeda, *Chem. Rev.*, 2016, **116**, 13752–13990.
- 87 E. Krieg, M. M. Bastings, P. Besenius and B. Rybtchinski, *Chem. Soc. Rev.*, 2016, **116**, 2414–2477.
- 88 B. Qin, Z. Yin, X. Tang, S. Zhang, Y. Wu, J.-F. Xu and X. Zhang, *Prog. Polym. Sci.*, 2020, **100**, 101167.
- 89 M. Hartlieb, E. D. H. Mansfield and S. Perrier, *Polym. Chem.*, 2020, **11**, 1083–1110.
- 90 C. Kulkarni, E. W. Meijer and A. R. A. Palmans, *Acc. Chem. Res.*, 2017, **50**, 1928–1936.
- 91 T. Mitchison and M. Kirschner, *Nature*, 1984, **312**, 237–242.
- 92 T. Horio and H. Hotani, *Nature*, 1986, **321**, 605–607.
- 93 T. E. Holy and S. Leibler, *Proc. Natl. Acad. Sci. U. S. A.*, 1994, **91**, 5682–5685.
- 94 D. A. Fletcher and R. D. Mullins, *Nature*, 2010, **463**, 485–492.
- 95 H. Hess and J. L. Ross, *Chem. Soc. Rev.*, 2017, **46**, 5570–5587.
- 96 J. M. Lehn, *Angew. Chem., Int. Ed. Engl.*, 1990, **29**, 1304–1319.
- 97 J.-M. Lehn, *Proc. Natl. Acad. Sci. U. S. A.*, 2002, **99**, 4763–4768.
- 98 J. M. Lehn, *Science*, 2002, **295**, 2400–2403.
- 99 J. A. A. W. Elemans, A. E. Rowan and R. J. M. Nolte, *J. Mater. Chem.*, 2003, **13**, 2661–2670.

- 100 R. F. Service, *Science*, 2005, **309**, 95.
- 101 S. Zhang, M. A. Greenfield, A. Mata, L. C. Palmer, R. Bitton, J. R. Mantei, C. Aparicio, M. O. de la Cruz and S. I. Stupp, *Nat. Mater.*, 2010, **9**, 594–601.
- 102 W.-J. Chung, J.-W. Oh, K. Kwak, B. Y. Lee, J. Meyer, E. Wang, A. Hexemer and S.-W. Lee, *Nature*, 2011, **478**, 364.
- 103 J.-M. Lehn, *Chem. Soc. Rev.*, 2007, **36**, 151–160.
- 104 Y. Tu, F. Peng, A. Adawy, Y. Men, L. K. E. A. Abdelmohsen and D. A. Wilson, *Chem. Rev.*, 2016, **116**, 2023–2078.
- 105 J.-F. Lutz, J.-M. Lehn, E. W. Meijer and K. Matyjaszewski, *Nat. Rev. Mater.*, 2016, **1**, 16024.
- 106 J. W. Steed and J. L. Atwood, *Supramolecular Chemistry*, Wiley, 2009.
- 107 J. Couet and M. Biesalski, *Soft Matter*, 2006, **2**, 1005–1014.
- 108 D. Zhao and J. S. Moore, *Chem. Commun.*, 2003, 807–818, DOI: 10.1039/B207442G.
- 109 J. S. Moore, *Acc. Chem. Res.*, 1997, **30**, 402–413.
- 110 S. Höger, *J. Polym. Sci., Part A: Polym. Chem.*, 1999, **37**, 2685–2698.
- 111 R. B. Martin, *Chem. Rev.*, 1996, **96**, 3043–3064.
- 112 A. S. Shetty, J. Zhang and J. S. Moore, *J. Am. Chem. Soc.*, 1996, **118**, 1019–1027.
- 113 S. Lahiri, J. L. Thompson and J. S. Moore, *J. Am. Chem. Soc.*, 2000, **122**, 11315–11319.
- 114 S. Rosselli, A. D. Ramminger, T. Wagner, B. Silier, S. Wiegand, W. Haeussler, G. Lieser, V. Scheumann and S. Höger, *Angew. Chem., Int. Ed.*, 2001, **40**, 3137–3141.
- 115 S. Höger, *Chem. – Eur. J.*, 2004, **10**, 1320–1329.
- 116 S. Rosselli, A.-D. Ramminger, T. Wagner, G. Lieser and S. Höger, *Chem. – Eur. J.*, 2003, **9**, 3481–3491.
- 117 N. Dingenouts, S. Klyatskaya, S. Rosenfeldt, M. Ballauff and S. Höger, *Macromolecules*, 2009, **42**, 5900–5902.
- 118 T. F. De Greef, M. M. Smulders, M. Wolfs, A. P. Schenning, R. P. Sijbesma and E. W. Meijer, *Chem. Rev.*, 2009, **109**, 5687–5754.
- 119 J. C. Gielen, A. Ver Heyen, S. Klyatskaya, W. Vanderlinden, S. Höger, J. C. Maan, S. De Feyter and P. C. M. Christianen, *J. Am. Chem. Soc.*, 2009, **131**, 14134–14135.
- 120 M. Fritzsche, S.-S. Jester, S. Höger, C. Klaus, N. Dingenouts, P. Linder, M. Drechsler and S. Rosenfeldt, *Macromolecules*, 2010, **43**, 8379–8388.
- 121 M. Lee and Y.-S. Yoo, *J. Mater. Chem.*, 2002, **12**, 2161–2168.
- 122 B. D. Olsen and R. A. Segalman, *Mater. Sci. Eng., R*, 2008, **62**, 37–66.
- 123 C.-L. Liu, C.-H. Lin, C.-C. Kuo, S.-T. Lin and W.-C. Chen, *Prog. Polym. Sci.*, 2011, **36**, 603–637.
- 124 J.-H. Ryu, D.-J. Hong and M. Lee, *Chem. Commun.*, 2008, 1043–1054, DOI: 10.1039/B713737K.
- 125 H. Wang, H. H. Wang, V. S. Urban, K. C. Littrell, P. Thiyagarajan and L. Yu, *J. Am. Chem. Soc.*, 2000, **122**, 6855–6861.
- 126 F. J. M. Hoeben, P. Jonkheijm, E. W. Meijer and A. P. H. J. Schenning, *Chem. Rev.*, 2005, **105**, 1491–1546.
- 127 B.-S. Kim, D.-J. Hong, J. Bae and M. Lee, *J. Am. Chem. Soc.*, 2005, **127**, 16333–16337.
- 128 J. Bae, J.-H. Choi, Y.-S. Yoo, N.-K. Oh, B.-S. Kim and M. Lee, *J. Am. Chem. Soc.*, 2005, **127**, 9668–9669.
- 129 W.-Y. Yang, E. Lee and M. Lee, *J. Am. Chem. Soc.*, 2006, **128**, 3484–3485.
- 130 J.-H. Ryu, N.-K. Oh and M. Lee, *Chem. Commun.*, 2005, 1770–1772, DOI: 10.1039/B419213C.
- 131 K.-S. Moon, H.-J. Kim, E. Lee and M. Lee, *Angew. Chem., Int. Ed.*, 2007, **46**, 6807–6810.
- 132 K.-I. Zhong, C. Yang, T. Chen, B. Yin, L. Y. Jin, Z. Huang and E. Lee, *Macromol. Res.*, 2010, **18**, 289–296.
- 133 H. Wang, W. You, P. Jiang, L. Yu and H. H. Wang, *Chem. – Eur. J.*, 2004, **10**, 986–993.
- 134 E. R. Zubarev, E. D. Sone and S. I. Stupp, *Chem. – Eur. J.*, 2006, **12**, 7313–7327.
- 135 E. R. Zubarev, M. U. Pralle, E. D. Sone and S. I. Stupp, *J. Am. Chem. Soc.*, 2001, **123**, 4105–4106.
- 136 G. Scheibe, *Kolloid-Z.*, 1938, **82**, 1–14.
- 137 G. Scheibe and L. Kandler, *Naturwissenschaften*, 1938, **26**, 412–413.
- 138 E. E. Jelley, *Nature*, 1936, **138**, 1009–1010.
- 139 Z. Chen, A. Lohr, C. R. Saha-Möller and F. Würthner, *Chem. Soc. Rev.*, 2009, **38**, 564–584.
- 140 D. Görl and F. Würthner, *Angew. Chem., Int. Ed.*, 2016, **55**, 12094–12098.
- 141 J. Baram, H. Weissman, Y. Tidhar, I. Pinkas and B. Rybtchinski, *Angew. Chem., Int. Ed.*, 2014, **53**, 4123–4126.
- 142 S. Chen, P. Slattum, C. Wang and L. Zang, *Chem. Rev.*, 2015, **115**, 11967–11998.
- 143 F. Würthner, C. R. Saha-Möller, B. Fimmel, S. Ogi, P. Leowanawat and D. Schmidt, *Chem. Rev.*, 2016, **116**, 962–1052.
- 144 E. Krieg, A. Niazov-Elkan, E. Cohen, Y. Tsarfati and B. Rybtchinski, *Acc. Chem. Res.*, 2019, **52**, 2634–2646.
- 145 F. Würthner, C. Thalacker, S. Diele and C. Tschierske, *Chem. – Eur. J.*, 2001, **7**, 2245–2253.
- 146 F. Würthner, *Chem. Commun.*, 2004, 1564–1579, DOI: 10.1039/b401630k.
- 147 A. Arnaud, J. Belleney, F. Boué, L. Bouteiller, G. Carrot and V. Wintgens, *Angew. Chem., Int. Ed.*, 2004, **43**, 1718–1721.
- 148 S. Rehm, V. Stepanenko, X. Zhang, T. H. Rehm and F. Würthner, *Chem. – Eur. J.*, 2010, **16**, 3372–3382.
- 149 S. Roy, D. Kumar Maiti, S. Panigrahi, D. Basak and A. Banerjee, *RSC Adv.*, 2012, **2**, 11053–11060.
- 150 C. D. Schmidt, C. Böttcher and A. Hirsch, *Eur. J. Org. Chem.*, 2009, 5337–5349.
- 151 R. F. Fink, J. Seibt, V. Engel, M. Renz, M. Kaupp, S. Lochbrunner, H.-M. Zhao, J. Pfister, F. Würthner and B. Engels, *J. Am. Chem. Soc.*, 2008, **130**, 12858–12859.
- 152 X. Zhang, D. Görl, V. Stepanenko and F. Würthner, *Angew. Chem., Int. Ed.*, 2014, **126**, 1294–1298.
- 153 W. Wagner, M. Wehner, V. Stepanenko and F. Würthner, *J. Am. Chem. Soc.*, 2019, **141**, 12044–12054.
- 154 X. Ma, Y. Zhang, Y. Zhang, Y. Liu, Y. Che and J. Zhao, *Angew. Chem., Int. Ed.*, 2016, **55**, 9539–9543.
- 155 C. Jarrett-Wilkins, X. He, H. E. Symons, R. L. Harniman, C. F. J. Faul and I. Manners, *Chem. – Eur. J.*, 2018, **24**, 15556–15565.
- 156 L. Tian, R. Szilluweit, R. Marty, L. Bertschi, M. Zerson, E.-C. Spitzner, R. Magerle and H. Frauenrath, *Chem. Sci.*, 2012, **3**, 1512–1521.
- 157 R. Marty, R. Szilluweit, A. Sánchez-Ferrer, S. Bolisetty, J. Adamcik, R. Mezzenga, E.-C. Spitzner, M. Feifer, S. N. Steinmann, C. Corminboeuf and H. Frauenrath, *ACS Nano*, 2013, **7**, 8498–8508.
- 158 R. Marty, R. Nigon, D. Leite and H. Frauenrath, *J. Am. Chem. Soc.*, 2014, **136**, 3919–3927.
- 159 E. Krieg and B. Rybtchinski, *Chem. – Eur. J.*, 2011, **17**, 9016–9026.
- 160 E. Shirman, A. Ustinov, N. Ben-Shitrit, H. Weissman, M. A. Iron, R. Cohen and B. Rybtchinski, *J. Phys. Chem. B*, 2008, **112**, 8855–8858.
- 161 M. A. Iron, R. Cohen and B. Rybtchinski, *J. Phys. Chem. B*, 2011, **115**, 2047–2056.
- 162 J. Baram, E. Shirman, N. Ben-Shitrit, A. Ustinov, H. Weissman, I. Pinkas, S. G. Wolf and B. Rybtchinski, *J. Am. Chem. Soc.*, 2008, **130**, 14966–14967.
- 163 E. Krieg, E. Shirman, H. Weissman, E. Shimoni, S. G. Wolf, I. Pinkas and B. Rybtchinski, *J. Am. Chem. Soc.*, 2009, **131**, 14365–14373.
- 164 G. Golubkov, H. Weissman, E. Shirman, S. G. Wolf, I. Pinkas and B. Rybtchinski, *Angew. Chem., Int. Ed.*, 2009, **121**, 944–948.
- 165 Y. Tidhar, H. Weissman, S. G. Wolf, A. Gulino and B. Rybtchinski, *Chem. – Eur. J.*, 2011, **17**, 6068–6075.
- 166 E. Krieg, H. Weissman, E. Shimoni, A. Bar On and B. Rybtchinski, *J. Am. Chem. Soc.*, 2014, **136**, 9443–9452.
- 167 E. Cohen, H. Weissman, I. Pinkas, E. Shimoni, P. Rehak, P. Král and B. Rybtchinski, *ACS Nano*, 2018, **12**, 317–326.
- 168 A. Ustinov, H. Weissman, E. Shirman, I. Pinkas, X. Zuo and B. Rybtchinski, *J. Am. Chem. Soc.*, 2011, **133**, 16201–16211.
- 169 M. R. Molla and S. Ghosh, *Chem. Mater.*, 2011, **23**, 95–105.
- 170 N. Narayanaswamy, M. B. Avinash and T. Govindaraju, *New J. Chem.*, 2013, **37**, 1302–1306.
- 171 A. Das and S. Ghosh, *Chem. Commun.*, 2016, **52**, 6860–6872.
- 172 A. Sikder, D. Ray, V. K. Aswal and S. Ghosh, *Angew. Chem., Int. Ed.*, 2019, **58**, 1606–1611.
- 173 P. Pramanik, D. Ray, V. K. Aswal and S. Ghosh, *Angew. Chem., Int. Ed.*, 2017, **129**, 3570–3574.
- 174 P. Dey, P. Rajdev, P. Pramanik and S. Ghosh, *Macromolecules*, 2018, **51**, 5182–5190.
- 175 T. Choynet, D. Canevet, M. Sallé, E. Nicol, F. Niepceron, J. Jestin and O. Colombani, *Chem. Commun.*, 2019, **55**, 9519–9522.
- 176 S. Cantekin, T. F. A. de Greef and A. R. A. Palmans, *Chem. Soc. Rev.*, 2012, **41**, 6125–6137.
- 177 M. A. Gillissen, M. M. Koenigs, J. J. Spiering, J. A. Vekemans, A. R. Palmans, I. K. Voets and E. W. Meijer, *J. Am. Chem. Soc.*, 2014, **136**, 336–343.
- 178 D. Weiss, K. Kreger and H. W. Schmidt, *Macromol. Mater. Eng.*, 2017, **302**, 1600390.

- 179 D. Ogata, T. Shikata and K. Hanabusa, *J. Phys. Chem. B*, 2004, **108**, 15503–15510.
- 180 L. Bouteiller, in *Hydrogen Bonded Polymers*, ed. W. Binder, 2007, vol. 207, pp. 79–112.
- 181 P. J. M. Stals, J. F. Haveman, R. Martin-Rapun, C. F. C. Fitie, A. R. A. Palmans and E. W. Meijer, *J. Mater. Chem.*, 2009, **19**, 124–130.
- 182 C. M. Leenders, L. Albertazzi, T. Mes, M. M. Koenigs, A. R. Palmans and E. W. Meijer, *Chem. Commun.*, 2013, **49**, 1963–1965.
- 183 A. Bernet, R. Q. Albuquerque, M. Behr, S. T. Hoffmann and H.-W. Schmidt, *Soft Matter*, 2012, **8**, 66–69.
- 184 D. Weiss, D. Skrybeck, H. Misslitz, D. Nardini, A. Kern, K. Kreger and H. W. Schmidt, *ACS Appl. Mater. Interfaces*, 2016, **8**, 14885–14892.
- 185 M. Blomenhofer, S. Ganzleben, D. Hanft, H.-W. Schmidt, M. Kristiansen, P. Smith, K. Stoll, D. Mäder and K. Hoffmann, *Macromolecules*, 2005, **38**, 3688–3695.
- 186 N. Mohmeyer, N. Behrendt, X. Q. Zhang, P. Smith, V. Altstadt, G. M. Sessler and H. W. Schmidt, *Polymer*, 2007, **48**, 1612–1619.
- 187 F. Abraham, S. Ganzleben, D. Hanft, P. Smith and H.-W. Schmidt, *Macromol. Chem. Phys.*, 2010, **211**, 171–181.
- 188 F. Abraham and H. W. Schmidt, *Polymer*, 2010, **51**, 913–921.
- 189 K. Petkau-Milroy, M. H. Sonntag, A. H. van Onzen and L. Brunsveld, *J. Am. Chem. Soc.*, 2012, **134**, 8086–8089.
- 190 M. H. Bakker, C. C. Lee, E. W. Meijer, P. Y. Dankers and L. Albertazzi, *ACS Nano*, 2016, **10**, 1845–1852.
- 191 M. Á. Alemán García, E. Magdalena Estirado, L.-G. Milroy and L. Brunsveld, *Angew. Chem., Int. Ed.*, 2018, **57**, 4976–4980.
- 192 S. P. W. Wijnands, W. Engelen, R. P. M. Lafleur, E. W. Meijer and M. Merckx, *Nat. Commun.*, 2018, **9**, 65.
- 193 K. K. Bejagam, G. Fiorin, M. L. Klein and S. Balasubramanian, *J. Phys. Chem. B*, 2014, **118**, 5218–5228.
- 194 M. Garzoni, M. B. Baker, C. M. A. Leenders, I. K. Voets, L. Albertazzi, A. R. A. Palmans, E. W. Meijer and G. M. Pavan, *J. Am. Chem. Soc.*, 2016, **138**, 13985–13995.
- 195 D. Bochicchio and G. M. Pavan, *ACS Nano*, 2017, **11**, 1000–1011.
- 196 T. Metzroth, A. Hoffmann, R. Martín-Rapún, M. M. J. Smulders, K. Pieterse, A. R. A. Palmans, J. A. J. M. Vekemans, E. W. Meijer, H. W. Spiess and J. Gauss, *Chem. Sci.*, 2011, **2**, 69–76.
- 197 Y. Nakano, T. Hirose, P. J. M. Stals, E. W. Meijer and A. R. A. Palmans, *Chem. Sci.*, 2012, **3**, 148–155.
- 198 L. Albertazzi, F. J. Martinez-Veracochea, C. M. A. Leenders, I. K. Voets, D. Frenkel and E. W. Meijer, *Proc. Natl. Acad. Sci. U. S. A.*, 2013, **110**, 12203–12208.
- 199 L. Albertazzi, D. van der Zwaag, C. M. Leenders, R. Fitzner, R. W. van der Hofstad and E. W. Meijer, *Science*, 2014, **344**, 491–495.
- 200 M. B. Baker, R. P. J. Gosens, L. Albertazzi, N. M. Matsumoto, A. R. A. Palmans and E. W. Meijer, *ChemBioChem*, 2016, **17**, 207–213.
- 201 L. Brunsveld, A. P. H. J. Schenning, M. A. C. Broeren, H. M. Janssen, J. A. J. M. Vekemans and E. W. Meijer, *Chem. Lett.*, 2000, 292–293.
- 202 A. R. Palmans and E. W. Meijer, *Angew. Chem., Int. Ed.*, 2007, **46**, 8948–8968.
- 203 M. B. Baker, L. Albertazzi, I. K. Voets, C. M. Leenders, A. R. Palmans, G. M. Pavan and E. W. Meijer, *Nat. Commun.*, 2015, **6**, 6234.
- 204 T. Mes, R. van der Weegen, A. R. Palmans and E. W. Meijer, *Angew. Chem., Int. Ed.*, 2011, **50**, 5085–5089.
- 205 T. Terashima, T. Mes, T. F. De Greef, M. A. Gillissen, P. Besenius, A. R. Palmans and E. W. Meijer, *J. Am. Chem. Soc.*, 2011, **133**, 4742–4745.
- 206 G. M. ter Huurne, M. A. J. Gillissen, A. R. A. Palmans, I. K. Voets and E. W. Meijer, *Macromolecules*, 2015, **48**, 3949–3956.
- 207 M. Artar, T. Terashima, M. Sawamoto, E. W. Meijer and A. R. A. Palmans, *J. Polym. Sci., Part A: Polym. Chem.*, 2014, **52**, 12–20.
- 208 P. J. M. Stals, M. A. J. Gillissen, T. F. E. Paffen, T. F. A. Greef, P. Lindner, E. W. Meijer, A. R. A. Palmans and I. K. Voets, *Macromolecules*, 2014, **47**, 2947–2954.
- 209 Y. Liu, S. Pujals, P. J. M. Stals, T. Paulohrl, S. I. Presolski, E. W. Meijer, L. Albertazzi and A. R. A. Palmans, *J. Am. Chem. Soc.*, 2018, **140**, 3423–3433.
- 210 A. P. P. Kröger and J. M. J. Paulusse, *J. Controlled Release*, 2018, **286**, 326–347.
- 211 T. Mes, M. M. E. Koenigs, V. F. Scalfani, T. S. Bailey, E. W. Meijer and A. R. A. Palmans, *ACS Macro Lett.*, 2012, **1**, 105–109.
- 212 J. Roosma, T. Mes, P. Leclere, A. R. Palmans and E. W. Meijer, *J. Am. Chem. Soc.*, 2008, **130**, 1120–1121.
- 213 N. Hosono, L. M. Pitet, A. R. A. Palmans and E. W. Meijer, *Polym. Chem.*, 2014, **5**, 1463–1470.
- 214 C. Li, J. Tan, Z. Guan and Q. Zhang, *Macromol. Rapid Commun.*, 2019, **0**, 1800909.
- 215 T. Klein, F. V. Gruschwitz, S. Rogers, S. Hoepfner, I. Nischang and J. C. Brendel, *J. Colloid Interface Sci.*, 2019, **557**, 488–497.
- 216 A. Duro-Castano, R. M. England, D. Razola, E. Romero, M. Oteo-Vives, M. A. Morcillo and M. J. Vicent, *Mol. Pharmaceutics*, 2015, **12**, 3639–3649.
- 217 A. Duro-Castano, V. J. Nebot, A. Nino-Pariente, A. Arminan, J. J. Arroyo-Crespo, A. Paul, N. Feiner-Gracia, L. Albertazzi and M. J. Vicent, *Adv. Mater.*, 2017, **29**, 1702888.
- 218 A. Heeres, C. van der Pol, M. Stuart, A. Friggeri, B. L. Feringa and J. van Esch, *J. Am. Chem. Soc.*, 2003, **125**, 14252–14253.
- 219 K. J. C. van Bommel, C. van der Pol, I. Muizebelt, A. Friggeri, A. Heeres, A. Meetsma, B. L. Feringa and J. van Esch, *Angew. Chem., Int. Ed.*, 2004, **43**, 1663–1667.
- 220 A. Friggeri, C. van der Pol, K. J. C. van Bommel, A. Heeres, M. C. A. Stuart, B. L. Feringa and J. van Esch, *Chem. – Eur. J.*, 2005, **11**, 5353–5361.
- 221 M. de Loos, J. H. van Esch, R. M. Kellogg and B. L. Feringa, *Tetrahedron*, 2007, **63**, 7285–7301.
- 222 K. P. van den Hout, R. Martín-Rapún, J. A. J. M. Vekemans and E. W. Meijer, *Chem. – Eur. J.*, 2007, **13**, 8111–8123.
- 223 Y. Dai, X. Zhao, X. Su, G. Li and A. Zhang, *Macromol. Rapid Commun.*, 2014, **35**, 1326–1331.
- 224 P. Besenius, G. Portale, P. H. Bomans, H. M. Janssen, A. R. Palmans and E. W. Meijer, *Proc. Natl. Acad. Sci. U. S. A.*, 2010, **107**, 17888–17893.
- 225 P. Besenius, K. P. van den Hout, H. M. Albers, T. F. de Greef, L. L. Olijve, T. M. Hermans, B. F. de Waal, P. H. Bomans, N. A. Sommerdijk, G. Portale, A. R. Palmans, M. H. van Genderen, J. A. Vekemans and E. W. Meijer, *Chemistry*, 2011, **17**, 5193–5203.
- 226 I. de Feijter, P. Besenius, L. Albertazzi, E. W. Meijer, A. R. A. Palmans and I. K. Voets, *Soft Matter*, 2013, **9**, 10025–10030.
- 227 H. Frisch, J. P. Unsleber, D. Lüdeker, M. Peterlechner, G. Brunklaus, M. Waller and P. Besenius, *Angew. Chem., Int. Ed.*, 2013, **52**, 10097–10101.
- 228 H. Frisch, Y. Nie, S. Raunser and P. Besenius, *Chem. – Eur. J.*, 2015, **21**, 3304–3309.
- 229 P. Ahlers, K. Fischer, D. Spitzer and P. Besenius, *Macromolecules*, 2017, **50**, 7712–7720.
- 230 M. von Gröning, I. de Feijter, M. C. A. Stuart, I. K. Voets and P. Besenius, *J. Mater. Chem. B*, 2013, **1**, 2008–2012.
- 231 R. Appel, J. Fuchs, S. M. Tyrrell, P. A. Korevaar, M. C. Stuart, I. K. Voets, M. Schonhoff and P. Besenius, *Chemistry*, 2015, **21**, 19257–19264.
- 232 R. Appel, S. Tacke, J. Klingauf and P. Besenius, *Org. Biomol. Chem.*, 2015, **13**, 1030–1039.
- 233 P. Ahlers, H. Frisch, D. Spitzer, Z. Vobecka, F. Vilela and P. Besenius, *Chem. – Asian J.*, 2014, **9**, 2052–2057.
- 234 B. Kemper, L. Zengerling, D. Spitzer, R. Otter, T. Bauer and P. Besenius, *J. Am. Chem. Soc.*, 2018, **140**, 534–537.
- 235 S. Chakraborty, C. M. Berac, B. Kemper, P. Besenius and T. Speck, *Macromolecules*, 2019, **52**, 7661–7667.
- 236 P. Ahlers, H. Frisch, R. Holm, D. Spitzer, M. Barz and P. Besenius, *Macromol. Biosci.*, 2017, **17**, 1700111.
- 237 D. Straßburger, N. Stergiou, M. Urschbach, H. Yurugi, D. Spitzer, D. Schollmeyer, E. Schmitt and P. Besenius, *ChemBioChem*, 2018, **19**, 912–916.
- 238 D. Spitzer, L. L. Rodrigues, D. Straßburger, M. Mezger and P. Besenius, *Angew. Chem., Int. Ed.*, 2017, **56**, 15461–15465.
- 239 H. Frisch, E.-C. Fritz, F. Stricker, L. Schmüser, D. Spitzer, T. Weidner, B. J. Ravoo and P. Besenius, *Angew. Chem., Int. Ed.*, 2016, **55**, 7242–7246.
- 240 S. Engel, D. Spitzer, L. L. Rodrigues, E.-C. Fritz, D. Straßburger, M. Schönhoff, B. J. Ravoo and P. Besenius, *Faraday Discuss.*, 2017, **204**, 53–67.
- 241 O. Zagorodko, V. J. Nebot and M. J. Vicent, *Polym. Chem.*, 2020, **11**, 1220–1229.
- 242 G. Fichman and E. Gazit, *Acta Biomater.*, 2014, **10**, 1671–1682.
- 243 D. J. Adams, *Macromol. Biosci.*, 2011, **11**, 160–173.
- 244 C. Tomasini and N. Castellucci, *Chem. Soc. Rev.*, 2013, **42**, 156–172.

- 245 M. Zhou, A. M. Smith, A. K. Das, N. W. Hodson, R. F. Collins, R. V. Ulijn and J. E. Gough, *Biomaterials*, 2009, **30**, 2523–2530.
- 246 R. Orbach, L. Adler-Abramovich, S. Zigerson, I. Mironi-Harpaz, D. Seliktar and E. Gazit, *Biomacromolecules*, 2009, **10**, 2646–2651.
- 247 C. Ou, J. Zhang, X. Zhang, Z. Yang and M. Chen, *Chem. Commun.*, 2013, **49**, 1853–1855.
- 248 Z. Yang, G. Liang, M. Ma, Y. Gao and B. Xu, *J. Mater. Chem.*, 2007, **17**, 850–854.
- 249 L. Chen, K. Morris, A. Laybourn, D. Elias, M. R. Hicks, A. Rodger, L. Serpell and D. J. Adams, *Langmuir*, 2010, **26**, 5232–5242.
- 250 Y. Zhang, Z. Yang, F. Yuan, H. Gu, P. Gao and B. Xu, *J. Am. Chem. Soc.*, 2004, **126**, 15028–15029.
- 251 S. Sutton, N. L. Campbell, A. I. Cooper, M. Kirkland, W. J. Frith and D. J. Adams, *Langmuir*, 2009, **25**, 10285–10291.
- 252 S. Roy and A. Banerjee, *Soft Matter*, 2011, **7**, 5300–5308.
- 253 J. Nanda, A. Biswas, B. Adhikari and A. Banerjee, *Angew. Chem., Int. Ed.*, 2013, **52**, 5041–5045.
- 254 J. Nanda, A. Biswas and A. Banerjee, *Soft Matter*, 2013, **9**, 4198–4208.
- 255 H. Cui, M. J. Webber and S. I. Stupp, *Pept. Sci.*, 2010, **94**, 1–18.
- 256 J. D. Hartgerink, E. Beniash and S. I. Stupp, *Science*, 2001, **294**, 1684–1688.
- 257 T. J. Moyer, H. A. Kassam, E. S. M. Bahnson, C. E. Morgan, F. Tantakitti, T. L. Chew, M. R. Kibbe and S. I. Stupp, *Small*, 2015, **11**, 2750–2755.
- 258 K. Sato, M. P. Hendricks, L. C. Palmer and S. I. Stupp, *Chem. Soc. Rev.*, 2018, **47**, 7539–7551.
- 259 S. E. Paramonov, H. W. Jun and J. D. Hartgerink, *J. Am. Chem. Soc.*, 2006, **128**, 7291–7298.
- 260 H. Jiang, M. O. Guler and S. I. Stupp, *Soft Matter*, 2007, **3**, 454–462.
- 261 J. D. Hartgerink, E. Beniash and S. I. Stupp, *Proc. Natl. Acad. Sci. U. S. A.*, 2002, **99**, 5133–5138.
- 262 A. Dehsorkhi, V. Castelletto and I. W. Hamley, *J. Pept. Sci.*, 2014, **20**, 453–467.
- 263 G. W. M. Vandermeulen and H.-A. Klok, *Macromol. Biosci.*, 2004, **4**, 383–398.
- 264 I. W. Hamley, *Angew. Chem., Int. Ed.*, 2007, **46**, 8128–8147.
- 265 H. G. Börner and H. Schlaad, *Soft Matter*, 2007, **3**, 394–408.
- 266 R. Otter and P. Besenius, *Org. Biomol. Chem.*, 2019, **17**, 6719–6734.
- 267 P. Thiyagarajan, T. S. Burkoth, V. Urban, S. Seifert, T. L. S. Benzinger, D. M. Morgan, D. Gordon, S. C. Meredith and D. G. Lynn, *J. Appl. Crystallogr.*, 2000, **33**, 535–539.
- 268 T. S. Burkoth, T. L. S. Benzinger, V. Urban, D. G. Lynn, S. C. Meredith and P. Thiyagarajan, *J. Am. Chem. Soc.*, 1999, **121**, 7429–7430.
- 269 T. S. Burkoth, T. L. S. Benzinger, D. N. M. Jones, K. Hallenga, S. C. Meredith and D. G. Lynn, *J. Am. Chem. Soc.*, 1998, **120**, 7655–7656.
- 270 J. H. Collier and P. B. Messersmith, *Adv. Mater.*, 2004, **16**, 907–910.
- 271 J. Hentschel, M. G. J. ten Cate and H. G. Börner, *Macromolecules*, 2007, **40**, 9224–9232.
- 272 J. Hentschel, E. Krause and H. G. Börner, *J. Am. Chem. Soc.*, 2006, **128**, 7722–7723.
- 273 D. Eckhardt, M. Groenewolt, E. Krause and H. G. Börner, *Chem. Commun.*, 2005, 2814–2816, DOI: 10.1039/B503275J.
- 274 S. Wiczorek, A. Dallmann, Z. Kochovski and H. G. Börner, *J. Am. Chem. Soc.*, 2016, **138**, 9349–9352.
- 275 I. W. Hamley, I. A. Ansari, V. Castelletto, H. Nuhn, A. Rösler and H. A. Klok, *Biomacromolecules*, 2005, **6**, 1310–1315.
- 276 V. Castelletto and I. W. Hamley, *Biophys. Chem.*, 2009, **141**, 169–174.
- 277 V. Castelletto, G. E. Newby, Z. Zhu, I. W. Hamley and L. Noirez, *Langmuir*, 2010, **26**, 9986–9996.
- 278 I. W. Hamley, G. Cheng and V. Castelletto, *Macromol. Biosci.*, 2011, **11**, 1068–1078.
- 279 V. Castelletto, G. Cheng, S. Fuzzeland, D. Atkins and I. W. Hamley, *Soft Matter*, 2012, **8**, 5434–5438.
- 280 V. Castelletto, R. J. Gouveia, C. J. Connon and I. W. Hamley, *Eur. Polym. J.*, 2013, **49**, 2961–2967.
- 281 D. Zanuy, I. W. Hamley and C. Alemán, *J. Phys. Chem. B*, 2011, **115**, 8937–8946.
- 282 S. Kirkham, V. Castelletto, I. W. Hamley, M. Reza, J. Ruokolainen, D. Hermida-Merino, P. Bilalis and H. Iatrou, *Biomacromolecules*, 2016, **17**, 1186–1197.
- 283 R. Otter, K. Klinker, D. Spitzer, M. Schinnerer, M. Barz and P. Besenius, *Chem. Commun.*, 2018, **54**, 401–404.
- 284 R. Otter, N. A. Henke, C. Berac, T. Bauer, M. Barz, S. Seiffert and P. Besenius, *Macromol. Rapid Commun.*, 2018, **39**, 1800459.
- 285 R. Otter, C. M. Berac, S. Seiffert and P. Besenius, *Eur. Polym. J.*, 2019, **110**, 90–96.
- 286 D. T. Bong, T. D. Clark, J. R. Granja and R. M. Ghadiri, *Angew. Chem., Int. Ed.*, 2001, **40**, 988–1011.
- 287 I. W. Hamley, *Angew. Chem., Int. Ed.*, 2014, **53**, 6866–6881.
- 288 P. de Santis, S. Morosetti and R. Rizzo, *Macromolecules*, 1974, **7**, 52–58.
- 289 R. M. Ghadiri, J. R. Granja, R. A. Milligan, D. E. McRee and N. Khazanovich, *Nature*, 1993, **366**, 324–327.
- 290 R. Chapman, M. Danial, M. L. Koh, K. A. Jolliffe and S. Perrier, *Chem. Soc. Rev.*, 2012, **41**, 6023–6041.
- 291 R. J. Brea, C. Reiriz and J. R. Granja, *Chem. Soc. Rev.*, 2010, **39**, 1448–1456.
- 292 N. Rodríguez-Vázquez, M. Amorín and J. R. Granja, *Org. Biomol. Chem.*, 2017, **15**, 4490–4505.
- 293 S. Fernandez-Lopez, H.-S. Kim, E. C. Choi, M. Delgado, J. R. Granja, A. Khasanov, K. Kraehenbuehl, G. Long, D. A. Weinberger, K. M. Wilcoxon and M. R. Ghadiri, *Nature*, 2001, **412**, 452–455.
- 294 W. S. Horne, C. M. Wiethoff, C. Cui, K. M. Wilcoxon, M. Amorin, M. R. Ghadiri and G. R. Nemerow, *Bioorg. Med. Chem.*, 2005, **13**, 5145–5153.
- 295 N. Ashkenasy, W. S. Horne and M. R. Ghadiri, *Small*, 2006, **2**, 99–102.
- 296 R. J. Brea, L. Castedo, J. R. Granja, M. Á. Herranz, L. Sánchez, N. Martín, W. Seitz and D. M. Guldi, *Proc. Natl. Acad. Sci. U. S. A.*, 2007, **104**, 5291–5294.
- 297 C. Reiriz, R. J. Brea, R. Arranz, J. L. Carrascosa, A. Garibotti, B. Manning, J. M. Valpuesta, R. Eritja, L. Castedo and J. R. Granja, *J. Am. Chem. Soc.*, 2009, **131**, 11335–11337.
- 298 K. Motesharei and M. R. Ghadiri, *J. Am. Chem. Soc.*, 1997, **119**, 11306–11312.
- 299 N. Rodríguez-Vázquez, M. Amorín, I. Alfonso and J. R. Granja, *Angew. Chem., Int. Ed.*, 2016, **55**, 4504–4508.
- 300 H. Shaikh, J. Y. Rho, L. J. Macdougall, P. Gurnani, A. M. Lunn, J. Yang, S. Huband, E. D. H. Mansfield, R. Peltier and S. Perrier, *Chem. – Eur. J.*, 2018, **24**, 19066–19074.
- 301 J. R. Granja and M. R. Ghadiri, *J. Am. Chem. Soc.*, 1994, **116**, 10785–10786.
- 302 R. M. Ghadiri, J. R. Granja and L. K. Buehler, *Nature*, 1994, **369**, 301–304.
- 303 R. García-Fandiño, M. Amorín, L. Castedo and J. R. Granja, *Chem. Sci.*, 2012, **3**, 3280–3285.
- 304 J. Montenegro, R. M. Ghadiri and J. R. Granja, *Acc. Chem. Res.*, 2013, **46**, 2955–2965.
- 305 J. Couet, J. D. J. S. Samuel, A. Kopyshv, S. Santer and M. Biesalski, *Angew. Chem., Int. Ed.*, 2005, **44**, 3297–3301.
- 306 J. Couet and M. Biesalski, *Macromolecules*, 2006, **39**, 7258–7268.
- 307 M. G. J. ten Cate, N. Severin and H. G. Börner, *Macromolecules*, 2006, **39**, 7831–7838.
- 308 J. Couet and M. Biesalski, *Small*, 2008, **4**, 1008–1016.
- 309 S. Loschonsky, J. Couet and M. Biesalski, *Macromol. Rapid Commun.*, 2008, **29**, 309–315.
- 310 S. C. Larnaudie, J. C. Brendel, K. A. Jolliffe and S. Perrier, *J. Polym. Sci., Part A: Polym. Chem.*, 2016, **54**, 1003–1011.
- 311 R. M. Ghadiri, K. Kobayashi, J. R. Granja, R. K. Chadha and D. E. McRee, *Angew. Chem., Int. Ed. Engl.*, 1995, **34**, 93–95.
- 312 R. Chapman, K. A. Jolliffe and S. Perrier, *Aust. J. Chem.*, 2010, **63**, 1169–1172.
- 313 R. Chapman, K. A. Jolliffe and S. Perrier, *Polym. Chem.*, 2011, **2**, 1956–1963.
- 314 R. Chapman, P. J. M. Bouten, R. Hoogenboom, K. A. Jolliffe and S. Perrier, *Chem. Commun.*, 2013, **49**, 6522–6524.
- 315 R. Chapman, K. A. Jolliffe and S. Perrier, *Adv. Mater.*, 2013, **25**, 1170–1172.
- 316 R. Chapman, M. L. Koh, G. G. Warr, K. A. Jolliffe and S. Perrier, *Chem. Sci.*, 2013, **4**, 2581–2589.
- 317 R. Chapman, G. G. Warr, S. Perrier and K. A. Jolliffe, *Chem. – Eur. J.*, 2013, **19**, 1955–1961.
- 318 M. Danial, C. My-Nhi Tran, P. G. Young, S. Perrier and K. A. Jolliffe, *Nat. Commun.*, 2013, **4**, 2780.
- 319 M. Danial, C. M. N. Tran, K. A. Jolliffe and S. Perrier, *J. Am. Chem. Soc.*, 2014, **136**, 8018–8026.
- 320 B. M. Blunden, R. Chapman, M. Danial, H. Lu, K. A. Jolliffe, S. Perrier and M. H. Stenzel, *Chemistry*, 2014, **20**, 12745–12749.

- 321 M. L. Koh, K. A. Jolliffe and S. Perrier, *Biomacromolecules*, 2014, **15**, 4002–4011.
- 322 M. L. Koh, P. A. FitzGerald, G. G. Warr, K. A. Jolliffe and S. Perrier, *Chem. – Eur. J.*, 2016, **22**, 18419–18428.
- 323 S. Catrouillet, J. C. Brendel, S. Larnaudie, T. Barlow, K. A. Jolliffe and S. Perrier, *ACS Macro Lett.*, 2016, **5**, 1119–1123.
- 324 S. C. Larnaudie, J. C. Brendel, K. A. Jolliffe and S. Perrier, *ACS Macro Lett.*, 2017, **6**, 1347–1351.
- 325 J. Y. Rho, J. C. Brendel, L. R. MacFarlane, E. D. H. Mansfield, R. Peltier, S. Rogers, M. Hartlieb and S. Perrier, *Adv. Funct. Mater.*, 2017, **28**, 1704569.
- 326 J. G. Binfield, J. C. Brendel, N. R. Cameron, A. M. Eissa and S. Perrier, *Macromol. Rapid Commun.*, 2018, **39**, 1700831.
- 327 S. C. Larnaudie, J. Sanchis, T.-H. Nguyen, R. Peltier, S. Catrouillet, J. C. Brendel, C. J. H. Porter, K. A. Jolliffe and S. Perrier, *Biomaterials*, 2018, **178**, 570–582.
- 328 S. C. Larnaudie, J. C. Brendel, I. Romero-Canelón, C. Sanchez-Cano, S. Catrouillet, J. Sanchis, J. P. C. Coverdale, J.-I. Song, A. Habtemariam, P. J. Sadler, K. A. Jolliffe and S. Perrier, *Biomacromolecules*, 2018, **19**, 239–247.
- 329 J. C. Brendel, J. Sanchis, S. Catrouillet, E. Czuba, M. Z. Chen, B. M. Long, C. Nowell, A. Johnston, K. A. Jolliffe and S. Perrier, *Angew. Chem., Int. Ed.*, 2018, **57**, 16678–16682.
- 330 J. C. Brendel, S. Catrouillet, J. Sanchis, K. A. Jolliffe and S. Perrier, *Polym. Chem.*, 2019, **10**, 2616–2625.
- 331 M. Hartlieb, S. Catrouillet, A. Kuroki, C. Sanchez-Cano, R. Peltier and S. Perrier, *Chem. Sci.*, 2019, **10**, 5476–5483.
- 332 Q. Song, J. Yang, J. Y. Rho and S. Perrier, *Chem. Commun.*, 2019, **55**, 5291–5294.
- 333 Q. Song, J. Yang, S. C. L. Hall, P. Gurnani and S. Perrier, *ACS Macro Lett.*, 2019, **8**, 1347–1352.
- 334 J. Y. Rho, H. Cox, E. D. H. Mansfield, S. H. Ellacott, R. Peltier, J. C. Brendel, M. Hartlieb, T. A. Waigh and S. Perrier, *Nat. Commun.*, 2019, **10**, 4708.
- 335 R. Chapman, G. G. Warr, S. Perrier and K. A. Jolliffe, *Chem. – Eur. J.*, 2013, **19**, 1955–1961.
- 336 E. D. H. Mansfield, M. Hartlieb, S. Catrouillet, J. Y. Rho, S. C. Larnaudie, S. E. Rogers, J. Sanchis, J. C. Brendel and S. Perrier, *Soft Matter*, 2018, **14**, 6320–6326.
- 337 S. Venkataraman, J. L. Hedrick, Z. Y. Ong, C. Yang, P. L. R. Ee, P. T. Hammond and Y. Y. Yang, *Adv. Drug Delivery Rev.*, 2011, **63**, 1228–1246.
- 338 N. P. Truong, A. K. Whittaker, C. W. Mak and T. P. Davis, *Expert Opin. Drug Delivery*, 2015, **12**, 129–142.
- 339 J. Jadzyn, M. Stockhausen and B. Zywucki, *J. Phys. Chem.*, 1987, **91**, 754–757.
- 340 J. van Esch, R. M. Kellogg and B. L. Feringa, *Tetrahedron Lett.*, 1997, **38**, 281–284.
- 341 M. George, G. Tan, V. T. John and R. G. Weiss, *Chem. – Eur. J.*, 2005, **11**, 3243–3254.
- 342 B. Isare, S. Pensec, M. Raynal and L. Bouteiller, *C. R. Chim.*, 2016, **19**, 148–156.
- 343 V. Simic, L. Bouteiller and M. Jalabert, *J. Am. Chem. Soc.*, 2003, **125**, 13148–13154.
- 344 A. J. Carr, R. Melendez, S. J. Geib and A. D. Hamilton, *Tetrahedron Lett.*, 1998, **39**, 7447–7450.
- 345 J. H. van Esch, F. Schoonbeek, M. de Loos, H. Kooijman, A. L. Spek, R. M. Kellogg and B. L. Feringa, *Chem. – Eur. J.*, 1999, **5**, 937–950.
- 346 F. Lortie, S. Boileau, L. Bouteiller, C. Chassenieux, B. Demé, G. Ducouret, M. Jalabert, F. Lauprêtre and P. Terech, *Langmuir*, 2002, **18**, 7218–7222.
- 347 T. Pinault, B. Isare and L. Bouteiller, *ChemPhysChem*, 2006, **7**, 816–819.
- 348 L. Bouteiller, *Adv. Polym. Sci.*, 2007, **207**, 79–112.
- 349 F. Ouhib, M. Raynal, B. Jouvet, B. Isare and L. Bouteiller, *Chem. Commun.*, 2011, **47**, 10683–10685.
- 350 L. Bouteiller, O. Colombani, F. Lortie and P. Terech, *J. Am. Chem. Soc.*, 2005, **127**, 8893–8898.
- 351 A. Pal, P. Besenius and R. P. Sijbesma, *J. Am. Chem. Soc.*, 2011, **133**, 12987–12989.
- 352 J. H. van Esch and B. L. Feringa, *Angew. Chem., Int. Ed.*, 2000, **39**, 2263–2266.
- 353 M. Yamanaka, *J. Inclusion Phenom. Macrocyclic Chem.*, 2013, **77**, 33–48.
- 354 X. Du, J. Zhou, J. Shi and B. Xu, *Chem. Rev.*, 2015, **115**, 13165–13307.
- 355 B. O. Okesola and D. K. Smith, *Chem. Soc. Rev.*, 2016, **45**, 4226–4251.
- 356 S. Pensec, N. Nouvel, A. Guilleman, C. Creton, F. Boué and L. Bouteiller, *Macromolecules*, 2010, **43**, 2529–2534.
- 357 S. Catrouillet, C. Fonteneau, L. Bouteiller, N. Delorme, E. Nicol, T. Nicolai, S. Pensec and O. Colombani, *Macromolecules*, 2013, **46**, 7911–7919.
- 358 S. Catrouillet, L. Bouteiller, E. Nicol, T. Nicolai, S. Pensec, B. Jacqueline, M. Le Bohec and O. Colombani, *Macromolecules*, 2015, **48**, 1364–1370.
- 359 C. Fonteneau, S. Pensec and L. Bouteiller, *Polym. Chem.*, 2014, **5**, 2496–2505.
- 360 S. Catrouillet, L. Bouteiller, O. Boyron, C. Lorthioir, E. Nicol, S. Pensec and O. Colombani, *Langmuir*, 2016, **32**, 8900–8908.
- 361 S. Han, G. Mellot, S. Pensec, J. Rieger, F. Stoffelbach, E. Nicol, O. Colombani, J. Jestin and L. Bouteiller, *Macromolecules*, 2020, **53**, 427–433.
- 362 E. Obert, M. Bellot, L. Bouteiller, F. Andrioletti, C. Lehen-Ferrenbach and F. Boué, *J. Am. Chem. Soc.*, 2007, **129**, 15601–15605.
- 363 S. Han, E. Nicol, F. Niepceron, O. Colombani, S. Pensec and L. Bouteiller, *Macromol. Rapid Commun.*, 2019, **40**, 1800698.
- 364 M. Fernandez-Castano Romera, R. P. M. Lafleur, C. Guibert, I. K. Voets, C. Storm and R. P. Sijbesma, *Angew. Chem., Int. Ed.*, 2017, **56**, 8771–8775.
- 365 A. Pal, S. Karthikeyan and R. P. Sijbesma, *J. Am. Chem. Soc.*, 2010, **132**, 7842–7843.
- 366 G. Mellot, J. M. Guigner, J. Jestin, L. Bouteiller, F. Stoffelbach and J. Rieger, *Macromolecules*, 2018, **51**, 10214–10222.
- 367 G. Mellot, J. M. Guigner, L. Bouteiller, F. Stoffelbach and J. Rieger, *Angew. Chem., Int. Ed.*, 2019, **58**, 3173–3177.
- 368 N. Chebotareva, P. H. H. Bomans, P. M. Frederik, N. A. J. M. Sommerdijk and R. P. Sijbesma, *Chem. Commun.*, 2005, 4967–4969, DOI: 10.1039/B507171B.
- 369 M. M. E. Koenigs, A. Pal, H. Mortazavi, G. M. Pawar, C. Storm and R. P. Sijbesma, *Macromolecules*, 2014, **47**, 2712–2717.
- 370 S. H. M. Söntjens, R. P. Sijbesma, M. H. P. van Genderen and E. W. Meijer, *J. Am. Chem. Soc.*, 2000, **122**, 7487–7493.
- 371 L. Brunsveld, B. J. B. Folmer, E. W. Meijer and R. P. Sijbesma, *Chem. Rev.*, 2001, **101**, 4071–4098.
- 372 Z.-T. Li and L.-Z. Wu, *Hydrogen Bonded Supramolecular Structures*, Springer, Heidelberg, 2015.
- 373 F. H. Beijer, H. Kooijman, A. L. Spek, R. P. Sijbesma and E. W. Meijer, *Angew. Chem., Int. Ed.*, 1998, **37**, 75–78.
- 374 F. H. Beijer, R. P. Sijbesma, H. Kooijman, A. L. Spek and E. W. Meijer, *J. Am. Chem. Soc.*, 1998, **120**, 6761–6769.
- 375 R. P. Sijbesma, F. H. Beijer, L. Brunsveld, B. J. B. Folmer, J. H. K. K. Hirschberg, R. F. M. Lange, J. K. L. Lowe and E. W. Meijer, *Science*, 1997, **278**, 1601–1604.
- 376 B. J. B. Folmer, R. P. Sijbesma, R. M. Versteegen, J. A. J. van der Rijt and E. W. Meijer, *Adv. Mater.*, 2000, **12**, 874–878.
- 377 B. J. B. Folmer and E. Cavini, *Chem. Commun.*, 1998, 1847–1848, DOI: 10.1039/A804797I.
- 378 J. H. K. K. Hirschberg, R. A. Koevoets, R. P. Sijbesma and E. W. Meijer, *Chem. – Eur. J.*, 2003, **9**, 4222–4231.
- 379 H. M. Keizer, R. P. Sijbesma and E. W. Meijer, *Eur. J. Org. Chem.*, 2004, 2553–2555.
- 380 M. Hutin, E. Burakowska-Meise, W. P. J. Appel, P. Y. W. Dankers and E. W. Meijer, *Macromolecules*, 2013, **46**, 8528–8537.
- 381 P. Y. W. Dankers, T. M. Hermans, T. W. Baughman, Y. Kamikawa, R. E. Kiełtyka, M. M. C. Bastings, H. M. Janssen, N. A. J. M. Sommerdijk, A. Larsen, M. J. A. van Luyn, A. W. Bosman, E. R. Popa, G. Fytas and E. W. Meijer, *Adv. Mater.*, 2012, **24**, 2703–2709.
- 382 N. E. Botterhuis, D. J. M. van Beek, G. M. L. van Gemert, A. W. Bosman and R. P. Sijbesma, *J. Polym. Sci., Part A: Polym. Chem.*, 2008, **46**, 3877–3885.
- 383 W. P. J. Appel, G. Portale, E. Wisse, P. Y. W. Dankers and E. W. Meijer, *Macromolecules*, 2011, **44**, 6776–6784.
- 384 H. Kautz, D. J. M. van Beek, R. P. Sijbesma and E. W. Meijer, *Macromolecules*, 2006, **39**, 4265–4267.
- 385 S. I. S. Hendrikse, S. P. W. Wijnands, R. P. M. Lafleur, M. J. Pouderoijen, H. M. Janssen, P. Y. W. Dankers and E. W. Meijer, *Chem. Commun.*, 2017, **53**, 2279–2282.
- 386 M. H. Bakker, R. E. Kiełtyka, L. Albertazzi and P. Y. W. Dankers, *RSC Adv.*, 2016, **6**, 110600–110603.
- 387 A. J. P. Teunissen, M. M. L. Nieuwenhuizen, F. Rodríguez-Llansola, A. R. A. Palmans and E. W. Meijer, *Macromolecules*, 2014, **47**, 8429–8436.

- 388 R. E. KIELTYKA, A. C. H. PAPE, L. ALBERTAZZI, Y. NAKANO, M. M. C. BASTINGS, I. K. VOETS, P. Y. W. DANKERS and E. W. MEIJER, *J. Am. Chem. Soc.*, 2013, **135**, 11159–11164.
- 389 R. E. KIELTYKA, M. M. C. BASTINGS, G. C. VAN ALMEN, P. BESENIUS, E. W. L. KEMPS and P. Y. W. DANKERS, *Chem. Commun.*, 2012, **48**, 1452–1454.
- 390 M. M. C. BASTINGS, S. KOUDESTAAL, R. E. KIELTYKA, Y. NAKANO, A. C. H. PAPE, D. A. M. FEYEN, F. J. VAN SLOCHTEREN, P. A. DOEVENDANS, J. P. G. SLUIJTER, E. W. MEIJER, S. A. J. CHAMULEAU and P. Y. W. DANKERS, *Adv. Healthcare Mater.*, 2014, **3**, 70–78.
- 391 R. IAN STORER, C. ACIRO and L. H. JONES, *Chem. Soc. Rev.*, 2011, **40**, 2330–2346.
- 392 N. BUSSCHAERT, I. L. KIRBY, S. YOUNG, S. J. COLES, P. N. HORTON, M. E. LIGHT and P. A. GALE, *Angew. Chem., Int. Ed.*, 2012, **51**, 4426–4430.
- 393 J. P. MALERICH, K. HAGIHARA and V. H. RAWAL, *J. Am. Chem. Soc.*, 2008, **130**, 14416–14417.
- 394 J. ALEMÁN, A. PARRA, H. JIANG and K. A. JØRGENSEN, *Chem. – Eur. J.*, 2011, **17**, 6890–6899.
- 395 F. R. WURM and H.-A. KLOK, *Chem. Soc. Rev.*, 2013, **42**, 8220–8236.
- 396 F. OLMO, C. ROTGER, I. RAMÍREZ-MACÍAS, L. MARTÍNEZ, C. MARÍN, L. CARRERAS, K. URBANOVÁ, M. VEGA, G. CHAVES-LEMAUR, A. SAMPEDEO, M. J. ROSALES, M. SÁNCHEZ-MORENO and A. COSTA, *J. Med. Chem.*, 2014, **57**, 987–999.
- 397 J. SCHILLER, J. V. ALEGRE-REQUENA, E. MARQUÉS-LÓPEZ, R. P. HERRERA, J. CASANOVAS, C. ALEMÁN and D. DÍAZ DÍAZ, *Soft Matter*, 2016, **12**, 4361–4374.
- 398 C. LÓPEZ, M. XIMENIS, F. ORVAY, C. ROTGER and A. COSTA, *Chem. – Eur. J.*, 2017, **23**, 7590–7594.
- 399 C. TONG, T. LIU, V. SAEZ TALENS, W. E. M. NOTEBORN, T. H. SHARP, M. M. R. M. HENDRIX, I. K. VOETS, C. L. MUMMERY, V. V. ORLOVA and R. E. KIELTYKA, *Biomacromolecules*, 2018, **19**, 1091–1099.
- 400 V. SAEZ TALENS, P. ENGLEBIENNE, T. T. TRINH, W. E. M. NOTEBORN, I. K. VOETS and R. E. KIELTYKA, *Angew. Chem., Int. Ed.*, 2015, **54**, 10502–10506.
- 401 V. SAEZ TALENS, D. M. M. MAKURAT, T. LIU, W. DAI, C. GUIBERT, W. E. M. NOTEBORN, I. K. VOETS and R. E. KIELTYKA, *Polym. Chem.*, 2019, **10**, 3146–3153.
- 402 W. E. M. NOTEBORN, V. SAEZ TALENS and R. E. KIELTYKA, *ChemBioChem*, 2017, **18**, 1995–1999.
- 403 V. SAEZ TALENS, G. ARIAS-ALPÍZAR, D. M. M. MAKURAT, J. DAVIS, J. BUSSMANN, A. KROS and R. E. KIELTYKA, *Biomacromolecules*, 2020, **21**, 1060–1068.
- 404 J.-M. LEHN, *Polym. Int.*, 2002, **51**, 825–839.
- 405 S. HECHT, *Angew. Chem., Int. Ed.*, 2003, **42**, 24–26.
- 406 A. BIRAUULT, E. MOLINA, P. TRENS, D. COT, G. TOQUER, N. MARCOTTE, C. CARCEL, J. R. BARTLETT, C. GÉRARDIN and M. WONG CHI MAN, *Eur. J. Inorg. Chem.*, 2019, 3157–3164.
- 407 S. P. W. WIJNANDS, E. W. MEIJER and M. MERKX, *Bioconjugate Chem.*, 2019, **30**, 1905–1914.
- 408 A. T. HAEDLER, K. KREGER, A. ISSAC, B. WITTMANN, M. KIVALA, N. HAMMER, J. KÖHLER, H.-W. SCHMIDT and R. HILDNER, *Nature*, 2015, **523**, 196–199.
- 409 S. M. CHIN, C. V. SYNATSCHKE, S. LIU, R. J. NAP, N. A. SATHER, Q. WANG, Z. ÁLVAREZ, A. N. EDELBROCK, T. FYRNER, L. C. PALMER, I. SZLEIFER, M. OLVERA DE LA CRUZ and S. I. STUPP, *Nat. Commun.*, 2018, **9**, 2395.
- 410 N. STERGIIOU, N. GAIDZIK, A.-S. HEIMES, S. DIETZEN, P. BESENIUS, J. JÄKEL, W. BRENNER, M. SCHMIDT, H. KUNZ and E. SCHMITT, *Cancer Immunol. Res.*, 2019, **7**, 113–122.
- 411 R. TOY, P. M. PEIRIS, K. B. GHAGHADA and E. KARATHANASIS, *Nano-medicine*, 2014, **9**, 121–134.
- 412 M. J. WEBBER and R. LANGER, *Chem. Soc. Rev.*, 2017, **46**, 6600–6620.
- 413 L. ALBERTAZZI, D. VAN DER ZWAAG, C. M. A. LEENDERS, R. FITZNER, M. OLVERA DE LA CRUZ and S. I. STUPP, *Nat. Commun.*, 2014, **5**, 491–495.
- 414 B. ADELIZZI, N. J. VAN ZEE, L. N. J. DE WINDT, A. R. A. PALMANS and E. W. MEIJER, *J. Am. Chem. Soc.*, 2019, **141**, 6110–6121.
- 415 W. ZHANG, W. JIN, T. FUKUSHIMA, A. SAEKI, S. SEKI and T. AIDA, *Science*, 2011, **334**, 340–343.
- 416 W. ZHANG, W. JIN, T. FUKUSHIMA, T. MORI and T. AIDA, *J. Am. Chem. Soc.*, 2015, **137**, 13792–13795.
- 417 L. H. BEUN, L. ALBERTAZZI, D. VAN DER ZWAAG, R. DE VRIES and M. A. COHEN STUART, *ACS Nano*, 2016, **10**, 4973–4980.
- 418 B. ADELIZZI, A. ALOI, N. J. VAN ZEE, A. R. A. PALMANS, E. W. MEIJER and I. K. VOETS, *ACS Nano*, 2018, **12**, 4431–4439.
- 419 B. ADELIZZI, A. ALOI, A. J. MARKVOORT, H. M. M. TEN EIKELDER, I. K. VOETS, A. R. A. PALMANS and E. W. MEIJER, *J. Am. Chem. Soc.*, 2018, **140**, 7168–7175.
- 420 S. OGI, K. SUGIYASU, S. MANNA, S. SAMITSU and M. TAKEUCHI, *Nat. Chem.*, 2014, **6**, 188.
- 421 S. OGI, V. STEPANENKO, J. THEIN and F. WÜRTHNER, *J. Am. Chem. Soc.*, 2016, **138**, 670–678.
- 422 W. WAGNER, M. WEHNER, V. STEPANENKO, S. OGI and F. WÜRTHNER, *Angew. Chem., Int. Ed.*, 2017, **56**, 16008–16012.
- 423 M. WEHNER and F. WÜRTHNER, *Nat. Rev. Chem.*, 2019, **4**, 38–53.
- 424 L. ALBERTAZZI, N. VAN DER VEEKEN, M. B. BAKER, A. R. PALMANS and E. W. MEIJER, *Chem. Commun.*, 2015, **51**, 16166–16168.
- 425 X. LOU, R. P. M. LAFLEUR, C. M. A. LEENDERS, S. M. C. SCHOENMAKERS, N. M. MATSUMOTO, M. B. BAKER, J. L. J. VAN DONGEN, A. R. A. PALMANS and E. W. MEIJER, *Nat. Commun.*, 2017, **8**, 15420.
- 426 S. M. C. SCHOENMAKERS, C. M. A. LEENDERS, R. P. M. LAFLEUR, X. LOU, E. W. MEIJER, G. M. PAVAN and A. R. A. PALMANS, *Chem. Commun.*, 2018, **54**, 11128–11131.
- 427 M. E. FOX, F. C. SZOKA and J. M. J. FRÉCHET, *Acc. Chem. Res.*, 2009, **42**, 1141–1151.

Publication P2

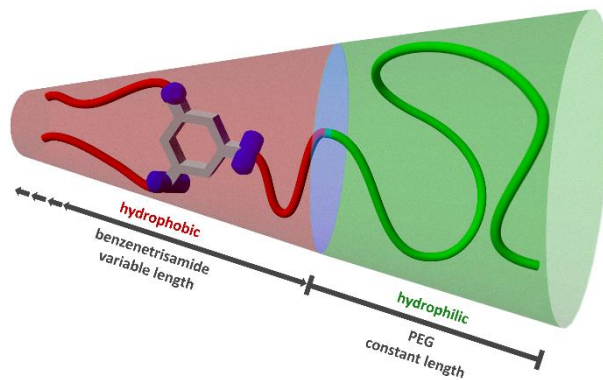
The influence of directed hydrogen bonds on the self-assembly of amphiphilic polymers in water

T. Klein[‡], F. V. Gruschwitz[‡], S. Rogers, S. Hoepfner, I. Nischang, J. C. Brendel, “”, *J. Colloid Interface Sci.* **2019**, *557*, 488-497.

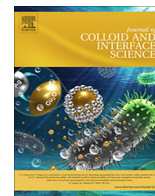
Reproduced by permission of Elsevier. Copyright © 2019.

The paper as well as the supporting information is available online:

doi.org/10.1016/j.jcis.2019.09.046



[‡] Equal contribution.



The influence of directed hydrogen bonds on the self-assembly of amphiphilic polymers in water

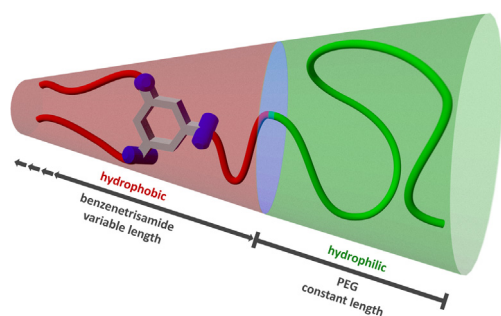
Tobias Klein^{a,b,1}, Franka V. Gruschwitz^{a,b,1}, Sarah Rogers^c, Stephanie Hoepfner^{a,b}, Ivo Nischang^{a,b}, Johannes C. Brendel^{a,b,*}

^aLaboratory of Organic and Macromolecular Chemistry (IOMC), Friedrich Schiller University Jena, Humboldtstraße 10, 07743 Jena, Germany

^bJena Center for Soft Matter (JCSM), Friedrich Schiller University Jena, Philosophenweg 7, 07743 Jena, Germany

^cISIS Neutron Facility, Rutherford Appleton Laboratory, Harwell Oxford, Didcot OX11 0QX, United Kingdom

GRAPHICAL ABSTRACT



ARTICLE INFO

Article history:

Received 14 June 2019

Revised 11 September 2019

Accepted 12 September 2019

Available online 13 September 2019

Keywords:

Supramolecular self-assembly

Block copolymers

Hydrogen bonds

Packing parameter

Amphiphilic materials

Benzenetrisamides

Analytical ultracentrifugation

ABSTRACT

Hypothesis: Molecules forming directed intermolecular hydrogen bonds, such as the well-known benzene-1,3,5-tricarboxamides (BTA) motif, are known to self-assemble into long fibrous structures. However, only a few of these systems have so far demonstrated the ability to form such anisotropic nanostructures, if they are combined with hydrophilic polymers to create an amphiphilic material. Here, we designed BTA-polymer conjugates to investigate whether the directionality of the hydrogen bonds or the ratio of hydrophobic to hydrophilic parts of the molecule, and thus the packing parameter, is decisive for obtaining anisotropic supramolecular structures in water.

Experiments: Poly(ethylene glycol) was conjugated to BTA moieties with varying lengths of hydrophobic alkyl spacers ranging from two to twelve methylene units. The resulting amphiphilic materials were characterized in aqueous solution by light and small-angle neutron scattering, analytical ultracentrifugation, and cryo-transmission electron microscopy.

Findings: While spherical micelles were observed for C₆ and C₁₀ alkyl spacers, anisotropic structures were only present in case of the C₁₂ spacer. The comparison to an analogous material, which lacks the directed hydrogen bonds, revealed that the BTA motif cannot provide a sufficient driving force to induce anisotropic structures, but increases the packing density in the hydrophobic part. Therefore, the packing parameter governs the appearance of anisotropic aggregates.

© 2019 Elsevier Inc. All rights reserved.

* Corresponding author at: Laboratory of Organic and Macromolecular Chemistry (IOMC), Friedrich Schiller University Jena, Humboldtstraße 10, 07743 Jena, Germany.

E-mail address: johannes.brendel@uni-jena.de (J.C. Brendel).

¹ The authors contributed equally to this work.

1. Introduction

Amphiphilic materials based on polymers have found widespread applications in several fields, such as biomedicine, nanolithography, and lubrication [1,2]. The self-assembly of amphiphiles in water is driven by the hydrophobic effect which minimizes the contact area between the hydrophobic domain and water [3]. This results in the formation of micellar morphologies, such as spheres, worms, worm-like micelles or vesicles, where the hydrophobic part is hidden inside of the structure and is surrounded by a corona formed by the hydrophilic part [4]. The morphologies of an amphiphile in aqueous solution can to some extent be predicted via the packing parameter, originally conceived by Israelachvili for small molecules [5]. It is defined as $p = V_c / (a_0 l_c)$ where V_c is the volume of the hydrophobic tail, a_0 the surface area of the hydrophilic head group of the aggregate and l_c the length of the hydrophobic chain [5,6]. In contrast to small molar mass amphiphiles, it is challenging to predict the surface area of the polar block in amphiphilic polymers and, as a consequence, the resulting morphology upon self-assembly in water [1]. This often results in a trial-and-error approach to control the self-assembly morphology by changing the type of polymers or the size of the individual parts. Moreover, mixtures of different morphologies are often observed for specific compositions [7–9].

An alternative approach to overcome this lack of control relies on the utilization of additional forces besides the hydrophobic effect. Well-known examples are the crystallization of the hydrophobic block [10–13] or the introduction of directing hydrogen bonds [14]. The latter was inspired by nature and often peptide sequences are used in this context as an illustrative example, as they enable the directed self-assembly of polymers via formation of β -sheets or α -helices [15]. Cyclic peptides represent a particularly interesting motif in this context. Made of an even number of alternating D- and L- α -amino acids, they adopt a flat ring conformation [16], and have been shown to assemble into cylindrical nanotubes through ring-stacking via hydrogen bonds, even if polymers are attached to the peptide rings [17–29]. Recently, it was reported that cyclic peptides incorporated at the block junction of an amphiphilic poly((polyethylene glycol) acrylate)-*b*-poly(*n*-butylacrylate) block copolymer can direct its self-assembly into tubular structures that were capable of perforating lysosomal membranes within cells [30]. The use of linear peptide sequences that form β -sheets and their impact on the self-assembly of peptide-polymer conjugates, consisting of a hydrophobic peptide segment and a hydrophilic polymer, has also been thoroughly studied [31–34]. In particular, the self-assembly of poly(ethylene glycol) (PEG) peptide block copolymers was investigated by Hamley and coworkers [35–43]. Castelletto et al. reported the self-assembly of a PEG in aqueous environment with a molar mass of 5000 g mol^{-1} , that was extended by four phenylalanine units, into straight fibrils [43]. In contrast to these peptide-based structures, we could only find one additional reported hydrogen motif suitable for directing the self-assembly of polymers. In this case, urea groups are introduced into the hydrophobic domain of the polymers to form cylindrical polymeric structures in water [44–51]. The limitation to this restricted number of motifs is somewhat surprising, considering the plethora of small molecules forming large aggregate structures by supramolecular interactions such as hydrogen bonds or π - π interactions [52–54].

To shed light on the general applicability of supramolecular motifs for the formation of anisotropic self-assembled polymer structures, we have chosen the well-known benzene-1,3,5-tricarboxamide (BTA) motif. BTAs are certainly among the most studied structures to form supramolecular polymers, however, so

far it has not been investigated whether this structure is also capable of directing the self-assembly of polymers. Low molar mass BTAs can self-assemble into fibers via a triple helix formation induced by the intermolecular hydrogen bonds [55,56]. Leenders et al. showed that BTAs can also self-assemble into fibers in water when equipped with hydrophilic tetraethylene glycol groups in the periphery and hydrophobic segments next to the core. Latter provide sufficient shielding of the hydrogen bonds in the core from penetrating water molecules [57,58]. Besides reported studies in which the BTA motif was used to drive the self-assembly of single-chain polymeric nanoparticles [59,60] or polypeptides [61,62], it has so far not been used to guide the self-assembly of amphiphilic polymer molecules into micelles.

Here, we modified PEG with a BTA-derived end group and studied its impact on the self-assembly in aqueous solution of the resulting PEG-amphiphile. We systematically varied the hydrophilic/hydrophobic block ratio of our polymeric compound by changing the length of the alkyl spacers around the BTA motif from two to twelve methylene groups, while keeping the length of the PEG constant. Afterwards, we performed a thorough solution characterization of the assemblies including cryoTEM, light and neutron scattering, and analytical ultracentrifugation in water. Our aim was to answer the question whether the hydrogen bonds of the BTA motif or the hydrophilic/hydrophobic block ratio are the main driving force to induce anisotropy of the formed polymer micelles.

2. Results and discussion

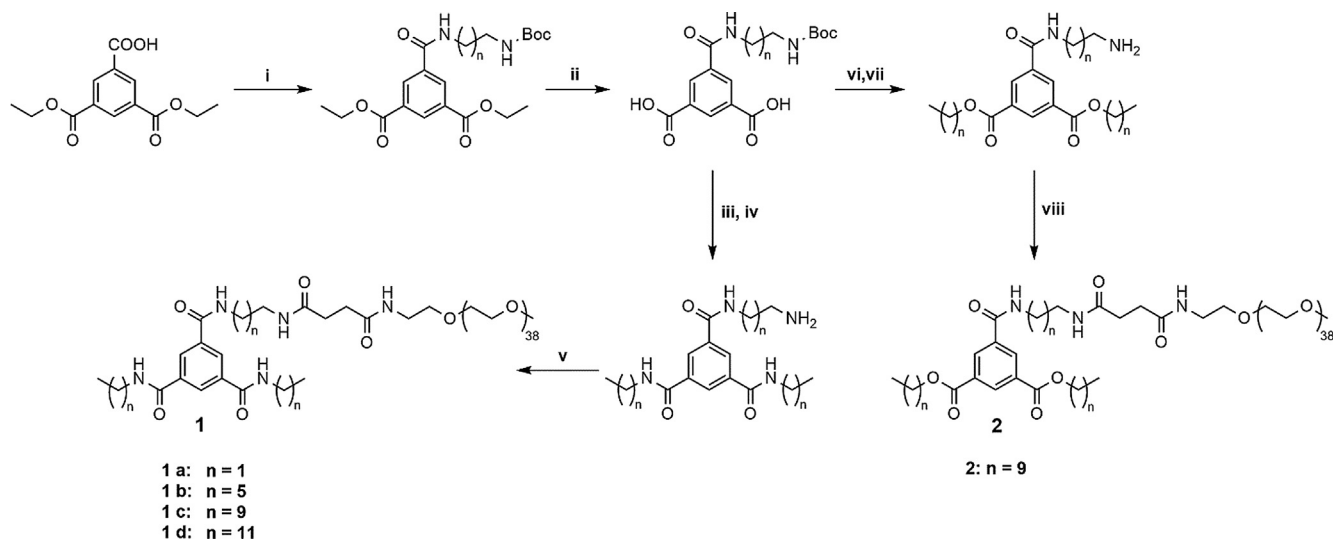
2.1. Synthesis of the supramolecular, amphiphilic polymers

Four BTA-modified PEG compounds (**1a–d**) were synthesized, in which only the length of the alkyl spacer next to the BTA motif was changed from two to twelve methylene groups in order to evaluate the impact of the hydrophilic/hydrophobic block ratio on the formed aggregate morphologies. Furthermore, a compound in which two amide groups were replaced with ester groups (**2**) was synthesized to study the influence of the number of hydrogen bonds on the self-assembly (Scheme 1; see SI for synthetic protocols and characterization of **1a–d** and **2** (Figures S1–2)) [63].

2.2. Self-assembly in water

2.2.1. Scattering experiments

Dynamic light scattering (DLS) was conducted to obtain a first indication of an aqueous solution self-assembly of the compounds. The formation of structures with a hydrodynamic diameter in the range of around 10–20 nm could be observed in the respective number-weighted distributions (Figure S3). The DLS correlograms show a shift to smaller diffusion coefficients (i.e., larger structures) with increasing length of the alkyl spacer. Furthermore, the addition of Nile red, a dye which is commonly used to determine the critical micelle concentration (CMC) of amphiphilic materials, resulted in a clear increase of the fluorescence intensity that is only observable if hydrophobic domains are present in the formed structures (see Figures S4–7 and Table S1 for further details) [64]. The corresponding CMC values for all compounds are summarized in Table S1 and, consequently, all characterization experiments were conducted at significantly higher concentrations to assure concentrations above the CMC. These first results already indicate that a minimum length of six CH_2 -groups in the spacer are necessary to induce the assembly of the polymers in water. However, since size estimations in standard DLS are based on the assumption of hydrodynamically equivalent spheres, the method



Scheme 1. Synthetic routes toward BTA compounds **1a–d** and BDEA compound **2**. (i) Semi-protected amine, DMAP, EDC, DCM, 25 °C, overnight; (ii) KOH in EtOH/H₂O 9:1, 80 °C, 30 min; (iii) Alkylamine, DMAP, EDC, DCM, 25 °C, overnight; (iv) TFA/TIPS/H₂O, DCM, 25 °C, 2 h; (v) Methoxy-PEG-NHS, TEA, DMF, 25 °C, overnight; (vi) Alkylamine, DMAP, EDC, DCM, 25 °C, overnight; (vii) TFA/TIPS/H₂O, DCM, 25 °C, 2 h; (viii) Methoxy-PEG-NHS, TEA, DMF, 25 °C, overnight.

is unsuitable for a straightforward identification of anisotropic morphologies.

Hence, we further used small-angle neutron-scattering (SANS) to elucidate the morphology of the compounds **1a–d** (Fig. 1) in solution.

The measured intensities in the low q region increase significantly from BTA-C₂ **1a** to BTA-C₆ **1b** and further to BTA-C₁₀ **1c**, which indicates a larger overall size of the scattering objects. The sample BTA-C₁₂ **1d** was measured at a higher concentration ($c = 10 \text{ mg mL}^{-1}$) and, therefore, a significantly higher intensity is observed in this case. For higher q -values, all samples exhibit a linear decay with slopes that scale with $q^{-5/3}$. In this q -region only features of smaller structures can be observed and the measured profile is typical for Gaussian coils, as they might be present in the corona of a polymeric micelle. The sample BTA-C₂ **1a** immediately approaches a plateau at lower q -values ($q < 0.1 \text{ \AA}^{-1}$), which is

representative for individually coiled polymer chains. All other samples show a steep increase of the scattering intensity at these lower q -values indicating the formation of larger assemblies, where the coil-like scattering behavior at high q -values ($>0.1 \text{ \AA}^{-1}$) reflects the presence of flexible chains in the corona. Closer to the Guinier regime ($q < 0.02 \text{ \AA}^{-1}$), the assembled samples display a similar scattering profile with a rollover between $q = 0.06 \text{ \AA}^{-1}$ and $q = 0.02 \text{ \AA}^{-1}$, but varying intensities in the final plateau. Such a profile is commonly observed for isotropic structures, e.g. spherical polymer micelles [66]. An initial Guinier plot (Figure S8) revealed an increasing radius of gyration (R_g) from BTA-C₆ **1b** to BTA-C₁₀ **1c**, while no further increase for BTA-C₁₂ **1d** is observed (details are given in the SI). In case of BTA-C₁₂ **1d**, even a slight decay of the scattering intensity is observed at very low q -values ($q < 0.01 \text{ \AA}^{-1}$), which is most likely related to a repulsive interaction of the assemblies, but a detailed analysis of this effect was beyond the scope of this study (a structure factor for a solid sphere was applied to fit the data, see SI for further details). In a first attempt to fit the data, a simple model for a solid sphere was chosen (Figure S9, details of the fit parameters are given in the SI), but in particular at higher q -values strong deviations from the scattering data were observed, which further indicates the presence of a polymer corona as in a spherical polymer micelle. From appropriate fits based on such a model, the radius for a solid core can be determined, which increases from BTA-C₆ **1b** ($R_{c,sphere} = 1.7 \text{ nm}$) to BTA-C₁₀ **1c** ($R_{c,sphere} = 3.6 \text{ nm}$), while it decreases again slightly for BTA-C₁₂ **1d** ($R_{c,sphere} = 3.4 \text{ nm}$) (details on the fitting parameters are given in the SI, Tables S2–S5). Deviations of some pronounced features in the fit (around q -values of 0.2) are diminished in the scattering data, which is most likely a result of the size distribution of the core and the corona, as well as an ill-defined interface between them. Overall, the obtained results suggest that the hydrogen bonds of the BTA cannot induce the formation of long cylindrical objects, which is commonly observed for the similar, but small molar mass variants [57]. In case of long fibrous structures, the scattering intensity is expected to scale with q^{-1} in the q -region below the rollover ($q < 0.02 \text{ \AA}^{-1}$), which is not observed here. An additional attempt to fit the data with a form factor of a cylindrical micelle results in an almost equal match of the scattering profile (see Figure S8) [66]. However, the lengths of the cylinders (BTA-C₆: $L_{cylinder} = 4.3 \text{ nm}$, BTA-C₁₀:

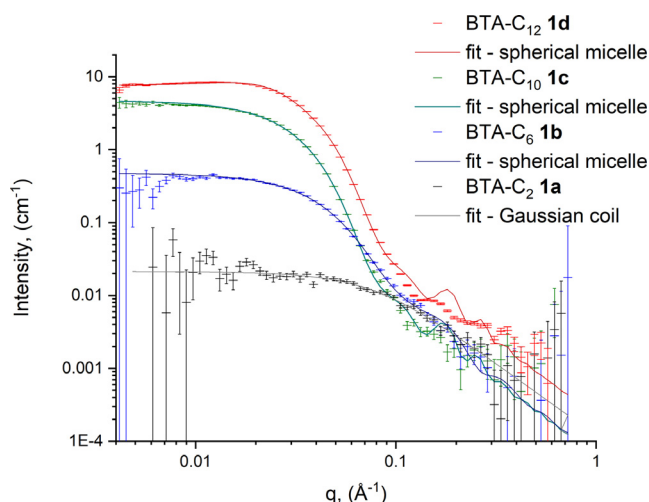


Fig. 1. Scattering profiles of the samples BTA-C₁₂ **1d** (red, $c = 10 \text{ mg mL}^{-1}$), BTA-C₁₀ **1c** (green, $c = 3 \text{ mg mL}^{-1}$), BTA-C₆ **1b** (blue, $c = 3 \text{ mg mL}^{-1}$), and BTA-C₂ **1a** (gray, $c = 3 \text{ mg mL}^{-1}$) obtained by SANS. The respective continuous lines represent the best fits for each sample using SASfit [65] (details are given in the SI). (For interpretation of the references to colour in this figure legend, the reader is referred to the web version of this article.)

$L_{c,cylinder} = 8.0$ nm, BTA-C₁₂: $L_{c,cylinder} = 8.4$ nm) is rather short in comparison to the diameter of the core (BTA-C₆: $2 \times R_{c,cylinder} = 2 \times 1.2$ nm = 2.4 nm, BTA-C₁₀: $2 \times R_{c,cylinder} = 2 \times 2.9$ nm = 5.8 nm, BTA-C₁₂: $2 \times R_{c,cylinder} = 2 \times 2.9$ nm = 5.8 nm), in particular, if the polymer corona is considered, and more or less symmetrical structures or at most prolate ellipsoids are observed by these fits. Despite some theoretical contradictions in case of BTA-C₁₀ (the estimated core radius of 3.6 nm exceeds the maximum theoretical lengths of the hydrophobic domain of 3.2 nm), which might be related to distribution effects in the fit or inclusion of PEG in the core, the most likely structure for these materials consequently remains a spherical micelle and no evidence for elongated structures can be drawn from the analysis by SANS.

2.2.2. Analytical ultracentrifugation (AUC)

The present set of polymers and their potential aggregates were further studied *in situ* via analytical ultracentrifugation, performed as described recently [67–69]. The determined partial specific volumes, v , of unimers/aggregates in water were determined by density measurements, respectively sedimentation coefficients in acetone/deuterated acetone for BTA-C₁₀ [70]. These are listed in Table S6. Fig. 2a shows normalized differential distributions of sedimentation coefficients, $c(s)$, obtained from a sedimentation-diffusion analysis of **1a–d** at a similar solution concentration of $c = 3$ mg mL⁻¹. The BTA-C₂ **1a** clearly behaved unimeric in nature, i.e. showed a narrow distribution of readily small sedimentation coefficients derived from sedimentation-diffusion analysis (black trace in Fig. 2a). The weight (signal) average sedimentation coefficients, s , (Figure S9) and fff_{sph} values were insensitive to solution concentration as expected for small molar mass species. The estimated values of $s = 0.25$ S and weight-average translational frictional ratios $fff_{sph} = 1.5$ are in agreement to recently reported values of varying α -end functional PEGs [69]. The molar mass of **1a** was calculated to $M_{s,f} = 2200$ g mol⁻¹ via the modified Svedberg equation. The resultant hydrodynamic diameter $d_h = 3\sqrt{2}\sqrt{[s]v}(f/f_{sph})^{3/2}$ was 2.5 nm where $[s] = s\eta_0/(1 - v\rho_0)$ is the intrinsic sedimentation coefficient, with η_0 being the viscosity of the solvent, ρ_0 the density of the solvent, and v the partial specific volume of the polymer (see Table S6). The calculated molar mass is in very good agreement with the expected molar mass of unimeric species.

The BTA-C₆ **1b** behaved differently. At higher concentrations ($c \geq 2$ mg mL⁻¹, Fig. 2A and S9) different species could clearly be seen in the sedimentation profiles, resulting in an additional distribution of species sedimenting between $s = 0.5$ – 3 S (red trace in Fig. 2a). In stark contrast, BTA-C₁₀ **1c** shows more than an order of magnitude larger sedimentation coefficients, s , than **1a**, appearing largely independent over the concentration range of 0.097 mg mL⁻¹ $\leq c \leq 3$ mg mL⁻¹ (green trace in Fig. 2A, Figure S9). Clearly **1c** assembles into well-defined aggregates with a frictional ratio of $fff_{sph} \approx 1.7$. The calculated molar mass of $M_{s,f} \approx 340000$ g mol⁻¹, together with a hydrodynamic diameter of $d_h \approx 17$ nm, supports the existence of aggregates in solution. These results suggest an apparent aggregation number of approximately $N_{agg} \approx 140$ for the sample in water, utilizing the unimers molar mass determined in acetone (vide infra). Aggregates in water appeared to be present down to concentrations of $c \leq 97.4$ μ g mL⁻¹ (Figure S9), which is in agreement with CMC values determined independently (Table S1).

The hydrodynamic equivalent spherical size estimate of these aggregates is in good agreement with number-weighted data from DLS (Figure S3). The sample BTA-C₁₂ **1d** as well resembles rather large species (blue trace in Fig. 2A) of a molar mass of $M_{s,f} \approx 313000$ g mol⁻¹ and a hydrodynamic diameter of $d_h = 16$ nm, resulting in a similar aggregation number $N_{agg} \approx 130$ as for BTA-C₁₀.

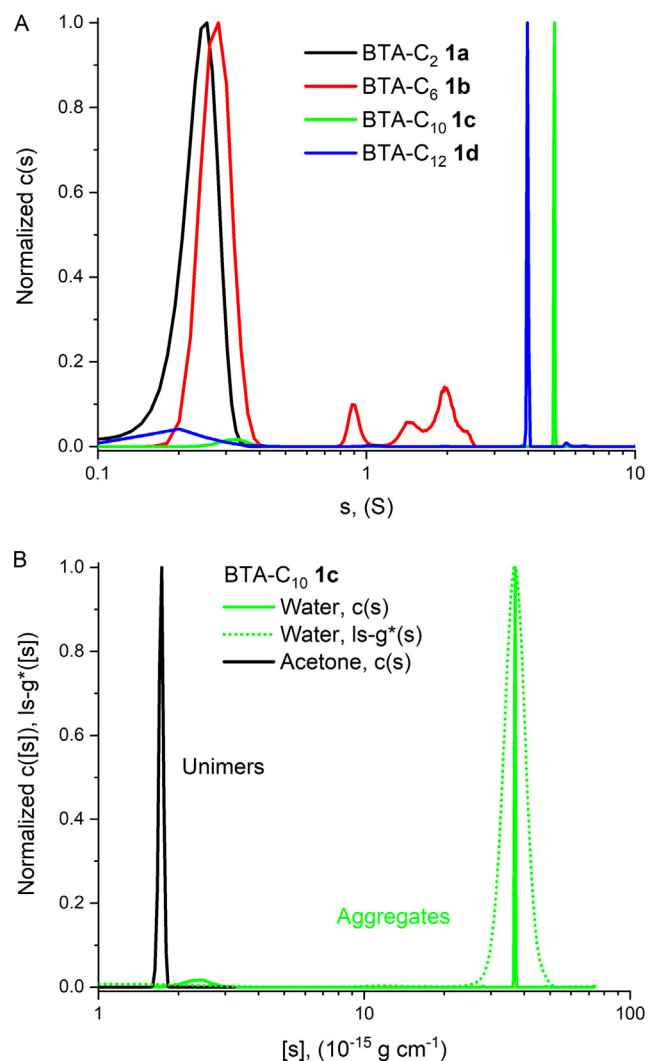


Fig. 2. Normalized differential distribution of sedimentation coefficients, s , of BTA samples **1a–d** from sedimentation-diffusion analysis, $c(s)$, at a comparable solution concentration of $c = 3$ mg mL⁻¹ (semi-logarithmic scale) (Fig. 2A). Comparison of normalized differential distribution of intrinsic sedimentation coefficients, $c([s])$, in acetone or water for BTA-C₁₀ **1c** (semi-logarithmic scale). For the aggregates in water (Fig. 2B) the sedimentation analysis without considering effects of diffusion, $ls - g^*([s])$, is shown as well.

In order to prove aggregation, we performed a comparison between the sedimentation coefficients, s , of BTA-C₁₀ **1c** measured in either water or acetone, the latter being a reasonably good solvent for both the more hydrophobic and the hydrophilic part of the PEG-amphiphile. Therefore, the initial sedimentation coefficients, s , were transformed into intrinsic sedimentation coefficients $[s]$ via the following relation $[s] = s\eta_0/(1 - v\rho_0)$ with η_0 being the viscosity of the solvent (water or acetone), ρ_0 the density of the solvent (water or acetone) and v the partial specific volume of the colloid (unimer or aggregate, see Table S6). In this way, the influence of solvent density and viscosity on sedimentation behavior of species of interest can be eliminated [68]. The agreement between both, the $c(s)$ model based on the numerical solution of the Lamm equation by assuming the same apparent weight-average translational frictional ratio [76] and the $ls - g^*(s)$ model, i.e. a least squares boundary modelling without considering diffusion, was used to support accuracy of estimated sedimentation coefficients, s [75]. These show excellent agreement (see solid green ($c([s])$) versus dotted green line ($ls - g^*([s])$) in Fig. 2B).

Fig. 2B also nicely shows that $[s]$ values differ largely when dissolving the sample in either water or acetone (see green versus black trace in Fig. 2B), indicating existence of aggregates in water, which are represented by an order of magnitude larger intrinsic sedimentation coefficients $[s]$. Sedimentation experiments of BTA-C₁₀ **1c** dissolved in acetone and the respective partial specific volume, v , resulted in an estimated molar mass of $M_{s,f} \approx 2400 \text{ g mol}^{-1}$, which is very close to the expected unimeric species.

2.2.3. cryoTEM

CryoTEM was used as a complementary technique to DLS, SANS, and AUC to visually verify the obtained results. In particular, the morphology was investigated to determine if spherical or cylindrical micelles are present for **1b-d** [70]. All samples were measured at concentrations above their CMC. BTA-C₁₂ **1d** and BTA-C₁₀ **1c** were measured at 3 mg/mL whereas BTA-C₆ **1b** was measured at 10 mg/mL, due to low contrast, resulting from the small size of the structures. For the BTA-C₂ **1a** no cryoTEM measurements were performed, since AUC measurements showed that BTA-C₂ **1a**, at a concentration of 3 mg mL⁻¹, behaves unimeric in nature, comparable to the behaviour of varying α -end functional PEGs [68]. An alkyl spacer length of six methylene groups (BTA-C₆ **1b**) resulted in the formation of spherical micelles with a diameter of approximately 6 nm (Fig. 3A) (for corresponding histograms, see Figure S10). The weak contrast does not allow for a direct discrimination of the core or corona features.

For BTA-C₁₀ **1c** the mean diameter of the micelles increased to approximately 8 nm (Fig. 3B). With further increasing the spacer length to twelve methylene groups (BTA-C₁₂ **1d**) (Fig. 3C) the diameter of the spherical micelles increases to approximately 11 nm. Although the latter matches well with the values observed in the SANS analysis, considering both core and shell size, it deviates for the sample BTA-C₁₀ **1c**. This discrepancy is most likely related to the difficulty to determine core and corona individually in the cryoTEM images. Furthermore, in case of BTA-C₁₂ **1d** both spherical and cylindrical structures can be observed in the cryoTEM images, which cannot be discriminated in the SANS data. Compared to the sizes of the aggregates, as revealed by AUC, the cryoTEM images provide a slightly smaller diameter, which might be due to the fact that the outer areas of the corona resemble a less dense packing of the chains which results in a weaker contrast in cryoTEM imaging. Furthermore, the fact that, in AUC the frictional properties and/or hydration are inherently affecting estimated sizes by their way of calculation (vide supra) might result in slight variations of the micelle sizes observed by cryoTEM imaging. However, in this case, first anisotropic structures appeared in the cryoTEM images, which had a diameter of about 9 nm (Figure S12). Their number was very limited and in total there were <1% (with regard to their number) of cylindrical structures present in the cryoTEM images. Therefore, it is not surprising that these structures could not be identified in the SANS data or the analysis via AUC.

In general, the majority of structures observed by cryoTEM are spherical, despite the ability of non-polymeric BTA molecules to form elongated supramolecular structures as known from the literature [56]. Only with increasing hydrophobic content (C₁₂ chain vs. C₁₀ chain) in the structures, first indications for a morphology transition can be observed. Considering the rather small molar mass of the PEG block (2000 g mol⁻¹), the size of the cores, in particular for BTA-C₁₀ (XX g mol⁻¹) and BTA-C₁₂ (729 g mol⁻¹) cannot be neglected in the considerations of the observed morphological transition. However, an improved hydrophobic shielding of the hydrogen bonds in the core has also to be considered, when changing the size of the alkyl chains, as less water might penetrate to the core and interfere with the hydrogen bonds. A similar observation was reported by Leenders et al. on C₃-symmetric BTA derivatives,

which revealed that supramolecular structures are only formed at spacer lengths of at least eleven CH₂ groups [58]. However, in contrast to the reported materials, structures presented here are C₂-symmetric and resemble more closely an amphiphilic polymer structure, which is clearly demonstrated by their ability to form micelles with even shorter spacers. Nevertheless, the question arises whether the observed onset of a morphological transition is a result of the increased shielding of the hydrogen bonds, or if it is simply due to the increased hydrophobic content in the material.

2.3. Impact of intermolecular hydrogen bonds on the aqueous self-assembly morphology

In order to answer whether hydrogen bonding or packing parameters determine the morphology of our amphiphilic polymers, we prepared analogous structures, in which two of the amide bonds on the benzene core are replaced by ester moieties (Scheme 1). The latter cannot form directed hydrogen bonds as they are common for supramolecular polymers of BTAs. The first material we synthesized was benzenediesteramide-PEG (BDEA-C₁₀) compound **2**, which contains C₁₀ alkyl spacers. CryoTEM images (Fig. 4) of **2** already revealed besides spherical micelles also a substantial number of cylindrical micelles of apparent lengths up to 1 μm and a diameter of 9 nm with an abundance of > 5% based on cryoTEM.

These results were confirmed by AUC measurements. A large range of sedimentation coefficients, s , with two apparent major populations could be found for BDEA-C₁₀ **2** (Fig. 5). Both the $c(s)$ and $ls - g^*(s)$ models again show good agreement. The persistent abundance of sedimentation coefficients between these two major species in both models suggests dynamic features between the observed smaller spherical and larger worm-like structures, as apparent in Fig. 5.

This result was somewhat unexpected, as we observed only spherical micelles for the BTA-C₁₀ **1c** with the same alkyl spacer length but more hydrogen bond forming amide groups. Based on this direct comparison of the formed aggregates of **1c** and **2**, we hypothesize that the transition onset from spherical to cylindrical morphologies is determined by the packing parameter, and not the presence of hydrogen bonds. In our opinion, the apparent discrepancy in the transition region for the BTAs compared to the ester analogues is likely due to a different packing density in the core of the micellar structures. Although AUC or SANS analysis might provide insight into the average aggregation number and the size of the structure, the rather broad distribution of the observed structures varying from small spherical micelles to short and long cylindrical micelles limits an appropriate estimation of the packing density in this case. One possibility for a denser packing of the BTAs might be their ability to form hydrogen bonds within the core of the spherical micelles. To prove this assumption, IR-spectra of BTA-C₁₀ **1c** in aqueous solution (D₂O) (Figure S14) were recorded. The presence of the typical amide I and amide II vibration at 1635 cm⁻¹ and 1473 cm⁻¹, respectively, can be observed. The strong shift of the amide II vibration (1539 cm⁻¹ to 1473 cm⁻¹) in comparison to the spectra in the solid state (Figure S15) is related to the exchange of hydrogen with deuterium, as reported previously [58]. The amide I vibration is mostly comprising the C=O and C-N stretching vibrations, which are more related to conformational changes and the presence of hydrogen bonds. The observed amide I vibration at 1635 cm⁻¹ is in good agreement to the reported values in the literature for aggregated BTAs [58], and thus confirms the presence of hydrogen bonds in the micellar structures in solution. Therefore, a denser packing can be expected compared to the sample BDEA-C₁₀ **2**, which can only form a single hydrogen-bond. Considering the definition of the packing param-

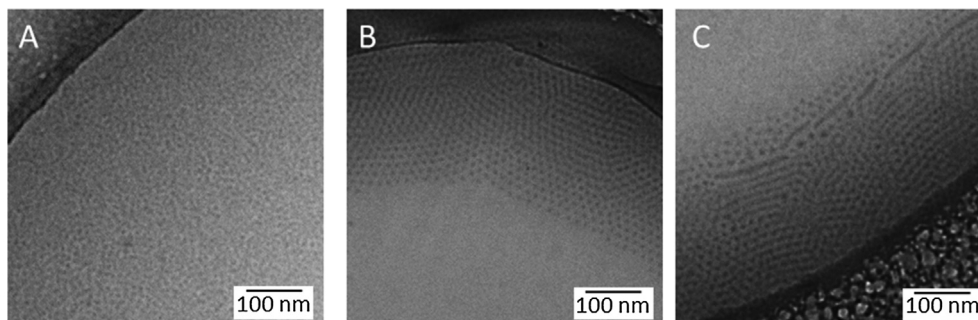


Fig. 3. CryoTEM images displaying spherical micelles for BTA-C₆ **1b** (A, 10 mg mL⁻¹), BTA-C₁₀ **1c** (B, 3 mg mL⁻¹), and mostly spherical micelles with some worm-like structures for BTA-C₁₂ **1d** (C, 3 mg mL⁻¹).

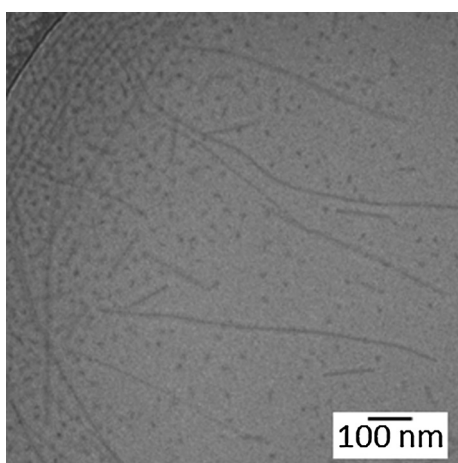


Fig. 4. CryoTEM images of spherical and cylindrical micelles for BDEA-C₁₀ **2** at a concentration of 3 mg mL⁻¹.

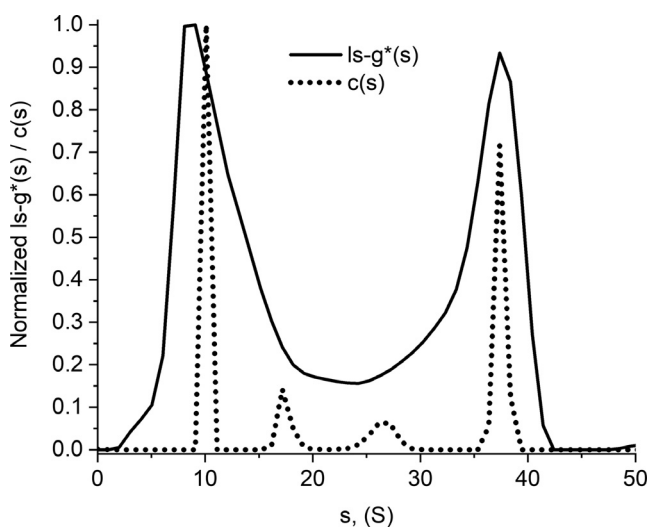


Fig. 5. Normalized differential distribution of sedimentation coefficients, s , of the BDEA-C₁₀ **2** samples from sedimentation-diffusion analysis, $c(s)$, (dotted line), and sedimentation analysis, $ls - g^*(s)$, (solid line) at a concentration of $c = 3$ mg mL⁻¹. Experiments were performed at a rotor velocity of 10,000 rpm.

ter p , this difference would result in a lower volume, V_c , of the hydrophobic part for **1c** compared to **2** and, hence, to a lower packing parameter value p , as the surface area a_0 of the hydrophilic part (here PEG) is the same for both compounds. Consequently, a transition from spherical ($p \leq 1/3$) to cylindrical ($1/3 \leq p \leq 1/2$)

micelles is only observed for the respective ester analogue BDEA-C₁₀ **2**.

3. Conclusion

In summary, four different BTA-modified PEGs were synthesized and their aqueous solution assembly was studied by SANS, cryoTEM, and AUC. We systematically varied the length of the alkyl spacer of the BTA moiety from two to twelve methylene units while keeping the length of the PEG component constant. In this way, we varied the hydrophilic/hydrophobic block ratio of our polymeric compound in order to investigate its impact on the formed micellar morphologies in water. No aggregation could be observed for BTA-C₂ **1a**. Spherical micelles were obtained for BTA-C₆ **1b** and BTA-C₁₀ **1c**, indicating that the hydrophobic BTA moiety needs to have a certain size compared to the hydrophilic PEG to enable assembly in water, corroborating the findings for non-polymeric BTA-derivatives [58]. For BTA-C₁₂ **1d**, a few cylindrical micelles were obtained. Yet, the majority of spherical micelles demonstrates that three hydrogens bonds are not sufficient to induce exclusively polymeric fibers.

Furthermore, we synthesized an ester derivative BDEA **2** with only one amide group, instead of three as for the BTA moiety. Surprisingly, we observed both spherical and cylindrical micelles by cryoTEM, suggesting that the hydrogen bonds of the BTA moiety are not the decisive parameter driving the micellar assemblies towards anisotropic structures with increasing alkyl spacer lengths. The earlier onset of the transition to asymmetry in case of the ester analogue is likely a result of a less dense packing in the micellar core of compound **2** compared to **1c**, although the overall size of the hydrophobic domain is expected to be similar. It has to be mentioned that theoretical considerations on the packing parameter are based on fluid-like structures and calculations for volumes, V_c , or chain lengths, l_c , respectively, rely on saturated aliphatic chains [71]. The previously mentioned bulk densities are usually not considered in theory, however, they are directly related to the real occupied volume keeping the influence of strong interactions such as hydrogen bonds in mind, which cause deviations from the fluid-like theory. Unfortunately, a measurement of the real density of the core of these micelles and thus the real volume of the hydrophobic tail, V_c , is hardly possible. Therefore, a real proof of our assumptions for the difference in the packing of the ester-based materials remains elusive.

Nevertheless, some theoretical considerations based on the obtained data can be drawn. While a direct estimation of the required surface area, a_0 , would be appreciable, typical Langmuir-Blodgett experiments do not apply for polymer-based surfactants, as their area depends largely on the chain conformation. More appropriate in this context is the equilibrium surface area, a_e , based on repulsive forces between adjacent chains, which

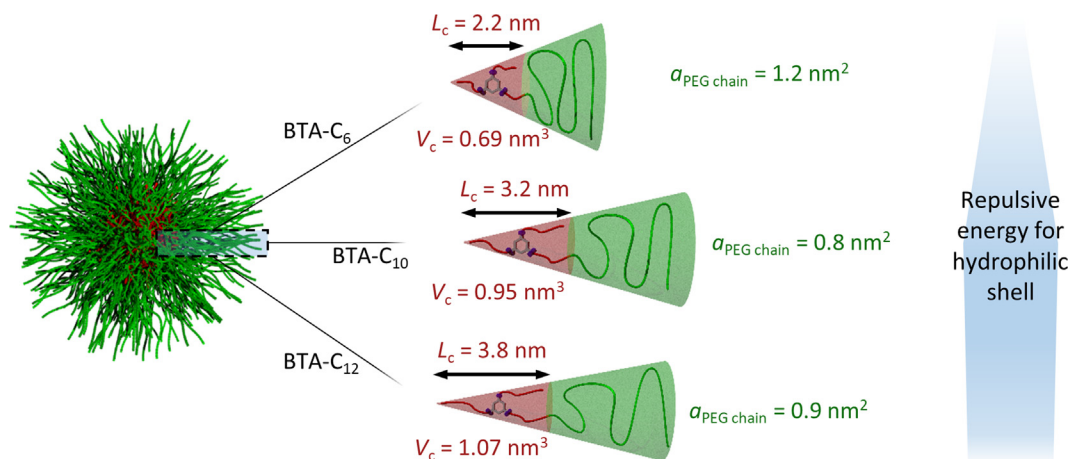


Fig. 6. Schematic representation of the configuration of individual units in the observed spherical micelles; the given values for a theoretical maximum length, L_c , and the theoretically occupied volume for each unit, V_c , are estimated from geometric considerations, while the surface area per PEG chain, $a_{\text{PEG chain}}$, was calculated from the representative spherical micelle fits.

contributes to the minimal Gibbs free energy [72,73]. As we assume a thermodynamic equilibrium for the observed micelles, the respective spherical micelle fits obtained from SANS data allow for an estimation of the effective surface area per hydrophilic head group or PEG chain, respectively. In contrast to BTA-C₁₀ **1c** and BTA-C₁₂ **1d**, the shorter alkyl chain in BTA-C₆ **1b** results in a significantly increased available surface area per PEG chain (Table S7, Fig. 6). Keeping in mind that in all cases the same PEG chain is attached, stronger repulsive forces are expected for the BTAs **1c** and **1d**, due to an increased crowding of chains, which may result in a transition from spherical to cylindrical structures due to a lower overall energy level [72]. Although, clear predictions of final morphologies based on this theory were beyond the scope of this work, these considerations support our assumption that the transition from spherical to cylindrical structure is dependent on the composition in the present work (i.e. the ratio of hydrophobic to hydrophilic domain), and not the presence of directed hydrogen bonds in the BTA motif itself.

The presented first integration of BTA units as structuring motif in amphiphilic polymers underlines, that despite the tendency to form directed hydrogen bonds, fibrous structures with pendant polymers are only present in case of a suitable packing parameter for cylindrical micelles. While hydrogen bonds are still present within the micelle, the directional force seems to not overcome the surface tension, as it has been reported, in particular, for cyclic [18–30] and linear [31–43] peptide-polymer conjugates but also for some urea modified polymers [44–51]. In comparison to the presented BTA unit, which by itself forms helical assemblies, the present systems feature linear configurations of the hydrogen bonds with mostly antiparallel alignment of the dipole moments. This fact, in combination with an increased number of hydrogen bonds, certainly accounts for the observed difference in the self-assembly properties. Nevertheless, the BTA-platform offers a modular approach to accurately tune the self-assembly strength, which opens up a variety of potential improvements on the interaction strength and the directional force including, for example, the introduction of peptide groups in order to drive the assembly toward more fiber-like supramolecular polymer brushes, as it has already been demonstrated for small molecules [74].

4. Experimental part

Complete experimental details, including synthetic protocols, chemical and physical characterization, imaging and scattering techniques, are reported in the accompanying ESI.

4.1. Materials and methods

All reagents and solvents were commercial products purchased from Sigma-Aldrich and were used without further purification. ¹H NMR spectra were measured with a Bruker spectrometer (300 MHz) equipped with an Avance I console, a dual ¹H and ¹³C sample head, and a 60 × BACS automatic sample changer. The chemical shifts of the peaks were determined by using the residual solvent signal as reference and are given in ppm in comparison to TMS. Size-exclusion chromatography (SEC) of polymers was performed on an Agilent system (series 1200) equipped with a PSS degasser, a G1310A pump, a G1362A refractive index detector and a PSS GRAM 30 and 1000 column with DMAc (+0.21 wt% LiCl) as eluent at a flow rate of 1 mL min⁻¹. The column oven was set to 40 °C and poly(ethylene glycol) (PEG) standards from PSS were used for calibration. Fluorescence spectra were recorded on a JASCO FP-8300 spectrometer equipped with a Peltier element. ITC dilution experiments were conducted with a standard volume Nano ITC by TA Instruments. IR spectra were recorded on an Affinity-1 Fourier transform infrared spectrophotometer from Shimadzu. DLS correlograms were measured on a ZetaSizer Nano ZS (Malvern, Herrenberg, Germany) equipped with a He–Ne laser with a wavelength of $\lambda = 633$ nm. CryoTEM measurements were performed on an FEI Tecnai G2 20 platform with a LaB₆ filament at 200 kV acceleration voltage. Small angle neutron scattering was carried out on the Sans2d small-angle diffractometer at the ISIS Pulsed Neutron Source (STFC Rutherford Appleton Laboratory, Didcot, U.K.).

4.2. DLS

A scattering angle of 173° was used to record intensity fluctuation counts of the different samples. All measurements were conducted in triplicate at 25 °C in macro cuvettes containing 2 mL solution after an equilibration time of 60 s, and an acquisition time of 60 s. The apparent distribution of number-weighted hydrodynamic radii, R_h , was calculated based on the Stokes–Einstein equation:

$$R_h = \frac{kT}{6\pi\eta_0 D}$$

with k being the Boltzmann constant, T the temperature in unit K, η_0 the viscosity of the solvent, and D the apparent translational diffusion coefficient.

4.3. CryoTEM

Samples were prepared on Ar plasma treated Quantifoil grids (R2/2). 8.5 μL of the solutions (3 mg mL^{-1} in H_2O , except for BTA-C₆: 10 mg mL^{-1}) were applied onto the grids and vitrified into liquid ethane utilizing a FEI Vitrobot Mark IV system (offset: –3 mm, blotting time: 1 s). Samples were transferred into the cryo holder (Gatan 626) utilizing the Gatan cryo stage, followed by transfer into the microscope keeping the temperature below –172 °C during the whole transfer and measurement process after vitrification. Images were acquired with a Mega View (OSIS, Olympus Soft Imaging Systems) or an Eagle 4 k CCD camera. In the cryoTEM images in this study, only specific regions of interest are shown, that are representative for the whole sample.

4.4. Analytical ultracentrifugation

Sedimentation velocity experiments were performed with a ProteomeLab XL-I analytical ultracentrifuge (Beckman Coulter Instruments, Brea, CA). The cells, containing double-sector epon centerpieces with a 12 mm optical path length, were placed in an An-50 Ti eight-hole rotor. A typical rotor speed of 42,000 rpm, unless otherwise noted, was used. The cells were filled with 420 μL sample solution in water or acetone and with 440 μL water or acetone as the reference. Depending on the sample, the experiments were conducted for variable timescales up to 24 h and at a temperature of $T = 20$ °C. Sedimentation profile scans were recorded with the interference optics (refractive index (RI)). A suitable selection of scans was used for data evaluation with Sedfit using the $ls - g^*(s)$ model, i.e. by least squares boundary modelling with a Tikhonov-Phillips regularization procedure and by assuming non-diffusing species [75]. This model results in an apparent differential distribution of sedimentation coefficients, s . Alternatively, the $c(s)$ model by assuming the same apparent, weight-average translational frictional ratio, f/f_{sph} , of the population of sedimenting species was used [76].

4.5. CMC determination

The critical micelle concentrations (CMC) were determined by measuring the fluorescence of Nile red incorporated in the benzenetrisamide (BTA) derivatives according to a literature procedure [77]. To this end, different BTA stock solutions were diluted with Milli-Q water to obtain solutions of $V = 180$ μL in a concentration range from $c = 1 \times 10^{-9}$ up to $c = 1$ mg mL^{-1} . Then, 18 μL of a Nile red stock solution in THF ($c = 1$ mg mL^{-1}) was added, and the samples equilibrated overnight in a thermoshaker device ($T = 20$ °C, $n = 200$ rpm). Afterwards, the samples were transferred to quartz cuvettes and the fluorescence of Nile red was recorded (wavelength measurement range: 550–800 nm) at an excitation wavelength of 535 ± 5 nm. Emission spectra were averaged over two scans. The CMC was determined as the intersection point of the linear fits (performed with OriginPRO 2015) from the emission intensity at a wavelength of 612 nm versus the log of concentration.

4.6. Synthesis

The detailed synthesis and purification steps for the BTA compounds **1a–d** and the BDEA compound **2** as well as their corresponding intermediates can be found in the [Supporting Information](#).

Acknowledgements

The authors thank Ulrich S. Schubert for substantial support. JCB, TK, and FG highly acknowledge the DFG for support

(Emmy-Noether Program, BR 4905/3-1). T.K. further thanks the Elitenetzwerk Bayern (ENB) for support. CryoTEM investigations were performed at the electron microscopy facilities of the Jena Center for Soft Matter (JCSM), which were established with grants from the DFG and the European funds for Regional Development (EFRE). I.N. and S.H. acknowledge support of this study by the DFG-funded Collaborative Research Center PolyTarget (SFB 1278, project Z01). We further thank Kristin Schreyer for the synthesis of several compounds and intermediates.

Declaration of Competing Interest

There are no conflicts to declare.

Appendix A. Supplementary material

Supplementary data to this article can be found online at <https://doi.org/10.1016/j.jcis.2019.09.046>.

References

- [1] U. Tritschler, S. Pearce, J. Gwyther, G.R. Whittell, I. Manners, 50th anniversary perspective: functional nanoparticles from the solution self-assembly of block copolymers, *Macromolecules* 50 (9) (2017) 3439–3463.
- [2] H. Cabral, K. Miyata, K. Osada, K. Kataoka, Block copolymer micelles in nanomedicine applications, *Chem. Rev.* 118 (14) (2018) 6844–6892.
- [3] D. Chandler, Interfaces and the driving force of hydrophobic assembly, *Nature* 437 (2005) 640–647.
- [4] Y. Mai, A. Eisenberg, Self-assembly of block copolymers, *Chem. Soc. Rev.* 41 (18) (2012) 5969–5985.
- [5] J.N. Israelachvili, D.J. Mitchell, B.W. Ninham, Theory of self-assembly of hydrocarbon amphiphiles into micelles and bilayers, *J. Chem. Soc. Faraday Trans. 2* (72) (1976) 1525–1568.
- [6] R. Nagarajan, Molecular packing parameter and surfactant self-assembly: the neglected role of the surfactant tail, *Langmuir* 18 (1) (2002) 31–38.
- [7] B. Karagoz, L. Esser, H.T. Duong, J.S. Basuki, C. Boyer, T.P. Davis, Polymerization-Induced Self-Assembly (PISA) – control over the morphology of nanoparticles for drug delivery applications, *Polym. Chem.* 5 (2) (2014) 350–355.
- [8] S.L. Canning, G.N. Smith, S.P. Armes, A critical appraisal of RAFT-mediated polymerization-induced self-assembly, *Macromolecules* 49 (6) (2016) 1985–2001.
- [9] M.J. Derry, L.A. Fielding, S.P. Armes, Polymerization-induced self-assembly of block copolymer nanoparticles via RAFT non-aqueous dispersion polymerization, *Prog. Polym. Sci.* 52 (Suppl C) (2016) 1–18.
- [10] X. Wang, G. Guerin, H. Wang, Y. Wang, I. Manners, M.A. Winnik, Cylindrical block copolymer micelles and co-micelles of controlled length and architecture, *Science* 317 (5838) (2007) 644–647.
- [11] T. Gädt, N.S. leong, G. Cambridge, M.A. Winnik, I. Manners, Complex and hierarchical micelle architectures from diblock copolymers using living, crystallization-driven polymerizations, *Nat. Mater.* 8 (2009) 144–150.
- [12] J.B. Gilroy, T. Gädt, G.R. Whittell, L. Chabanne, J.M. Mitchels, R.M. Richardson, M.A. Winnik, I. Manners, Monodisperse cylindrical micelles by crystallization-driven living self-assembly, *Nat. Chem.* 2 (2010) 566.
- [13] N. Petzetakis, A.P. Dove, R.K. O'Reilly, Cylindrical micelles from the living crystallization-driven self-assembly of poly(lactide)-containing block copolymers, *Chem. Sci.* 2 (5) (2011) 955–960.
- [14] J.C. Brendel, F.H. Schacher, Block copolymer self-assembly in solution—quo vadis?, *Chem Asian J.* 13 (3) (2018) 230–239.
- [15] H.G. Börner, H. Schlaad, Bioinspired functional block copolymers, *Soft Matter* 3 (4) (2007) 394–408.
- [16] R.M. Ghadiri, J.R. Granja, R.A. Milligan, D.E. McRee, N. Khazanovich, Self-assembling organic nanotubes based on a cyclic peptide architecture, *Nature* 366 (1993) 324–327.
- [17] J. Couet, J.D.J.S. Samuel, A. Kopyshv, S. Santer, M. Biesalski, Peptide-polymer hybrid nanotubes, *Angew. Chem. Int. Ed.* 44 (21) (2005) 3297–3301.
- [18] J. Couet, M. Biesalski, Surface-initiated ATRP of N-isopropylacrylamide from initiator-modified self-assembled peptide nanotubes, *Macromolecules* 39 (21) (2006) 7258–7268.
- [19] J. Couet, M. Biesalski, Conjugating self-assembling rigid rings to flexible polymer coils for the design of organic nanotubes, *Soft Matter* 2 (12) (2006) 1005–1014.
- [20] J. Couet, M. Biesalski, Polymer-wrapped peptide nanotubes: peptide-grafted polymer mass impacts length and diameter, *Small* 4 (7) (2008) 1008–1016.
- [21] S. Loschonsky, J. Couet, M. Biesalski, Synthesis of peptide/polymer conjugates by solution ATRP of Butylacrylate using an initiator-modified cyclic D-alt-L-peptide, *Macromol. Rapid Commun.* 29 (4) (2008) 309–315.
- [22] M.G.J. ten Cate, N. Severin, H.G. Börner, Self-assembling peptide-polymer conjugates comprising (d-alt-l)-cyclopeptides as aggregator domains, *Macromolecules* 39 (23) (2006) 7831–7838.

- [23] R. Chapman, K.A. Jolliffe, S. Perrier, Modular design for the controlled production of polymeric nanotubes from polymer/peptide conjugates, *Polym. Chem.* 2 (9) (2011) 1956–1963.
- [24] R. Chapman, M. Daniai, M.L. Koh, K.A. Jolliffe, S. Perrier, Design and properties of functional nanotubes from the self-assembly of cyclic peptide templates, *Chem. Soc. Rev.* 41 (18) (2012) 6023–6041.
- [25] S.C. Larnaudie, J.C. Brendel, I. Romero-Cañelón, C. Sanchez-Cano, S. Catrouillet, J. Sanchis, J.P.C. Coverdale, J.-I. Song, A. Habtemariam, P.J. Sadler, K.A. Jolliffe, S. Perrier, Cyclic peptide-polymer nanotubes as efficient and highly potent drug delivery systems for organometallic anticancer complexes, *Biomacromolecules* 19 (1) (2018) 239–247.
- [26] S.C. Larnaudie, J. Sanchis, T.-H. Nguyen, R. Peltier, S. Catrouillet, J.C. Brendel, C.J. H. Porter, K.A. Jolliffe, S. Perrier, Cyclic peptide-poly(HPMA) nanotubes as drug delivery vectors: In vitro assessment, pharmacokinetics and biodistribution, *Biomaterials* 178 (2018) 570–582.
- [27] E.D.H. Mansfield, M. Hartlieb, S. Catrouillet, J.Y. Rho, S.C. Larnaudie, S.E. Rogers, J. Sanchis, J.C. Brendel, S. Perrier, Systematic study of the structural parameters affecting the self-assembly of cyclic peptide-poly(ethylene glycol) conjugates, *Soft Matter* 14 (2018) 6320–6326.
- [28] S. Catrouillet, J.C. Brendel, S. Larnaudie, T. Barlow, K.A. Jolliffe, S. Perrier, Tunable length of cyclic peptide-polymer conjugate self-assemblies in water, *ACS Macro Lett.* 5 (10) (2016) 1119–1123.
- [29] J.C. Brendel, S. Catrouillet, J. Sanchis, K.A. Jolliffe, S. Perrier, Shaping block copolymer micelles by supramolecular polymerization: making ‘tubosomes’, *Polym. Chem.* (2019).
- [30] J.C. Brendel, J. Sanchis, S. Catrouillet, E. Czuba, M.Z. Chen, B.M. Long, C. Nowell, A. Johnston, K.A. Jolliffe, S. Perrier, Secondary self-assembly of supramolecular nanotubes into tubosomes and their activity on cells, *Angewandte Chemie International Edition in English* 57 (2018) 16678–16882.
- [31] T.S. Burkoth, T.L.S. Benzinger, D.N.M. Jones, K. Hallenga, S.C. Meredith, D.G. Lynn, C-terminal PEG blocks the irreversible step in β -amyloid(10–35) fibrillogenesis, *J. Am. Chem. Soc.* 120 (30) (1998) 7655–7656.
- [32] D. Eckhardt, M. Groenewolt, E. Krause, H.G. Börner, Rational design of oligopeptide organizers for the formation of poly(ethylene oxide) nanofibers, *Chem. Commun.* 22 (2005) 2814–2816.
- [33] R. Otter, N.A. Henke, C. Berac, T. Bauer, M. Barz, S. Seiffert, P. Besenius, Secondary structure-driven hydrogelation using foldable telechelic polymer-peptide conjugates, *Macromol. Rapid Commun.* 39 (2018) 1800459.
- [34] R. Otter, K. Klinker, D. Spitzer, M. Schinnerer, M. Barz, P. Besenius, Folding induced supramolecular assembly into pH-responsive nanorods with a protein repellent shell, *Chem. Commun.* 54 (4) (2018) 401–404.
- [35] I.W. Hamley, M.J. Krysmann, Effect of PEG Crystallization on the self-assembly of PEG/peptide copolymers containing amyloid peptide fragments, *Langmuir* 24 (15) (2008) 8210–8214.
- [36] I.W. Hamley, I.A. Ansari, V. Castelletto, H. Nuhn, A. Rösler, H.A. Klok, Solution self-assembly of hybrid block copolymers containing poly(ethylene glycol) and amphiphilic β -strand peptide sequences, *Biomacromolecules* 6 (3) (2005) 1310–1315.
- [37] H.-A. Klok, G.W.M. Vandermeulen, H. Nuhn, A. Rösler, I.W. Hamley, V. Castelletto, H. Xu, S.S. Sheiko, Peptide mediated formation of hierarchically organized solution and solid state polymer nanostructures, *Faraday Discuss.* 128 (2005) 29–41.
- [38] V. Castelletto, R.J. Gouveia, C.J. Connon, I.W. Hamley, Self-assembly and bioactivity of a polymer/peptide conjugate containing the RGD cell adhesion motif and PEG, *Eur. Polym. J.* 49 (10) (2013) 2961–2967.
- [39] V. Castelletto, G. Cheng, S. Furlzeland, D. Atkins, I.W. Hamley, Control of strand registry by attachment of PEG chains to amyloid peptides influences nanostructure, *Soft Matter* 8 (20) (2012) 5434–5438.
- [40] I.W. Hamley, G. Cheng, V. Castelletto, A thermoresponsive hydrogel based on telechelic PEG end-capped with hydrophobic dipeptides, *Macromol. Biosci.* 11 (8) (2011) 1068–1078.
- [41] V. Castelletto, J.E. McKendrick, I.W. Hamley, U. Olsson, C. Cenker, PEGylated amyloid peptide nanocontainer delivery and release system, *Langmuir* 26 (14) (2010) 11624–11627.
- [42] V. Castelletto, G.E. Newby, Z. Zhu, I.W. Hamley, L. Noirez, Self-assembly of PEGylated peptide conjugates containing a modified amyloid β -peptide fragment, *Langmuir* 26 (12) (2010) 9986–9996.
- [43] V. Castelletto, I.W. Hamley, Self assembly of a model amphiphilic phenylalanine peptide/polyethylene glycol block copolymer in aqueous solution, *Biophys. Chem.* 141 (2) (2009) 169–174.
- [44] N. Chebotareva, P.H.H. Bomans, P.M. Frederik, N.A.J.M. Sommerdijk, R.P. Sijbesma, Morphological control and molecular recognition by bis-urea hydrogen bonding in micelles of amphiphilic tri-block copolymers, *Chem. Commun.* 39 (2005) 4967–4969.
- [45] S.I.S. Hendrikse, S.P.W. Wijnands, R.P.M. Lafleur, M.J. Pouderoijen, H.M. Janssen, P.Y.W. Dankers, E.W. Meijer, Controlling and tuning the dynamic nature of supramolecular polymers in aqueous solutions, *Chem. Commun.* 53 (14) (2017) 2279–2282.
- [46] S. Han, E. Nicol, F. Niepceron, O. Colombani, S. Pensec, L. Bouteiller, Oligo-urea with no alkylene unit self-assembles into rod-like objects in water, *Macromol. Rapid Commun.* 1800698 (2019).
- [47] G. Mellot, J.-M. Guigner, J. Jestin, L. Bouteiller, F. Stoffelbach, J. Rieger, Bisurea-functionalized RAFT agent: A straightforward and versatile tool toward the preparation of supramolecular cylindrical nanostructures in water, *Macromolecules* 51 (24) (2018) 10214–10222.
- [48] G. Mellot, J.M. Guigner, L. Bouteiller, F. Stoffelbach, J. Rieger, Templated PISA: driving polymerization-induced self-assembly towards fibre morphology, *Angew. Chem. Int. Ed. Engl.* 58 (10) (2019) 3173–3177.
- [49] S. Catrouillet, L. Bouteiller, O. Boyron, C. Lorthioir, E. Nicol, S. Pensec, O. Colombani, Patchy supramolecular bottle-brushes formed by solution self-assembly of bis(urea)s and tris(urea)s decorated by two incompatible polymer arms, *Langmuir* 32 (35) (2016) 8900–8908.
- [50] S. Catrouillet, L. Bouteiller, E. Nicol, T. Nicolai, S. Pensec, B. Jacqueline, M. Le Bohec, O. Colombani, Self-assembly and critical solubility temperature of supramolecular polystyrene bottle-brushes in cyclohexane, *Macromolecules* 48 (5) (2015) 1364–1370.
- [51] S. Catrouillet, C. Fonteneau, L. Bouteiller, N. Delorme, E. Nicol, T. Nicolai, S. Pensec, O. Colombani, Competition between steric hindrance and hydrogen bonding in the formation of supramolecular bottle brush polymers, *Macromolecules* 46 (19) (2013) 7911–7919.
- [52] L. Brunsveld, B.J.B. Folmer, E.W. Meijer, R.P. Sijbesma, Supramolecular polymers, *Chem. Rev.* 101 (12) (2001) 4071–4098.
- [53] L. Bouteiller, Assembly via Hydrogen Bonds of Low Molar Mass Compounds into Supramolecular Polymers, 207 (2007) 79–112.
- [54] E. Krieg, M.M.C. Bastings, P. Besenius, B. Rybtchinski, Supramolecular polymers in aqueous media, *Chem. Rev.* 116 (4) (2016) 2414–2477.
- [55] M.P. Lightfoot, F.S. Mair, R.G. Pritchard, J.E. Warren, New supramolecular packing motifs: [small pi]-stacked rods encased in triply-helical hydrogen bonded amide strands, *Chem. Commun.* 19 (1999) 1945–1946.
- [56] S. Cantekin, T.F.A. de Greef, A.R.A. Palmans, Benzene-1,3,5-tricarboxamide: a versatile ordering moiety for supramolecular chemistry, *Chem. Soc. Rev.* 41 (18) (2012) 6125–6137.
- [57] C.M.A. Leenders, L. Albertazzi, T. Mes, M.M.E. Koenigs, A.R.A. Palmans, E.W. Meijer, Supramolecular polymerization in water harnessing both hydrophobic effects and hydrogen bond formation, *Chem. Commun.* 49 (19) (2013) 1963–1965.
- [58] C.M.A. Leenders, M.B. Baker, I.A.B. Pijpers, R.P.M. Lafleur, L. Albertazzi, A.R.A. Palmans, E.W. Meijer, Supramolecular polymerisation in water; elucidating the role of hydrophobic and hydrogen-bond interactions, *Soft Matter* 12 (11) (2016) 2887–2893.
- [59] T. Mes, R. van der Weegen, A.R.A. Palmans, E.W. Meijer, Single-chain polymeric nanoparticles by stepwise folding, *Angew. Chem. Int. Ed.* 50 (22) (2011) 5085–5089.
- [60] P.J.M. Stals, M.A.J. Gillissen, T.F.E. Paffen, T.F.A. de Greef, P. Lindner, E.W. Meijer, A.R.A. Palmans, I.K. Voets, Folding polymers with pendant hydrogen bonding motifs in water: the effect of polymer length and concentration on the shape and size of single-chain polymeric nanoparticles, *Macromolecules* 47 (9) (2014) 2947–2954.
- [61] A. Duro-Castano, V.J. Nebot, A. Niño-Pariente, A. Armiñán, J.J. Arroyo-Crespo, A. Paul, N. Feiner-Gracia, L. Albertazzi, M.J. Vicent, Capturing “Extraordinary” soft-assembled charge-like polypeptides as a strategy for nanocarrier design, *Adv. Mater.* 29 (39) (2017) 1702888.
- [62] A. Duro-Castano, R.M. England, D. Razola, E. Romero, M. Oteo-Vives, M.A. Morcillo, M.J. Vicent, Well-defined star-shaped polyglutamates with improved pharmacokinetic profiles as excellent candidates for biomedical applications, *Mol. Pharm.* 12 (10) (2015) 3639–3649.
- [63] F.G. Brunetti, C. Romero-Nieto, J. López-Andarias, C. Atienza, J.L. López, D.M. Guldi, N. Martín, Self-ordering electron donor-acceptor nanohybrids based on single-walled carbon nanotubes across different scales, *Angew. Chem. Int. Ed.* 52 (8) (2013) 2180–2184.
- [64] M.C. Stuart, J. van de Pas, J.B. Engberts, The use of Nile Red to monitor the aggregation behavior in ternary surfactant–water–organic solvent systems, *J. Phys. Org. Chem.* 18 (9) (2005) 929–934.
- [65] I. Bressler, J. Kohlbrecher, A.F. Thunemann, SASfit: a tool for small-angle scattering data analysis using a library of analytical expressions, *J. Appl. Crystallogr.* 48 (5) (2015) 1587–1598.
- [66] J. Pedersen, Form factors of block copolymer micelles with spherical, ellipsoidal and cylindrical cores, *J. Appl. Crystallogr.* 33 (3 Part 1) (2000) 637–640.
- [67] M. Grube, M.N. Leiske, U.S. Schubert, I. Nischang, POx as an alternative to PEG? a hydrodynamic and light scattering study, *Macromolecules* 51 (2018) 1905–2116.
- [68] I. Muljajew, C. Weber, I. Nischang, U.S. Schubert, PMMA-g-OEtOx graft copolymers: influence of grafting degree and side chain length on the conformation in aqueous solution, *Materials* 11 (4) (2018) 528.
- [69] I. Nischang, I. Perevyazko, T. Majdanski, J. Vitz, G. Festag, U.S. Schubert, Hydrodynamic analysis resolves the pharmaceutically-relevant absolute molar mass and solution properties of synthetic poly(ethylene glycol)s created by varying initiation sites, *Anal. Chem.* 89 (2) (2017) 1185–1193.
- [70] W. Mächtle, Charakterisierung von dispersionen durch gekoppelte H₂O/D₂O-ultrazentrifugenmessungen, *Makromol. Chem.* 185 (5) (1984) 1025–1039.
- [71] J.N. Israelachvili, Soft and biological structures, in: J.N. Israelachvili (Ed.), *Intermolecular and Surface Forces*, third ed., Academic Press, San Diego, 2011, pp. 535–576.
- [72] R. Nagarajan, Constructing a molecular theory of self-assembly: Interplay of ideas from surfactants and block copolymers, *Adv. Colloid Interface Sci.* 244 (2017) 113–123.
- [73] C. Tanford, Theory of micelle formation in aqueous solutions, *J. Phys. Chem.* 78 (24) (1974) 2469–2479.

- [74] P. Besenius, Y. Goedegebure, M. Driesse, M. Koay, P.H.H. Bomans, A.R.A. Palmans, P.Y.W. Dankers, E.W. Meijer, Peptide functionalised discotic amphiphiles and their self-assembly into supramolecular nanofibres, *Soft Matter* 7 (18) (2011) 7980–7983.
- [75] P. Schuck, P. Rossmanith, Determination of the sedimentation coefficient distribution by least-squares boundary modeling, *Biopolymers* 54 (5) (2000) 328–341.
- [76] P. Schuck, Size-distribution analysis of macromolecules by sedimentation velocity ultracentrifugation and Lamm equation modeling, *Biophys. J.* 78 (3) (2000) 1606–1619.
- [77] M.K. Gupta, T.A. Meyer, C.E. Nelson, C.L. Duvall, Poly(PS-*b*-DMA) micelles for reactive oxygen species triggered drug release, *J. Control. Release* 162 (3) (2012) 591–598.

The influence of directed hydrogen bonds on the self-assembly of amphiphilic polymers in water

Tobias Klein,^{a,b,†} Franka Gruschwitz,^{a,b,†} Sarah Rogers,^c Stephanie Hoepfener,^{a,b} Ivo Nischang,^{a,b} Johannes C. Brendel,^{a,b,*}

a Laboratory of Organic and Macromolecular Chemistry (IOMC), Friedrich Schiller University Jena, Humboldtstraße 10, 07743 Jena, Germany

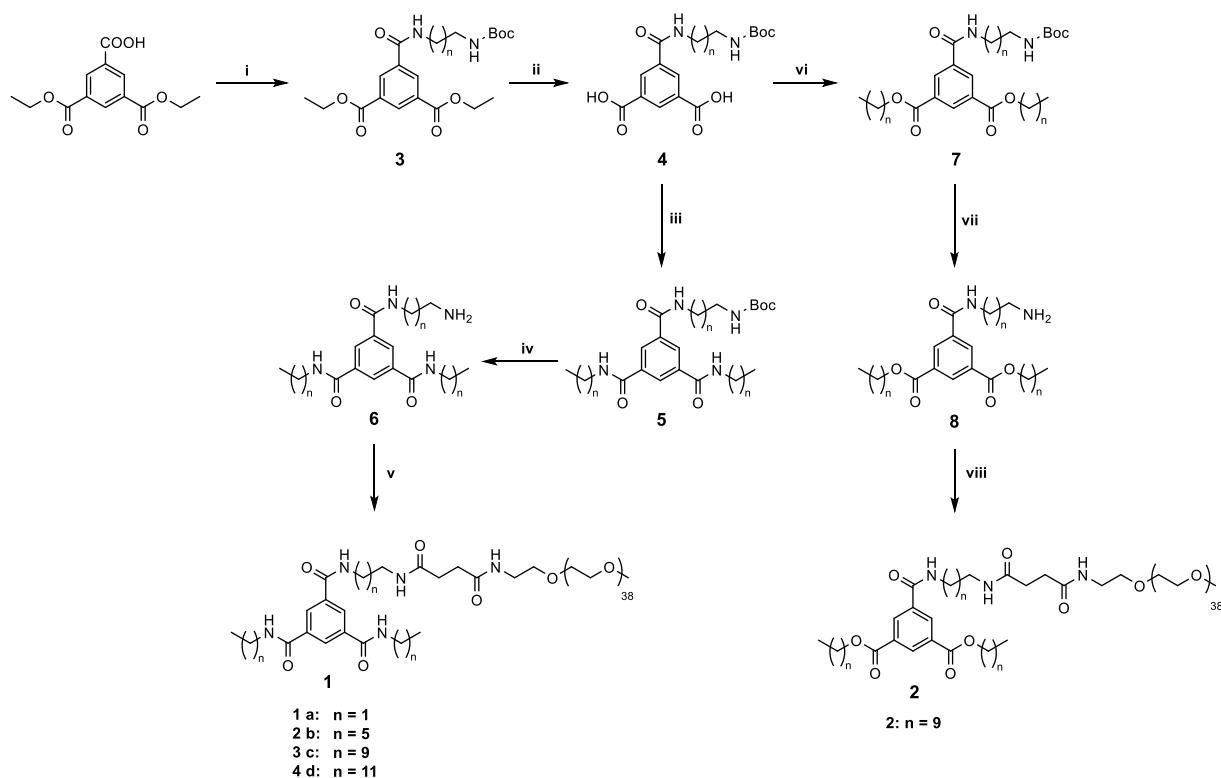
b Jena Center for Soft Matter (JCSM), Friedrich Schiller University Jena, Philosophenweg 7, 07743 Jena, Germany

c ISIS Neutron Facility, Rutherford Appleton Laboratory, Harwell Oxford, Didcot OX11 0QX, United Kingdom

† The authors contributed equally to this work

*corresponding author: johannes.brendel@uni-jena.de

Synthesis



Scheme S1: Schematic representation of the synthetic route toward BTAs. Details on the synthesis are detailed below. BTAs **1a-d** and **2**. i) Semi-protected amine, DMAP, EDC, DCM, 25 °C, overnight; ii) KOH in EtOH/H₂O 9:1, 80 °C, 30 min; iii) Alkylamine, DMAP, EDC, DCM, 25 °C, overnight; iv) TFA/TIPS/H₂O, DCM, 25 °C, 2 h; v) Methoxy-PEG-NHS, TEA, DMF, 25 °C, overnight; vi) Alkylamine, DMAP, EDC, DCM, 25 °C, overnight; vii) TFA/TIPS/H₂O, DCM, 25 °C, 2 h; viii) Methoxy-PEG-NHS, TEA, DMF, 25 °C, overnight.

Diethyl 5-(2-(tert-butoxycarbonylamino)dodecylcarbamoyle)isophthalate (3d).

3,5-bis(ethoxycarbonyl)benzoic acid (1 g, 3.76 mmol), DMAP (0.046 g, 0.376 mmol) and *tert*-butyl 12-aminododecylcarbamate (1.072 g, 3.57 mmol) were dissolved in dry CH₂Cl₂ (Volume: 30 mL). Under stirring at 25 °C EDC (0.864 g, 4.51 mmol) was added and the reaction solution was stirred for 20 h at 25 °C under argon. The organic phase was successively washed with saturated NaHCO₃ (3 x 50 mL), and sat. NH₄Cl (3x50 mL). The organic layer was dried over Na₂SO₄, filtered and purified by column chromatography on silica gel with CH₂Cl₂/MeOH 20:1 as eluent. ¹H NMR (300 MHz, DMSO-d₆) δ [ppm]: 8.91 (s, 1H), 8.62-8.69 (m, 3H), 8.56 (t, J=1.60 Hz, 1H), 6.75 (br t, J=5.37 Hz, 1H), 4.39 (q, J=7.16 Hz, 4H), 3.24-3.30 (m, 2H), 2.87 (q, J=6.59 Hz, 2H), 1.52 (br d, J=6.78 Hz, 2H), 1.34-1.39 (m, 18H), 1.21-1.30 (m, 16H).

Diethyl 5-(2-(tert-butoxycarbonylamino)ethylcarbamoyl)isophthalate (3a). In a 50 mL round-bottom flask 3,5-bis(ethoxycarbonyl)benzoic acid (1 g, 3.76 mmol) was dissolved in DMF (Volume: 20 mL). HBTU (1.709 g, 4.51 mmol) and TEA (0.628 ml, 4.51 mmol) were subsequently added and after stirring at room temperature for 15 min, *tert*-butyl 2-aminoethylcarbamate (0.662 g, 4.13 mmol) was slowly added. The reaction mixture was stirred with a magnetic stirrer at room temperature for 3 h and monitored by TLC. The solvent was removed under reduced pressure and the residue was redissolved in CH₂Cl₂ (50 mL). The organic phase was successively washed with sat. NaHCO₃ (3 x 50 mL), and sat. NH₄Cl (3x50 mL). The organic layer was dried over Na₂SO₄, filtered and concentrated to obtain a pale yellow powder without further purification. ¹H NMR (300 MHz, DMSO-d₆) δ [ppm]: 8.91 (br s, 1H), 8.63 (br s, 2H), 8.55 (br s, 1H), 6.93 (br s, 1H), 5.74 (s, 2H), 4.38 (q, J=6.66 Hz, 4H), 3.06-3.16 (m, 2H), 2.67 (s, 2H), 1.35 (s, 15H).

Diethyl 5-(2-(tert-butoxycarbonylamino)hexylcarbamoyl)isophthalate (3b). Under argon, 3,5-bis(ethoxycarbonyl)benzoic acid (2 g, 7.51 mmol), *tert*-butyl 6-aminohexylcarbamate (1.625 g, 7.51 mmol), DMAP (0.092 g, 0.751 mmol) were dissolved in CH₂Cl₂ (Volume: 40 mL) in a 250 mL round-bottomed flask. Subsequently, EDC (1.728 g, 9.01 mmol) was slowly added under stirring. The reaction was kept at room temperature for 16 h and monitored by TLC. The organic phase was diluted with 100 mL diethyl ether and successively washed with 1M HCl (2 x 50 mL) and sat. NaHCO₃ (2 x 50 mL). The organic layer was dried over Na₂SO₄, filtered and concentrated to obtain a white wax-like solid after keeping it at room temperature overnight. The product was purified by column chromatography with ethyl acetate/hexane as eluent. ¹H NMR (300 MHz, CHLOROFORM-d) δ [ppm]: 8.79 (t, J=1.60 Hz, 1H), 8.64 (d, J=1.32 Hz, 1H), 8.57-8.71 (m, 1H), 6.56-6.81 (m, 1H), 4.43 (q, J=7.16 Hz, 4H), 3.49 (q, J=6.78 Hz, 2H), 3.14 (q, J=6.15 Hz, 2H), 1.66 (quin, J=6.92 Hz, 2H), 1.29-1.58 (m, 21H).

Diethyl-5-(2-(tert-butoxycarbonylamino)decylcarbamoyl)isophthalate (3c).

3,5-bis(ethoxycarbonyl)benzoic acid (0.5 g, 1.878 mmol), *tert*-butyl 10-aminodecylcarbamate (0.512 g, 1.878 mmol) and DMAP (0.023 g, 0.188 mmol) were dissolved in dry CH₂Cl₂ (Volume: 10 mL). EDC (0.432 g, 2.254 mmol) was slowly added under stirring. The reaction mixture was stirred at room temperature for 20 h. The organic phase was diluted with 100 mL diethyl ether and washed with 1M HCl (2 x 50 mL) and saturated NaHCO₃ (2 x 50 mL). The organic layer was dried over Na₂SO₄, filtered and concentrated to obtain a white wax-like solid after keeping it at room temperature overnight. ¹H NMR (300 MHz, CHLOROFORM-d) δ

[ppm]: 8.79 (t, $J=1.51$ Hz, 1H), 8.61 (d, $J=1.51$ Hz, 2H), 6.22-6.48 (m, 1H), 4.34-4.57 (m, 5H), 3.44-3.54 (m, 2H), 3.11 (q, $J=6.59$ Hz, 2H), 1.55-1.75 (m, 4H), 1.20-1.50 (m, 30H).

5-((2-((tert-butoxycarbonyl)amino)dodecyl)carbamoyl)isophthalic acid (4d).

Diethyl 5-(2-(tert-butoxycarbonylamino)dodecylcarbamoyl)isophthalate (**3d**) (1.4 g, 2.55 mmol) was added to a solution of a 2 M KOH (5.4 g, 102 mmol) in EtOH (ratio: 9, Volume: 33.1 mL)/water (ratio: 1.000, Volume: 3.67 mL). The resulting suspension was stirred at reflux for 30 min. After addition of HCl to neutralize the base, the mixture was extracted with ethyl acetate (3 x 100 mL). The organic phase was dried over Na₂SO₄, filtered and concentrated to yield a white solid. ¹H NMR (300 MHz, DMSO-d₆) δ [ppm]: 8.83-8.93 (m, 1H), 8.62 (d, $J=1.70$ Hz, 2H), 8.56 (t, $J=1.51$ Hz, 1H), 6.69-6.80 (m, 1H), 3.27 (br d, $J=6.03$ Hz, 4H), 2.85-2.90 (m, 2H), 1.53 (br s, 2H), 1.35 (s, 12H), 1.21-1.30 (m, 17H).

5-((2-((tert-butoxycarbonyl)amino)ethyl)carbamoyl)isophthalic acid (4a). The compound was prepared according to the previous procedure. ¹H NMR (300 MHz, DMSO-d₆) δ [ppm]: 8.85 (br t, $J=5.27$ Hz, 1H), 8.59-8.66 (m, 2H), 8.51-8.59 (m, 1H), 6.92 (br t, $J=5.84$ Hz, 1H), 3.21-3.28 (m, 2H), 3.07-3.15 (m, 2H), 1.35 (s, 9H).

5-((2-((tert-butoxycarbonyl)amino)hexyl)carbamoyl)isophthalic acid (4b). The compound was prepared according to the previous procedure. ¹H NMR (300 MHz, DMSO-d₆) δ [ppm]: 8.80-8.92 (m, 1H), 8.63 (d, $J=1.70$ Hz, 2H), 8.56 (t, $J=1.60$ Hz, 1H), 6.78 (s, 1H), 2.89 (q, $J=6.59$ Hz, 2H), 1.48-1.59 (m, 2H), 1.36 (s, 11H), 1.29 (br s, 4H).

5-((2-((tert-butoxycarbonyl)amino)decyl)carbamoyl)isophthalic acid (4c). The compound was prepared according to the previous procedure. ¹H NMR (300 MHz, DMSO-d₆) δ [ppm]: 8.86 (br t, $J=5.46$ Hz, 1H), 8.62 (d, $J=1.51$ Hz, 2H), 8.55-8.59 (m, 1H), 6.75 (s, 1H), 2.83-2.92 (m, 2H), 1.53 (br s, 2H), 1.15-1.41 (m, 25H).

tert-butyl 2-(3,5-bis(dodecylcarbamoyl)benzamido)dodecylcarbamate (5d). Under argon 5-(12-(tert-butoxycarbonylamino)dodecylcarbamoyl)isophthalic acid (0.57 g, 1.157 mmol), dodecylamine (0.515 g, 2.78 mmol) and DMAP (0.014 g, 0.116 mmol) were stirred in CH₂Cl₂. EDC (0.395 g, 2.55 mmol) in 1 mL of CH₂Cl₂ was added and the solution was stirred for 20 h at 25 °C. The organic phase was diluted with 100 mL CH₂Cl₂ and successively washed with 1M HCl (2 x 50 mL) and saturated NaHCO₃ (2 x 50 mL). The organic layer was dried over Na₂SO₄, filtered and concentrated to obtain a white solid. The product was purified by column chromatography on silica gel with CH₂Cl₂/MeOH 20:1 as an eluent. ¹H NMR (300 MHz, DMSO-d₆) δ [ppm]: 8.64 (t, $J=5.65$ Hz, 3H), 8.35 (s, 3H), 6.75 (br s, 1H), 3.23-3.30 (m, 6H),

2.84-2.91 (m, 2H), 1.52 (br d, $J=6.97$ Hz, 6H), 1.36 (s, 11H), 1.21-1.31 (m, 52H), 0.81-0.89 (m, 6H).

tert-butyl 2-(3,5-bis(ethylcarbamoyl)benzamido)ethylcarbamate (5a). In a 0.1 M solution of LiCl (0.080 g, 1.892 mmol) in DMF (Volume: 18.92 mL), 5-(2-(*tert*-butoxycarbonylamino)ethylcarbamoyl)isophthalic acid (**4a**) (0.4 g, 1.135 mmol) was dissolved under argon. HBTU (1.033 g, 2.72 mmol) and TEA (0.380 mL, 2.72 mmol) were added. After stirring at room temperature for 15 min, ethylamine (1.249 mL, 2.498 mmol) was slowly added. The reaction mixture was stirred for further 24 h at room temperature. The reaction mixture was precipitated into water and the resulting white precipitate was filtered off and washed 2 times with water. If necessary the product was recrystallized from DMF. ^1H NMR (300 MHz, DMSO- d_6) δ [ppm]: 8.66 (br t, $J=5.37$ Hz, 3H), 8.36 (s, 3H), 6.92 (s, 1H), 3.23-3.32 (m, 6H), 3.04-3.13 (m, 2H), 1.35 (s, 9H), 1.11-1.16 (m, 6H).

tert-butyl 2-(3,5-bis(hexylcarbamoyl)benzamido)hexylcarbamate (5b). Under argon, 5-(6-(*tert*-butoxycarbonylamino)hexylcarbamoyl)isophthalic acid (**4b**) (1 g, 2.448 mmol), hexan-1-amine (0.712 mL, 5.39 mmol) and DMAP (0.030 g, 0.245 mmol) were dissolved in CH_2Cl_2 (Volume: 24.48 mL). EDC (1.126 g, 5.88 mmol) was added and the gelated mixture was sonicated for 5 min. After the gel dissolved, the reaction mixture was stirred at room temperature for 16 h. The organic phase was diluted with 100 mL CH_2Cl_2 and successively washed with 1M HCl (2 x 50 mL) and sat. NaHCO_3 (2 x 50 mL). The organic layer was dried over Na_2SO_4 , filtered and concentrated to obtain a brittle (foamlike) solid. ^1H NMR (300 MHz, DMSO- d_6) δ [ppm]: 8.66 (t, $J=5.56$ Hz, 3H), 8.35 (s, 3H), 6.68-6.86 (m, 1H), 3.23-3.32 (m, 6H), 2.89 (q, $J=6.53$ Hz, 2H), 1.52 (br d, $J=6.78$ Hz, 6H), 1.36 (s, 11H), 1.22-1.33 (m, 16H), 0.82-0.91 (m, 6H).

tert-butyl 2-(3,5-bis(decylcarbamoyl)benzamido)decylcarbamate (5c). The compound was prepared according to the previous procedure with the use of decylamine. ^1H NMR (300 MHz, DMSO- d_6) δ [ppm]: 8.64 (t, $J=5.56$ Hz, 3H), 8.35 (s, 3H), 6.75 (br t, $J=5.75$ Hz, 1H), 3.16-3.31 (m, 6H), 2.87 (q, $J=6.66$ Hz, 2H), 1.52 (br d, $J=6.59$ Hz, 6H), 1.36 (s, 11H), 1.21-1.32 (m, 40H), 0.81-0.89 (m, 6H).

*Didecyl 5-((10-((*tert*-butoxycarbonyl)amino)decyl)carbamoyl)isophthalate (7)*. Under argon, 5-(10-(*tert*-butoxycarbonylamino)decylcarbamoyl)isophthalic acid (0.3 g, 0.646 mmol), decan-1-ol (0.225 g, 1.421 mmol) and DMAP (7.89 mg, 0.065 mmol) were dissolved in DCM (Volume: 12.92 mL). EDC (0.297 g, 1.550 mmol) was slowly added and the mixture was stirred

at room temperature for 16 h. The organic phase was diluted with 100 mL CH₂Cl₂ and successively washed with 1M HCl (2 x 50 mL) and sat. NaHCO₃ (2 x 50 mL). The organic layer was dried over Na₂SO₄, filtered and concentrated to obtain a brittle (foamlike) solid. ¹H NMR (300 MHz, CHLOROFORM-d) δ [ppm]: 8.79 (t, J=1.60 Hz, 1H), 8.61 (d, J=1.51 Hz, 2H), 6.28 (s, 1H), 4.38 (s, 4H), 3.50 (q, J=6.59 Hz, 2H), 3.06-3.17 (m, 2H), 1.76-1.85 (m, 4H), 1.63-1.71 (m, 2H), 1.46 (s, 15H), 1.24-1.37 (m, 38H), 0.88-0.93 (m, 6H).

N1-(2-aminododecyl)-N3,N5-didodecylbenzene-1,3,5-tricarboxamide (TFA salt) (6d). A mixture of *tert*-butyl-12-(3,5-bis(dodecylcarbamoyl)benzamido)dodecylcarbamate (0.1 g, 0.121 mmol) and triisopropylsilane (0.050 mL, 0.242 mmol) in water (4.36 μL, 0.242 mmol) was stirred in CH₂Cl₂ (Volume: 2 mL). TFA (0.335 mL, 4.35 mmol) was added and stirred at room temperature for 2 h. The reaction mixture was precipitated into cold ether, resulting in a white precipitate that was filtered off and washed twice with ether. ¹H NMR (300 MHz, DMSO-d₆) δ [ppm]: 8.61-8.71 (m, 3H), 8.38 (s, 3H), 7.77 (br s, 3H), 3.27 (q, J=6.59 Hz, 6H), 2.71-2.81 (m, 2H), 1.52 (br s, 8H), 1.18-1.36 (m, 56H), 0.79-0.89 (m, 6H).

N1-(2-aminoethyl)-N3,N5-diethylbenzene-1,3,5-tricarboxamide (TFA salt) (6a). The compound was prepared according to the previous procedure. ¹H NMR (300 MHz, DMSO-d₆) δ [ppm]: 8.83 (br t, J=5.46 Hz, 1H), 8.72 (br t, J=5.56 Hz, 2H), 8.37-8.46 (m, 3H), 7.84 (br s, 3H), 3.50-3.54 (m, 2H), 3.25-3.37 (m, 4H), 2.95-3.07 (m, 2H), 1.14 (s, 6H).

N1-(2-aminohexyl)-N3,N5-dihexylbenzene-1,3,5-tricarboxamide (TFA salt) (6b). The compound was prepared according to the previous procedure. ¹H NMR (300 MHz, DMSO-d₆) δ [ppm]: 8.62-8.74 (m, 3H), 8.37 (s, 3H), 7.70 (br s, 3H), 3.23-3.35 (m, 6H), 2.73-2.87 (m, 2H), 1.47-1.59 (m, 8H), 1.25-1.38 (m, 16H), 0.82-0.92 (m, 6H).

N1-(2-aminodecyl)-N3,N5-didecylbenzene-1,3,5-tricarboxamide (TFA salt) (6c). The compound was prepared according to the previous procedure. ¹H NMR (300 MHz, DMSO-d₆) δ [ppm]: 8.61-8.71 (m, 3H), 8.36 (s, 3H), 7.65 (br s, 3H), 3.23-3.32 (m, 6H), 2.70-2.82 (m, 2H), 1.52 (br d, J=6.59 Hz, 8H), 1.25 (br d, J=6.78 Hz, 40H), 0.80-0.89 (m, 6H).

Dodecyl 5-((10-aminodecyl)carbamoyl)isophthalate (8). The compound was prepared according to the previous procedure. ¹H NMR (300 MHz, DMSO-d₆) δ [ppm]: 8.93 (s, 1H), 8.64 (d, J=1.51 Hz, 2H), 8.55-8.58 (m, 1H), 7.64 (br s, 2H), 4.33 (t, J=6.40 Hz, 4H), 2.72-2.79 (m, 2H), 1.68-1.80 (m, 4H), 1.52 (br d, J=4.90 Hz, 4H), 1.40 (br d, J=8.67 Hz, 4H), 1.16-1.37 (m, 38H), 0.79-0.89 (m, 6H).

PEG-N1-(2-aminododecyl)-N3,N5-didodecylbenzene-1,3,5-tricarboxamide (**1d**). N1-(2-aminododecyl)-N3,N5-didodecylbenzene-1,3,5-tricarboxamide (TFA salt) (0.06 g, 0.083 mmol) and methoxy-PEG-NHS (0.166 g, 0.083 mmol) were dissolved in DMF (Volume: 2 mL). TEA (2 mL, 14.35 mmol) was added and the solution was stirred for 20 h at room temperature. The reaction mixture was precipitated into ether, resulting in a white precipitate that was filtered off and washed twice with ether. ¹H NMR (300 MHz, DMSO-d₆) δ [ppm]: 8.64 (t, *J*=5.27 Hz, 3H), 8.35 (s, 3H), 7.85-7.90 (m, 1H), 7.73-7.79 (m, 1H), 3.51 (s, 152H), 3.39-3.44 (m, 16H), 3.27 (br d, *J*=6.40 Hz, 6H), 3.24 (s, 3H), 3.14-3.20 (m, 2H), 2.93-3.06 (m, 4H), 2.27 (s, 4H), 1.53 (br s, 6H), 1.18-1.36 (m, 54H), 0.85 (s, 6H). IR (solid/film) ν [cm⁻¹]: 2900 (w), 2886 (m), 1639 (w), 1550 (w), 1466 (w), 1342 (w), 1281 (w), 1146 (w), 1111 (s), 1061 (w), 964 (w), 845 (w).

PEG-N1-(2-aminoethyl)-N3,N5-diethylbenzene-1,3,5-tricarboxamide (1a). The compound was prepared according to the previous procedure. ¹H NMR (300 MHz, DMSO-d₆) δ [ppm]: 8.69 (br d, J=5.84 Hz, 3H), 8.38 (s, 3H), 7.96-8.02 (m, 1H), 7.87-7.94 (m, 1H), 3.40-3.46 (m, 6H), 3.29-3.40 (m, 154H), 3.24 (s, 3H), 3.13-3.21 (m, 2H), 2.59 (s, 2H), 2.27-2.35 (m, 4H), 1.15 (t, J=7.25 Hz, 6H)
IR (solid/film) ν [cm⁻¹]: 3588 (w), 3356 (w), 2870 (m), 1659 (e), 1539 (w), 1454 (w), 1366 (w), 1354 (w), 1288 (w), 1215 (w), 1103 (s), 1042 (w).

PEG-N1-(2-aminoethyl)-N3,N5-dihexylbenzene-1,3,5-tricarboxamide (1b). The compound was prepared according to the previous procedure. ¹H NMR (300 MHz, DMSO-d₆) δ [ppm]: 8.66 (t, J=5.56 Hz, 3H), 8.36 (s, 3H), 7.83-7.92 (m, 1H), 7.78 (t, J=5.46 Hz, 1H), 3.51 (s, 152H), 3.39-3.44 (m, 4H), 3.34 (s, 38H), 3.25-3.31 (m, 6H), 3.24 (s, 3H), 3.17 (br d, J=5.65 Hz, 2H), 3.01 (br d, J=6.03 Hz, 2H), 2.28 (s, 4H), 1.48-1.58 (m, 6H), 1.25-1.38 (m, 18H), 0.83-0.90 (m, 6H)
IR (solid/film) ν [cm⁻¹]: 2866 (m), 1740 (w), 1655 (w), 1539 (w), 1458 (w), 1350 (w), 1288 (w), 1258 (w), 1103 (s), 949 (w), 914 (w).

PEG-N1-(2-aminodecyl)-N3,N5-didecylbenzene-1,3,5-tricarboxamide (1c). The compound was prepared according to the previous procedure. ¹H-NMR (300 MHz, DMSO-d₆) δ [ppm]: 8.64 (br t, J=5.27 Hz, 3H), 8.35 (s, 3H), 7.84-7.94 (m, 1H), 7.76 (t, J=5.56 Hz, 1H), 3.51 (s, 152H), 3.40 (br s, 1H), 3.34 (s, 36H), 3.25-3.31 (m, 6H), 3.24 (s, 3H), 3.17 (br d, J=5.65 Hz, 2H), 2.99 (br d, J=6.03 Hz, 2H), 2.27 (s, 4H), 1.52 (br d, J=6.59 Hz, 6H), 1.21-1.35 (m, 42H), 0.80-0.89 (m, 6H)
IR (solid/film) ν [cm⁻¹]: 3525 (w), 2920 (w), 2882 (m), 1651 (w), 1539 (w), 1458 (w), 1350 (w), 1288 (w), 1254 (w), 1099 (w), 1036 (s), 949 (w).

PEG-Dodecyl 5-((10-aminodecyl)carbamoyl)isophthalate (2). The compound was prepared according to the previous procedure. ¹H NMR (300 MHz, DMSO-d₆) δ [ppm]: 8.85-8.97 (m, 1H), 8.63-8.67 (m, 2H), 8.55-8.59 (m, 1H), 7.83-7.91 (m, 1H), 7.72-7.80 (m, 1H), 4.31-4.38 (m, 4H), 3.46-3.56 (m, 152H), 3.42-3.45 (m, 6H), 3.22-3.25 (m, 2H), 3.11-3.22 (m, 2H), 2.93-3.05 (m, 2H), 2.27 (s, 4H), 1.75 (br d, J=6.59 Hz, 4H), 1.54 (br s, 2H), 1.24 (br s, 46H), 0.79-0.88 (m, 6H)
IR (solid/film) ν [cm⁻¹]: 2920 (w), 2882 (m), 1636 (w), 1543 (w), 1466 (w), 1342 (w), 1281 (w), 1134 (w), 1103 (s), 961 (w), 845 (w).

^1H NMR, DMSO, 300 MHz

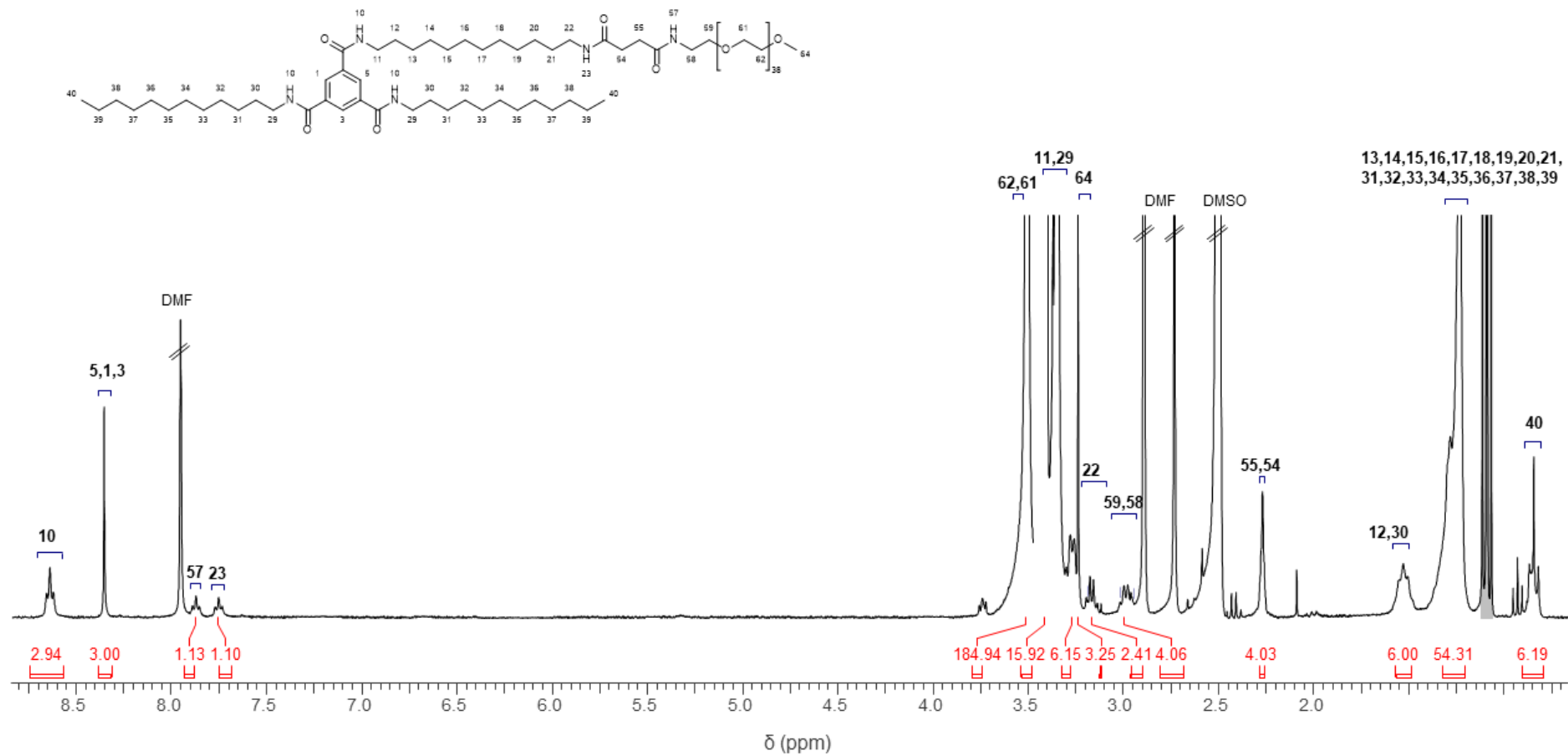


Figure S1: ^1H -NMR spectrum in DMSO- d_6 of BTA **1d**.

Size exclusion chromatograms of 1a-d and 2:

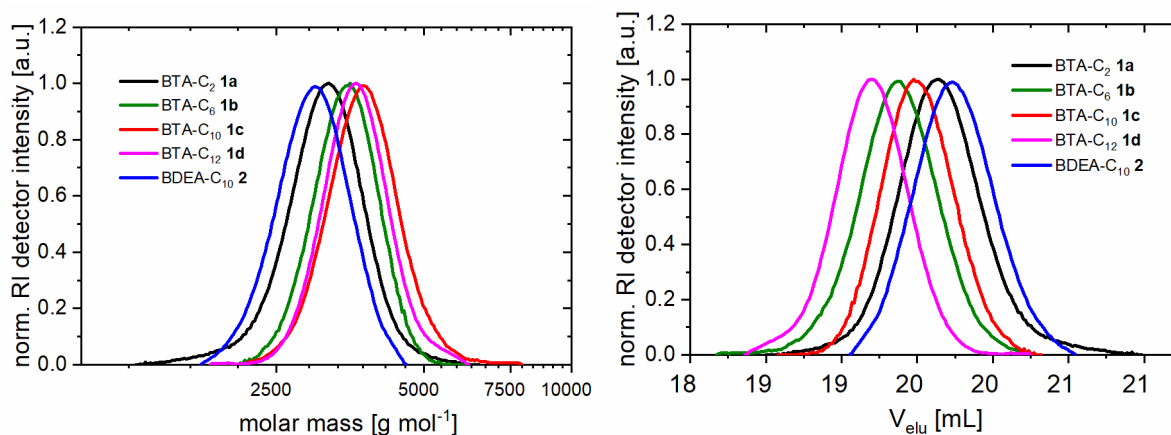


Figure S2: Size exclusion chromatograms of **1a-d** and **2** (left: normalized detector intensity vs. molar mass; right: normalized detector intensity vs. elution volume).

Dynamic light scattering:

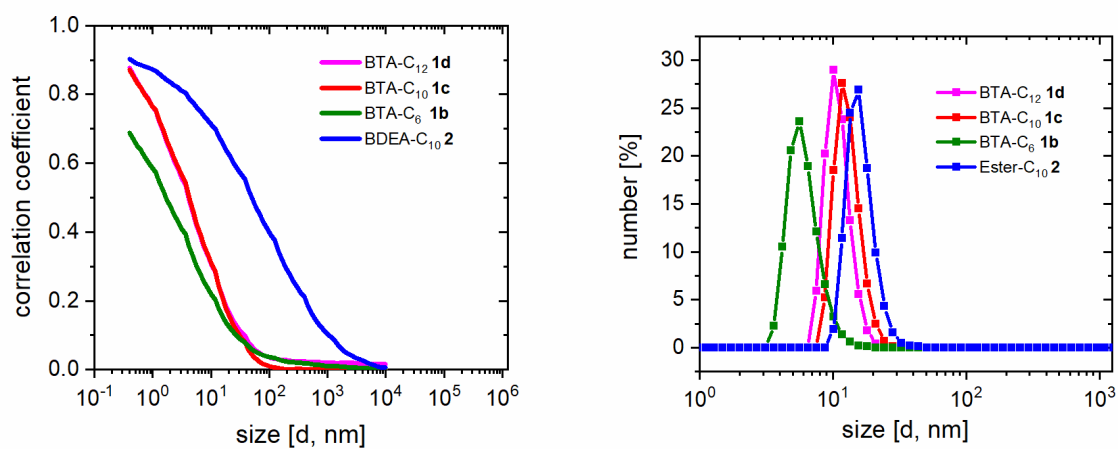


Figure S3: DLS correlograms (left) and distribution of the number-weighted hydrodynamic diameters (right) of **1a-d** and **2** at a concentration of $c=3 \text{ mg mL}^{-1}$.

CMC Determination via Nile red fluorescence

The micellar stability of the compounds was studied in more detail by determining the critical micelle concentration (CMC) using Nile red (NR) as fluorescent probe, according to a previously published protocol.⁶ Hence, aqueous solutions of **1b-d** were prepared in a concentration range from $c=1 \text{ mg mL}^{-1}$ down to $c=1 \times 10^{-9} \text{ mg mL}^{-1}$ and incubated with NR overnight. The fluorescence intensity of the NR emission was then measured as a function of the concentration (Figures S11-14). No solution was prepared for BTA-C₂ **1a**, as no aggregation could be observed via DLS, SANS and AUC. The CMC was determined as the intersection of the linear fits in the fluorescence intensity vs. the logarithmic concentration plots (Table S1). As expected, the CMC decreases from $215 \text{ } \mu\text{mol L}^{-1}$ for **1b** to $89 \text{ } \mu\text{mol L}^{-1}$ and $47 \text{ } \mu\text{mol L}^{-1}$ for **1c** and **1d**, respectively, due to the increasing hydrophobicity with increasing alkyl spacer length.

Table S1: CMC values of **1a-d** in $\mu\text{mol L}^{-1}$ and $\mu\text{g mL}^{-1}$ using Nile red as a fluorescent probe.

Compounds	CMC ($\mu\text{g mL}^{-1}$)	CMC ($\mu\text{mol L}^{-1}$)
BTA-C ₂ 1a	- ^a	- ^a
BTA-C ₆ 1b	495	215
BTA-C ₁₀ 1c	132	53
BTA-C ₁₂ 1d	120	47
BDEA-C ₁₀ 2	63	26

^a CMC values for BTA-C₂ were not determined as no aggregation could be observed in SANS, and AUC.

BTA-C₆ **1b**

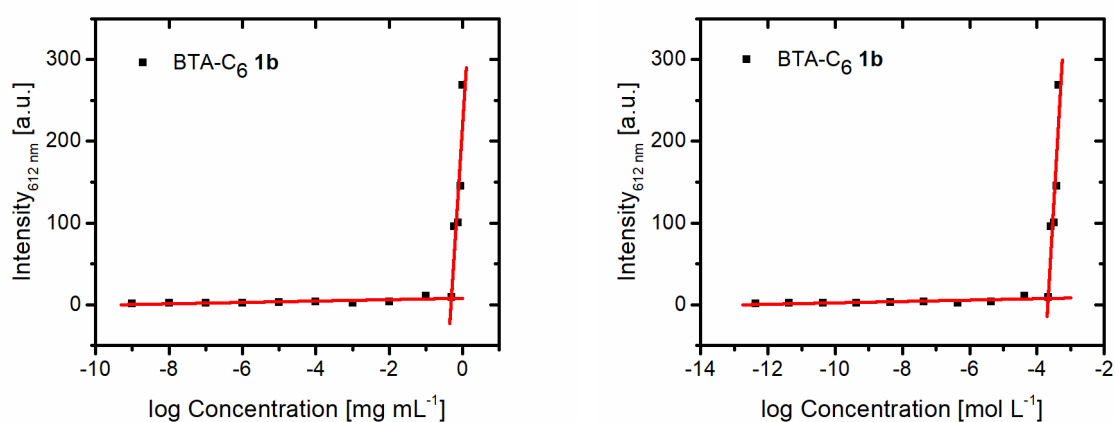


Figure S4: CMC determination of **1b** via the Nile red fluorescence intensity method. Left: Fluorescence intensity at 612 nm vs. logarithmic concentration in mg mL^{-1} ; right: Fluorescence intensity at 612 nm vs. logarithmic concentration in mol L^{-1} .

BTA-C₁₀ 1c

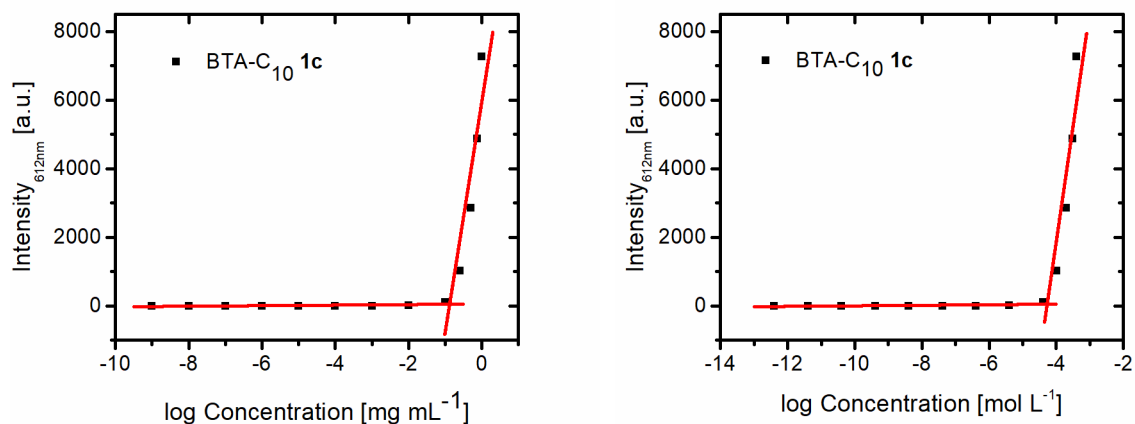


Figure S5: CMC determination of **1c** via the Nile red fluorescence intensity method. Left: Fluorescence intensity at 612 nm vs. logarithmic concentration in mg mL⁻¹; right: Fluorescence intensity at 612 nm vs. logarithmic concentration in mol L⁻¹.

BTA-C₁₂ 1d

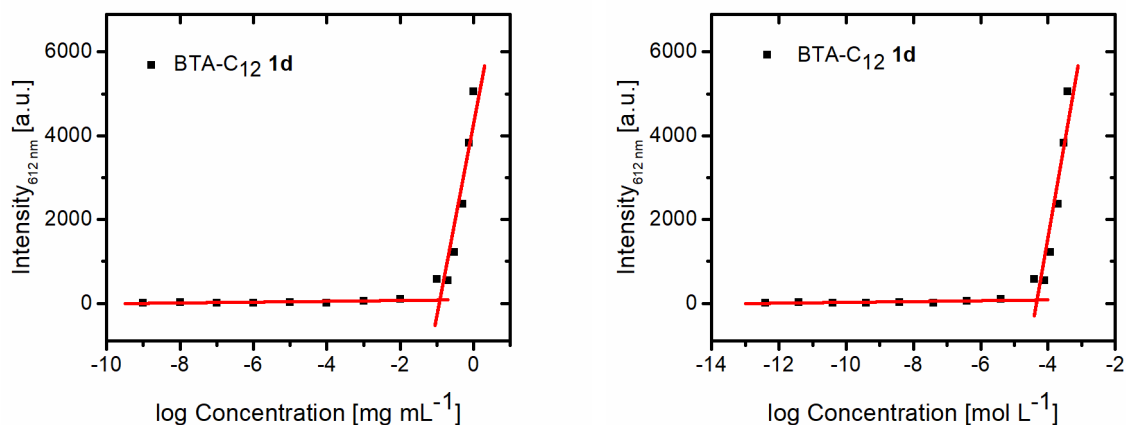


Figure S6: CMC determination of **1d** via the Nile red fluorescence intensity method. Left: Fluorescence intensity at 612 nm vs. logarithmic concentration in mg mL⁻¹; right: Fluorescence intensity at 612 nm vs. logarithmic concentration in mol L⁻¹.

BDEA 2

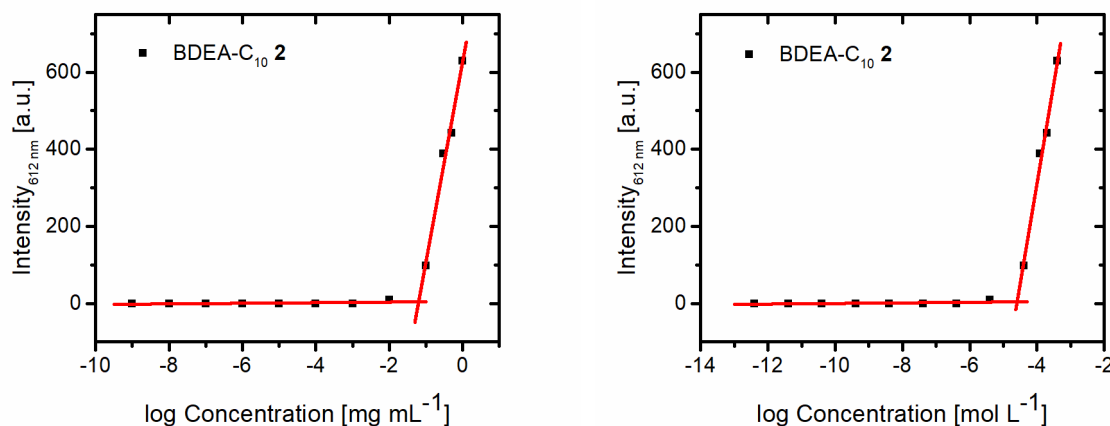


Figure S7: CMC determination of **2** via the Nile red fluorescence intensity method. Left: Fluorescence intensity at 612 nm vs. logarithmic concentration in mg mL⁻¹; right: Fluorescence intensity at 612 nm vs. logarithmic concentration in mol L⁻¹.

Small angle neutron scattering (SANS):

Small angle neutron scattering was carried out on the Sans2d small-angle diffractometer at the ISIS Pulsed Neutron Source (STFC Rutherford Appleton Laboratory, Didcot, U.K.).¹ A collimation length of 4 m and incident wavelength range of 1.75 – 16.5 Å was employed. Data were measured simultaneously on two 1 m² detectors to acquire a q-range of 0.0045 to 1.00 Å⁻¹. The small-angle detector was positioned 4 m from the sample and the vertical offset was 60 mm and sideways 100 mm. The wide-angle detector was positioned 2.4 m from the sample, offset sideways by 980 mm and rotated to face the sample. q is defined as:

$$q = \frac{4\pi \sin \frac{\theta}{2}}{\lambda} \quad (\text{Equation S1})$$

where θ is the scattered angle and λ is the incident neutron wavelength. The beam diameter was 8 mm. Each raw scattering data set was corrected for the detector efficiencies, sample transmission, background scattering, and finally converted to the scattering cross-section data ($\partial \Sigma / \partial \Omega$ vs. q) using the instrument-specific software.² These data were placed on an absolute scale (cm⁻¹) using the scattering from a standard sample (a solid blend of hydrogenous and per-deuterated polystyrene) in accordance with established procedures.³ The obtained reduced data was analyzed with the open access software SASfit.⁴ A form factor for a hypothetical Gaussian coil was used to fit the data obtained for BTA-C₂ (Table S2).

Table S2: Fitting parameters for BTA-C₂ using a form factor of a Gaussian coil.

Parameter	Values	
R_g , ^a (Å)	18.93 ± 0.70	Fitted
N	$3.17 \times 10^{13} \pm 8.01 \times 10^{11}$	
b_{polymer} ^b (Å)	2.62×10^{-8}	Calculated
V_{polymer} ^c (Å ³)	692.4	
ρ_{solvent} ^d (cm ⁻¹)	6.37×10^{-6}	
Background subtracted	1.65×10^{-3}	

^a Radius of gyration (R_g) of the polymer;

^b The scattering lengths b of the polymer was calculated using the calculator given in SASfit;

^c The volume of the whole conjugate was calculated as the sum of the individual parts;

^d The scattering lengths density (SLD) of the materials was calculated using the calculator given in SASfit.

In the other cases, scattering intensities were much higher, which indicated presence of larger structures. To estimate an average size, a radius of gyration was calculated from the slope in the Guinier plot (Figure S8) according to the following equation:

$$\ln(I) = \ln(I_0) - \frac{q^2 R_g^2}{3} \quad (\text{Equation S2})$$

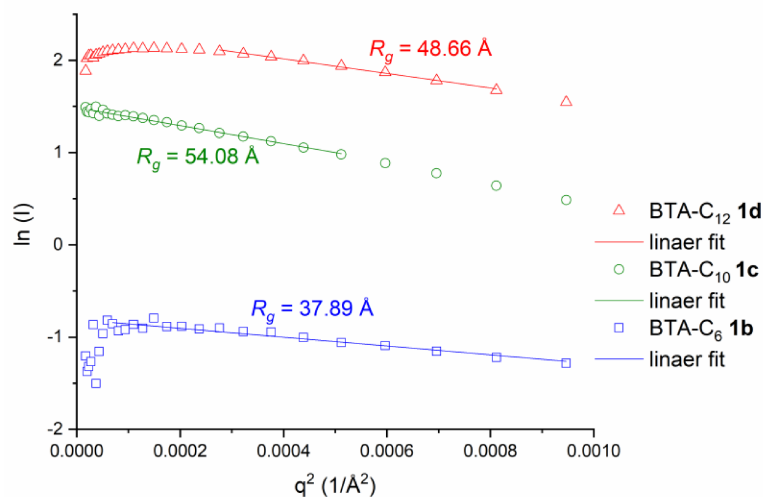


Figure S8: Guinier plot of the samples BTA-C₁₂ (red, $c = 10 \text{ mg mL}^{-1}$), BTA-C₁₀ (green, $c = 3 \text{ mg mL}^{-1}$), and BTA-C₆ (blue, $c = 3 \text{ mg mL}^{-1}$) obtained by SANS. The respective continuous lines represent linear fits for each sample in the linear part of the Guinier region of the scattering data ($qR_g \leq \sqrt{3}$), while the resulting radii of gyration (R_g) are given next to the curves.

For a more detailed analysis, the form factors, first for solid spheres but later also for spherical and cylindrical micelles were applied to fit the data (BTA-C₆: Table S3; BTA-C₁₀: Table S4; BTA-C₁₂: Table S5).⁵ The scattering data and the respective fits using a form factor for a solid sphere or a cylindrical micelle are plotted in Figure S9 and Figure S10, respectively.

Table S3: Fitting parameters for BTA-C₆ using a form factor for a sphere (top), spherical micelle (middle), and a cylindrical polymer micelle (bottom).

<i>Sphere</i>		
Parameter	Values	
R (Å)	45.09 ± 0.09	<i>(Fitted without distribution)</i>
σ (Gaussian standard deviation)	4.38 ± 0.12	Fitted
N	7.99 × 10 ⁻² ± 3.39 × 10 ⁻⁴	
ρ ^d (cm ⁻¹)	4.23 × 10 ⁻⁷	Calculated
ρ _{solvent} ^d (cm ⁻¹)	6.37 × 10 ⁻⁶	
Background subtracted	4.40 × 10 ⁻³	
Hard sphere radius (Å) ^f	120	

<i>Spherical polymer micelle</i>		
Parameter	Values	
N _{agg} ^a	28.21 ± 0.56	Fitted
R _{core} (Å)	16.71 ± 0.11	
R _{g, corona} ^b (Å)	18.27 ± 0.12	
N	1.54 × 10 ⁰ ± 6.07 × 10 ⁻²	
V _{core} ^c (Å ³)	692.4	Calculated
V _{corona} ^c (Å ³)	2788.5	
ρ _{core} ^d (cm ⁻¹)	8.73 × 10 ⁻⁷	
ρ _{corona} ^d (cm ⁻¹)	6.86 × 10 ⁻⁷	
ρ _{solvent} ^d (cm ⁻¹)	6.37 × 10 ⁻⁶	
d ^e	1	
Background subtracted	2.90 × 10 ⁻³	

<i>Cylindrical polymer micelle</i>		
Parameter	Values	
N _{agg}	27.99 ± 1.06	Fitted
R _{core} ^a (Å)	11.99 ± 0.54	
L _{core} ^a (Å)	42.92 ± 4.24	
R _{g, corona} ^b (Å)	16.02 ± 0.27	
N	1.54 × 10 ⁰ ± 7.53 × 10 ⁻²	Calculated
V _{core} ^c (Å ³)	692.4	
V _{corona} ^c (Å ³)	2788.5	
ρ _{core} ^d (cm ⁻¹)	8.73 × 10 ⁻⁷	
ρ _{corona} ^d (cm ⁻¹)	6.86 × 10 ⁻⁷	
ρ _{solvent} ^d (cm ⁻¹)	6.37 × 10 ⁻⁶	
d ^e	1	
Background subtracted	2.90 × 10 ⁻³	

^a The number of aggregation (N_{agg}) was calculated from the volume of the whole core (calculated from the radius or length and radius, respectively) divided by the volume of a single core unit (BTA);

^b Radius of gyration (R_g) of a single chain in the corona;

^c The volume of the core (BTA) or corona (PEG) was estimated from the M_n, divided by the Avogadro constant and assuming a density of 1.1 g/cm³;

^d The scattering lengths density (SLD) of the materials was calculated using the calculator given in SASfit;

^e d represents a penetration factor for chains of the brush entering the core with no penetration giving a value of 1.

Table S4: Fitting parameters for BTA-C₁₀ using a form factor for a sphere (top), spherical polymer micelle (middle), and a cylindrical polymer micelle (bottom).

<i>Sphere</i>		
Parameter	Values	
R (Å)	56.18 ± 0.16	
σ (Gaussian standard deviation)	13.59 ± 0.10	Fitted
N	1.24 × 10 ⁻¹ ± 8.15 × 10 ⁻⁴	
ρ ^d (cm ⁻¹)	4.23 × 10 ⁻⁷	Calculated
ρ _{solvent} ^d (cm ⁻¹)	6.37 × 10 ⁻⁶	
Background subtracted	4.40 × 10 ⁻³	
Hard sphere radius (Å) ^f	120	

<i>Spherical polymer micelle</i>		
Parameter	Values	
N _{agg} ^a	199.52 ± 0.67	Fitted
R _{core} (Å)	35.59 ± 0.04	
R _{g, corona} ^b (Å)	20.22 ± 0.06	
N	2.58 × 10 ⁻¹ ± 2.06 × 10 ⁻³	
V _{core} ^c (Å ³)	946.5	Calculated
V _{corona} ^c (Å ³)	2788.5	
ρ _{core} ^d (cm ⁻¹)	5.33 × 10 ⁻⁷	
ρ _{corona} ^d (cm ⁻¹)	6.86 × 10 ⁻⁷	
ρ _{solvent} ^d (cm ⁻¹)	6.37 × 10 ⁻⁶	
d ^e	1	
Background subtracted	2.50 × 10 ⁻³	

<i>Cylindrical polymer micelle</i>		
Parameter	Values	
N _{agg}	220.63 ± 0.83	Fitted
R _{core} ^a (Å)	28.81 ± 0.10	
L _{core} ^a (Å)	80.10 ± 1.69	
R _{g, corona} ^b (Å)	16.14 ± 0.21	
N	2.09 × 10 ⁰ ± 7.32 × 10 ⁻³	
V _{core} ^c (Å ³)	946.5	Calculated
V _{corona} ^c (Å ³)	2788.5	
ρ _{core} ^d (cm ⁻¹)	5.33 × 10 ⁻⁷	
ρ _{corona} ^d (cm ⁻¹)	6.86 × 10 ⁻⁷	
ρ _{solvent} ^d (cm ⁻¹)	6.37 × 10 ⁻⁶	
d ^e	1	
Background subtracted	2.50 × 10 ⁻³	

^a The number of aggregation (N_{agg}) was calculated from the volume of the whole core (calculated from the radius or length and radius, respectively) divided by the volume of a single core unit (BTA);

^b Radius of gyration (R_g) of a single chain in the corona;

^c The volume of the core (BTA) or corona (PEG) was estimated from the M_n, divided by the Avogadro constant and assuming a density of 1.1 g/cm³;

^d The scattering lengths density (SLD) of the materials was calculated using the calculator given in SASfit;

^e d represents a penetration factor for chains of the brush entering the core with no penetration giving a value of 1.

Table S5: Fitting parameters for BTA-C₁₂ using a form factor for a sphere (top), a spherical polymer micelle (middle), and a cylindrical polymer micelle (bottom).

<i>Sphere</i>		
Parameter	Values	
R (Å)	51.03 ± 0.04	
σ (Gaussian standard deviation)	12.76 ± 0.02	Fitted
N	5.00 × 10 ⁻¹ ± 7.89 × 10 ⁻⁴	
ρ ^d (cm ⁻¹)	4.23 × 10 ⁻⁷	Calculated
ρ _{solvent} ^d (cm ⁻¹)	6.37 × 10 ⁻⁶	
Background subtracted	4.40 × 10 ⁻³	
Hard sphere radius (Å) ^f	120	

<i>Spherical polymer micelle</i>		
Parameter	Values	
N _{agg} ^a	157.18 ± 0.14	Fitted
R _{core} (Å)	34.31 ± 0.01	
R _{g, corona} ^b (Å)	18.23 ± 0.01	
N	9.17 × 10 ⁻¹ ± 1.44 × 10 ⁻³	
V _{core} ^c (Å ³)	1073.5	Calculated
V _{corona} ^c (Å ³)	2788.5	
ρ _{core} ^d (cm ⁻¹)	4.23 × 10 ⁻⁷	
ρ _{corona} ^d (cm ⁻¹)	6.86 × 10 ⁻⁷	
ρ _{solvent} ^d (cm ⁻¹)	6.37 × 10 ⁻⁶	
d ^e	1	
Background subtracted	4.40 × 10 ⁻³	
Hard sphere radius (Å) ^f	120	

<i>Cylindrical polymer micelle</i>		
Parameter	Values	
N _{agg}	201.07 ± 0.29	Fitted
R _{core} ^a (Å)	28.62 ± 0.04	
L _{core} ^a (Å)	83.9 ± 0.4	
R _{g, corona} ^b (Å)	11.96 ± 0.09	
N	5.32 × 10 ⁻¹ ± 8.12 × 10 ⁻³	
V _{core} ^c (Å ³)	1073.5	Calculated
V _{corona} ^c (Å ³)	2788.5	
ρ _{core} ^d (cm ⁻¹)	4.23 × 10 ⁻⁷	
ρ _{corona} ^d (cm ⁻¹)	6.86 × 10 ⁻⁷	
ρ _{solvent} ^d (cm ⁻¹)	6.37 × 10 ⁻⁶	
d ^e	1	
Background subtracted	4.40 × 10 ⁻³	
Hard sphere radius (Å) ^f	120	

^a The number of aggregation (N_{agg}) was calculated from the volume of the whole core (calculated from the radius or length and radius, respectively) divided by the volume of a single core unit (BTA);

^b Radius of gyration (R_g) of a single chain in the corona;

^c The volume of the core (BTA) or corona (PEG) was estimated from the M_n, divided by the Avogadro constant and assuming a density of 1.1 g/cm³;

^d The scattering lengths density (SLD) of the materials was calculated using the calculator given in SASfit;

^e d represents a penetration factor for chains of the brush entering the core with no penetration giving a value of 1.

^f A structure factor of a hard sphere was applied to account for repulsive interactions in the sample.

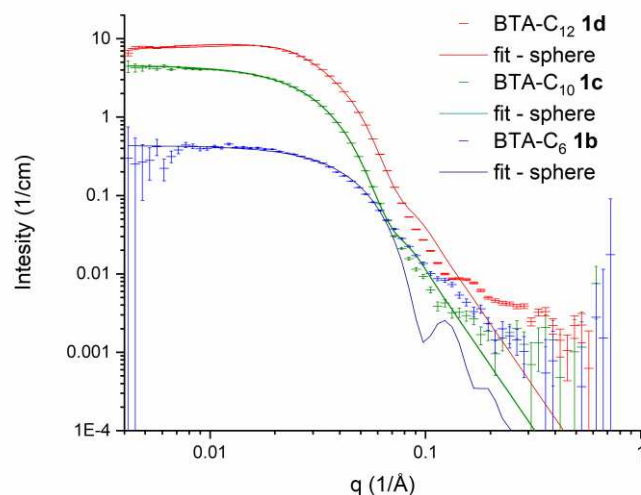


Figure S9: Scattering profiles of the samples BTA-C₁₂ 1d (red, $c = 10 \text{ mg mL}^{-1}$), BTA-C₁₀ 1c (green, $c = 3 \text{ mg mL}^{-1}$) and BTA-C₆ 1b (blue, $c = 3 \text{ mg mL}^{-1}$) obtained by SANS. The respective continuous lines represent the most appropriate fits for each sample using a form factor of a solid sphere.

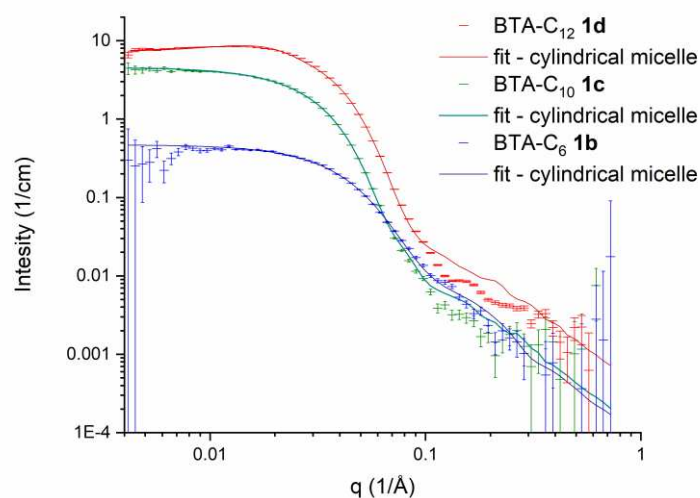


Figure S10: Scattering profiles of the samples BTA-C₁₂ 1d (red, $c = 10 \text{ mg mL}^{-1}$), BTA-C₁₀ 1c (green, $c = 3 \text{ mg mL}^{-1}$), BTA-C₆ 1b (blue, $c = 3 \text{ mg mL}^{-1}$), and BTA-C₂ 1a (gray, $c = 3 \text{ mg mL}^{-1}$) obtained by SANS. The respective continuous lines represent the most appropriate fits for each sample using a form factor of a cylindrical polymer micelle.

Analytical ultracentrifugation (AUC)

Table S6: Determined partial specific volumes, v , of the polymers/aggregates in solution from density increment measurements as described recently.⁷

Compound	$v, \text{cm}^3 \text{g}^{-1}$
BTA-C ₂ 1a	0.82
BTA-C ₆ 1b	0.84
BTA-C ₁₀ 1c	0.87 (0.89*)
BTA-C ₁₂ 1d	0.87
BDEA-C ₁₀ 2	0.86

*The value in brackets refers to an estimate in acetone according to the procedure described by Mächtle *et al.*⁸

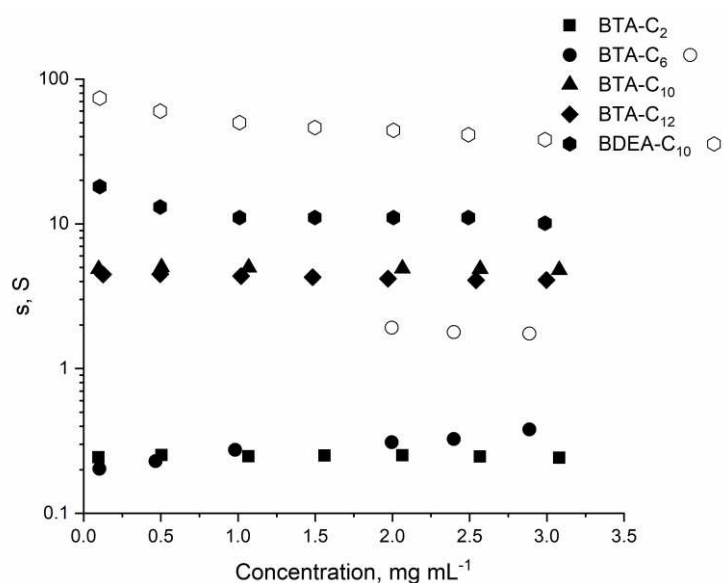


Figure S11: Plot of sedimentation coefficients, s , derived from sedimentation diffusion analysis, $c(s)$, against solution concentration for the polymers/aggregates (semilogarithmic). For the BTA-C₆ and the BDEA-C₁₀ two distinct populations, indicated by the filled and open symbols, are seen.

CryoTEM:

In each of the selected images the diameter of 100 micelles was counted and the diameter of the worms was measured for 50 times at different positions. The respective histograms could be established.

BTA-C₆ 1b

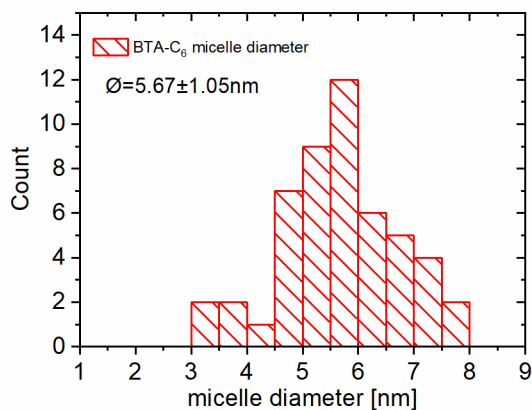


Figure S12: cryoTEM histogram of **1b**.

BTA-C₁₀ 1c

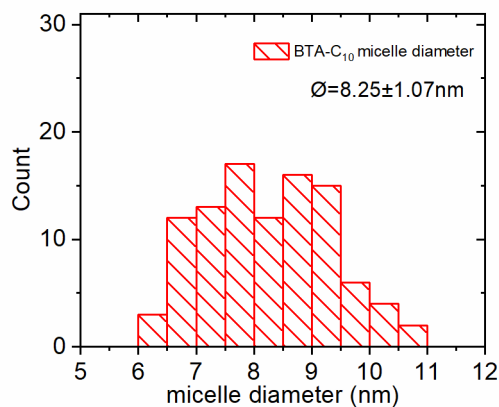


Figure S13: cryoTEM histogram of **1c**.

BTA-C₁₂ 1d

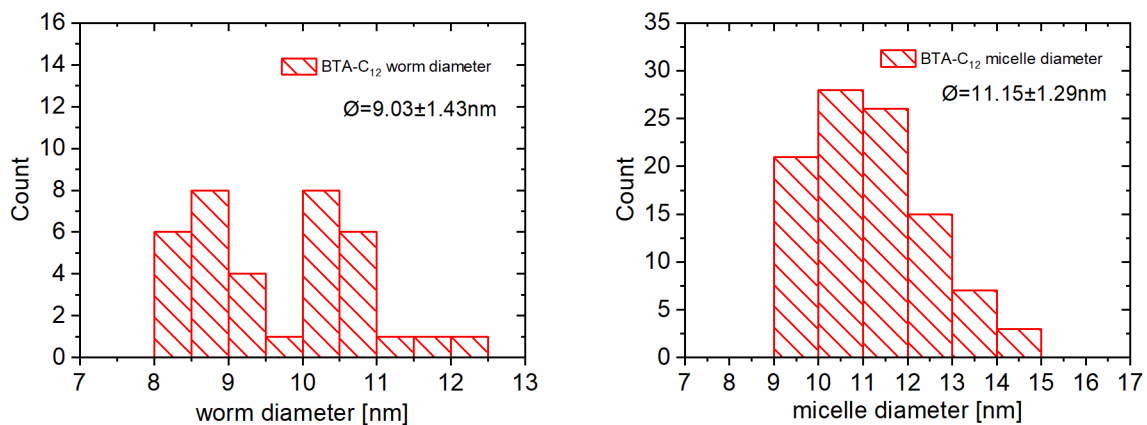


Figure S14: *cryo*TEM histograms of **1d** for the diameters of its worms (left) and spherical micelles (right).

BDEA-C₁₀ 2

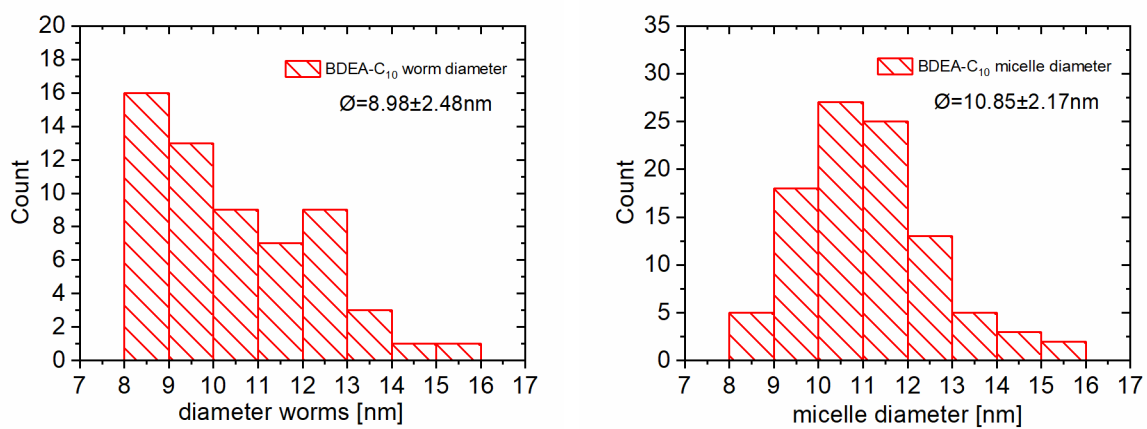


Figure S15: *cryo*TEM histograms of **2** for the diameters of its worms (left) and spherical micelles (right).

FTIR spectroscopy:

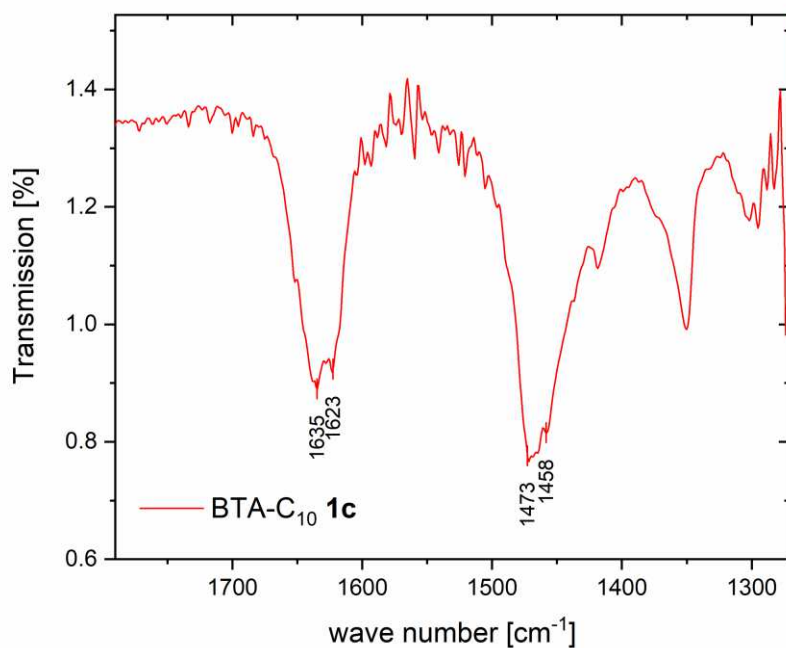


Figure S16: Solution-IR spectra of BTA-C₁₀ **1c** in D₂O.

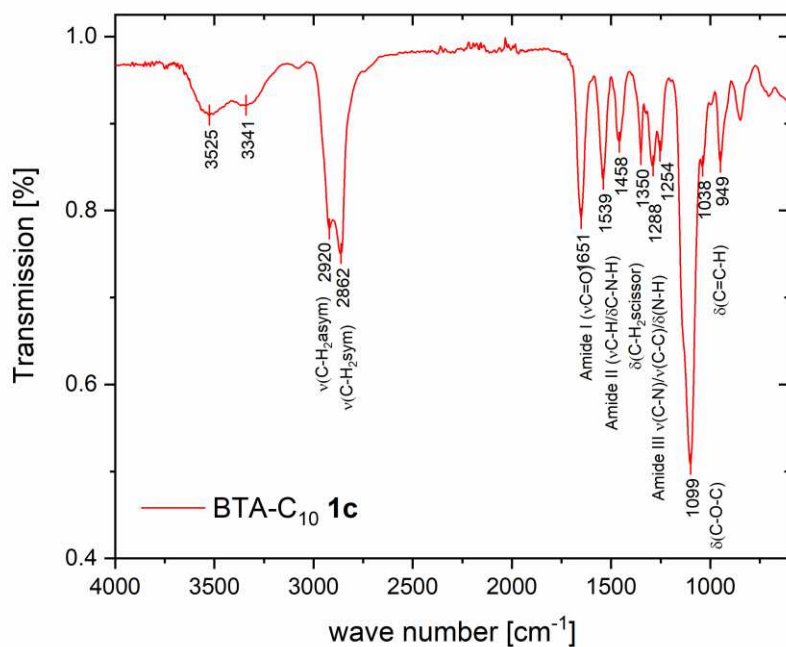


Figure S17: FTIR spectrum of BTA **1c** in the solid state.

Calculation of the surface area available for the hydrophilic headgroup by assumption of a solid sphere:

The area, a_0 , was calculated via the surface of a sphere, A , of a radius, r_c , obtained from fitting of SANS data, divided by the aggregation number, also calculated from fitted SANS data.

$$A = 4 \pi r_c^2 \quad (\text{Equation S3})$$

$$a_0 = A/N_{agg} \quad (\text{Equation S4})$$

Table S7: Calculation of surface area available for the hydrophilic headgroup

Substance	r_c (from SANS)	N_{agg} (from SANS)	a_0
BTA-C ₆ 1b	1.671 nm	28.21	1.244 nm ²
BTA-C ₁₀ 1c	3.559 nm	199.52	0.798 nm ²
BTA-C ₁₂ 1d	3.431 nm	157.18	0.941 nm ²

References:

1. R. K. Heenan, S. E. Rogers, D. Turner, A. E. Terry, J. Treadgold and S. M. King, *Neutron News*, 2011, **22**, 19-21.
2. <http://www.mantidproject.org>, 2015.
3. G. D. Wignall and F. S. Bates, *J. Appl. Crystallogr.*, 1987, **20**, 28-40.
4. I. Bressler, J. Kohlbrecher and A. F. Thunemann, *J. Appl. Crystallogr.*, 2015, **48**, 1587-1598.
5. J. Pedersen, *J. Appl. Crystallogr.*, 2000, **33**, 637-640.
6. M. K. Gupta, T. A. Meyer, C. E. Nelson and C. L. Duvall, *J Control Release*, 2012, **162**, 591-598.
7. M. Grube, M. N. Leiske, U. S. Schubert and I. Nischang, *Macromolecules*, 2018, DOI: 10.1021/acs.macromol.7b02665.
8. W. Mächtle, *Die Makromolekulare Chemie*, 1984, **185**, 1025-1039.

Publication P3

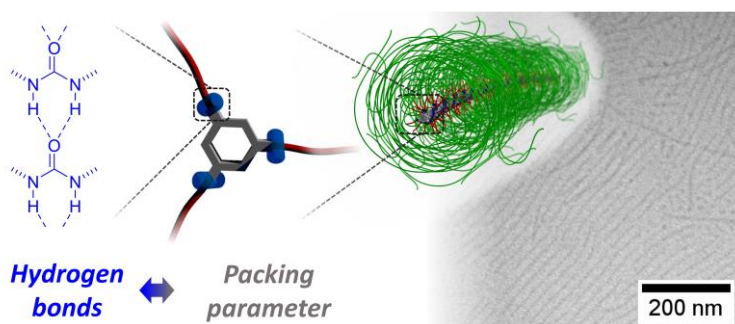
Unraveling decisive structural parameters for the self-assembly of supramolecular polymer bottlebrushes based on benzene trisureas

F. V. Gruschwitz, M.-C. Fu, T. Klein, R. Takahashi, T. Higashihara, S. Hoepfner, I. Nischang, K. Sakurai, J. C. Brendel, *Macromolecules* **2020**, *53*, 7552-7560.

Reproduced permission of the American Chemical Society. Copyright © 2020.

The paper as well as the supporting information is available online:

doi.org/10.1021/acs.macromol.0c01361



Unraveling Decisive Structural Parameters for the Self-Assembly of Supramolecular Polymer Bottlebrushes Based on Benzene Trisureas

Franka V. Gruschwitz, Mao-Chun Fu, Tobias Klein, Rintaro Takahashi, Tomoya Higashihara, Stephanie Hoepfner, Ivo Nischang, Kazuo Sakurai, and Johannes C. Brendel*

Cite This: *Macromolecules* 2020, 53, 7552–7560

Read Online

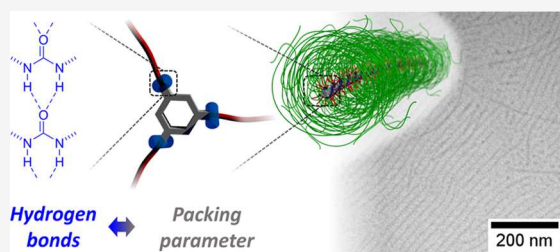
ACCESS |

Metrics & More

Article Recommendations

Supporting Information

ABSTRACT: By introducing strong directed hydrogen bonds to an amphiphilic polymer, we demonstrate that phase transitions from spherical to cylindrical morphologies in aqueous solutions can significantly be shifted to favor the assembly of supramolecular polymer bottlebrushes. In water, a forced self-assembly of polymers into cylindrical structures remains a challenge as the often required hydrophobic shielding induces forces, which tend to minimize the surface area. The herein presented novel benzene trisureas can overcome these limitations due to strong hydrogen bonds and alter the morphology to cylinders despite an unfavorable packing parameter, which dominated the previously reported trisamide analogues. The systematic variation of composition and architecture revealed that a transition to spherical morphologies still occurs, but the phase-transition boundaries appear to be shifted to tolerate larger hydrophilic polymer chains. The strength of the directing interactions appears to be decisive for the shift, though we additionally observed that any restrictions of lateral aggregation can diminish the effect of the directing hydrogen bonds. Overall, the straightforward synthesis and versatile design render the presented systems an interesting blueprint for the development of more advanced supramolecular polymer bottlebrushes and multifunctional nanostructures.



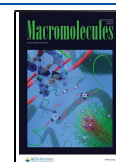
INTRODUCTION

Hierarchical structuring up to the mesoscopic scale is a key factor in life and of tremendous importance in biological systems such as proteins or membrane structures. The elongated shape of the tobacco mosaic virus¹ and the actin filaments and microtubules of the cytoskeleton^{2–4} are just a few examples of nature's hierarchical and functional supramolecular structuring concepts. Transferring this concept to synthetic materials has, therefore, gained increasing attention and inspired the design of artificial macromolecules, which feature intrinsic self-assembly properties.^{5,6} In particular, the assembly of functional polymers into cylindrical nanostructures, such as the above-mentioned examples from nature, promises unprecedented possibilities for areas of research such as nanomedicine,^{7,8} rheology,⁹ photonics, or organic electronics.^{10–12} In contrast to covalently linked materials,^{13–15} supramolecular systems offer a new assembly concept to mimic nature's structural ordering by facilitating dynamic processes within the assemblies.^{16–20}

A promising class of molecules prone to supramolecular self-assembly are peptides, which assemble into stable secondary structures such as β -sheets, thus offering a directional nonspherical assembly for their use in supramolecular chemistry (e.g., formation of supramolecular fiberlike structures).^{21,22} Their ability to form several parallel hydrogen bonds creates a sufficient supramolecular driving force to

assemble even large macromolecules into hierarchical structures.^{23,24} Apart from linear peptides, cyclic analogues comprising alternating L- and D-amino acids have attracted considerable attention,²⁵ as their strong tendency to aggregate tolerates the conjugation with various polymer chains resulting in the formation of supramolecular polymer bottlebrushes in solution.^{26–29} Despite numerous small molecules forming supramolecular polymers,^{17,20,30–34} non-peptide-based building blocks with the ability to organize polymers into supramolecular bottlebrushes remain scarce so far, in particular, if aqueous environments are considered.^{35–37} Only recently, efforts by the group of Rieger demonstrated the potential of such systems to drive the block-copolymer self-assembly toward cylindrical morphologies.^{38,39} Further synthetic alternatives to replace the most frequently used peptide motif as a structural organization unit could offer the advantage of scalable and straightforward synthetic procedures compared to the elaborate and sometimes costly peptide preparation. Typically, the formation of stable hydrogen bonds in the

Received: June 10, 2020
 Revised: August 3, 2020
 Published: August 20, 2020



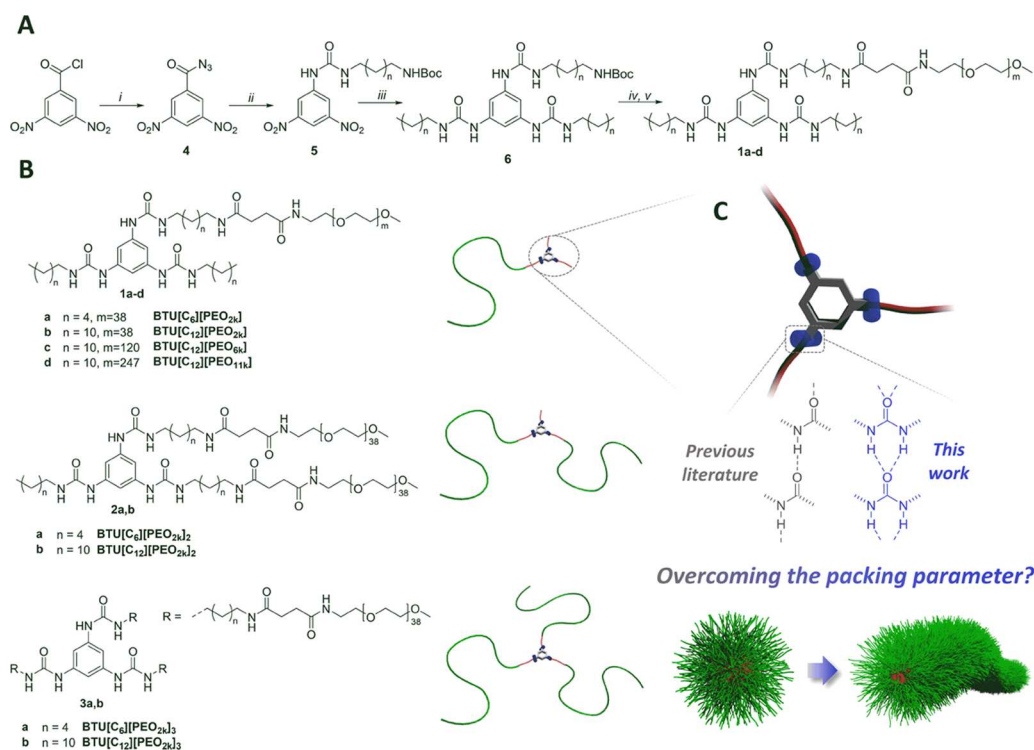


Figure 1. (A) Synthetic procedure for the synthesis of the BTU core with one polymer chain attached: (i) NaN_3 (aq); (ii) *tert*-butyl *n*-aminoalkylcarbamate; (iii) H_2 , Pd/C, alkylisocyanate; (iv) TFA; (v) NHS-PEO, TEA. (The detailed synthesis protocols for the BTU cores with two or three polymer chains attached can be found Schemes S2–S4 of the Supporting Information.) (B) Chemical structures of the molecular building blocks. (C) Schematic representation of the interactions in the self-assembly of benzene trisureas in comparison to the analogous amides published previously⁴⁷ to form supramolecular polymer bottlebrushes.

presence of water as a prime competitor for such interactions poses a challenge in promoting assembly in an aqueous environment. This issue could be overcome if multiple hydrogen-bonding units are combined in synergy as reported by Han et al.³⁶ A more common way is to shield the hydrogen-bond-forming groups from the water molecules by hydrophobic domains, usually consisting of aliphatic chains, which, in the case of a connected hydrophilic polymer generates an amphiphilic macromolecular structure.^{35,40,41} A key driving force for the assembly is then the hydrophobic effect, which, however, strives to minimize the surface area of the aggregates.^{42,43} Most amphiphilic polymers, therefore, tend to form spherical structures (spherical micelles or vesicles), and only in a small composition range (i.e., ratio of hydrophobic to hydrophilic domain), cylindrical morphologies are thermodynamically favored, although in reality, frequently mixed structures occur.^{44–46}

To investigate the impact of directed hydrogen bonds on supramolecular polymer assemblies, we previously studied a library of amphiphilic polymers comprising 1,3,5-benzene triscarboxamide (BTA) units.⁴⁷ Despite the presence of this well-known supramolecular building block, the composition or the packing parameter, respectively, remained the decisive parameter for the resulting morphology. This result motivated the question, whether the influence of the packing parameter can be minimized by adjusting the supramolecular forces created by the hydrogen bonds. In this work, we, therefore, designed similar amphiphilic polymers based on 1,3,5-substituted benzene trisureas (BTU)s to maintain comparable composition ratios but to increase the interaction strength. Urea groups are known for their ability to enable stronger

interaction forces due to a higher number of hydrogen bonds compared to, e.g., amides.⁴⁸ All materials were then thoroughly analyzed for their self-assembly behavior using electron microscopy, scattering techniques, and analytical ultracentrifugation to comprehensively evaluate the resulting morphology and composition.

EXPERIMENTAL SECTION

Synthesis. The synthesis of all BTU compounds and characterization by ¹H NMR, electrospray ionization-mass spectrometry (ESI-MS), matrix-assisted laser desorption ionization time-of-flight-mass spectrometry (MALDI-TOF-MS), and size exclusion chromatography (SEC) are described in detail in Supporting Information Section 1.

Cryogenic Transmission Electron Microscopy (cryoTEM). The cryoTEM measurements were performed on an FEI Tecnai G² 20 platform with an LaB₆ filament operated at 200 kV acceleration voltage. Samples were prepared on Quantifoil grids (R2/2), which were treated with Ar plasma prior to use for hydrophilization and cleaning. The solution (8.5 μL , 3 mg mL^{-1} in H_2O) was applied onto the grids utilizing an FEI Vitrobot Mark IV system (offset: -5 mm, blotting time: 1 s). After blotting, the samples were immediately plunged into liquid ethane to achieve vitrification. The samples were transferred to a Gatan cryo stage and subsequently into a Gatan cryo holder (Gatan 626) and were then transferred into a microscope by maintaining a temperature below -168 °C during the whole transfer and measurement process after vitrification. Images were acquired with a MegaView (OSIS, Olympus Soft Imaging Systems) or an Eagle 4k CCD camera. Micrographs were adapted in terms of brightness and contrast using the software ImageJ 1.47v. Full-sized images can be found in Supporting Information Section 2.

Light Scattering. Dynamic light scattering (DLS) was performed on a ZetaSizer Nano ZS (Malvern, Herrenberg, Germany) equipped with a He–Ne laser operating at a wavelength of $\lambda = 633$ nm. Measurements were performed at 25 °C and a scattering angle of

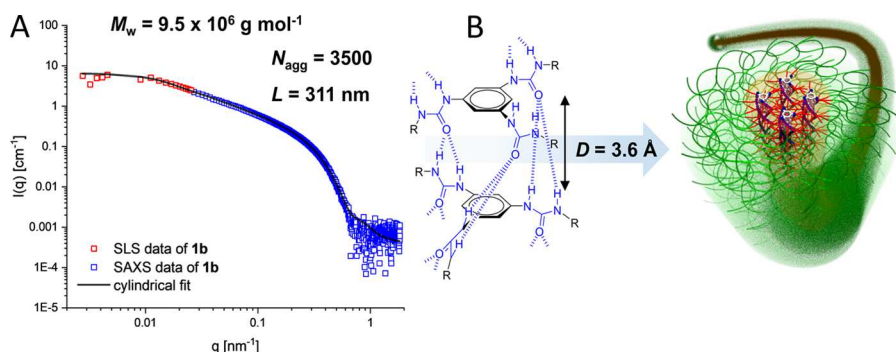


Figure 2. (A) Scattering profile of BTU[C₁₂][PEO_{2k}] **1b** obtained by SLS (red squares) and SAXS (blue squares) and a cylindrical fit (black line) of the combined data ($c = 1.5 \text{ mg mL}^{-1}$). (B) Proposed arrangement of BTU[C₁₂][PEO_{2k}] molecules in the cross section of the formed fibers based on the results obtained from the scattering data and assuming a distance of 3.6 Å between the BTU cores.

173° in quartz glass cuvettes in triplicate with an acquisition time of 60 s after an equilibration time of 60 s.

Static light scattering (SLS) measurements of compound **1b** were conducted at scattering angles of $\theta = 12\text{--}150^\circ$ (scattering vector q varying from 2.76×10^{-3} to $2.56 \times 10^{-2} \text{ nm}^{-1}$) on an ALVCGS-3 instrument with a He–Ne laser operating at a wavelength of $\lambda_0 = 633 \text{ nm}$ at 25 °C. Detailed information on light scattering experiments and data treatment can be found in Supporting Information Section 3.

Small-Angle X-ray Scattering (SAXS). Synchrotron SAXS measurements were conducted at the beamline BL40B2, SPring-8, Hyogo, Japan. The sample solution was poured into a quartz capillary cell and maintained at 25 °C. The scattering intensity $I(q)$ was detected by PILATUS (Dectris, Barden, Switzerland) at a sample-to-detector distance of 1 or 4 m. The obtained reduced data were analyzed with the open-access software SASfit.⁴⁹ All fit parameters and additional treatment of the data can be found in Supporting Information Section 3.

Analytical Ultracentrifugation (AUC). Sedimentation velocity experiments were performed with a ProteomeLab XL-I analytical ultracentrifuge (Beckman Coulter Instruments, Brea, CA). The cells, containing double-sector epon centerpieces with a 12 mm optical solution path length, were placed in an An-50 Ti eight-hole rotor. A typical rotor speed of 42 000 rpm was used. The cells were filled with 420 μL of sample solution in water and with 440 μL of water in the reference sector. The experiments were typically conducted for 24 h and at a temperature of $T = 20.0 \text{ }^\circ\text{C}$. Sedimentation velocity profile scans were recorded with interference optics (refractive index (RI)). A suitable selection of scans was used for data evaluation with Sedit using the $ls - g^*(s)$ model, i.e., by least-squares boundary modeling with a Tikhonov–Phillips regularization procedure and by assuming nondiffusing species.⁵⁰ This model results in an apparent differential distribution of sedimentation coefficients, s . The differential distributions of the sedimentation coefficients, $ls - g^*(s)$, of BTU[C₆][PEO_{2k}] **1a** and additional data evaluation using the $c(s)$ model⁵¹ can be found in Supporting Information Section 4.

RESULTS AND DISCUSSION

Synthesis. Conveniently, the synthesis of the presented materials is based on well-established isocyanate chemistry, which favors a straightforward synthetic access to a variety of modifications based on the BTU motif (see Figure 1A for details). Starting from commercially available 3,5-dinitrobenzoyl chloride, first, the corresponding carbonyl azide **4** was synthesized. A subsequent Curtius rearrangement yielded the isocyanate, which was in situ reacted with a mono-boc-protected alkyl (hexyl or dodecyl) diamine (C₆ or C₁₂ spacer). After hydrogenation of the nitro groups on **5**, alkyl-isocyanates of the corresponding lengths were attached to the resulting amino groups to finalize the trisurea core motif **6**. The poly(ethylene oxide) polymers (PEO) were then connected to

these cores by amide groups, which were formed from an activated *N*-hydroxysuccinimide (NHS) ester, after removal of the boc-group. Following this procedure, we synthesized a small library of benzene trisurea compounds (BTUs **1–3**) (Figure 1B) to evaluate their structure-forming ability (synthetic procedures for two- and three-armed compounds can be found in Schemes S3 and S4 of the Supporting Information). In accordance with our previous work, the length of the alkyl spacer was varied to comprise 6 or 12 methylene units, which results in two different overall compositions in case of shorter PEO (PEO_{2k}, $M_n = 1900 \text{ g mol}^{-1}$ according to SEC). To further extend the tested compositions, the length of the hydrophilic polymer was varied from 5600 g mol^{-1} (PEO_{6k}) to 11 200 g mol^{-1} (PEO_{11k}). The increased chain length of the polymer should also provide insight into the impact of the steric constraint of the attached chains on the self-assembly (Figure 1C). In addition, we further evaluated the influence of the number of PEO polymer chains attached to our supramolecular core motifs, which not only causes an increased steric demand but may also hamper an additional lateral aggregation or bundling of columnar stacks of the unimers. To vary the number of attached polymers to the core motifs, the synthesis was slightly adapted (for details, see Schemes S3 and S4 of the Supporting Information). Overall, all materials could be obtained in reasonable yields, quantities, and purity, circumventing chromatographic purification procedures (see the Supporting Information for experimental details).

For convenience, a comparable nomenclature for all compounds is introduced. BTU[C_{*n*}][PEO_{*x*}]_{*y*} refers to the benzene trisurea (BTU) analogous to the previously used benzene trisamides (BTA)s as the core motifs,⁴⁷ n represents the respective alkyl spacer length for hexyl [C₆] or dodecyl [C₁₂] chains, and x describes the molar mass of the PEO as already mentioned above ($x = 2 = 2k, 6k, \text{ or } 11k$), while y refers to the number of attached polymer chains to the core unit ($y = 1, 2, 3$).

Morphology after Self-Assembly in Aqueous Solution. Just upon dissolution of the compounds in water, aggregation could be proven for all compounds by DLS measurements, except for BTU[C₆][PEO_{2k}]₂ **2a** and BTU[C₆][PEO_{2k}]₃ **3a** (Figure S18). The latter compounds were, therefore, not further considered in the following study. All other samples were analyzed in more detail by cryoTEM to provide visual indication of the resulting apparent morphologies. In case of compound BTU[C₆][PEO_{2k}] **1a**, only very small

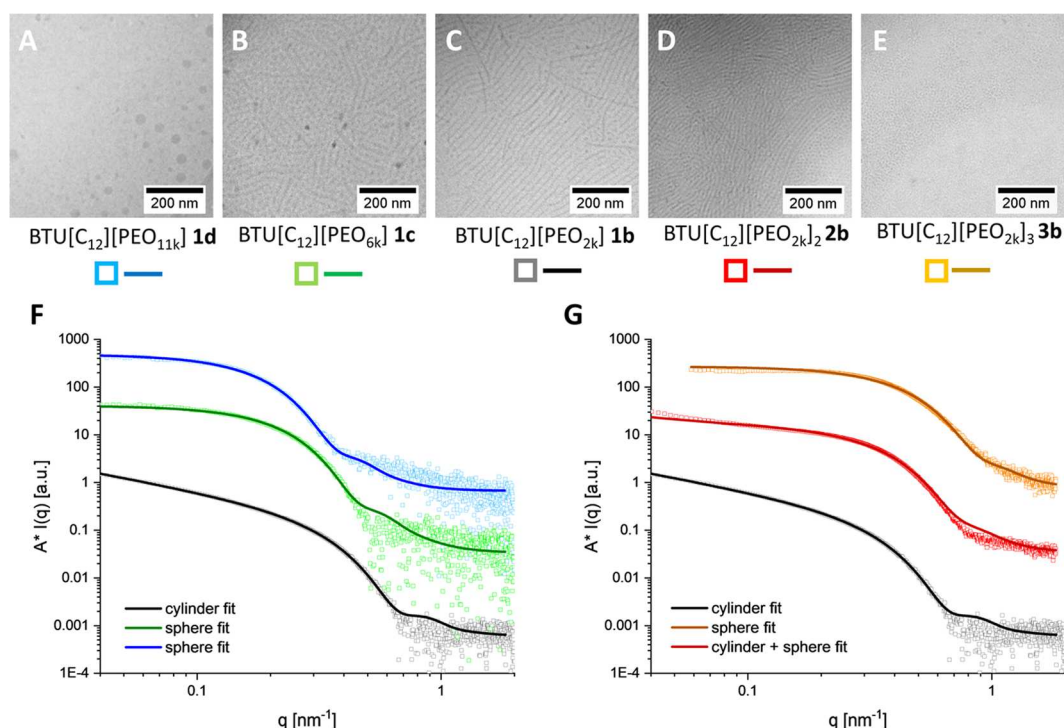


Figure 3. cryoTEM images of BTU[C₁₂][PEO_{11k}] **1d** (A), BTU[C₁₂][PEO_{6k}] **1c** (B), BTU[C₁₂][PEO_{2k}] **1b** (C), BTU[C₁₂][PEO_{2k}]₂ **2b** (D), and BTU[C₁₂][PEO_{2k}]₃ **3b** (E) in water at $c = 5 \text{ mg mL}^{-1}$ (full-sized images can be found in Supporting Information Figure S20). Scattering profiles of **1b** (gray), **1c** (green), and **1d** (blue) at a concentration of $c = 1.5 \text{ mg mL}^{-1}$ (F). Scattering profiles of **3b** (red) and **2b** (orange) at a concentration of $c = 10 \text{ mg mL}^{-1}$, and **1b** (gray) (depicted again for comparison) (G) obtained by SAXS. In the case of **2b**, the extended q range ($q < 0.06$) was not further examined as a constant plateau was already observed.

spherical micelles were observed, which are comparable to the previously reported assemblies formed by the respective amide analogue (Figures S19 and S21, Table S1).⁴⁷ However, an increase of the spacer length to 12 methylene units in compound BTU[C₁₂][PEO_{2k}] **1b** resulted in the appearance of pure fiberlike structures (Figure 3C) with an apparent average diameter of 7.6 nm. A clear estimation of the lengths from cryoTEM is challenging, since the ends of the fibers are exceeding the imaged area (full-sized images and histograms of distributions in the diameter estimated from cryoTEM for all compounds can be found in Figures S20 and S21 of the Supporting Information). The fiber morphology is particularly interesting, considering the similarity of the used unimeric compounds and our previously reported BTA analogue, which mostly formed spherical micelles. The only difference appears to be the presence of urea groups instead of amide moieties.⁴⁷

Additionally, small-angle X-ray scattering (SAXS) measurements confirmed the morphology as the scattering intensity $[I(q)]$ scales with q^{-1} at low q values, which is indicative of the formation of cylindrical structures (Figure 3F,G), where q denotes the magnitude of the scattering vector. However, the SAXS data provide no further information about the average length of these cylinders as the q^{-1} dependence still continues at the lower limit of detection. To extend the accessible window of observation, we additionally analyzed the samples by static light scattering (SLS) experiments (Figure S27). Even in this case, a q^{-1} dependence can be observed closer to the upper q -limit, but a plateau is formed at q values below $9 \times 10^{-3} \text{ nm}^{-1}$. Combining the data of both scattering techniques⁵² (Figure 2A; see the Supporting Information for details), a model of a cylinder with a radius R_{cyl} of 5.0 nm and a length L_{cyl} of 311 nm can be fitted. A Gaussian distribution was

applied to the radius to match the observed smooth oscillation at high q values, which is most likely related to the distribution and the fuzzy nature of the PEO shell with solvated chains reaching into the solvent. Furthermore, the radius of gyration of the cross section R_{cs} was determined via a cross-sectional plot to be 6.2 nm (Figure S26). Assuming a solid cylinder, the previously described radii should follow the relationship $R_{\text{cs}} = R_{\text{cyl}}/\sqrt{2}$. The deviation from this relationship is related to a more complex core-shell structure of the cylindrical micelles with the solvated hydrophilic polymer chains protruding into the solvent, instead of a uniform electron density profile applied in the cylindrical model.⁵³ The Guinier analysis results in a radius of gyration (R_g) of 66 nm, fitting the plateau at low q values. Considering an average length of 311 nm from the fit, and an intermolecular distance of 3.6 Å between the BTU units, as reported previously for similar systems,⁵⁴ rationally, a maximum number of about 840 unimers can then be stacked in the average cylinder. However, the overall molar mass was determined by SLS to be $9.5 \times 10^6 \text{ g mol}^{-1}$, which results in a number of aggregation of unimeric building units to $N_{\text{agg}} = 3500$ per cylinder considering a molar mass of 2800 g mol^{-1} for the unimer. This discrepancy can only be explained if the assembly of BTU[C₁₂][PEO_{2k}] **1b** is not considered a single columnar stack, but contains a lateral arrangement of four unimers per unit cross section (Figure 2B, Tables S5 and S6, eqs S4 and S5).

To further elucidate the impact of the composition on this assembly, the compounds **1c** and **1d** were examined next, which feature longer polymer chains (PEO_{6k} or PEO_{11k}). For BTU[C₁₂][PEO_{6k}] **1c**, a plateau is observed at high q values in the SAXS data (Figure 3F), which already indicates a morphology transition from elongated structures found for

1b to considerably shorter assemblies. The corresponding cryoTEM images (Figure 3B) confirm the presence of mostly spherical structures, but some cylinders can still be identified, indicating that the system is close to a phase-transition boundary from spherical to cylindrical morphologies. Despite the mixed morphologies in the images, the SAXS data can be well fitted with a spherical model, which confirms the preponderance of the isotropic spherical morphology (Figure 3A). Hereby, a radius R_{sphere} of 8.6 nm is determined (a Gaussian distribution was applied; see SI for details, Table S1) and the Guinier plot analysis results in an R_g of 8.6 nm (Figure S26). Similar to the above-discussed relationship between R_{cs} and R_{cyl} , the deviation from the expected correlation $R_g = \sqrt{\frac{3}{5}} R_{\text{sphere}}$ is related to the polymer corona of the assemblies. These PEO chains are solvated and do not reflect a sharp interface as considered in the applied spherical fit. With an overall molar mass of $1.0 \times 10^6 \text{ g mol}^{-1}$ obtained by SAXS measurements, an N_{agg} of approximately 165 was calculated (Table S1, Figure S26). Considering the limited extension of the hydrophobic domain in the polymer molecules, their arrangement into a spherical morphology would mean structural irregularities for such a rather high number of aggregation. In addition, a model of a short cylinder was therefore tested as an alternative morphology (Figure S25A). A similarly adequate fit is obtained with cylinder dimensions of $L_{\text{cyl}} = 14.7 \text{ nm}$ and with an R_{cyl} of 8.0 nm (for R_{cyl} , a Gaussian distribution was applied; see Table S2). Due to the random orientation of these small cylinders in the vitrified ice film in cryoTEM, it is reasonable to assume that the projection of the aggregates results in a spherical-like appearance of the aggregates. Furthermore, the estimated length from the fit corresponds to 41 stacked units (vide supra), which nicely matches the number of aggregation of 165, if again a cross section comprising four molecules is assumed, as found for compound **1b** (eq S5). For compound $\text{BTU}[\text{C}_{12}][\text{PEO}_{11k}]$ **1d**, finally, no further cylindrical structures are present in the cryoTEM images, but rather ill-defined spherical structures are observed (Figure 3A). This result confirms an increased interference of the longer polymer chains on the self-assembly process. In SAXS, an R_{sphere} of 10.5 nm (for R_{sphere} , a Gaussian distribution was applied; Table S1) can be calculated by fitting the corresponding data with a spherical model (Figure 3F) and the Guinier analysis (Table S1, Figure S26) provides an R_g of 10.6 nm with a molar mass of $1.1 \times 10^6 \text{ g mol}^{-1}$ ($N_{\text{agg}} = 98$). Similar to the compounds **1b** and **1c**, we also tested a cylindrical model for **1b**, and the fit gave an L_{cyl} of 17.2 nm and an R_{cyl} of 10.6 nm (for R_{cyl} , a Gaussian distribution was applied; see Table S2 and Figure S25A). Apparently, in this case, the calculated N_{agg} does not correlate to the length of the above-discussed cylindrical aggregates (**1b** and **1c**, four molecules in the cross section). Only about two molecules can be present in the cross section if the length L_{cyl} of 17 nm and an N_{agg} of 98 are used for the corresponding calculation (eq S5). Since compound **1d** comprises a considerably longer PEO chain compared to **1c** and **1b**, stronger steric demands are expected, which might impede a similar lateral aggregation. Overall, these results corroborate the impact of the composition and the importance of the packing parameter for these amphiphilic polymers, although the boundaries of the phase transition can be shifted by the presence of urea groups inducing strong directional hydrogen bonds.

An additional aspect, which needs to be considered in such self-assembled nanostructures, is the design and architecture of the amphiphile. The compounds $\text{BTU}[\text{C}_{12}][\text{PEO}_{2k}]_2$ **2b** and $\text{BTU}[\text{C}_{12}][\text{PEO}_{2k}]_3$ **3b** comprise two or three polymer chains attached to the core motifs, respectively, creating a bola-amphiphilic structure. According to cryoTEM images, $\text{BTU}[\text{C}_{12}][\text{PEO}_{2k}]_2$ **2b** mostly aggregated in the form of fibers (Figure 3D), but in comparison to **1b**, a significant population of smaller aggregates is visible as well. For this material, the presence of a mixed population morphology is further supported by the $q^{-0.6}$ decay in the low- q region of the SAXS measurements (Figure 3G), which can be fitted by a combination of two models for smaller spherical structures and long cylinders. Due to the limited information on the length of the long cylinders, the ratio between both the present morphologies cannot be calculated from the SAXS data. Nevertheless, an estimation of the radius of the structures is possible, which gives an R_{sphere} of 5.1 nm and an R_{cyl} of 4.3 nm for the spheres and cylinders, respectively (for R_{cyl} and R_{sphere} , a Gaussian distribution was applied; Table S3). Due to the rather high difference in these radii, we also considered a fit using the same long cylinder, but replacing the spherical model with a short cylinder model, as already applied for the compounds **1c** and **1d**. Although such a combination of models is accompanied by some uncertainties, the scattering data can be similarly well fitted with two different cylinders (Figure S25B), which gives an $R_{\text{cyl_short}}$ of 4.8 nm and an $R_{\text{cyl_long}}$ of 4.3 nm for the short and long cylinders, respectively (for $R_{\text{cyl_short}}$ and $R_{\text{cyl_long}}$, a Gaussian distribution was applied; Table S4). Unfortunately, a calculation of the cross section as for the previous compounds (**1b–1d**) is not possible, as the overall molar mass could not be determined. However, the radius for the cylinders of **2b** is smaller than for compound **1b**, although an additional polymer chain is present. Therefore, we conclude that the lateral aggregation is already impaired. A further increase of the number of polymer arms to three ($\text{BTU}[\text{C}_{12}][\text{PEO}_{2k}]_3$ **3b**) resulted in a purely spherical morphology, which is indicated by a plateau in the Guinier region at low q values (Figure 3G). From the corresponding sphere fit, an R_{sphere} of 4.2 nm is estimated, while the Guinier plot gives a radius of gyration R_g of 4.1 nm (for R_{sphere} , a Gaussian distribution was applied; Table S1, Figure S26). These results are further corroborated by cryoTEM, where only very small particles can be observed (Figure 3E). Considering the results on compounds **1** featuring only one polymer chain, a morphology transition can certainly be expected due to the increased ratio of hydrophilic to hydrophobic content by the additional polymer chains. Nevertheless, it is noteworthy that the radii decrease for compounds **2b** and **3b** in comparison to compound **1b**, while an increase is seen in the case of **1c** and **1d**. This becomes most obvious by the respective shifts of the rollovers in the SAXS data (Figures 3, S23, and S24). In particular, the decrease in radius from **1b** to **2b** and **3b** must, therefore, be accompanied by a reduced number of units per cross section. To further support this assumption of an impaired lateral aggregation, again a cylinder fit was applied for **3b**, resulting in an L_{cyl} of 5.8 nm and an R_{cyl} of 5.3 nm (for R_{cyl} , a Gaussian distribution was applied; Table S2 and Figure S25B). In contrast to **2b**, an N_{agg} of 16 is calculated for $\text{BTU}[\text{C}_{12}][\text{PEO}_{2k}]_3$ **3b** from the Guinier analysis, which indeed is in excellent agreement with a single molecule per cross section, assuming the same stacking distance of 3.6 Å (eq S5). Interestingly, while still mostly cylindrical structures are

formed in the case of **2b**, the symmetrical attachment of three polymers (**3b**) finally impedes the formation of long cylindrical structures, although the overall size of the hydrophilic and hydrophobic domains of the latter (**3b**) is similar to that for **1c** (BTU[C₁₂][PEO_{6k}]), which still formed some cylindrical structures (Figure 3B,F). From this comparison, we assume that the lateral aggregation, which is still present for **1c**, induces a cooperative effect for the formation of cylindrical structures, as any defects in the stacked, hydrogen-bond-forming ureas might be compensated by the parallel alignment of neighboring stacks in such bundles of aggregates. Similar effects have already been shown for other supramolecular systems.^{55,56} Therefore, the architecture of the unimeric building block and resulting structural constraints clearly have an effect on the final morphology, but the composition of the unimers and thus the packing parameter remain the more important parameters for the final shape of the self-assembled nanostructures.

In Situ Investigation of Population Distributions. To gain further insight into the assembly behavior of the BTUs, solution characterization was conducted by sedimentation velocity analytical ultracentrifugation (AUC) experiments of the BTU-PEO conjugates and their assemblies in water. These sedimentation velocity experiments allow for the determination of potentially different solution populations and differential distributions of sedimentation coefficients, *s*, via least-squares boundary modeling, as described recently.^{47,51} The BTU containing the shorter C₆ methylene spacer BTU[C₆][PEO_{2k}] **1a** with one arm only, shows a distribution of relatively small sedimentation coefficients located around 3 S (Figure S28). This agrees with relatively small aggregates, as observed in cryoTEM images and in the SAXS data (Figures S19 and S22). Increasing the spacer length to 12 methylene units (BTU[C₁₂][PEO_{2k}] **1b**), which led to fiber formation according to SAXS and cryoTEM data, results in a broad distribution of relatively large sedimentation coefficients (Figure 4A, black line). Therefore, it can be concluded that large and disperse aggregates are present in solution. This finding is well supported by the cryoTEM images, which also revealed a large variety in the lengths of the fiber structures (Figure 3C). Increasing the PEO arm length, for BTU[C₁₂][PEO_{6k}] **1c** and BTU[C₁₂][PEO_{11k}] **1d**, compared to BTU[C₁₂][PEO_{2k}] **1b**, leads to populations showing smaller average sedimentation coefficients under otherwise identical conditions. These distributions of aggregates are at least bimodal in nature (green and blue lines in Figure 4A), indicating population heterogeneity in solution, again in agreement with cryoTEM imaging, showing the presence of a mixture of objects (Figure 2A,B). In turn, increasing the number of arms from one to two, i.e., BTU[C₁₂][PEO_{2k}]₂ **2b**, results in a population of sedimentation coefficients shifting to lower values (compared to BTU[C₁₂][PEO_{2k}] **1b**). Those were centered around 5S. However, a barely resolvable small population of large sedimentation coefficients is still found (>10 S) as well as rather small species. For BTU[C₁₂][PEO_{2k}]₃ **3b**, a further reduction toward even smaller average sedimentation coefficients with different populations is observed (Figure 4B) that yet significantly exceed those of the unimeric species. It is apparent that an increase in the arm length or the number of arms at fixed arm lengths leads to a diminution of the aggregation. Additionally, when modeling these data from the last scans, where the majority of the larger assemblies have sedimented according to the Lamm equation and considering

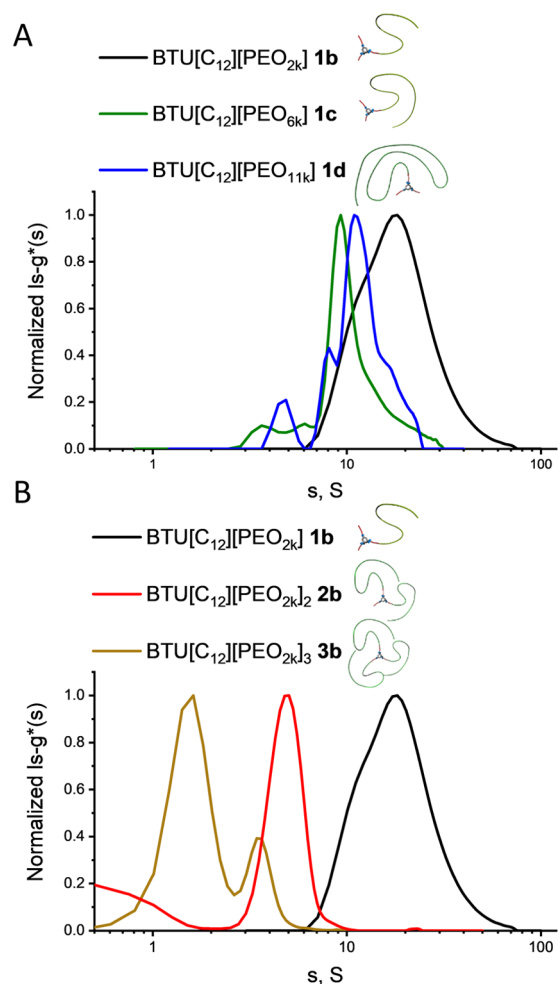


Figure 4. Normalized semilogarithmic plot of the differential distributions of sedimentation coefficients, $Is-g^*(s)$, for BTUs with (A) an increased arm length at a fixed number of arms and (B) an increased number of arms at a fixed arm length. The concentration of each sample in water was 3 mg mL⁻¹.

effects of diffusion, as described recently,^{47,57,58} mostly small concentrations of unimeric species can still be found in all samples (see normalized differential distributions of sedimentation coefficients, $c(s)$, as dashed lines in Figure S29). Qualitatively, these species correspond to the different molar masses of the corresponding unimers assembling to rather large aggregates. The presence of such unimeric species in the solution may be due to a critical aggregation concentration or possible kinetic trapping, which prevents any further assembly of remaining unimers. An exact determination of the remaining unimeric species in solutions containing mostly large assemblies is often neglected in comparable supramolecular systems but may offer new insights into the assembly process.³⁷ More detailed investigations in this direction are currently ongoing. In this context also, the AUC may represent a powerful tool, as it enables a detailed investigation of the supramolecular assemblies ranging from unimers of a few thousand grams per mole (Figure S29) to large (an)isotropic structures (Figure 4).

CONCLUSIONS

Overall, we confirmed that the multiple hydrogen bonds formed by the urea groups in the BTU motif are strong enough

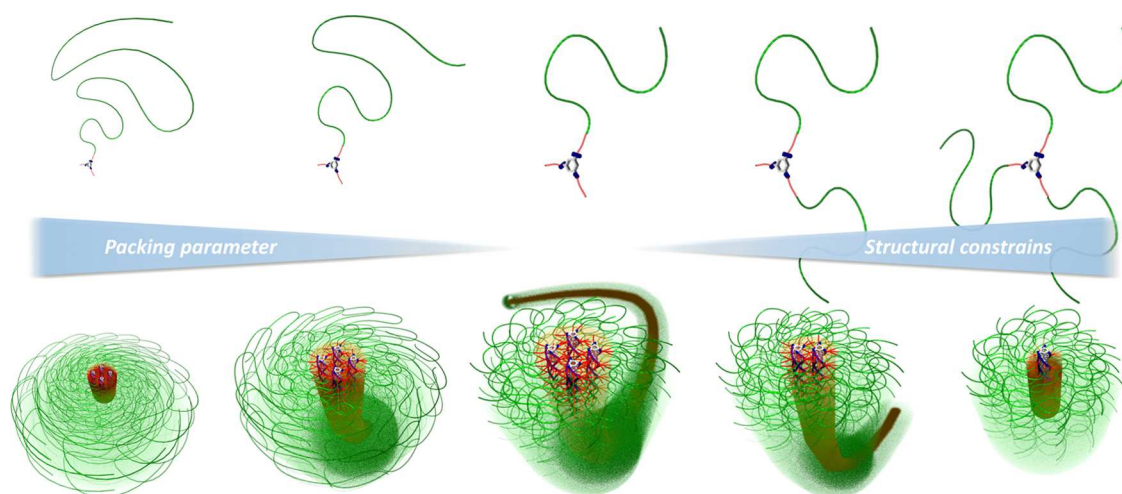


Figure 5. Schematic depiction of the different assembly behavior (bottom) observed for the tested BTUs (top), which is influenced by either the structural arrangement of the hydrophilic polymer chains (right) or the packing parameter (left).

to induce a directional self-assembly into supramolecular polymer bottlebrushes. In contrast to the previously presented amide bonds, the driving force created by the urea groups is sufficient to compensate for the energy penalty caused by the additional surface area and crowding of polymer chains in the cylindrical aggregates compared to their spherical analogues.⁴⁷ The packing parameter, which we previously claimed to be the main driving forces for isotropic self-assembly of BTAs,⁴⁷ can therefore be challenged by stronger directional forces created by a sufficient number of directed hydrogen bonds in the case of BTU as opposed to BTA. Notwithstanding, this enhanced interaction seems to only shift the phase boundaries of the morphology transitions, since decreasing the relative size of the hydrophobic core of the unimers by increasing the length of hydrophilic polymer again results in a transition toward the isotropic structures (Figure 5, left). Besides this change of composition with variation of spacer or polymer length, an increase in the number of polymer chains (from one to two or three) attached to the core motif resulted in a similar trend on the first glance. The resulting bolaamphiphilic structures again caused a gradual transition from cylindrical to mostly spherical structures via a mixed population. A closer look, however, reveals that the modified structural arrangement clearly affects the molecular packing of the building units in the cross section of the assemblies. For BTU[C₁₂][PEO_{2k}] **1b** with only a single polymer chain, four units are found in the cross section. As the radius decreases in the case of BTU[C₁₂][PEO_{2k}]₂ and BTU[C₁₂][PEO_{2k}]₃, this lateral aggregation must be diminished, if more polymer chains are attached to the BTU motifs (Figure 5, right). We, therefore assume that not only the increased steric demand of the polymers induces a phase transition but the limited lateral aggregation further hampers any cooperative assembly effect and, as a consequence, reduces the effective force originating from the directing hydrogen bonds.

The strengthening of directional interaction forces by increasing the number of hydrogen bonds enables a broadening of the usually narrow composition window for cylindrical self-assembled structures. With a comparable design of the core motif, a direct evaluation of different key aspects became feasible, which compares the impact of the packing parameter, hydrophobic interactions, directional interactions of hydrogen bonds, and steric restrictions on the self-assembly. The

morphology formed by the supramolecular aggregation of the presented polymer systems depends on a fine balance of all of the underlying forces. Our results demonstrate that tuning of these interactions can drive the formation of purely cylindrical morphologies or supramolecular polymer bottlebrushes, respectively. We believe that these fundamental studies set the basis for further systematic developments in this area of research and that the design of functional supramolecular polymer bottlebrushes finds applications, for instance, as carrier systems in nanomedicine or as dynamic scaffolds for cell proliferation.

■ ASSOCIATED CONTENT

SI Supporting Information

The Supporting Information is available free of charge at <https://pubs.acs.org/doi/10.1021/acs.macromol.0c01361>.

Synthesis of all BTUs **1–3 a–d**, ¹H NMR, ESI-MS, SEC, MALDI-TOF, DLS data, full-sized cryoTEM images, additional data for light and X-ray scattering, and additional AUC experiments (PDF)

■ AUTHOR INFORMATION

Corresponding Author

Johannes C. Brendel – Laboratory of Organic and Macromolecular Chemistry (IOMC) and Jena Center for Soft Matter (JCSM), Friedrich Schiller University Jena, 07743 Jena, Germany; orcid.org/0000-0002-1206-1375; Email: johannes.brendel@uni-jena.de

Authors

Franka V. Gruschwitz – Laboratory of Organic and Macromolecular Chemistry (IOMC) and Jena Center for Soft Matter (JCSM), Friedrich Schiller University Jena, 07743 Jena, Germany

Mao-Chun Fu – Department of Organic Materials Science, Yamagata University, Yonezawa, Yamagata 992-8510, Japan

Tobias Klein – Laboratory of Organic and Macromolecular Chemistry (IOMC) and Jena Center for Soft Matter (JCSM), Friedrich Schiller University Jena, 07743 Jena, Germany; orcid.org/0000-0001-9404-7739

Rintaro Takahashi – Department of Chemistry and Biochemistry, University of Kitakyushu, Kitakyushu, Fukuoka 808-0135, Japan

Tomoya Higashihara – Department of Organic Materials Science, Yamagata University, Yonezawa, Yamagata 992-8510, Japan; orcid.org/0000-0003-2115-1281

Stephanie Hoeppe – Laboratory of Organic and Macromolecular Chemistry (IOMC) and Jena Center for Soft Matter (JCSM), Friedrich Schiller University Jena, 07743 Jena, Germany

Ivo Nischang – Laboratory of Organic and Macromolecular Chemistry (IOMC) and Jena Center for Soft Matter (JCSM), Friedrich Schiller University Jena, 07743 Jena, Germany; orcid.org/0000-0001-6182-5215

Kazuo Sakurai – Department of Chemistry and Biochemistry, University of Kitakyushu, Kitakyushu, Fukuoka 808-0135, Japan; orcid.org/0000-0002-9737-0061

Complete contact information is available at:

<https://pubs.acs.org/10.1021/acs.macromol.0c01361>

Notes

The authors declare no competing financial interest.

ACKNOWLEDGMENTS

The SAXS experiments were carried out at SPring-8 upon the approval by JASRI (proposal numbers: 2017B1481, 2018A1454, and 2018B1370). J.C.B., F.V.G., and T.K. further thank the German Science Foundation (DFG) for generous funding within the Emmy-Noether Programme (Project-ID: 358263073). cryoTEM investigations were performed at the electron microscopy facilities of the Jena Center for Soft Matter (JCSM), which were purchased with grants from the DFG and the European funds for Regional Development (EFRE). Funding within the collaborative research center PolyTarget, projects A05 and Z01 (Project-ID: 316213987—SFB 1278) by the DFG, and Grant-in-Aid from CREST-JST (JPMJCR1521) are also acknowledged. Furthermore, Prof. U.S. Schubert is acknowledged for his continuous support and providing access to excellent research facilities.

REFERENCES

- (1) Klug, A. The tobacco mosaic virus particle: structure and assembly. *Philos. Trans. R. Soc., B* **1999**, *354*, 531–535.
- (2) Fletcher, D. A.; Mullins, R. D. Cell mechanics and the cytoskeleton. *Nature* **2010**, *463*, 485–492.
- (3) Wu, K. C.-W.; Yang, C.-Y.; Cheng, C.-M. Using cell structures to develop functional nanomaterials and nanostructures – case studies of actin filaments and microtubules. *Chem. Commun.* **2014**, *50*, 4148–4157.
- (4) Hess, H.; Ross, J. L. Non-equilibrium assembly of microtubules: from molecules to autonomous chemical robots. *Chem. Soc. Rev.* **2017**, *46*, 5570–5587.
- (5) Zhao, Y.; Sakai, F.; Su, L.; Liu, Y.; Wei, K.; Chen, G.; Jiang, M. Progressive macromolecular self-assembly: from biomimetic chemistry to bio-inspired materials. *Adv. Mater.* **2013**, *25*, 5215–5256.
- (6) Foster, J. C.; Varlas, S.; Couturaud, B.; Coe, Z.; O'Reilly, R. K. Getting into Shape: Reflections on a New Generation of Cylindrical Nanostructures' Self-Assembly Using Polymer Building Blocks. *J. Am. Chem. Soc.* **2019**, *141*, 2742–2753.
- (7) Petkau-Milroy, K.; Sonntag, M. H.; van Onzen, A. H.; Brunsveld, L. Supramolecular polymers as dynamic multicomponent cellular uptake carriers. *J. Am. Chem. Soc.* **2012**, *134*, 8086–8089.

(8) Wijnands, S. P. W.; Engelen, W.; Lafleur, R. P. M.; Meijer, E. W.; Merckx, M. Controlling protein activity by dynamic recruitment on a supramolecular polymer platform. *Nat. Commun.* **2018**, *9*, No. 65.

(9) Golkaram, M.; Boetje, L.; Dong, J.; Suarez, L. E. A.; Fodor, C.; Maniar, D.; van Ruymbeke, E.; Faraji, S.; Portale, G.; Loos, K. Supramolecular Mimic for Bottlebrush Polymers in Bulk. *ACS Omega* **2019**, *4*, 16481–16492.

(10) Hill, J. P.; Jin, W.; Kosaka, A.; Fukushima, T.; Ichihara, H.; Shimomura, T.; Ito, K.; Hashizume, T.; Ishii, N.; Aida, T. Self-Assembled Hexa-peri-hexabenzocoronene Graphitic Nanotube. *Science* **2004**, *304*, 1481–1483.

(11) Miyake, G. M.; Piunova, V. A.; Weitekamp, R. A.; Grubbs, R. H. Precisely Tunable Photonic Crystals From Rapidly Self-Assembling Brush Block Copolymer Blends. *Angew. Chem., Int. Ed.* **2012**, *51*, 11246–11248.

(12) Jin, X.-H.; Price, M. B.; Finnegan, J. R.; Boott, C. E.; Richter, J. M.; Rao, A.; Menke, S. M.; Friend, R. H.; Whittell, G. R.; Manners, I. Long-range exciton transport in conjugated polymer nanofibers prepared by seeded growth. *Science* **2018**, *360*, 897–900.

(13) Sheiko, S. S.; Sumerlin, B. S.; Matyjaszewski, K. Cylindrical molecular brushes: Synthesis, characterization, and properties. *Prog. Polym. Sci.* **2008**, *33*, 759–785.

(14) Verduzco, R.; Li, X.; Pesek, S. L.; Stein, G. E. Structure, function, self-assembly, and applications of bottlebrush copolymers. *Chem. Soc. Rev.* **2015**, *44*, 2405–2420.

(15) Pelras, T.; Mahon, C. S.; Müllner, M. Synthesis and Applications of Compartmentalised Molecular Polymer Brushes. *Angew. Chem., Int. Ed.* **2018**, *57*, 6982–6994.

(16) Baker, M. B.; Albertazzi, L.; Voets, I. K.; Leenders, C. M.; Palmans, A. R.; Pavan, G. M.; Meijer, E. W. Consequences of chirality on the dynamics of a water-soluble supramolecular polymer. *Nat. Commun.* **2015**, *6*, No. 6234.

(17) Krieg, E.; Bastings, M. M.; Besenius, P.; Rybtchinski, B. Supramolecular Polymers in Aqueous Media. *Chem. Rev.* **2016**, *116*, 2414–2477.

(18) da Silva, R. M. P.; van der Zwaag, D.; Albertazzi, L.; Lee, S. S.; Meijer, E. W.; Stupp, S. I. Super-resolution microscopy reveals structural diversity in molecular exchange among peptide amphiphile nanofibers. *Nat. Commun.* **2016**, *7*, No. 11561.

(19) Thota, B. N. S.; Lou, X.; Bochicchio, D.; Paffen, T. F. E.; Lafleur, R. P. M.; van Dongen, J. L. J.; Ehrmann, S.; Haag, R.; Pavan, G. M.; Palmans, A. R. A.; Meijer, E. W. Supramolecular Copolymerization as a Strategy to Control the Stability of Self-Assembled Nanofibers. *Angew. Chem., Int. Ed.* **2018**, *57*, 6843–6847.

(20) Qin, B.; Yin, Z.; Tang, X.; Zhang, S.; Wu, Y.; Xu, J.-F.; Zhang, X. Supramolecular polymer chemistry: From structural control to functional assembly. *Prog. Polym. Sci.* **2020**, *100*, No. 101167.

(21) Hartgerink, J. D.; Beniash, E.; Stupp, S. I. Self-Assembly and Mineralization of Peptide-Amphiphile Nanofibers. *Science* **2001**, *294*, 1684–1688.

(22) Hamley, I. W. Peptide Fibrillization. *Angew. Chem., Int. Ed.* **2007**, *46*, 8128–8147.

(23) Eckhardt, D.; Groenewolt, M.; Krause, E.; Börner, H. G. Rational design of oligopeptide organizers for the formation of poly(ethylene oxide) nanofibers. *Chem. Commun.* **2005**, 2814–2816.

(24) Hamley, I. W.; Cheng, G.; Castelletto, V. A Thermoresponsive Hydrogel Based on Telechelic PEG End-Capped with Hydrophobic Dipeptides. *Macromol. Biosci.* **2011**, *11*, 1068–1078.

(25) Ghadiri, M. R.; Granja, J. R.; Milligan, R. A.; McRee, D. E.; Khazanovich, N. Self-assembling organic nanotubes based on a cyclic peptide architecture. *Nature* **1993**, *366*, 324–327.

(26) Couet, J.; Samuel, J. D.; Kopyshev, A.; Santer, S.; Biesselski, M. Peptide-polymer hybrid nanotubes. *Angew. Chem., Int. Ed.* **2005**, *44*, 3297–3301.

(27) Ruiz, L.; Ketten, S. Directing the self-assembly of supra-biomolecular nanotubes using entropic forces. *Soft Matter* **2014**, *10*, 851–861.

(28) Mansfield, E. D. H.; Hartlieb, M.; Catrouillet, S.; Rho, J. Y.; Larnaudie, S. C.; Rogers, S. E.; Sanchis, J.; Brendel, J. C.; Perrier, S.

Systematic study of the structural parameters affecting the self-assembly of cyclic peptide-poly(ethylene glycol) conjugates. *Soft Matter* **2018**, *14*, 6320–6326.

(29) Brendel, J. C.; Catrouillet, S.; Sanchis, J.; Jolliffe, K. A.; Perrier, S. Shaping block copolymer micelles by supramolecular polymerization: making ‘tubosomes’. *Polym. Chem.* **2019**, *10*, 2616–2625.

(30) Brunsveld, L.; Folmer, B. J. B.; Meijer, E. W.; Sijbesma, R. P. Supramolecular Polymers. *Chem. Rev.* **2001**, *101*, 4071–4098.

(31) De Greef, T. F.; Smulders, M. M.; Wolffs, M.; Schenning, A. P.; Sijbesma, R. P.; Meijer, E. W. Supramolecular polymerization. *Chem. Rev.* **2009**, *109*, 5687–5754.

(32) Yamanaka, M. Urea derivatives as low-molecular-weight gelators. *J. Inclusion Phenom. Macrocyclic Chem.* **2013**, *77*, 33–48.

(33) Yashima, E.; Ousaka, N.; Taura, D.; Shimomura, K.; Ikai, T.; Maeda, K. Supramolecular Helical Systems: Helical Assemblies of Small Molecules, Foldamers, and Polymers with Chiral Amplification and Their Functions. *Chem. Rev.* **2016**, *116*, 13752–13990.

(34) Hartlieb, M.; Mansfield, E. D. H.; Perrier, S. A guide to supramolecular polymerizations. *Polym. Chem.* **2020**, *11*, 1083–1110.

(35) Obert, E.; Bellot, M.; Bouteiller, L.; Andrioletti, F.; Lehen-Ferrenbach, C.; Boue, F. Both water- and organo-soluble supramolecular polymer stabilized by hydrogen-bonding and hydrophobic interactions. *J. Am. Chem. Soc.* **2007**, *129*, 15601–15605.

(36) Han, S.; Nicol, E.; Niepceron, F.; Colombani, O.; Pensec, S.; Bouteiller, L. Oligo-Urea with No Alkylene Unit Self-Assembles into Rod-Like Objects in Water. *Macromol. Rapid Commun.* **2019**, *40*, No. e1800698.

(37) Gruschwitz, F. V.; Klein, T.; Catrouillet, S.; Brendel, J. C. Supramolecular polymer bottlebrushes. *Chem. Commun.* **2020**, *56*, 5079–5110.

(38) Mellot, G.; Guigner, J. M.; Jestin, J.; Bouteiller, L.; Stoffelbach, F.; Rieger, J. Bisurea-Functionalized RAFT Agent: A Straightforward and Versatile Tool toward the Preparation of Supramolecular Cylindrical Nanostructures in Water. *Macromolecules* **2018**, *51*, 10214–10222.

(39) Mellot, G.; Guigner, J. M.; Bouteiller, L.; Stoffelbach, F.; Rieger, J. Templated PISA: Driving Polymerization-Induced Self-Assembly towards Fibre Morphology. *Angew. Chem., Int. Ed.* **2019**, *58*, 3173–3177.

(40) Leenders, C. M.; Albertazzi, L.; Mes, T.; Koenigs, M. M.; Palmans, A. R.; Meijer, E. W. Supramolecular polymerization in water harnessing both hydrophobic effects and hydrogen bond formation. *Chem. Commun.* **2013**, *49*, 1963–1965.

(41) Leenders, C. M.; Baker, M. B.; Pijpers, I. A.; Lafleur, R. P.; Albertazzi, L.; Palmans, A. R.; Meijer, E. W. Supramolecular polymerisation in water; elucidating the role of hydrophobic and hydrogen-bond interactions. *Soft Matter* **2016**, *12*, 2887–2893.

(42) Blokzijl, W.; Engberts, J. B. F. N. Hydrophobic Effects. Opinions and Facts. *Angew. Chem., Int. Ed.* **1993**, *32*, 1545–1579.

(43) Biedermann, F.; Nau, W. M.; Schneider, H. J. The hydrophobic effect revisited—studies with supramolecular complexes imply high-energy water as a noncovalent driving force. *Angew. Chem., Int. Ed.* **2014**, *53*, 11158–11171.

(44) Israelevili, J. N.; Mitchell, D. J.; Ninham, B. W. Theory of Self-Assembly of Hydrocarbon Amphiphiles into Micelles and Bilayers. *J. Chem. Soc., Faraday Trans. 2* **1976**, *72*, 1525–1568.

(45) Nagarajan, R. Molecular Packing Parameter and Surfactant Self-Assembly: The Neglected Role of the Surfactant Tail†. *Langmuir* **2002**, *18*, 31–38.

(46) Mai, Y.; Eisenberg, A. Self-assembly of block copolymers. *Chem. Soc. Rev.* **2012**, *41*, 5969–5985.

(47) Klein, T.; Gruschwitz, F. V.; Rogers, S.; Hoepfener, S.; Nischang, I.; Brendel, J. C. The influence of directed hydrogen bonds on the self-assembly of amphiphilic polymers in water. *J. Colloid Interface Sci.* **2019**, *557*, 488–497.

(48) Van Gorp, J. J.; Vekemans, J. A.; Meijer, E. W. C3-symmetrical supramolecular architectures: fibers and organic gels from discotic trisamides and trisureas. *J. Am. Chem. Soc.* **2002**, *124*, 14759–14769.

(49) Breßler, I.; Kohlbrecher, J.; Thünemann, A. F. SASfit: a tool for small-angle scattering data analysis using a library of analytical expressions. *J. Appl. Crystallogr.* **2015**, *48*, 1587–1598.

(50) Schuck, P.; Rossmann, P. Determination of the sedimentation coefficient distribution by least-squares boundary modeling. *Biopolymers* **2000**, *54*, 328–341.

(51) Schuck, P. Size-distribution analysis of macromolecules by sedimentation velocity ultracentrifugation and lamm equation modeling. *Biophys. J.* **2000**, *78*, 1606–1619.

(52) Han, S. Y.; Mellot, G.; Pensec, S.; Rieger, J.; Stoffelbach, F.; Nicol, E.; Colombani, O.; Jestin, J.; Bouteiller, L. Crucial Role of the Spacer in Tuning the Length of Self-Assembled Nanorods. *Macromolecules* **2020**, *53*, 427–433.

(53) Livsey, I. Neutron scattering from concentric cylinders. Intraparticle interference function and radius of gyration. *J. Chem. Soc., Faraday Trans. 2* **1987**, *83*, 1445–1452.

(54) Lortie, F.; Boileau, S.; Bouteiller, L.; Chassenieux, C.; Demé, B.; Ducouret, G.; Jalabert, M.; Lauprêtre, F.; Terech, P. Structural and Rheological Study of a Bis-urea Based Reversible Polymer in an Apolar Solvent. *Langmuir* **2002**, *18*, 7218–7222.

(55) Appel, W. P. J.; Portale, G.; Wisse, E.; Dankers, P. Y. W.; Meijer, E. W. Aggregation of Ureido-Pyrimidinone Supramolecular Thermoplastic Elastomers into Nanofibers: A Kinetic Analysis. *Macromolecules* **2011**, *44*, 6776–6784.

(56) Teunissen, A. J. P.; Nieuwenhuizen, M. M. L.; Rodríguez-Llansola, F.; Palmans, A. R. A.; Meijer, E. W. Mechanically Induced Gelation of a Kinetically Trapped Supramolecular Polymer. *Macromolecules* **2014**, *47*, 8429–8436.

(57) Nischang, I.; Perevyazko, I.; Majdanski, T.; Vitz, J.; Festag, G.; Schubert, U. S. Hydrodynamic Analysis Resolves the Pharmaceutically-Relevant Absolute Molar Mass and Solution Properties of Synthetic Poly(ethylene glycol)s Created by Varying Initiation Sites. *Anal. Chem.* **2017**, *89*, 1185–1193.

(58) Grube, M.; Leiske, M. N.; Schubert, U. S.; Nischang, I. POx as an Alternative to PEG? A Hydrodynamic and Light Scattering Study. *Macromolecules* **2018**, *51*, 1905–1916.

Supporting Information

Unraveling decisive structural parameters for the self-assembly of supramolecular polymer bottlebrushes based on benzene trisureas

Franka V. Gruschwitz,^{a,b} Mao-Chun Fu,^c Tobias Klein,^{a,b} Rintaro Takahashi,^d Tomoya Higashihara,^c Stephanie Hoepfener,^{a,b} Ivo Nischang,^{a,b} Kazuo Sakurai,^d Johannes C. Brendel,^{a,b,*}

a Laboratory of Organic and Macromolecular Chemistry (IOMC), Friedrich Schiller University Jena, Humboldtstraße 10, 07743 Jena, Germany

b Jena Center for Soft Matter (JCSM), Friedrich Schiller University Jena, Philosophenweg 7, 07743 Jena, Germany

c Department of Organic Materials Science, Yamagata University, 4-3-16 Jonan, Yonezawa, Yamagata 992-8510, Japan

d Department of Chemistry and Biochemistry, University of Kitakyushu, 1-1 Hibikino, Kitakyushu, Fukuoka 808-0135, Japan

*corresponding author: johannes.brendel@uni-jena.de

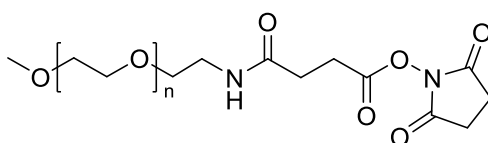
Contents:

1. Synthesis	2
2. Dynamic light scattering	27
3. cryoTEM	28
4. X-ray scattering experiments	31
5. Static light scattering	36
6. Analytical ultracentrifugation	39

1. Synthesis

1.1 Materials and methods

All reagents and solvents were commercial products purchased from Sigma-Aldrich, TCI, or Alfa Aesar, and were used without further purification. The different PEO-NHS esters (Structure in Scheme S 1) were purchased from RAPP and also used without further purification.



Scheme S1. Chemical structure of PEG-NHS ester ($n = 2k, 6k, 11k$).

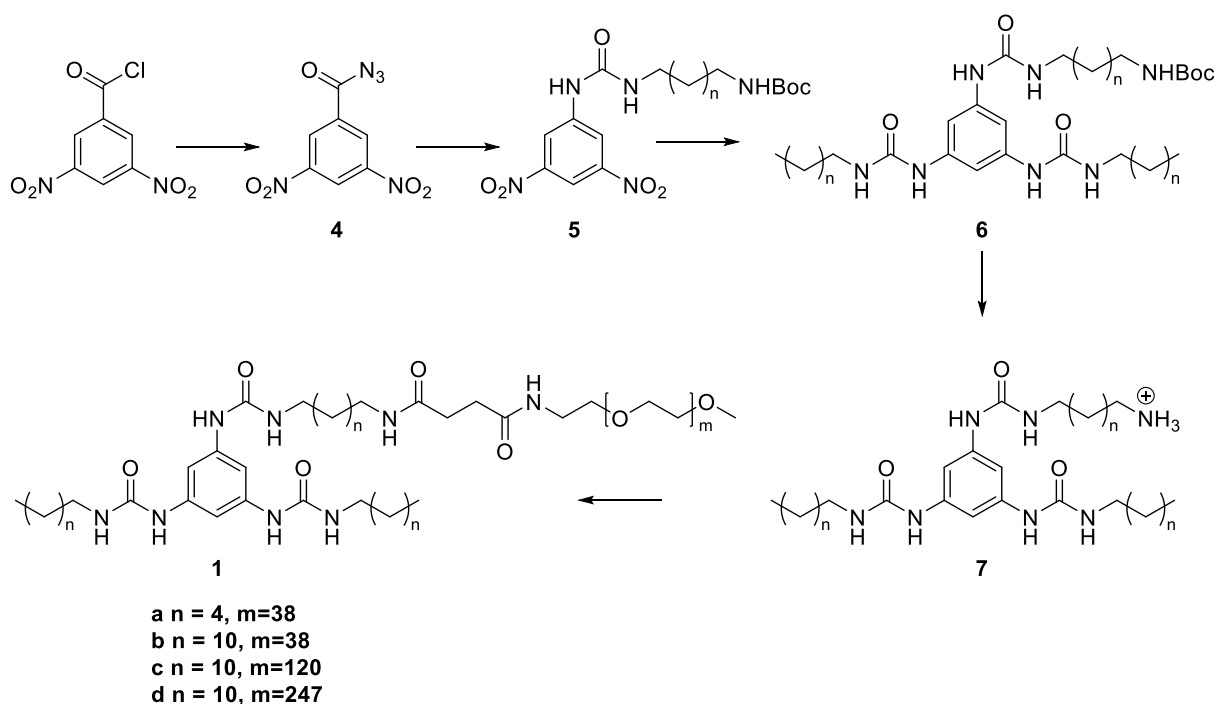
Equipment. $^1\text{H-NMR}$ spectra were measured with a Bruker spectrometer (300 MHz) equipped with an Avance I console, a dual ^1H and ^{13}C sample head and a 60 x BACS automatic sample changer. The chemical shifts of the peaks were determined by using the residual solvent signal as reference and are given in ppm in comparison to TMS. All NMR data was analyzed with the ACD/Spectrum Processor 2016.1.1. Size-exclusion chromatography (SEC) of polymers was performed on an Agilent system (series 1200) equipped with a PSS degasser, a G1310A pump, a G1362A refractive index detector and a PSS GRAM 30 and 1000 column with DMAc (+ 0.21 wt.% LiCl) as eluent and a flow rate of 1 mL min^{-1} . The column oven was set to $40 \text{ }^\circ\text{C}$ and poly(ethylene oxide) (PEO) standards were used for calibration.

ESI. Electrospray ionization mass spectrometry was conducted using a micrOTOF Q-II (Bruker Daltonics) mass spectrometer equipped with an automatic syringe pump from KD Scientific for sample injection. The ESI-Q-ToF mass spectrometer was operating at 4.5 kV, at a desolvation temperature of $180 \text{ }^\circ\text{C}$, in the positive ion mode. Nitrogen was used as the nebulizer and drying gas. All fractions were injected using a constant flow rate ($3 \text{ } \mu\text{L min}^{-1}$) of sample solution. The instrument was calibrated in the m/z range 50–3000 using a calibration standard (ESI-L Low Concentration Tuning Mix), which was supplied from Agilent Technologies. All data were processed via Bruker Data Analysis software version 4.2.

MALDI. Matrix-assisted laser desorption ionization mass spectrometry (MALDI-MS) measurements were carried out using an Ultraflex III ToF/ToF instrument (Bruker Daltonics)

equipped with a Nd-YAG laser. All spectra were measured in the positive mode using α -Cyano-4-hydroxycinnamic acid (CHCA) or 2,5-Dihydroxybenzoic acid (DHB) as a matrix.

1.2 Synthesis of the BTU with one PEO-arm



Scheme S2. Synthetic procedure for the one-armed BTU **1a-d**.

3,5-Dinitrobenzoyl azide (**4**).

A solution of 3,5-dinitrobenzoyl chloride (5.00 g, 21.7 mmol) in acetone (30 mL) was stirred at 0 °C. NaN₃ (2.12 g, 32.5 mmol) in water (20 ml) was added dropwise over 1 h and stirred for 12 h at 0 °C. Acetone was removed under reduced pressure and the reaction mixture was extracted with EtOAc (30 mL x 3). The combined organic layers were dried over MgSO₄ and the solvent was evaporated *in vacuo* to obtain a green crystalline powder. Yield: 4.10 g (80%) ¹H NMR (300 MHz, DMSO-*d*₆) δ [ppm]: 9.08 (t, *J*=2.07 Hz, 1H), 8.89 (d, *J*=2.07 Hz, 2H).

tert-butyl (3-(3-(3,5-dinitrophenyl)ureido)hexyl)carbamate (**5a**). Under argon 3,5-dinitrobenzoyl azide **4** (3.00 g, 12.7 mmol) was dissolved in toluene (50 mL) and stirred at 80 °C for 2 h. To the reaction solution of **4** *tert*-butyl 6-aminohexylcarbamate (2.95 g, 13.6 mmol) was added and stirred for 5 h at 60 °C. The reaction mixture was filtered over silica gel and washed off with THF. After evaporation *in vacuo* a yellow powder was obtained. Yield: 3.27 g (61%) ¹H NMR (300 MHz, DMSO-*d*₆) δ [ppm]: 9.50 (s, 1H), 8.70 (d, *J*=2.05 Hz, 2H), 8.33 (t, *J*=2.10 Hz, 1H), 7.22-7.33 (m, 2H), 7.11-7.22 (m, 3H), 6.77 (br t, *J*=5.40 Hz, 1H), 6.60 (t, *J*=5.54 Hz, 1H), 5.76 (s, 2H), 3.07-3.31 (m, 2H), 2.90 (q, *J*=6.58 Hz, 2H), 2.30 (s, 3H), 1.46

(br s, 2H), 1.37 (s, 11H), 1.28 (br s, 4H). ^{13}C NMR (75 MHz, DMSO- d_6) δ [ppm]: 154.5, 148.2, 143.1, 137.3, 125.3, 116.8, 109.7, 77.3, 54.9, 29.5, 28.3, 26.0, 21.0.

tert-butyl (3-(3-(3,5-dinitrophenyl)ureido)dodecyl)carbamate (5b). Under argon, 3,5-dinitrobenzoyl azide **4** (3.23 g, 13.6 mmol) was dissolved in toluene (50 mL) and stirred at 80 °C for 2 h. To the reaction solution of **4**, *tert-butyl* 12-aminododecylcarbamate (4.09 g, 13.6 mmol) was added and stirred for 5 h at 60 °C. The reaction mixture was filtered over silica gel and washed off with THF. After evaporation *in vacuo*, a yellow powder was obtained. Yield: 4.80 g (75%) ^1H NMR (300 MHz, DMSO- d_6) δ [ppm]: 9.54-9.61 (m, 1H), 8.80 (d, $J=2.07$ Hz, 2H), 8.34 (t, $J=2.07$ Hz, 1H), 6.71-6.82 (m, 1H), 6.63 (t, $J=5.46$ Hz, 1H), 3.21 (q, $J=6.66$ Hz, 2H), 2.99 (br d, $J=6.40$ Hz, 3H), 1.43 (s, 13H), 1.22-1.30 (m, 16H) ^{13}C NMR (75 MHz, DMSO- d_6) δ [ppm]: 155.0, 148.7, 143.5, 129.3, 128.6, 125.8, 117.3, 110.1, 107.4, 97.6, 77.7, 30.0, 29.5, 29.3, 29.2, 29.2, 28.7, 26.8, 26.7, 21.5. ESI(positiveMode): 532.2725 m/z [$\text{M}+\text{Na}^+$], 548.2462 m/z [$\text{M}+\text{K}^+$].

tert-butyl (3-(3-(3,5-bis(3-hexylureido)phenyl)ureido)hexyl)carbamate (6a). Compound **5a** (2.00 g, 4.70 mmol) was dissolved in MeOH (8 mL). Palladium catalyst on active charcoal (0.1 g) was added and the reaction was performed under 3 bar H_2 pressure at 60 °C for 24 h. The mixture was filtered over silica gel, the solvent was evaporated to yield a yellow powder. 0.800 g (2.30 mmol) of this powder was immediately dissolved in THF (15 mL). Hexylisocyanate (0.585 g, 4.60 mmol) was added and stirred for 12 h. The solution was filtered over celite. After drying *in vacuo* a yellow solid was obtained. Yield: 1.06 g (74%) ^1H NMR (300 MHz, DMSO- d_6) δ [ppm]: 8.28 (s, 3H), 7.09 (s, 3H), 6.78 (s, 1H), 5.96 (br t, $J=5.56$ Hz, 3H), 3.04 (q, $J=6.34$ Hz, 6H), 2.89 (q, $J=6.47$ Hz, 2H), 1.37 (s, 17H), 1.24-1.32 (m, 16H), 0.82-0.92 (m, 6H). ^{13}C NMR (75 MHz, DMSO- d_6) δ [ppm]: 155.1, 140.9, 100.0, 67.0, 31.0, 29.7, 28.2, 26.0, 25.1, 22.1, 15.1, 13.9.

tert-butyl (3-(3-(3,5-bis(3-dodecylureido)phenyl)ureido)dodecyl)carbamate (6b). Compound **5b** (3.00 g, 5.89 mmol) was dissolved in THF (15 mL). Palladium catalyst on active charcoal (0.1 g) was added and the reaction was performed under 5 bar H_2 pressure at 80 °C for 24 h. Dodecylisocyanate (3.17g, 14.98 mmol) was added at 50 °C and stirred for 5 h. The solution was filtered over Celite. After drying *in vacuo* an orange solid was obtained. Yield: 3.10 g (58%). ^1H NMR (300 MHz, DMSO- d_6) δ [ppm]: 8.27 (s, 3H), 7.10 (s, 3H), 6.74 (br s, 1H), 5.94 (br t, $J=5.18$ Hz, 3H), 3.04 (br d, $J=5.65$ Hz, 6H), 2.84-2.91 (m, 2H), 1.36 (s, 15H), 1.24 (br s, 54H), 0.85 (s, 6H). ^{13}C NMR (75 MHz, DMSO- d_6) δ [ppm]: 155.6, 141.3, 107.4, 100.6, 97.6,

77.7, 67.4, 67.0, 66.1, 33.6, 31.8, 30.2, 29.5, 29.2, 28.6, 26.8, 24.0, 23.7, 22.5, 14.3
ESI(positiveMode): 894.714 m/z [M+Na⁺], 910.688 m/z [M+K⁺].

1-(3-aminohexyl)-3-(3,5-bis(3-hexyllureido)phenyl)urea (TFA salt) (7a). To a solution of **6a** (0.543 g, 0.870 mmol) in triisopropylsilane (0.400 mL, 1.75 mmol) and water (0.2 mL), trifluoroacetic acid (0.240 mL, 3.07 mmol) was added and stirred for 2 h at 25 °C. The solution was precipitated in ether, centrifuged, washed twice with ether and dried *in vacuo* to yield a greenish solid. Yield: 0.550 g (100%). ¹H NMR (300 MHz, DMSO- *d*₆) δ [ppm]: 8.26-8.36 (m, 3H), 7.02-7.15 (m, 3H), 6.03 (br s, 3H), 3.04 (br s, 6H), 2.71-2.85 (m, 2H), 1.47-1.58 (m, 2H), 1.36-1.46 (m, 6H), 1.16-1.36 (m, 18H), 0.82-0.91 (m, 6H) ¹³C NMR (75 MHz, DMSO- *d*₆) δ [ppm]: 171.4, 171.1, 155.1, 140.9, 71.3, 69.8, 69.6, 69.1, 58.0, 31.0, 30.8, 29.7, 26.1, 26.1, 26.0, 22.1, 13.9 ESI(positiveMode): 570.3968 m/z [M+H⁺]

1-(3-aminohexyl)-3-(3,5-bis(3-dodecylureido)phenyl)urea (TFA salt) (7b). The compound was prepared according to the previous procedure. Yield: 0.400 g (100%). ¹H NMR (300 MHz, DMSO- *d*₆) δ [ppm]: 8.27 (s, 3H), 7.10 (s, 3H), 6.74 (br s, 1H), 5.94 (br t, *J*=5.18 Hz, 3H), 3.04 (br d, *J*=5.65 Hz, 6H), 2.84-2.91 (m, 2H), 1.36 (s, 15H), 1.24 (br s, 54H), 0.85 (s, 6H) ¹³C NMR (75 MHz, DMSO- *d*₆) δ [ppm]: 159.1, 158.6, 155.6, 141.4, 117.9, 114.0, 100.6, 31.8, 30.2, 29.5, 29.4, 29.3, 29.2, 29.0, 27.4, 26.2, 22.5, 14.3, 12.5

*N1-(3-(3-(3,5-bis(3-hexyllureido)phenyl)ureido)hexyl)-N4-((PEO_{2k})succinamide
BTU[C₆][PEO_{2k}] (1a)*.

The deprotected core **7a** (0.180 g, 0.340 mmol) was dissolved in DMF (5 mL). Triethylamine (1.90 mL, 1.60 mmol) and PEO-NHS ester (0.670 g, 0.340 mmol) were added and stirred for 20 h at 25 °C. The solution was precipitated in ether, centrifuged, washed twice with ether and dried *in vacuo* to yield a white powder. Yield: 0.840 g (100%). ¹H NMR (300 MHz, DMSO- *d*₆) δ [ppm]: 8.26 (s, 3H), 7.88 (s, 1H), 7.78 (s, 1H), 7.09 (s, 3H), 5.95-5.97 (m, 3H), 3.33-3.44 (m, 144H), 3.23 (s, 3H), 3.17 (br d, *J*=5.84 Hz, 2H), 2.96-3.10 (m, 8H), 2.27 (s, 4H), 1.39 (br d, *J*=6.40 Hz, 8H), 1.26 (br s, 16H), 0.83-0.88 (m, 6H). ¹³C NMR (75 MHz, DMSO- *d*₆) δ [ppm]: 171.9, 155.5, 141.4, 100.5, 71.7, 70.2, 58.5, 31.5, 31.3, 30.2, 26.5, 22.5, 14.4

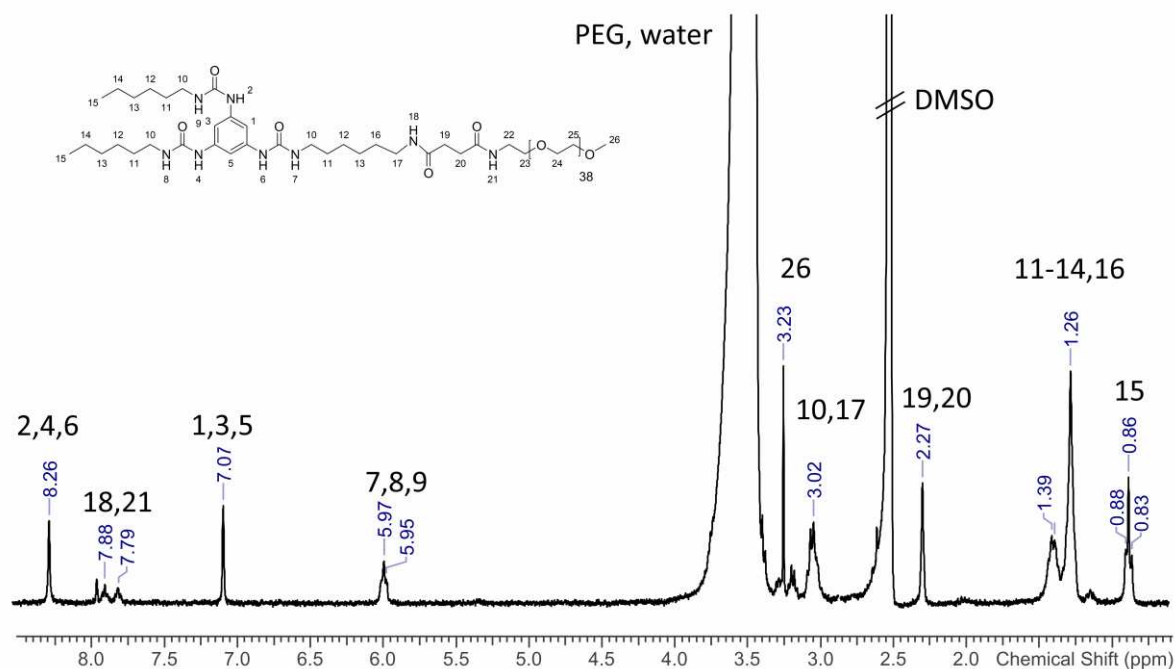


Figure S1. $^1\text{H-NMR}$ of $\text{BTU}[\text{C}_6][\text{PEO}_{2k}]$ (**1a**).

N1-(3-(3-(3,5-bis(3-dodecylureido)phenyl)ureido)dodecyl)-N4-(PEO_{2k})succinamide BTU[C₁₂][PEO_{2k}] (1b). The deprotected core **7b** (0.463 g, 0.600 mmol) was dissolved in DMF (2 mL). Triethylamine (0.500 mL, 3.60 mmol) and 2 kDa-PEO-NHS ester (1.204 g, 0.600 mmol) were added and stirred for 20 h at 25 °C. The solution was precipitated in ether, centrifuged, washed twice with ether and dried *in vacuo* to yield a slightly yellowish powder. Yield: 1.60 g (100%). $^1\text{H NMR}$ (300 MHz, $\text{DMSO-}d_6$) δ [ppm]: 8.27 (s, 3H), 7.87 (m, 1H), 7.76 (br t, $J=4.80$ Hz, 1H), 7.09 (s, 3H), 5.87-6.04 (m, 3H), 3.34 (m, 152H), 3.24 (s, 3H), 3.17 (br d, $J=5.65$ Hz, 2H), 2.98-3.07 (m, 8H), 2.26-2.30 (m, 4H), 1.39 (br s, 8H), 1.24 (br s, 52H), 0.85 (s, 6H). $^{13}\text{C NMR}$ (75 MHz, $\text{DMSO-}d_6$) δ [ppm]: 171.9, 171.5, 155.5, 141.4, 100.5, 71.7, 70.3, 69.6, 58.5, 31.8, 31.3, 30.2, 29.5, 29.2, 26.8, 22.5, 14.4

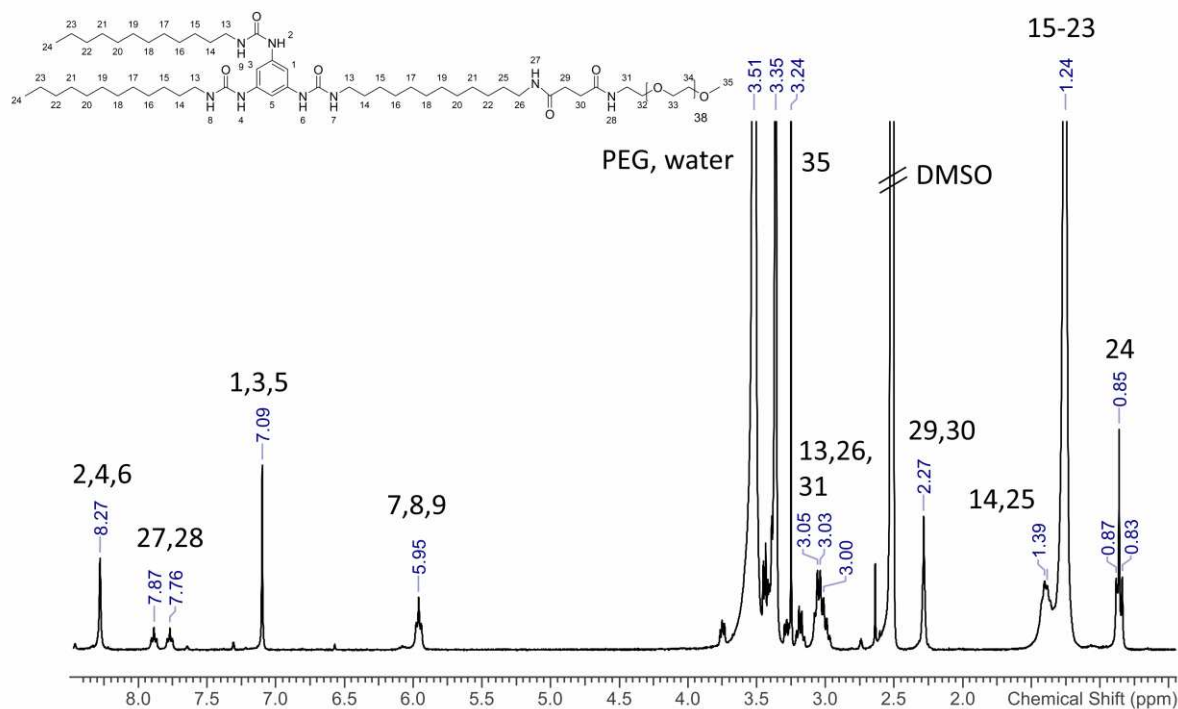


Figure S2. $^1\text{H-NMR}$ of $\text{BTU}[\text{C}_{12}][\text{PEO}_{2k}]$ (**1b**).

N1-(3-(3-(3,5-bis(3-dodecylureido)phenyl)ureido)docecyl)-N4-(PEO_{6k})succinamide
BTU[**C**₁₂][**PEO**_{6k}] (**1c**).

The deprotected core **7b** (0.500 g, 0.560 mmol) was dissolved in DMF (2 mL). Triethylamine (0.160 mL, 1.13 mmol) and 6 kDa-PEO-NHS ester (0.314 g, 0.560 mmol) were added and stirred for 20 h at 25 °C. The solution was precipitated in ether, centrifuged, washed twice with ether and dried *in vacuo* to yield a white powder. Yield: 3.50 g (100%). $^1\text{H NMR}$ (300 MHz, $\text{DMSO-}d_6$) δ [ppm]: 8.27 (s, 3H), 7.87 (br t, $J=5.46$ Hz, 1H), 7.76 (br t, $J=5.37$ Hz, 1H), 7.09 (s, 3H), 5.95 (br t, $J=5.56$ Hz, 3H), 3.35 (s, 240H), 3.24 (s, 3H), 2.92-3.09 (m, 10H), 2.27 (s, 4H), 1.34-1.42 (m, 8H), 1.24 (br s, 52H), 0.84-0.88 (m, 6H).

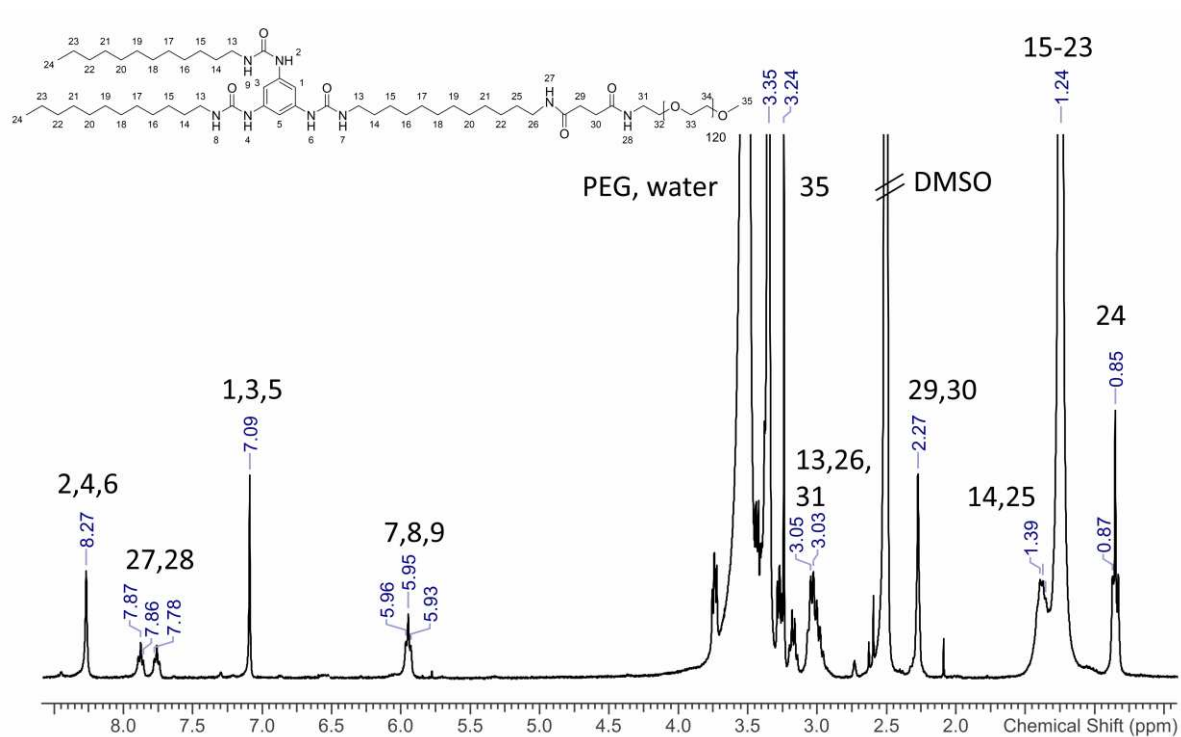


Figure S3. $^1\text{H-NMR}$ of $\text{BTU}[\text{C}_{12}][\text{PEO}_{6k}]$ (**1c**).

*N*1-(3-(3-(3,5-bis(3-dodecylureido)phenyl)ureido)dodecyl)-*N*4-(PEO_{11k})succinamide **BTU**[C_{12}][PEO_{11k}] (**1d**).

The deprotected core **7b** (0.077 g, 0.087 mmol) was dissolved in DMF (2 mL). Triethylamine (0.250 mL, 1.70 mmol) and 11 kDa-PEO-NHS ester (0.969 g, 0.087 mmol) were added and stirred for 20 h at 25 °C. The solution was precipitated in ether, centrifuged, washed twice with ether and dried *in vacuo* to yield a white powder. Yield: 1.00 g (100%). $^1\text{H NMR}$ (300 MHz, $\text{DMSO-}d_6$) δ [ppm]: 8.27 (m, 3H), 7.89 (m, 1H), 7.76 (m, 1H), 7.09 (m, 3H), 5.94 (br s, 3H), 3.35 (s, 494H), 3.24 (s, 3H), 2.94-3.13 (m, 10H), 2.27-2.28 (m, 4H), 1.34-1.44 (m, 8H), 1.24 (br s, 52H), 0.85 (s, 6H).

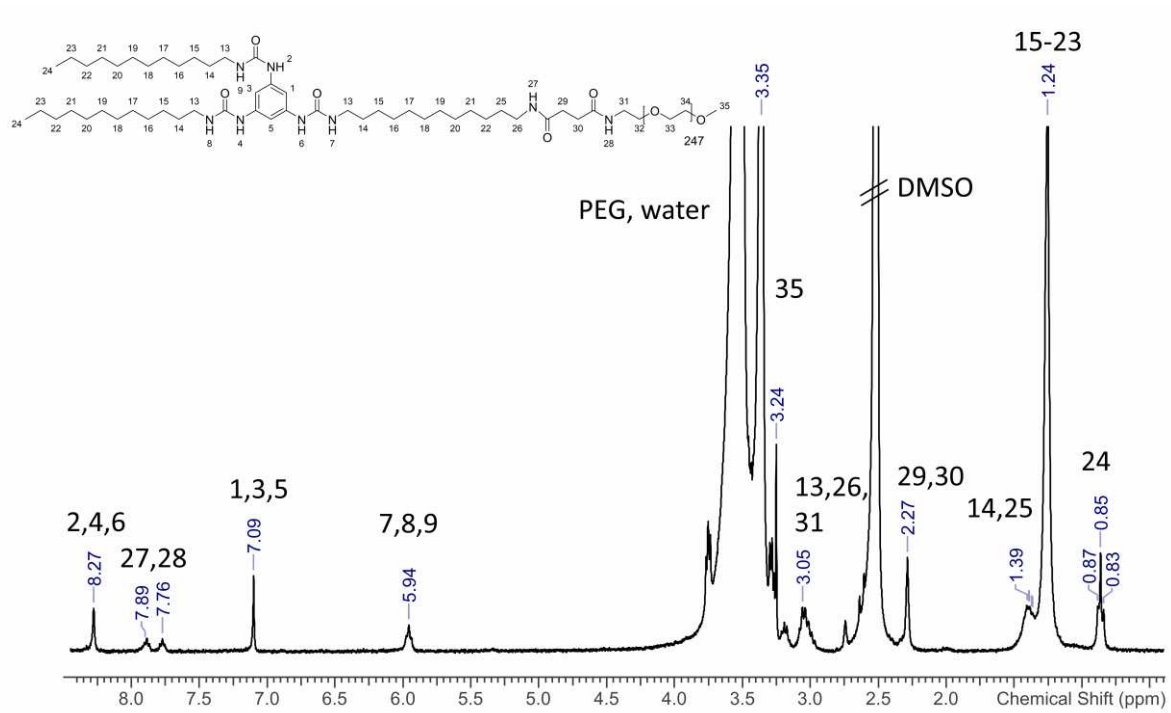
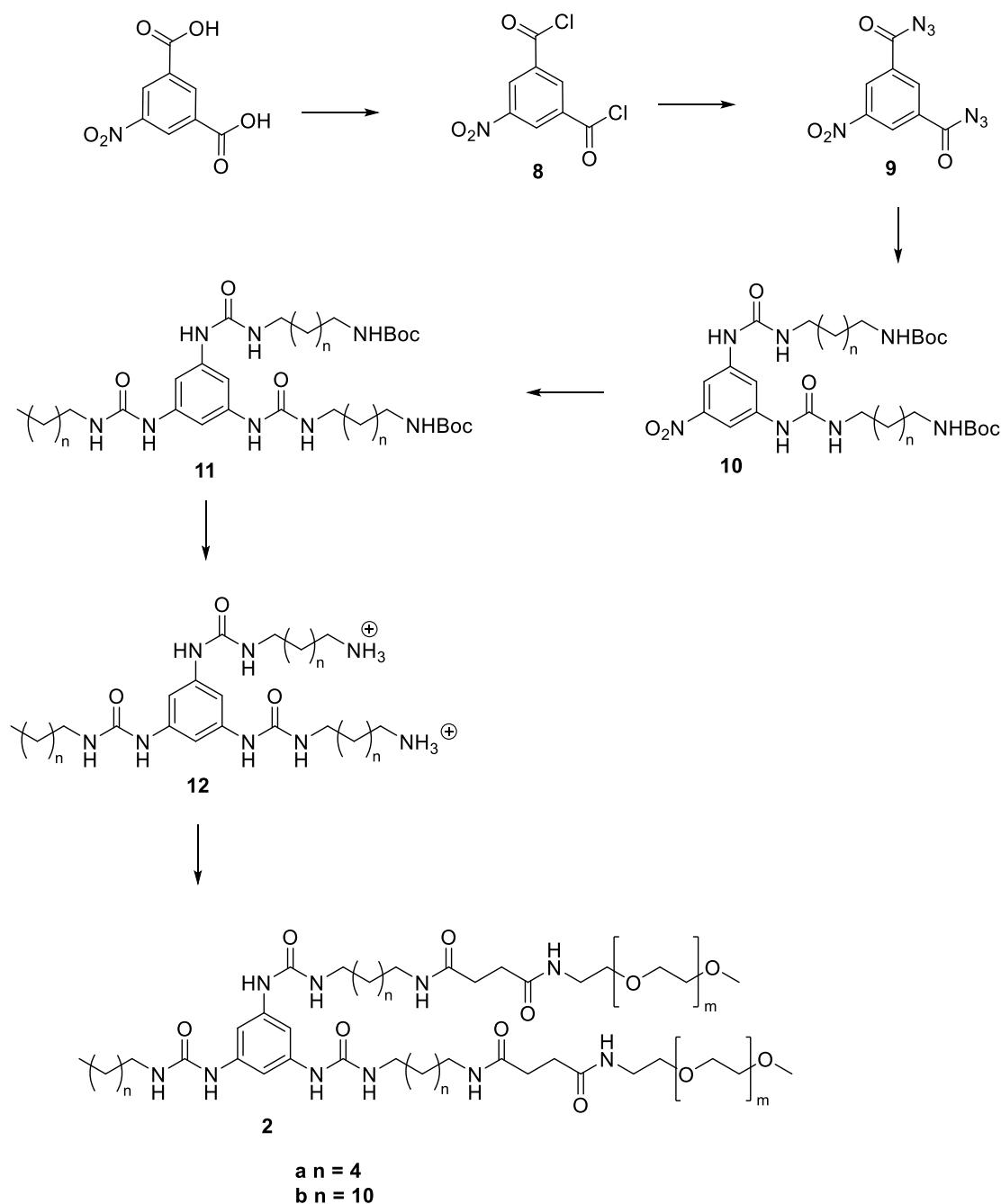


Figure S4. ¹H-NMR of BTU[C₁₂][PEO_{11k}] (**1d**).

1.3 Synthesis of the BTU with two PEO-arms



Scheme S3. Synthetic procedure for the two-armed BTU **2a-b**.

5-nitroisophthaloyl dichloride (**8**). 5-Nitroisophthalic acid (5.00 g, 23.7 mmol) was stirred at 100 °C for 24 h in sulphurous dichloride (24.1 mL, 332 mmol). Remaining sulphurous dichloride was evaporated *in vacuo* to yield a white/yellowish solid. Yield: 5.80 g (99%). ¹H NMR (300 MHz, DMSO-*d*₆) δ [ppm]: 8.74 (d, *J*=1.51 Hz, 2H), 8.69-8.73 (m, 1H). ¹³C NMR (75 MHz, DMSO-*d*₆) δ [ppm]: 164.8, 148.3, 135.1, 133.2, 127.3.

5-nitroisophthaloyl diazide (**9**). 5-nitroisophthaloyl dichloride **8** (5.00 g, 20.1 mmol) was dissolved in DCM (30 mL). The solution was added dropwise to a solution of sodium azide (2.00 g, 30.3 mmol) in 30 mL 1 M aq. NaOH at 0 °C. The mixture was stirred for 20 h at 0 °C -> RT. The phases were separated and the organic phase was washed with water. The solution was dried over Na₂SO₄ and the solvent was evaporated *in vacuo* to yield a white solid. Yield: 4.90 g (79%). ¹H NMR (300 MHz, DMSO-*d*₆) δ [ppm]: 9.08 (s, 1H), 8.89 (d, *J*=2.07 Hz, 2H). ¹³C NMR (75 MHz, DMSO- *d*₆) δ [ppm]: 169.6, 148.6, 133.8, 132.6, 128.1.

di-tert-butyl((((5-nitro-1,3-phenylene)bis(azanediyl))bis(carbonyl))bis(azanediyl))bis(hexane-3,1-diyl))dicarbamate (**10a**). 5-nitroisophthaloyl diazide **9** (4.00 g, 15.3 mmol) was stirred under reflux in toluene (120 mL) for 25 h. Then, *tert*-butyl (6-aminohexyl)carbamate (6.63 g, 30.6 mmol) was added at 50 °C and stirred for another 20 h under argon. A yellow precipitate was visible which was centrifuged off after cooling to room temperature. The obtained solid was washed three times with toluene and dried *in vacuo* to yield a yellow powder. Yield: 3.85 g (38%). ¹H NMR (300 MHz, DMSO- *d*₆) δ [ppm]: 8.82-8.98 (m, 2H), 7.99 (s, 2H), 7.68 (d, *J*=1.13 Hz, 1H), 6.68-6.86 (m, 2H), 6.20 (br s, 2H), 3.07 (q, *J*=5.97 Hz, 4H), 2.90 (q, *J*=6.09 Hz, 4H), 1.36 (s, 24H), 1.26 (br s, 8H). ¹³C NMR (75 MHz, DMSO- *d*₆) δ [ppm]: 156.0, 155.3, 150.3, 142.3, 135.1, 104.9, 77.8, 41.4, 30.1, 29.9, 28.7, 26.5. MS-ESI (positiveMode): 660.3699 m/z [M+Na⁺].

di-tert-butyl((((5-nitro-1,3-phenylene)bis(azanediyl))bis(carbonyl))bis(azanediyl))bis(dodecane-3,1-diyl))dicarbamate (**10b**). 5-nitroisophthaloyl diazide **9** (2 g, 7.66 mmol) was stirred under reflux in toluene (60 mL) for 2 h under argon. Then, *tert*-butyl (6-aminododecyl)carbamate (3.90 g, 17.6 mmol) was added at 50 °C and stirred for another 20 h under argon. The solution was filtered over silica and dried *in vacuo* to yield a yellow powder. Yield: 4.20 g (68%). ¹H NMR (300 MHz, DMSO- *d*₆) δ [ppm]: 9.12 (s, 2H), 8.01 (d, *J*=1.88 Hz, 2H), 7.62 (s, 1H), 6.75 (br t, *J*=5.37 Hz, 2H), 6.40 (br t, *J*=5.46 Hz, 2H), 3.00-3.11 (m, 4H), 2.83-2.91 (m, 4H), 1.36 (s, 25H), 1.23 (br s, 32H). ¹³C NMR (75 MHz, DMSO- *d*₆) δ [ppm]: 156.0, 155.4, 148.9, 142.4, 104.7, 77.7, 30.1, 29.9, 29.5, 29.4, 29.2, 29.2, 28.7, 26.8, 26.7 MS-ESI (positiveMode): 844.5270 m/z [M+Na⁺].

di-tert-butyl (((((5-(3-hexylureido)-1,3-phenylene)bis(azanediyl))bis(carbonyl))bis(azanediyl))bis(hexane-3,1-diyl))dicarbamate (**11a**). Compound **10a** (0.800 g, 1.25 mmol) was dissolved in MeOH (10 mL). Palladium catalyst on active charcoal (0.1 g) was added and the reaction performed under 4 bar H₂ pressure at 50 °C for 24 h. Hexylisocyanate (0.175 g, 1.38 mmol) was added *in situ* and stirred for 20 h. The solution was filtered over Celite and

dried *in vacuo* to obtain a yellow solid. Yield: 0.500 g (45%). ¹H NMR (300 MHz, DMSO- *d*₆) δ [ppm]: 8.26 (s, 3H), 7.08 (s, 3H), 6.77 (br t, *J*=5.09 Hz, 2H), 5.89-6.04 (m, 3H), 3.03 (br d, *J*=5.84 Hz, 6H), 2.89 (br d, *J*=6.22 Hz, 4H), 1.36 (s, 28H), 1.26 (br s, 14H), 0.83-0.89 (m, 3H). ¹³C NMR (75 MHz, DMSO- *d*₆) δ [ppm]: 156.0, 155.6, 141.4, 100.5, 77.7, 31.5, 30.2, 30.2, 29.9, 28.7, 26.5, 26.5, 22.5, 22.5, 14.4. MS-ESI (positiveMode): 757.4935 m/z [M+Na⁺].

di-tert-butyl (((((5-(3-dodecylureido)-1,3-phenylene)bis(azanediyl))bis(carbonyl))bis(azanediyl))bis(dodecane-3,1-diyl))dicarbamate (**11b**). Compound **10b** (1.00 g, 1.24 mmol) was dissolved in THF (15 mL). Palladium catalyst on active coal (0.1 g) was added and under 5 bar H₂ pressure at 60 °C reacted for 24 h. Dodecylisocyanate (0.315 g, 1.49 mmol) was added *in situ* and stirred for 20 h. The solution was filtered over celite. After drying *in vacuo* a white solid was obtained. Yield: 1.00 g (86%). ¹H NMR (300 MHz, DMSO- *d*₆) δ [ppm]: 8.26 (s, 3H), 7.04-7.18 (m, 3H), 6.70-6.81 (m, 2H), 5.89-5.99 (m, 3H), 3.03 (br d, *J*=5.65 Hz, 6H), 2.87 (q, *J*=6.59 Hz, 4H), 1.36 (s, 28H), 1.24 (br s, 50H), 0.85 (br t, *J*=6.50 Hz, 3H). ¹³C NMR (75 MHz, DMSO- *d*₆) δ [ppm]: 155.5, 141.4, 111.2, 100.5, 77.7, 40.0, 31.7, 30.2, 29.5, 28.7, 26.8, 22.5, 14.4. MS-ESI (positiveMode): 1009.7683 m/z [M+Na⁺].

1,1'-(5-(3-hexylureido)-1,3-phenylene)bis(3-(3-aminohexyl)urea) (TFA salt) (12a). To a solution of **11a** (0.500 g, 0.506 mmol) in triisopropylsilane (1.5 mL, 7.60 mmol) and water (0.5 mL), trifluoroacetic acid (1.50 mL, 20.3 mmol) was added and stirred for 2 h at 25 °C. The solution was precipitated in ether, centrifuged, and dried *in vacuo* to obtain a brown solid. Yield: 0.200 g (80%). ¹H NMR (300 MHz, DMSO- *d*₆) δ [ppm]: 8.29-8.38 (m, 3H), 7.05-7.12 (m, 3H), 6.02-6.14 (m, 3H), 3.05 (br d, *J*=5.09 Hz, 6H), 2.71-2.83 (m, 4H), 1.45-1.60 (m, 5H), 1.40 (br d, *J*=6.03 Hz, 6H), 1.25-1.34 (m, 14H), 0.84-0.89 (m, 3H). ¹³C NMR (75 MHz, DMSO- *d*₆) δ [ppm]: 155.6, 141.4, 31.5, 31.3, 30.2, 27.5, 26.5, 26.3, 26.0, 22.5, 14.4.

1,1'-(5-(3-dodecylureido)-1,3-phenylene)bis(3-(3-aminododecyl)urea) (TFA salt) (12b). The compound was prepared according to the previous procedure. Yield: 0.335 g (84%). ¹H NMR (300 MHz, DMSO- *d*₆) δ [ppm]: 8.32 (s, 3H), 7.73 (br s, 6H), 7.08 (s, 3H), 6.07 (br s, 3H), 3.03 (q, *J*=6.34 Hz, 6H), 2.72-2.80 (m, 4H), 1.47-1.56 (m, 4H), 1.39 (br s, 6H), 1.25 (br s, 50H), 0.81-0.89 (m, 3H). ¹³C NMR (75 MHz, DMSO- *d*₆) δ [ppm]: 155.6, 141.4, 100.7, 31.7, 30.2, 29.5, 29.4, 29.3, 29.2, 29.0, 27.4, 26.8, 26.2, 22.5, 14.4.

N1,N1'-((((5-(3-hexylureido)-1,3-phenylene)bis(azanediyl))bis(carbonyl))bis(azanediyl))bis(hexane-3,1-diyl))bis(N4-(PEO_{2k})succinamide) BTU[C₆][PEO_{2k}]₂ (2a). The deprotected core **12a** (0.200 g, 0.340

mmol)) was dissolved in DMF (5 mL). Triethylamine (1.90 mL, 1.60 mmol) and 2kDa-PEO-NHS ester (1.20 g, 0.640 mmol) were added and stirred for 20 h at 25 °C. The solution was precipitated in ether, centrifuged, washed twice with ether and dried *in vacuo* to yield a white powder. Yield: 1.50 g (100%). ¹H NMR (300 MHz, DMSO- *d*₆) δ [ppm]: 8.27 (s, 3H), 7.87 (br t, *J*=5.37 Hz, 2H), 7.78 (br t, *J*=5.18 Hz, 2H), 7.09 (s, 3H), 5.80-6.11 (m, 3H), 3.32-3.40 (m, 304H), 3.23 (s, 6H), 3.10-3.21 (m, 6H), 2.98-3.06 (m, 10H), 2.28 (s, 8H), 1.38 (br d, *J*=6.59 Hz, 10H), 1.26 (br s, 14H), 0.88 (s, 3H). ¹³C NMR (75 MHz, DMSO- *d*₆) δ [ppm]: 171.9, 171.5, 155.5, 141.4, 100.5, 71.7, 70.3, 69.6, 58.5, 31.5, 31.3, 30.2, 29.6, 26.6, 22.5, 14.4.

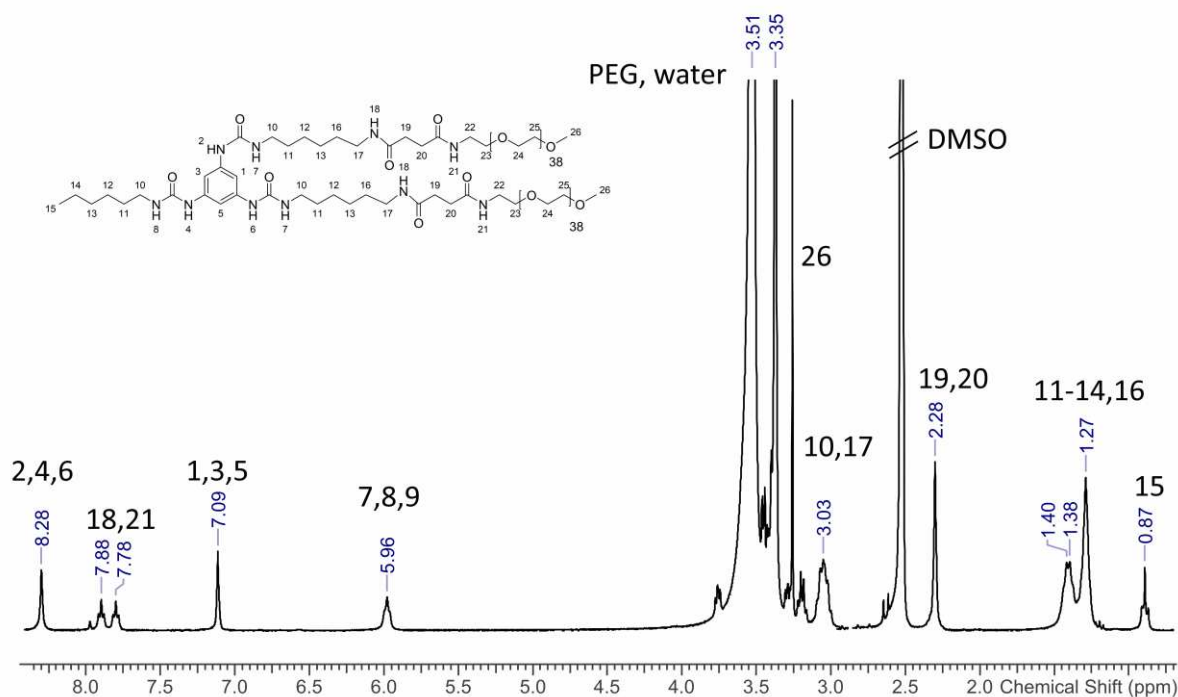


Figure S5. ¹H-NMR of BTU[C₆][PEO_{2k}]₂ (**2a**).

N1,N1'-((((5-(3-dodecylureido)-1,3-phenylene)bis(azanediy))bis(carbonyl))bis(azanediy))bis(dodecane-3,1-diyl))bis(*N4*-(PEO_{2k})succinamide) **BTU**[C₁₂][PEO_{2k}]₂ (**2b**). The compound was prepared according to the previous procedure. Yield: 1 g (100%). ¹H NMR (300 MHz, DMSO-*d*₆) δ [ppm]: 8.26 (s, 3H), 7.87 (s, 2H), 7.75 (s, 2H), 7.09 (s, 3H), 5.94 (br s, 3H), 3.30-3.44 (m, 304H), 3.23 (s, 8H), 3.14-3.20 (m, 4H), 3.01 (br dd, *J*=6.40, 13.37 Hz, 12H), 2.27 (s, 8H), 1.33-1.41 (m, 10H), 1.24 (br s, 50H), 0.82-0.88 (m, 3H). ¹³C NMR (75 MHz, DMSO-*d*₆) δ [ppm]: 171.9, 171.5, 155.5, 141.4, 100.5, 70.3, 58.5, 31.8, 31.3, 30.2, 29.5, 29.3, 26.9, 22.6, 14.4.

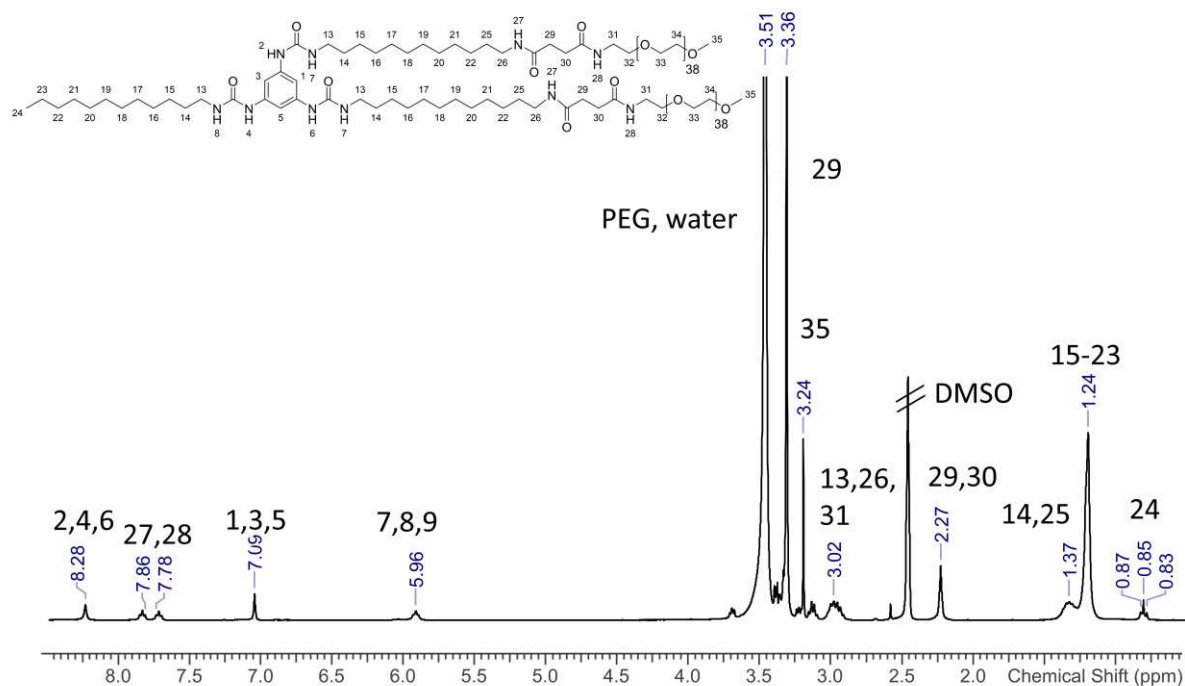
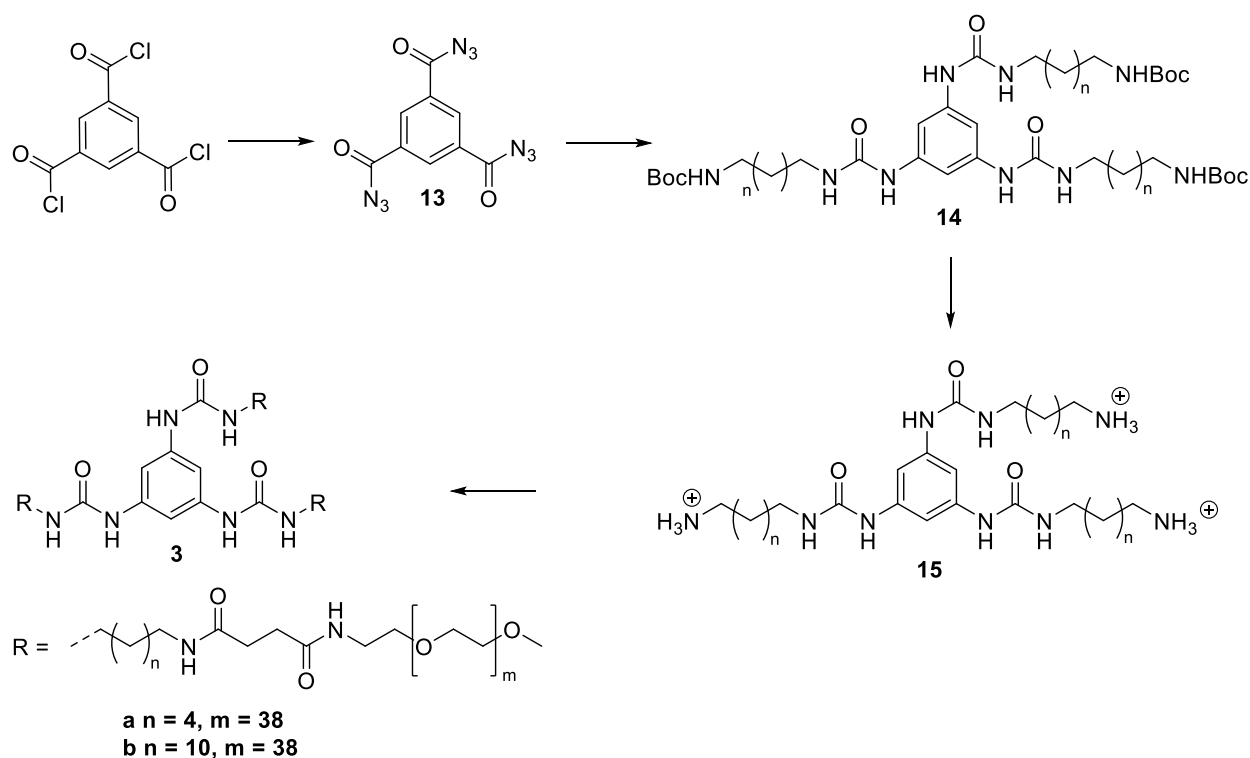


Figure S6. ¹H-NMR of BTU[C₁₂][PEO_{2k}]₂ (**2b**).

1.4 Synthesis of the BTU with three PEO-arms



Scheme S4. synthetic procedure for the three-armed BTU **3a-b**.

1,3,5-Benzenetricarbonyl triazide (13). Compound **13** was prepared according to a procedure in literature.¹ A solution of 1,3,5-benzenetricarbonyl trichloride (0.265 g, 1.00 mmol) in dry tetrahydrofuran (0.7 mL) was added dropwise to a solution of NaN₃ (0.260 g, 4.00 mmol) in water (2.0 mL) while cooling with an ice bath. Immediately, the desired product was formed as a white solid, which was stirred in suspension for 1.5 h. To the reaction mixture toluene (8 mL) and a saturated solution of NaHCO₃ in water (13 mL) were added respectively. After phase separation the aqueous layer was extracted twice more with toluene (2 × 5 mL). The combined organic layers were washed with saturated NaHCO₃ and NaCl solutions in water and dried with MgSO₄·H₂O. After filtration the solution of 1,3,5-benzenetricarbonyl triazide in toluene was concentrated by evaporating until a volume of 10 mL was reached. This yielded a 0.1 M solution of (**13**) in toluene. ¹H NMR (300 MHz, toluene-*d*₈) δ [ppm]: 8.36 (s, 3H).

tri-tert-butyl (((benzene-1,3,5-triyltris(azanediyl))tris(carbonyl))tris(azanediyl))tris(hexane-3,1-diyl))tricarbamate (14a). A 0.1 M solution of **13** (1.00 mmol, 1.0 eq) was heated to 100 °C for 1 h till gas evolution stopped. *tert*-butyl (6-aminohexyl)carbamate (0.720 mL, 0.695 g, 3.20 mmol, 3.2 eq) was added and the solution was kept at 80 °C for 18 h. Subsequently the mixture was cooled to room temperature and the gel-like product was purified by precipitation

and centrifugation in ethyl acetate, yielding (**14a**) as a white powder. Yield: 0.381 g (45%). ¹H NMR (300 MHz, DMSO- *d*₆) δ [ppm]: 8.13 (s, 3H), 7.09 (s, 3H), 6.75 (br, s, 3H), 5.90 (br s, 3H), 3.07 (q, br, 6H), 2.93 (q, br, 6H), 1.32-1.42 (br, 12H), 1.29 (br, 12H). ESI(positiveMode): 872.5576 m/z [M+Na⁺].

tri-tert-butyl((((benzene-1,3,5-triyltris(azanediyl))tris(carbonyl))tris(azanediyl))tris(dodecane-3,1-diyl))tricarbamate (**14b**). 15 mL of a 0.1 M solution of **13** in toluene (1.50 mmol, 1.0 eq) was heated to 100 °C for 1 h till gas evolution stopped. *tert*-butyl(12-aminododecyl)carbamate (1.44 g, 4.80 mmol, 3.2 eq) was added and the solution was kept at 80 °C for 18 h. Subsequently the mixture was cooled to room temperature and the gel-like product was purified by precipitation and centrifugation in ethyl acetate, yielding (**14a**) as a white powder. Yield: 1.22 g (74%). ¹H NMR (300 MHz, DMSO- *d*₆) δ [ppm]: 8.27 (s, 3H), 7.09 (s, 3H), 6.75 (br, s, 3H), 5.96 (br s, 3H), 3.04 (q, br, 6H), 2.88 (q, br, 6H), 1.33-1.47 (br, 12H), 1.23-1.25 (br, 48H). ESI(positiveMode): 1124.8297 m/z [M+Na⁺].

N1,N1',N1''-((((benzene-1,3,5-triyltris(azanediyl))tris(carbonyl))tris(azanediyl))tris(hexane-6,1-diyl))tris(N4-(PEO_{2k})succinamide) **BTU[C₆][PEO_{2k}]₃** (**3a**)

Deprotection in TFA (**15**) and attachment of PEO (**3a**) was done according to the previous mentioned procedures for **1** and **2**. Yield: 0.600 g (100%). ¹H NMR (300 MHz, DMSO- *d*₆) δ [ppm]: 8.28 (s, 3H), 7.88 (s, 2H), 7.78 (s, 2H), 7.10 (s, 3H), 5.96 (br s, 3H), 3.43-3.50 (m, 465H), 3.24 (s, 9H), 3.18 (m, 6H), 3.02 (br, 12H), 2.28 (s, 12H), 1.33-1.47 (br, 12H), 1.24 (br s, 12H). ¹³C NMR (75 MHz, DMSO- *d*₆) δ [ppm]: 171.9, 171.5, 155.5, 141.4, 100.5, 70.3, 58.5, 31.3, 30.2, 29.5, 26.6.

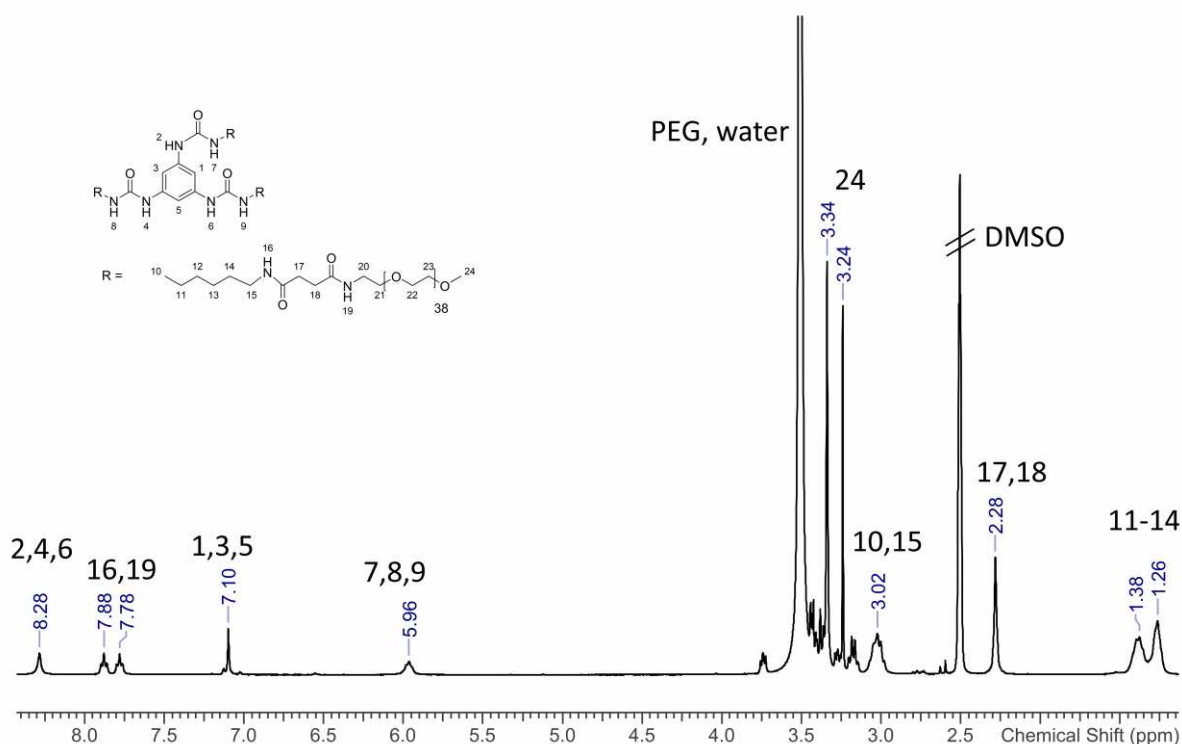


Figure S7. $^1\text{H-NMR}$ of $\text{BTU}[\text{C}_6][\text{PEO}_{2k}]_3$ (**3a**).

$N1,N1',N1''$ -((((benzene-1,3,5-triyltris(azanediyl))tris(carbonyl))tris(azanediyl))tris(dodecyl-6,1-diyl))tris($N4$ -(PEO_{2k})succinamide) **$\text{BTU}[\text{C}_{12}][\text{PEO}_{2k}]_3$** (**3b**)

Deprotection in TFA (**15**) and attachment of PEO (**3b**) was done according to the previous mentioned procedures for **1** and **2**. Yield: 0.650 g (93%). $^1\text{H NMR}$ (300 MHz, $\text{DMSO-}d_6$) δ [ppm]: 8.28 (s, 3H), 7.88 (s, 2H), 7.78 (s, 2H), 7.09 (s, 3H), 5.96 (br s, 3H), 3.43-3.50 (m, 465H), 3.24 (s, 9H), 3.18 (q, 6H), 2.96-3.04 (br, 12H), 2.27 (s, 12H), 1.35-1.39 (br, 12H), 1.24 (br s, 48H). $^{13}\text{C NMR}$ (75 MHz, $\text{DMSO-}d_6$) δ [ppm]: 171.9, 171.5, 155.5, 141.4, 100.5, 70.3, 58.5, 31.3, 30.2, 29.5, 26.9.

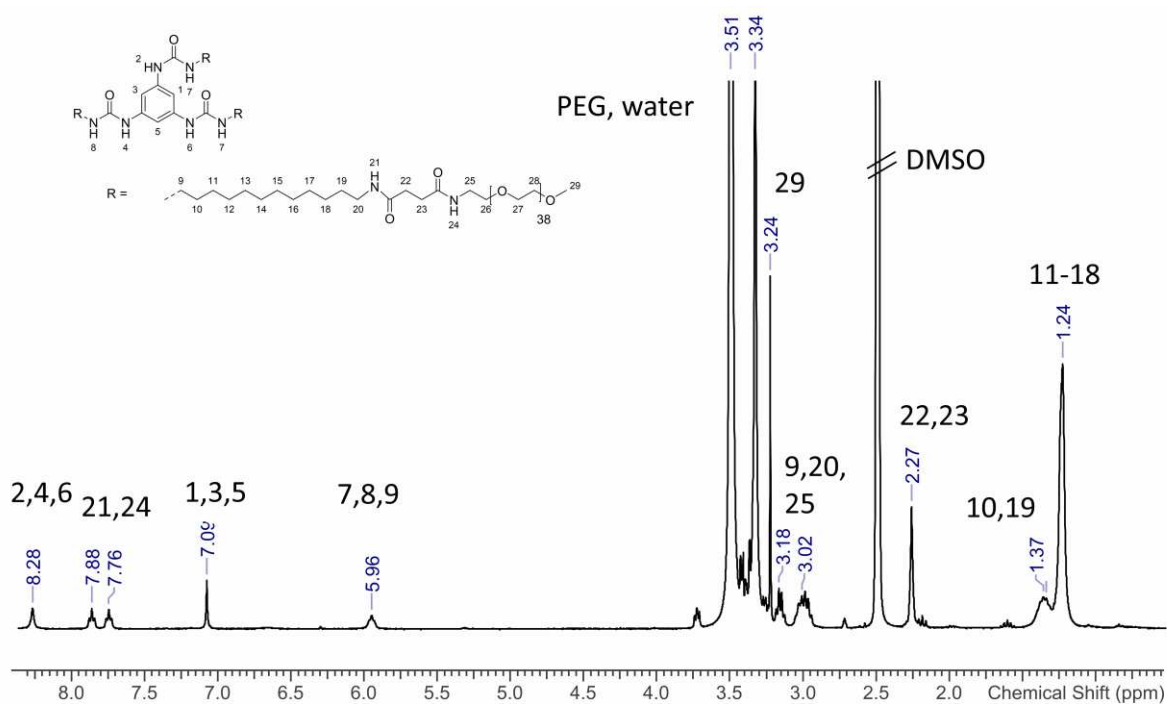


Figure S8. $^1\text{H-NMR}$ of BTU[C₁₂][PEO_{2k}]₃ (**3b**).

1.5 SEC

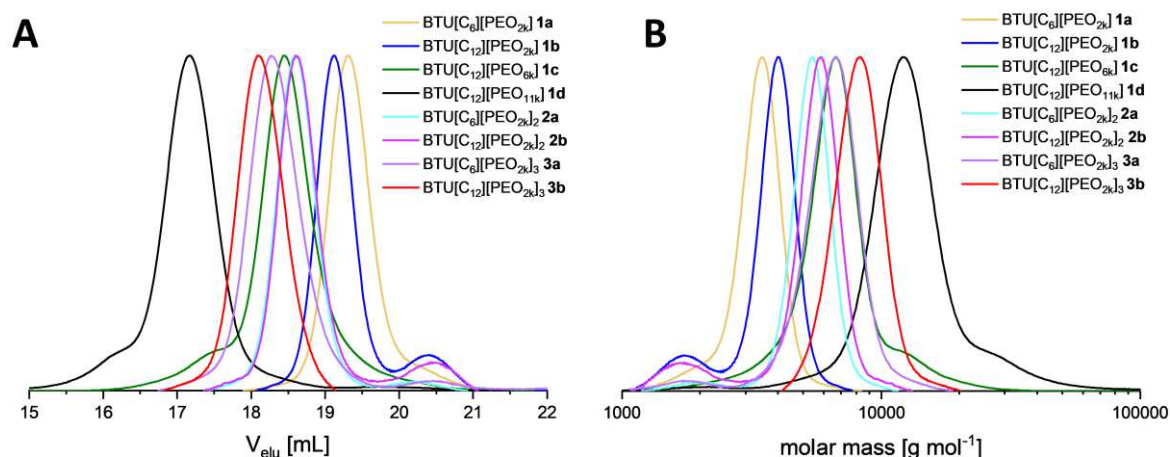


Figure S9. SEC-curves (A) and molar mass distribution (B) obtained by SEC (DMAc/LiCl, 25°C, RI Detection, PEO-Calibration) of all compounds.

Some SEC traces indicate the presence of additional PEG chains in the sample (in particular **1b** and **2b**). However, the content of this unreacted PEG remains below 4 wt% in all cases (determined from the integration of the respective peak areas). Therefore, the additional polymer was not considered in further calculations.

1.6 MALDI-TOF.

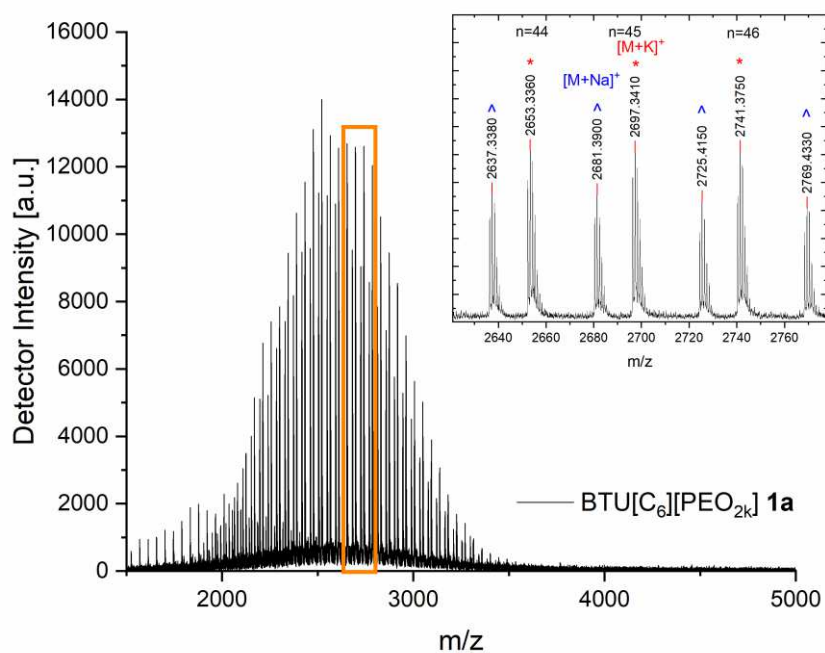


Figure S10. MALDI-TOF spectra of BTU[C₆][PEO_{2k}] **1a** and zoomed region (inlet) measured with CHCA as matrix material.

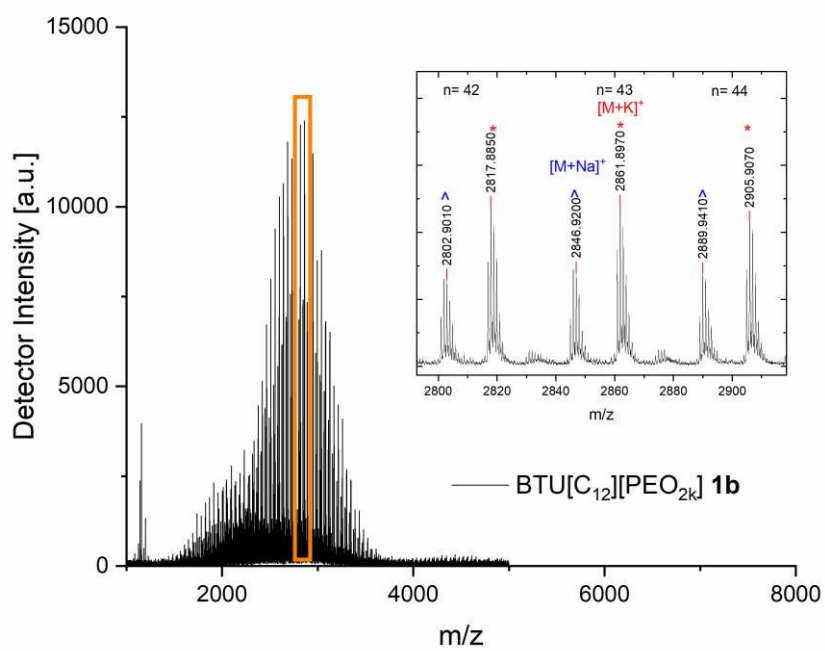


Figure S11. MALDI-TOF spectra of BTU[C₁₂][PEO_{2k}] **1b** and zoomed region (inlet) measured with CHCA as matrix material.

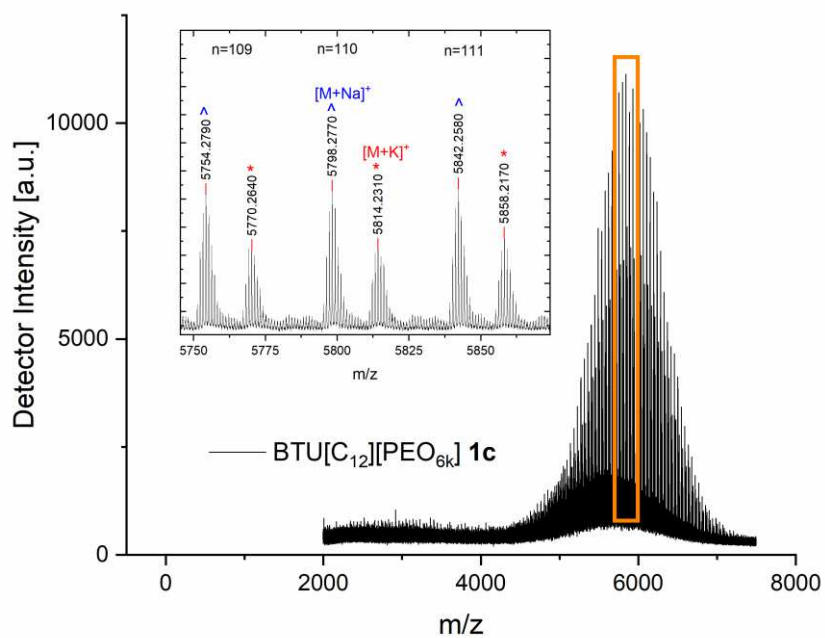


Figure S12. MALDI-TOF spectra of BTU[C₁₂][PEO_{6k}] **1c** and zoomed region (inlet) measured with CHCA as matrix material.

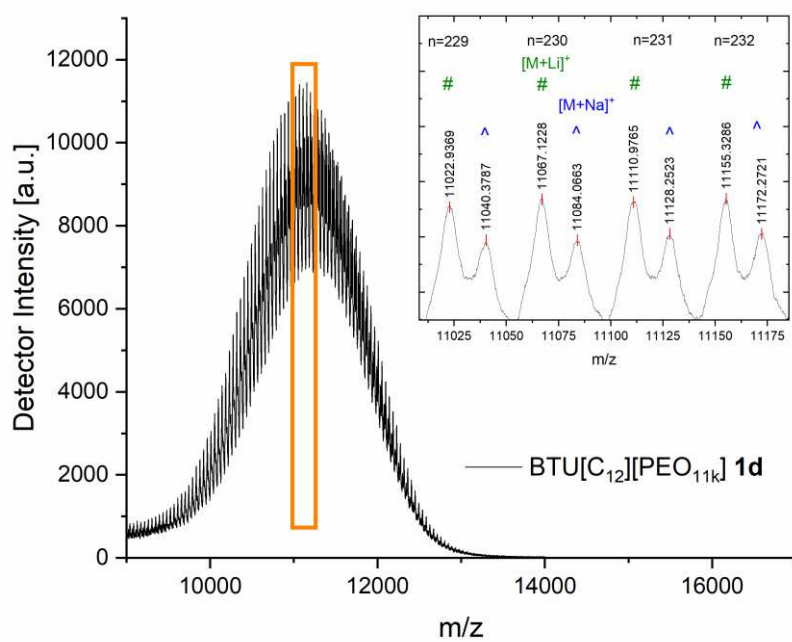


Figure S13. MALDI-TOF spectra of BTU[C₁₂][PEO_{11k}] **1d** and zoomed region (inlet) measured with CHCA as matrix material.

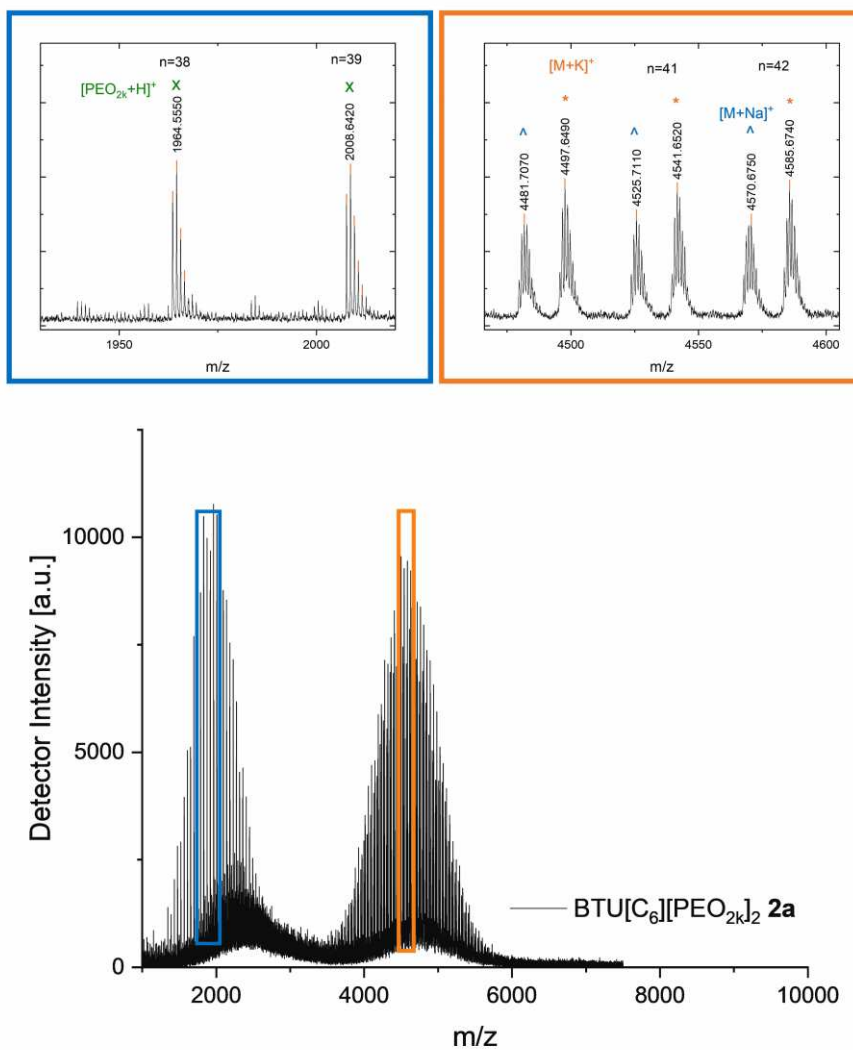


Figure S14. MALDI-TOF spectra of BTU[C₆][PEO_{2k}]₂ 2a and zoomed region (right inset) measured with CHCA as matrix material. The overestimated signals (see SEC data, Figure S9 for details) at low molar masses (< 3000 g/mol) can be attributed to uncoupled PEO chains derived from the initial NHS-PEO after hydrolysis.

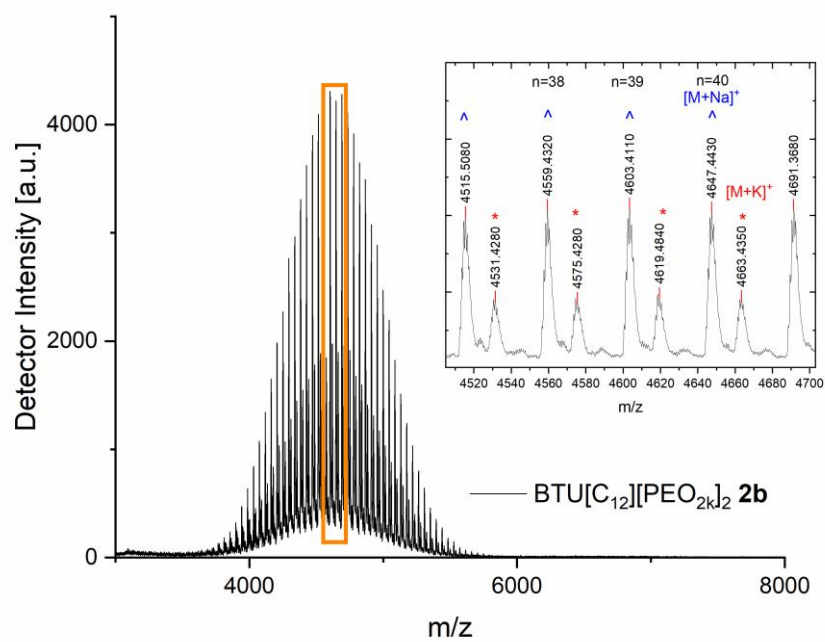


Figure S15. MALDI-TOF spectra of BTU[C₁₂][PEO_{2k}]₂ **2b** and zoomed region (inlet) measured with CHCA as matrix material.

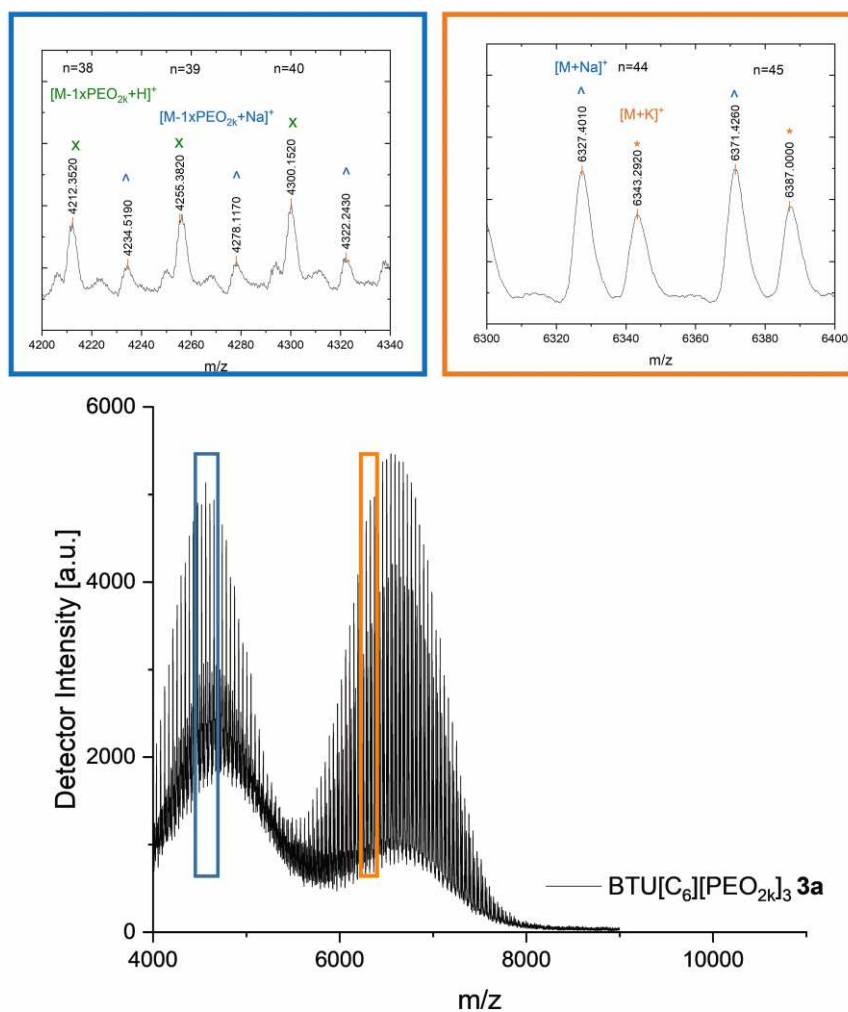


Figure S16. MALDI-TOF spectra of BTU[C₆](PEO_{2k})₃ **3a** and zoomed region (right inlet) measured with DHB as matrix material. The overestimated signals at low molar masses (< 5000 g/mol) can be attributed to the BTU where only two PEO arms are attached (left inlet).

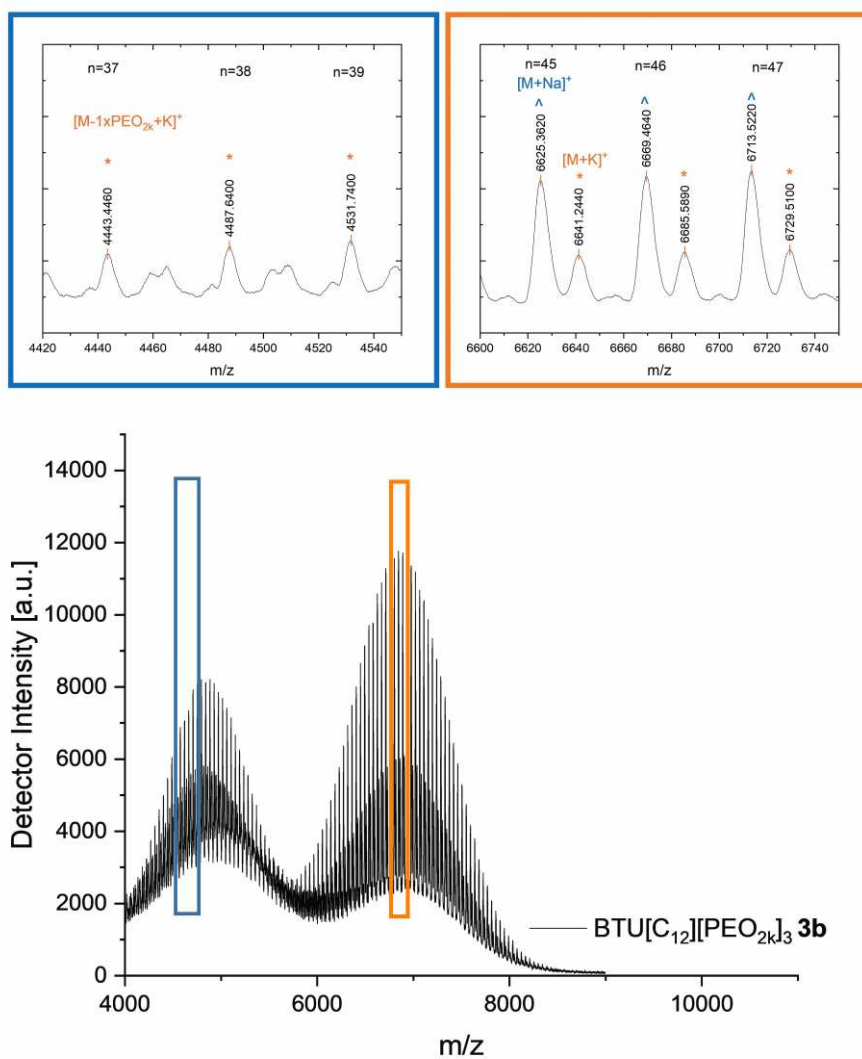


Figure S17. MALDI-TOF spectra of BTU[C₆][PEO_{2k}]₃ **3b** and zoomed region (inlet) measured with DHB as matrix material. The overestimated signals at low molar masses (< 5000 g/mol) can be attributed to the BTU where only two PEO arms are attached (left inlet).

2. Dynamic light scattering (DLS)

The hydrodynamic radius, R_h , was calculated based on the Stokes–Einstein equation:

$$R_h = \frac{kT}{6\pi\eta_0 D} \quad \text{Eq. S1}$$

with k being the Boltzmann constant, T the temperature in unit K, η_0 the viscosity of the solvent, and D the apparent translational diffusion coefficient.

The resulting intensity-weighted apparent distribution of hydrodynamic radii was converted to a number-weighted distribution (Figure S18B).

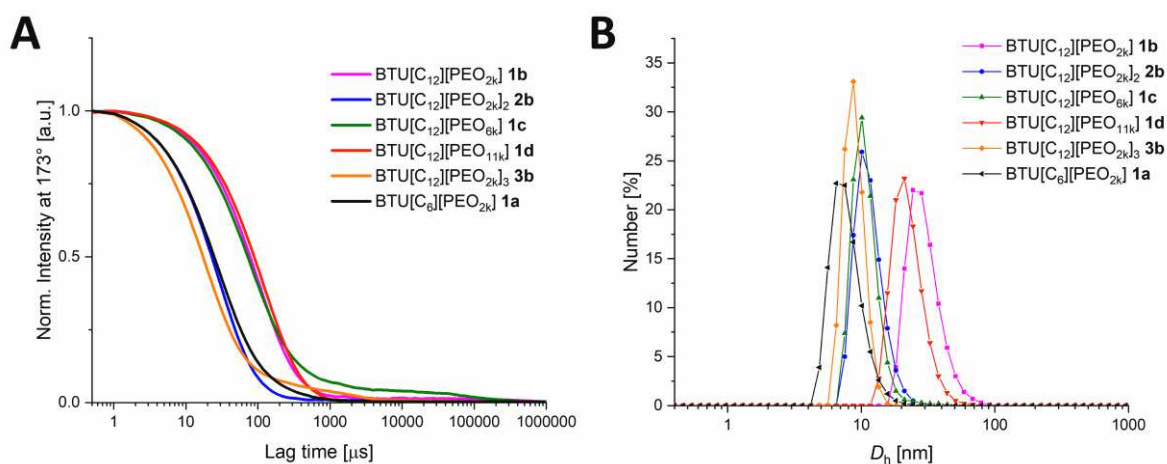


Figure S18. Intensity correlation curves (A) and number distributions of the hydrodynamic diameter D_h (B) of the BTUs at a 173° scattering angle in water at $T = 25.0$ °C at a concentration of 3 mg mL^{-1} of all samples in water.

3. cryoTEM

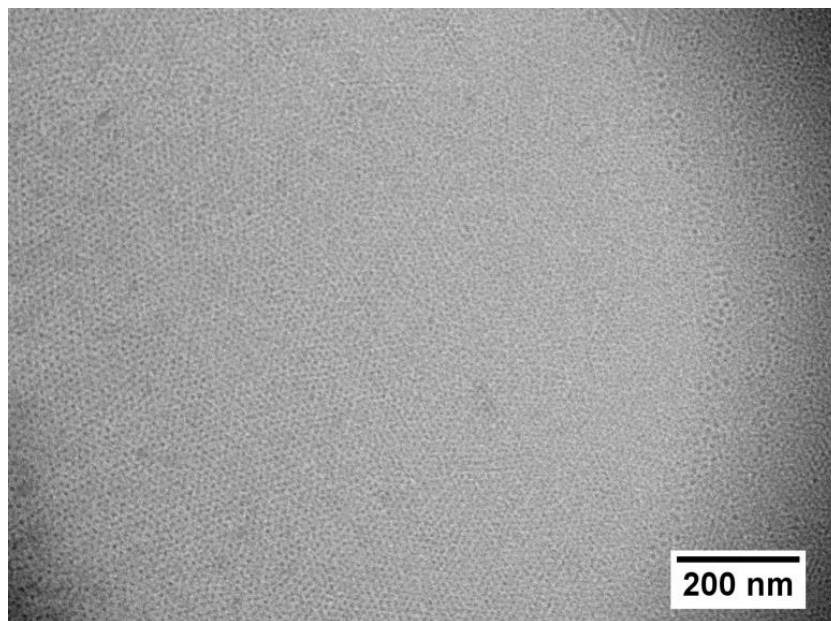


Figure S19. CryoTEM image of BTU[C₆][PEO_{2k}] **1a** in water at $c = 5 \text{ mg mL}^{-1}$.

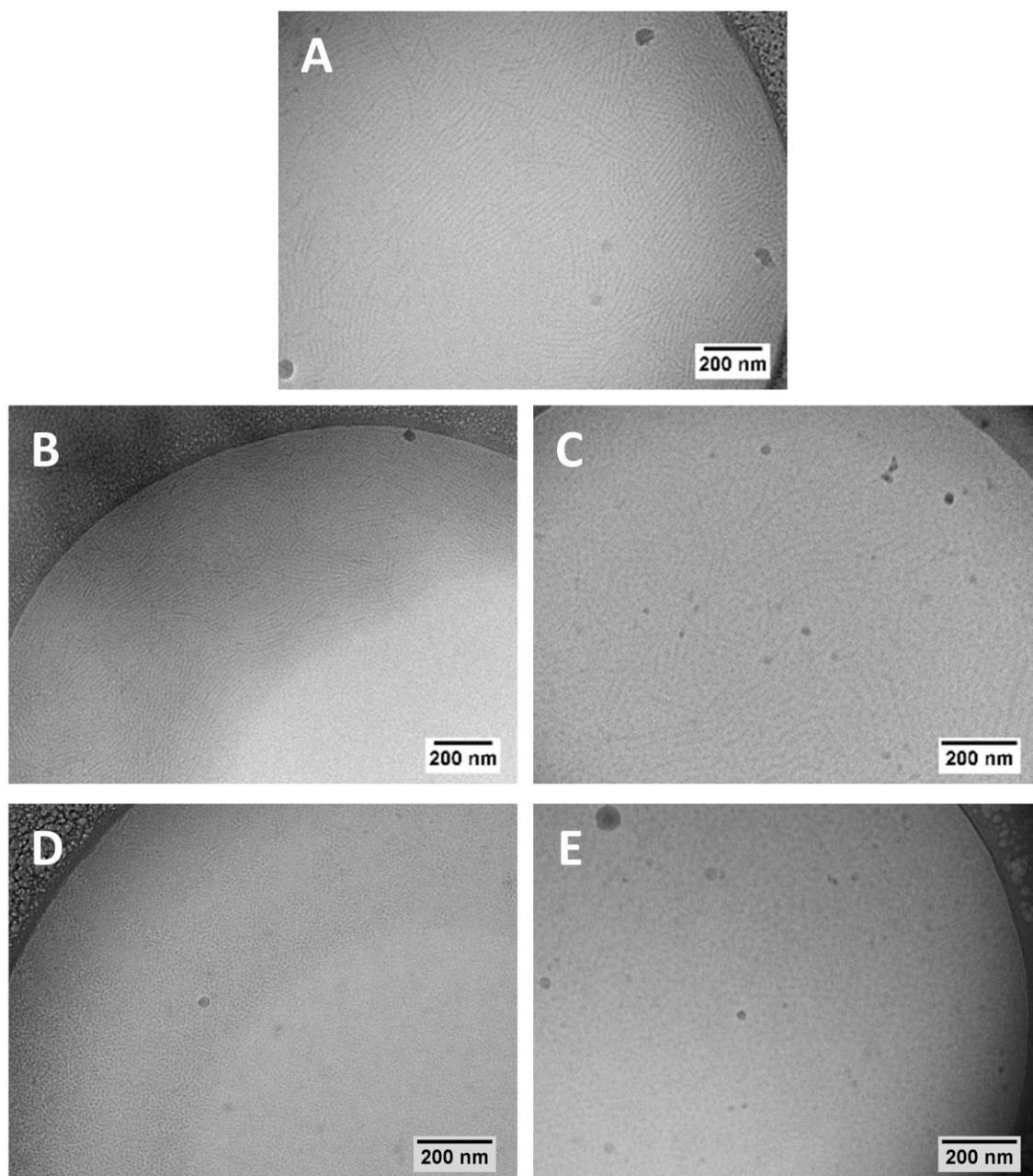


Figure S20. Full-sized cryoTEM images of BTU[C₁₂][PEO_{2k}] **1b** (A), BTU[C₁₂][PEO_{2k}]₂ **2b** (B), BTU[C₁₂][PEO_{6k}] **1c** (C), BTU[C₁₂][PEO_{2k}]₃ **3b** (D), and BTU[C₁₂][PEO_{11k}] **1d** (E) all prepared in water at $c = 5 \text{ mg mL}^{-1}$.

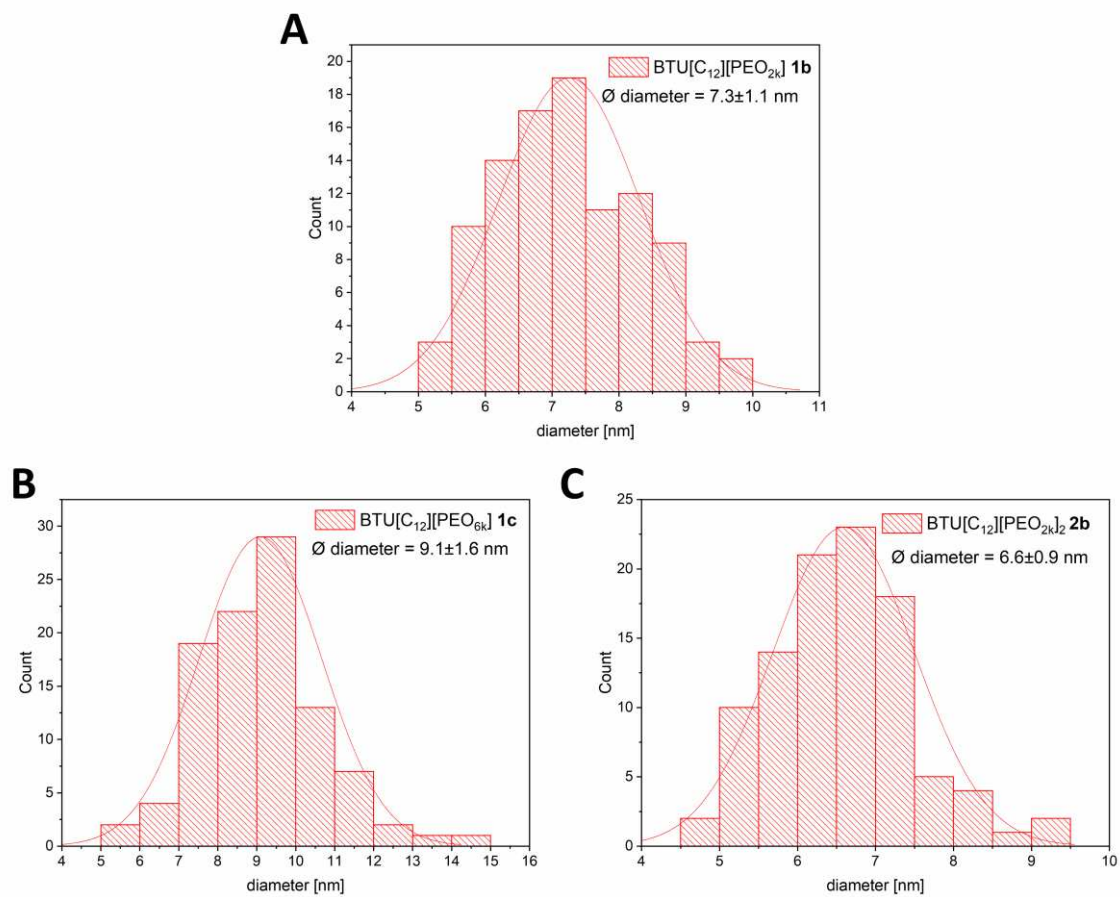


Figure S21. Histograms of the size distribution of the fiber diameter of BTU[C₁₂][PEO_{2k}] **1b** (A), BTU[C₁₂][PEO_{6k}] **1c** (B), and BTU[C₁₂][PEO_{2k}]₂ **2b** (C) (estimated from cryoTEM (n=100)).

4. Small angle X-Ray scattering (SAXS)

Table S1. Fitted parameters from SAXS compounds **1a**, **3b**, **1c**, **1d** using a spherical fit with a Gaussian distribution of the radius R_{sphere} .

#Compound	1a	3b	1c	1d
R_{sphere} [nm]	3.93	4.20	8.61	10.51
σ^1	1.11	1.05	1.88	2.31
N	1.56	1.27	3.019×10^2	1.074×10^2
δ^2 [nm ⁻²]	0.001018	0.001019	0.00102	0.00102
background	5.000×10^{-4}	7.458×10^{-4}	3.358×10^{-4}	6.689×10^{-4}
R_g [nm]	4.30^3	4.06^b	8.63^c	10.62^c
MW^4 [g mol ⁻¹]		0.1×10^6	1.0×10^6	1.1×10^6
N_{agg}		16.46	164.78	97.91
ν^5 [cm ³ g ⁻¹]		0.8499^6	0.8499	0.8443

Table S2. Fitted parameters from SAXS compounds **1c**, **1d** using a cylindrical fit with Gaussian distribution of the radius R_{sphere} .

#Compound	3b	1c	1d
R_{cyl} [nm]	5.35	8.01	10.6
L_{cyl} [nm]	5.77	14.6	17.2
σ^a	0.40	2.28	2.31
N	0.93	0.030	0.0097
δ^7 [nm ⁻²]	0.001019	0.00102	0.00102
background	7.458×10^{-4}	3.358×10^{-4}	6.689×10^{-4}

¹ Deviation derived from the Gaussian distribution of the radius.

² The scattering lengths density (SLD) of the materials was calculated using the calculator given in SASfit assuming a density of 1.1 g/cm³

³ R_g is calculated via Guinier plot of $\ln(I(q))$ vs. q^2 . Graphical depiction can be found in FigureS25 and S26.

⁴ Calculated from Guinier plot of $\ln(I(q)/K/c)$ vs. q^2 . Graphical depiction can be found in FigureS23 and S24.

⁵ The partial specific volume ν was calculated from density measurements at different concentration and subsequent linear fitting. The slope of the linear fit represents $d\rho/dc$. With $(1 - d\rho/dc)/\rho_0 = \nu$ the specific volume is obtained.

⁶ The partial specific volume ν was estimated from density measurements for **1c**, since the chemical composition is comparable.

⁷ The scattering lengths density (SLD) of the materials was calculated using the calculator given in SASfit assuming a density of 1.1 g/cm³

Table S3. Fitted parameters from SAXS for BTU[C₁₂][PEO_{2k}]₂ **2b** by combination of a spherical and a cylindrical fit.

Parameters for compound 2b	Contribution of cylindrical fit 1 (long cylinders)	Contribution of spherical fit
<i>N</i>	0.00187588	0.732201
<i>X</i> ₀ [nm]	4.31422 ⁸	5.08781 ⁹
Σ	1.12311	1.32483
<i>L</i> _{cylinder} [nm]	603.394 ¹⁰	-
δ^a [nm ⁻²]	0.001020	
Background	1.3500 x 10 ⁻³	

Table S4. Fitted parameters from SAXS for BTU[C₁₂][PEO_{2k}]₂ **2b** by combination of a long and a short cylindrical fit.

Parameters for compound 2b	Contribution of cylindrical fit 1 (long cylinders) ¹¹	Contribution of cylindrical fit 2 (short cylinders)
<i>N</i>	0.00187588	0.684476
<i>X</i> ₀ [nm]	4.31422 ¹²	4.76984 ¹³
σ	1.12311	1.60837
<i>L</i> _{cylinder} [nm]	603.394 ⁱ	9.13961
δ^a [nm ⁻²]	0.001020	
Background	1.3500 x 10 ⁻³	

⁸ Denoted as *R*_{cyl_long} in the manuscript.⁹ Denoted as *R*_{sphere} in the manuscript.¹⁰ The range for fitting of this parameter was set from 550-650 nm according to the cryoTEM images.¹¹ Data derived from cylindrical fit 1 Table S3.¹² Denoted as *R*_{cyl_long} in the manuscript.¹³ Denoted as *R*_{cyl_short} in the manuscript.

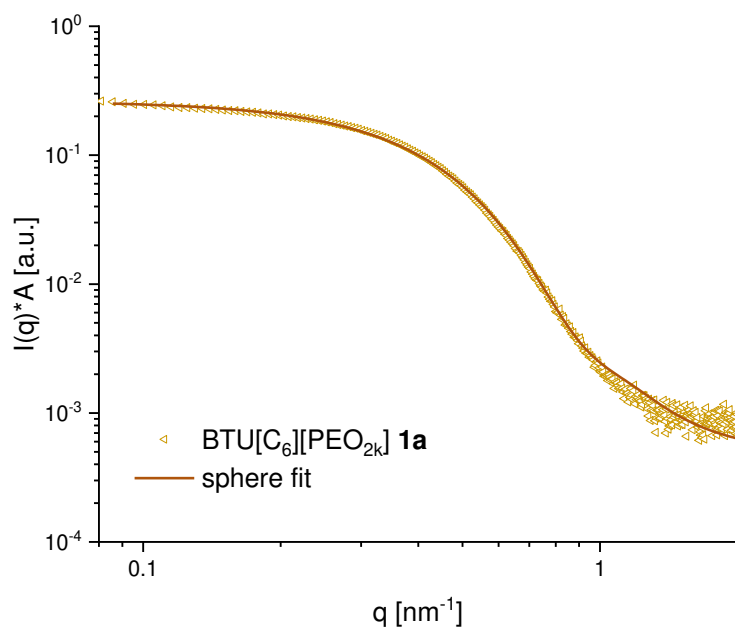


Figure S22. Scattering profile of **1a** at a concentration of $c = 10 \text{ mg mL}^{-1}$ obtained by SAXS.

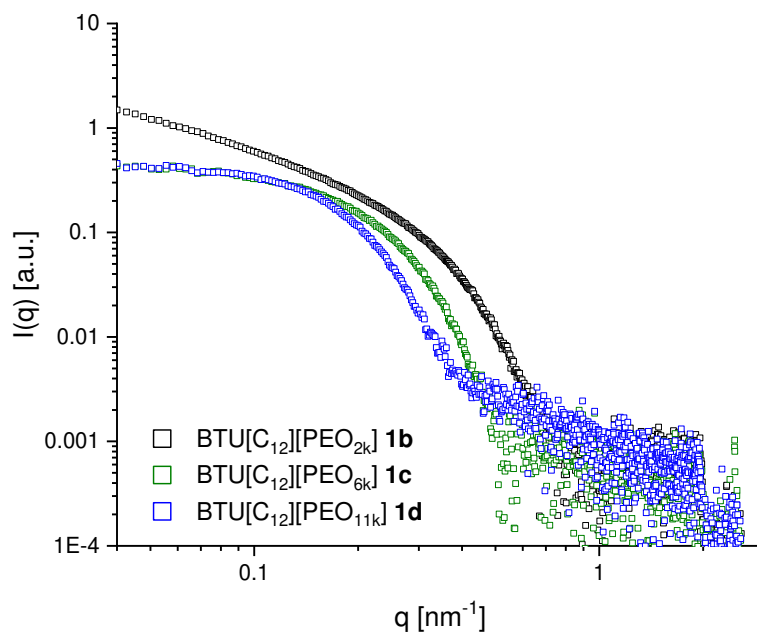


Figure S23. Scattering profiles of **1b** (black), **1c** (green) and **1d** (blue) at a concentration of $c = 1.5 \text{ mg mL}^{-1}$ obtained by SAXS without offset.

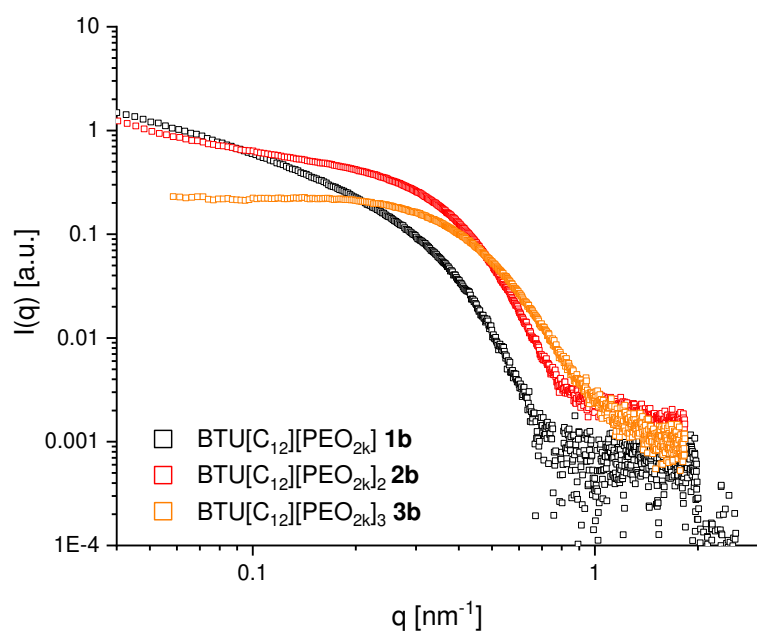


Figure S24. Scattering profiles of **3b** (red), **2b** (magenta) at a concentration of $c = 10 \text{ mg mL}^{-1}$ and **1b** (back) at a concentration of $c = 1.5 \text{ mg mL}^{-1}$ obtained by SAXS without offset.

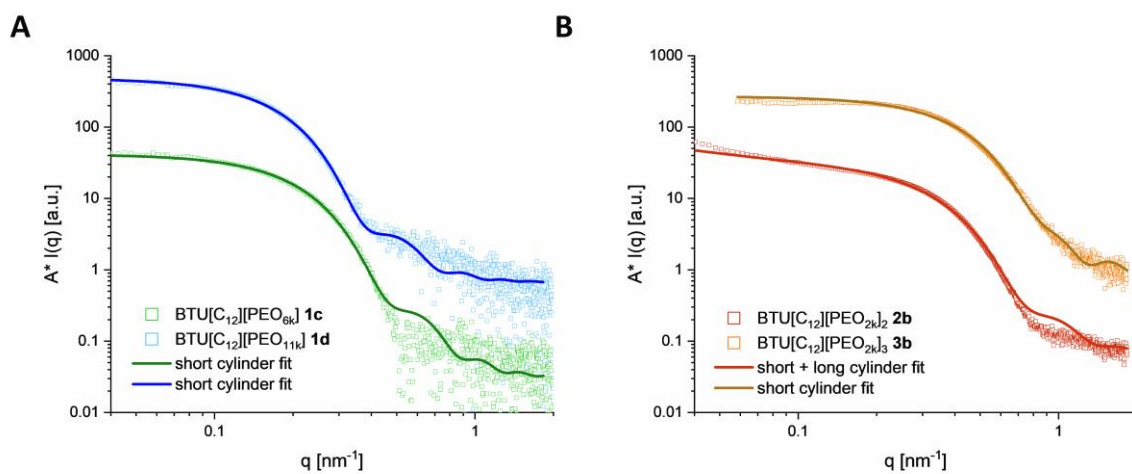


Figure S25. SAXS profiles of **1c** (green), **1d** (blue) (A) and **2b** (red), **3b** (orange) (B) with cylindrical fits obtained by SAXS.

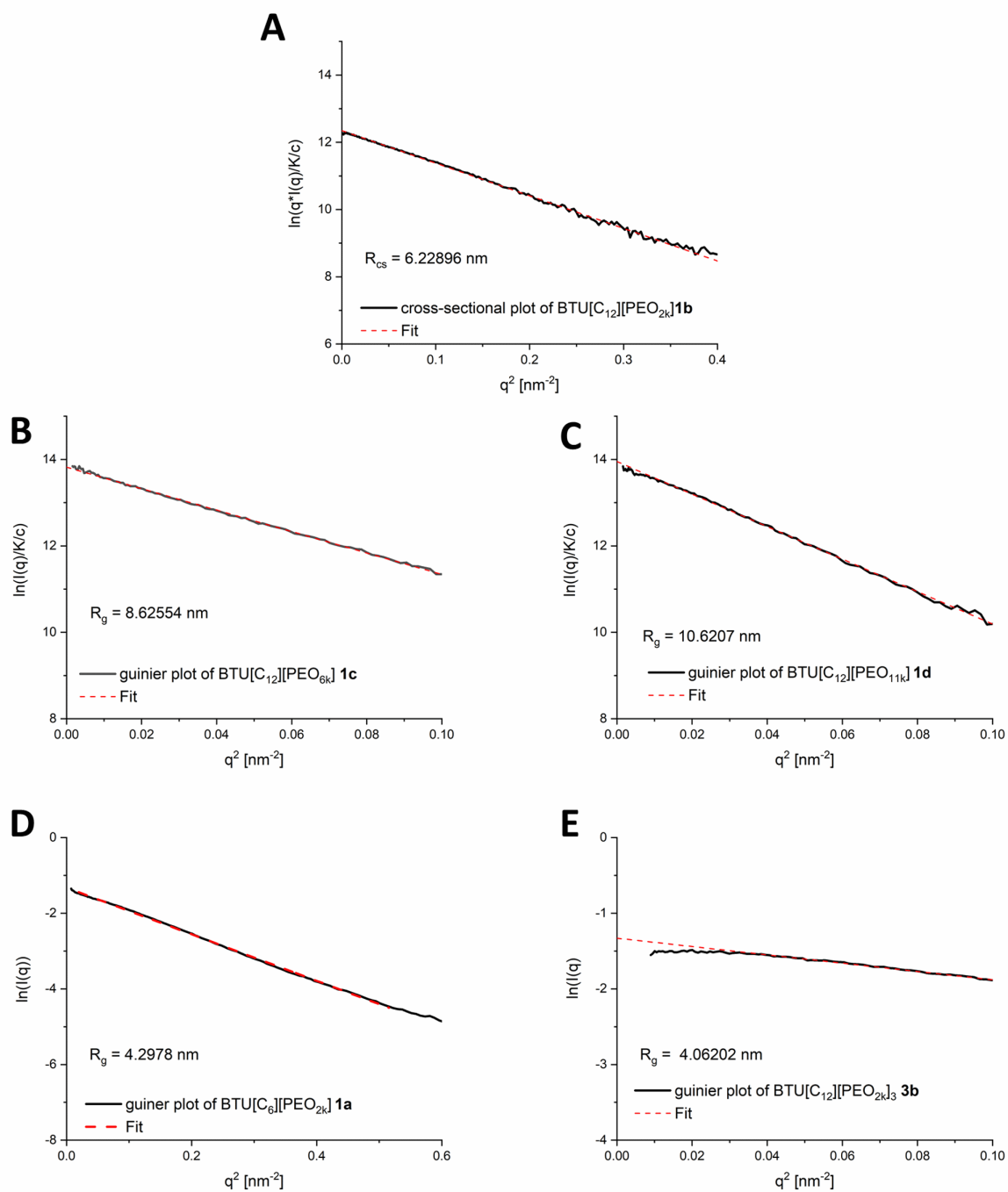


Figure S26. Cross-sectional plot for BTU[C₁₂][PEO_{2k}] **1b** (A) and Guinier plot for BTU[C₁₂][PEO_{6k}] **1c** (B), BTU[C₁₂][PEO_{11k}] **1d** (C), BTU[C₆][PEO_{2k}] **1a** (D) and BTU[C₁₂][PEO_{2k}]₃ **3b** (E). Linear fits were calculated using the software OriginPro 2018b.

5. Static light scattering (SLS)

The absolute scattering intensity R_θ in cm^{-1} was determined according to

$$R_\theta = \frac{I_{\text{solution}}(\theta) - I_{\text{solvent}}(\theta)}{I_{\text{toluene}}(\theta)} \times \left(\frac{n_{\text{solvent}}}{n_{\text{toluene}}} \right)^2 R_{\text{toluene}} \quad \text{Eq. S2}$$

With I_{toluene} , I_{solvent} , I_{solution} being the average scattering intensities by toluene, solvent and solution, respectively. $n_{\text{toluene}} = 1.496$, $n_{\text{solvent}} = n_{\text{water}} = 1.33$, and $R_{\text{toluene}} = 1.35 \cdot 10^{-5} \text{ cm}^{-1}$ at the wavelength of $\lambda_0 = 633 \text{ nm}$.

The contrast factor K was calculated by

$$K = \frac{4\pi^2 n_{\text{solvent}}^2}{\lambda^4 N_a} \times \left(\frac{\partial n}{\partial c} \right)^2 \quad \text{Eq. S3}$$

Where N_a is Avogadro number and $\left(\frac{\partial n}{\partial c} \right)$ is the refractive index increment of the polymer **BTU** **1b** determined to be 0.147 mL/g .

Different concentrations were investigated to ensure that interactions between the aggregates can be neglected (Figure S27).

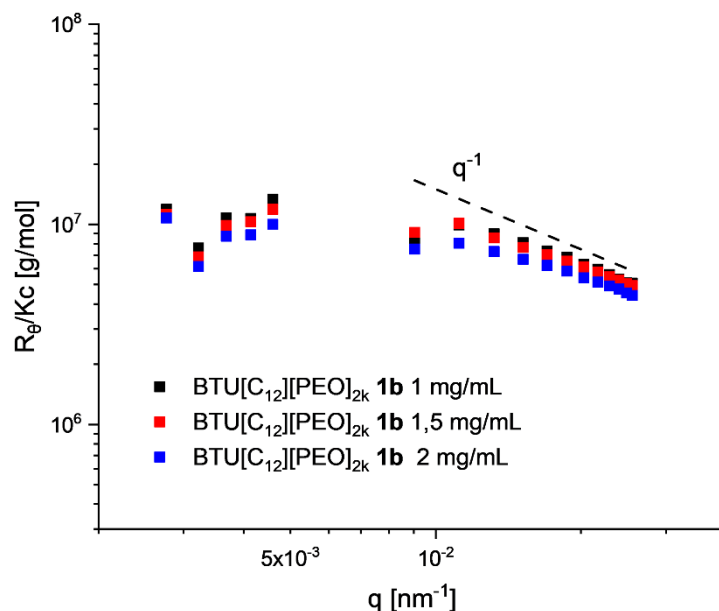


Figure S27. Concentration-dependent evolution of R_θ/Kc versus the scattering vector q for BTU[C₁₂][PEO]_{2k} **1b** in water (dashed black line as a guide to the eye for a q^{-1} dependency).

5.1 Combination of SAXS with SLS data.

To get a superimposed graph of SAXS and SLS data the intensities obtained from SLS from BTU[C₁₂][PEO_{2k}] **1b** at 1.5 mg mL⁻¹ were multiplied by a factor of 1.6. This slight correction was necessary because the data did not superimpose perfectly. A reason for this might be the intrinsic experimental error of around 10-20% of both measurements techniques.²

Fitted parameters using a cylindrical fit with a Gaussian distribution of the radius R_{cylinder} for compound **1b**:

Table S5. Fitted parameters from SAXS combined with SLS for BTU[C₁₂][PEO_{2k}] **1b**.

#Compound	1b
R_{cyl} [nm]	5.03
Σ	1.12
N	7.33×10^{-3}
L_{cyl}	311
δ^{14} [nm ⁻²]	0.001058
Background	5.000×10^{-4}
R_{cs}^{15} [nm]	6.2
ν^{16} [cm ³ g ⁻¹]	0.8779541

For BTU[C₁₂][PEO_{2k}] **1b** the following values were calculated:

Table S6. Molecular weight and aggregation number calculated from SLS^h and SAXSⁱ.

$M_{\text{w,unimer}}$ [g/mol]	M_{w} [g/mol]	L_{cylinder} [nm]	N_{agg}	n_{cross}
2779.62	9 516 135 ^h	311 ⁱ	3 424	3.96

¹⁴ The scattering lengths density (SLD) of the materials was calculated using the calculator given in SASfit assuming a density of 1.1 g/cm³

¹⁵ $R_{\text{cross-sectional}}$ calculated via cross-sectional plot of $\ln(q^*I(q)/K/c)$ vs. q^2 .

¹⁶ The partial specific volume was calculated from density measurements.

With:

$$N_{agg} = \frac{M_w}{M_{w,unimer}} \quad \text{Eq. S4}$$

$$\# \text{ molecules in the cross - section} = n_{cross} = \frac{N_{agg}}{\frac{L_{cylinder}}{d_{stacking}}} \quad \text{Eq. S5}$$

6. Analytical Ultracentrifugation (AUC)

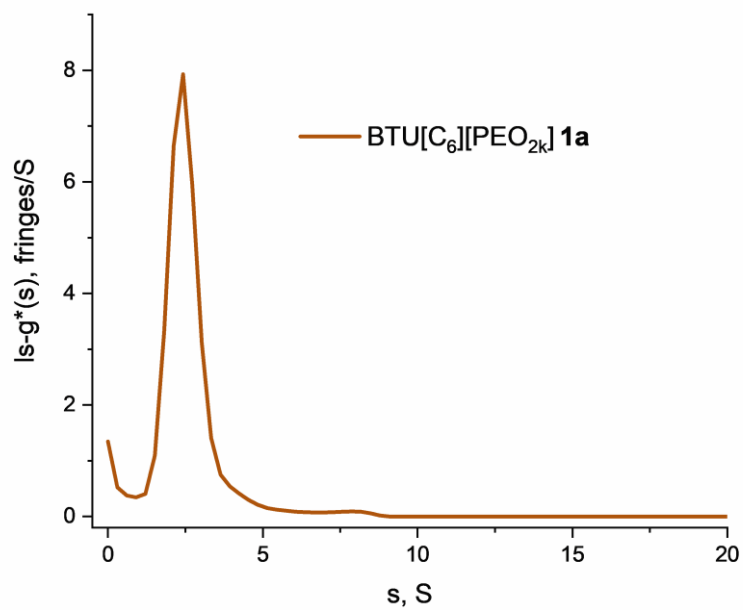


Figure S28. Differential distribution of sedimentation coefficients, $ls-g^*(s)$, of BTU[C₆][PEO_{2k}] **1a** at 3 mg mL⁻¹ in water from sedimentation velocity AUC experiments.

Alternatively to the $ls - g^*(s)$ model, solving for the apparent differential distribution of sedimentation coefficients as specified in the experimental section,³ the $c(s)$ model can be used. Hereby, for resolving residual rather small unimeric species, sedimentation-diffusion analysis was carried out (Figure S29).⁴

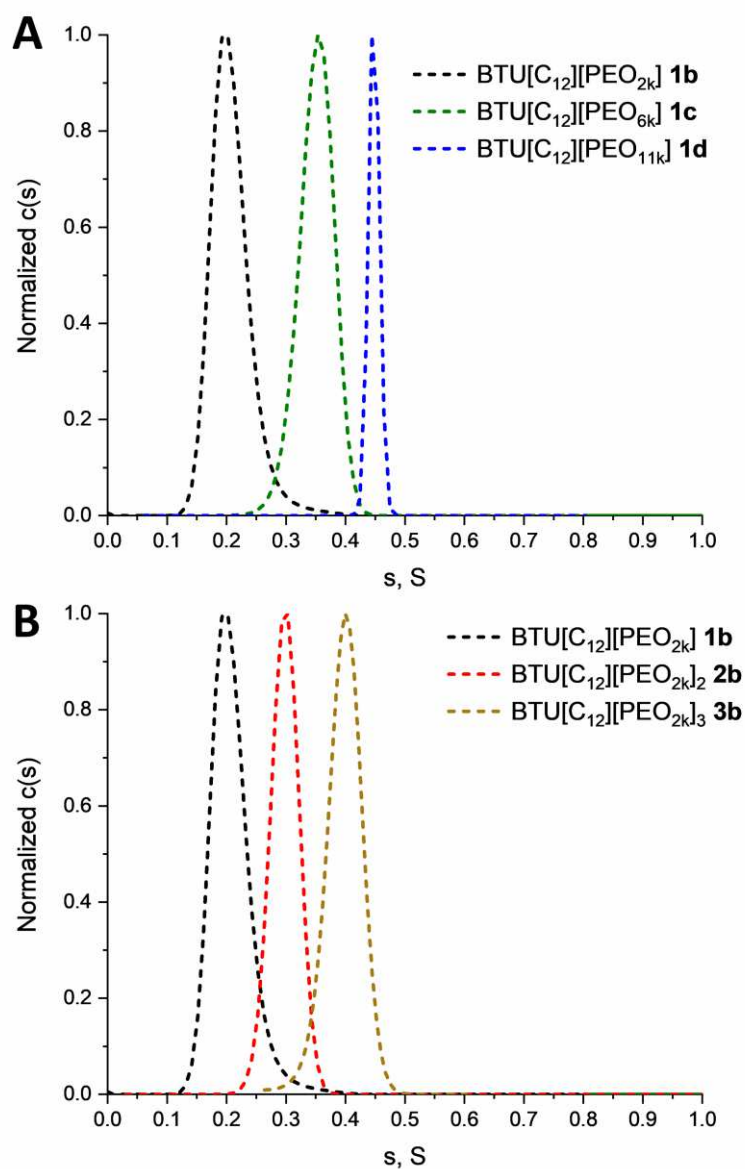


Figure S29. Normalized differential distributions of sedimentation coefficients, $c(s)$, for all BTUs with (A) increased arm length at a fixed number of arms, and (B) an increased number of arms at a fixed arm length. The analysis was focused on the apparently existing residual non-assembled small unimeric species using sedimentation-diffusion analysis. The total concentration of each sample was 3mg/mL in water.

7. References.

1. Van Gorp, J. J.; Vekemans, J. A.; Meijer, E. W. C3-symmetrical supramolecular architectures: fibers and organic gels from discotic trisamides and trisureas. *J. Am. Chem. Soc.* **2002**, 124 (49), 14759-69 DOI: 10.1021/ja020984n.
2. Han, S. Y.; Mellot, G.; Pensec, S.; Rieger, J.; Stoffelbach, F.; Nicol, E.; Colombani, O.; Jestin, J.; Bouteiller, L. Crucial Role of the Spacer in Tuning the Length of Self-Assembled Nanorods. *Macromolecules* **2020**, 53 (1), 427-433 DOI: 10.1021/acs.macromol.9b01928.
3. Schuck, P.; Rossmannith, P. Determination of the sedimentation coefficient distribution by least-squares boundary modeling. *Biopolymers* **2000**, 54 (5), 328-41 DOI: 10.1002/1097-0282(20001015)54:5<328::AID-BIP40>3.0.CO;2-P.
4. Nischang, I.; Perevyazko, I.; Majdanski, T.; Vitz, J.; Festag, G.; Schubert, U. S. Hydrodynamic Analysis Resolves the Pharmaceutically-Relevant Absolute Molar Mass and Solution Properties of Synthetic Poly(ethylene glycol)s Created by Varying Initiation Sites. *Anal. Chem.* **2017**, 89 (2), 1185-1193 DOI: 10.1021/acs.analchem.6b03615.

Publication P4

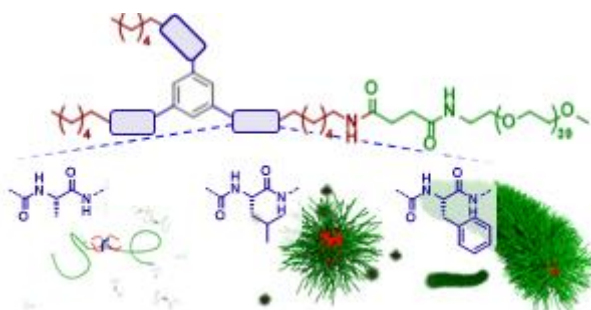
Impact of amino acids on the aqueous self-assembly of benzenetrisepptides into supramolecular polymer bottlebrushes

T. Klein, H. F. Ulrich, F. V. Gruschwitz, M. T. Kuchenbrod, R. Takahashi, S. Fujii, S. Hoepfner, I. Nischang, K. Sakurai, J. C. Brendel, *Polym. Chem.* **2020**, *11*, 6763-6771.

Reproduced by permission of Royal Society of Chemistry. Copyright © 2020.

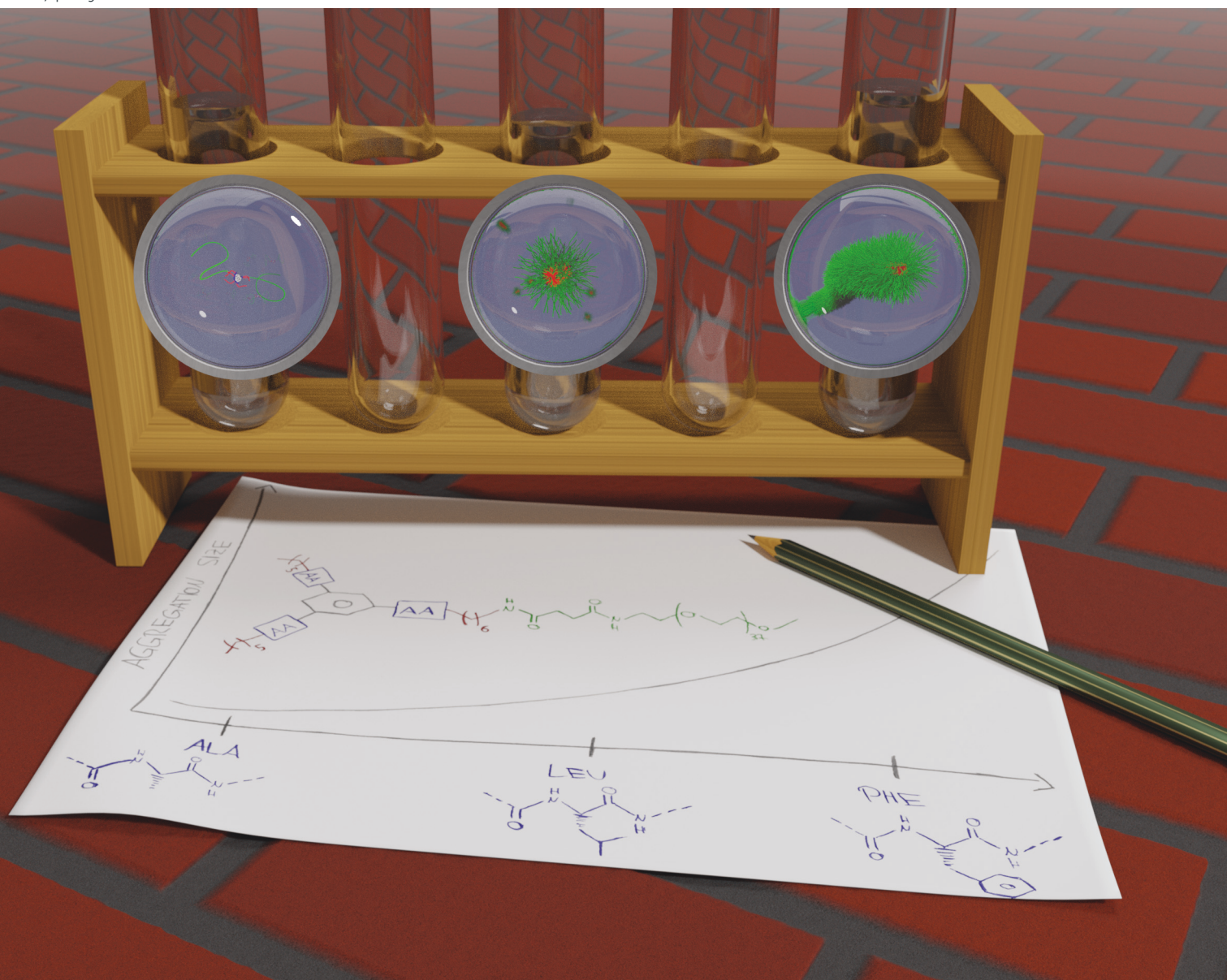
The paper as well as the supporting information is available online:

doi.org/10.1039/d0py01185a



Polymer Chemistry

rsc.li/polymers



ISSN 1759-9962



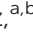
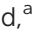






PAPER

Johannes C. Brendel *et al.*
Impact of amino acids on the aqueous self-assembly
of benzenetrispeptides into supramolecular polymer
bottlebrushes



Cite this: *Polym. Chem.*, 2020, **11**, 6763

Impact of amino acids on the aqueous self-assembly of benzenetrispeptides into supramolecular polymer bottlebrushes†

Tobias Klein, ^{a,b} Hans F. Ulrich, ^{a,b} Franka V. Gruschwitz, ^{a,b} Maren T. Kuchenbrod, ^{a,b} Rintaro Takahashi, ^c Shota Fujii, ^c Stephanie Hoepfner, ^{a,b} Ivo Nischang, ^{a,b} Kazuo Sakurai ^c and Johannes C. Brendel ^{*a,b}

In contrast to covalent polymer brushes, directional supramolecular forces such as hydrogen bonds or π - π -interactions govern the formation of supramolecular polymer bottlebrushes (SPBs) in a self-assembly process starting from single polymer building units. In an attempt to broaden our understanding of these processes and the required supramolecular forces, we here investigated the benzenetrispeptide (BTP) motif to self-assemble polyethylene oxide (PEO) chains into SPBs in water. For this purpose, we synthesized a library of BTP-PEO conjugates, in which we varied the amino acid unit (alanine vs. leucine vs. phenylalanine), the hydrophobic spacer (C_6 vs. C_{12}), and the steric hindrance imposed by PEO (2 vs. 5 vs. 10 kg mol⁻¹, one vs. three polymer chains). In particular, the type of amino acid was hypothesized to have a crucial influence on the final morphology. A detailed characterization of the respective solutions revealed that for the C_6 spacer and one PEO_{2k} chain, only phenylalanine containing core units formed the desirable SPBs, while in the other cases only spherical micelles (leucine) or barely any aggregation (alanine) was observed. In contrast, the more hydrophobic C_{12} spacer resulted in an exclusive formation of SPBs, whereas the choice of the amino acid moiety had a minor influence on the observed morphology. Increasing the steric hindrance finally resulted in a transition from cylindrical toward spherical micelles. The broad structural variety offered by the choice of amino acids not only allows for an excellent control of the solution morphologies but also the potential integration of functional units to the core.

Received 20th August 2020,
Accepted 28th September 2020
DOI: 10.1039/d0py01185a

rsc.li/polymers

1. Introduction

Much research in the last 20 years has been devoted to the development of synthetic protocols toward anisotropic polymeric aggregates¹ as these materials offer promising properties for applications *e.g.* in nanomedicine,^{2,3} as rheology modifiers⁴⁻⁶ or in electronic and photonic applications.⁷⁻⁹ However, only a narrow range of volume fractions (solvophobic vs. solvophilic block), which is related to the packing parameter p for small molar mass amphiphiles,¹⁰ results in the formation of cylindrical micelles.^{11,12} Furthermore, the accurate

prediction of this parameter p remains challenging for polymers and obtaining the desired solution morphologies often requires systematic variations of the copolymer composition.¹² Advanced approaches such as the polymerization induced self-assembly (PISA) certainly improved the access to anisotropic polymeric structures, but predictions of morphologies remain mostly elusive due to potential kinetically trapped states of the structures.¹³⁻¹⁶ To obtain anisotropic polymeric aggregates in solution over a broad composition range, an additional driving force must be introduced to overcome the thermodynamically often favoured formation of spherical structures.¹⁶⁻¹⁹ A successful concept relies, *e.g.*, on the crystallization-driven self-assembly (CDSA),²⁰⁻²³ but despite its unrivalled dimensional control, the synthetic effort and the demands for highly crystalline polymers renders this technique rather challenging and less suitable for widespread applications.²⁴⁻²⁶ A straightforward approach relies on the utilization of π - π -interactions or hydrogen bonds (H-bonds) which govern the solution self-assembly of polymers into so-called supramolecular polymer bottlebrushes (SPBs) comprising a non-covalent backbone structure.²⁷ Despite a growing number of available supramole-

^aLaboratory of Organic and Macromolecular Chemistry (IOMC), Friedrich Schiller University Jena, Humboldtstraße 10, 07743 Jena, Germany. E-mail: johannes.brendel@uni-jena.de

^bJena Center for Soft Matter (JCSM), Friedrich Schiller University Jena, Philosophenweg 7, 07743 Jena, Germany

^cDepartment of Chemistry and Biochemistry, University of Kitakyushu, 1-1 Hibikino, Wakamatsu-ku, Kitakyushu, Fukuoka 808-0135, Japan

†Electronic supplementary information (ESI) available. See DOI: 10.1039/d0py01185a

cular motifs, SPBs still remain a niche, although their inherently dynamic nature makes them appealing in areas such as nanomedicine.^{28–35}

Focussing on H-bonds, aqueous self-assembly of polymers becomes particularly challenging due to the competitive character of water. Only recently, Han *et al.* compared the aqueous self-assembly of urea motifs consisting of three, four or five urea groups and only the latter was able to form SPBs in water.³⁶ As an alternative concept, synergetic effects between H-bonds and an associated hydrophobic shielding have been employed to further strengthen the self-assembly in water.^{37–45} In addition, sufficient hydrophilicity must be introduced by the attachment of hydrophilic polymers to guarantee solubility in water. In general, the steric constraints imposed by those tethered polymers significantly impact the self-assembly behaviour depending on polymer chain length, number of attached chains, and their bulkiness.^{39,46–52} In the case of aqueous solution systems, we recently discovered that amphiphilic supramolecular building blocks still obey the general idea of the above-mentioned packing parameter, but an increasing number of H-bonds formed by the core unit are able to shift the assembly morphology phase boundaries and extend the range of the cylindrical assemblies.^{51,53} Those studies utilized the 1,3,5-benzenetrisamide (BTA) and 1,3,5-benzenetrisurea (BTU) motifs, capable of assembling into cylindrical structures by the formation of a H-bond triple helix.^{54–57} An opportunity to further increase the number of H-bonds is the attachment of amino acids to the central BTA core resulting in benzenetrispeptides (BTPs) as shown by the Besenius group for non-polymeric compounds^{58–66} and more recently by Zagorodko *et al.*⁶⁷

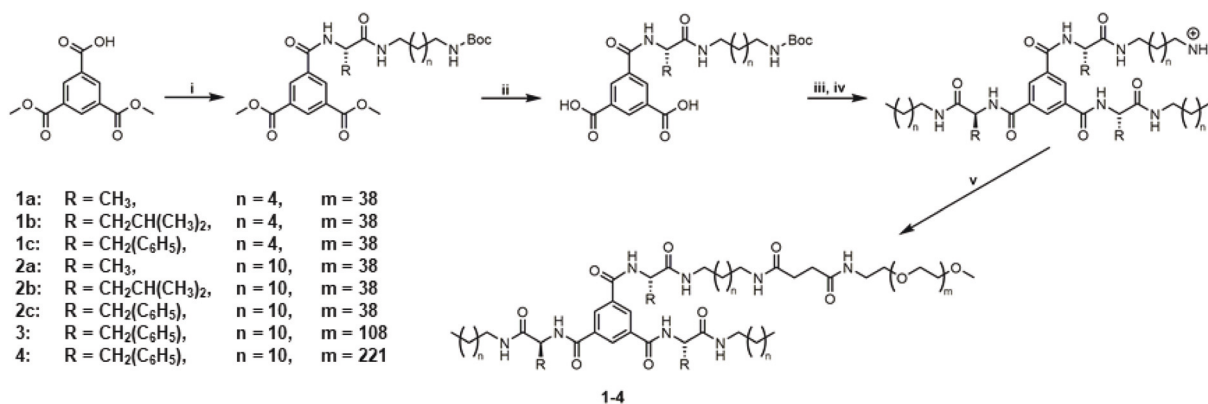
Intrigued by the results and the versatility of the 1,3,5-substituted benzene motif, we sought of extending our understanding of this assembly process and gain a better control of the resultant solution structure. In particular, the choice of amino acids represents an interesting possibility to fine tune the strength of the interaction.^{68–70} Taking advantage of this

adaptability, we created several 1,3,5-substituted benzenetrispeptides (BTP) conjugated with poly(ethylene oxide) (PEO). The amino acids were systematically varied from alanine to leucine and finally phenylalanine to increase the hydrophobicity and the tendency to form β -sheet-like assemblies.^{71–73} In accordance with our previous studies, short and long hydrophobic linkers (C_6 vs. C_{12}) were compared and the impact of the number (one vs. three) as well as the length of attached PEO chains (2 vs. 5 vs. 10 kg mol⁻¹) was examined to obtain a comprehensive structure-assembly correlation. An in-depth solution characterization of this library of compounds was performed by combining scattering (dynamic light scattering (DLS), small angle X-ray scattering (SAXS)), spectroscopic (circular dichroism (CD)), microscopic (cryo-transmission electron microscopy (cryoTEM)) and hydrodynamic (analytical ultracentrifugation (AUC)) techniques.

2. Results and discussion

2.1. Synthesis of BTP-PEO conjugates

The BTP-PEO conjugates (**1a–c**, **2a–c**, **3**, **4** and **5**) were synthesized similarly to the previously reported BTA-PEO compounds (Scheme 1 and Schemes S1–S5; see ESI† for synthetic protocols).⁵³ Starting from commercially available trimethyl benzene-1,3,5-tricarboxylate, a selective hydrolysis of one methyl ester yielded 3,5-bis(methoxycarbonyl)benzoic acid to which amino acid containing chains were attached *via* sequential amide couplings and selective deprotections. The incorporated amino acids were previously modified with hexyl or dodecyl alkyl-chains using an orthogonal protecting strategy comprising Boc- and Cbz-protecting groups (see Schemes S2–4†). After deprotection of the one terminal Boc-group, PEO polymers could be tethered to the central BTP motif *via* amide formation initiated by an activated *N*-hydroxysuccinimide (NHS) ester on the terminus of the polymers resulting in BTP-PEO conjugates **1a–c**, **2a–c**, **3**, and **4** (the synthetic route to



Scheme 1 Synthetic route toward BTP compounds **1a–c**, **2a–c**, **3**, and **4**. (i) *N*-Boc-protected, alkylated amino acid, DMAP, EDC-HCl, CHCl₃, rt, overnight; (ii) KOH in EtOH/H₂O 9 : 1, reflux, 30 min; (iii) alkylated amino acid, DMAP, EDC-HCl, CHCl₃ or DMF, rt, overnight; (iv) TFA/TIPS/H₂O, DCM, rt, 2 h; (v) MeO-PEO-NHS, TEA, DMF, rt, overnight. The detailed synthetic protocols and the scheme for the BTP-PEO bearing three polymer chains can be found in the ESI (Scheme S6†).

compound BTP-PEO 5 bearing three PEO chains can be found in Scheme S6†). To ensure a monomodal distribution of the BTP-PEO conjugates, excess PEO and unconjugated core motifs could be successfully removed by washing using centrifugal filters (membrane molecular weight cut-off: 10 kDa).

2.2. Impact of the hydrophobicity of the amino acid on the self-assembly

Amino acids differ significantly in their hydrophobicity, which is a crucial aspect for the self-assembly of peptides.⁷³ As our previous studies revealed that dodecyl (C₁₂) in contrast to hexyl (C₆) spacers provide a sufficient hydrophobic shielding,^{51,53} we here deliberately chose the short spacer to evaluate the effect of the respective amino acids. While leucine and phenylalanine might introduce sufficient hydrophobicity, solely the additional H-bond formation might compensate for the reduced hydrophobic shielding in the case of alanine. To evaluate this aspect, the aqueous self-assembly of compounds **1a–c** were investigated, that are all endowed with one PEO_{2k} chain but different amino acids (**1a**: alanine; **1b**: leucine; **1c**: phenylalanine; for sample preparation: see ESI†). DLS in water was performed as pre-screening to gain first insights into their solution self-assembly. The very small intensity-weighted, average hydrodynamic diameter, d_H , of 9.0 ± 2.0 nm for **1a** indicates no or hardly any

solution aggregation. In contrast to this, an increasing d_H from 16.2 ± 4.2 nm for **1b** to 115.0 ± 81.2 nm for **1c** could be observed (Fig. S19†). These first results already indicate that the strength of the H-bonds in case of alanine might not be sufficient to compensate the limited hydrophobic shielding of the C₆ spacer.

As the values for the hydrodynamic diameters obtained by DLS have to be taken with care, we further performed SAXS experiments to study the actual morphologies of the compounds **1a–c** in water (Fig. 1D). For **1a**, the SAXS trace indicates molecularly dissolved unimers, corroborating the results from DLS. In contrast, the scattering profile for **1b** displays much higher intensities $I(q)$ with a plateau at low q -values followed by a $I(q) \propto q^{-4}$ regime, which is indicative for the presence of spherical polymer micelles.⁷⁴ The data set of **1b** was thus best modelled by applying a form factor of a sphere (details of all fits are given in the ESI†). A Guinier plot provided a radius of gyration R_g of 5.3 nm (Fig. S4†). The appearance of large cylindrical aggregates was first observed for **1c**, which was assigned by the characteristic decay at low q -values scaling with $I(q) \propto q^{-1}$. The scattering profile could be best fitted with a cylindrical form factor. The radius of gyration of the cross-section, R_{cs} , was calculated to be 6.1 nm (Fig. S22†). An average length could not be estimated due to the lack of a plateau at low q values.

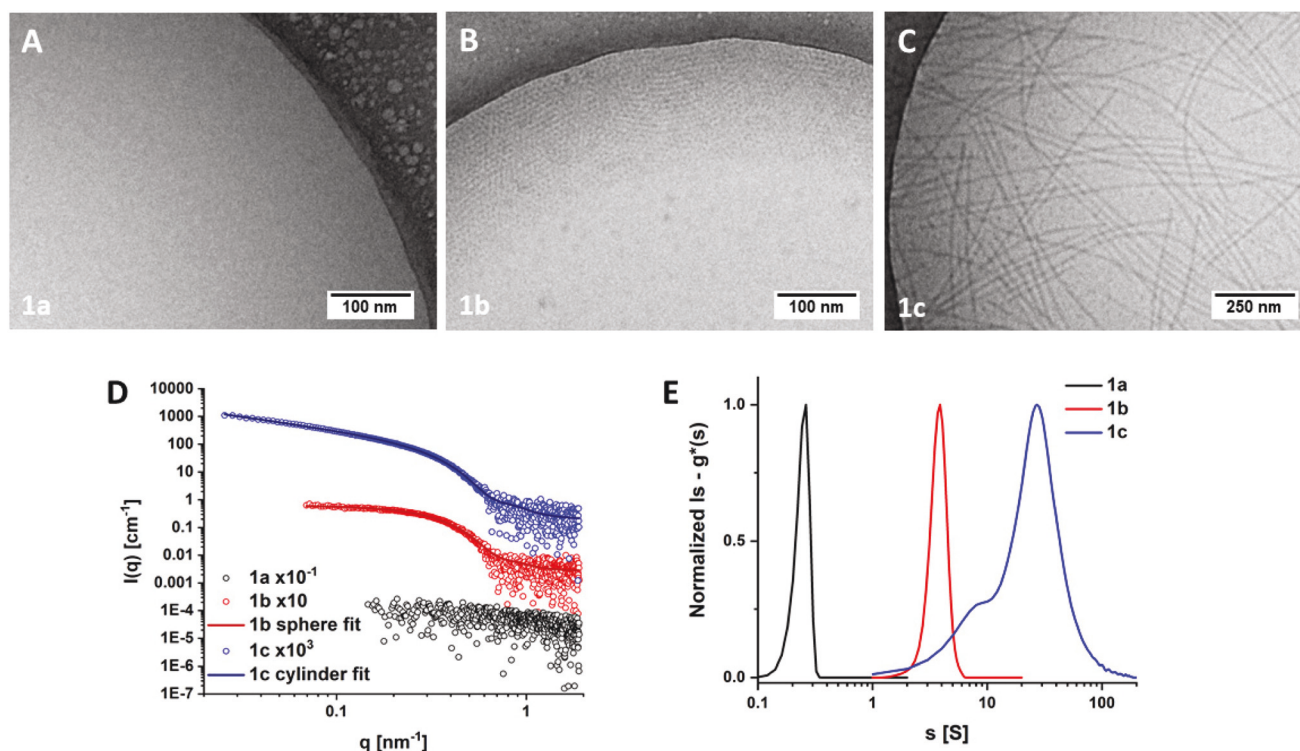


Fig. 1 (A–C) CryoTEM images of **1a–c** in water ($c = 3$ mg mL⁻¹). Full-sized images can be found in the ESI, Fig. S35–37.† (D) SAXS scattering profiles of the samples **1a** (black), **1b** (red), and **1c** (blue), measured in water ($c = 1.5$ mg mL⁻¹). The traces of **1b** and **1c** were shifted by multiplication for reasons of clarity as indicated in the figure legend. The respective solid lines represent the best fits for **1b** and **1c** using SASfit (details are given in the ESI†).⁸² (E) Normalized differential distribution of sedimentation coefficients, of compounds **1a** from sedimentation-diffusion analysis, $c(s)$ (black), and from sedimentation analysis, $ls - g^*(s)$, for **1b** (red) and **1c** (blue) in water ($c = 3$ mg mL⁻¹).

CryoTEM was then applied as a complementary technique to DLS and SAXS to visualize the solution morphologies of **1a–c** and to gain more information on the length of the cylindrical aggregates of **1c**.⁷⁵ As expected, no aggregates are visible for **1a** (Fig. 1A). For **1b**, spherical micelles with an average diameter of 8 ± 1 nm can be seen (Fig. 1B), slightly smaller than the obtained $2R_g$ from the Guinier plot of **1b**. This difference might be attributed to the limited contrast of the PEO-corona in cryoTEM imaging.^{76–79} The presence of long cylindrical structures for **1c**, as observed in SAXS, can be confirmed (Fig. 1C). The formed SPBs exhibit an extremely high aspect ratio with lengths exceeding several microns, but also display a broad length distribution. An average diameter of 9 ± 1 nm was determined, which is again slightly smaller than $2R_{cs}$ obtained from the SAXS data.

Compounds **1a–c** were then also examined *via* sedimentation velocity experiments in AUC to investigate the presence of potentially different solution populations, reflected by sedimentation profiles, respectively, differential distributions of sedimentation coefficients, *s*, *via* least squares boundary modelling assuming non-diffusing species or sedimentation-diffusion analysis in case of rather small species (Fig. 1E).^{51,53,80} In agreement with DLS, SAXS, and cryoTEM, only species with a very small signal (weight) average sedimentation coefficient of 0.2 S obtained by sedimentation-diffusion analysis were observed for **1a**.⁸¹ Compound **1b** exhibits more than an order of magnitude larger signal (weight) average sedimentation coefficients ($s = 3.9$ S) than **1a**, characterized by a well-defined monomodal distribution of sedimentation coefficients, obtainable by least squares boundary modelling. For **1c**, again one order of magnitude larger signal (weight) average sedimentation coefficients ($s = 38.5$ S) were observed. As indicated above, compound **1c** forms large asymmetric structures that display a rather broad length distribution in the cryoTEM images. AUC additionally indicates a population heterogeneity of the self-assembled structures covering roughly two orders of magnitude of the observed sedimentation coefficients.

We were further interested in the molecular packing of our BTP motifs within the formed aggregates and the question if helical arrangements are present, similar to many reports of BTA and BTP compounds.^{6,55,61,63,70,83,84} To this end, we applied circular dichroism (CD) spectroscopy to aqueous solutions of compounds **1a–c** (Fig. S44†). For all compounds, a positive Cotton effect could be observed, indicative of right-handed, helical superstructures.^{83,84} Surprisingly, even compound **1a** shows a CD signal, despite no indication of a solution self-assembly seen *via* SAXS, cryoTEM, and AUC. We hypothesize that the BTP units still interact and reversibly assemble to small aggregates such as dimers or trimers. Unfortunately, we could not find a suitable organic solvent in which the assembly is fully suppressed (Fig. S47†). Interestingly, the solution morphology has no impact on the observed helicities as can be seen by comparing **1b** (spherical micelles) to **1c** (cylindrical micelles) (Fig. S44†). Consequently, small helical superstructures of BTP units must also be present in the interior of the spherical micelles. To substantiate

this hypothesis, we re-fitted the SAXS data of **1b** by applying a form factor for a short cylinder. A similarly adequate fit could be obtained with dimensions of $R_{cyl} = 6.2$ nm and $L_{cyl} = 8.11$ nm for the radius and the length of the cylinder, respectively (see Table S2 and Fig. S23†), supporting the assumption of a potential cylindrical stacking of **1b** inside the micellar interior.

The presented comparison of only weakly shielded motifs (short hydrophobic C₆ spacer) clearly reveals the impact of the amino acid unit on the solution morphology of the respective BTP-PEO conjugates **1a–c** in water. A sufficient hydrophobicity of the chosen amino acid, as in the case for leucine and phenylalanine containing compounds **1b** and **1c** is required to enable the formation of aggregates in water. In contrast, no clear aggregation could be observed for the alanine analogue **1a**. The morphology transformation from **1b** (spherical micelles) to **1c** (cylindrical micelles) cannot be related solely to the increasing hydrophobicity of phenylalanine when compared to leucine. We consider the π - π interactions between the phenyl moieties to provide an additional driving force in this case. As a result, extraordinary long fibers are obtained for **1c** which exemplifies once more the potential of strong directional forces to promote formation of cylindrical morphologies.

2.3. Influence of the amino acid unit on the interaction strength

In order to individually assess the influence of the amino acid structure on the H-bonding interaction, we further examined the self-assembly behaviour of the respective BTP compounds with a C₁₂ spacer and PEO_{2k}. Such a long aliphatic chain has previously been proven to provide sufficient shielding and enable an assembly of BTA- and BTU-based compounds in water,⁵⁶ while the final morphology depends on the interaction strength as reported recently.^{51,53} Based on these experiences, we should be able to evaluate a direct impact of the tested amino acids on the directing forces from the resulting nanostructures, *i.e.* their resulting lengths and length distributions.

A first indication of the formation of more stable aggregates was obtained by determining the critical aggregation concentration (CAC) of compounds **2a–c** in comparison to the previous compounds **1a–c** (Fig. S48–53†). A clear decrease of the CAC values was observed with the increased hydrophobic spacer length (Table S12†). Light scattering experiments were again performed as a pre-screening into the solution self-assembly behaviour. DLS experiments revealed the formation of significantly larger aggregates in cases of **2a–c** compared to **1a–c**, with intensity-average d_H values of 113.0 ± 71.4 nm (**2a**), 95.6 ± 63.5 nm (**2b**) and 84.5 ± 65.9 nm (**2c**) (Fig. S20†). The subsequent SAXS measurements indicated the formation of cylindrical morphologies for all the samples **2a–c** (Fig. 2D). The SAXS profiles were thus all fitted by applying a cylinder model as the form factor (see ESI† for details). Radii of gyration of the cross-section R_{cs} of 7.3 nm (**2a**), 8.0 nm (**2b**) and 7.2 nm (**2c**) could be calculated (Fig. S25–27†). Those values

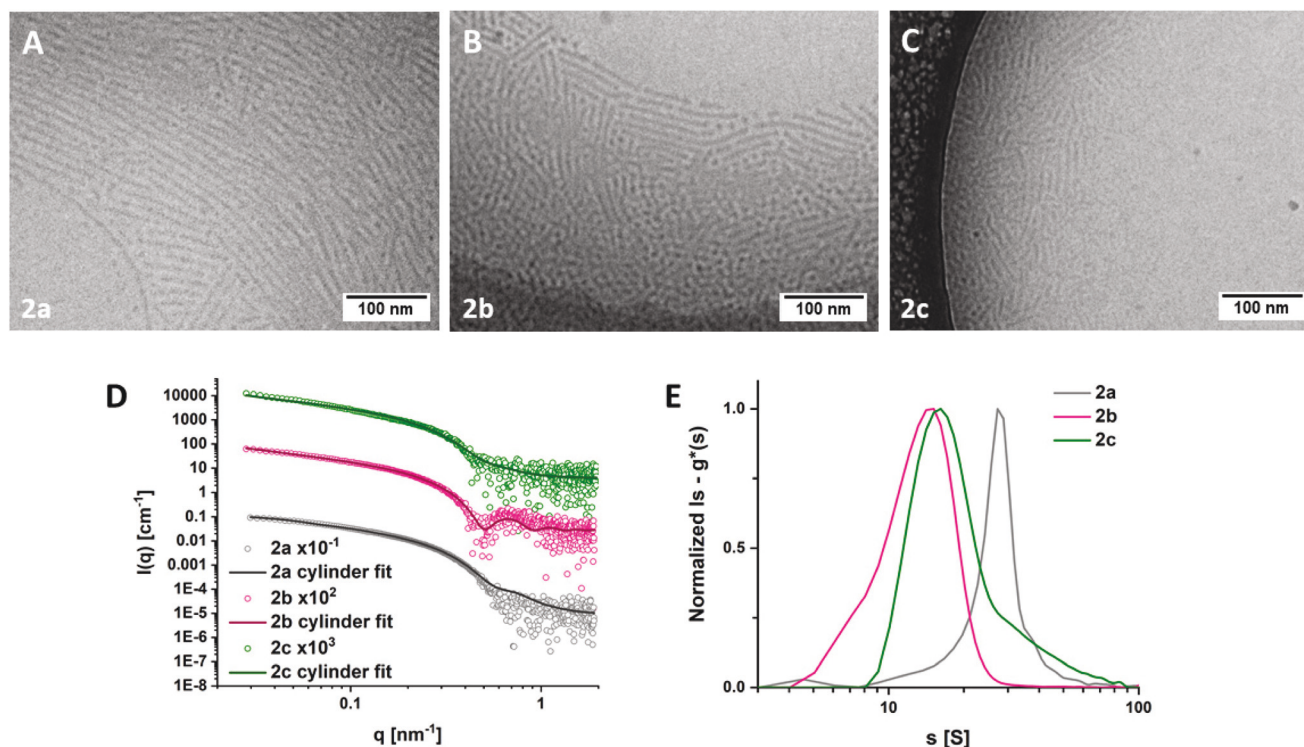


Fig. 2 (A–C) CryoTEM images of **2a–c** in water ($c = 3 \text{ mg mL}^{-1}$). Full-sized images can be found in the ESI, Fig. S38–40.† (D) SAXS scattering profiles of the samples **2a** (grey), **2b** (magenta), and **2c** (green), measured in water ($c = 1.5 \text{ mg mL}^{-1}$). The traces of **2b** and **2c** were shifted by multiplication for reasons of clarity as indicated in the figure legend. The respective solid lines represent the best fits for **2a–c** using SASfit (details are given in the ESI†).⁸² (E) Normalized differential distribution of sedimentation coefficients, $l_s - g^*(s)$, of compounds **2a** (grey), **2b** (magenta), and **2c** (green) from sedimentation analysis in water ($c = 3 \text{ mg mL}^{-1}$).

are slightly larger compared to **1c**, reflecting the increased size of the hydrophobic spacers for **2a–c**.

CryoTEM was used to visualize if any differences in the size distributions of the expected cylindrical structures can be identified. For **2a**, SPBs of a wide range of aspect ratios can be found (Fig. 2A), displaying an average diameter of $9 \pm 1 \text{ nm}$ and very broad length distributions with lengths ranging up to more than one micron. **2b** formed SPBs with similar average diameters of $8 \pm 1 \text{ nm}$, but lengths below 600 nm (Fig. 2B). Similarly, cryoTEM images of **2c** showed SPBs with an average diameter of $10 \pm 2 \text{ nm}$. However, the maximum lengths decreased further down to 250 nm (Fig. 2C). Additionally, spherical aggregates can be seen for **2b** and **2c**, exhibiting diameters of $10 \pm 1 \text{ nm}$ and $10 \pm 2 \text{ nm}$, respectively. However, due to the display of an ideal $I(q) \propto q^{-1}$ power law regime in the respective SAXS profiles, we assume that these assemblies are rather truncated cylindrical micelles, oriented orthogonally to the cryoTEM grid, than spherical micelles. This hypothesis is supported by the slightly higher contrast seen for some spherical aggregates in additional cryoTEM images (Fig. S38–40†).

Sedimentation velocity measurements *via* AUC were then performed to examine if the choice of amino acid has any influence on the sedimentation coefficient distributions of the formed cylindrical structures (Fig. 2E). An increase of the signal (weight) average sedimentation coefficient from **2b**

(15.2 S) to **2a** (30.6 S) can be seen, which is in accordance with the structures found in the cryoTEM images. **2c** exhibits a smaller average value of 26.0 S , with a prominent tailing. The pronounced tailing towards higher sedimentation coefficients in case of **2c** indicates the presence of some larger structures. This result agrees with the previously observed strong interaction of these core units, although they could not be identified in the TEM images. The absence of any smaller sedimentation coefficients for **2b** and **2c** further supports our hypothesis of the truncated cylinders seen as spheres in the respective cryoTEM images.

We used CD spectroscopy again, to also examine the supposed helical arrangement of the compounds **2a–c**. Likewise to the C_6 -spacer bearing compounds **1a–c**, aqueous solutions of the BTP-PEO conjugates **2a–c** all exhibit a positive Cotton effect caused by a right-handedness of the helical aggregates (Fig. S45†).^{82,84} Compared to **1a–c**, the molar ellipticity substantially increases with doubling of the spacer length from C_6 to C_{12} (Fig. S46†). This effect is particularly significant from **1a** (hardly any assembly) to **2a** (SPBs) and from **1b** (spherical micelles) to **2b** (SPBs), illustrating the influence of the increased hydrophobic shielding on the degree of H-bonding between subunits and, thus, self-assembly in water.⁶ In this regard, a less pronounced but still present increase of the molar ellipticity can be seen from **1c** to **2c**, as both systems form SPBs.

Summarizing these results, all compounds equipped with a C_{12} spacer (**2a–c**) formed cylindrical SPBs, which corroborates the significant impact of the hydrophobic shielding. The C_{12} spacer appears to generally provide sufficient hydrophobic shielding for any H-bonding subunit around the benzene core, obviating the need for an additional hydrophobic shielding by the amino acid unit to enable the formation of SPBs. Although this aspect seems to minimize the influence of the type of amino acid, we still observed that the size distribution of the SPBs differ depending on the amino acid, apparent from the larger aggregates formed by **2a** compared to **2b** and **2c**. Such a trend is rather unexpected due to the lower tendency of alanine (**2a**) to form β -sheets in comparison to leucine (**2b**) or phenylalanine (**2c**).^{71,72} We hypothesise that the combination of a hydrophobic amino acid with a C_{12} spacer, as for **2b** and **2c**, results in a very hydrophobic core, which is hindered to freely assemble into extended SPBs. This hindrance may result in kinetically trapped structures in the aqueous environment. Further investigations of these kinetically trapped states and pathway complexities are currently ongoing. This explanation could also be the reason for the greater lengths observed in the cryoTEM images of **1c** compared to **2a–c**, despite its shorter alkyl spacer and the less favoured composition. Apparently, the combination of a C_6 spacer with the highly hydrophobic amino acid phenylalanine seems to be an ideal balance between sufficient hydrophobic shielding and yet adequate solubility and mobility in water to enable the formation of SPBs of extraordinary length and aspect ratio.

2.4. Impact of steric constraints on the self-assembly

Our previous studies on similar conjugates clearly revealed that the morphology transition from cylindrical to spherical micelles can be shifted with increased interaction strength.^{51,53} Following this strategy, we aimed to evaluate whether the additional H-bonds compared to the previously used urea or amide units can further extend these phase boundaries. According to the above described results, the BTP core unit comprising phenylalanine units seems to provide the strongest interaction strength. Therefore, we have chosen **2c** as our starting material and first varied the molar mass of the attached PEO chains.

To this end, we conjugated PEO chains of 5 kg mol^{-1} (**3**) or 10 kg mol^{-1} (**4**) to the central unit. In addition, we synthesised compound **5**, consisting of the same BTP core unit but connected to three PEO_{2k} chains (see Scheme S6† for synthesis route).⁶⁹

CryoTEM images were recorded to image the solution morphologies of **3–5**. For **3**, a mixture of spherical (diameter of $15 \pm 3 \text{ nm}$) and cylindrical (diameter of $10 \pm 2 \text{ nm}$; $L = 20\text{--}400 \text{ nm}$) micelles can be seen (Fig. 3A and Fig. S41†). With increasing PEO chain length, only spherical micelles with a diameter of $16 \pm 3 \text{ nm}$ are visible for **4** (Fig. 3B). Compound **5** displays smaller, well-defined spherical micelles with a diameter of $9 \pm 2 \text{ nm}$ (Fig. 3C).

SAXS measurement of **3** corroborated the mixture of spherical and cylindrical aggregates seen in cryoTEM. Although a further continuous increase is visible at low q -values, the slope is lower than the typical q^{-1} relationship expected for pure cylinders. Therefore, the SAXS data of **3** could only be fitted well by a form factor with contributions from both a sphere and a cylinder geometry (see Fig. S28 and Tables S7, 8†). The SAXS traces of compounds **4** and **5** both showed a plateau at low q values, characteristic for spherical aggregates. Guinier plots provided radii of gyration of 13.1 nm for **4** and 4.2 nm for **5** (see Fig. S30 and 32†).

AUC measurements were again conducted to determine the differential distributions of sedimentation coefficients of the aggregates in water. A decrease of the average sedimentation coefficient s from **2c** ($s = 26.0 \text{ S}$) to **3** ($s = 9.6 \text{ S}$), **4** ($s = 8.0 \text{ S}$), and finally **5** ($s = 2.4 \text{ S}$) was observed (Fig. S54†). As expected, increasing the molar mass of the tethered PEO chain from 2 kg mol^{-1} for **2c** to 5 kg mol^{-1} for **3** resulted in a significant reduction of average sedimentation coefficients indicating smaller assemblies. The apparently monomodal distribution of the sedimentation coefficients for **3** indicates that the majority of aggregates should roughly contain one type of species only. However, the population tails toward higher values of s , indicating the presence of some larger species, likely the existence of a small number of cylindrical aggregates (see Fig. S55†). Further increasing the molar mass of the PEO to 10 kg mol^{-1} for **4** only caused a minor decrease of average s values. Compound **5** displays the smallest s value, despite having a lower overall molar mass of PEO chains when com-

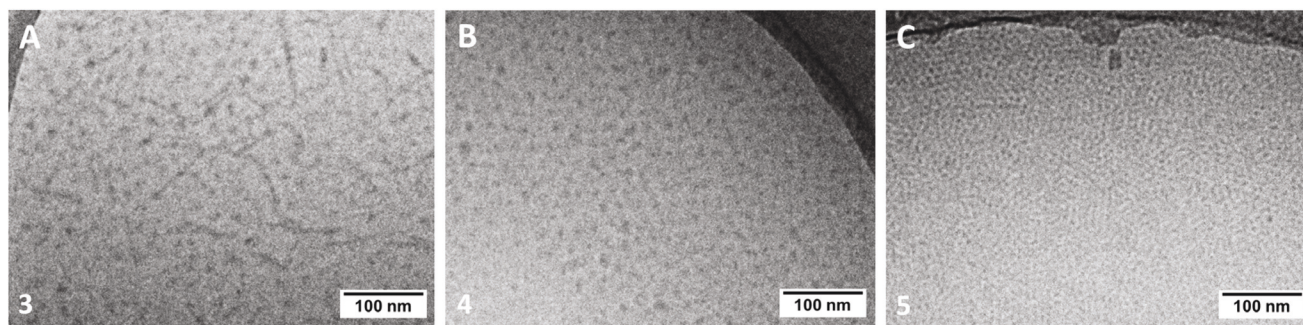


Fig. 3 (A–C) CryoTEM images of **3**, **4** and **5** in water ($c = 3 \text{ mg mL}^{-1}$). Full-sized images can be found in the ESI, Fig. S41–43.†

pared to **4** ($3 \times 2 \text{ kg mol}^{-1}$ vs. 10 kg mol^{-1}). The majority of structures refers to rather small spherical micelles (Fig. 3C).

This suggests, that not solely the molar mass, but also the molecular architecture determined by the number of arms (**2c**, **3**, **4**: one PEO chain; **5**: three PEO chains) influences the self-assembly in water. Considering our earlier findings for a very similar urea-based compound bearing three PEO chains,⁵¹ we hypothesize that the lateral aggregation is also impeded for **5**. To quantify this assumption, we determined the weight-average molar mass, M_w , from the Guinier plot of the SAXS data (Fig. S33†).⁵¹ Assuming a cylindrical arrangement of the BTP-PEO compound inside the micelles *via* the formation of a triple helix as known for benzenetrisamides (Table S11 and Fig. S34†),⁵⁴ and a previously reported intermolecular distance of 3.62 Å between BTA units,⁸⁵ a number of aggregation, N_{agg} , of 12.3 and from this, the number of molecules per cross-section could be determined to be 0.87. As this value is even smaller than 1, we conclude that the backbone of the SPB of **5** must consist of only one molecule in the cross-section. The value below 1 is probably caused by deviations from the intermolecular distance. The reported value 3.62 Å was found in a crystal structure of a BTA that was only equipped with methoxyethyl-substituents.⁸⁵ In compound **5**, however, sterically more demanding phenylalanine units were incorporated, most likely resulting in a slightly increased intermolecular distance.

Despite the higher number of H-bonds and increased hydrophobicity of the phenylalanine C_{12} core unit compared to our previously tested compounds, no shift of the phase boundary for the transition from cylindrical to spherical aggregates toward higher PEO molar masses was observed. However, kinetic trapping, similar to **2c**, cannot be fully excluded and more detailed investigations are currently performed. In addition, the type of polymer architecture also plays a crucial role – next to the overall molar mass – as seen for the absence of any cylindrical micelles for **5**.

3. Conclusion

We synthesized a small library of BTP-PEO conjugates in which we systematically varied structural segments to establish a structure-assembly correlation by studying the corresponding aqueous self-assembly *via* DLS, SAXS, AUC, cryoTEM, and CD. For a shorter C_6 spacer, we observed a significant influence of the chosen amino acid moiety on the observed aggregate solution morphology. As the hydrophobic shielding of the short spacer is not sufficient to efficiently shield the H-bonds in the core from interference with surrounding water molecules, only the hydrophobic amino acids leucine (**1b**) and phenylalanine (**1c**) were able to stimulate self-assembly. On the contrary, hardly any assembly was identifiable for the corresponding alanine analogue (**1a**). While leucine (**1b**) resulted in purely spherical structures, phenylalanine (**1c**) enabled the formation of very large SPBs with lengths of several microns. This significant difference in the self-assembly is attributed to an amplification of the directional driving force by a synergistic effect of

H-bonds and additional π - π -interactions of the corresponding phenyl moieties of the amino acid.

These observations clearly demonstrate the necessity of a sufficient hydrophobic shielding of H-bonds to allow for the formation of cylindrical self-assembly structures in water.^{37,39,51,53,56} By extending the hydrophobic spacer to twelve methylene units, the impact of the nature of the applied amino acid is diminished, as in all cases exclusively SPBs were formed. Notwithstanding, the overall lengths of the SPBs decreased from **2a** to **2b** to **2c**, which indicates an increased driving force toward anisotropic assemblies for the alanine containing compound. However, kinetic trapping of the structures in water cannot be excluded, considering the very hydrophobic nature of the BTP units comprising leucine or phenylalanine. Despite the high number of H-bonds and the increased size of the hydrophobic core in case of the phenylalanine-based unit with a C_{12} spacer, the increase of molar mass of the attached PEO chains from 2 kg mol^{-1} to 10 kg mol^{-1} resulted in a transition from cylindrical toward spherical micelles. The increased steric demand of the higher molar mass polymer chains and the resulting shift in the packing parameter appears to be paramount in this context and further shifts of the phase boundary from spherical to cylindrical aggregates seem to require even stronger H-bonds as directional driving forces for SPBs.

Overall, the here presented incorporation of amino acid moieties demonstrates the potential of the BTP core units and adds another level of modularity to the already versatile platform based on 1,3,5-substituted benzene units for the self-assembly of SPBs. Addition of further amino acid moieties in each “arm” of the BTP unit might even enable the extended adjustment of the interaction strength toward SBPs.⁶⁷ The introduction of functional amino acids would certainly broaden the scope of the resulting SPBs and their response to external stimuli.^{58,60,61,64,65,86,87} Conclusively, this may set the basis for further developments of functional SPBs.

Conflicts of interest

The authors declare no conflicts of interest.

Acknowledgements

The authors thank Prof. Ulrich S. Schubert for his continuous support and access to excellent research facilities. J. C. B., T. K., H. F. U., and F. V. G. further thank the German Science Foundation (DFG) for generous funding within the Emmy-Noether Programme (Project-ID: 358263073). CryoTEM investigations were performed at the electron microscopy facilities of the Jena Center for Soft Matter (JCSM), which were established with grants from the DFG and the European funds for Regional Development (EFRE). I. N., S. H., and M. T. K. acknowledge support of this study by the DFG-funded Collaborative Research Center PolyTarget (SFB 1278, project

number 316213987, project Z01). The SAXS experiments were carried out at SPring-8 under the approval by JASRI (Proposal number: 2018A1454, 2018B1396, 2019A1327, and 2019B1207). We further thank Maria Strumpf for the continuous support in the laboratory.

References

- N. P. Truong, J. F. Quinn, M. R. Whittaker and T. P. Davis, *Polym. Chem.*, 2016, **7**, 4295–4312.
- P. Ascenzi, A. Bocedi, J. Heptonstall, M. R. Capobianchi, A. Di Caro, E. Mastrangelo, M. Bolognesi and G. Ippolito, *Mol. Aspects Med.*, 2008, **29**, 151–185.
- S. Venkataraman, J. L. Hedrick, Z. Y. Ong, C. Yang, P. L. R. Ee, P. T. Hammond and Y. Y. Yang, *Adv. Drug Delivery Rev.*, 2011, **63**, 1228–1246.
- R. Verber, A. Blanazs and S. P. Armes, *Soft Matter*, 2012, **8**, 9915–9922.
- W. Zhang, B. Charleux and P. Cassagnau, *Soft Matter*, 2013, **9**, 2197–2205.
- C. M. A. Leenders, T. Mes, M. B. Baker, M. M. E. Koenigs, P. Besenius, A. R. A. Palmans and E. W. Meijer, *Mater. Horiz.*, 2014, **1**, 116–120.
- O. Azzaroni, *J. Polym. Sci., Part A: Polym. Chem.*, 2012, **50**, 3225–3258.
- G. Sun, S. Cho, C. Clark, S. V. Verkhoturov, M. J. Eller, A. Li, A. Pavia-Jiménez, E. A. Schweikert, J. W. Thackeray, P. Trefonas and K. L. Wooley, *J. Am. Chem. Soc.*, 2013, **135**, 4203–4206.
- X.-H. Jin, M. B. Price, J. R. Finnegan, C. E. Boott, J. M. Richter, A. Rao, S. M. Menke, R. H. Friend, G. R. Whittell and I. Manners, *Science*, 2018, **360**, 897–900.
- J. N. Israelachvili, D. J. Mitchell and B. W. Ninham, *J. Chem. Soc., Faraday Trans. 2*, 1976, **72**, 1525–1568.
- Y. Mai and A. Eisenberg, *Chem. Soc. Rev.*, 2012, **41**, 5969–5985.
- U. Tritschler, S. Pearce, J. Gwyther, G. R. Whittell and I. Manners, *Macromolecules*, 2017, **50**, 3439–3463.
- B. Charleux, G. Delaittre, J. Rieger and F. D'Agosto, *Macromolecules*, 2012, **45**, 6753–6765.
- N. J. Warren and S. P. Armes, *J. Am. Chem. Soc.*, 2014, **136**, 10174–10185.
- J. Rieger, *Macromol. Rapid Commun.*, 2015, **36**, 1458–1471.
- G. Mellot, J.-M. Guigner, L. Bouteiller, F. Stoffelbach and J. Rieger, *Angew. Chem., Int. Ed.*, 2019, **58**, 3173–3177.
- Y. Yan, Y. Lin, Y. Qiao and J. Huang, *Soft Matter*, 2011, **7**, 6385–6398.
- J. C. Brendel and F. H. Schacher, *Chem. – Asian J.*, 2018, **13**, 230–239.
- G. Mellot, J.-M. Guigner, J. Jestin, L. Bouteiller, F. Stoffelbach and J. Rieger, *Macromolecules*, 2018, **51**, 10214–10222.
- J. B. Gilroy, T. Gädt, G. R. Whittell, L. Chabanne, J. M. Mitchels, R. M. Richardson, M. A. Winnik and I. Manners, *Nat. Chem.*, 2010, **2**, 566–570.
- T. Gädt, N. S. Jeong, G. Cambridge, M. A. Winnik and I. Manners, *Nat. Mater.*, 2009, **8**, 144–150.
- Z. M. Hudson, C. E. Boott, M. E. Robinson, P. A. Rugar, M. A. Winnik and I. Manners, *Nat. Chem.*, 2014, **6**, 893–898.
- S. Ganda and M. H. Stenzel, *Prog. Polym. Sci.*, 2019, **101**, 101195.
- J. R. Finnegan, X. He, S. T. G. Street, J. D. Garcia-Hernandez, D. W. Hayward, R. L. Harniman, R. M. Richardson, G. R. Whittell and I. Manners, *J. Am. Chem. Soc.*, 2018, **140**, 17127–17140.
- Y. He, J.-C. Eloi, R. L. Harniman, R. M. Richardson, G. R. Whittell, R. T. Mathers, A. P. Dove, R. K. O'Reilly and I. Manners, *J. Am. Chem. Soc.*, 2019, **141**, 19088–19098.
- Q. Yu, M. G. Roberts, S. Pearce, A. M. Oliver, H. Zhou, C. Allen, I. Manners and M. A. Winnik, *Macromolecules*, 2019, **52**, 5231–5244.
- F. V. Gruschwitz, T. Klein, S. Catrouillet and J. C. Brendel, *Chem. Commun.*, 2020, **56**, 5079–5110.
- B. M. Blunden, R. Chapman, M. Danial, H. Lu, K. A. Jolliffe, S. Perrier and M. H. Stenzel, *Chem. – Eur. J.*, 2014, **20**, 12745–12749.
- R. Dong, Y. Zhou, X. Huang, X. Zhu, Y. Lu and J. Shen, *Adv. Mater.*, 2015, **27**, 498–526.
- M. J. Webber and R. Langer, *Chem. Soc. Rev.*, 2017, **46**, 6600–6620.
- J. Y. Rho, J. C. Brendel, L. R. MacFarlane, E. D. H. Mansfield, R. Peltier, S. Rogers, M. Hartlieb and S. Perrier, *Adv. Funct. Mater.*, 2017, **28**, 1704569.
- J. C. Brendel, J. Sanchis, S. Catrouillet, E. Czuba, M. Z. Chen, B. M. Long, C. Nowell, A. Johnston, K. A. Jolliffe and S. Perrier, *Angew. Chem., Int. Ed.*, 2018, **57**, 16678–16882.
- S. C. Larnaudie, J. C. Brendel, I. Romero-Canelón, C. Sanchez-Cano, S. Catrouillet, J. Sanchis, J. P. C. Coverdale, J.-I. Song, A. Habtemariam, P. J. Sadler, K. A. Jolliffe and S. Perrier, *Biomacromolecules*, 2018, **19**, 239–247.
- S. C. Larnaudie, J. Sanchis, T.-H. Nguyen, R. Peltier, S. Catrouillet, J. C. Brendel, C. J. H. Porter, K. A. Jolliffe and S. Perrier, *Biomaterials*, 2018, **178**, 570–582.
- J. Yang, J.-I. Song, Q. Song, J. Y. Rho, E. D. H. Mansfield, S. C. L. Hall, M. Sambrook, F. Huang and S. Perrier, *Angew. Chem.*, 2020, **59**, 8860–8863.
- S. Han, E. Nicol, F. Niepceron, O. Colombani, S. Pensec and L. Bouteiller, *Macromol. Rapid Commun.*, 2019, **40**, 1800698.
- E. Obert, M. Bellot, L. Bouteiller, F. Andrioletti, C. Lehen-Ferrenbach and F. Boué, *J. Am. Chem. Soc.*, 2007, **129**, 15601–15605.
- E. Krieg, M. M. C. Bastings, P. Besenius and B. Rybtchinski, *Chem. Rev.*, 2016, **116**, 2414–2477.
- V. Saez Talens, D. M. M. Makurat, T. Liu, W. Dai, C. Guibert, W. E. M. Noteborn, I. K. Voets and R. E. Kielyka, *Polym. Chem.*, 2019, **10**, 3146–3153.
- M. Tharcis, T. Breiner, J. Belleney, F. Boué and L. Bouteiller, *Polym. Chem.*, 2012, **3**, 3093–3099.

- 41 T. Choynet, D. Canevet, M. Sallé, E. Nicol, F. Niepceon, J. Jestin and O. Colombani, *Chem. Commun.*, 2019, **55**, 9519–9522.
- 42 N. Chebotareva, P. H. H. Bomans, P. M. Frederik, N. A. J. M. Sommerdijk and R. P. Sijbesma, *Chem. Commun.*, 2005, **39**, 4967–4969.
- 43 A. Pal, S. Karthikeyan and R. P. Sijbesma, *J. Am. Chem. Soc.*, 2010, **132**, 7842–7843.
- 44 A. Pal, P. Besenius and R. P. Sijbesma, *J. Am. Chem. Soc.*, 2011, **133**, 12987–12989.
- 45 V. Saez Talens, P. Englebienne, T. T. Trinh, W. E. M. Noteborn, I. K. Voets and R. E. Kieltyka, *Angew. Chem., Int. Ed.*, 2015, **54**, 10502–10506.
- 46 J. Couet and M. Biesalski, *Small*, 2008, **4**, 1008–1016.
- 47 V. Castelletto, G. E. Newby, Z. Zhu, I. W. Hamley and L. Noirez, *Langmuir*, 2010, **26**, 9986–9996.
- 48 M. Danial, C. My-Nhi Tran, P. G. Young, S. Perrier and K. A. Jolliffe, *Nat. Commun.*, 2013, **4**, 2780.
- 49 R. Chapman, M. L. Koh, G. G. Warr, K. A. Jolliffe and S. Perrier, *Chem. Sci.*, 2013, **4**, 2581–2589.
- 50 E. D. H. Mansfield, M. Hartlieb, S. Catrouillet, J. Y. Rho, S. C. Larnaudie, S. E. Rogers, J. Sanchis, J. C. Brendel and S. Perrier, *Soft Matter*, 2018, **14**, 6320–6326.
- 51 F. V. Gruschwitz, M.-C. Fu, T. Klein, R. Takahashi, T. Higashihara, S. Hoepfener, I. Nischang, K. Sakurai and J. C. Brendel, *Macromolecules*, 2020, **53**, 7552–7560.
- 52 S. Catrouillet, L. Bouteiller, E. Nicol, T. Nicolai, S. Pensec, B. Jacquette, M. Le Bohec and O. Colombani, *Macromolecules*, 2015, **48**, 1364–1370.
- 53 T. Klein, F. V. Gruschwitz, S. Rogers, S. Hoepfener, I. Nischang and J. C. Brendel, *J. Colloid Interface Sci.*, 2019, **557**, 488–497.
- 54 S. Cantekin, T. F. A. de Greef and A. R. A. Palmans, *Chem. Soc. Rev.*, 2012, **41**, 6125–6137.
- 55 C. M. A. Leenders, L. Albertazzi, T. Mes, M. M. E. Koenigs, A. R. A. Palmans and E. W. Meijer, *Chem. Commun.*, 2013, **49**, 1963–1965.
- 56 C. M. A. Leenders, M. B. Baker, I. A. B. Pijpers, R. P. M. Lafleur, L. Albertazzi, A. R. A. Palmans and E. W. Meijer, *Soft Matter*, 2016, **12**, 2887–2893.
- 57 M. B. Baker, L. Albertazzi, I. K. Voets, C. M. A. Leenders, A. R. A. Palmans, G. M. Pavan and E. W. Meijer, *Nat. Commun.*, 2015, **6**, 6234.
- 58 C. M. Berac, L. Zengerling, D. Straßburger, R. Otter, M. Urschbach and P. Besenius, *Macromol. Rapid Commun.*, 2020, **41**, 1900476.
- 59 B. Kemper, L. Zengerling, D. Spitzer, R. Otter, T. Bauer and P. Besenius, *J. Am. Chem. Soc.*, 2018, **140**, 534–537.
- 60 D. Spitzer, L. L. Rodrigues, D. Strassburger, M. Mezger and P. Besenius, *Angew. Chem., Int. Ed.*, 2017, **56**, 15461–15465.
- 61 P. Ahlers, H. Frisch, R. Holm, D. Spitzer, M. Barz and P. Besenius, *Macromol. Biosci.*, 2017, **17**, 1700111.
- 62 H. Frisch, E.-C. Fritz, F. Stricker, L. Schmäser, D. Spitzer, T. Weidner, B. J. Ravoo and P. Besenius, *Angew. Chem., Int. Ed.*, 2016, **55**, 7242–7246.
- 63 R. Appel, J. Fuchs, S. M. Tyrrell, P. A. Korevaar, M. C. A. Stuart, I. K. Voets, M. Schönhoff and P. Besenius, *Chem. – Eur. J.*, 2015, **21**, 19257–19264.
- 64 P. Ahlers, H. Frisch and P. Besenius, *Polym. Chem.*, 2015, **6**, 7245–7250.
- 65 H. Frisch, Y. Nie, S. Raunser and P. Besenius, *Chem. – Eur. J.*, 2015, **21**, 3304–3309.
- 66 P. Besenius, G. Portale, P. H. H. Bomans, H. M. Janssen, A. R. A. Palmans and E. W. Meijer, *Proc. Natl. Acad. Sci. U. S. A.*, 2010, **107**, 17888–17893.
- 67 O. Zagorodko, V. J. Nebot and M. J. Vicent, *Polym. Chem.*, 2020, **11**, 1220–1229.
- 68 K. P. van den Hout, R. Martín-Rapún, J. A. J. M. Vekemans and E. W. Meijer, *Chem. – Eur. J.*, 2007, **13**, 8111–8123.
- 69 M. de Loos, J. H. van Esch, R. M. Kellogg and B. L. Feringa, *Tetrahedron*, 2007, **63**, 7285–7301.
- 70 Y. Dai, X. Zhao, X. Su, G. Li and A. Zhang, *Macromol. Rapid Commun.*, 2014, **35**, 1326–1331.
- 71 C. K. Smith, J. M. Withka and L. Regan, *Biochemistry*, 1994, **33**, 5510–5517.
- 72 D. L. Minor and P. S. Kim, *Nature*, 1994, **367**, 660–663.
- 73 C. P. Moon and K. G. Fleming, *Proc. Natl. Acad. Sci. U. S. A.*, 2011, **108**, 10174–10177.
- 74 J. Pedersen, *J. Appl. Crystallogr.*, 2000, **33**, 637–640.
- 75 J. P. Patterson, M. P. Robin, C. Chassenieux, O. Colombani and R. K. O'Reilly, *Chem. Soc. Rev.*, 2014, **43**, 2412–2425.
- 76 J. Baram, E. Shirman, N. Ben-Shitrit, A. Ustinov, H. Weissman, I. Pinkas, S. G. Wolf and B. Rybtchinski, *J. Am. Chem. Soc.*, 2008, **130**, 14966–14967.
- 77 G. Golubkov, H. Weissman, E. Shirman, S. G. Wolf, I. Pinkas and B. Rybtchinski, *Angew. Chem.*, 2009, **121**, 944–948.
- 78 E. Krieg, E. Shirman, H. Weissman, E. Shimoni, S. G. Wolf, I. Pinkas and B. Rybtchinski, *J. Am. Chem. Soc.*, 2009, **131**, 14365–14373.
- 79 Y. Tidhar, H. Weissman, S. G. Wolf, A. Gulino and B. Rybtchinski, *Chem. – Eur. J.*, 2011, **17**, 6068–6075.
- 80 P. Schuck and P. Rossmanith, *Biopolymers*, 2000, **54**, 328–341.
- 81 I. Nischang, I. Perevyazko, T. Majdanski, J. Vitz, G. Festag and U. S. Schubert, *Anal. Chem.*, 2017, **89**, 1185–1193.
- 82 I. Bressler, J. Kohlbrecher and A. F. Thunemann, *J. Appl. Crystallogr.*, 2015, **48**, 1587–1598.
- 83 M. M. J. Smulders, T. Buffeteau, D. Cavagnat, M. Wolffs, A. P. H. J. Schenning and E. W. Meijer, *Chirality*, 2008, **20**, 1016–1022.
- 84 S. Cantekin, D. W. R. Balkenende, M. M. J. Smulders, A. R. A. Palmans and E. W. Meijer, *Nat. Chem.*, 2011, **3**, 42–46.
- 85 M. P. Lightfoot, F. S. Mair, R. G. Pritchard and J. E. Warren, *Chem. Commun.*, 1999, **19**, 1945–1946.
- 86 D. Spitzer, V. Marichez, G. J. M. Formon, P. Besenius and T. M. Hermans, *Angew. Chem., Int. Ed.*, 2018, **57**, 11349–11353.
- 87 H. Frisch, J. P. Unsleber, D. Lüdeker, M. Peterlechner, G. Brunklaus, M. Waller and P. Besenius, *Angew. Chem., Int. Ed.*, 2013, **52**, 10097–10101.

Impact of amino acids on the aqueous self-assembly of benzenetrispeptides into supramolecular polymer bottlebrushes

Tobias Klein^{a,b}, Hans F. Ulrich^{a,b}, Franka V. Gruschwitz^{a,b}, Maren Kuchenbrod^{a,b}, Rintaro Takahashi^c, Shota Fujii^c, Stephanie Hoepfener^{a,b}, Ivo Nischang^{a,b}, Kazuo Sakurai^c, Johannes C. Brendel^{a,b,*}

a Laboratory of Organic and Macromolecular Chemistry (IOMC), Friedrich Schiller University Jena, Humboldtstraße 10, 07743 Jena, Germany

b Jena Center for Soft Matter (JCSM), Friedrich Schiller University Jena, Philosophenweg 7, 07743 Jena, Germany

c Department of Chemistry and Biochemistry, University of Kitakyushu, 1-1 Hibikino, Wakamatsu-ku, Kitakyushu, Fukuoka 808-0135, Japan

*corresponding author: johannes.brendel@uni-jena.de

Content

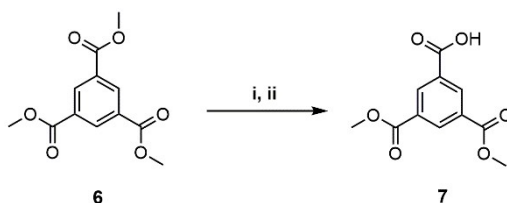
1. Synthesis	3
1.1 Synthetic routes	4
1.2 Synthetic protocols.....	6
1.2.1 Core unit.....	6
1.2.2 Amino acid arms	7
1.2.3 Benzenetrispeptide building blocks bearing one PEO chain	21
1.2.4 Benzenetrispeptide building blocks bearing three PEO chains	51
2. Characterisation	55
2.1 Sample preparation.....	55
2.2 Dynamic Light Scattering (DLS)	55
2.3 Small Angle X-Ray Scattering (SAXS).....	57
2.4 CryoTransmission Electron Microscopy (cryoTEM)	69
2.5 Circular Dichroism (CD) spectroscopy.....	78
2.6 CAC Determination.....	80
2.7 Analytical Ultracentrifugation (AUC)	83
3. References.....	85

1. Synthesis

Materials and Methods. All reagents and solvents were commercial products purchased from Sigma-Aldrich, abcr, Iris BioTech, Rapp Polymere or TCI and were used without further purification. Flash chromatography was performed on a *CombiFlash* Rf 4x Module by TeledyneIsco using a UV detector for compound purity monitoring. ¹H-NMR spectra were measured with a Bruker spectrometer (300 MHz) equipped with an Avance I console, a dual ¹H and ¹³C sample head and a 120x BACS automatic sample changer. The chemical shifts of the peaks were determined by using the residual solvent signal as reference and are given in ppm in comparison to TMS. Size-exclusion chromatography (SEC) of polymers was performed on an Agilent system (series 1200) equipped with a PSS degasser, a G1310A pump, a G1362A refractive index detector and a PSS GRAM 30 and 1000 column with DMAc (+ 0.21 wt.% LiCl) as eluent at a flow rate of 1 mL min⁻¹. The column oven was set to 40 °C and poly(ethylene glycol) (PEO) standards were used for calibration. Fluorescence spectra were recorded on a JASCO FP-8300 spectrometer equipped with a Peltier element. DLS correlograms were measured on a ZetaSizer Nano ZS (Malvern, Herrenberg, Germany) equipped with a He–Ne laser with a wavelength of $\lambda = 633$ nm. *Cryo*TEM measurements were performed on a FEI Tecnai G2 20 platform with a LaB6 filament at 200 kV acceleration voltage. Analytical ultracentrifuge experiments were performed with a ProteomeLab XL-I analytical ultracentrifuge (Beckman Coulter Instruments, Brea, CA). Small angle X-ray scattering was performed at the beamline BL40B2 of the Super Photon Ring – 8 GeV (SPring-8) in Hyōgo Prefecture, Japan. CD spectra were measured using a JASCO J-820KS spectrophotometer.

1.1 Synthetic routes

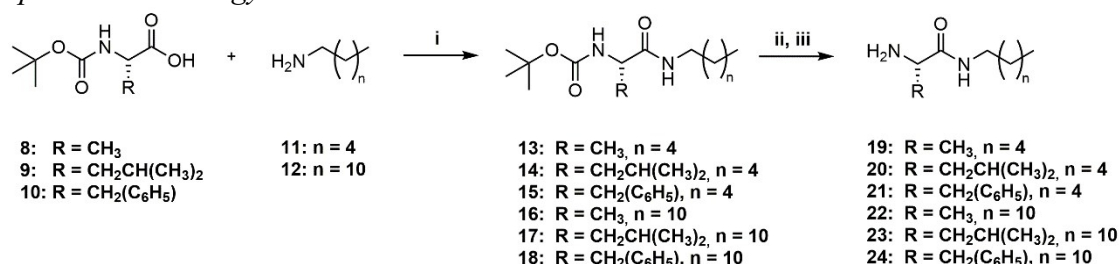
Core unit



Scheme S 1: Synthesis of 3,5-bis(methoxycarbonyl)benzoic acid **7**. i) NaOH (aq), MeOH, overnight; ii) 1M HCl, H₂O.

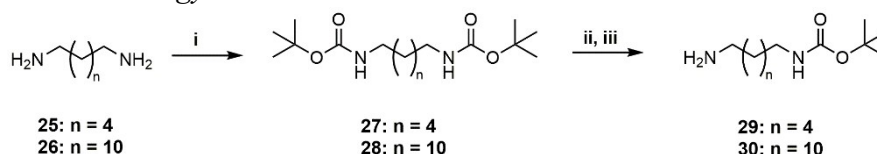
Amino acid arms

Boc-protection strategy

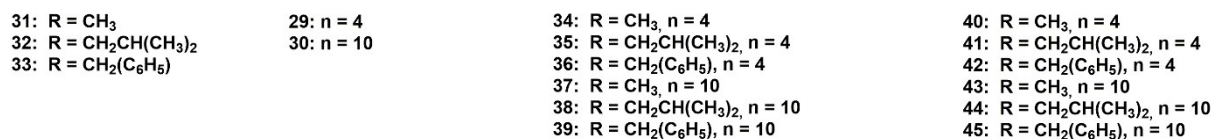
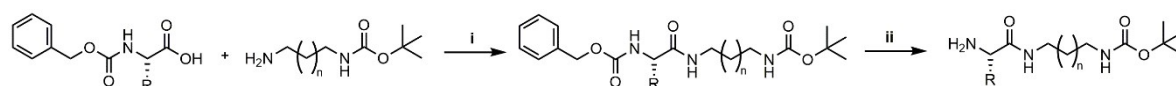


Scheme S 2: Synthesis of alkylated amino acids **19-24**. i) DMAP, EDC-HCl, DCM, 20 °C, 6 h; ii) TFA, TIPS, H₂O, DCM, 20 °C, 6 h; iii) Na₂CO₃ (aq), 20 °C, overnight.

Cbz-Boc-protection strategy



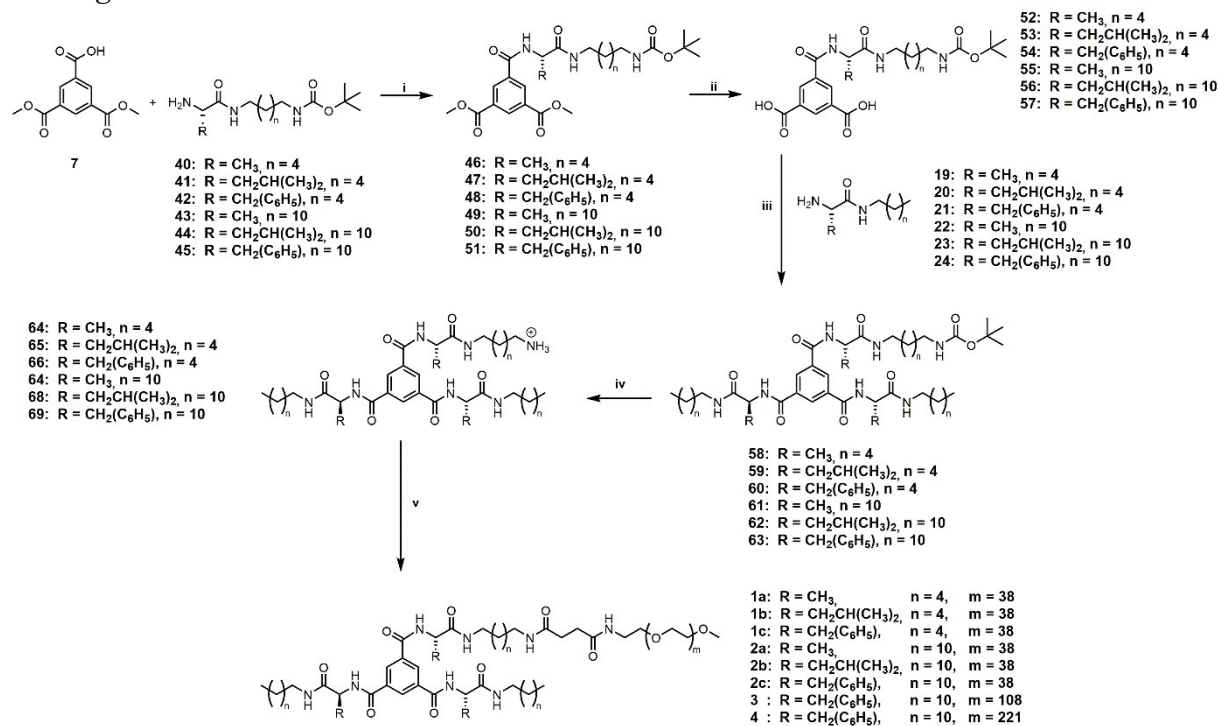
Scheme S 3: Synthesis of semi-Boc-protected hexyl- and dodecyl-diamines **29** and **30**, respectively. i) DiBoc, DCM/MeOH 1:1, 20 °C, overnight; ii) HCl, DCM/Et₂O 1:1, 20 °C, overnight; iii) NaHCO₃ (aq), 20 °C, overnight.



Scheme S 4: Synthesis of alkylated amino acids bearing a terminal Boc-protected amino group **40-45**. i) DMAP, EDC-HCl, DCM, 20 °C, 6 h; ii) H₂, Pd-C, MeOH or THF, 20 °C, overnight.

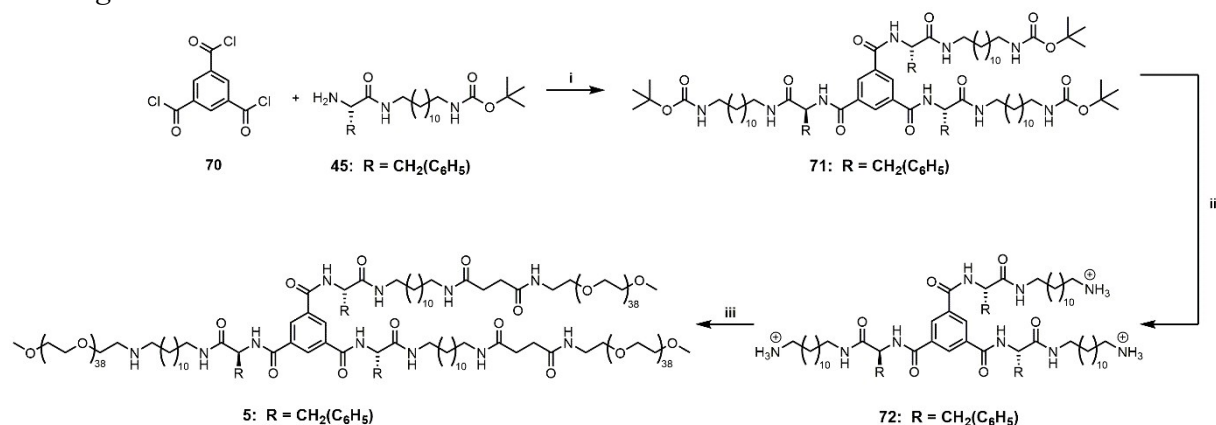
Benzenetrispeptide building blocks

Bearing one PEO chain



Scheme S 5: Synthetic route to the benzenetrispeptide conjugates **1a**, **1b**, **1c**, **2a**, **2b**, **2c**, **3** and **4** bearing one PEO chain. i) DMAP, EDC-HCl, CHCl₃, rt, overnight; ii) KOH, EtOH/H₂O, reflux, 30 min; iii) DMAP, EDC-HCl, CHCl₃ or DMF, rt, overnight; iv) TFA/TIPS/H₂O, DCM, rt, 2 h; v) MeO-PEO-NHS, TEA, DMF, rt, overnight.

Bearing three PEO chains

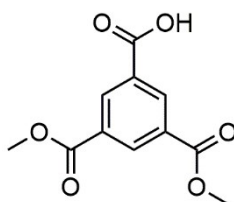


Scheme S 6: Synthetic route to the benzenetrispeptide conjugate **5** bearing three PEO chains. i) TEA, CHCl₃, 0 °C, overnight; ii) TFA, TIPS, H₂O, DCM, 20 °C, 2 h; iii) MeO-PEO-NHS, TEA, DMF, 20 °C, overnight.

1.2 Synthetic protocols

1.2.1 Core unit

3,5-bis(methoxycarbonyl)benzoic acid - 7



7

Trimethyl benzene-1,3,5-tricarboxylate (30 g, 119 mmol, 1.0 eq) was dissolved in 1.5 L methanol and 107 mL of a 1 M aq. NaOH solution (107 mmol, 0.9 eq) dropwise added under vigorous stirring and the solution stirred overnight at rt. Afterwards, the solvent was removed under reduced pressure and the residue resuspended in DCM to dissolve residual starting material. The suspension was then filtered and the solid residue dried in a vacuum oven (40 °C) overnight. To convert the sodium-carboxylate into its corresponding carboxylic acid, the dried solid (27.7 g, 106.5 mmol) was dissolved in 500 mL water to which 106.5 mL of a 1 M aq. HCl solution (106.5 mmol) were added dropwise under vigorous stirring. The formed precipitate was filtered and wash with a little amount of water to remove remaining sodium-carboxylate. The obtained white solid was dried overnight in the vacuum oven (40 °C).

Yield: 20 g, 84 mmol (78%), white solid.

Molecular formula: C₁₁H₁₀O₆.

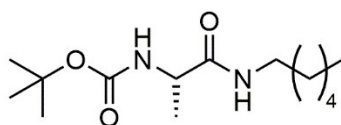
¹H-NMR (300 MHz, d₆-DMSO, 298 K): δ [ppm] = 13.69 (s, 1H, COOH), 8.61 (d, *J* = 1.6 Hz, 2H, CH_{aromat}), 8.58 (t, *J* = 1.6 Hz, 1H, CH_{aromat}), 2.50 (s, 6H, CH₃).

ESI-ToF-MS (negative mode, acetonitrile) (m/z): calculated for [M-H]⁻: 237.0405; found: 237.0351.

1.2.2 Amino acid arms

Boc-protection strategy

Boc-L-Ala-C(O)NH-C₆ - **13**



13

Boc-L-Ala-OH **8** (10 g, 52.9 mmol, 1.0 eq) and DMAP (646 mg, 5.29 mmol, 0.1 eq) were dissolved in 192 mL DCM. To this solution 7.64 mL hexylamine (58.1 mmol, 1.1 eq) were added dropwise. Thereafter, 12.16 g EDC-HCl (63.4 mmol, 1.2 eq) were added portion wise under vigorous stirring and the solution stirred for 4 h at rt. Afterwards, the reaction mixture was extracted with 1 M HCl (3x 50 mL), sat. aq. NaHCO₃ (1x, 50 mL) and brine (1x, 50 mL). The combined organic phases were dried over MgSO₄, filtered and reduced *in vacuo*. The obtained product was dried in the vacuum oven (40 °C) overnight.

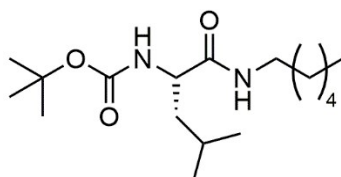
Yield: 13.23 g, 48.6 mmol (92%), yellowish liquid.

Molecular formula: C₁₄H₂₈N₂O₃.

¹H-NMR (300 MHz, CDCl₃, 298 K): δ [ppm] = 6.42 (s, 1H, NH), 5.18 (d, J = 6.8 Hz, 1H, NH), 4.21 – 4.04 (m, 1H, CH), 3.20 (q, J = 6.9, 6.4 Hz, 2H, CH₂), 1.46 (m, 2H, CH₂), 1.42 (s, 9H, CH₃), 1.32 (d, J = 7.0 Hz, 3H, CH₃), 1.25 (m, 4H, CH₂), 0.85 (t, J = 6 Hz, 3H, CH₃).

ESI-ToF-MS (positive mode, acetonitrile) (m/z): calculated for [M+Na]⁺: 295.1992; found: 295.1984.

Boc-L-Leu-C(O)NH-C₆ – **14**



14

The compound was synthesized according to the procedure of compound **13**.

Yield: 24.064 g, 76.5 mmol (95%), yellowish liquid.

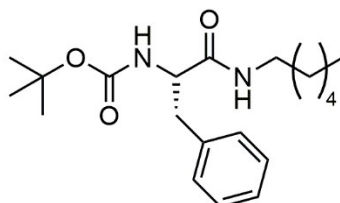
Molecular formula: C₁₇H₃₄N₂O₃.

¹H-NMR (300 MHz, d₆-DMSO, 298 K): δ [ppm] = 7.74 (d, J = 5.7 Hz, 1H, NH), 6.77 (d, J = 8.5 Hz, 1H, NH), 3.89 (q, J = 8.6 Hz, 1H, CH), 3.02 (dt, J = 13.9, 6.9 Hz, 2H, CH₂), 1.36 (dd,

J = 12.6, 7.5 Hz, 1H, CH₂ CH), 1.36 (m, 13H, CH₃, CH₂), 1.23 (s, 6H, CH₂), 0.84 (m, 9H, CH₃) ppm.

ESI-ToF-MS (positive mode, acetonitrile) (m/z): calculated for [M+Na]⁺: 337.2462; found: 337.2472.

Boc-L-Phe-C(O)NH-C₆ - **15**



15

The compound was synthesized according to the procedure of compound **13**.

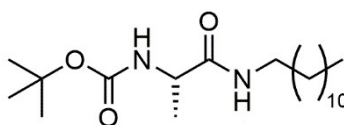
Yield: 25.66 g, 73.6 mmol (98%), white solid.

Molecular formula: C₂₀H₃₂N₂O₃.

¹H-NMR (300 MHz, d₆-DMSO, 298 K): δ [ppm] = 7.82 (t, J = 5.4 Hz, 1H, NH), 7.24 (m, 5H, CH_{aromat}), 6.86 (d, J = 8.5 Hz, 1H, NH), 4.09 (td, J = 9.3, 5.1 Hz, 1H, CH), 3.12 – 2.94 (m, 2H, CH₂), 2.89 (dd, J = 13.6, 5.0 Hz, 1H, CH₂), 2.72 (dd, J = 13.5, 9.8 Hz, 1H, CH₂), 1.26 (m, 17H, CH₃, CH₂, CH₂, CH₂, CH₂), 0.85 (t, J = 6.7 Hz, 3H).

ESI-ToF-MS (positive mode, acetonitrile) (m/z): calculated for [M+Na]⁺: 371.2305; found: 371.2314.

Boc-L-Ala-C(O)NH-C₁₂ - **16**



16

Boc-L-Ala-OH **8** (5 g, 26.4 mmol, 1.0 eq) and DMAP (323 mg, 2.64 mmol, 0.1 eq) were dissolved in 117 mL DCM. To this solution 4.41 g dodecylamine (23.78 mmol, 0.9 eq) were added. Thereafter, 6.08 g EDC-HCl (31.7 mmol, 1.2 eq) were added portion wise under vigorous stirring and the solution stirred for 4 h at rt. Afterwards, the reaction mixture was extracted with 1 M HCl (4x, 50 mL), sat. aq. NaHCO₃ (3x, 50 mL) and brine (1x, 50 mL). The combined organic phases were dried over MgSO₄, filtered and reduced *in vacuo*. The obtained product was dried in the vacuum oven (40 °C) overnight.

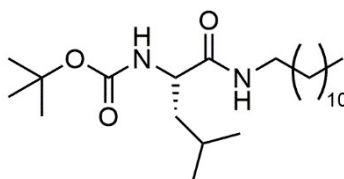
Yield: 8.52 g, 23.9 mmol (90%), white solid.

Molecular formula: C₂₀H₄₀N₂O₃.

¹H-NMR (300 MHz, CDCl₃, 298 K): δ [ppm] = 6.12 (s, 1H, NH), 4.98 (s, 1H, NH), 4.10 (p, J = 6.2 Hz, 1H, CH), 3.23 (q, J = 6.6 Hz, 2H, CH₂), 1.44 (m, 7H, CH₂, CH₃), 1.34 (d, J = 7.1 Hz, 3H, CH₃), 1.25 (m, 11H, CH₂), 0.87 (t, J = 7.5 Hz, 3H, CH₃).

ESI-ToF-MS (positive mode, acetonitrile) (m/z): calculated for [M+Na]⁺: 379.2931; found: 379.2940.

Boc-L-Leu-C(O)NH-C₁₂ – **17**



17

The compound was synthesized according to the procedure of compound **16**.

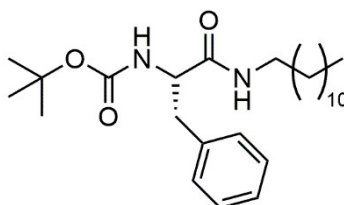
Yield: 22.91 g, 57.5 mmol (89%), yellow liquid.

Molecular formula: C₂₃H₄₆N₂O₃.

¹H-NMR (300 MHz, CDCl₃, 298 K): δ [ppm] = 6.05 (t, J = 4.9 Hz, 1H, NH), 4.83 (s, 1H, NH), 4.01 (q, J = 8.2 Hz, 1H, CH), 3.21 (q, J = 6.8 Hz, 2H, CH₂), 1.64 (dt, J = 12.0, 6.7 Hz, 2H, CH₂), 1.42 (m, 13H, CH₂, CH₃), 1.23 (m, 18H, CH₂), 0.91 (dd, J = 6.2, 2.2 Hz, 6H, CH₃), 0.86 (t, J = 7.5 Hz, 3H, CH₃).

ESI-ToF-MS (positive mode, acetonitrile) (m/z): calculated for [M+Na]⁺: 421.3401; found: 421.3332.

Boc-L-Phe-C(O)NH-C₁₂ - **18**



18

The compound was synthesized according to the procedure of compound **16**.

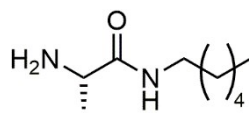
Yield: 23.3 g, 56.5 mmol (95%), white solid.

Molecular formula: C₂₆H₄₄N₂O₃.

¹H-NMR (300 MHz, CDCl₃, 298 K): δ [ppm] = 7.36 – 7.15 (m, 4H, C_{aromat}), 5.64 (s, 1H, NH), 5.08 (s, 1H, NH), 4.25 (q, J = 7.5 Hz, 1H, CH), 3.21 – 2.93 (m, 4H, CH₂), 1.41 (s, 9H, CH₃), 1.28 (m, 20H, CH₂), 0.88 (t, J = 7.5 Hz, 3H, CH₃).

ESI-ToF-MS (positive mode, acetonitrile) (m/z): calculated for [M+Na]⁺: 455.3244; found: 455.3255.

H₂N-L-Ala-C(O)NH-C₆ - **19**



19

Compound **13** (3.07 g, 11.28 mmol, 1.0 eq) was dissolved in 26 mL DCM. To this solution, 26.1 mL trifluoroacetic acid (338 mmol, 25.0 eq) added dropwise under vigorous stirring. Afterwards, the reaction mixture was stirred for 4 h at rt. Then, the reaction mixture was reduced *in vacuo*. The residue was re-dissolved in 250 mL DCM and again reduced *in vacuo*. This step was repeated 4x in order to remove most of the residual TFA. The obtained salt product (3.5 g) was then dissolved in 55 mL sat. NaHCO₃ (aq.) and stirred overnight in order to convert the ammonium-TFA salt into the free amine. The aqueous solution was then extracted with DCM (5x, 50 mL). The combined organic phases were then washed with brine (1x, 50 mL), dried over MgSO₄, filtered and reduced *in vacuo*. The obtained product was dried in the vacuum oven (40 °C) overnight.

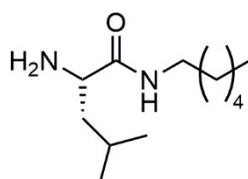
Yield: 1.55 g, 9 mmol (80%), yellow liquid.

Molecular formula: C₉H₂₀N₂O.

¹H-NMR (300 MHz, d₆-DMSO, 298 K): δ [ppm] = 7.78 (s, 1H, NH), 3.22 (q, J = 6.9 Hz, 1H, CH), 3.04 (q, J = 6.6 Hz, 2H, CH₂), 2.06 (s, 2H, NH₂), 1.37 (q, J = 6.6 Hz, 2H, CH₂), 1.23 (m, 6H, CH₂), 1.09 (d, J = 6.9 Hz, 3H, CH₃), 0.84 (t, J = 7.5 Hz, 3H, CH₃).

ESI-ToF-MS (positive mode, acetonitrile) (m/z): calculated for [M+H]⁺: 173.1648; found: 173.1649.

H₂N-L-Leu-C(O)NH-C₆ - **20**



20

The compound was synthesized according to the procedure of compound **19**.

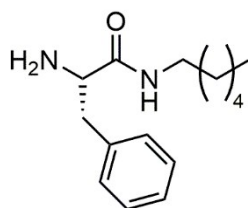
Yield: 13.82 g, 64.5 mmol (85%), white solid.

Molecular formula: C₁₂H₂₆N₂O.

¹H-NMR (300 MHz, d₆-DMSO, 298 K): δ [ppm] = 7.80 (t, J = 5.4 Hz, 1H, NH), 3.06 (m, 3H, CH, CH₂), 1.66 (dq, J = 12.9, 6.5 Hz, 2H), 1.36 (ddd, J = 13.5, 8.2, 5.6 Hz, 2H, CH₂), 1.24 (m, 3H, CH, CH₂), 0.85 (m, 9H, CH₃).

ESI-ToF-MS (positive mode, acetonitrile) (m/z): calculated for [M+H]⁺: 215.2118; found: 215.2177.

H₂N-L-Phe-C(O)NH-C₆ - **21**



21

The compound was synthesized according to the procedure of compound **19**.

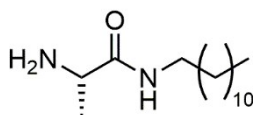
Yield: 7.63 g, 30.7 mmol (93%), white solid.

Molecular formula: C₁₅H₂₄N₂O.

¹H-NMR (300 MHz, d₆-DMSO, 298 K): δ [ppm] = 7.76 (t, J = 5.1 Hz, 1H, NH), 7.31 – 7.13 (m, 4H, C_{aromat}), 3.01 (hept, J = 6.6 Hz, 2H, CH₂), 2.88 (dd, J = 13.0, 5.0 Hz, 1H, CH₂), 2.60 (dd, J = 13.1, 7.9 Hz, 1H, CH₂), 1.63 (s, 2H, NH₂), 1.39 – 1.12 (m, 8H, CH₂), 0.85 (t, J = 6.1 Hz, 3H, CH₃).

ESI-ToF-MS (positive mode, acetonitrile) (m/z): calculated for [M+H]⁺: 249.1961; found: 249.1978.

H₂N-L-Ala-C(O)NH-C₁₂ – **22**



22

The compound was synthesized according to the procedure of compound **19**.

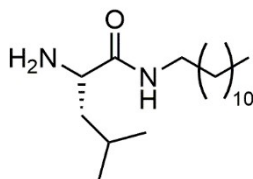
Yield: 4.94 g, 19.3 mmol (88%), yellowish solid.

Molecular formula: C₁₅H₃₂N₂O.

¹H-NMR (300 MHz, d₆-DMSO, 298 K): δ [ppm] = 7.73 (t, J = 5.5 Hz, 1H, NH), 3.19 (q, J = 7.9, 7.0 Hz, 1H, CH), 3.02 (q, J = 6.5 Hz, 2H, CH₂), 1.45 – 1.31 (m, 2H, CH₂), 1.23 (m, 16H, CH₂), 1.08 (d, J = 5.6 Hz, 3H, CH₃), 0.85 (t, J = 6.1 Hz, 3H, CH₃).

ESI-ToF-MS (positive mode, acetonitrile) (m/z): calculated for [M+H]⁺: 257.2587; found: 257.2638.

H₂N-L-Leu-C(O)NH-C₁₂ – **23**



23

The compound was synthesized according to the procedure of compound **19**.

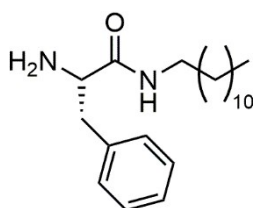
Yield: 15.7 g, 52.6 mmol (93%), yellowish solid.

Molecular formula: C₁₈H₃₈N₂O.

¹H-NMR (300 MHz, d₆-DMSO, 298 K): δ [ppm] = 7.79 (t, J = 5.5 Hz, 1H), 3.12 – 2.93 (m, 3H, CH, CH₂), 1.67 (m, 3H, NH₂, CH), 1.43 – 1.29 (m, 4H, CH₂), 1.23 (m, 18H, CH₂), 0.85 (m, 9H, CH₃).

ESI-ToF-MS (positive mode, acetonitrile) (m/z): calculated for [M+H]⁺: 299.3057; found: 299.3051.

H₂N-L-Phe-C(O)NH-C₁₂ – **24**



24

The compound was synthesized according to the procedure of compound **19**.

Yield: 14.56 g, 43.8 mmol (95%), yellow resin-like liquid.

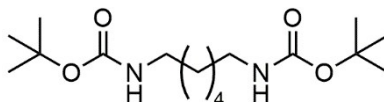
Molecular formula: C₂₁H₃₆N₂O.

¹H-NMR (300 MHz, d₆-DMSO, 298 K): δ [ppm] = 7.75 (t, J = 4.7 Hz, 1H, NH), 7.30 – 7.12 (m, 4H, C_{aromat}), 3.00 (m, 2H, CH₂), 2.87 (dd, J = 13.6, 4.8 Hz, 1H, CH₂), 2.60 (dd, J = 12.6, 8.5 Hz, 1H, CH₂), 1.67 (s, 2H, NH₂), 1.23 (m, 20H, CH₂), 0.85 (t, J = 5.8 Hz, 3H, CH₃).

ESI-ToF-MS (positive mode, acetonitrile) (m/z): calculated for [M+H]⁺: 333.2900; found: 333.2910.

Cbz-Boc-protection strategy

N,N'-Boc-1,6-hexanediamine – **27**



27

Hexane-1,6-diamine **25** (15 g, 129 mmol, 1.0 eq) were dissolved in 430 mL DCM/MeOH (1:1 v:v). To this solution, 62.3 mL di-*tert*-butyl dicarbonate (59.2 g, 271 mmol, 2.1 eq) were added dropwise under vigorous stirring. The reaction mixture was stirred overnight at rt. Afterwards, the solvents were removed under reduced pressure and the obtained crude product recrystallised from methanol. The obtained crystals were dried in the vacuum oven (40 °C) overnight.

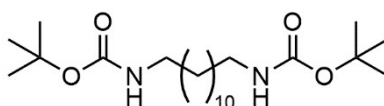
Yield: 40.7 g, 129 mmol (100%), white powder.

Molecular formula: C₁₆H₃₂N₂O₄.

¹H-NMR (300 MHz, d₄-MeOD, 298 K): δ [ppm] = 3.02 (t, J = 6.9 Hz, 4H, CH₂), 1.43 (m, 22H, CH₂, CH₃), 1.32 (dt, J = 7.4, 3.4 Hz, 4H, CH₂).

ESI-ToF-MS (positive mode, acetonitrile) (m/z): calculated for [M+K]⁺: 355.1994; found: 355.2068.

N,N'-Boc-1,12-dodecanediamine – **28**



28

The compound was synthesized according to the procedure of compound **27**.

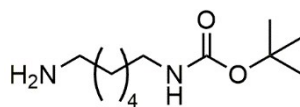
Yield: 33.2 g, 83 mmol (95%), white powder.

Molecular formula: C₂₂H₄₄N₂O₄.

¹H-NMR (300 MHz, d₄-MeOD, 298 K): δ [ppm] = 3.01 (t, J = 7.0 Hz, 4H, CH₂), 1.43 (m, 22H, CH₂, CH₃), 1.30 (m, 16H, CH₂).

ESI-ToF-MS (positive mode, acetonitrile) (m/z): calculated for [M+Na]⁺: 423.3193; found: 423.3144.

N-Boc-1,6-hexanediamine – **29**



29

Compound **27** (20 g, 63.2 mmol, 1.0 eq) was dissolved in 95 mL DCM. To this 95 mL of a 1 M HCl in diethyl ether (190 mmol, 3.0 eq) was added dropwise under vigorous stirring. The solution turned turbid (precipitation of product) and was further stirred overnight at rt. The precipitate was filtered and washed with cold diethyl ether (3x, 50 mL). The obtained ammonium chloride salt product was dried in the vacuum oven (40 °C) overnight. Afterwards, the crude product was dissolved in sat. NaHCO₃ (aq., 700 mL) and stirred overnight at rt in order to obtain the free amine. Thereafter, the aqueous solution was extracted with DCM (5x, 100 mL). The combined organic phases were dried over MgSO₄, filtered and reduced *in vacuo*.

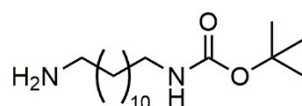
Yield: 10.603 g, 49 mmol (78%), white solid.

Molecular formula: C₁₁H₂₄N₂O₂.

¹H-NMR (300 MHz, d₄-MeOD, 298 K): δ [ppm] = 3.02 (t, J = 6.9 Hz, 2H, CH₂), 2.66 (t, J = 7.2 Hz, 2H, CH₂), 1.42 (m, 13H, CH₂, CH₃), 1.39 – 1.29 (m, 4H, CH₂).

ESI-ToF-MS (positive mode, acetonitrile) (m/z): calculated for [M+H]⁺: 217.1911; found: 217.1896.

N-Boc-1,12-dodecanediamine – **30**



30

Compound **28** (33 g, 82 mmol, 1.0 eq) was dissolved in 124 mL DCM. To this 124 mL of a 1 M HCl in diethyl ether (247 mmol, 3.0 eq) was added dropwise under vigorous stirring. The solution turned turbid (precipitation of product) and was further stirred overnight at rt. The precipitate was filtered and washed with cold diethyl ether (3x, 50 mL). The obtained ammonium chloride salt product was dried in the vacuum oven (40 °C) overnight. Afterwards, the crude product was dissolved in sat. NaHCO₃ (aq., 350 mL) and stirred overnight at rt in order to obtain the free amine. Thereafter, the formed precipitate was filtered and thoroughly washed with water to remove residual salt traces. The obtained product was dried in the vacuum oven (40 °C) overnight.

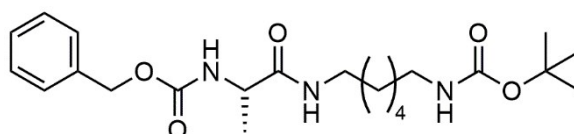
Yield: 24.163 g, 80 mmol (98%), white solid.

Molecular formula: C₁₇H₃₆N₂O₂.

¹H-NMR (300 MHz, d₄-MeOD, 298 K): δ [ppm] = 3.01 (t, J = 7.0 Hz, 2H, CH₂), 2.80 – 2.73 (m, 2H, CH₂), 1.61 – 1.51 (m, 2H, CH₂), 1.43 (m, 11H, CH₂, CH₃), 1.31 (m, 16H, CH₂).

ESI-ToF-MS (positive mode, acetonitrile) (m/z): calculated for [M+H]⁺: 301.2850; found: 301.3650.

Cbz-L-Ala-C(O)NH-C₆-NH-Boc – **34**



34

Cbz-L-Ala-OH **31** (3 g, 13.44 mmol, 1.0 eq) and DMAP (164 mg, 1.34 mmol, 0.1 eq) were dissolved in 59.7 mL DCM. To this solution 3.2 g tert-butyl 6-aminohexylcarbamate **29** (14.78 mmol, 1.1 eq) were added. Thereafter, 3.09 g EDC-HCl (16.13 mmol, 1.2 eq) were added portion wise under vigorous stirring and the solution stirred for 4 h at rt. Afterwards, the reaction mixture was extracted with 1 M HCl (3x, 50 mL), sat. aq. NaHCO₃ (1x, 50 mL) and brine (1x, 50 mL). The combined organic phases were dried over MgSO₄, filtered and reduced *in vacuo*. The obtained product was dried in the vacuum oven (40 °C) overnight.

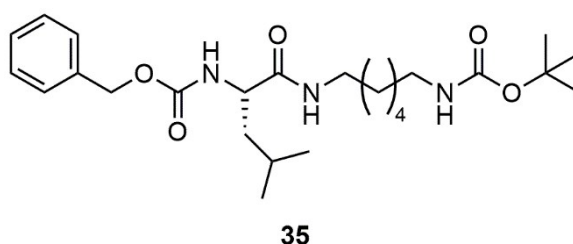
Yield: 4.99 g, 11.84 mmol (88%), white solid.

Molecular formula: C₂₂H₃₅N₃O₅.

¹H-NMR (300 MHz, d₆-DMSO, 298 K): δ [ppm] = 7.80 (t, J = 5.5 Hz, 1H, NH), 7.34 (m, 6H, C_{aromat}, NH), 6.77 (t, J = 5.4 Hz, 1H, NH), 5.00 (d, J = 2.6 Hz, 2H, CH₂), 3.97 (p, J = 7.0 Hz, 1H, CH), 3.02 (hept, J = 6.4 Hz, 3H, CH₂), 2.88 (q, J = 6.5 Hz, 2H, CH₂), 1.36 (m, 13H, CH₂, CH₃), 1.21 (m, 4H, CH₂), 1.17 (d, J = 7.2 Hz, 3H, CH₃).

ESI-ToF-MS (positive mode, acetonitrile) (m/z): calculated for [M+Na]⁺: 444.2469; found: 444.2487.

Cbz-L-Leu-C(O)NH-C₆-NH-Boc – **35**



The compound was synthesized according to the procedure of compound **34**.

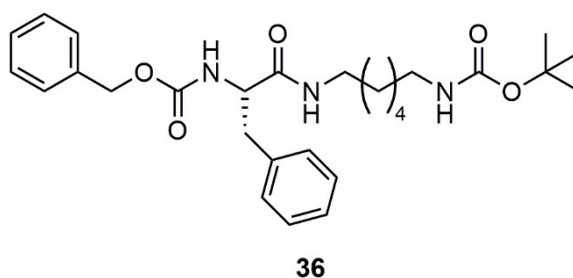
Yield: 11.191 g, 24.13 mmol (83%), yellow liquid.

Molecular formula: C₂₅H₄₁N₃O₅.

¹H-NMR (300 MHz, d₆-DMSO, 298 K): δ [ppm] = 7.86 (t, J = 5.7 Hz, 1H, NH), 7.34 (m, 6H, C_{aromat}, NH), 6.77 (t, J = 5.3 Hz, 1H, NH), 5.01 (s, 2H, CH₂), 4.04 – 3.89 (m, 1H, CH), 3.11 – 2.91 (m, 2H, CH₂), 2.87 (q, J = 6.4 Hz, 2H, CH₂), 1.56 (m, 2H, CH₂), 1.36 (m, 15H, CH₂, CH₃), 1.21 (m, 4H, CH₂), 0.85 (t, J = 6.9 Hz, 6H, CH₃).

ESI-ToF-MS (positive mode, acetonitrile) (m/z): calculated for [M+Na]⁺: 486.2938; found: 486.2897.

Cbz-L-Phe-C(O)NH-C₆-NH-Boc – **36**



The compound was synthesized according to the procedure of compound **34**.

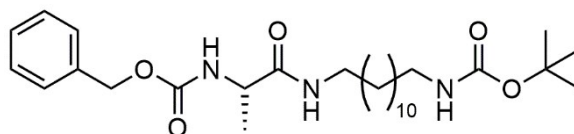
Yield: 5.655 g, 11.36 mmol (68%), yellowish solid.

Molecular formula: C₂₈H₃₉N₃O₅.

¹H-NMR (300 MHz, d₆-DMSO, 298 K): δ [ppm] = 7.94 (t, J = 5.4 Hz, 1H, NH), 7.47 (d, J = 8.6 Hz, 1H, NH), 7.39 – 7.13 (m, 10H, C_{aromat}), 6.77 (t, J = 5.5 Hz, 1H, NH), 4.94 (s, 2H, CH₂), 4.18 (td, J = 9.6, 5.0 Hz, 1H, CH), 2.96 (m, 5H, CH₂), 2.74 (dd, J = 13.5, 10.0 Hz, 1H, CH₂), 1.37 (m, 13H, CH₂, CH₃), 1.19 (m, 4H, CH₂).

ESI-ToF-MS (positive mode, acetonitrile) (m/z): calculated for [M+Na]⁺: 520.2782; found: 520.2785.

Cbz-L-Ala-C(O)NH-C₁₂-NH-Boc – **37**



37

The compound was synthesized according to the procedure of compound **34**.

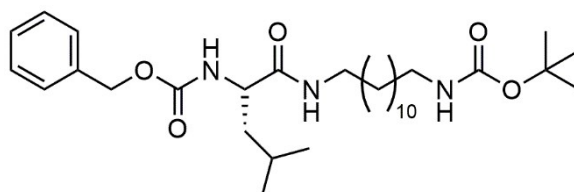
Yield: 6.87 g, 13.59 mmol (82%), white solid.

Molecular formula: C₂₈H₄₇N₃O₅.

¹H-NMR (300 MHz, d₆-DMSO, 298 K): δ [ppm] = 7.79 (t, J = 5.4 Hz, 1H, NH), 7.44 – 7.24 (m, 5H, C_{aromat}, NH), 6.75 (t, J = 5.6 Hz, 1H, NH), 5.00 (s, 2H, CH₂), 3.96 (q, J = 7.3 Hz, 1H, CH), 3.02 (hept, J = 6.5 Hz, 3H, CH₂), 2.87 (q, J = 6.6 Hz, 2H, CH₂), 1.36 (m, 13H, CH₂, CH₃), 1.22 (m, 16H, CH₂), 1.17 (d, J = 7.2 Hz, 3H, CH₃).

ESI-ToF-MS (positive mode, acetonitrile) (m/z): calculated for [M+Na]⁺: 528.3408; found: 528.3412.

Cbz-L-Leu-C(O)NH-C₁₂-NH-Boc – **38**



38

The compound was synthesized according to the procedure of compound **34**.

Yield: 14.341 g, 26.18 mmol (98%), white solid.

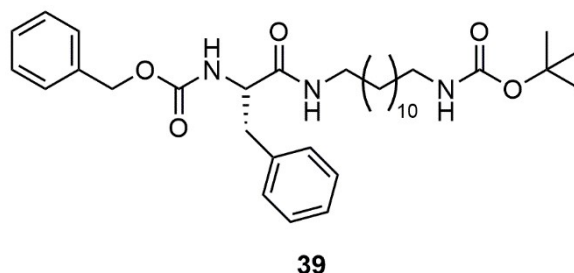
Molecular formula: C₃₁H₅₃N₃O₅.

¹H-NMR (300 MHz, d₆-DMSO, 298 K): δ [ppm] = 7.85 (t, J = 5.4 Hz, 1H, NH), 7.33 (m, 6H, C_{aromat}, NH), 6.75 (t, J = 5.3 Hz, 1H, NH), 5.01 (s, 2H, CH₂), 4.03 – 3.90 (m, 1H, CH), 3.01 (m,

2H, CH₂), 2.87 (q, J = 6.5 Hz, 2H, CH₂), 1.64 – 1.51 (m, 2H, CH₂), 1.36 (m, 15H, CH₂, CH₃), 1.22 (m, 16H, CH₂), 0.85 (t, J = 6.9 Hz, 6H, CH₃).

ESI-ToF-MS (positive mode, acetonitrile) (m/z): calculated for [M+Na]⁺: 570.3877; found: 570.3772.

Cbz-L-Phe-C(O)NH-C₁₂-NH-Boc – **39**



The compound was synthesized according to the procedure of compound **34**.

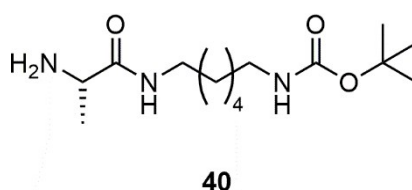
Yield: 7.82 g, 13.44 mmol (81%), white solid.

Molecular formula: C₃₄H₅₁N₃O₅.

¹H-NMR (300 MHz, d₆-DMSO, 298 K): δ [ppm] = 7.93 (t, J = 5.5 Hz, 1H, NH), 7.47 (d, J = 8.6 Hz, 1H, NH), 7.41 – 7.13 (m, 10H, C_{aromat}), 6.75 (t, J = 5.3 Hz, 1H, NH), 4.94 (s, 2H, CH₂), 4.18 (td, J = 9.6, 4.9 Hz, 1H, CH), 3.13 – 2.82 (m, 5H, CH₂), 2.74 (dd, J = 13.7, 10.0 Hz, 1H, CH₂), 1.36 (m, 13H, CH₂, CH₃), 1.22 (m, 16H, CH₂).

ESI-ToF-MS (positive mode, acetonitrile) (m/z): calculated for [M+Na]⁺: 604.3721 ; found: 604.3721.

H₂N-L-Ala-C(O)NH-C₆-NH-Boc – **40**



Cbz-L-Ala-C(O)NH-C₆-NH-Boc **34** (7 g, 17.18 mmol, 1.0 eq) was dissolved in 68.7 mL methanol. To this solution 700 mg palladium on activated charcoal (10 wt%) were added and the flask sealed with a septum. By using a balloon, hydrogen was purged through this solution 5x and afterwards a sixth balloon was left on the flask as a hydrogen reservoir. The reaction mixture was stirred overnight at rt. The solution was then filtered over Celite® and reduced *in vacuo*. The obtained product was dried in the vacuum oven (40 °C) overnight.

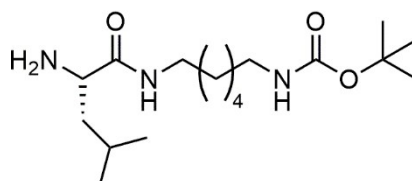
Yield: 4.78 g, 16.63 mmol (98%), white/brownish solid.

Molecular formula: C₁₄H₂₉N₃O₃.

¹H-NMR (300 MHz, CDCl₃, 298 K): δ [ppm] = 7.28 (s, 1H, NH), 4.59 (s, 1H, NH), 3.46 (q, J = 5.8 Hz, 1H, CH), 3.21 (q, J = 6.8 Hz, 2H, CH₂), 3.08 (q, J = 6.5 Hz, 2H, CH₂), 1.63 (s, 2H, NH₂), 1.42 (m, 13H, CH₂, CH₃), 1.31 (m, 7H, CH₂, CH₃).

ESI-ToF-MS (positive mode, acetonitrile) (m/z): calculated for [M+H]⁺: 288.2282; found: 288.2347.

H₂N-L-Leu-C(O)NH-C₆-NH-Boc – **41**



41

The compound was synthesized according to the procedure of compound **40**.

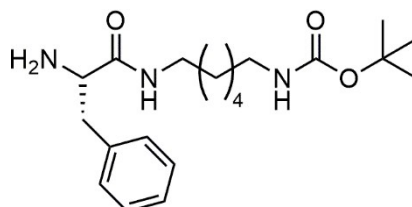
Yield: 3.341 g, 10.14 mmol (93%), white solid.

Molecular formula: C₁₇H₃₅N₃O₃.

¹H-NMR (300 MHz, d₆-DMSO, 298 K): δ [ppm] = 7.82 (t, J = 5.5 Hz, 1H, NH), 6.77 (t, J = 5.4 Hz, 1H, NH), 3.18 – 2.95 (m, 3H, CH₂, CH), 2.88 (q, J = 6.6 Hz, 2H, CH₂), 1.90 (s, 2H, NH₂), 1.65 (m, 1H, CH), 1.36 (m, 13H, CH₂, CH₃), 1.22 (m, 4H, CH₂), 0.85 (d, J = 10.1, 6.6 Hz, 6H, CH₃).

ESI-ToF-MS (positive mode, acetonitrile) (m/z): calculated for [M+H]⁺: 330.2751; found: 330.2759.

H₂N-L-Phe-C(O)NH-C₆-NH-Boc – **42**



42

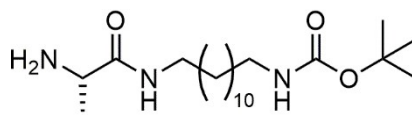
The compound was synthesized according to the procedure of compound **40**.

Yield: 1.313 g, 3.61 mmol (90%), yellowish wax/solid.

Molecular formula: C₂₀H₃₃N₃O₃.

¹H-NMR (300 MHz, CDCl₃, 298 K): δ [ppm] = 7.37 – 7.16 (m, 5H, C_{aromat}), 4.54 (s, 1H, NH), 3.59 (dd, J = 9.3, 4.1 Hz, 1H, CH), 3.32 – 3.17 (m, 3H, CH₂), 3.10 (q, J = 6.5 Hz, 1H, CH₂), 2.69 (dd, J = 13.7, 9.3 Hz, 1H, CH₂), 1.44 (m, 16H, CH₂, CH₃, NH₂), 1.36 – 1.26 (m, 4H, CH₂).
ESI-ToF-MS (positive mode, acetonitrile) (m/z): calculated for [M+H]⁺: 364.2595; found: 364.2605.

H₂N-L-Ala-C(O)NH-C₁₂-NH-Boc – **43**



43

The compound was synthesized according to the procedure of compound **40**.

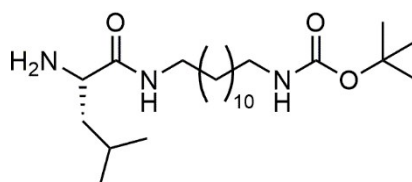
Yield: 3.265 g, 8.79 mmol (89%), yellowish solid.

Molecular formula: C₂₀H₄₁N₃O₃.

¹H-NMR (300 MHz, CDCl₃, 298 K): δ [ppm] = 7.24 (s, 1H, NH), 4.51 (s, 1H, NH), 3.50 (q, J = 7.0 Hz, 1H, CH), 3.23 (q, J = 7.0 Hz, 2H, CH₂), 3.09 (q, J = 6.7 Hz, 2H, CH₂), 1.69 (s, 2H, NH₂), 1.44 (m, 13H, CH₂, CH₃), 1.33 (d, J = 7.0 Hz, 3H, CH₃), 1.25 (m, 16H, CH₂).

ESI-ToF-MS (positive mode, acetonitrile) (m/z): calculated for [M+H]⁺: 372.3221; found: 372.3207.

H₂N-L-Leu-C(O)NH-C₁₂-NH-Boc – **44**



44

The compound was synthesized according to the procedure of compound **40**.

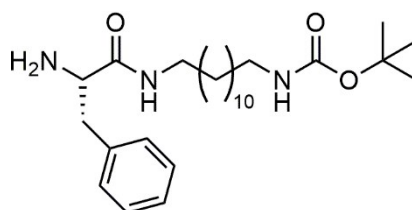
Yield: 6.944 g, 16.79 mmol (92%), white solid.

Molecular formula: C₂₃H₄₇N₃O₃.

¹H-NMR (300 MHz, d₆-DMSO, 298 K): δ [ppm] = 7.79 (t, J = 5.6 Hz, 1H, NH), 6.76 (t, J = 5.5 Hz, 1H, NH), 3.13 – 2.96 (m, 3H, CH, CH₂), 2.87 (q, J = 6.5 Hz, 2H, CH₂), 1.67 (m, 2H, CH₂), 1.36 (m, 15H, CH₂, CH₃), 1.23 (m, 16H, CH₂), 0.85 (dd, J = 10.3, 6.6 Hz, 6H, CH₃).

ESI-ToF-MS (positive mode, acetonitrile) (m/z): calculated for [M+H]⁺: 414.3690; found: 414.3690.

H₂N-L-Phe-C(O)NH-C₁₂-NH-Boc – **45**



45

The compound was synthesized according to the procedure of compound **40**.

Yield: 5.535 g, 12.36 mmol (91%), white solid.

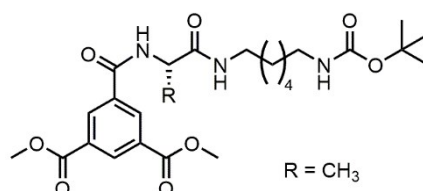
Molecular formula: C₂₆H₄₅N₃O₃.

¹H-NMR (300 MHz, CDCl₃, 298 K): δ [ppm] = 7.37 – 7.15 (m, 5H, C_{aromat}), 4.51 (s, 1H, NH), 3.59 (dd, J = 9.3, 4.1 Hz, 1H, CH), 3.33 – 3.16 (m, 3H, CH, CH₂), 3.09 (q, J = 6.6 Hz, 2H, CH₂), 2.69 (dd, J = 13.7, 9.3 Hz, 1H, CH₂), 1.59 (s, 2H, NH₂), 1.44 (m, 13H, CH₂, CH₃), 1.25 (m, 16H, CH₂).

ESI-ToF-MS (positive mode, acetonitrile) (m/z): calculated for [M+H]⁺: 448.3539; found: 448.3509.

1.2.3 Benzenetrispeptide building blocks bearing one PEO chain

(S)-dimethyl 5-(1-(6-(*tert*-butoxycarbonylamino)hexylamino)-1-oxopropan-2-ylcarbamoyl)-isophthalate – **46**



46

3,5-bis(methoxycarbonyl)benzoic acid **7** (0.5 g, 2.099 mmol, 1.0 eq) and DMAP (26 mg, 0.21 mmol, 0.1 eq) were dissolved in 10.5 mL chloroform. Compound **40** (0.664 g, 2.309 mmol, 1.1 eq) was added to the reaction mixture. Afterwards, EDC-HCl (0.483 g, 2.52 mmol, 1.2 eq) was added portion wise and the reaction mixture stirred overnight at rt. After removal of the solvent, the crude product was purified via flash chromatography (DCM/MeOH 96.5:3.5, v:v).

Yield: 0.834 g, 1.643 mmol (78%), white solid.

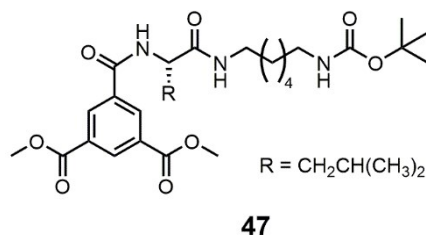
Molecular formula: C₂₅H₃₇N₃O₈.

¹H-NMR (300 MHz, d₆-DMSO, 298 K): δ [ppm] = 9.02 (d, J = 7.4 Hz, 1H, NH), 8.72 (d, J = 1.6 Hz, 2H, CH_{aromat}), 8.58 (t, J = 1.5 Hz, 1H, CH_{aromat}), 6.74 (t, J = 5.4 Hz, 1H, NH), 4.46 (t, J

= 7.3 Hz, 1H, CH), 3.93 (s, 6H, CH₃), 3.05 (p, J = 6.8 Hz, 2H, CH₂), 2.87 (q, J = 6.6 Hz, 2H, CH₂), 1.44 – 1.29 (m, 16H, CH₂, CH₃), 1.29 – 1.17 (m, 4H, CH₂).

ESI-ToF-MS (positive mode, acetonitrile) (m/z): calculated for [M+Na]⁺: 530.2473; found: 530.2468.

dimethyl (*S*)-5-((1-((6-((*tert*-butoxycarbonyl)amino)hexyl)amino)-4-methyl-1-oxopentan-2-yl)carbamoyl)isophthalate – **47**



The compound was synthesized according to the procedure of compound **46**, except using a different eluent composition (here: DCM/MeOH 96:4, v:v) for flash chromatography.

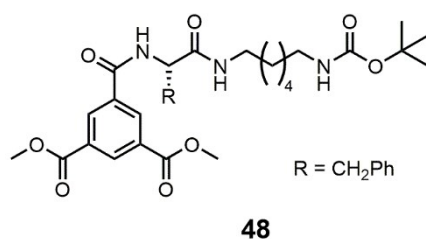
Yield: 1.736 g, 3.158 mmol (83%), white solid.

Molecular formula: C₂₈H₄₃N₃O₈.

¹H-NMR (300 MHz, d₆-DMSO, 298 K): δ [ppm] = 8.99 (d, J = 8.1 Hz, 1H, NH), 8.73 (d, J = 1.6 Hz, 2H, CH_{aromat}), 8.59 (t, J = 1.5 Hz, 1H, CH_{aromat}), 6.75 (t, J = 4.8 Hz, 1H, NH), 4.56 – 4.43 (m, 1H, CH), 3.93 (s, 6H, CH₃), 3.12 – 2.96 (m, 2H, CH₂), 2.86 (q, J = 7.3, 6.7 Hz, 2H), 1.76 – 1.46 (m, 3H, CH, CH₂), 1.36 (m, 13H, CH₂, CH₃), 1.21 (m, 4H, CH₂), 0.88 (dd, J = 11.2, 6.1 Hz, 6H, CH₃).

ESI-ToF-MS (positive mode, acetonitrile) (m/z): calculated for [M+Na]⁺: 572.2942; found: 572.2926.

dimethyl (*S*)-5-((1-((6-((*tert*-butoxycarbonyl)amino)hexyl)amino)-1-oxo-3-phenylpropan-2-yl)carbamoyl)isophthalate – **48**



The compound was synthesized according to the procedure of compound **46**, except using a different eluent composition (here: DCM/MeOH 97:3, v:v) for flash chromatography.

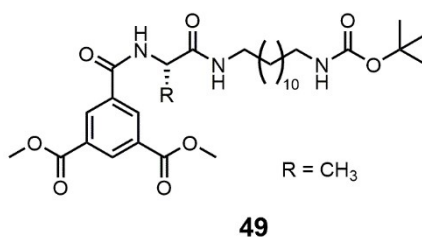
Yield: 0.307 g, 0.526 mmol (84%), white solid.

Molecular formula: C₃₁H₄₁N₃O₈.

¹H-NMR (300 MHz, d₆-DMSO, 298 K): δ [ppm] = 9.15 (d, J = 8.5 Hz, 1H, NH), 8.63 (d, J = 1.5 Hz, 2H, CH_{aromat}), 8.56 (t, J = 1.5 Hz, 1H, CH_{aromat}), 8.11 (t, J = 5.4 Hz, 1H, NH), 7.34 – 7.10 (m, 5H, CH_{aromat}), 6.76 (t, J = 5.5 Hz, 1H, NH), 4.76 – 4.64 (m, 1H, CH), 3.93 (s, 6H, CH₃), 3.14 – 2.93 (m, 4H, CH₂), 2.87 (q, J = 6.3 Hz, 2H, CH₂), 1.42 – 1.27 (m, 13H, CH₂, CH₃), 1.27 – 1.12 (m, 2H, CH₂).

ESI-ToF-MS (positive mode, acetonitrile) (m/z): calculated for [M+Na]⁺: 606.2786; found: 606.2802.

(S)-dimethyl 5-(1-(12-(*tert*-butoxycarbonylamino)dodecylamino)-1-oxopropan-2-ylcarbamoyl)isophthalate – **49**



The compound was synthesized according to the procedure of compound **46**, except using a different eluent composition (here: DCM/MeOH 98:2, v:v) for flash chromatography.

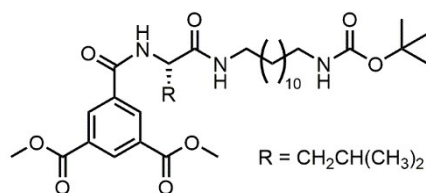
Yield: 0.738 g, 3.158 mmol (79%), white solid.

Molecular formula: C₃₁H₄₉N₃O₈.

¹H-NMR (300 MHz, d₆-DMSO, 298 K): δ [ppm] = 9.04 (d, J = 7.3 Hz, 1H, NH), 8.73 (d, J = 1.6 Hz, 2H, CH_{aromat}), 8.59 (t, J = 1.6 Hz, 1H, CH_{aromat}), 7.93 (t, J = 5.6 Hz, 1H, NH), 6.75 (t, J = 5.3 Hz, 1H, NH), 4.46 (p, J = 7.1 Hz, 1H, CH), 3.93 (s, 6H, CH₃), 3.04 (q, J = 6.2 Hz, 2H, CH₂), 2.87 (q, J = 6.5 Hz, 2H, CH₂), 1.44 – 1.29 (m, 16H, CH₂, CH₃), 1.20 (m, 16H, CH₂).

ESI-ToF-MS (positive mode, acetonitrile) (m/z): calculated for [M+Na]⁺: 614.3412; found: 614.3447.

dimethyl (*S*)-5-((1-((12-((*tert*-butoxycarbonyl)amino)dodecyl)amino)-4-methyl-1-oxopentan-2-yl)carbamoyl)isophthalate – **50**



50

The compound was synthesized according to the procedure of compound **46**, except using a different eluent composition (here: DCM/MeOH 96:4, v:v) for flash chromatography.

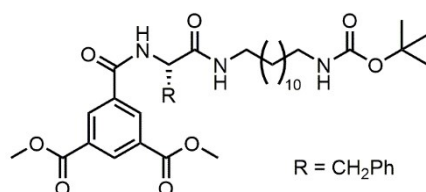
Yield: 1.736 g, 2.739 mmol (83%), white solid.

Molecular formula: C₃₄H₅₅N₃O₈.

¹H-NMR (300 MHz, d₆-DMSO, 298 K): δ [ppm] = 8.99 (d, *J* = 8.1 Hz, 1H, NH), 8.73 (d, *J* = 1.6 Hz, 2H, CH_{aromat}), 8.59 (t, *J* = 1.5 Hz, 1H, CH_{aromat}), 8.01 (t, *J* = 5.5 Hz, 1H, NH), 6.75 (t, *J* = 5.1 Hz, 1H, NH), 4.57 – 4.45 (m, 1H, CH), 3.93 (s, 6H, CH₃), 3.11 – 2.98 (m, 2H, CH₂), 2.87 (q, *J* = 6.6 Hz, 2H, CH₂), 1.77 – 1.45 (m, 3H, CH, CH₂), 1.36 (m, 13H, CH₂, CH₃), 1.19 (m, 16H, CH₂), 0.88 (dd, *J* = 11.2, 6.1 Hz, 6H, CH₃).

ESI-ToF-MS (positive mode, acetonitrile) (m/z): calculated for [M+Na]⁺: 656.3881; found: 656.3789.

(*S*)-dimethyl 5-(1-(12-((*tert*-butoxycarbonyl)amino)dodecyl)amino)-1-oxo-3-phenylpropan-2-ylcarbamoyl)isophthalate – **51**



51

The compound was synthesized according to the procedure of compound **46**, except using a different eluent composition (here: DCM/MeOH 96:4, v:v) for flash chromatography.

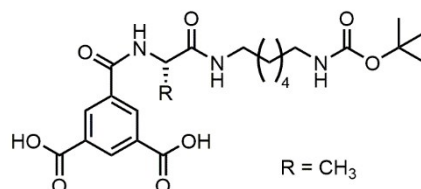
Yield: 1.174 g, 2.739 mmol (93%), white solid.

Molecular formula: C₃₇H₅₃N₃O₈.

¹H-NMR (300 MHz, d₆-DMSO, 298 K): δ [ppm] = 9.15 (d, *J* = 8.4 Hz, 1H, NH), 8.63 (d, *J* = 1.6 Hz, 2H, CH_{aromat}), 8.56 (t, *J* = 1.6 Hz, 1H, CH_{aromat}), 8.09 (t, *J* = 5.5 Hz, 1H, NH), 7.35 – 7.10 (m, 5H, CH_{aromat}), 6.75 (t, *J* = 5.4 Hz, 1H, NH), 4.72 (m, 1H, CH), 3.92 (s, 6H, CH₃), 3.07 (m, 4H, CH₂), 2.87 (q, *J* = 6.6 Hz, 2H, CH₂), 1.36 (m, 13H, CH₂, CH₃), 1.20 (m, 16H, CH₂).

ESI-ToF-MS (positive mode, acetonitrile) (m/z): calculated for $[M+Na]^+$: 690.3725; found: 690.3733.

(S)-5-(1-(6-(*tert*-butoxycarbonylamino)hexylamino)-1-oxopropan-2-ylcarbamoyl)isophthalic acid – **52**



52

Compound **46** (0.819 g, 1.614 mmol, 1.0 eq) was dissolved in 32.23 ml EtOH/H₂O (9:1, v:v) and stirred under reflux for 30 min. Afterwards, 1M aq. HCl was added dropwise under vigorous stirring until the product starts to precipitate. Then, the ethanol was removed *in vacuo* in order to allow an extraction with ethyl acetate. The remaining aqueous phase was extracted with ethyl acetate (3x, 50 mL). The combined organic phases were washed with brine, dried over MgSO₄, filtered and reduced *in vacuo*. The obtained product was then dried in the vacuum oven (40 °C) overnight.

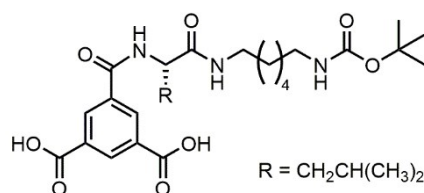
Yield: 0.549 g, 1.145 mmol (71%), white solid.

Molecular formula: C₂₃H₃₃N₃O₈

¹H-NMR (300 MHz, d₆-DMSO, 298 K): δ [ppm] = 13.47 (s, 2H, COOH), 8.97 (d, J = 7.4 Hz, 1H, NH), 8.68 (d, J = 1.6 Hz, 2H, CH_{aromat}), 8.58 (t, J = 1.6 Hz, 1H, CH_{aromat}), 7.93 (t, J = 5.6 Hz, 1H, NH), 6.75 (t, J = 5.6 Hz, 1H, NH), 4.45 (p, J = 7.1 Hz, 1H, CH), 3.04 (m, 4H, CH₂), 2.87 (q, J = 6.6 Hz, 2H, CH₂), 1.35 (m, 16H, CH₂, CH₃), 1.22 (m, 4H, CH₂).

ESI-ToF-MS (positive mode, acetonitrile) (m/z): calculated for $[M+Na]^+$: 502.2160; found: 502.2158.

(S)-5-((1-((6-((*tert*-butoxycarbonyl)amino)hexyl)amino)-4-methyl-1-oxopentan-2-yl)carbamoyl)isophthalic acid – **53**



53

The compound was synthesized according to the procedure of compound **52**.

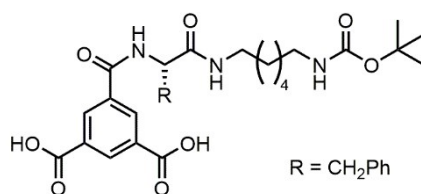
Yield: 0.323 g, 0.619 mmol (99%), white solid.

Molecular formula: C₂₆H₃₉N₃O₈

¹H-NMR (300 MHz, d₆-DMSO, 298 K): δ [ppm] = 13.48 (s, 2H, COOH), 8.92 (d, J = 8.1 Hz, 1H, NH), 8.68 (d, J = 1.6 Hz, 2H, CH_{aromat}), 8.57 (t, J = 1.6 Hz, 1H, CH_{aromat}), 8.00 (t, J = 5.6 Hz, 1H, NH), 6.75 (t, J = 5.7 Hz, 1H, NH), 4.55 – 4.44 (m, 1H, CH), 3.03 (m, 2H, CH₂), 2.87 (q, J = 6.7 Hz, 2H, CH₂), 1.75 – 1.47 (m, 4H, CH₂), 1.33 (m, 13H, CH₂, CH₃), 1.23 (s, 4H, CH₂), 0.88 (dd, J = 11.1, 6.2 Hz, 6H, CH₃).

ESI-ToF-MS (positive mode, acetonitrile) (m/z): calculated for [M+Na]⁺: 544.2690; found: 544.2557.

(S)-5-((1-((6-((*tert*-butoxycarbonyl)amino)hexyl)amino)-1-oxo-3-phenylpropan-2-yl)carbamoyl)isophthalic acid – **54**



54

The compound was synthesized according to the procedure of compound **52**.

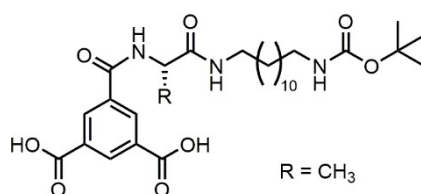
Yield: 0.248 g, 0.446 mmol (99%), white solid.

Molecular formula: C₂₉H₃₇N₃O₈

¹H-NMR (300 MHz, d₆-DMSO, 298 K): δ [ppm] = 9.08 (d, J = 8.0 Hz, 1H, NH), 8.59 (d, J = 1.5 Hz, 2H, CH_{aromat}), 8.55 (t, J = 1.4 Hz, 1H, CH_{aromat}), 8.11 (t, J = 5.1 Hz, 1H, NH), 7.36 – 7.10 (m, 5H, CH_{aromat}), 6.77 (t, J = 5.3 Hz, 1H, NH), 4.76 – 4.63 (m, 1H, CH), 3.15 – 2.94 (m, 4H, CH₂), 2.87 (q, J = 6.8 Hz, 2H, CH₂), 1.42 – 1.27 (m, 13H, CH₂, CH₃), 1.27 – 1.14 (m, 4H, CH₂).

ESI-ToF-MS (positive mode, acetonitrile) (m/z): calculated for [M+Na]⁺: 578.2473; found: 578.2467.

(S)-5-(1-(12-((*tert*-butoxycarbonyl)amino)dodecyl)amino)-1-oxopropan-2-ylcarbamoyl)isophthalic acid – **55**



55

The compound was synthesized according to the procedure of compound **52**.

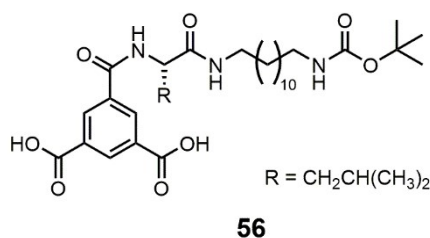
Yield: 0.511 g, 0.907 mmol (94%), white solid.

Molecular formula: C₂₉H₄₅N₃O₈

¹H-NMR (300 MHz, d₆-DMSO, 298 K): δ [ppm] = 13.50 (s, 2H, COOH), 8.97 (d, J = 7.3 Hz, 1H, NH), 8.73 – 8.65 (m, 2H, CH_{aromat}), 8.60 – 8.56 (m, 1H, CH_{aromat}), 7.90 (t, J = 5.2 Hz, 1H, NH), 6.79 – 6.70 (m, 1H, NH), 4.45 (p, J = 6.9, 6.4 Hz, 1H), 3.04 (q, J = 7.3, 6.8 Hz, 2H, CH₂), 2.87 (q, J = 6.2 Hz, 2H, CH₂), 1.35 (m, 17H, CH₂, CH₃), 1.20 (m, 16H, CH₂).

ESI-ToF-MS (negative mode, acetonitrile) (m/z): calculated for [M-H]⁻: 638.3447; found: 638.3283.

(S)-5-((1-((12-((*tert*-butoxycarbonyl)amino)dodecyl)amino)-4-methyl-1-oxopentan-2-yl)carbamoyl)isophthalic acid – **56**



The compound was synthesized according to the procedure of compound **52**.

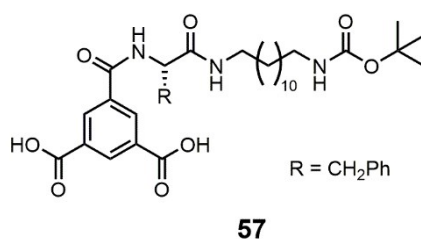
Yield: 1.404 g, 2.318 mmol (94%), white solid.

Molecular formula: C₃₂H₅₁N₃O₈

¹H-NMR (300 MHz, d₆-DMSO, 298 K): δ [ppm] = 8.93 (d, J = 8.5 Hz, 1H, NH), 8.67 (d, J = 1.6 Hz, 2H, CH_{aromat}), 8.57 (t, J = 1.5 Hz, 1H, CH_{aromat}), 8.00 (t, J = 5.5 Hz, 1H, NH), 6.75 (t, J = 5.5 Hz, 1H, NH), 4.54 – 4.43 (m, 1H, CH), 3.08 – 2.99 (m, 2H, CH₂), 2.86 (q, J = 6.5 Hz, 2H, CH₂), 1.75 – 1.48 (m, 3H, CH, CH₂), 1.35 (m, 13H, CH₂, CH₃), 1.19 (m, 16H, CH₂), 0.88 (dd, J = 11.3, 6.2 Hz, 6H, CH₃).

ESI-ToF-MS (positive mode, acetonitrile) (m/z): calculated for [M+Na]⁺: 628.3568; found: 628.3444.

(S)-5-(1-(12-((*tert*-butoxycarbonyl)amino)dodecylamino)-1-oxo-3-phenylpropan-2-yl)carbamoyl)isophthalic acid – **57**



The compound was synthesized according to the procedure of compound **52**.

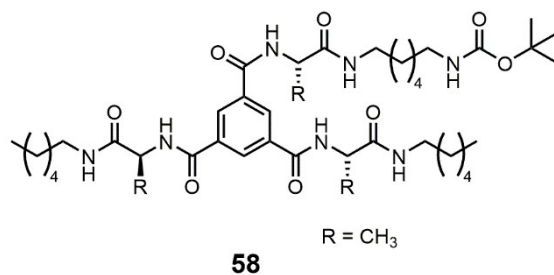
Yield: 1.029 g, 1.608 mmol (99%), white solid.

Molecular formula: C₃₅H₄₉N₃O₈

¹H-NMR (300 MHz, d₆-DMSO, 298 K): δ [ppm] = 13.34 (s, 1H, COOH), 9.08 (d, J = 8.4 Hz, 1H, NH), 8.60 (d, J = 1.6 Hz, 2H, CH_{aromat}), 8.55 (t, J = 1.5 Hz, 1H, CH_{aromat}), 8.07 (t, J = 5.5 Hz, 1H, NH), 7.34 – 7.10 (m, 5H, CH_{aromat}), 6.75 (t, J = 5.2 Hz, 1H, NH), 4.70 (td, J = 9.5, 5.1 Hz, 1H, CH), 3.13 – 2.94 (m, 4H, CH₂), 2.87 (q, J = 6.6 Hz, 2H, CH₂), 1.36 (m, 13H, CH₂, CH₃), 1.20 (m, 16H, CH₂).

ESI-ToF-MS (negative mode, acetonitrile) (m/z): calculated for [M-H]⁻: 638.3447; found: 638.3283.

[B][Ala][C₆] Boc-protected – **58**



Compound **52** (0.549 g, 1.145 mmol, 1.0 eq) and DMAP (14 mg, 0.114 mmol, 0.1 eq) were dissolved in 5.7 mL chloroform. To this, compound **19** (0.434 g, 2.52 mmol, 2.2 eq) was added. Consequently, EDC-HCl (0.658 g, 3.43 mmol, 3 eq) was added and the solution stirred overnight at rt. Afterwards, the solvent was removed and crude product purified via flash chromatography (DCM/MeOH, 92:8, v:v).

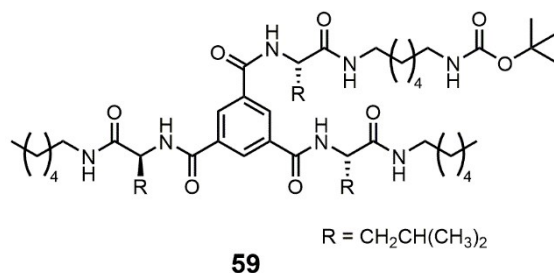
Yield: 0.703 g, 0.892 mmol (78%), white solid.

Molecular formula: C₄₁H₆₉N₇O₈

¹H-NMR (300 MHz, d₆-DMSO, 298 K): δ [ppm] = 8.67 (d, J = 7.4 Hz, 3H, NH), 8.47 (d, J = 1.1 Hz, 3H, CH_{aromat}), 7.96 (t, J = 5.3 Hz, 3H, NH), 6.77 (t, J = 5.4 Hz, 1H, NH), 4.50 (p, J = 7.2 Hz, 3H, CH), 3.05 (m, 6H, CH₂), 2.88 (q, J = 6.5 Hz, 2H, CH₂), 1.34 (m, 23H, CH₂, CH₃), 1.24 (m, 16H, CH₂), 0.84 (t, J = 7.5 Hz, 6H, CH₃).

ESI-ToF-MS (positive mode, acetonitrile) (m/z): calculated for [M+Na]⁺: 810.5100; found: 810.5124.

[B][Leu][C₆] Boc-protected – 59



The compound was synthesized according to the procedure of compound **58**, except using a different eluent composition (here: DCM/MeOH 96:4, v:v) for flash chromatography.

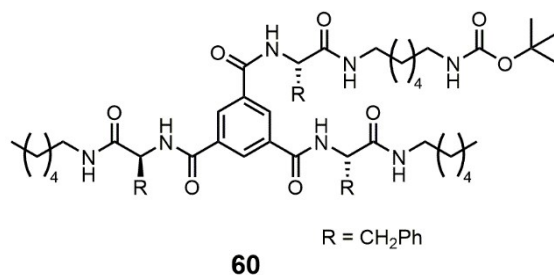
Yield: 0.155 g, 0.157 mmol (44%), light yellow solid.

Molecular formula: C₅₀H₈₇N₇O₈

¹H-NMR (300 MHz, d₆-DMSO, 298 K): δ [ppm] = 8.63 (d, J = 8.2 Hz, 3H, NH), 8.43 (s, 3H, CH_{aromat}), 8.01 (t, J = 5.3 Hz, 3H, NH), 6.75 (t, J = 5.4 Hz, 1H, NH), 4.54 (m, 3H, CH), 3.14 – 2.96 (m, 6H, CH₂), 2.87 (q, J = 6.6 Hz, 2H, CH₂), 1.73 – 1.58 (m, 6H, CH₂), 1.57 – 1.46 (m, 3H, CH), 1.45 – 1.30 (m, 17H, CH₂, CH₃), 1.29 – 1.15 (m, 16H, CH₂), 0.90 (dd, J = 9.0, 6.4 Hz, 18H, CH₃), 0.84 (t, J = 7.5 Hz, 6H, CH₃).

ESI-ToF-MS (positive mode, acetonitrile) (m/z): calculated for [M+Na]⁺: 936.6508; found: 936.6489.

[B][Phe][C₆] Boc-protected – 60



The compound was synthesized according to the procedure of compound **58**, except using DMF as reaction solvent and a different eluent composition (here: DCM/MeOH 90:10, v:v) for flash chromatography.

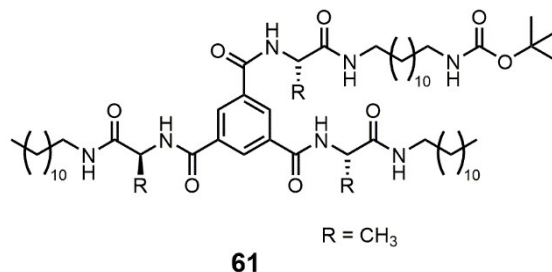
Yield: 0.765 g, 0.753 mmol (49%), light yellow solid.

Molecular formula: C₅₉H₈₁N₇O₈

¹H-NMR (300 MHz, d₆-DMSO, 298 K): δ [ppm] = 8.75 – 8.63 (m, 3H, NH), 8.34 – 8.25 (m, 3H, CH_{aromat}), 8.15 – 8.06 (m, 3H, NH), 7.37 – 7.11 (m, 15H, CH_{aromat}), 6.76 (t, J = 5.4 Hz, 1H, NH), 4.77 – 4.68 (m, 3H, CH), 3.14 – 2.94 (m, 12H, CH₂), 2.88 (q, J = 6.1 Hz, 3H, CH₂), 1.36 (m, 17H, CH₂, CH₃), 1.22 (m, 16H, CH₂), 0.84 (t, J = 6.9 Hz, 6H, CH₃).

ESI-ToF-MS (positive mode, acetonitrile) (m/z): calculated for $[M+Na]^+$: 1038.6039; found: 1038.6000.

[B][Ala][C₁₂] Boc-protected – **61**



The compound was synthesized according to the procedure of compound **58**, except using DMF as reaction solvent and a different eluent composition (here: DCM/MeOH 96:4, v:v) for flash chromatography.

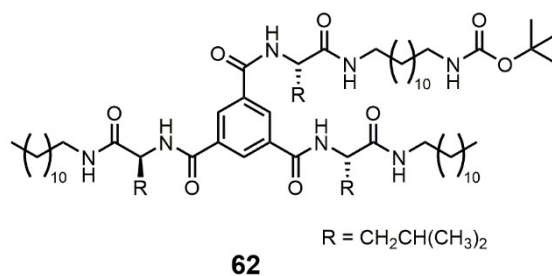
Yield: 0.605 g, 0.581 mmol (37.5%), light yellow solid.

Molecular formula: C₅₉H₁₀₅N₇O₈

¹H-NMR (300 MHz, d₆-DMSO, 298 K): δ [ppm] = 8.66 (d, J = 7.5 Hz, 3H, NH), 8.47 (d, J = 1.0 Hz, 3H, CH_{aromat}), 7.95 (t, J = 7.5 Hz, 3H, NH), 6.75 (t, J = 5.6 Hz, 1H, NH), 4.49 (p, J = 7.0 Hz, 3H, CH), 3.05 (q, J = 6.3, 5.9 Hz, 6H, CH₂), 2.88 (q, J = 6 Hz, 1H), 1.45 – 1.30 (m, 26H, CH₂, CH₃), 1.22 (m, 52H, CH₂), 0.84 (t, J = 7.5 Hz, 6H, CH₃).

ESI-ToF-MS (positive mode, acetonitrile) (m/z): calculated for $[M+Na]^+$: 1062.7917; found: 1062.7879.

[B][Leu][C₁₂] Boc-protected – **62**



The compound was synthesized according to the procedure of compound **58**, except using a different eluent composition (here: DCM/MeOH 96:4, v:v) for flash chromatography.

Yield: 0.288 g, 0.247 mmol (74%), light yellow solid.

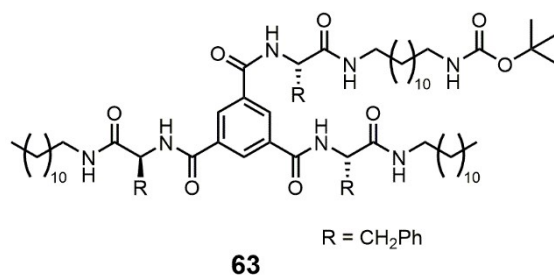
Molecular formula: C₆₈H₁₂₃N₇O₈

¹H-NMR (300 MHz, d₆-DMSO, 298 K): δ [ppm] = 8.63 (d, J = 8.3 Hz, 3H, NH), 8.43 (s, 3H, CH_{aromat}), 8.01 (t, J = 5.4 Hz, 3H, NH), 6.74 (t, J = 5.3 Hz, 1H, NH), 4.58 – 4.47 (m, 3H, CH),

3.05 (hept, $J = 6.5$ Hz, 6H, CH₂), 2.87 (q, $J = 6.7$ Hz, 2H, CH₂), 1.75 – 1.47 (m, 9H, CH, CH₂), 1.36 (m, 17H, CH₂, CH₃), 1.21 (s, 52H, CH₂), 0.98 – 0.77 (m, 24H, CH₃).

ESI-ToF-MS (positive mode, acetonitrile) (m/z): calculated for [M+Na]⁺: 1188.9325; found: 1188.9310.

[B][Phe][C₁₂] Boc-protected – **63**



The compound was synthesized according to the procedure of compound **58**, except using DMF as reaction solvent and a different eluent composition (here: DCM/MeOH 96:4, v:v) for flash chromatography.

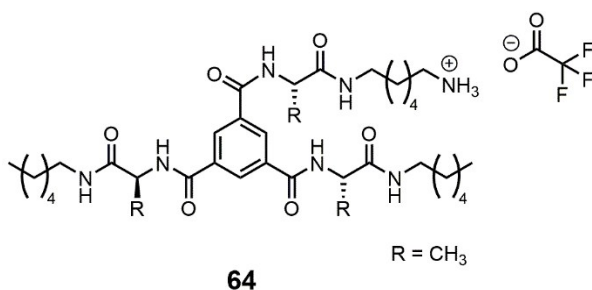
Yield: 0.442 g, 0.348 mmol (45%), light yellow solid.

Molecular formula: C₇₇H₁₁₇N₇O₈

¹H-NMR (300 MHz, d₆-DMSO, 298 K): δ [ppm] = 8.72 (t, $J = 7.9$ Hz, 3H, NH), 8.35 – 8.25 (m, 3H, CH_{aromat}), 8.16 – 8.04 (m, 3H, NH), 7.37 – 7.09 (m, 15H, CH_{aromat}), 6.75 (t, $J = 5.2$ Hz, 1H, NH), 4.80 – 4.63 (m, 3H, CH), 3.16 – 2.92 (m, 12H, CH₂), 2.87 (q, $J = 6.6$ Hz, 2H, CH₂), 1.36 (m, 17H, CH₂, CH₃), 1.21 (m, 52H, CH₂), 0.84 (t, $J = 6.6$ Hz, 6H, CH₃).

ESI-ToF-MS (positive mode, acetonitrile) (m/z): calculated for [M+Na]⁺: 1290.8856; found: 1290.8791.

[B][Ala][C₆] Boc-deprotected – **64**



Compound **58** (0.690 g, 0.876 mmol, 1.0 eq) was dissolved in 8.76 mL DCM. To this, 2.82 mL of an 18:1:1 solution of TFA/TIPS/H₂O (TFA: 2.429 mL, 31.5 mmol, 36 eq; TIPS: 0.359 mL, 1.751 mmol, 2 eq; H₂O: 0.032 mL, 1.751 mmol, 2 eq) was added dropwise and the solution stirred for 2 h at rt. Afterwards, half of the DCM volume was removed and the concentrated

reaction mixture precipitated in cold diethyl ether. The suspension was centrifuged (3 min, 8,000 rpm) and the supernatant decanted. The obtained product was dried in the vacuum oven (40 °C overnight).

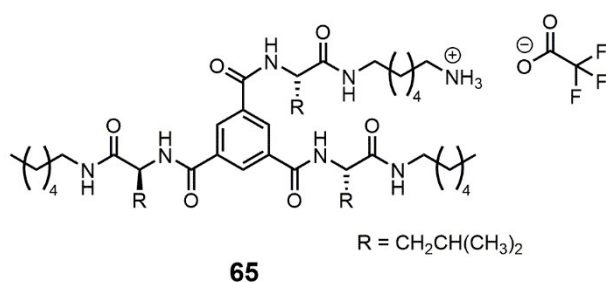
Yield: 0.636 g, 0.739 mmol (91%), white solid.

Molecular formula: C₃₂H₆₂N₇O₂F₃

¹H-NMR (300 MHz, d₆-DMSO, 298 K): δ [ppm] = 8.67 (t, J = 6.5 Hz, 3H, NH), 8.50 – 8.45 (m, 3H, CH_{aromat}), 7.98 (t, J = 5.4 Hz, 3H, NH), 7.63 (s, 3H, NH₃), 4.49 (p, J = 6.2, 5.5 Hz, 3H, CH), 3.06 (hept, J = 6.3 Hz, 6H, CH₂), 2.84 – 2.69 (m, 2H, CH₂), 1.57 – 1.46 (m, 2H, CH₂), 1.36 (m, 11H, CH₂, CH₃), 1.26 (m, 16H), 0.85 (t, J = 7.5 Hz, 6H, CH₃).

ESI-ToF-MS (positive mode, acetonitrile) (m/z): calculated for [M+H]⁺: 688.4756; found: 688.4741.

[B][Leu][C₆] Boc-protected – **65**



The compound was synthesized according to the procedure of compound **64**.

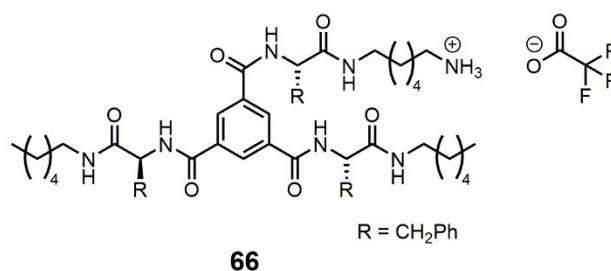
Yield: 0.099 g, 0.107 mmol (98%), white solid.

Molecular formula: C₄₂H₈₀N₇O₂F₃

¹H-NMR (300 MHz, d₆-DMSO, 298 K): δ [ppm] = 8.63 (d, J = 8.3 Hz, 3H, NH), 8.43 (s, 3H, CH_{aromat}), 8.03 (t, J = 5.2 Hz, 3H, NH), 7.60 (s, 3H, NH₃), 4.52 (t, J = 7.0 Hz, 3H, CH), 3.07 (m, 6H, CH₂), 2.83 – 2.69 (m, 2H, CH₂), 1.75 – 1.32 (m, 17H, CH, CH₂), 1.24 (m, 16H, CH₂), 0.98 – 0.75 (m, 24H, CH₃).

ESI-ToF-MS (positive mode, acetonitrile) (m/z): calculated for [M+H]⁺: 814.6165; found: 814.6142.

[B][Phe][C₆] Boc-deprotected – 66



The compound was synthesized according to the procedure of compound **64**.

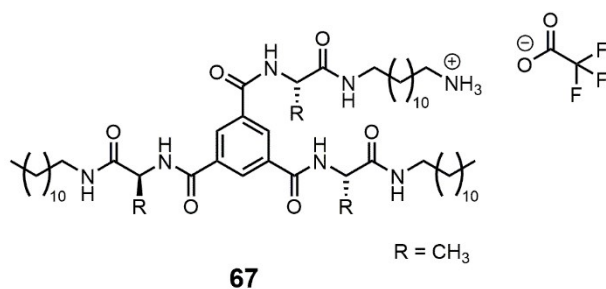
Yield: 0.621 g, 0.603 mmol (88%), white solid.

Molecular formula: C₅₂H₇₄N₇O₂F₃

¹H-NMR (300 MHz, d₆-DMSO, 298 K): δ [ppm] = 8.80 – 8.64 (m, 3H, NH), 8.37 – 8.25 (m, 3H, CH_{aromat}), 8.22 – 8.07 (m, 3H, NH), 7.79 (s, 3H, NH₃), 7.39 – 7.08 (m, 15H, CH_{aromat}), 4.82 – 4.64 (m, 3H, CH_{aromat}), 3.19 – 2.92 (m, 12H, CH₂), 2.84 – 2.68 (m, 2H, CH₂), 1.50 (q, J = 7.6, 7.0 Hz, 2H, CH₂), 1.37 (m, 6H, CH₂), 1.22 (m, 17H, CH₂), 0.84 (t, J = 6.5 Hz, 6H, CH₃).

ESI-ToF-MS (mode, acetonitrile) (m/z): calculated for [M+H]⁺: 916.5695; found: 916.5658.

[B][Ala][C₁₂] Boc-deprotected – 67



The compound was synthesized according to the procedure of compound **64**.

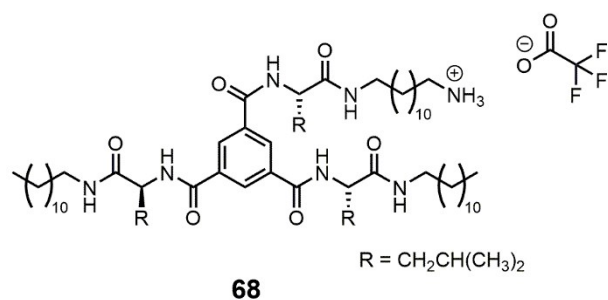
Yield: 0.533 g, 0.505 mmol (87%), white solid.

Molecular formula: C₅₆H₉₈N₇O₈F₃

¹H-NMR (300 MHz, d₆-DMSO, 298 K): δ [ppm] = 8.67 (d, J = 7.4 Hz, 3H, NH), 8.48 (d, J = 1.4 Hz, 3H, CH_{aromat}), 7.97 (t, J = 5.5 Hz, 3H, NH), 7.70 (s, 3H, NH₃), 4.49 (p, J = 6.9 Hz, 3H, CH), 3.06 (q, J = 6.6 Hz, 6H, CH₂), 2.76 (dq, J = 12.8, 5.7 Hz, 2H, CH₂), 1.59 – 1.46 (m, 2H, CH₂), 1.36 (m, 15H, CH₂, CH₃), 1.23 (m, 48H, CH₂), 0.85 (t, J = 7.5 Hz, 6H, CH₃).

ESI-ToF-MS (positive mode, acetonitrile) (m/z): calculated for [M+H]⁺: 940.7573; found: 940.7574.

[B][Leu][C₁₂] Boc-deprotected – 68



The compound was synthesized according to the procedure of compound 64.

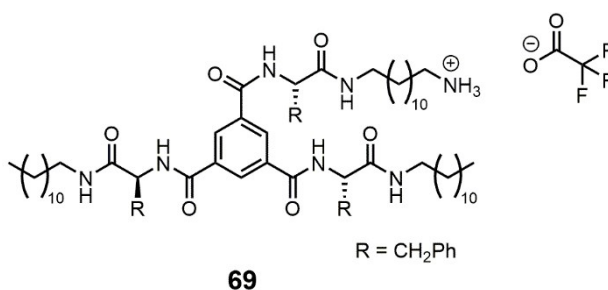
Yield: 0.195 g, 0.165 mmol (96%), white solid.

Molecular formula: C₆₅H₁₁₆N₇O₈F₃

¹H-NMR (300 MHz, d₆-DMSO, 298 K): δ [ppm] = 8.63 (d, J = 8.2 Hz, 3H, NH), 8.43 (s, 3H, CH_{aromat}), 8.02 (t, J = 5.3 Hz, 3H, NH), 7.59 (s, 3H, NH₃), 4.62 – 4.45 (m, 3H, CH), 3.13 – 2.95 (m, 6H, CH₂), 2.81 – 2.74 (m, 2H, CH₂), 1.75 – 1.33 (m, 17H, CH₂, CH₃), 1.22 (m, 52H, CH₂), 0.97 – 0.74 (m, 24H, CH₃).

ESI-ToF-MS (positive mode, acetonitrile) (m/z): calculated for [M+H]⁺: 1066.8982; found: 1066.8958.

[B][Phe][C₁₂] Boc-deprotected – 69



The compound was synthesized according to the procedure of compound 64.

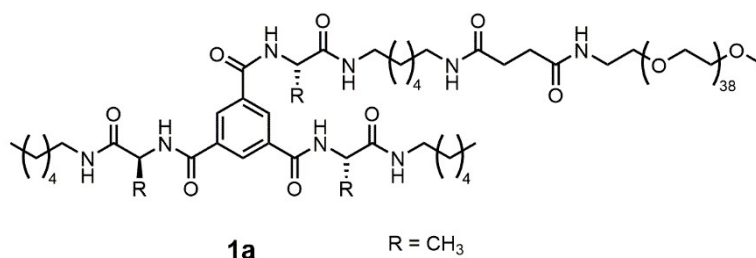
Yield: 0.311 g, 0.242 mmol (80%), white solid.

Molecular formula: C₇₄H₁₁₀N₇O₈F₃

¹H-NMR (300 MHz, d₆-DMSO, 298 K): δ [ppm] = 8.73 (t, J = 7.4 Hz, 3H, NH), 8.38 – 8.24 (m, 3H, CH_{aromat}), 8.11 (t, J = 4.7 Hz, 3H, NH), 7.70 (s, 3H, NH₃), 7.38 – 7.08 (m, 15H, CH_{aromat}), 4.72 (q, J = 8.9 Hz, 3H, CH), 3.18 – 2.91 (m, 12H, CH₂), 2.83 – 2.64 (m, 2H, CH₂), 1.59 – 1.44 (m, 2H, CH₂), 1.36 (m, 6H, CH₂), 1.22 (m, 52H, CH₂), 0.84 (t, J = 6.5 Hz, 6H, CH₃).

ESI-ToF-MS (mode, acetonitrile) (m/z): calculated for [M+H]⁺: 1168.8512; found: 1168.8467.

[B][Ala]₃[C₆]₃[PEO_{2k}] – **1a**



Compound **64** (0.599 g, 0.747 mmol, 1.0 eq) was dissolved in 9.96 mL DMF. To this, 1.041 mL triethylamine (7.47 mmol, 10 eq) were added dropwise. After stirring at rt for 15 min, 1.784 g of MeO-PEO_{2k}-NHS ester (0.896 mmol, 1.2 eq) were added and the reaction mixture stirred at rt overnight. Afterwards, the reaction mixture was precipitated into cold diethyl ether, the suspension centrifuged (3 min, 8,000 rpm) and the supernatant decanted. Then a mixture of diethyl ether and acetone (9:1, v:v) was added to the precipitate and the suspension exposed to sonication for 5 min in order to remove all residual DMF and some unconjugated MeO-PEO_{2k}-NHS ester. Afterwards, the suspension was again centrifuged (3 min, 8,000 rpm) and the supernatant decanted. Still remaining MeO-PEO_{2k}-NHS ester was then removed via continuous centrifugal washing using Amicon® Ultra-15 centrifugal filter units (MWCO: 10 kDa). The obtained product was then dissolved in water and lyophilised overnight.

Yield: 1.734 g, 0.677 mmol (91%), white powder.

Molecular formula: C₁₂₁H₂₂₈N₈O₄₈

¹H-NMR (300 MHz, d₆-DMSO, 298 K): δ [ppm] = 8.66 (d, J = 7.4 Hz, 3H, NH), 8.47 (s, 3H, CH_{aromat}), 7.96 (t, J = 5.0 Hz, 3H, NH), 7.87 (t, J = 5.3 Hz, 1H, NH), 7.76 (t, J = 5.2 Hz, 1H, NH), 4.49 (p, J = 6.6 Hz, 3H, CH), 3.77 – 3.70 (m, 2H, CH₂), 3.50 (s, 148H, PEO), 3.45 – 3.41 (m, 2H, CH₂), 3.23 (s, 2H, CH₂), 3.16 (q, J = 5.6 Hz, 2H, CH₂), 3.12 – 2.93 (m, 6H, CH₂), 2.27 (s, 4H, CH₂), 1.47 – 1.30 (m, 11H, CH₂, CH₃), 1.24 (s, 16H, CH₂), 0.84 (t, J = 6.4 Hz, 6H, CH₃).

MALDI-ToF-MS (positive mode, DHB) (m/z): calculated for [C₁₁₉H₂₂₄N₈O₄₇Na]⁺: 2541.5309; found: 2541.6358.

SEC (DMAc + 0.21 wt.% LiCl): M_n = 2,400 g mol⁻¹; M_w = 3,000 g mol⁻¹; Đ = 1.26.

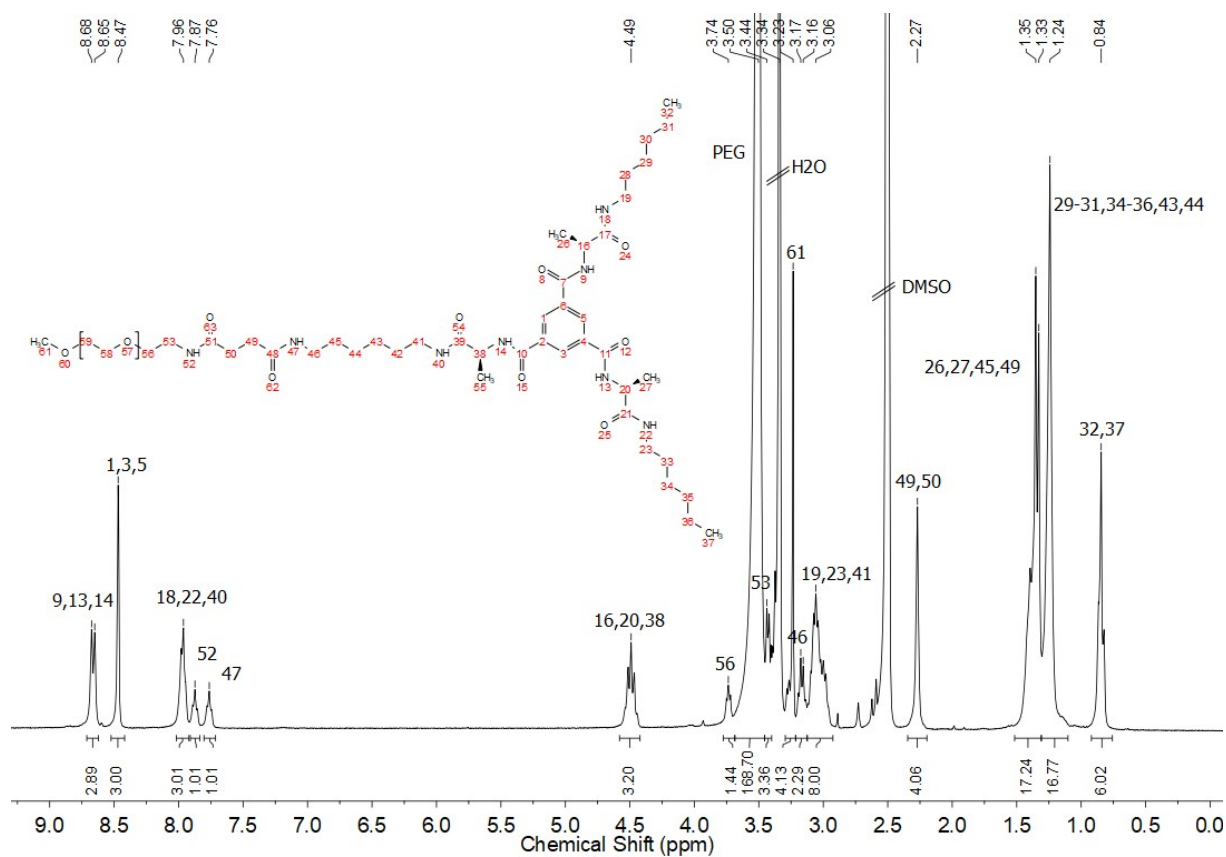


Figure S 1: ¹H-NMR spectrum of **1a** measured in d₆-DMSO.

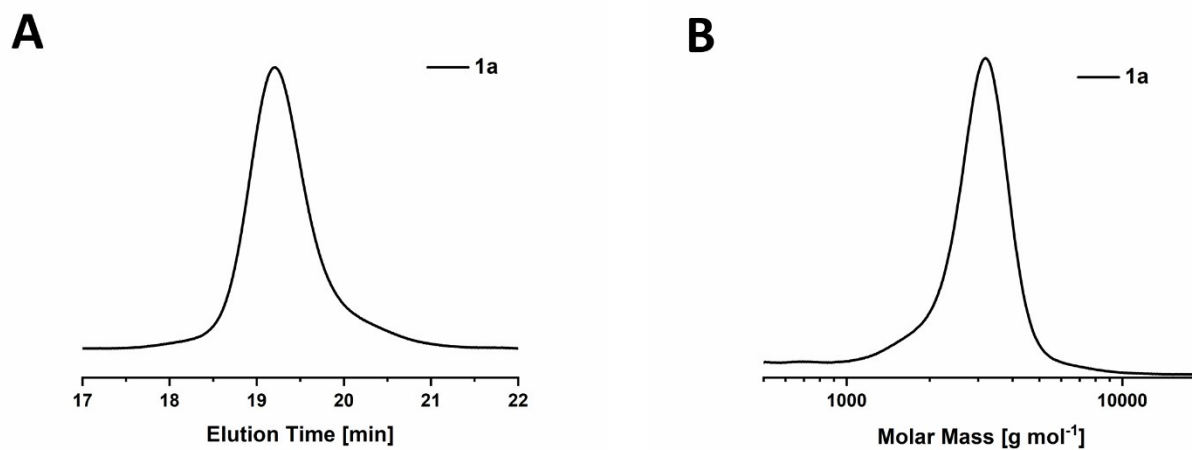
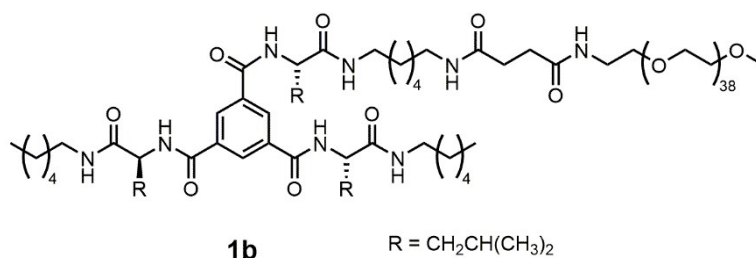


Figure S 2: SEC traces of **1a** recorded in DMAc (+0.21 wt% LiCl; 25 °C, RI, detection, PEO-Standard). A) Elution profile, B) Molar Mass distribution.

[B][Leu]₃[C₆]₃[PEO_{2k}] – **1b**



The compound was synthesized according to the procedure of compound **1a**.

Yield: 0.148 g, 0.055 mmol (68%), white powder.

Molecular formula: C₁₃₀H₂₄₆N₈O₄₈

¹H-NMR (300 MHz, d₆-DMSO, 298 K): δ [ppm] = 8.65 (d, J = 8.1 Hz, 3H, NH), 8.43 (s, 3H, CH_{aromat}), 8.03 (t, J = 4.8 Hz, 3H, NH), 7.87 (t, J = 5.1 Hz, 1H, NH), 7.76 (t, J = 4.7 Hz, 1H, NH), 4.60 – 4.47 (m, 3H, CH), 3.78 – 3.70 (m, 2H, CH₂), 3.50 (s, 148H, PEO), 3.45 – 3.41 (m, 2H, CH₂), 3.23 (s, 2H, CH₂), 3.17 (q, J = 5.4 Hz, 2H, CH₂), 3.13 – 2.94 (m, 8H, CH₂), 2.27 (s, 4H, CH₂), 1.66 (q, J = 8.1, 6.5 Hz, 6H, CH₂), 1.59 – 1.46 (m, 3H, CH), 1.46 – 1.32 (m, 8H, CH₂), 1.24 (s, 14H, CH₂), 0.90 (t, J = 6.2 Hz, 18H, CH₃), 0.84 (t, J = 6.2 Hz, 6H, CH₃).

MALDI-ToF-MS (positive mode, DHB) (m/z): calculated for [C₁₂₈H₂₄₂N₈O₄₇Na]⁺: 2667.6718; found: 2667.8208.

SEC (DMAc + 0.21 wt.% LiCl): M_n = 3,100 g mol⁻¹; M_w = 3,200 g mol⁻¹; Đ = 1.05.

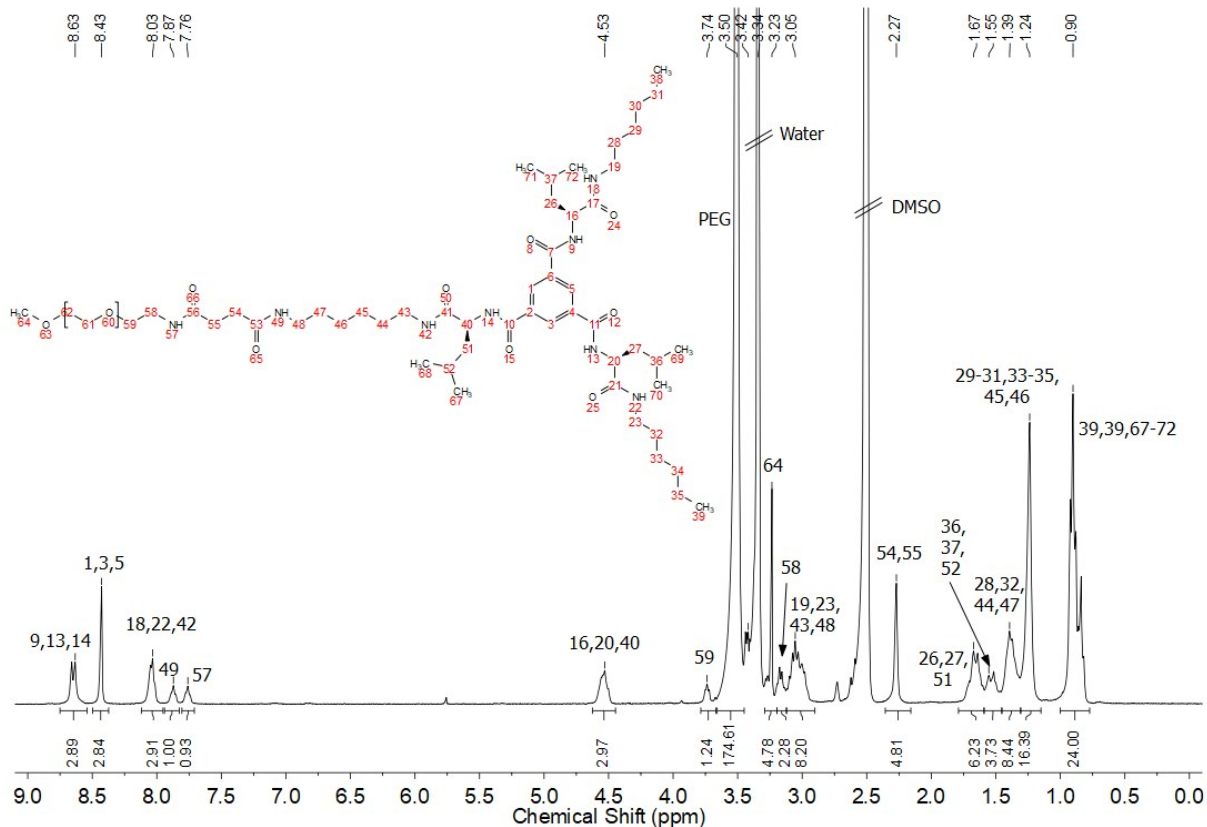


Figure S 3: $^1\text{H-NMR}$ spectrum of **1b** measured in $d_6\text{-DMSO}$.

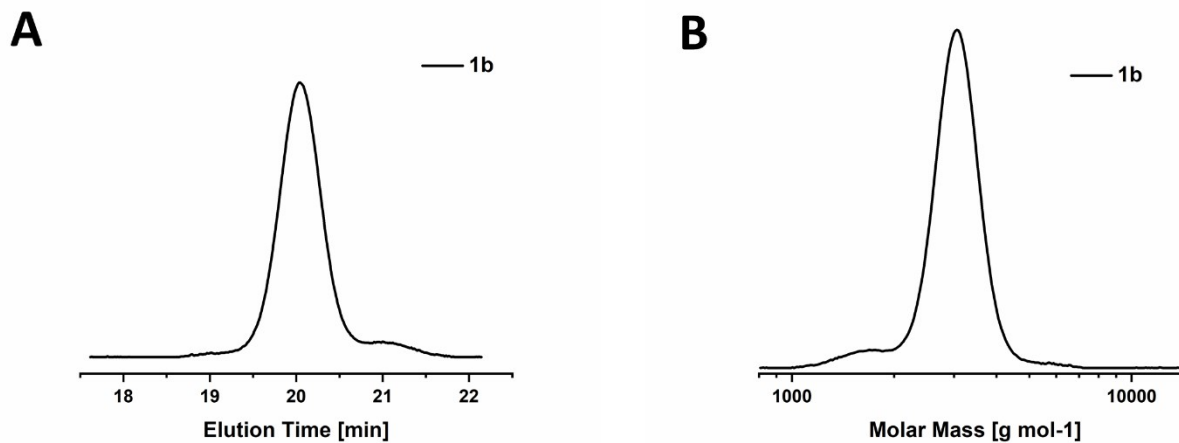
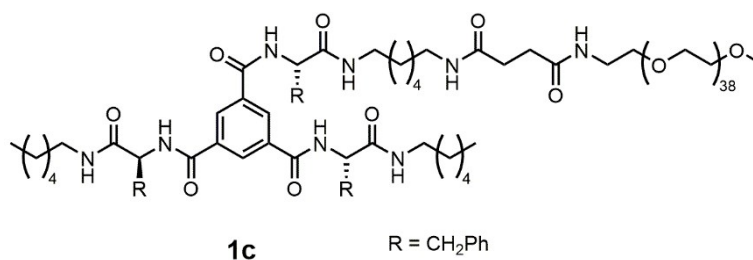


Figure S 4: SEC traces of **1b** recorded in DMAc (+0.21 wt% LiCl; 25 °C, RI, detection, PEO-Standard). A) Elution profile, B) Molar Mass distribution.

[B][Phe]₃[C₆]₃[PEO_{2k}] – **1c**



The compound was synthesized according to the procedure of compound **1a**.

Yield: 1.191 g, 0.427 mmol (75%), white powder.

Molecular formula: C₁₃₉H₂₄₀N₈O₄₈

¹H-NMR (300 MHz, d₆-DMSO, 298 K): δ [ppm] = 8.78 – 8.62 (m, 3H, NH), 8.36 – 8.23 (m, 3H, CH_{aromat}), 8.17 – 8.05 (m, 3H, NH), 7.87 (t, J = 5.4 Hz, 1H, NH), 7.76 (t, J = 5.8 Hz, 1H, NH), 7.37 – 7.09 (m, 15H, CH_{aromat}), 4.79 – 4.64 (m, 3H, CH), 3.78 – 3.70 (m, 2H, CH₂), 3.50 (s, 148H, PEO), 3.45 – 3.40 (m, 2H, CH₂), 3.23 (s, 2H, CH₂), 3.17 (q, J = 5.9 Hz, 2H, CH₂), 3.13 – 2.92 (m, 12H, CH₂), 2.28 (s, 4H, CH₂), 1.36 (m, 8H, CH₂), 1.22 (m, 18H, CH₂), 0.84 (t, J = 6.6 Hz, 6H, CH₃).

MALDI-ToF-MS (positive mode, DHB) (m/z): calculated for [C₁₃₇H₂₃₈N₈O₄₇Na]⁺: 2769.6249; found: 2769.8914.

SEC (DMAc + 0.21 wt.% LiCl): M_n = 2,700 g mol⁻¹; M_w = 3,100 g mol⁻¹; Đ = 1.16.

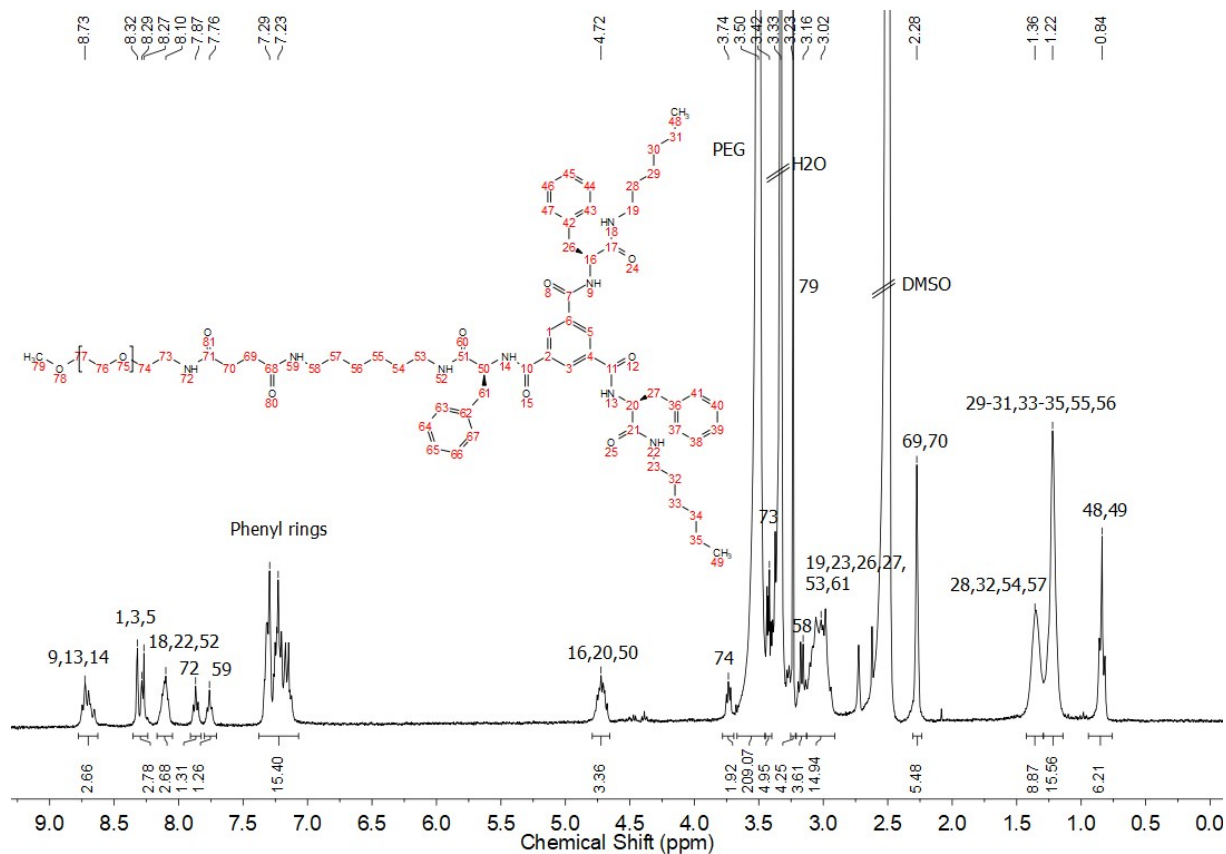


Figure S 5: ^1H -NMR spectrum of **1c** measured in d_6 -DMSO.

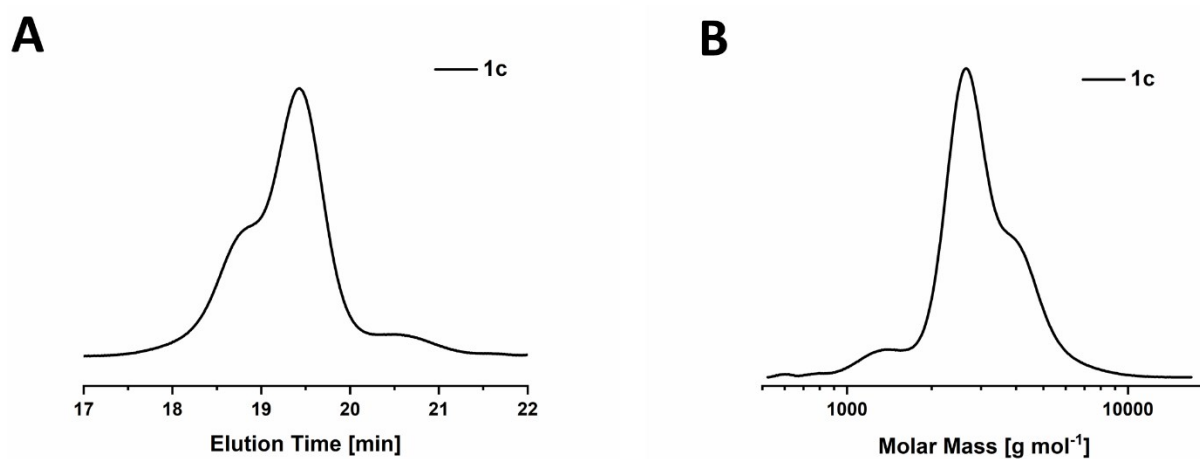
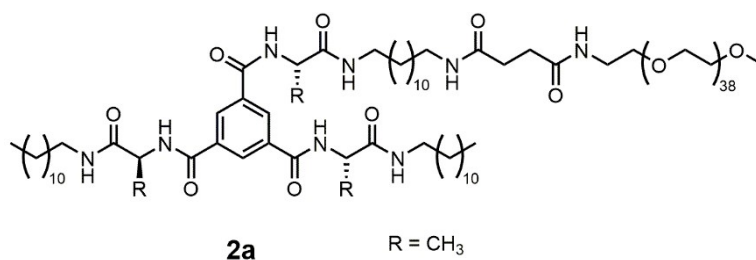


Figure S 6: SEC traces of **1c** recorded in DMAc (+0.21 wt% LiCl; 25 °C, RI, detection, PEO-Standard). A) Elution profile, B) Molar Mass distribution. The peak at around 1500 g mol^{-1} is caused by residual NHS-PEO2k-MeO and the shoulder at higher molar masses most likely originates from assembly of **1c**.

[B][Ala]₃[C₁₂]₃[PEO_{2k}] – **2a**



The compound was synthesized according to the procedure of compound **1a**.

Yield: 0.359 g, 0.128 mmol (90%), white powder.

Molecular formula: C₁₃₉H₂₆₄N₈O₄₈

¹H-NMR (300 MHz, d₆-DMSO, 298 K): δ [ppm] = 8.65 (d, J = 7.4 Hz, 3H, NH), 8.47 (s, 3H, CH_{aromat}), 7.95 (t, J = 5.5 Hz, 3H), 7.87 (t, J = 5.5 Hz, 1H, NH), 7.75 (t, J = 5.4 Hz, 1H, NH), 4.49 (p, J = 6.9 Hz, 3H, CH), 3.74 (t, J = 4.8 Hz, 2H, CH₂), 3.50 (s, 148H, PEO), 3.46 – 3.39 (m, 2H, CH₂), 3.23 (s, 2H, CH₂), 3.16 (q, J = 5.9 Hz, 2H, CH₂), 3.12 – 2.93 (m, 6H, CH₂), 2.27 (s, 4H, CH₂), 1.46 – 1.30 (m, 17H, CH₂, CH₃), 1.22 (m, 54H, CH₂), 0.89 – 0.80 (m, 6H, CH₃).

MALDI-ToF-MS (positive mode, DHB) (m/z): calculated for [C₁₃₇H₂₆₀N₈O₄₇Na]⁺: 2793.8127; found: 2793.8134.

SEC (DMAc + 0.21 wt.% LiCl): M_n = 3,500 g mol⁻¹; M_w = 3,700 g mol⁻¹; Đ = 1.06.

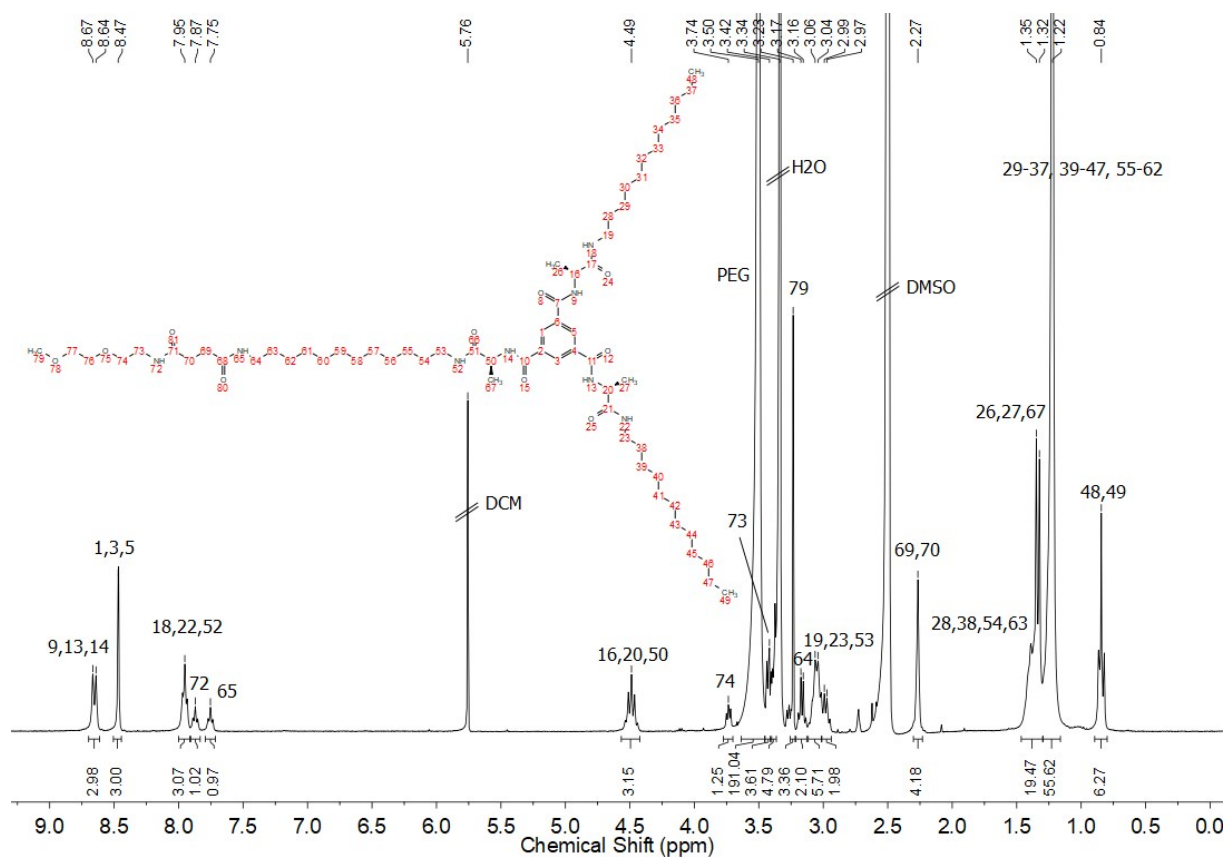


Figure S 7: $^1\text{H-NMR}$ spectrum of **2a** measured in $\text{d}_6\text{-DMSO}$.

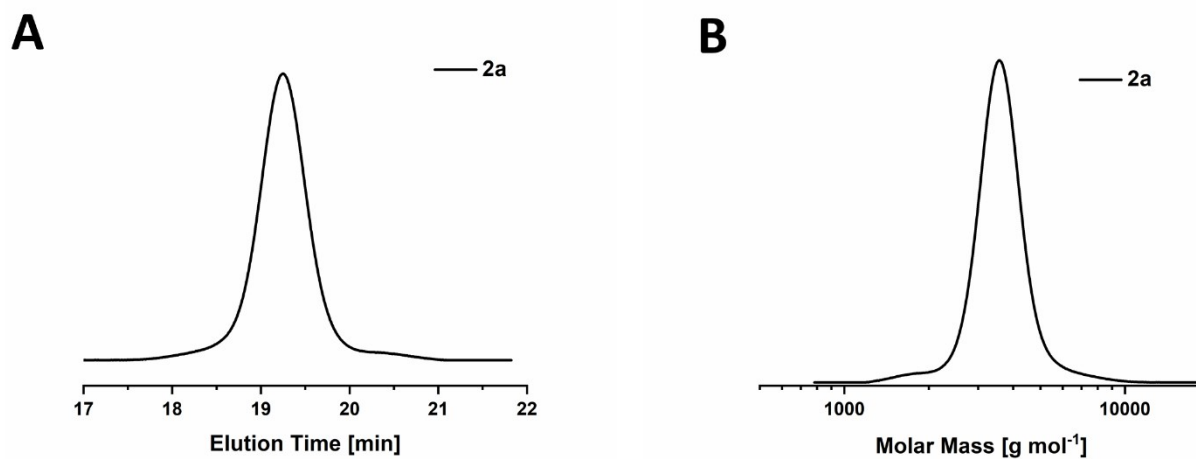
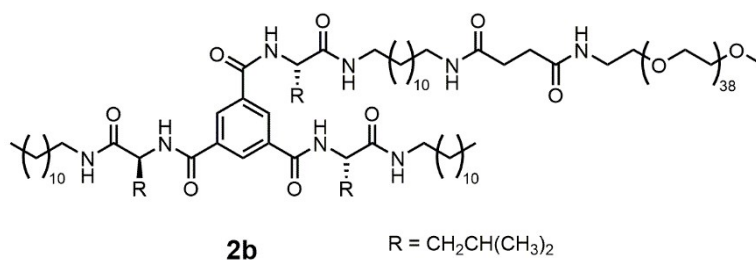


Figure S 8: SEC traces of **2a** recorded in DMAc (+0.21 wt% LiCl; 25 °C, RI, detection, PEO-Standard). A) Elution profile, B) Molar Mass distribution.

[B][Leu]₃[C₁₂]₃[PEO_{2k}] – **2b**



The compound was synthesized according to the procedure of compound **1a**.

Yield: 0.221 g, 0.075 mmol (97%), white powder.

Molecular formula: C₁₄₈H₂₈₂N₈O₄₈

¹H-NMR (300 MHz, d₆-DMSO, 298 K): δ [ppm] = 8.63 (d, J = 8.1 Hz, 3H, NH), 8.43 (s, 3H, CH_{aromat}), 8.02 (t, J = 4.9 Hz, 3H, NH), 7.87 (t, J = 5.1 Hz, 1H, NH), 7.75 (t, J = 5.4 Hz, 1H, NH), 4.61 – 4.48 (m, 3H, CH), 3.78 – 3.70 (m, 2H, CH₂), 3.50 (s, 148H, PEO), 3.28 (m, 2H, CH₂), 3.23 (s, 2H, CH₂), 3.17 (q, J = 5.6 Hz, 2H, CH₂), 3.13 – 2.93 (m, 6H, CH₂), 2.27 (s, 4H, CH₂), 1.75 – 1.32 (m, 17H, CH, CH₂), 1.22 (m, 54H, CH₂), 0.90 (t, J = 6.4 Hz, 18H, CH₃), 0.84 (t, J = 6.7 Hz, 3H, CH₃).

MALDI-ToF-MS (positive mode, DHB) (m/z): calculated for [C₁₄₆H₂₇₈N₈O₄₇Na]⁺: 2919.9537; found: 2919.8889.

SEC (DMAc + 0.21 wt.% LiCl): M_n = 3,600 g mol⁻¹; M_w = 3,800 g mol⁻¹; Đ = 1.05.

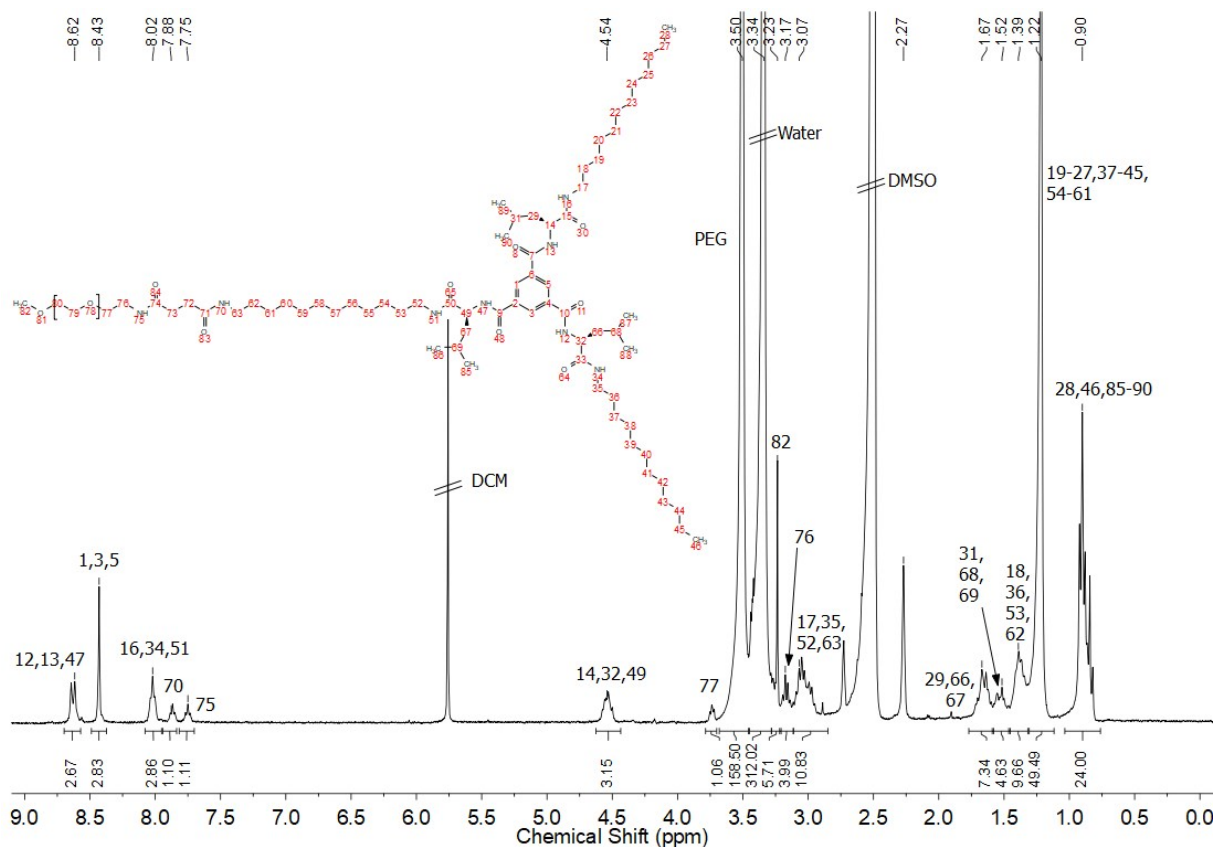


Figure S 9: $^1\text{H-NMR}$ spectrum of **2b** measured in $d_6\text{-DMSO}$.

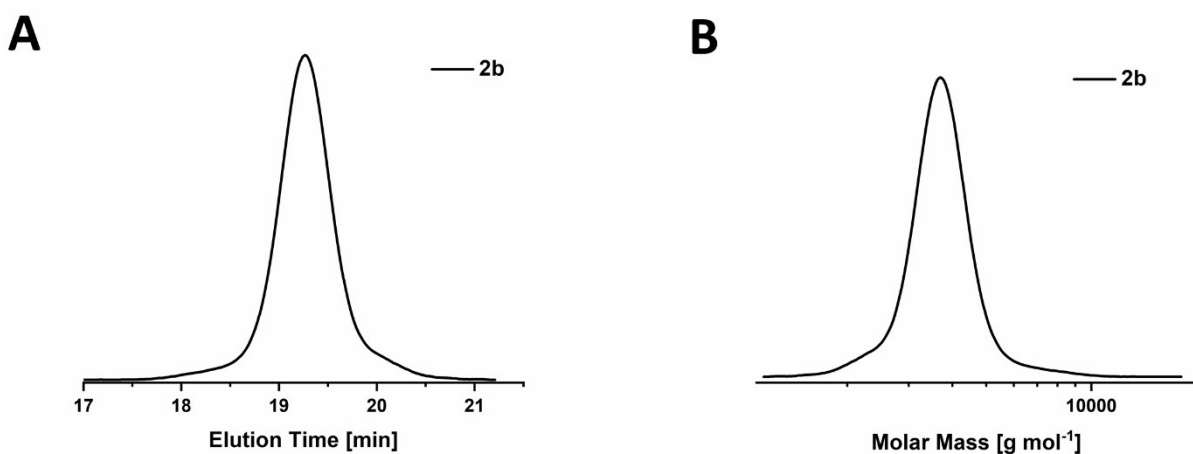
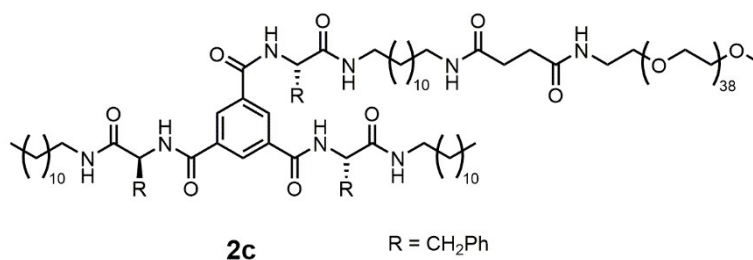


Figure S 10: SEC traces of **2b** recorded in DMAc (+0.21 wt% LiCl; 25 °C, RI, detection, PEO-Standard). A) Elution profile, B) Molar Mass distribution.

[B][Phe]₃[C₁₂]₃[PEO_{2k}] – **2c**



The compound was synthesized according to the procedure of compound **1a**.

Yield: 0.7 g, 0.230 mmol (97%), white powder.

Molecular formula: C₁₅₇H₂₇₆N₈O₄₈

¹H-NMR (300 MHz, d₆-DMSO, 298 K): δ [ppm] = 8.72 (t, J = 7.6 Hz, 3H, NH), 8.36 – 8.24 (m, 3H, CH_{aromat}), 8.09 (s, 3H, NH), 7.87 (t, J = 5.5 Hz, 1H, NH), 7.75 (t, J = 5.1 Hz, 1H, NH), 7.37 – 7.08 (m, 15H, CH_{aromat}), 4.78 – 4.63 (m, 3H, CH), 3.78 – 3.70 (m, 2H, CH₂), 3.50 (s, 148H, PEO), 3.46 – 3.40 (m, 2H, CH₂), 3.23 (s, 2H, CH₂), 3.16 (q, J = 5.6 Hz, 2H, CH₂), 3.12 – 2.89 (m, 12H, CH₂), 2.27 (s, 4H, CH₂), 1.35 (m, 8H, CH₂), 1.22 (m, 54H), 0.84 (t, J = 6.4 Hz, 6H, CH₃).

MALDI-ToF-MS (positive mode, DHB) (m/z): calculated for [C₁₅₅H₂₇₂N₈O₄₇Na]⁺: 3021.9070; found: 3021.8116.

SEC (DMAc + 0.21 wt.% LiCl): M_n = 3,400 g mol⁻¹; M_w = 3,700 g mol⁻¹; Đ = 1.07.

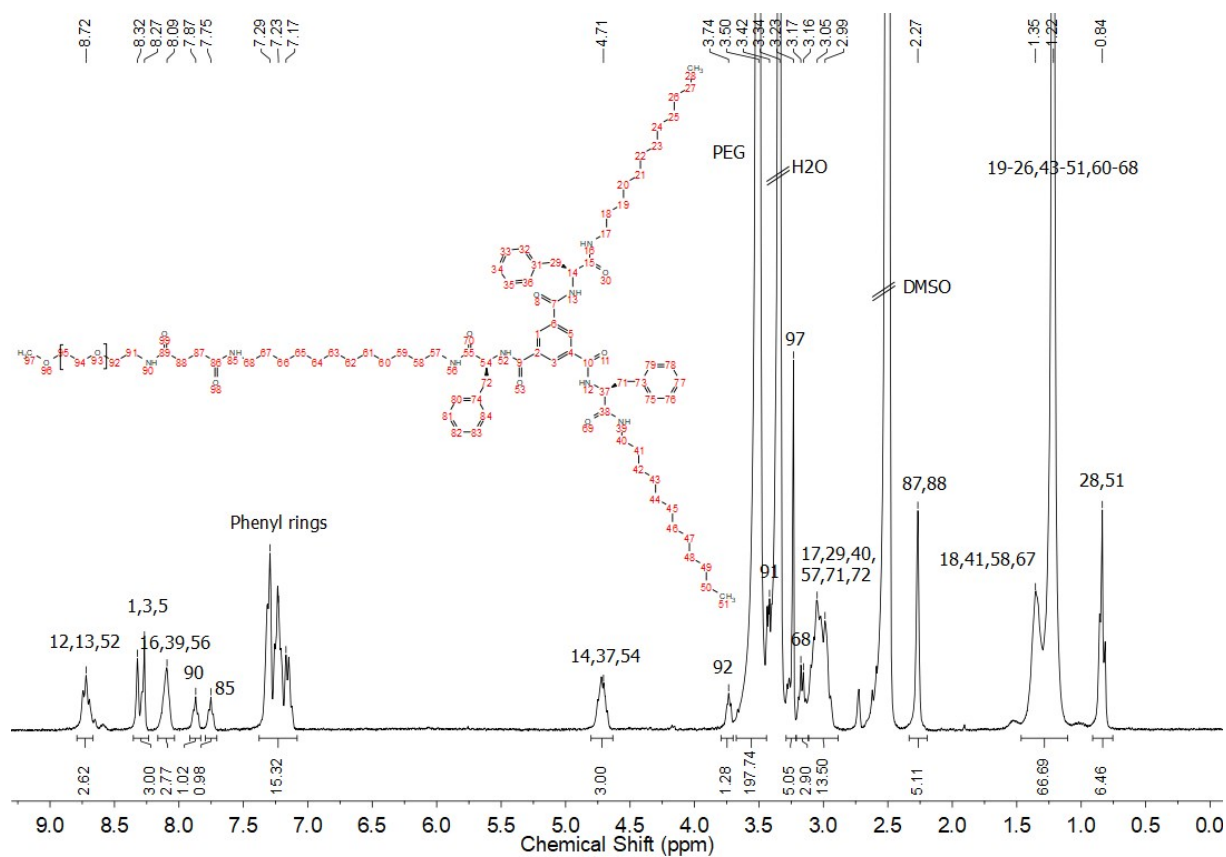


Figure S 11: $^1\text{H-NMR}$ spectrum of **2c** measured in $d_6\text{-DMSO}$.

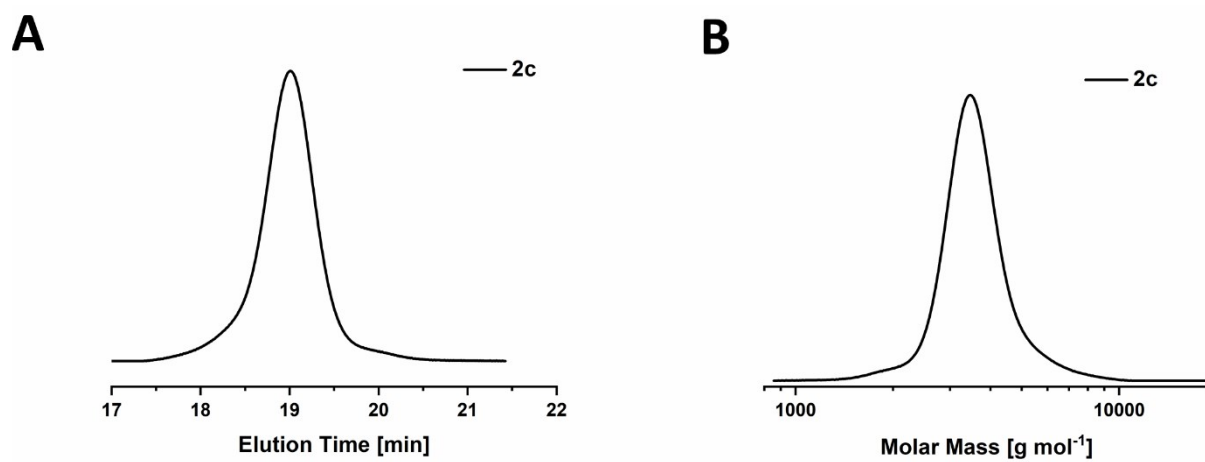
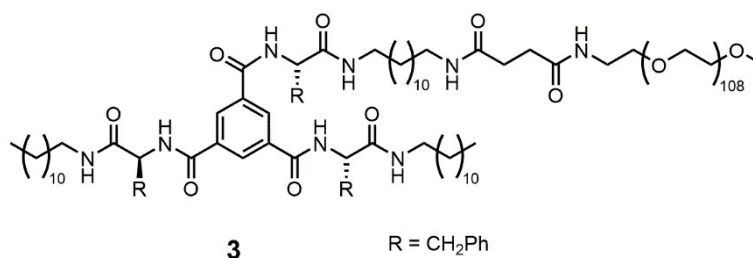


Figure S 12: SEC traces of **2c** recorded in DMAc (+0.21 wt% LiCl; 25 °C, RI, detection, PEO-Standard). A) Elution profile, B) Molar Mass distribution.

[B][Phe]₃[C₁₂]₃[PEO_{5k}] – 3



The compound was synthesized according to the procedure of compound **1a**.

Yield: 0.846 g, 0.139 mmol (119%, residual PEO_{5k} left), white powder.

Molecular formula: C₂₉₅H₅₅₂N₈O₁₁₇

¹H-NMR (300 MHz, d₆-DMSO, 298 K): δ [ppm] = 8.72 (t, J = 7.4 Hz, 3H, NH), 8.37 – 8.24 (m, 3H, CH_{aromat}), 8.09 (m, 3H, NH), 7.87 (t, J = 5.2 Hz, 1H, NH), 7.75 (t, J = 4.9 Hz, 1H, NH), 7.37 – 7.03 (m, 15H, CH_{aromat}), 4.78 – 4.66 (m, 3H, CH), 3.78 – 3.70 (m, 2H, CH₂), 3.50 (s, 432H, PEO), 3.45 – 3.41 (m, 2H, CH₂), 3.23 (s, 2H, CH₂), 3.17 (q, J = 5.8 Hz, 2H, CH₂), 3.12 – 2.92 (m, 12H, CH₂), 2.27 (s, 4H, CH₂), 1.36 (m, 8H, CH₂), 1.22 (m, 54H, CH₂), 0.84 (t, J = 6.5 Hz, 6H, CH₃).

MALDI-ToF-MS (positive mode, DHB) (m/z): calculated for [C₃₀₃H₅₆₈N₈O₁₂₁Na]⁺: 6281.9637; found: 6282.000.

SEC (DMAc + 0.21 wt.% LiCl): M_n = 6,200 g mol⁻¹; M_w = 6,900 g mol⁻¹; Đ = 1.11.

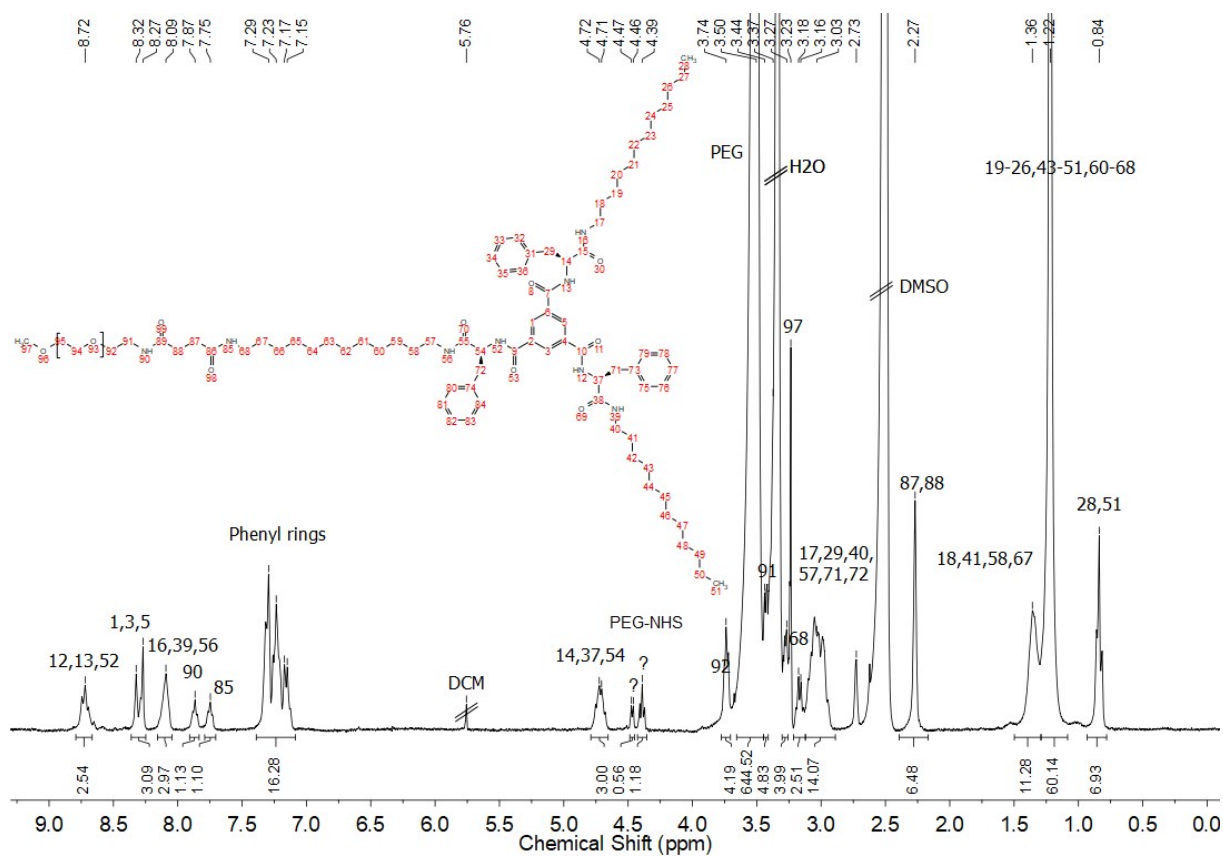


Figure S 13: $^1\text{H-NMR}$ spectrum of **3** measured in $\text{d}_6\text{-DMSO}$.

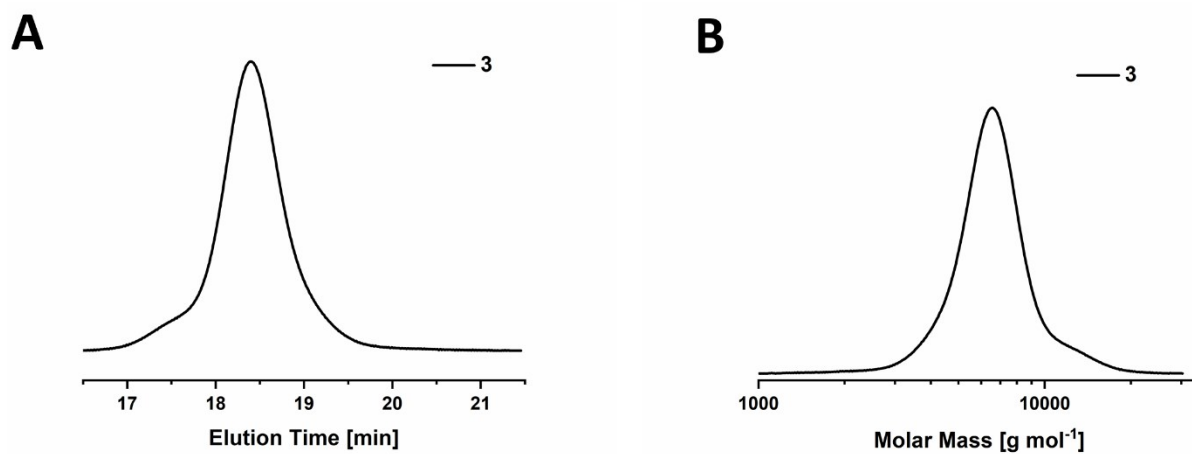
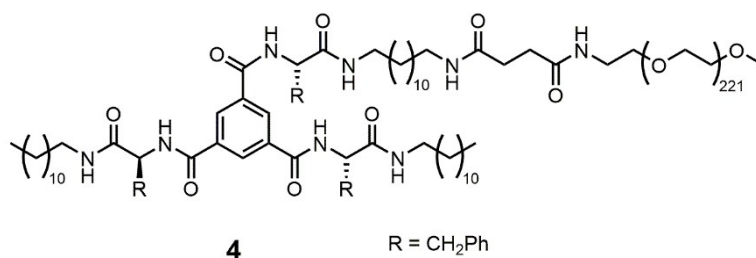


Figure S 14: SEC traces of **3** recorded in DMAc (+0.21 wt% LiCl; 25 °C, RI, detection, PEO-Standard). A) Elution profile, B) Molar Mass distribution.

[B][Phe]₃[C₁₂]₃[PEO_{10k}] – 4



The compound was synthesized according to the procedure of compound **1a**.

Yield: 0.914 g, 0.083 mmol (141%, residual PEO_{10k} left), white powder.

Molecular formula: C₅₂₁H₁₀₀₄N₈O₂₃₀

¹H-NMR (300 MHz, d₆-DMSO, 298 K): δ [ppm] = 8.74 (t, J = 7.6 Hz, 3H, NH), 8.36 – 8.26 (m, 3H, CH_{aromat}), 8.10 (s, 3H, NH), 7.87 (t, J = 5.2 Hz, 1H, NH), 7.75 (t, J = 5.0 Hz, 1H, NH), 7.37 – 7.07 (m, 15H, CH_{aromat}), 4.78 – 4.64 (m, 3H, CH), 3.79 – 3.68 (m, 2H, CH₂), 3.50 (s, 884H, PEO), 3.44 (m, 2H, CH₂), 3.24 (s, 2H, CH₂), 3.22 – 3.11 (m, 2H, CH₂), 3.12 – 2.92 (m, 12H, CH₂), 2.27 (s, 4H, CH₂), 1.36 (m, 8H, CH₂), 1.22 (m, 54H, CH₂), 0.84 (t, J = 6.7 Hz, 6H, CH₃).

MALDI-ToF-MS (positive mode, CHCA) (m/z): calculated for [C₅₂₁H₁₀₀₄N₈O₂₃₀Na]⁺: 11,083.4190; found: 11,083.3760.

SEC (DMAc + 0.21 wt.% LiCl): M_n = 11,800 g mol⁻¹; M_w = 13,600 g mol⁻¹; Đ = 1.15.

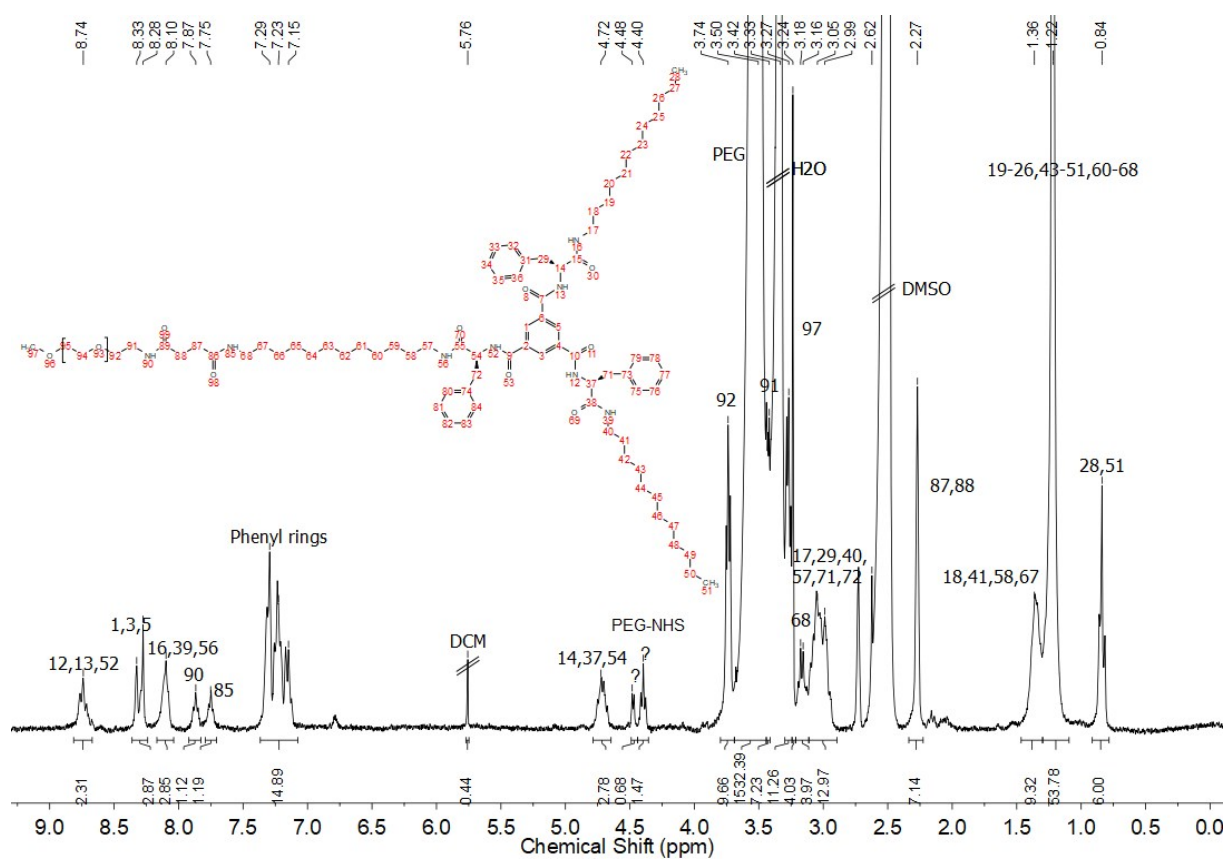


Figure S 15: $^1\text{H-NMR}$ spectrum of **4** measured in $\text{d}_6\text{-DMSO}$.

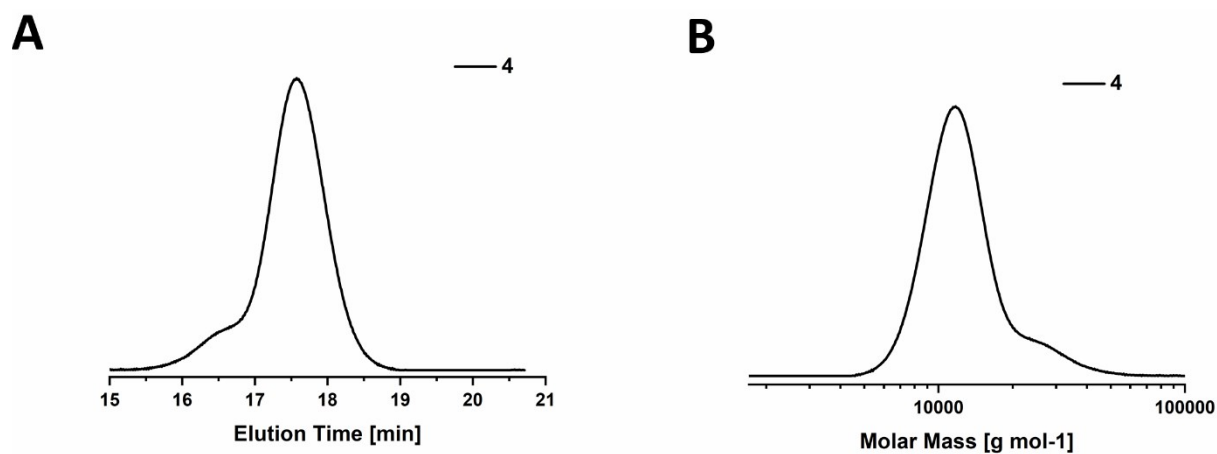
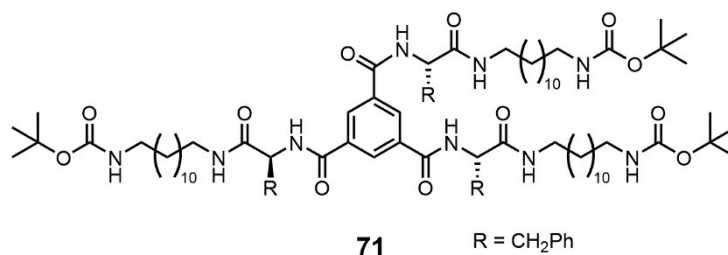


Figure S 16: SEC traces of **4** recorded in DMAc (+0.21 wt% LiCl; 25 °C, RI, detection, PEO-Standard). A) Elution profile, B) Molar Mass distribution.

1.2.4 Benzenetrispeptide building blocks bearing three PEO chains

[B][Phe]₃[C₁₂]₃ Boc-protected – 71



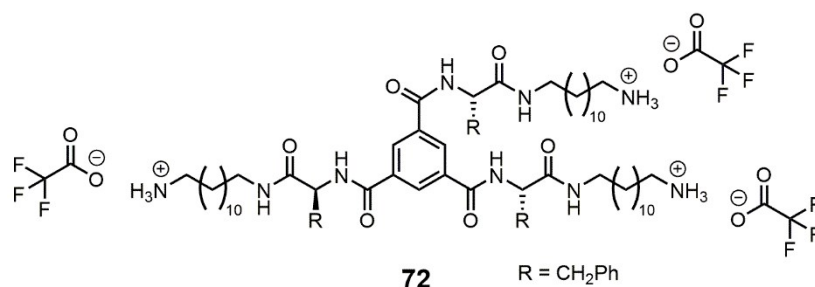
Benzene-1,3,5-tricarbonyl trichloride (96 mg, 0.360 mmol, 1.0 eq) was dissolved in 7.21 mL anhydrous chloroform under Argon atmosphere and the solution cooled to 0 °C. Compound **45** (0.5 g, 1.117 mmol, 3.1 eq) and triethylamine (201 μL, 1.441 mmol, 4 eq) were added. The solution was allowed to warm to rt and then stirred overnight. The solvent was removed and the crude product purified via flash chromatography (DCM/MeOH; 93:7, v:v). The obtained product was dried in the vacuum oven (40 °C) overnight.

Yield: 0.238 g, 0.159 mmol (44%), white solid.

Molecular formula: C₈₇H₁₃₅N₉O₁₂

¹H-NMR (300 MHz, d₆-DMSO, 298 K): δ [ppm] = 8.74 (d, J = 8.4 Hz, 3H, NH), 8.27 (s, 3H, CH_{aromat}), 8.09 (t, J = 5.4 Hz, 3H, NH), 7.35 – 7.09 (m, 15H, CH_{aromat}), 6.75 (t, J = 5.4 Hz, 3H, NH), 4.79 – 4.64 (m, 3H, CH), 3.17 – 2.93 (m, 12H, CH₂), 2.87 (q, J = 6.6 Hz, 6H, CH₂), 1.36 (m, 43H, CH₂, CH₃), 1.21 (m, 48H, CH₂).

[B][Phe]₃[C₁₂]₃ Boc-protected – 72



Compound **71** (0.24 g, 0.16 mmol, 1.0 eq) was dissolved in 1.6 mL DCM. To this, 515 μ L of an 18:1:1 solution of TFA/TIPS/H₂O (TFA: 444 μ L, 5.76 mmol, 36 eq; TIPS: 66 μ L, 0.32 mmol, 2 eq; H₂O: 5 μ L, 0.32 mmol, 2 eq) was added dropwise and the solution stirred for 3 h at rt. Afterwards, half of the DCM volume was removed and the concentrated reaction mixture precipitated in cold diethyl ether. The suspension was centrifuged (3 min, 8,000 rpm) and the supernatant decanted. The obtained product was dried in the vacuum oven (40 °C) overnight.

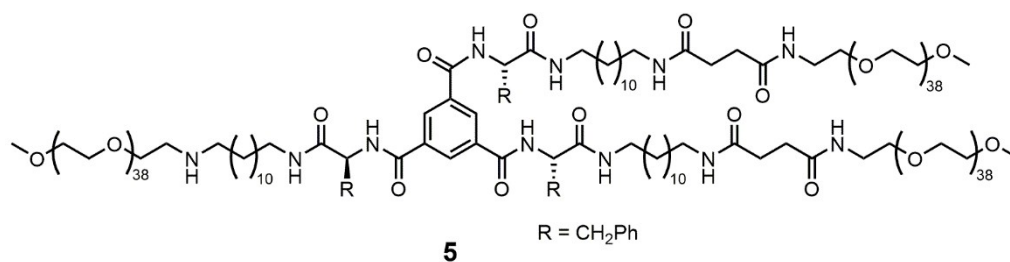
Yield: 0.171 g, 0.111 mmol (69%), light yellow wax.

Molecular formula: C₇₈H₁₁₄N₉O₁₂F₉

¹H-NMR (300 MHz, d₆-DMSO, 298 K): δ [ppm] = 8.73 (d, J = 8.4 Hz, 3H, NH), 8.27 (s, 3H, CH_{aromat}), 8.12 (t, J = 5.5 Hz, 3H, NH), 7.69 (s, 9H, NH₃), 7.36 – 7.11 (m, 15H, CH_{aromat}), 4.79 – 4.65 (m, 3H, CH), 3.18 – 2.91 (m, 12H, CH₂), 2.83 – 2.67 (m, 6H, CH₂), 1.57 – 1.40 (m, 6H, CH₂), 1.42 – 1.31 (m, 6H, CH₂), 1.23 (m, 48H, CH₂).

ESI-ToF-MS (positive mode, acetonitrile) (m/z): calculated for [M+2H]²⁺: 599.9401; found: 599.9424.

[B][Phe]₃[C₁₂]₃[PEO_{2k}]₃ – 5



Compound **72** (0.171 g, 0.111 mmol, 1.0 eq) was dissolved in 9.96 mL DMF. To this, 0.309 mL triethylamine (2.22 mmol, 20 eq) were added dropwise. After stirring at rt for 15 min, 0.663 g of MeO-PEO_{2k}-NHS ester (0.333 mmol, 3.0 eq) were added and the reaction mixture stirred at rt overnight. Afterwards, the reaction mixture was precipitated into cold diethyl ether, the suspension centrifuged (3 min, 8,000 rpm) and the supernatant decanted. Then a mixture of diethyl ether and acetone (9:1, v:v) was added to the precipitate and the suspension exposed to sonication for 5 min in order to remove all residual DMF and some unconjugated MeO-PEO_{2k}-NHS ester. Afterwards, the suspension was again centrifuged (3 min, 8,000 rpm) and the supernatant decanted. Still remaining MeO-PEO_{2k}-NHS ester was then removed via continuous centrifugal washing using Amicon® Ultra-15 centrifugal filter units (MWCO: 10 kDa). The obtained product was then dissolved in water and lyophilised overnight.

Yield: 0.622 g, 0.091 mmol (82%), white powder.

Molecular formula: C₃₂₇H₆₁₂N₁₂O₁₃₂

¹H-NMR (300 MHz, d₆-DMSO, 298 K): δ [ppm] = 8.72 (d, J = 7.8 Hz, 3H, NH), 8.26 (s, 3H, CH_{aromat}), 8.09 (t, J = 5.0 Hz, 3H, NH), 7.87 (t, J = 5.3 Hz, 3H, NH), 7.75 (t, J = 5.5 Hz, 3H, NH), 7.34 – 7.08 (m, 15H, CH_{aromat}), 4.71 (q, J = 8.8 Hz, 3H, CH), 3.78 – 3.70 (m, 6H, CH₂), 3.50 (m, 468H, PEO), 3.29 – 3.25 (m, 6H, CH₂), 3.23 (s, 6H, CH₂), 3.16 (q, J = 5.8 Hz, 6H, CH₂), 3.12 – 2.91 (m, 12H, CH₂), 2.27 (s, 12H, CH₂), 1.34 (m, 12H, CH₂), 1.21 (m, 48H, CH₂).

MALDI-ToF-MS (positive mode, dithranol) (m/z): calculated for [C₃₂₇H₆₁₂N₁₂O₁₃₂Na]⁺: 6847.0805; found: 6843.9496.

SEC (DMAc + 0.21 wt.% LiCl): M_n = 6,600 g mol⁻¹; M_w = 7,200 g mol⁻¹; Đ = 1.16.

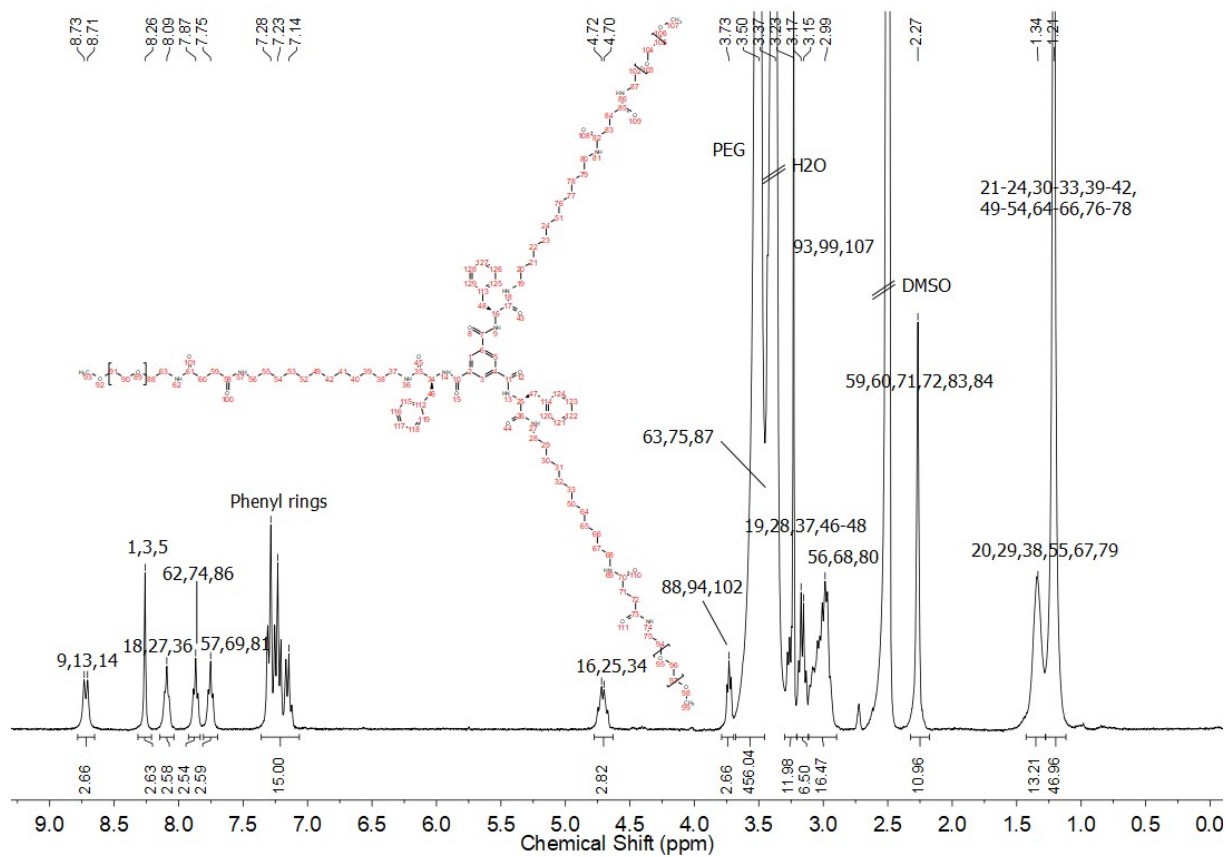


Figure S 17: ¹H-NMR spectrum of **5** measured in d₆-DMSO.

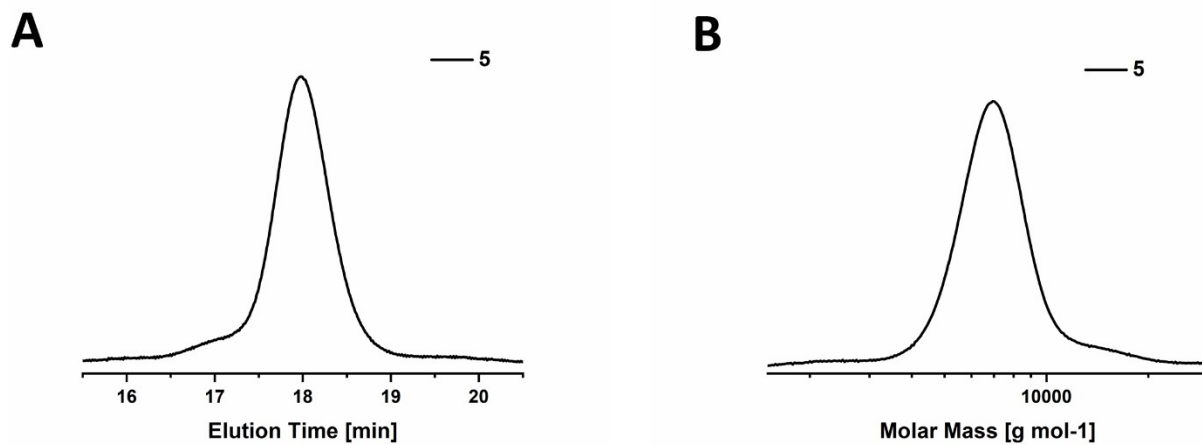


Figure S 18: SEC traces of **5** recorded in DMAc (+0.21 wt% LiCl; 25 °C, RI, detection, PEO-Standard). A) Elution profile, B) Molar Mass distribution.

2. Characterisation

2.1 Sample preparation

All investigated samples were initially dissolved in water and lyophilized afterwards, in order to obtain a fluffy powder. We observed that this powder dissolves easier in water compared to the precipitate obtained out of the PEO-conjugation reaction.

Prior to characterization, the powder was dissolved in MilliQ water at the desired concentration. For dissolution, the solution was put into the vortex and shaken at room temperature until the solution was fully clear (at least 24 h). No stirring, heating, sonication or filtration was applied to facilitate the dissolution in water, in order to keep the parameters affecting dissolution and self-assembly to a minimum.

2.2 Dynamic Light Scattering (DLS)

A scattering angle of 173° was used to record intensity fluctuations of the different samples in solution. All measurements were conducted in triplicate at a temperature of 25°C in disposable macro cuvettes containing 3 mL solution and after allowing for an equilibration time of 60 s. The acquisition time was 60 s. The apparent distribution of intensity-weighted hydrodynamic radii, d_h , was obtained from the Stokes–Einstein equation:

$$d_h = \frac{kT}{3\pi\eta D} \quad (\text{Equation S1})$$

with k being the Boltzmann constant, T the temperature in units K, η the viscosity of the solvent, and D the apparent translational diffusion coefficient at the utilized concentrations. The intensity-weighted distributions were transformed into number-weighted distributions.

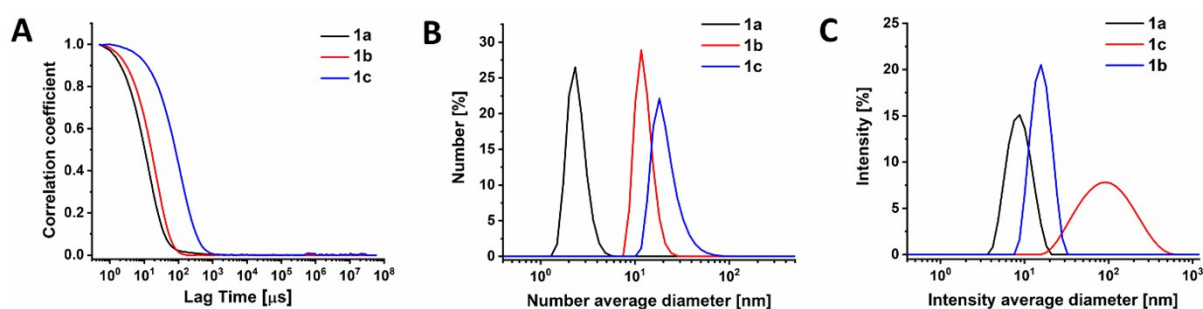


Figure S19: A) DLS correlograms of **1a** (black), **1b** (red) and **1c** (blue); B) corresponding distributions of the number-weighted hydrodynamic diameter (**1a**: $d_{H,number} = 2.5 \pm 0.2$ nm; **1b**: $d_{H,number} = 11.5 \pm 0.1$ nm; **1c**: $d_{H,number} = 16.2 \pm 5.0$ nm) and C) intensity-weighted hydrodynamic diameter (**1a**: $d_{H,intensity} = 9.0 \pm 2.0$ nm; **1b**: $d_{H,intensity} = 16.2 \pm 4.2$ nm; **1c**: $d_{H,intensity} = 115.0 \pm 81.2$ nm) at a concentration of 5 mg mL^{-1} .

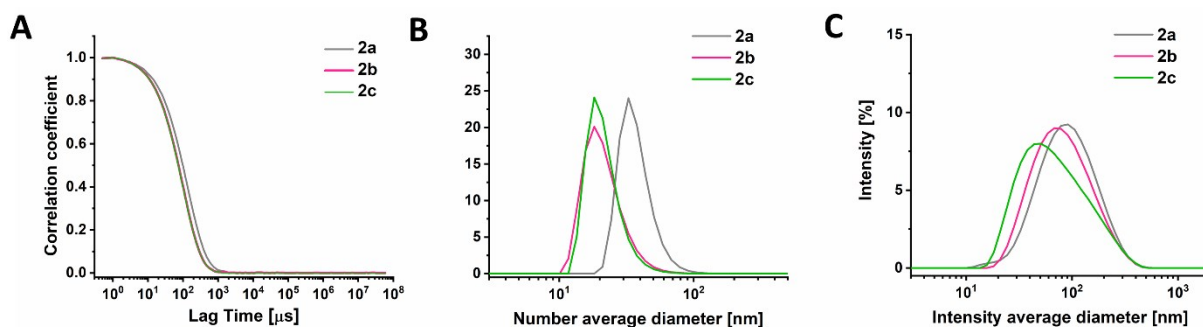


Figure S 20: A) DLS correlograms of **2a** (grey), **2b** (magenta) and **2c** (green); B) corresponding distributions of the number-weighted hydrodynamic diameter (**2a**: $d_{H,number} = 27.0 \pm 9.3$ nm; **2b**: $d_{H,number} = 20.3 \pm 8.1$ nm; **2c**: $d_{H,number} = 22.6 \pm 1.0$ nm) and C) intensity-weighted hydrodynamic diameter (**2a**: $d_{H,intensity} = 113.0 \pm 71.4$ nm; **2b**: $d_{H,intensity} = 95.6 \pm 63.5$ nm; **2c**: $d_{H,intensity} = 84.5 \pm 65.9$ nm) at a concentration of 5 mg mL⁻¹.

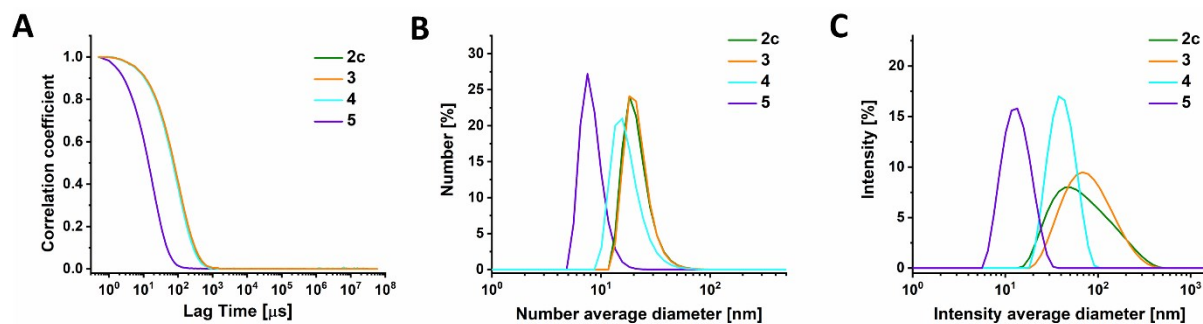


Figure S 21: A) DLS correlograms of **2c** (green), **3** (orange), **4** (cyan) and **5** (purple); B) corresponding distributions of the number-weighted hydrodynamic diameter (**2c**: $d_{H,number} = 22.6 \pm 1.0$ nm; **3**: $d_{H,number} = 22.4 \pm 2.7$ nm; **4**: $d_{H,number} = 23.3 \pm 4.8$ nm; **5**: $d_H = 8.5 \pm 0.2$ nm) and C) intensity-weighted hydrodynamic diameter (**2c**: $d_{H,intensity} = 84.5 \pm 65.9$ nm; **3**: $d_{H,intensity} = 90.9 \pm 57.8$ nm; **4**: $d_{H,intensity} = 42.4 \pm 13.4$ nm; **5**: $d_{H,intensity} = 13.9 \pm 4.7$ nm) at a concentration of 5 mg mL⁻¹.

2.3 Small Angle X-Ray Scattering (SAXS)

Small angle X-ray scattering was performed at the beamline BL40B2 of the Super Photon Ring – 8 GeV (SPring-8) in Hyogo Prefecture, Japan. The sample-to-detector distance was 4.0 m (detector: PILATUS 2M (Dectris)) and the wavelength of the incident beam (λ) was adjusted to 0.10 nm. Each sample was measured at a concentration of 1.5 mg mL⁻¹ in water at 25 °C and exposed for 180 s.

Each recorded 2D profile was azimuthally averaged to obtain 1D profile of $I(q)$ vs. q , followed by being divided by the incident X-ray intensity. After that, the solvent scattering data (background scattering) was subtracted from the solution data to obtain the excess scattering intensity. The excess scattering intensity was normalized to be the differential scattering cross-section (absolute intensity) by using the scattering intensity of water.¹

The obtained reduced SAXS data was analysed with the open access software SASfit (version: 0.94.11).² All parameters for the respective fits can be found in the following tables. The radius of the sphere or cylinder were fitted by applying a Gaussian distribution to the fit, which has a concentration parameter N , a width parameter σ and a mean radius parameter R .

1b – [B][Leu]₃[C₆]₃[PEO_{2k}]

Table S 1: SAXS fitting parameters for compound **1b** using a form factor for a sphere.

Parameter	Values
R_{sphere} [nm]	5.27
Σ	1.32
N	7.45×10^{-2}
<i>subtracted background</i>	2.70×10^{-4}
η^a [nm ⁻²]	1.019×10^{-3}

^a The X-ray scattering length density (SLD) η was calculated using the SLD calculator given in SASfit.

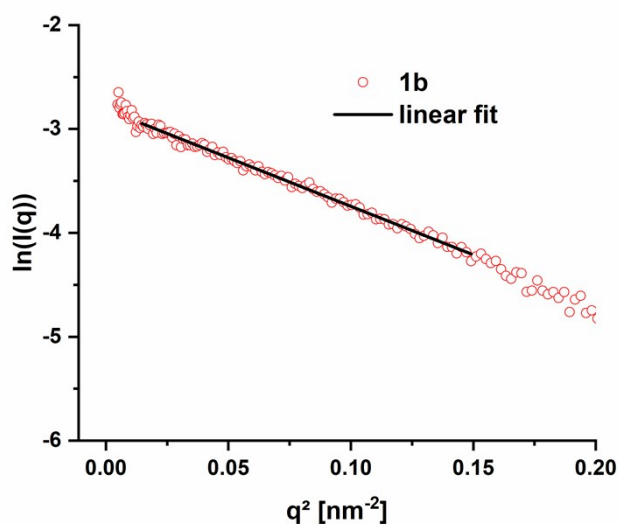


Figure S 22: Guinier plot ($\ln(I(q))$ vs. q^2) of the SAXS data of compound **1b**. The slope of the linear fit was used to determine the radius of gyration R_g (here: $R_g = 5.3$ nm) using the Guinier approximation.

Table S 2: SAXS fitting parameters for compound **1b** using a form factor for a cylinder.

Parameter	Values
R_{cylinder} [nm]	6.24
L_{cylinder} [nm]	8.12
Σ	0.52
N	5.5×10^{-2}
<i>subtracted background</i>	2.70×10^{-4}
η^a [nm ⁻²]	1.019×10^{-3}

^a The X-ray scattering length density (SLD) η was calculated using the SLD calculator given in SASfit.

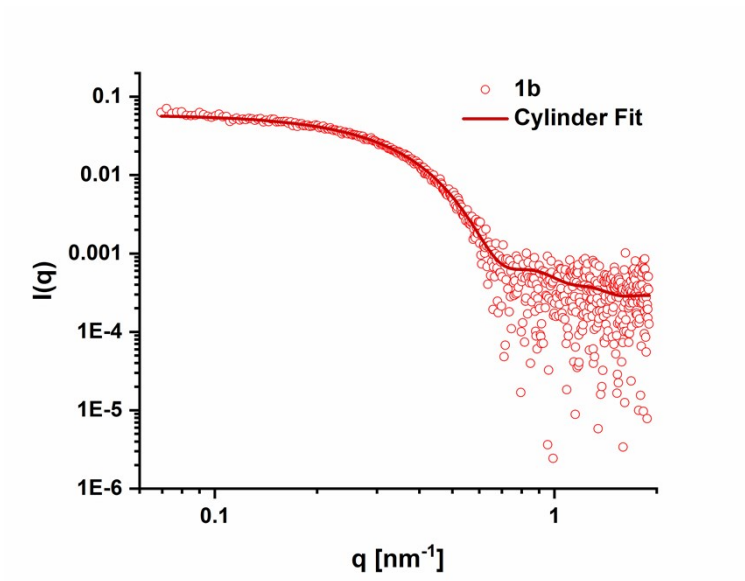


Figure S 23: SAXS trace for **1b** (circles) in water ($c = 1.5 \text{ mg mL}^{-1}$) fitted with form factor for cylinder (solid line).

1c – [B][Phe]₃[C₆]₃[PEO]_{2k}

Table S 3: SAXS fitting parameters for compound **1c** using a form factor for a cylinder.

Parameter	Values
R_{cylinder} [nm]	5.08
L_{cylinder}^a [nm]	700
Σ	1.22
N	1.59×10^{-3}
subtracted background	2.00×10^{-4}
η^b [nm ⁻²]	1.014×10^{-3}

^a The length L for the cylinder fit was estimated from the lengths observed in the corresponding cryoTEM images of compound **1c**. Due to the absence of a plateau at low q -values for the SAXS data, this value does not represent the real average cylinder length.

^b The X-ray scattering length density (SLD) η was calculated using the SLD calculator given in SASfit.

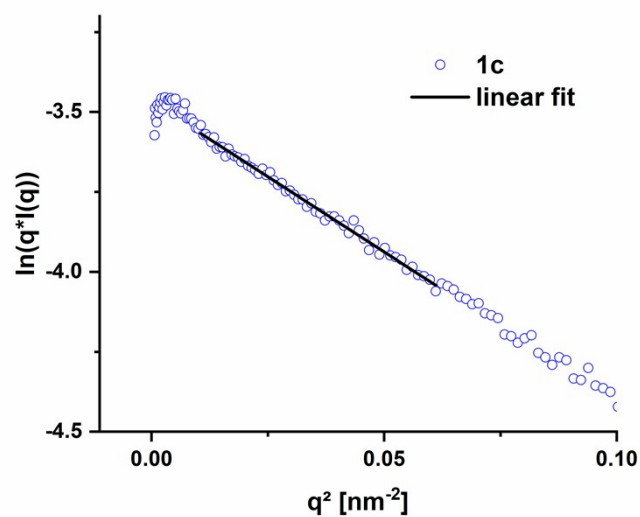


Figure S 24: Cross-sectional diameter plot ($\ln(qI(q))$ vs. q^2) of the SAXS data of compound **1c**. The slope of the linear fit was used to determine the cross-sectional radius $R_{\text{c-s}}$ (here: $R_{\text{c-s}} = 6.1$ nm).

2a – [B][Ala]₃[C₁₂]₃[PEO_{2k}]

Table S 4: SAXS fitting parameters for compound **2a** using a form factor for a cylinder.

Parameter	Values
R_{cylinder} [nm]	6.14
L_{cylinder}^a [nm]	100
Σ	1.36
N	6.43×10^{-2}
<i>subtracted background</i>	9.00×10^{-5}
η^b [nm ⁻²]	1.021×10^{-3}

^a The length L for the cylinder fit was estimated from the lengths observed in the corresponding cryoTEM images of compound **2a**. Due to the absence of a plateau at low q -values for the SAXS data, this value does not represent the real average cylinder length.

^b The X-ray scattering length density (SLD) η was calculated using the SLD calculator given in SASfit.

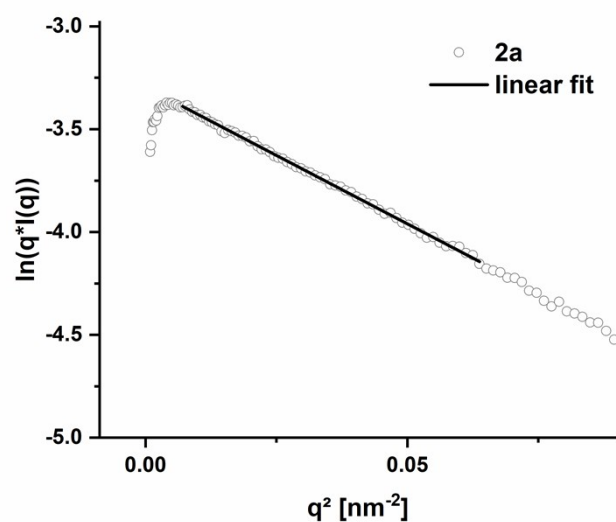


Figure S 25: Cross-sectional diameter plot ($\ln(qI(q))$ vs. q^2) of the SAXS data of compound **2a**. The slope of the linear fit was used to determine the cross-sectional radius $R_{\text{c-s}}$ (here: $R_{\text{c-s}} = 7.3$ nm).

2b – [B][Leu]₃[C₁₂]₃[PEO]_{2k}

Table S 5: SAXS fitting parameters for compound **2b** using a form factor for a cylinder.

Parameter	Values
R_{cylinder} [nm]	7.57
L_{cylinder}^a [nm]	320
Σ	4.00×10^{-3}
N	5.02×10^{-4}
<i>subtracted background</i>	2.71×10^{-4}
η^b [nm ⁻²]	1.023×10^{-3}

^a The length L for the cylinder fit was estimated from the lengths observed in the corresponding cryoTEM images of compound **2b**. Due to the absence of a plateau at low q -values for the SAXS data, this value does not represent the real average cylinder length.

^b The X-ray scattering length density (SLD) η was calculated using the SLD calculator given in SASfit.

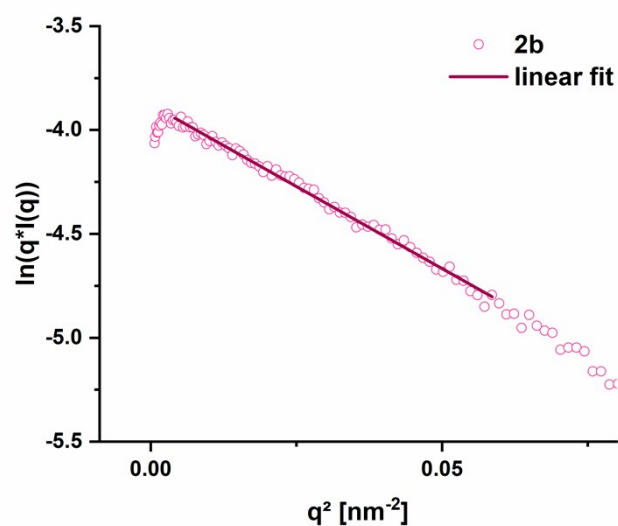


Figure S 26: Cross-sectional diameter plot ($\ln(qI(q))$ vs. q^2) of the SAXS data of compound **2b**. The slope of the linear fit was used to determine the cross-sectional radius $R_{\text{c-s}}$ (here: $R_{\text{c-s}} = 8.0$ nm).

2c – [B][Phe]₃[C₁₂]₃[PEO]_{2k}

Table S 6: SAXS fitting parameters for compound **2c** using a form factor for a cylinder.

Parameter	Values
R_{cylinder} [nm]	6.56
L_{cylinder}^a [nm]	200
Σ	1.42
N	1.91×10^{-3}
<i>subtracted background</i>	1.00×10^{-4}
η^b [nm ⁻²]	1.018×10^{-3}

^a The length L for the cylinder fit was estimated from the lengths observed in the corresponding cryoTEM images of compound **2c**. Due to the absence of a plateau at low q -values for the SAXS data, this value does not represent the real average cylinder length.

^b The X-ray scattering length density (SLD) η was calculated using the SLD calculator given in SASfit.

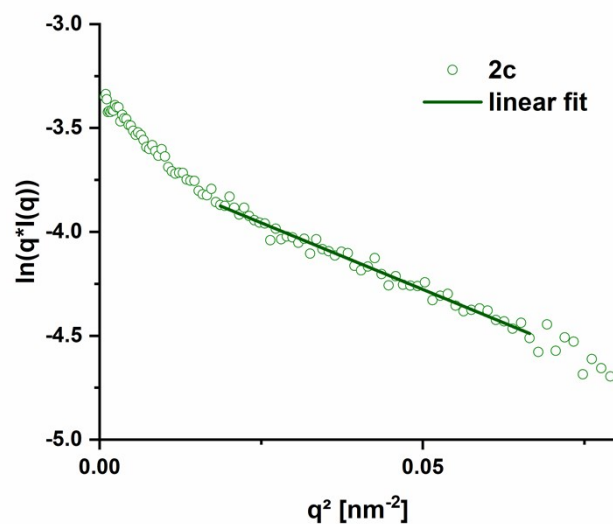


Figure S 27: Cross-sectional diameter plot ($\ln(q^2 I(q))$ vs. q^2) of the SAXS data of compound **2c**. The slope of the linear fit was used to determine the cross-sectional radius $R_{\text{c-s}}$ (here: $R_{\text{c-s}} = 7.2$ nm).

3 – [B][Phe]₃[C₁₂]₃[PEO]_{5k}

Table S 7: SAXS fitting parameters for compound **3** using a form factor contribution for a sphere.

Parameter	Values
R_{sphere} [nm]	9.34
Σ	3.34
N	4.87×10^{-3}
<i>subtracted background</i>	4.00×10^{-4}
η^a [nm ⁻²]	1.018×10^{-3}

^a The X-ray scattering length density (SLD) η was calculated using the SLD calculator given in SASfit.

Table S 8: SAXS fitting parameters for compound **3** using a form factor contribution for a cylinder.

Parameter	Values
R_{cylinder} [nm]	9.87
L_{cylinder}^a [nm]	200
Σ	1.03
N	1.45×10^{-4}
<i>subtracted background</i>	1.00×10^{-4}
η^b [nm ⁻²]	1.018×10^{-3}

^a The length L for the cylinder fit was estimated from the lengths observed in the corresponding cryoTEM images of compound **3**. Due to the absence of a plateau at low q -values for the SAXS data, this value does not represent the real average cylinder length.

^b The X-ray scattering length density (SLD) η was calculated using the SLD calculator given in SASfit.

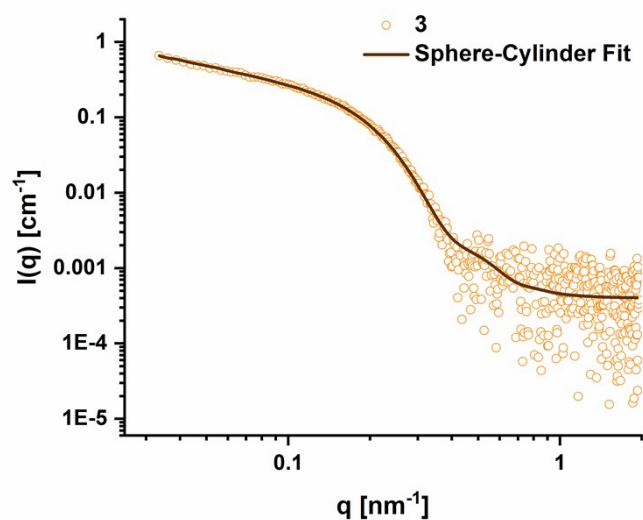


Figure S 28: SAXS trace for **3** (circles) in water ($c = 1.5 \text{ mg mL}^{-1}$) fitted with form factor contributions for a sphere and cylinder (solid line).

4 – [B][Phe]₃[C₁₂]₃[PEO]_{10k}

Table S 9: SAXS fitting parameters for compound 4 using a form factor for a sphere.

Parameter	Values
R_{sphere} [nm]	10.53
Σ	4.85
N	2.10×10^{-3}
<i>subtracted background</i>	4.00×10^{-4}
η^a [nm ⁻²]	1.019×10^{-3}

^a The X-ray scattering length density (SLD) η was calculated using the SLD calculator given in SASfit.

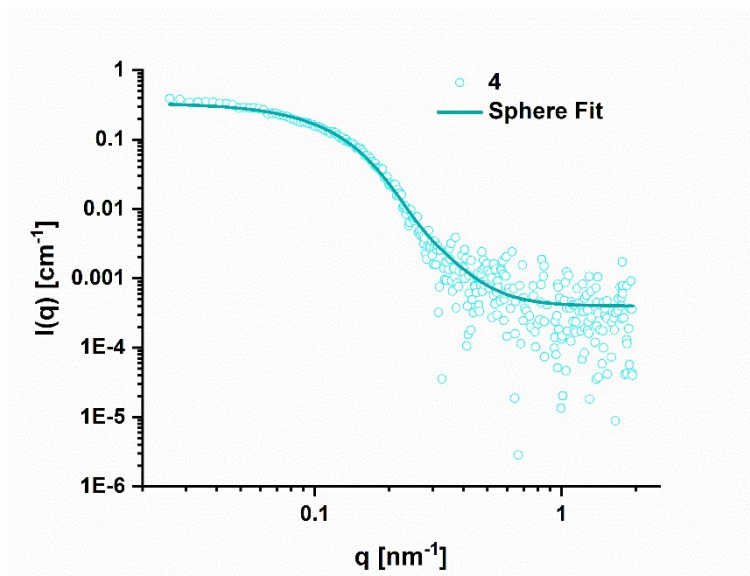


Figure S 29: SAXS trace for 4 (circles) in water ($c = 1.5 \text{ mg mL}^{-1}$) fitted with a form factor for a sphere (solid line).

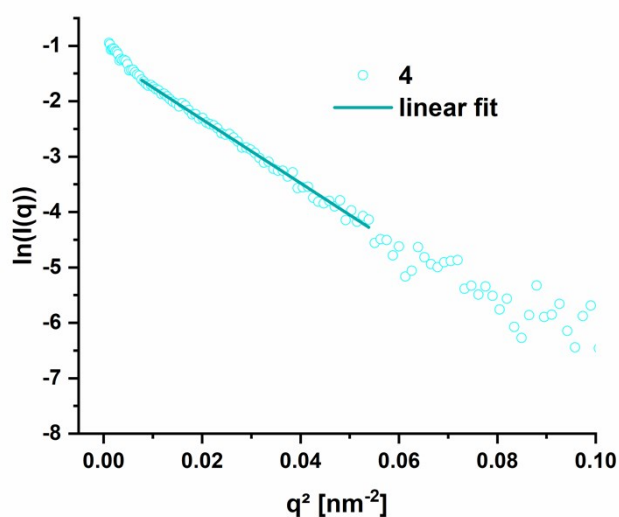


Figure S 30: Guinier plot ($\ln(I(q))$ vs. q^2) of the SAXS data of compound 4. The slope of the linear fit was used to determine the radius of gyration R_g (here: $R_g = 13.1 \text{ nm}$) using the Guinier approximation.

5 – [B][Phe]₃[C₁₂]₃[PEO_{2k}]₃

Table S 10: SAXS fitting parameters for compound **4** using a form factor for a sphere.

Parameter	Values
R_{sphere} [nm]	3.91
Σ	1.05
N	2.10×10^{-3}
<i>subtracted background</i>	4.00×10^{-4}
η^a [nm ⁻²]	1.019×10^{-3}

^a The X-ray scattering length density (SLD) η was calculated using the SLD calculator given in SASfit.

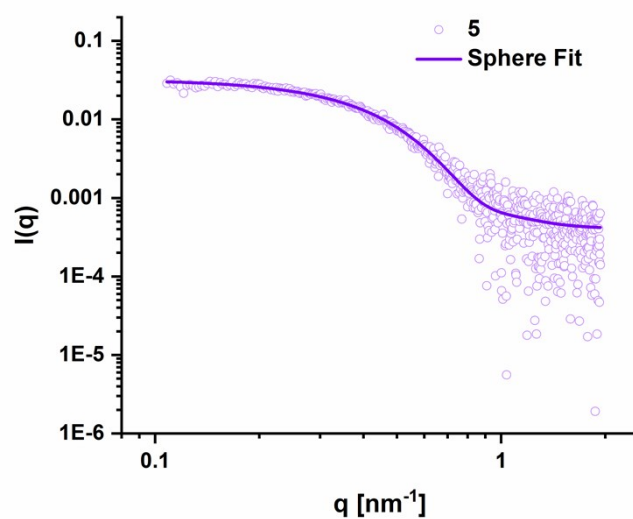


Figure S 31: SAXS trace for **5** (circles) in water ($c = 1.5 \text{ mg mL}^{-1}$) fitted with a form factor for a sphere (solid line).

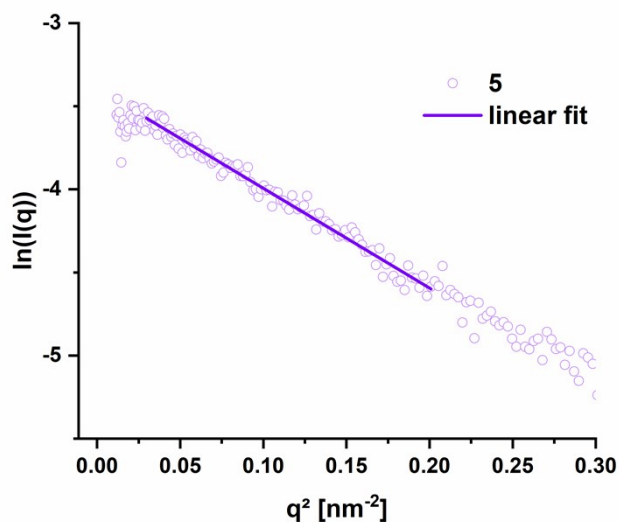


Figure S 32: Guinier plot ($\ln(I(q))$ vs. q^2) of the SAXS data of compound **5**. The slope of the linear fit was used to determine the radius of gyration R_g (here: $R_g = 4.2 \text{ nm}$) using the Guinier approximation.

Molecules per cross-section calculation

The weight-average molar mass, M_w , of the spherical aggregates of **5** can be calculated from a Guinier plot of $\ln\left(\frac{I(q)}{K \cdot C}\right)$ against q^2 . To this end, the intersection of the linear plot with the y-axis is determined which yields the weight-average molar mass according to the following equation:³

$$M_w = e^{y, \text{intersection}} = e^{\left(\frac{I(q)}{K \cdot C}\right)_{x,0}} \quad (\text{Equation S2})$$

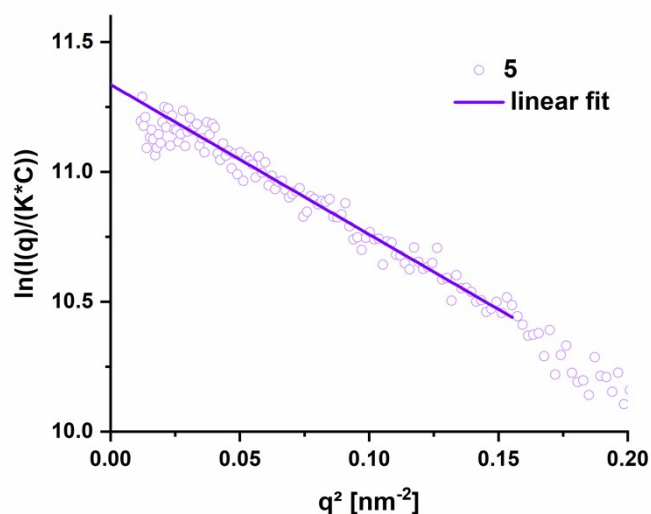


Figure S 33: Weight-average molar mass, M_w , calculation from a Guinier plot of $\ln(I(q)/(K \cdot C))$ against q^2 . M_w can be derived from the intersection of the linear fit with the y-axis.

This results in a M_w of 83800 g mol⁻¹ for the spherical micelle of **5**. Assuming a cylindrical arrangement of the BTP-PEO compound inside the micelles via the formation of a triple helix as known for benzenetrisamides,⁴ the number of aggregation, N_{agg} , and from this the number of molecules per cross-section can be determined. To support the assumption of a cylindrical arrangement of **5** within the spherical micelle, we fitted the SAXS data of **5** with a cylindrical form factor. The resulting fit was of similar quality as the originally applied fit using a spherical form factor (Table S 11 and Figure S 34).

Table S 11: SAXS fitting parameters for compound **5** using a form factor contribution for a cylinder.

Parameter	Values
R_{cylinder} [nm]	5.14
L_{cylinder} [nm]	5.28
σ	0.55
N	1.49×10^{-1}
<i>subtracted background</i>	4.00×10^{-4}
η^a [nm ⁻²]	1.017×10^{-3}

^a The X-ray scattering length density (SLD) η was calculated using the SLD calculator given in SASfit.

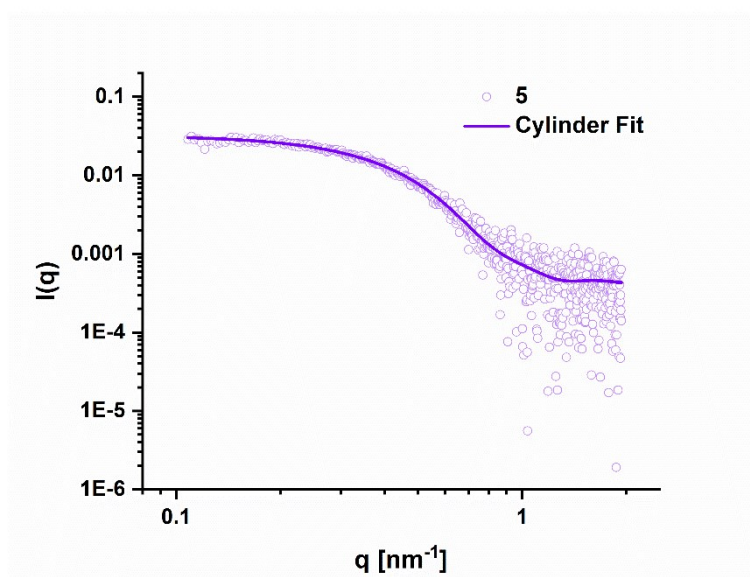


Figure S 34: SAXS trace for **5** (circles) in water ($c = 1.5 \text{ mg mL}^{-1}$) fitted with a form factor for a cylinder (solid line).

The number of aggregation, N_{agg} , can then be calculated by dividing M_w by the molar mass of compound **5**.

$$N_{\text{agg}} = \frac{M_w}{M_{w,5}} \quad (\text{Equation S3})$$

This yields a N_{agg} of 12.3. Assuming an intermolecular distance of 0.362 nm between individual BTP-PEO molecules,⁵ the number of molecules per cross-section, $\#_{\text{cross}}$, can be calculated when considering the length of the cylinder, L_{cyl} , obtained from the cylindrical fit (Table S 11):

$$\#_{\text{cross}} = \frac{N_{\text{agg}}}{\left(\frac{L_{\text{cyl}}}{0.362 \text{ nm}} \right)} \quad (\text{Equation S4})$$

According to this, approximately 0.87 molecules of **5** are present in the cross-section of the spherical micelles.

2.4 CryoTransmission Electron Microscopy (cryoTEM)

Samples were prepared on Ar plasma treated Quantifoil grids (R2/2). 8.5 μL of the solutions (3 mg mL^{-1} in H_2O) were applied onto the grids and vitrified into liquid ethane utilizing a FEI Vitrobot Mark IV system (offset: -3 mm, blotting time: 1 s). Samples were transferred into the cryo holder (Gatan 626) utilizing the Gatan cryo stage, followed by transfer into the microscope keeping the temperature below -172 $^\circ\text{C}$ during the whole transfer and measurement process after vitrification. Measurements were performed using a FEI Technai G² 20 at an acceleration voltage of 200 kV. Images were acquired with a Mega View (OSIS, Olympus Soft Imaging Systems) or an Eagle 4k CCD camera. In the cryoTEM images in this study, only specific regions of interest are shown, that are representative for the whole sample.

1a – [B][Ala]₃[C₆]₃[PEO_{2k}]

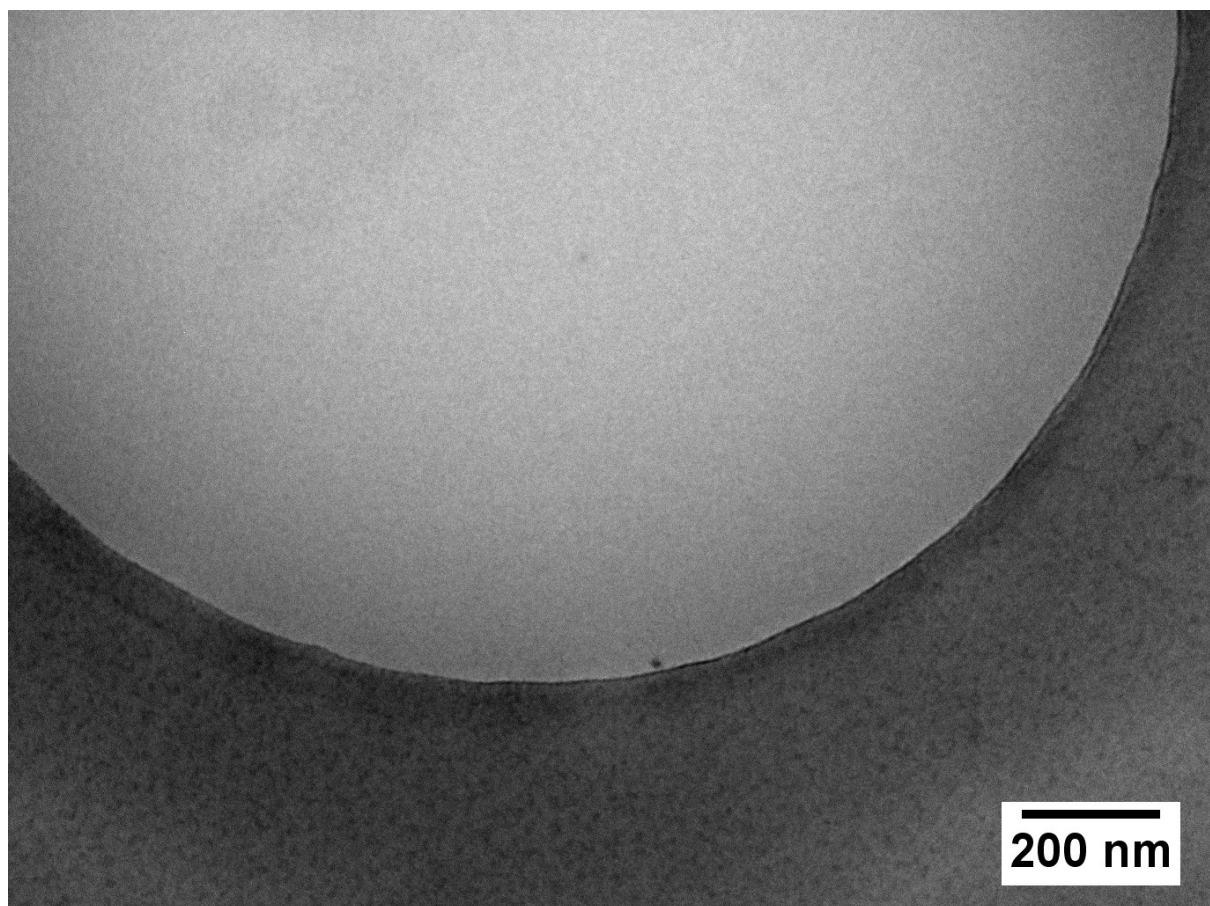


Figure S 35: cryoTEM micrograph of **1a** in water (3 mg mL^{-1}).

1b – [B][Leu]₃[C₆]₃[PEO_{2k}]

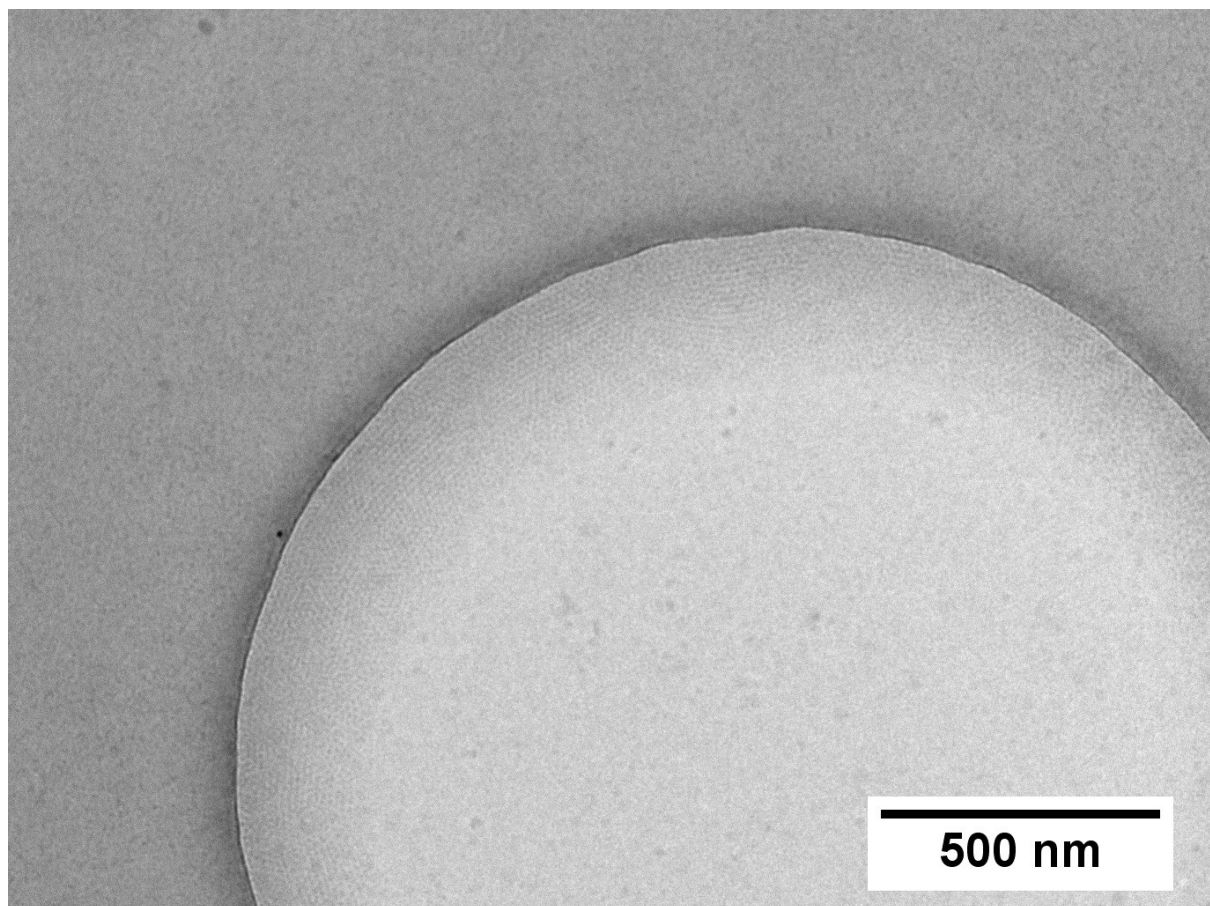


Figure S 36: cryoTEM micrograph of **1b** in water (3 mg mL⁻¹).

1c – [B][Phe]₃[C₆]₃[PEO_{2k}]

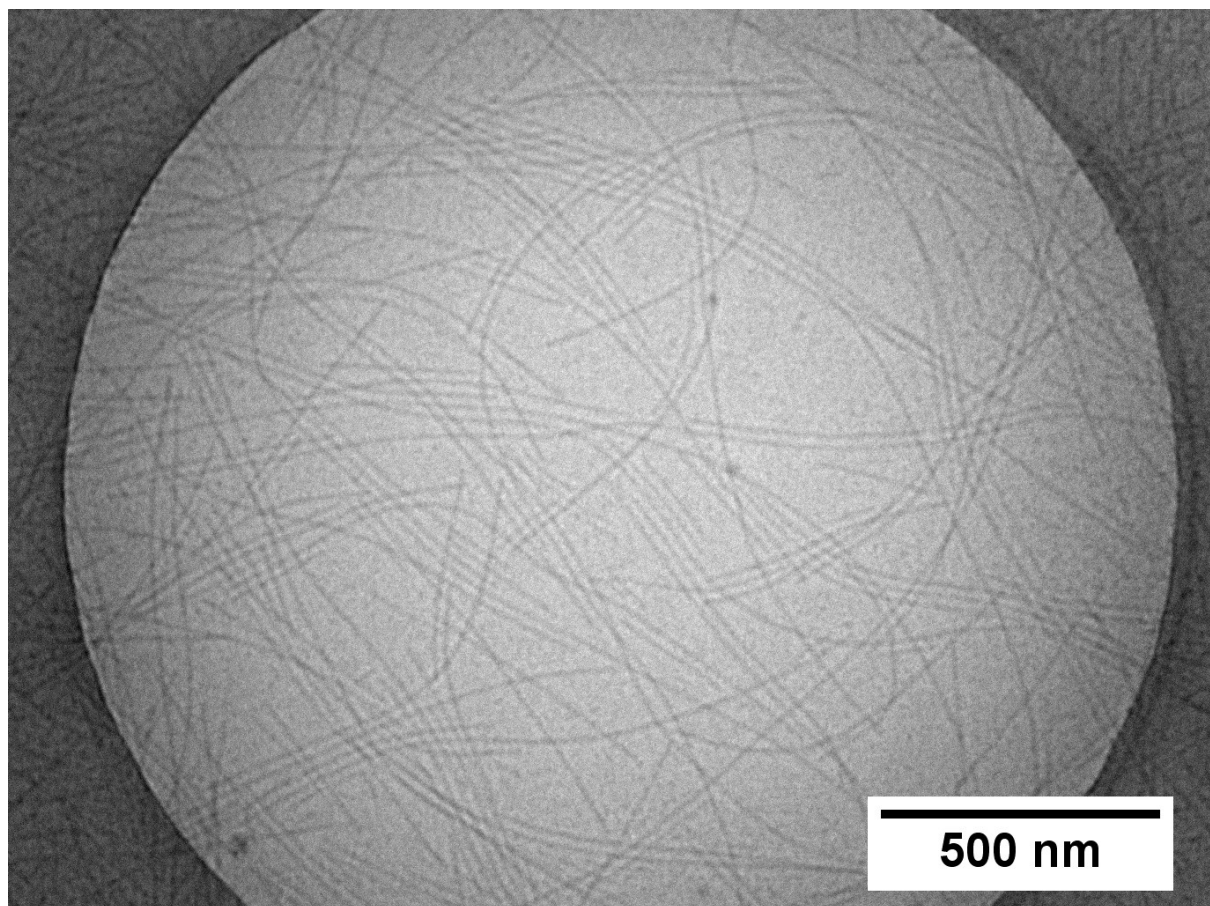


Figure S 37: cryoTEM micrograph of **1c** in water (3 mg mL⁻¹).

2a – [B][Ala]₃[C₁₂]₃[PEO_{2k}]

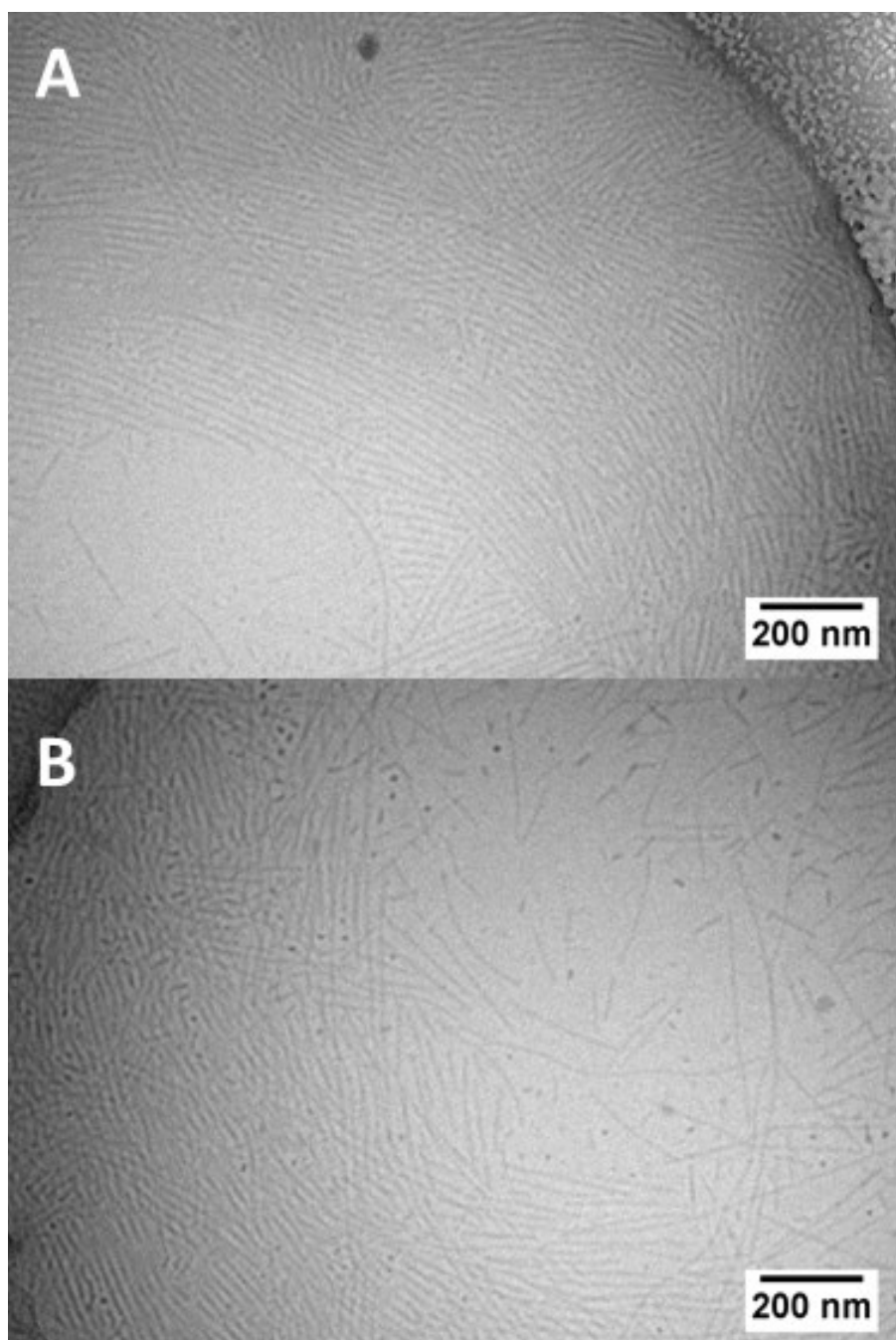


Figure S 38: cryoTEM micrographs of **2a** in water (3 mg mL⁻¹).

2b – [B][Leu]₃[C₁₂]₃[PEO_{2k}]

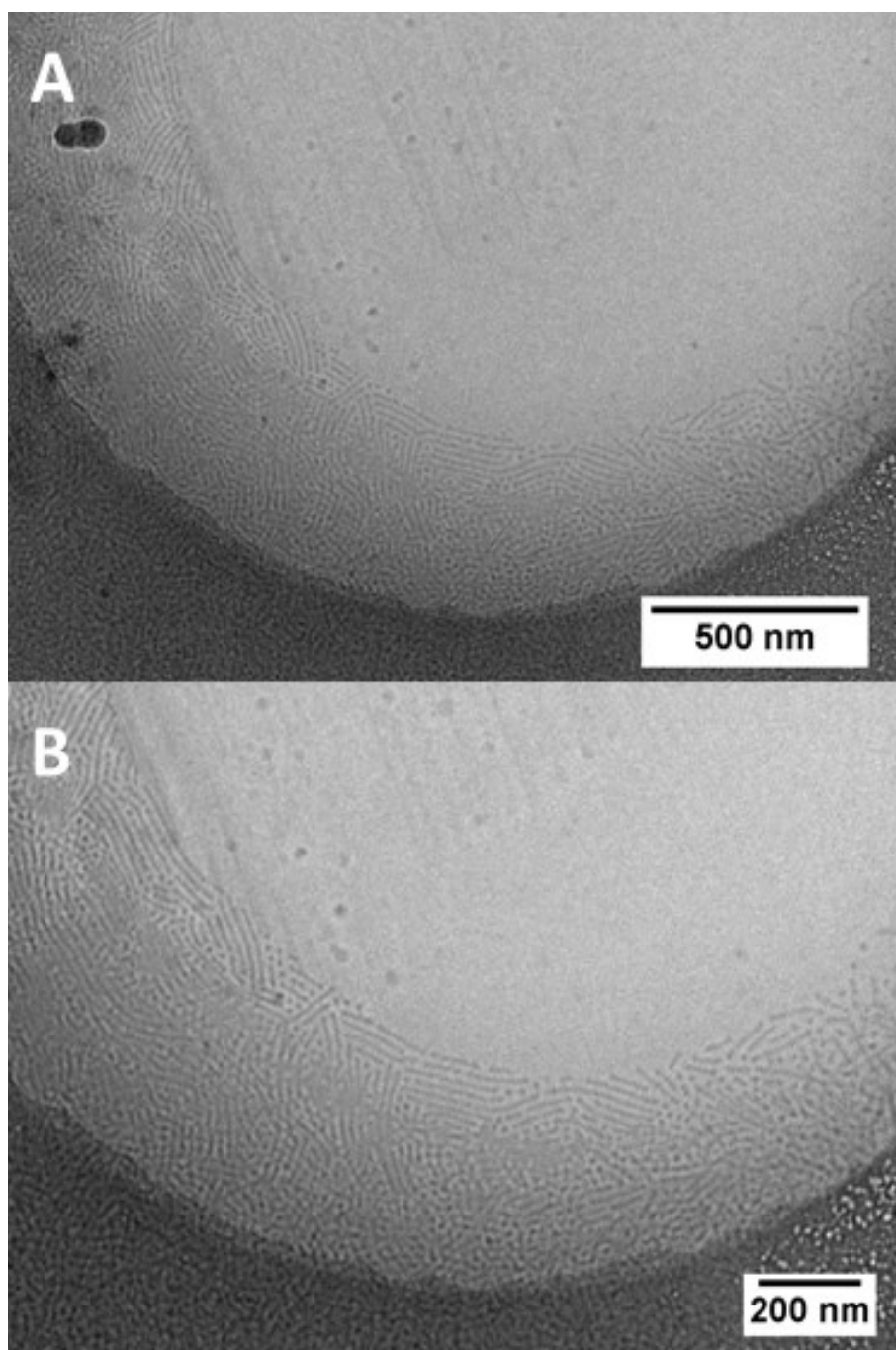


Figure S 39: cryoTEM micrographs of **2b** in water (3 mg mL⁻¹).

2c – [B][Phe]₃[C₁₂]₃[PEO_{2k}]

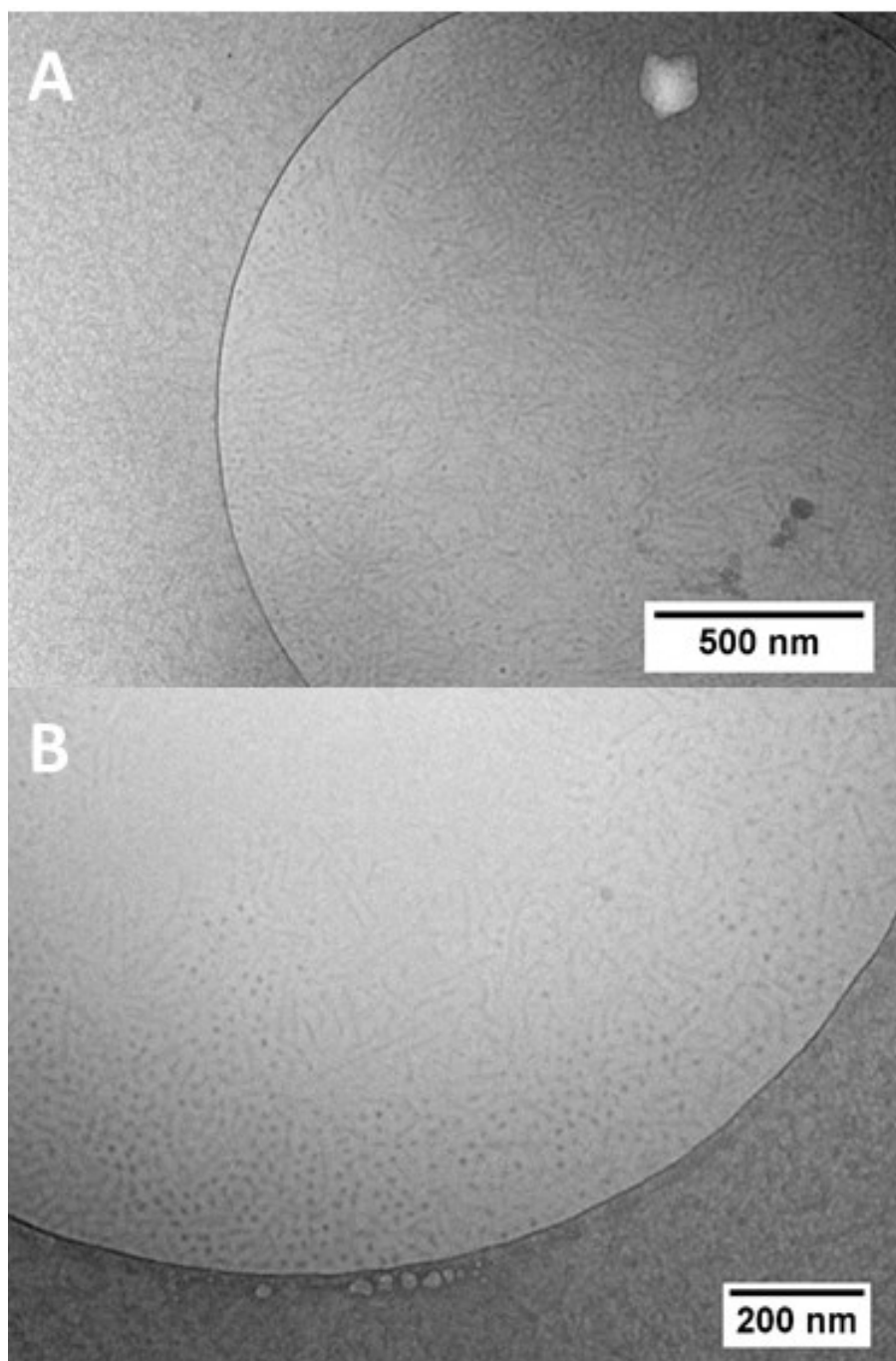


Figure S 40: cryoTEM micrographs of **2c** in water (3 mg mL⁻¹).

3 – [B][Phe]₃[C₁₂]₃[PEO]_{5k}

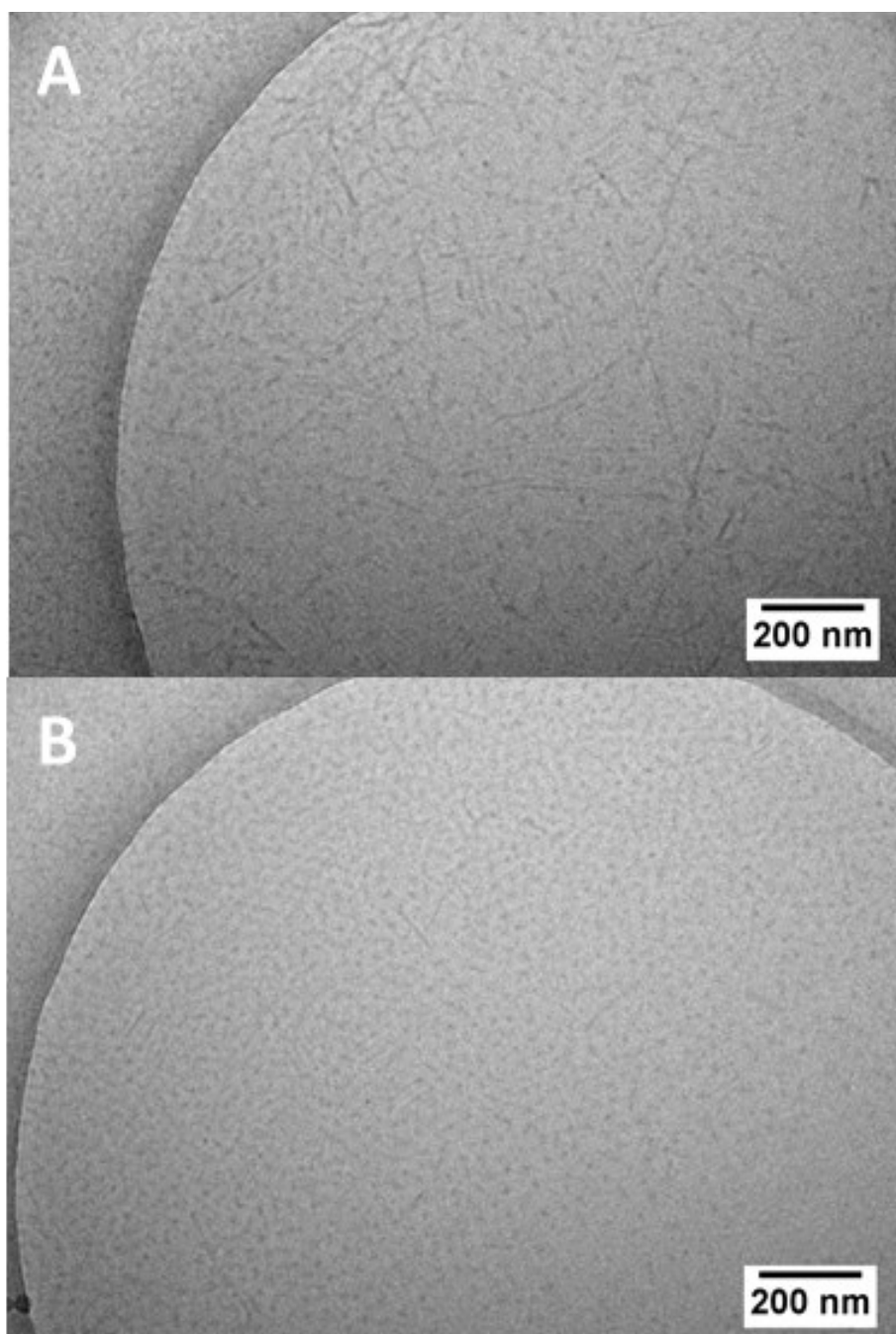


Figure S 41: cryoTEM micrographs of **3** in water (3 mg mL⁻¹).

4 – [B][Phe]₃[C₁₂]₃[PEO]_{10k}

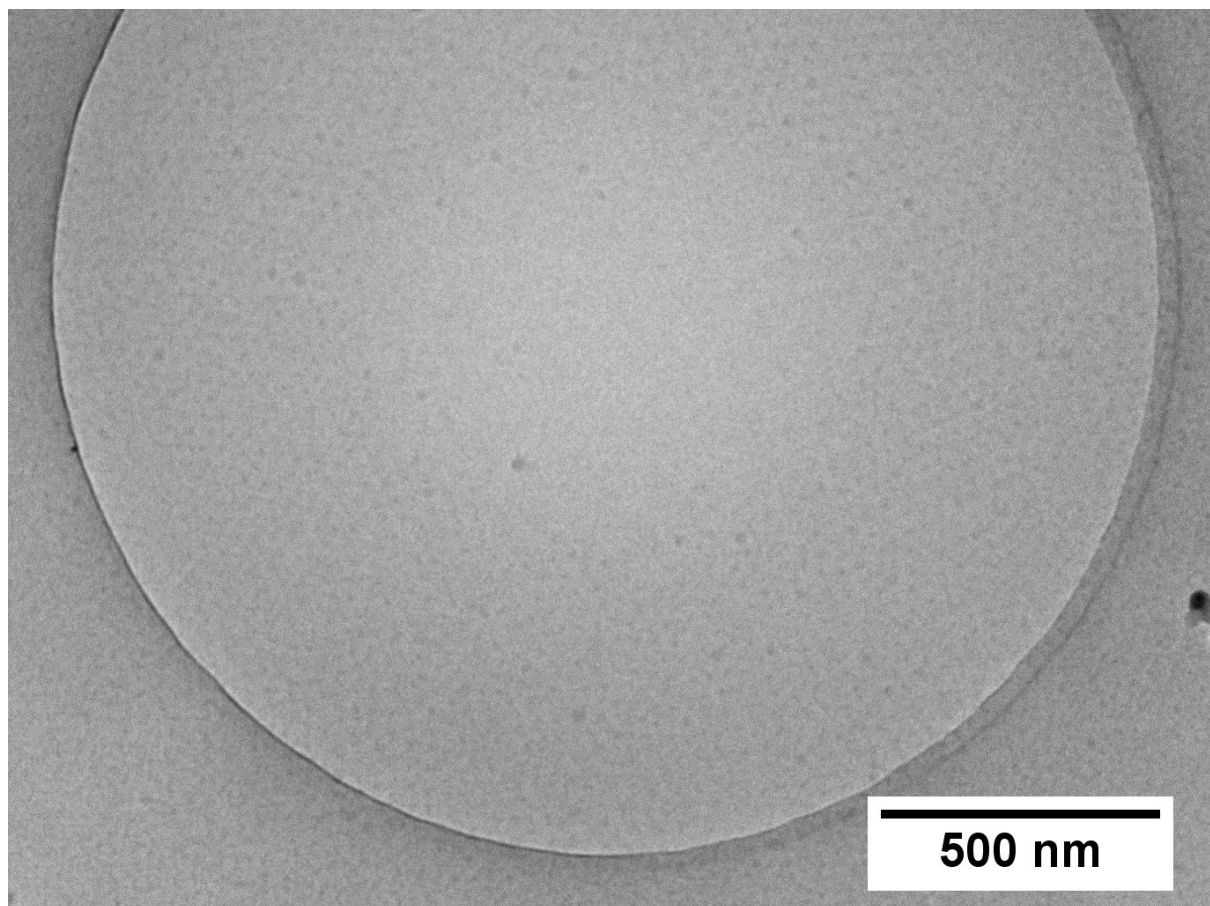


Figure S 42: cryoTEM micrograph of **4** in water (3 mg mL^{-1}).

5 – [B][Phe]₃[C₁₂]₃[PEO_{2k}]₃

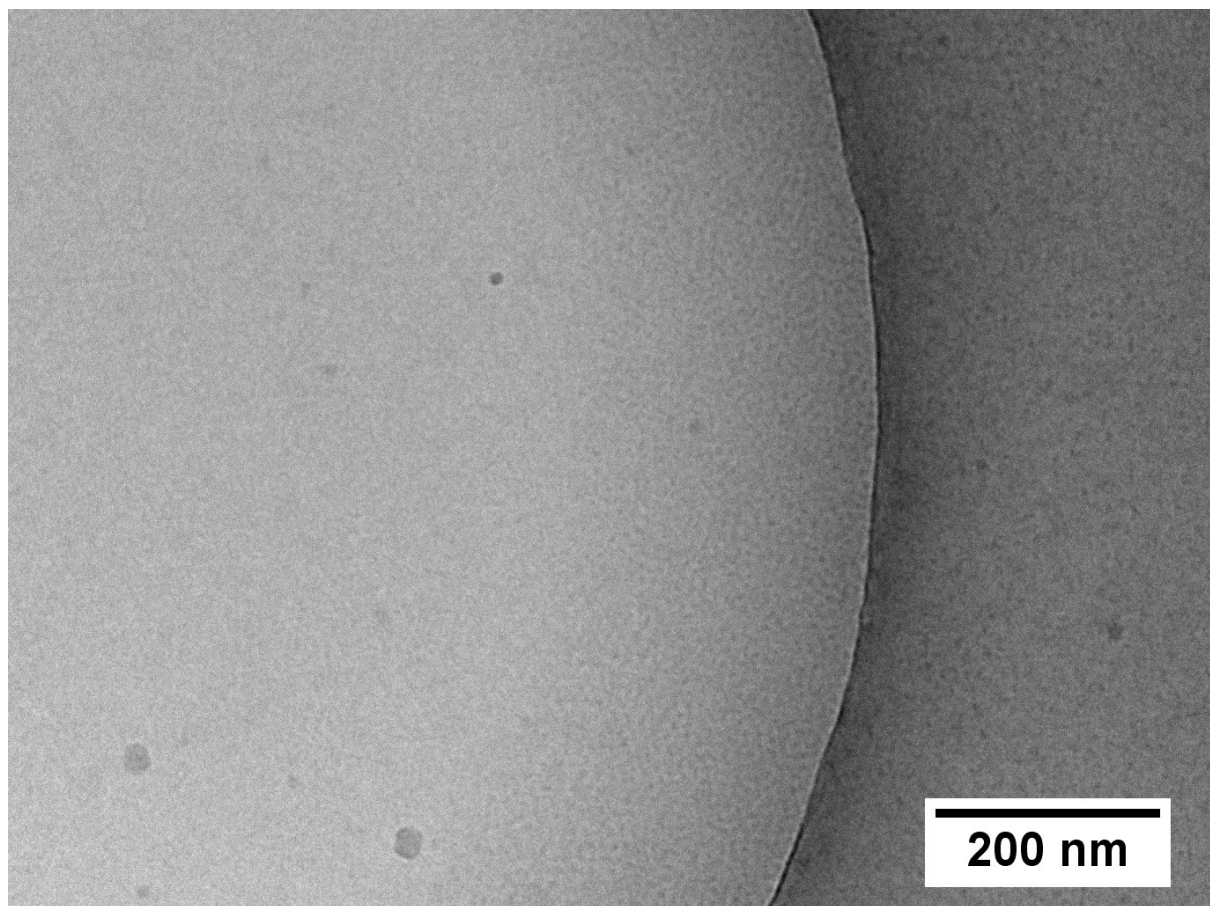


Figure S 43: cryoTEM micrograph of **5** in water (3 mg mL⁻¹).

2.5 Circular Dichroism (CD) spectroscopy

CD spectra were recorded on a JASCO J-820KS spectrophotometer. Each sample was measured five times at a concentration of 1.5 mg mL^{-1} in water using a quartz cell with a path length of 1 mm.

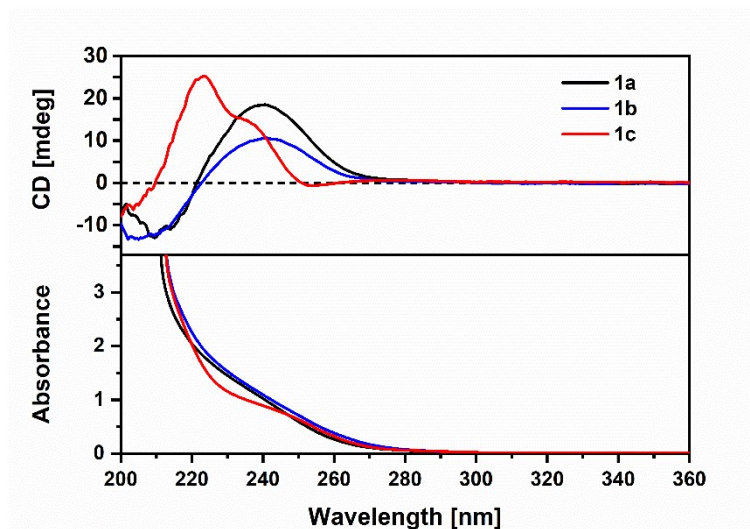


Figure S 44: CD (top) and UV absorption (bottom) spectra for compounds **1a** (black line), **1b** (red line) and **1c** (blue line) recorded in MilliQ water at a concentration of 1.5 mg mL^{-1} .

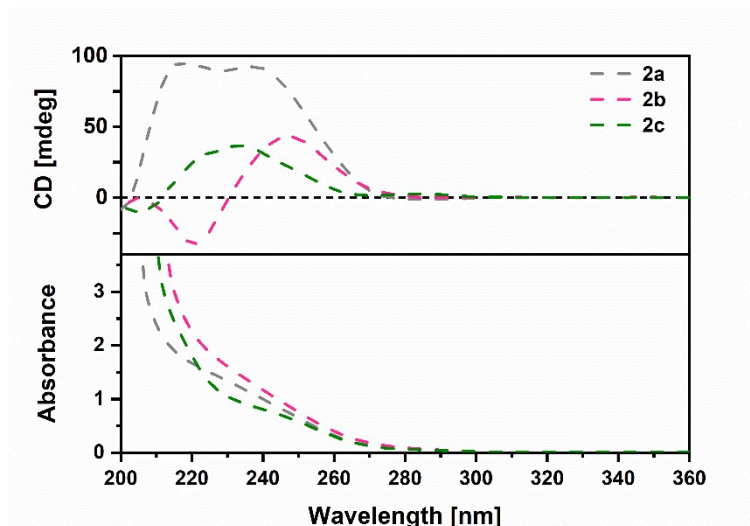


Figure S 45: CD (top) and UV absorption (bottom) spectra for compounds **2a** (grey line), **2b** (magenta line) and **2c** (green line) recorded in MilliQ water at a concentration of 1.5 mg mL^{-1} .

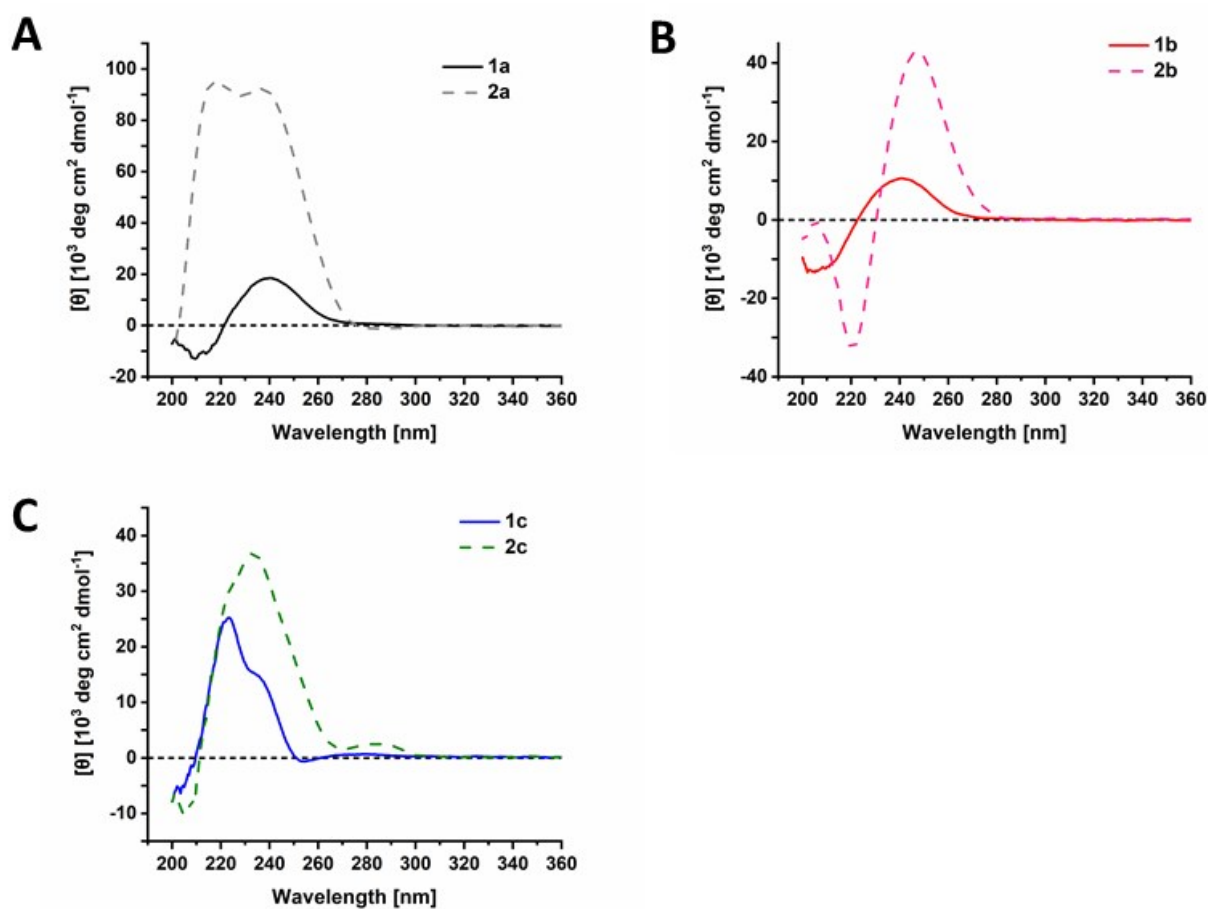


Figure S 46: CD spectra for compounds (A) **1a** (black line) and **2a** (grey line), (B) **1b** (red line) and **2b** (magenta line) and (C) **1c** (blue line) and **2c** (green line) recorded in MilliQ water at a concentration of 1.5 mg mL^{-1} .

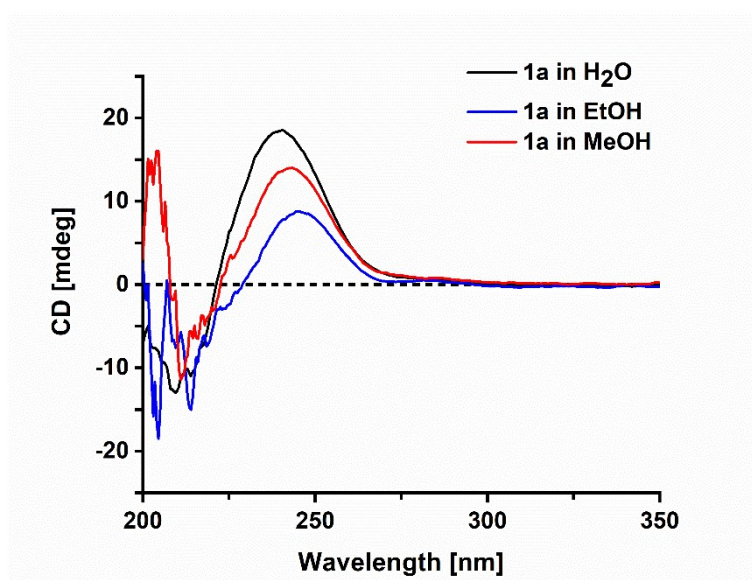


Figure S 47: CD spectra of 1a recorded in water (black), ethanol (blue), and methanol (red).

2.6 CAC Determination

The critical aggregation concentrations (CAC) were determined by measuring the fluorescence intensity of Nile red incorporated in the benzenetrispeptide (BTP) poly(ethylene glycol) conjugates according to a literature procedure.⁶ To this end, BTP stock solutions were diluted with MilliQ water to obtain solutions of $V = 180 \mu\text{L}$ in a concentration range from $c = 1 \times 10^{-9}$ up to $c = 3 \text{ mg mL}^{-1}$. Then, $18 \mu\text{L}$ of a Nile red stock solution in THF ($c = 1 \text{ mg mL}^{-1}$) was added, and the samples equilibrated overnight in a thermoshaker device ($T = 25 \text{ }^\circ\text{C}$, 400 rpm). Afterwards, the samples were transferred to quartz cuvettes and the fluorescence of Nile red recorded (wavelength measurement range: 550 – 800 nm) from an excitation at a wavelength of $535 \pm 5 \text{ nm}$. The CAC was determined as the intersection point of the linear fits (performed with OriginPRO 2018b) from the emission intensity at a wavelength of 612 nm versus the \log of the BTP concentration.

Table S 12: CAC values of **1a-c** and **2a-c** in $\mu\text{g mL}^{-1}$ and $\mu\text{mol L}^{-1}$ using Nile red as a fluorescent probe.

Compound	CAC _{612nm} [$\mu\text{g mL}^{-1}$]	CAC _{612nm} [$\mu\text{mol L}^{-1}$]
1a	694.4	268.8
1b	177.7	66.2
1c	171.2	61.3
2a	125.9	44.5
2b	149.5	50.9
2c	113.2	37.2

1a – [B][Ala]₃[C₆]₃[PEO_{2k}]

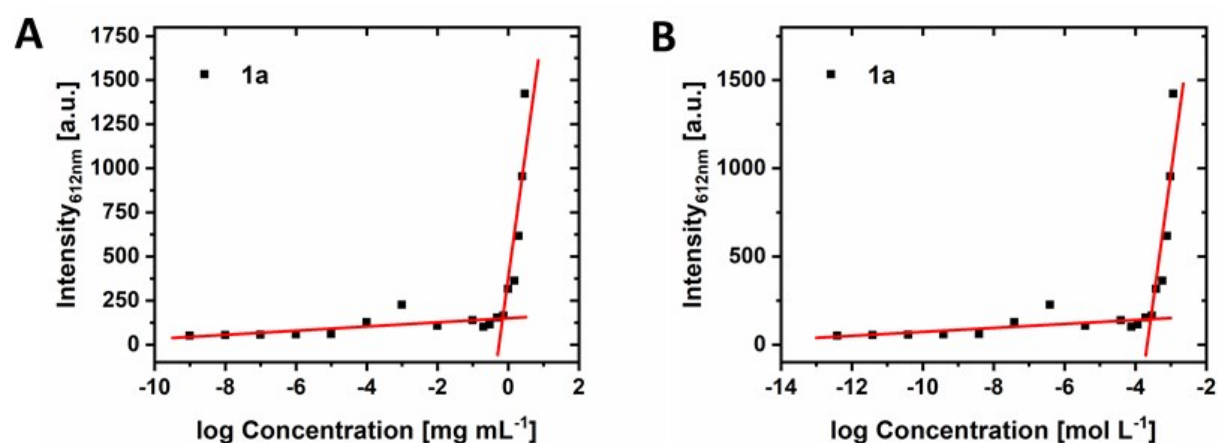


Figure S 48: CAC determination of **1a** via the Nile red fluorescence intensity method. A) Fluorescence intensity at 612 nm vs. logarithmic concentration in mg mL^{-1} (CAC: $694.4 \mu\text{g mL}^{-1}$) and B) Fluorescence intensity at 612 nm vs. logarithmic concentration in mol L^{-1} (CAC: $268.8 \mu\text{mol L}^{-1}$).

1b – [B][Leu]₃[C₆]₃[PEO_{2k}]

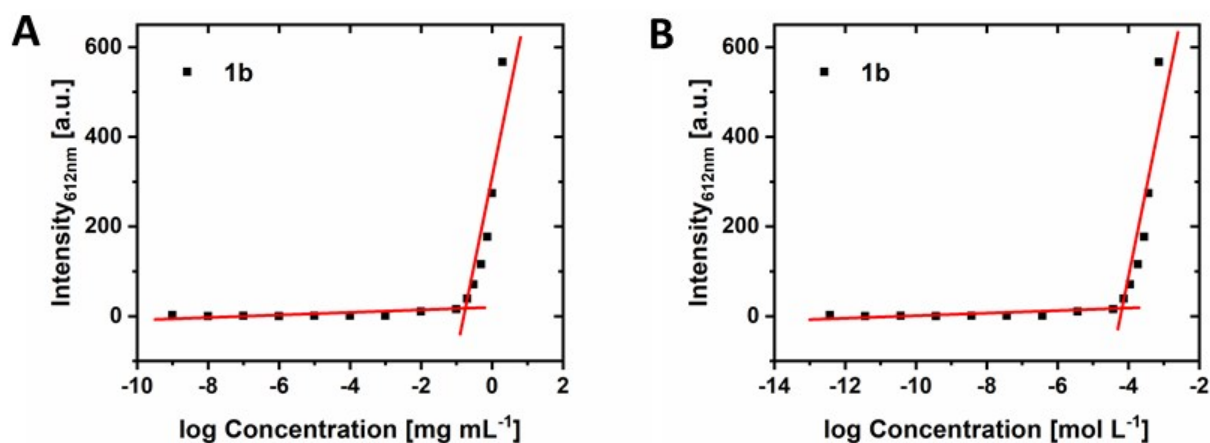


Figure S 49: CAC determination of **1b** via the Nile red fluorescence intensity method. A) Fluorescence intensity at 612 nm vs. logarithmic concentration in mg mL⁻¹ (CAC: 177.7 $\mu\text{g mL}^{-1}$) and B) Fluorescence intensity at 612 nm vs. logarithmic concentration in mol L⁻¹ (CAC: 66.2 $\mu\text{mol L}^{-1}$).

1c – [B][Phe]₃[C₆]₃[PEO_{2k}]

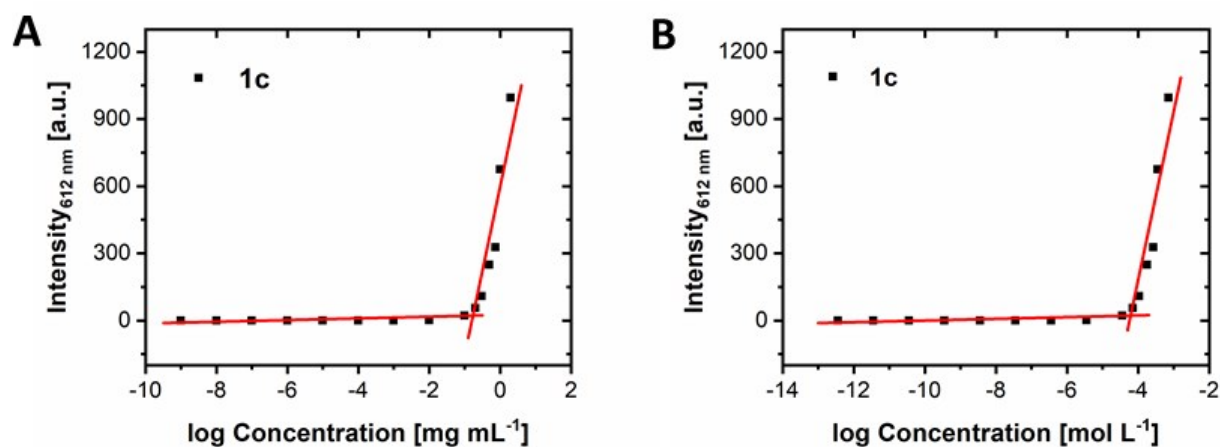


Figure S 50: CAC determination of **1c** via the Nile red fluorescence intensity method. A) Fluorescence intensity at 612 nm vs. logarithmic concentration in mg mL⁻¹ (CAC: 171.2 $\mu\text{g mL}^{-1}$) and B) Fluorescence intensity at 612 nm vs. logarithmic concentration in mol L⁻¹ (CAC: 61.3 $\mu\text{mol L}^{-1}$).

2a – [B][Ala]₃[C₁₂]₃[PEO_{2k}]

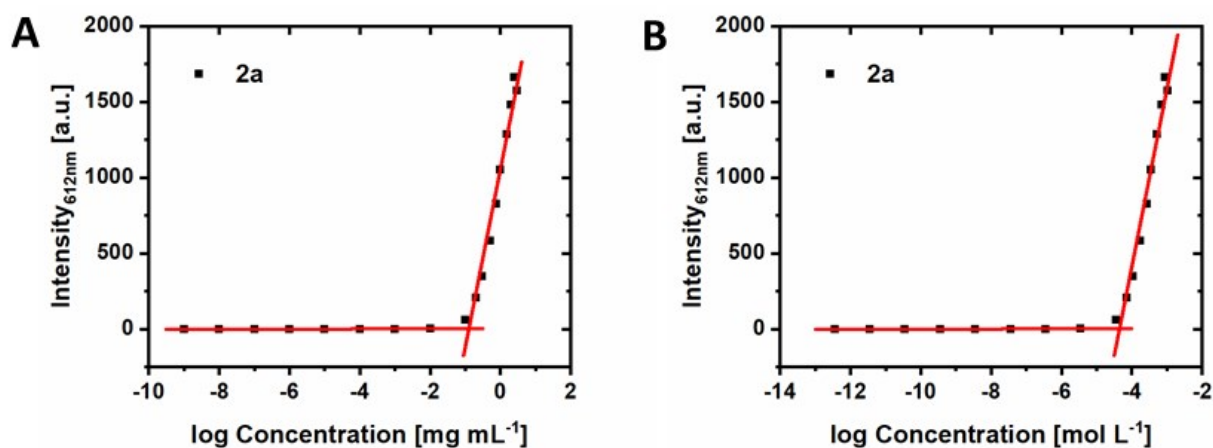


Figure S 51: CAC determination of **2a** via the Nile red fluorescence intensity method. A) Fluorescence intensity at 612 nm vs. logarithmic concentration in mg mL⁻¹ (CAC: 125.9 $\mu\text{g mL}^{-1}$) and B) Fluorescence intensity at 612 nm vs. logarithmic concentration in mol L⁻¹ (CAC: 44.5 $\mu\text{mol L}^{-1}$).

2b – [B][Leu]₃[C₁₂]₃[PEO_{2k}]

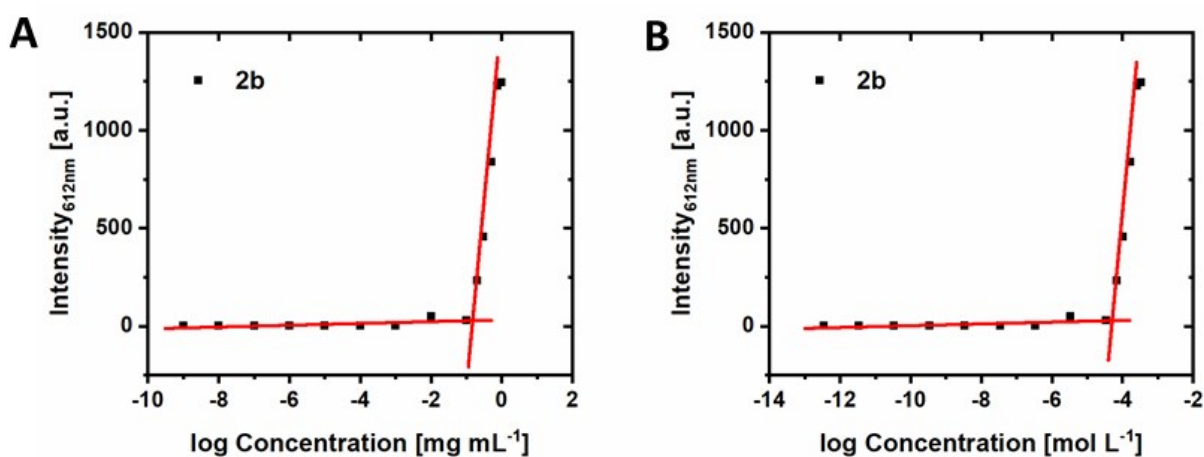


Figure S 52: CAC determination of **2b** via the Nile red fluorescence intensity method. A) Fluorescence intensity at 612 nm vs. logarithmic concentration in mg mL⁻¹ (CAC: 149.5 $\mu\text{g mL}^{-1}$) and B) Fluorescence intensity at 612 nm vs. logarithmic concentration in mol L⁻¹ (CAC: 50.9 $\mu\text{mol L}^{-1}$).

2c – [B][Phe]₃[C₁₂]₃[PEO_{2k}]

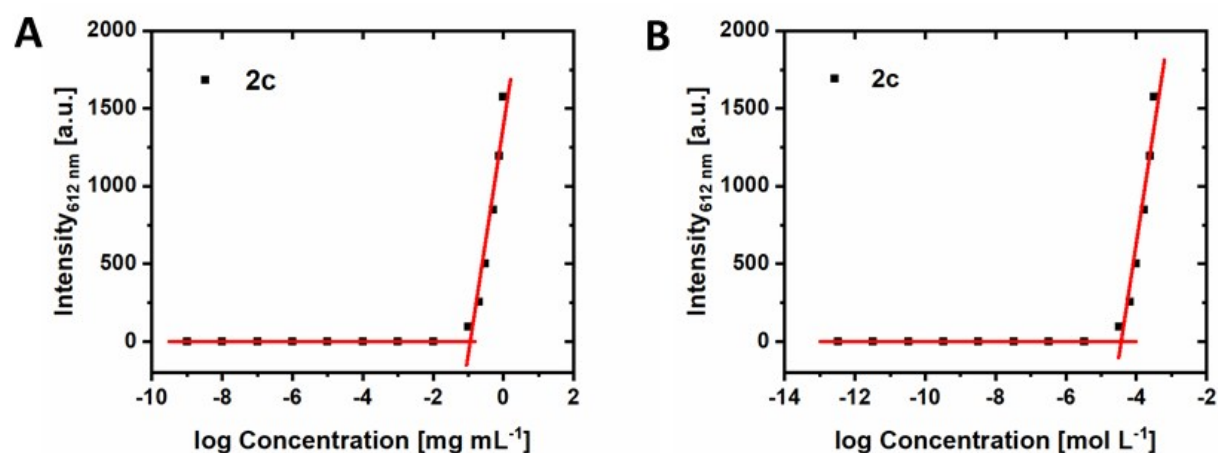


Figure S 53: CAC determination of 2c via the Nile red fluorescence intensity method. A) Fluorescence intensity at 612 nm vs. logarithmic concentration in mg mL⁻¹ (CAC: 113.2 μg mL⁻¹) and B) Fluorescence intensity at 612 nm vs. logarithmic concentration in mol L⁻¹ (CAC: 37.2 μmol L⁻¹).

2.7 Analytical Ultracentrifugation (AUC)

Sedimentation velocity experiments were performed with a ProteomeLab XL-I analytical ultracentrifuge (Beckman Coulter Instruments, Brea, CA). The cells, containing double-sector epon centerpieces with a 12 mm optical solution path length, were placed in an An-50 Ti eight-hole rotor. A rotor speed of 42,000 rpm was used. The cells were filled with 420 μL sample solution in water and with 440 μL of the solvent water in the reference sector. Typically, the experiments were conducted for a timescale of at least 24 hours and at a temperature of $T = 20$ °C. Sedimentation profile scans were recorded with the interference optics (refractive index (RI)).

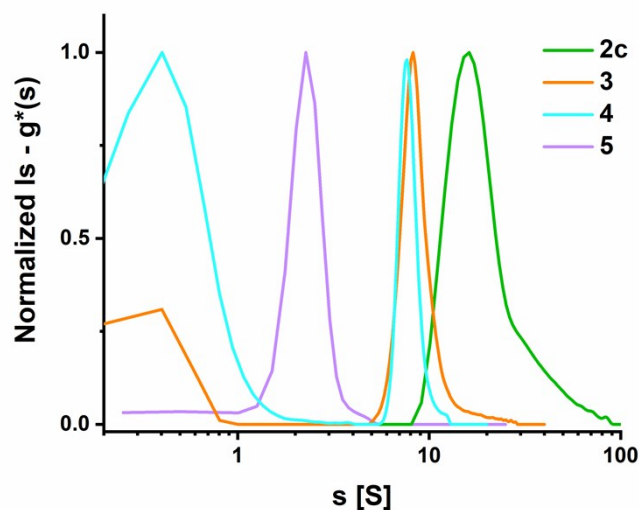


Figure S 54: Normalized differential distribution of sedimentation coefficients, $ls-g^*(s)$, of **2c** (green), **3** (orange), **4** (cyan) and **5** (purple) from sedimentation analysis in water ($c = 3 \text{ mg mL}^{-1}$). The signals below $S < 1$, visible in the curves of **3** and **4** originate from residual PEO_{5k} and PEO_{10k} unimeric species, respectively.⁷ These could not be removed from the BTP-PEO compounds via centrifugal washing, as described in the procedures in Chapter 1.

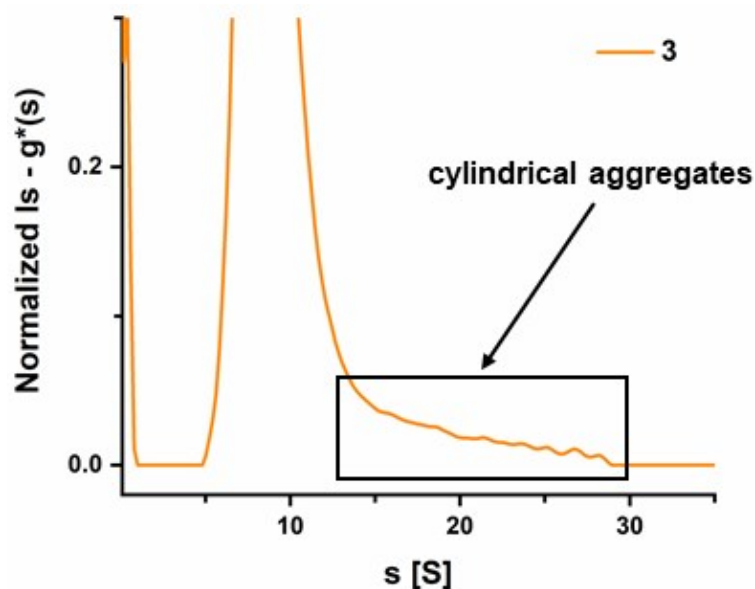


Figure S 55: Normalized differential distribution of sedimentation coefficients, $ls-g^*(s)$, of **3** from sedimentation-diffusion analysis in water ($c = 3 \text{ mg mL}^{-1}$). Zoomed view to clearly illustrate the presence of a minority of larger, cylindrical aggregates in accordance with the SAXS data and cryoTEM images of **3**.

3. References

1. D. Orthaber, A. Bergmann and O. Glatter, *J. Appl. Crystallogr.*, 2000, **33**, 218-225.
2. I. Bressler, J. Kohlbrecher and A. F. Thunemann, *J. Appl. Crystallogr.*, 2015, **48**, 1587-1598.
3. F. V. Gruschwitz, M.-C. Fu, T. Klein, R. Takahashi, T. Higashihara, S. Hoepfener, I. Nischang, K. Sakurai and J. C. Brendel, *Macromolecules*, 2020, **53**, 7552-7560.
4. S. Cantekin, T. F. A. de Greef and A. R. A. Palmans, *Chem. Soc. Rev.*, 2012, **41**, 6125-6137.
5. M. P. Lightfoot, F. S. Mair, R. G. Pritchard and J. E. Warren, *Chem. Commun.*, 1999, **19**, 1945-1946.
6. M. K. Gupta, T. A. Meyer, C. E. Nelson and C. L. Duvall, *J. Control. Release*, 2012, **162**, 591-598.
7. I. Nischang, I. Perevyazko, T. Majdanski, J. Vitz, G. Festag and U. S. Schubert, *Anal. Chem.*, 2017, **89**, 1185-1193.

Publication P5

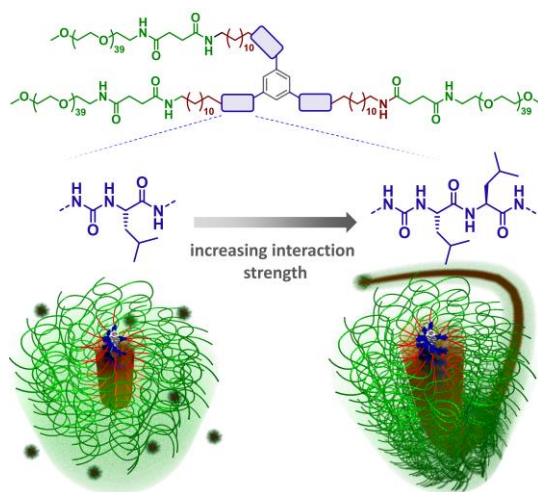
Overcoming the Necessity of a Lateral Aggregation in the Formation of Supramolecular Polymer Bottlebrushes in Water

T. Klein, H. F. Ulrich, F. V. Gruschwitz, M. T. Kuchenbrod, R. Takahashi, S. Hoepfener, I. Nischang, K. Sakurai, J. C. Brendel, *Macromol. Rapid Commun.* **2021**, *42*, e2000585.

Reproduced by permission of John Wiley and Sons. Copyright © 2020.

The paper as well as the supporting information is available online:

doi.org/10.1002/marc.202000585





Overcoming the Necessity of a Lateral Aggregation in the Formation of Supramolecular Polymer Bottlebrushes in Water

Tobias Klein, Hans F. Ulrich, Franka V. Gruschwitz, Maren T. Kuchenbrod, Rintaro Takahashi, Stephanie Hoepfener, Ivo Nischang, Kazuo Sakurai, and Johannes C. Brendel*

The assembly of supramolecular polymer bottlebrushes in aqueous systems is, in most cases, associated with a lateral aggregation of the supramolecular building blocks in addition to their axial stacking. Here, it is demonstrated that this limitation can be overcome by attaching three polymer chains to a central supramolecular unit that possesses a sufficiently high number of hydrogen bonding units to compensate for the increased steric strain. Therefore, a 1,3,5-benzenetrisurea-polyethylene oxide conjugate is modified with different peptide units located next to the urea groups which should facilitate self-assembly in water. For a single amino acid per arm, spherical micelles are obtained for all three tested amino acids (alanine, leucine, and phenylalanine) featuring different hydrophobicities. Only a slight increase in size and solution stability of spherical micelles is observed with increasing hydrophobicity of amino acid unit. In contrast, introducing two amino acid units per arm and thus increasing the number of hydrogen bonds per unimer molecule results in the formation of cylindrical structures, that is, supramolecular polymer bottlebrushes, despite a suppressed lateral aggregation. Consequently, it can be concluded that the number of hydrogen bonds has a more profound impact on the resulting solution morphology than the hydrophobicity of the amino acid unit.

The self-assembly of amphiphilic polymers in water is mainly governed by the hydrophobic effect, causing a minimization of the contact area between the hydrophobic part of the molecule and the surrounding water, mostly resulting in the formation of spherical aggregates.^[1] Recently, more attention has been paid to introducing motifs capable of forming directional, supramolecular interaction forces such as π - π interactions or hydrogen bonds (H-bonds) that can allow to direct the polymer assembly into elongated structures, such as cylinders, that would otherwise not be accessible.^[2-7] In particular, the so-called supramolecular polymer bottlebrushes (SPBs) have gained increasing interest due to their potential applications in areas such as nanomedicine,^[8] rheology^[9], electronics, and photonics.^[10,11]

The design of many supramolecular core units within such nanostructures relies on a combination of hydrophobic

elements repelling the aqueous environment with multiple strong H-bonding units, as demonstrated, for example, for urea based sticker motifs, the benzene/toluene bisureas, squaramides or 1,3,5-substituted benzene units featuring either amide, urea, or peptide units.^[12-27] Considering the latter, we have previously shown that the number of H-bonds per central motif, and thus the interaction strength, is decisive to obtain SPBs.^[28-30] However, next to the strength of the supramolecular interaction and the main axial assembly, a lateral assembly appears to be crucial for the formation of cylindrical structures, which is similarly observed for other of the above-mentioned motifs.

Here, we aim on answering the question if this requirement can be overcome by firstly blocking a lateral aggregation via by the attachment of polyethylene oxide (PEO) chains and secondly by gradually increasing the number of H-bonds per central motif and adjustment of the hydrophobicity in their immediate environment. Based on our previous work, the starting point was the symmetrically substituted benzene trisurea (BTU) conjugate bearing three polyethylene oxide PEO (2 kg mol⁻¹) chains, which formed small spherical aggregates

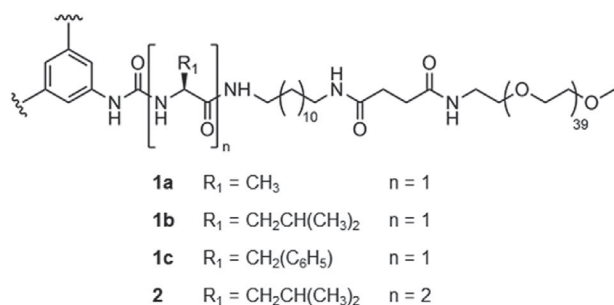
T. Klein, H. F. Ulrich, F. V. Gruschwitz, M. T. Kuchenbrod, Dr. S. Hoepfener, Dr. I. Nischang, Dr. J. C. Brendel
Laboratory of Organic and Macromolecular Chemistry (IOMC)
Friedrich Schiller University Jena
Humboldtstraße 10, 07743 Jena, Germany
E-mail: johannes.brendel@uni-jena.de

T. Klein, H. F. Ulrich, F. V. Gruschwitz, M. T. Kuchenbrod, Dr. S. Hoepfener, Dr. I. Nischang, Dr. J. C. Brendel
Jena Center for Soft Matter (JCSM)
Friedrich Schiller University Jena
Philosophenweg 7, 07743 Jena, Germany
Dr. R. Takahashi, Prof. K. Sakurai
Department of Chemistry and Biochemistry
University of Kitakyushu
1-1 Hibikino, Wakamatsu-ku, Kitakyushu, Fukuoka 808-0135, Japan

The ORCID identification number(s) for the author(s) of this article can be found under <https://doi.org/10.1002/marc.202000585>.

© 2020 The Authors. Macromolecular Rapid Communications published by Wiley-VCH GmbH. This is an open access article under the terms of the Creative Commons Attribution License, which permits use, distribution and reproduction in any medium, provided the original work is properly cited.

DOI: 10.1002/marc.202000585



Scheme 1. Chemical structures of the BTUPs **1a–c** and **2**. All three substituents tethered to the central benzene unit are identical and two of them were omitted due to reasons of clarity as indicated by the wavy curled lines.

with a fully suppressed lateral aggregation. To increase the interaction strength, additional amino acid units were integrated next to the urea units and the central benzene core (**Scheme 1**). Variation of the type of amino acid allows further subtle structural adjustments, that is, an increase of hydrophobicity or the introduction of π - π interactions. The resulting assemblies were then thoroughly characterized by small-angle X-ray scattering (SAXS), cryo-transmission electron microscopy (cryoTEM), and sedimentation velocity experiments in an analytical ultracentrifuge (AUC).

For the preparation of our C_3 -symmetric benzenetrisurea-peptide-PEO conjugates (BTUPs), we combined the previously reported syntheses of C_3 -symmetric BTU and benzenetrispeptide (BTP) conjugates (Schemes S1 and S2, Supporting Information).^[28–31] Different amino acids (alanine, leucine, and phenylalanine) were chosen to study the impact of the hydrophobicity of the respective amino acid and their ability to form additional π - π interactions in case of phenylalanine on the self-assembled structures in water. The low solubility of the resulting compounds simplified the purification by precipitation, but the overall yields remained low due to the formation of gels during the reactions.^[31] After removal of the NH-Boc groups, three PEO chains with terminal *N*-hydroxysuccinimide esters were tethered to the central moiety resulting in bolaamphiphilic polymers **1a–c**. To further examine the impact of the number of hydrogen H-bonds, we further increased the number of H-bonds for compound **2** by introducing two leucine units per arm.

Dynamic light scattering (DLS) experiments allowed to obtain first insights into their self-assembly in water (Figure S9, Supporting Information). The rather small intensity-weighted hydrodynamic diameters, d_{H} , of 9.0 ± 2.8 nm (**1a**), 13.5 ± 4.4 nm (**1b**), and 15.1 ± 4.5 nm (**1c**) already indicated that no large aggregates are present. To examine the solution morphology in more detail, we further performed SAXS experiments (Figure 1A). The SAXS trace of **1a** could be best fit by a form factor for a Gaussian coil (details of all fits are given in the Supporting Information), indicating that hardly any assembly takes place for the alanine analogue. We assume that the rather hydrophilic character of the alanine, compared to the leucine or phenylalanine, provides a weaker driving force for aggregation, despite the presence of the adjacent dodecane units, which should provide adequate shielding from the surrounding water.^[23,27]

Consequently, other impeding factors for the self-assembly seem to prevail, such as steric hindrance and entropic penalty due to the stretching of PEO chains. For **1b** and **1c**, the plateau at low q values was followed by a $I(q) \propto q^{-4}$ regime, which is indicative for the presence of spherical polymer micelles. This allowed to fit the SAXS profiles with a form factor of a sphere. R_{sphere} of 3.3 nm (**1b**) and 4.3 nm (**1c**) were determined. Guinier plots for both data sets provided values for R_g of 4.2 nm (Figure S11, Supporting Information) and 4.6 nm (Figure S12, Supporting Information) for **1b** and **1c**, respectively. The deviation from the expected correlation $R_g = \sqrt{\frac{3}{5}} R_{\text{sphere}}$ is caused by the inhomogeneous PEO corona of the spherical micelles, which is in contrast to the sharp interfaces as assumed in the sphere fits.^[32] Similarly, the observed difference between R_{H} and R_{sphere} might also be related to the soft character of the structure compared to the model of a hard sphere which was assumed in the fit or a size distribution. However, this was not investigated in

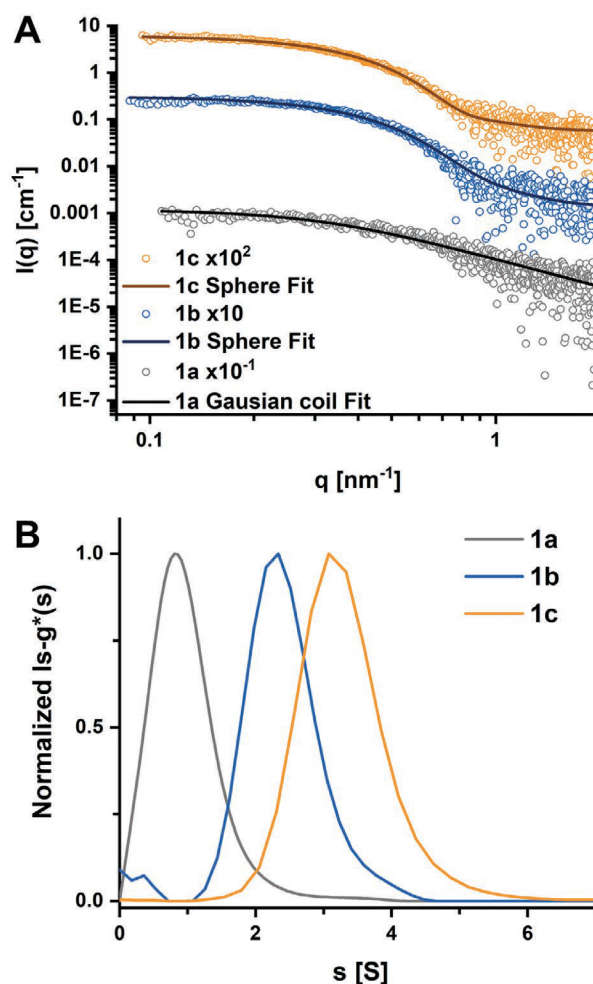


Figure 1. A) SAXS profiles of the samples **1a** (grey), **1b** (blue), and **1c** (orange), measured in water ($c = 1.5$ mg mL⁻¹). The traces were shifted for reasons of clarity as indicated in the figure legend. The respective continuous lines represent the best fits using SASfit (details are given in the Supporting Information).^[34] B) Normalized differential distribution of sedimentation coefficients, $I_s\text{-}g^*(s)$, of **1a** (grey), **1b** (blue), and **1c** (orange) from sedimentation analysis in water ($c = 3$ mg mL⁻¹).

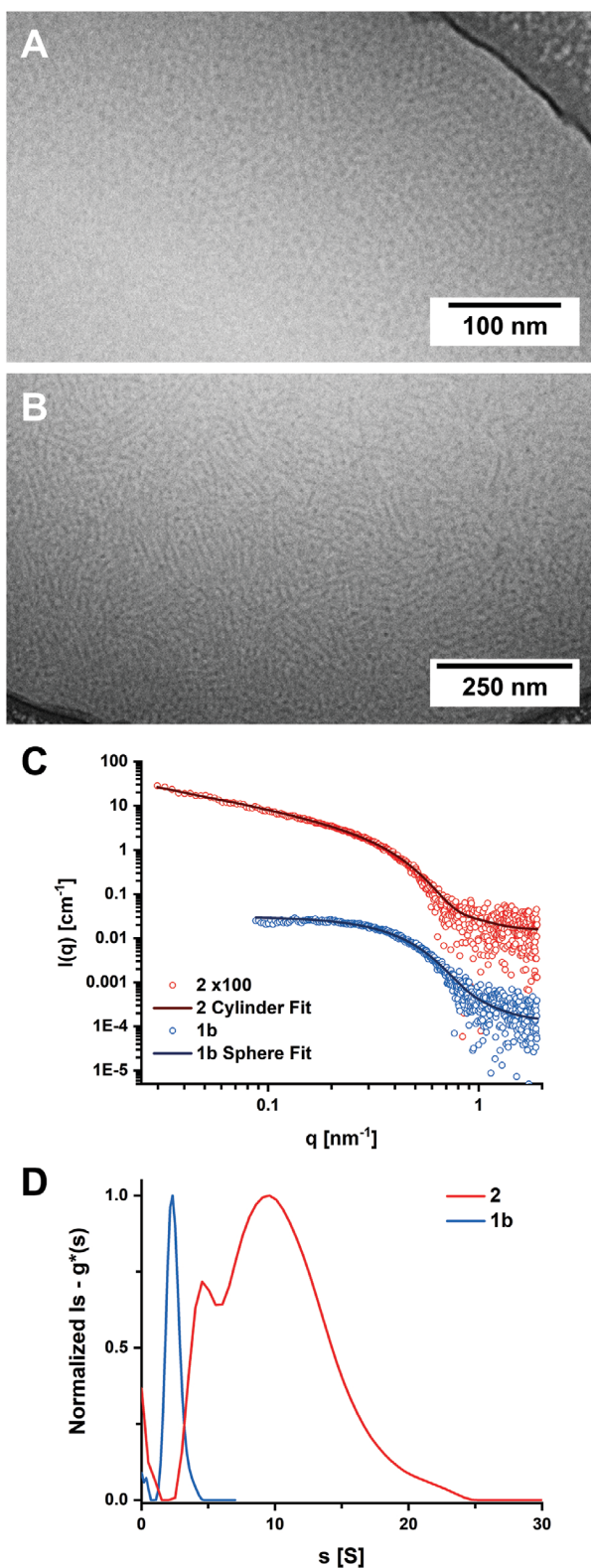


Figure 2. CryoTEM images of **1b** (A) and **2** (B) in water ($c = 3 \text{ mg mL}^{-1}$). Full-sized images can be found in Figures S16 and S18, Supporting Information. C) SAXS scattering profiles of the samples **1b** (blue, $c = 1.5 \text{ mg mL}^{-1}$) and **2** (red, $c = 0.8 \text{ mg mL}^{-1}$), measured in water. The trace of **2** was shifted by multiplication for reasons of clarity as indicated in the figure

more detail. Considering the difference to **1a**, the self-assembly of **1b** and **1c** is most likely caused by an increased hydrophobicity of the amino acids leucine (**1b**) and phenylalanine (**1c**) when compared to alanine (**1a**), but a clear evidence for the formation of cylindrical stacks due to hydrogen bonds is not provided by the data.

CryoTEM analysis corroborated the SAXS results, as spherical micelles with diameters of $7 \pm 1 \text{ nm}$ and $10 \pm 1 \text{ nm}$ can be seen for **1b** and **1c**, respectively (Figures S16 and S17, Supporting Information). For **1a**, no clear structures can be identified in the images (Figure S15, Supporting Information).

Compounds **1a–c** were further studied via sedimentation velocity experiments in the AUC to resolve apparent distributions of the sedimentation coefficients, s (Figure 1B).^[28,29,33] For all three compounds, roughly monomodal distributions of s were observed with signal (weight) average sedimentation coefficients of $s = 1.0 \text{ S}$ (**1a**), $s = 2.4 \text{ S}$ (**1b**), and $s = 3.3 \text{ S}$ (**1c**). The very small s -value for **1a** is in accordance with the SAXS and cryoTEM results indicate the presence of unimers next to small aggregates.

The presented data for **1a–c** clearly reveal that the interaction strength between the BTUPs was not large enough to enable the formation of cylindrical SPBs, despite the presence of nine binding sites which are able to potentially form H-bonds. The steric strain imposed by the three tethered PEO chains appears to be too high in order to be compensated by the additional H-bonding interactions. The type of the amino acid moiety had only a minor impact on the solution morphology. The increased hydrophobicity of **1b** (leucine) and **1c** (phenylalanine) compared to **1a** (alanine) only induced the assembly into spherical structures, but no morphology transition from spherical to cylindrical structures was observed.

Inspired by a recent report of Zagorodko et al., who reported the formation of SPBs based on the BTP motif with three amino acid units per arm, we further increased the number of H-bonds to identify the critical step for the formation of SPBs in our system.^[35] For this purpose, we synthesized compound **2** comprising two leucine units per arm (Schemes S3 and S5, Supporting Information). We deliberately chose leucine in this case due to its sufficient hydrophobicity to shield the core H-bonds compared to alanine.

DLS measurements of **2** yielded an intensity-weighted hydrodynamic diameter, d_{H} , of $81.9 \pm 56.5 \text{ nm}$ and, thus, almost twice the apparent hydrodynamic size of its analogue **1b** with only one leucine unit per arm (Figure S10, Supporting Information). In contrast to the spherical micelles observed for **1b** (Figure 2A), the cryoTEM images of **2** revealed the formation of cylindrical micelles with an average diameter of $8 \pm 1 \text{ nm}$ and apparent lengths up to 265 nm (Figure 2B). A few spherical aggregates can also be identified in the image. Some of them exhibit a higher contrast, which could be related to short, truncated, cylindrical micelles that are oriented orthogonally with respect to the vitrified ice film,^[30] but an unequivocal proof cannot be derived from the data.

legend. The respective continuous lines represent the best fits using SAS fit (details are given in the Supporting Information).^[34] D) Normalized differential distribution of sedimentation coefficients, $Is - g^*(s)$, of **1b** (blue) and **2** (red) from sedimentation analysis in water ($c = 3 \text{ mg mL}^{-1}$).

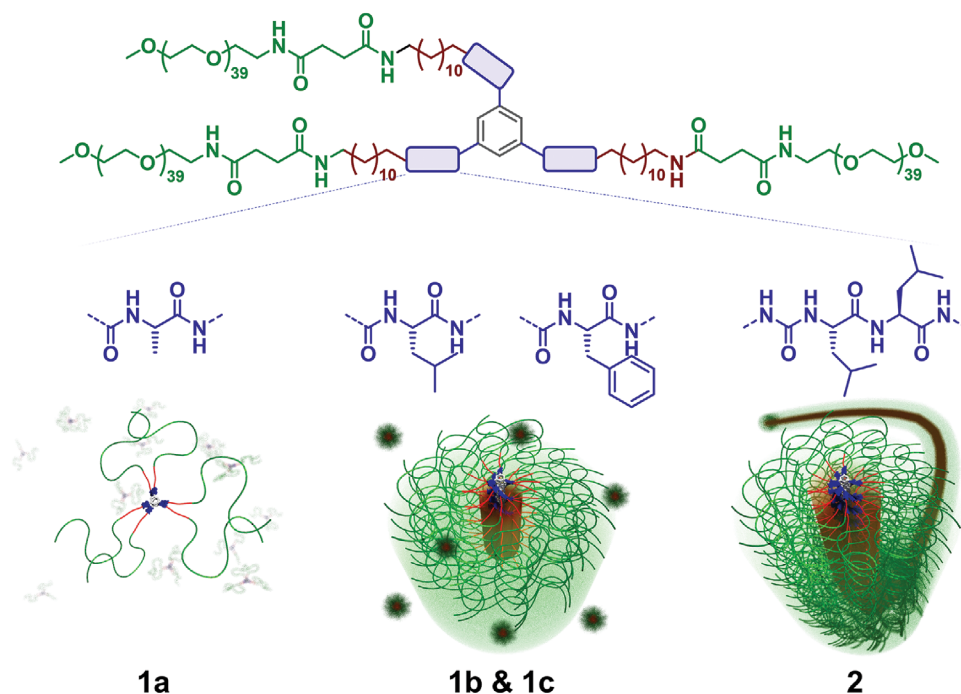
To further support this assumption, we performed SAXS to investigate the ensemble solution morphology of **2**.^[36] An ideal $I(q) \propto q^{-1}$ relationship was found for small q -values, indicative of the exclusive presence of cylindrical aggregates (Figure 2C). The scattering profile could thus be best fit by using a form factor of a cylinder (Table S4, Supporting Information), yielding $R_{\text{cyl}} = 4.0$ nm. An average cylinder length could not be determined from the SAXS data of **2**, as no plateau at very low q values was obtained. The radius of gyration of the cross-section R_{cs} was determined to be 4.8 nm via a cross-sectional plot (Figure S13, Supporting Information). Likewise to the above-discussed relationship between R_{g} and R_{sphere} , the deviation from the expected correlation of $R_{\text{cs}} = R_{\text{cyl}}/\sqrt{2}$ results from the inhomogeneous formation of the cylinder corona by the three PEO chains in water.^[32] The small value for R_{cyl} is a first indication that the backbone of the SPB of **2** could potentially consist of only one columnar stack of BTUP units.^[29] To further investigate this, the molar mass per unit length M_{L} of the SPB **2** could be derived from the $I(q) \propto q^{-1}$ dependence at low q -values according to $(I(q)/Kc)q = M_{\text{L}}\pi$. It was determined to be $M_{\text{L}} = 1.11 \times 10^4$ g mol⁻¹ nm⁻¹ (Figure S14, Supporting Information).^[14,17] Assuming the previously reported intermolecular distance of 4.6 Å between urea crystals,^[37] a theoretical $M_{\text{L,stack}} = M_{\text{w,compound 2}} / 0.46$ nm = 1.55×10^4 g mol⁻¹ nm⁻¹ is expected for a unimolecular SPB backbone. As M_{L} is even lower than $M_{\text{L,stack}}$, we conclude that the backbone of the SPB of **2** consists of one molecule in the cross section only. The further deviation is likely caused by a different intermolecular distance between unimers. The reported value of 4.6 Å was found for *N,N'*-dimethylurea.^[37] In compound **2**, however, the urea-groups are flanked by sterically more demanding

leucine dipeptide units. This, most likely, causes a larger intermolecular distance and, consequently, lower $M_{\text{L,stack}}$ values, resulting in $M_{\text{L}}/M_{\text{L,stack}}$ values closer to one. Furthermore, due to the presence of some unconjugated PEO in **2** (see Figure S8, Supporting Information) and the filtration of the sample before SAXS measurement to remove undissolved aggregates, the real concentration of **2** in the SAXS measurement could be slightly lower than assumed for the calculations (0.8 mg mL⁻¹). Consequently, a higher value for M_{L} is expected which would result in give a $M_{\text{L}}/M_{\text{L,stack}}$ ratio closer to one.

In addition, a sedimentation-velocity experiment for **2** was performed (Figure 2D). A broad distribution of sedimentation coefficients was observed with a signal (weight) average sedimentation coefficient of $s = 9.9$ S. The partly resolved population at smaller sedimentation coefficients with a maximum at $s = 4.5$ S indicates the presence of some smaller aggregates, that, however, still sediment faster than the spherical aggregates observed for **1b**.

Increasing the number of H-bonds and thus the interaction strength by incorporating a second amino acid unit, here leucine, appeared to be the key factor for overcoming the steric strain imposed by the three PEO chains on the core motif and their unfavorable entropy of stretching upon self-assembly. Consequently, a morphology transition from spherical to cylindrical micelles (**Scheme 2**) is observed.

In summary, we investigated the impact of structural modifications (type and number of incorporated amino acid moieties) of symmetrically substituted BTUPs on the self-assembly structures formed in water. Variations of the amino acid unit (alanine, leucine, and phenylalanine) had only a minor influence



Scheme 2. Schematic representations of the observed solution morphologies for BTUPs in this study: hardly any assembly for **1a**, spherical micelles for **1b** and **1c**, and cylindrical micelles for **2** were found.

on the solution assembly. While **1a** showed hardly any assembly, small spherical micelles were obtained for compounds **1b-c**. The more hydrophobic amino acids leucine (**1b**) and phenylalanine (**1c**) were, therefore, able to trigger an assembly, but did not facilitate the formation of cylindrical structures, despite multiple directing H-bonding sites and potentially existing π - π interactions (**1c**), which favor a 1D supramolecular stacking. We assume the large steric demands of the three pendant PEO chains to still suppress an extended aggregation. Furthermore, increasing the number of H-bonds by introducing a second leucine unit resulted in the formation of cylindrical micelles for compound **2** featuring only a unimolecular backbone. This study, thus, demonstrates that despite the high steric strain imposed by the three polymer chains suppressing the lateral aggregation, the formation of cylindrical SPBs is still possible if directional, supramolecular forces of sufficient strength are incorporated into the central unimer motifs.

Supporting Information

Supporting Information is available from the Wiley Online Library or from the author.

Acknowledgements

The authors thank Prof. Ulrich S. Schubert for his continuous support and access to excellent research facilities. J.C.B., T.K., H.F.U., and F.V.G. further thank the German Science Foundation (DFG) for generous funding within the Emmy-Noether Programme (Project-ID: 358263073). CryoTEM investigations were performed at the electron microscopy facilities of the Jena Center for Soft Matter (JCSM), which were established with grants from the DFG and the European Funds for Regional Development (EFRE). I.N., S.H., and M.T.K. acknowledge support of this study by the DFG-funded Collaborative Research Center PolyTarget (SFB 1278, project number 316213987, project Z01). The SAXS experiments were carried out at SPring-8 under the approval by JASRI (Proposal Number: 2018A1454, 2018B1396, 2019A1327, and 2019B1207).

Open access funding enabled and organized by Projekt DEAL.

Conflict of Interest

The authors declare no conflict of interest.

Keywords

bottlebrush polymers, hydrogen bonds, lateral aggregation, self-assembly, supramolecular polymers

Received: October 2, 2020
Revised: November 12, 2020
Published online:

- [1] Y. Mai, A. Eisenberg, *Chem. Soc. Rev.* **2012**, *41*, 5969.
[2] F. V. Gruschwitz, T. Klein, S. Catrouillet, J. C. Brendel, *Chem. Commun.* **2020**, *56*, 5079.
[3] G. Mellot, J.-M. Guigner, L. Bouteiller, F. Stoffelbach, J. Rieger, *Angew. Chem., Int. Ed.* **2019**, *58*, 3173.

- [4] G. Mellot, P. Beaunier, J.-M. Guigner, L. Bouteiller, J. Rieger, F. Stoffelbach, *Macromol. Rapid Commun.* **2019**, *40*, 1800315.
[5] Z. Hua, J. R. Jones, M. Thomas, M. C. Arno, A. Souslov, T. R. Wilks, R. K. O'Reilly, *Nat. Commun.* **2019**, *10*, 5406.
[6] J. C. Brendel, F. H. Schacher, *Chem. Asian J.* **2018**, *13*, 230.
[7] J. C. Brendel, S. Catrouillet, J. Sanchis, K. A. Jolliffe, S. Perrier, *Polym. Chem.* **2019**, *10*, 2616.
[8] S. P. W. Wijnands, W. Engelen, R. P. M. Lafleur, E. W. Meijer, M. Merckx, *Nat. Commun.* **2018**, *9*, 65.
[9] M. Golkaram, L. Boetje, J. Dong, L. E. A. Suarez, C. Fodor, D. Maniar, E. van Ruymbeke, S. Faraji, G. Portale, K. Loos, *ACS Omega* **2019**, *4*, 16481.
[10] G. M. Miyake, V. A. Piunova, R. A. Weitekamp, R. H. Grubbs, *Angew. Chem., Int. Ed.* **2012**, *51*, 11246.
[11] X.-H. Jin, M. B. Price, J. R. Finnegan, C. E. Boott, J. M. Richter, A. Rao, S. M. Menke, R. H. Friend, G. R. Whittell, I. Manners, *Science* **2018**, *360*, 897.
[12] S. Cantekin, T. F. A. de Greef, A. R. A. Palmans, *Chem. Soc. Rev.* **2012**, *41*, 6125.
[13] S. Han, G. Mellot, S. Pensec, J. Rieger, F. Stoffelbach, E. Nicol, O. Colombani, J. Jestin, L. Bouteiller, *Macromolecules* **2020**, *53*, 427.
[14] S. Han, E. Nicol, F. Niepceron, O. Colombani, S. Pensec, L. Bouteiller, *Macromol. Rapid Commun.* **2019**, *40*, 1800698.
[15] S. Catrouillet, L. Bouteiller, O. Boyron, C. Lorthioir, E. Nicol, S. Pensec, O. Colombani, *Langmuir* **2016**, *32*, 8900.
[16] S. Catrouillet, L. Bouteiller, E. Nicol, T. Nicolai, S. Pensec, B. Jacqueline, M. Le Bohec, O. Colombani, *Macromolecules* **2015**, *48*, 1364.
[17] S. Catrouillet, C. Fonteneau, L. Bouteiller, N. Delorme, E. Nicol, T. Nicolai, S. Pensec, O. Colombani, *Macromolecules* **2013**, *46*, 7911.
[18] R. Appel, J. Fuchs, S. M. Tyrrell, P. A. Korevaar, M. C. A. Stuart, I. K. Voets, M. Schönhoff, P. Besenius, *Chem. - Eur. J.* **2015**, *21*, 19257.
[19] P. Besenius, K. P. van den Hout, H. M. H. G. Albers, T. F. A. de Greef, L. L. C. Olijve, T. M. Hermans, B. F. M. de Waal, P. H. H. Bomans, N. A. J. M. Sommerdijk, G. Portale, A. R. A. Palmans, M. H. P. van Genderen, J. A. J. M. Vekemans, E. W. Meijer, *Chem. - Eur. J.* **2011**, *17*, 5193.
[20] P. Besenius, Y. Goedegebure, M. Driesse, M. Koay, P. H. H. Bomans, A. R. A. Palmans, P. Y. W. Dankers, E. W. Meijer, *Soft Matter* **2011**, *7*, 7980.
[21] V. Saez Talens, D. M. M. Makurat, T. Liu, W. Dai, C. Guibert, W. E. M. Noteborn, I. K. Voets, R. E. Kielyka, *Polym. Chem.* **2019**, *10*, 3146.
[22] V. Saez Talens, P. Englebienne, T. T. Trinh, W. E. M. Noteborn, I. K. Voets, R. E. Kielyka, *Angew. Chem., Int. Ed.* **2015**, *54*, 10502.
[23] M. Tharcis, T. Breiner, J. Bellenev, F. Boué, L. Bouteiller, *Polym. Chem.* **2012**, *3*, 3093.
[24] T. Choynet, D. Canevet, M. Sallé, E. Nicol, F. Niepceron, J. Jestin, O. Colombani, *Chem. Commun.* **2019**, *55*, 9519.
[25] N. Chebotareva, P. H. H. Bomans, P. M. Frederik, N. A. J. M. Sommerdijk, R. P. Sijbesma, *Chem. Commun.* **2005**, *39*, 4967.
[26] A. Pal, P. Besenius, R. P. Sijbesma, *J. Am. Chem. Soc.* **2011**, *133*, 12987.
[27] A. Pal, S. Karthikeyan, R. P. Sijbesma, *J. Am. Chem. Soc.* **2010**, *132*, 7842.
[28] T. Klein, F. V. Gruschwitz, S. Rogers, S. Hoepfener, I. Nischang, J. C. Brendel, *J. Colloid Interface Sci.* **2019**, *557*, 488.
[29] F. V. Gruschwitz, M.-C. Fu, T. Klein, R. Takahashi, T. Higashihara, S. Hoepfener, I. Nischang, K. Sakurai, J. C. Brendel, *Macromolecules* **2020**, *53*, 7552.



- [30] T. Klein, H. F. Ulrich, F. V. Gruschwitz, M. T. Kuchenbrod, R. Takahashi, S. Fujii, S. Hoepfner, I. Nischang, K. Sakurai, J. C. Brendel, *Polym. Chem.* **2020**, *11*, 6763.
- [31] M. de Loos, J. H. van Esch, R. M. Kellogg, B. L. Feringa, *Tetrahedron* **2007**, *63*, 7285.
- [32] I. Livsey, *J. Chem. Soc., Faraday Trans.* **1987**, *83*, 1445.
- [33] P. Schuck, P. Rossmanith, *Biopolymers* **2000**, *54*, 328.
- [34] I. Bressler, J. Kohlbrecher, A. F. Thunemann, *J. Appl. Crystallogr.* **2015**, *48*, 1587.
- [35] O. Zagorodko, V. J. Nebot, M. J. Vicent, *Polym. Chem.* **2020**, *11*, 1220.
- [36] J. P. Patterson, M. P. Robin, C. Chassenieux, O. Colombani, R. K. O'Reilly, *Chem. Soc. Rev.* **2014**, *43*, 2412.
- [37] J. Pérez-Folch, J. A. Subirana, J. Aymami, *J. Chem. Crystallogr.* **1997**, *27*, 367.



Supporting Information

for *Macromol. Rapid Commun.*, DOI: 10.1002/marc.202000585

Overcoming the Necessity of a Lateral Aggregation in
the Formation of Supramolecular Polymer Bottlebrushes
in Water

Tobias Klein, Hans F. Ulrich, Franka V. Gruschwitz,
Maren T. Kuchenbrod, Rintaro Takahashi, Stephanie
Hoeppener, Ivo Nischang, Kazuo Sakurai, and Johannes
C. Brendel*

Supporting information for

Overcoming the necessity of a lateral aggregation in the formation of supramolecular polymer bottlebrushes in water

Tobias Klein^{a,b}, Hans F. Ulrich^{a,b}, Franka V. Gruschwitz, Maren T. Kuchenbrod^{a,b}, Rintaro Takahashi^c, Stephanie Hoepfener^{a,b}, Ivo Nischang^{a,b}, Kazuo Sakurai^c, Johannes C. Brendel^{a,b,*}

a Laboratory of Organic and Macromolecular Chemistry (IOMC), Friedrich Schiller University Jena, Humboldtstraße 10, 07743 Jena, Germany

b Jena Center for Soft Matter (JCSM), Friedrich Schiller University Jena, Philosophenweg 7, 07743 Jena, Germany

c Department of Chemistry and Biochemistry, University of Kitakyushu, 1-1 Hibikino, Wakamatsu-ku, Kitakyushu, Fukuoka 808-0135, Japan

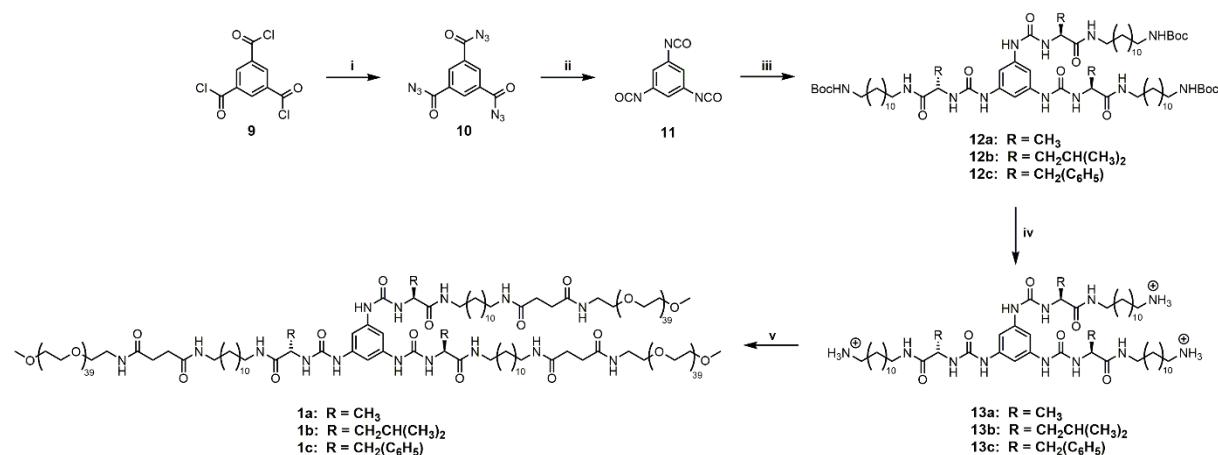
*corresponding author: johannes.brendel@uni-jena.de

Content

1. Synthesis	3
2. Characterisation	21
2.1 Sample preparation	21
2.2 Dynamic Light Scattering (DLS)	22
2.3 Small Angle X-Ray Scattering (SAXS)	23
2.4 Cryogenic Transmission Electron Microscopy (cryoTEM)	28
2.5 Analytical Ultracentrifugation (AUC).....	32
3. References.....	32

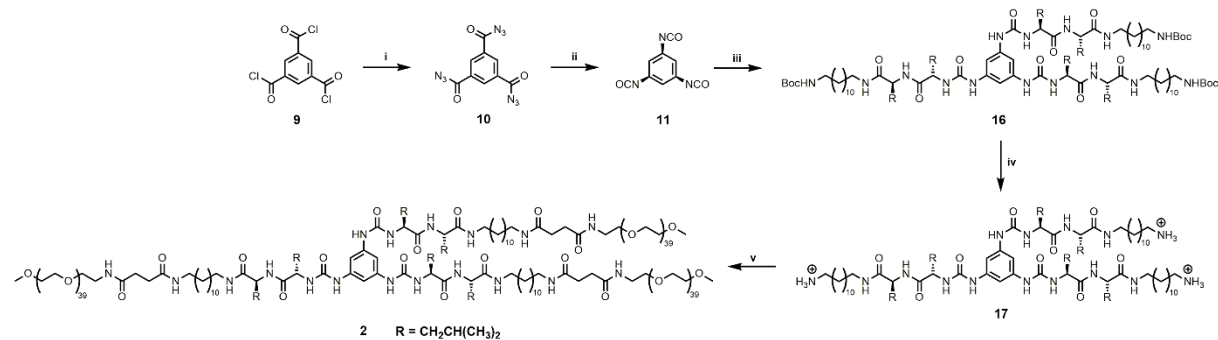
Benzenetrisureapeptide building blocks

With one amino acid per arm



Scheme S 4: Synthetic route to the benzenetrisureapeptide conjugates **1a-c** bearing three PEO chains. i) NaN₃, H₂O/THF 3:1, 0 °C, 90 min; ii) Toluene; 80 °C; 1 h; iii) alkylated amino acids; toluene, 90 °C, overnight; iv) TFA/TIPS/H₂O, DCM, rt, 2 h; v) MeO-PEO_{2k}-NHS, TEA, DMF, rt, overnight.

With two amino acids per arm

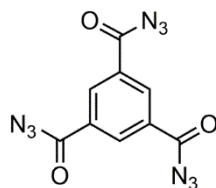


Scheme S 5: Synthetic route to the benzenetrisureapeptide conjugate **2** bearing three PEO chains. i) NaN₃, H₂O/THF 3:1, 0 °C, 90 min; ii) Toluene; 80 °C; 1 h; iii) alkylated di-leucine; toluene, 90 °C, overnight; iv) TFA/TIPS/H₂O, DCM, rt, 2 h; v) MeO-PEO_{2k}-NHS, TEA, DMF, rt, overnight.

Synthetic protocols

Core units

Benzene-1,3,5-tricarbonyl azide – **10**



10

Benzene-1,3,5-tricarbonyl trichloride (0.56 g, 2.109 mmol, 1.0 eq) was dissolved in 1.465 mL anhydrous THF and cooled to 0 °C. In a separate flask, sodium azide (0.549 g, 8.44 mmol, 4.0 eq) was dissolved in 4.39 mL water and dropwise added to the THF solution. The reaction mixture was stirred for 90 min at 0 °C. Afterwards, 13 mL of toluene and 27 mL of a sat. NaHCO₃ (aq.) solution were added. The aqueous phase was then 3x extracted with toluene (10 mL). The combined organic phases were then once washed with brine, dried over MgSO₄ and filtered. Afterwards, the organic solution was reduced *in vacuo* to approximately 11 mL (corresponding to a 0.19 M solution).

Due to its explosive nature, benzene-1,3,5-tricarbonyl azide **10** was not concentrated and characterized, but straight away used in the subsequent reaction.

Yield: -

Molecular formula: -

¹H-NMR (300 MHz, d₆-DMSO, 298 K): -

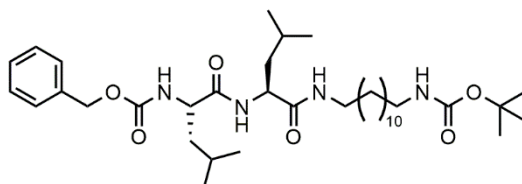
ESI-ToF-MS (positive mode, acetonitrile) (m/z): -

Amino acid arms

Compounds 4-8

The synthetic protocols for compounds 4-8 were reported recently.^[1]

Cbz-L-Leu-C(O)NH-L-Leu-C(O)NH-C₁₂-NH-Boc – 14



14

Cbz-L-Leu-OH **6b** (1.069 g, 4.029 mmol, 1.0 eq) and DMAP (44 mg, 0.363 mmol, 0.1 eq) were dissolved in 18.15 mL chloroform. To this solution 1.5 g Cbz-L-Leu-C(O)NH-C₁₂-NH-Boc **8b** (3.626 mmol, 0.9 eq) were added. Thereafter, 0.834 g EDC-HCl (4.351 mmol, 1.2 eq) were added portion wise under vigorous stirring and the solution stirred overnight at rt. Afterwards, the reaction mixture was extracted with 1 M HCl (3x, 50 mL), sat. aq. NaHCO₃ (1x, 50 mL) and brine (1x, 50 mL). The combined organic phases were dried over MgSO₄, filtered and reduced *in vacuo*. The obtained product was dried in the vacuum oven (40 °C) overnight.

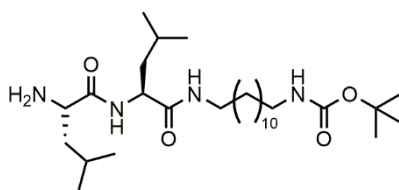
Yield: 1.817 g, 2.749 mmol (76%), white solid.

Molecular formula: C₃₇H₆₄N₄O₆.

¹H-NMR (300 MHz, d₆-DMSO, 298 K): δ [ppm] = 7.81 (t, J = 8.1 Hz, 2H, NH), 7.44 (d, J = 8.3 Hz, 1H, NH), 7.41 – 7.25 (m, 4H, CH_{aromat}), 6.76 (t, J = 5.6 Hz, 1H, NH), 5.02 (s, 2H, CH₂), 4.25 (q, J = 8.1, 7.6 Hz, 1H, CH), 4.07 – 3.97 (m, 1H, CH), 3.01 (dq, J = 13.2, 7.1 Hz, 2H, CH₂), 2.87 (q, J = 6.7 Hz, 2H, CH₂), 1.68 – 1.49 (m, 2H, CH), 1.49 – 1.28 (m, 17H, CH₂, CH₃), 1.22 (s, 16H, CH₂), 0.93 – 0.73 (m, 12H, CH₃).

ESI-ToF-MS (positive mode, acetonitrile) (m/z): calculated for [M+Na]⁺: 683.4718; found: 683.4878.

H₂N-L-Leu-C(O)NH-L-Leu-C(O)NH-C₁₂-NH-Boc – **15**



15

Cbz-L-Leu-C(O)NH-L-Leu-C(O)NH-C₁₂-NH-Boc **14** (1.6 g, 2.421 mmol, 1.0 eq) were dissolved in 14.2 mL methanol. To this solution 160 mg palladium on activated charcoal (10 wt%) were added and the flask sealed with a septum. By using a balloon, hydrogen was purged through this solution 5x and afterwards a sixth balloon was left on the flask as a hydrogen reservoir. The reaction mixture was stirred overnight at rt. The solution was then filtered over Celite and reduced *in vacuo*. The obtained product was dried in the vacuum oven (40 °C) overnight.

Yield: 1.132 g, 2.155 mmol (89%), yellow liquid.

Molecular formula: C₂₉H₅₈N₄O₄.

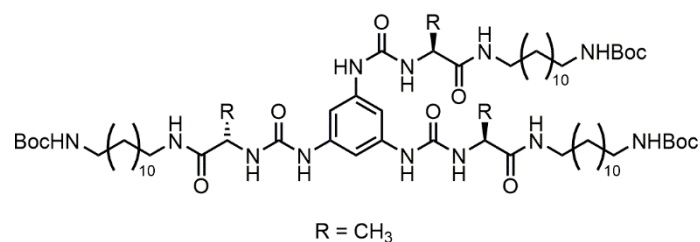
¹H-NMR (300 MHz, d₆-DMSO, 298 K): δ [ppm] = 7.92 (q, J = 7.1, 5.8 Hz, 2H, NH), 6.76 (t, J = 5.3 Hz, 1H, NH), 4.27 (q, J = 7.3 Hz, 1H, CH), 4.11 (q, J = 5.4 Hz, 1H, CH), 3.01 (dt, J = 13.6, 6.9 Hz, 2H, CH₂), 2.87 (q, J = 6.6 Hz, 2H, CH₂), 1.96 (s, 2H, NH₂), 1.69 (dd, J = 14.5, 6.5 Hz, 1H, CH), 1.60 – 1.46 (m, 1H, CH), 1.46 – 1.29 (m, 17H, CH₂, CH₃), 1.22 (s, 16H, CH₂), 0.85 (dd, J = 9.6, 6.5 Hz, 12H, CH₃).

ESI-ToF-MS (positive mode, acetonitrile) (m/z): calculated for [M+Na]⁺: 549.4350; found: 549.4616.

Benzenetrispeptide building blocks

With one amino acid per arm

[B][U-Ala]₃[C₁₂]₃ Boc-protected – **12a**



12a

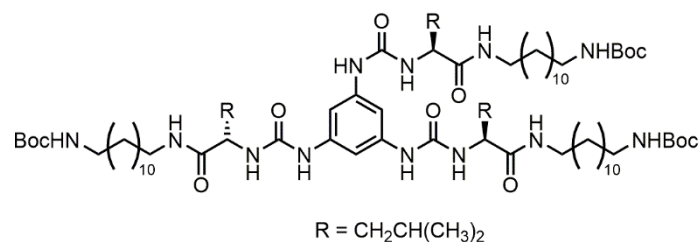
Under argon, 5.5 mL of a 0.19 M solution of benzene-1,3,5-tricarbonyl azide **10** (0.3 g, 1.052 mmol, 1.0 eq) in toluene was heated to 100 °C to *in situ* generate 1,3,5-triisocyanatobenzene **11**. After 1 h, the temperature was reduced to 90 °C, as no more N₂ gas development was visible. To this, a solution of 1.251 g H₂N- L-Ala-C(O)NH-C₁₂-NH-Boc **8a** (3.37 mmol, 3.2 eq) in 15 mL anhydrous toluene was added dropwise and the reaction mixture stirred overnight at 90 °C. Afterwards, the solvent was removed under reduced pressure and the residue suspended in THF (starting materials: soluble; product: insoluble). The suspension was then centrifuged (3 min, 8,000 rpm) and the supernatant discarded. The precipitate was two more times suspended in THF and centrifuged in order to fully remove residual starting materials. The obtained product was dried in the vacuum oven (40 °C) overnight.

Yield: 0.104 g, 0.079 mmol (8%), white solid.

Molecular formula: C₆₉H₁₂₆N₁₂O₁₂.

¹H-NMR (300 MHz, d₆-DMSO, 298 K): δ [ppm] = 8.54 (s, 3H, NH), 7.98 (t, J = 5.3 Hz, 3H, NH), 7.07 (s, 3H, CH_{aromat}), 6.75 (t, J = 5.4 Hz, 3H, NH), 6.28 (d, J = 8.0 Hz, 3H, NH), 4.17 (p, J = 7.1 Hz, 3H, CH), 3.11 – 2.97 (m, 6H, CH₂), 2.87 (q, J = 6.6 Hz, 6H, CH₂), 1.46 – 1.29 (m, 39H, CH₂, CH₃), 1.29 – 1.12 (m, 57H, CH₂, CH₃).

[B][U-Leu]₃[C₁₂]₃ Boc-protected – **12b**



12b

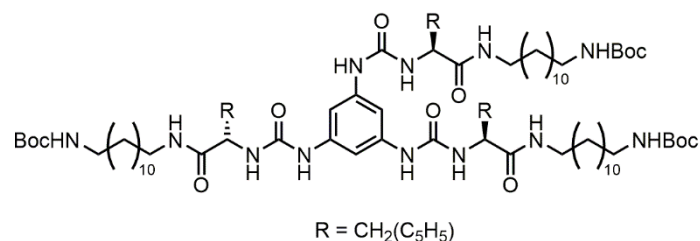
The compound was synthesised according to the procedure of compound **12a**, instead of purifying the obtained crude product via flash chromatography (SiO₂, DCM/MeOH 96.5:3.4).

Yield: 0.137 g, 24.13 mmol (17%), yellow liquid.

Molecular formula: C₇₉H₁₄₆N₁₂O₁₂.

¹H-NMR (300 MHz, d₆-DMSO, 298 K): δ [ppm] = 8.48 (s, 3H, NH), 8.04 (t, J = 5.6 Hz, 3H, NH), 7.07 (s, 3H, CH_{aromat}), 6.75 (t, J = 5.7 Hz, 3H, NH), 6.18 (d, J = 8.1 Hz, 3H, NH), 4.23 – 4.11 (m, 3H, CH), 3.13 – 2.92 (m, 6H, CH₂), 2.87 (q, J = 6.7 Hz, 6H, CH₂), 1.67 – 1.48 (m, 3H, CH), 1.46 – 1.28 (m, 39H, CH₂, CH₃), 1.29 – 1.10 (m, 48H, CH₂), 0.89 (d, J = 6.6 Hz, 18H, CH₃).

[B][U-Phe]₃[C₁₂]₃ Boc-protected – **12c**



12c

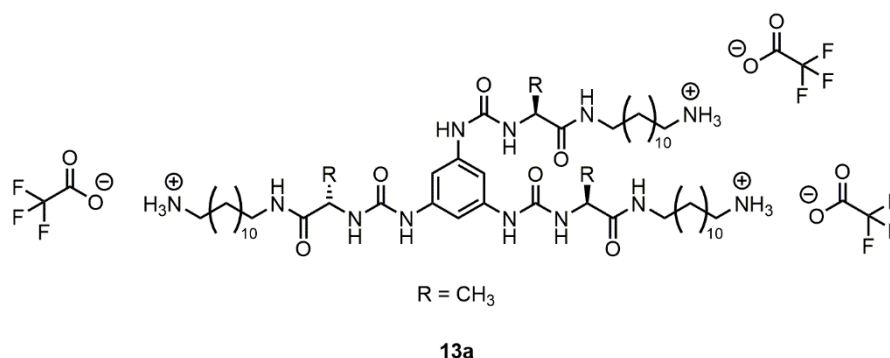
The compound was synthesised according to the procedure of compound **12a**, instead of precipitating the obtained crude product in ethyl acetate.

Yield: 0.541 g, 0.35 mmol (33%), white solid.

Molecular formula: C₈₇H₁₃₈N₁₂O₁₂.

¹H-NMR (300 MHz, d₆-DMSO, 298 K): δ [ppm] = 8.53 (s, 3H, NH), 8.00 (t, J = 5.5 Hz, 3H, NH), 7.33 – 7.11 (m, 15H, CH_{aromat}), 7.04 (s, 3H), CH_{aromat}, 6.75 (t, J = 5.4 Hz, 3H, NH), 6.22 (d, J = 7.9 Hz, 3H, NH), 4.39 (q, J = 7.2 Hz, 3H, CH), 3.13 – 2.74 (m, 18H, CH₂), 1.49 – 1.27 (m, 39H, CH₂, CH₃), 1.27 – 1.07 (m, 48H, CH₂).

[B][U-Ala]₃[C₁₂]₃ Boc-protected – **13a**



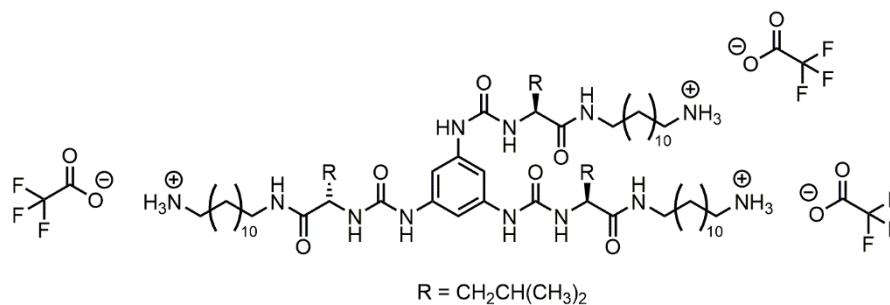
Compound **12a** (0.085 g, 0.065 mmol, 1.0 eq) was dissolved in 0.646 mL DCM. To this, 207 μ L of an 18:1:1 solution of TFA/TIPS/H₂O (TFA: 179 μ L, 2.326 mmol, 36 eq; TIPS: 26 μ L, 0.129 mmol, 2 eq; H₂O: 2.3 μ L, 0.129 mmol, 2 eq) was added dropwise and the solution stirred for 3 h at rt. Afterwards, half of the DCM volume was removed and the concentrated reaction mixture precipitated in cold diethyl ether. The suspension was centrifuged (3 min, 8,000 rpm) and the supernatant decanted. The obtained product was dried in the vacuum oven (40 °C overnight).

Yield: 0.049 g, 0.036 mmol (56%), white solid.

Molecular formula: C₆₀H₁₀₅N₁₂O₁₂F₁₉.

¹H-NMR (300 MHz, d₆-DMSO, 298 K): δ [ppm] = 8.56 (s, 3H, NH), 8.00 (t, J = 5.3 Hz, 3H, NH), 7.64 (s, 9H, NH₃), 7.07 (s, 3H, CH_{aromat}), 6.30 (d, J = 7.5 Hz, 3H, NH), 4.17 (p, J = 7.5, 6.8 Hz, 3H, CH), 3.04 (qt, J = 12.8, 6.7 Hz, 6H, CH₂), 2.86 – 2.67 (m, 6H, CH₂), 1.58 – 1.45 (m, 6H, CH₂), 1.44 – 1.34 (m, 6H, CH₂), 1.24 (s, 48H), 1.19 (d, J = 6.9 Hz, 9H, CH₃).

[B][U-Leu]₃[C₁₂]₃ Boc-protected – **13b**



13b

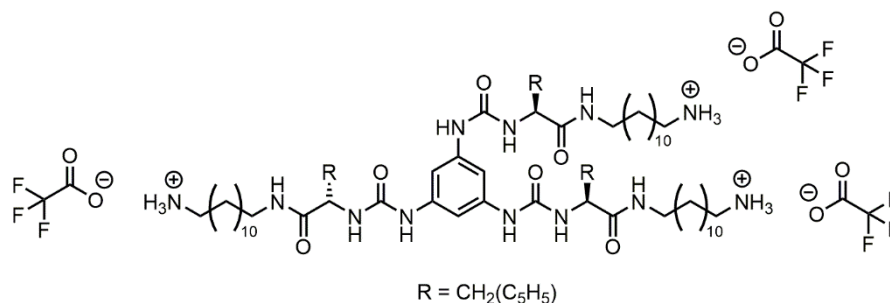
The compound was synthesised according to the procedure of compound **12a**.

Yield: 0.137 g, 0.091 mmol (100%), white solid.

Molecular formula: C₇₀H₁₂₅N₁₂O₁₂F₉.

¹H-NMR (300 MHz, d₆-DMSO, 298 K): δ [ppm] = 8.49 (s, 3H, NH), 8.05 (t, J = 5.3 Hz, 3H, NH), 7.65 (s, 9H, NH₃), 7.07 (s, 3H, CH_{aromat}), 6.19 (d, J = 8.2 Hz, 3H, NH), 4.17 (q, J = 8.1 Hz, 3H, CH), 3.18 – 2.88 (m, 6H, CH₂), 2.76 (dq, J = 12.8, 5.7 Hz, 6H, CH₂), 1.66 – 1.45 (m, 9H, CH, CH₂), 1.44 – 1.33 (m, 12H, CH₂), 1.33 – 1.14 (m, 48H, CH₂), 0.89 (d, J = 6.5 Hz, 18H, CH₃).

[B][U-Phe]₃[C₁₂]₃ Boc-protected – **13c**



13c

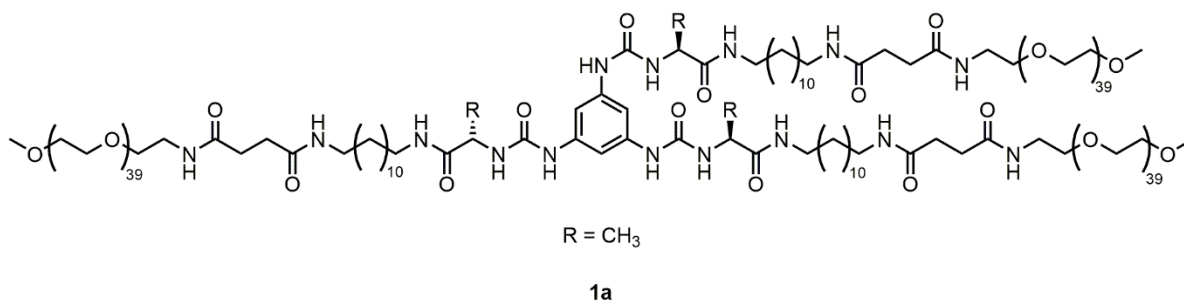
The compound was synthesised according to the procedure of compound **13a**.

Yield: 0.473 g, 0.298 mmol (92%), white solid.

Molecular formula: C₇₈H₁₁₇N₁₂O₁₂F₉.

¹H-NMR (300 MHz, d₆-DMSO, 298 K): δ [ppm] = 8.54 (s, 3H, NH), 8.02 (t, J = 5.5 Hz, 3H, NH), 7.66 (s, 9H, NH₃), 7.28 – 7.16 (m, 15H, CH_{aromat}), 7.03 (s, 3H, CH_{aromat}), 6.23 (d, J = 7.9 Hz, 3H, NH), 4.39 (q, J = 7.1 Hz, 3H, CH), 3.16 – 3.00 (m, 3H, CH₂), 3.00 – 2.86 (m, 6H, CH₂), 2.86 – 2.68 (m, 9H, CH₂), 1.59 – 1.40 (m, 6H, CH₂), 1.40 – 1.09 (m, 48H, CH₂).

[B][U-Ala]₃[C₁₂]₃[PEO_{2k}]₃ – **1a**



Compound **13a** (0.037 g, 0.027 mmol, 1.0 eq) was dissolved in 0.363 mL DMF. To this, 0.038 mL triethylamine (0.273 mmol, 10 eq) were added dropwise. After stirring at rt for 15 min, 0.174 g of MeO-PEO_{2k}-NHS ester (0.087 mmol, 3.2 eq) were added and the reaction mixture was stirred at rt overnight. Afterwards, the reaction mixture was precipitated into cold diethyl ether, the suspension centrifuged (3 min, 8,000 rpm) and the supernatant decanted. Then a mixture of diethyl ether and acetone (9:1, v:v) was added to the precipitate and the suspension exposed to sonication for 5 min in order to remove all residual DMF and some unconjugated MeO-PEO_{2k}-NHS ester. Afterwards, the suspension was again centrifuged (3 min, 8,000 rpm) and the supernatant decanted. Still remaining MeO-PEO_{2k}-NHS ester was then removed via continuous centrifugal washing using Amicon® Ultra-15 centrifugal filter units (MWCO: 10 kDa). The obtained product was then dissolved in water and lyophilised overnight.

Yield: 0.138 g, 0.021 mmol (76%), white powder.

Molecular formula: C₃₀₉H₆₀₃N₁₅O₁₃₂.

¹H-NMR (300 MHz, d₆-DMSO, 298 K): δ [ppm] = 8.54 (s, 3H, NH), 7.99 (t, J = 4.9 Hz, 3H, NH), 7.87 (t, J = 4.6 Hz, 3H, NH), 7.75 (t, J = 4.7 Hz, 3H, NH), 7.07 (s, 3H, CH_{aromat}), 6.29 (d, J = 7.6 Hz, 3H, NH), 4.18 (q, J = 7.3 Hz, 3H, CH), 3.79 – 3.69 (m, 6H, CH₂), 3.50 (s, 468H, PEO), 3.23 (s, 9H, CH₃), 3.21 – 3.12 (m, 6H, CH₂), 3.12 – 2.92 (m, 6H, CH₂), 2.27 (s, 12H, CH₂), 1.48 – 1.29 (m, 12H, CH₂), 1.29 – 1.12 (m, 48H, CH₂).

Elemental analysis: calculated: C: 55.88; H: 9.15; N: 3.16; found: C: 56.09; H: 9.07; N: 3.27.

MALDI-ToF-MS (positive mode, CHCA) (m/z): calculated for [C₃₀₉H₆₀₃N₁₅O₁₃₂K]⁺: 6679.9272; found: 6677.421.

SEC (DMAc + 0.21 wt.% LiCl): M_n = 7,300 g mol⁻¹; M_w = 7,800 g mol⁻¹; Đ = 1.07.

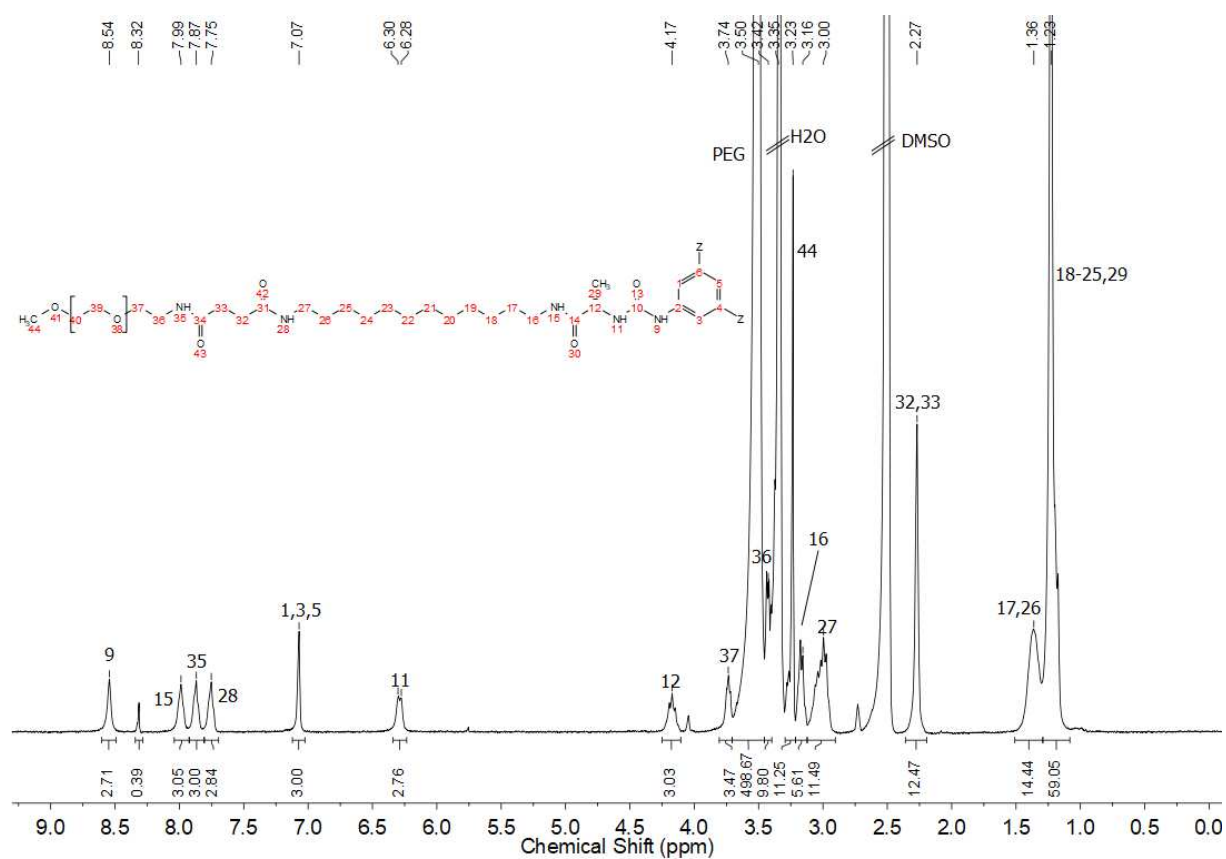


Figure S 1: ^1H -NMR spectrum of **1a** measured in d_6 -DMSO. As all three benzene substituents are the same, two of them were omitted for reasons of clarity and abbreviated as “Z”.

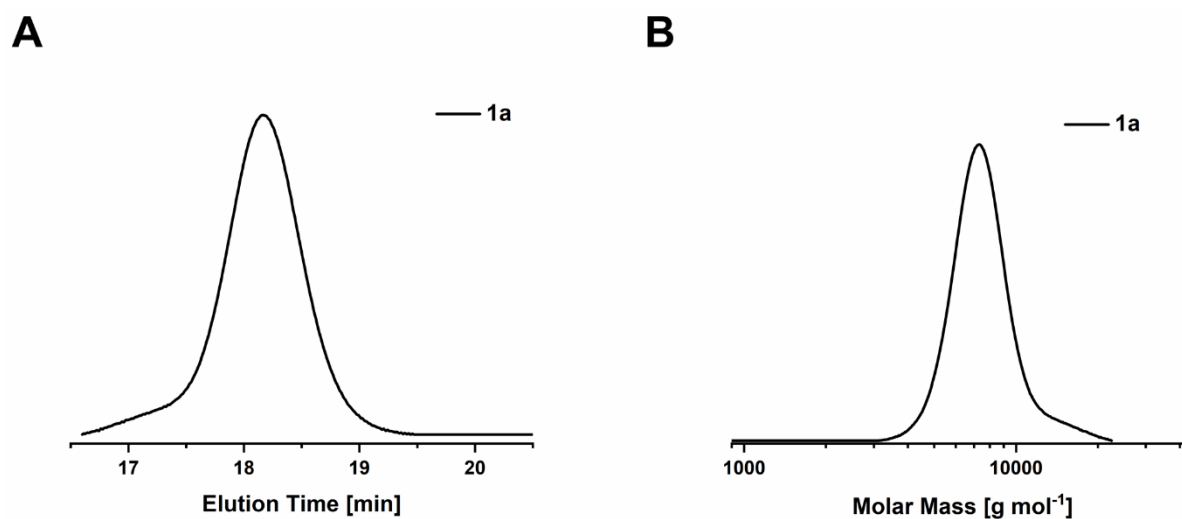
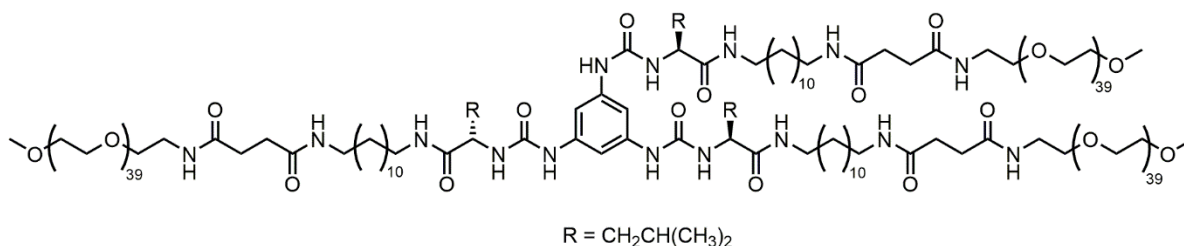


Figure S 2: SEC traces of **1a** recorded in DMAc (+0.21 wt% LiCl; 25 °C, RI, detection, PEO-Standard). A) Elution profile, B) Molar Mass distribution.

[B][U-Leu]₃[C₁₂]₃[PEO_{2k}]₃ – **1b**



1b

The compound was synthesised according to the procedure of compound **1a**.

Yield: 0.189 g, 0.028 mmol (82%), white powder.

Molecular formula: C₃₁₈H₆₂₁N₁₅O₁₃₂.

¹H-NMR (300 MHz, d₆-DMSO, 298 K): δ [ppm] = 8.47 (s, 3H, NH), 8.10 – 7.98 (m, 3H, NH), 7.87 (t, J = 6.1 Hz, 3H, NH), 7.75 (t, J = 5.7 Hz, 3H, NH), 7.07 (s, 3H, CH_{aromat}), 6.17 (d, J = 8.0 Hz, 3H, NH), 4.25 – 4.09 (m, 3H, CH), 3.79 – 3.69 (m, 6H, CH₂), 3.65 – 3.45 (m, 468H, PEO), 3.23 (s, 9H, CH₃), 3.17 (q, J = 5.9, 5.4 Hz, 6H, CH₂), 2.98 (q, J = 6.5 Hz, 6H, CH₂), 2.27 (s, 12H, CH₂), 1.67 – 1.50 (m, 3H, CH), 1.46 – 1.29 (m, 12H), 1.30 – 1.13 (m, 48H, CH₂), 0.89 (d, J = 6.4 Hz, 18H, CH₃).

Elemental analysis: calculated: C: 56.44; H: 9.25; N: 3.19; found: C: 56.56; H: 9.33; N: 3.05.

MALDI-ToF-MS (positive mode, CHCA) (m/z): calculated for [C₃₁₈H₆₂₁N₁₅O₁₃₂Na]⁺: 6790.0751; found: 6789.990.

SEC (DMAc + 0.21 wt.% LiCl): M_n = 6,900 g mol⁻¹; M_w = 7,500 g mol⁻¹; Đ = 1.08.

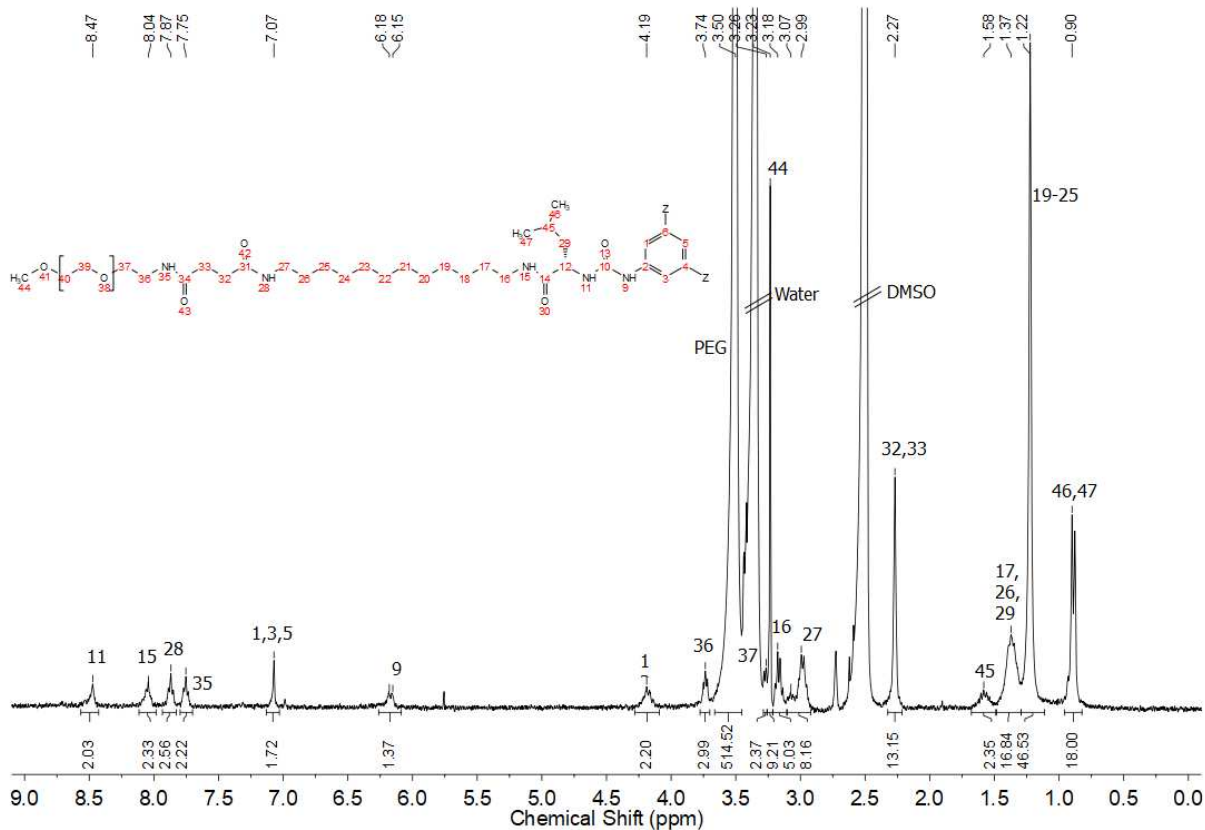


Figure S 3: ^1H -NMR spectrum of **1b** measured in d_6 -DMSO. As all three benzene substituents are the same, two of them were omitted for reasons of clarity and abbreviated as “Z”.

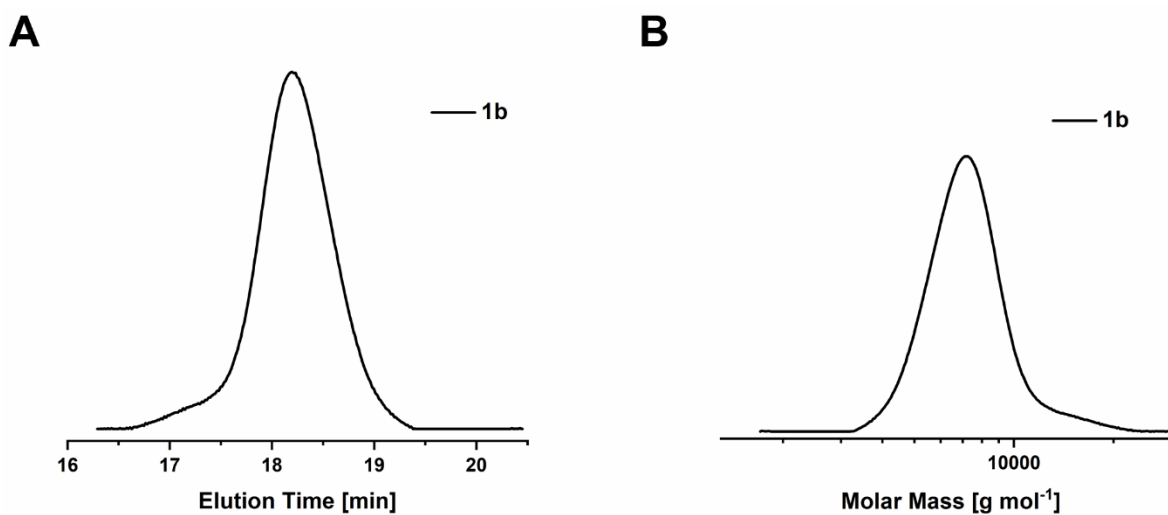
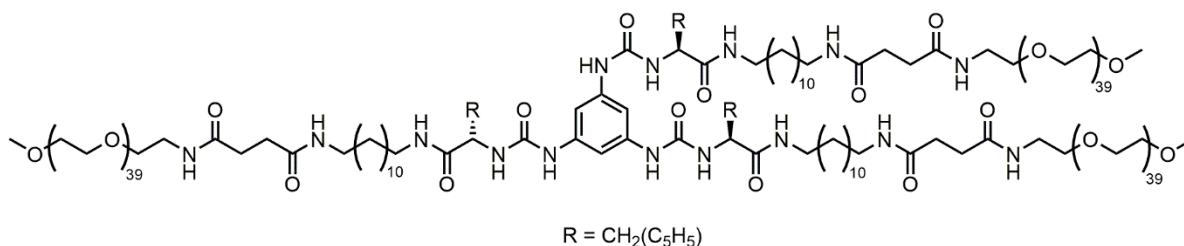


Figure S 4: SEC traces of **1b** recorded in DMAc (+0.21 wt% LiCl; 25 °C, RI, detection, PEO-Standard). A) Elution profile, B) Molar Mass distribution.

[B][U-Phe]₃[C₁₂]₃[PEO_{2k}]₃ – **1c**



1c

The compound was synthesised according to the procedure of compound **1a**.

Yield: 0.944 g, 0.137 mmol (87%), white powder.

Molecular formula: C₃₂₇H₆₁₅N₁₅O₁₃₂.

¹H-NMR (300 MHz, d₆-DMSO, 298 K): δ [ppm] = 8.52 (s, 3H, NH), 8.06 – 7.95 (m, 3H, NH), 7.91 – 7.82 (m, 3H, NH), 7.80 – 7.70 (m, 3H, NH), 7.33 – 7.10 (m, 15H, CH_{aromat}), 7.03 (s, 3H, CH_{aromat}), 6.21 (d, J = 5.6 Hz, 3H, NH), 4.48 – 4.32 (m, 3H, CH), 3.78 – 3.70 (m, 6H, CH₂), 3.63 – 3.45 (m, 468H, PEO), 3.27 – 3.21 (m, 9H, CH₃), 3.21 – 3.12 (m, 6H, CH₂), 3.09 – 2.71 (m, 12H, CH₂), 2.27 (s, 12H, CH₂), 1.42 – 1.27 (m, 12H, CH₂), 1.28 – 1.08 (m, 48H, CH₂).

Elemental analysis: calculated: C: 57.17; H: 9.02; N: 3.06; found: C: 56.91; H: 8.87; N: 3.13.

MALDI-ToF-MS (positive mode, CHCA) (m/z): calculated for [C₃₂₇H₆₁₅N₁₅O₁₃₂Na]⁺: 6892.1248; found: 6889.029.

SEC (DMAc + 0.21 wt.% LiCl): M_n = 7,400 g mol⁻¹; M_w = 8,100 g mol⁻¹; Đ = 1.10.

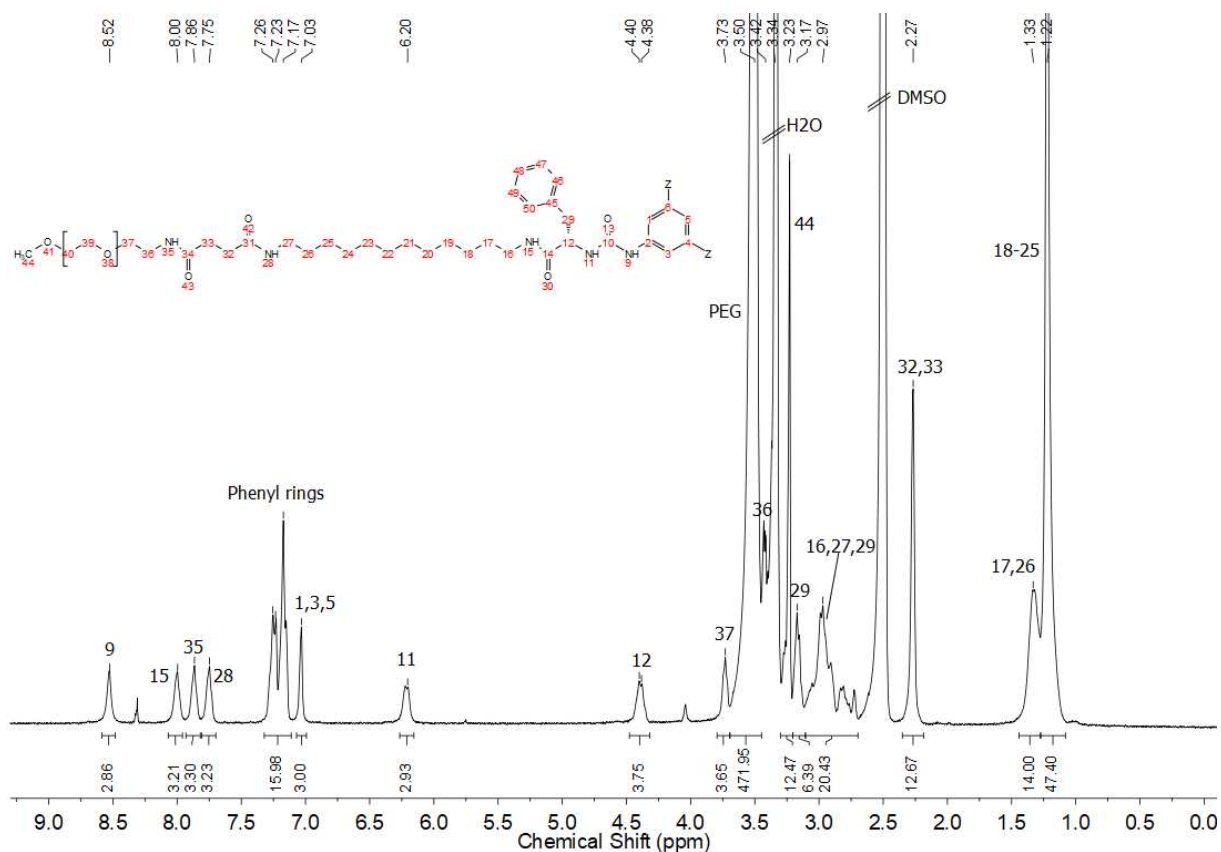


Figure S 5: ^1H -NMR spectrum of **1c** measured in d_6 -DMSO. As all three benzene substituents are the same, two of them were omitted for reasons of clarity and abbreviated as “Z”.

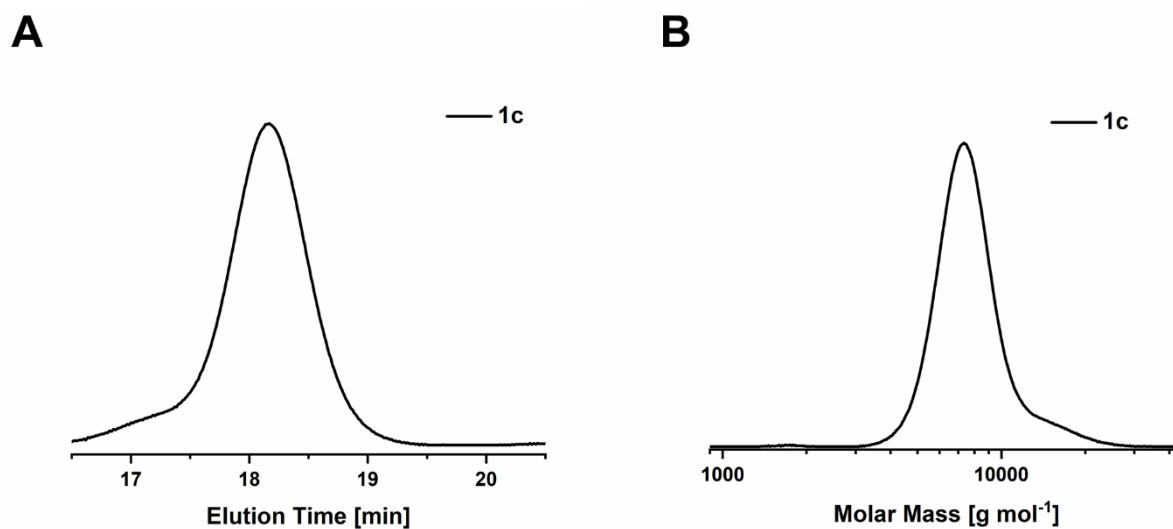
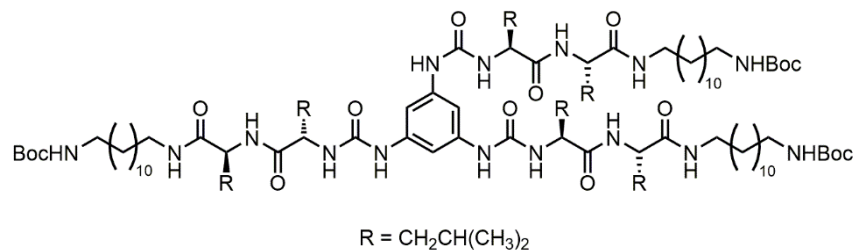


Figure S 6: SEC traces of **1c** recorded in DMAc (+0.21 wt% LiCl; 25 °C, RI, detection, PEO-Standard). A) Elution profile, B) Molar Mass distribution.

With two amino acids per arm

[B][U-Leu-Leu]₃[C₁₂]₃ Boc-protected – 16



16

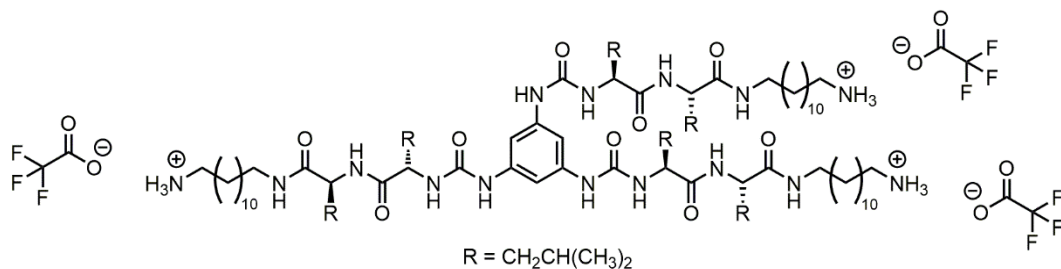
The compound was synthesised according to the procedure of compound **12a**. However, the precipitation was performed in MeOH.

Yield: 0.016 g, 0.009 mmol (3%), yellow solid.

Molecular formula: C₉₇H₁₇₉N₁₅O₁₅.

¹H-NMR (300 MHz, d₆-DMSO, 298 K): δ [ppm] = 8.50 (s, 3H, NH), 8.06 (d, J = 8.1 Hz, 3H, NH), 7.78 (t, J = 5.8 Hz, 3H, NH), 7.10 (s, 3H, CH_{aromat}), 6.74 (t, J = 5.1 Hz, 3H, NH), 6.19 (d, J = 8.2 Hz, 3H, NH), 4.34 – 4.12 (m, 6H, CH), 3.01 (dt, J = 12.3, 6.4 Hz, 6H, CH₂), 2.87 (q, J = 6.4 Hz, 6H, CH₂), 1.70 – 1.50 (m, 6H, CH₂), 1.46 – 1.41 (m, 6H, CH), 1.39 – 1.28 (m, 39H, CH₂, CH₃), 1.27 – 1.12 (m, 48H, CH₂), 0.94 – 0.74 (m, 36H, CH₃).

[B][U-Leu-Leu]₃[C₁₂]₃ Boc-deprotected – 17



17

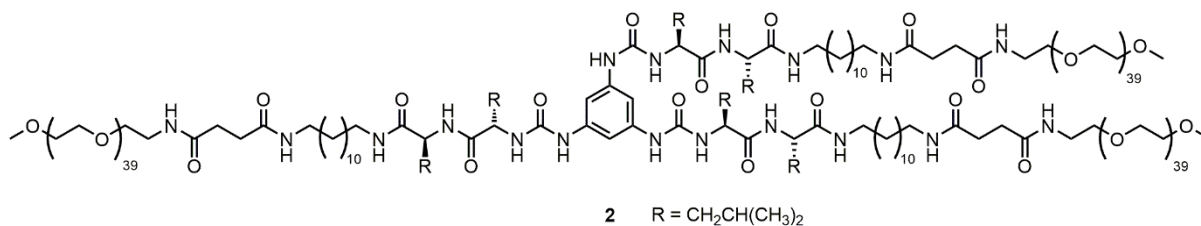
The compound was synthesised according to the procedure of compound **13a**.

Yield: 2 mg, 0.001 mmol (14%), white solid.

Molecular formula: C₈₈H₁₅₈N₁₅O₁₅F₉.

¹H-NMR (300 MHz, d₆-DMSO, 298 K): δ [ppm] = 8.51 (s, 3H, NH), 8.07 (d, J = 7.4 Hz, 3H, NH), 7.80 (d, J = 5.3 Hz, 3H, NH), 7.62 (s, 9H, NH₃), 7.10 (s, 3H, CH_{aromat}), 6.21 (d, J = 5.9 Hz, 3H, NH), 4.25 (q, J = 8.6 Hz, 6H, CH), 3.10 – 2.93 (m, 6H, CH₂), 2.82 – 2.68 (m, 6H, CH₂), 1.64 – 1.44 (m, 14H, CH, CH₂), 1.39 – 1.30 (m, 6H, CH₂), 1.30 – 1.15 (m, 48H, CH₂), 0.94 – 0.71 (m, 36H, CH₃).

[B][U-Leu-Leu]₃[C₁₂]₃[PEO_{2k}]₃ – 2



The compound was synthesised according to the procedure of compound **1a**.

Yield: 0.008 g, 0.001 mmol (95%), white powder.

Molecular formula: C₃₃₇H₆₅₆N₁₈O₁₃₅.

¹H-NMR (300 MHz, d₆-DMSO, 298 K): δ [ppm] = 8.53 (s, 3H, NH), 8.08 (d, J = 8.5 Hz, 3H, NH), 7.87 (t, J = 5.9 Hz, 3H, NH), 7.83 – 7.71 (m, 3H, NH), 7.10 (s, 3H, CH_{aromat}), 6.75 (s, 3H, NH), 6.24 (s, 3H, NH), 4.34 – 4.12 (m, 6H, CH), 3.73 (t, J = 4.4 Hz, 6H, CH₂), 3.65 – 3.43 (m, 468H, PEO), 3.23 (s, 9H, CH₃), 3.17 (dd, J = 10.9, 5.6 Hz, 6H, CH₂), 3.08 – 2.92 (m, 6H, CH₂), 2.27 (s, 12H, CH₂), 1.70 – 1.50 (m, 1H), 1.50 – 1.27 (m, 30H, CH, CH₂), 1.22 (s, 48H, CH₂), 1.01 – 0.75 (m, 36H, CH₃).

MALDI-ToF-MS (positive mode, CHCA) (m/z): calculated for [C₃₃₆H₆₅₄N₁₈O₁₃₅Na]⁺: 7129.5519; found: 7129.552.

SEC (DMAc + 0.21 wt.% LiCl): M_n = 6,000 g mol⁻¹; M_w = 6,400 g mol⁻¹; Đ = 1.07.

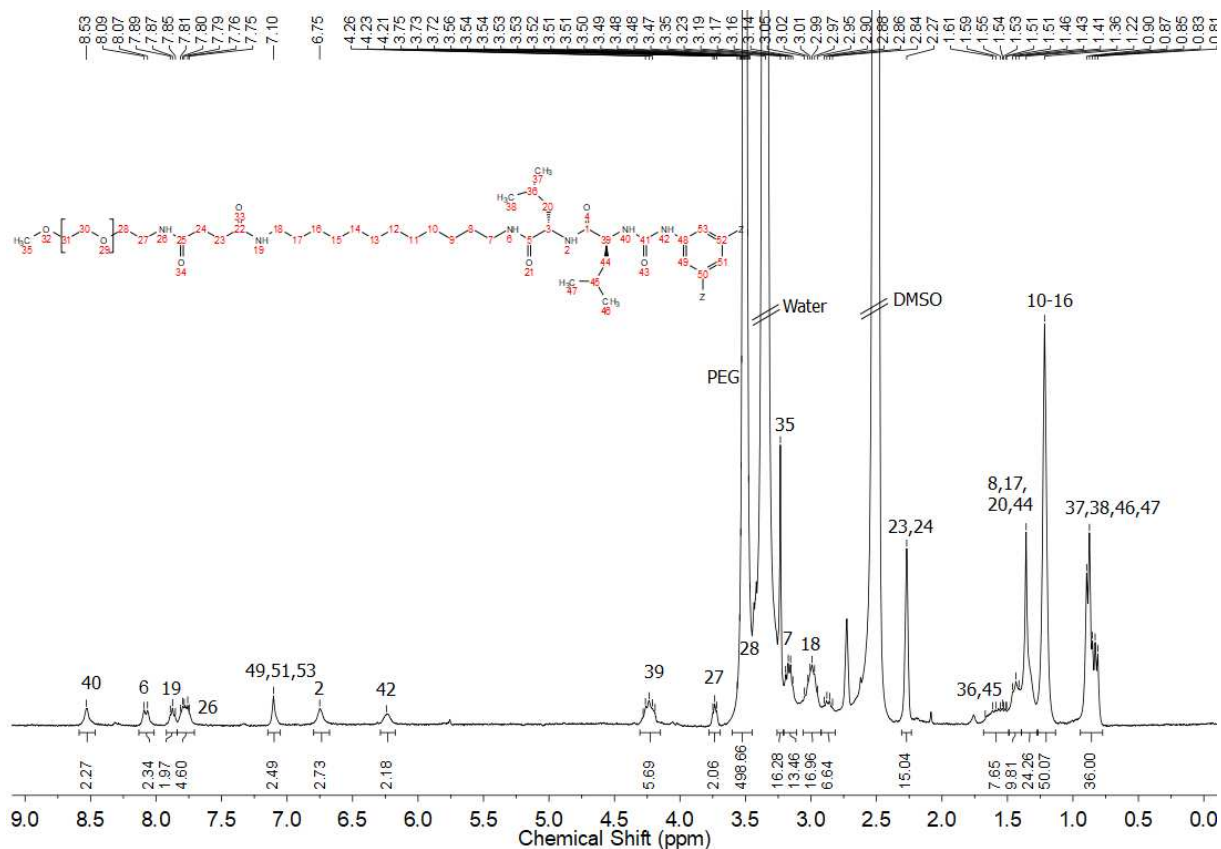


Figure S 7: ^1H -NMR spectrum of **2** measured in d_6 -DMSO. As all three benzene substituents are the same, two of them were omitted for reasons of clarity and abbreviated as “R”.

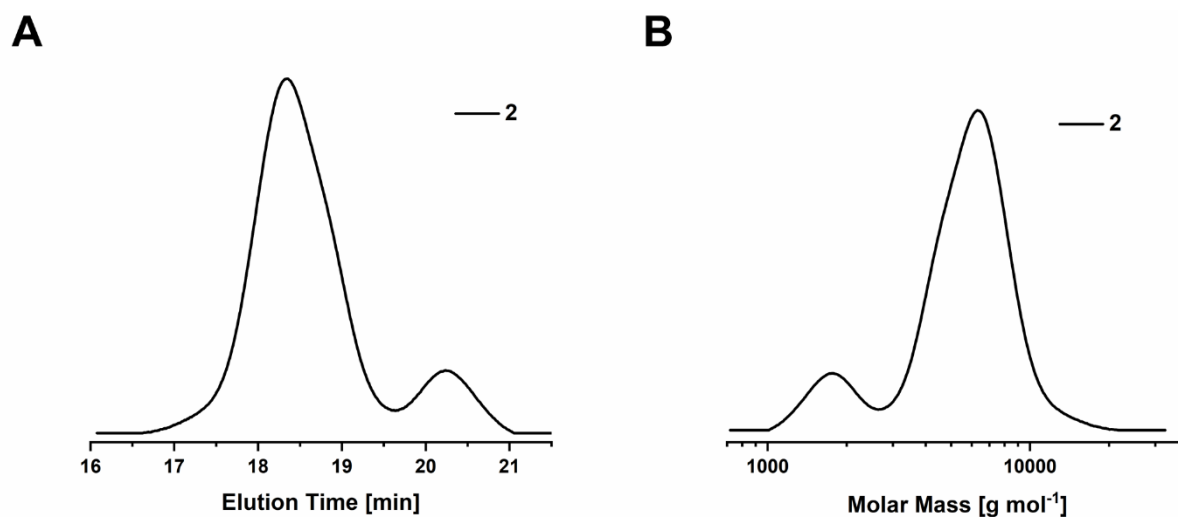


Figure S 8: SEC traces of **2** recorded in DMAc (+0.21 wt% LiCl; 25 °C, RI, detection, PEO-Standard). A) Elution profile, B) Molar Mass distribution. The peak at longer elution times/lower molar mass is caused by residual MeO-PEO-NHS from the conjugation reaction. Due to the very low yield of the reactions, a removal of this excess PEO was not attempted.

2. Characterisation

Materials and Methods. All reagents and solvents were commercial products purchased from Sigma-Aldrich, abcr, Iris BioTech, Rapp Polymere or TCI and were used without further purification. Flash chromatography was performed on a *CombiFlash* Rf 4x Module by TeledyneIsco using a UV detector for compound purity monitoring. ^1H -NMR spectra were measured with a Bruker spectrometer (300 MHz) equipped with an Avance I console, a dual ^1H and ^{13}C sample head and a 120x BACS automatic sample changer. The chemical shifts of the peaks were determined by using the residual solvent signal as reference and are given in ppm in comparison to TMS. Size-exclusion chromatography (SEC) of polymers was performed on an Agilent system (series 1200) equipped with a PSS degasser, a G1310A pump, a G1362A refractive index detector and a PSS GRAM 30 and 1000 column with DMAc (+ 0.21 wt.% LiCl) as eluent at a flow rate of 1 mL min^{-1} . The column oven was set to $40\text{ }^\circ\text{C}$ and poly(ethylene glycol) (PEG) standards were used for calibration.

2.1 Sample preparation

All investigated samples were initially dissolved in water and lyophilized afterwards, in order to obtain a fluffy powder. We observed that this powder dissolves easier in water compared to the precipitate obtained out of the PEO-conjugation reaction.

Prior to characterization, the powder was dissolved in MilliQ water at the desired concentration. For dissolution, the solution was put into the vortex and shaken at room temperature until the solution was fully clear (at least 24 h). No stirring, heating, sonication or filtration was applied to facilitate the dissolution in water, in order to keep the parameters affecting dissolution and self-assembly to a minimum. For the SAXS measurement of compound **2**, the sample had to be filtered due to very slow dissolution and the presence of undissolved aggregates. A subsequent concentration determination via lyophilization yielded a new concentration of $c = 0.8\text{ mg mL}^{-1}$. This value was also used in the calculation of M_L for **2**.

2.2 Dynamic Light Scattering (DLS)

A scattering angle of 173° was used to record intensity fluctuations of the different samples in solution. All measurements were conducted in triplicate at a temperature of 25°C in disposable macro cuvettes containing 3 mL solution and after allowing for an equilibration time of 60 s. The acquisition time was 60 s. The apparent distribution of intensity-weighted hydrodynamic radii, d_H , was obtained from the Stokes–Einstein equation:

$$d_H = \frac{kT}{3\pi\eta D} \quad (\text{Equation S1})$$

with k being the Boltzmann constant, T the temperature in units K, η the viscosity of the solvent, and D the apparent translational diffusion coefficient at the utilized concentrations. The intensity-weighted distributions were transformed into number-weighted distributions.

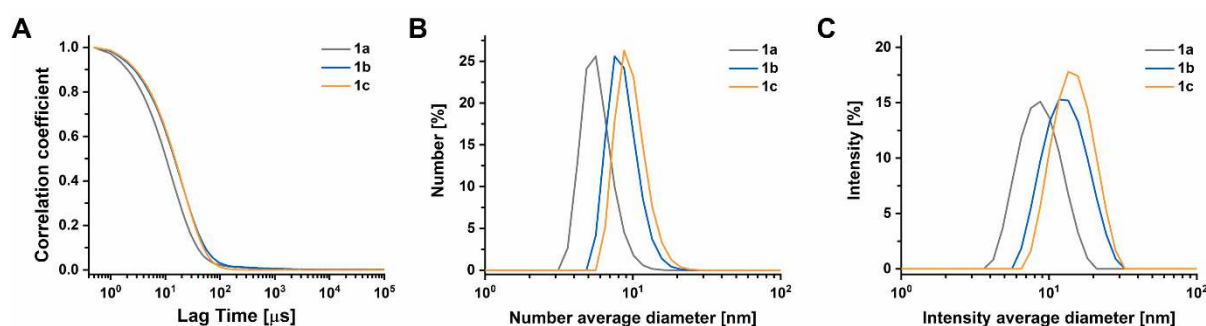


Figure S 9: A) DLS correlograms of **1a** (grey), **1b** (blue) and **1c** (orange); B) corresponding distributions of the number-weighted hydrodynamic diameter (**1a**: $d_{H,\text{number}} = 7.0 \pm 0.1$ nm; **1b**: $d_{H,\text{number}} = 8.9 \pm 0.4$ nm; **1c**: $d_{H,\text{number}} = 10.0 \pm 0.1$ nm) and C) intensity-weighted hydrodynamic diameter (**1a**: $d_{H,\text{intensity}} = 9.0 \pm 2.8$ nm; **1b**: $d_{H,\text{intensity}} = 13.5 \pm 4.4$ nm; **1c**: $d_{H,\text{intensity}} = 15.1 \pm 4.5$ nm) all at a concentration of 5 mg mL^{-1} .

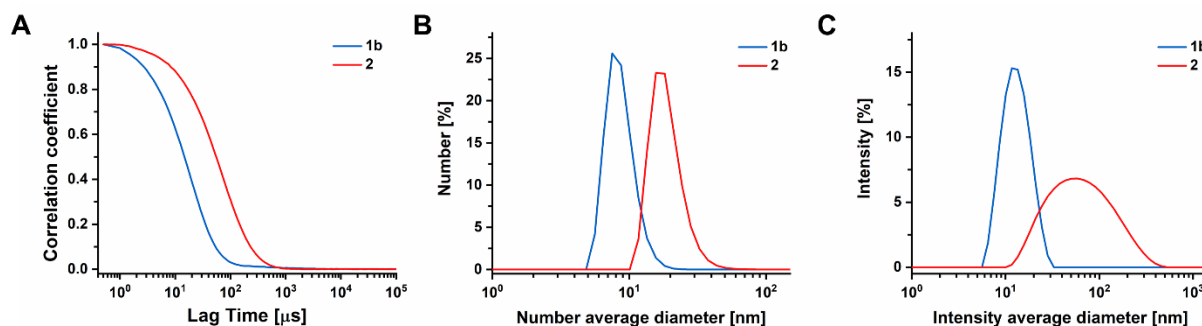


Figure S 10: A) DLS correlograms **1b** (blue) and **2** (red); B) corresponding distributions of the number-weighted hydrodynamic diameter (**1b**: $d_{H,\text{number}} = 8.9 \pm 0.4$ nm; **2**: $d_{H,\text{number}} = 17.2 \pm 1.7$ nm) and C) intensity-weighted hydrodynamic diameter (**1b**: $d_{H,\text{intensity}} = 13.5 \pm 4.4$ nm; **2**: $d_{H,\text{intensity}} = 81.9 \pm 56.5$ nm) all at a concentration of 5 mg mL^{-1} .

2.3 Small Angle X-Ray Scattering (SAXS)

Small angle X-ray scattering was performed at the beamline BL40B2 of the Super Photon Ring – 8 GeV (SPring-8) in Hyogo Prefecture, Japan. The sample-to-detector distance was 4.0 m (detector: PILATUS 2M (Dectris)) and the wavelength of the incident beam (λ) was adjusted to 0.10 nm. Each sample was measured at a concentration of 1.5 mg mL⁻¹ in water at 25 °C and exposed for 180 s.

Each recorded 2D profile was azimuthally averaged to obtain 1D profile of $I(q)$ vs. q , followed by being divided by the incident X-ray intensity. After that, the solvent scattering data (background scattering) was subtracted from the solution data to obtain the excess scattering intensity. The excess scattering intensity was normalized to be the differential scattering cross-section (absolute intensity) by using the scattering intensity of water.^[2]

The obtained reduced SAXS data was analysed with the open access software SASfit (version: 0.94.11).^[3] All parameters for the respective fits can be found in the following tables. The radius of the sphere or cylinder were fitted by applying a Gaussian distribution to the fit, which has a concentration parameter N , a width parameter σ and a mean radius parameter R .

[B][U-Ala]₃[C₁₂]₃[PEO_{2k}]₃ – 1a

Table S 1: SAXS fitting parameters for compound **1a** using a form factor for a Gaussian coil.

Parameter	Values
R_g [nm]	4.7
I_0 <i>subtracted background</i>	1.20×10^{-2} 0
η^a [nm ⁻²]	1.018×10^{-3}

^a The X-ray scattering length density (SLD) η was calculated using the SLD calculator given in SASfit.

[B][U-Leu]₃[C₁₂]₃[PEO_{2k}]₃ – **1b**

Table S 2: SAXS fitting parameters for compound **1b** using a form factor for a sphere.

Parameter	Values
R_{sphere} [nm]	3.33
σ	1.34
N	2.59×10^{-1}
<i>subtracted background</i>	1.30×10^{-4}
η^a [nm ⁻²]	1.019×10^{-3}

^a The X-ray scattering length density (SLD) η was calculated using the SLD calculator given in SASfit.

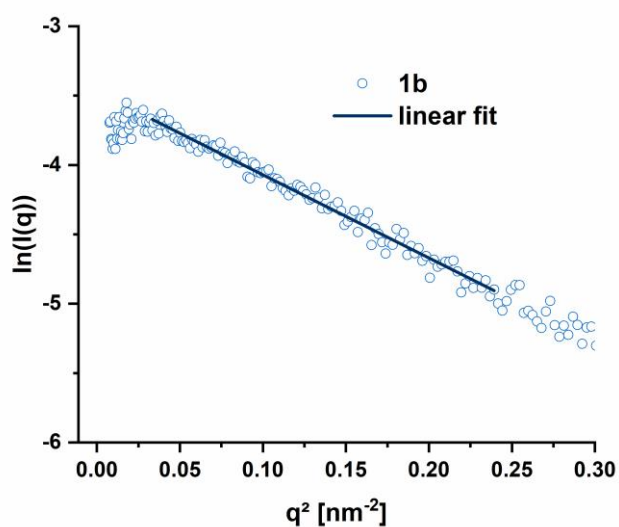


Figure S 11: Guinier plot ($\ln(I(q))$ vs. q^2) of the SAXS data of compound **1b**. The slope of the linear fit was used to determine the radius of gyration R_g (here: $R_g = 4.2$ nm) using the Guinier approximation.

[B][U-Phe]₃[C₁₂]₃[PEO_{2k}]₃ – 1c

Table S 3: SAXS fitting parameters for compound **1c** using a form factor for a sphere.

Parameter	Values
R_{sphere} [nm]	4.33
σ	1.13
N	2.29×10^{-1}
<i>subtracted background</i>	5.56×10^{-4}
η^a [nm ⁻²]	1.017×10^{-3}

^a The X-ray scattering length density (SLD) η was calculated using the SLD calculator given in SASfit.

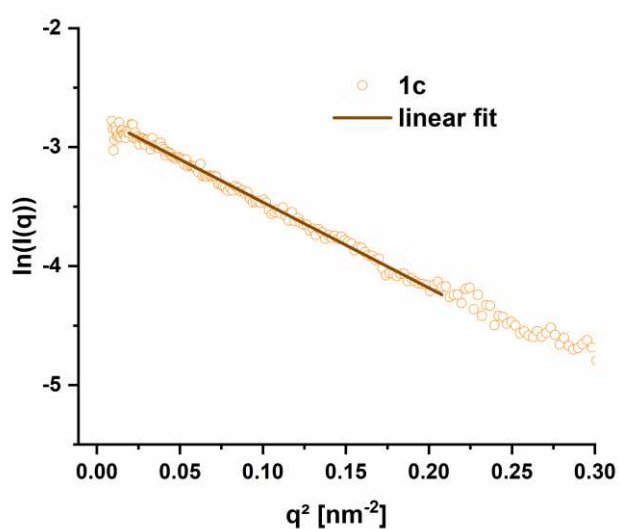


Figure S 12: Guinier plot ($\ln(I(q))$ vs. q^2) of the SAXS data of compound **1c**. The slope of the linear fit was used to determine the radius of gyration R_g (here: $R_g = 4.6$ nm) using the Guinier approximation.

[B][U-Leu-Leu]₃[C₁₂]₃[PEO_{2k}]₃ – 2

Table S 4: SAXS fitting parameters for compound **2** using a form factor for a cylinder.

Parameter	Values
R_{cylinder} [nm]	4.00
L_{cylinder}^a [nm]	150
σ	1.10
N	4.84×10^{-3}
<i>subtracted background</i>	1.50×10^{-4}
η^b [nm ⁻²]	1.02×10^{-3}

^a The length L for the cylinder fit was estimated from the lengths observed in the corresponding cryoTEM images of compound **2**. Due to the absence of a plateau at low q -values for the SAXS data, this value does not represent the real average cylinder length.

^b The X-ray scattering length density (SLD) η was calculated using the SLD calculator given in SASfit.

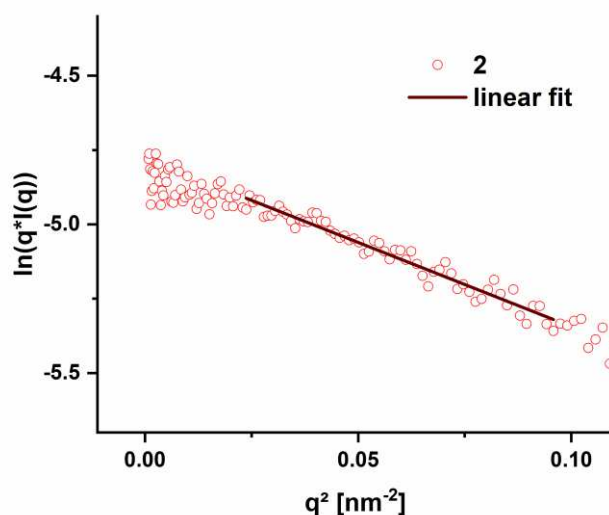


Figure S 13: Cross-sectional diameter plot ($\ln(qI(q))$ vs. q^2) of the SAXS data of compound **2**. The slope of the linear fit was used to determine the radius of gyration of the cross-section $R_{\text{c-s}}$ (here: $R_{\text{c-s}} = 4.8$ nm).

Due to the $I(q) \propto q^{-1}$ regime at low q values, the molar mass per unit of length, M_L , could be determined according to the following equation:^[4, 5]

$$\frac{I(q)}{Kc} = M_L \cdot \pi \cdot q^{-1} \quad (\text{Equation S2})$$

The plateau in the low q region yields $M_L = 1.1 \times 10^{11}$ g mol⁻¹ cm⁻¹ and hence $M_L = 1.1 \times 10^4$ g mol⁻¹ nm⁻¹ (Figure S 14).

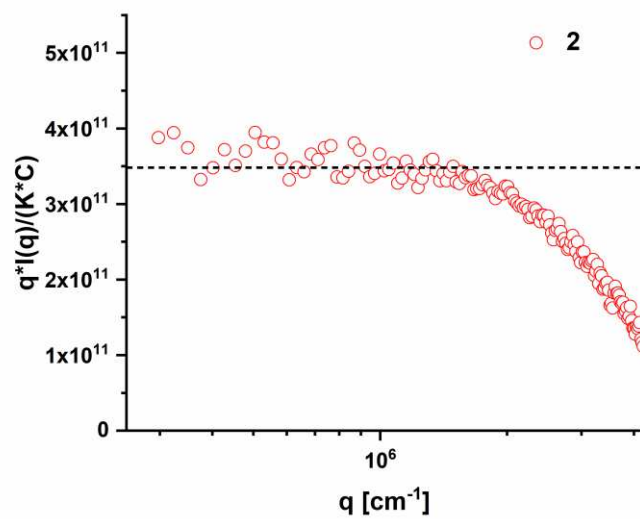


Figure S 14: Plot of $q^*I(q)/(Kc)$ against q for **2** determined by SAXS. The data points approach a plateau at low q values from which M_L can be derived according to equation S1 and yields $M_L = 1.1 \times 10^{11} \text{ g mol}^{-1} \text{ cm}^{-1}$ and hence $M_L = 1.1 \times 10^4 \text{ g mol}^{-1} \text{ nm}^{-1}$.

2.4 Cryogenic Transmission Electron Microscopy (cryoTEM)

Samples were prepared on Ar plasma treated Quantifoil grids (R2/2, Quantifoil, Germany). 8.5 μL of the solutions (3 mg mL^{-1} in H_2O) were applied onto the grids and vitrified into liquid ethane utilizing a FEI Vitrobot Mark IV system (offset: -3 mm , blotting time: 1 s). Samples were transferred into the cryo holder (Gatan 626) utilizing the Gatan cryo stage, followed by transfer into the microscope keeping the temperature below $-172 \text{ }^\circ\text{C}$ during the whole transfer and measurement process after vitrification. Measurements were performed using a FEI Technai G² 20 at an acceleration voltage of 200 kV . Images were acquired with a Mega View (OSIS, Olympus Soft Imaging Systems) or an Eagle 4k CCD camera. CryoTEM images in this study depict only specific regions of interest, which are representative for the whole sample.

[B][U-Ala]₃[C₁₂]₃[PEO_{2k}]₃ – 1a

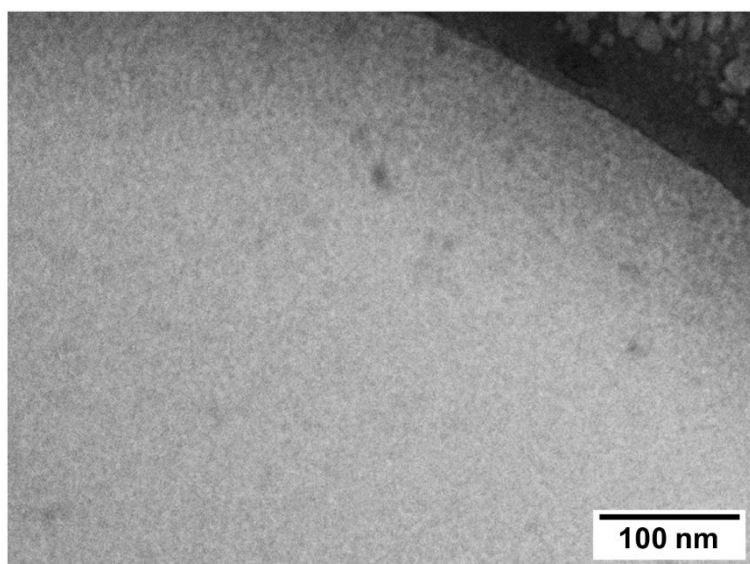


Figure S 15: cryoTEM micrographs of **1a** in water (3 mg mL^{-1}).

[B][U-Leu]₃[C₁₂]₃[PEO_{2k}]₃ – **1b**

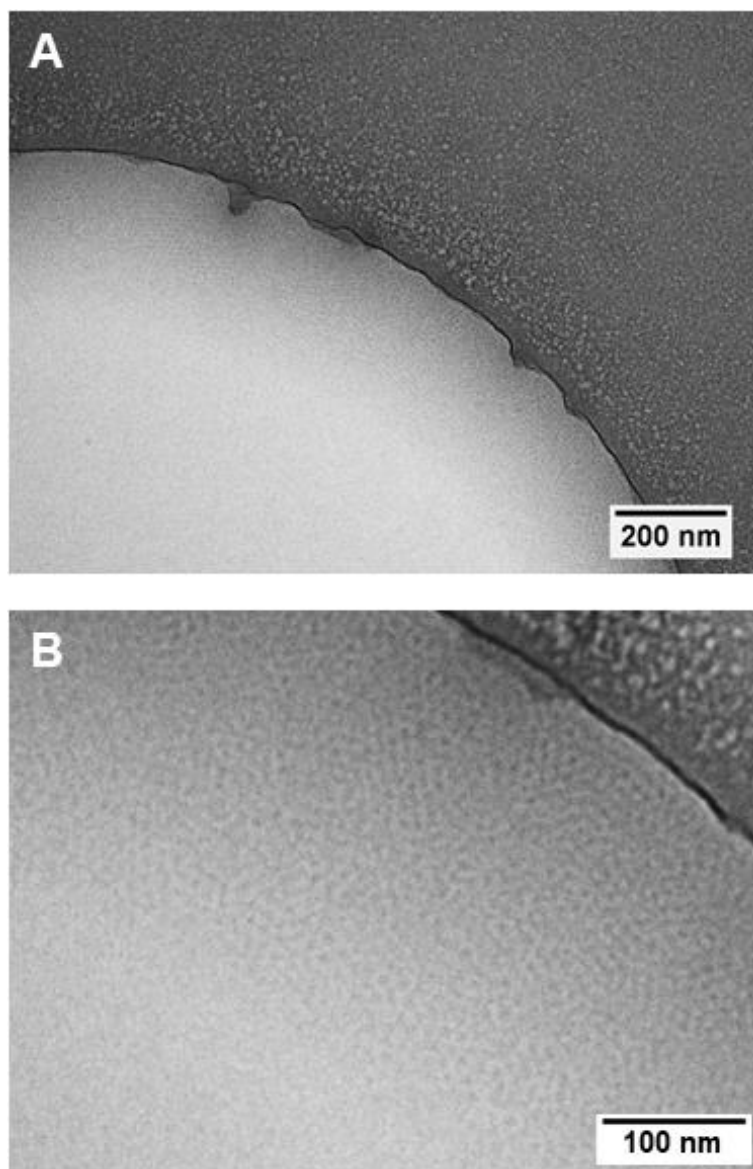


Figure S 16: cryoTEM micrographs of **1b** in water (3 mg mL⁻¹).

[B][U-Phe]₃[C₁₂]₃[PEO_{2k}]₃ - 1c

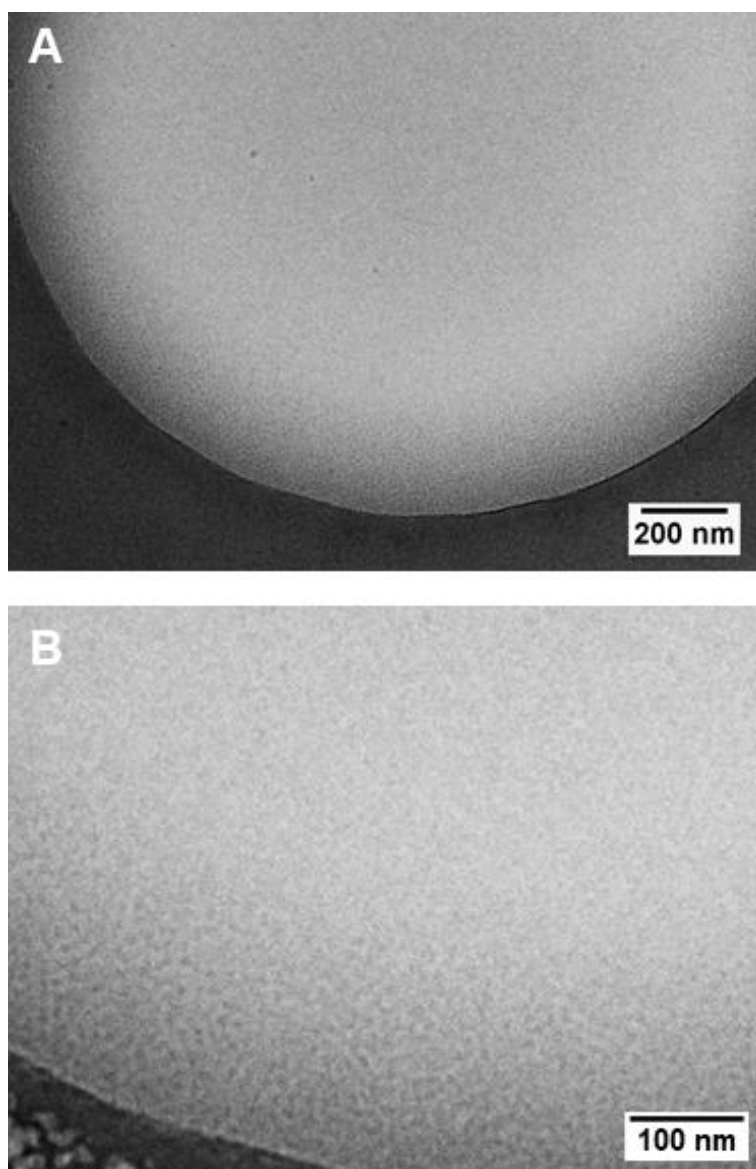


Figure S 17: cryoTEM micrographs of 1c in water (3 mg mL⁻¹).

[B][U-Leu-Leu]₃[C₁₂]₃[PEO_{2k}]₃ – 2

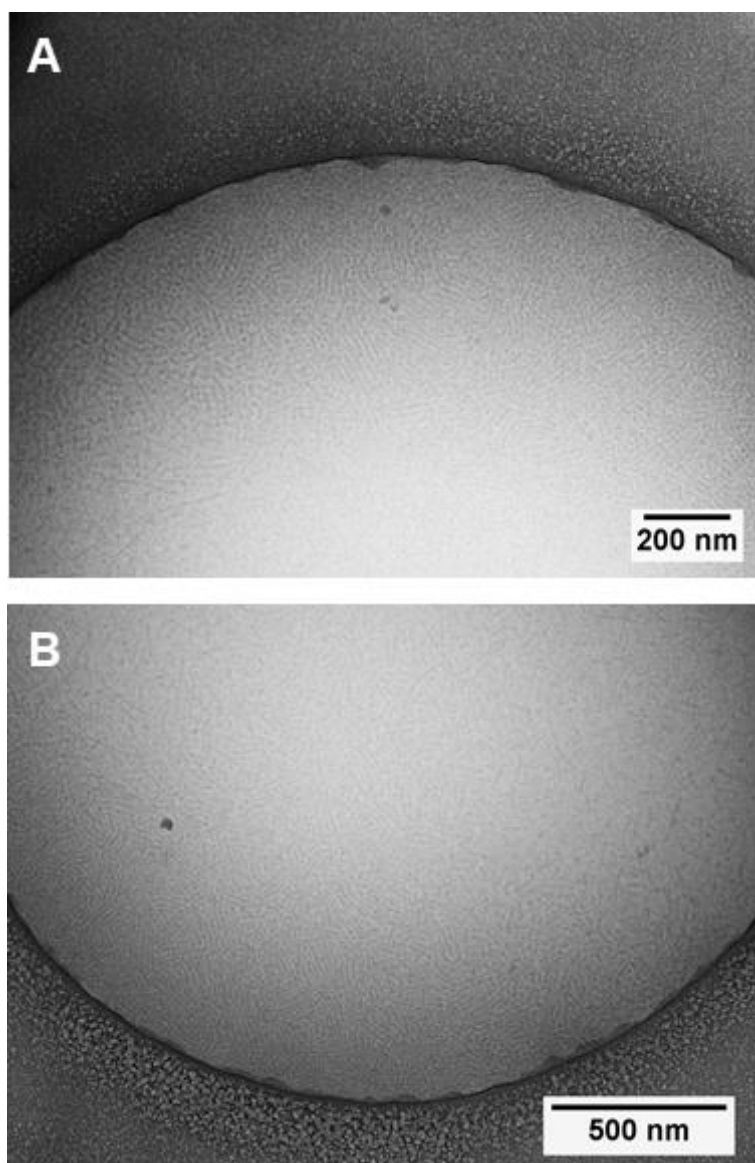


Figure S 18: cryoTEM micrographs of **2** in water (3 mg mL^{-1}). The darker spherical spots are most likely truncated cylinders that are aligned orthogonally to the cryoTEM grid as observed before.

2.5 Analytical Ultracentrifugation (AUC)

Sedimentation velocity experiments were performed with a ProteomeLab XL-I analytical ultracentrifuge (Beckman Coulter Instruments, Brea, CA). The cells, containing double-sector epon centerpieces with a 12 mm optical solution path length, were placed in an An-50 Ti eight-hole rotor. A rotor speed of 42,000 rpm was used. The cells were filled with 420 μL sample solution in water and with 440 μL of the solvent water in the reference sector. The experiments were conducted at a temperature of $T = 20\text{ }^{\circ}\text{C}$. Sedimentation velocity profile scans were recorded with the interference optics (refractive index (RI) detection). The data were evaluated via least squares boundary modelling assuming non-diffusing species, $ls-g^*(s)$.

3. References

- [1] T. Klein, H. F. Ulrich, F. V. Gruschwitz, M. T. Kuchenbrod, R. Takahashi, S. Fujii, S. Hoepfner, I. Nischang, K. Sakurai, J. C. Brendel, *Polym. Chem.* **2020**, *11*, 6763.
- [2] D. Orthaber, A. Bergmann, O. Glatter, *J. Appl. Crystallogr.* **2000**, *33*, 218.
- [3] I. Bressler, J. Kohlbrecher, A. F. Thunemann, *J. Appl. Crystallogr.* **2015**, *48*, 1587.
- [4] S. Han, E. Nicol, F. Niepceron, O. Colombani, S. Pensec, L. Bouteiller, *Macromol. Rapid Commun.* **2019**, *40*, 1800698.
- [5] S. Catrouillet, C. Fonteneau, L. Bouteiller, N. Delorme, E. Nicol, T. Nicolai, S. Pensec, O. Colombani, *Macromolecules* **2013**, *46*, 7911.

Publication P6

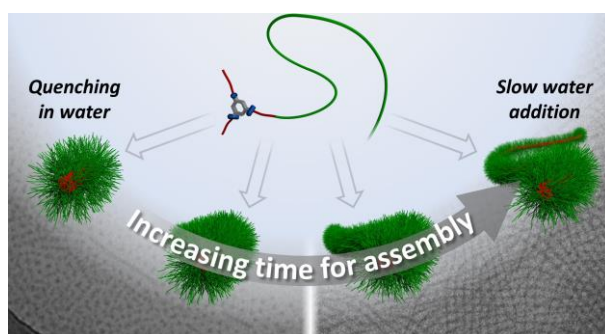
Kinetically Controlling the Length of Self-Assembled Polymer Nanofibers Formed by Intermolecular Hydrogen Bonds

F. V. Gruschwitz[‡], T. Klein[‡], M. T. Kuchenbrod, N. Moriyama, S. Fujii, I. Nischang, S. Hoepfner, K. Sakurai, U. S. Schubert, J. C. Brendel, *ACS Macro Lett.* **2021**, 837-843.

Reproduced by permission of American Chemical Society. Copyright © 20201.

The paper as well as the supporting information is available online:

doi.org/10.1021/acsmacrolett.1c00296



[‡] Equal contribution.

Kinetically Controlling the Length of Self-Assembled Polymer Nanofibers Formed by Intermolecular Hydrogen Bonds

Franka V. Gruschwitz,[‡] Tobias Klein,[‡] Maren T. Kuchenbrod, Naoto Moriyama, Shota Fujii, Ivo Nischang, Stephanie Hoepfener, Kazuo Sakurai, Ulrich S. Schubert, and Johannes C. Brendel*



Cite This: *ACS Macro Lett.* 2021, 10, 837–843



Read Online

ACCESS |



Metrics & More

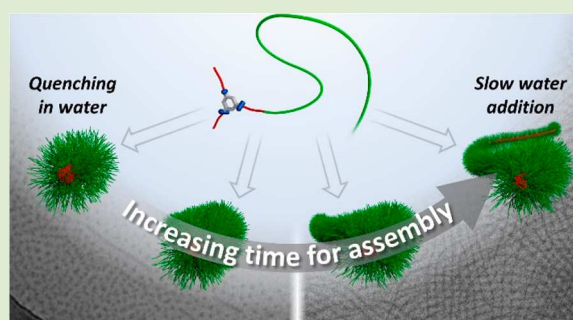


Article Recommendations



Supporting Information

ABSTRACT: Strong directional hydrogen bonds represent a suitable supramolecular force to drive the one-dimensional (1D) aqueous self-assembly of polymeric amphiphiles resulting in cylindrical polymer brushes. However, our understanding of the kinetics in these assembly processes is still limited. We here demonstrate that the obtained morphologies for our recently reported benzene tris-urea and tris-peptide conjugates are strongly pathway-dependent. A controlled transfer from solutions in organic solvents to aqueous environments enabled a rate-dependent formation of kinetically trapped but stable nanostructures ranging from small cylindrical or spherical objects (<50 nm) to remarkably large fibers (>2 μm). A detailed analysis of the underlying assembly mechanism revealed a cooperative nature despite the steric demands of the polymers. Nucleation is induced by hydrophobic interactions crossing a critical water content, followed by an elongation process due to the strong hydrogen bonds. These findings open an interesting new pathway to control the length of 1D polymer nanostructures.



Self-assembly of amphiphilic polymers in water has been the focus of research for several decades and has resulted in various complex hierarchical structures.^{1–6} However, the complexity of the assembly of natural macromolecules, that is, proteins, is yet still beyond reach, in particular, if fibrous structures are considered.⁷ While several approaches provide access to fiber- or wormlike morphologies, control of the length of such structures still remains a challenge.^{8,9} Certainly, a breakthrough in this regard was the development of the crystallization-driven self-assembly (CDSA). However, it remains the only viable method to gain real control of the fiber length, particularly in seldomly reported aqueous systems.^{10–15} Strong directional supramolecular interactions such as π - π interactions or hydrogen bonds represent an interesting and more dynamic alternative to crystallization processes in order to guide the assembly of polymeric building blocks.¹⁶ However, a similar length control in such complex assemblies, as reported for CDSA, has yet to be realized. Interestingly, the understanding of supramolecular polymerization of small molecular building blocks has taken a leap in the past decade. Several exciting systems with excellent size control have been reported based on a profound knowledge of thermodynamics and kinetics of the self-assembly process.^{17–20} A more detailed analysis of the underlying mechanism revealed the strong cooperative nature of their aggregation.²¹ The growth into large aggregates is, in this case, favored as soon as an initial nucleus is formed. It has to be mentioned that this aspect not yet implies a living character of the assembly, but

represents a major prerequisite for controlling the aggregation process.²² Interestingly, most reported systems based on hydrogen bonds appear to follow a cooperative mechanism, but a comprehensive comparison of derivatives of the well-studied benzene-1,3,5-tricarboxamides (BTA) revealed a strong dependence on the molecular structure.²³ In particular, sterically demanding groups seem to impede a cooperative self-assembly. In consequence, the implementation of a cooperative supramolecular assembly into macromolecular building blocks appears to be difficult to realize.

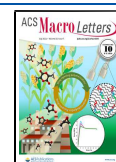
Nonetheless, the group of Rybtchinski already demonstrated that various kinetically trapped structures can be accessed based on a pathway-dependent assembly of amphiphilic perylene diimide-PEO conjugates in water, reflecting characteristics of a cooperative assembly.^{24–27} More recently, also the group of Bouteiller reported hydrogen bond-based systems, which resulted in different morphologies based on the preparation pathway.²⁸

Inspired by these studies, we intended to evaluate the impact of the self-assembly pathway on our recently reported BTU

Received: April 30, 2021

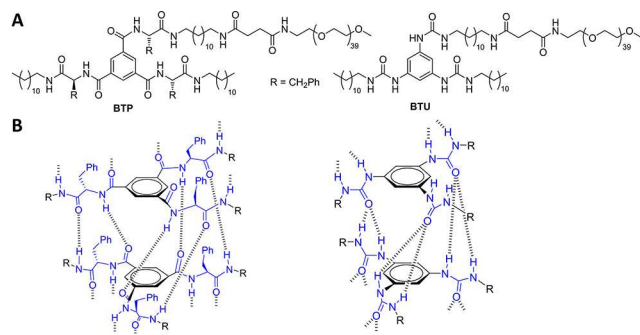
Accepted: June 15, 2021

Published: June 23, 2021



and BTP conjugates (Scheme 1). Those formed fibrous polymer nanostructures that we coined supramolecular

Scheme 1. Schematic Representation of the Chemical Structures of BTU and BTP and Their Aggregation Pattern



polymer bottlebrushes (SPBs).^{29–31} Fibrillar structures with average lengths of around 300 nm for BTU and lengths up to several μm for BTP, depending on the integrated amino acid, could be obtained upon direct dissolution in water.^{30,31} To investigate if the self-assembly of these two compounds is influenced by the conditions of the self-assembly process and thus exhibits a pathway complexity, we started here from a homogeneous solution in organic solvents (THF or DMF) to which an excess of water was added at various rates to induce the assembly process (details of the preparation procedures can be found in the Supporting Information). Starting with 1 mL h^{-1} , the cryoTEM images of BTU THF 1 mL h^{-1} and BTP THF 1 mL h^{-1} revealed the formation of long cylindrical

aggregates for both assembled compounds (Figures 1A, S7, S9, and S10, DLS: Figure S1), which is in stark contrast to the previously observed short cylinders formed upon direct dissolution in water.^{30,31}

Those new aggregates exceed, in most cases, the dimensions of the holes in the cryoTEM grid, impeding a thorough length determination. Nevertheless, at the lowest magnification, several fibers with lengths up to 2.5 μm could be observed (Figure S10). A more detailed analysis of the size distribution was achieved by asymmetrical flow field-flow fractionation (AF4) coupled to a UV- and multiangle laser light scattering (MALLS) detector.^{32–34} For BTU THF 1 mL h^{-1} , an elution profile with a peak maximum of the UV trace at approximately 80 min can be observed (Figure 1F). The structures eluting at >60 min, however, exceed the linear region of the Zimm plot extrapolation. This limits the accuracy in size and mass estimations (Figure S18). The maximum length of the structures observed in MALLS is larger than 1.5 μm , corroborating the length observed in TEM images (Figure S17).

The slow solvent switch appears to have a crucial impact on the resulting SPBs and confirms a dependence of the self-assembly process on the preparation pathway in a repeatable manner (Figures S2 and S21). Subsequently, the water addition rates were increased from 1 mL h^{-1} up to 100 mL h^{-1} . A continuous decrease of the SPB lengths was observed for BTP with increasing addition rates (Figures 1B–D and S20A), as the peak maximum shifts gradually toward smaller elution times in the AF4 (Figure 1E) and a decrease of the average fiber lengths in the cryoTEMs becomes apparent (Figures S8–S15). For the fastest addition rate of 100 mL h^{-1} ,

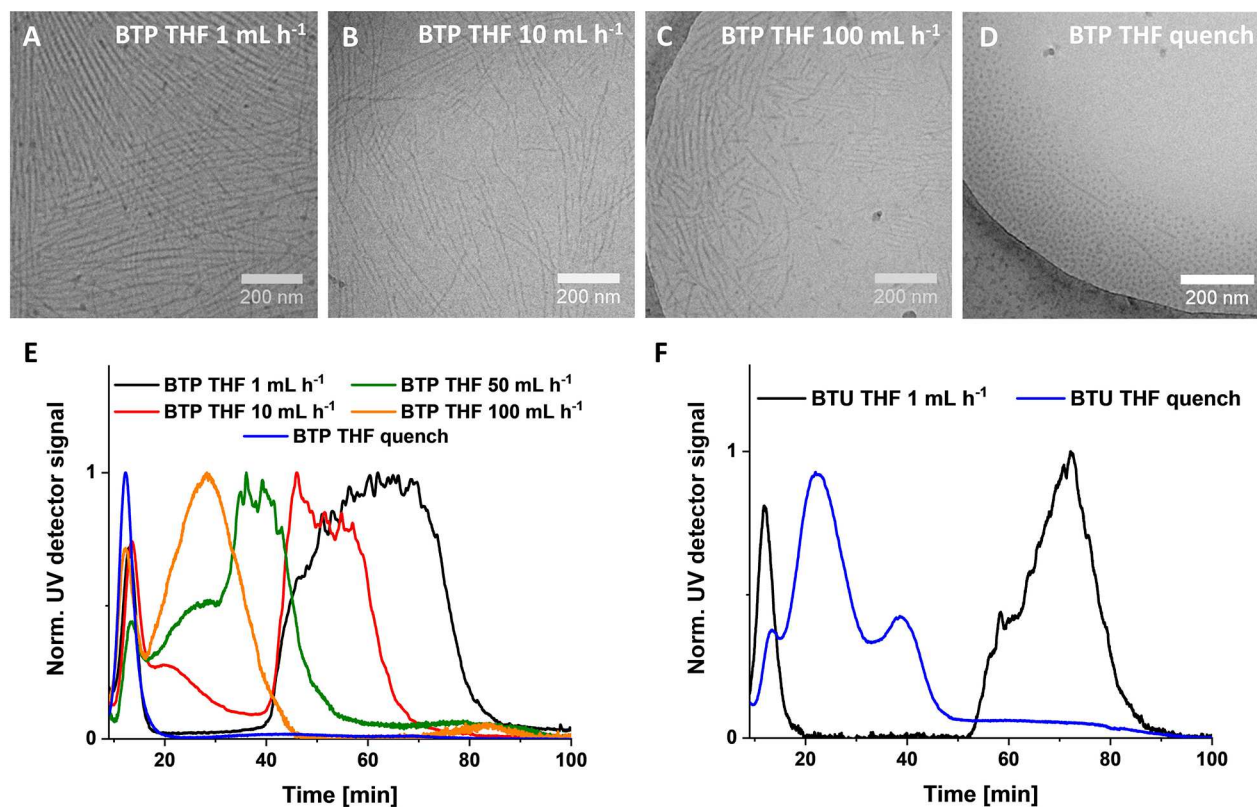


Figure 1. cryoTEM images of (A) BTP THF 1 mL h^{-1} , (B) BTP THF 10 mL h^{-1} , (C) BTP THF 100 mL h^{-1} , and (D) BTP THF quench ($c = 1 \text{ mg mL}^{-1}$). AF4-UV traces at 280 nm of BTP THF (E) and BTU THF (F). The injection peaks were omitted for reasons of clarity.

significantly smaller structures with an average R_g of 34 nm were obtained (Figure S20B). In an extreme case, the THF solution was rapidly quenched into an excess of water (BTP THF quench), which repeatedly resulted in the formation of almost exclusively spherical structures besides a few larger fibers (Figures 1D and S19C). This result was confirmed by AF4 measurements, as mostly oligomers were detected at very low elution times, while the number of the few larger structures seen in the TEM images is too low to be distinguished from the baseline (Figure 1E). This systematic decrease of lengths with increasing rate of water addition exemplifies the significant impact of kinetics on the structure formation. In the case of BTU THF, a similar trend was observed. However, the different addition rates did not affect the size of the structures in the same way as found for BTP (Figure S20C), as in all cases still rather large structures were observed, indicated by the minor shift of elution times in AF4 measurements compared to BTU THF 1 mL h^{-1} . We relate this difference to a more rapid growth of the BTU sample, which is further exemplified in the quenching experiment. Even this rapid quenching in water (BTU THF quench, Figures 1F, S8, and S19) resulted in the formation of cylinders with a length of around 100 nm and thus significantly larger structures than the ones found for BTP. The very fast aggregation for BTU further appears to be very sensitive to subtle variations in the quenching procedure, limiting the repeatability of the results (Figure S19A,B).

We subsequently monitored the temporal stability of several BTP and BTU assemblies and even mixtures thereof by DLS and AF4 to verify that the resulting structures are kinetically trapped in water. None of the samples showed any significant changes over time periods of up to one year (Figures S3 and S22–S24), indicating the long-term stability of the structures. Interestingly, all samples revealed the presence of small oligomers or potential unimers next to the considerably larger supramolecular aggregates. As the presence of non-aggregated building blocks is indicative of a cooperative self-assembly mechanism, we aimed to investigate, if the assembly into SPBs proceeds via a nucleation-elongation process. Hereby, we expected that aggregate formation occurs rapidly when exceeding a certain water threshold.^{8,35–38} To this end, we monitored the aggregate formation with increasing water content by DLS. For both BTU THF and BTP THF, the derived count rate rapidly rises at 37 v% or 50 v% water content, respectively (Figure 2A,B), indicative of a cooperative nature of the assembly and a nucleation-elongation process.³⁵ Hence, even subtle molecular variations can have an impact on the onset of the cooperative self-assembly process.²³ Below this threshold, hardly any change in the count rate can be observed. For both compounds, a decrease in the count rate was observed for high water contents due to increasing dilution upon water addition. The characteristic immediate aggregate formation can also be observed for BTP comprising other amino acids such as alanine or leucine instead of phenylalanine (Figure S6B). The shift of the critical water content is not only related to the hydrophobicity of the amino acid but also to steric demands and the initial solubility in THF.

The self-assembly behavior of the BTP compound with phenylalanine was further characterized by ^1H NMR (Figure 3A).³⁹ The main aromatic signals shift, and adjacent signals appear with increasing water addition until all signals start to vanish at water contents $>60 \text{ v}\%$. The latter is clearly reflecting the previously observed strong aggregation at this water

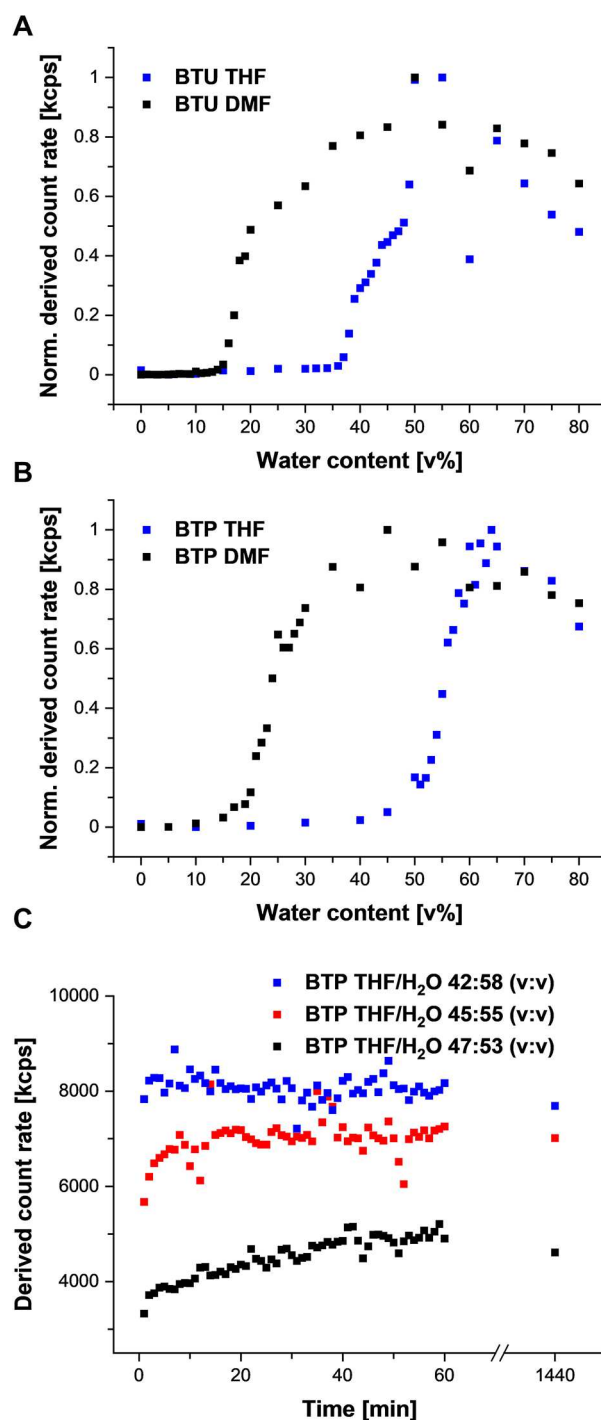


Figure 2. DLS solvent switch method experiments to determine the onset of the self-assembly of BTP and BTU into SPBs. After initial dissolution in THF or DMF, water was slowly added and the count rate was determined for each solvent mixture composition. Normalized derived count rates against the water content for (A) BTU DMF (black) and BTU THF (blue) and (B) BTP DMF (black) and BTP THF (blue). The decrease in the normalized derived count rate at high water contents is caused due to the increasing dilution. Time-dependent evolution of derived count rates for (C) BTP THF at 53, 55, and 58 v% water.

content. Interestingly, the shift and change of the aromatic signal indicates an alteration of the structure at low water content. To gain further insight into this structural change circular dichroism (CD) measurements of BTP in different

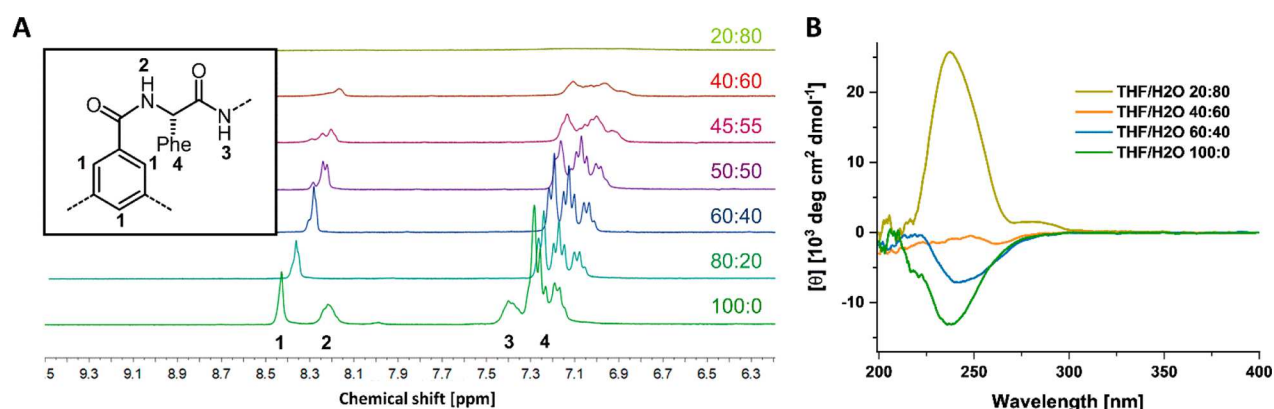


Figure 3. ^1H NMR measurements of BTP in different solvent compositions ($v:v$, THF- d_8 / D_2O), where the hydrophobic shielding of the aromatic units of BTP can be visualized by the vanishing of the respective signals with increasing D_2O content. A complete ^1H NMR spectrum of BTP can be found in Figure S28 (A). CD measurements of BTP in THF/ H_2O ($v:v$) mixtures (B).

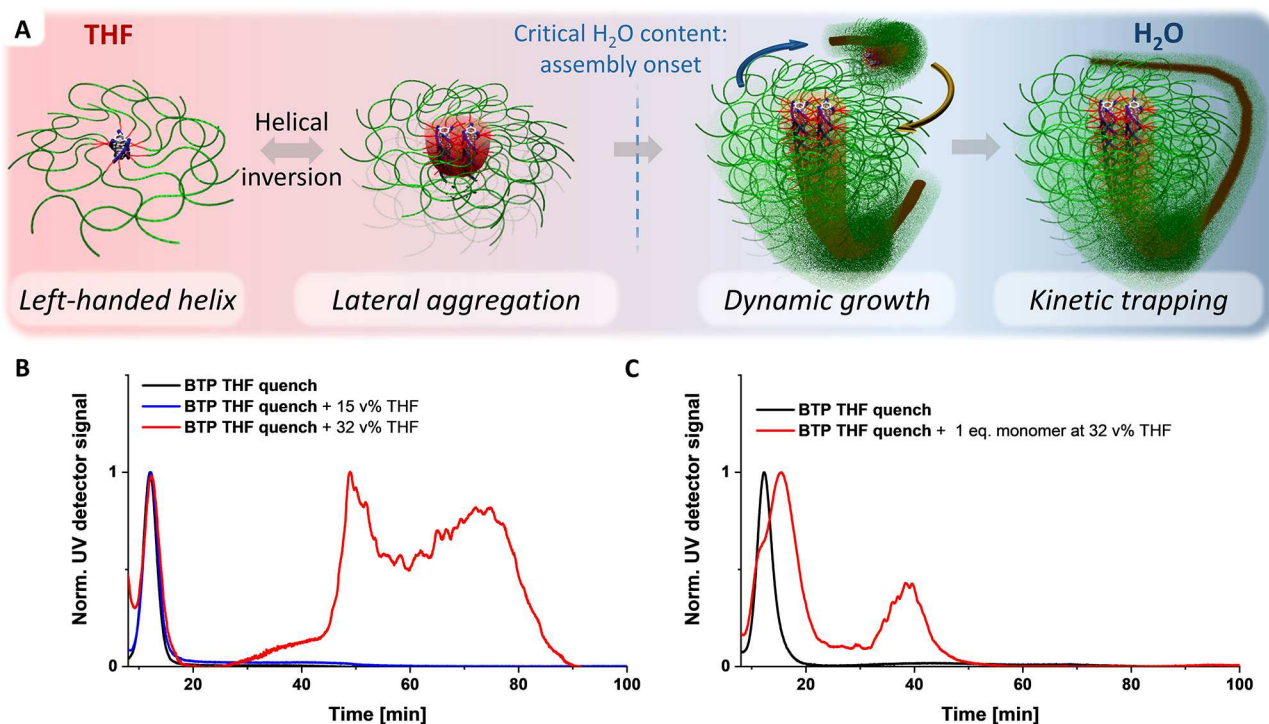


Figure 4. Schematic depiction of the self-assembly process of BTP upon changing from THF to H_2O (A). AF4-UV measurements at 280 nm of BTP THF quench after the addition of pure THF (B) and after the addition of BTP in THF/ H_2O mixtures at a final THF content of 32 v% (C). THF was removed by evaporation before measuring and the injection peaks were omitted for reasons of clarity.

THF/water mixtures were performed (Figure 3B).⁴⁰ Although no larger structures were observed in DLS and distinct signals appear in NMR, the CD spectra indicate the presence of a left-handed helix in THF.⁴¹ The hydrogen bonds, consequently, seem to induce the preaggregation of a few BTP units into small and dynamic aggregates. An increase in the water content is accompanied by an inversion of the helicity, which finally resulted in a right-handed helix at >60 v% water. This inversion appears to be a turning point during the assembly process. While the hydrogen bonds already lead to the formation of short stacks in THF, the cooperative aggregation into long fibers must be induced by the hydrophobic assembly of the BTP core unit of the amphiphilic molecule.^{42–45} This hypothesis is supported by the fact that the addition speed of water does not influence the aggregation onset (Figure S6A). Hydrophobic interactions are known for their

cooperative nature, and it appears to be the predominant driving force in this assembly process, too.⁴³ Nevertheless, the hydrogen bonds introduce the directionality needed for 1D growth once critical nuclei sizes are reached and define the local arrangement of the molecules, which is supported by the presence of the characteristic amide I and II bonds in FT-IR measurements (Figure S27).⁴⁶

A closer investigation of the final fiber structure (Figure S30) by static light scattering (SLS) and small-angle X-ray scattering (SAXS) revealed a lateral arrangement of at least two BTP moieties, which is in agreement with our previous observations for the BTU compound.³⁰ This lateral aggregation hints at a plausible explanation for the observed helix inversion. While the small stacks in THF allow a favored arrangement of the attached polymer chains according to their steric demands, the lateral aggregation at critical water content

forces the chains of the individual stacks to point at similar directions (Figure 4A). In order to maintain the hydrogen bonds, the helical structure in the individual stacks has to be rearranged during the hydrophobic assembly, finally resulting in the right-handed helix in aqueous solution. Interestingly, this inversion of the helix was also observed in the small structures obtained during quenching (BTP THF quench), which reflects the rapid formation of the lateral aggregates, which we consider the nucleation points (Figure S26). However, the impeded growth also corroborates an early kinetic trapping preventing any further addition of unimers or further condensation of the nuclei. This trapped state was tested by further addition of a THF solution of the BTP compound. In a living system, a seeded growth of the small aggregates is expected. However, no elongation of our assembled structures was observed at an overall low THF content (~10 v%), which corroborates the trapped state of the aggregates preventing a further growth (Figure S25A). Instead, the added BTP units seemed to nucleate rapidly and become quenched in their growth again. The situation changed, when the THF content was increased (32 v% THF). A partial shift of the main population became apparent which correlates with our expectations for a seeded growth (Figure 4B). However, much larger structures were formed in addition, indicating a competing aggregation process. Indeed, the addition of pure THF to the sample BTP THF quench also resulted in a size increase when reaching 32 v% of THF, as observed in DLS and AF4 measurements (Figures 4C and S5). While the system is kinetically trapped at lower THF content, the dynamics of the system seem to increase at this stage and enable further growth by aggregation, resulting in the rather broad distribution of the sample. Addition of more THF (≥ 58 v%) finally resulted in the disassembly of all aggregates (Figure S5). The occurrence of increased dynamics at these conditions rule out a controlled living growth as seen for small supramolecular building blocks or in CDSA.^{9,22,47,48} At lower THF content, the growth at the chain ends is impeded, which we assume to be related to an increased shielding from the water and a limited accessibility for further addition of unimers, as it was reported previously.²⁵ Similar observations were made for BTU upon sequential monomer additions (Figure S25B,C). In this case, the dynamics appear to be further enhanced as much larger structures were formed at increasing THF content, which exceeded even the limits of the AF4 setup. The fast dynamics are in good agreement to the rather fast aggregation of BTU compared to BTP at different addition rates of water. To examine the effect of different organic solvents on the self-assembly process, we repeated the experiment with DMF, which was found to be another good solvent for both tested compounds. Unfortunately, the absorbance of DMF in the region of interest impedes a detailed analysis by CD spectroscopy. Nevertheless, the DLS studies indicated again a nucleation-elongation mechanism for BTU DMF as well as for BTP DMF (Figure 2A,B). Interestingly, both samples started to assemble at lower water contents compared to the THF samples. Similar to the different amino acids, the choice of solvent seems to play an important role concerning the assembly onset, that is, when the solvent conditions are poor enough to drive the hydrophobic assembly of the core units to form the larger structures.

Due to the rapid aggregation of BTU, we focused on BTP for further kinetic studies. To this end, the derived count rate was monitored for 1 h and again 24 h after the water addition

(Figure 2C). Reaching a water content of 53 v% for BTP THF, the derived count rate continuously increased for up to 1 h, but then remained constant. The high initial value indicates that the assembly after the addition of a critical amount of water proceeds almost instantaneously (the short time period for addition and starting the measurement has to be kept in mind), followed by a slower growth of the SPBs over a short time of 60 min. When reaching 55 v% of water, only a slight increase was visible for the first 10 min, whereas for 58 v% water, the count rates remained constant, thus, indicating that no further assembly processes occur. From the DLS data it is not clear if the increase in count rate at 55 v% and 58 v% water stems from prolonging the present SPBs or from the formation of new SPBs, but it corroborates the previously detected dynamic nature of the system, which seems to be impeded at water contents >58 v%. For BTP DMF, the assembly seems to proceed faster and dynamics appear to stop earlier, as no increase in the derived count rate can be observed within the first hour after the water addition, even for the early stages of the solvent switch (Figure S4).

To exclude the presence of any other intermediate structures formed in the course of the assembly and verify our theory of a nucleation–elongation mechanism, further SAXS studies were performed at different stages of the assembly (Figure 5). As only a limited number of steps could be monitored, we had to slightly adapt the assembly procedure, changing from addition of pure water to the addition of a solvent mixture in the first steps. This should prevent any unwanted growth at the injection site, as in the preparation of these samples, no continuous addition could be realized. DMF was chosen as the starting solvent, as self-assembly sets in at a lower water content and no further time-dependent processes might interfere. No aggregates were found at 0 and 11 v% water content in the scattering profiles of the SAXS measurements. When increasing the water content to 23 v%, a scattering profile with a $I(q) \propto q^{-1}$ dependency for low q -values could immediately be observed, indicating cylindrical aggregates. Interestingly, no plateau at low q -values appeared, confirming the instant growth into large cylinders (>130 nm). Consequently, no intermediate species, such as spherical micelles, are formed and the unimers directly assemble into cylindrical SPBs. Further increase in the water content did not lead to any further significant morphological changes. Noteworthy, the cylinder radius remained constant throughout the solvent switch (Figure 5B, Table S1). As the assembly relies on a hydrophobic aggregation of the BTP core, we also tested a cylinder fit with a core–shell structure, which should resemble the structure in more detail. The obtained fit was of similar quality, although it has to be mentioned that the strong scattering of the data at high q -values might not allow an accurate determination of core and shell individually. Nevertheless, also in this case no significant increase of the cylinder radius could be observed at water contents >23 v% (Figure S29, Table S2). This consistency indicates that the lateral aggregation of the BTP moieties inside the SPBs is not changing over the course of the assembly process, which further corroborates our theory of a nucleation–elongation process.

In conclusion, an inherently strong dependency of the self-assembly of BTU and BTP on the parameters of the preparation process and their kinetic stability enabled us to adjust the length distributions of self-assembled polymer nanofibers based on BTUs and BTPs. Polymer nanofibers of

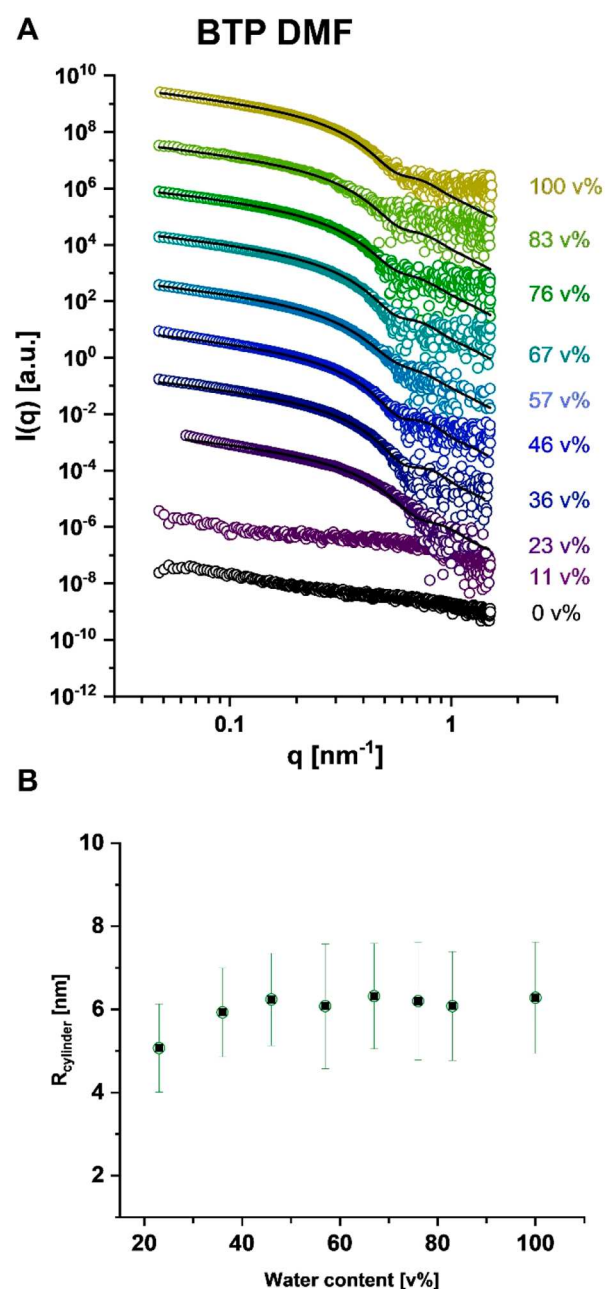


Figure 5. (A) SAXS scattering profiles of BTP DMF for different water contents (v%). The traces were shifted by multiplication for reasons of clarity. The respective solid black lines represent the best fits obtained for a cylinder. (B) Corresponding values for the radius of the cylinder obtained from fitting.

various lengths, ranging from short cylinders or nearly spherical structures to structures of several micrometers in length and high aspect ratios (>100) could be created, solely by adjusting the solvent exchange rate, which indicates a strong pathway complexity of the assembly. We identified a cooperative assembly mechanism crossing a critical water to solvent ratio, which was found to rely on the strong hydrophobic effect induced by the core unit. Following a nucleation by lateral aggregation of small oligomers, the 1D elongation process is a result of the local stacking of the units due to the directional hydrogen bonds. At high water contents, the structures become kinetically trapped, impeding any further growth, but also implementing a remarkable kinetic

stability of all different structures over extended time scales (up to one year). However, the presence of a critical amount of solvent (for v% water > nucleation point) can retain a dynamic nature that enables an extension of the fibers, but also facilitates their fragmentation and recombination. A real living assembly of these SPBs is, therefore, still beyond reach,^{9,22} but the control of the processing parameters opens a straightforward pathway to adjust the length of these 1D polymer assemblies, which has so far solely been achieved by crystallization. Our current efforts are focusing on understanding the dynamics of these systems, which might finally unveil the path to a living growth.

■ ASSOCIATED CONTENT

Supporting Information

The Supporting Information is available free of charge at <https://pubs.acs.org/doi/10.1021/acsmacrolett.1c00296>.

Details on the preparation procedure and characterization methods (PDF)

■ AUTHOR INFORMATION

Corresponding Author

Johannes C. Brendel – Laboratory of Organic and Macromolecular Chemistry (IOMC), Friedrich Schiller University Jena, 07743 Jena, Germany; orcid.org/0000-0002-1206-1375; Email: johannes.brendel@uni-jena.de

Authors

Franka V. Gruschwitz – Laboratory of Organic and Macromolecular Chemistry (IOMC), Friedrich Schiller University Jena, 07743 Jena, Germany

Tobias Klein – Laboratory of Organic and Macromolecular Chemistry (IOMC), Friedrich Schiller University Jena, 07743 Jena, Germany; orcid.org/0000-0001-9404-7739

Maren T. Kuchenbrod – Laboratory of Organic and Macromolecular Chemistry (IOMC), Friedrich Schiller University Jena, 07743 Jena, Germany

Naoto Moriyama – Department of Chemistry and Biochemistry, University of Kitakyushu, Wakamatsu-ku, Kitakyushu, Fukuoka 808-0135, Japan

Shota Fujii – Department of Chemistry and Biochemistry, University of Kitakyushu, Wakamatsu-ku, Kitakyushu, Fukuoka 808-0135, Japan; orcid.org/0000-0002-6594-5211

Ivo Nischang – Laboratory of Organic and Macromolecular Chemistry (IOMC), Friedrich Schiller University Jena, 07743 Jena, Germany; orcid.org/0000-0001-6182-5215

Stephanie Hoepfner – Laboratory of Organic and Macromolecular Chemistry (IOMC), Friedrich Schiller University Jena, 07743 Jena, Germany; orcid.org/0000-0002-5770-5197

Kazuo Sakurai – Department of Chemistry and Biochemistry, University of Kitakyushu, Wakamatsu-ku, Kitakyushu, Fukuoka 808-0135, Japan; orcid.org/0000-0002-9737-0061

Ulrich S. Schubert – Laboratory of Organic and Macromolecular Chemistry (IOMC), Friedrich Schiller University Jena, 07743 Jena, Germany; orcid.org/0000-0003-4978-4670

Complete contact information is available at: <https://pubs.acs.org/doi/10.1021/acsmacrolett.1c00296>

Author Contributions

[‡]These authors contributed equally to this work.

Notes

The authors declare no competing financial interest.

ACKNOWLEDGMENTS

F.V.G., T.K., and J.C.B. thank the German Science Foundation (DFG) for generous funding within the Emmy-Noether Programme (Project-ID: 358263073). CryoTEM investigations were performed at the electron microscopy facilities of the Jena Center for Soft Matter (JCSM), which were purchased with grants from the DFG and the European funds for Regional Development (EFRE). The funding of the collaborative research center SFB1278 (“PolyTarget”), Projects A05 and Z01 (Project-ID: 316213987 – SFB 1278) by the DFG, and Grant-in-Aid from CREST-JST (JPMJCR1521) are acknowledged. All SAXS measurements were carried out at SPring-8 BL40B2 (Proposal Nos. 2018B1396, 2019B1207, and 2020A1228).

REFERENCES

- (1) Wong, C. K.; Qiang, X.; Müller, A. H. E.; Gröschel, A. H. *Prog. Polym. Sci.* **2020**, *102*, 101211.
- (2) Qiang, X.; Franzka, S.; Dai, X.; Gröschel, A. H. *Macromolecules* **2020**, *53* (11), 4224–4233.
- (3) Wong, C. K.; Heidelmann, M.; Dulle, M.; Qiang, X.; Förster, S.; Stenzel, M. H.; Gröschel, A. H. *J. Am. Chem. Soc.* **2020**, *142* (25), 10989–10995.
- (4) Steinhaus, A.; Chakroun, R.; Müllner, M.; Nghiem, T.-L.; Hildebrandt, M.; Gröschel, A. H. *ACS Nano* **2019**, *13* (6), 6269–6278.
- (5) Gröschel, A. H.; Walther, A.; Löblich, T. I.; Schacher, F. H.; Schmalz, H.; Müller, A. H. E. *Nature* **2013**, *503* (7475), 247–251.
- (6) Gröschel, A. H.; Schacher, F. H.; Schmalz, H.; Borisov, O. V.; Zhulina, E. B.; Walther, A.; Müller, A. H. E. *Nat. Commun.* **2012**, *3* (1), 710.
- (7) Fletcher, D. A.; Mullins, R. D. *Nature* **2010**, *463* (7280), 485–92.
- (8) Wehner, M.; Würthner, F. *Nat. Rev. Chem.* **2020**, *4*, 38–53.
- (9) Hartlieb, M.; Mansfield, E. D. H.; Perrier, S. *Polym. Chem.* **2020**, *11*, 1083–1110.
- (10) MacFarlane, L.; Zhao, C.; Cai, J.; Qiu, H.; Manners, I. *Chem. Sci.* **2021**, *12* (13), 4661–4682.
- (11) Street, S. T. G.; He, Y.; Jin, X.-H.; Hodgson, L.; Verkade, P.; Manners, I. *Chem. Sci.* **2020**, *11*, 8394.
- (12) Yu, Q.; Roberts, M. G.; Pearce, S.; Oliver, A. M.; Zhou, H.; Allen, C.; Manners, I.; Winnik, M. A. *Macromolecules* **2019**, *52* (14), 5231–5244.
- (13) Gilroy, J. B.; Gädt, T.; Whittell, G. R.; Chabanne, L.; Mitchels, J. M.; Richardson, R. M.; Winnik, M. A.; Manners, I. *Nat. Chem.* **2010**, *2*, 566–570.
- (14) Gädt, T.; Jeong, N. S.; Cambridge, G.; Winnik, M. A.; Manners, I. *Nat. Mater.* **2009**, *8*, 144–150.
- (15) Finnegan, J.; Pilkington, E.; Alt, K.; Rahim, M. A.; Kent, S. J.; Davis, T. P.; Kempe, K. *Chem. Sci.* **2021**, *12*, 7350.
- (16) Brendel, J. C.; Schacher, F. H. *Chem. - Asian J.* **2018**, *13* (3), 230–239.
- (17) Kang, J.; Miyajima, D.; Mori, T.; Inoue, Y.; Itoh, Y.; Aida, T. *Science* **2015**, *347* (6222), 646–651.
- (18) Ogi, S.; Sugiyasu, K.; Manna, S.; Samitsu, S.; Takeuchi, M. *Nat. Chem.* **2014**, *6*, 188–195.
- (19) Wagner, W.; Wehner, M.; Stepanenko, V.; Ogi, S.; Würthner, F. *Angew. Chem., Int. Ed.* **2017**, *56* (50), 16008–16012.
- (20) Robinson, M. E.; Lunn, D. J.; Nazemi, A.; Whittell, G. R.; De Cola, L.; Manners, I. *Chem. Commun.* **2015**, *51* (88), 15921–15924.
- (21) Smulders, M. M.; Nieuwenhuizen, M. M.; de Greef, T. F.; van der Schoot, P.; Schenning, A. P.; Meijer, E. W. *Chem. - Eur. J.* **2010**, *16*, 362–367.
- (22) van der Zwaag, D.; de Greef, T. F. A.; Meijer, E. W. *Angew. Chem., Int. Ed.* **2015**, *54*, 8334–8336.
- (23) Kulkarni, C.; Meijer, E. W.; Palmans, A. R. A. *Acc. Chem. Res.* **2017**, *50*, 1928–1936.
- (24) Cohen, E.; Weissman, H.; Pinkas, I.; Shimoni, E.; Rehak, P.; Král, P.; Rybtchinski, B. *ACS Nano* **2018**, *12* (1), 317–326.
- (25) Baram, J.; Weissman, H.; Rybtchinski, B. *J. Phys. Chem. B* **2014**, *118* (41), 12068–12073.
- (26) Baram, J.; Weissman, H.; Tidhar, Y.; Pinkas, I.; Rybtchinski, B. *Angew. Chem., Int. Ed.* **2014**, *53* (16), 4123–4126.
- (27) Tidhar, Y.; Weissman, H.; Wolf, S. G.; Gulino, A.; Rybtchinski, B. *Chem. - Eur. J.* **2011**, *17* (22), 6068–6075.
- (28) Han, S.; Nicol, E.; Niepceron, F.; Colombani, O.; Pensec, S.; Bouteiller, L. *Macromol. Rapid Commun.* **2019**, *40*, 1800698.
- (29) Gruschwitz, F. V.; Fu, M.-C.; Klein, T.; Takahashi, R.; Higashihara, T.; Hoepfener, S.; Nischang, I.; Sakurai, K.; Brendel, J. C. *Macromolecules* **2020**, *53* (17), 7552–7560.
- (30) Klein, T.; Ulrich, H. F.; Gruschwitz, F. V.; Kuchenbrod, M. T.; Takahashi, R.; Fujii, S.; Hoepfener, S.; Nischang, I.; Sakurai, K.; Brendel, J. C. *Polym. Chem.* **2020**, *11* (42), 6763–6771.
- (31) Gruschwitz, F. V.; Klein, T.; Catrouillet, S.; Brendel, J. C. *Chem. Commun.* **2020**, *56*, 5079–5110.
- (32) Podzimek, S. *Asymmetric Flow Field Flow Fractionation. In Light Scattering, Size Exclusion Chromatography and Asymmetric Flow Field Flow Fractionation*; Wiley, 2011; pp 259–305.
- (33) Ratanathanawongs Williams, S. K.; Lee, D. J. *Sep. Sci.* **2006**, *29* (12), 1720–1732.
- (34) Wagner, M.; Holzschuh, S.; Traeger, A.; Fahr, A.; Schubert, U. S. *Anal. Chem.* **2014**, *86* (11), 5201–5210.
- (35) De Greef, T. F.; Smulders, M. M.; Wolffs, M.; Schenning, A. P.; Sijbesma, R. P.; Meijer, E. W. *Chem. Rev.* **2009**, *109*, 5687–5754.
- (36) Korevaar, P. A.; Newcomb, C. J.; Meijer, E. W.; Stupp, S. I. *J. Am. Chem. Soc.* **2014**, *136* (24), 8540–8543.
- (37) Ahlers, P.; Frisch, H.; Holm, R.; Spitzer, D.; Barz, M.; Besenius, P. *Macromol. Biosci.* **2017**, *17* (10), 1700111.
- (38) Korevaar, P. A.; Schaefer, C.; de Greef, T. F.; Meijer, E. W. *J. Am. Chem. Soc.* **2012**, *134*, 13482–13491.
- (39) Yagai, S.; Iwashima, T.; Karatsu, T.; Kitamura, A. *Chem. Commun.* **2004**, 1114–1115.
- (40) Cantekin, S.; Balkenende, D. W.; Smulders, M. M.; Palmans, A. R.; Meijer, E. W. *Nat. Chem.* **2011**, *3*, 42–46.
- (41) Smulders, M. M. J.; Buffeteau, T.; Cavagnat, D.; Wolffs, M.; Schenning, A. P. H. J.; Meijer, E. W. *Chirality* **2008**, *20*, 1016–1022.
- (42) Krieg; Weissman, H.; Shimoni, E.; Bar On, A.; Rybtchinski, B. *J. Am. Chem. Soc.* **2014**, *136*, 9443–9452.
- (43) Jiang, L.; Cao, S.; Cheung, P. P.-H.; Zheng, X.; Leung, C. W. T.; Peng, Q.; Shuai, Z.; Tang, B. Z.; Yao, S.; Huang, X. *Nat. Commun.* **2017**, *8*, 15639.
- (44) Chandler, D. *Nature* **2005**, *437*, 640–647.
- (45) Martinez, C. R.; Iverson, B. L. *Chem. Sci.* **2012**, *3*, 2191–2201.
- (46) Leenders, C. M. A.; Baker, M. B.; Pijpers, I. A. B.; Lafleur, R. P. M.; Albertazzi, L.; Palmans, A. R. A.; Meijer, E. W. *Soft Matter* **2016**, *12*, 2887–2893.
- (47) Huang, Z.; Qin, B.; Chen, L.; Xu, J.-F.; Faul, C. F. J.; Zhang, X. *Macromol. Rapid Commun.* **2017**, *38*, 1700312.
- (48) Wagner, W.; Wehner, M.; Stepanenko, V.; Würthner, F. *J. Am. Chem. Soc.* **2019**, *141*, 12044–12054.

Supporting Information

Kinetically controlling the length of self-assembled polymer nanofibers formed by intermolecular hydrogen bonds

Franka Gruschwitz,^{a,b,‡} Tobias Klein,^{a,b,‡} Maren T. Kuchenbrod,^{a,b} Naoto Moriyama,^c Shota Fujii,^c Ivo Nischang,^{a,b} Stephanie Hoepfener,^{a,b} Kazuo Sakurai,^c Ulrich S. Schubert,^{a,b} Johannes C. Brendel,^{a,b,*}

a Laboratory of Organic and Macromolecular Chemistry (IOMC), Friedrich Schiller University Jena, Humboldtstraße 10, 07743 Jena, Germany

b Jena Center for Soft Matter (JCSM), Friedrich Schiller University Jena, Philosophenweg 7, 07743 Jena, Germany

c Department of Chemistry and Biochemistry, University of Kitakyushu, 1-1 Hibikino, Wakamatsu-ku, Kitakyushu, Fukuoka 808-0135, Japan

‡ These authors contributed equally to this work

*corresponding author: johannes.brendel@uni-jena.de

Content

1. Synthesis & Procedures	3
2. Characterization.....	4
2.1 Dynamic Light Scattering (DLS)	4
2.2 CryoTransmission Electron Microscopy (cryoTEM).....	8
2.3 Asymmetrical Flow Field-Flow Fractionation (AF4)	14
2.4 Small angle x-ray scattering.....	21
3. References	22

1. Synthesis & Procedures

Materials and Methods. All reagents and solvents were commercial products purchased from Sigma-Aldrich, abcr, Iris BioTech, Rapp Polymere or TCI and were used without further purification.

Synthesis.

The benzenetrisurea-polyethylene oxide (BTU) and benzenetrispeptide-polyethylene oxide (BTP) conjugates were synthesized according to previously published protocols.¹⁻²

Self-assembly procedures.

Solvent switch method

5 mg of **BTU** or **BTP** were dissolved in 1 mL of the respective organic solvent (DMF, THF, acetone or ethanol) and stirred overnight to guarantee complete dissolution. To this, 4 mL of MilliQ water were added at the specified speed (1 to 100 ml h⁻¹) using a syringe pump under vigorous stirring to reach a final water content of 80 v%. For this purpose, the needle of the syringe was immersed in the organic **BTP** or **BTU** solution to enable a constant release of MilliQ water from the syringe and avoid the formation of drops that would result in high local water concentrations at the spot where the drop immerses into the solution. Afterwards, the solution was transferred to float-analyzer® tubings with a molecular weight cutoff of 3.5 kD and dialyzed for five days against water to remove all organic solvent traces.

Quenching method

5 mg of **BTU** or **BTP** were dissolved in 1 mL of the respective organic solvent (DMF, THF, acetone or ethanol) and stirred overnight to guarantee complete dissolution. This organic solution was added to 4 mL MilliQ water using a syringe pump (1 mL h⁻¹) under vigorous stirring to reach a final water content of 80 v%. For this purpose, the needle of the syringe was immersed in the MilliQ water to enable a constant release of organic **BTP** or **BTU** solution from the syringe and avoid the formation of drops that would result in high local **BTP** or **BTU** solution concentrations at the spot where the drop immerses into the solution. Afterwards, the solution was transferred to float-analyzer® tubings with a molecular weight cutoff of 3.5 kD and dialyzed for five days against water to remove all organic solvent traces.

2. Characterization

2.1 Dynamic Light Scattering (DLS)

A scattering angle of 173° was used to record intensity fluctuations of the different samples in solution. All measurements were conducted in triplicate at a temperature of 25 °C in disposable macro cuvettes containing 2 mL solution and after allowing for an equilibration time of 60 s. The acquisition time was 60 s. The apparent distribution of intensity-weighted hydrodynamic radii, d_h , was obtained from the Stokes–Einstein equation:

$$d_h = \frac{kT}{3\pi\eta D} \quad \text{Eq. 1}$$

with k being the Boltzmann constant, T the temperature in units K, η the viscosity of the solvent, and D the apparent translational diffusion coefficient at the utilized concentrations.

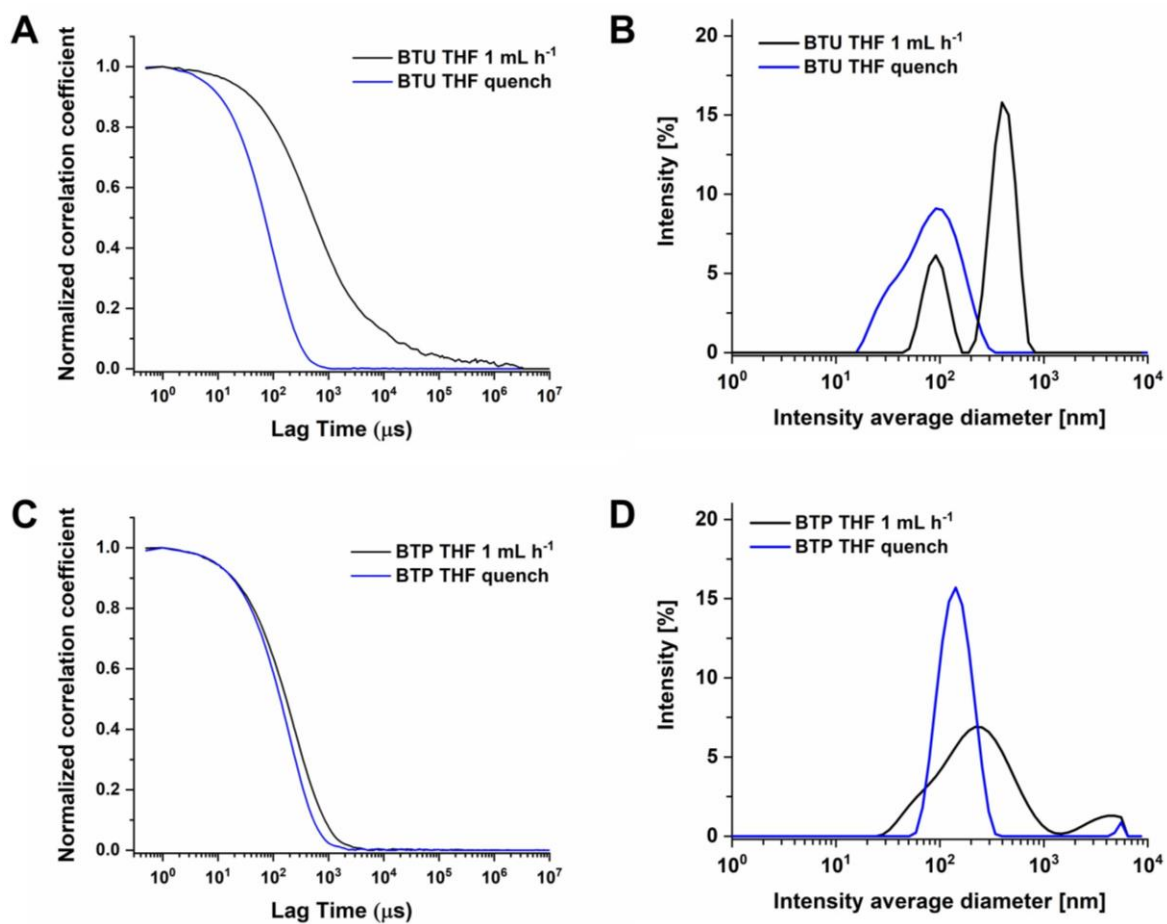


Figure S1: DLS correlograms of **BTU** (A) and **BTP** (B) in water for the solvent switch (**THF 1 mL h⁻¹**; black) and the quenching procedure (**THF quench**; blue). Correlograms were recorded in MilliQ water at a concentration of 1 mg mL⁻¹. The corresponding intensity average diameters for **BTU** and **BTP** can be seen in (C) and (D), respectively.

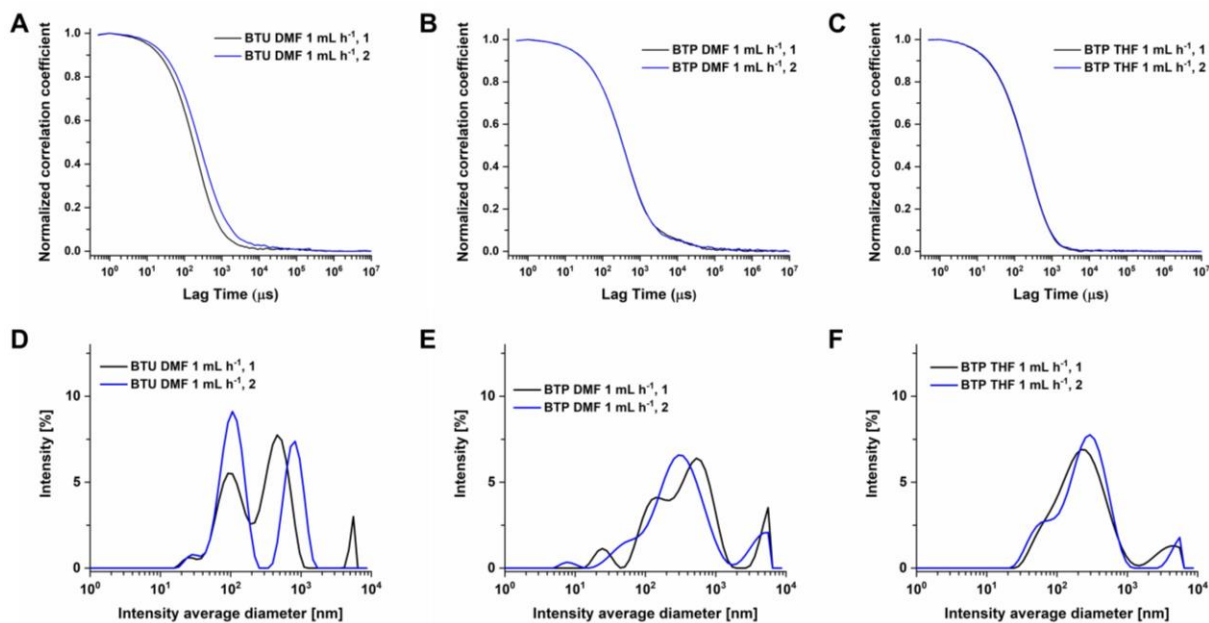


Figure S2: DLS correlograms showing the reproducibility of the applied assembly procedure. A) **BTU DMF 1 mL h⁻¹**, B) **BTP DMF 1 mL h⁻¹**, and C) **BTP THF 1 mL h⁻¹**. Each assembly procedure was performed twice, indicated by the numbers “1” and “2” in the legends. The corresponding intensity average diameters for the assembled **BTU** and **BTP** samples can be seen in (D) and (E & F), respectively.

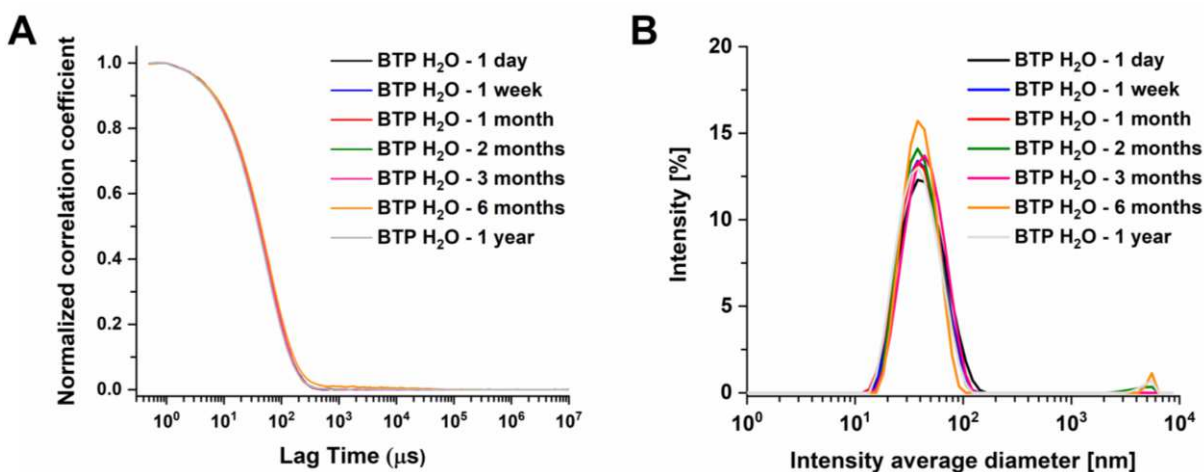


Figure S3: DLS stability test of **BTP H₂O**. A) Correlograms were recorded at a concentration of 3 mg mL⁻¹ over a period of one year. B) The corresponding intensity average diameters for the different time points.

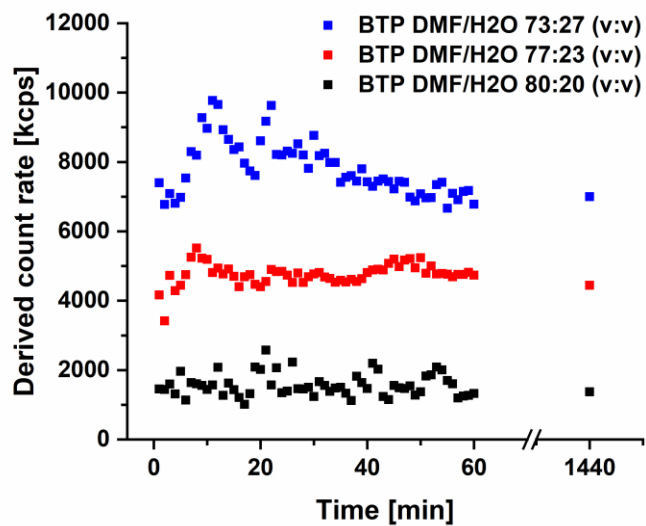


Figure S4: Time dependent evolution of derived count rates determined via DLS for **BTP DMF** at 20, 23 and 27 v% water.

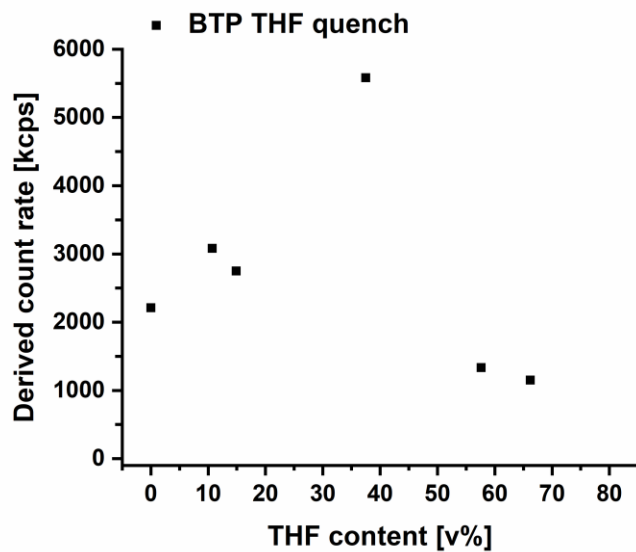


Figure S5: DLS derived count rates for **BTP THF quench** for adding more and more THF.

2.2 CryoTransmission Electron Microscopy (cryoTEM)

Samples were prepared on Ar plasma treated Quantifoil grids (R2/2). 8.5 μL of the solutions (3 mg mL^{-1} in H_2O) were applied onto the grids and vitrified in liquid ethane utilizing a FEI Vitrobot Mark IV system (offset: -3 mm, blotting time: 1 s). Samples were transferred into the cryo holder (Gatan 626) utilizing the Gatan cryo stage, followed by transfer into the microscope keeping the temperature below -172 $^\circ\text{C}$ during the whole transfer and measurement process after vitrification. Measurements were performed using a FEI Technai G² 20 operated at an acceleration voltage of 200 kV. Images were acquired with a Mega View (OSIS, Olympus Soft Imaging Systems) or an Eagle 4k CCD camera. cryoTEM images in this study display only specific regions of interest that are representative for the whole sample.

THF 1 mL h^{-1} vs. THF quench

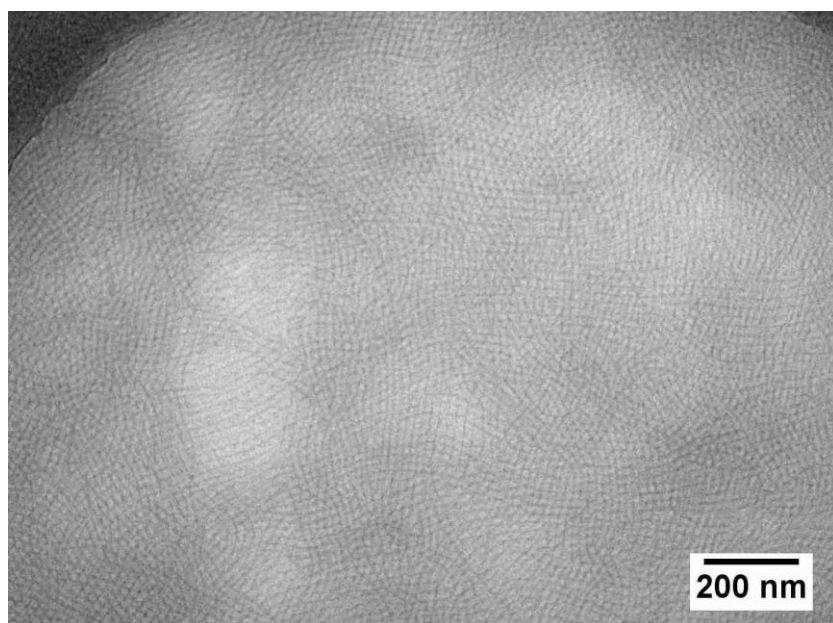


Figure S6: cryoTEM image of BTU THF 1 mL h^{-1} in water ($c = 1$ mg mL^{-1}).

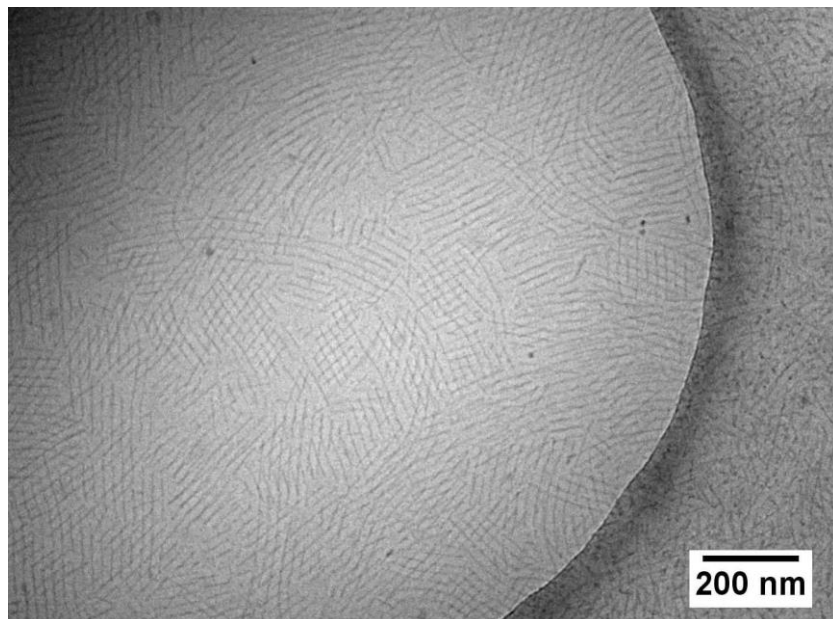


Figure S7: cryoTEM image of **BTU THF quench** in water ($c = 1 \text{ mg mL}^{-1}$).

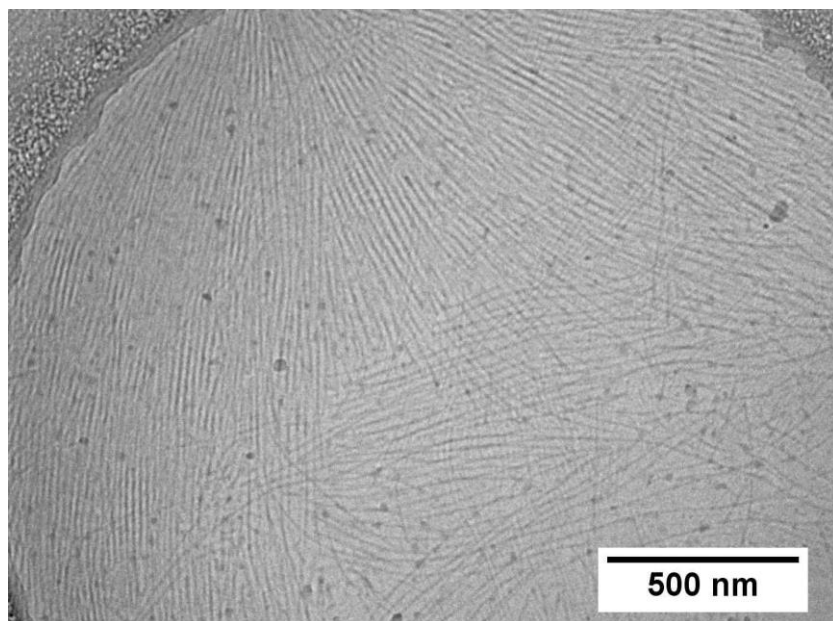


Figure S8: cryoTEM image of **BTP THF 1 mL h⁻¹** in water ($c = 1 \text{ mg mL}^{-1}$).

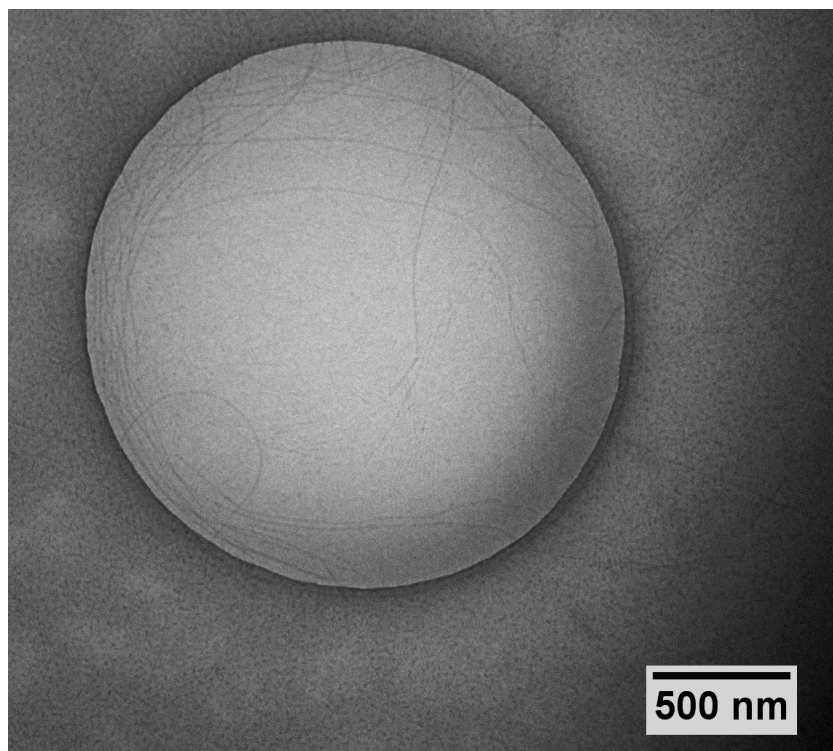


Figure S9: cryoTEM image of **BTP THF 1 mL h⁻¹** in water ($c = 1 \text{ mg mL}^{-1}$) at low magnification.

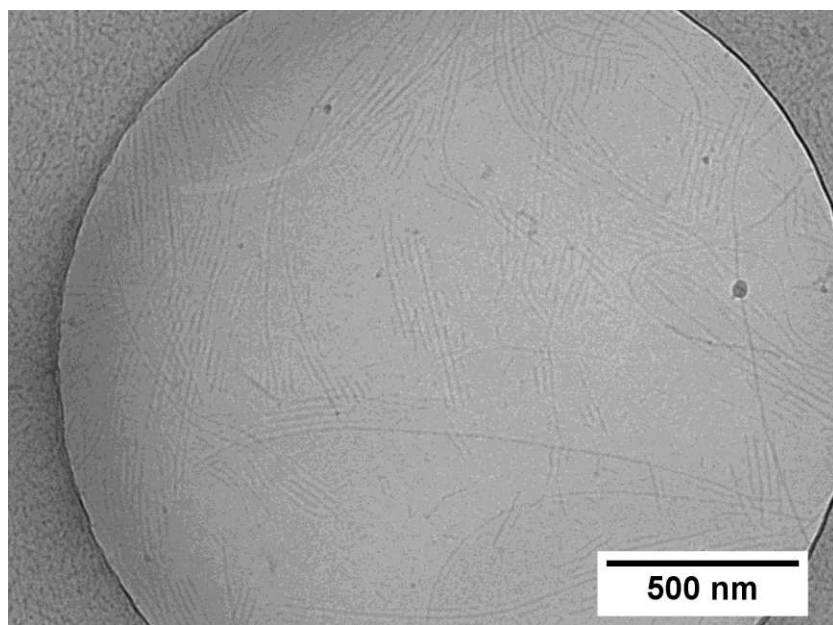


Figure S10: cryoTEM image of **BTP THF 10 mL h⁻¹** in water ($c = 1 \text{ mg mL}^{-1}$).

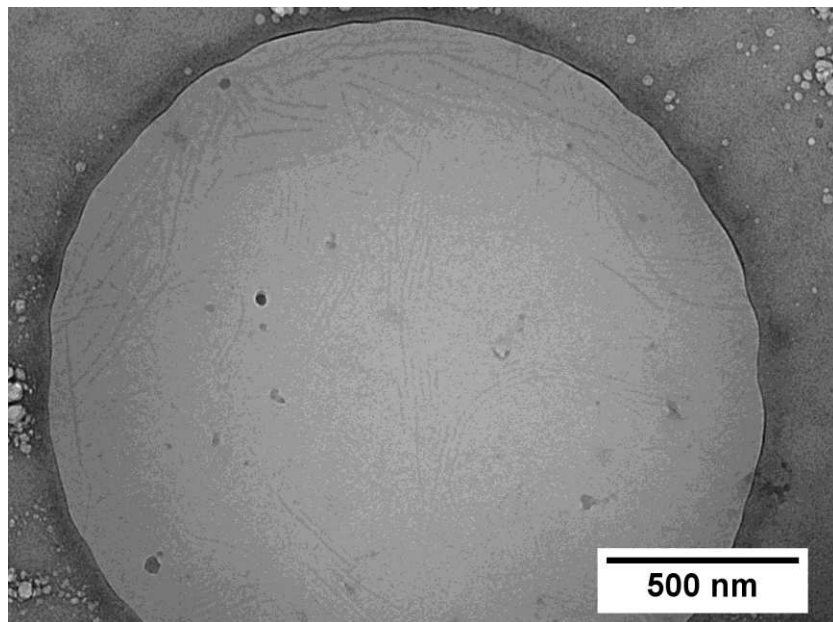


Figure S11: cryoTEM image of **BTP THF 50 mL h⁻¹** in water ($c = 1 \text{ mg mL}^{-1}$).

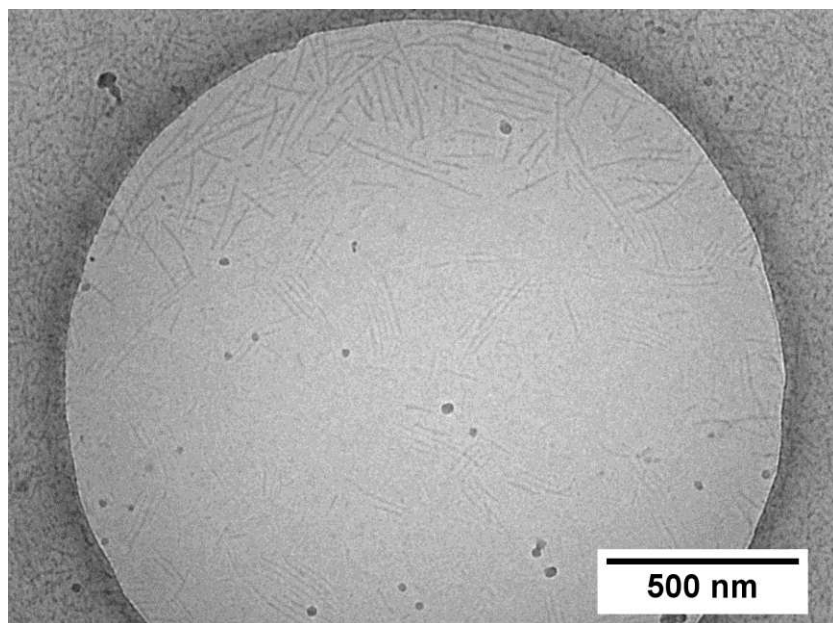


Figure S12: cryoTEM image of **BTP THF 100 mL h⁻¹** in water ($c = 1 \text{ mg mL}^{-1}$).

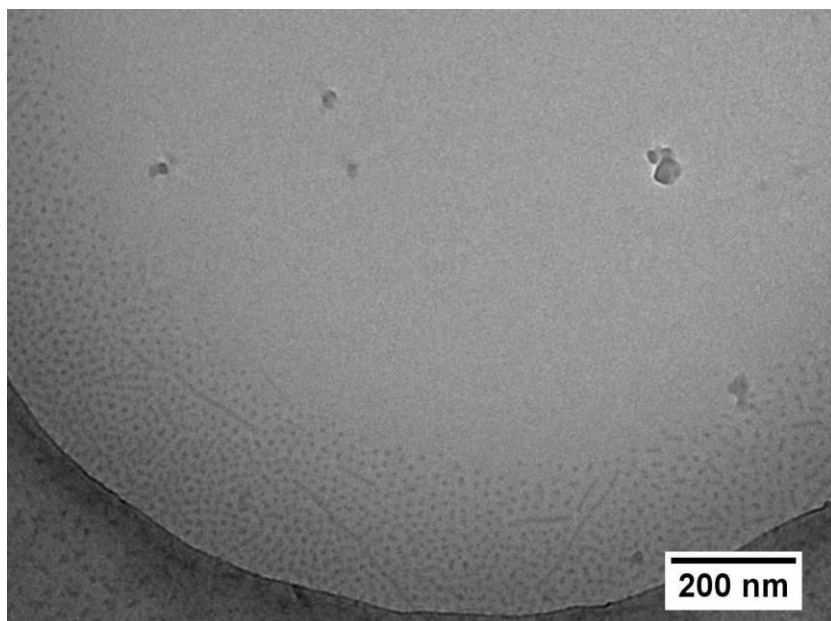


Figure S13: cryoTEM image of **BTP THF quench** in water ($c = 1 \text{ mg mL}^{-1}$).

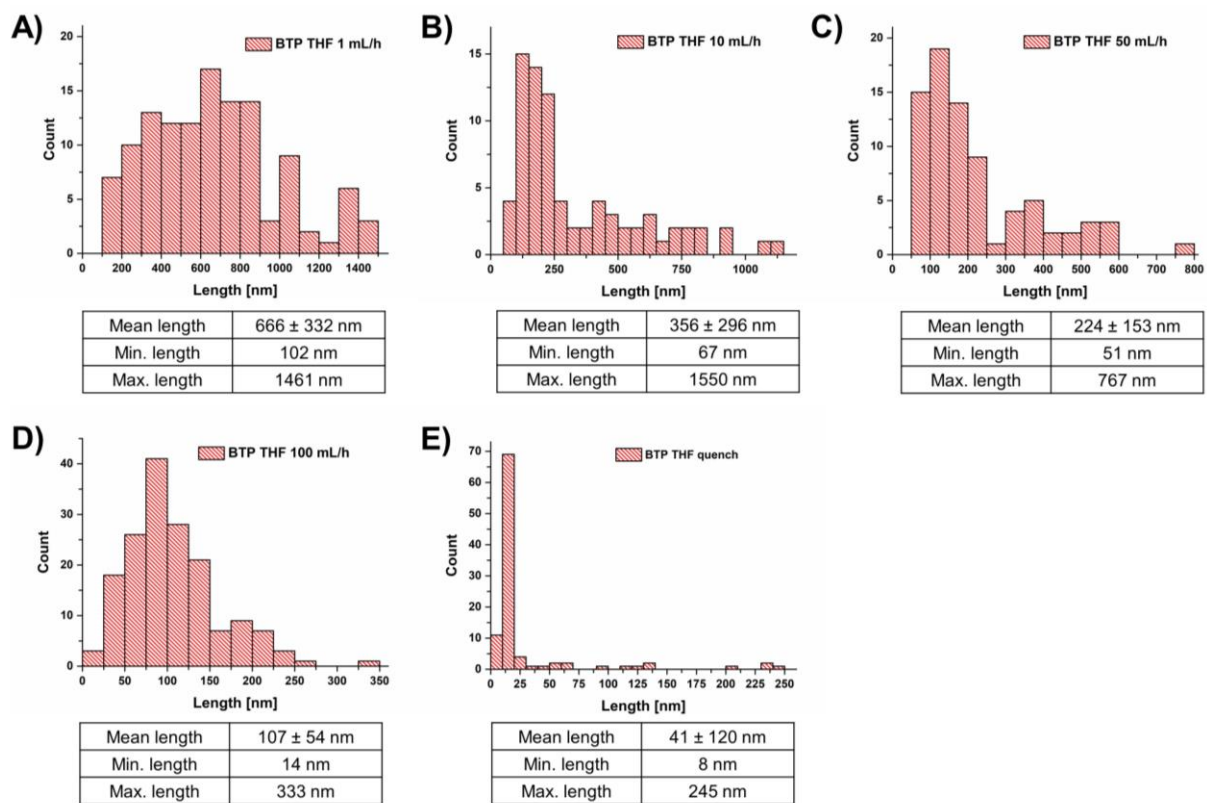


Figure S14: Histograms of fiber lengths obtained from cryoTEM images of **BTP THF 1 mL h⁻¹** (A), **BTP THF 10 mL h⁻¹** (B), **BTP THF 50 mL h⁻¹** (C), **BTP THF 100 mL h⁻¹** (D) and **BTP quench** (E).

2.3 Asymmetrical Flow Field-Flow Fractionation (AF4)

AF4 measurements were performed on an AF2000 MT System from Postnova Analytics GmbH (Landsberg, Germany), equipped with a tip and focus pump (PN1130), an autosampler (PN5300), and a channel oven unit (PN4020) set to 25 °C. The channel was coupled to a multiangle laser light scattering (MALLS) detector (PN3621) equipped with a 532 nm laser and measuring 21 angles (only 28° to 148° have been used for calculation of R_g and M_w), a refractive index (RI) detector (PN3150), and a UV-detector (PN3212) operating at a wavelength of 280 nm. The channel had a trapezoidal geometry with a nominal height of 350 μm . A regenerated cellulose (RC) membrane from Postnova Analytics GmbH (10 kDa RC membrane) with a molar mass cutoff of 10 kDa was used as accumulation wall. As the mobile phase, an aqueous solution with 0.002 w% of NaN_3 was used. 50 μL of the sample at a concentration of 1 mg mL^{-1} was injected with an injection flow rate of 0.2 mL min^{-1} , a focus flow rate of 0.8 mL min^{-1} , and a cross-flow rate of 0.7 mL min^{-1} , resulting in a detector flow rate of 0.3 mL min^{-1} . The focusing time was 4 min before switching to elution at an exponentially decaying crossflow from 0.7 mL min^{-1} to 0.2 mL min^{-1} within 76.2 min. Thereafter, the crossflow profile was set to decay in a linear way from 0.05 mL min^{-1} to 0.04 mL min^{-1} within 71 min (Figure S21). Before the start of the next measurement, a rinsing step was performed at 1.5 mL min^{-1} flow of the tip pump only for 20 min. After each sample measurement, a blank measurement was run, which was subtracted from the data of the sample measurement for analysis. The RI-detector was used as the concentration-sensitive detector ($\text{dn}/\text{dc}_{\text{BTU}}$ 1.47 mL/g and $\text{dn}/\text{dc}_{\text{BTP}}$ 1.48 mL/g) and the MALLS data was analysed via a ZIMM plot analysis to obtain the radii of gyration (R_g) and the molar mass at the specified elution times.

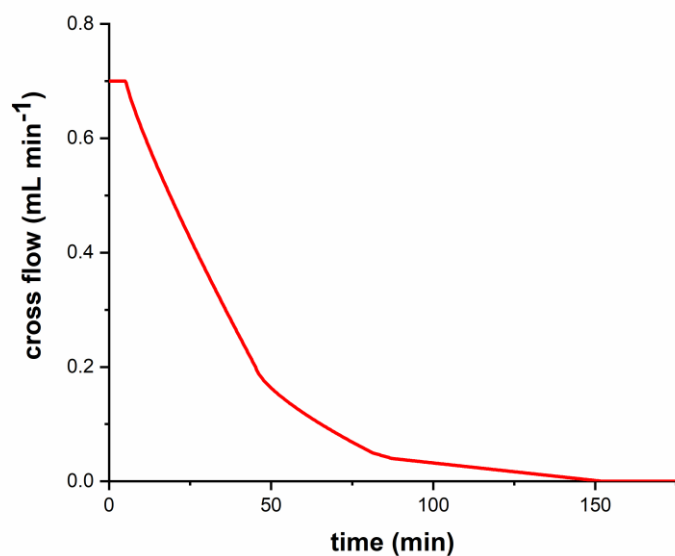


Figure S15: Cross-flow profile applied for all AF4-MALLS measurements in this manuscript.

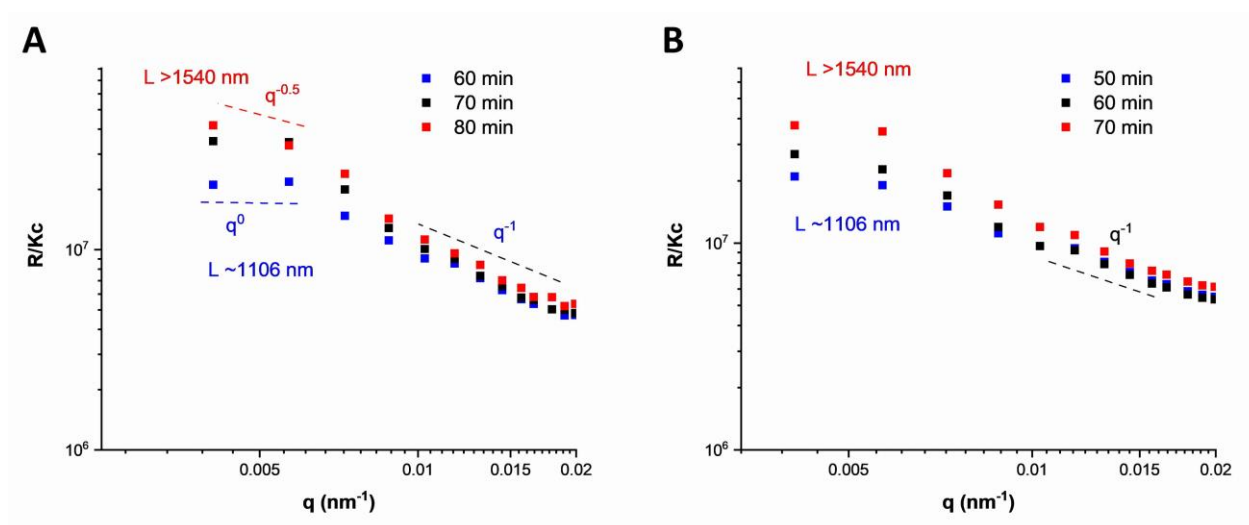


Figure S16: Scattering intensity plotted against the scattering vector q for **BTU THF 1 mL h⁻¹** (A) and **BTP THF 1 mL h⁻¹** (B) and the maximum observable length derived from the change of the q^{-1} dependency to a q^0 plateau at low scattering values.

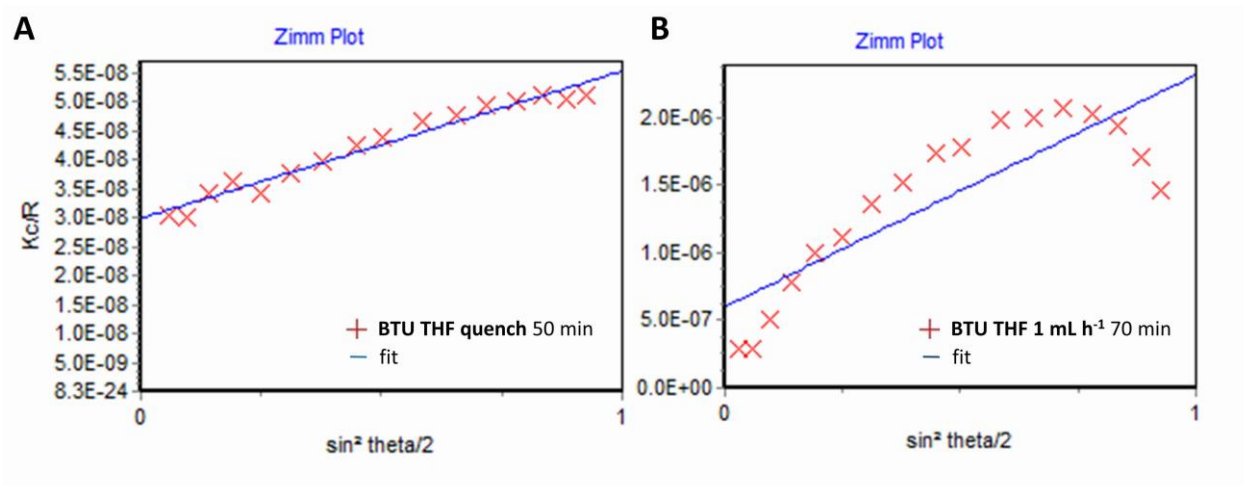


Figure S17: Zimm plots for **BTU THF quench** at 50 min resulting in an R_g of 80 nm (A) and for **BTU THF 1 mL h⁻¹** at 70 min where Zimm fitting is not accurate anymore (B).

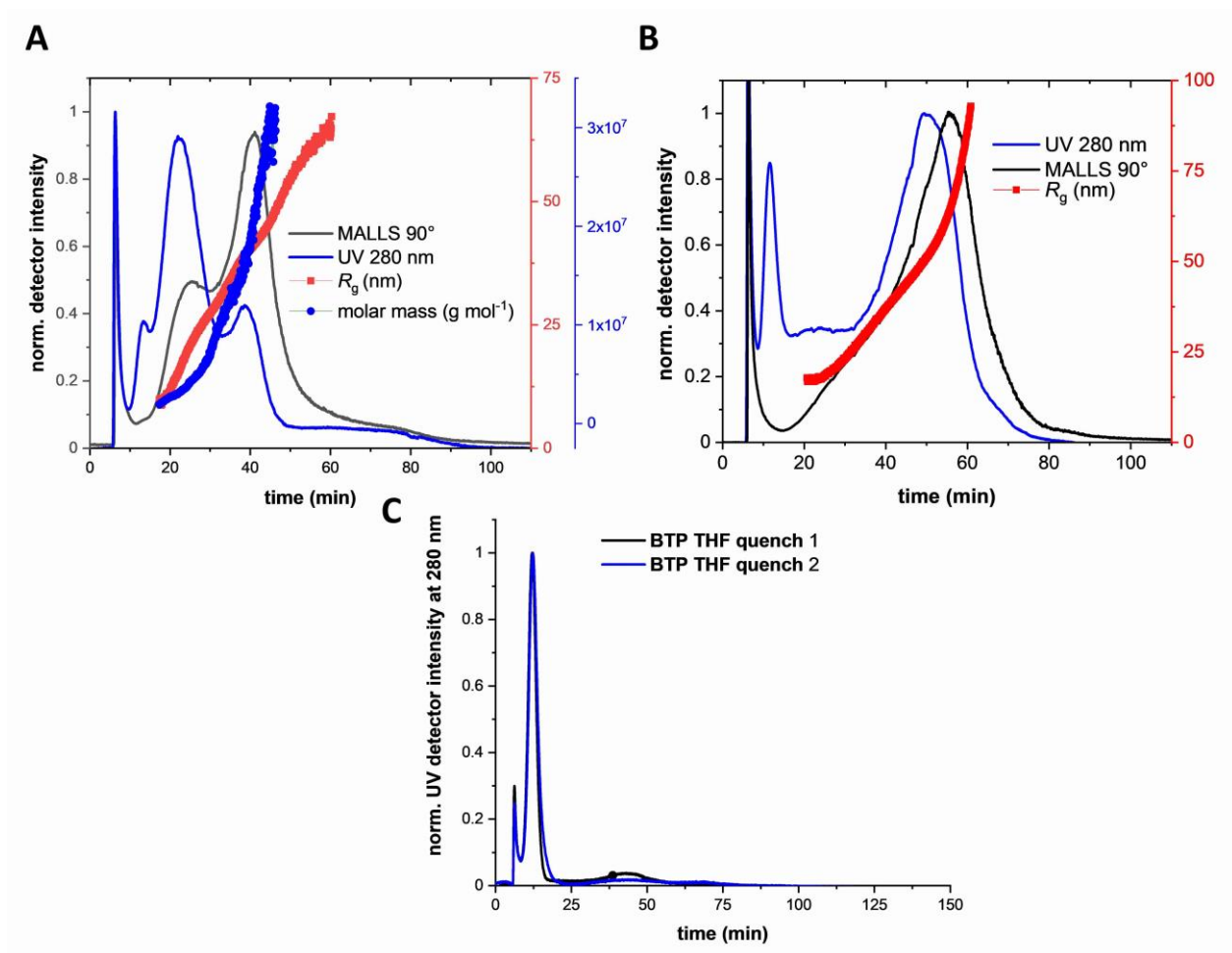


Figure S18: MALLS 90° (black), UV trace (blue), R_g (red) and molar mass (blue) obtained by Zimm analysis for **BTU THF quench 1** (A) and **BTU THF quench 2** (C). cryoTEM image of **BTU THF quench 1** ($c = 1 \text{ mg mL}^{-1}$). **BTP THF quench 1 and 2** (D).

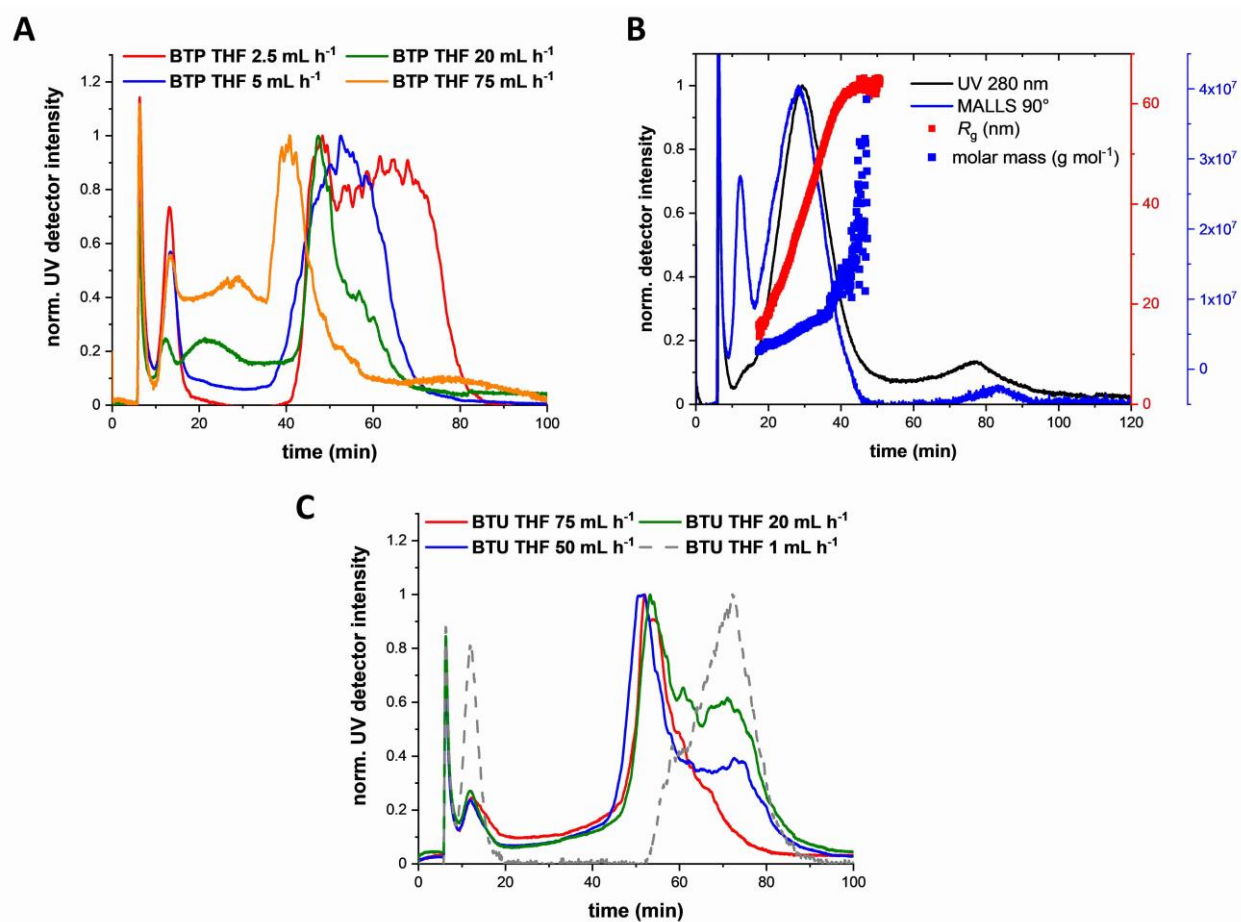


Figure S19: Impact of the water addition rate on the resulting **BTP THF** assemblies (A) and **BTU THF** assemblies (C) (elution profile monitored via UV detector). MALLS 90° (black), UV trace (blue) and R_g (red) obtained via Zimm plot for **BTP THF** 100 mL h⁻¹ (B).

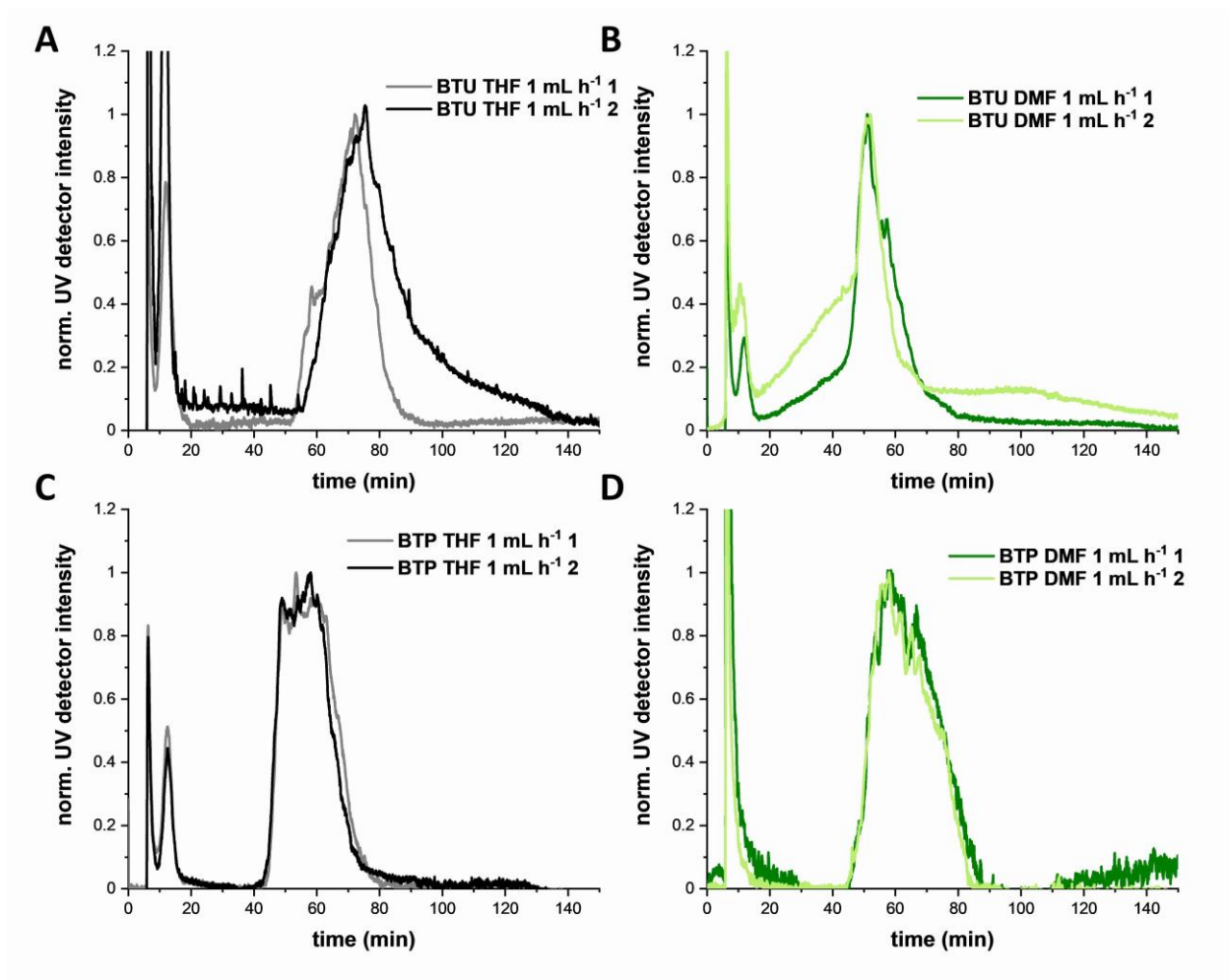


Figure S20: Reproducibility of the solvent switch procedure shown for **BTU THF 1 mL h⁻¹** (A), **BTU DMF 1 mL h⁻¹** (B), **BTP THF 1 mL h⁻¹** (C) and **BTP DMF 1 mL h⁻¹** (D).

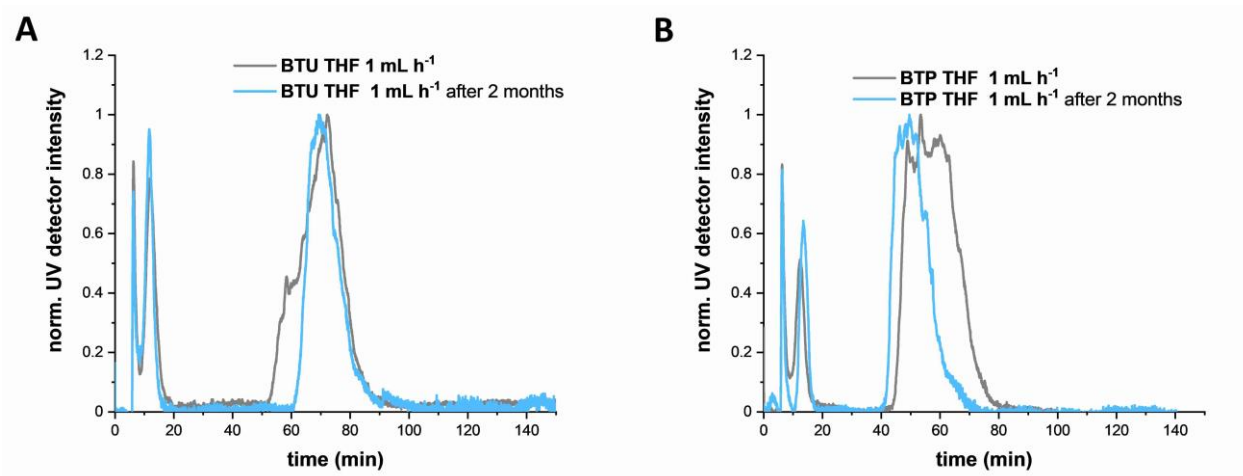


Figure S21: Normalized UV traces of **BTU THF 1 mL h⁻¹** (A) and **BTP THF 1 mL h⁻¹** (B) (grey) and after 2 months (blue). Slight deviations result from variations in the membranes and pressure differences in the AF4 system.

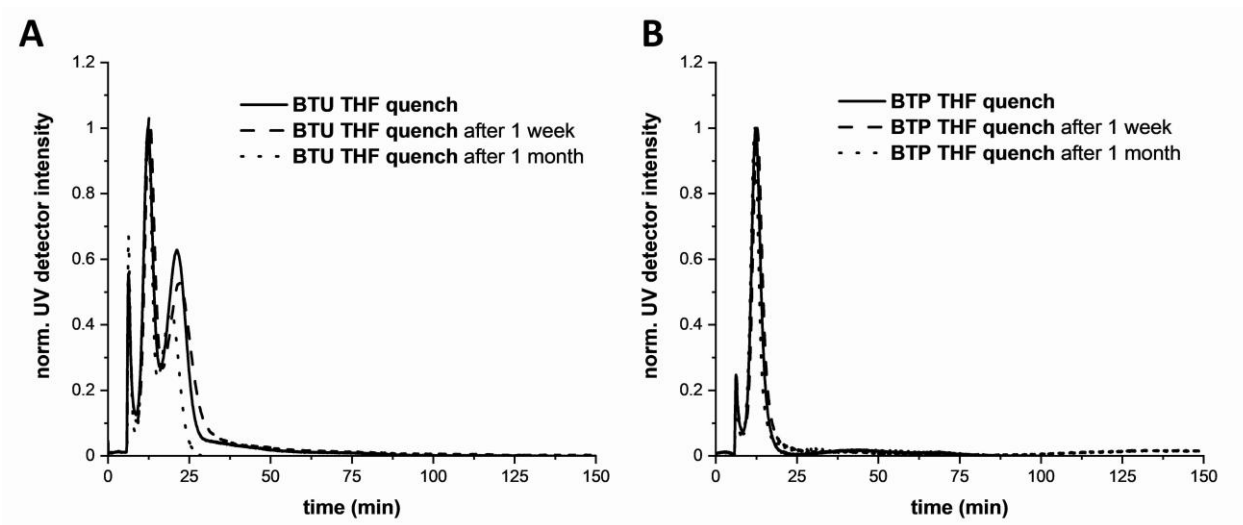


Figure S22: Normalized UV traces of **BTU THF quench** (A) and **BTP THF quench** (B) (solid) and after 1 week (dashed).

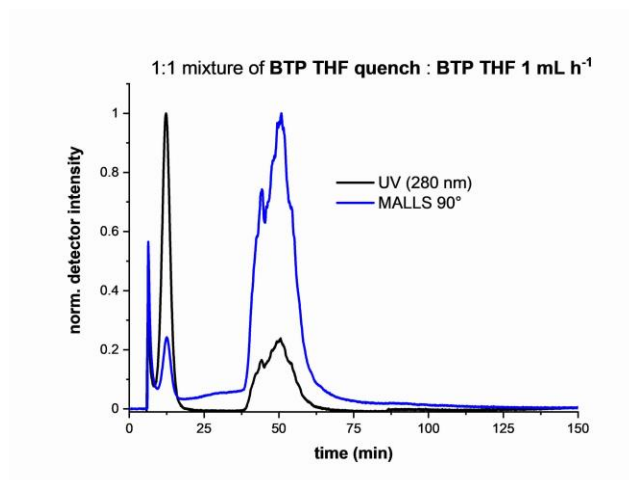


Figure S23: AF4 elution profile proving the stability of a 1:1 (v/v) mixture of **BTP THF 1 mL h⁻¹** and **BTU THF quench (B)** measured after several days (B).

2.4 Small angle x-ray scattering

The SAXS measurements in DMF/H₂O solvent mixtures were performed at BL-40B2 at SPring-8, Hyogo Prefecture, Japan. The distances between the sample and detector were 4 m. The wavelength was 0.1 nm. The sample was prepared at a starting concentration of 10 mg mL⁻¹ and diluted successively to 0.3 mg mL⁻¹ by addition of water. For the fitting of the fibrillar SAXS profiles, a model of a core-shell cylinder was used, described by the following expression:

$$I(q) = \frac{L\pi}{q} * \left\{ 2\pi R_c^2 (\rho_c - \rho_s) \frac{J_1(qR_c)}{qR_c} + 2\pi R_s^2 \rho_s \frac{J_1(qR_s)}{qR_s} \right\}^2 \quad \text{Eq 2}$$

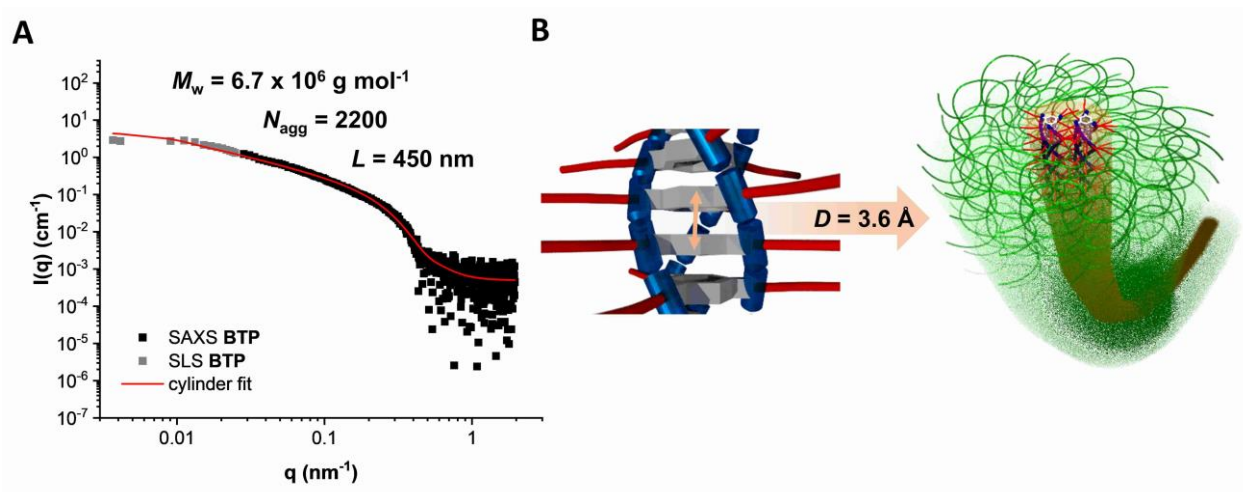


Figure S24: (A) Scattering profile of BTP directly dissolved in water, obtained by SLS (gray squares) and SAXS (black squares) and a cylindrical fit (red line) of the combined data ($c = 1.5 \text{ mg mL}^{-1}$). Fitting parameter: $R_{\text{cyl}} = 6.3 \pm 1.97 \text{ nm}$, $L_{\text{cyl}} = 451.97 \text{ nm}$, $N = 1.01557 \times 10^{-3}$, $SLD = 1.0118 \times 10^{-3}$. (B) Proposed arrangement of BTP molecules in the cross section assuming a stacking distance of 3.6 \AA between the BTP cores. For further experimental details of these measurements and calculation, the reader is referred to reference [1] where the analog procedure is employed.

3. References

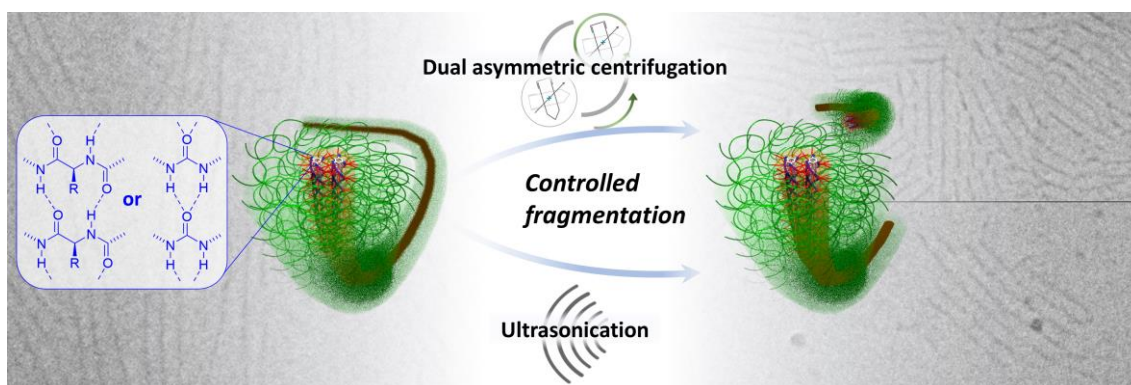
1. Gruschwitz, F. V.; Fu, M.-C.; Klein, T.; Takahashi, R.; Higashihara, T.; Hoepfner, S.; Nischang, I.; Sakurai, K.; Brendel, J. C., *Macromolecules* **2020**, *53* (17), 7552-7560.
2. Klein, T.; Ulrich, H. F.; Gruschwitz, F. V.; Kuchenbrod, M. T.; Takahashi, R.; Fujii, S.; Hoepfner, S.; Nischang, I.; Sakurai, K.; Brendel, J. C., *Polym. Chem.* **2020**, *11* (42), 6763-6771.

Publication P7

Adjusting the length of supramolecular polymer bottlebrushes by top-down approaches

T. Klein[‡], F. V. Gruschwitz[‡], I. Nischang, S. Hoepfner, J. C. Brendel, *Beilstein J.* **2021**, submitted.

Reproduced by permission of T. Klein, F. V. Gruschwitz, I. Nischang, S. Hoepfner, J. C. Brendel.



[‡]Equal contribution.

Adjusting the length of supramolecular polymer bottlebrushes by top-down approaches

Tobias Klein,^{a,b,‡} Franka V. Gruschwitz,^{a,b,‡} Maren T. Kuchenbrod,^{a,b} Ivo Nischang,^{a,b} Stephanie Hoepfner,^{a,b} Johannes C. Brendel,^{a,b,*}

a Laboratory of Organic and Macromolecular Chemistry (IOMC), Friedrich Schiller University Jena, Humboldtstraße 10, 07743 Jena, Germany

b Jena Center for Soft Matter (JCSM), Friedrich Schiller University Jena, Philosophenweg 7, 07743 Jena, Germany

‡ These authors contributed equally to this work

*corresponding author: johannes.brendel@uni-jena.de

Keywords: dual centrifugation; self-assembly; distribution; filomicelles; ultrasonication.

Abstract

Controlling the length of one-dimensional polymer nanostructures remains a key challenge on their way toward applications. Here, we demonstrate that top-down processing facilitates a straightforward adjustment of the length of polyethylene oxide (PEO) based supramolecular polymer bottlebrushes (SPBs) in aqueous solutions. These cylindrical structures self-assemble via directional hydrogen bonds formed by benzenetrisurea (BTU) or benzenetrisepptide (BTP) motifs located within the hydrophobic core of the fiber. A slow transition from different organic solvents to water leads first to the formation of μm -long fibers, which can subsequently be fragmented by

ultrasonication or dual asymmetric centrifugation. The latter allows for a better adjustment of applied shear stresses and, thus, enables access to differently sized fragments depending on time and rotation rate. Extended sonication and scission analysis further allowed an estimation of tensile strengths of around 16 MPa for both, the BTU and BTP systems. In combination with the high kinetic stability of these SPBs, the applied top-down methods represent an easily implementable technique toward one-dimensional polymer nanostructures with adjustable lengths in the range of interest for perspective biomedical applications.

Introduction

Cylindrical polymer nanostructures in solution have received increasing attention during the last two decades related to their high surface-to-volume ratio which is particularly attractive for targeted carrier materials in biomedical applications. In addition, cylindrical drug delivery vehicles appear to be advantageous compared to their spherical analogues with regard to blood circulation time, drug loading, and tumor penetration abilities.[1-3] The straightforward preparation of cylindrical polymer aggregates with defined and reproducible lengths, however, still remains challenging, but represents a prerequisite for the desired applications in nanomedicine.[4, 5] A key factor in this regard are formulation strategies, which allow a straightforward implementation into established processes which are, e.g., in accordance with a Good Manufacturing Practice (GMP).[6] Approaches such as the crystallization-driven self-assembly (CDSA) or the synthesis of covalently bound cylindrical polymer brushes (CPBs) offer access to defined fiber lengths.[7-16] However, they also suffer from disadvantages, such as significant experimental effort to evaluate suitable reaction procedures for the synthesis or the conditions for the assembly process, and are therefore often limited to specific materials. An alternative is the use of molecular motifs

capable of forming directional supramolecular interaction forces, such as hydrogen bonds or π -interactions, to guide the one-dimensional (1D) assembly of established, commercial polymers in solution.[17] We recently reported the self-assembly of polyethylene oxide (PEO) polymers into cylindrical nanostructures, also called supramolecular polymer bottlebrushes (SPBs), based on their end group modification with hydrogen bond forming benzenetrisurea (BTU) and benzenetrisepptide (BTP) motifs.[18-20] The resulting amphiphilic character of the materials facilitated a control of the kinetic assembly which provided access to stable nanostructures in a broad range of lengths (<100 nm – 2 μ m). While the process enables a good adjustment of length, it relies on a precise control of the assembly pathway and requires the use of organic solvents such as THF and DMF, which limits the applicability in pharmaceutical formulations.[21] For an application in nanomedicine, lengths in the range of 100-200 nm are particularly attractive to ensure cellular uptake and to access the known size window for a potential enhanced permeability and retention effect (EPR).[22, 23] As an alternative for the assembly pathway control, we opted to apply easy-to-use top-down approaches to tune the length distributions in a straightforward fashion over the above-mentioned length range of interest. While ultrasonication (US) represents a standard, but a rather harsh fragmentation technique, we additionally introduce dual asymmetric centrifugation (DAC) as an excellent alternative top-down method for effective, more controlled, and adaptable preparation of polymer nanostructures.[24-28] Both methods are applied for fragmentation of initially μ m-long SPBs based on BTU- and BTP-PEO conjugates. The resulting nanofibers were characterized in detail by cryo transmission electron microscopy (cryo-TEM), as well as asymmetrical flow field-flow fractionation measurements coupled to an UV- and a multi angle laser light scattering detector (AF4-MALLS) to estimate apparent structure lengths and length distribution of the SPBs.

Results and discussion

The general structure of the tested BTP and BTU is depicted in Figure 1.[19, 20] While the hydrogen bonding moieties are either urea- or peptide-based (i.e. phenylalanine) units, the dodecyl chains act as hydrophobic shields to induce the amphiphilic assembly in water and prevent the surrounding water from interfering with the hydrogen bonds in the interior.[29] Attaching a hydrophilic PEO chain (2 kg mol^{-1}), the compounds self-assemble into long fiber structures consisting of 2-4 lateral core units upon transfer into water as reported previously.[19-21] A slow solvent switch from a THF solution to water resulted in μm -long fibers in both cases (**BTU** or **BTP**).

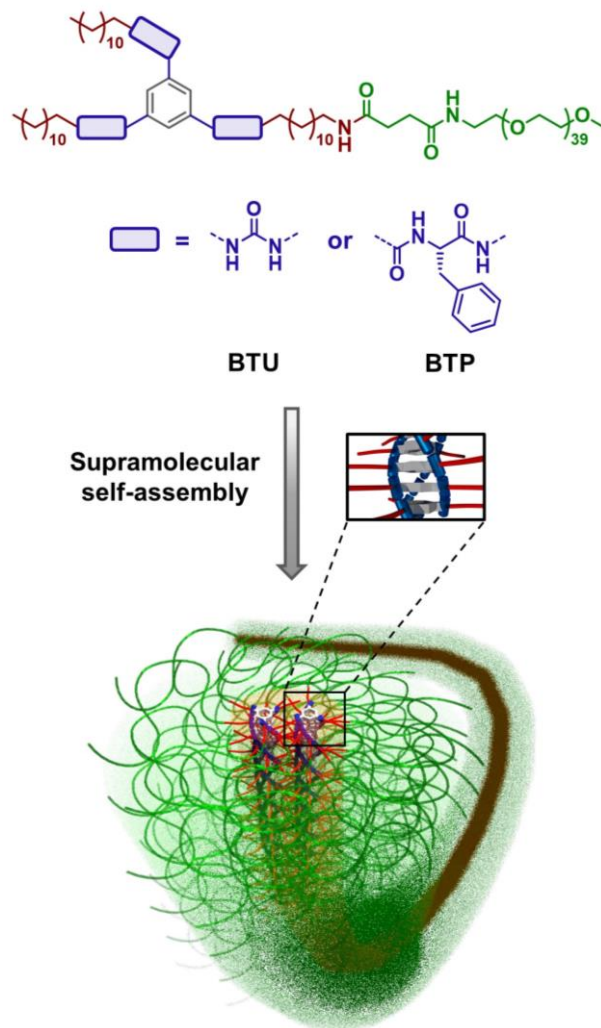


Figure 1: Schematic representation of the chemical structures of **BTU** and **BTP** and their supramolecular self-assembly into SPBs.

An initial attempt to tune the fiber lengths by changing the initial organic solvent was not successful. As seen in the corresponding cryoTEM investigations/images (Figures S1-6) and AF4 measurements (Figure S10), all tested organic solvents yielded similarly μm -long fibers, exemplifying the surprisingly minor influence of the initial organic solvent on the resulting fiber lengths. Targeted sizes below $1 \mu\text{m}$ can be, alternatively, achieved by top-down strategies inducing strong shear forces. Typically, ultrasonication (US) is applied to fragment supramolecular

structures.[7, 30-33] However, US causes cavitation within the sample whose collapse is accompanied by very high local heating. Alternative approaches rely on inducing strong shear forces by strong mixers or dispersers. An interesting method in this regard is the use of the dual asymmetric centrifugation (DAC), which is also considered to be a speed-mix technology due to the rapid mixing of the sample.[28] In DAC, the sample holder performs an additional rotation besides the main rotor rotation, resulting in a continuous change of the direction of the centrifugal force.[28] This change induces a strong agitation of the solution and generates large shear forces. DAC has mainly been used to create drug composites, but recently found application in the formulation of liposomes or the direct nano-dispersion of pharmaceutically active ingredients.[24-28] The technique resembles nano-milling methods, but allows much smaller sample scales, which renders it particularly attractive for testing its suitability to fragment fiber-like supramolecular assemblies in solution.[34]

We started with a rotational speed of 1000 rpm and treated the initial fibers for 10 min (samples **BTU DAC (10 min, 1000 rpm)** and **BTP DAC (10 min, 1000 rpm)**). This comparably mild treatment already caused a significant fragmentation of the μm long fibers resulting in structures of 50-200 nm length according to the cryo-TEM images after 10 min of treatment (Figure 2). Average fiber lengths of 92 ± 51 nm and 74 ± 39 nm for **BTU DAC (10 min, 1000 rpm)** and **BTP DAC (10 min, 1000 rpm)**, respectively, were apparent according to cryoTEM.

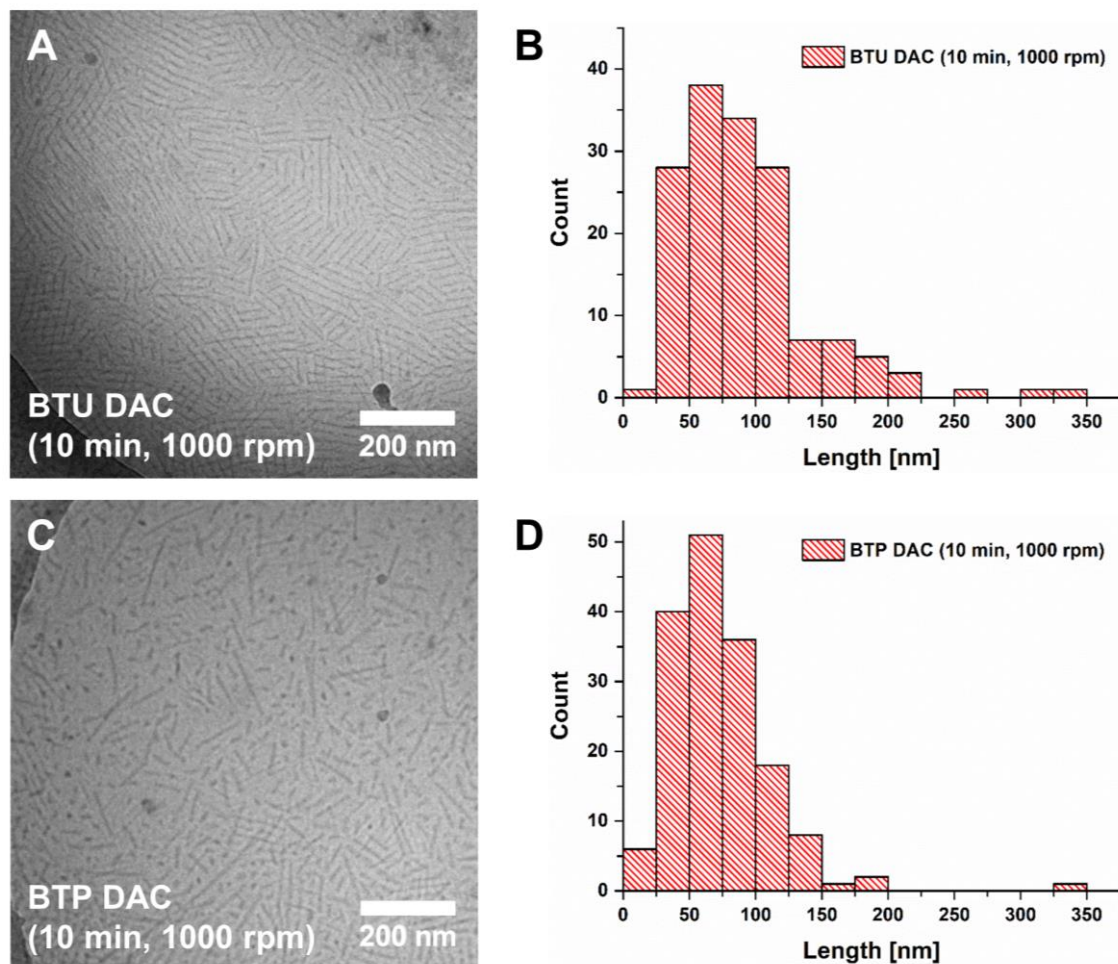


Figure 2: CryoTEM images of **BTU DAC (10 min, 1000 rpm)** (A) and **BTP DAC (10 min, 1000 rpm)** (C) and the corresponding histograms (B and D) showing the length distributions of **BTU DAC (10 min, 1000 rpm)** (B, mean length: 92 ± 51 nm) and **BTP DAC (10 min, 1000 rpm)** (D, mean length: 74 ± 39 nm).

This can further be supported by AF4 measurements (Figure 3A and B). Here, fibers featuring an average radius of gyration $R_g \sim 20$ nm and a weight-average molar mass M_w of $3\,099\,000$ g mol⁻¹ corresponding to a number of aggregation, N_{agg} , of ca. 1200 and a length of 110 nm for **BTU** (assuming four units per cross-section), and a weight-average molar mass M_w of $4\,406\,000$ g mol⁻¹ corresponding to a number of aggregation, N_{agg} , of ca. 490 and a length of 120 nm (assuming two

units per cross-section) for **BTP**, can be observed after 10 min at 1000 rpm (Figure S12 A and B).[19, 21]

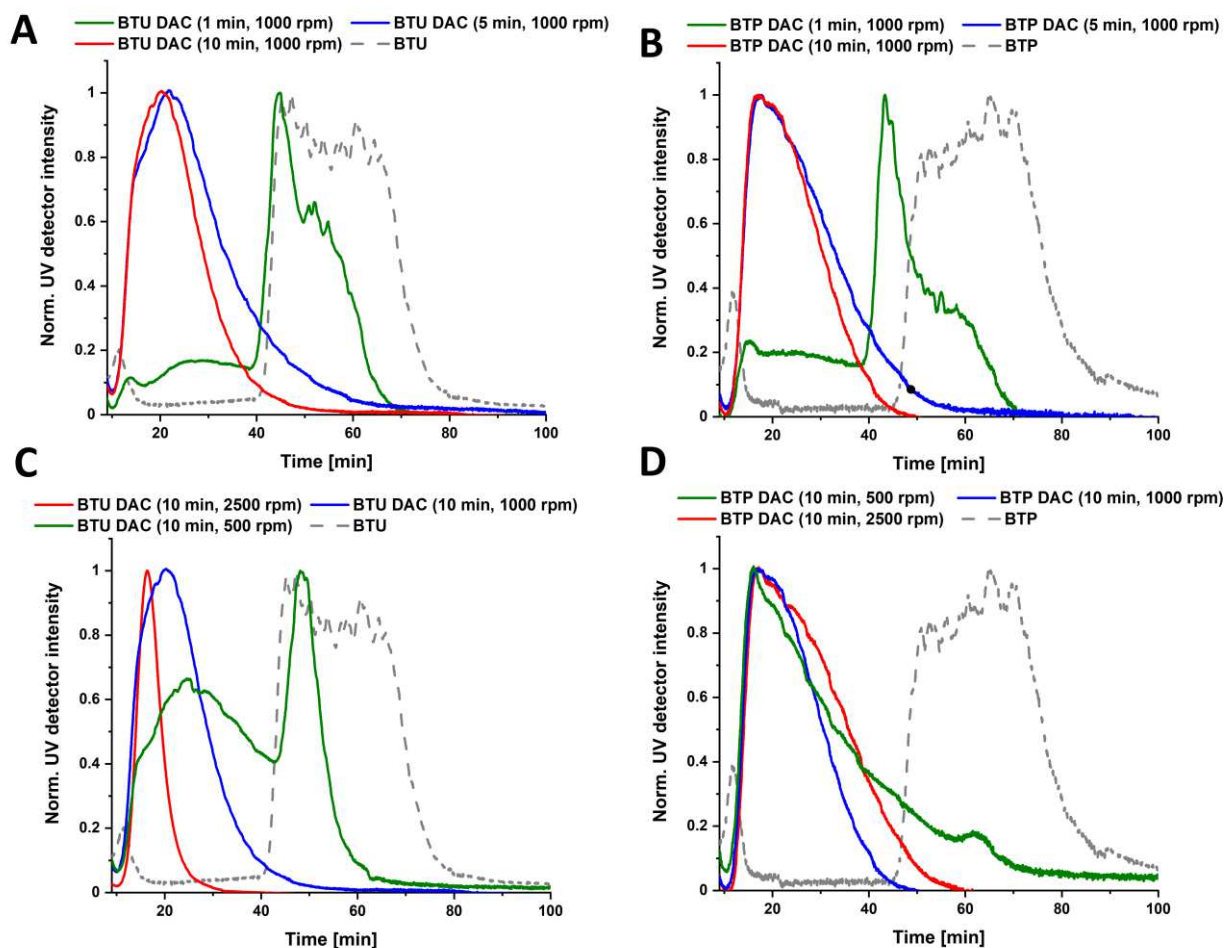


Figure 3: AF4 elution profiles showing the stability against dual centrifugation over different time ranges at rotation speeds of 1000 rpm (A and B) and 2500 rpm (C and D) of **BTU** and **BTP**, respectively. Injection peaks were omitted for reasons of clarity.

As a consequence, we scrutinized the influence of time and rotation speed on the sizes of the fragments which were analyzed by AF4 (Figure 3). First, samples were treated for 1, 5, and 10 min at a rotation speed of 1000 rpm (Figure 3A and B, S12A and B) to investigate if an extended exposure time can break up the aggregates even further. In case of **BTU**, already after 1 min of mixing the peak maximum of the UV trace is shifted from 60 min to 45 min (Figure 3A). After 5 min of centrifugation, no further change can be observed since the peak at this low elution time

already corresponds to very small oligomers (Figure 3A). For **BTP**, a stronger downward shift of the peak maximum from 70 to 45 min can be observed after 1 min of mixing. Similar to the **BTU**, the increase of centrifugation time to 5 min leads to a more pronounced fragmentation, which is not further enhanced by additional time of DAC.

To determine the influence of the strength of the shear forces, we also increased or decreased the centrifugal speed to 2500 and 500 rpm, respectively (Figure 3C and D). At 2500 rpm, the fragmentation of the aggregates occurs more rapidly and a significant shift in AF4 elution times is observed for both samples, **BTU** and **BTP**, within 1 min DAC (Figure S11A and B). In case of **BTU**, the samples were further fragmented with extended time at this speed and the smallest structures were obtained for **BTU** with an $R_g < 3$ nm (Figure S12C). On the contrary, the reduction of the applied shear forces (500 rpm) limited the fragmentation rate for both samples. In case of **BTU** and after 10 min a significant amount of the large structures (> 40 min elution time) remains intact (Figure 3C and D, S11C and D). Overall, DAC represents as a straightforward technique to adjust the size of these supramolecular assemblies, which can easily be tuned by variation of rotational speed and treatment time. Nevertheless, the distribution of the aggregate size remains rather broad. Increasing the time of treatment, the length of the fibers appears to approach a lower size-limit depending on the speed of rotation, which becomes particularly apparent for the **BTU** compounds. Even extended mixing times (3 h) at 2500 rpm did not significantly change the observed distributions compared to 10 min treatment (Figure S13).

For comparison to more established techniques, we tested the impact of ultrasonication (US) on the same fibers by variation of the exposure times to a US sonication probe (Figure 4).

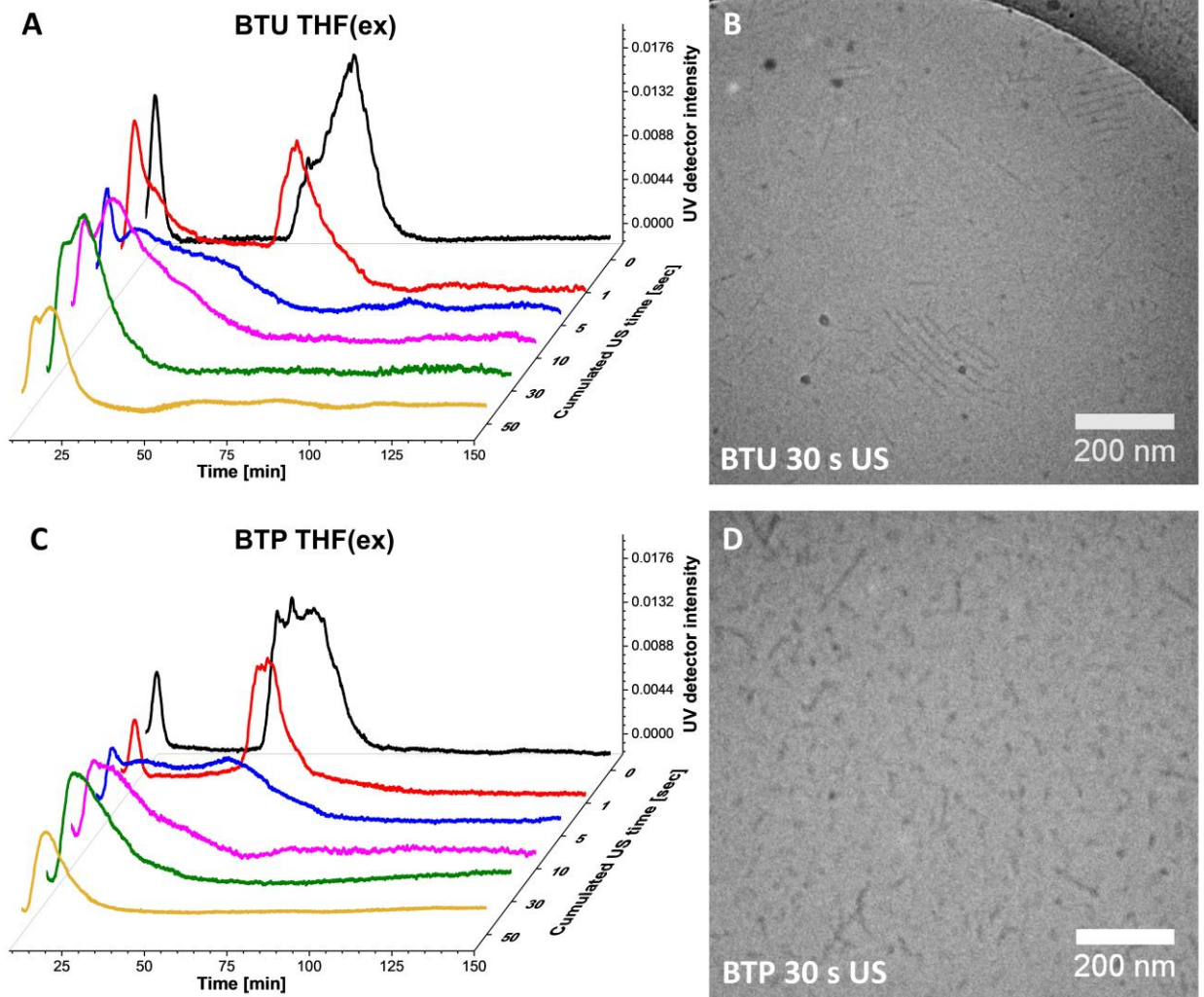


Figure 4: AF4-UV elution profiles after ultrasonication (US) for the cumulated time of 0 s (black), 1 s (red), 5 s (blue), 10 s (magenta), 30 s (green), and 50 s (yellow) for **BTU** (A) and **BTP** (C). The injection peaks were omitted for reasons of clarity. CryoTEM images of **BTU** (B) and **BTP** (D) after 30 s of ultrasonication exposure ($c = 1 \text{ mg mL}^{-1}$).

Already after 1 s of US, a significant decrease in length of the fibers can be seen for both samples (Figure 4A and C), substantiating the rather harsh forces induced by this technique. The peak maxima at around 80 min (**BTU**) and 65 min (**BTP**) decrease slightly and shift to lower elution times. In case of the **BTU** sample, even a new peak is formed at 10 to 20 min, corresponding to the formation of short structures. Continuing US for a cumulated time of 5 s resulted in the

disappearance of the main peaks and the appearance of a broad distribution ranging from 15 min to 70 min elution time for both samples. The severe broadening of the distribution and the immediate formation of very small structures suggests a shearing off of small fragments during US. A further increase of time (up to 30 s) narrows the length distribution once again and only the small aggregates remain in solution, which appear to be stable during further sonication (50 s of cumulated US time). The resulting fibers feature an average $R_g \sim 15$ nm (Figure S14) and a weight-average molar mass M_w of 3 633 000 g mol⁻¹ corresponding to a number of aggregation, N_{agg} , of 1400 and a length of 125 nm for **BTU** (assuming four units per cross-section). For **BTP** a weight-average molar mass M_w of 2 910 000 g mol⁻¹, corresponding to a number of aggregation, N_{agg} , of 440 and a length of 80 nm (assuming two units per cross-section) is calculated.[19, 21] Correlating well with the AF4 results, cryoTEM images of both samples (Figure 4B and 1D) show mainly short cylinders after a cumulated US time of 30 s with average fiber lengths of 124 ± 65 nm and 69 ± 41 nm for **BTU** and **BTP**, respectively (Figure S8). It is important to note, that all obtained fibers remained unchanged over several months after the top-down processing, demonstrating the previously described excellent kinetic stability of these supramolecular aggregates (Figures S15 and S16).[21]

Inspired by work of Lamour *et al.*, we estimated a similar limit length L_{lim} upon extensive US treatment.[35] This length allows an indirect estimation of the tensile strength of our fibers according to $L_{lim} = \sqrt{\frac{d^2 \sigma^*}{2\eta (\dot{R}_l/R_l)}}$, where R_l is the radius of the cavitation bubble, \dot{R}_l is the wall velocity of the collapsing bubble, d is the fiber diameter, and η is the viscosity of the solvent.[36] By assuming typical values for the wall velocity, bubble radius and viscosity of the solvent, the equation simplifies to: $L_{lim} = 7 \times 10^{-4} d \sqrt{\sigma^*}$. [37, 38] We exposed the **BTU** and **BTP** fibers to

extended US (> 1 h). No further scission could be observed after 2-3 h of US. AF4-MALLS measurements of the fibers after 3 h US revealed a weight-average molar mass at the elution peak maximum of 843 000 g mol⁻¹ and 943 000 g mol⁻¹ for **BTU** and **BTP**, respectively (Figure S17). This translates to a fiber length of 29 nm for **BTU** by assuming a stacking distance of 0.36 nm and 4 molecules per cross-section,[19] and 28 nm for **BTP** assuming a similar stacking distance and 2 molecules per cross-section.[21] Based on a fiber diameter of 12 nm (estimated from small angle X-ray scattering experiments),[19, 20] the resulting tensile strength for both compounds is approximately 16 to 17 MPa (Table S1). This strength is in the range of Elastin filaments and significantly lower, as for instance, the tensile strengths of amyloid fibrils.[35, 39] Overall the observed values for the fibers correspond well to their sensitivity to shear forces, however, the core-shell structure of our supramolecular systems has to be considered in this regard. E.g., significant steric strains induced by the polymer chains act on the core structure, limiting the strength of the supramolecular assembly.

Conclusion

In conclusion, the remarkable long-term stability of BTU- and BTP-PEO fibers in water, that were prepared via bottom-up self-assembly, enabled us to apply two straightforward top-down approaches (ultrasonication and dual asymmetric centrifugation) to tune the length distributions of the supramolecular fibers. Exposing the SPBs to ultrasonication resulted in a rapid fragmentation of the fibers into small rod-like fragments. Dual asymmetric centrifugation, on the other hand, allowed to adjust the length distributions in a more controlled manner by adjusting the time and rotation speed. This study, thus, demonstrates that easy-to-use top-down methods can be a feasible

approach to obtain some control over the length distributions of one-dimensional polymer nanostructures and make them thus more likely to be applied in biomedicine, where dimensional control is a prerequisite.

Acknowledgements

The authors thank Prof. Ulrich S. Schubert for his continuous support and access to excellent research facilities. TK, FVG, and JCB thank the German Science Foundation (DFG) for generous funding within the Emmy-Noether Programme (Project-ID: 358263073). CryoTEM investigations were performed at the electron microscopy facilities of the Jena Center for Soft Matter (JCSM), which were purchased with grants from the DFG and the European funds for Regional Development (EFRE). The funding of the collaborative research center PolyTarget, projects A05 and Z01 (Project-ID: 316213987 – SFB 1278) by the DFG are acknowledged.

References

1. Truong, N. P.; Whittaker, A. K.; Mak, C. W.; Davis, T. P. *Expert Opin. Drug Del.* **2015**, *12* (1), 129-142.
2. Toy, R.; Peiris, P. M.; Ghaghada, K. B.; Karathanasis, E. *Nanomedicine* **2014**, *9* (1), 121-134.
3. Liu, Y.; Tan, J.; Thomas, A.; Ou-Yang, D.; Muzykantov, V. R. *Therapeutic delivery* **2012**, *3* (2), 181-194.
4. Müllner, M. *Macromol. Chem. Phys.* **2016**, *217* (20), 2209-2222.
5. Truong, N. P.; Quinn, J. F.; Whittaker, M. R.; Davis, T. P. *Polym. Chem.* **2016**, *7* (26), 4295-4312.
6. Shkodra-Pula, B.; Vollrath, A.; Schubert, U. S.; Schubert, S. Chapter 9 - Polymer-based nanoparticles for biomedical applications. In *Frontiers of Nanoscience*; Parak, W. J.; Feliu, N., Eds.; Elsevier: 2020; Vol. 16, pp 233-252.

7. Gilroy, J. B.; Gädt, T.; Whittell, G. R.; Chabanne, L.; Mitchels, J. M.; Richardson, R. M.; Winnik, M. A.; Manners, I. *Nat. Chem.* **2010**, *2*, 566-570, Article.
8. Finnegan, J.; Pilkington, E.; Alt, K.; Rahim, M. A.; Kent, S. J.; Davis, T. P.; Kempe, K. *Chem. Sci.* **2021**, *12*, 7350-7360.
9. Finnegan, J. R.; He, X.; Street, S. T. G.; Garcia-Hernandez, J. D.; Hayward, D. W.; Harniman, R. L.; Richardson, R. M.; Whittell, G. R.; Manners, I. *J. Am. Chem. Soc.* **2018**, *140* (49), 17127-17140.
10. He, Y.; Eloi, J.-C.; Harniman, R. L.; Richardson, R. M.; Whittell, G. R.; Mathers, R. T.; Dove, A. P.; O'Reilly, R. K.; Manners, I. *J. Am. Chem. Soc.* **2019**, *141* (48), 19088-19098.
11. Street, S. T. G.; He, Y.; Jin, X.-H.; Hodgson, L.; Verkade, P.; Manners, I. *Chem. Sci.* **2020**, *11*, 8394-8408.
12. Niederberger, A.; Pelras, T.; Manni, L. S.; FitzGerald, P. A.; Warr, G. G.; Müllner, M. *Macromol. Rapid Commun.* **2021**, *42* (13), 2100138.
13. Müllner, M.; Yang, K.; Kaur, A.; New, E. J. *Polym. Chem.* **2018**, *9* (25), 3461-3465.
14. Mullner, M.; Mehta, D.; Nowell, C. J.; Porter, C. J. H. *Chem. Commun.* **2016**, *52* (58), 9121-9124.
15. Müllner, M.; Müller, A. H. E. *Polymer* **2016**, *98*, 389-401.
16. Müllner, M.; Dodds, S. J.; Nguyen, T.-H.; Senyschyn, D.; Porter, C. J. H.; Boyd, B. J.; Caruso, F. *ACS Nano* **2015**, *9* (2), 1294-1304.
17. Gruschwitz, F. V.; Klein, T.; Catrouillet, S.; Brendel, J. C. *Chem. Commun.* **2020**, *56*, 5079-5110.
18. Klein, T.; Ulrich, H. F.; Gruschwitz, F. V.; Kuchenbrod, M. T.; Takahashi, R.; Hoepfner, S.; Nischang, I.; Sakurai, K.; Brendel, J. C. *Macromol. Rapid Commun.* **2021**, *42*, 2000585.
19. Gruschwitz, F. V.; Fu, M.-C.; Klein, T.; Takahashi, R.; Higashihara, T.; Hoepfner, S.; Nischang, I.; Sakurai, K.; Brendel, J. C. *Macromolecules* **2020**, *53* (17), 7552-7560.
20. Klein, T.; Ulrich, H. F.; Gruschwitz, F. V.; Kuchenbrod, M. T.; Takahashi, R.; Fujii, S.; Hoepfner, S.; Nischang, I.; Sakurai, K.; Brendel, J. C. *Polym. Chem.* **2020**, *11* (42), 6763-6771.
21. Gruschwitz, F. V.; Klein, T.; Kuchenbrod, M. T.; Moriyama, N.; Fujii, S.; Nischang, I.; Hoepfner, S.; Sakurai, K.; Schubert, U. S.; Brendel, J. C. *ACS Macro Lett.* **2021**, 837-843.
22. Maeda, H. *Adv. Drug Del. Rev.* **2015**, *91*, 3-6.
23. Maeda, H.; Nakamura, H.; Fang, J. *Adv. Drug Del. Rev.* **2013**, *65* (1), 71-79.

24. Krämer, W.; Schubert, R.; Massing, U. *Int. J. Pharm.* **2019**, *572*, 118753.
25. Hagedorn, M.; Liebich, L.; Bögershausen, A.; Massing, U.; Hoffmann, S.; Mende, S.; Rischer, M. *Int. J. Pharm.* **2019**, *565*, 187-198.
26. Hagedorn, M.; Bögershausen, A.; Rischer, M.; Schubert, R.; Massing, U. *Int. J. Pharm.* **2017**, *530* (1), 79-88.
27. Hirsch, M.; Zirolì, V.; Helm, M.; Massing, U. *J. Control. Release* **2009**, *135* (1), 80-88.
28. Massing, U.; Cicko, S.; Zirolì, V. *J. Control. Release* **2008**, *125* (1), 16-24.
29. Krieg, E.; Bastings, M. M. C.; Besenius, P.; Rybtchinski, B. *Chem. Rev.* **2016**, *116* (4), 2414-2477.
30. Gädt, T.; Jeong, N. S.; Cambridge, G.; Winnik, M. A.; Manners, I. *Nat. Mater.* **2009**, *8*, 144-150.
31. Rho, J. Y.; Cox, H.; Mansfield, E. D. H.; Ellacott, S. H.; Peltier, R.; Brendel, J. C.; Hartlieb, M.; Waigh, T. A.; Perrier, S. *Nat. Commun.* **2019**, *10* (1), 4708.
32. Steinlein, C.; Kreger, K.; Schmidt, H.-W. *Macromol. Mater. Eng.* **2019**, *304* (10), 1900258.
33. Guérin, G.; Wang, H.; Manners, I.; Winnik, M. A. *J. Am. Chem. Soc.* **2008**, *130* (44), 14763-14771.
34. Peltonen, L.; Hirvonen, J. *J. Pharm. Pharmacol.* **2010**, *62* (11), 1569-1579.
35. Lamour, G.; Nassar, R.; Chan, P. H. W.; Bozkurt, G.; Li, J.; Bui, J. M.; Yip, C. K.; Mayor, T.; Li, H.; Wu, H.; Gsponer, J. A. *Biophys. J.* **2017**, *112* (4), 584-594.
36. Huang, Y. Y.; Knowles, T. P. J.; Terentjev, E. M. *Adv. Mater.* **2009**, *21* (38-39), 3945-3948.
37. Nguyen, T. Q.; Liang, Q. Z.; Kausch, H.-H. *Polymer* **1997**, *38* (15), 3783-3793.
38. Henrich, F.; Krupke, R.; Arnold, K.; Rojas Stütz, J. A.; Lebedkin, S.; Koch, T.; Schimmel, T.; Kappes, M. M. *J. Phys. Chem. B* **2007**, *111* (8), 1932-1937.
39. Paparcone, R.; Buehler, M. J. *Biomaterials* **2011**, *32* (13), 3367-3374.

Supporting Information

Adjusting the length of supramolecular polymer bottlebrushes by top down-approaches

Tobias Klein,^{a,b,‡} Franka V. Gruschwitz,^{a,b,‡} Maren T. Kuchenbrod,^{a,b} Ivo Nischang,^{a,b} Stephanie Hoepfner,^{a,b} Johannes C. Brendel,^{a,b,*}

a Laboratory of Organic and Macromolecular Chemistry (IOMC), Friedrich Schiller University Jena, Humboldtstraße 10, 07743 Jena, Germany

b Jena Center for Soft Matter (JCSM), Friedrich Schiller University Jena, Philosophenweg 7, 07743 Jena, Germany

‡ These authors contributed equally to this work

*corresponding author: johannes.brendel@uni-jena.de

Content

1. Synthesis & Procedures	3
2. Characterization.....	4
2.1 CryoTransmission Electron Microscopy (cryoTEM).....	4
2.2 Asymmetrical Flow Field-Flow Fractionation (AF4)	13
3. References	20

1. Synthesis & Procedures

Materials and Methods

All reagents and solvents were commercial products purchased from Sigma-Aldrich, abcr, Iris BioTech, Rapp Polymere or TCI and were used without further purification.

Synthesis

The benzenetrisurea-polyethylene oxide (BTU) and benzenetrispeptide-polyethylene oxide (BTP) conjugates were synthesized according to previously published protocols.^[1]

Self-assembly procedures

Solvent switch method

The self-assembly was conducted according to previous publications,^[2] where 5 mg of **BTU** or **BTP** were dissolved in 1 mL of THF and stirred overnight to guarantee complete dissolution. To this, 4 mL of MilliQ water were added (1-100 mL h⁻¹) using a syringe pump under vigorous stirring to reach a final water content of 80 v%. For this purpose, the needle of the syringe was immersed in the organic **BTP** or **BTU** solution to enable a constant release of MilliQ water from the syringe and avoid the formation of drops that would result in high local water concentrations at the spot where the drop immerses into the solution. Afterwards, the solution was transferred to float-analyzer® tubings with a molecular weight cutoff of 3.5 kD and dialyzed for five days against water to remove all THF traces.

Ultrasonication procedure

BTP and **BTU** samples assembled from THF at a concentration of 1 mg mL⁻¹ in MilliQ water were exposed to ultrasonication using a sonication probe (Hielscher ultrasonic processor UP200St, 100% amplitude, 20 W) for different durations up to a cumulated time of 50 s (1 s + 2 s + 2 s + 5 s + 5 s + 15 s + 20 s).

For the experiments concerning the mechanical stability the maximal power of 200 W of the ultrasonicator was applied for periods of 5 sec, with a 3 sec pause for 59 min each time.

Dual centrifugation procedure

Dual centrifugation was performed using a Hettich ZentriMix 380 R equipped with a ZentriMix rotor. **BTU** and **BTP** at a concentration of 1 mg mL^{-1} in MilliQ water were added to 2 mL vials and centrifuged for different durations (1 min, 5 min, 10 min, and 180 min) at different rotation speeds (500 rpm, 1000 rpm, and 2500 rpm). No milling beads were added to the vials to just rely on the shear forces caused by the dual rotor setup.

2. Characterization

2.1 CryoTransmission Electron Microscopy (cryoTEM)

Samples were prepared on Ar plasma treated Quantifoil grids (R2/2). $8.5 \mu\text{L}$ of the solutions (3 mg mL^{-1} in H_2O) were applied onto the grids and vitrified in liquid ethane utilizing a FEI Vitrobot Mark IV system (offset: -3 mm , blotting time: 1 s). Samples were transferred into the cryo holder (Gatan 626) utilizing the Gatan cryo stage, followed by transfer into the microscope keeping the temperature below $-172 \text{ }^\circ\text{C}$ during the whole transfer and measurement process after vitrification. Measurements were performed using a FEI Technai G² 20 operated at an acceleration voltage of 200 kV . Images were acquired with a Mega View (OSIS, Olympus Soft Imaging Systems) or an Eagle 4k CCD camera. cryoTEM images in this study display only specific regions of interest that are representative for the whole sample.

BTU Acetone

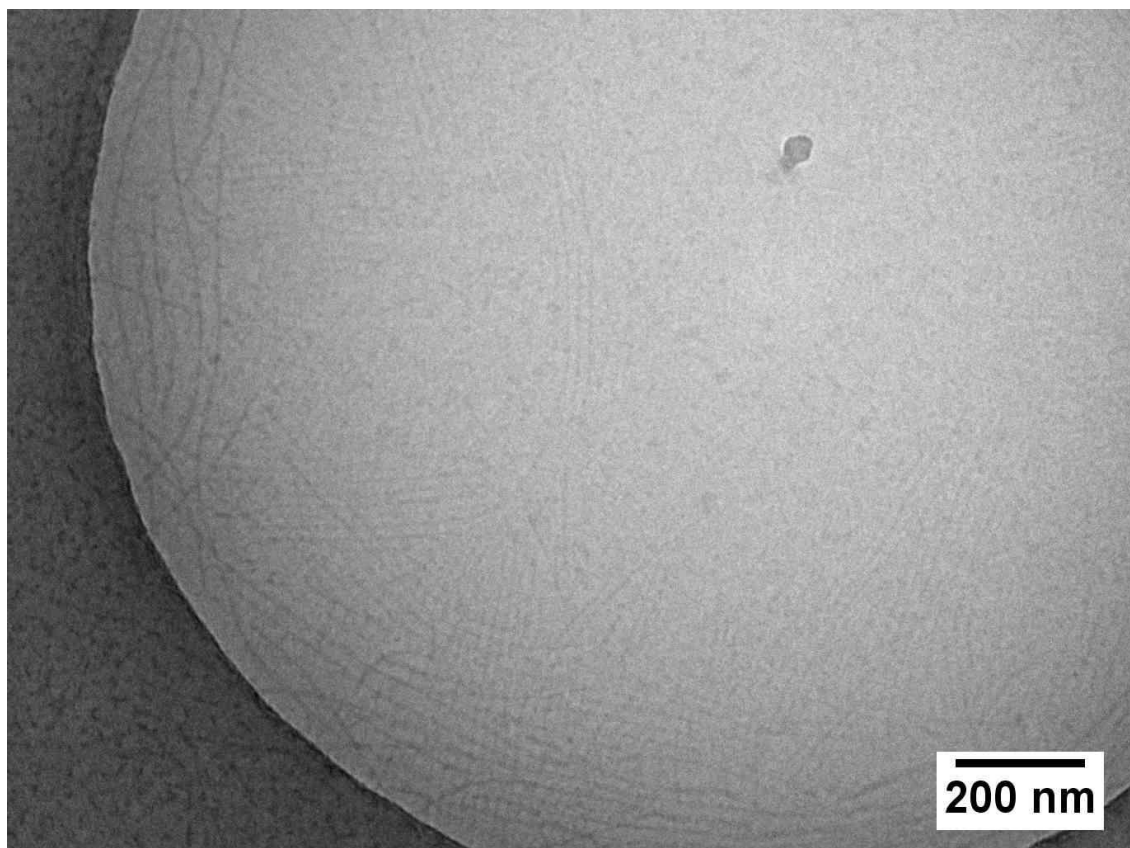


Figure S 1: cryoTEM image of **BTU Acetone** in water ($c = 1 \text{ mg mL}^{-1}$).

BTU DMF

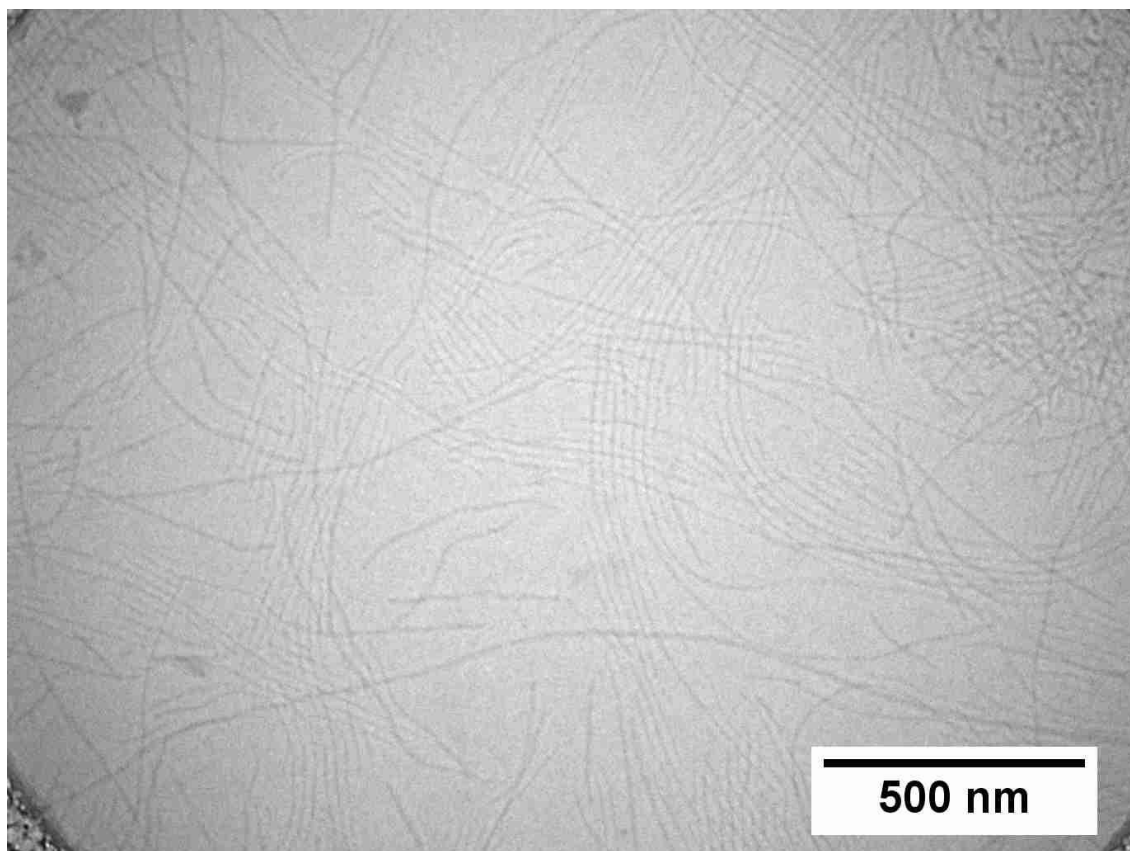


Figure S 2: cryoTEM image of **BTU DMF** in water ($c = 1 \text{ mg mL}^{-1}$).

BTU EtOH

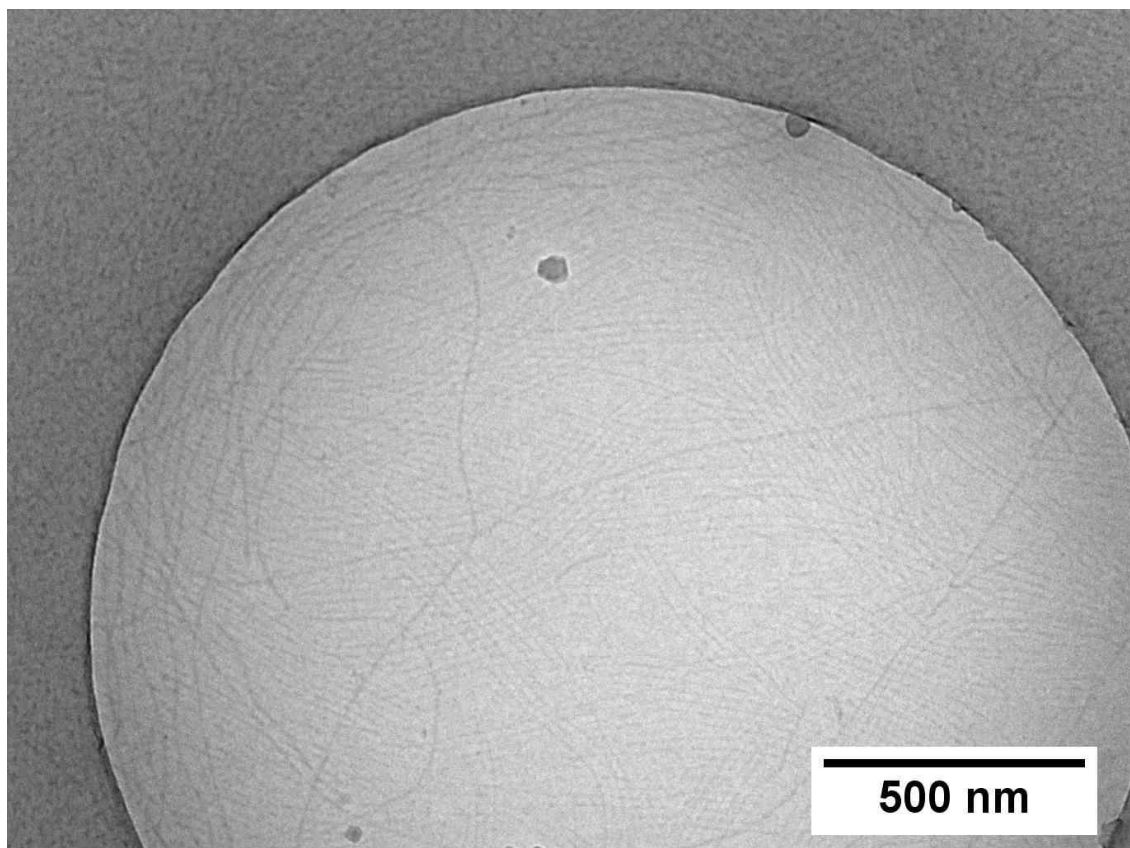


Figure S 3: cryoTEM image of **BTU EtOH** in water ($c = 1 \text{ mg mL}^{-1}$).

BTP Acetone

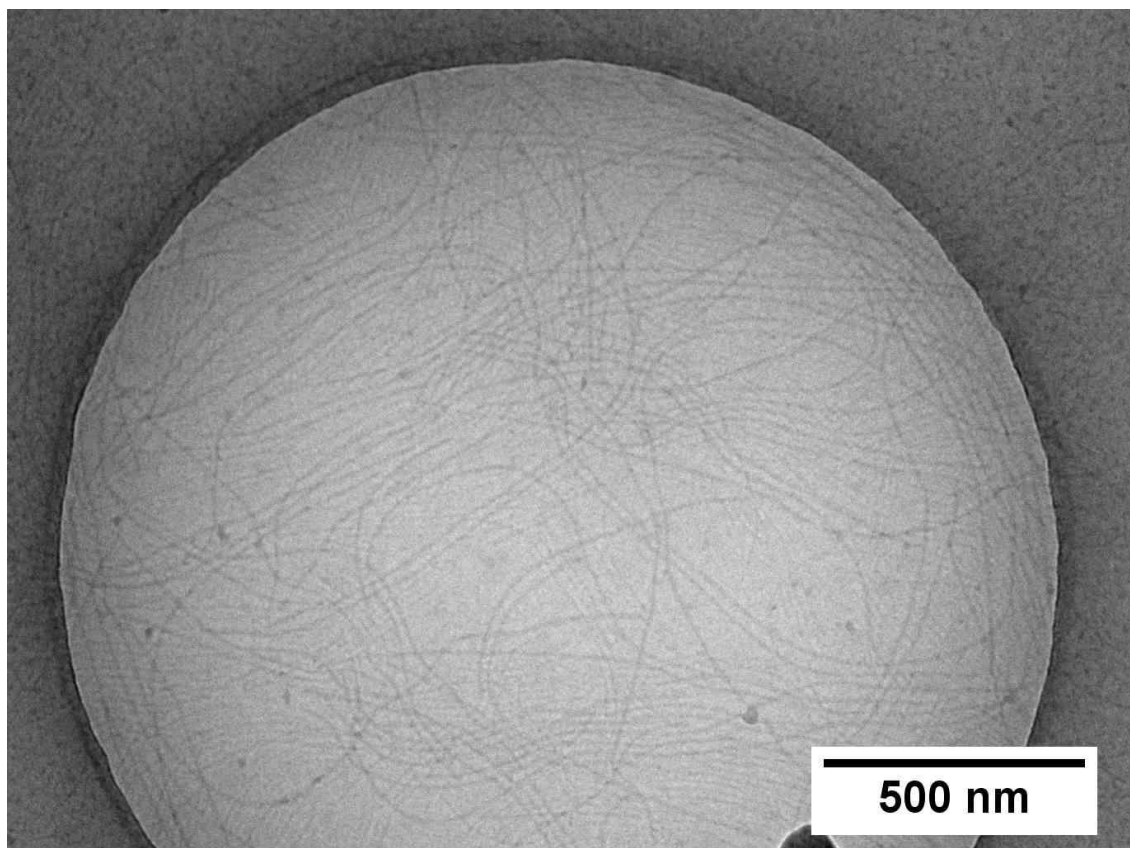


Figure S 4: cryoTEM image of **BTP Acetone** in water ($c = 1 \text{ mg mL}^{-1}$).

BTP DMF

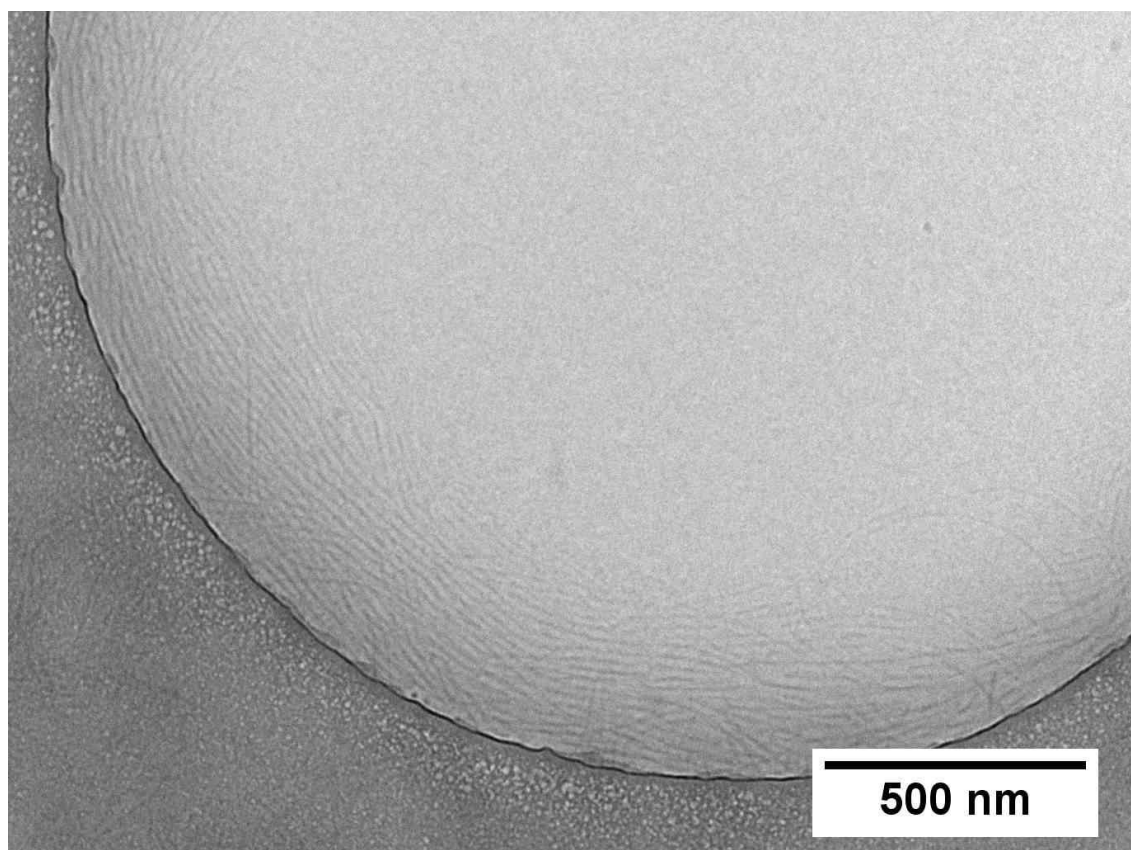


Figure S 5: cryoTEM image of **BTP DMF** in water ($c = 1 \text{ mg mL}^{-1}$).

BTP EtOH

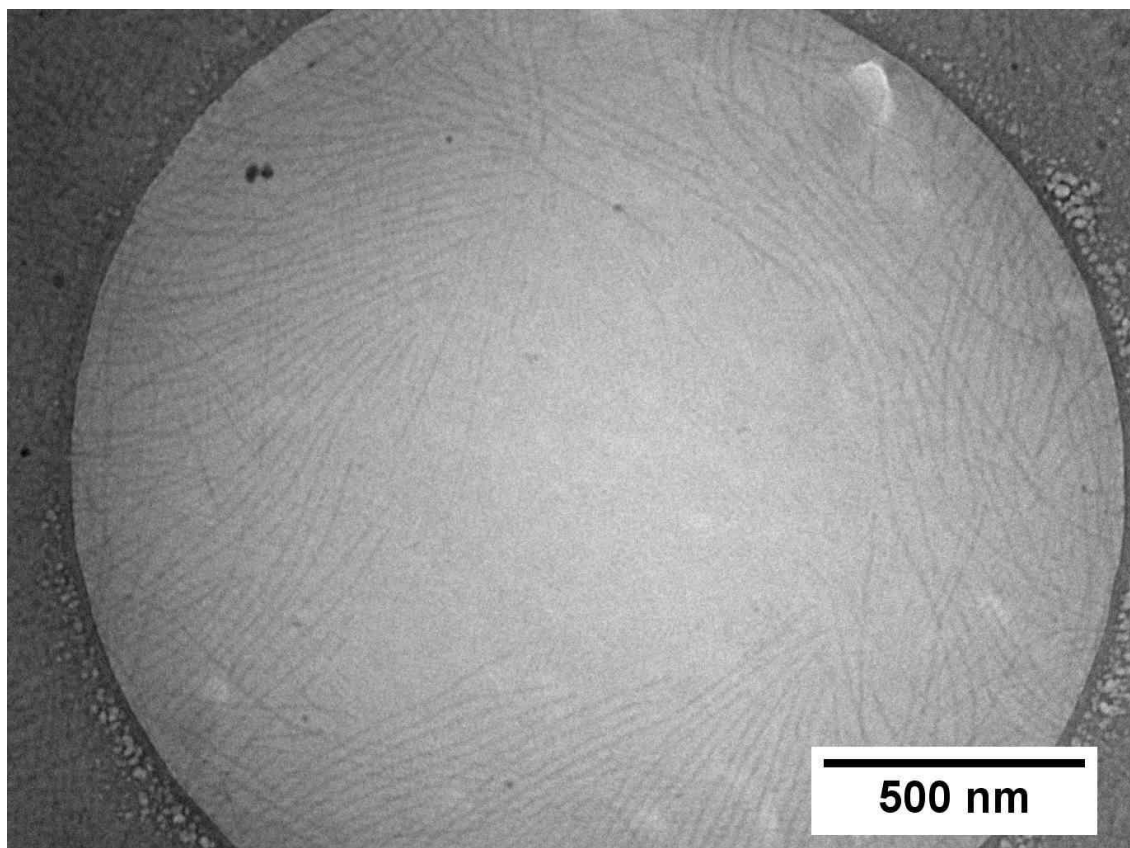


Figure S 6: cryoTEM image of **BTP EtOH** in water ($c = 1 \text{ mg mL}^{-1}$).

BTP US 1 s

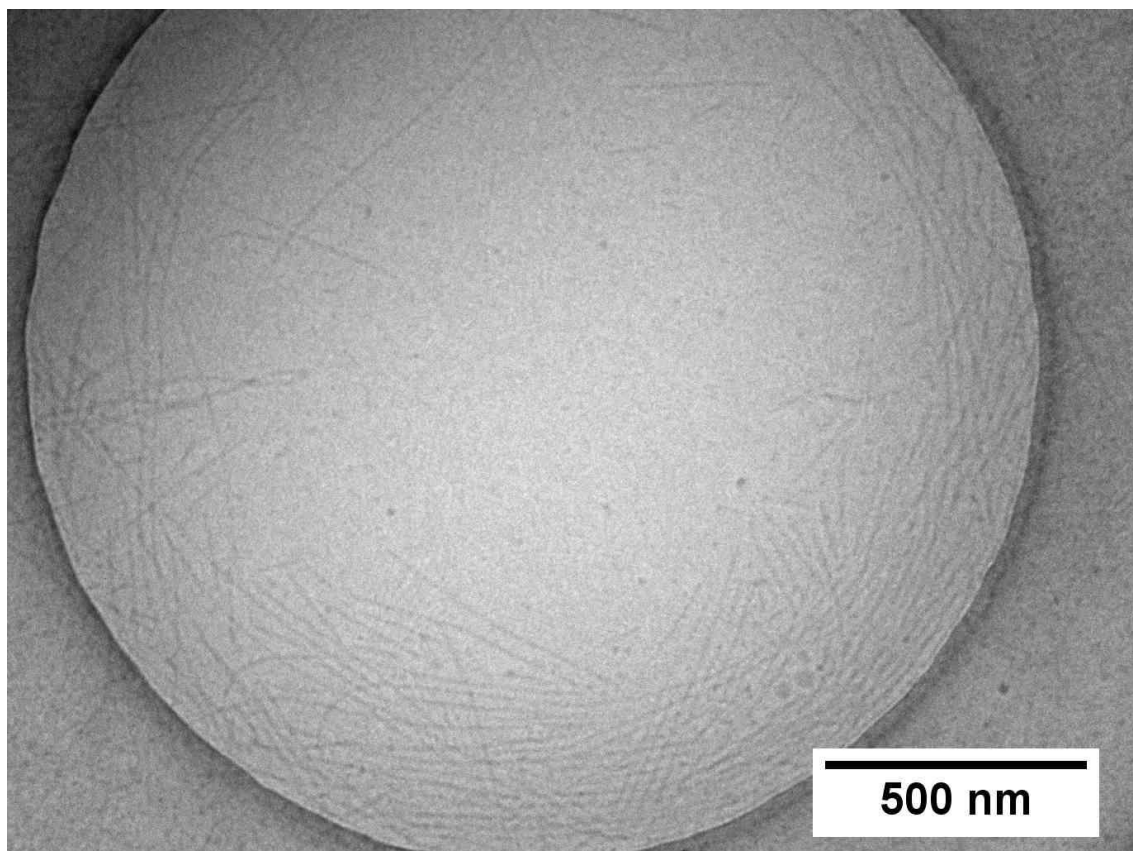


Figure S 7: cryoTEM image of **BTP** after ultrasonication for a cumulated time of 1 s (water; $c = 1 \text{ mg mL}^{-1}$).

BTU US 30 s & BTP US 30 s – cryoTEM histograms

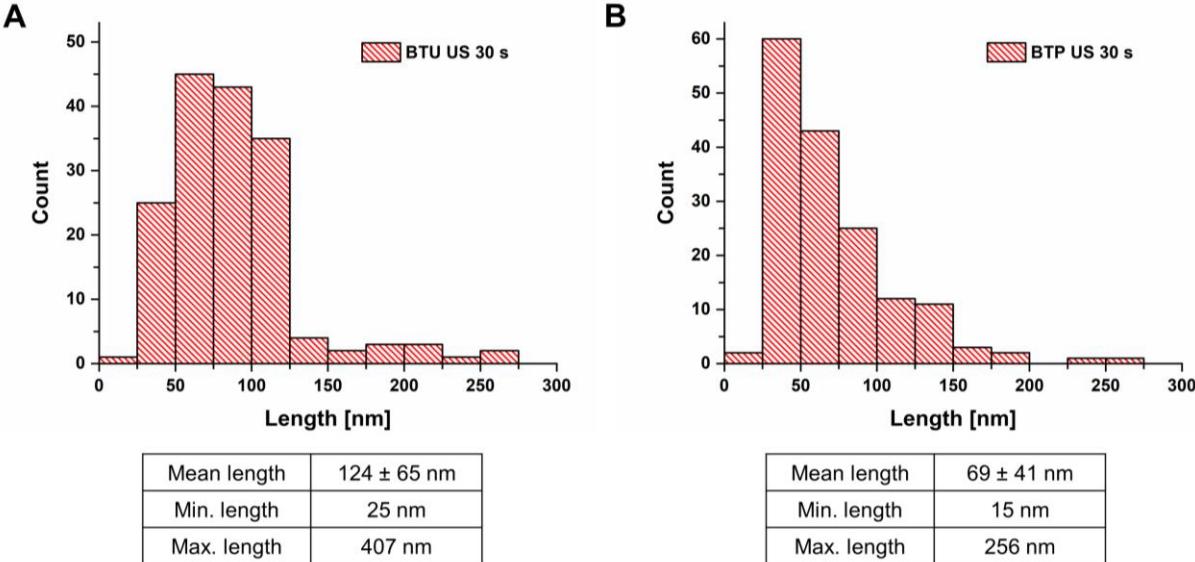


Figure S 8: CryoTEM histograms for **BTU US 30 s** (A) and **BTP US 30 s** (B).

2.2 Asymmetrical Flow Field-Flow Fractionation (AF4)

AF4 measurements were performed on an AF2000 MT System from Postnova Analytics GmbH (Landsberg, Germany), equipped with a tip and focus pump (PN1130), an autosampler (PN5300), and a channel oven unit (PN4020) set to 25 °C. The channel was coupled to a multiangle laser light scattering (MALLS) detector (PN3621) equipped with a 532 nm laser and an overall of 21 angles (only 28° - 148° have been used for calculation of R_g and M_w), a refractive index (RI) detector (PN3150), and a UV-detector (PN3212) operating at a wavelength of 280 nm. The channel had a trapezoidal geometry with a nominal height of 350 μm . A regenerated cellulose (RC) membrane from Postnova Analytics GmbH (10 kDa RC membrane) with a molar mass cutoff of 10 kDa was used as accumulation wall. As the mobile phase, an aqueous solution with 0.002 w% of NaN_3 was used. 50 μL of the sample at a concentration of 1 mg mL^{-1} was injected with an injection flow rate of 0.2 mL min^{-1} , a focus flow rate of 0.8 mL min^{-1} , and a cross-flow rate of 0.7 mL min^{-1} , resulting in a detector flow rate of 0.3 mL min^{-1} . The focusing time was 4 min before switching to elution at an exponentially decaying crossflow from 0.7 mL min^{-1} to 0.2 mL min^{-1} within 76.2 min. Thereafter, the crossflow profile was set to decay in a linear way from 0.05 mL min^{-1} to 0.04 mL min^{-1} within 71 min (Figure S21). Before the start of the next measurement, a rinsing step was performed at 1.5 mL min^{-1} flow of the tip pump only for 20 min. After each sample measurement, a blank measurement at identical detector conditions was run, which was subtracted from the traces of the sample measurement for analysis. The RI-detector was used as the concentration-sensitive detector ($\text{dn/dc}_{\text{BTU}}$ 1.47 mL/g and $\text{dn/dc}_{\text{BTP}}$ 1.48 mL/g) and the MALLS data was analysed via a ZIMM plot analysis to obtain the radii of gyration (R_g) and the molar mass at the specified elution times.

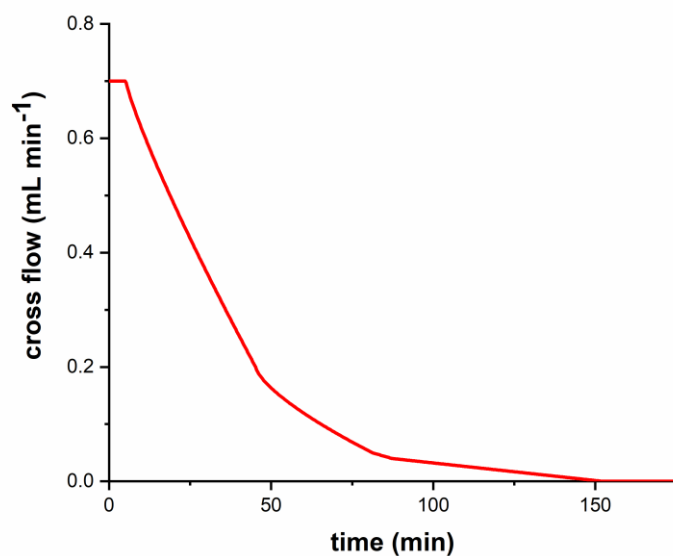


Figure S 9: Cross-flow profile applied for all AF4-MALLS measurements in this manuscript.

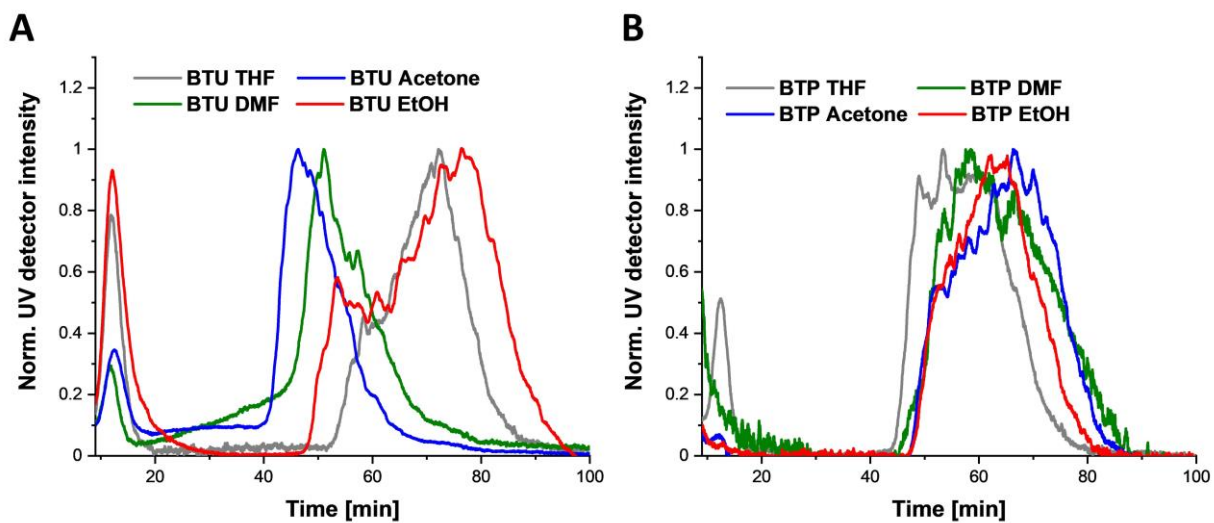


Figure S 10: Normalized UV traces at 280 nm of **BTU** (A) and **BTP** (B) assembled from different organic solvents. The injection peaks were omitted for reasons of clarity.

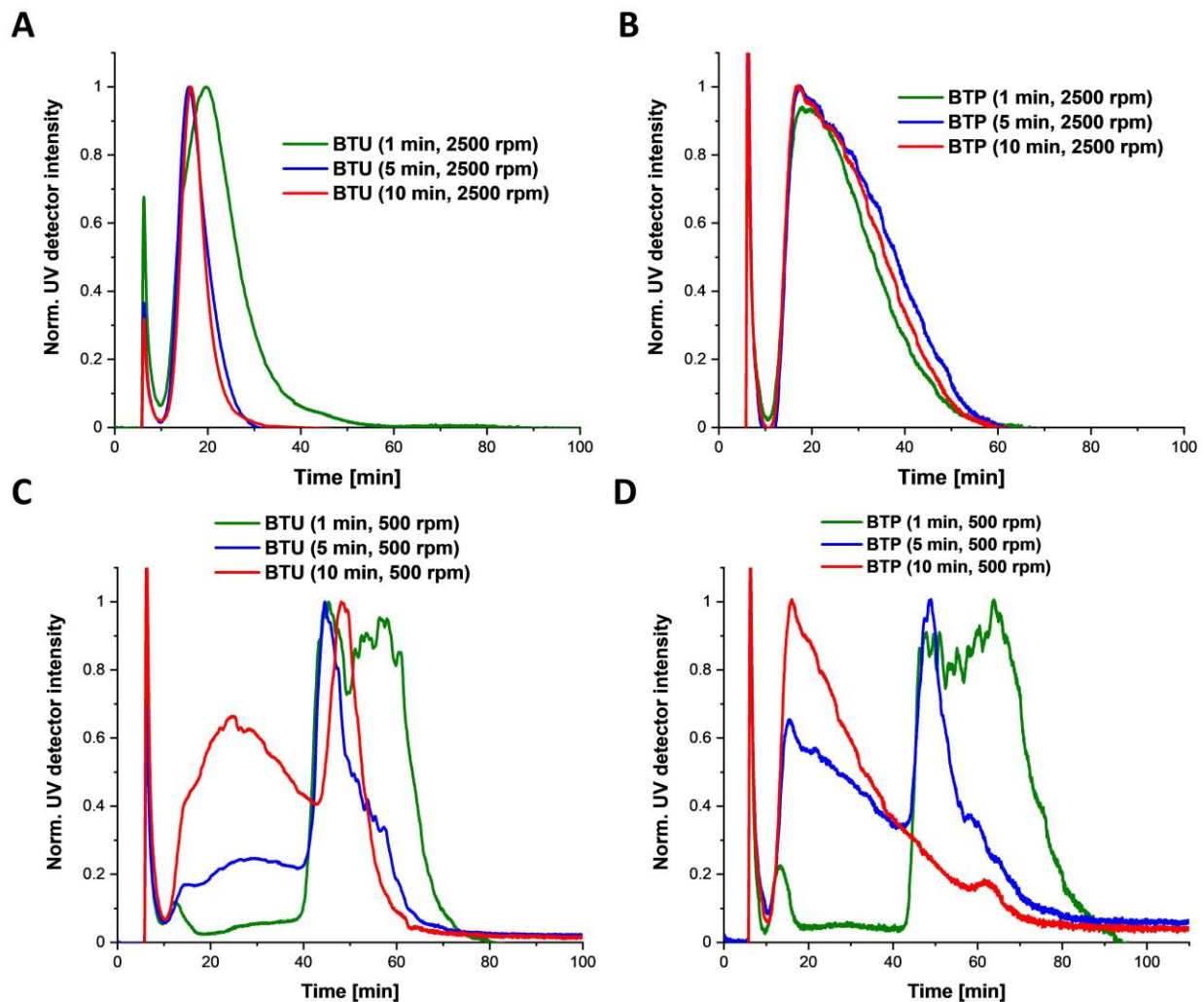


Figure S 11: AF4 elution profile showing the stability against dual centrifugation at different rotation speeds of 2500 rpm (A and B) and 500 rpm (C and D) of **BTU** and **BTP**, respectively.

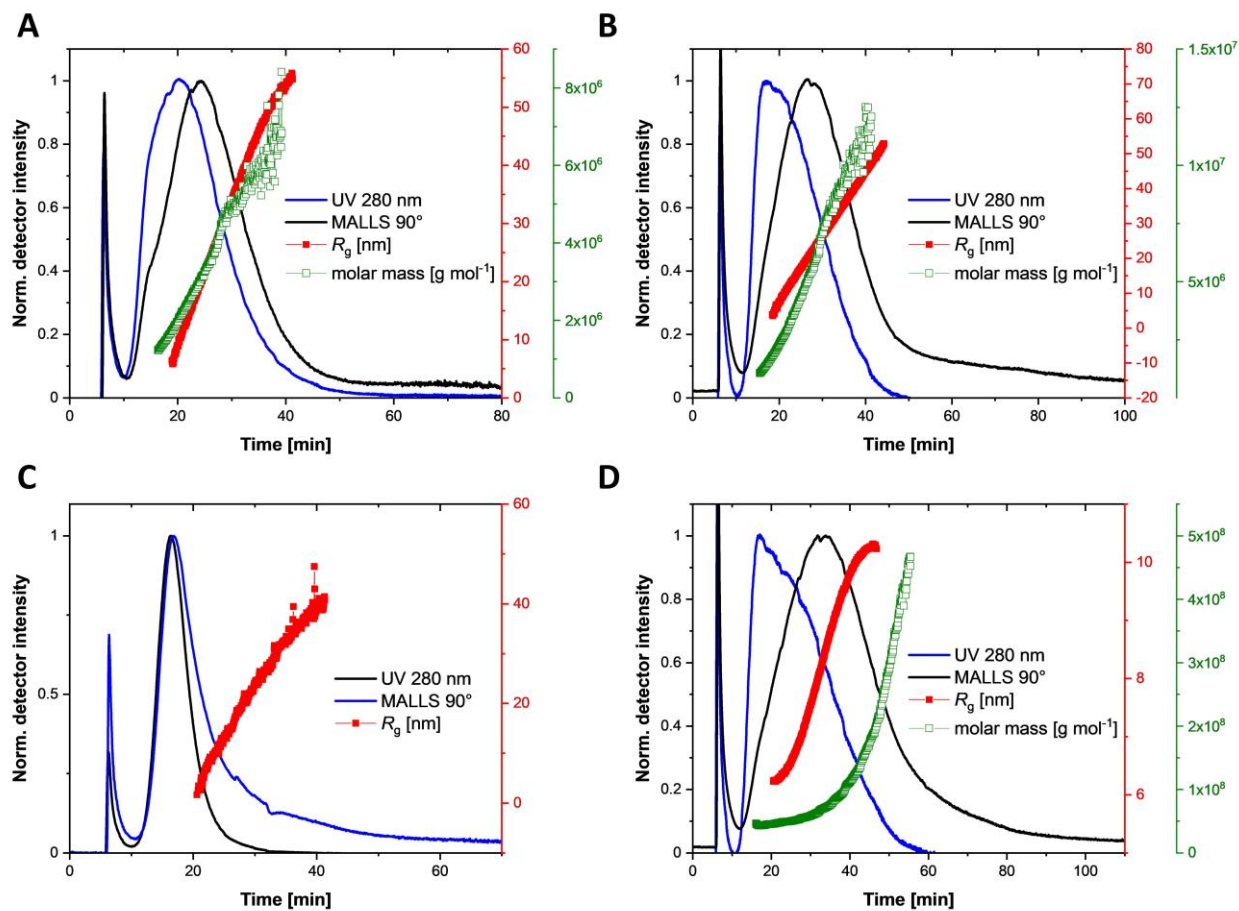


Figure S 12: Normalized MALLS 90° (black) and UV (blue) traces of **BTU** at 1000 rpm (A) and 2500 rpm (C), and **BTP** at 1000 rpm (B) and 2500 rpm (D) for 10 min. R_g (red) and molar mass (green) obtained via the Zimm plot of light scattering data from AF4-MALLS measurements. For **BTU (10 min, 2500 rpm)** (C), estimation of molar mass was not possible.

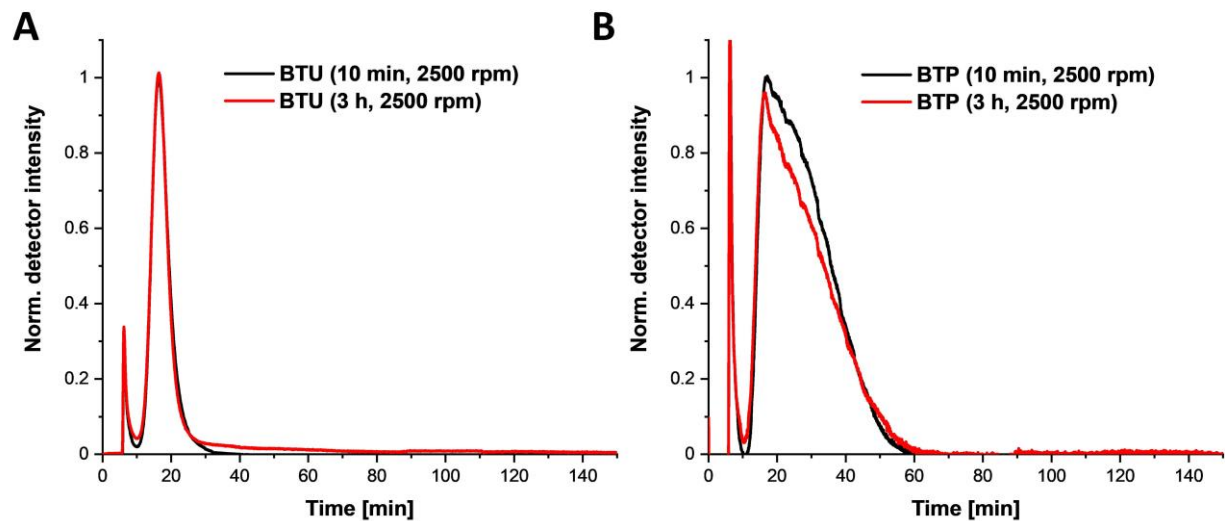


Figure S 13: AF4-UV traces (at 280 nm) of **BTP** (A) and **BTU** (B) after extended centrifugation times of 3 h.

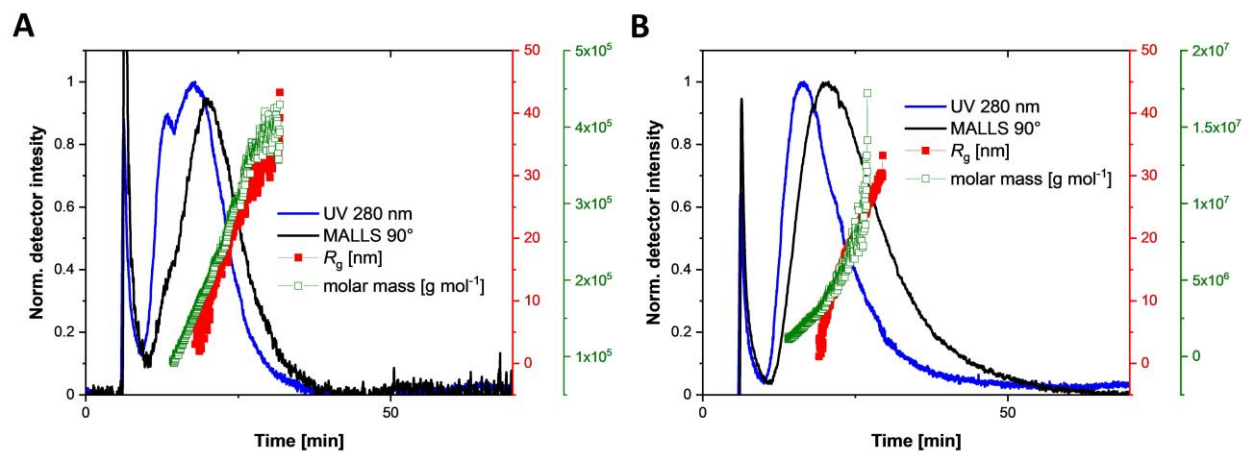


Figure S 14: Normalized MALLS 90° (black) and UV (blue) traces of **BTU** (A) and **BTP** (B), after a cumulated time of 50 s ultrasonication (black). R_g (red) and molar mass (green) obtained via the Zimm plot of light scattering data from AF4-MALLS measurements.

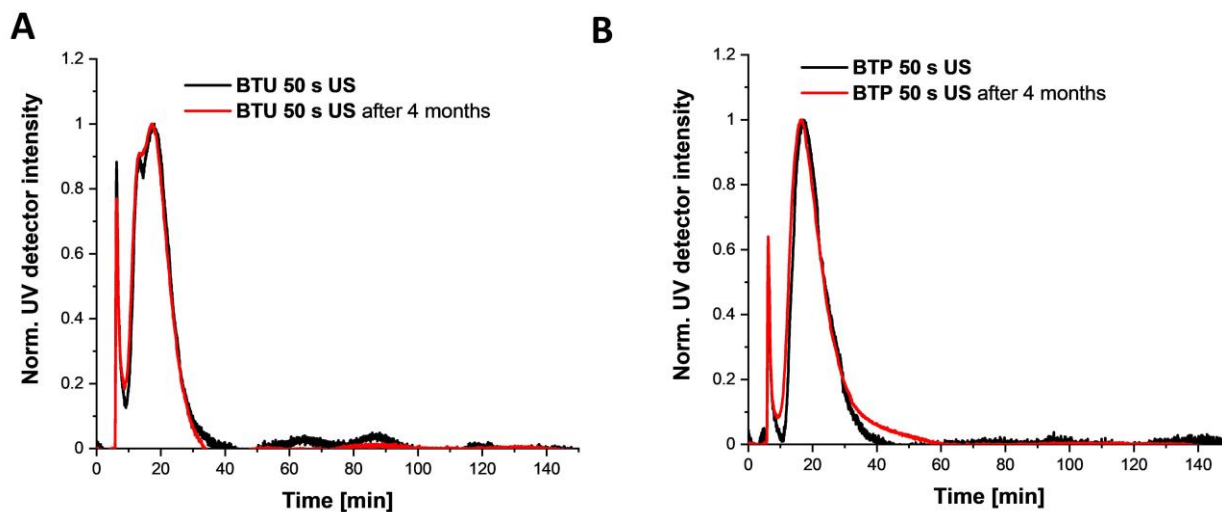


Figure S 15: Stability of the samples **BTP THF** (A) and **BTU THF** (B) after 50 s of ultrasound (US) exposure measured directly afterwards (black) and after four months (red).

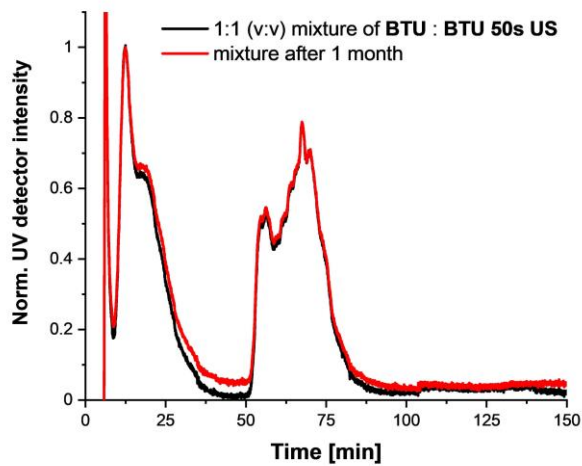


Figure S 16: AF4 elution profile proving the stability of a 1:1 (v/v) mixture of **BTU 50 s US** and **BTU** over months. Slight deviations in the traces might result from variations in the membrane and pressure differences between the measurements in the AF4 setup.

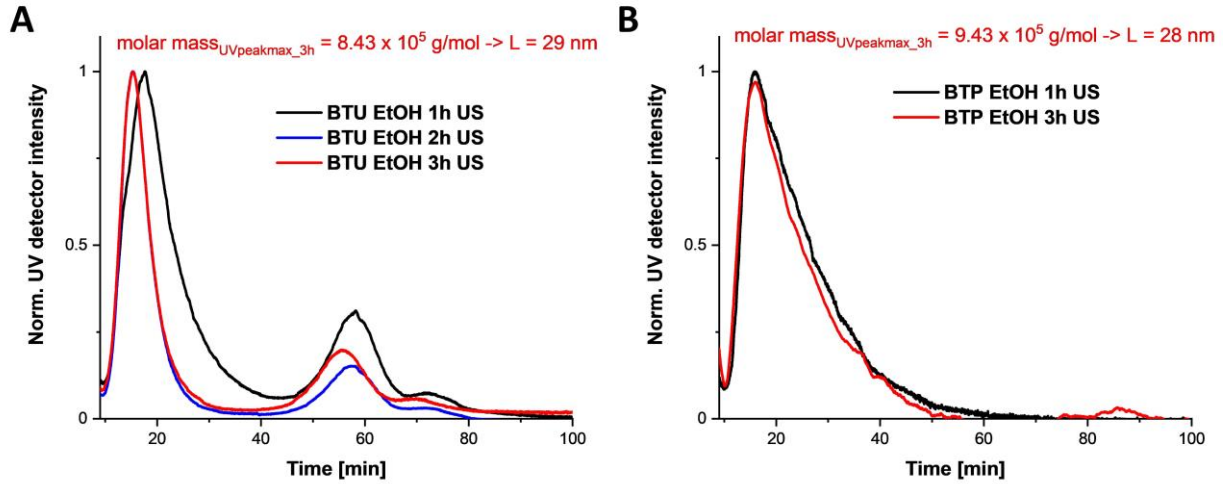


Figure S 17: AF4-UV traces of **BTU** (A) and **BTP** (B) after extended ultrasonication exposures of 1 to 3 h. The injection peaks were omitted for reasons of clarity. The molar mass at the UV peak maximum (280 nm) of the elution curve after 3 h was calculated by Zimm plotting the data obtained by the MALLS detector. The length was estimated from the number of aggregation and the literature known stacking distance of the unimers of approximately 0.36 nm. After correction by the number of molecules in the cross-section, as published recently,^[2] an approximate length of the assemblies at this point of elution can be calculated.

Calculation of σ^* from the obtained limit length after US

$$L_{lim} \approx 7 * 10^{-4} d \sqrt{\sigma^*} \quad \text{Eq. 1}$$

$$\sigma^* \approx \left(\frac{L_{lim}}{7 * 10^{-4} * d} \right)^2 \quad \text{Eq. 2}$$

Table S 1: Values calculated for σ^* for BTU and BTP from their respective limit length after 3h of US.

	L_{lim} (nm)	σ^* (MPa)
BTU	29	17
BTP	28	16

3. References

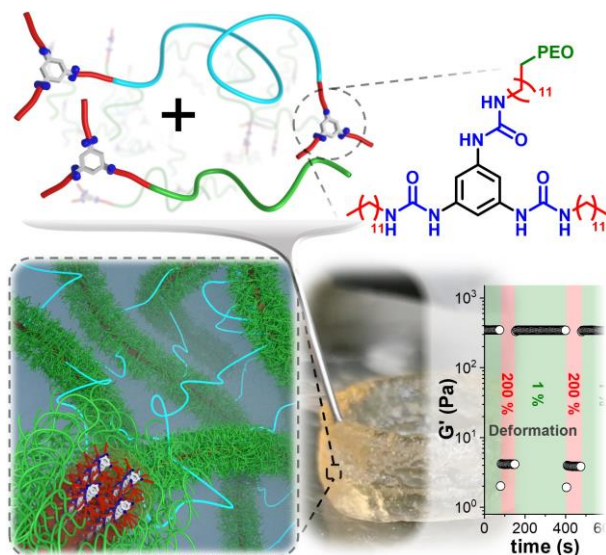
- [1] a) F. V. Gruschwitz, M.-C. Fu, T. Klein, R. Takahashi, T. Higashihara, S. Hoepfener, I. Nischang, K. Sakurai, J. C. Brendel, *Macromolecules* **2020**, *53*, 7552-7560; b) T. Klein, H. F. Ulrich, F. V. Gruschwitz, M. T. Kuchenbrod, R. Takahashi, S. Fujii, S. Hoepfener, I. Nischang, K. Sakurai, J. C. Brendel, *Polym. Chem.* **2020**, *11*, 6763-6771.
- [2] F. V. Gruschwitz, T. Klein, M. T. Kuchenbrod, N. Moriyama, S. Fujii, I. Nischang, S. Hoepfener, K. Sakurai, U. S. Schubert, J. C. Brendel, *ACS Macro Lett.* **2021**, 837-843.

Publication P8

Dynamic hydrogels from crosslinked supramolecular polymeric nanofibers

F. V. Gruschwitz, F. Hausig, P. Schüler, J. Kimmig, D. Pretzel, U.S. Schubert, S. Catrouillet, J. C. Brendel, *Adv. Func. Mater.* **2021**, submitted.

Reproduced by permission of F. V. Gruschwitz, F. Hausig, P. Schüler, J. Kimmig, D. Pretzel, U.S. Schubert, S. Catrouillet, J. C. Brendel.



Dynamic hydrogels from crosslinked supramolecular polymeric nanofibers

Franka V. Gruschwitz,^{a,b} Franziska Hausig,^{a,b} Philipp Schüler,^c Julian Kimmig,^b , David Pretzel,^b Ulrich S. Schubert,^{a,b} Sylvain Catrouillet,^{d,*} Johannes C. Brendel,^{a,b,*}

a Laboratory of Organic and Macromolecular Chemistry (IOMC), Friedrich Schiller University Jena, Humboldtstraße 10, 07743 Jena, Germany

b Jena Center for Soft Matter (JCSM), Friedrich Schiller University Jena, Philosophenweg 7, 07743 Jena, Germany

c IOMC/IAAC NMR platform, Friedrich Schiller University Jena, Humboldtstraße 10, 07743 Jena, Germany

d ICGM, Université de Montpellier, CNRS, ENSCM, Montpellier, France

*corresponding author: sylvain.catrouillet@umontpellier.fr; johannes.brendel@uni-jena.de

Keywords: supramolecular polymer bottlebrushes; self-assembly; polymer nanostructures; bioprinting; shear thinning;

Abstract

Hydrogels based on fibrillar nanostructures are attractive biomimetic materials for applications in tissue engineering, protection of stem cells, or drug reservoirs. The supramolecular assembly of small molecules represents a promising approach to create a dynamic scaffold for rapid shear-thinning and recovery. Other systems rely on the wormlike self-assembly of amphiphilic polymers with a dense polymer corona that minimizes undesired protein interactions while enabling versatile functionalization to control cellular adhesion. Here, we demonstrate that the advantages of both systems can synergistically be combined in hydrogels based on supramolecular polymer bottlebrushes. The incorporation of bivalent crosslinkers transforms these one-dimensional polymer nanofibers into strong but surprisingly dynamic gels, which can be tuned by variation of the linker content, the length of the linker, and the overall concentration. Their excellent stability

in various conditions including cell medium allows unaffected cell proliferation in close proximity to the gel, while the polyethylene oxide (PEO) corona of the fibers prevents cell adhesion on the gels. The low viscosity at high strain and rapid recovery after relief of strain facilitates the straightforward extrusion from thin needles and even printing of self-supporting structures, which renders these hydrogels promising materials for application in cell scaffolds or as injectable drug reservoirs.

Introduction

Gels and particularly hydrogels have found a wide range of applications for instance in cosmetics and personal care or in industry as lubricants due to their viscoelastic properties. But hydrogels also enter more sophisticated areas, particularly in biomedicine, where they promise injectable drug reservoirs for local delivery or the buildup of printable artificial cell scaffolds for tissue engineering.^[1] Prerequisites for these applications are, however, more demanding, as excellent biocompatibility and biomimetic elasticity have to be guaranteed, which requests a careful design of the applied hydrogels.^[2] Besides natural gelators,^[3] covalent crosslinking of established biocompatible polymers – most commonly polyethylene oxide (PEO) – represents a straightforward approach to create suitable hydrophilic 3D networks for the formation of biocompatible hydrogels for such applications.^[4] Covalently linked polymeric gel networks provide sufficient stability and enable the tuning of their elastic properties, however, an inherent drawback is the usually irreversible bond formation in the covalent links, which necessitates the crosslinking reactions to occur subsequent to any injection or printing steps and limits any dynamic reconfiguration.^[1b] An alternative approach addressing such features relies on the incorporation of physical crosslinks to construct the gel network. Such crosslinking points feature a dynamic character and offer the possibility for degradation due to supramolecular erosion.^[5] This can either be achieved by employing block copolymer self-assembly to build up transient networks formed by crosslinking of micellar structures,^[6] or by incorporation of supramolecular crosslinking motifs in conventional covalent polymers.^[1f, 7] By employing fibrillar structures and their entanglement, branching, or bundling, hydrogels can also be formed solely relying on supramolecular self-assembly.^[1a] Low molecular weight gelators (LMWG), which assemble into long cylindrical aggregates, due to supramolecular interactions such as directing hydrogen bonds, are employed to

synthesize highly dynamic gels.^[8] The crosslinking to 3D networks arises hereby from the bundling of multiple fibers and the formation of entanglements.^[1a, 8c, 9] The formation of entanglements as the basis for gelation is also used in the synthesis of gels from worm-like micelles by block-copolymer self-assembly.^[10] Here several advantages, such as stimuli-responsiveness or the possibility for additional functionalization, arise due to the brush-like structure.^[10e, 11] However, targeting solely, e.g. worm-like morphology phases in block copolymer self-assembly is often rather difficult, and in most cases, high concentrations of 10 wt% and additional crosslinking of the cylindrical micelles are required to obtain stable gels.^[10c, 12] Therefore, combining the polymeric self-assembly with supramolecular polymerization, gives access to supramolecular polymer bottlebrush (SPB) structures, which pave the way to the formation of potentially dynamic, responsive, and yet stable gels bearing different functionalities.^[1c, 7d, 9] By employing the brush-like structure, the thickness of a single fiber is increased and lateral aggregation is controlled, thus resulting in a rather defined and tunable network size. Due to their hydrated polymer exterior, stealth- and even functional properties can be introduced, making these gels in particular suitable for the application in nanomedicine^[7g, 13] e.g. as injectable hydrogel drug reservoir^[1c, 1f, 1g, 5, 7e, 7g, 11d] or in tissue engineering.^[1a]

Previously published supramolecular polymer bottlebrushes (SPBs) based on benzene trisurea-functionalized PEO-conjugates exhibited fiber-like morphologies with lengths exceeding 3 μm .^[14] Due to their size, these structures are expected to gel at a certain concentration via entanglement formation and produce stable but potentially dynamic gels. In this study, we evaluate their gel-forming abilities and the tuning of the gel strength and responsiveness by additional crosslinking. The great possibilities for functionalization render such SPB-hydrogels interesting for potential applications in nanomedicine. However, some prerequisites such as biocompatibility have to be taken into account. Additionally, further preliminary tests have been conducted to prove good processability and high stability, since shaping and structuring of hydrogels are crucial for its application e.g. as scaffold for cell growth^[15] or the adaption to the cellular environment when injected as a drug reservoir.^[1c]

Results and Discussion

The previously published BTU-PEO_{2k} **1** (Figure 1A)^[16] was evaluated concerning its gelation ability using a solvent switch method.^[14] Hereby, the bulk material is molecularly dissolved in an organic solvent and water is added to the mixture at 1 mL h⁻¹ while stirring. The water addition initiates self-assembly of the unimer due to trifold hydrogen bonding between the urea groups. After the addition of 66 v% of water to the volume of the organic solvent, the latter is removed by evaporation. Surprisingly, BTU-PEO_{2k} **1** exhibits no gelation in water at a concentration as high as 1 to 20 mg mL⁻¹ despite its ability to form fibers of up to 3 μm.^[14] This is astonishing since the overlap concentration of these structures in water is calculated to be 0.05 mg mL⁻¹. Gelation of these structures, however, could only be observed at concentrations > 20 mg mL⁻¹ (Figure 1B). Since this concentration is 400 times higher compared to the calculated overlap concentration, the fibers seem to be remarkably stiff and thus, entanglement is prevented at lower concentrations. Additionally, the interactions between the fibers might be reduced due to the sterically demanding hydrated brush structure, and crosslinking by defects in the structure or branching can be excluded, since in such cases also lower gelation concentrations could be expected. Bundling seems further to be unlikely due to the dense and extended hydrophilic shell of the SPB.

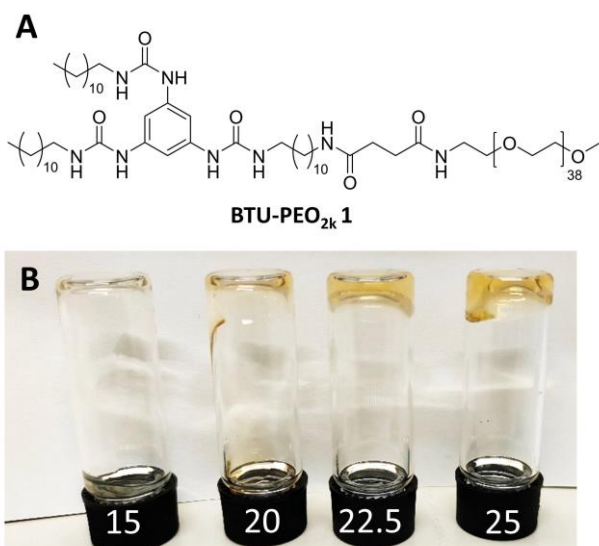


Figure 1 Schematic representation of the chemical structure of **BTU-PEO_{2k} 1** (A). Inverted vial test of **BTU-PEO_{2k} 1** hydrogels prepared by the solvent switch method at concentrations of 10 to 25 mg mL⁻¹ (B).

To assess the strength of the gel of **1**, frequency-sweep measurements of the gel were conducted at 25 mg mL^{-1} immersed in water to prevent drying (Figure 2E, further details can be found in the Supporting Information, Figure S11). The observed plateau-like curve between 1 and 10 rad s^{-1} is typical for the formation of entanglements of the SPB fibers (Figure 2E). Toward lower frequencies, a decrease of the storage modulus can be observed which already indicates an upcoming crossover of storage and loss modulus, although this Maxwellian behavior was not further investigated. The maximum storage modulus G' of around 10 kPa is rather low, which again reflects the weak interaction of the fibers. The reason thereof is considered to be the core-shell structure of the SPBs (Figure 2B) and their high stiffness, which results in fewer entanglements. A well-known strategy to improve the strength of gels is to introduce crosslinking.^[1c, 9, 17] To do so, a bivalent linker consisting of a PEO chain of 20 kD and BTU endgroups was added before the solvent switch (Figure 2A). With incorporation of these endgroups into distinct nanofibers, a significant number of crosslinking points can be formed, thus, the network gets denser and the moduli should increase (Figure 2D). This effect can already be observed with adding just 1 % of bivalent linker **2a**. The mechanical strength of the gel increased by a factor of 10 (Figure 2E). Interestingly, the pure bivalent crosslinker at 25 mg mL^{-1} results in similar weak networks as pure **1**, which corroborates a synergistic effect. All gels show a yield point in strain-sweep measurements at strains $> 40 \%$, indicating a breakdown of the network above these strains (Figure 2F). Macroscopically, the gel liquefies if sufficient shear stress is applied, which is further discussed later (*vide infra*).

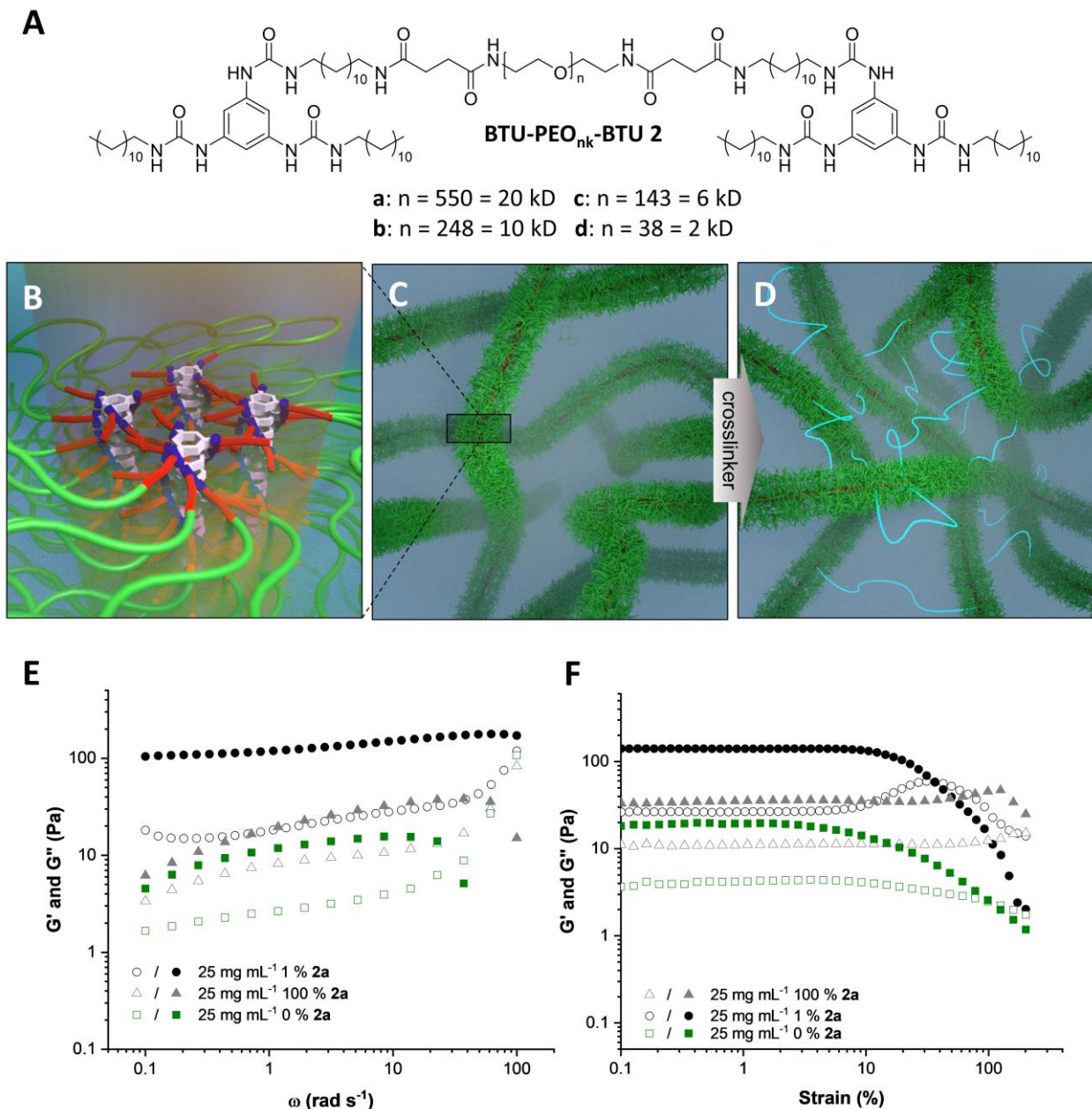


Figure 2 Schematic representation of the chemical structure of **BTU-PEO_{nk}-BTU 2** (A). Schematic depiction of the cross-section of the SPB fiber (B), the gel without (C), and with 1 % crosslinker (D). Frequency-sweep measurement of **1** (green), **1** with 1% **2a** (black) and **2a** hydrogels at a concentration of 25 mg mL⁻¹ (E). Strain-sweep measurements (D) of **1** (green), **1** with 1% **2a** (black) and **2a** hydrogels at a concentration of 25 mg mL⁻¹ (F).

Light scattering experiments were conducted to get an idea about the internal structure of the gel. The correlation functions of a solution of the crosslinked BTU gel (**1** + 1% **2a**, 25 mg mL⁻¹) at various scattering wave vectors show two clear relaxation modes. The correlation length ξ can be determined using static light scattering (SLS) whereas the hydrodynamic correlation length ξ_H is

determined using dynamic light scattering (DLS). As soon as the polymers form a transient network, the correlation length no longer contains information about the size of the individual chains, but it reflects the mesh size ξ_m of the network. With SLS, the average mesh size of the transient polymer network is measured, whereas DLS measures the average diffusion coefficient of the meshes. Using Figure S2 and equation S2 it is possible to determine a mesh size by SLS of the solution of the crosslinked BTU gel (**1** + 1% **2a**, 25 mg mL⁻¹) of 34 nm, which is reasonable considering the length of the fibers and the amount of crosslinker. Using DLS a ξ_H of 81 nm was determined. The value obtained is different but of the same order of magnitude as already seen in similar systems.^[18] To determine the origin of the two relaxations, the correlation functions have been represented versus t (Figure S5A) and normalized with q^2 (Figure S5B). The normalization with q^2 shows that only the first mode is superimposed. Therefore, it is due to the cooperative scattering of the network. On the contrary, the second mode is q^2 independent (Figure S4) and the amplitude of the first mode varies with q (Figure S3). It means that the second mode is probably due to the relaxation of the chains in the network. The average of the measured values at different q is taken as Γ_{slow} , and the reciprocal of this equals τ_{slow} . A value of 1,55 s is obtained for this system. Unfortunately, this relaxation value cannot be compared with our rheology experiments as no cross-over was observed during the frequency sweep experiments. Additionally, similar systems led to large discrepancies between rheology and DLS on studying the relaxation time, which is why we did not consider any further investigations in this direction.^[18]

The general stability of these hydrogels can already be seen by the bare eye, when compact solid gel structures are generated via a molding technique. For this purpose, small Teflon or silicone molds were filled with the solution of **1** with 1 % **2a** and the THF was evaporated to a final concentration of 25 mg mL⁻¹ (Figure 3A and S1). After the gel was released from the mold, it keeps its form on a glass slide for more than an hour before severe drying is observed (Figure S1B). Furthermore, it is possible to cut and rearrange the gel resulting in a solid attachment of the two components (Figure 3B). Interestingly, immersion in aqueous environment for multiple weeks does not alter the gel. No swelling or degradation can be observed (Figure 3C). Here, also no change in the rheological properties could be measured (Figure S12). Stable gels were still formed even in the presence of up to 33 v% THF (Figure S10). The gel formation tolerates even very acidic (pH 2) and basic media (pH 11), the presence of salt and serum proteins (Figure S6). This again holds

great potential for a wide range of applications, e.g. *in vitro* and *in vivo*. The incorporation of cells in hydrogels, for instance, requires the presence of media with its corresponding nutrients. The possibility to directly add media instead of water for the preparation of the gel paves the way for application in cell culturing.

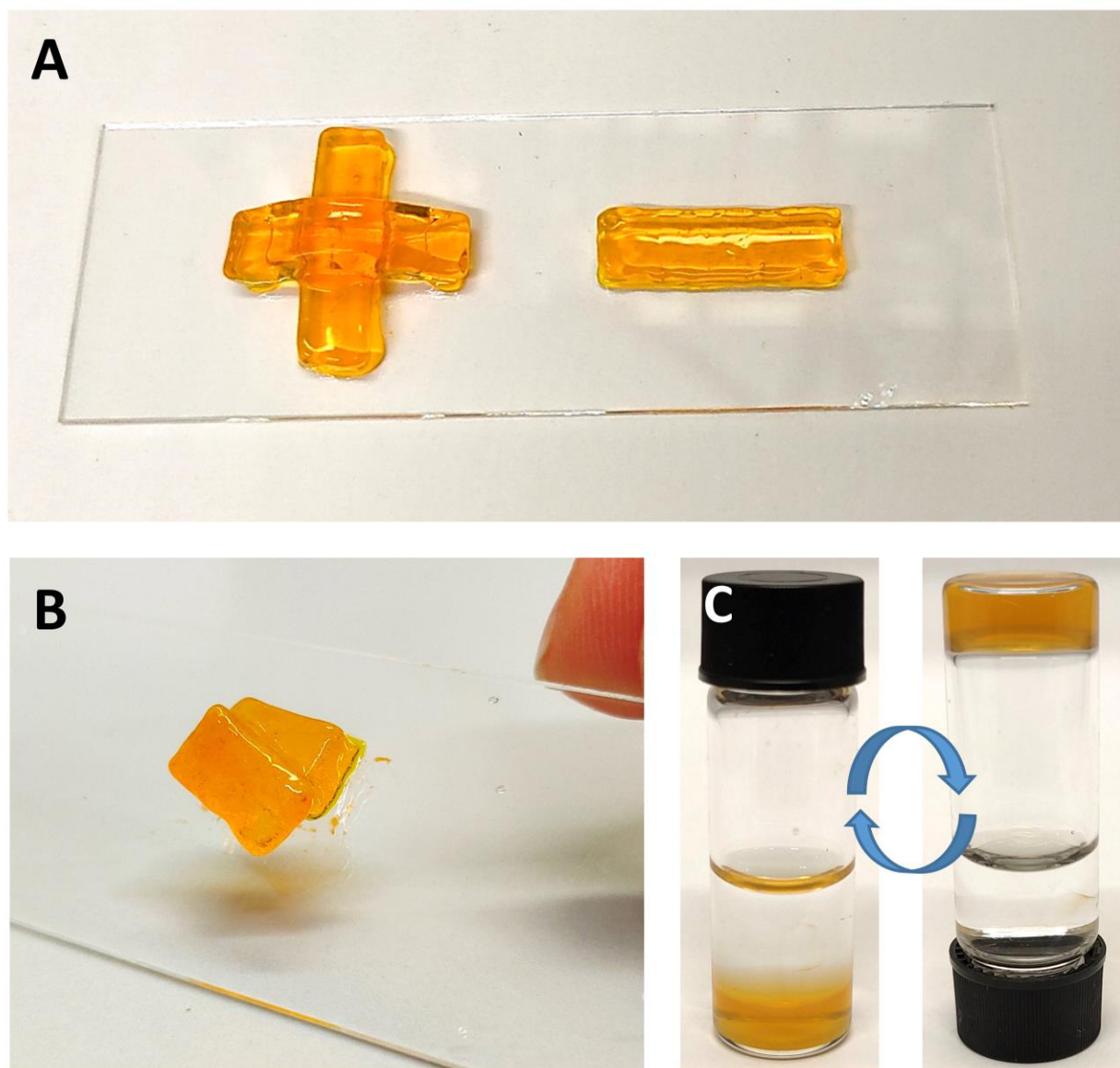


Figure 3 Gels (stained with Na-Fluorescein for better visibility) of **1** with 1 % **2a** ($c = 25 \text{ mg mL}^{-1}$) molded in silicone molds (A). Molded blocks were cut and stacked (B). Stability of a gel in water (C). After immersion in water for one week, the vial could be inverted and no degradation or swelling of the gel could be observed.

The most important factor to keep in mind, when aiming for an application e.g. *in vivo* is to ensure the biocompatibility of the hydrogel material. The gel will be in contact with the cellular environment so it should be non-toxic. The biocompatibility of a gel of **1** with 1 % **2a** at 25 mg mL⁻¹ was investigated using the adherent murine cell line L929. Therefore, the gel was tested by applying a small amount of gel in 24-well plates, which were then incubated with L929 cells over 24 h and the cell viability was assessed via the PrestoBlue assay. Here, two incubation modes were applied, one where the gel was initially placed in the well and then the cell suspension was added (preparation way 1), and one where the gel was added later to the cell suspension (preparation way 2). Independent of the preparation procedure, the gel seems to be non-toxic since viabilities of 81 ± 3 % and 96 ± 2 % could be measured for preparation ways 1 and 2, respectively (Table S1). The difference between the two preparation procedures is attributed to the lower surface area in the well which is available for the cells in case of preparation way 1. Due to the PEO-functionalization of the gel, a stealth behavior is expected. Microscopy images were recorded on gels incubated for 24 h with L929 cells (Figure S7). As expected, no cells could adhere to the PEGylated gel structure, however, already at the border of the gel, cells proliferated unaffected (Figure S7A and B). From this data, we conclude that biocompatibility is ensured, but growth of cells on the hydrogel will require additional functionalization. The limited adherence, however, also represents the opportunity to selectively introduce specific receptors in structured cell scaffolds, as it has very recently been shown for LMWH.^[1h] Further research in this direction is currently planned. In any potential application (cell scaffold or drug delivery reservoir), the diffusion of substances in the gel should be given in addition to good stability and biocompatibility. The diffusion of nutrients or other substances is mandatory for cell proliferation on the scaffold and the time-dependent release of active pharmaceutical ingredients from a hydrogel drug reservoir. To obtain an impression of the diffusion of macromolecules in the gel, pulse-field-gradient (PFG) NMR spectra were recorded of poly(ethyl oxazoline) (PEtOx) of different molar mass in the pure BTU gel (**1**, 25 mg mL⁻¹) and the crosslinked BTU gel (**1** + 1% **2a**, 25 mg mL⁻¹) (further details can be found in the Supporting Information). By comparison of the free diffusion coefficient D_0 of the PEtOx in water to the diffusion coefficient D of PEtOx in the gel, a strong retardation can be observed for PEtOx in both gels. However, no complete trapping could be observed but a very slow diffusion (Table S2, Figure S8 and S9). This might be the result of the highly hydrated brush structure where the PEO chains

of the SPBs extend far into the water and significantly prevent the free diffusion of the probe along the network pores (Figure 2B-D). Macroscopically, this diffusion was monitored by measuring the fluorescence intensity of gels covered with water. TRITC-dextran was incorporated into the gel during the assembly process, similar to the PEtOx polymers in PFG-NMR experiments, and the fluorescence intensity in the supernatant aqueous solution was monitored over time (Figure 4, S10).^[4c] A continuous release is observed, which scales with the size of the applied FITC-dextran. In the first few minutes, the intensity increases rapidly which is presumably due to probe molecules attached to the gel surface or in the outer layers of the gel. By fitting an exponential model a similar exponent could be calculated for all dextran sizes, meaning the same diffusion mechanism independent of the size of the probe molecule can be expected (Figure 4A). This slow release over days might already be favorable for the application in nanomedicine to ensure delivery of active pharmaceutical ingredients over larger time scales at a constant level. Interestingly, even low-molar mass substances can be trapped in the gel and continuously released over several hours, which is again attributed to the hydration of the PEO chains and their extension into the aqueous phase of the gel. We exemplarily demonstrate this effect with the sodium salt of fluorescein (Figure S10B). Here an exponential function can be fitted with an exponent of 0.5 resembling the Fickian diffusion and no sign of a strong burst release in the beginning.^[19] After 80 h a quantitative release is observed (equal intensities in both gel and supernatant). The Fickian diffusion indicates that the dye is not significantly interacting with the polymer network, while the high density of the PEO-chains appears to significantly slow down the diffusion of the small molecule. Such a controlled and continuous release of small molecules over several hours is highly desirable for the design of hydrogel reservoirs and usually requires gels of very small mesh sizes,^[20] which we can circumvent by our dense but flexible PEO-chains extending into the aqueous matrix of the gel. These diffusion tests further corroborate the excellent stability of the gel, as even after seven days of immersion in water, no swelling and degradation of the gel become apparent (Figure 4B).

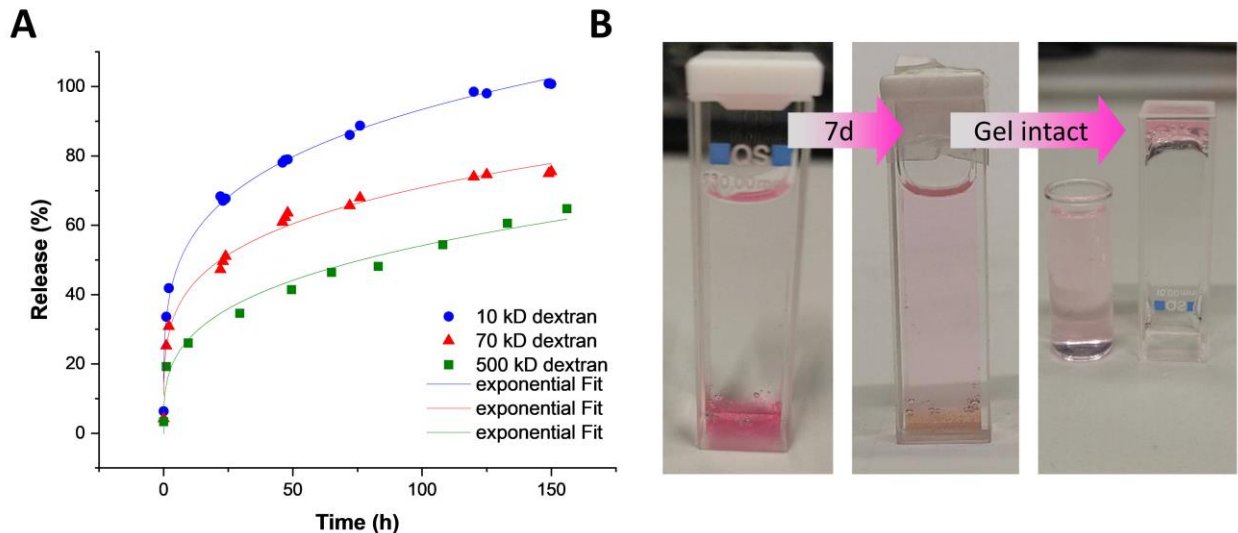


Figure 4 Diffusion kinetics of TRITC-dextran of different molar mass followed by fluorescence spectroscopy (A). Color-change of the water in the cuvette after seven days and high stability of the gel even after immersion in water (B)

For the application of hydrogels in cellular environment, careful design of the mechanical properties is necessary.^[21] Properties like elasticity and surface modification influence the cell-attachment and proliferation to a great extent.^[22] Due to the high versatility of the system, several parameters are available to tune the gel strength. Since already 1 % of an additional crosslinker yielded significantly stronger gels, the influence of the crosslinker content on the gel strength was tested in more detail. In frequency-sweep measurements of gels at 25 mg mL⁻¹ with different amounts of 20 kD crosslinker **2a** a maximum strength can be observed for gels with 10 % crosslinker (Figure 5A, S13C). This might be the result of increased backfolding of the crosslinker and an increasing number of micellar aggregates at higher crosslinker contents, as already observed for other supramolecular gel systems.^[1c]

Additionally, the influence of the length of the linker on the mechanical properties of the hydrogel was evaluated by frequency sweep of the gels at 25 mg mL⁻¹ and 1 % of crosslinker (Figure 5A, S13B). If the length of the crosslinker is decreased from 20 (**2a**) to 6 kD (**2c**) and 2 kD (**2d**) already a strong decrease of the plateau moduli can be observed. Here very weak gels can be observed since two nanofibers equipped with a 2kD PEO corona will not get in sufficient close proximity, so crosslinker **2d** or **2c** could link them. Such a nearly touching contact is unfavorable due to the hydrated PEO corona. Consequently, backfolding of the PEO chain of the crosslinker will be

avored. Surprisingly, this decrease in crosslinking probability can already be observed for crosslinker lengths of 10 kD (**2b**) which are still five times the size of the PEO corona (2 kD) of the SPB.

Another parameter to tune the gel strength is the concentration. If the concentration of the hydrogel is increased, a strong increase in storage and loss modulus can be observed (Figure 5C, S 13A). Due to an overall higher number of fibers, the number of entanglements in the network increases, and thus the gel strength is enhanced. This correlates well with other known systems where gelation is favored for higher concentrations.^[1c, 9] Interestingly, a plateau is reached at a concentration of 50 mg mL⁻¹ (Figure 5C). Therefore, the optimum composition for the strongest gel of this system with a storage modulus of 1 kPa could be observed for a gel with a concentration of 50 mg mL⁻¹ and 10 % crosslinker **2a** (Figure 5D, S16).

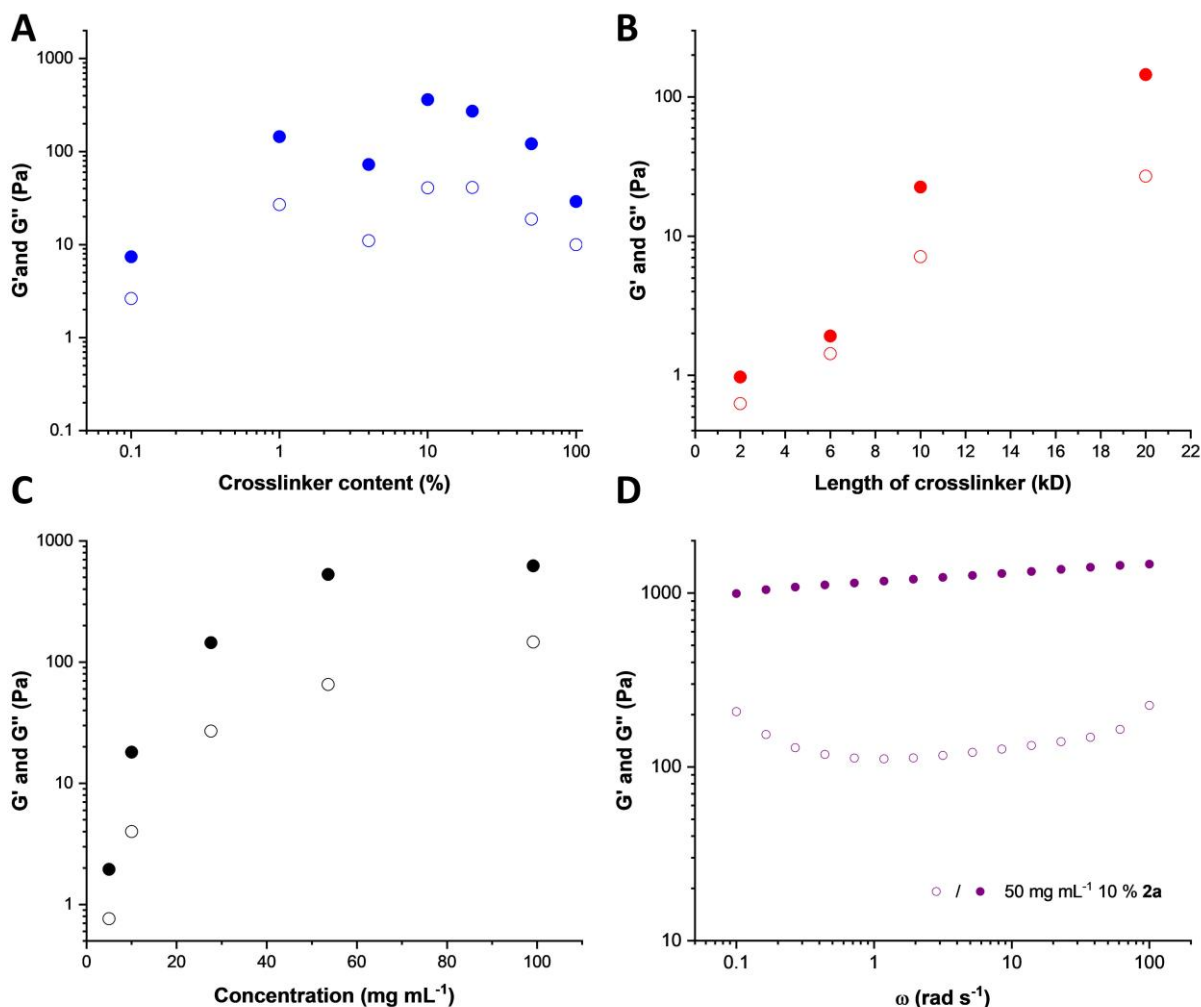


Figure 5 Plateau modulus of hydrogels with different amounts of crosslinker **2a** ($c = 25 \text{ mg mL}^{-1}$) (A), plateau modulus of hydrogels with 1 % crosslinker of different lengths ($c = 25 \text{ mg mL}^{-1}$) (B), and concentration-dependent plateau modulus of hydrogels with 1 % of **2a** crosslinker at different concentrations (C). Frequency-sweep measurement of a hydrogel of **1** with 10 % of **2a** at 50 mg mL^{-1} (D).

To assess the dynamics of the gel network in absence of any shear forces, a gel was examined by fluorescence recovery after photo-bleaching (FRAP). To do so, the network structure of a covalently labeled gel of **1** with 1 % AF-594 labeled BTU + 1% **2a** at a concentration of 25 mg mL^{-1} was bleached for 30 min with a UV laser. The bleached part was examined after 6 and 24 h. No recovery of the fluorescence can be observed in the bleached parts of the sample (Figure 6, Figure S20), meaning the mobility of individual building blocks must be impeded in the gel network. This result again exemplifies the high stability of the gel structure which also relates to the kinetic trapping observed for BTU fibers in aqueous environment previously.^[14] We conclude

that gels of **1** with 1 % crosslinker form mostly static gel networks, which do not permit an exchange of individual building blocks and limit the swelling of the gel if immersed in water.

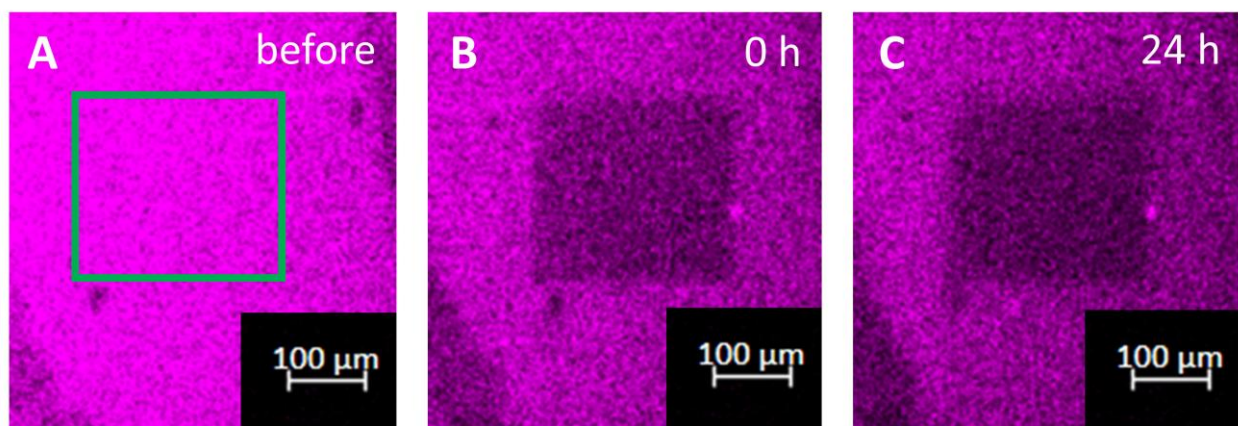


Figure 6 Fluorescence recovery after photo-bleaching experiment of a covalently labeled gel (**1** + 1% AF-594 labeled BTU + 1% **2a** at 25 mg mL⁻¹) before bleaching (A), directly after bleaching (B) and after 24 h (C).

Nonetheless, we tested the response of the gel to amplitude sweeps. A decrease of gel strength can be measured at specific strains for all gels with a gel comprising 50 % **2a** at 25 mg mL⁻¹ featuring the highest yield stress (Figure S15D). The highest storage moduli, however, could be measured for the 1 % and 10 % **2a** containing samples (Figure S15C). Subsequently to these experiments we further applied dynamic step-strain experiments to evaluate any remaining dynamics as observed for other supramolecular gels.^[1b, 7g, 7i] To our surprise and contrary to the previous dynamic studies, these experiments revealed excellent reversibility and full recovery of the initial gel strength upon relief of the shear stress without any sign of irreversible degradation (Figure 7A, S14). At high deformation (200%), the supramolecular interactions in the gel must be disrupted and the storage modulus is decreased by a factor of 43 for a gel of **1** with 1 % **2a** at 25 mg mL⁻¹ falling below the loss modulus (Figure 7A). The gel exhibits therefore liquid-like properties. Relieving the stress, the gel recovers its strength immediately (< 5 s) without any signs of delay. The supramolecular interactions must reform immediately, which we relate to the strong intramolecular hydrogen bonds and the hydrophobic effect of the supramolecular core units. This effect is astonishing considering the limited dynamics of single building blocks and the high kinetic stability of small fibers found previously. We assume that the fibers rupture upon exposition to shear forces, resulting in fragments that feature reactive chain ends that are not saturated with PEO chains on their surface.

These hydrophobic surfaces then represent a strong driving force to reconnect the fiber ends and minimize the exposed hydrophobic core to the surrounding water. Since the gel strength is recovered to 100 % each cycle, nearly every active chain end must reconnect. Similar dynamic behavior is also found for all other gel compositions (Figure S14). The difference in G' between periods of high and low deformation varies, however, and is much lower for BTU gel **1** and the pure crosslinker **2a** as well as the time to recover increases (Figure 7a). The gel consisting of **1** + 10% **2a** at 25 mg mL⁻¹ sets a benchmark for the G' ratio between high and low deformation and reaches a value of 90 in these step-strain measurements while retaining the rapid recovery.

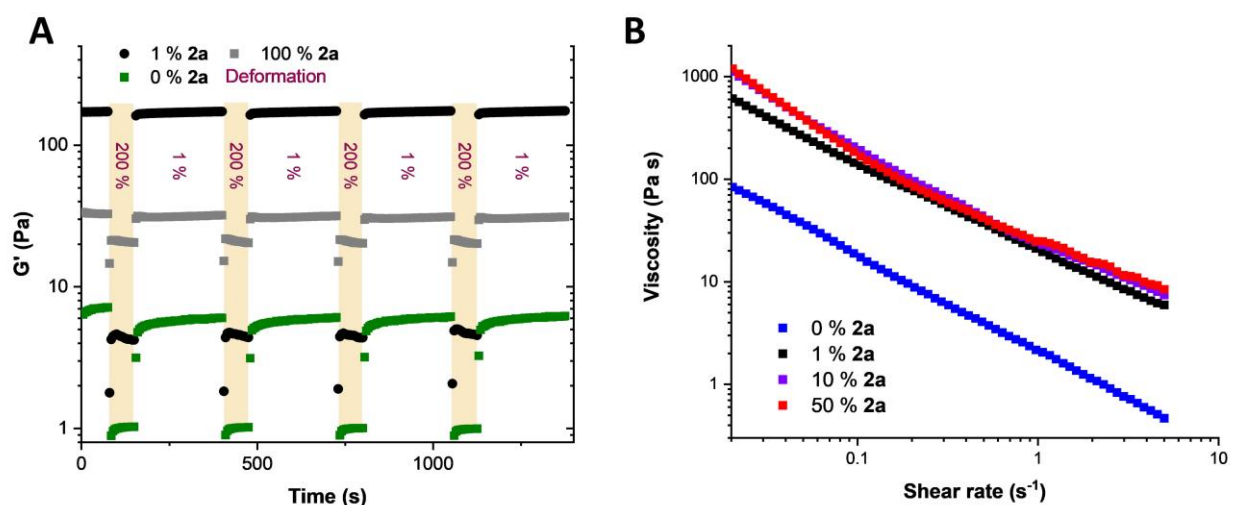


Figure 7 Step-strain measurements of gels of **1**, of **1** with 1 % **2a** and of pure **2a** ($c = 25 \text{ mg mL}^{-1}$) (A) Shear rate-dependent viscosity behavior of pure BTU gel **1** and gel of **1** with different amounts of crosslinker **2a** ($c = 25 \text{ mg mL}^{-1}$) (B).

Since a liquid-like behavior is expected at ratios $G'/G'' < 1$, rheology measurements under continuous shear stress were conducted to evaluate the proportionality of the shear rate $\dot{\gamma}$ on the viscosity. A potential shear-thinning behavior is highly advantageous in the design of injectable hydrogels to facilitate, for instance, subcutaneous administration, and for printing applications to enable a fast printing process.^[23] Figure 7B depicts the response of viscosity with increasing shear rate, which reveals a linear decrease in this double logarithmic plot, as it appears for nearly all compositions at higher shear rates (Figure S17A). Interestingly, no yield point can be observed in the measured shear rate and shear stress regime for gels with concentrations $> 5 \text{ mg mL}^{-1}$ (Figure S17B and C). Since the measured data is characteristic of the flow regime, the yield point is

expected to occur at even lower shear rates and stresses, which is rather surprising considering the strength of the gel in oscillating measurements. The viscosity decreases rapidly for all gel compositions increasing the shear rates which implies an enhanced shear-thinning behavior. Very low viscosity is already reached at limited shear rates of 5 s^{-1} which resemble characteristics of PEO in water at similar concentrations although with higher average molar masses (around 10^6 g mol^{-1}).^[24] The addition of the crosslinker increases the viscosity in general by approximately a factor of 10 compared to the non-crosslinked gel **1** with 0 % **2a**, which is similar to the improvement in the modulus. The shear-thinning behavior can further be quantified by fitting the linear regime of the viscosity to a power law that is described by the consistency index, K , and shear-thinning parameter, n (Eq. 1).^[23c, 25] Therefore, only the linear regions at higher shear rates were considered for the suitable samples (Table 1, Figure S18). Interestingly, the herein presented systems gave very low values for both n and K compared to established systems like Alginate or Poloxamer polymers, which either feature higher values for n or K , respectively.^[26]

$$\eta = K\dot{\gamma}^{n-1} \quad \text{Eq. 1}$$

Table 1 Fitted shear-thinning parameter n and consistency index K for different gel compositions.

Gel	n	$K \text{ (Pa s}^n\text{)}$
0 % 2a , 25 mg mL ⁻¹	0.07979	2.1272
1 % 2a , 25 mg mL ⁻¹	0.14637	22.96811
10 % 2a , 25 mg mL ⁻¹	0.27144	24.40954
50 % 2a , 25 mg mL ⁻¹	0.31115	25.56372
1 % 2a , 5 mg mL ⁻¹	0.09689	0.71141
1 % 2a , 10 mg mL ⁻¹	0.14439	1.45285
10 % 2a , 50 mg mL ⁻¹	0.14202	142.97

Transferring these results to an application, it is feasible to calculate the force needed to administer such gels e.g. as injectable hydrogel. For example, a 1 mL syringe equipped with cannulas of 27 to 33 gauge (length 1 inch) are often used in oncological treatments to administer drugs at a speed of approx. 6 mL/min.^[20, 27] It is expected that a force of 50 N is still acceptable for the doctor to

administer and the patient to feel comfortable with. We can see that the herein presented hydrogels require only very limited forces for administration with a syringe at such rates (Figure S19A). Even if cannulas with a very small diameter (Gauge 33) are used, the force for extrusion is around 10 N for the strongest gels 2.5 wt%. These considerations match our practical experience handling the gels, as the resistance of ejecting the gel through a cannula into the wells for biological tests appears only marginally higher than for pure water. In consequence, pressures occurring during administration of such a gel can be kept very low, allowing an improved dosage control and, thus, limited formation of hematoma at the injection site.^[1c] We assume that the shear-thinning behavior is strongly enhanced by the supramolecular nature and brush structure of the SPB hydrogel as compared, for instance, to physically linked Poloxamer and poly(ethylene glycol)–diacrylate (PEG-DA) hydrogels.^[26b]

The low viscosity and pressure are further beneficial for fast printing methods, which gain increasing attention. In rapid prototyping, an accelerated printing procedure offers possibilities for the processing of sensitive materials.^[15a, 23b, 26a, 28] Since in such strongly shear-thinning materials high shear forces only occur near the cannula wall and low forces are present in a broad range in the center,^[26a] we expect these gels to be suitable to extrude and print cell containing hydrogels at rather high speeds, which further limits the time of exposure of cells to this stress.^[23] Similar considerations as for the injection above reveal that even for strong gels with increased crosslinker content of 10 % and a concentration of 50 mg mL, printing velocities of more than 10^2 mm s⁻¹ are achievable at very low pressures of 120 kPa considering a 27 gauge cannula (Figure S19B). Summarizing all properties, our supramolecular polymer brush gels feature sufficient strength, pronounced shear-thinning properties, rapid recovery after stress relief, and high stability, which distinguishes them from many other known systems. To further evaluate their suitability for application in printing techniques, a rapid-prototyping (RP) setup was used to produce individually shaped structures from CAD models.^[29] A common 3D printer can be employed to print prototypes by attaching a cannula to it which is further connected to a syringe pump *via* flexible tubings (Figure S21A). We started the tests by printing single straight lines of the gels with 1 % **2a** at 10, 25, and 50 mg mL⁻¹ at printing velocities of 36 mm s⁻¹. For the highest concentration of 50 mg mL⁻¹, some limitations became obvious, as irregular clogging of the capillary was observed at this speed (using a 20 Gauge cannula) (Figure 8A). However, we did not further optimize the conditions at

17

this stage and considered the ordinary setup. The lower concentrations of 25 and 10 mg mL⁻¹ did not result in any clogging and smooth lines could be extruded. For both gels, the viscosity at the apparent shear rate is sufficiently low to facilitate an easy extrusion through the nozzle. Apart from a good extrusion through the needle, the gel should reform immediately after leaving the needle tip, meaning the gel should exhibit no or weak thixotropy to form defined structures. Additionally, the formed structures should be stable, implying the gel to be of a certain strength. These prerequisites are not met by a gel of 10 mg mL⁻¹, since it already shows a slight line broadening, meaning thixotropic behavior. Using the 25 mg mL⁻¹ gel with 1% crosslinker **2a** defined lines could be printed due to its suitable balance between shear-thinning and mechanical strength at zero stress. Since the gel recovers rapidly after extrusion from the needle tip, even irregular shapes such as stars could be printed (Figure 8B). The high strength of this gel even enables the printing of lines on top of each other. In consequence, we were able to print a hollow self-supporting cylinder as a proof of concept (Figure 8C, Movie). Lower concentrations of 10 mg mL⁻¹ show decreased mechanical strength compared to higher concentrated gels and, thus, prints are not able to support their weight (Figure S21B). This processability of the gels in 3D printing methods, even at high printing speeds with low shear forces present in the cannula, could pave the way for a future application, e.g. as a bioscaffold for tissue engineering.^[21, 28a, 29a, 30]

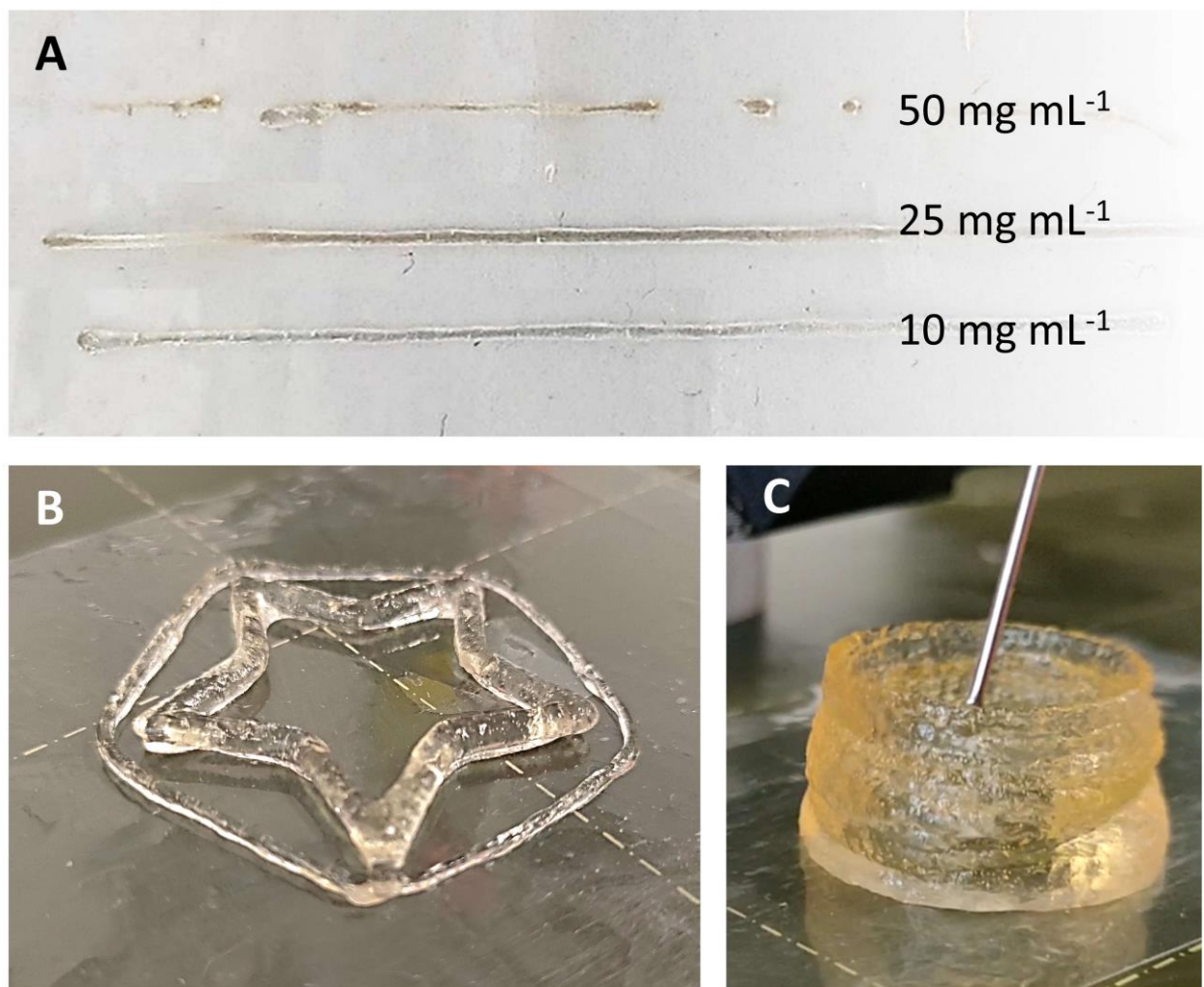


Figure 8 Printed straight lines of 50, 25 and 10 mg mL⁻¹ gels of **1** with 1 % **2a** (A). 3D printed star with a gel of **1** with 1 % **2a** ($c = 25$ mg mL⁻¹) (B). 3D printed hollow cylinder with a gel of **1** with 1 % **2a** ($c = 25$ mg mL⁻¹) (C).

Conclusion

The introduction of bifunctional, crosslinking building blocks into 1D polymer self-assemblies formed by supramolecular interactions creates a stable network. The brush-like fibers macroscopically produce robust hydrogels with storage moduli of up to the kPa range. These hydrogels show exceptional stability even when they are immersed in water. The gel formation tolerates acidic or basic conditions as well as the presence of salt or serum-containing media, which makes the system attractive for biomedical applications. In this regard, preliminary cell tests

revealed that cells still proliferate normally in close proximity to the gel, while they cannot adhere to the gel surface. We assume that the dense PEO corona in the bottlebrush fibers prevents the cellular adherence, which opens the opportunity to control cell growth by introduction of specific receptors and growth factors. The diffusion of compounds within and out of gel is further maintained, although PFG-NMR measurements reveal a strong retardation of macromolecules, which is again related to the hydrated polymer corona of the fibers. Interestingly, a similar retardation is observed for small molecules as exemplarily demonstrated for a dye, which opens up interesting opportunities for controlled drug release applications. Most surprisingly, the obtained gels feature a strong shear thinning behavior with a rapid (< 5 s) and complete recovery of strength as soon as the strain is relieved, despite demonstrating very limited dynamics in the exchange of single building blocks as known from other supramolecular hydrogels. We assume that at high strain the supramolecular fibers break and reactive end-groups are formed, which rapidly re-aggregate in the absence of shear forces. Nonetheless, further detailed investigations are required to gain insight into this unusual behavior. The combination of strong shear thinning and rapid recovery of gel strength set the basis for further tests on the printing capabilities of these materials. Adjusting the composition, self-sustaining cylindrical structures could be printed, corroborating the rapid solidification of the hydrogel and its high stability. Overall, the excellent biocompatibility, the strong shear-thinning properties together with the very rapid recovery renders these supramolecular polymer bottlebrush hydrogels promising candidates for potential applications as injectable hydrogel reservoir or 3D cell scaffold, as it has been demonstrated for other supramolecular systems.^[21, 31] The high density of the polymer corona on the fibrillar microstructure not only minimizes undesired protein adsorption and cellular interactions but also opens up the opportunity for versatile functionalization without corrupting the gel stability.

Supporting Information

Experimental details, detailed characterization and further information can be found in the Supporting Information, which is available from the Wiley Online Library or from the author.

Acknowledgements

FVG and JCB thank the German Science Foundation (DFG) for generous funding within the Emmy-Noether Programme (Project-ID: 358263073). C. Kellner is thanked for conducting the cell culture maintenance and her help in cytotoxicity studies. M. Dirauf, N. Göppert and M. Kleinsteuber are acknowledged for synthesizing the PEtOx polymers.

References

- [1] a) E. Prince, E. Kumacheva, *Nat. Rev. Mater.* **2019**, *4*, 99-115; b) L. Saunders, P. X. Ma, *Macromol. Biosci.* **2019**, *19*, 1800313; c) J. Cheng, D. Amin, J. Latona, E. Heber-Katz, P. B. Messersmith, *ACS Nano* **2019**, *13*, 5493-5501; d) V. M. P. Vieira, L. L. Hay, D. K. Smith, *Chem. Sci.* **2017**, *8*, 6981-6990; e) V. M. P. Vieira, A. C. Lima, M. de Jong, D. K. Smith, *Chem. Eur. J.* **2018**, *24*, 15112-15118; f) P. Y. W. Dankers, T. M. Hermans, T. W. Baughman, Y. Kamikawa, R. E. Kieltyka, M. M. C. Bastings, H. M. Janssen, N. A. J. M. Sommerdijk, A. Larsen, M. J. A. van Luyn, A. W. Bosman, E. R. Popa, G. Fytas, E. W. Meijer, *Adv. Mater.* **2012**, *24*, 2703-2709; g) P. Y. W. Dankers, M. J. A. van Luyn, A. Huizinga-van der Vlag, G. M. L. van Gemert, A. H. Petersen, E. W. Meijer, H. M. Janssen, A. W. Bosman, E. R. Popa, *Biomaterials* **2012**, *33*, 5144-5155; h) M. Zhou, A. M. Smith, A. K. Das, N. W. Hodson, R. F. Collins, R. V. Ulijn, J. E. Gough, *Biomaterials* **2009**, *30*, 2523-2530.
- [2] a) J. Y. C. Lim, Q. Lin, K. Xue, X. J. Loh, *Mater. Today Adv.* **2019**, *3*, 100021; b) X. Du, J. Zhou, J. Shi, B. Xu, *Chem. Rev.* **2015**, *115*, 13165-13307.
- [3] M. Watase, K. Arakawa, *Bull. Chem. Soc. Jpn.* **1968**, *41*, 1830-1834.
- [4] a) S. Hong, D. Sycks, H. F. Chan, S. Lin, G. P. Lopez, F. Guilak, K. W. Leong, X. Zhao, *Adv. Mater.* **2015**, *27*, 4035-4040; b) O. Erol, A. Pantula, W. Liu, D. H. Gracias, *Advanced Materials Technologies* **2019**, *4*, 1900043; c) V. Hagel, T. Haraszti, H. Boehm, *Biointerphases* **2013**, *8*, 36.
- [5] M. J. Webber, E. T. Pashuck, *Adv. Drug Del. Rev.* **2021**, *172*, 275-295.
- [6] a) R. R. Taribagil, M. A. Hillmyer, T. P. Lodge, *Macromolecules* **2010**, *43*, 5396-5404; b) C. Tsitsilianis, *Soft Matter* **2010**, *6*, 2372-2388; c) J. Qian, M. Zhang, I. Manners, M. A. Winnik, *Trends Biotechnol.* **2010**, *28*, 84-92.
- [7] a) A. Noro, M. Hayashi, Y. Matsushita, *Soft Matter* **2012**, *8*, 6416-6429; b) T. Rossow, S. Seiffert, *Polym. Chem.* **2014**, *5*, 3018-3029; c) R. F. M. Lange, M. Van Gurp, E. W. Meijer, *J. Polym. Sci., Part A: Polym. Chem.* **1999**, *37*, 3657-3670; d) I. W. Hamley, G. Cheng, V. Castelletto, *Macromol. Biosci.* **2011**, *11*, 1068-1078; e) G. M. Pawar, M. Koenigs, Z. Fahimi, M. Cox, I. K. Voets, H. M. Wyss, R. P. Sijbesma, *Biomacromolecules* **2012**, *13*, 3966-3976; f) A. J. P. Teunissen, M. M. L. Nieuwenhuizen, F. Rodríguez-Llansola, A. R. A. Palmans, E. W. Meijer, *Macromolecules* **2014**, *47*, 8429-8436; g) M. M. C. Bastings, S. Koudstaal, R. E. Kieltyka, Y. Nakano, A. C. H. Pape, D. A. M. Feyen, F. J. van Slochteren, P. A. Doevendans, J. P. G. Sluijter, E. W. Meijer, S. A. J. Chamuleau, P. Y. W. Dankers,

- Adv. Healthcare Mater.* **2014**, *3*, 70-78; h) R. Murphy, D. P. Walsh, C. A. Hamilton, S.-A. Cryan, M. in het Panhuis, A. Heise, *Biomacromolecules* **2018**, *19*, 2691-2699; i) S. Strandman, X. X. Zhu, *Gels* **2016**, *2*, 16.
- [8] a) G. Cheng, V. Castelletto, C. M. Moulton, G. E. Newby, I. W. Hamley, *Langmuir* **2010**, *26*, 4990-4998; b) Y. Gao, F. Zhao, Q. Wang, Y. Zhang, B. Xu, *Chem. Soc. Rev.* **2010**, *39*, 3425-3433; c) S. Zhang, M. A. Greenfield, A. Mata, L. C. Palmer, R. Bitton, J. R. Mantei, C. Aparicio, M. O. de la Cruz, S. I. Stupp, *Nat. Mater.* **2010**, *9*, 594-601; d) H. Yokoi, T. Kinoshita, S. Zhang, *Proc. Natl. Acad. Sci. U.S.A* **2005**, *102*, 8414; e) S. S. Babu, V. K. Praveen, A. Ajayaghosh, *Chem. Rev.* **2014**, *114*, 1973-2129; f) D. Higashi, M. Yoshida, M. Yamanaka, *Chem. - Asian J.* **2013**, *8*, 2584-2587; g) L. A. Estroff, A. D. Hamilton, *Angew. Chem. Int. Ed.* **2000**, *39*, 3447-3450.
- [9] R. E. Kieltyka, A. C. H. Pape, L. Albertazzi, Y. Nakano, M. M. C. Bastings, I. K. Voets, P. Y. W. Dankers, E. W. Meijer, *J. Am. Chem. Soc.* **2013**, *135*, 11159-11164.
- [10] a) P. Malo de Molina, M. Gradzielski, *Gels* **2017**, *3*, 30; b) Y.-Y. Won, H. T. Davis, F. S. Bates, *Science* **1999**, *283*, 960; c) Y.-Y. Won, K. Paso, H. T. Davis, F. S. Bates, *J. Phys. Chem. B* **2001**, *105*, 8302-8311; d) S. R. Raghavan, J. F. Douglas, *Soft Matter* **2012**, *8*, 8539-8546; e) R. Verber, A. Blanazs, S. P. Armes, *Soft Matter* **2012**, *8*, 9915-9922; f) J. R. Lovett, L. P. D. Ratcliffe, N. J. Warren, S. P. Armes, M. J. Smallridge, R. B. Cracknell, B. R. Saunders, *Macromolecules* **2016**, *49*, 2928-2941.
- [11] a) A. Blanazs, R. Verber, O. O. Mykhaylyk, A. J. Ryan, J. Z. Heath, C. W. I. Douglas, S. P. Armes, *J. Am. Chem. Soc.* **2012**, *134*, 9741-9748; b) M. Sponchioni, C. T. O'Brien, C. Borchers, E. Wang, M. N. Rivolta, N. J. W. Penfold, I. Canton, S. P. Armes, *Chem. Sci.* **2020**, *11*, 232-240; c) N. J. W. Penfold, J. R. Whatley, S. P. Armes, *Macromolecules* **2019**, *52*, 1653-1662; d) A. L. A. Binch, L. P. D. Ratcliffe, A. H. Milani, B. R. Saunders, S. P. Armes, J. A. Hoyland, *Biomacromolecules* **2021**, *22*, 837-845; e) M. K. Gupta, J. R. Martin, T. A. Werfel, T. Shen, J. M. Page, C. L. Duvall, *J. Am. Chem. Soc.* **2014**, *136*, 14896-14902.
- [12] A. Blanazs, J. Madsen, G. Battaglia, A. J. Ryan, S. P. Armes, *J. Am. Chem. Soc.* **2011**, *133*, 16581-16587.
- [13] I. Canton, N. J. Warren, A. Chahal, K. Amps, A. Wood, R. Weightman, E. Wang, H. Moore, S. P. Armes, *ACS Cent. Sci.* **2016**, *2*, 65-74.
- [14] F. V. Gruschwitz, T. Klein, M. T. Kuchenbrod, N. Moriyama, S. Fujii, I. Nischang, S. Hoepfener, K. Sakurai, U. S. Schubert, J. C. Brendel, *ACS Macro Lett.* **2021**, *10*, 837-843.
- [15] a) P. R. A. Chivers, D. K. Smith, *Nat. Rev. Mater.* **2019**, *4*, 463-478; b) T. Jungst, W. Smolan, K. Schacht, T. Scheibel, J. Groll, *Chem. Rev.* **2016**, *116*, 1496-1539.
- [16] F. V. Gruschwitz, M.-C. Fu, T. Klein, R. Takahashi, T. Higashihara, S. Hoepfener, I. Nischang, K. Sakurai, J. C. Brendel, *Macromolecules* **2020**, *53*, 7552-7560.
- [17] a) E. Vereroudakis, M. Bantawa, R. P. M. Lafleur, D. Parisi, N. M. Matsumoto, J. W. Peeters, E. Del Gado, E. W. Meijer, D. Vlassopoulos, *ACS Cent. Sci.* **2020**, *6*, 1401-1411; b) W. E. M. Noteborn, D. N. H. Zwagerman, V. S. Talens, C. Maity, L. van der Mee, J. M. Poolman, S. Mytnyk, J. H. van Esch, A. Kros, R. Eelkema, R. E. Kieltyka, *Adv. Mater.* **2017**, *29*, 1603769.
- [18] W. Knoben, N. A. M. Besseling, L. Bouteiller, M. A. Cohen Stuart, *Phys. Chem. Chem. Phys.* **2005**, *7*, 2390-2398.
- [19] P. L. Ritger, N. A. Peppas, *J. Control. Release* **1987**, *5*, 37-42.

- [20] S. Correa, A. K. Grosskopf, H. Lopez Hernandez, D. Chan, A. C. Yu, L. M. Stapleton, E. A. Appel, *Chem. Rev.* **2021**.
- [21] Y. Wang, J. Li, Y. Li, B. Yang, *Nano Today* **2021**, *39*, 101180.
- [22] W. Zhou, J. M. Stukel, H. L. Cebull, R. K. Willits, *Macromol. Biosci.* **2016**, *16*, 535-544.
- [23] a) P. A. Amorim, M. A. d'Ávila, R. Anand, P. Moldenaers, P. Van Puyvelde, V. Bloemen, *Bioprinting* **2021**, *22*, e00129; b) A. Blaeser, D. F. Duarte Campos, U. Puster, W. Richtering, M. M. Stevens, H. Fischer, *Adv. Healthcare Mater.* **2016**, *5*, 326-333; c) N. Zandi, E. S. Sani, E. Mostafavi, D. M. Ibrahim, B. Saleh, M. A. Shokrgozar, E. Tamjid, P. S. Weiss, A. Simchi, N. Annabi, *Biomaterials* **2021**, *267*, 120476.
- [24] a) P. Gonzalez-Tello, F. Camacho, G. Blazquez, *Journal of Chemical & Engineering Data* **1994**, *39*, 611-614; b) K. W. Ebagninin, A. Benchabane, K. Bekkour, *J. Colloid Interface Sci.* **2009**, *336*, 360-367.
- [25] C. W. Macosko, *Rheology: Principles, Measurements, and Applications*, Wiley-VCH, New York, **1994**.
- [26] a) N. Paxton, W. Smolan, T. Bock, F. Melchels, J. Groll, T. Jungst, *Biofabrication* **2017**, *9*, 044107; b) G. Kraut, L. Yenchesky, F. Prieto, G. E. M. Tovar, A. Southan, *J. Appl. Polym. Sci.* **2017**, *134*, 45083.
- [27] H. Lopez Hernandez, J. W. Souza, E. A. Appel, *Macromol. Biosci.* **2021**, *21*, 2000295.
- [28] a) L. Moroni, J. A. Burdick, C. Highley, S. J. Lee, Y. Morimoto, S. Takeuchi, J. J. Yoo, *Nat Rev Mater* **2018**, *3*, 21-37; b) M. C. Nolan, A. M. Fuentes Caparrós, B. Dietrich, M. Barrow, E. R. Cross, M. Bleuel, S. M. King, D. J. Adams, *Soft Matter* **2017**, *13*, 8426-8432; c) N. A. Sather, H. Sai, I. R. Sasselli, K. Sato, W. Ji, C. V. Synatschke, R. T. Zambrotta, J. F. Edelbrock, R. R. Kohlmeier, J. O. Hardin, J. D. Berrigan, M. F. Durstock, P. Mirau, S. I. Stupp, *Small* **2021**, *17*, 2005743.
- [29] a) R. Landers, A. Pfister, U. Hübner, H. John, R. Schmelzeisen, R. Mülhaupt, *J. Mater. Sci.* **2002**, *37*, 3107-3116; b) L. A. Hockaday, K. H. Kang, N. W. Colangelo, P. Y. C. Cheung, B. Duan, E. Malone, J. Wu, L. N. Girardi, L. J. Bonassar, H. Lipson, C. C. Chu, J. T. Butcher, *Biofabrication* **2012**, *4*, 035005-035005; c) B. Duan, L. A. Hockaday, K. H. Kang, J. T. Butcher, *J. Biomed. Mater. Res. A* **2013**, *101*, 1255-1264.
- [30] K. Schacht, T. Jüngst, M. Schweinlin, A. Ewald, J. Groll, T. Scheibel, *Angew. Chem. Int. Ed.* **2015**, *54*, 2816-2820.
- [31] M. Diba, S. Spaans, S. I. S. Hendrikse, M. M. C. Bastings, M. J. G. Schotman, J. F. van Sprang, D. J. Wu, F. J. M. Hoeben, H. M. Janssen, P. Y. W. Dankers, *Adv. Mater.* **2021**, *n/a*, 2008111.

Supporting Information

Dynamic hydrogels from crosslinked supramolecular polymeric nanofibers

Franka V. Gruschwitz,^{a,b} Franziska Hausig,^{a,b} Philipp Schüler,^c Julian Kimmig,^b David Pretzel,^b Ulrich S. Schubert,^{a,b} Sylvain Catrouillet,^{d,*} Johannes C. Brendel,^{a,b,*}

a Laboratory of Organic and Macromolecular Chemistry (IOMC), Friedrich Schiller University Jena, Humboldtstraße 10, 07743 Jena, Germany

b Jena Center for Soft Matter (JCSM), Friedrich Schiller University Jena, Philosophenweg 7, 07743 Jena, Germany

c IOMC/IAAC NMR platform, Friedrich Schiller University Jena, Humboldtstraße 10, 07743 Jena, Germany

d ICGM, Univ Montpellier, CNRS, ENSCM, Montpellier, France

*corresponding authors: sylvain.catrouillet@umontpellier.fr, johannes.brendel@uni-jena.de,

Content

1. Synthesis and characterization	3
2. Preparation of the gels	5
3. Moldability.....	6
4. Light scattering measurments	6
5. Stability of the gels.....	10
6. Cytotoxicity measurements.....	11
7. Pulse-field-gradient NMR spectroscopy	12
8. Fluorescence spectroscopy	15
9. Rheology.....	16
10. Photo-bleaching recovery measurements.....	22
11. 3D printing	23
References.....	24

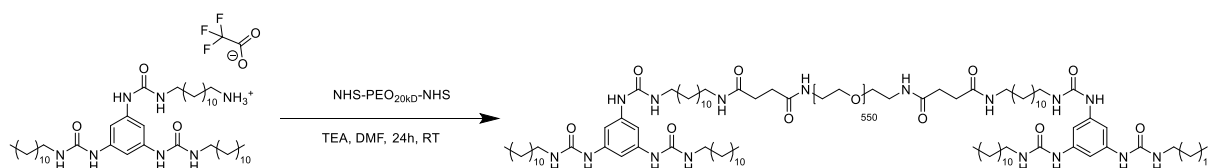
1. Synthesis and characterization

Materials and methods. All reagents and solvents were commercial products purchased from Sigma-Aldrich, Alfa Aesar, Rapp Polymere or TCI and were used without further purification. ^1H -NMR spectra were measured with a Bruker spectrometer (300 MHz) equipped with an Avance I console, a dual ^1H and ^{13}C sample head and a 120x BACS automatic sample changer. The chemical shifts of the peaks were determined by using the residual solvent signal as reference and are given in ppm in comparison to TMS. Size-exclusion chromatography (SEC) of polymers was performed on an Agilent system (series 1200) equipped with a PSS degasser, a G1310A pump, a G1362A refractive index detector and a PSS GRAM 30 and 1000 column with DMAc (+ 0.21 wt.% LiCl) as eluent at a flow rate of 1 mL min^{-1} . The column oven was set to $40\text{ }^\circ\text{C}$ and poly(ethylene oxide) (PEO) standards were used for calibration. Matrix-assisted laser desorption ionization mass spectrometry (MALDI-MS) measurements were carried out using an Ultraflex III ToF/ToF instrument (Bruker Daltonics) equipped with a Nd-YAG laser. All spectra were measured in the positive mode using α -cyano-4-hydroxycinnamic acid (CHCA) as matrix material.

Synthesis of BTU-PEO_{2k} 1

The detailed synthesis procedure of BTU-PEO_{2k} was published elsewhere.^[1]

Synthesis of the crosslinker BTU-PEO_{20k}-BTU 2a



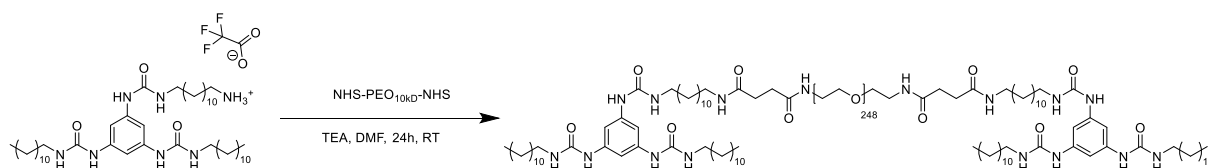
Scheme S 1 Schematic representation of the synthetic procedure for the crosslinker **BTU-PEO_{20k}-BTU 2a**.

The deprotected BTU core^[1] (0.020 g, 0.026 mmol, 2.0 eq) was dissolved in 3 mL DMF. To this, 0.04 mL triethylamine (0.26 mmol, 20 eq) were added dropwise. After stirring at rt for 15 min, 0.320 g of NHS-PEO_{20k}-NHS ester (0.013 mmol, 1.0 eq) were added and the reaction mixture stirred at rt overnight. Afterwards, the reaction mixture was precipitated into cold diethyl ether, the suspension centrifuged (10 min, 5,000 rpm) and the supernatant decanted. Then a mixture of diethyl ether and acetone (9:1, v:v) was added to the precipitate and the suspension exposed to sonication for 5 min in order to remove remaining unconjugated NHS-PEO_{20k}-NHS ester. Afterwards, the suspension was again centrifuged (10 min, 5,000 rpm) and the supernatant decanted. The obtained product was lyophilized overnight.

¹H-NMR (300 MHz, d₆-DMSO, 298 K): δ [ppm] = 8.27 (s, 6H, NH), 7.87 (t, J = 5.48, 2H, NH), 7.75 (s, J = 5.71 2H, NH), 7.09 (s, 6H, CH_{aromat}), 5.95 (t, J = 5.48 Hz, 6H, NH), 3.51 (s, 2267H, PEO), 3.18 (q, 6H, CH₂), 3.05 (m, 20H, CH₂), 2.27 (s, 8H, CH₂), 1.39 (m, 16H, CH₂), 1.24 (m, 116H, CH₂), 0.85 (t, J = 6.85 Hz, 12H, CH₃).

SEC (DMAc + 0.21 wt. % LiCl, PEO-Calibration): $M_n = 25,030 \text{ g mol}^{-1}$; $M_w = 30,066 \text{ g mol}^{-1}$; $\text{Đ} = 1.21$.

Synthesis of the crosslinker BTU-PEO_{10k}-BTU 2b



Scheme S 2 Schematic representation of the synthetic procedure for the crosslinker **BTU-PEO_{10k}-BTU 2b**.

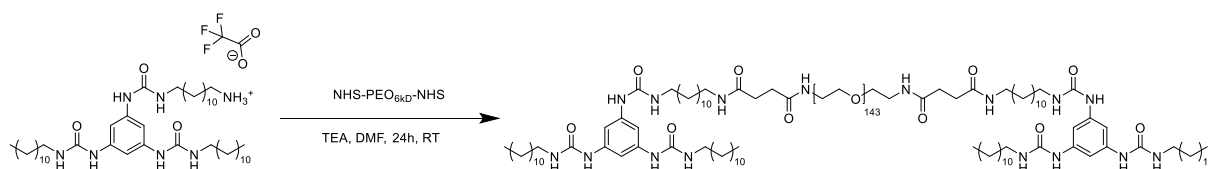
The compound was synthesized according to the procedure of compound **2a**.

¹H-NMR (300 MHz, d₆-DMSO, 298 K): δ [ppm] = 8.26 (s, 6H, NH), 7.86 (t, J = 5.48, 2H, NH), 7.75 (s, J = 5.71 2H, NH), 7.08 (s, 6H, CH_{aromat}), 5.94 (t, J = 5.48 Hz, 6H, NH), 3.51 (s, 992H, PEO), 3.18 (q, 6H, CH₂), 3.02 (m, 20H, CH₂), 2.27 (s, 8H, CH₂), 1.39 (m, 16H, CH₂), 1.24 (m, 120H, CH₂), 0.85 (t, J = 6.85 Hz, 12H, CH₃).

SEC (DMAc + 0.21 wt. % LiCl, PEO-Calibration): $M_n = 17,398 \text{ g mol}^{-1}$; $M_w = 21,464 \text{ g mol}^{-1}$; $\text{Đ} = 1.21$.

MALDI-ToF-MS (positive mode, CHCA) (m/z): calculated for DP = 220 [C₅₄₀H₁₀₆₂N₁₆O₂₃₀Na]⁺: 11,483.4713; found: 11, 483.477.

Synthesis of the crosslinker BTU-PEO_{6k}-BTU 2c



Scheme S 3 Schematic representation of the synthetic procedure for the crosslinker **BTU-PEO_{6k}-BTU 2c**.

The compound was synthesized according to the procedure of compound **2a**

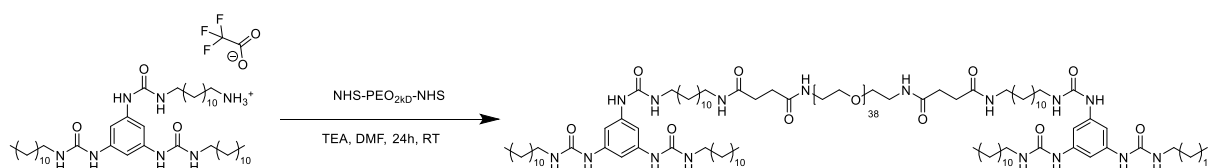
¹H-NMR (300 MHz, d₆-DMSO, 298 K): δ [ppm] = 8.26 (s, 6H, NH), 7.85 (t, J = 5.48, 2H, NH), 7.77 (s, J = 5.71 2H, NH), 7.09 (s, 6H, CH_{aromat}), 5.94 (t, J = 5.48 Hz, 6H, NH), 3.51 (s,

727H, PEO), 3.18 (q, 6H, CH₂), 3.03 (m, 20H, CH₂), 2.27 (s, 8H, CH₂), 1.38 (m, 16H, CH₂), 1.24 (m, 119H, CH₂), 0.85 (t, J = 6.85 Hz, 12H, CH₃).

SEC (DMAc + 0.21 wt. % LiCl, PEO-Calibration): $M_n = 10,961 \text{ g mol}^{-1}$; $M_w = 12,231 \text{ g mol}^{-1}$; $\bar{D} = 1.13$.

MALDI-ToF-MS (positive mode, CHCA) (m/z): calculated for DP = 120 $[\text{C}_{340}\text{H}_{662}\text{N}_{16}\text{O}_{130}\text{Na}]^+$: 7,077.5083; found: 7,077.2760.

Synthesis of the crosslinker BTU-PEO_{2k}-BTU 2d



Scheme S 4 Schematic representation of the synthetic procedure for the crosslinker **BTU-PEO_{2k}-BTU 2d**.

The compound was synthesized according to the procedure of compound **2a**

¹H-NMR (300 MHz, d₆-DMSO, 298 K): δ [ppm] = 8.26 (s, 6H, NH), 7.87 (t, J = 5.48, 2H, NH), 7.77 (s, J = 5.71 2H, NH), 7.09 (s, 6H, CH_{aromat}), 5.95 (t, J = 5.48 Hz, 6H, NH), 3.51 (s, 179H, PEO), 3.18 (q, J = 5.94 Hz, 6H, CH₂), 3.03 (m, 16H, CH₂), 2.27 (s, 8H, CH₂), 1.39 (m, 16H, CH₂), 1.24 (m, 116H, CH₂), 0.85 (t, J = 6.85 Hz, 12H, CH₃).

SEC (DMAc + 0.21 wt. % LiCl, PEO-Calibration): $M_n = 8,314 \text{ g mol}^{-1}$; $M_w = 9,083 \text{ g mol}^{-1}$; $\bar{D} = 1.12$.

MALDI-ToF-MS (positive mode, CHCA) (m/z): calculated for DP = 22

$[\text{C}_{144}\text{H}_{270}\text{N}_{16}\text{O}_{32}\text{Na}]^+$: 2,759.9917; found: 2,759.5420.

2. Preparation of the gels

The procedure resembles the solvent switch method published previously.^[2] The respective amount of BTU-PEO_{2k} **1** and crosslinker **2** were dissolved in 0.5 mL of THF and stirred for 10 min to guarantee complete dissolution. Subsequently, 1 mL of MilliQ water was added (1 mL h⁻¹) using a syringe pump under stirring to reach a final water content of 66 v%. The solution was transferred either to the measurement setup and left to evaporate for approx. 0.5 h or was filled in a syringe without the stamp to evaporate and gelate in the syringe for printing till all THF was evaporated. Transfer of the gel after evaporation was not feasible due to the strength of the gel and the formation of entrapped air bubbles, which would prevent a continuous

printing process. Removal of THF was ensured by $^1\text{H-NMR}$ spectroscopy and weighing of the sample.

3. Moldability

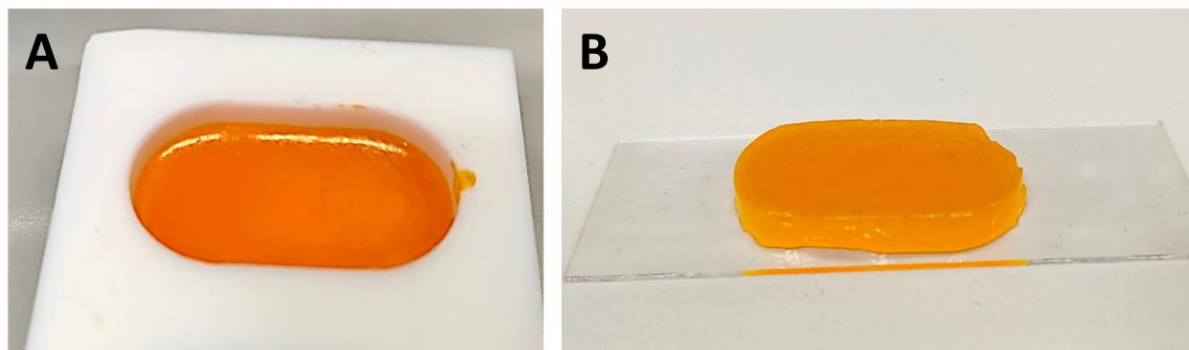


Figure S 1 Gels of **1** with 1 % **2a** ($c = 25 \text{ mg mL}^{-1}$) molded in Teflon molds (A) were stable on a glass slide (B).

4. Light scattering measurements

The water (refractive index $n_0 = 1.333$) was filtered. Light Scattering measurements were performed on a LSInstrument spectrometer operating with a vertically polarized laser with wavelength $\lambda = 660 \text{ nm}$. The measurements were done at 20°C over a range of scattering wave vectors ($q = 4\pi n \sin(\theta/2)/\lambda$, with θ the angle of observation and n the refractive index of the solvent).

Static light scattering: The time-averaged scattered intensity of samples (I_{sample}) was measured at 10° intervals at scattering angles between 20° and 150° (corresponding to values of q between 4.4×10^6 and $2.5 \times 10^7 \text{ m}^{-1}$). The scattered intensity of the pure solvent (I_{solvent}) was also measured. The reduced scattered intensity, denoted as $I(q)$, was used for further calculations:

$$I(q) = \frac{I_{\text{sample}}(q) - I_{\text{solvent}}(q)}{I_{\text{solvent}}(q)} \quad \text{Eq. S1}$$

By using $I(q)$ instead of the absolute scattered intensity, both scattering from the solvent and the angular dependence of the scattering volume are taken into account and corrected for.

Measurements were taken from 20 to 150° each 10° during 500s.

From the q dependence of the intensity, information about the characteristic length scales in the sample can be derived. The segment density correlation length in the solution can be found using the Ornstein-Zernike equation for the structure factor:^[3]

$$I(q) \approx \frac{1}{1 + q^2 \xi^2} \quad \text{Eq. S2}$$

In dilute solutions, the polymer chains do not interact, and the correlation length gives information about the (average) size of the individual molecules. If the solution is concentrated and chains start to overlap (beyond the overlap concentration c^*), the polymers form a transient network and the correlation length no longer contains information about the size of the individual chains, but it reflects the mesh size ξ_m of the network.

Dynamic light scattering: The scattered intensity was measured at scattering angles between 20° and 150° (corresponding to values of q between 4.4×10^6 and $2.5 \times 10^7 \text{m}^{-1}$). between 20° and 150° (corresponding to values of q between 4.4×10^6 and $2.5 \times 10^7 \text{m}^{-1}$). To obtain correlation functions of sufficient quality, measuring times of 500s per angle were used.

Dynamic light scattering (DLS) measures temporal fluctuations of the scattered intensity arising from motion of the scatterers.^[3] From the scattered intensity as a function of time, the intensity correlation function $g^{(2)}(\tau)$ is calculated for a number of time intervals τ :

$$g^{(2)}(\tau) = \frac{\langle I(t)I(t + \tau) \rangle}{\langle I(t) \rangle^2} \quad \text{Eq. S3}$$

The intensity correlation function is related to the normalized field correlation function $g^{(1)}(\tau)$ by the Siegert equation:^[3] $g^{(2)}(\tau) = 1 + A [g^{(1)}(\tau)]^2$ Eq. S4

where A is a constant of order unity depending on the geometry of the experimental setup. De Gennes developed a scaling theory for semidilute polymer solutions using a transient gel model.^[4] According to this theory $g^{(1)}(\tau)$ is an exponentially decreasing function with a single decay rate constant Γ , which is determined by the scattering vector q and the so-called gel diffusion coefficient D_g , according to

$$g^{(1)}(\tau) = e^{-\Gamma\tau} = e^{-q^2 D_g \tau} \quad \text{Eq. S5}$$

D_g is given by

$$D_g = D_c \frac{M_g + M_0}{M_0} \quad \text{Eq. S6}$$

where M_g is the gel modulus (the elastic or Young's modulus of the transient gel), M_o the osmotic modulus, defined as $c(d\Pi/dc)$, and D_c the collective diffusion coefficient, which is in turn related to the hydrodynamic correlation length ξ_H by the Stokes-Einstein equation^[3]

$$D_c = \frac{k_B T}{6\pi\eta_0 \xi_H} \quad \text{Eq. S7}$$

where η_0 is the solvent viscosity. For polymers in a good solvent, $M_o \gg M_g$ and D_c is effectively equal to D_g . Experimentally, a distribution of decay rate constants Γ is generally measured, each with its own weight w , so $g^{(1)}_{(\tau)}$ is given by

$$g^{(1)}_{(\tau)} = \int_0^{\infty} w(\Gamma) e^{-\Gamma\tau} d\Gamma \quad \text{Eq. S8}$$

Mostly, the value of Γ at the peak of the distribution is taken as “the” decay rate constant and used for further calculations.

In the concentrated regimes, the hydrodynamic correlation length corresponds to the hydrodynamic mesh size of the transient network, the average distance between entanglement points. With SLS, the average mesh size of the transient polymer network is measured, whereas DLS measures the average diffusion coefficient of the meshes. From this diffusion coefficient and the viscosity of the solvent, the size of the mesh can be calculated with eq 5. The hydrodynamic correlation length $\hat{e}H$ measured by DLS is thus not equal to the static correlation length \hat{e} , but it is of the same order of magnitude and it scales in the same way with concentration.

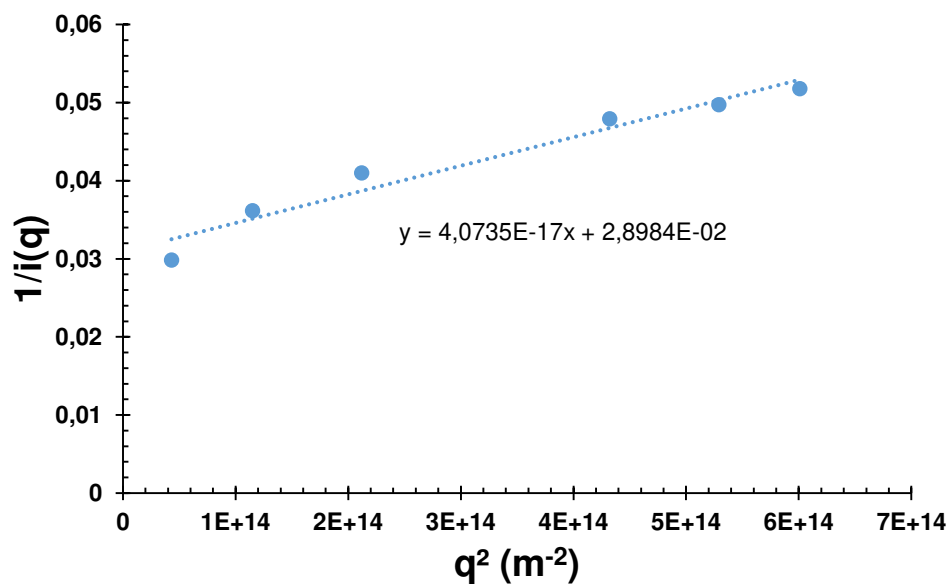


Figure S 2 Reciprocal reduced scattered intensity as a function of q^2 for the crosslinked BTU gel (1 + 1% 2a, 25 mg mL^{-1}). The line is linear fit to the data.

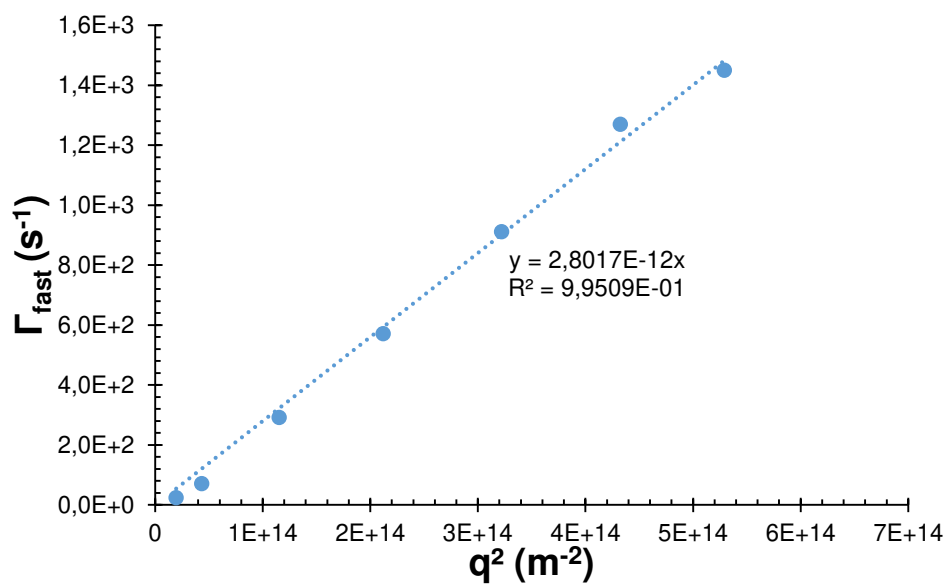


Figure S 3 q^2 dependence of Γ_{fast} for the crosslinked BTU gel (1 + 1% 2a, 25 mg mL^{-1}). Γ_{fast} is proportional to q^2 , as indicated by the linear fit, which corresponds to $\Gamma_{\text{fast}} + 2.8017 \times 10^{-12}q^2$.

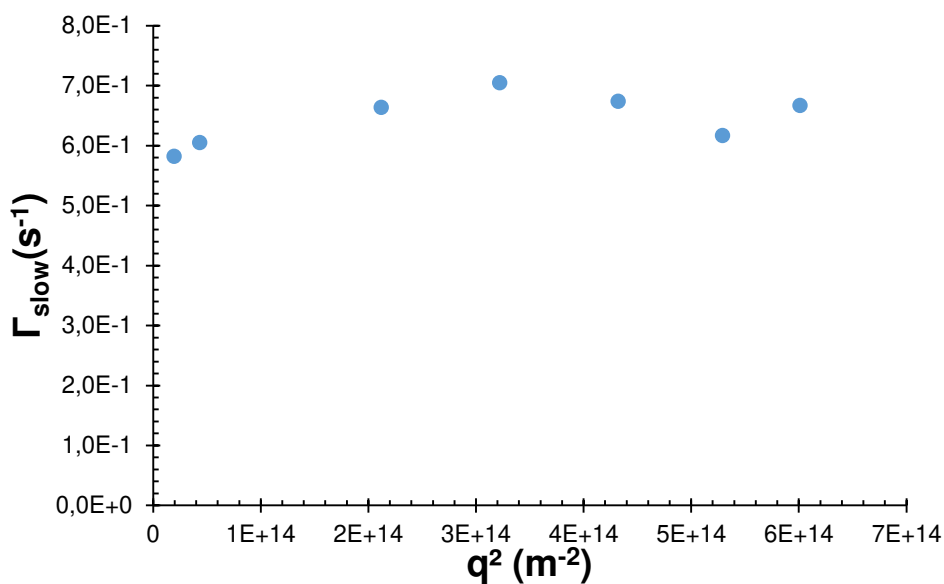


Figure S 4 q^2 dependence of Γ_{slow} for the crosslinked BTU gel (**1** + 1% **2a**, 25 mg mL⁻¹). The horizontal line at $\Gamma_{\text{slow}} = 0.645 \text{ s}^{-1}$ shows that the slow mode does not depend significantly on q .

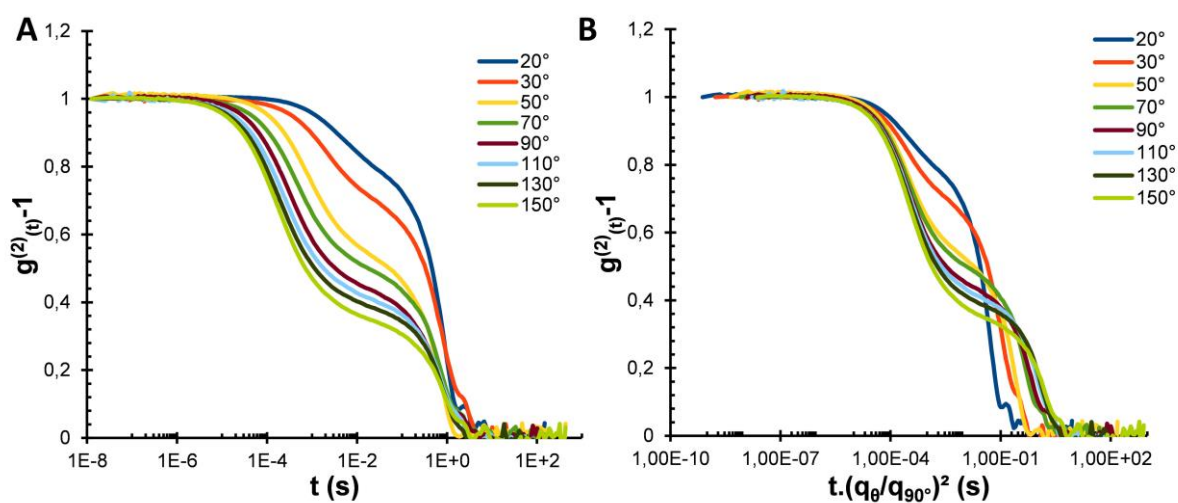


Figure S 5 q dependence of the correlation functions for the crosslinked BTU gel (**1** + 1% **2a**, 25 mg mL⁻¹) (A). Same data as in figure (A) after q^2 normalization (B).

5. Stability of the gels

Gels were prepared according to the already mentioned procedure. Instead of pure water, water at pH 2 (addition of HCl), pH 11 (addition of NaOH) was added to the solution of **1** and **2** in THF. For the salt containing gel, 1.8% NaCl aq. solution, and for the media containing gel DMEM + 10% serum protein was added instead of pure water in the gel preparation.

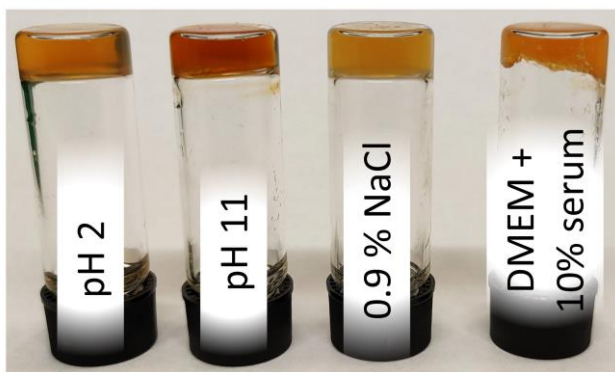


Figure S 6 Gel of **1** + 1% **2a** at 25 mg mL⁻¹ prepared in acid, basic, salt- and serum-containing media.

6. Cytotoxicity measurements

Cytotoxicity studies were performed using the mouse fibroblast cell line L929 (400620, CLS), as recommended by ISO10993-5. L929 cells were routinely cultured in Dulbecco's modified eagle's medium with 2 mM L-glutamine (Biochrom, Germany) supplemented with 10% fetal calf serum (FCS, Capricorn Scientific, Germany), 100 U mL⁻¹ penicillin, and 100 µg mL⁻¹ streptomycin (Biochrom, Germany) at 37 °C under a humidified 5% (v/v) CO₂ atmosphere. For the cell experiments, a gel of **1** with 1% **2a** at 25 mg mL⁻¹ was either added prior to the addition of the cell suspension on a part of the well plate bottom or post to the freshly added cell suspension. Experiments were done in duplicate. In detail, cells were seeded at 10⁴ cells mL⁻¹ (10⁴ cells per well) in a 24 well plate (VWR, Germany) and incubated for 24 h. Subsequently, the medium was replaced by a mixture of a fresh culture medium and the resazurin-based solution PrestoBlue (Thermo Fisher, Germany, prepared according to the manufacturer's instructions). After further incubation for 45 min at 37 °C under a humidified 5% (v/v) CO₂ atmosphere, the fluorescence was measured at $\lambda_{\text{ex}} = 560 \text{ nm}/\lambda_{\text{em}} = 590 \text{ nm}$ with gain set to optimal (Infinite M200 PRO microplate reader, Tecan, Germany), with untreated cells on the same well plate serving as negative controls. Cell viability below 70% was considered to be indicative of cytotoxicity. The experiments were conducted with approx. 0.1 to 0.2 mL of two gels of **1** with 1% **2a** at 25 mg mL⁻¹ per well, including Blanks and negative controls. Data are expressed as mean \pm SD. In addition, cells were imaged with a transmitted light microscope (Axio Observer Vert.A1, Zeiss, Germany) equipped with a 10x objective using brightfield imaging prior to the PrestoBlue assay. Images were acquired using the ZEN lite software (2012, Zeiss).

Table S 1 Cell viabilities dependent on the preparation procedure.

Procedure	Mean viability (%)	Standard deviation (%)
First gel addition, then seeding of cells	81.3	2.8
First seeding of cells, then gel addition	96.0	1.7

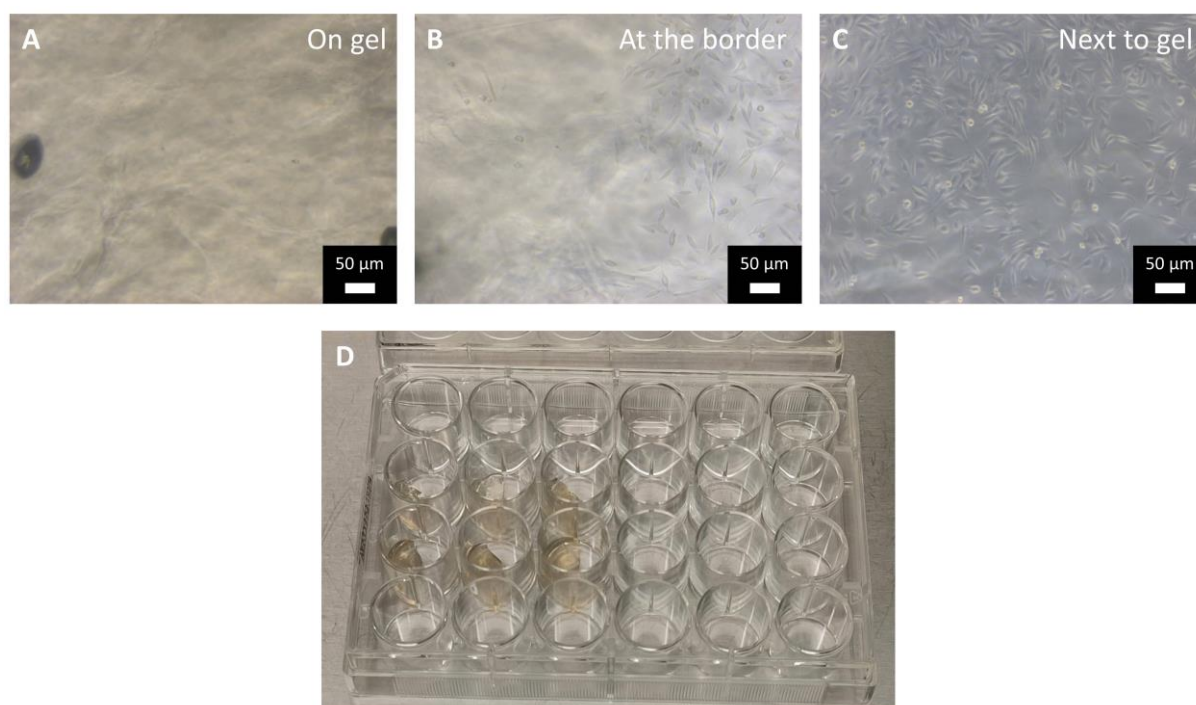


Figure S 7 Microscopy images of the gel (A), the cells at the border of the gel (B) and next to the gel at the bottom of the well (C). Image of the well-plate design, with wells half-filled with the gel (D).

7. Pulse-field-gradient NMR spectroscopy

Poly(ethyloxazoline) (PEtOx) with a degree of polymerization of 20 and 60, resulting in hydrodynamic radii of 0.44 and 2.43 nm (calculated by Stokes-Einstein equation), respectively, were incorporated into the pure BTU gel (**1**, 25 mg mL⁻¹) and the crosslinked BTU gel (**1** + 1% **2a**, 25 mg mL⁻¹) and measured in PFG-NMR. The diffusion coefficient was extracted by fitting a gamma function to the obtained data, to correct for the molar mass distribution of the polymer. To do so, 12.5 mg of **1**, 1.25 mg of **2a** and 1 mg of PEtOx20 or PEtOx60 were dissolved in

0.1 mL THF. 0.5 mL D₂O was added, the mixture was transferred to an NMR tube and the THF was evaporated.

DOSY experiments were performed at 24 °C on a Bruker Avance III (400 MHz, BBFO). The maximum z-gradient was 50 G cm⁻¹. The gradient strength was calibrated using the “doped water” standard. All PFG-experiments performed using the convection compensated pulse program *dstebpgp3s* with $\delta = 4$ ms, $\Delta = 0.75$ s, and increments (gradient) = 64 or 32. Raw data was processed with Topspin 4.1 with phase and baseline correction. Gradient depended signal decays were extracted using the T1/T2 modul in Topspin 4.1. Exact diffusion gradients were calculated using Origin 2020b by fitting to a Gamma function.^[5]

$$A(k) = A(0) \cdot \left(\frac{\beta}{\beta + k} \right)^\alpha \quad \text{Eq. S9}$$

with $k = (\gamma g \delta)^2 (\Delta - \gamma/3)$

The mean diffusion coefficient easily calculated by $\langle D \rangle = \alpha/\beta$. The standard derivation σ was calculated using $\sigma = \frac{\sqrt{\alpha}}{\beta}$.

The following values could be calculated:

Table S 2 Calculated diffusion coefficients of PEtOx₂₀ and PEtOx₆₀ in different gels and pure D₂O fitted by a Gamma function.

Gel	α	β	$\langle D \rangle_{PEtOx20}$ ($\cdot 10^{-10} \text{ m}^2 \text{ s}^{-1}$)	α	β	$\langle D \rangle_{PEtOx60}$ ($\cdot 10^{-10} \text{ m}^2 \text{ s}^{-1}$)
pure 1 at 25 mg mL ⁻¹	73.03	$1.1 \cdot 10^{12}$	0.663±0.078	52.32	$1.17 \cdot 10^{12}$	0.447±0.062
1 + 1% 2a at 25 mg mL ⁻¹	207.9	$6.67 \cdot 10^{11}$	0.3.12±0.22	1044.65	$3.3 \cdot 10^{13}$	0.317±0.009
pure D ₂ O	617.32	$1.1 \cdot 10^{12}$	5.59± 0.23	21.31	$2.1 \cdot 10^{-10}$	1.01±0.22

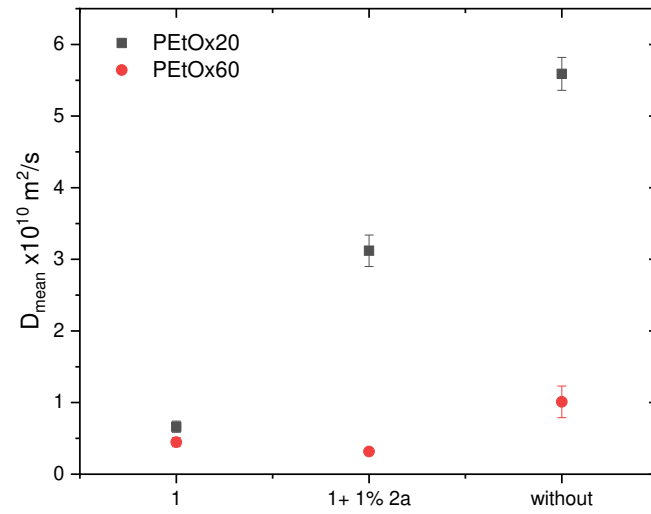


Figure S 8 Calculated mean diffusion coefficients of PEtOx₂₀ and PEtOx₆₀ in different gels and pure D₂O fitted by a Gamma function.

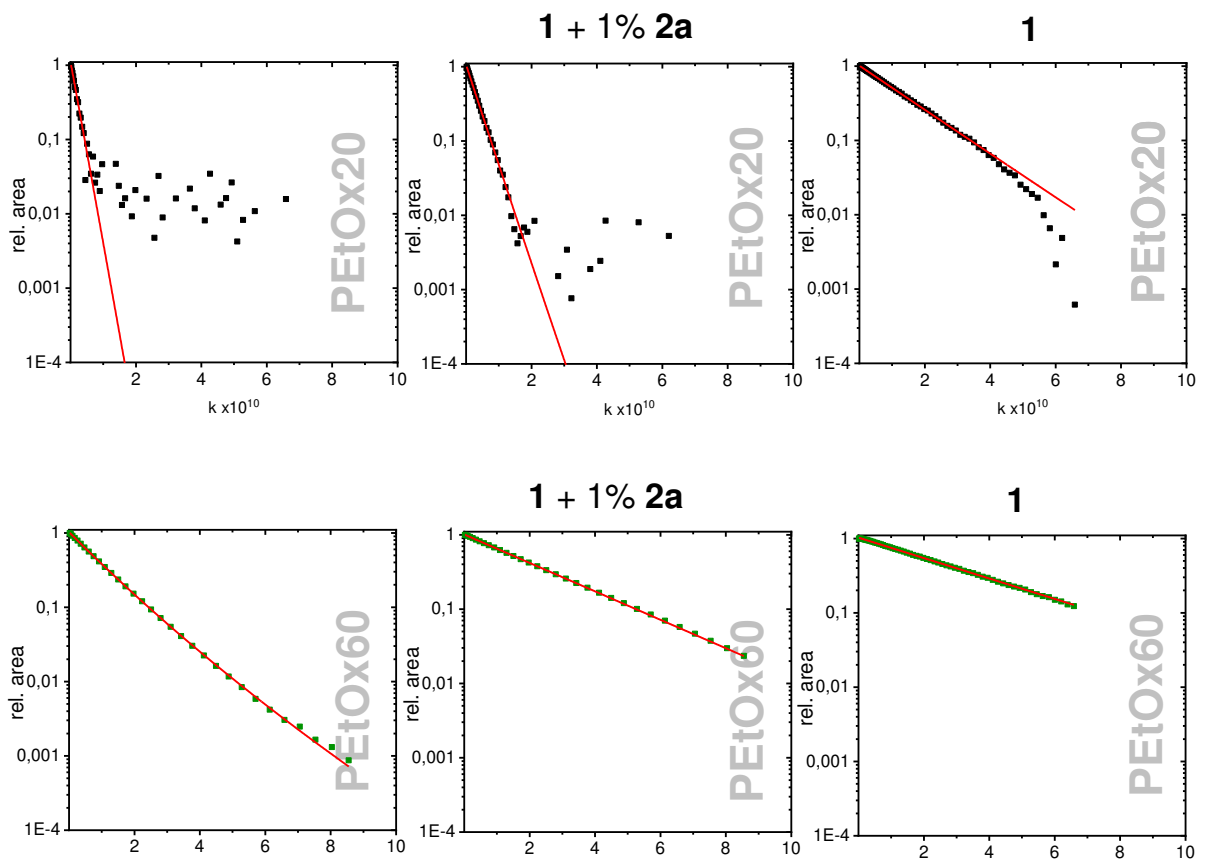


Figure S 9 Fitting curves of normalized signal areas in dependence of $k = (\gamma g \delta)^2 (\Delta - \gamma/3)$ of PEtOx₂₀ and PEtOx₆₀ in different gels and pure D₂O using gamma fit function.

8. Fluorescence spectroscopy

Fluorescence spectroscopy was measured on a Spectrofluorometer FP-8500 from JASCO, in 4 mL quartz cuvettes. 0.5 mL of the gel **1** with 1% **2a** was prepared in the cuvette. To do so, 0.6 mg of the crosslinker **2a** and 6 mg of **1** were dissolved in 0.05 mL THF. 0.250 mL of an aqueous solution of the TRITC labeled dextran ($c = 0.1 \text{ mg mL}^{-1}$) was slowly added to the solution. After evaporation of the THF to an end concentration of 25 mg mL^{-1} the resulting gel was overlaid with 3 mL of water and the spectra measurement was started immediately at an excitation wavelength of 550 nm and measured for every 60 min.

For the Na-fluorescein diffusion experiment, the procedure was adapted. Here 0.25 mL of a 0.001 mg mL^{-1} solution of Na-fluorescein in water was added. The spectra were measured at an excitation wavelength of 490 nm every 30 min.

The diffusion was fitted the Fickian law:

$$\frac{M_t}{M_\infty} = kt^n \quad \text{Eq. S10}$$

with M_t/M_∞ being the amount of released drug, k being the rate constant and n the diffusional exponent.^[6]

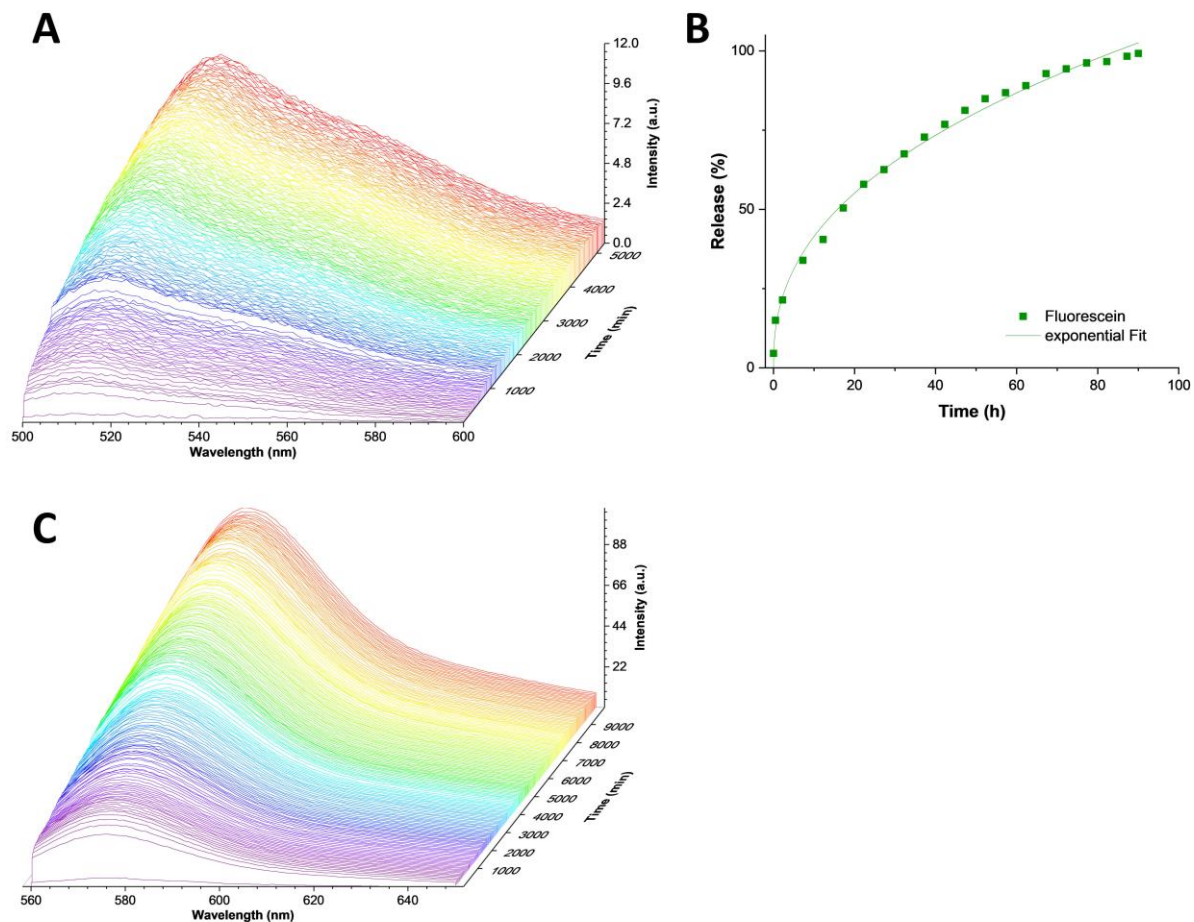


Figure S 10 Time-dependent fluorescence spectra of Na-fluorescein (A) and its release kinetics (B) at an excitation wavelength of 490. Time-dependent fluorescence spectra of TRITC-dextran (500 kD) (C) at an excitation wavelength of 550 nm.

9. Rheology

Methods and materials

The oscillatory dynamic measurements were performed with a Physica Modular Compact MCR301 Rheometer from Anton Paar (Germany). Mechanical properties of the viscoelastic hydrogel material were assayed using a parallel (PP 25 sandblasted)-plate geometry. The linear viscoelastic regime of the samples was obtained from amplitude sweep experiments that were performed from 0.1 to 200% strain at 6.36 rad s^{-1} angular frequency. Frequency sweep measurements were recorded from 0.1 to 100 rad s^{-1} at 1% strain. Measurements were performed at 20 °C unless stated otherwise.

Measurement data

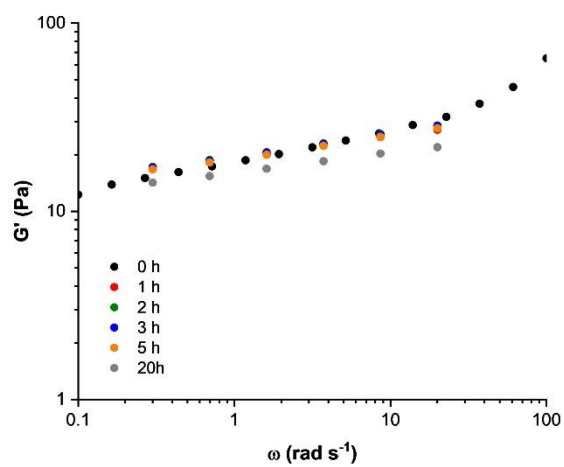


Figure S 11 Frequency-sweep measurements of gel **1** with 1% **2a** ($c = 25 \text{ mg mL}^{-1}$) after exposure to water for a distinct time.

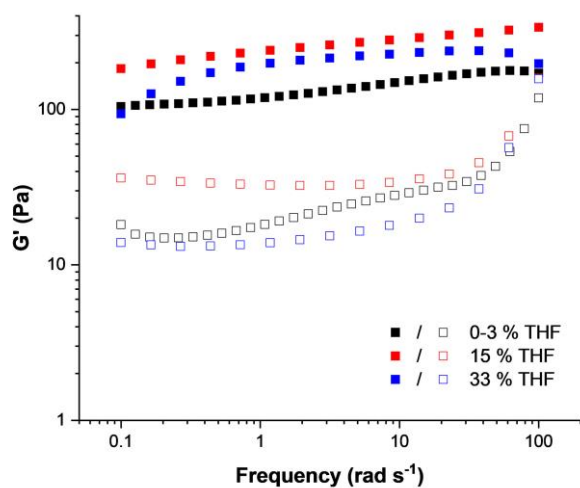


Figure S 12 Frequency-sweep measurements of gel **1** with 1% **2a** ($c = 25 \text{ mg mL}^{-1}$) and different amounts of THF.

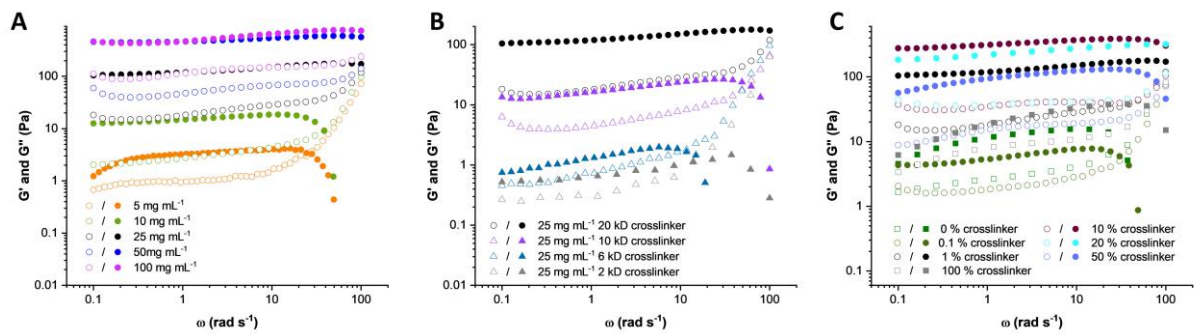


Figure S 13 Frequency-sweep measurements of gels of **1** with 1% **2a** at different concentrations (A), of **1** with 1% crosslinker of different lengths at a concentration of 25 mg mL⁻¹ (B), and with different amount of **2a** crosslinker at 25 mg mL⁻¹ (C).

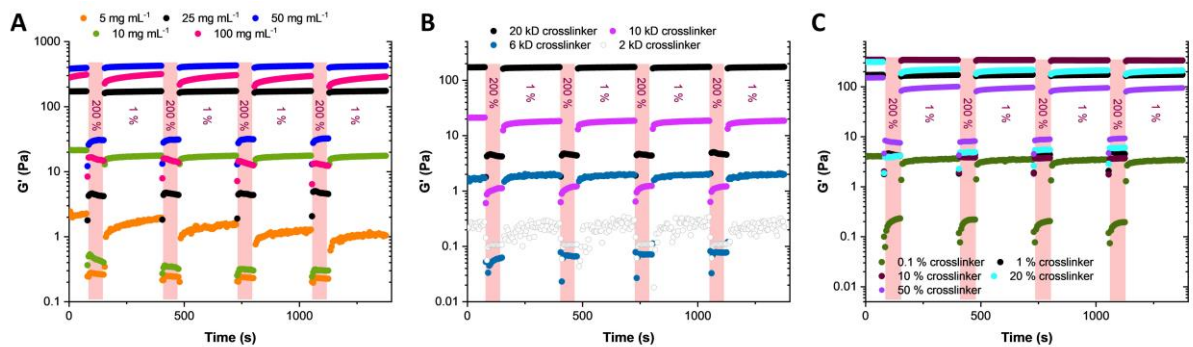


Figure S 14 Step-strain measurements of gels of **1** with 1% of crosslinker **2a** at different concentrations (A), with 1% of different lengths of crosslinkers at 25 mg mL⁻¹ (B) and with different amounts of crosslinker **2a** at 25 mg mL⁻¹ (C). The periods of high deformation (200%) are marked in red.

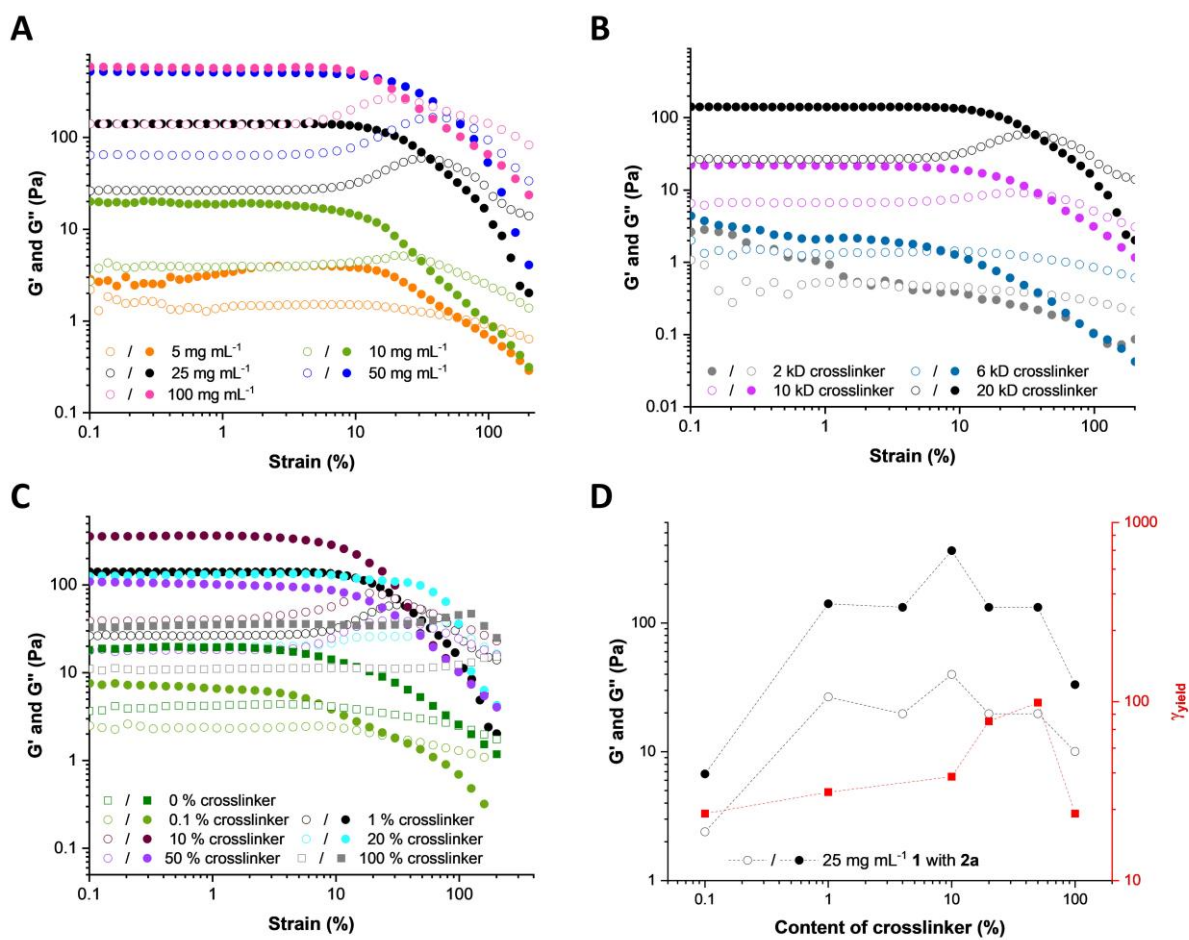


Figure S 15 Deformation measurements of gels of **1** with 1% **2a** at different concentrations (A), of **1** with 1% crosslinker of different lengths at a concentration of 25 mg mL⁻¹ (B), and with different amount of **2a** crosslinker at 25 mg mL⁻¹ (C). Dependence of the yield stress γ_{yield} and the storage/loss module on the amount of crosslinker **2a** ($c = 25 \text{ mg mL}^{-1}$) (D).

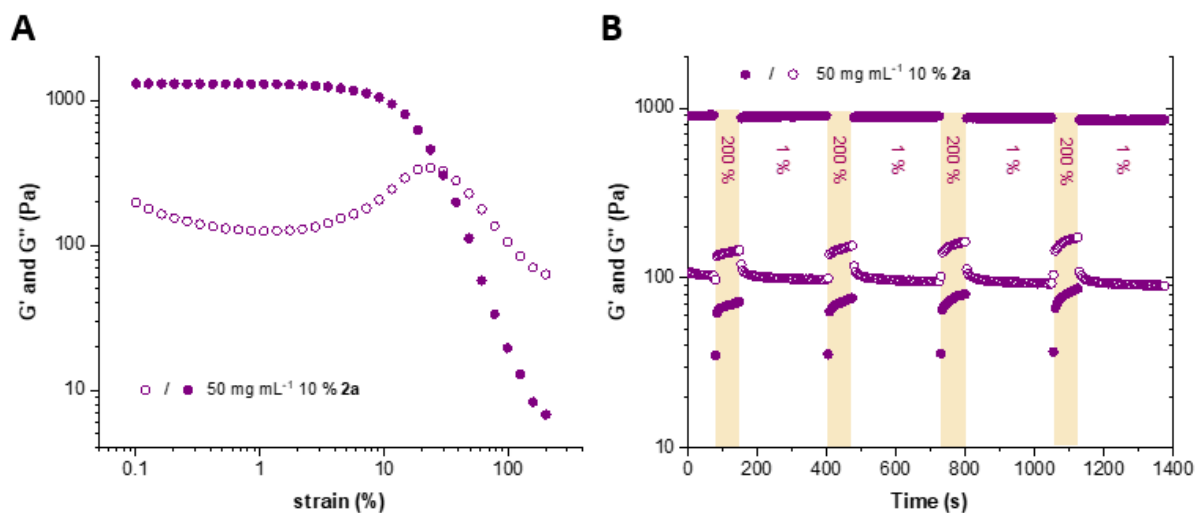


Figure S 16 Strain-sweep (A) and step-strain measurements (B) of gel **1** with 10% **2a** at 50 mg mL⁻¹.

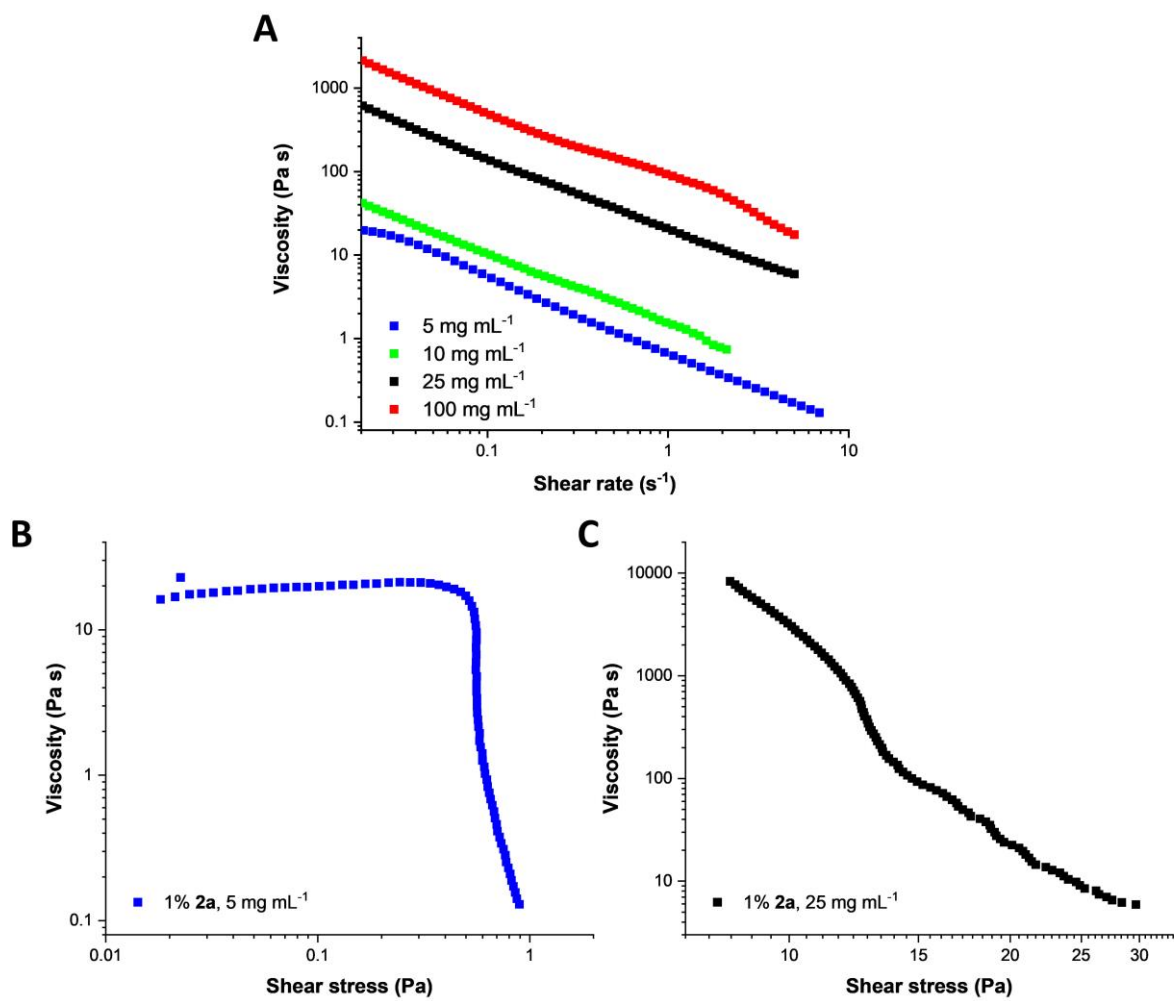


Figure S 17 Shear-rate dependent viscosity of gel of **1** with 1 % **2a** at different concentrations (A) and shear stress dependent viscosity of gel **1** with 1 % **2a** at 5 mg mL⁻¹ (B) and of gel **1** with 1 % **2a** at 25 mg mL⁻¹ (C).

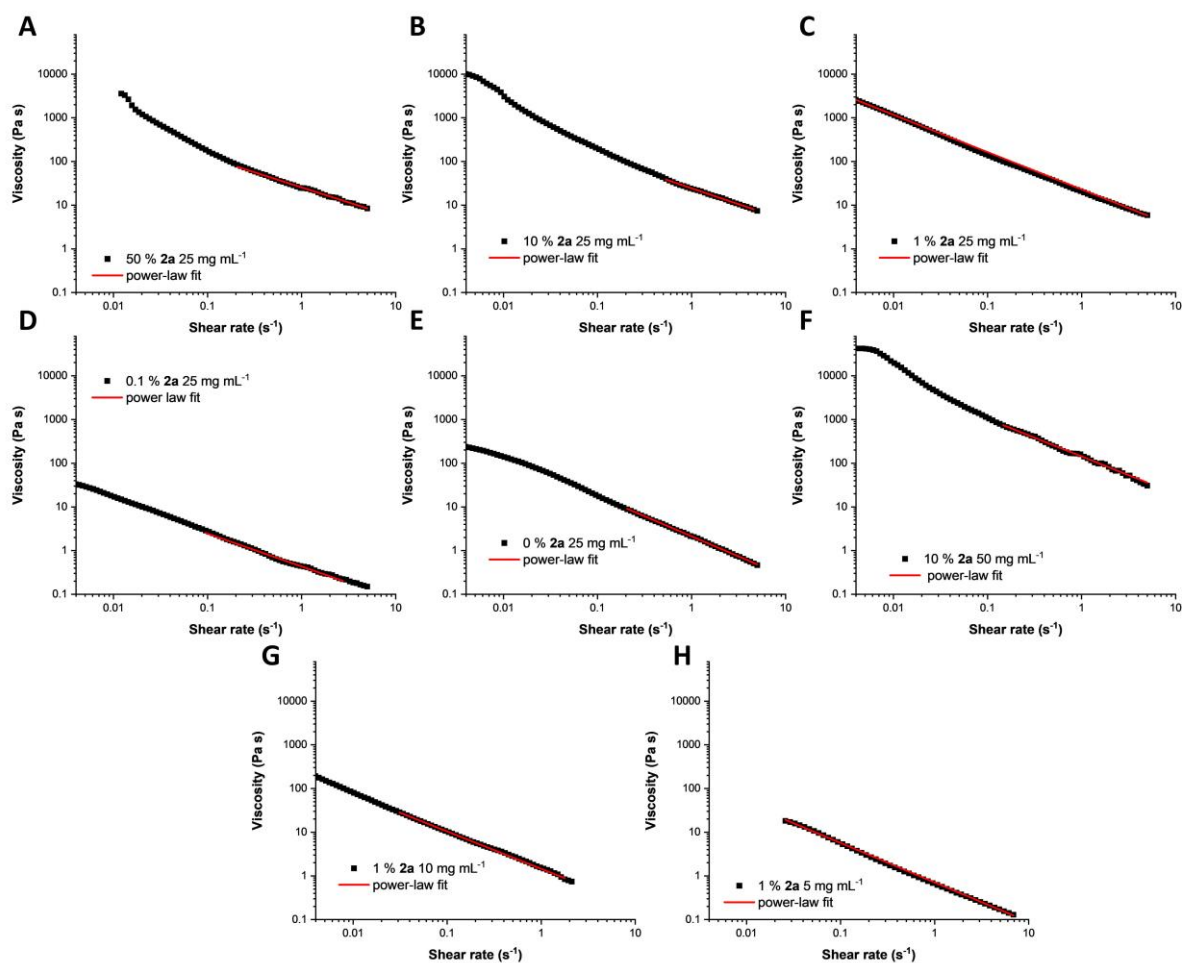


Figure S 18 Power-law fits of the viscosity of different gel compositions. If non-linear behavior could be observed, only the data at higher shear rates was fitted.

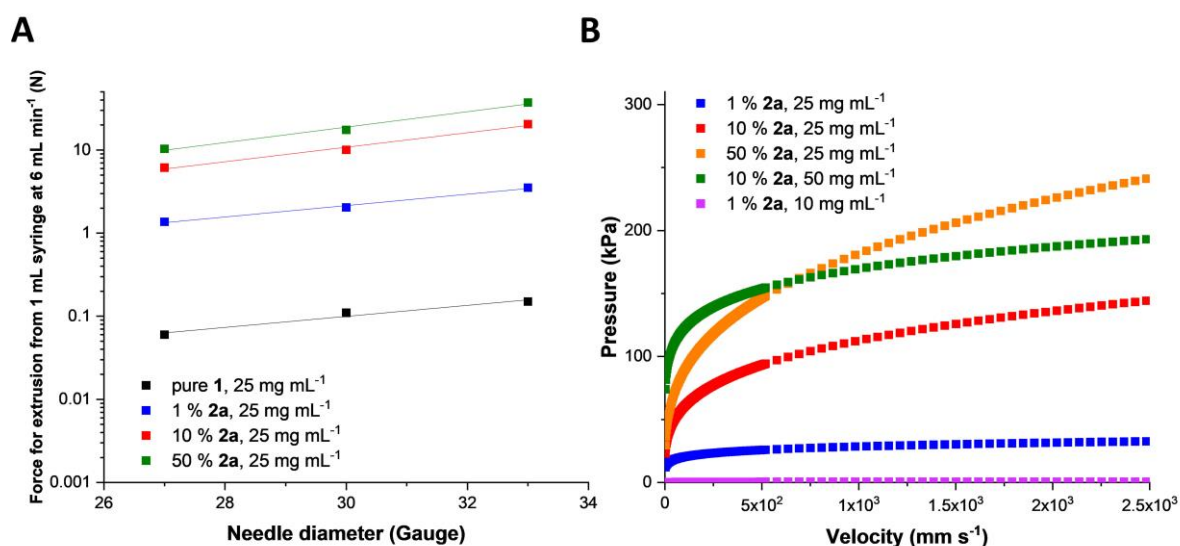


Figure S 19 Force needed for extrusion of the gels of different amount of crosslinker **2a** ($c = 25 \text{ mg mL}^{-1}$) out of a 1 mL syringe at 6 mL min^{-1} in dependence of the needle diameter (needle length 1 inch) (A). Pressure needed for printing gels of different amount of crosslinker **2a** and different concentration from a 1 mL syringe equipped with a cannula (gauge 27, $\frac{1}{2}$ inch) dependent on the velocity (B).

The flow rate Q was calculated by^[7]:

$$Q = \pi \left(\frac{P}{2kl} \right)^{\frac{1}{n}} \frac{n}{3n+1} R^{\frac{3n+1}{n}} \quad \text{Eq.S11}$$

With P being the pressure, n the shear-thinning parameter, k the consistency index, l the length and R the radius of the cannula.

Or rearranging:

$$P = \left(\frac{3n+1}{n} \right)^n k \left(\frac{Q}{\pi} \right)^n \frac{2l}{R^{3n+1}} \quad \text{Eq.S12}$$

The velocity v was calculated by:

$$v = \frac{Q}{\pi R^2} \quad \text{Eq.S13}$$

10. Photo-bleaching recovery measurements

The measurement was conducted using confocal laser scanning microscopy (CLSM) employing a LSM880, Elyra PS.1 system (Zeiss, Oberkochen, Germany) applying the He-Ne laser for excitation at 561 nm (2%) and emission filters for AF-594 (573 – 732 nm) with a gain of 638.8 and a digital detector amplification of 8.1. The pinhole was set to 0.93 AU. For magnification, a 10 × 0.3 EC Plan-Neofluar objective was applied. Images were acquired and analyzed using the ZEN software, version 2.3 SP1 (Zeiss). For bleaching, the UV laser was applied at 355 nm (100%) for 33 min 50 s. The pinhole was set to 0.84 AU.

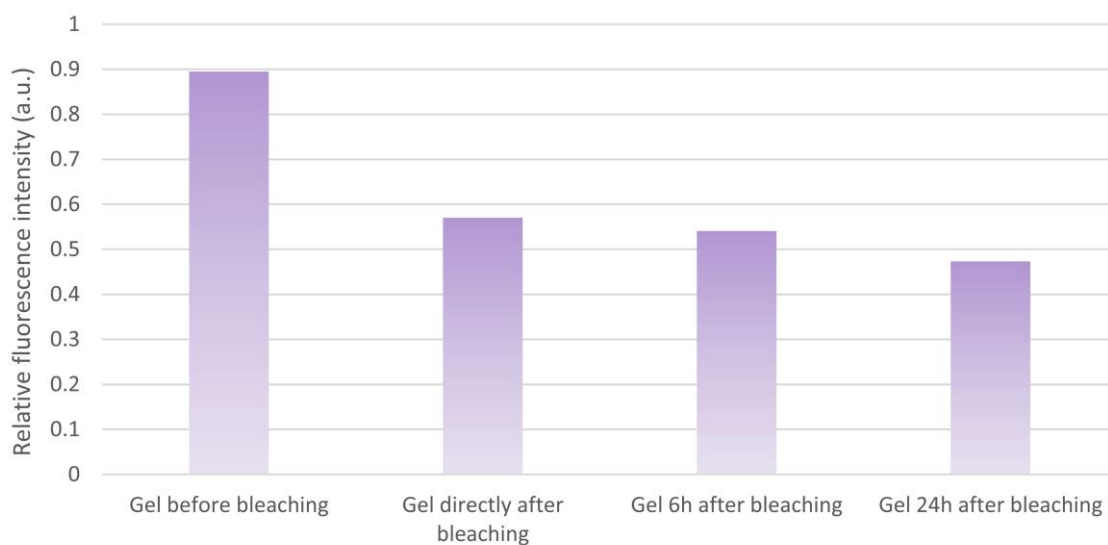


Figure S 20 Relative fluorescence intensity (bleached vs. non-treated area) before and directly after bleaching, after 6 and after 24h.

11. 3D printing

For 3D printing of the gels a Prusa i3 MKS printer was used. To the extruder of the printer, a cannula was fixed, which was connected to a syringe pump via a capillary. This way, parallel to the gel-print, a PLA print was produced as a control-geometry. The printer speed was set to 36 mm/s and the syringe pump to 15 mL h⁻¹. The printing bed was heated to 60 °C for good PLA adhesion and equipped with a nafion foil under the print area for the gel, to enable transfer of the printed structures.

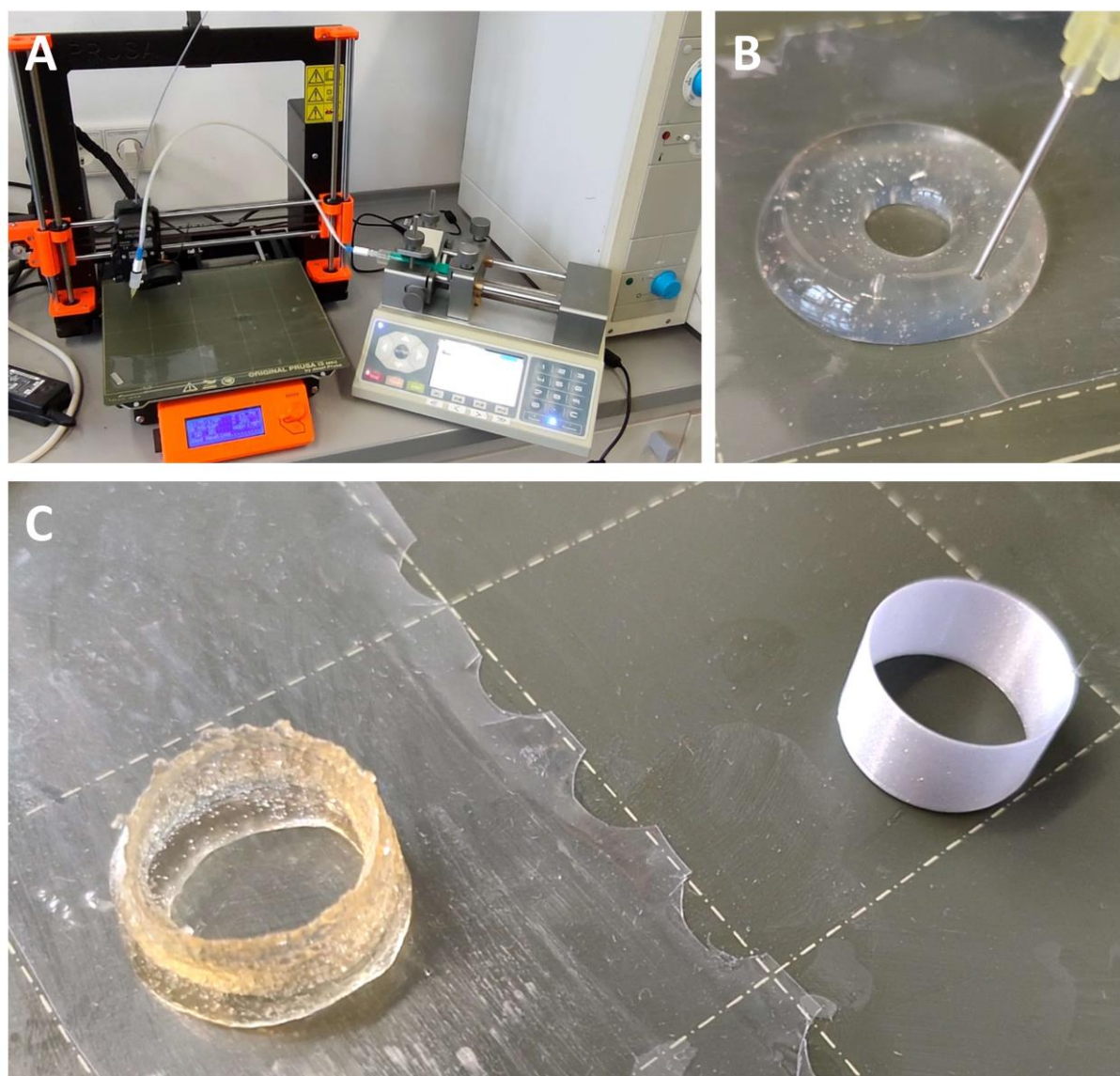


Figure S 21 3D-printing setup (A), 3D printing of a gel **1** with 1% **2a** ($c = 10 \text{ mg mL}^{-1}$) (B), and 3D printed hollow cylinder from gel **1** with 1% **2a** ($c = 25 \text{ mg mL}^{-1}$) next to the PLA model (C).

References

- [1] F. V. Gruschwitz, M.-C. Fu, T. Klein, R. Takahashi, T. Higashihara, S. Hoepfner, I. Nischang, K. Sakurai, J. C. Brendel, *Macromolecules* **2020**, *53*, 7552-7560.
- [2] F. V. Gruschwitz, T. Klein, M. T. Kuchenbrod, N. Moriyama, S. Fujii, I. Nischang, S. Hoepfner, K. Sakurai, U. S. Schubert, J. C. Brendel, *ACS Macro Lett.* **2021**, *10*, 837-843.
- [3] W. Brown, *Light Scattering: Principles and Development*, Clarendon Press Oxford, **1996**.
- [4] P. G. de Gennes, P. P. G. Gennes, C. U. Press, *Scaling Concepts in Polymer Physics*, Cornell University Press, **1979**.
- [5] N. H. Williamson, M. Nydén, M. Röding, *J. Mag. Reson.* **2016**, *267*, 54-62.
- [6] P. L. Ritger, N. A. Peppas, *J. Control. Release* **1987**, *5*, 37-42.
- [7] H. Lopez Hernandez, J. W. Souza, E. A. Appel, *Macromol. Biosci.* **2021**, *21*, 2000295.

Publication addendum

Note: Publication P7 was accepted by the Beilstein J. Org. Chem. in the meantime
and published in the following form:



Adjusting the length of supramolecular polymer bottlebrushes by top-down approaches

Tobias Klein^{‡1,2}, Franka V. Gruschwitz^{‡1,2}, Maren T. Kuchenbrod^{1,2}, Ivo Nischang^{1,2}, Stephanie Hoepfner^{1,2} and Johannes C. Brendel^{*1,2}

Letter

Open Access

Address:

¹Laboratory of Organic and Macromolecular Chemistry (IOMC), Friedrich Schiller University Jena, Humboldtstraße 10, 07743 Jena, Germany and ²Jena Center for Soft Matter (JCSM), Friedrich Schiller University Jena, Philosophenweg 7, 07743 Jena, Germany

Email:

Johannes C. Brendel* - johannes.brendel@uni-jena.de

* Corresponding author ‡ Equal contributors

Keywords:

distribution; dual centrifugation; filomicelles; self-assembly; ultrasonication

Beilstein J. Org. Chem. **2021**, *17*, 2621–2628.

<https://doi.org/10.3762/bjoc.17.175>

Received: 30 July 2021

Accepted: 29 September 2021

Published: 21 October 2021

This article is part of the thematic issue "Polymer chemistry: fundamentals and applications".

Guest Editor: B. V. K. J. Schmidt

© 2021 Klein et al.; licensee Beilstein-Institut.

License and terms: see end of document.

Abstract

Controlling the length of one-dimensional (1D) polymer nanostructures remains a key challenge on the way toward the applications of these structures. Here, we demonstrate that top-down processing facilitates a straightforward adjustment of the length of polyethylene oxide (PEO)-based supramolecular polymer bottlebrushes (SPBs) in aqueous solutions. These cylindrical structures self-assemble via directional hydrogen bonds formed by benzenetrisurea (BTU) or benzenetrispeptide (BTP) motifs located within the hydrophobic core of the fiber. A slow transition from different organic solvents to water leads first to the formation of μm -long fibers, which can subsequently be fragmented by ultrasonication or dual asymmetric centrifugation. The latter allows for a better adjustment of applied shear stresses, and thus enables access to differently sized fragments depending on time and rotation rate. Extended sonication and scission analysis further allowed an estimation of tensile strengths of around 16 MPa for both the BTU and BTP systems. In combination with the high kinetic stability of these SPBs, the applied top-down methods represent an easily implementable technique toward 1D polymer nanostructures with an adjustable length in the range of interest for perspective biomedical applications.

Introduction

Cylindrical polymer nanostructures in solution have received increasing attention during the last two decades, related to the high surface-to-volume ratio, which is particularly attractive for targeted carrier materials in biomedical applications. In addition, cylindrical drug delivery vehicles appear to be advantageous compared to the spherical analogues with regard to blood

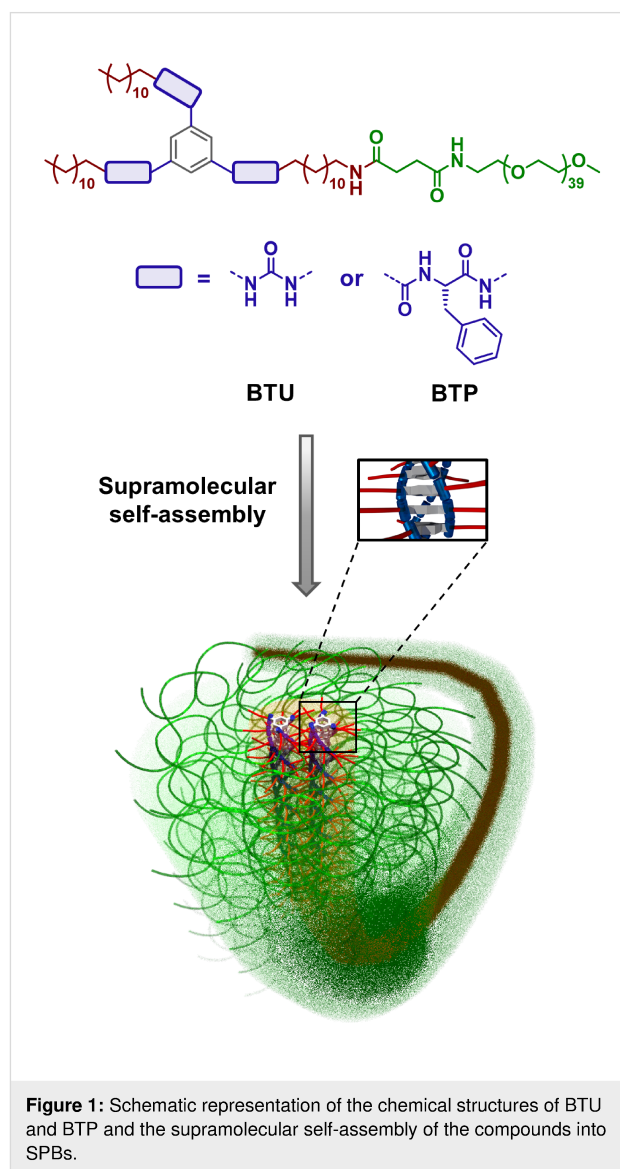
circulation time, drug loading, and tumor penetration abilities [1-3]. However, the straightforward preparation of cylindrical polymer aggregates with defined and reproducible length still remains challenging but represents a prerequisite for the desired applications in nanomedicine [4,5]. A key factor in this regard are formulation strategies, which allow a straightforward imple-

mentation into established processes that are, e.g., in accordance with good manufacturing practice (GMP) [6]. Approaches such as the crystallization-driven self-assembly (CDSA) or the synthesis of covalently bound cylindrical polymer brushes (CPBs) offer access to a defined fiber length [7-16]. However, they also suffer from disadvantages, such as significant experimental effort to evaluate suitable reaction procedures for the synthesis or the conditions for the assembly process, and are therefore often limited to specific materials. An alternative is the use of molecular motifs capable of forming directional supramolecular interaction forces, such as hydrogen bonds or π -interactions, to guide the one-dimensional (1D) assembly of established, commercial polymers in solution [17]. We recently reported the self-assembly of polyethylene oxide (PEO) polymers into cylindrical nanostructures, also called supramolecular polymer bottlebrushes (SPBs), based on the end group modification with hydrogen bond forming benzenetrisurea (BTU) and benzenetrispeptide (BTP) motifs [18-20]. The resulting amphiphilic character of the materials facilitated a control of the kinetic assembly, which provided access to stable nanostructures on a broad length range (<100 nm–2 μ m). While the process enables a good adjustment of the length, it relies on a precise control of the assembly pathway and requires the use of organic solvents, such as THF and DMF, which limits the applicability in pharmaceutical formulations [21]. For an application in nanomedicine, a length in the range of 100–200 nm is particularly attractive to ensure cellular uptake and to access the known size window for a potential enhanced permeability and retention effect (EPR) [22,23]. As an alternative for the assembly pathway control, we opted to apply easy-to-use top-down approaches to tune the length distribution in a straightforward fashion over the above-mentioned length range of interest. While ultrasonication (US) represents a standard but rather harsh fragmentation technique, we additionally introduced dual asymmetric centrifugation (DAC) as an excellent alternative top-down method for effective, more controlled, and adaptable preparation of polymer nanostructures [24-28]. Both methods are applied for fragmentation of initially μ m-long SPBs based on BTU-PEO and BTP-PEO conjugates. The resulting nanofibers were characterized in detail by cryogenic transmission electron microscopy (cryoTEM), as well as by asymmetrical flow field-flow fractionation measurements coupled to a UV detector and a multiangle laser light scattering detector (AF4-MALLS technique) to estimate the apparent structure length and the length distribution of the SPBs.

Results and Discussion

The general structure of the tested BTP and BTU is depicted in Figure 1 [19,20]. While the hydrogen bonding moieties are either urea-based or peptide-based (i.e., phenylalanine) units, the dodecyl chains act as hydrophobic shields to induce the

amphiphilic assembly in water and prevent the surrounding water from interfering with the hydrogen bonds in the interior [29]. Attaching a hydrophilic PEO chain (2 kg·mol⁻¹), the compounds self-assemble into long fiber structures consisting of 2–4 lateral core units upon transfer into water, as reported previously [19-21]. A slow solvent change from a THF solution to water resulted in μ m-long fibers in both cases (BTU or BTP).

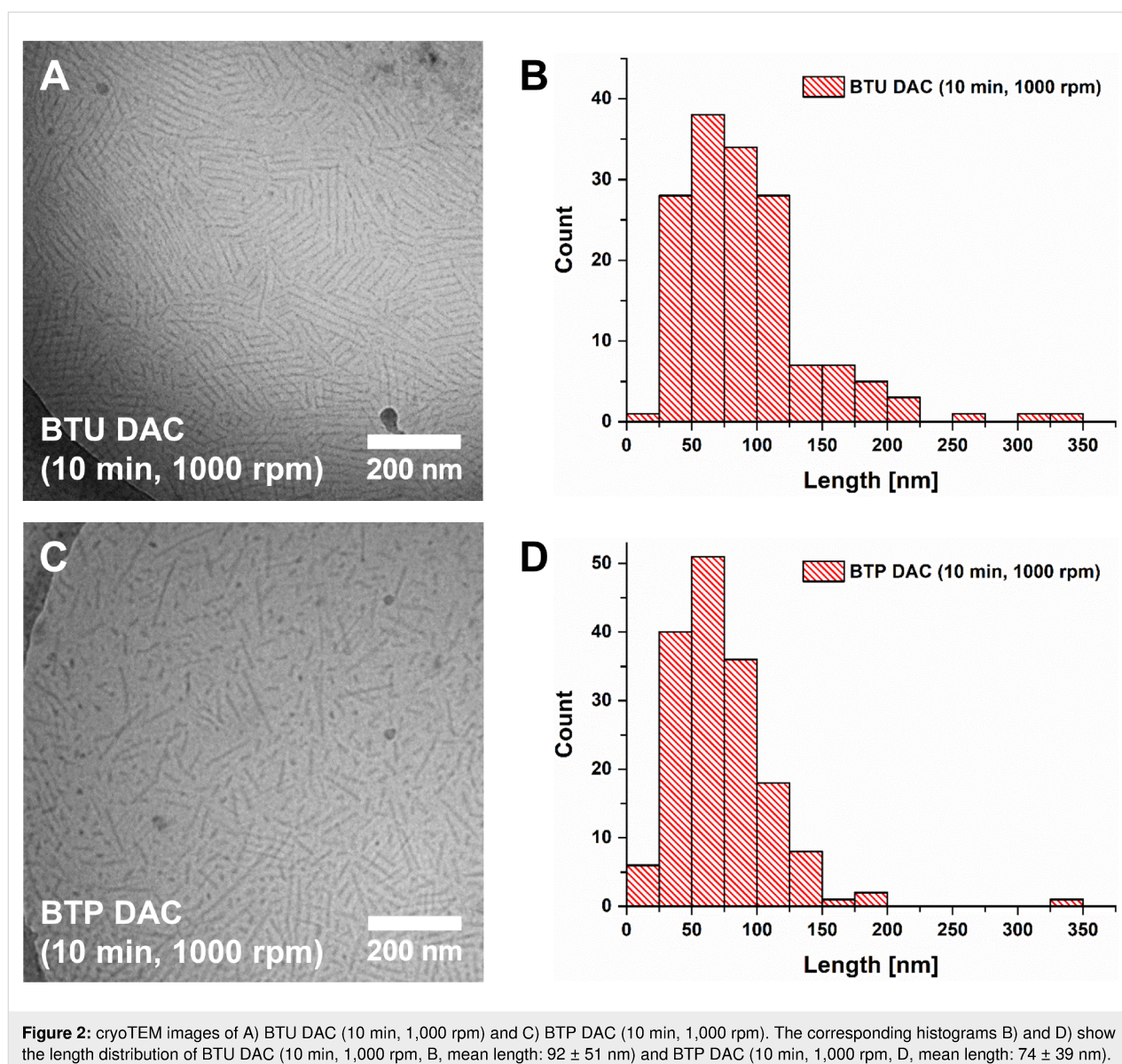


An initial attempt to tune the fiber length by changing the initial organic solvent was not successful. As seen in the corresponding cryoTEM images (Figures S1–S6, Supporting Information File 1) as well as AF4 measurements (Figure S10, Supporting Information File 1), all tested organic solvents yielded similarly μ m-long fibers, exemplifying the surprisingly minor influence of the initial organic solvent on the resulting fiber length. Alternatively, a targeted size below 1 μ m can be achieved by top-

down strategies inducing strong shear forces. Typically, US is applied to fragment supramolecular structures [7,30–33]. However, US causes cavitation within the sample, the collapse of which is accompanied by very high local heating. Alternative approaches rely on inducing strong shear forces by strong mixers or dispersers. An interesting method in this regard is the use of DAC, which is also considered to be a speed-mix technology due to the rapid mixing of the sample [28]. In DAC, the sample holder performs an additional rotation besides the main rotor rotation, resulting in a continuous change of the direction of the centrifugal force [28]. This change induces a strong agitation of the solution and generates large shear forces. DAC has mainly been used to create drug composites but recently found application in the formulation of liposomes or the direct nanodispersion of pharmaceutically active ingredients [24–28].

The technique resembles nanomilling methods but allows a much smaller sample scale, which renders it particularly attractive for testing the suitability to fragment fiber-like supramolecular assemblies in solution [34].

We started with a rotational speed of 1,000 rpm and treated the initial fibers for 10 min using samples BTU DAC (10 min, 1,000 rpm) and BTP DAC (10 min, 1,000 rpm). This comparably mild treatment already caused a significant fragmentation of the μm -long fibers, resulting in structures of 50–200 nm length according to the cryoTEM images after 10 min of treatment (Figure 2). An average fiber length of 92 ± 51 nm and 74 ± 39 nm for BTU DAC (10 min, 1,000 rpm) and BTP DAC (10 min, 1,000 rpm), respectively, were apparent according to cryoTEM.

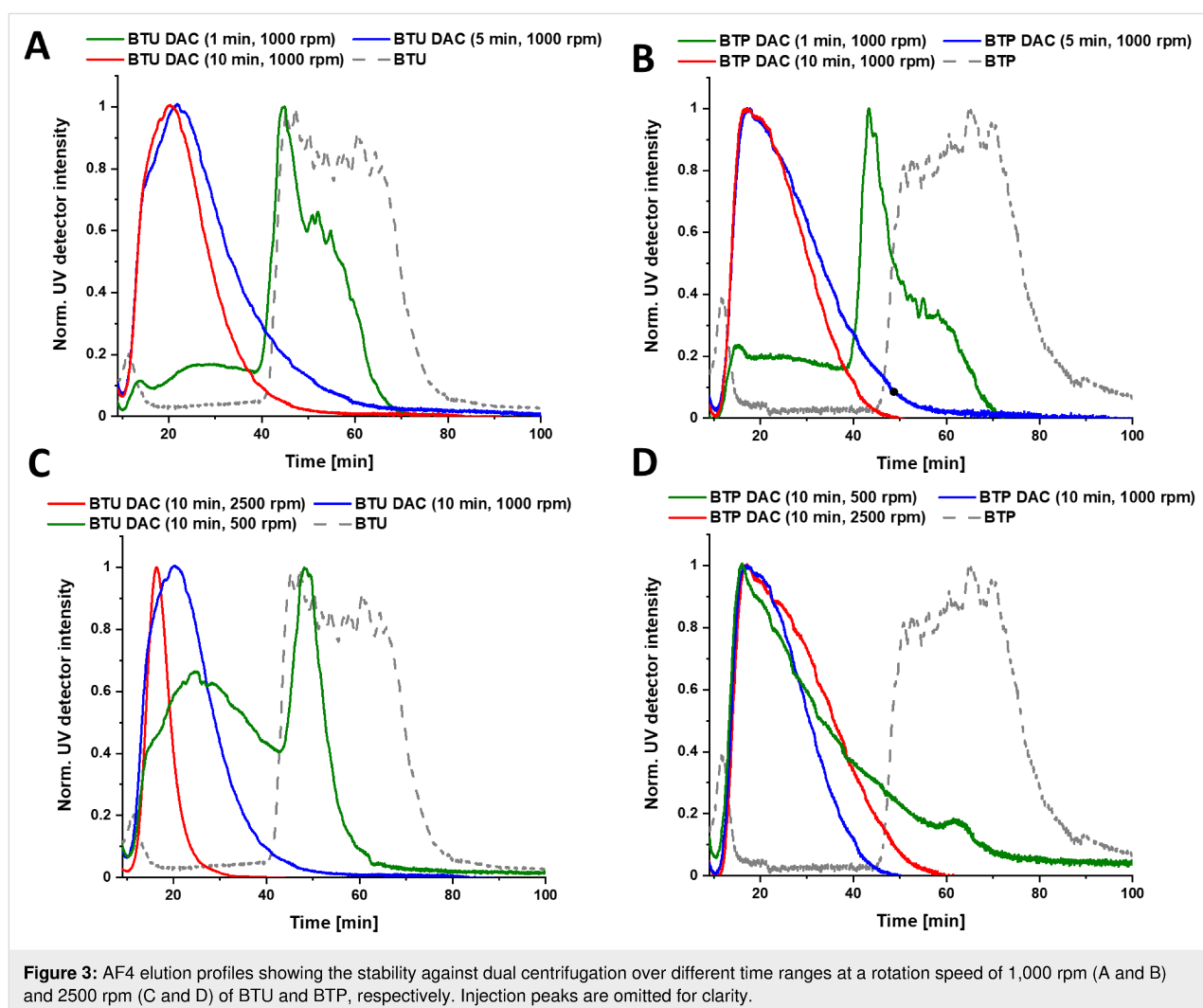


This could further be supported by AF4 measurements (Figure 3A and 3B). Here, fibers featuring an average radius of gyration of $R_g \approx 20$ nm and a weight-average molar mass of $M_w = 3,099,000$ g·mol⁻¹, corresponding to a number of aggregation of $N_{agg} \approx 1,200$ and a length of 110 nm for BTU (assuming four units per cross-section), as well as a weight-average molar mass of $M_w = 4,406,000$ g·mol⁻¹, corresponding to a number of aggregation of $N_{agg} \approx 490$ and a length of 120 nm (assuming two units per cross-section) for BTP, could be observed after 10 min at 1,000 rpm (Figure S12A and S12B, Supporting Information File 1) [19,21].

As a consequence, we scrutinized the influence of time and rotation speed on the size of the fragments, which were analyzed by AF4 (Figure 3). First, samples were treated for 1, 5, and 10 min at a rotation speed of 1,000 rpm (Figure 3A and 3B as well as Figure S12A and S12B, Supporting Information File 1) to investigate if an extended exposure time can break up the aggregates even further. For BTU, the peak maximum of the

UV trace was shifted from 60 min to 45 min already after 1 min of mixing (Figure 3A). After 5 min of centrifugation, no further change could be observed since the peak at this low elution time already corresponded to very small oligomers (Figure 3A). For BTP, a stronger downward shift of the peak maximum from 70 to 45 min could be observed after 1 min of mixing. Similar to BTU, the increase in centrifugation time to 5 min led to a more pronounced fragmentation, which was not further enhanced by prolonged DAC.

To determine the influence of the strength of the shear forces, we also increased or decreased the centrifugal speed to 2,500 and 500 rpm, respectively (Figure 3C and 3D). At 2,500 rpm, the fragmentation of the aggregates occurred more rapidly, and a significant shift in AF4 elution time was observed for both samples, BTU and BTP, within 1 min of DAC (Figure S11A and S11B, Supporting Information File 1). For BTU, the samples were further fragmented with extended time at this speed, and the smallest structures were obtained for BTU with

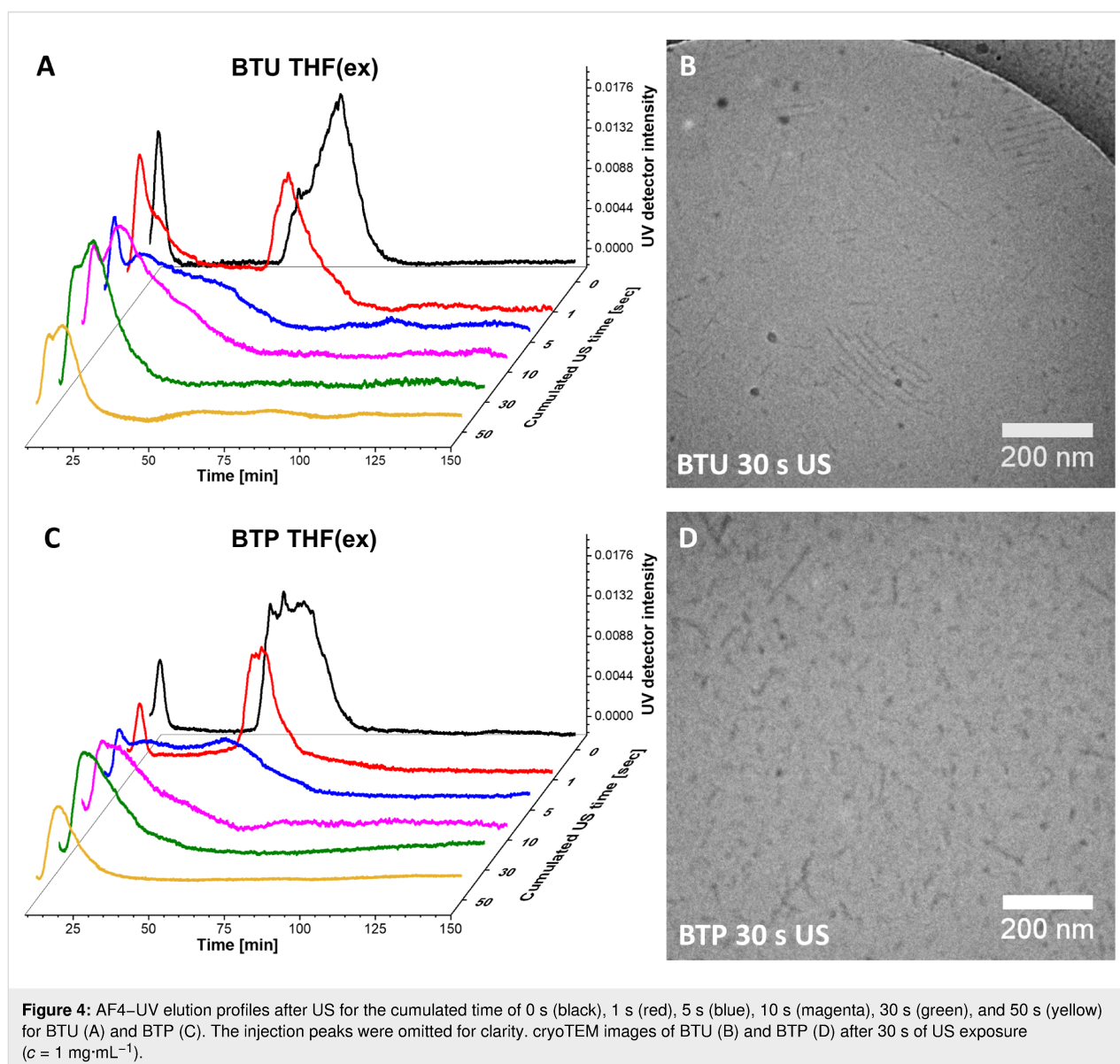


$R_g < 3$ nm (Figure S12C, Supporting Information File 1). On the contrary, the reduction of the applied shear forces (500 rpm) limited the fragmentation rate for both samples. For BTU and after 10 min, a significant amount of the large structures (>40 min elution time) remained intact (Figure 3C and 3D as well as Figure S11C and S11D, Supporting Information File 1). Overall, DAC represents a straightforward technique to adjust the size of these supramolecular assemblies, which could easily be tuned by variation of rotational speed and treatment time. Nevertheless, the distribution of the aggregate size remained rather broad. Increasing the time of treatment, the length of the fibers appeared to approach a lower size limit depending on the speed of rotation, which became particularly apparent for the BTU compounds. Even an extended mixing time of 3 h at 2,500 rpm did not significantly change the observed distribu-

tions compared to 10 min treatment (Figure S13, Supporting Information File 1).

For comparison to more established techniques, we tested the impact of US on the same fibers. Initial tests on treating fibers within an ultrasound bath ($\approx 11.5 \text{ W}\cdot\text{L}^{-1}$) did not reveal any changes in the structure. Therefore, we decided to apply a US probe at higher power (200 W) and varied the exposure times (Figure 4).

Already after 1 s of US, a significant decrease in the length of the fibers could be seen for both samples (Figure 4A and 4C), substantiating the rather harsh forces induced by this technique at the applied conditions. A reduction of the applied power might represent a suitable way to further limit the shear forces



on the sample and gain more control, but this was not further tested. The peak maxima at around 80 min (BTU) and 65 min (BTP) decreased slightly and shifted to a lower elution time. For the BTU sample, even a new peak was formed at 10 to 20 min, corresponding to the formation of short structures. Continuous US for a cumulated time of 5 s resulted in the disappearance of the main peaks and the appearance of a broad distribution ranging from 15 min to 70 min elution time for both samples. The severe broadening of the distribution and the immediate formation of very small structures suggests a shearing off of small fragments during US. A further increase of the time (up to 30 s) narrowed the length distribution once again, and only the small aggregates remained in solution, which appeared to be stable during further sonication (50 s of cumulated US time). The resulting fibers featured an average R_g value of ≈ 15 nm (Figure S14, Supporting Information File 1) and a weight-average molar mass of $M_w = 3,633,000$ g·mol⁻¹, corresponding to a number of aggregation of $N_{agg} = 1400$ and a length of 125 nm for BTU (assuming four units per cross-section). For BTP, a weight-average molar mass of $M_w = 2,910,000$ g·mol⁻¹, corresponding to a number of aggregation of $N_{agg} = 440$ and a length of 80 nm (assuming two units per cross-section) was calculated [19,21]. Correlating well with the AF4 results, cryoTEM images of both samples (Figure 4B and 1D) showed mainly short cylinders after a cumulated US time of 30 s, with an average fiber length of 124 ± 65 nm and 69 ± 41 nm for BTU and BTP, respectively (Figure S8, Supporting Information File 1). It is important to note that all obtained fibers remained unchanged over several months after the top-down processing, demonstrating the previously described excellent kinetic stability of these supramolecular aggregates (Figures S15 and S16, Supporting Information File 1) [21].

Inspired by work of Lamour et al., we estimated a similar limit length L_{lim} upon extensive US treatment [35]. This length allows an indirect estimation of the tensile strength σ^* of our fibers according to

$$L_{lim} = \sqrt{\frac{d^2 \cdot \sigma^*}{2 \cdot \eta \cdot (\dot{R}_l / R_l)}}$$

where R_l is the radius of the cavitation bubble, \dot{R}_l is the wall velocity of the collapsing bubble, d is the fiber diameter, and η is the viscosity of the solvent [36]. By assuming typical values for the wall velocity, bubble radius, and viscosity of the solvent, the equation simplifies [37,38] to

$$L_{lim} = 7 \cdot 10^{-4} \cdot d \cdot \sqrt{\sigma^*}$$

We exposed the BTU and BTP fibers to extended US (>1 h). No further scission could be observed after 2–3 h of US. AF4–MALLS measurements of the fibers after 3 h US revealed a M_w at the elution peak maximum of 843,000 g·mol⁻¹ and 943,000 g·mol⁻¹ for BTU and BTP, respectively (Figure S17, Supporting Information File 1). This translates to a fiber length of 29 nm for BTU by assuming a stacking distance of 0.36 nm and 4 molecules per cross-section [19], and 28 nm for BTP by assuming a similar stacking distance and 2 molecules per cross-section [21]. Based on a fiber diameter of 12 nm (estimated from small-angle X-ray scattering experiments) [19,20], the resulting tensile strength for both compounds was approximately 16 to 17 MPa (Table S1, Supporting Information File 1). This strength was in the range of Elastin filaments and significantly lower as, for instance, the tensile strength of amyloid fibrils [35,39]. Overall, the observed values for the fibers corresponded well to the sensitivity to shear forces. However, the core–shell structure of our supramolecular systems has to be considered in this regard. For example, significant steric strains induced by the polymer chains act on the core structure, limiting the strength of the supramolecular assembly.

Conclusion

In conclusion, the remarkable long-term stability of BTU–PEO and BTP–PEO fibers in water, which were prepared via bottom-up self-assembly, enabled us to apply two straightforward top-down approaches (US and dual asymmetric centrifugation) to tune the length distributions of the supramolecular fibers. Exposing the SPBs to US resulted in a rapid fragmentation of the fibers into small rod-like fragments. Dual asymmetric centrifugation, on the other hand, allowed to adjust the length distribution in a more controlled manner by adjusting the time and rotation speed. Thus, this study demonstrates that easy-to-use top-down methods can be a feasible approach to obtain some control over the length distributions of 1D polymer nanostructures, and thus this makes them more likely to be applied in biomedicine, where dimensional control is a prerequisite.

Supporting Information

Supporting Information File 1

Synthesis, procedures, and characterization.

[<https://www.beilstein-journals.org/bjoc/content/supplementary/1860-5397-17-175-S1.pdf>]

Acknowledgements

The authors thank Prof. Ulrich S. Schubert for his continuous support and access to excellent research facilities.

Funding

T. K., F. V. G., and J. C. B. thank the German Science Foundation (DFG) for generous funding within the Emmy Noether Programme (Project-ID: 358263073). cryoTEM investigations were performed at the electron microscopy facilities of the Jena Center for Soft Matter (JCSM), which were purchased with grants from the DFG and the European funds for Regional Development (EFRE). The funding of the collaborative research center PolyTarget, projects A05 and Z01 (Project-ID: 316213987 – SFB 1278), by the DFG is acknowledged.

ORCID® IDs

Tobias Klein - <https://orcid.org/0000-0001-9404-7739>

Johannes C. Brendel - <https://orcid.org/0000-0002-1206-1375>

References

- Truong, N. P.; Whittaker, M. R.; Mak, C. W.; Davis, T. P. *Expert Opin. Drug Delivery* **2015**, *12*, 129–142. doi:10.1517/17425247.2014.950564
- Toy, R.; Peiris, P. M.; Ghaghada, K. B.; Karathanasis, E. *Nanomedicine (London, U. K.)* **2014**, *9*, 121–134. doi:10.2217/nnm.13.191
- Liu, Y.; Tan, J.; Thomas, A.; Ou-Yang, D.; Muzykantov, V. R. *Ther. Delivery* **2012**, *3*, 181–194. doi:10.4155/tde.11.156
- Müllner, M. *Macromol. Chem. Phys.* **2016**, *217*, 2209–2222. doi:10.1002/macp.201600086
- Truong, N. P.; Quinn, J. F.; Whittaker, M. R.; Davis, T. P. *Polym. Chem.* **2016**, *7*, 4295–4312. doi:10.1039/c6py00639f
- Shkodra-Pula, B.; Vollrath, A.; Schubert, U. S.; Schubert, S. Polymer-based nanoparticles for biomedical applications. In *Frontiers of Nanoscience*; Parak, W. J.; Feliu, N., Eds.; Elsevier: Amsterdam, Netherlands, 2020; Vol. 16, pp 233–252. doi:10.1016/b978-0-08-102828-5.00009-7
- Gilroy, J. B.; Gädt, T.; Whittell, G. R.; Chabanne, L.; Mitchels, J. M.; Richardson, R. M.; Winnik, M. A.; Manners, I. *Nat. Chem.* **2010**, *2*, 566–570. doi:10.1038/nchem.664
- Finnegan, J. R.; Pilkington, E. H.; Alt, K.; Rahim, M. A.; Kent, S. J.; Davis, T. P.; Kempe, K. *Chem. Sci.* **2021**, *12*, 7350–7360. doi:10.1039/d1sc00938a
- Finnegan, J. R.; He, X.; Street, S. T. G.; Garcia-Hernandez, J. D.; Hayward, D. W.; Harniman, R. L.; Richardson, R. M.; Whittell, G. R.; Manners, I. *J. Am. Chem. Soc.* **2018**, *140*, 17127–17140. doi:10.1021/jacs.8b09861
- He, Y.; Eloi, J.-C.; Harniman, R. L.; Richardson, R. M.; Whittell, G. R.; Mathers, R. T.; Dove, A. P.; O'Reilly, R. K.; Manners, I. *J. Am. Chem. Soc.* **2019**, *141*, 19088–19098. doi:10.1021/jacs.9b09885
- Street, S. T. G.; He, Y.; Jin, X.-H.; Hodgson, L.; Verkade, P.; Manners, I. *Chem. Sci.* **2020**, *11*, 8394–8408. doi:10.1039/d0sc02593c
- Niederberger, A.; Pelras, T.; Manni, L. S.; FitzGerald, P. A.; Warr, G. G.; Müllner, M. *Macromol. Rapid Commun.* **2021**, *42*, 2100138. doi:10.1002/marc.202100138
- Müllner, M.; Yang, K.; Kaur, A.; New, E. J. *Polym. Chem.* **2018**, *9*, 3461–3465. doi:10.1039/c8py00703a
- Müllner, M.; Mehta, D.; Nowell, C. J.; Porter, C. J. H. *Chem. Commun.* **2016**, *52*, 9121–9124. doi:10.1039/c6cc00447d
- Müllner, M.; Müller, A. H. E. *Polymer* **2016**, *98*, 389–401. doi:10.1016/j.polymer.2016.03.076
- Müllner, M.; Dodds, S. J.; Nguyen, T.-H.; Senyschyn, D.; Porter, C. J. H.; Boyd, B. J.; Caruso, F. *ACS Nano* **2015**, *9*, 1294–1304. doi:10.1021/nn505125f
- Gruschwitz, F. V.; Klein, T.; Catrouillet, S.; Brendel, J. C. *Chem. Commun.* **2020**, *56*, 5079–5110. doi:10.1039/d0cc01202e
- Klein, T.; Ulrich, H. F.; Gruschwitz, F. V.; Kuchenbrod, M. T.; Takahashi, R.; Hoepfener, S.; Nischang, I.; Sakurai, K.; Brendel, J. C. *Macromol. Rapid Commun.* **2021**, *42*, 2000585. doi:10.1002/marc.202000585
- Gruschwitz, F. V.; Fu, M.-C.; Klein, T.; Takahashi, R.; Higashihara, T.; Hoepfener, S.; Nischang, I.; Sakurai, K.; Brendel, J. C. *Macromolecules* **2020**, *53*, 7552–7560. doi:10.1021/acs.macromol.0c01361
- Klein, T.; Ulrich, H. F.; Gruschwitz, F. V.; Kuchenbrod, M. T.; Takahashi, R.; Fujii, S.; Hoepfener, S.; Nischang, I.; Sakurai, K.; Brendel, J. C. *Polym. Chem.* **2020**, *11*, 6763–6771. doi:10.1039/d0py01185a
- Gruschwitz, F. V.; Klein, T.; Kuchenbrod, M. T.; Moriyama, N.; Fujii, S.; Nischang, I.; Hoepfener, S.; Sakurai, K.; Schubert, U. S.; Brendel, J. C. *ACS Macro Lett.* **2021**, *10*, 837–843. doi:10.1021/acsmacrolett.1c00296
- Maeda, H. *Adv. Drug Delivery Rev.* **2015**, *91*, 3–6. doi:10.1016/j.addr.2015.01.002
- Maeda, H.; Nakamura, H.; Fang, J. *Adv. Drug Delivery Rev.* **2013**, *65*, 71–79. doi:10.1016/j.addr.2012.10.002
- Krämer, W.; Schubert, R.; Massing, U. *Int. J. Pharm.* **2019**, *572*, 118753. doi:10.1016/j.ijpharm.2019.118753
- Hagedorn, M.; Liebich, L.; Bögershausen, A.; Massing, U.; Hoffmann, S.; Mende, S.; Rischer, M. *Int. J. Pharm.* **2019**, *565*, 187–198. doi:10.1016/j.ijpharm.2019.04.082
- Hagedorn, M.; Bögershausen, A.; Rischer, M.; Schubert, R.; Massing, U. *Int. J. Pharm.* **2017**, *530*, 79–88. doi:10.1016/j.ijpharm.2017.07.047
- Hirsch, M.; Zirolì, V.; Helm, M.; Massing, U. *J. Controlled Release* **2009**, *135*, 80–88. doi:10.1016/j.jconrel.2008.11.029
- Massing, U.; Cicko, S.; Zirolì, V. *J. Controlled Release* **2008**, *125*, 16–24. doi:10.1016/j.jconrel.2007.09.010
- Krieg, E.; Bastings, M. M. C.; Besenius, P.; Rytbchinski, B. *Chem. Rev.* **2016**, *116*, 2414–2477. doi:10.1021/acs.chemrev.5b00369
- Gädt, T.; leong, N. S.; Cambridge, G.; Winnik, M. A.; Manners, I. *Nat. Mater.* **2009**, *8*, 144–150. doi:10.1038/nmat2356
- Rho, J. Y.; Cox, H.; Mansfield, E. D. H.; Ellacott, S. H.; Peltier, R.; Brendel, J. C.; Hartlieb, M.; Waigh, T. A.; Perrier, S. *Nat. Commun.* **2019**, *10*, 4708. doi:10.1038/s41467-019-12586-8
- Steinlein, C.; Kreger, K.; Schmidt, H.-W. *Macromol. Mater. Eng.* **2019**, *304*, 1900258. doi:10.1002/mame.201900258
- Guérin, G.; Wang, H.; Manners, I.; Winnik, M. A. *J. Am. Chem. Soc.* **2008**, *130*, 14763–14771. doi:10.1021/ja805262v
- Peltonen, L.; Hirvonen, J. *J. Pharm. Pharmacol.* **2010**, *62*, 1569–1579. doi:10.1111/j.2042-7158.2010.01022.x
- Lamour, G.; Nassar, R.; Chan, P. H. W.; Bozkurt, G.; Li, J.; Bui, J. M.; Yip, C. K.; Mayor, T.; Li, H.; Wu, H.; Gsponer, J. A. *Biophys. J.* **2017**, *112*, 584–594. doi:10.1016/j.bpj.2016.12.036
- Huang, Y. Y.; Knowles, T. P. J.; Terentjev, E. M. *Adv. Mater. (Weinheim, Ger.)* **2009**, *21*, 3945–3948. doi:10.1002/adma.200900498
- Nguyen, T. Q.; Liang, Q. Z.; Kausch, H.-H. *Polymer* **1997**, *38*, 3783–3793. doi:10.1016/s0032-3861(96)00950-0

38. Hennrich, F.; Krupke, R.; Arnold, K.; Rojas Stütz, J. A.; Lebedkin, S.; Koch, T.; Schimmel, T.; Kappes, M. M. *J. Phys. Chem. B* **2007**, *111*, 1932–1937. doi:10.1021/jp065262n
39. Paparcone, R.; Buehler, M. J. *Biomaterials* **2011**, *32*, 3367–3374. doi:10.1016/j.biomaterials.2010.11.066

License and Terms

This is an Open Access article under the terms of the Creative Commons Attribution License (<https://creativecommons.org/licenses/by/4.0>). Please note that the reuse, redistribution and reproduction in particular requires that the author(s) and source are credited and that individual graphics may be subject to special legal provisions.

The license is subject to the *Beilstein Journal of Organic Chemistry* terms and conditions: (<https://www.beilstein-journals.org/bjoc/terms>)

The definitive version of this article is the electronic one which can be found at: <https://doi.org/10.3762/bjoc.17.175>



Supporting Information

for

Adjusting the length of supramolecular polymer bottlebrushes by top-down approaches

Tobias Klein, Franka V. Gruschwitz, Maren T. Kuchenbrod, Ivo Nischang, Stephanie Hoepfner and Johannes C. Brendel

Beilstein J. Org. Chem. **2021**, *17*, 2621–2628. [doi:10.3762/bjoc.17.175](https://doi.org/10.3762/bjoc.17.175)

Synthesis, procedures, and characterization

Content

1. Synthesis and procedures	S2
2. Characterization	S3
2.1 Cryogenic transmission electron microscopy (cryoTEM).....	S3
2.2 Asymmetrical flow field-flow fractionation (AF4)	S12
3. References	S19

1. Synthesis and procedures

Materials and Methods

All reagents and solvents were commercial products purchased from Sigma-Aldrich, abcr, Iris BioTech, Rapp Polymere, or TCI and were used without further purification.

Synthesis

The benzenetrisurea–polyethylene oxide (BTU) and benzenetrispeptide–polyethylene oxide (BTP) conjugates were synthesized according to previously published protocols [1].

Self-assembly procedures

Solvent switch method

The self-assembly was conducted according to previous publications [2], where 5 mg of BTU or BTP were dissolved in 1 mL of THF and stirred overnight to guarantee complete dissolution. To this, 4 mL of MilliQ water were added ($1\text{--}100\text{ mL}\cdot\text{h}^{-1}$) using a syringe pump under vigorous stirring to reach a final water content of 80 vol %. For this purpose, the needle of the syringe was immersed in the organic BTP or BTU solution to enable a constant release of MilliQ water from the syringe and to avoid the formation of drops that would result in high local water concentrations at the spot where the drop immerses into the solution. Afterwards, the solution was transferred to float-a-lyzer® tubings with a molecular weight cutoff of 3.5 kD and dialyzed for five days against water to remove all THF traces.

Ultrasonication procedure

BTP and BTU samples assembled from THF at a concentration of $1\text{ mg}\cdot\text{mL}^{-1}$ in MilliQ water were exposed to ultrasonication using a sonication probe (Hielscher ultrasonic processor UP200St, 100% amplitude, 20 W) for different durations up to a cumulated time of 50 s (1 s + 2 s + 2 s + 5 s + 5 s + 15 s + 20 s).

For the experiments concerning the mechanical stability, the maximal power of 200 W of the ultrasonicator was applied for periods of 5 s, with a 3 s pause for 59 min each time.

Dual centrifugation procedure

Dual centrifugation was performed using a Hettich ZentriMix 380 R equipped with a ZentriMix rotor. BTU and BTP at a concentration of $1 \text{ mg}\cdot\text{mL}^{-1}$ in MilliQ water were added to 2 mL vials and centrifuged for different durations (1 min, 5 min, 10 min, and 180 min) at different rotation speeds (500 rpm, 1,000 rpm, and 2,500 rpm). No milling beads were added to the vials, to rely just on the shear forces caused by the dual rotor setup.

2. Characterization

2.1 Cryogenic transmission electron microscopy (cryoTEM)

Samples were prepared on Ar plasma treated Quantifoil grids (R2/2). $8.5 \text{ }\mu\text{L}$ of the solutions ($3 \text{ mg}\cdot\text{mL}^{-1}$ in H_2O) were applied onto the grids and vitrified in liquid ethane utilizing a FEI Vitrobot Mark IV system (offset: -3 mm , blotting time: 1 s). Samples were transferred into the cryo holder (Gatan 626) utilizing the Gatan cryo stage, followed by transfer into the microscope keeping the temperature below $-172 \text{ }^\circ\text{C}$ during the whole transfer and measurement process after vitrification. Measurements were performed using a FEI Technai G² 20 operated at an acceleration voltage of 200 kV . Images were acquired with a Mega View (OSIS, Olympus Soft Imaging Systems) or an Eagle 4k CCD camera. cryoTEM images in this study display only specific regions of interest that are representative for the whole sample.

BTU acetone

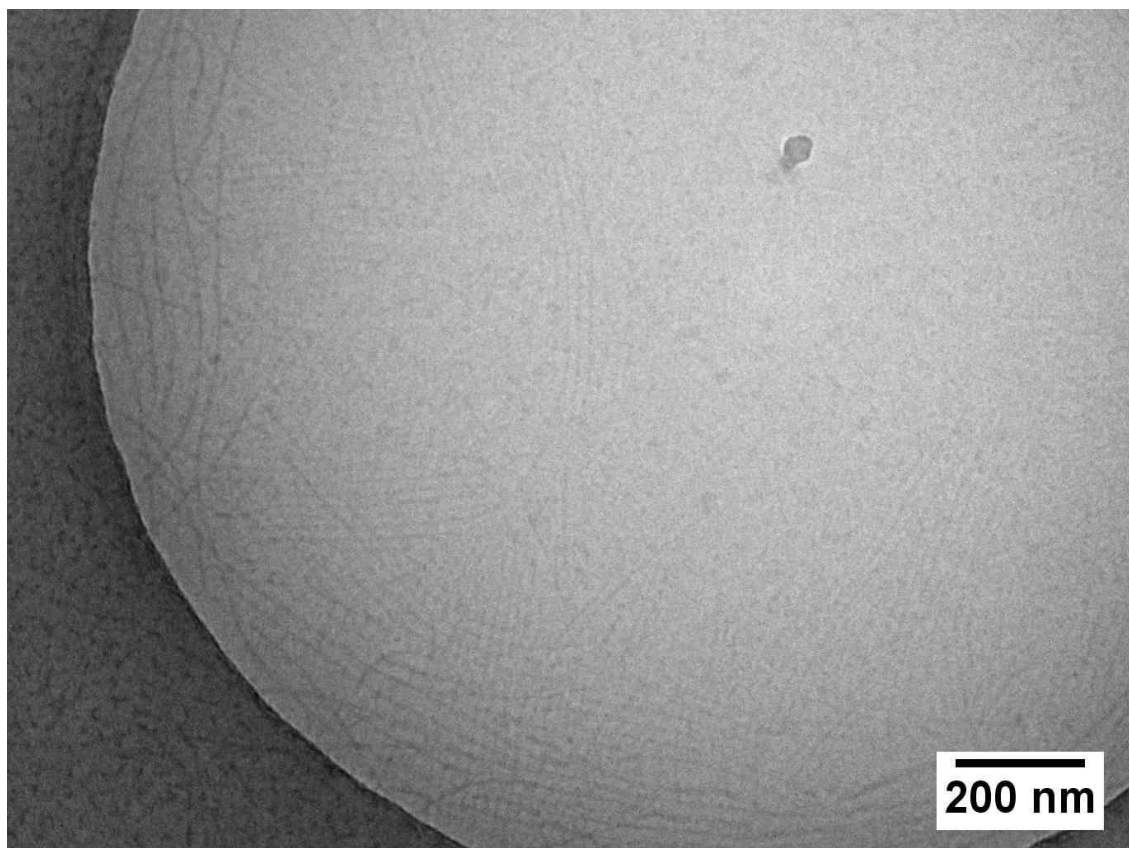


Figure S1: cryoTEM image of BTU acetone in water ($c = 1 \text{ mg}\cdot\text{mL}^{-1}$) assembled at $1 \text{ mL}\cdot\text{h}^{-1}$ water addition rate.

BTU DMF

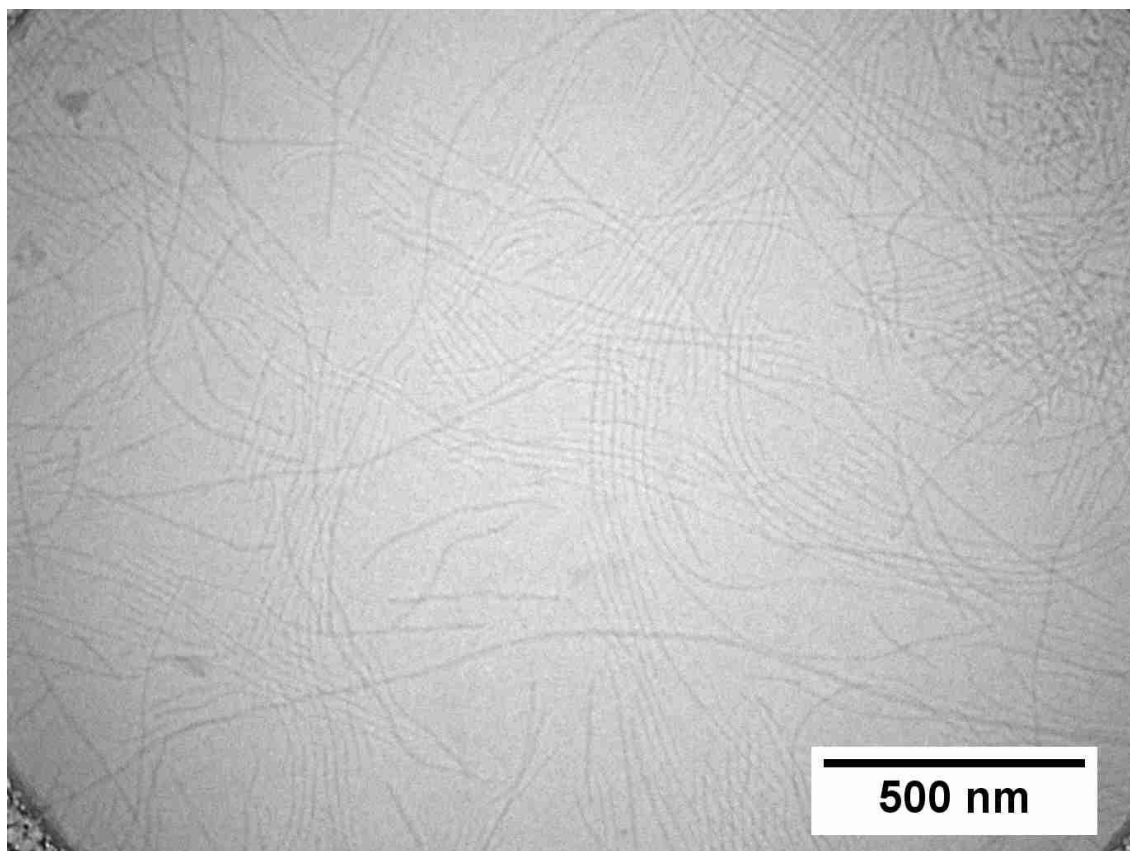


Figure S2: cryoTEM image of BTU DMF in water ($c = 1 \text{ mg}\cdot\text{mL}^{-1}$) assembled at $1 \text{ mL}\cdot\text{h}^{-1}$ water addition rate.

BTU EtOH

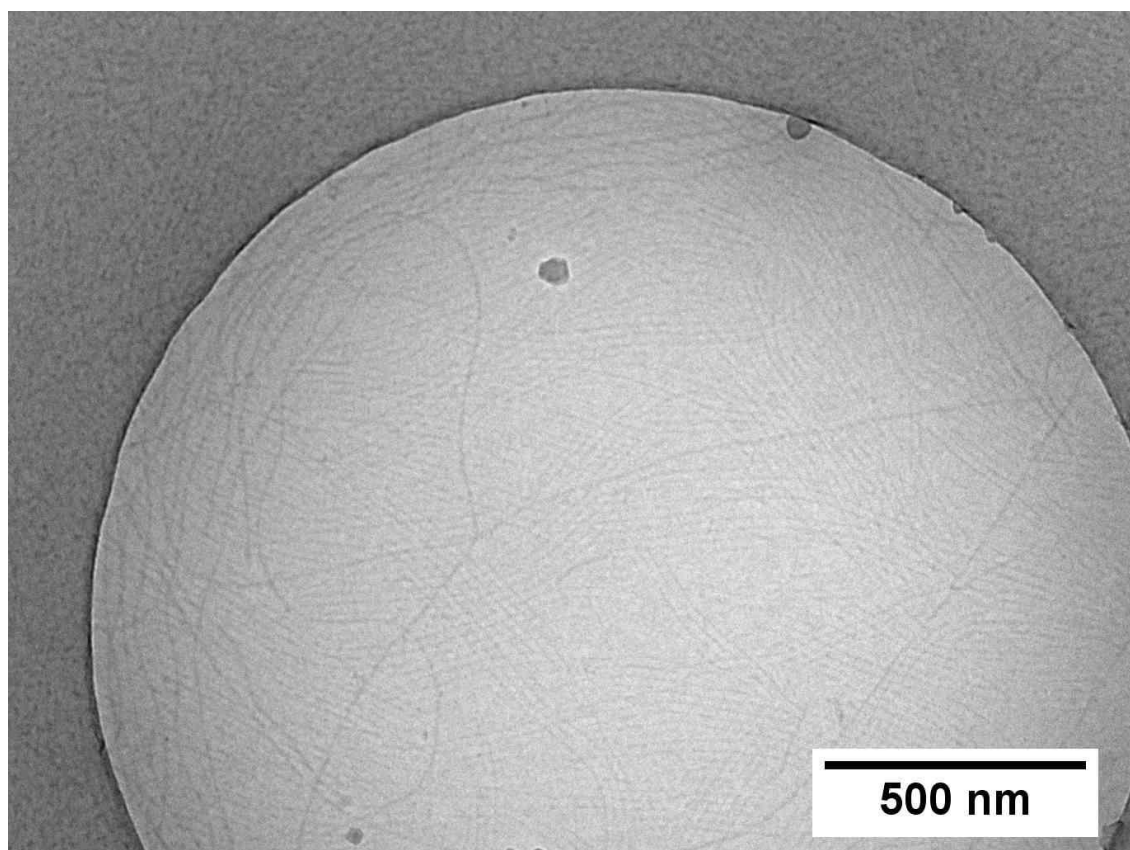


Figure S3: cryoTEM image of BTU EtOH in water ($c = 1 \text{ mg}\cdot\text{mL}^{-1}$) assembled at $1 \text{ mL}\cdot\text{h}^{-1}$ water addition rate.

BTP acetone

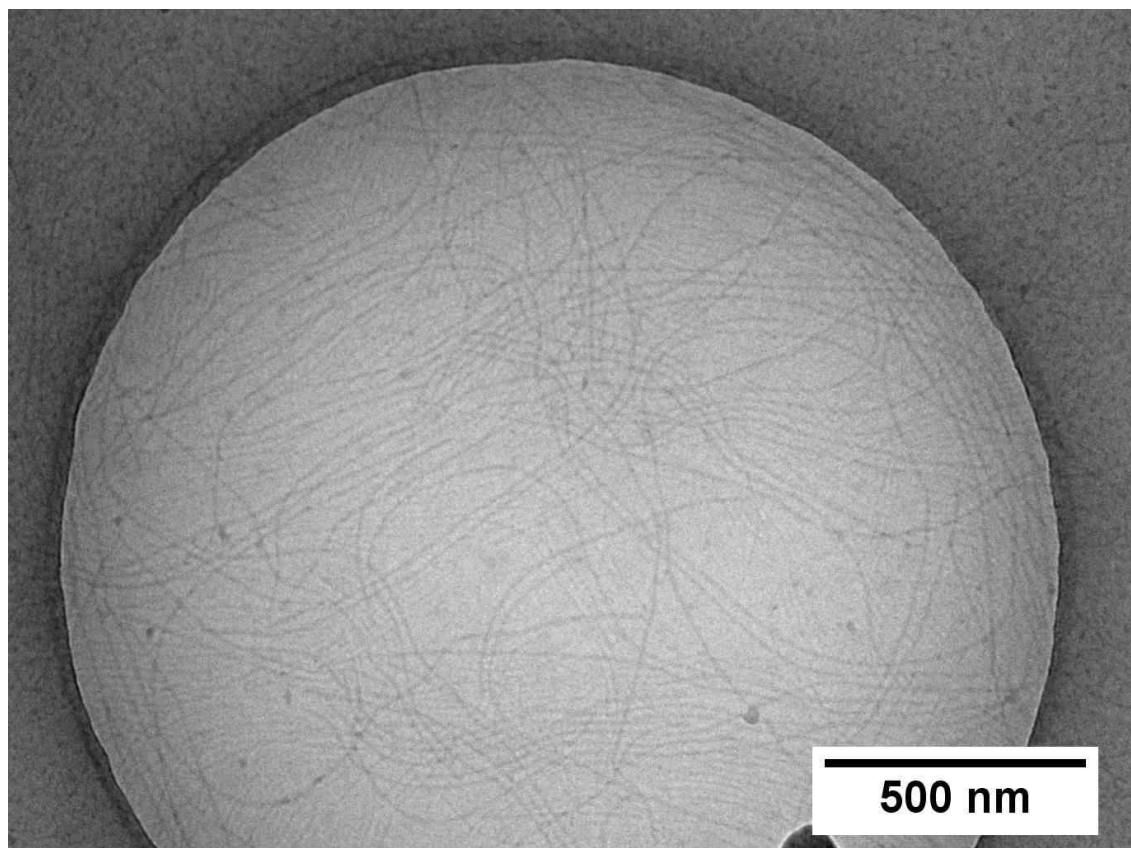


Figure S4: cryoTEM image of BTP acetone in water ($c = 1 \text{ mg}\cdot\text{mL}^{-1}$) assembled at $1 \text{ mL}\cdot\text{h}^{-1}$ water addition rate.

BTP DMF

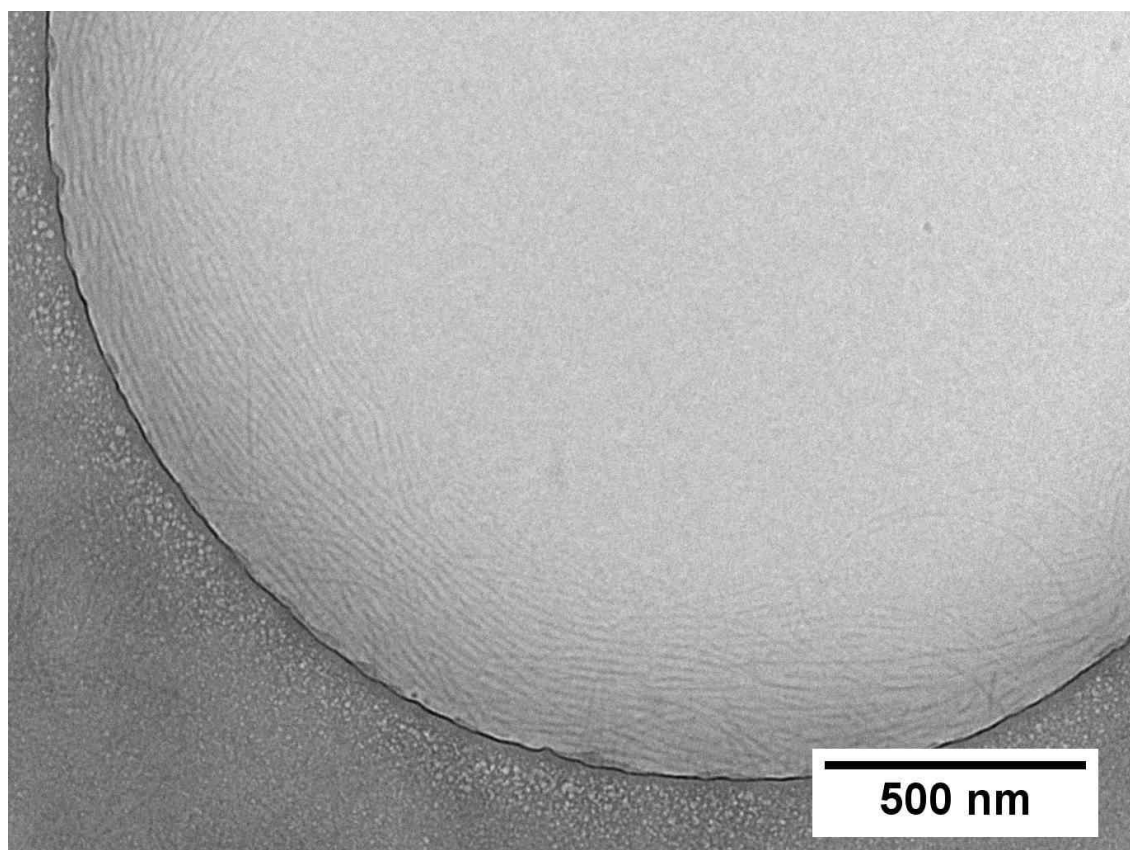


Figure S5: cryoTEM image of BTP DMF in water ($c = 1 \text{ mg}\cdot\text{mL}^{-1}$) assembled at $1 \text{ mL}\cdot\text{h}^{-1}$ water addition rate.

BTP EtOH

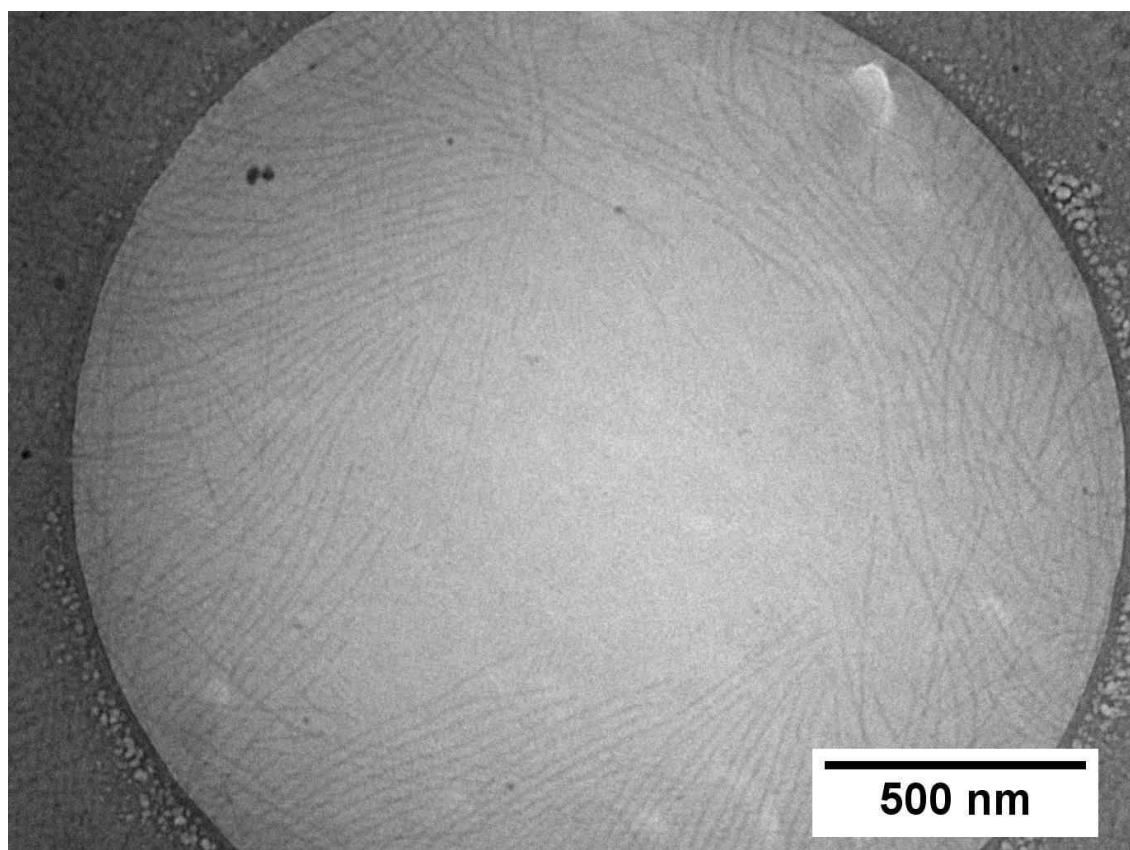


Figure S6: cryoTEM image of BTP EtOH in water ($c = 1 \text{ mg}\cdot\text{mL}^{-1}$) assembled at $1 \text{ mL}\cdot\text{h}^{-1}$ water addition rate.

BTP US 1 s

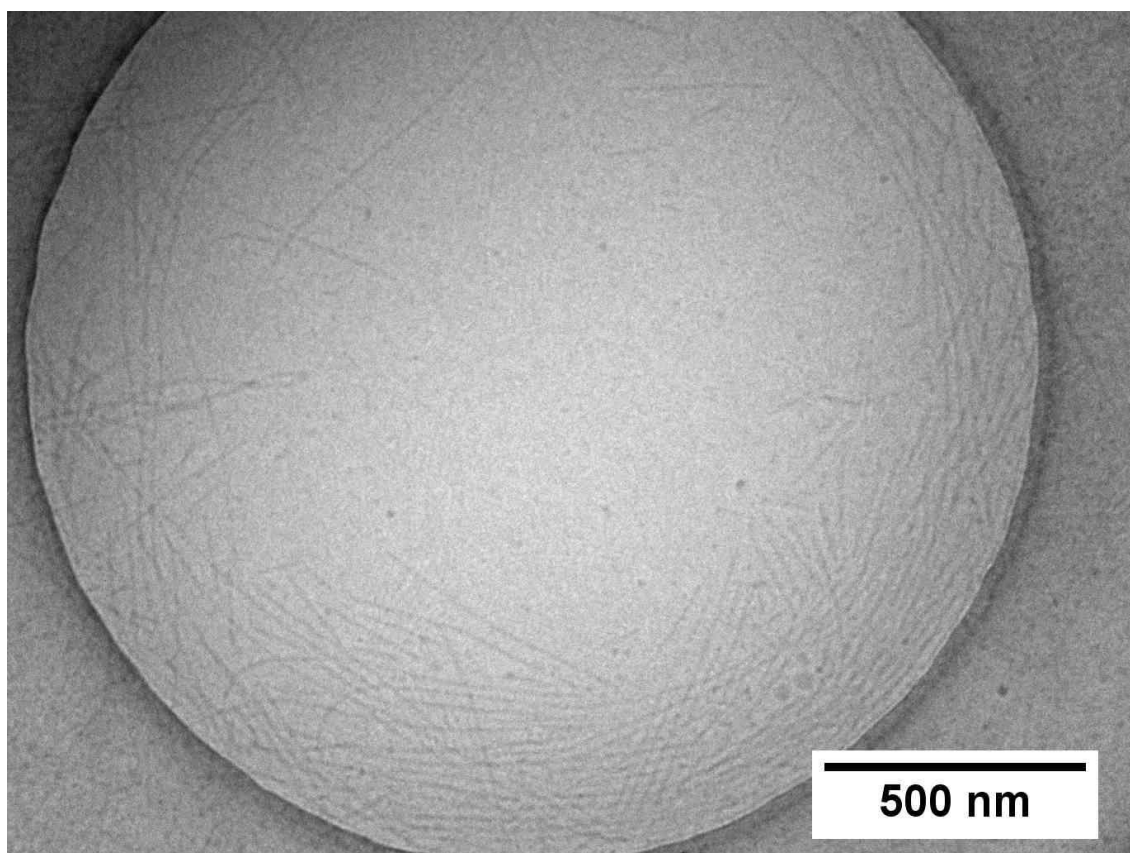


Figure S7: cryoTEM image of BTP after ultrasonication for a cumulated time of 1 s in water ($c = 1 \text{ mg}\cdot\text{mL}^{-1}$).

BTU US 30 and BTP US 30 s: cryoTEM histograms

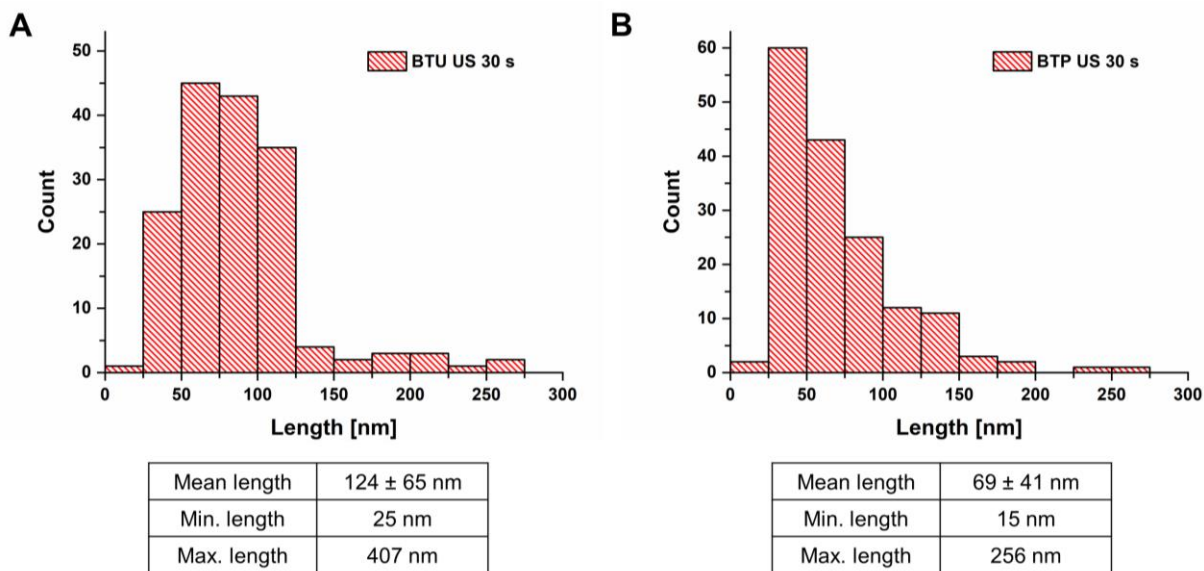


Figure S8: cryoTEM histograms for BTU US 30 s (A) and BTP US 30 s (B).

2.2 Asymmetrical flow field-flow fractionation (AF4)

AF4 measurements were performed on an AF2000 MT System from Postnova Analytics GmbH (Landsberg, Germany), equipped with a tip and focus pump (PN1130), an autosampler (PN5300), and a channel oven unit (PN4020) set to 25 °C. The channel was coupled to a multiangle laser light scattering (MALLS) detector (PN3621) equipped with a 532 nm laser and an overall of 21 angles (only 28°–148° have been used for calculation of R_g and M_w), a refractive index (RI) detector (PN3150), and a UV detector (PN3212) operating at a wavelength of 280 nm. The channel had a trapezoidal geometry with a nominal height of 350 μm . A regenerated cellulose (RC) membrane from Postnova Analytics GmbH (10 kDa RC membrane) with a molar mass cutoff of 10 kDa was used as the accumulation wall. As the mobile phase, an aqueous solution with 0.002 wt % of NaN_3 was used. 50 μL of the sample at a concentration of 1 $\text{mg}\cdot\text{mL}^{-1}$ was injected with an injection flow rate of 0.2 $\text{mL}\cdot\text{min}^{-1}$, a focus flow rate of 0.8 $\text{mL}\cdot\text{min}^{-1}$, and a cross-flow rate of 0.7 $\text{mL}\cdot\text{min}^{-1}$, resulting in a detector flow rate of 0.3 $\text{mL}\cdot\text{min}^{-1}$. The focusing time was 4 min before switching to elution at an exponentially decaying crossflow from 0.7 $\text{mL}\cdot\text{min}^{-1}$ to 0.2 $\text{mL}\cdot\text{min}^{-1}$ within 76.2 min. Thereafter, the crossflow profile was set to decay in a linear way from 0.05 $\text{mL}\cdot\text{min}^{-1}$ to 0.04 $\text{mL}\cdot\text{min}^{-1}$ within 71 min (Figure S9). Before the start of the next measurement, a rinsing step was performed at 1.5 $\text{mL}\cdot\text{min}^{-1}$ tip flow for 20 min. After each sample measurement, a blank measurement at identical detector conditions was run, which was subtracted from the traces of the sample measurement for analysis. The RI detector was used as the concentration-sensitive detector ($\text{dn}/\text{dc}_{\text{BTU}}$ 1.47 mL/g and $\text{dn}/\text{dc}_{\text{BTP}}$ 1.48 mL/g), and the MALLS data was analysed via a ZIMM plot analysis to obtain the R_g values and the molar mass at the specified elution times.

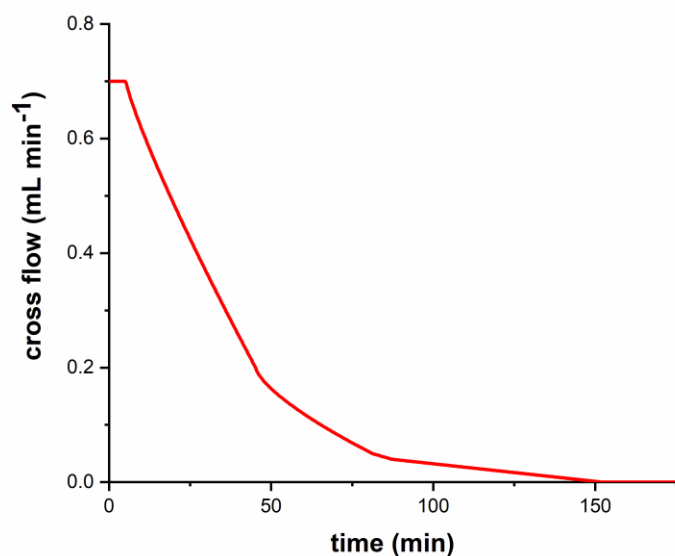


Figure S9: Cross-flow profile applied for all AF4–MALLS measurements in this manuscript.

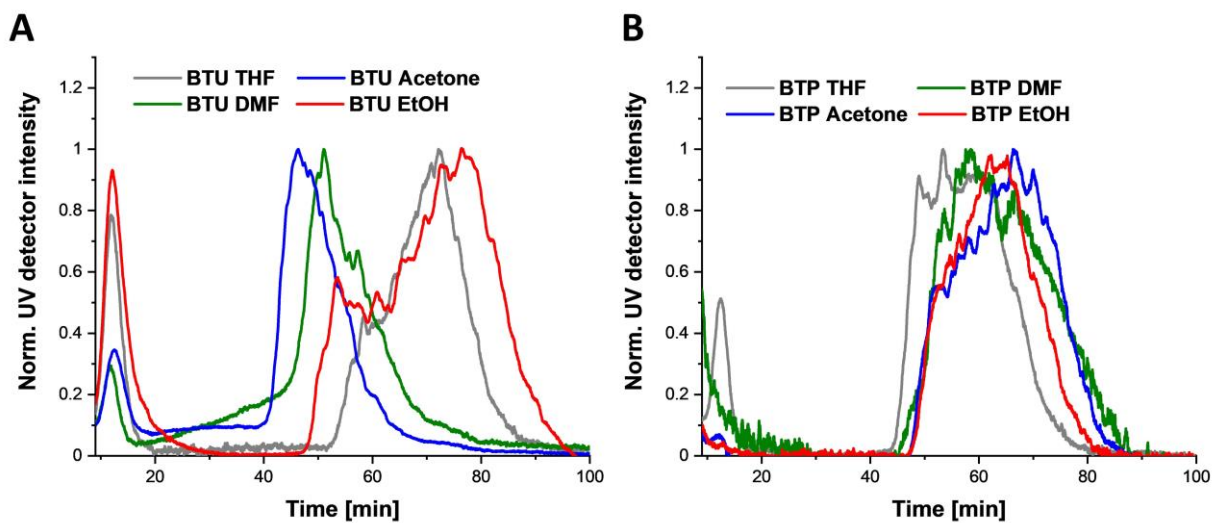


Figure S10: Normalized UV traces at 280 nm of BTU (A) and BTP (B) assembled from different organic solvents. The injection peaks were omitted for reasons of clarity.

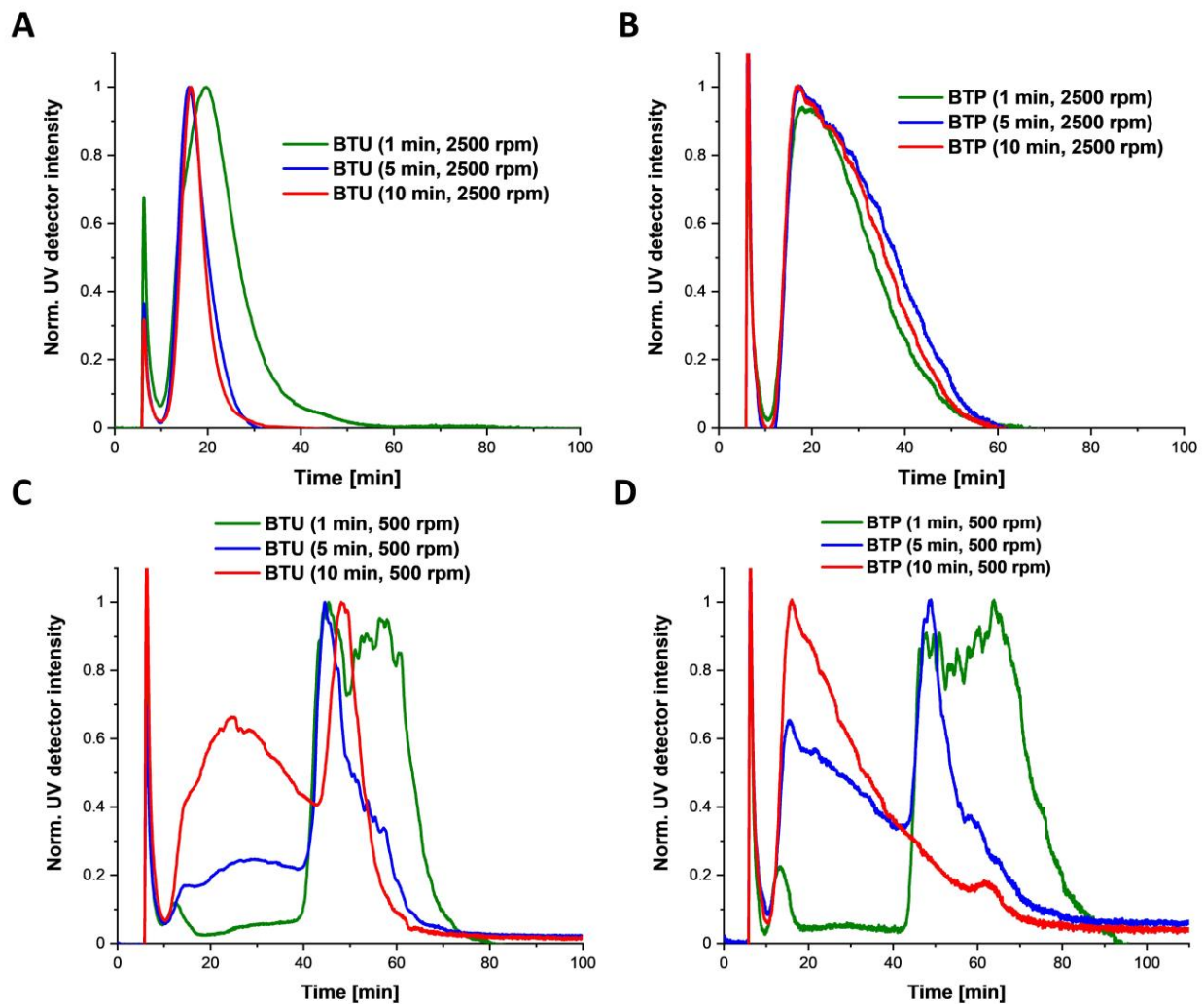


Figure S11: AF4 elution profile showing the stability against dual centrifugation at different rotation speeds of 2,500 rpm (A and B) and 500 rpm (C and D) of BTU and BTP, respectively.

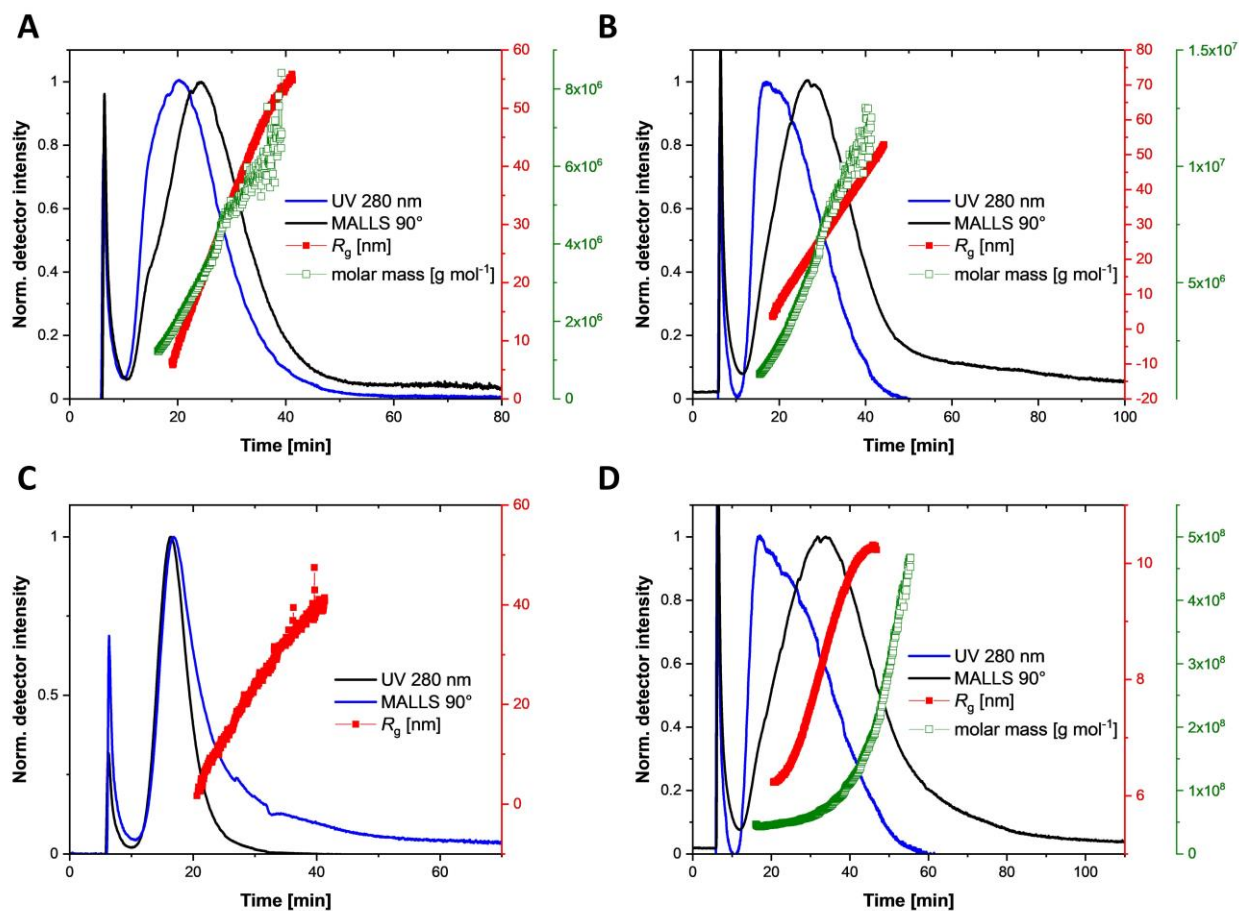


Figure S12: Normalized MALLS 90° (black) and UV (blue) traces of BTU at 1,000 rpm (A) and 2,500 rpm (C), and BTP at 1,000 rpm (B) and 2,500 rpm (D) for 10 min each. R_g (red) and molar mass (green) obtained via the Zimm plot of light scattering data from AF4–MALLS measurements. For BTU (10 min, 2,500 rpm) (C), estimation of the molar mass was not possible.

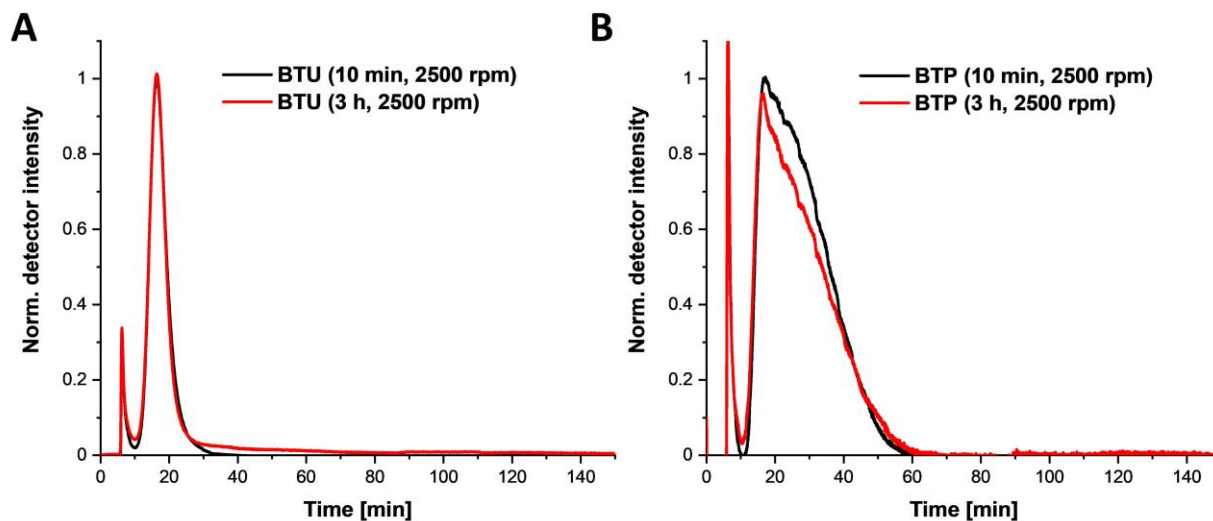


Figure S13: AF4–UV traces (at 280 nm) of BTP (A) and BTU (B) after extended centrifugation times of 3 h.

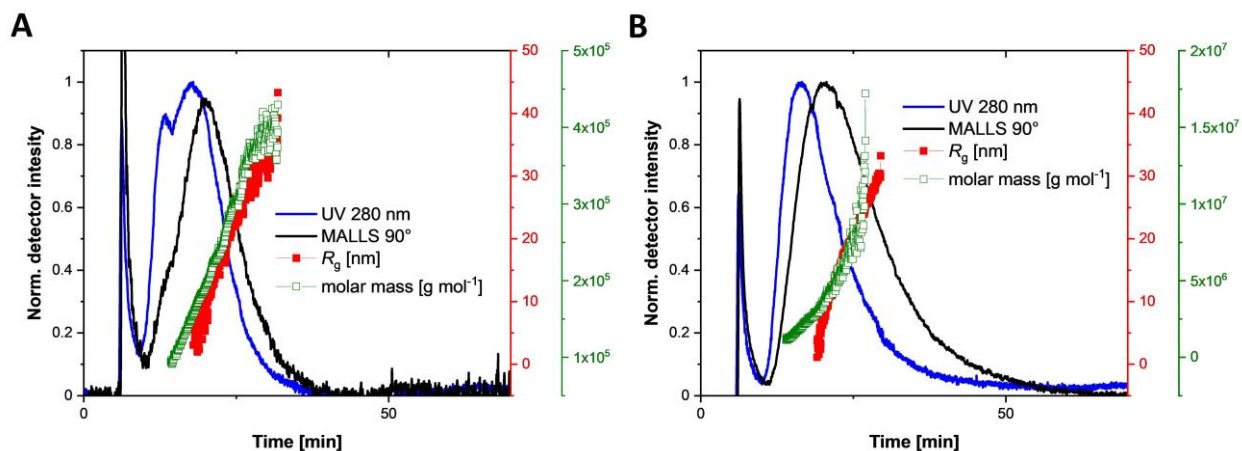


Figure S14: Normalized MALLS 90° (black) and UV (blue) traces of BTU (A) and BTP (B), after a cumulated time of 50 s ultrasonication (black). R_g (red) and molar mass (green) obtained via the Zimm plot of light scattering data from AF4–MALLS measurements.

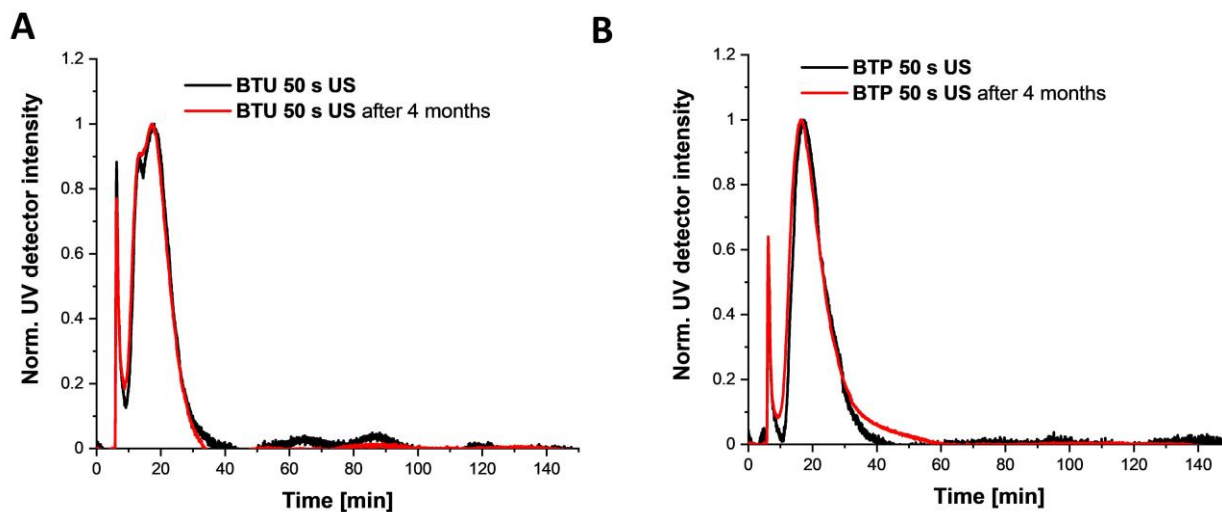


Figure S15: Stability of the samples BTP THF (A) and BTU THF (B) after 50 s of ultrasound exposure measured directly afterwards (black) and after four months (red).

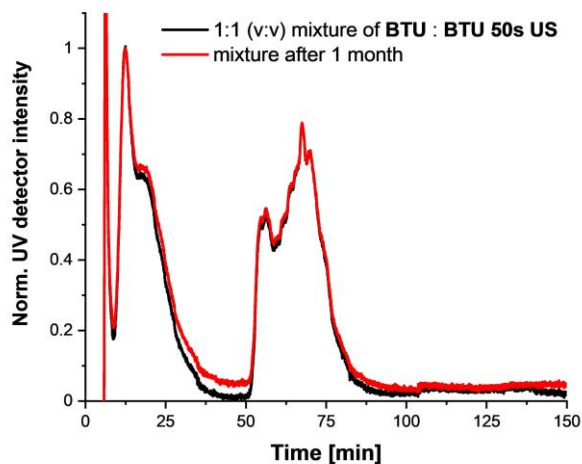


Figure S16: AF4 elution profile proving the stability of a 1:1 (v/v) mixture of BTU 50 s US and BTU over months. Slight deviations in the traces might result from variations in the membrane and pressure differences between the measurements in the AF4 setup.

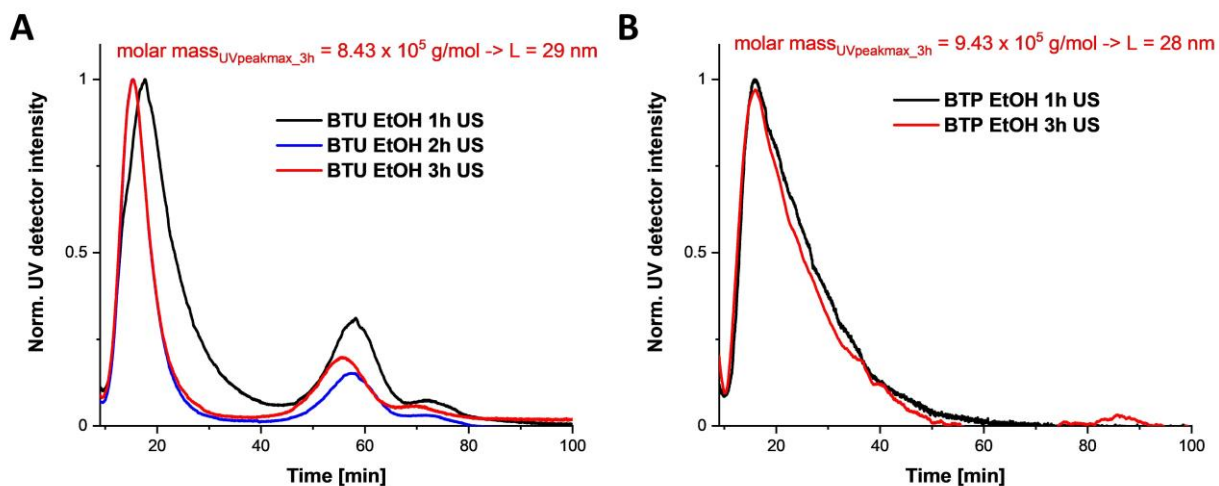


Figure S17: AF4–UV traces of BTU (A) and BTP (B) after extended ultrasonication exposures of 1 to 3 h. The injection peaks were omitted for clarity. The molar mass at the UV peak maximum (280 nm) of the elution curve after 3 h was calculated by Zimm plotting the data obtained by the MALLS detector. The length was estimated from the number of aggregation and the literature known stacking distance of the unimers of approximately 0.36 nm. After correction by the number of molecules in the cross-section, as published recently [2], an approximate length of the assemblies at this point of elution can be calculated.

Calculation of σ^* from the obtained limit length after US

$$L_{lim} \approx 7 * 10^{-4} d \sqrt{\sigma^*} \quad \text{Eq. 1}$$

$$\sigma^* \approx \left(\frac{L_{lim}}{7 * 10^{-4} * d} \right)^2 \quad \text{Eq. 2}$$

Table S1: Values calculated for σ^* for BTU and BTP from the respective limit length after 3 h of US.

	L_{lim} (nm)	σ^* (MPa)
BTU	29	17
BTP	28	16

3. References

- [1] a) F. V. Gruschwitz, M.-C. Fu, T. Klein, R. Takahashi, T. Higashihara, S. Hoepfener, I. Nischang, K. Sakurai, J. C. Brendel, *Macromolecules* **2020**, *53*, 7552-7560; b) T. Klein, H. F. Ulrich, F. V. Gruschwitz, M. T. Kuchenbrod, R. Takahashi, S. Fujii, S. Hoepfener, I. Nischang, K. Sakurai, J. C. Brendel, *Polym. Chem.* **2020**, *11*, 6763-6771.
- [2] F. V. Gruschwitz, T. Klein, M. T. Kuchenbrod, N. Moriyama, S. Fujii, I. Nischang, S. Hoepfener, K. Sakurai, U. S. Schubert, J. C. Brendel, *ACS Macro Lett.* **2021**, 837-843.

Note: Publication P8 was rejected by Advanced Functional Materials in the meantime and resubmitted in the following form at Chemistry of Materials on the 15.11.2021

Shear-thinning and rapidly recovering hydrogels of polymeric nanofibers formed by supramolecular self-assembly

Franka V. Gruschwitz,^{a,b} Franziska Hausig,^{a,b} Philipp Schüler,^c Julian Kimmig,^{a,b} David Pretzel,^{a,b} Ulrich S. Schubert,^{a,b} Sylvain Catrouillet,^{d,*} Johannes C. Brendel,^{a,b,*}

a Laboratory of Organic and Macromolecular Chemistry (IOMC), Friedrich Schiller University Jena, Humboldtstraße 10, 07743 Jena, Germany

b Jena Center for Soft Matter (JCSM), Friedrich Schiller University Jena, Philosophenweg 7, 07743 Jena, Germany

c IOMC/IAAC NMR platform, Friedrich Schiller University Jena, Humboldtstraße 10, 07743 Jena, Germany

d ICGM, Université de Montpellier, CNRS, ENSCM, Montpellier, France

*corresponding author: sylvain.catrouillet@umontpellier.fr; johannes.brendel@uni-jena.de

Keywords: supramolecular polymer bottlebrushes; self-assembly; polymer nanostructures; bioprinting, crosslinking;

Abstract

The self-assembly of amphiphilic polymers into wormlike micelles represents a versatile approach to create hydrogels, where interactions and functionalities are widely customizable by the chemistry of the hydrophilic block. However, processing options for such gels remain a bottleneck, as fragmentation is often irreversible due to limited dynamics of the assemblies. We here demonstrate that shear-thinning hydrogels can reversibly be formed by amphiphilic polymers, which assemble into supramolecular polymer nanofibers due to additional directing hydrogen bonds. The addition of bifunctional crosslinkers resulted in robust gels, which feature a surprisingly strong shear-thinning character but recover fully in absence of shear stress despite the lack of a dynamic exchange of individual building blocks. In addition to increasing the concentration, the strength of the gel can be tuned by varying the content or the length of the bivalent crosslinker. Low viscosities under shear load and the rapid recovery (< 5s) after relief

of strain facilitates an effortless extrusion through even thin needles and subsequent formation of self-supporting structures in a printing process. The polymer fiber structure further bestows the gels with an excellent stability in various conditions and good biocompatibility while minimizing cell adhesion. Comprising sufficient mesh sizes, even large macromolecules can still diffuse through the gel, but retardation is observed even for small molecules due to the dense polymer brush structure. This unique set of properties renders these polymer fiber hydrogels a versatile and easily processible scaffold for future applications for example as adaptable cell scaffold or injectable drug depot.

Introduction

In the last decades, much effort has been made to create one-dimensional (1D) structures resembling those found in nature, for example in the cytoskeleton or the extracellular matrix.¹⁻⁶ These structures form a dense network and resemble the scaffold for cellular life. A versatile approach to create such fiber-like structures relies on the self-assembly of amphiphilic polymers into worm-like or fibrous micellar structures.⁷⁻¹¹ Thermodynamically, the formation of these 1D morphologies in water is only governed in a narrow composition range which is overall challenging to predict. Moreover, kinetic trapping might impede a morphological transition due to a lack of dynamic exchange of polymer chains. But despite these challenges, a variety of approaches have been developed to reliably form the desired 1D morphologies for polymer self-assemblies in water.¹² For instance, additional driving forces were introduced such as a crystallization of the core or directing hydrogen bonds, which guide the self-assembly of the polymers into a 1D or fiber-like structure.^{13, 14} Other attempts take advantage of polymerization-induced self-assembly (PISA), where nanostructure formation occurs in situ and thus simplifies the targeting of specific morphologies. This approach results in high concentrations of polymers, and often gels are obtained if worm-like micelles are formed.¹⁵ In general, 1D polymer nanostructures form networks or hydrogels crossing a certain threshold concentration as fibers entangle or associate.¹⁶⁻²¹ The fibrillar structure of the network introduces interesting characteristics to the hydrogel as all fibers are covered by a dense layer of hydrophilic polymer. This polymer corona opens the possibility to control cellular interactions and for example influence the differentiation of human stem cells, as Armes and coworkers reported in several examples.^{15, 20, 22-24} These reports underline the potential of such fibrillar hydrogels and further opportunities reside within the versatile options to functionalize the polymer scaffold, for example an introduction of crosslinking which allows for tuning of the mechanical strength.^{25, 26} A challenge however remains in the limited processability of such hydrogels based on polymer

self-assemblies. While in the case of the above-mentioned examples a reversible transition from worms to spheres at low temperatures offers a unique tool for processing, most polymer self-assemblies are lacking such features or the required dynamic adaptability to external stress.^{27, 28} Therefore, bioprinting processes or direct injection of such scaffolds *in vivo* as demonstrated for dynamic supramolecular fibrillar assemblies seem still beyond reach.²⁹⁻³⁴

An integration of such a reversible and shear-dependent network formation as reported for the supramolecular fibers would certainly expand the scope of the polymer-based fibrillar hydrogels. Dynamics in polymer self-assembly can for example be enhanced by increasing the solubility of the hydrophobic block, but also supramolecular interactions such as hydrogen bonds appear suitable to introduce reversible interactions. We have recently reported that such supramolecular forces introduced by benzene trisureas (BTU) or trispeptide units enable the formation of polymer fibers from poly(ethylene oxide) (PEO) conjugates that reach lengths of several micrometers.³⁵ Intrigued by the above-mentioned unique properties of polymer-based fibrillar hydrogels we were interested in testing whether these fibers have a similar potential to form hydrogels and if the supramolecular structures induce a reversible network formation. Therefore, various concentrations were examined to estimate the critical point for gelation. Furthermore, we tested the impact of bifunctional crosslinker to tune the gel properties and investigated the dynamic response to shear stress in rheological studies. Considering a potential biomedical application further *in vitro* tests on biocompatibility were included.

Results and Discussion

In a first attempt, the previously published sample BTU-PEO_{2k} **1** (Figure 1A) was evaluated concerning its gelation ability at various concentrations.³⁶ To ensure the formation of large fibers a similar assembly procedure was applied as previously reported.³⁵ In brief, the bulk material is first molecularly dissolved in an organic solvent, and water is subsequently added at 1 mL h⁻¹ to induce the assembly. The organic solvent is finally removed by evaporation. To our surprise, BTU-PEO_{2k} **1** exhibits no gelation in water at concentrations between 1 and 20 mg mL⁻¹ despite its ability to form fibers of up to 3 μm,³⁵ which would correlate to an overlap concentration of around 0.05 mg mL⁻¹. Gelation occurs only at concentrations > 20 mg mL⁻¹ (Figure 1B). Since this concentration is 400 times higher compared to the calculated overlap concentration, the fibers seem to be remarkably stiff and thus, entanglement is prevented at lower concentrations. A similar behaviour was observed for worm-like polymer micelles, which show gelation at similar high concentrations, the interactions between the fibers appear to be

reduced due to the sterically demanding hydrated brush structure, which impedes crosslinking by branching of the structure or bundling of fibers.

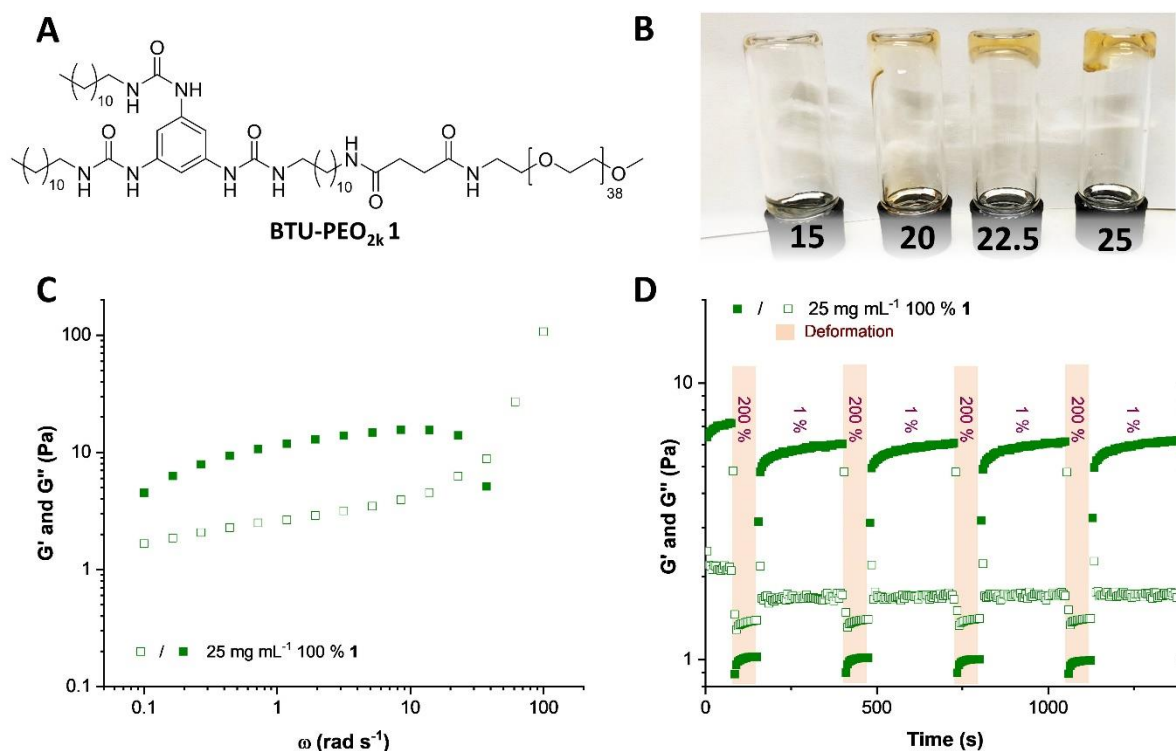


Figure 1 Schematic representation of the chemical structure of **BTU-PEO_{2k} 1** (A). Inverted vial test of **BTU-PEO_{2k} 1** hydrogels prepared by the solvent switch method at concentrations of 10 to 25 mg mL⁻¹ (B). Frequency-sweep (C) and step-strain (D) measurement of **1** at 25 mg mL⁻¹.

Exemplarily the strength of the gel of **1** at 25 mg mL⁻¹ was assessed in frequency-sweep measurements (Figure 1C, further details can be found in the Supporting Information, Figure S3). A plateau-like curve between 1 and 10 rad s⁻¹ is observed which is typical for the formation of entanglements between fibers (Figure 1C). Toward lower frequencies, a decrease of the storage modulus can be observed which already indicates an upcoming crossover of storage and loss modulus, although this Maxwellian behavior was not further investigated. The maximum storage modulus G' of around 10 Pa is rather low, which again reflects the weak interaction of the fibers as described above.

Interestingly, during our measurements, we observed that the gel reformed after relieving the deformation force. Therefore, additional dynamic step-strain experiments were applied to evaluate in more detail the reversibility of the gel formation after deformation.³⁷⁻³⁹ To our surprise and contrary to most worm-like micelles, the gel recovered upon relief of the shear stress slowly reaching almost its initial strength (Figure 1D, S4). At high deformation (200%), liquid-like properties appear as $G'' > G'$. At this stage, it was not clear whether this behavior is a result of the breakage of the fibers or their simple disentangling related to their very weak

interaction, which is also reflected in the overall low strength of the observed gels. An interesting strategy to improve the strength of gels is the introduction of crosslinking units as in the case of common ABA triblock copolymers. Recently, this strategy was adapted for supramolecular fibers.^{29, 31, 40, 41} We adjusted the latter systems and synthesized a bivalent linker consisting of a PEO chain of 20 kD and two BTU endgroups (**2a**) which was added at different ratios to **1** before the solvent switch (Figure 2A). With incorporation of the two endgroups into different nanofibers, additional crosslinking points are formed strengthening the gel and preventing a disentanglement (Figure 2D). A strong effect is already observed with adding just 1 % of this bivalent linker **2a**. The mechanical strength of the gel increased by a factor of 10 (Figure S3C). Further addition of crosslinker has only a marginal effect, while at contents of 50% a decrease in strength is observed. Interestingly, the pure bivalent crosslinker at 25 mg mL⁻¹ forms a similar weak networks as pure **1**. We assume that following our previous studies, the fiber formation is hampered due to the high molar mass of the polymer chain in the linker. Similar observations were also made for supramolecular gels based on low molecular weight building blocks.⁴⁰

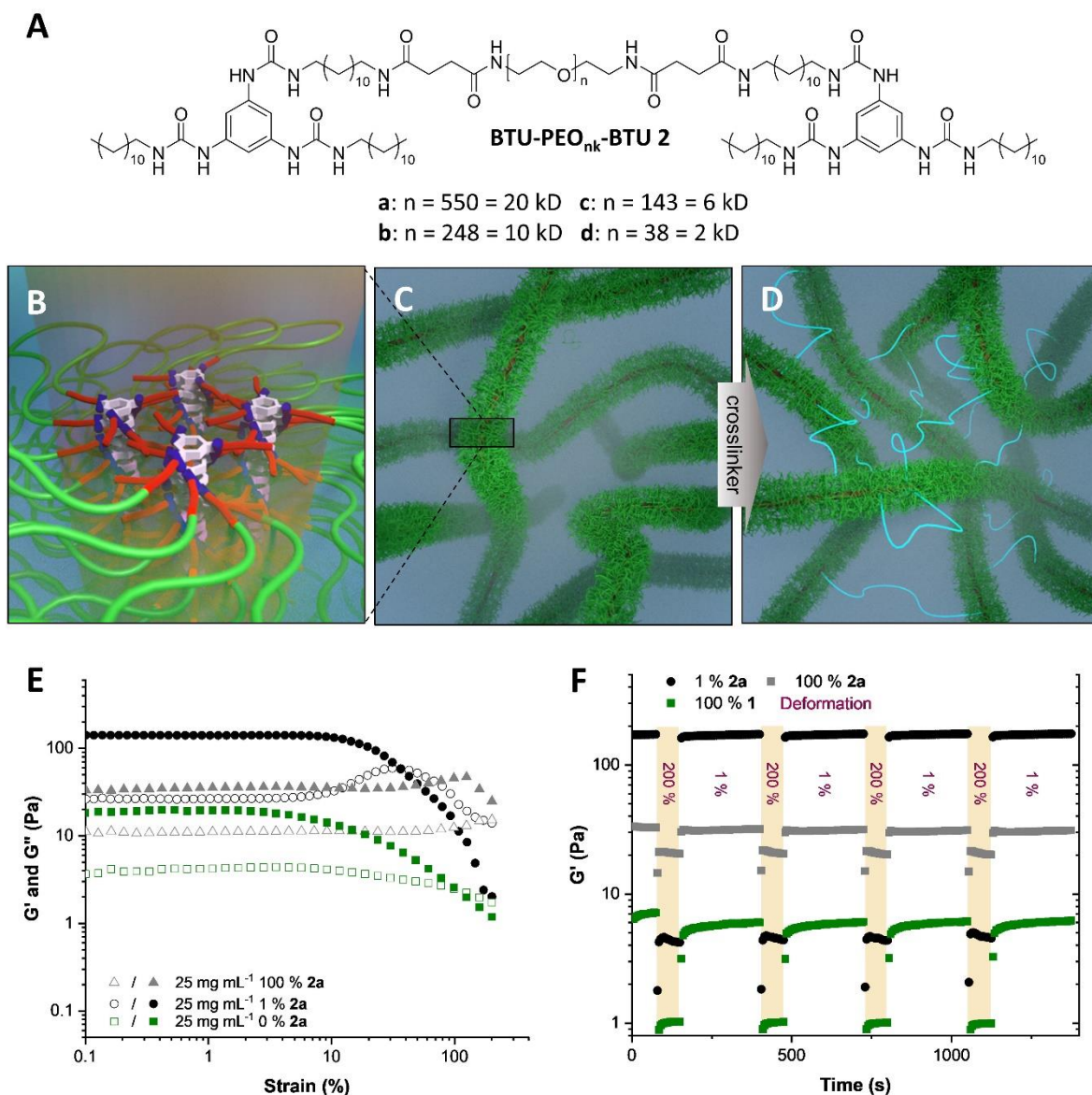


Figure 2 Schematic representation of the chemical structure of **BTU-PEO_{nk}-BTU 2** (A). Schematic depiction of the cross-section of the SPB fiber (B), the gel without (C), and with 1 % crosslinker (D). Strain-sweep measurements (E) and step-strain measurements (F) of **1** (green), **1** with 1% **2a** (black) and **2a** hydrogels at a concentration of 25 mg mL⁻¹.

All gels show a yield point in strain-sweep measurements at strains $> 40 \%$, indicating a breakdown of the network above these strains (Figure 2E, S5). Macroscopically, the gels liquefy if sufficient shear stress is applied. This liquification appears again reversible despite the presence of the crosslinker. Most astonishingly the gel of **1** + 1% **2a** at 25 mg mL⁻¹ recovers within less than 5 s to their full strength in contrast to the slow recovery of the gel formed by pure compound **1**. Similar rapid recovery is also found for gels with higher and lower crosslinker content (Figure S4). The difference in G' between periods of high and low deformation varies with crosslinker content similar to the overall strength but appears to be much lower for the pure monovalent structure **1** and the pure crosslinker **2a** (Figure 2F). The gel consisting of **1** + 10% **2a** at 25 mg mL⁻¹ sets a benchmark for the G' ratio between high and

low deformation and reaches a value of 90 in these step-strain measurements while retaining the rapid recovery.

Considering the fact that these BTU hydrogels should resemble a static network due to the crosslinking, the fibers must fragment under the applied shear forces and reassemble once the stress is relieved. In the case of low molecular weight gelators, such behavior is related to the dynamics of the system, as individual building blocks can exchange, and thus the fibrous structure is reformed after deformation.⁴²⁻⁴⁴ Our polymer-based fibers, however, did so far not demonstrate any dynamic behavior in aqueous systems as it is reflected by the possibility to kinetically trap structures with different sizes.³⁵ The addition of the crosslinker might however influence the assembly behavior. Therefore, the dynamics of the gels were examined in more detail by fluorescence recovery after photo-bleaching (FRAP). To do so, the gel containing 1% **2a** was covalently labeled with AF-594 and bleached for 30 min with a UV laser. The bleached part was examined after 6 and 24 h. No recovery of the fluorescence can be observed in the bleached parts of the sample (Figure 3, Figure S10), meaning the mobility of individual building blocks must be impeded in the gel network and therefore the above-considered dynamics within the gel are absent. The result coincides with the previously observed kinetic trapping and corroborates the high stability of the gel structure.³⁵

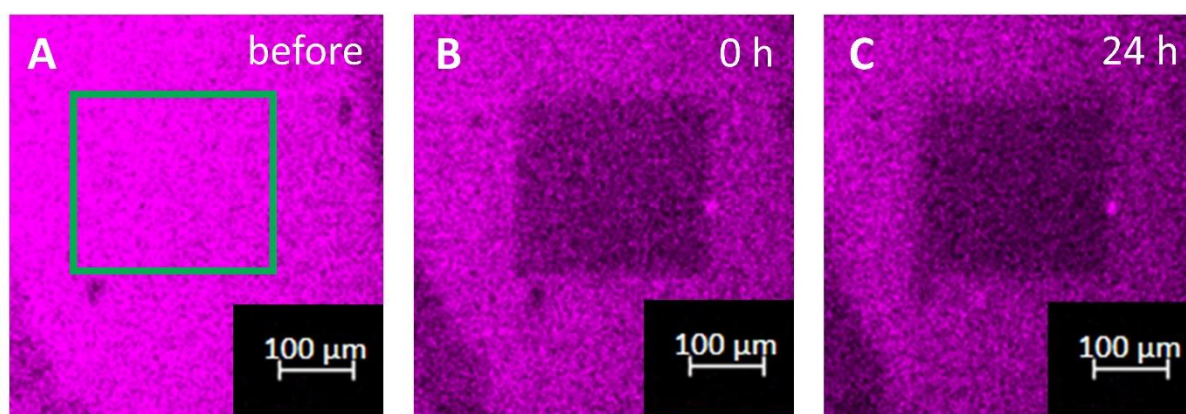


Figure 3 Fluorescence recovery after photo-bleaching experiment of a covalently labeled gel (**1** + 1% AF-594 labeled BTU + 1% **2a** at 25 mg mL⁻¹) before bleaching (A), directly after bleaching (B) and after 24 h (C).

In consequence, the observed liquification and rapid recovery of the gel must be related to a different mechanism. As the supramolecular interactions must reform immediately, we assume the strong intramolecular hydrogen bonds combined with the hydrophobic effect of the supramolecular core units induce the effect. The fibers rupture upon exposition to shear forces, resulting in fragments that feature reactive chain ends that are not saturated with PEO chains on their surface. These hydrophobic surfaces then represent a strong driving force to reconnect

the fiber ends and minimize the exposed hydrophobic core to the surrounding water. Since the gel strength is recovered to 100 % each cycle, nearly every active chain end must reconnect.

Intrigued by these unexpected properties we investigated whether the properties of the gels can be further optimized by variations of the composition. Besides the above-mentioned impact of the crosslinker content summarized in Figure 4A (Figure S3C), the influence of the length of the linker on the mechanical properties of the hydrogel was evaluated on gels (25 mg mL^{-1}) containing 1 % of crosslinker (Figure 4B, S3B). If the length of the crosslinker is decreased from 20 (**2a**) to 6 kD (**2c**) and 2 kD (**2d**) a strong decrease of the plateau moduli can be observed. In this case, only weak gels are formed. We assume that two nanofibers equipped with a 2kD PEO corona will not get in sufficient proximity, so crosslinker **2d** or **2c** could link them. Such a nearly touching contact is unfavorable due to the hydrated PEO corona. Consequently, backfolding of the PEO chain of the crosslinker will be favored. Surprisingly, this decrease in crosslinking probability can already be observed for crosslinker lengths of 10 kD (**2b**) which are still five times the size of the PEO corona (2 kD) of the SPB.

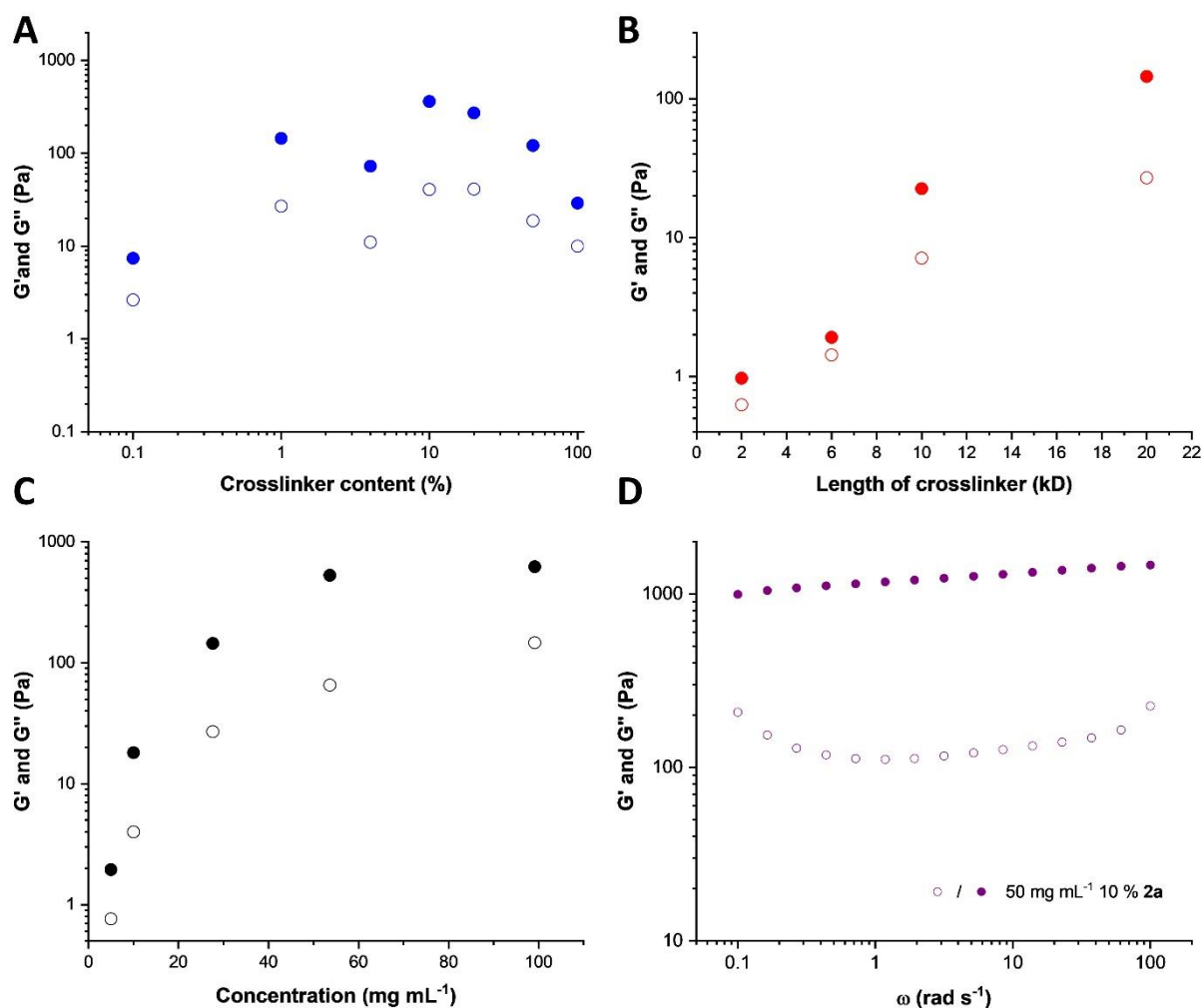


Figure 4 Plateau modulus of hydrogels with different amounts of crosslinker **2a** ($c = 25 \text{ mg mL}^{-1}$) (A), plateau modulus of hydrogels with 1 % crosslinker of different lengths ($c = 25 \text{ mg mL}^{-1}$) (B), and concentration-dependent plateau modulus of hydrogels with 1 % of **2a** crosslinker at different concentrations (C). Frequency-sweep measurement of a hydrogel of **1** with 10 % of **2a** at 50 mg mL^{-1} (D).

Another parameter to tune the gel strength is the concentration. If the concentration of the hydrogel is increased, a strong increase in storage and loss modulus can be observed (Figure 4C, S3A). Due to an overall higher number of fibers, the number of entanglements in the network increases, and thus the gel strength is enhanced. This correlates well with other known systems where gelation is favored for higher concentrations.^{29, 31} Interestingly, a plateau is reached at a concentration of 50 mg mL^{-1} (Figure 4C). In consequence, the strongest gel based on this system was obtained at a concentration of 50 mg mL^{-1} and 10 % crosslinker **2a** which reached a storage modulus of 1 kPa (Figure 4D, S6).

We further tested the response of the gels to amplitude sweeps. A crossover of G' and G'', and thus, a breakdown of the gel network can be measured at specific strains for all gels. All crosslinked gels remain stable with strains < 10 % and feature the yield stresses > 20 Pa (Figure

S5D). Overall, all crosslinked gels appear very soft but tolerate surprisingly high deformations before yielding (Figure S5).

The general stability of these hydrogels can already be seen by the bare eye when compact solid gel structures are generated via a molding technique. For this purpose, small Teflon or silicone molds were filled with the solution of **1** with 1 % **2a** and the THF was evaporated to a final concentration of 25 mg mL⁻¹ (Figure 5A and S13). After the gel was released from the mold, it keeps its form on a glass slide for more than an hour before severe drying is observed (Figure S13B). Furthermore, it is possible to cut and rearrange the gel resulting in a solid attachment of the two components (Figure 5B). Interestingly, even immersion in aqueous environment for multiple weeks does not alter the gel, which corroborates the absence of dynamic exchange of building blocks in this system. No swelling or degradation can be observed (Figure 5C) what resembles the characteristics of hydrogels derived from block-copolymers in contrast to more dynamic supramolecular structures, which would finally swell and dissolve into the addition aqueous phase. Here, also no change in the rheological properties could be observed (Figure S1) and stable gels are even formed in the presence of up to 33 v% THF (Figure S2).

This high stability of the gels intrigued us to further investigate their tolerance for different conditions and media during the formation process. Besides very acidic (pH 2) and basic media (pH 11), the presence of salt and serum proteins (Figure S11) did not visibly impact the network formation and in all cases, stable gels were obtained. In first preliminary tests, we also assessed the biocompatibility of the gels. Therefore, the gels were added to cell cultures and their impact on the viability of the L929 cells was evaluated according to ISO10993-5. The presence of the gel appears to not significantly affect the cell growth next to the cell, however, we already observed that cells were not able to adhere to the gel itself, which exemplifies the impact of the dense PEO layer on the fibers (Table S1, Figure S12A and B). Further, more detailed studies on cellular interactions are currently in preparation.

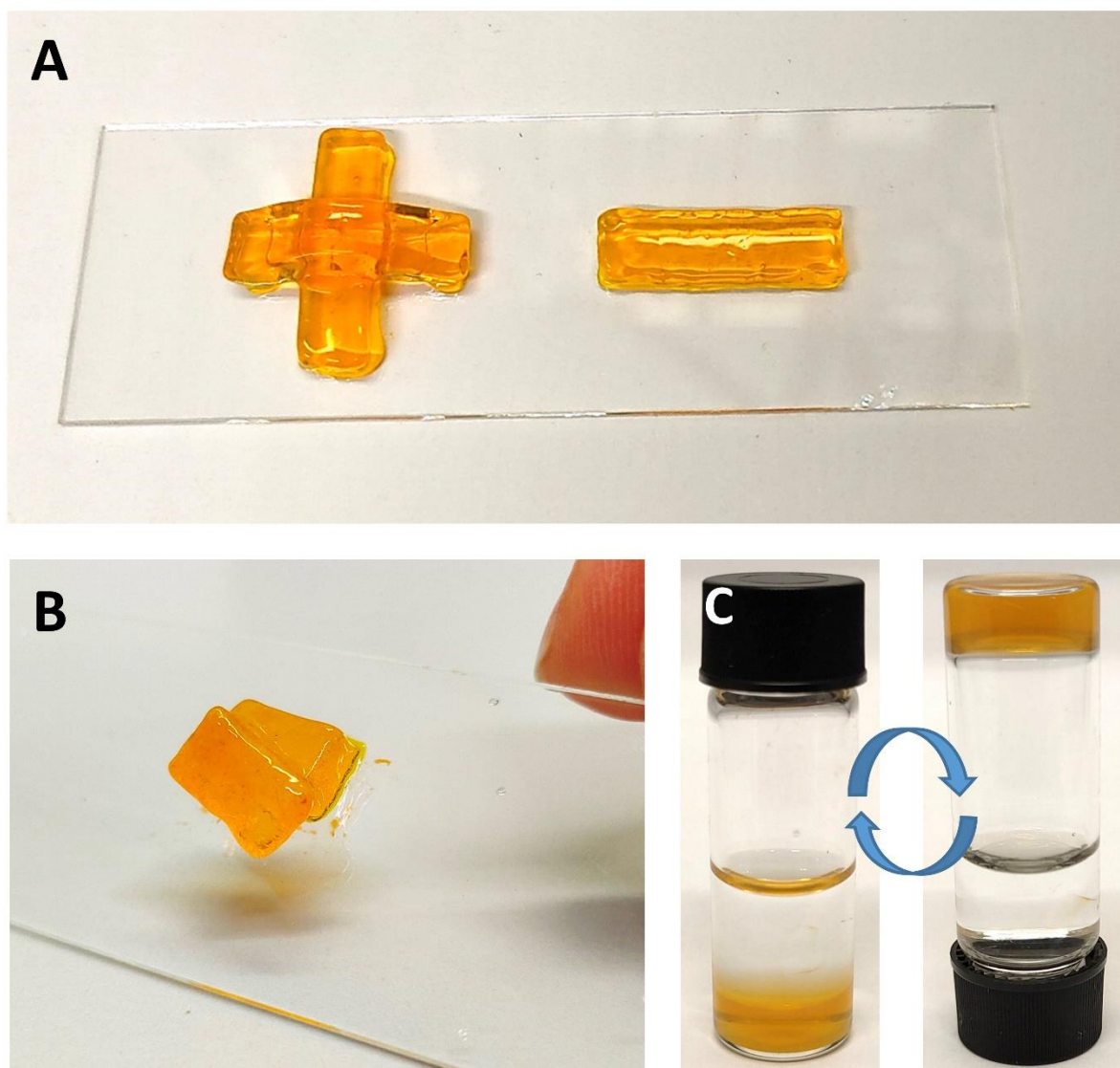


Figure 5 Gels (stained with Na-fluorescein for better visibility) of **1** with 1 % **2a** ($c = 25 \text{ mg mL}^{-1}$) molded in silicone molds (A). Molded blocks were cut and stacked (B). Stability of a gel in water (C). After immersion in water for one week, the vial could be inverted and no degradation or swelling of the gel could be observed.

Light scattering experiments were conducted to gain information on the internal structure of the gel. The correlation functions of a solution of the crosslinked BTU gel (**1** + 1% **2a**, 25 mg mL^{-1}) at various scattering wave vectors show two clear relaxation modes. The correlation length ξ can be determined using static light scattering (SLS) whereas the hydrodynamic correlation length ξ_H is determined using dynamic light scattering (DLS). As soon as the polymers form a transient network, the correlation length no longer contains information about the size of the individual chains, but it reflects the mesh size ξ_m of the network. With SLS, the average mesh size of the transient polymer network is measured, whereas DLS measures the average diffusion coefficient of the meshes. Using Figure S14 and equation S5 it is possible to determine a mesh size by SLS of the solution of the crosslinked BTU gel (**1** + 1% **2a**, 25 mg mL^{-1}) of 34 nm, which is reasonable considering the length of the fibers and the amount of crosslinker. Using

DLS a ξ_H of 81 nm was determined. The value obtained is different but of the same order of magnitude as already seen in similar systems.⁴⁵ To determine the origin of the two relaxations, the correlation functions have been represented versus t (Figure S17A) and normalized with q^2 (Figure S17B). The normalization with q^2 shows that only the first mode is superimposed. Therefore, it is due to the cooperative scattering of the network. On the contrary, the second mode is q^2 independent (Figure S16) and the amplitude of the first mode varies with q (Figure S15). It means that the second mode is probably due to the relaxation of the chains in the network. The average of the measured values at different q is taken as Γ_{slow} , and the reciprocal of this equals τ_{slow} . A value of 1,55 s is obtained for this system. Unfortunately, this relaxation value cannot be compared with our rheology experiments as no cross-over was observed during the frequency sweep experiments. Additionally, similar systems led to large discrepancies between rheology and DLS on studying the relaxation time, which is why we did not consider any further investigations in this direction.⁴⁵

Since these gels are constructed from strongly hydrated brush-like polymer fibers we were further interested whether these structures affect the diffusion of molecules through the gel. Applying pulse-field-gradient (PFG) NMR, the diffusion of well-defined poly(ethyl oxazolines) (PEtOx) was evaluated. Two PEtOx of different molar masses were enclosed in the crosslinked gel (**1** + 1% **2a**, 25 mg mL⁻¹) and the pure BTU gel (**1**, 25 mg mL⁻¹) for comparison (further details can be found in the Supporting Information). By comparison of the free diffusion coefficient D_0 of the PEtOx in water to the diffusion coefficient D of PEtOx in the gel, a strong retardation can be observed for PEtOx in both gels. However, the polymers were not completely trapped but a very slow diffusion was estimated (Table S2, Figure S18 and S19). As mentioned above, this retardation might be the result of the highly hydrated brush structure where the PEO chains of the SPBs extend far into the water and significantly prevent the free diffusion of the probe along the network pores (Figure 2B-D). Due to the high stability of gels even if immersed in water, we were further able to investigate diffusion processes macroscopically. Therefore, TRITC-labelled dextrans of different sizes were incorporated into the gel during the assembly process and the fluorescence intensity in the supernatant aqueous solution was monitored over time (Figure 6, S20).⁴⁶ A continuous release for all dextrans is observed, which scales with their size. In the first few minutes, the intensity increases rapidly which is presumably due to probe molecules attached to the gel surface or enclosed in the outermost layer of the gel. By fitting an exponential model, a similar exponent could be calculated for all dextran sizes, meaning the same diffusion mechanism independent of the size of the probe molecule can be expected (Figure 6A). Interestingly, even low-molar mass

substances can be enclosed in the gel and continuously released over several hours, which is again attributed to the hydration of the PEO chains and their extension into the aqueous phase of the gel. We exemplarily demonstrate this effect with the sodium salt of fluorescein (Figure S20B). Here an exponential function can be fitted with an exponent of 0.5 resembling the Fickian diffusion and no sign of a strong burst release in the beginning.⁴⁷ After 80 h a quantitative release is observed (equal intensities in both gel and supernatant). The Fickian diffusion indicates that the dye is not significantly interacting with the polymer network, while the high density of the PEO-chains appears to significantly slow down the diffusion of the small molecule. These diffusion tests further corroborate the excellent stability of the gel, as even after seven days of immersion in water, no swelling and degradation of the gel become apparent (Figure 6B).

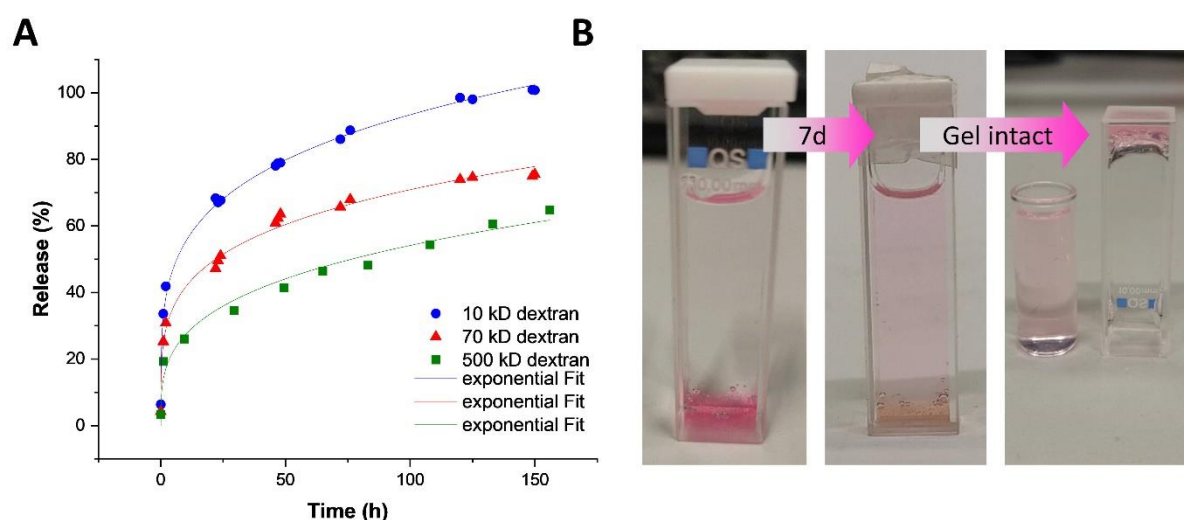


Figure 6 Diffusion kinetics of TRITC-dextrans of different molar mass followed by fluorescence spectroscopy (A). Color-change of the water in the cuvette after seven days and high stability of the gel even after immersion in water (B)

Besides these intrinsic properties of the gel state, we were further interested in the behavior of the materials under shear, since the observed liquification may open opportunities to inject or even print these gels similar to other shear-thinning materials.⁴⁸⁻⁵⁰ Therefore, rheology measurements under continuous shear stress were conducted to evaluate the proportionality of the shear rate $\dot{\gamma}$ on the viscosity. Figure 7A depicts the response of viscosity with increasing shear rate, which reveals a linear decrease in this double logarithmic plot, as it appears for nearly all compositions at higher shear rates (Figure S7A). Interestingly, no yield point can be observed in the measured shear rate and shear stress regime for gels with concentrations $> 5 \text{ mg mL}^{-1}$ (Figure S7B and C). Since the measured data is characteristic of the flow regime, the yield point is expected to occur at even lower shear rates and stresses, which is rather surprising considering the strength of the gel in oscillating measurements. The viscosity

decreases rapidly for all gel compositions at increasing shear rates, which implies an enhanced shear-thinning behavior. Very low viscosities are already reached for all samples at limited shear rates of 5 s^{-1} which resemble characteristics of PEO in water at similar concentrations although with higher average molar masses (around 10^6 g mol^{-1}).^{51, 52} The addition of the crosslinker increases the viscosity in general by approximately a factor of 10 compared to the non-crosslinked gel **1** with 0 % **2a**, which is similar to the improvement in the modulus. The shear-thinning behavior can further be quantified by fitting the linear regime of the viscosity to a power law that is described by the consistency index, K , and shear-thinning parameter, n (Eq. 1).^{50, 53} Therefore, only the linear regions at higher shear rates were considered for the suitable samples (Table 1, Figure S8). Interestingly, the herein presented systems gave very low values for both n and K compared to established systems like Alginate or Poloxamer polymers, which either feature higher values for n or K , respectively.^{54, 55} We assume that the shear-thinning behavior is strongly enhanced by the supramolecular nature and brush structure of the SPB hydrogel as compared, for instance, to physically linked Poloxamer and poly(ethylene glycol)–diacrylate (PEG-DA) hydrogels.⁵⁵

$$\eta = K\dot{\gamma}^{n-1} \quad \text{Eq. 1}$$

Table 1 Fitted shear-thinning parameter n and consistency index K for different gel compositions.

Gel	n	K (Pa s ^{n})
0 % 2a , 25 mg mL ⁻¹	0.07979	2.1272
1 % 2a , 25 mg mL ⁻¹	0.14637	22.96811
10 % 2a , 25 mg mL ⁻¹	0.27144	24.40954
50 % 2a , 25 mg mL ⁻¹	0.31115	25.56372
1 % 2a , 5 mg mL ⁻¹	0.09689	0.71141
1 % 2a , 10 mg mL ⁻¹	0.14439	1.45285
10 % 2a , 50 mg mL ⁻¹	0.14202	142.97

These low viscosities and the rapid recovery intrigued us further to test the potential of the material for direct printing. To evaluate their suitability for this processing technique, we established a simple rapid-prototyping (RP) setup to test the printing of various shapes based

on simple CAD models.⁵⁶⁻⁵⁸ Therefore, a common 3D printer was modified by attaching a cannula to its print head, which is further connected to a syringe pump *via* flexible tubings providing a continuous flow of liquified gel (Figure S21A). We started the tests by printing single straight lines of the gels of **1** with 1 % **2a** at 10, 25, and 50 mg mL⁻¹ at printing velocities of 36 mm s⁻¹. Using concentrations of 25 and 10 mg mL⁻¹ smooth lines could be extruded, which corroborates that for both gels, the viscosity at the apparent shear rate is sufficiently low to facilitate an easy extrusion through the nozzle. For a higher concentration of 50 mg mL⁻¹, some limitations became obvious, as irregular clogging of the capillary was observed at the applied speed (using a 20 Gauge cannula) (Figure 7C). We did not further consider optimizing the conditions for this material and focused on the lower concentrations. Apart from their good extrusion through the needle, the gel should also reform immediately after leaving the needle tip, meaning the gel should exhibit no or weak thixotropy to form defined structures. Additionally, the formed structures should be stable, implying the gel to be of a certain strength. These prerequisites are not met by a gel of 10 mg mL⁻¹, since it already shows a slight line broadening, meaning thixotropic behavior. Using the 25 mg mL⁻¹ gel with 1% crosslinker **2a** more defined lines could be printed due to its suitable balance between shear-thinning and mechanical strength at zero stress. Since the gel recovers rapidly after extrusion from the needle tip, even irregular shapes such as stars could be printed (Figure 7D). The high strength of this gel even enables the printing of lines on top of each other. In consequence, we were able to print a hollow self-supporting cylinder as a first proof of concept for creating 3-dimensional self-sustaining structures (Figure 7B, Movie in SI), which is astonishing considering the underlying nanostructure of the gel. Similar to the line tests, the lower concentration of 10 mg mL⁻¹ lacks the required mechanical strength and, thus, prints are not able to support their weight (Figure S21B).

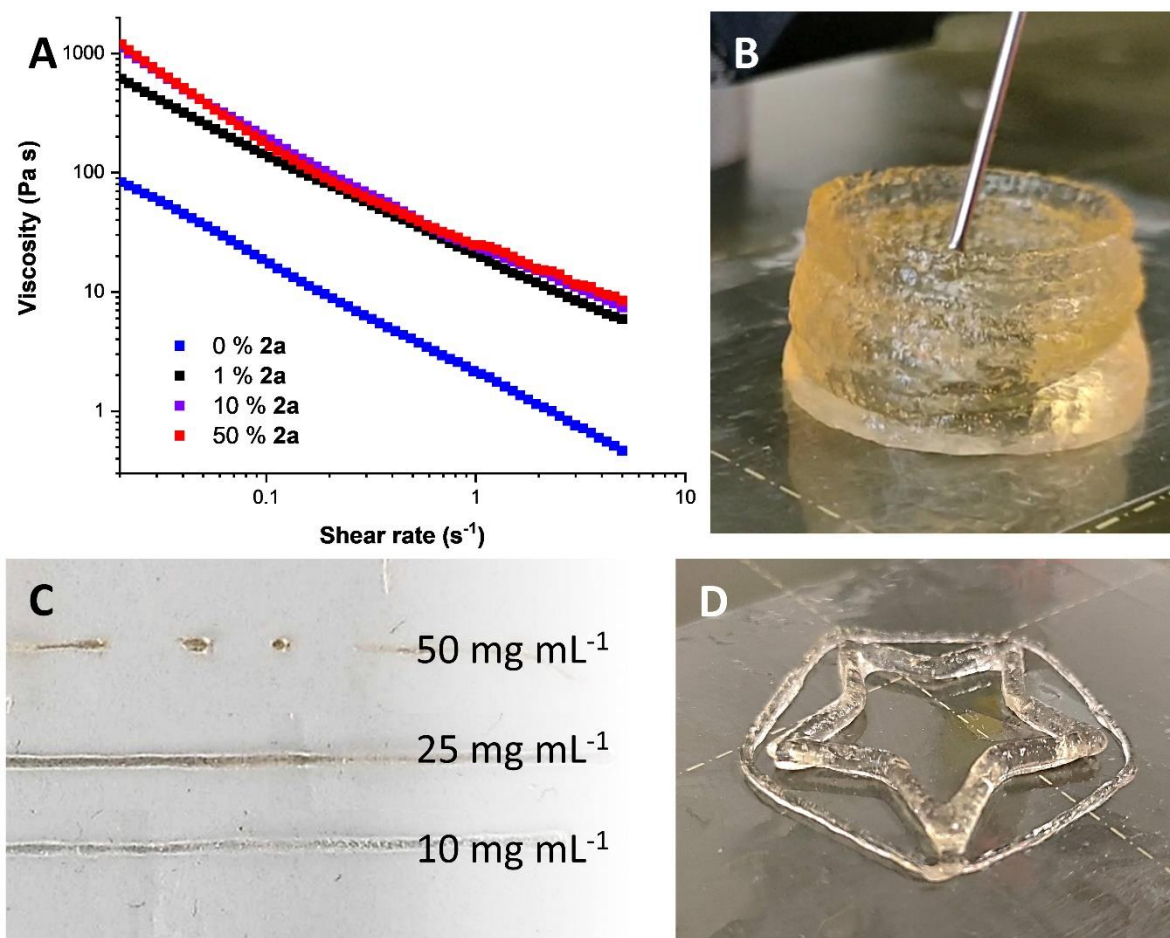


Figure 7 Shear rate-dependent viscosity behavior of pure BTU gel **1** and gel of **1** with different amounts of crosslinker **2a** ($c = 25 \text{ mg mL}^{-1}$) (A). 3D printed hollow cylinder with a gel of **1** with 1% **2a** ($c = 25 \text{ mg mL}^{-1}$) (B). Printed straight lines of 50, 25 and 10 mg mL⁻¹ gels of **1** with 1% **2a** (C). 3D printed star with a gel of **1** with 1% **2a** ($c = 25 \text{ mg mL}^{-1}$) (D).

Conclusion

The presented 1D polymer self-assemblies based on supramolecular interactions facilitate the preparation of hydrogels which resemble much of the character of fibrillar networks based on amphiphilic block copolymers. While the pure structures form rather weak gels solely based on entanglements, the introduction of a bifunctional crosslinker significantly enhances the strength of the network due to the bridging between individual fibers resulting in robust hydrogels with storage moduli up to the kPa range. In contrast to most other fibrillar polymer structures, the gels feature a strong shear thinning character but reform rapidly as soon as the stress is relieved. Full recovery of the initial strength is observed within seconds. Dynamic exchange of single building blocks as known from other supramolecular gelators however is absent and a different mechanism must account for the observed effect. We assume that at high strain the supramolecular fibers break and hydrophobic patches are formed at the extremities of the

broken fibers, which rapidly re-aggregate in the absence of shear forces. Due to the lack of dynamics, these hydrogels feature exceptional stability and remain unaffected even when immersed in water. The gel formation further tolerates acidic or basic conditions as well as the presence of salt or serum-containing media. Further preliminary cell tests revealed that cells still proliferate normally in close proximity to the gel, while they cannot adhere to the gel surface. We assume that the dense PEO corona in the bottlebrush fibers prevents cellular adherence, which may open the opportunity to selectively control cell growth by introduction of specific receptors and growth factors. The diffusion of compounds within and out of gel is further maintained, although PFG-NMR measurements reveal strong retardation of macromolecules, which is again related to the hydrated polymer corona of the fibers. Interestingly, similar retardation is observed for small molecules as exemplarily demonstrated for a dye, is challenging to realize in hydrogels and usually requires the modification of the small compounds with reversibly bound polymers.⁵⁹

Overall, the excellent self-healing abilities, the strong shear-thinning properties together with preliminary biocompatibility renders these supramolecular polymer bottlebrush hydrogels promising candidates for potential applications as injectable hydrogel reservoir or 3D cell scaffold, as it has been demonstrated for other supramolecular systems.^{34, 56, 60-62} Considering rapid prototyping, high stability even serum-containing media, and the low pressure required for extrusion might open opportunities for an accelerated printing procedure, offering possibilities for the processing of sensitive materials.^{48-50, 54, 62-65} Additionally, the application as a hydrogel drug reservoir would be feasible due to the limited force needed to administer the compound via subcutaneous injection (Figure S9).^{29, 59, 66} Hereby, the fibrillar microstructure with a dense polymer corona on the surface not only minimizes undesired protein adsorption and cellular interactions but also opens up the opportunity for versatile functionalization without corrupting the gel stability.

Associated content

Experimental details, detailed characterization, preparation of the gels, rheological measurements, stability tests by photo-bleaching recovery measurements, cytotoxicity tests, light scattering and pulse-field-gradient NMR measurements, fluorescence spectroscopy and 3D-printing.

The following files are available free of charge.

Supporting information (PDF)

3D-printing of **1** + 1% **2a** at 25 mg mL⁻¹ (movie)

Author Information

Corresponding Author

Johannes Christopher Brendel - Laboratory of Organic and Macromolecular Chemistry (IOMC), Friedrich Schiller University Jena, Humboldtstraße 10, 07743 Jena, Germany; Email: johannes.brendel@uni-jena.de; orchid.org/0000-0002-1206-1375

Authors

Franka V. Gruschwitz - Laboratory of Organic and Macromolecular Chemistry (IOMC), Friedrich Schiller University Jena, Humboldtstraße 10, 07743 Jena, Germany

Franziska Hausig - Laboratory of Organic and Macromolecular Chemistry (IOMC), Friedrich Schiller University Jena, Humboldtstraße 10, 07743 Jena, Germany

Philipp Schüler - Laboratory of Organic and Macromolecular Chemistry (IOMC)/ Institute for Inorganic and Analytical Chemistry (IAAC) NMR platform, Friedrich Schiller University Jena, Humboldtstraße 10, 07743 Jena, Germany

Julian Kimmig - Laboratory of Organic and Macromolecular Chemistry (IOMC), Friedrich Schiller University Jena, Humboldtstraße 10, 07743 Jena, Germany

David Pretzel - Laboratory of Organic and Macromolecular Chemistry (IOMC), Friedrich Schiller University Jena, Humboldtstraße 10, 07743 Jena, Germany

Ulrich S. Schubert - Laboratory of Organic and Macromolecular Chemistry (IOMC), Friedrich Schiller University Jena, Humboldtstraße 10, 07743 Jena, Germany; orchid.org/0000-0003-4978-4670

Sylvain Catrouillet - ICGM, Université de Montpellier, CNRS, ENSCM, Montpellier, France

Author Contributions

The manuscript was written through contributions of all authors. All authors have given approval to the final version of the manuscript.

Acknowledgements

FVG and JCB thank the German Science Foundation (DFG) for generous funding within the Emmy-Noether Programme (Project-ID: 358263073). C. Kellner is thanked for conducting the cell culture maintenance and her help in cytotoxicity studies. M. Dirauf, N. Göppert and M. Kleinstaubler are acknowledged for synthesizing the PEtOx polymers.

References

1. Truong, N. P.; Quinn, J. F.; Whittaker, M. R.; Davis, T. P., Polymeric filomicelles and nanoworms: two decades of synthesis and application. *Polym. Chem.* **2016**, 7, (26), 4295-4312.
2. Prince, E.; Kumacheva, E., Design and applications of man-made biomimetic fibrillar hydrogels. *Nat. Rev. Mater.* **2019**, 4, (2), 99-115.
3. Goor, O. J. G. M.; Hendrikse, S. I. S.; Dankers, P. Y. W.; Meijer, E. W., From supramolecular polymers to multi-component biomaterials. *Chem. Soc. Rev.* **2017**, 46, (21), 6621-6637.
4. Theocharis, A. D.; Skandalis, S. S.; Gialeli, C.; Karamanos, N. K., Extracellular matrix structure. *Adv. Drug Del. Rev.* **2016**, 97, 4-27.
5. Hess, H.; Ross, J. L., Non-equilibrium assembly of microtubules: from molecules to autonomous chemical robots. *Chem. Soc. Rev.* **2017**, 46, (18), 5570-5587.
6. MacKintosh, F. C.; Käs, J.; Janmey, P. A., Elasticity of Semiflexible Biopolymer Networks. *Phys. Rev. Lett.* **1995**, 75, (24), 4425-4428.
7. Taribagil, R. R.; Hillmyer, M. A.; Lodge, T. P., Hydrogels from ABA and ABC Triblock Polymers. *Macromolecules* **2010**, 43, (12), 5396-5404.
8. Tsitsilianis, C., Responsive reversible hydrogels from associative "smart" macromolecules. *Soft Matter* **2010**, 6, (11), 2372-2388.
9. Qian, J.; Zhang, M.; Manners, I.; Winnik, M. A., Nanofiber micelles from the self-assembly of block copolymers. *Trends Biotechnol.* **2010**, 28, (2), 84-92.
10. Israelachvili, J., Physical Principles of Surfactant Self-Association Into Micelles, Bilayers, Vesicles and Microemulsion Droplets. In *Surfactants in Solution*, Mittal, K. L.; Bothorel, P., Eds. Springer US: Boston, MA, 1986; pp 3-33.
11. Israelachvili, J. N.; Mitchell, D. J.; Ninham, B. W., Theory of Self-Assembly of Hydrocarbon Amphiphiles into Micelles and Bilayers. *J. Chem. Soc., Faraday Trans. 2* **1976**, 72, (0), 1525-1568.
12. Brendel, J. C.; Schacher, F. H., Block Copolymer Self-Assembly in Solution-Quo Vadis? *Chem Asian J* **2018**, 13, (3), 230-239.
13. Gruschwitz, F. V.; Klein, T.; Catrouillet, S.; Brendel, J. C., Supramolecular polymer bottlebrushes. *Chem. Commun.* **2020**, 56, (38), 5079-5110.
14. Schmelz, J.; Schacher, F. H.; Schmalz, H., Cylindrical crystalline-core micelles: pushing the limits of solution self-assembly. *Soft Matter* **2013**, 9, (7), 2101-2107.
15. Blanazs, A.; Verber, R.; Mykhaylyk, O. O.; Ryan, A. J.; Heath, J. Z.; Douglas, C. W. I.; Armes, S. P., Sterilizable Gels from Thermoresponsive Block Copolymer Worms. *J. Am. Chem. Soc.* **2012**, 134, (23), 9741-9748.
16. Malo de Molina, P.; Gradzielski, M., Gels Obtained by Colloidal Self-Assembly of Amphiphilic Molecules. *Gels* **2017**, 3, (3), 30.
17. Won, Y.-Y.; Davis, H. T.; Bates, F. S., Giant Wormlike Rubber Micelles. *Science* **1999**, 283, (5404), 960.

18. Won, Y.-Y.; Paso, K.; Davis, H. T.; Bates, F. S., Comparison of Original and Cross-linked Wormlike Micelles of Poly(ethylene oxide-*b*-butadiene) in Water: Rheological Properties and Effects of Poly(ethylene oxide) Addition. *J. Phys. Chem. B* **2001**, 105, (35), 8302-8311.
19. Raghavan, S. R.; Douglas, J. F., The conundrum of gel formation by molecular nanofibers, wormlike micelles, and filamentous proteins: gelation without cross-links? *Soft Matter* **2012**, 8, (33), 8539-8546.
20. Verber, R.; Blanazs, A.; Armes, S. P., Rheological studies of thermo-responsive diblock copolymer worm gels. *Soft Matter* **2012**, 8, (38), 9915-9922.
21. Lovett, J. R.; Ratcliffe, L. P. D.; Warren, N. J.; Armes, S. P.; Smallridge, M. J.; Cracknell, R. B.; Saunders, B. R., A Robust Cross-Linking Strategy for Block Copolymer Worms Prepared via Polymerization-Induced Self-Assembly. *Macromolecules* **2016**, 49, (8), 2928-2941.
22. Sponchioni, M.; O'Brien, C. T.; Borchers, C.; Wang, E.; Rivolta, M. N.; Penfold, N. J. W.; Canton, I.; Armes, S. P., Probing the mechanism for hydrogel-based stasis induction in human pluripotent stem cells: is the chemical functionality of the hydrogel important? *Chem. Sci.* **2020**, 11, (1), 232-240.
23. Penfold, N. J. W.; Whatley, J. R.; Armes, S. P., Thermoreversible Block Copolymer Worm Gels Using Binary Mixtures of PEG Stabilizer Blocks. *Macromolecules* **2019**, 52, (4), 1653-1662.
24. Canton, I.; Warren, N. J.; Chahal, A.; Amps, K.; Wood, A.; Weightman, R.; Wang, E.; Moore, H.; Armes, S. P., Mucin-Inspired Thermoresponsive Synthetic Hydrogels Induce Stasis in Human Pluripotent Stem Cells and Human Embryos. *ACS Cent. Sci.* **2016**, 2, (2), 65-74.
25. Simon, K. A.; Warren, N. J.; Mosadegh, B.; Mohammady, M. R.; Whitesides, G. M.; Armes, S. P., Disulfide-Based Diblock Copolymer Worm Gels: A Wholly-Synthetic Thermoreversible 3D Matrix for Sheet-Based Cultures. *Biomacromolecules* **2015**, 16, (12), 3952-3958.
26. Warren, N. J.; Rosselgong, J.; Madsen, J.; Armes, S. P., Disulfide-Functionalized Diblock Copolymer Worm Gels. *Biomacromolecules* **2015**, 16, (8), 2514-2521.
27. Nicolai, T.; Colombani, O.; Chassenieux, C., Dynamic polymeric micelles versus frozen nanoparticles formed by block copolymers. *Soft Matter* **2010**, 6, (14), 3111-3118.
28. Hayward, R. C.; Pochan, D. J., Tailored Assemblies of Block Copolymers in Solution: It Is All about the Process. *Macromolecules* **2010**, 43, (8), 3577-3584.
29. Cheng, J.; Amin, D.; Latona, J.; Heber-Katz, E.; Messersmith, P. B., Supramolecular Polymer Hydrogels for Drug-Induced Tissue Regeneration. *ACS Nano* **2019**, 13, (5), 5493-5501.
30. Hamley, I. W.; Cheng, G.; Castelletto, V., A Thermoresponsive Hydrogel Based on Telechelic PEG End-Capped with Hydrophobic Dipeptides. *Macromol. Biosci.* **2011**, 11, (8), 1068-1078.
31. KIELTYKA, R. E.; PAPE, A. C. H.; ALBERTAZZI, L.; NAKANO, Y.; BASTINGS, M. M. C.; VOETS, I. K.; DANKERS, P. Y. W.; MEIJER, E. W., Mesoscale Modulation of Supramolecular Ureidopyrimidinone-Based Poly(ethylene glycol) Transient Networks in Water. *J. Am. Chem. Soc.* **2013**, 135, (30), 11159-11164.
32. Gao, Y.; Zhao, F.; Wang, Q.; Zhang, Y.; Xu, B., Small peptide nanofibers as the matrices of molecular hydrogels for mimicking enzymes and enhancing the activity of enzymes. *Chem. Soc. Rev.* **2010**, 39, (9), 3425-3433.
33. Yokoi, H.; Kinoshita, T.; Zhang, S., Dynamic reassembly of peptide RADA16 nanofiber scaffold. *Proc. Natl. Acad. Sci. U.S.A* **2005**, 102, (24), 8414.

34. Wang, Y.; Li, J.; Li, Y.; Yang, B., Biomimetic bioinks of nanofibrillar polymeric hydrogels for 3D bioprinting. *Nano Today* **2021**, *39*, 101180.
35. Gruschwitz, F. V.; Klein, T.; Kuchenbrod, M. T.; Moriyama, N.; Fujii, S.; Nischang, I.; Hoepfner, S.; Sakurai, K.; Schubert, U. S.; Brendel, J. C., Kinetically Controlling the Length of Self-Assembled Polymer Nanofibers Formed by Intermolecular Hydrogen Bonds. *ACS Macro Lett.* **2021**, *10*, (7), 837-843.
36. Gruschwitz, F. V.; Fu, M.-C.; Klein, T.; Takahashi, R.; Higashihara, T.; Hoepfner, S.; Nischang, I.; Sakurai, K.; Brendel, J. C., Unraveling Decisive Structural Parameters for the Self-Assembly of Supramolecular Polymer Bottlebrushes Based on Benzene Trisureas. *Macromolecules* **2020**, *53*, (17), 7552-7560.
37. Saunders, L.; Ma, P. X., Self-Healing Supramolecular Hydrogels for Tissue Engineering Applications. *Macromol. Biosci.* **2019**, *19*, (1), 1800313.
38. Strandman, S.; Zhu, X. X., Self-Healing Supramolecular Hydrogels Based on Reversible Physical Interactions. *Gels* **2016**, *2*, (2), 16.
39. Bastings, M. M. C.; Koudstaal, S.; Kieltyka, R. E.; Nakano, Y.; Pape, A. C. H.; Feyen, D. A. M.; van Slochteren, F. J.; Doevendans, P. A.; Sluijter, J. P. G.; Meijer, E. W.; Chamuleau, S. A. J.; Dankers, P. Y. W., A Fast pH-Switchable and Self-Healing Supramolecular Hydrogel Carrier for Guided, Local Catheter Injection in the Infarcted Myocardium. *Adv. Healthcare Mater.* **2014**, *3*, (1), 70-78.
40. Vereroudakis, E.; Bantawa, M.; Lafleur, R. P. M.; Parisi, D.; Matsumoto, N. M.; Peeters, J. W.; Del Gado, E.; Meijer, E. W.; Vlassopoulos, D., Competitive Supramolecular Associations Mediate the Viscoelasticity of Binary Hydrogels. *ACS Cent. Sci.* **2020**, *6*, (8), 1401-1411.
41. Noteborn, W. E. M.; Zwagerman, D. N. H.; Talens, V. S.; Maity, C.; van der Mee, L.; Poolman, J. M.; Mytnyk, S.; van Esch, J. H.; Kros, A.; Eelkema, R.; Kieltyka, R. E., Crosslinker-Induced Effects on the Gelation Pathway of a Low Molecular Weight Hydrogel. *Adv. Mater.* **2017**, *29*, (12), 1603769.
42. Baker, M. B.; Gosens, R. P. J.; Albertazzi, L.; Matsumoto, N. M.; Palmans, A. R. A.; Meijer, E. W., Exposing Differences in Monomer Exchange Rates of Multicomponent Supramolecular Polymers in Water. *ChemBioChem* **2016**, *17*, (3), 207-213.
43. Mukhopadhyay, P.; Fujita, N.; Takada, A.; Kishida, T.; Shirakawa, M.; Shinkai, S., Regulation of a Real-Time Self-Healing Process in Organogel Tissues by Molecular Adhesives. *Angew. Chem. Int. Ed.* **2010**, *49*, (36), 6338-6342.
44. Xu, Z.; Peng, J.; Yan, N.; Yu, H.; Zhang, S.; Liu, K.; Fang, Y., Simple design but marvelous performances: molecular gels of superior strength and self-healing properties. *Soft Matter* **2013**, *9*, (4), 1091-1099.
45. Knoben, W.; Besseling, N. A. M.; Bouteiller, L.; Cohen Stuart, M. A., Dynamics of reversible supramolecular polymers: Independent determination of the dependence of linear viscoelasticity on concentration and chain length by using chain stoppers. *Phys. Chem. Chem. Phys.* **2005**, *7*, (11), 2390-2398.
46. Hagel, V.; Haraszti, T.; Boehm, H., Diffusion and interaction in PEG-DA hydrogels. *Biointerphases* **2013**, *8*, (1), 36.
47. Ritger, P. L.; Peppas, N. A., A simple equation for description of solute release II. Fickian and anomalous release from swellable devices. *J. Control. Release* **1987**, *5*, (1), 37-42.
48. Amorim, P. A.; d'Ávila, M. A.; Anand, R.; Moldenaers, P.; Van Puyvelde, P.; Bloemen, V., Insights on shear rheology of inks for extrusion-based 3D bioprinting. *Bioprinting* **2021**, *22*, e00129.

49. Blaeser, A.; Duarte Campos, D. F.; Puster, U.; Richtering, W.; Stevens, M. M.; Fischer, H., Controlling Shear Stress in 3D Bioprinting is a Key Factor to Balance Printing Resolution and Stem Cell Integrity. *Adv. Healthcare Mater.* **2016**, 5, (3), 326-333.
50. Zandi, N.; Sani, E. S.; Mostafavi, E.; Ibrahim, D. M.; Saleh, B.; Shokrgozar, M. A.; Tamjid, E.; Weiss, P. S.; Simchi, A.; Annabi, N., Nanoengineered shear-thinning and bioprintable hydrogel as a versatile platform for biomedical applications. *Biomaterials* **2021**, 267, 120476.
51. Gonzalez-Tello, P.; Camacho, F.; Blazquez, G., Density and Viscosity of Concentrated Aqueous Solutions of Polyethylene Glycol. *Journal of Chemical & Engineering Data* **1994**, 39, (3), 611-614.
52. Ebagninin, K. W.; Benchabane, A.; Bekkour, K., Rheological characterization of poly(ethylene oxide) solutions of different molecular weights. *J. Colloid Interface Sci.* **2009**, 336, (1), 360-367.
53. Macosko, C. W., *Rheology: Principles, Measurements, and Applications*. Wiley-VCH: New York, 1994.
54. Paxton, N.; Smolan, W.; Bock, T.; Melchels, F.; Groll, J.; Jungst, T., Proposal to assess printability of bioinks for extrusion-based bioprinting and evaluation of rheological properties governing bioprintability. *Biofabrication* **2017**, 9, (4), 044107.
55. Kraut, G.; Yenchsky, L.; Prieto, F.; Tovar, G. E. M.; Southan, A., Influence of shear thinning and material flow on robotic dispensing of poly(ethylene glycol) diacrylate/poloxamer 407 hydrogels. *J. Appl. Polym. Sci.* **2017**, 134, (29), 45083.
56. Landers, R.; Pfister, A.; Hübner, U.; John, H.; Schmelzeisen, R.; Mülhaupt, R., Fabrication of soft tissue engineering scaffolds by means of rapid prototyping techniques. *J. Mater. Sci.* **2002**, 37, (15), 3107-3116.
57. Hockaday, L. A.; Kang, K. H.; Colangelo, N. W.; Cheung, P. Y. C.; Duan, B.; Malone, E.; Wu, J.; Girardi, L. N.; Bonassar, L. J.; Lipson, H.; Chu, C. C.; Butcher, J. T., Rapid 3D printing of anatomically accurate and mechanically heterogeneous aortic valve hydrogel scaffolds. *Biofabrication* **2012**, 4, (3), 035005-035005.
58. Duan, B.; Hockaday, L. A.; Kang, K. H.; Butcher, J. T., 3D bioprinting of heterogeneous aortic valve conduits with alginate/gelatin hydrogels. *J. Biomed. Mater. Res. A* **2013**, 101, (5), 1255-1264.
59. Correa, S.; Grosskopf, A. K.; Lopez Hernandez, H.; Chan, D.; Yu, A. C.; Stapleton, L. M.; Appel, E. A., Translational Applications of Hydrogels. *Chem. Rev.* **2021**.
60. Diba, M.; Spaans, S.; Hendrikse, S. I. S.; Bastings, M. M. C.; Schotman, M. J. G.; van Sprang, J. F.; Wu, D. J.; Hoeben, F. J. M.; Janssen, H. M.; Dankers, P. Y. W., Engineering the Dynamics of Cell Adhesion Cues in Supramolecular Hydrogels for Facile Control over Cell Encapsulation and Behavior. *Adv. Mater.* **2021**, 33, (37), e2008111.
61. Schacht, K.; Jüngst, T.; Schweinlin, M.; Ewald, A.; Groll, J.; Scheibel, T., Biofabrication of Cell-Loaded 3D Spider Silk Constructs. *Angew. Chem. Int. Ed.* **2015**, 54, (9), 2816-2820.
62. Moroni, L.; Burdick, J. A.; Highley, C.; Lee, S. J.; Morimoto, Y.; Takeuchi, S.; Yoo, J. J., Biofabrication strategies for 3D in vitro models and regenerative medicine. *Nat. Rev. Mater.* **2018**, 3, (5), 21-37.
63. Chivers, P. R. A.; Smith, D. K., Shaping and structuring supramolecular gels. *Nat. Rev. Mater.* **2019**, 4, (7), 463-478.
64. Nolan, M. C.; Fuentes Caparrós, A. M.; Dietrich, B.; Barrow, M.; Cross, E. R.; Bleuel, M.; King, S. M.; Adams, D. J., Optimising low molecular weight hydrogels for automated 3D printing. *Soft Matter* **2017**, 13, (45), 8426-8432.
65. Sather, N. A.; Sai, H.; Sasselli, I. R.; Sato, K.; Ji, W.; Synatschke, C. V.; Zambrotta, R. T.; Edelbrock, J. F.; Kohlmeyer, R. R.; Hardin, J. O.; Berrigan, J. D.; Durstock, M. F.; Mirau, P.;

Stupp, S. I., 3D Printing of Supramolecular Polymer Hydrogels with Hierarchical Structure. *Small* **2021**, 17, (5), 2005743.

66. Lopez Hernandez, H.; Souza, J. W.; Appel, E. A., A Quantitative Description for Designing the Extrudability of Shear-Thinning Physical Hydrogels. *Macromol. Biosci.* **2021**, 21, (2), 2000295.

Supporting Information

Shear-thinning and rapidly recovering hydrogels of polymeric nanofibers formed by supramolecular self-assembly

Franka V. Gruschwitz,^{a,b} Franziska Hausig,^{a,b} Philipp Schüler,^c Julian Kimmig,^b David Pretzel,^b Ulrich S. Schubert,^{a,b} Sylvain Catrouillet,^{d,*} Johannes C. Brendel,^{a,b,*}

a Laboratory of Organic and Macromolecular Chemistry (IOMC), Friedrich Schiller University Jena, Humboldtstraße 10, 07743 Jena, Germany

b Jena Center for Soft Matter (JCSM), Friedrich Schiller University Jena, Philosophenweg 7, 07743 Jena, Germany

c IOMC/IAAC NMR platform, Friedrich Schiller University Jena, Humboldtstraße 10, 07743 Jena, Germany

d ICGM, Université de Montpellier, CNRS, ENSCM, Montpellier, France

*corresponding author: sylvain.catrouillet@umontpellier.fr; johannes.brendel@uni-jena.de

Content

1. Synthesis and characterization	26
2. Preparation of the gels	28
3. Rheology	29
4. Photo-bleaching recovery measurements	34
5. Stability of the gels	35
6. Cytotoxicity measurements	36
7. Moldability	37
8. Light scattering measurements	38
9. Pulse-field-gradient NMR spectroscopy	42
10. Fluorescence spectroscopy	45
11. 3D printing	46
References	47

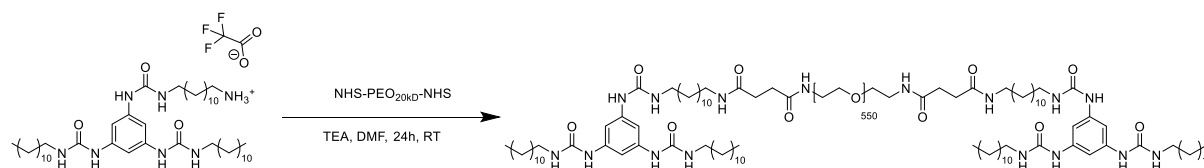
1. Synthesis and characterization

Materials and methods. All reagents and solvents were commercial products purchased from Sigma-Aldrich, Alfa Aesar, Rapp Polymere or TCI and were used without further purification. ^1H -NMR spectra were measured with a Bruker spectrometer (300 MHz) equipped with an Avance I console, a dual ^1H and ^{13}C sample head and a 120x BACS automatic sample changer. The chemical shifts of the peaks were determined by using the residual solvent signal as reference and are given in ppm in comparison to TMS. Size-exclusion chromatography (SEC) of polymers was performed on an Agilent system (series 1200) equipped with a PSS degasser, a G1310A pump, a G1362A refractive index detector and a PSS GRAM 30 and 1000 column with DMAc (+ 0.21 wt.% LiCl) as eluent at a flow rate of 1 mL min^{-1} . The column oven was set to $40\text{ }^\circ\text{C}$ and poly(ethylene oxide) (PEO) standards were used for calibration. Matrix-assisted laser desorption ionization mass spectrometry (MALDI-MS) measurements were carried out using an Ultraflex III ToF/ToF instrument (Bruker Daltonics) equipped with a Nd-YAG laser. All spectra were measured in the positive mode using α -cyano-4-hydroxycinnamic acid (CHCA) as matrix material.

Synthesis of BTU-PEO_{2k} 1

The detailed synthesis procedure of BTU-PEO_{2k} was published elsewhere.^[1]

Synthesis of the crosslinker BTU-PEO_{20k}-BTU 2a



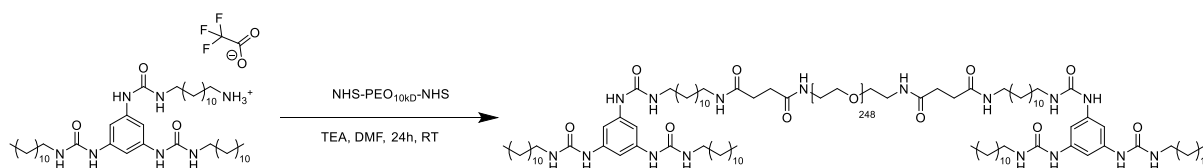
Scheme S 1 Schematic representation of the synthetic procedure for the crosslinker **BTU-PEO_{20k}-BTU 2a**.

The deprotected BTU core^[1] (0.020 g, 0.026 mmol, 2.0 eq) was dissolved in 3 mL DMF. To this, 0.04 mL triethylamine (0.26 mmol, 20 eq) were added dropwise. After stirring at rt for 15 min, 0.320 g of NHS-PEO_{20k}-NHS ester (0.013 mmol, 1.0 eq) were added and the reaction mixture stirred at rt overnight. Afterwards, the reaction mixture was precipitated into cold diethyl ether, the suspension centrifuged (10 min, 5,000 rpm) and the supernatant decanted. Then a mixture of diethyl ether and acetone (9:1, v:v) was added to the precipitate and the suspension exposed to sonication for 5 min in order to remove remaining unconjugated NHS-PEO_{20k}-NHS ester. Afterwards, the suspension was again centrifuged (10 min, 5,000 rpm) and the supernatant decanted. The obtained product was lyophilized overnight.

¹H-NMR (300 MHz, d₆-DMSO, 298 K): δ [ppm] = 8.27 (s, 6H, NH), 7.87 (t, J = 5.48, 2H, NH), 7.75 (s, J = 5.71 2H, NH), 7.09 (s, 6H, CH_{aromat}), 5.95 (t, J = 5.48 Hz, 6H, NH), 3.51 (s, 2267H, PEO), 3.18 (q, 6H, CH₂), 3.05 (m, 20H, CH₂), 2.27 (s, 8H, CH₂), 1.39 (m, 16H, CH₂), 1.24 (m, 116H, CH₂), 0.85 (t, J = 6.85 Hz, 12H, CH₃).

SEC (DMAc + 0.21 wt. % LiCl, PEO-Calibration): $M_n = 25,030 \text{ g mol}^{-1}$; $M_w = 30,066 \text{ g mol}^{-1}$; $\text{Đ} = 1.21$.

Synthesis of the crosslinker BTU-PEO_{10k}-BTU 2b



Scheme S 2 Schematic representation of the synthetic procedure for the crosslinker **BTU-PEO_{10k}-BTU 2b**.

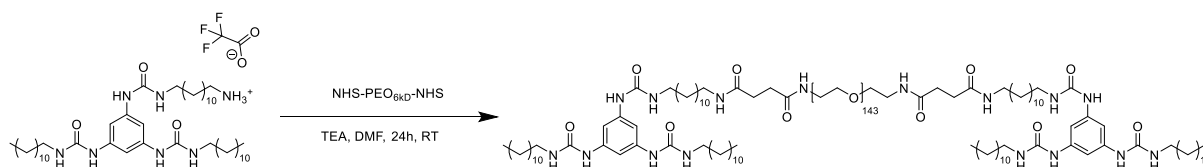
The compound was synthesized according to the procedure of compound **2a**.

¹H-NMR (300 MHz, d₆-DMSO, 298 K): δ [ppm] = 8.26 (s, 6H, NH), 7.86 (t, J = 5.48, 2H, NH), 7.75 (s, J = 5.71 2H, NH), 7.08 (s, 6H, CH_{aromat}), 5.94 (t, J = 5.48 Hz, 6H, NH), 3.51 (s, 992H, PEO), 3.18 (q, 6H, CH₂), 3.02 (m, 20H, CH₂), 2.27 (s, 8H, CH₂), 1.39 (m, 16H, CH₂), 1.24 (m, 120H, CH₂), 0.85 (t, J = 6.85 Hz, 12H, CH₃).

SEC (DMAc + 0.21 wt. % LiCl, PEO-Calibration): $M_n = 17,398 \text{ g mol}^{-1}$; $M_w = 21,464 \text{ g mol}^{-1}$; $\text{Đ} = 1.21$.

MALDI-ToF-MS (positive mode, CHCA) (m/z): calculated for DP = 220 [C₅₄₀H₁₀₆₂N₁₆O₂₃₀Na]⁺: 11,483.4713; found: 11,483.477.

Synthesis of the crosslinker BTU-PEO_{6k}-BTU 2c



Scheme S 3 Schematic representation of the synthetic procedure for the crosslinker **BTU-PEO_{6k}-BTU 2c**.

The compound was synthesized according to the procedure of compound **2a**

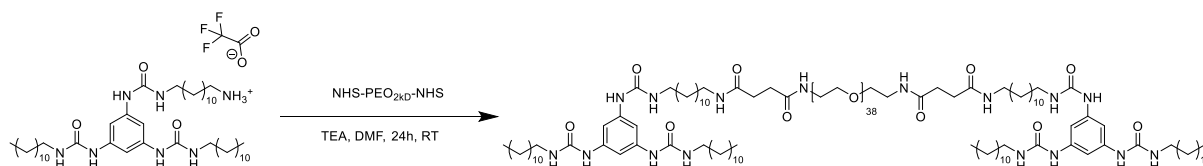
¹H-NMR (300 MHz, d₆-DMSO, 298 K): δ [ppm] = 8.26 (s, 6H, NH), 7.85 (t, J = 5.48, 2H, NH), 7.77 (s, J = 5.71 2H, NH), 7.09 (s, 6H, CH_{aromat}), 5.94 (t, J = 5.48 Hz, 6H, NH), 3.51 (s,

727H, PEO), 3.18 (q, 6H, CH₂), 3.03 (m, 20H, CH₂), 2.27 (s, 8H, CH₂), 1.38 (m, 16H, CH₂), 1.24 (m, 119H, CH₂), 0.85 (t, J = 6.85 Hz, 12H, CH₃).

SEC (DMAc + 0.21 wt. % LiCl, PEO-Calibration): $M_n = 10,961 \text{ g mol}^{-1}$; $M_w = 12,231 \text{ g mol}^{-1}$; $\bar{D} = 1.13$.

MALDI-ToF-MS (positive mode, CHCA) (m/z): calculated for DP = 120 $[\text{C}_{340}\text{H}_{662}\text{N}_{16}\text{O}_{130}\text{Na}]^+$: 7,077.5083; found: 7,077.2760.

Synthesis of the crosslinker BTU-PEO_{2k}-BTU 2d



Scheme S 4 Schematic representation of the synthetic procedure for the crosslinker **BTU-PEO_{2k}-BTU 2d**.

The compound was synthesized according to the procedure of compound **2a**

¹H-NMR (300 MHz, d₆-DMSO, 298 K): δ [ppm] = 8.26 (s, 6H, NH), 7.87 (t, J = 5.48, 2H, NH), 7.77 (s, J = 5.71 2H, NH), 7.09 (s, 6H, CH_{aromat}), 5.95 (t, J = 5.48 Hz, 6H, NH), 3.51 (s, 179H, PEO), 3.18 (q, J = 5.94 Hz, 6H, CH₂), 3.03 (m, 16H, CH₂), 2.27 (s, 8H, CH₂), 1.39 (m, 16H, CH₂), 1.24 (m, 116H, CH₂), 0.85 (t, J = 6.85 Hz, 12H, CH₃).

SEC (DMAc + 0.21 wt. % LiCl, PEO-Calibration): $M_n = 8,314 \text{ g mol}^{-1}$; $M_w = 9,083 \text{ g mol}^{-1}$; $\bar{D} = 1.12$.

MALDI-ToF-MS (positive mode, CHCA) (m/z): calculated for DP = 22

$[\text{C}_{144}\text{H}_{270}\text{N}_{16}\text{O}_{32}\text{Na}]^+$: 2,759.9917; found: 2,759.5420.

2. Preparation of the gels

The procedure resembles the solvent switch method published previously.^[2] The respective amount of BTU-PEO_{2k} **1** and crosslinker **2** were dissolved in 0.5 mL of THF and stirred for 10 min to guarantee complete dissolution. Subsequently, 1 mL of MilliQ water was added (1 mL h⁻¹) using a syringe pump under stirring to reach a final water content of 66 v%. The solution was transferred either to the measurement setup and left to evaporate for approx. 0.5 h or was filled in a syringe without the stamp to evaporate and gelate in the syringe for printing till all THF was evaporated. Transfer of the gel after evaporation was not feasible due to the strength of the gel and the formation of entrapped air bubbles, which would prevent a continuous

printing process. Removal of THF was ensured by $^1\text{H-NMR}$ spectroscopy and weighing of the sample.

3. Rheology

Methods and materials

The oscillatory dynamic measurements were performed with a Physica Modular Compact MCR301 Rheometer from Anton Paar (Germany). Mechanical properties of the viscoelastic hydrogel material were assayed using a parallel (PP 25 sandblasted)-plate geometry. The linear viscoelastic regime of the samples was obtained from amplitude sweep experiments that were performed from 0.1 to 200% strain at 6.36 rad s^{-1} angular frequency. Frequency sweep measurements were recorded from 0.1 to 100 rad s^{-1} at 1% strain. Measurements were performed at $20 \text{ }^\circ\text{C}$ unless stated otherwise.

Measurement data

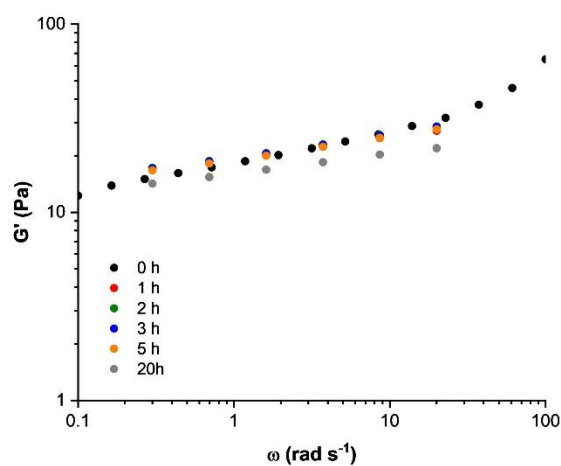


Figure S 1 Frequency-sweep measurements of gel 1 with 1% **2a** ($c = 25 \text{ mg mL}^{-1}$) after exposure to water for a distinct time.

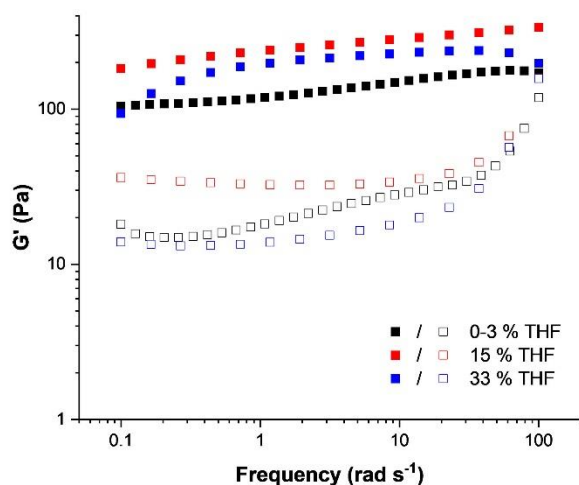


Figure S 2 Frequency-sweep measurements of gel **1** with 1% **2a** ($c = 25 \text{ mg mL}^{-1}$) and different amounts of THF.

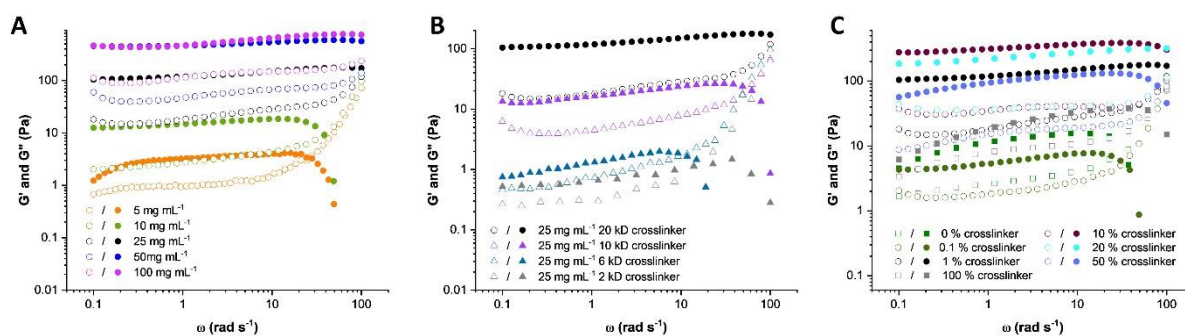


Figure S 3 Frequency-sweep measurements of gels of **1** with 1% **2a** at different concentrations (A), of **1** with 1% crosslinker of different lengths at a concentration of 25 mg mL^{-1} (B), and with different amount of **2a** crosslinker at 25 mg mL^{-1} (C).

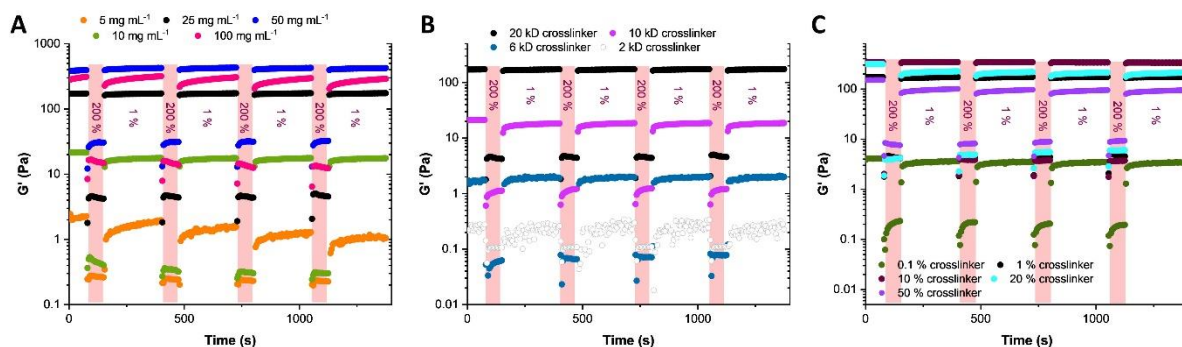


Figure S 4 Step-strain measurements of gels of **1** with 1% of crosslinker **2a** at different concentrations (A), with 1% of different lengths of crosslinkers at 25 mg mL^{-1} (B) and with different amounts of crosslinker **2a** at 25 mg mL^{-1} (C). The periods of high deformation (200%) are marked in red.

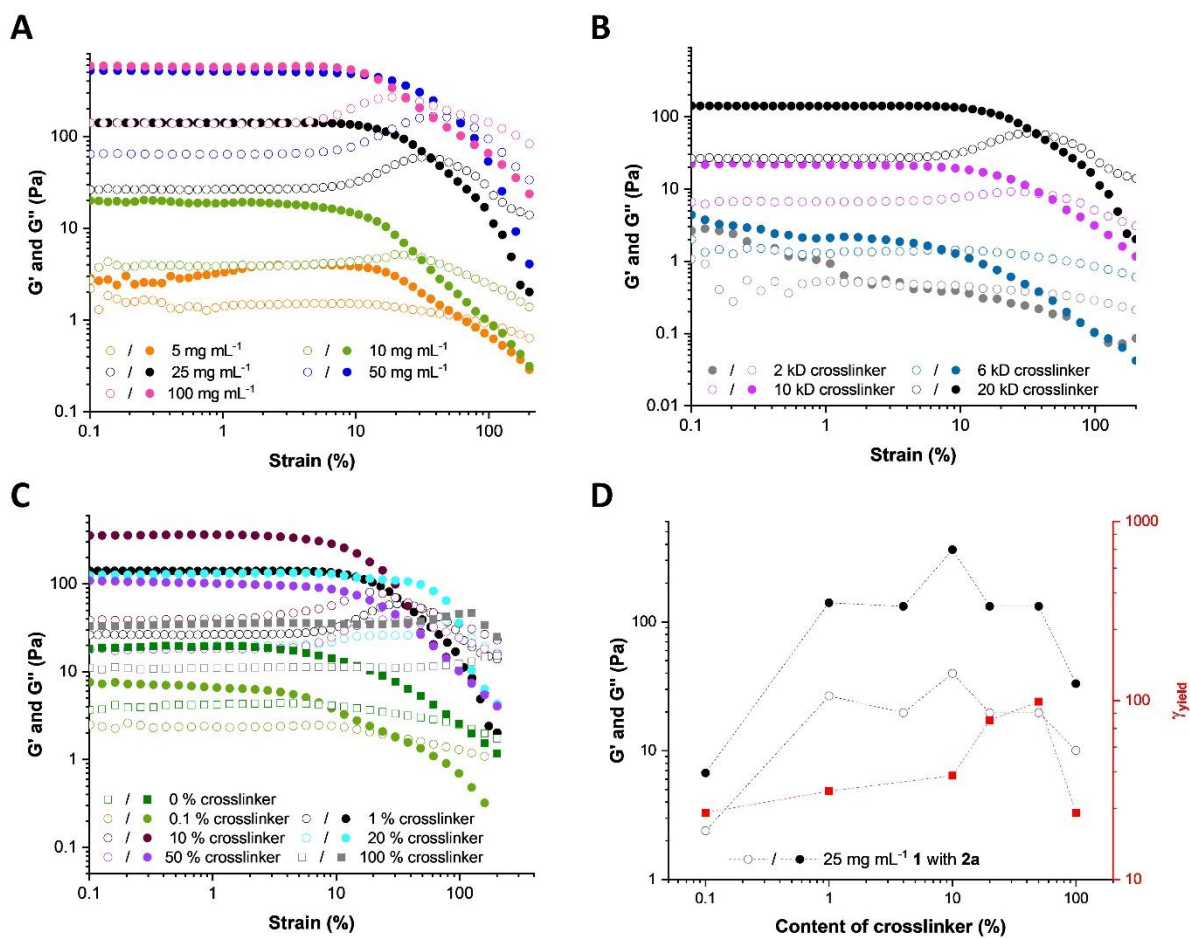


Figure S 5 Deformation measurements of gels of **1** with 1% **2a** at different concentrations (A), of **1** with 1% crosslinker of different lengths at a concentration of 25 mg mL⁻¹ (B), and with different amount of **2a** crosslinker at 25 mg mL⁻¹ (C). Dependence of the yield stress γ_{yield} and the storage/loss module on the amount of crosslinker **2a** ($c = 25 \text{ mg mL}^{-1}$) (D).

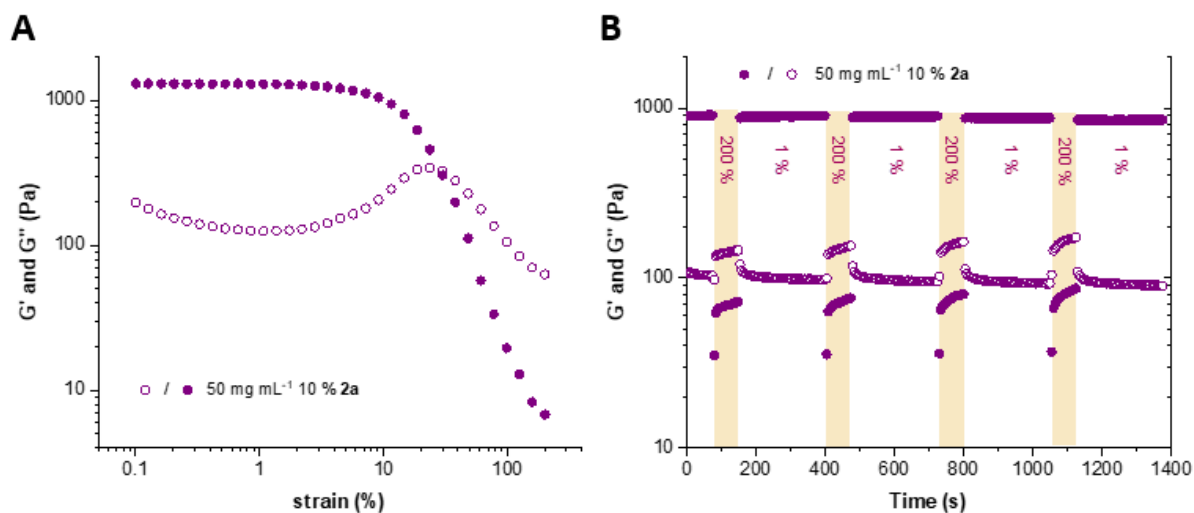


Figure S 6 Strain-sweep (A) and step-strain measurements (B) of gel **1** with 10% **2a** at 50 mg mL⁻¹.

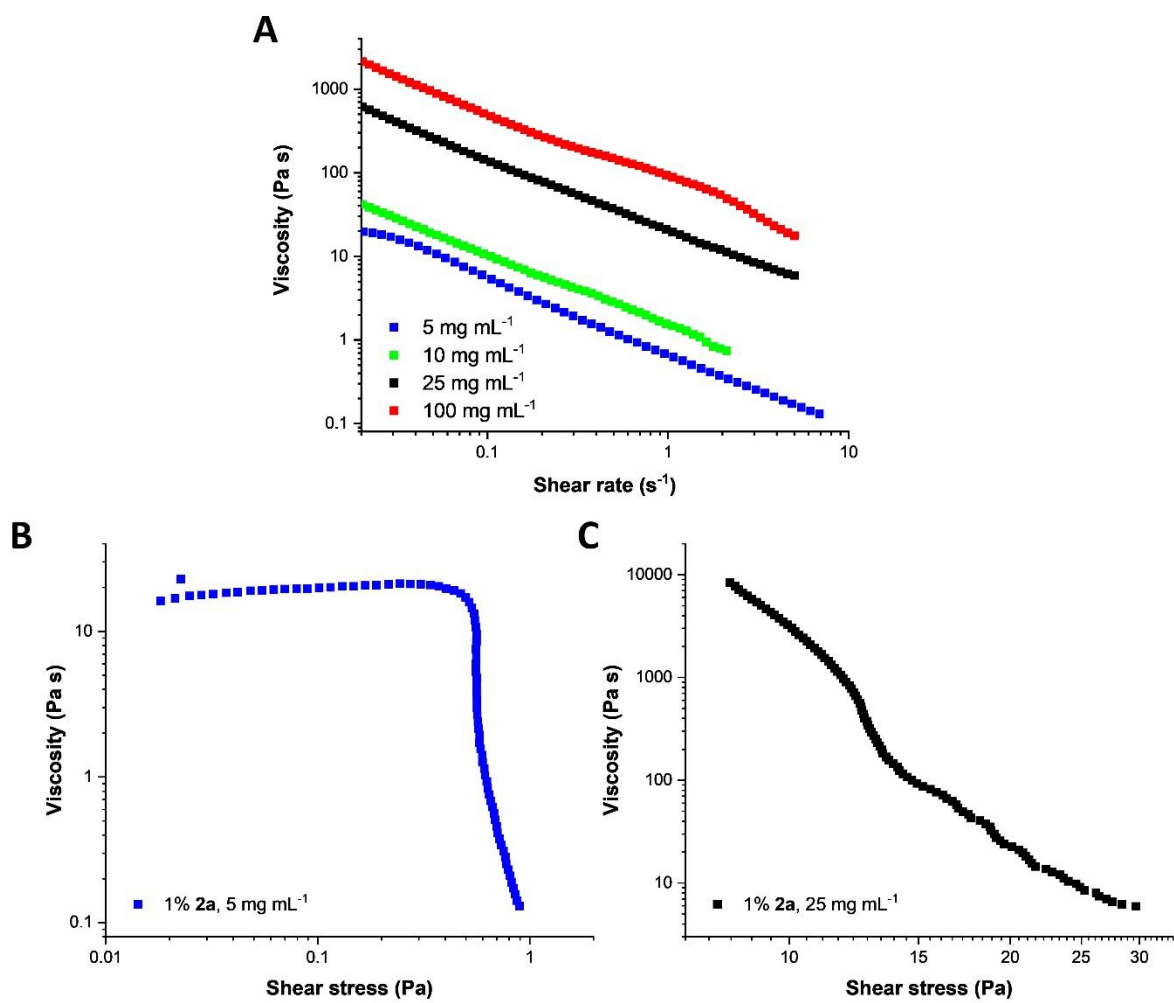


Figure S 7 Shear-rate dependent viscosity of gel of **1** with 1 % **2a** at different concentrations (A) and shear stress dependent viscosity of gel **1** with 1 % **2a** at 5 $mg mL^{-1}$ (B) and of gel **1** with 1 % **2a** at 25 $mg mL^{-1}$ (C).

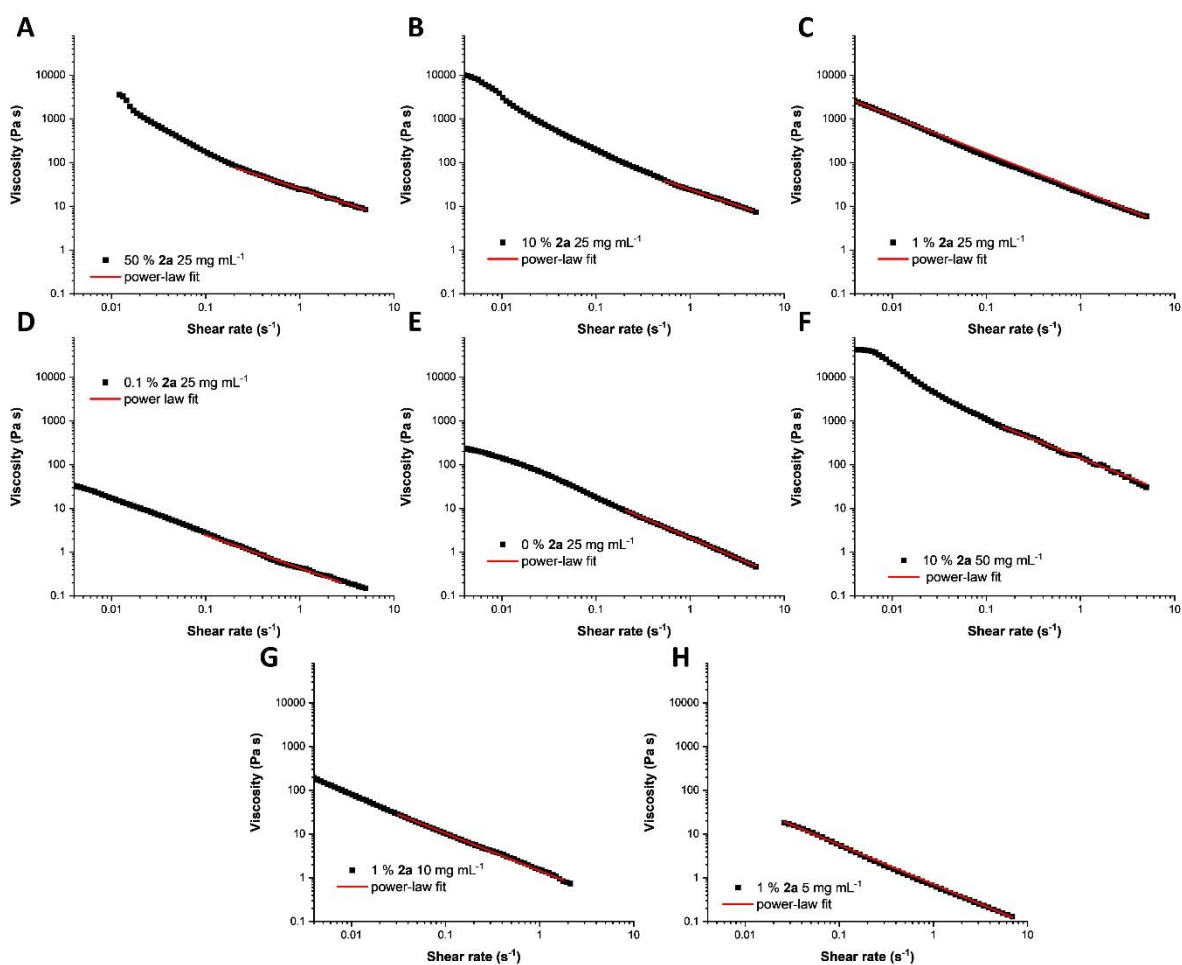


Figure S 8 Power-law fits of the viscosity of different gel compositions. If non-linear behavior could be observed, only the data at higher shear rates was fitted.

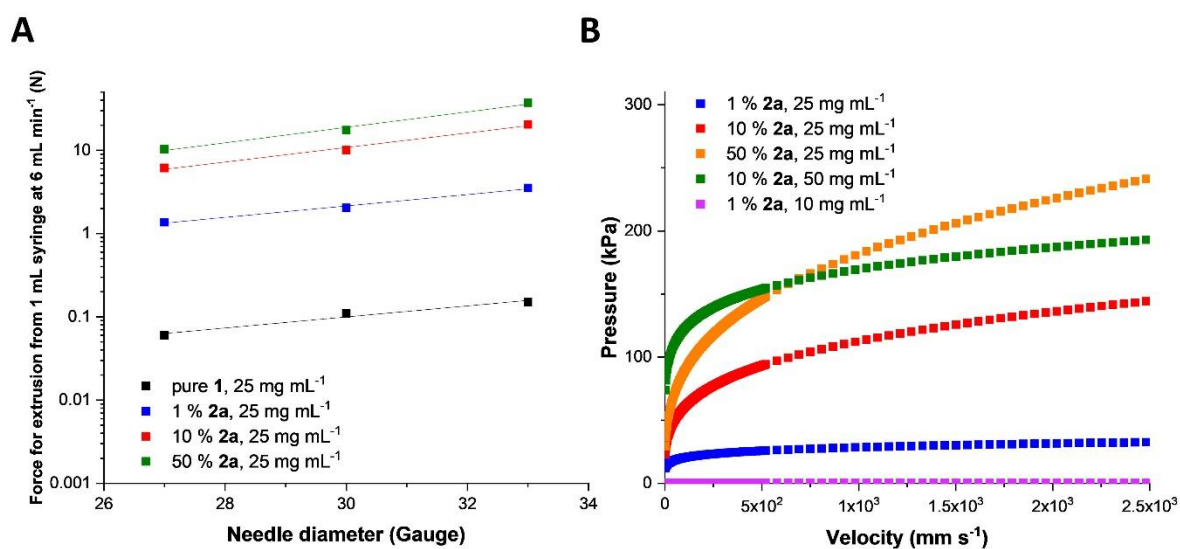


Figure S 9 Force needed for extrusion of the gels of different amount of crosslinker **2a** ($c = 25 \text{ mg mL}^{-1}$) out of a 1 mL syringe at 6 mL min^{-1} in dependence of the needle diameter (needle length 1 inch) (A). Pressure needed for printing gels of different amount of crosslinker **2a** and different concentration from a 1 mL syringe equipped with a cannula (gauge 27, $\frac{1}{2}$ inch) dependent on the velocity (B).

The flow rate Q was calculated by^[3]:

$$Q = \pi \left(\frac{P}{2kl} \right)^{\frac{1}{n}} \frac{n}{3n+1} R^{\frac{3n+1}{n}} \quad \text{Eq.S1}$$

With P being the pressure, n the shear-thinning parameter, k the consistency index, l the length and R the radius of the cannula.

Or rearranging:

$$P = \left(\frac{3n+1}{n} \right)^n k \left(\frac{Q}{\pi} \right)^n \frac{2l}{R^{3n+1}} \quad \text{Eq.S2}$$

The velocity v was calculated by:

$$v = \frac{Q}{\pi R^2} \quad \text{Eq.S3}$$

For example, a 1 mL syringe equipped with cannulas of 27 to 33 gauge (length 1 inch) are often used in oncological treatments to administer drugs at a speed of approx. 6 mL/min.^[3-4] It is expected that a force of 50 N is still acceptable for the doctor to administer and the patient to feel comfortable with. We can see that the herein presented hydrogels require only very limited forces for administration with a syringe at such rates. Even if cannulas with a very small diameter (Gauge 33) are used, the force for extrusion is around 10 N for the strongest gels 2.5 wt%. Similar considerations as for the injection above reveal that even for strong gels with increased crosslinker content of 10 % and a concentration of 50 mg mL, printing velocities of more than 10^2 mm s^{-1} are achievable at very low pressures of 120 kPa considering a 27 gauge cannula (Figure S9B).

4. Photo-bleaching recovery measurements

The measurement was conducted using confocal laser scanning microscopy (CLSM) employing a LSM880, Elyra PS.1 system (Zeiss, Oberkochen, Germany) applying the He-Ne laser for excitation at 561 nm (2%) and emission filters for AF-594 (573 – 732 nm) with a gain of 638.8 and a digital detector amplification of 8.1. The pinhole was set to 0.93 AU. For magnification, a 10×0.3 EC Plan-Neofluar objective was applied. Images were acquired and

analyzed using the ZEN software, version 2.3 SP1 (Zeiss). For bleaching, the UV laser was applied at 355 nm (100%) for 33 min 50 s. The pinhole was set to 0.84 AU.

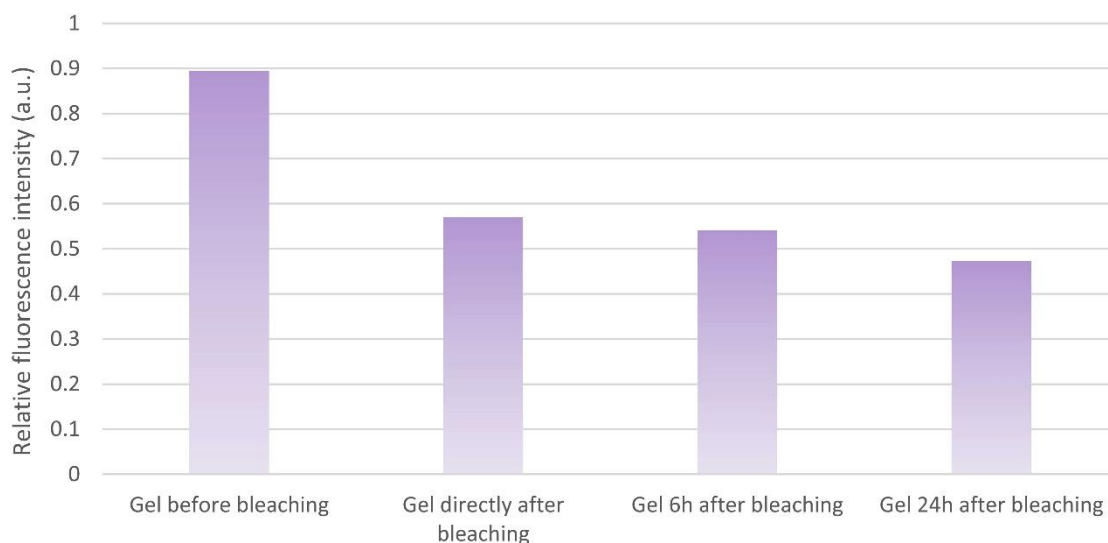


Figure S 10 Relative fluorescence intensity (bleached vs. non-treated area) before and directly after bleaching, after 6 and after 24h.

5. Stability of the gels

Gels were prepared according to the already mentioned procedure. Instead of pure water, water at pH 2 (addition of HCl), pH 11 (addition of NaOH) was added to the solution of **1** and **2** in THF. For the salt containing gel, 1.8% NaCl aq. solution, and for the media containing gel DMEM + 10% serum protein was added instead of pure water in the gel preparation.

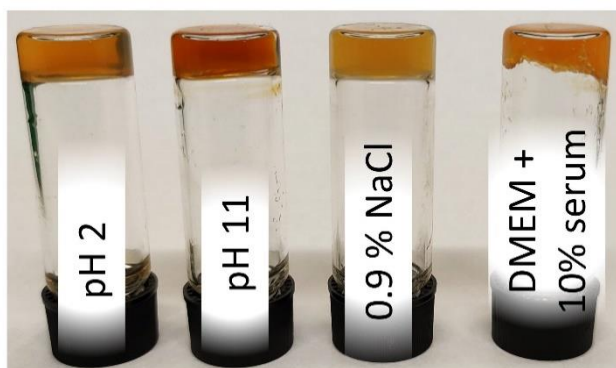


Figure S 11 Gel of **1** + 1% **2a** at 25 mg mL⁻¹ prepared in acid, basic, salt- and serum-containing media.

6. Cytotoxicity measurements

Cytotoxicity studies were performed using the mouse fibroblast cell line L929 (400620, CLS), as recommended by ISO10993-5. L929 cells were routinely cultured in Dulbecco's modified eagle's medium with 2 mM L-glutamine (Biochrom, Germany) supplemented with 10% fetal calf serum (FCS, Capricorn Scientific, Germany), 100 U mL⁻¹ penicillin, and 100 µg mL⁻¹ streptomycin (Biochrom, Germany) at 37 °C under a humidified 5% (v/v) CO₂ atmosphere. For the cell experiments, a gel of **1** with 1% **2a** at 25 mg mL⁻¹ was either added prior to the addition of the cell suspension on a part of the well plate bottom (preparation way 1) or post to the freshly added cell suspension (preparation way 2). Experiments were done in duplicate. In detail, cells were seeded at 10⁴ cells mL⁻¹ (10⁴ cells per well) in a 24 well plate (VWR, Germany) and incubated for 24 h. Subsequently, the medium was replaced by a mixture of a fresh culture medium and the resazurin-based solution PrestoBlue (Thermo Fisher, Germany, prepared according to the manufacturer's instructions). After further incubation for 45 min at 37 °C under a humidified 5% (v/v) CO₂ atmosphere, the fluorescence was measured at $\lambda_{\text{ex}} = 560 \text{ nm}/\lambda_{\text{em}} = 590 \text{ nm}$ with gain set to optimal (Infinite M200 PRO microplate reader, Tecan, Germany), with untreated cells on the same well plate serving as negative controls. Cell viability below 70% was considered to be indicative of cytotoxicity. The experiments were conducted with approx. 0.1 to 0.2 mL of two gels of **1** with 1% **2a** at 25 mg mL⁻¹ per well, including Blanks and negative controls. Data are expressed as mean \pm SD. In addition, cells were imaged with a transmitted light microscope (Axio Observer Vert.A1, Zeiss, Germany) equipped with a 10x objective using brightfield imaging prior to the PrestoBlue assay. Images were acquired using the ZEN lite software (2012, Zeiss).

Table S 1 Cell viabilities dependent on the preparation procedure.

<i>Procedure</i>	<i>Mean viability (%)</i>	<i>Standard deviation (%)</i>
<i>First gel addition, then seeding of cells</i>	81.3	2.8
<i>First seeding of cells, then gel addition</i>	96.0	1.7

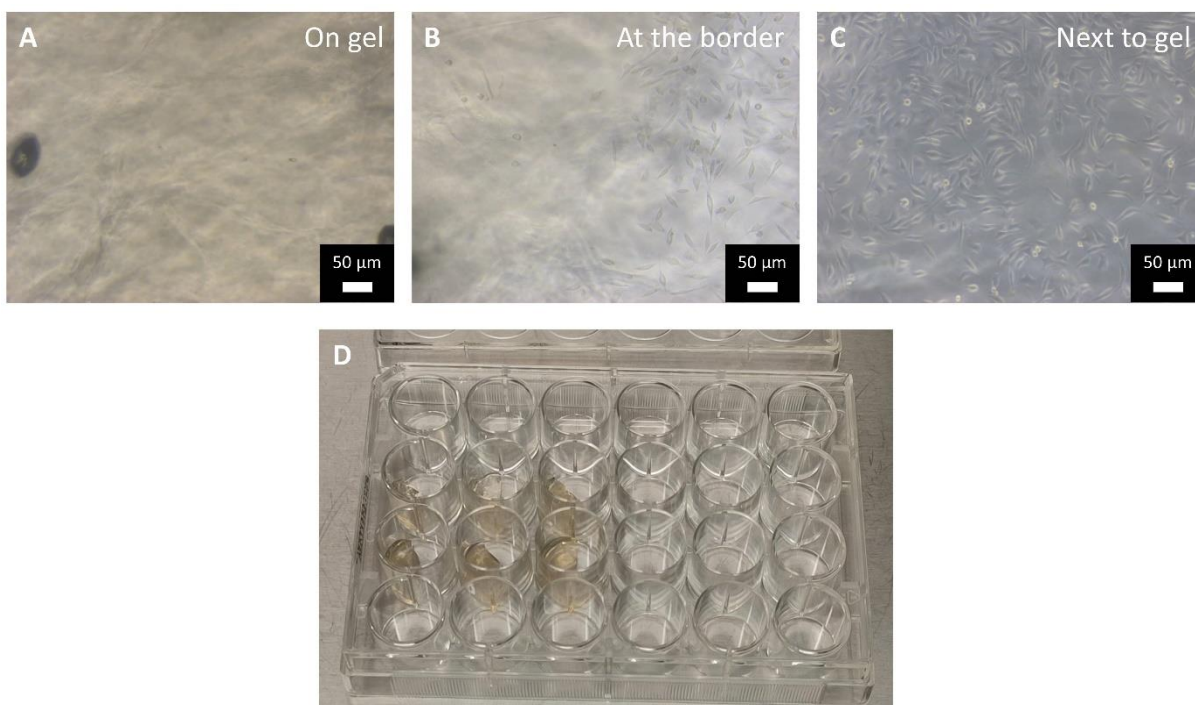


Figure S 12 Microscopy images of the gel (A), the cells at the border of the gel (B) and next to the gel at the bottom of the well (C). Image of the well-plate design, with wells half-filled with the gel (D).

Independent of the preparation procedure, the gel seems to be non-toxic since viabilities of $81 \pm 3 \%$ and $96 \pm 2 \%$ could be measured for preparation ways 1 and 2, respectively. The difference between the two preparation procedures is attributed to the lower surface area in the well which is available for cell attachment in case of preparation way 1. Due to the PEO-functionalization of the gel, a stealth behavior is expected. As it can be concluded from the microscopy images, no cells could adhere to the PEGylated gel structure, however, already at the border of the gel, cells proliferated unaffected.

7. Moldability

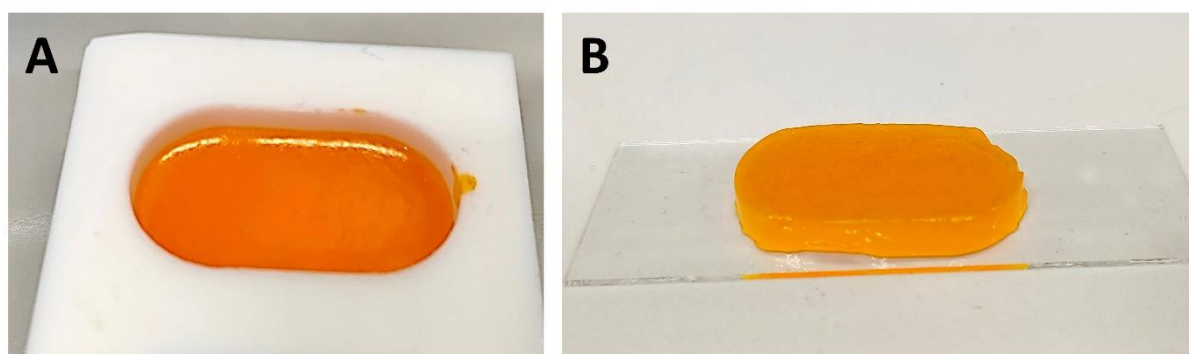


Figure S 13 Gels of **1** with 1 % **2a** ($c = 25 \text{ mg mL}^{-1}$) molded in Teflon molds (A) were stable on a glass slide (B).

8. Light scattering measurements

The water (refractive index $n_0 = 1.333$) was filtered. Light Scattering measurements were performed on a LSInstrument spectrometer operating with a vertically polarized laser with wavelength $\lambda = 660$ nm. The measurements were done at 20 °C over a range of scattering wave vectors ($q = 4\pi n \sin(\theta/2)/\lambda$, with θ the angle of observation and n the refractive index of the solvent).

Static light scattering: The time-averaged scattered intensity of samples (I_{sample}) was measured at 10° intervals at scattering angles between 20° and 150° (corresponding to values of q between 4.4×10^6 and $2.5 \times 10^7 \text{m}^{-1}$). The scattered intensity of the pure solvent (I_{solvent}) was also measured. The reduced scattered intensity, denoted as $I(q)$, was used for further calculations:

$$I(q) = \frac{I_{\text{sample}}(q) - I_{\text{solvent}}(q)}{I_{\text{solvent}}(q)} \quad \text{Eq. S4}$$

By using $I(q)$ instead of the absolute scattered intensity, both scattering from the solvent and the angular dependence of the scattering volume are taken into account and corrected for.

Measurements were taken from 20 to 150° each 10° during 500s.

From the q dependence of the intensity, information about the characteristic length scales in the sample can be derived. The segment density correlation length in the solution can be found using the Ornstein-Zernike equation for the structure factor:^[5]

$$I(q) \approx \frac{1}{1 + q^2 \xi^2} \quad \text{Eq. S5}$$

In dilute solutions, the polymer chains do not interact, and the correlation length gives information about the (average) size of the individual molecules. If the solution is concentrated and chains start to overlap (beyond the overlap concentration c^*), the polymers form a transient network and the correlation length no longer contains information about the size of the individual chains, but it reflects the mesh size ξ_m of the network.

Dynamic light scattering: The scattered intensity was measured at scattering angles between 20° and 150° (corresponding to values of q between 4.4×10^6 and $2.5 \times 10^7 \text{m}^{-1}$). To obtain correlation functions of sufficient quality, measuring times of 500s per angle were used.

Dynamic light scattering (DLS) measures temporal fluctuations of the scattered intensity arising from motion of the scatterers.^[5] From the scattered intensity as a function of time, the intensity correlation function $g^{(2)}(\tau)$ is calculated for a number of time intervals τ :

$$g^{(2)}(\tau) = \frac{\langle I(t)I(t + \tau) \rangle}{\langle I(t) \rangle^2} \quad \text{Eq. S6}$$

The intensity correlation function is related to the normalized field correlation function $g^{(1)}(\tau)$ by the Siegert equation:^[5] $g^{(2)}(\tau) = 1 + A [g^{(1)}(\tau)]^2$ Eq. S7

where A is a constant of order unity depending on the geometry of the experimental setup. De Gennes developed a scaling theory for semidilute polymer solutions using a transient gel model.^[6] According to this theory $g^{(1)}(\tau)$ is an exponentially decreasing function with a single decay rate constant Γ , which is determined by the scattering vector q and the so-called gel diffusion coefficient D_g , according to

$$g^{(1)}(\tau) = e^{-\Gamma\tau} = e^{-q^2 D_g \tau} \quad \text{Eq. S8}$$

D_g is given by

$$D_g = D_c \frac{M_g + M_o}{M_o} \quad \text{Eq. S9}$$

where M_g is the gel modulus (the elastic or Young's modulus of the transient gel), M_o the osmotic modulus, defined as $c(d\Pi/dc)$, and D_c the collective diffusion coefficient, which is in turn related to the hydrodynamic correlation length ξ_H by the Stokes-Einstein equation^[5]

$$D_c = \frac{k_B T}{6\pi\eta_0 \xi_H} \quad \text{Eq. S10}$$

where η_0 is the solvent viscosity. For polymers in a good solvent, $M_o \gg M_g$ and D_c is effectively equal to D_g . Experimentally, a distribution of decay rate constants Γ is generally measured, each with its own weight w , so $g^{(1)}(\tau)$ is given by

$$g^{(1)}(\tau) = \int_0^\infty w(\Gamma) e^{-\Gamma\tau} d\Gamma \quad \text{Eq. S11}$$

Mostly, the value of Γ at the peak of the distribution is taken as “the” decay rate constant and used for further calculations.

In the concentrated regimes, the hydrodynamic correlation length corresponds to the hydrodynamic mesh size of the transient network, the average distance between entanglement points. With SLS, the average mesh size of the transient polymer network is measured, whereas DLS measures the average diffusion coefficient of the meshes. From this diffusion coefficient and the viscosity of the solvent, the size of the mesh can be calculated with eq 10. The hydrodynamic correlation length ζ_H measured by DLS is thus not equal to the static correlation length ξ , but it is of the same order of magnitude and it scales in the same way with concentration.

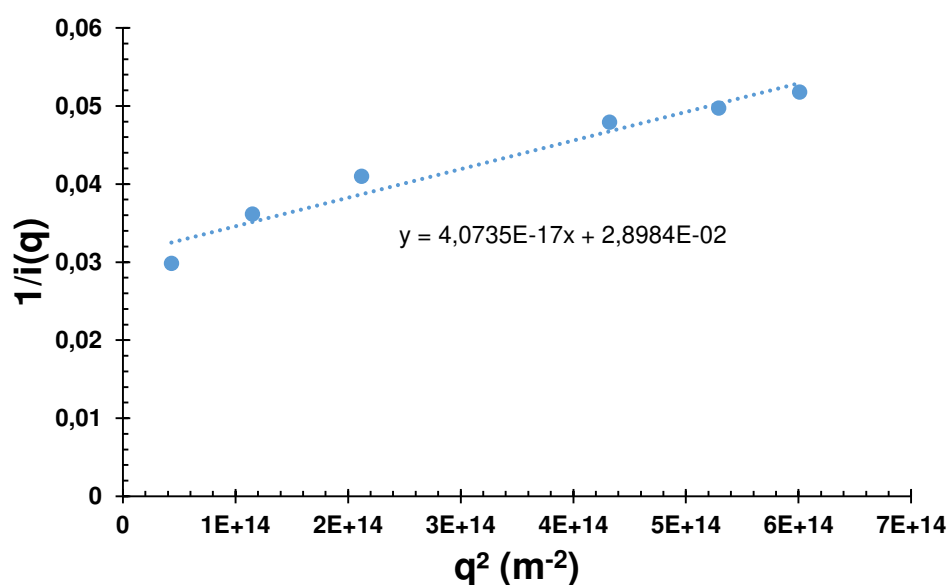


Figure S 14 Reciprocal reduced scattered intensity as a function of q^2 for the crosslinked BTU gel (1 + 1% **2a**, 25 mg mL⁻¹). The line is linear fit to the data.

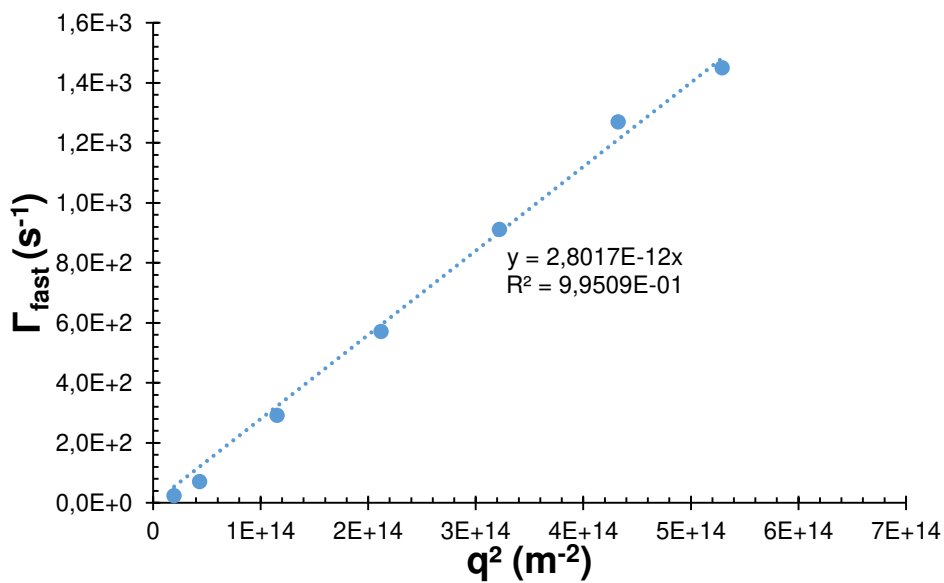


Figure S 15 q^2 dependence of Γ_{fast} for the crosslinked BTU gel (1 + 1% **2a**, 25 mg mL⁻¹). Γ_{fast} is proportional to q^2 , as indicated by the linear fit, which corresponds to $\Gamma_{fast} + 2.8017 \times 10^{-12}q^2$.

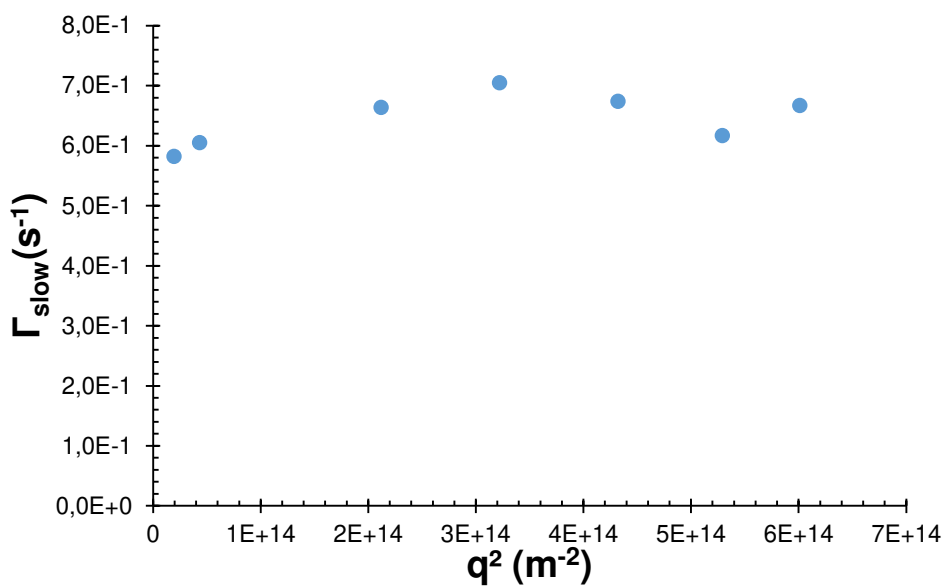


Figure S 16 q^2 dependence of Γ_{slow} for the crosslinked BTU gel (1 + 1% **2a**, 25 mg mL⁻¹). The horizontal line at $\Gamma_{slow} = 0.645$ s⁻¹ shows that the slow mode does not depend significantly on q .

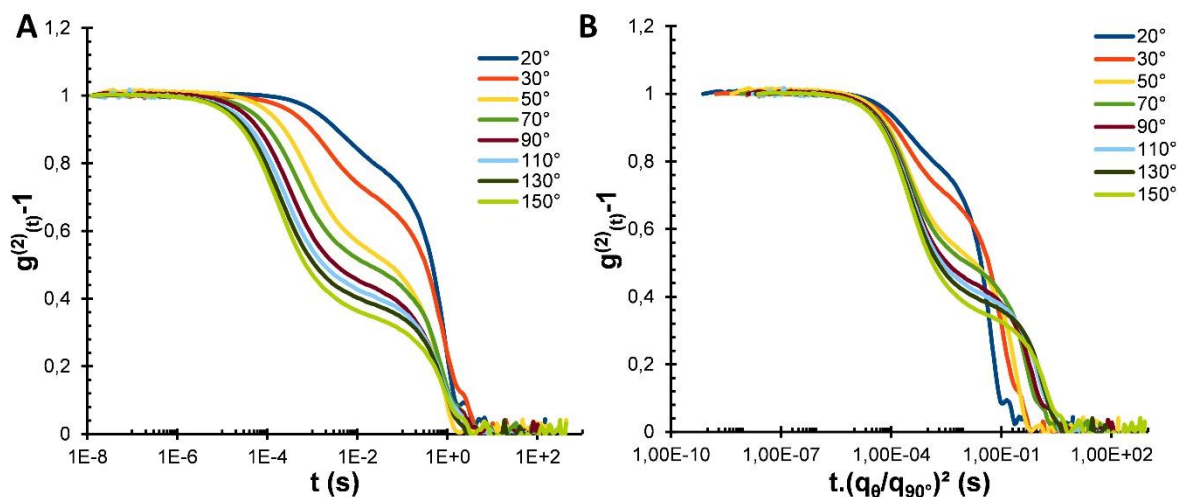


Figure S 17 q dependence of the correlation functions for the crosslinked BTU gel (**1** + 1% **2a**, 25 mg mL⁻¹) (A). Same data as in figure (A) after q² normalization (B).

9. Pulse-field-gradient NMR spectroscopy

Poly(ethyloxazoline) (PEtOx) with a degree of polymerization of 20 and 60, resulting in hydrodynamic radii of 0.44 and 2.43 nm (calculated by Stokes-Einstein equation), respectively, were incorporated into the pure BTU gel (**1**, 25 mg mL⁻¹) and the crosslinked BTU gel (**1** + 1% **2a**, 25 mg mL⁻¹) and measured in PFG-NMR. The diffusion coefficient was extracted by fitting a gamma function to the obtained data, to correct for the molar mass distribution of the polymer. To do so, 12.5 mg of **1**, 1.25 mg of **2a** and 1 mg of PEtOx20 or PEtOx60 were dissolved in 0.1 mL THF. 0.5 mL D₂O was added, the mixture was transferred to an NMR tube and the THF was evaporated.

DOSY experiments were performed at 24 °C on a Bruker Avance III (400 MHz, BBFO). The maximum z-gradient was 50 G cm⁻¹. The gradient strength was calibrated using the “doped water” standard. All PFG-experiments performed using the convection compensated pulse program *dstebpgp3s* with $\delta = 4$ ms, $\Delta = 0.75$ s, and increments (gradient) = 64 or 32. Raw data was processed with Topspin 4.1 with phase and baseline correction. Gradient depended signal decays were extracted using the T1/T2 modul in Topspin 4.1. Exact diffusion gradients were calculated using Origin 2020b by fitting to a Gamma function.^[7]

$$A(k) = A(0) \cdot \left(\frac{\beta}{\beta + k} \right)^\alpha \quad \text{Eq. S12}$$

with $k = (\gamma g \delta)^2 (\Delta - \gamma/3)$

The mean diffusion coefficient easily calculated by $\langle D \rangle = \alpha/\beta$. The standard derivation σ was calculated using $\sigma = \frac{\sqrt{\alpha}}{\beta}$.

The following values could be calculated:

Table S 2 Calculated diffusion coefficients of PEtOx₂₀ and PEtOx₆₀ in different gels and pure D₂O fitted by a Gamma function.

<i>Gel</i>	α	β	$\langle D \rangle_{PEtOx20}$ ($\cdot 10^{-10} m^2 s^{-1}$)	α	β	$\langle D \rangle_{PEtOx60}$ ($\cdot 10^{-10} m^2 s^{-1}$)
<i>pure 1 at 25 mg mL⁻¹</i>	73.03	$1.1 \cdot 10^{12}$	0.663±0.078	52.32	$1.17 \cdot 10^{12}$	0.447±0.062
<i>1 + 1% 2a at 25 mg mL⁻¹</i>	207.9	$6.67 \cdot 10^{11}$	0.3.12±0.22	1044.65	$3.3 \cdot 10^{13}$	0.317±0.009
<i>pure D₂O</i>	617.32	$1.1 \cdot 10^{12}$	5.59± 0.23	21.31	$2.1 \cdot 10^{-10}$	1.01±0.22

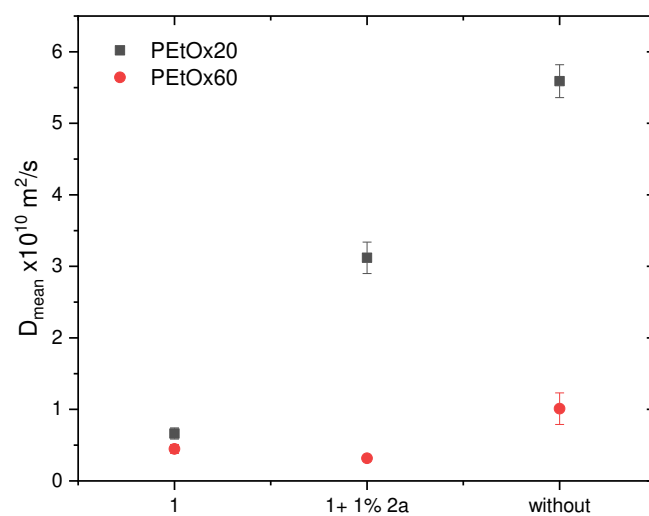


Figure S 18 Calculated mean diffusion coefficients of PEtOx₂₀ and PEtOx₆₀ in different gels and pure D₂O fitted by a Gamma function.

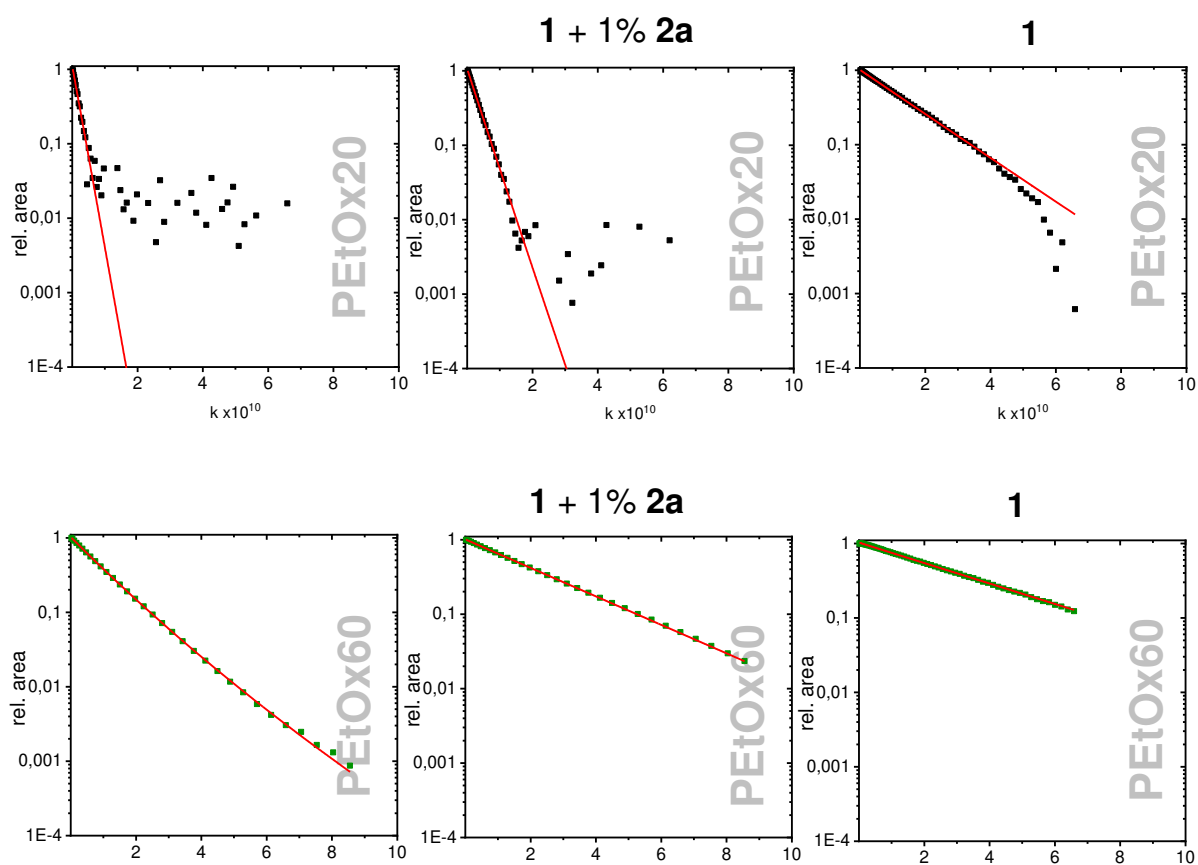


Figure S 19 Fitting curves of normalized signal areas in dependence of $k = (\gamma g \delta)^2 (\Delta - \gamma/3)$ of PEtOx₂₀ and PEtOx₆₀ in different gels and pure D₂O using gamma fit function.

10. Fluorescence spectroscopy

Fluorescence spectroscopy was measured on a Spectrofluorometer FP-8500 from JASCO, in 4 mL quartz cuvettes. 0.5 mL of the gel **1** with 1% **2a** was prepared in the cuvette. To do so, 0.6 mg of the crosslinker **2a** and 6 mg of **1** were dissolved in 0.05 mL THF. 0.250 mL of an aqueous solution of the TRITC labeled dextran ($c = 0.1 \text{ mg mL}^{-1}$) was slowly added to the solution. After evaporation of the THF to an end concentration of 25 mg mL^{-1} the resulting gel was overlaid with 3 mL of water and the spectra measurement was started immediately at an excitation wavelength of 550 nm and measured for every 60 min.

For the Na-fluorescein diffusion experiment, the procedure was adapted. Here 0.25 mL of a 0.001 mg mL^{-1} solution of Na-fluorescein in water was added. The spectra were measured at an excitation wavelength of 490 nm every 30 min.

The diffusion was fitted the Fickian law:

$$\frac{M_t}{M_\infty} = kt^n \quad \text{Eq. S13}$$

with M_t/M_∞ being the amount of released drug, k being the rate constant and n the diffusional exponent.^[8]

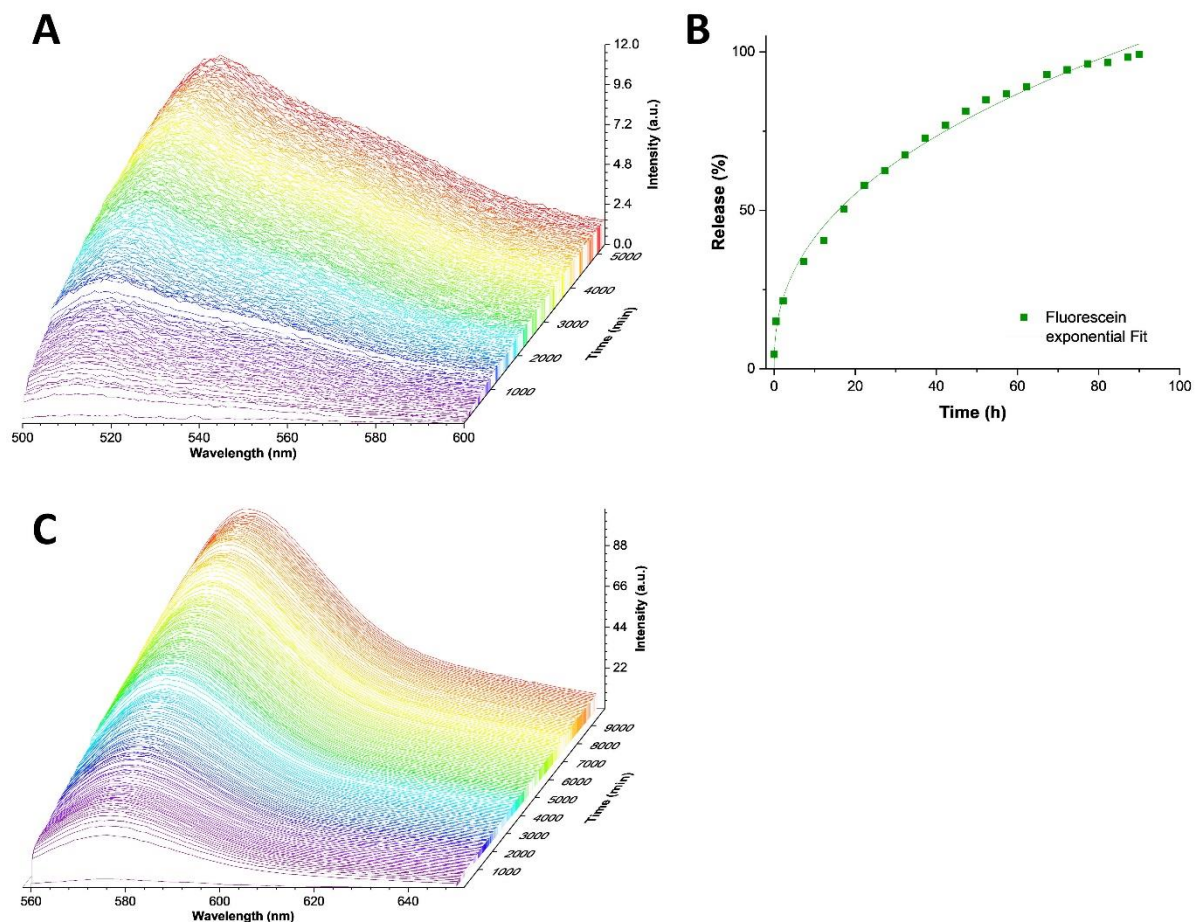


Figure S 20 Time-dependent fluorescence spectra of Na-fluorescein (A) and its release kinetics (B) at an excitation wavelength of 490. Time-dependent fluorescence spectra of TRITC-dextran (500 kD) (C) at an excitation wavelength of 550 nm.

11. 3D printing

For 3D printing of the gels a Prusa i3 MKS printer was used. To the extruder of the printer, a cannula was fixed, which was connected to a syringe pump via a capillary. This way, parallel to the gel-print, a PLA print was produced as a control-geometry. The printer speed was set to 36 mm/s and the syringe pump to 15 mL h⁻¹. The printing bed was heated to 60 °C for good PLA adhesion and equipped with a nafion foil under the print area for the gel, to enable transfer of the printed structures.

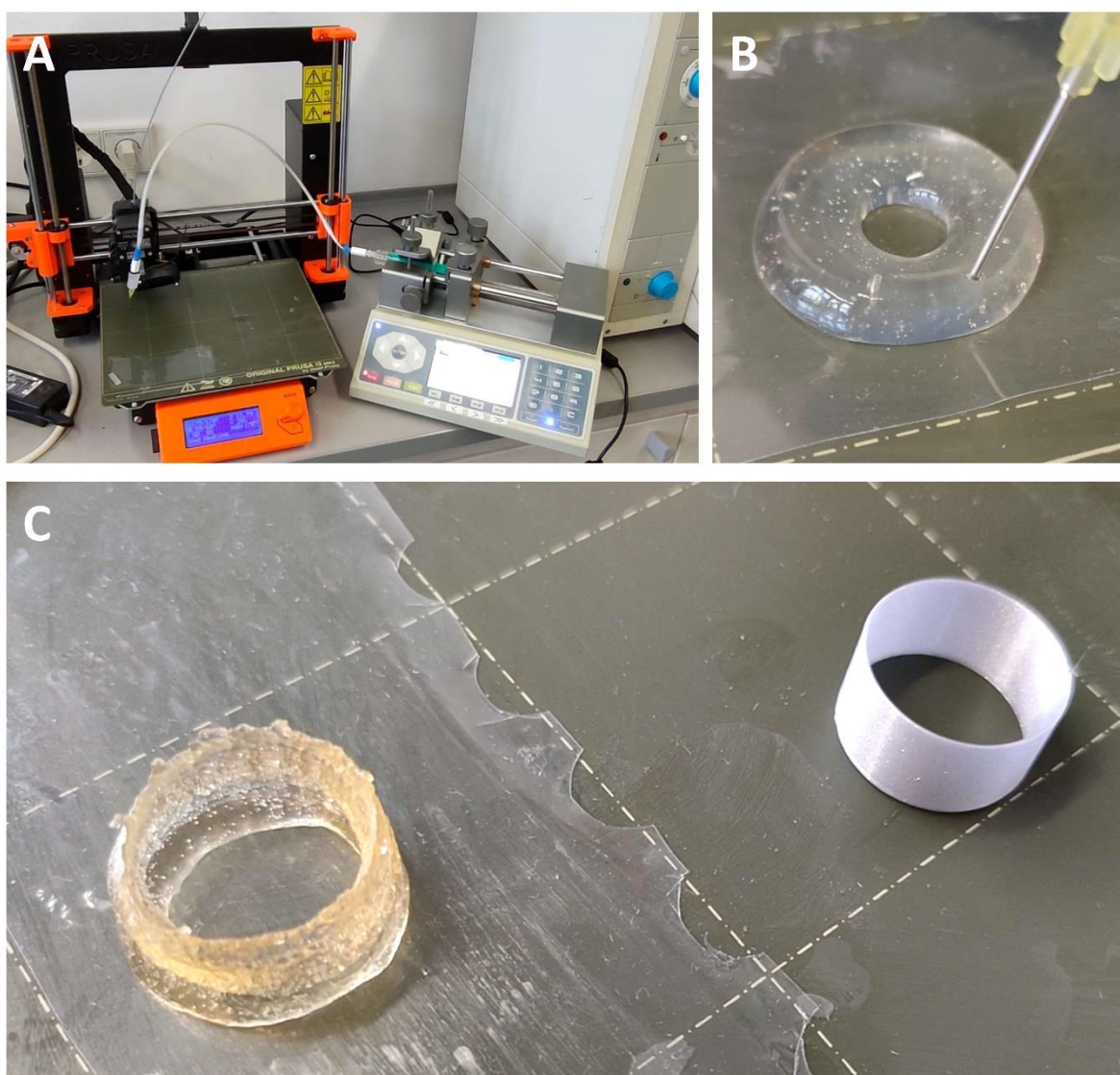


Figure S 21 3D-printing setup (A), 3D printing of a gel **1** with 1% **2a** ($c = 10 \text{ mg mL}^{-1}$) (B), and 3D printed hollow cylinder from gel **1** with 1% **2a** ($c = 25 \text{ mg mL}^{-1}$) next to the PLA model (C).

References

- [1] F. V. Gruschwitz, M.-C. Fu, T. Klein, R. Takahashi, T. Higashihara, S. Hoepfner, I. Nischang, K. Sakurai, J. C. Brendel, *Macromolecules* **2020**, *53*, 7552-7560.
- [2] F. V. Gruschwitz, T. Klein, M. T. Kuchenbrod, N. Moriyama, S. Fujii, I. Nischang, S. Hoepfner, K. Sakurai, U. S. Schubert, J. C. Brendel, *ACS Macro Lett.* **2021**, *10*, 837-843.
- [3] H. Lopez Hernandez, J. W. Souza, E. A. Appel, *Macromol. Biosci.* **2021**, *21*, 2000295.
- [4] S. Correa, A. K. Grosskopf, H. Lopez Hernandez, D. Chan, A. C. Yu, L. M. Stapleton, E. A. Appel, *Chem. Rev.* **2021**.
- [5] W. Brown, *Light Scattering: Principles and Development*; Clarendon Press Oxford, **1996**.
- [6] P. G. de Gennes, P. P. G. Gennes, C. U. Press, *Scaling Concepts in Polymer Physics*, Cornell University Press, **1979**.
- [7] N. H. Williamson, M. Nydén, M. Röding, *J. Mag. Reson.* **2016**, *267*, 54-62.
- [8] P. L. Ritger, N. A. Peppas, *J. Control. Release* **1987**, *5*, 37-42.